Adaptation strategies of *Streptococcus pneumoniae* and *Staphylococcus aureus* under infection conditions

Inaugural-Dissertation

to obtain the academic degree
Doctor rerum naturalium (Dr. rer. nat.)

submitted to the

Department of Biology, Chemistry, Pharmacy
of Freie Universität Berlin

by

Verena Nadin Fritsch

Berlin 2022

1st reviewer: Prof. Dr. Haike Antelmann
Institute of Biology-Microbiology, Freie Universität Berlin

2nd reviewer: Prof. Dr. Markus C. Wahl
Institute of Structural Biochemistry, Freie Universität Berlin

Date of defense: 09th November 2022

Acknowledgement

At this point, I would like to thank everyone who supported me during my scientific career and especially during the preparation of my doctoral thesis.

First, I would like to express my gratitude to Prof. Dr. Haike Antelmann for giving me the opportunity to work on different microbial projects within the interesting field of redox biology. I am very grateful for her supervision, including the many constructive discussions during the project planning, experimental work, data analyses and writing process. A heartfelt thank you for her professional guidance and subject-specific support during the time of my dissertation. Thank you also for giving me the many opportunities to discuss my work with other researchers at conferences and internal meetings.

Additionally, I would like to thank Prof. Dr. Markus Wahl for the willing acquisition of the second review and the scientific support as a cooperation partner.

Also, I thank a lot all other cooperation partners for their help with my scientific projects and valuable discussions. Especially, I would like to thank Dr. Tobias Busche, Dr. Christoph Weise and Dr. Benno Kuropka for their expert support with the transcriptome and proteomic analyses.

I want to express thanks to the whole team in the laboratory of Prof. Dr. Haike Antelmann for their support and the pleasant working atmosphere.

I'm particularly thankful to Dr. Vu Van Loi for his never-ending patience when he introduced me to new methods or was available to answer any questions regarding experiments. Not only with his tips and tricks but also with his scientific work, he contributed enormously to this work. Special thanks to Dr. Nico Linzner for his support and the very constructive discussions over the last years. Also, I would like to thank Dr. Quach Ngoc Tung for his help with certain experiments. I would also like to thank Franziska Kiele for her encouraging words and help in the lab, especially with the protein purifications. Also, I am grateful for the support of Dr. Eberhard Klauck. Besides specific microbiological questions, he was always eager to discuss other scientific and social topics. Often, he reminded me that a five-minute break can increase the efficiency of my work.

I wish to acknowledge the Deutsche Forschungsgemeinschaft within the SFB-TR84 project B06 for the financial support.

At last, I want to thank my mother for her entire support throughout my study. I am very grateful for her emotional support throughout my study and life.

Statement of authorship

Hereby, I certify that this thesis has not been submitted for the purpose of doctorate at Freie Universität Berlin or any other institution. I declare that I have written this thesis by myself under the guidance and supervision of Prof. Dr. Haike Antelmann, Institute for Biology-Microbiology, Freie Universität Berlin. Furthermore, I did not take any text sections of a third person without identification.

Berlin, 29.09.2022

_____

Verena Fritsch

Table of contents

Summary

Human pathogenic bacteria, such as *Staphylococcus aureus* and *Streptococcus pneumoniae*, that cause life-threatening diseases and are resistant to many antibiotics, pose a serious health risk and, thus, a global social challenge. Therefore, further elucidation of bacterial resistance mechanisms to antimicrobial substances and the host immune defense is urgently required to improve existing treatment options and to develop new therapeutic approaches. The stringent response, which confers a non-specific stress resistance and facilitates the survival of bacteria, is induced in response to unfavorable environmental influences, such as nutrient starvation, by the accumulation of the alarmones guanosine tetra- or pentaphosphate ((p)ppGpp). While it was demonstrated that the stringent response is associated with increased antibiotic resistance, virulence and persistence, the underlying molecular mechanisms, particularly in Gram-positive bacteria, are still incompletely understood. Within this dissertation, it could be shown that (p)ppGpp is also essential for the oxidative stress resistance of *S. aureus* in the stationary phase **(chapter 1)**. Quantitative analyses revealed higher respiratory chain activity and elevated total and free iron levels, causing increased intracellular levels of reactive oxygen species (ROS) in the (p)ppGpp^0 mutant. Accordingly, the addition of iron chelators and antioxidants restored these physiological changes and mitigated the increased sensitivity of the (p)ppGpp^0 mutant to oxidative stress and antibiotics. Thus, the maintenance of the intracellular iron and redox homeostasis was identified as a key mechanism of (p)ppGpp to promote increased stress resistance and antibiotic tolerance in *S. aureus*.

The host immune system produces ROS and reactive chlorine species (RCS), such as H_2O_2 and hypochlorous acid (HOCl), as a central defense strategy. Consequently, the resistance of human pathogens to these reactive species is essential for their survival in the host. Low molecular weight thiols, such as glutathione (GSH) and bacillithiol (BSH), represent an important defense mechanism. Despite their function as antioxidants, they also protect thiol groups of proteins from irreversible over-oxidation through post-translational modification via *S*-thiolations. While the redox pathway for the regeneration of *S*-glutathionylated proteins has been fully elucidated, the equivalent process in Gram-positive Firmicutes, which use BSH instead of GSH, was incompletely understood. As presented in **chapter 2**, this work contributed to elucidate this further. It was demonstrated that the BSH redox pathway, consisting of BSH, bacilliredoxin A (BrxA) and the NADPH-dependent flavin oxidoreductase YpdA, is essential for the survival of *S. aureus* in the presence of H_2O_2 and HOCl.

In addition, pathogens, such as *S. aureus*, encode for redox-sensing transcription factors, which utilize conserved cysteine residues to sense and respond to redox stress conditions via

post-translational thiol modifications **(chapter 3)**. Since these regulators control regulons that represent important enzymatic and non-enzymatic resistance mechanisms in bacteria, the work in hand focused on the identification and characterization of further transcription factors of the bacterial thiol-stress defense. For that purpose, RNA-seq analyses were used to investigate the bacterial stress response of *S. pneumoniae* to HOCl **(chapter 4)**. The NmlR regulon was most strongly induced by HOCl stress and identified as an important resistance mechanism against oxidative stress and for the survival inside human macrophages. It consists of the *nmlR* and *adhC* genes that encode for the MerR-family transcriptional regulator NmlR and the Zn^{2+}-dependent class III alcohol dehydrogenase AdhC. While NmlR was characterized previously as an aldehyde sensor, within this work, it was shown that NmlR also activates the transcription of the *nmlR-adhC* operon in response to oxidants. Molecular analyses revealed that the conserved cysteine (Cys52) is required for redox sensing by intermolecular disulfide formation and *S*-glutathionylation of NmlR.

Although quinones are applied as potent antimicrobials since centuries, the bacterial resistance mechanisms are still incompletely resolved. Therefore, this work focussed on the characterization of the quinone stress response of *S. aureus*. The transcription profiles of the methylhydroquinone (MHQ) and lapachol stress responses revealed a high overlap of the provoked expression changes **(chapters 5 and 6)**. For example, both quinones induced the oxidative stress response and the quinone-specific MhqR and QsrR regulons. Further analysis showed that, in contrast to MHQ, lapachol does not act as an electrophile but exerts its toxicity through the production of ROS **(chapter 5)**. The antimicrobial effect of lapachol was oxygen-dependent and could be reduced significantly by microaerophilic growth conditions. Phenotype analyses identified the H_2O_2 detoxifying catalase (KatA) and the BrxA/BSH/YpdA/NADPH redox pathway as important resistance mechanisms against lapachol stress in *S. aureus*. In contrast, the MhqR regulon conferred protection against MHQ but not lapachol. This finding suggests a substrate specificity of the enzymes MhqE and MhqD **(chapter 6)**. Since the single cysteine residue (Cys95) of MhqR is not required for DNA binding and quinone sensing, it can be concluded that the MhqR repressor is not inactivated by a thiol-based mechanism but probably through ligand binding. In contrast, QsrR, another quinone-specific regulator of *S. aureus*, was shown to be regulated by different thiol switches **(chapter 7)**. Unlike the MhqR regulon, the QsrR regulon was not only strongly induced by quinones but also by various oxidants. While QsrR was shown to sense oxidants by an intermolecular disulfide formation between the redox-active Cys4 and Cys29', allicin caused the *S*-thioallylation of all three cysteine residues (Cys4, Cys29, Cys32) *in vitro*. Northern blot analyses indicated that the

S-thioallylation of Cys4 is sufficient for the QsrR inactivation, while Cys4 and either Cys29' or Cys32' are required for the induction of the QsrR regulon by oxidants *in vivo.* Further transcriptional analysis and functional characterization revealed that the MhqR and QsrR regulons are also implicated in the resistance to various antibiotics, including ciprofloxacin and rifampicin **(chapters 6 and 7)**. In addition, the Δ*mhqR* mutant showed an increased survival rate in long-term infection experiments with murine macrophages compared to the wild type, indicating that the MhqR regulon might function in persistence.

Additionally, within the present work, the function of the GbaA regulon in the thiol stress response was examined **(chapter 8)**. While the deletion of the *SACOL2592-nmrA-2590* operon caused an enhanced susceptibility to diamide, allicin and aldehydes, the Δ*gbaB* mutant was impaired in its survival upon MHQ stress. It was further revealed that the conserved cysteines Cys55 and Cys104 of GbaA are required for the stress resistance against electrophiles.

Substances that interfere with the bacterial redox homeostasis, either through the production of ROS, their electrophilic properties, or the inhibition of proteins, are currently developed and tested as alternatives to antibiotics **(chapter 9)**. Especially ROS-generating substances represent promising treatment options since their non-specific mode of action minimizes the likelihood of resistance evolution. However, based on the usually lower cytotoxicity, specific inhibitors, e.g., of the low molecular weight thiol biosynthesis, might be more suitable for clinical application. Incited by the current global problem of the pandemic caused by the SARS-CoV-2 virus, the question of the antiviral activity of redox-based substances arose. Since the antimicrobial effect of allicin has been studied in detail, and previous studies suggested that allicin exerts an immunomodulatory effect, the antiviral activity of allicin on SARS-CoV-2 was investigated in a cell culture model within a collaboration project with the working group of Prof. Dr. Drosten **(chapter 10)**. It was demonstrated that the administration of biocompatible allicin doses to SARS-CoV-2 infected cells reduced the viral RNA amount and the number of infectious viral particles by up to 70%. Using label-free quantitative proteomics, it was shown that SARS-CoV-2 causes the profound reprogramming of several host pathways, including gene expression and metabolism. In addition, a strong induction of the interferon signaling pathway and the interferon-stimulated gene signature was detected. Allicin treatment reverted several SARS-CoV-2 induced changes, including the expression of the interferon pathways, to levels of uninfected cells and reduced the expression of viral proteins significantly.

The demonstrated antimicrobial activity of thiol-based substances suggests that they can be used in a modified form to combat infectious diseases. Lapachol, whose mode of action in

S. aureus was elucidated in the present work, but also allicin, could serve as lead compounds to create more stable and less cytotoxic derivates. In addition, by combining global transcriptome analyses with molecular and microbiological assays, the present work contributed to the elucidation of bacterial adaptation strategies. In particular, the transcription factors NmlR, MhqR and QsrR were identified as important resistance mechanisms of the human pathogenic bacteria *S. pneumoniae* and *S. aureus*. Since the expression of these regulons is associated with increased bacterial resistance to the immune system and antibiotics, these proteins represent promising molecular targets for drug development.

Zusammenfassung

Humanpathogene Bakterien, die wie *Staphylococcus aureus* und *Streptococcus pneumoniae*, lebensbedrohliche Krankheiten verursachen und gegen eine Vielzahl an Antibiotika resistent sind, stellen eine gesundheitliche Gefährdung und damit eine globale gesellschaftliche Herausforderung dar. Die weitere Aufklärung von bakteriellen Resistenzmechanismen gegen antimikrobielle Substanzen und die wirtsspezifische Abwehr ist daher essenziell, um bestehende Behandlungsmethoden effektiver gestalten zu können, und neue Therapieansätze zu entwickeln. Als Mediator einer unspezifischen Resistenz ermöglicht die sogenannte „Stringent Response" die Adaptation von Bakterien an zahlreiche Umweltbedingungen. Sie wird z.B. durch Nährstoffmangel und in Folge von anderen ungünstigen Umwelteinflüssen durch die Akkumulation der Alarmone Guanosin-Tetra- bzw. Pentaphosphat ((p)ppGpp) ausgelöst. Während bereits nachgewiesen wurde, dass die „Stringent Response" mit einer erhöhten Antibiotikaresistenz, Virulenz und Persistenz einhergeht, sind die zugrundeliegenden molekularen Mechanismen, insbesondere in Gram-positiven Bakterien, noch unzureichend aufgeklärt. Wie in **Kapitel 1** dargestellt, konnte in der vorliegenden Dissertation gezeigt werden, dass (p)ppGpp auch für die oxidative Stressresistenz von *S. aureus* in der stationären Phase essenziell ist. Mittels quantitativer Analysen konnten erhöhte intrazelluläre Eisenlevel, eine gesteigerte Atmungskettenaktivität und infolgedessen eine höhere endogene Produktion reaktiver Sauerstoffspezies (ROS) in der (p)ppGpp^0 Mutante nachgewiesen werden. Durch die Zugabe von Eisenchelatoren und Antioxidantien konnten diese physiologischen Veränderungen sowie die erhöhte Sensitivität der (p)ppGpp^0 Mutante gegenüber oxidativem Stress und Antibiotika abgemildert werden. Somit wurde die Funktion von (p)ppGpp in der Aufrechterhaltung der intrazellulären Eisen- und Redoxhomöostase als wesentlicher Faktor für die erhöhte Stressresistenz und Antibiotikatoleranz identifiziert.

Im Rahmen der Immunantwort werden ROS und reaktive Chlor-Spezies (RCS), wie z.B. H_2O_2 und hypochlorige Säure (HOCl), als zentraler Abwehrmechanismus gebildet. Für humanpathogene Bakterien ist daher die Resistenz gegen diese reaktiven Spezies essenziell für ihr Überleben im Wirt. Niedermolekulare Thiolverbindungen, wie z.B. Glutathion (GSH) und Bacillithiol (BSH), nehmen hierbei eine besondere Stellung ein. Sie fungieren nicht nur als Antioxidantien, sondern schützen auch Thiolgruppen von Proteinen durch die post-translationale Modifikation in Form einer *S*-Thiolierung vor einer irreversiblen Überoxidation. Während die Kaskade zur Regeneration von *S*-glutathionylierten Proteinen bereits vollständig aufgeklärt wurde, war der äquivalente Prozess in Gram-positiven Firmicutes-Bakterien, die BSH anstelle von GSH nutzen, nur unvollständig erforscht. Wie in **Kapitel 2** dargelegt, trug die vorliegende

Arbeit dazu bei, diesen weiter aufzuklären. Es konnte gezeigt werden, dass das Zusammenspiel von BSH, dem Bacilliredoxin A (BrxA) und der NADPH-abhängigen Flavin-Oxidoreduktase YpdA innerhalb des sogenannten BrxA/BSH/YpdA/NADPH Redoxweges in Anwesenheit von H_2O_2 und HOCl für das Überleben von *S. aureus* wichtig ist.

Zudem verfügen Pathogene, wie z.B. *S. aureus*, über spezifische Transkriptionsfaktoren, die in Reaktion auf reaktive Spezies die Expression von enzymatischen und nicht-enzymatischen Resistenzmechanismen induzieren **(Kapitel 3)**. Diese Regulatoren fungieren dabei als sogenannte Redox-Sensoren, deren Aktivität durch post-translationale Modifikationen ihrer Thiolgruppen reguliert wird. Da die von ihnen kontrollierten Regulons wichtige Resistenzmechanismen von Bakterien darstellen, lag der Schwerpunkt der vorliegenden Arbeit auf der Identifizierung und Charakterisierung weiterer Transkriptionsfaktoren der bakteriellen Stressreaktion. Dafür wurde die bakterielle Stressantwort von *S. pneumoniae* nach Zugabe von HOCl mittels RNA-seq Transkriptomanalysen genauer untersucht **(Kapitel 4)**. Im Zuge dessen wurde das NmlR Regulon als wichtiger Resistenzmechanismus gegen oxidativen Stress und der humanen Immunabwehr identifiziert. Das NmlR Regulon besteht aus den Genen *nmlR* und *adhC*, die für den zur MerR-Familie gehörenden Regulator NmlR und eine Zn^{2+}-abhängigen Klasse III Alkohol Dehydrogenase kodieren. Während der Regulator NmlR zuvor als Aldehyd-Sensor klassifiziert wurde, konnte innerhalb dieser Arbeit gezeigt werden, dass NmlR auch in Folge von verschiedenen Oxidantien die Transkription des *nmlR-adhC* Operons aktiviert. Mittels molekularer Analysen wurde nachgewiesen, dass das konservierte Cystein (Cys52) essenziell für die reversible Thioloxidation ist. Dabei ließ sich sowohl eine intermolekulare Disulfidbrückenbildung als auch *S*-Glutathionylierung detektieren.

Obwohl die antimikrobielle Wirkung zahlreicher Chinone seit Jahrhunderten genutzt wird, sind die bakteriellen Resistenzmechanismen bisher unzureichend aufgeklärt. Daher lag der Fokus der vorliegenden Arbeit auf der Charakterisierung der Chinon-Stressantwort von *S. aureus*. Ein Vergleich der Transkriptionsprofile nach Methylhydrochinon (MHQ) und Lapachol Stress ergab, dass sich die induzierten Stressreaktionen nur geringfügig voneinander unterscheiden **(Kapitel 5 und 6)**. Beispielsweise induzierten beide Chinone die oxidative Stressantwort und die Chinon-spezifischen MhqR und QsrR Regulons. Anhand weiterer Analysen ließ sich zeigen, dass Lapachol, anders als MHQ, nicht als Elektrophil agiert, sondern seine Toxizität durch die Produktion von ROS ausübt **(Kapitel 5)**. Die antimikrobielle Wirkung von Lapachol erwies sich als sauerstoffabhängig und konnte durch mikroaerophile Wachstumsbedingungen deutlich vermindert werden. Phänotypanalysen identifizierten die Katalase (KatA), die die Detoxifizierung von H_2O_2 katalysiert, zusammen mit dem BrxA/BSH/YpdA/NADPH Redox-

weg als wichtige Resistenzmechanismen von *S. aureus* gegen Lapachol. Im Gegensatz dazu vermittelte das MhqR Regulon nur gegen MHQ, nicht aber gegen Lapachol, einen Schutz, was auf eine Substratspezifität der MhqR regulierten Enzyme MhqE und MhqD hindeutet **(Kapitel 6)**. Da der einzige Cysteinrest von MhqR (Cys95) keine elementare Funktion bei der DNA-Bindung und Chinonerkennung hatte, lässt sich schließen, dass die Repressorinaktivierung nicht über einen Thiol-basierten Mechanismus, sondern wahrscheinlich durch eine Ligandenbindung erfolgt. Wie in **Kapitel 7** beschrieben, konnte nachgewiesen werden, dass im Gegensatz dazu QsrR, ein weiterer Chinon-spezifischer Regulator von *S. aureus*, durch verschiedene Thiol-basierte Mechanismen reguliert wird. Anders als das MhqR Regulon wurde das QsrR Regulon nicht nur stark durch Chinone, sondern auch durch verschiedene Oxidantien, gegen die es einen signifikanten Schutz vermittelte, induziert. Während Oxidantien eine intermolekulare Disulfidbrückenbildung zwischen dem redox-aktiven Cys4 und dem Cys29‘ induzierten, führte Allicin zu einer *S*-Thioallylierung aller 3 Cysteinreste (Cys4, Cys29, Cys32) *in vitro*. Northern Blot Analysen deuten darauf hin, dass *in vivo* die *S*-Thioallylierung von Cys4 ausreichend ist, während die Inaktivierung von QsrR durch Oxidantien sowohl das Vorhandensein von Cys4 als auch von Cys29‘ oder Cys32‘ erfordert. Weitere Transkriptionsanalysen und funktionelle Charakterisierungen ergaben, dass die MhqR und QsrR Regulons auch durch verschiedene Antibiotika, einschließlich Ciprofloxacin und Rifampicin, induziert werden und gegen diese eine Resistenz vermitteln **(Kapitel 6 und 7)**. Zudem wies die Δ*mhqR* Mutante verglichen mit dem Wildtyp eine erhöhte Überlebensrate in 48 Stunden andauernden Infektionsversuchen mit murinen Makrophagen auf. Dieser Befund deutet auf eine Funktion des MhqR Regulons in der Persistenz hin.

Im Rahmen der vorliegenden Arbeit wurde auch die Funktion des GbaA Regulons in der Thiol-Stressantwort genauer untersucht **(Kapitel 8)**. Während die Deletion des *SACOL2592-nmrA-2590* Operons eine erhöhte Sensitivität gegen Diamid, Allicin und Aldehyden bedingte, wies die Δ*gbaB* Mutante ein vermindertes Überleben nach MHQ-Stress auf. Zudem konnte gezeigt werden, dass die konservierten Cysteine Cys55 und Cys104 von GbaA für die elekrophile Stressresistenz erforderlich sind.

Substanzen, die entweder durch die Produktion von ROS, ihren elektrophilen Eigenschaften oder durch die Inhibierung von Proteinen mit der bakteriellen Redox-Homöostase interferieren, werden gegenwärtig als Alternative zu Antibiotika entwickelt und getestet **(Kapitel 9)**. Insbesondere ROS-produzierende Substanzen gelten als vielversprechend, da sie durch ihre unspezifische Wirkungsweise die Wahrscheinlichkeit einer Resistenzbildung minimieren. Dadurch steigt jedoch das Risiko von cytotoxischen Effekten, sodass spezifischere Inhibitoren, die

beispielsweise die Biosynthese von niedermolekularen Thiolverbindungen hemmen, geeigneter sein könnten. Angeregt durch das derzeitige globale Problem der Pandemie, ausgelöst durch das SARS-CoV-2 Virus, stellte sich die Frage nach der antiviralen Wirksamkeit redox-basierter Substanzen. Da die antimikrobielle Wirkung von Allicin bereits eingehend untersucht wurde und Allicin zudem immunmodulatorisch wirkt, wurde innerhalb eines Kooperationsprojekts mit der Arbeitsgruppe von Prof. Dr. Drosten, die antivirale Wirkung von Allicin auf SARS-CoV-2 in Zellkulturmodellen untersucht **(Kapitel 10)**. Biokompatible Allicin-Konzentrationen, die nach einer erfolgten SARS-CoV-2 Infektion verabreicht wurden, reduzierten die virale RNA-Menge und Anzahl an viralen Partikeln bis zu 70 %. Mittels Proteomstudien konnte gezeigt werden, dass eine SARS-CoV-2 Infektion mit einer ausgeprägten Veränderung des Wirtsmetabolismus und der Genexpression einhergeht. Zudem wurde eine starke Induktion des antiviralen Interferon-Signalweges festgestellt. Durch die Gabe von Allicin wurden diese durch SARS-CoV-2 induzierten Veränderungen rückgängig gemacht und die Expression der viralen Proteine signifikant vermindert.

Die nachgewiesene antimikrobielle Wirksamkeit von Thiol-basierten Substanzen legen nahe, diese in modifizierter Form zur Bekämpfung von Infektionskrankheiten nutzbar zu machen. Insbesondere Lapachol, dessen Wirkmechanismus in *S. aureus* in der vorliegenden Arbeit aufgeklärt wurde, könnte, wie auch Allicin, als Ausgangssubstanz zur Entwicklung von stabileren und weniger cytotoxischen Derivaten dienen. Außerdem konnten in der vorliegenden Arbeit durch die Kombination von globalen Transkriptomanalysen mit molekularen und mikrobiologischen Assays die Adaptationsstrategien von Bakterien weiter aufgeklärt werden. Dabei wurden insbesondere die Transkriptionsfaktoren NmlR, MhqR und QsrR als wichtige Resistenzmechanismen der humanpathogenen Bakterien *S. pneumoniae* und *S. aureus* identifiziert. Da die Expression dieser Regulons mit einer erhöhten Resistenz der Bakterien gegen das Immunsystem und gegen Antibiotika einhergeht, stellen diese Proteine interessante Ansatzpunkte für die Medikamentenentwicklung dar.

List of publications within this dissertation

1) Linzner N, Loi VV, **Fritsch VN**, Tung QN, Stenzel S, Wirtz M, Hell R, Hamilton C, Tedin K, Fulde M and Antelmann H. *Staphylococcus aureus* uses the bacilliredoxin (BrxAB)/bacillithiol disulfide reductase (YpdA) redox pathway to defend against oxidative stress under infections. *Front. Microbiol* 10:1355, 2019. **(Original Article)**

2) **Fritsch VN**, Loi VV, Busche T, Sommer A, Tedin K, Nürnberg DJ, Kalinowski J, Bernhardt J, Fulde M and Antelmann H. The MarR-type repressor MhqR confers quinone and antimicrobial resistance in *Staphylococcus aureus*. *Antioxid Redox Signal* 31(16):1235-1252, 2019. **(Original Article)**

3) **Fritsch VN**, Loi VV, Busche T, Tung QN, Lill R, Horvatek P, Wolz C, Kalinowski J and Antelmann H. The alarmone (p)ppGpp confers tolerance to oxidative stress during the stationary phase by maintenance of redox and iron homeostasis in *Staphylococcus aureus*. *Free Radic Biol Med.* 161:351-364, 2020. **(Original Article)**

4) Linzner N*, **Fritsch VN***, Busche T, Tung QN, Loi VV, Bernhardt J, Kalinowski J and Antelmann H. The plant-derived naphthoquinone lapachol causes an oxidative stress response in *Staphylococcus aureus*. *Free Radic Biol Med.* 158:126-136, 2020. **(Original Article)**

5) Linzner N, Loi VV, **Fritsch VN** and Antelmann H. Thiol-based redox switches in the major pathogen *Staphylococcus aureus. Biol Chem* 402(3):333-361, 2021. **(Review Article)**

6) Mösbauer K*, **Fritsch VN***, Adrian L, Bernhardt J, Gruhlke MCH, Slusarenko AJ, Niemeyer D and Antelmann H. The effect of allicin on the proteome of SARS-CoV-2 infected Calu-3 cells. *Front Microbiol* 12:746795, 2021. **(Original Article)**

7) Loi VV, Busche T, **Fritsch VN**, Weise C, Gruhlke MCH, Slusarenko AJ, Kalinowski J and Antelmann H. The two-Cys-type TetR repressor GbaA confers resistance under disulfide and electrophile stress in *Staphylococcus aureus*. *Free Radic Biol Med.* 177:120-131, 2021. **(Original Article)**

8) **Fritsch VN** and Antelmann H. Thiol targets in drug development to combat bacterial infections. Book chapter no. 28, Book title "Redox Chemistry and Biology of Thiols", Editors: Alvarez B, Comini M, Salinas G and Trujillo M, *Academic Press*, 2022. **(Review Article)**

9) **Fritsch VN**, Loi VV, Kuropka B, Gruhlke MCH, Weise C and Antelmann H. The MarR/DUF24-family QsrR repressor senses quinones and oxidants by thiol switch mechanisms in *Staphylococcus aureus. Antioxid Redox Signal.* Accepted on September 24th, 2022 **(Original Article)**

10) **Fritsch VN,** Linzner N, Busche T, Said N, Weise C, Kalinowski J, Wahl MC and Antelmann H. The MerR-family regulator NmlR is involved in the defense against HOCl stress in *Streptococcus pneumoniae. Mol Microbiol.* Under major revision **(Original Article)**

*Shared first authorships

Declaration of personal contribution to the publications

1) Linzner *et al.*, 2019: *Staphylococcus aureus* uses the bacilliredoxin (BrxAB)/ bacillithiol disulfide reductase (YpdA) redox pathway to defend against oxidative stress under infections.

I carried out the RNA isolation and Northern blot analyses to study the transcriptional regulation of *brxA, brxB*, and *ypdA* under control and thiol-specific stress conditions (Fig. 2). Together with Dr. Nico Linzner, I performed phenotype analyses to investigate the role of BrxAB and YpdA under HOCl and H_2O_2. I did the data analysis of these experiments and drafted the corresponding figures (Fig. 6 and 7).

2) Fritsch *et al.*, 2019: The MarR-type repressor MhqR confers quinone and antimicrobial resistance in *Staphylococcus aureus*.

I contributed to the concept of this paper, performed most of the experiments, and created the corresponding figures. Parts of the experiments were performed within my master thesis. This included the construction of the Δ*qsrR* deletion mutant and *mhqR* complemented strain, Fig. 4B,D,E; Fig. S7A and to some extent Fig. 4C. My experimental work during my doctoral thesis included the Northern blot analyses under different stress conditions and electrophoretic mobility shift assays (EMSAs) to the mutated inverted repeat (Fig. 4A,C), murine macrophage infection assays (Fig. 8A,B), ATP measurements, determination of the oxygen consumption rates with methylene blue and with the help of Dr. Dennis Nürnberg by using a Clark-type electrode (Fig. 9). Preliminary growth and survival assays during my master thesis were finalised and extended (Fig. 6-8; S1; S6; S8). I also measured the Brx-roGFP2 biosensor oxidation after H_2O_2 addition (Fig. S7B). Alongside the protein sequence alignments (Fig. S3), I designed figure S4 and wrote the manuscript together with Prof. Dr. Haike Antelmann.

3) Fritsch *et al.*, 2020: The alarmone (p)ppGpp confers tolerance to oxidative stress during the stationary phase by maintenance of redox and iron homeostasis in *Staphylococcus aureus*.

As the first author, I conducted most of the experiments. Thereby I was involved in phenotype analyses to investigate the ability of *S. aureus* to acquire a non-specific stress tolerance during the stationary phase and the role of (p)ppGpp (Fig. 1). Together with Dr. Quach Ngoc Tung, Dr. Tobias Busche and Prof. Dr. Haike Antelmann, I was responsible for the transcriptome data analysis and the further research design. I helped to characterize the function of (p)ppGpp in the iron and redox homeostasis by measuring the catalase activity and the intracellular amount of reactive oxygen species using the $DCFH_2$-DA dye (Fig. 5D,F). Additionally, I determined oxygen consumption rates (Fig. 6) and performed the Northern blots in Fig. 8A and S3. For quantification of intracellular iron levels, I applied the ferene-s assay and prepared the samples for ICP-MS analysis (Fig. 7C,D). Moreover, I performed phenotype analyses to characterize the susceptibility of the *S. aureus* strains to iron limitation, different antibiotics, and reactive oxygen species (ROS) in dependence on the endogenous iron and ROS levels (Fig. 7E,F; 9; 10; S4; S5). I drafted the initial manuscript and prepared with the co-authors the figures for publication.

4) Linzner et al., 2020: The plant-derived naphthoquinone lapachol causes an oxidative stress response in *Staphylococcus aureus*.

Together with Prof. Dr. Haike Antelmann, I developed the idea to compare the stress response of *S. aureus* against different quinones, including lapachol. My contribution to this paper included the first assessment of the antimicrobial activity of lapachol against *S. aureus* (Fig. 1A). Further, I was involved in the analysis of the mode of action of lapachol by performing

survival assays under different oxygen conditions and ROS levels (Fig. 5). To characterize the resistance mechanisms of *S. aureus* in more detail, I prepared the RNA-seq samples (Fig. 2) and performed phenotype analyses of different mutant strains (Fig. 7; S3). I did the data analysis and figure drafts for the experiments I executed, and together with all other authors, I participated in the literature review and correction of the manuscript.

5) Linzner *et al.*, 2021: Thiol-based redox switches in the major pathogen *Staphylococcus aureus.*

Together with all other authors, I was involved in the literature search and writing of initial manuscript sections. My focus was on the sections about the quinone sensing and stress resistance mechanisms, the SrrAB two-component system, and the defense mechanism of *S. aureus* against reactive nitrogen and sulfur species (RNS, RSS).

6) Mösbauer et al., 2021: The effect of allicin on the proteome of SARS-CoV-2 infected Calu-3 cells.

Prof. Dr. Haike Antelmann and I conducted the study and wrote the manuscript. My experimental research part included the sample preparation for the proteomics study and the measurement of the glutathione and glutathione disulfide levels (Fig. 1C). I was heavily involved in the analysis and interpretation of the proteomic data (Tables 1; S1-3; Fig. 5). Further, I did the statistical data analysis of all experiments and drafted figures 1-4.

7) Loi *et al.*, 2021: The two-Cys-type TetR repressor GbaA confers resistance under disulfide and electrophile stress in *Staphylococcus aureus*.

I helped to elucidate the function of the GbaA regulon in *S. aureus* by performing phenotype analyses under different thiol-stress conditions (Fig. 8; S9). Additionally, I contributed to the clarification of the redox-sensing mechanism of GbaA *in vivo* by analyzing the survival of the GbaA Cys mutants (Fig. 9).

8) Fritsch and Antelmann 2022: Thiol targets in drug development to combat bacterial infections.

My work on this book chapter included the literature search to develop, together with Prof. Dr. Haike Antelmann, the outline of this review article. During the writing process, I drafted most parts of the manuscript and created the blueprints for Fig. 2-6.

9) Fritsch *et al.*, 2022: The MarR/DUF24-family QsrR repressor senses quinones and oxidants by thiol switch mechanisms in *Staphylococcus aureus.*

Together with Prof. Dr. Haike Antelmann, I designed the concept of this study, wrote the methods section, and edited the manuscript. Furthermore, I performed most of the experiments. Thereby, I created together with Dr. Vu Van Loi the mutant strains and performed the Northern blot analyses of Fig. 1A. I analyzed the function of the QsrR regulon in the thiol-stress resistance and the role of the three cysteine residues for DNA binding and redox sensing by conducting phenotype analyses, Northern and Western blots, EMSAs and (non-)reducing SDS-PAGEs (Fig. 1C,E,G; 2-7; 9A,B; S1; S2). I made the quantitative and statistical evaluation of the experimental data, including Fig. 1B,D,F,H, and created all figures corresponding to the mentioned experiments.

10) Fritsch *et al.*, 2022: The MerR-family regulator NmlR is involved in the defense against HOCl stress in *Streptococcus pneumoniae.*

To assess the HOCl-stress response of *S. pneumoniae*, I prepared the RNA for the RNA-seq analysis performed by Dr. Tobias Busche. After I analyzed the obtained data, I developed together with Prof. Dr. Haike Antelmann the concept of this research project. Together with Dr. Nico Linzner, I performed the murine macrophage infection assays and assisted him with the mutant constructions. To investigate the function of the NmlR regulon and elucidate the redox-sensing mechanism, I used phenotype analyses, qRT-PCR, EMSAs and (non-)reducing SDS-PAGE analyses (Fig. 2; 3; 5; 7; 8; S1 and S2). Additionally, I performed the structural modeling shown in Fig. S3, the data analysis, and created the figures for the experiments I conducted. Additionally, I drafted the initial manuscript.

Introduction and general conclusions

1 Antibiotic resistance as a global public health threat

Within their natural niche, bacteria accomplish to resist various adverse conditions (1). Their adaptability is particularly evident in their ability to evade the immune system and to survive antibiotic treatment (2). The worldwide misuse and the lack of new antibiotics fostered the increasing prevalence of multi-drug-resistant bacteria and treatment failures (3-5). According to the WHO, "[a]ntibiotic resistance is one of the biggest threats to global health, food security, and development today."(6). In 2022, it was retrospectively estimated that 4.95 million deaths worldwide were associated with drug-resistant infections, of which, in 2019, 1.27 million deaths were directly attributable to antibiotic resistance (7). Studies indicated that acquired resistance mechanisms, which are often associated with high energy costs, will persist even in the absence of the antibiotic as selection pressure due to compensatory mutations (8, 9). This underscores the importance and urgency of solving the problem of increasing antibiotic resistance. Regardless of resistant bacteria, persister cells that are phenotypically tolerant to antibiotics despite the absence of resistance genes represent an additional serious health threat. Especially the finding of certain mutations that can increase the persister fraction within a population, their implication in persistent and difficult-to-treat infections and the increased likelihood of antibiotic-tolerant bacteria to become resistant is concerning (10-12). Redox-based drugs and compounds that specifically target proteins involved in the bacterial redox homeostasis are currently developed and tested as alternative treatment options or adjuvants (13). It is thought that they have a lower potential for resistance evolution than conventional antibiotics, but they often have a more cytotoxic effect on human cells (13). However, the sensory pathways and resistance mechanisms to withstand various environmental stresses, including redox stress, are still insufficiently investigated in bacteria. To identify new drug targets and to evaluate potential antimicrobials, comprehensive analyses of the intrinsic and acquired adaptation strategies of the major human pathogens are urgently required. In my dissertation, I characterized the redox stress response of the two human pathogens *Streptococcus pneumoniae* and *Staphylococcus aureus.* Hence, I will focus in the following elaboration on these two pathogens and, if applicable, refer to similar mechanisms in related bacteria.

1.1 Impact of the priority pathogens *Streptococcus pneumoniae* and *Staphylococcus aureus*

The Gram-positive bacteria *Streptococcus pneumoniae* and *Staphylococcus aureus* represent two human commensals that colonize the mucosal surfaces of the human upper respiratory tract.

While *S. pneumoniae* asymptomatically colonizes up to 65% of children and is less prevalent (<10%) in adults (14, 15), around 50% of the adult population are asymptomatic carriers of *S. aureus* on their skin or mucosae (16). However, both bacteria of the phylum Firmicutes can cause life-threatening diseases, such as pneumonia, meningitis, and sepsis. The type and progression of infection are mainly determined by the immune status of the host and the virulence of the strain (15, 17). Through the increased prevalence of antibiotic-resistant strains, the treatment of staphylococcal and pneumococcal infections has become difficult (7). According to the Centers for Disease Control and Prevention (CDC) report from 2019, methicillin-resistant *S. aureus* (MRSA) and drug-resistant *S. pneumoniae* caused presumably 10,600 and 3,600 deaths, respectively, in the United States (U.S.) (18).

Shortly after the introduction of penicillin in the 1940s, penicillin-resistant *S. aureus* and *S. pneumoniae* strains were identified (19, 20). Nevertheless, it took until the 1960/70s before β-lactam-resistant strains appeared as a medical problem. Both bacteria were found to express alternative penicillin-binding proteins, which have lower affinities to different β-lactams causing β-lactam antibiotic resistance (16, 21). While initially, MRSA strains were mainly healthcare-associated and termed hospital-acquired MRSA, this changed in the mid-1990s and 2004 when community-acquired MRSA and livestock-associated MRSA infections appeared, respectively (20). In contrast, it is thought that penicillin-resistant *S. pneumoniae* mainly emerged and spread in the community (21). Since then, both bacteria evolved resistances to other antibiotic classes, including macrolides, tetracyclines, and fluoroquinolones (9, 21-23). In both bacteria, the macrolide resistance is mediated by antibiotic efflux systems, encoded by *msr* and *mef* genes, and by target alterations. Post-transcriptional modifications of the 23S rRNA structure by methylase, encoded by *erm* family genes, as well as mutations in ribosomal proteins, were shown to prevent macrolide binding (24, 25). Furthermore, enzymatic macrolide inactivation confers resistance against this antibiotic class in *S. aureus* (25). Similar resistance mechanisms, including target alterations by amino acid changes of the topoisomerase IV or DNA gyrase, and increased drug efflux, are responsible for the fluoroquinolone resistance in these bacteria (9, 23) **(Fig. 1)**. The CDC reported in 2019 that strains resistant to one or more clinically relevant antibiotics are responsible for 30% of all *S. pneumoniae* infections in the U.S. (18). Based on their health and economic impact, their (probable) incidence, current treatment and prevention options, *S. aureus* and *S. pneumoniae* are listed alongside nine other human pathogens as "serious threats" by the CDC (18). *S. aureus* further belongs to the group of six so-called ESKAPE pathogens that are recognized as increasingly difficult to treat due to the rising number of antibiotic-resistant strains (26).

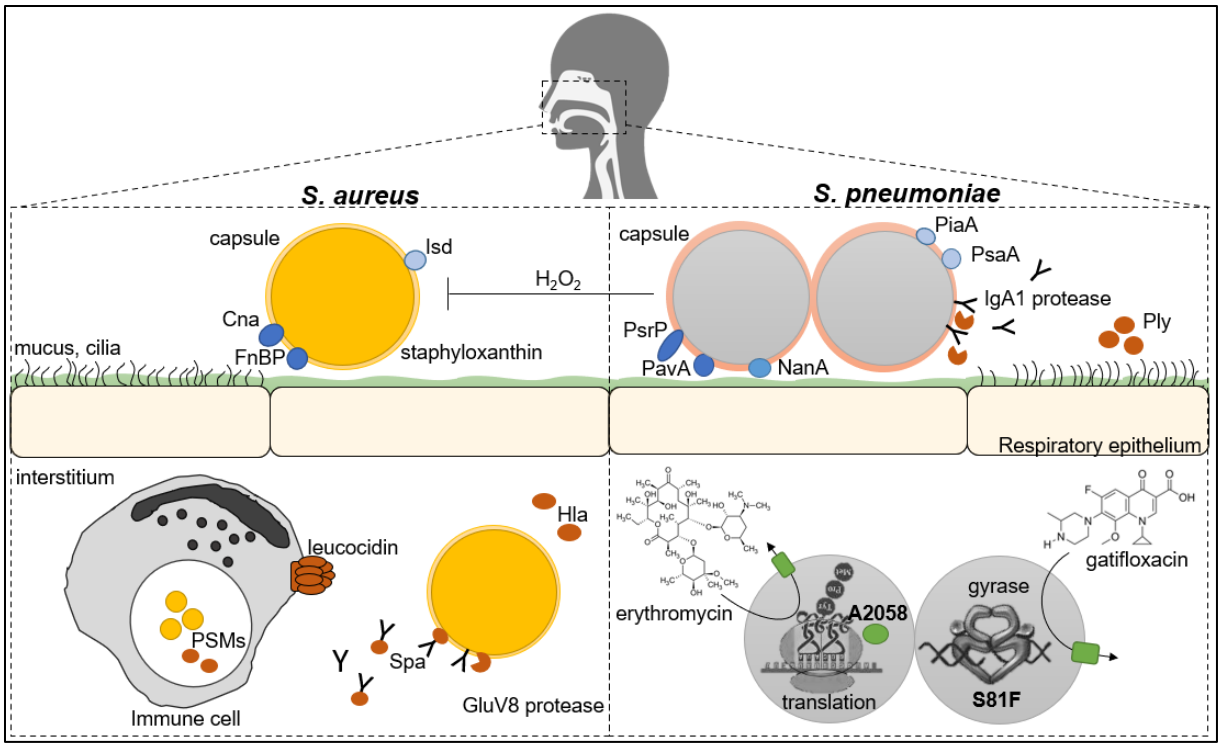

Figure 1: Virulence factors and antibiotic resistance mechanisms contributing to the pathogenesis of *S. aureus* (left) and *S. pneumoniae* (right) infections. The adhesion to the host tissue is mediated by the fibronectin-binding proteins (FnBPA/B) and the collagen-binding adhesin (Cna) of *S. aureus,* the pneumococcal adherence and virulence factor A (PavA), and the pneumococcal serine-rich repeat protein (PsrP) of *S. pneumoniae*. The capsule, the mucus degrading enzyme NanA and the toxin pneumolysin (Ply) inhibit mucociliary clearance. *S. pneumoniae* produces H_2O_2 to outcompete other bacteria. *S. aureus* possesses the carotenoid pigment staphyloxanthin as a defense mechanism against oxidants. Metal acquisition systems, such as the iron-specific ABC transporter PiaA, the manganese uptake system PsaA and the Isd system for heme acquisition, are used to overcome nutritional immunity. *S. aureus* secretes toxins, including leucocidins, phenol soluble modulins (PSMs), and alpha-hemolysin (Hla), to destroy host tissue. The protein A (Spa), the GluV8 and IgA1 proteases sequester or degrade immunoglobulins. Drug efflux pumps mediate antimicrobial resistance against fluoroquinolones (e.g., gatifloxacin) and macrolides (e.g., erythromycin). Further target modifications, such as the S81F point mutation at the gyrase A subunit or the dimethylation of A2058 at the 23S rRNA by a methylase, block antibiotic binding and render them ineffective. The figure is adapted from (14, 27-29).

Besides their ability to resist medical treatment options, both bacteria express a plethora of different virulence factors **(Fig. 1)**, which can have toxic implications on the host. Their tight regulation, depending on the growth, infection state and site, is critical for successful colonization and evasion of the host immune system (30-32). For example, surface proteins, such as the fibronectin-binding proteins FnBPA/B in *S. aureus* and the pneumococcal adherence and virulence factor A and B PavA/B in *S. pneumoniae,* are involved in the process of adherence and invasion. Additionally, several surface proteins contribute to immune evasion, metal homeostasis and biofilm formation (33-35). As a so-called "spreading factor", hyaluronidases, expressed by *S. aureus* and *S. pneumoniae,* facilitate the dissemination within the host by degradation of hyaluronan, a component of the extracellular matrix (ECM) (36, 37). Both pathogens also express various proteases, which are partly engaged in the processing of surface and secreted proteins. However, most proteases are mainly implicated in nutrient

acquisition, dissemination, and immune evasion, e.g., by cleavage of immunoglobulins, complement proteins and degradation of antimicrobial peptides (37-39).

Of special interest, due to their disruptive effect on eukaryotic cells, are toxins, which either work in a receptor-mediated or receptor-independent fashion (37, 40). While *S. aureus* possesses different cytolytic toxins, such as the alpha-hemolysin, the Panton-Valentine leucocidin, the gamma-toxin and phenol-soluble modulins (37, 41), *S. pneumoniae* only encodes for the cholesterol-dependent cytolysin pneumolysin. As a key pneumococcal virulence factor, pneumolysin was shown to not only exhibit cytolytic activity but to interfere directly with different host responses, e.g., by activation of the complement system (34, 42, 43). In *S. aureus*, superantigens modulate the adaptive immune system and cause, inter alia, the toxic shock syndrome via activation of T cells and cytokine release (44, 45).

The capsular polysaccharides represent important antigen targets of *S. aureus* and *S. pneumoniae*. The capsule promotes the survival inside the host by inhibiting the mucociliary clearance during colonization, and by interfering with the phagocytosis by neutrophils (46-48). The capsular diversity of *S. pneumoniae* is much higher than in *S. aureus,* as reflected by the 97 known *S. pneumoniae* compared to 11 *S. aureus* serotypes (49). While in 75% of encapsulated clinical *S. aureus* strains, the serotypes 5 and 8 are the most frequent, the serotype distribution in *S. pneumoniae* is more dynamic, which has serious implications on vaccination strategies (44, 47, 49). Upon introduction of the pneumococcal conjugate vaccine, the number of pneumococcal infections caused by (antibiotic-resistant) vaccine strains decreased, especially in children, significantly (18). However, this success was accompanied by increased serotype switching and replacement events, leading to an elevated frequency of non-vaccine serotypes (50, 51). Despite huge efforts, there is currently, except for two veterinarian vaccines, no vaccine available for *S. aureus*. Nevertheless, new approaches and vaccine candidates are currently being tested, which will hopefully help to combat *S. aureus* and *S. pneumoniae* infections (52, 53).

2 Redox-stress resistance mechanism under infection conditions

Upon bacterial infections, the innate and adaptive immune responses are activated and act synergistically to eliminate the invading pathogens. Thereby, the innate immune response represents the first line of defense and is characterized by a large influx of neutrophils to the sites of bacterial infections. Especially the oxidant-dependent killing mechanism, whereby large amounts of reactive oxygen species (ROS) are produced by neutrophils, macrophages, and monocytes, was shown to be crucial for successful bacterial clearance (54). Deficiencies in

this process, as observed in patients with chronic granulomatous disease, lead to an increased susceptibility to certain pathogens and recurrent and severe bacterial infections (55, 56). *S. pneumoniae* and *S. aureus* have evolved various mechanisms to evade and protect themselves against the immune response. Adaptive-regulatory networks that control enzymatic and non-enzymatic defense mechanisms allow *S. aureus* to survive and replicate inside neutrophils and macrophages (57, 58). Therefore, it is of supreme importance to investigate the resistance mechanisms in more detail to establish adequate treatment options and combat *S. aureus* and *S. pneumoniae* infections. The following sections will provide an overview of the reactive species with which pathogens are confronted and their destructive effect, with a special emphasis on protein thiols. As the overall goal of this thesis was to establish how *S. aureus* and *S. pneumoniae* sense and resist quinone and hypochlorous acid stress, the main focus are the newly identified defense strategies against these compounds.

2.1 Sources and thiol chemistry of reactive oxygen and chlorine species

The generation of ROS by specialized phagocytes is termed as oxidative or respiratory burst. The nicotinamide adenine dinucleotide phosphate (NADPH) oxidase NOX2 is rapidly activated upon phagocytosis and assembled to a multisubunit enzyme at the phagosomal membrane (59, 60). NOX2 catalyzes the one-electron reduction of oxygen (O_2) to superoxide anion radicals ($O_2^{\cdot -}$). The spontaneous dismutation and enzymatical conversion of $O_2^{\cdot -}$ by the superoxide dismutase (SOD) and myeloperoxidase (MPO) leads to hydrogen peroxide (H_2O_2) **(Fig. 2)** (61-64). In neutrophils, the MPO is released into the phagosome upon fusion with primary (azurophilic) granules (65, 66). The MPO catalyzes the reaction of H_2O_2 with (pseudo)halides to different hypohalous acids, such as the reactive chlorine species (RCS) hypochlorous acid (HOCl) (66). According to kinetic models, HOCl is produced inside the phagosome at a constant rate of 134 mM/min and a yield of 80% (61, 67). As a strong oxidant, HOCl reacts with different cellular macromolecules, leading, among others, to protein thiol oxidation and aggregation, and ultimately kills the pathogen (68, 69). Additionally, HOCl reacts with primary amines to chloramines **(Fig. 2)** (61). The MPO and other heme peroxidases, such as the lactoperoxidase (LPO), further catalyze the generation of hypothiocyanous acid (HOSCN) (70, 71). HOSCN reacts with thiolates to sulfenyl thiocyanates that hydrolyze to sulfenic acids (66, 72, 73). Of note, mitochondria-derived ROS were shown to contribute to the capability of macrophages to kill bacteria, including MRSA (74-76).

The assumption is made that most antibiotics indirectly cause an increased ROS formation in bacteria, by leading to an alteration of the metabolism, cellular respiration, iron

homeostasis and cellular damage (77-80). However, whether ROS accumulation contributes to bacterial killing by antibiotics is still a matter of debate (78, 81-84). The antimicrobial surface coating AGXX® has been shown to exhibit its antibacterial activity via ROS production (13, 85-88). Ebselen and suramin contribute indirectly to elevated ROS levels by inhibiting antioxidant enzymes (13, 89). The potential of these antimicrobial therapies will be discussed in more detail in section 2.8 **(chapter 9)** (13).

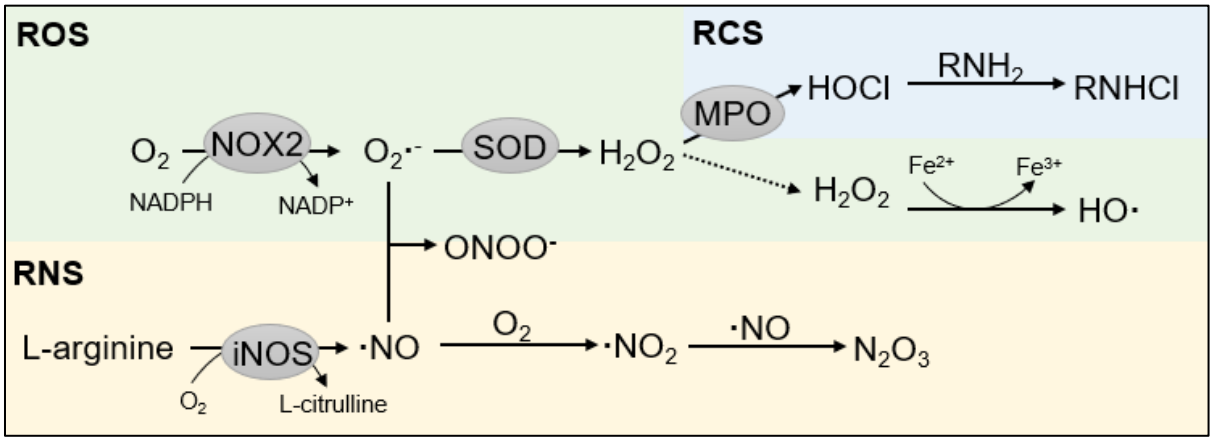

Figure 2: Sources of reactive species during infection conditions. During the oxidative burst, the NADPH oxidase (NOX2) generates superoxide anion radicals ($O_2^{\cdot -}$). This reactive oxygen species (ROS) is converted by the superoxide dismutase (SOD) to hydrogen peroxide (H_2O_2). In the Fenton reaction, ferrous iron (Fe^{2+}) promotes the production of the hydroxyl radical (HO·). The myeloperoxidase (MPO) generates the reactive chlorine species (RCS) hypochlorous acid (HOCl) using H_2O_2 and chloride. HOCl reacts with primary amines (RNH_2) to chloramines (RNHCl). The inducible nitrite oxide synthase (iNOS) produces the reactive nitrogen species (RNS) nitric oxide (·NO), which is auto-oxidized to nitrogen dioxide ($\cdot NO_2$). The reaction of ·NO with $O_2^{\cdot -}$ and $\cdot NO_2$ yields the peroxynitrite anion ($ONOO^-$) and dinitrogen trioxide (N_2O_3), respectively. The figure is adapted from (90).

Furthermore, endogenous ROS are produced due to the incomplete reduction of molecular O_2 within the electron transport chain and by the auto-oxidations of flavoenzymes (91, 92). In the strictly fermentative organism *S. pneumoniae*, which lacks cytochromes and heme-containing proteins (93), the oxidative decarboxylation of pyruvate to acetyl phosphate by SpxB generates millimolar concentrations of H_2O_2. This enables *S. pneumoniae* to outcompete other bacteria, including *S. aureus*, in the respiratory tract **(Fig. 1)** (94-96).

ROS, such as $O_2^{\cdot -}$ and H_2O_2, differ in their diffusion properties, kinetics, and reactions (76, 97-99), and react with most cellular macromolecules, e.g., DNA, RNA, proteins, and lipids (100, 101). However, the nucleophilic thiol group of proteins represents a preferential target for ROS (98). As the thiol group of cysteines is required for a variety of cellular functions, including protein folding, metal coordination, and catalytic reactions of redox enzymes, post-translational thiol modifications can lead to the inactivation of various cellular processes (99). Therefore, the bacterial cytoplasm is kept in a strongly reducing state (102, 103). The unbalancement towards oxidants through the depletion of antioxidant systems by ROS is

defined as oxidative stress, which is associated with a disruption of the redox homeostasis, oxidative damage, and ultimately the bacterial cell death (97, 104). Alterations in the cellular redox state by ROS and RCS are caused via the oxidation of sulfhydryl groups. The two-electron oxidation of a thiol group by ROS leads to the formation of instable Cys-sulfenic acids (Cys-SOH) **(Fig. 3)** (98). Also in the reaction of HOCl with thiols, Cys-SOH is generated through hydrolysis of the initially formed sulfenyl chloride (Cys-SCl). In the presence of strong oxidants, Cys-SOH is further oxidized to sulfinic- and sulfonic acids, causing irreversible protein damage (76). However, in the presence of adjacent thiols, Cys-SOH can undergo reversible thiol oxidations to inter- and intramolecular disulfides, or mixed protein disulfides, termed generically as *S*-thiolations (103, 105). Additionally, Cys-SCl and Cys-SOH can react with amines and amides, producing sulfenamides, which can be further oxidized to sulfonamides (69).

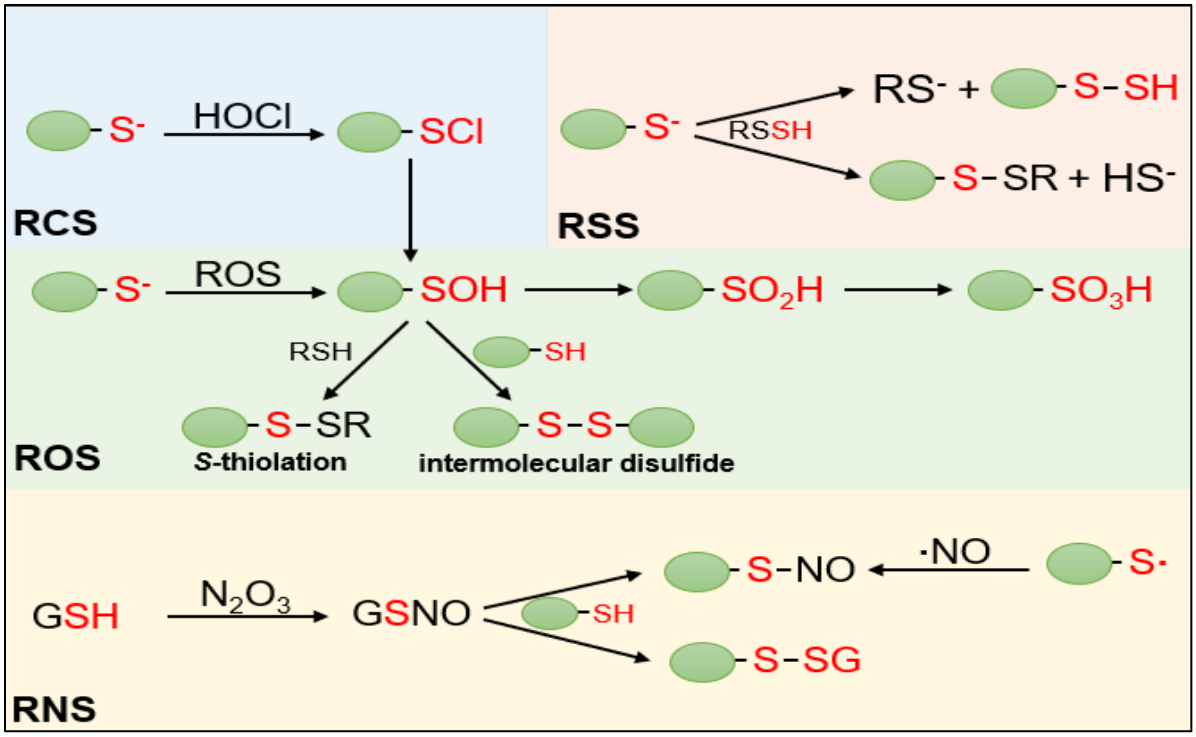

Figure 3: Reactive chlorine (RCS), sulfur (RSS), oxygen (ROS), and nitrogen (RNS) species cause various post-translational thiol modifications. Thiol groups are chlorinated by HOCl to sulfenylchloride, which is hydrolyzed to sulfenic acid (R-SOH). Through thiol oxidation, R-SOH can also be generated by ROS. R-SOH reacts with other thiol groups, leading to the formation of intermolecular disulfides. Upon reaction with low molecular weight thiols (RSH), mixed disulfides, termed *S*-thiolations, are formed. R-SOH can be also irreversibly overoxidized to sulfinic (RSO_2H) and sulfonic acids (RSO_3H). The protein persulfidation is mediated by hydropersulfides (RSSH), leading, among others, to mixed disulfides and hydrosulfides (HS^-). The one-electron oxidation reactions of thiyl radicals ($RS^{\cdot}$) by ·NO yield *S*-nitrosothiols. In contrast, dinitrogen trioxide (N_2O_3) mediates the two-electron oxidation of thiol groups. Upon reaction with glutathione (GSH), *S*-nitrosoglutathione (GSNO) is generated. GSNO causes the *S*-nitrosylation and *S*-glutathionylation of proteins. The illustration is adapted from (105).

The reactivity of thiols with ROS, such as H_2O_2, is determined by the accessibility, proximity to titratable groups, oxidation state and pK_a of the thiol group (106, 107). The pK_a value is highly dependent on the relative localization of the thiol group within the protein and the surrounding amino acids (108). Consequently, post-translational thiol modifications are regarded as site-specific cellular events with profound implications on various cellular functions (98). In contrast, an inverse relation of the HOCl reactivity and the pK_a value of the thiol group was not detected, indicating the indiscriminative reactivity of HOCl with thiols (109). These different reactivities with thiol groups are also apparent from the second-order rate constants of 18-26 $M^{-1}s^{-1}$ and 1.24-3.6x10^8 $M^{-1}s^{-1}$ for H_2O_2 and HOCl, respectively (105, 110). Importantly, most redox-responsive transcriptional regulators possess critical cysteine residues that are more reactive towards certain reactive species. For example, the rate constant for the reaction of H_2O_2 with the redox-regulator OxyR is approximately 10^7 $M^{-1}s^{-1}$, allowing the fast transcriptional response by this redox sensor (111). The chemical properties of thiol groups make cysteines to important constituents of the redox-signaling network in bacterial cells and the antioxidant defense (112, 113). Certain conserved cysteines of transcriptional factors serve hereby as molecular switches, which integrate different redox-based post-translational modifications into gene expression changes, as will be discussed in the following chapters.

2.2 Sources and thiol chemistry of reactive electrophilic species

Compounds with electron-deficient centers are termed as reactive electrophilic species (RES), including aldehydes and quinones (103, 114). The α-oxoaldehydes glyoxal and methylglyoxal (MG) are generated endogenously during the glycolysis and degradation of glycated proteins (115). Lipid peroxidation, amino acid and DNA oxidation can lead to aldehyde generation (116-120). Additionally, the decomposition of HOCl-derived chloramines produces α-hydroxy and α,β-unsaturated aldehydes, highlighting the relevance of RES sensing systems under infection conditions (121, 122). Most RES react preferentially with nucleophilic thiol groups, leading to irreversible *S*-alkylation via 1,4-Michael addition and subsequent enzyme inactivation (115, 123). MG stress was associated with increased ROS levels, contributing to the toxic effects of this RES (124). Since most RES detoxification pathways require the $NAD(P)^+$/NAD(P)H redox couple, RES also aid indirectly to a depletion of cellular reductants (114, 125).

Quinones comprise diketones with the general structure $O{=}C{-}(C{=}C)_n{-}C{=}O$ (126). Based on their aromatic carbon skeleton, quinones can be allocated to four different structural groups, namely the benzoquinones, naphthoquinones, anthraquinones, and N-heterocyclic quinones (quinone-imines) (127, 128). As quinones and their derivatives are components of different

industrial products and produced by various organisms as defense strategies, quinones are highly abundant in the environment (126, 129-134). Several quinone-derivates represent established drugs to treat various diseases **(chapter 9)** (13, 135-141). Quinones can be formed during the metabolism of benzene, phenols and certain drugs in the human body (129). For example, acetaminophen (Paracetamol) is degraded to the N-acetyl-*p*-benzoquinone imine (123). The spontaneous and metal ion-catalyzed auto-oxidation of siderophore-derived catechol and host-derived catecholamines, such as dopamine and norepinephrine, leads to the formation of quinones and semiquinone radicals. Therefore, Fe^{3+}-catecholate complexes, which are used by pathogens as an iron source under infections, represent a physiological quinone source (130, 142-149).

Membrane-associated quinones are essential electron carriers of the respiratory chain. While *S. pneumoniae* lacks a functional cytochrome-like respiratory system, including quinones (150), in *S. aureus*, menaquinone shuttles the electrons within the branched-chain respiratory pathway to the heme-containing cytochrome *bd* and cytochrome aa_3 quinol-oxidases (151, 152). Interestingly, the synthetic menaquinone precursor menadione and menaquinone analogs showed potent antimicrobial activity against *S. aureus* (153, 154), indicating that bacteria require effective resistance mechanisms to cope with exogenous and endogenous quinones.

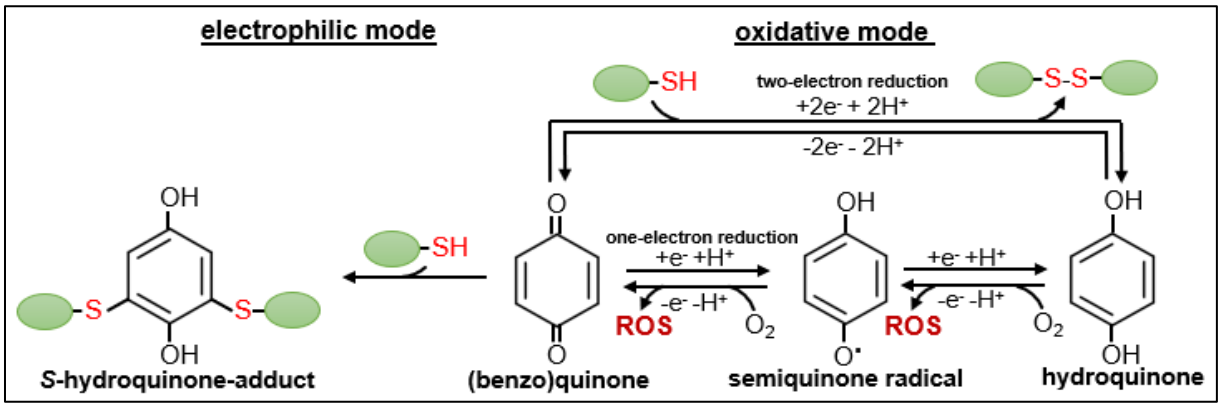

Figure 4: Molecular mechanisms of quinone toxicity. As electrophiles, quinones can react with thiol groups of proteins by a reductive 1,4-Michael addition, leading to the formation of *S*-hydroquinone-adducts. The one- and two-electron reduction of quinones generates the semiquinone radical and hydroquinone, respectively. The oxidation of both reaction products is associated with the reduction of molecular oxygen (O_2) to generate reactive oxygen species (ROS). Within the two-electron reduction, adjacent thiol groups can be oxidized, leading to the formation of disulfides. Both modes of action contribute to the intracellular thiol depletion and alteration of the cellular redox state. The figure is adapted from (155).

Pathogens are also exposed to antibiotics and quorum-sensing molecules with quinone-like elements (128, 156, 157). While certain phenazines and quinolones were shown to substitute for quinones in the respiratory chain, for others their antimicrobial activity is well established (158, 159). The fluoroquinolone ciprofloxacin is commonly prescribed for the

treatment of infectious diseases caused by *S. aureus* (160). The phenazine pyocyanin is produced as a potent antimicrobial by *Pseudomonas aeruginosa* (161), a pathogen that often co-infects the lungs of cystic fibrosis patients with *S. aureus* (162). Both quinone-like compounds contain the structural element of a quinone-imine (163, 164).

In general, quinones can either act as oxidants or as electrophiles. Thereby, they can alter e.g., the RNA and protein biosynthesis, respiratory chain activity and ATP synthesis (128, 165). As electrophiles, quinones lead to the thiol-(*S*)-alkylation of nucleophilic thiol groups and the formation of the *S*-hydroquinone-adduct (166) **(Fig. 4)**. Upon subsequent oxidation and 1,4-reductive Michael-type addition reactions, the quinone can be fully substituted (167). Thereby, quinones lead to irreversible protein aggregates and the depletion of the reduced cellular thiol pool (155). The alkylating ability of quinones with a free position in conjugation to one of the carbonyls is influenced by the adjacent substituent, modulating the accessibility and electrophilicity (166, 168). As oxidants, quinones can lead to the production of ROS within their redox cycle (169, 170) **(Fig. 4)**. Quinones must undergo a one-electron reduction to form the semiquinone radical, which is re-oxidized to the corresponding quinone by the reduction of molecular oxygen to ROS (155, 166, 171). ROS can also be generated through the oxidation of the hydroquinone to the semiquinone radical, followed by the reduction of the oxidized species (166, 172). The two-electron reduction of the quinone to the corresponding hydroquinone can be coupled to the oxidation of cellular thiols to disulfides (173). The primary mode of action of a certain quinone is not only dependent on the physicochemical properties but also the cellular concentration and conditions, such as oxygen level (169).

2.3 Sources and thiol chemistry of reactive nitrogen and sulfur species

During infections, the inducible nitric oxide synthase (iNOS) in macrophages and neutrophils aids in the bacterial killing by producing the reactive nitrogen species (RNS) nitric oxide (·NO) (174-179). Commensal bacteria are exposed to ·NO generated in the respiratory epithelium and on the skin (176, 180). The auto-oxidation of ·NO can lead to nitrogen dioxide (·NO_2), which further reacts with ·NO to dinitrogen trioxide (N_2O_3) (179) **(Fig. 2)**. Through the reaction with $O_2^{\cdot -}$, ·NO can also give rise to the peroxynitrite anion ($OONO^-$), a potent two-electron oxidant that leads to the formation of nitrite and sulfenic acid upon reaction with thiol groups (181-184). Additionally, ·NO can react with hydrogen sulfide (H_2S) to thionitrous acid (HSNO) (106, 185).

Reactive sulfur species (RSS) are redox-active organic or inorganic sulfur-containing molecules, including allicin, H_2S, and persulfides (RSSH). Most RSS represent either natural

compounds from plants or are formed as secondary products within ROS- and RNS-dependent reactions (186). Low amounts of endogenously produced ·NO and H_2S in bacteria have been associated with increased resistance to oxidative stress, antibiotics, and the host-immune defense (179, 180, 187-194).

The reversible oxidation of protein thiols by RSS is termed as protein persulfidation (195, 196). The reaction of RSSH with thiol groups can either involve the attack on the terminal sulfane sulfur or the internal sulfur atom **(Fig. 3)**. While in the transpersulfidation reaction, the persulfide is transferred within a thiol-disulfide exchange reaction to the attacking thiol, in the latter reaction, a mixed disulfide and H_2S is formed (195, 197, 198). In the case of allicin, the thiol-disulfide exchange reaction with glutathione (GSH) leads to the formation of the *S*-allylmercaptoglutathione (GSSA) and GSH depletion (199-201). In *S. aureus*, sublethal amounts of allicin caused bacillithiol (BSH) depletion, *S*-thioallylations of 57 proteins and a strong thiol-specific oxidative and sulfur stress response (202).

By damaging lipids, proteins, and DNA, RNS have been shown to interfere with different cellular processes, whereby the inhibition of DNA replication and respiration seem to be the most prevalent ones (203, 204). RNS cause, via one- and two-electron oxidation reactions, post-translational thiol modifications (181, 205, 206). During the *S*-nitrosylation process, a nitrosyl group is added to the thiol group, leading to the formation of *S*-nitrosothiol (SNO) (205) **(Fig. 3)**. *S*-nitrosylated proteins can also react with adjacent thiols to form inter- or intramolecular disulfides or *S*-thiolations (207). The reaction of GSH with ·NO leads to *S*-nitrosoglutathione (GSNO). While GSNO can cause *S*-glutathionylation, it can also propagate further *S*-nitrosylations of proteins by transnitrosation and is often employed as a ·NO donor (179, 208).

Bacteria possess an arsenal of inducible defense systems to counteract the described deleterious effects of ROS, RCS, RES, RNS and RSS. Within their environments, bacteria are most likely not exposed to only one individual reactive species but a plethora of different reactive species (185, 209). Thereby, the relative composition of the formed reactive species will determine the intracellular targets and the precise stress response, mediated by the previously explained reversible thiol modifications, including sulfenylation, thiolation, alkylation, nitrosylation and persulfidation of the thiol proteome. Thus, studying each stress response separately helps to understand to what extent certain defense strategies are conserved across bacterial species and to determine key regulators and key enzymes as potential drug targets.

2.4 The interconnection of the metal and redox homeostasis in pathogenic bacteria

As structural and catalytic cofactors, trace metals, such as zinc (Zn^{2+}), ferrous iron (Fe^{2+}), manganese (Mn^{2+}) and cupric ion (Cu^{2+}), are implicated in various cellular processes, including respiration and signal transduction (210). Accordingly, the frequency of metalloenzymes in all six Enzyme Commission classes ranges between 36% to 59%, whereby Fe^{2+} is the predominant metal involved in redox-catalysis (211). To limit the access of bacteria to essential metals, host cells export Zn^{2+}, Mn^{2+}, and Fe^{2+} from the phagosome and phagolysosome and chelate extracellular metals to keep their concentration extremely low in human body fluids. Thus, pathogenic bacteria encode for various high-affinity metal-chelating compounds, such as sidero- and zincophores, and other virulence factors involved in metal acquisition to counteract this nutritional immunity (143, 212-216). By inducing the expression of antioxidant enzymes and proteins involved in the limitation and remedying of oxidative damage, metal starvation has been identified as a priming factor for an increased resistance toward ROS (217, 218). Vice versa, ROS induce zinc and manganese uptake, iron-sulfur cluster assembly systems and ferritins (92, 219, 220). The tight connection between metals and ROS becomes even more evident when the role of metals in the oxidative stress defense is contemplated. As cofactors of ROS detoxifying enzymes, such as SOD, metals are critical for the bacterial defense against oxidative stress (221). Additionally, Mn^{2+} and Zn^{2+} protect thiol groups from oxidation by replacing the redox-active Fe^{2+} and Cu^{2+} from metalloproteins, reducing oxidative damage (212, 222, 223). Furthermore, Mn^{2+} was shown to reduce $O_2^{\cdot -}$ with a rate constant of approximately 10^6 M^{-1} s^{-1} and to contribute significantly to the oxidative stress resistance of different bacteria, including *S. pneumoniae* (92, 224). However, Mn^{2+} excess interferes with various cellular processes, underlining the significance of a tightly regulated metal homeostasis (225, 226). Interestingly, in *B. subtilis,* Mn^{2+} intoxication was suppressed by induction of the MhqR regulon (s. section 2.7.1) (225).

By increasing the amounts of cuprous ion (Cu^{1+}) and Zn^{2+} inside the phagolysosome, metal intoxication is employed by host cells as an alternative strategy to kill invading pathogens (227, 228). Host-derived reactive species further contribute to elevated intracellular free iron levels by targeting metalloenzymes and iron-sulfur clusters (219, 229-232). Upon ROS exposure, the $[4Fe\text{-}4S]^{2+}$ cluster is converted to a $[2Fe\text{-}2S]^{+}$ cluster, leading to the release of Fe^{2+} and ferric iron (Fe^{3+}), and finally, cluster degradation and formation of apo-proteins (92, 233-235). Interestingly, *S. pneumoniae* lacks $[4Fe\text{-}4S]^{2+}$ clusters and possesses few iron-sulfur cluster proteins, contributing to its H_2O_2 resistance (93).

Elevated $Cu^{1+/2+}$ and Zn^{2+} levels interfere with protein folding and enzymatic functions, for example, by catalyzing the formation of non-native disulfide bonds, mis-metalation, binding to free thiol groups and damaging of iron-sulfur clusters and their biogenesis (222, 223, 227, 228). While Zn^{2+} is redox-inert, Cu^{1+} and Fe^{2+} contribute as redox-active trace metal ions to the intracellular ROS levels. Therefore, iron enrichment renders under aerobic conditions *S. aureus* and other bacteria more sensitive toward H_2O_2 (236, 237). According to the Fenton reaction, the oxidation of Fe^{2+} or Cu^{1+} by H_2O_2 leads to the formation of Fe^{3+} or Cu^{2+} and the hydroxyl radical (HO·) (238) **(Fig. 2)**. This highly reactive radical initiates lipid peroxidation and damages DNA bases, sugar moieties and proteins at diffusion-limited rates. However, as Fe^{2+} binds directly to the phosphodiester backbone, the DNA is thought to represent the primary target (92, 222). To inhibit the detrimental metal-mediated redox-reactions, most of the intracellular Fe^{2+} is bound or sequestered, e.g., by (mini)ferritins, and iron uptake is tightly controlled, especially under oxidative stress by metalloregulators, such as Fur and PerR (239, 240). While Fur senses changes in intracellular Fe^{2+} levels (241, 242), PerR of *S. aureus* acts as a metal and peroxide sensor. In response to peroxides, the Fe^{2+}-catalyzed histidine oxidation of PerR induces the expression of genes functioning in the oxidative stress defense and metal homeostasis, such as the catalase *katA*, the alkyl hydroperoxide reductase *ahpC*, the thioredoxin reductase *trxB*, the miniferritin *dps* and the ferritin *ftnA* (243, 244). Moreover, PerR negatively regulates the expression of Fur, which co-regulates the expression of *katA, ahpC, dps* and *ftnA*, but not of other PerR regulon members (241, 242, 245). In the presence of $O_2^{\cdot -}$ or cellular reductants, Fe^{3+} and Cu^{2+} are reduced non-enzymatically back to Fe^{2+} and Cu^{1+}, making them again accessible to the Fenton reaction (238, 246). The redox-active mode of Cu^{2+} and the inhibition of the iron-sulfur cluster biosynthesis contribute to its toxicity in different bacteria (223, 247-253). Independently, Cu^{2+} promotes ROS formation by catalyzing the oxidation of hydroquinones to semiquinone radicals, leading to an enhanced expression of quinone detoxifying enzymes in *Lactococcus lactis* (254, 255).

2.5 The small alarmone (p)ppGpp as mediator of the stringent response

Bacteria are constantly faced with growth-limiting challenges, such as toxic reactive species and starvation for nutrients, such as metal ions, amino acids, and carbon sources. Despite stress-specific resistance mechanisms, which will be discussed using the examples of HOCl and quinones in the following sections (s. section 2.6 and 2.7), bacteria can acquire a non-specific, general stress resistance (256, 257). In reaction to multiple signals, bacteria accumulate, for instance, the small alarmones guanosine tetra- and pentaphosphate (p)ppGpp to induce the

stringent response. The stringent response leads to an altered gene expression profile, characterized by repression of genes for active growth and activation of genes required for amino acid biosynthesis and transport, nutrient acquisition, and stress survival (258, 259). This is accomplished by interfering, depending on the intracellular (p)ppGpp concentrations, in a hierarchical order with different physiological processes, including DNA replication, ribosome synthesis and maturation, transcription, and translation (260). In *S. aureus*, the bifunctional synthase/hydrolase RSH/Rel of the RelA-SpoT homolog (RSH) family (261) catalyzes the synthesis and degradation of (p)ppGpp. Together with the two small alarmone synthetases (SASs) RelP and RelQ, RSH catalyzes the pyrophosphate transfer from ATP to the hydroxyl group on carbon three of the ribose moiety of GDP or GTP, generating (p)ppGpp (261, 262). Although a conserved sequence motif of these proteins determines the specificity for guanine nucleotides, the catalytic efficiencies, preference for GDP or GTP and regulatory mechanisms differ between these enzymes (262-267). The SASs and hydrolase activity of Rel are important for maintaining low basal levels of (p)ppGpp during the exponential growth phase, modulating the bacterial growth rate and metabolism (264, 268-270). The intramolecular switch of Rel from the hydrolase to the synthetase activity, mediated by the C-terminal regulatory domain, is essential for the rapid accumulation of (p)ppGpp in response to amino acid limitation (264, 271). Consistent with the reported preference of Rel for GTP, the pppGpp levels reached ~0.175 nmol/mg cell dry weight and were approximately 2.3-fold higher than the amount of ppGpp upon mupirocin-mediated amino acid starvation in *S. aureus.* This distinction is probably facilitated by the RXKD motif in the substrate-binding pocket (263, 270).

Studies on Firmicutes have shown that the targets and molecular mechanisms of (p)ppGpp to achieve the same overall physiological changes are different from the ones in Gammaproteobacteria (262, 272-274). The conformational variability of (p)ppGpp, especially of the 3' and 5' phosphate moieties, enables the binding of (p)ppGpp to different targets (275). (p)ppGpp binds preferentially to GTP- and phosphoribosyl pyrophosphate (PRPP)-binding pockets of proteins in Gram-positive bacteria (274). Additionally, (p)ppGpp exerts its activity by acting as an allosteric effector to induce conformational changes of the active sites or protein oligomerization.

Until today, no physical interaction of (p)ppGpp with the RNA polymerase could be detected in Firmicutes or Actinobacteria (273, 276). Instead, (p)ppGpp mediates broad physiological alterations by modulation of the intracellular purine concentrations. In *S. aureus*, the induction of the stringent response by mupirocin resulted in sixfold lower GTP and threefold higher ATP levels, respectively (277). Similar trends were also observed for other guanine and

adenine nucleotides, such as GDP, ADP, and AMP (278). The consumption of GTP for the (p)ppGpp production, as well as the inhibition of the GTP biosynthesis pathway by (p)ppGpp, contribute to decreased GTP levels (279, 280) **(Fig. 5A)**. The enzymes HprT, Gmk and XPRT of the GTP biosynthesis pathway appear hereby as the main targets of (p)ppGpp (280, 281). Additionally, (p)ppGpp inhibits the purine nucleotide biosynthesis by competitive binding to the transcriptional repressor PurR and hindering its inactivation by PRPP (282). Low GTP levels block the transcription of ribosomal RNAs that require GTP as initiating NTPs, while genes that are activated by ATP, such as branched-chain amino acid biosynthesis genes (277, 283-286), are induced **(Fig. 5A)**. The inverse relationship between (p)ppGpp and GTP also affects the DNA-binding activity of the global transcription factor CodY, conserved in Firmicutes (279, 287, 288). In *S. aureus*, CodY negatively regulates the expression of amino acid biosynthesis pathways and represses either directly or indirectly virulence genes and biofilm formation. The CodY-dependent regulation accounted for 143 of the 150 upregulated genes upon induction of the stringent response by leucine and valine starvation (289).

Furthermore, (p)ppGpp hinders the DNA replication by binding to the active site of the primase DnaG. The abrogation of mRNA translation is achieved by interfering with the activity of the elongation factors EF-TU and EF-G as well as the translational initiation factor 2 (IF2) (290, 291) **(Fig. 5A)**. Although GTP and ppGpp bind to the same nucleotide-binding site of the translational GTPase IF-2, their effects on IF-2 activity were found to be contrary. While GTP enables the formation of the 30S and 70S initiation complexes, the binding of (p)ppGpp interferes with the association of the fMet-$tRNA^{Met}$ and thereby with the IF-2-dependent translation initiation complex formation (290, 292-294). Further studies showed that (p)ppGpp interferes with protein synthesis by binding to five GTPases (RsgA, RbgA, Era, HflX and ObgE) of *S. aureus* and homologs in other bacteria that are implicated in ribosome assembly and maturation. As a result, the intracellular amount of 70S ribosomes is reduced, and the 100S ribosome disassembly is inhibited (293, 295-298) **(Fig. 5A)**. Recent studies indicate that guanosine-5′-monophosphate-3′-diphosphate (pGpp) functions as a third alarmone in bacteria (281, 299-302).

Although changes in the nucleotide pool and the inhibition of CodY account for most transcriptional changes in *S. aureus* during the stringent response, some effects are CodY independent and require the identification of further molecular targets of (p)ppGpp (278, 289).

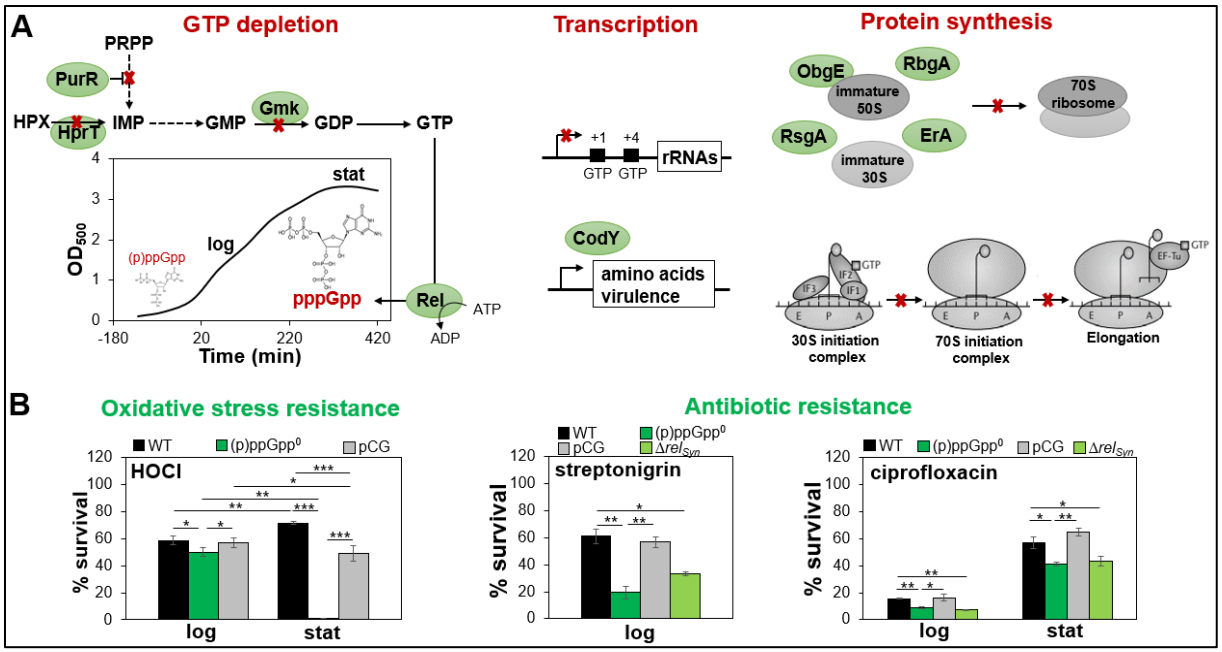

Figure 5: The alarmone (p)ppGpp affects several physiological processes to mediate cellular survival under growth-limiting conditions. (A) In response to nutrient limitation, (p)ppGpp is synthesized by Rel from GTP and GDP to induce the stringent response. The GTP levels are decreased through the inactivation of the GTPases involved in the GTP biosynthesis. HprT and Gmk catalyze the synthesis of inosine monophosphate (IMP) and GDP from hypoxanthine (HPX) and GMP, respectively. The derepression of the PurR regulon enables the synthesis of IMP from phosphoribosyl pyrophosphate (PRPP). This process is inhibited by the direct binding of (p)ppGpp to PurR. Decreased GTP levels abolish the transcription of ribosomal RNAs, which require GTP as initiating NTPs. In contrast, genes implicated in virulence and amino acid biosynthesis are transcribed due to the inactivation of the GTP-sensing CodY repressor. (p)ppGpp interferes with ribosome biogenesis by destabilizing the association of the GTPases RbgA, RsgA and Era with the ribosome subunits, and by increasing the affinity of the anti-association factor ObgE to the 50S subunit. The binding of (p)ppGpp to the translational initiation factor 2 (IF2) and the elongation factor EF-TU abolish the mRNA translation. **(B)** Survival assays using the wild type (WT), the (p)ppGpp^0 strain, and the complemented strain, expressing the (p)ppGpp synthetase Rel_{Syn} (pCG), revealed that (p)ppGpp confers tolerance to HOCl stress in the logarithmic (log) and especially in the stationary (stat) phase in *S. aureus*. The (p)ppGpp^0 and Δrel_{syn} mutants were also more susceptible to the antibiotics ciprofloxacin and streptonigrin. The latter exerts its toxicity in the presence of iron through ROS production, indicating an elevated labile iron pool in cells lacking (p)ppGpp. The figure is adapted from (276, 280, 293) and chapter 1 (303), where the experimental procedures are described. *p<0.05; **p>0.01; ***p<0.001.

2.5.1 The function of (p)ppGpp in the redox and iron homeostasis

The signal molecule (p)ppGpp is also required for the viability, biofilm formation, long-term persistence, and virulence in many bacteria, including *S. aureus* and *S. pneumoniae* (276, 304-313). The stringent response and elevated (p)ppGpp levels render different bacteria more tolerant toward antibiotics (314-321). For example, two different mutations in the *rel* gene found in a clinical *S. aureus* isolate led to higher (p)ppGpp levels and mediated increased tolerance to five antibiotic classes (322). Further analyses indicated that the transcription and translation of the *mecA* gene are altered in dependence on the (p)ppGpp levels (323, 324). Additionally, decreased growth and metabolic rates because of the stringent response account for the increased antibiotic tolerance (322). However, the *S. aureus relP* and *relQ* mutants were highly sensitive towards cell wall-targeting antibiotics, such as vancomycin, despite showing

similar growth rates as the wild type (264), highlighting the need for a better understanding of the molecular mechanisms of (p)ppGpp.

Until today, several models have been proposed to link mechanistically (p)ppGpp with bacterial persistence, such as efflux pumps, toxin-antitoxin systems, and ribosome dimerization. However, due to a lack of experimental evidence and sometimes contradicting results, the question is still unanswered (307). Interestingly, increased antibiotic tolerance during the stringent response could be also a secondary effect based on the role of (p)ppGpp in the cellular redox homeostasis. Thiol stress was shown previously to cause the rise of intracellular (p)ppGpp levels in some bacteria, including *B. subtilis* (325-327). However, the precise molecular mechanism of (p)ppGpp synthesis in response to oxidative stress is still uncertain. It was suggested that oxidative protein damage might lead to an impaired uptake and biosynthesis of amino acids and an accumulation of uncharged tRNA, which is sensed (325, 326). Accordingly, the (p)ppGpp mediated upregulation of branched-chain amino acid biosynthesis genes, and subsequent translation of proteins implicated in the stress defense was shown to confer resistance against nitrosative stress in *Salmonella enterica* serovar Typhimurium (326).

A decreased oxidative stress resistance was also found in *Bacillus subtilis, Brucella suis* and *Francisella tularensis* strains with diminished (p)ppGpp levels (317, 325, 328). Furthermore, in *Vibrio cholerae, Enterococcus faecalis* and *P. aeruginosa*, (p)ppGpp was shown to affect the intracellular ROS levels (329). In *V. cholerae,* (p)ppGpp was suggested to downregulate proteins involved in the TCA cycle and inhibit the iron-uptake transporter FbpA, thereby leading to reduced endogenous ROS formation (314). (p)ppGpp in *P. aeruginosa* increased the expression of ROS detoxifying enzymes and decreased the pro-oxidant 4-hydroxy-2-alkylquinolines expression, causing elevated ROS levels in strains lacking (p)ppGpp (315, 316, 330). Similarly, a Δ*relA*Δ*spoT* mutant in *Escherichia coli* was characterized by a lower catalase activity and increased intracellular ROS levels (330). Mupirocin treatment indicated that the ROS detoxifying enzymes AhpC and KatA might be regulated by (p)ppGpp in *S. aureus* (259). As (p)ppGpp plays a central role in virulence, stress resistance and persistence of bacteria, it represents a potential drug target to control infections (331). However, for a successful application, the underlying targets and physiological mechanisms concerning (p)ppGpp, should be further elucidated. Since the molecular regulatory mechanisms of (p)ppGpp were shown to vary between bacterial species (269, 332), and comprehensive studies in *S. aureus* were missing, we aimed to investigate the role of (p)ppGpp in the thiol stress

resistance of this major human pathogen in more detail as one main part of this doctoral thesis (303) **(chapter 1)**.

Using survival assays, I could demonstrate that *S. aureus* acquires a non-specific thiol-stress tolerance against HOCl and methylhydroquinone (MHQ), indicated by the approximately 2- and 40-fold higher survival rate of stationary (stat) phase cells compared to logarithmic (log) grown bacteria, respectively (303). Remarkably, the stat phase resistance towards HOCl was completely abolished in the (p)ppGpp^0 mutant **(Fig. 5B)**. These results indicate that (p)ppGpp contributes to the thiol-stress response of *S. aureus* in the log, and especially in the stat phase. Since the effect after the addition of MHQ was not as pronounced, it can be concluded that other resistance mechanisms compensate for the lack of (p)ppGpp. For example, we observed a 2.5–5.3-fold upregulation of the QsrR regulon in the (p)ppGpp^0 mutant in the stat phase (303). The QsrR regulon is implicated in the quinone stress resistance in *S. aureus* **(chapter 6 and 7)**. Interestingly, other studies reported that external H_2O_2 treatment does not induce the stringent response in *S. aureus* (278). Nevertheless, also in this study (p)ppGpp was identified as essential for the oxidative stress resistance, indicated by the high susceptibility of the (p)ppGpp^0 mutant towards H_2O_2 (278).

Transcriptome analyses by colleagues confirmed the previously reported main targets of the (p)ppGpp mediated reprogramming of cellular processes, including CodY-regulated genes, ribosomal proteins, translation elongation factors and aminoacyl-tRNA synthetases. Moreover, our analysis indicated that the (p)ppGpp^0 mutant in RPMI medium, but not in rich LB medium, might suffer from increased ROS levels. The oxidative stress response of the mutant was characterized by the strong upregulation of the PerR and sulfur stress-specific CstR regulons and the proteases and chaperones, belonging to the CtsR and HrcA regulons as well as genes for cysteine and BSH biosynthesis (303). Based on the 8 to 31-fold upregulation of *dps* and *ftnA*, the strong induction of iron-sulfur cluster biosynthesis genes, and the pronounced downregulation of the Fur-controlled iron, heme and siderophore uptake systems, the results further suggested an altered iron homeostasis. Previous studies demonstrated that RPMI medium simulates the conditions in human plasma under infection conditions characterized by high expression levels of iron-regulated genes (333). Thus, the Fur-mediated downregulation of these genes in the (p)ppGpp^0 mutant was surprising and indicative of elevated intracellular iron levels. Growth deficiencies of (p)ppGpp^0 mutants in *E. coli* and *B. suis* in minimal media, but not nutrient-rich media, were linked to the auxotrophy for certain amino acids (328, 331). However, amino acid supplementations were not sufficient to restore the growth phenotype in *B. subtilis* after nutrient starvation (334), indicating that further cellular processes are affected

by (p)ppGpp. Since I could demonstrate in Northern blot analyses that the oxidative and iron stress response of the mutant was abrogated in the (p)ppGpp complemented pCG327 strain in *S. aureus*, my further experiments were directed to investigate these observations in more detail (303).

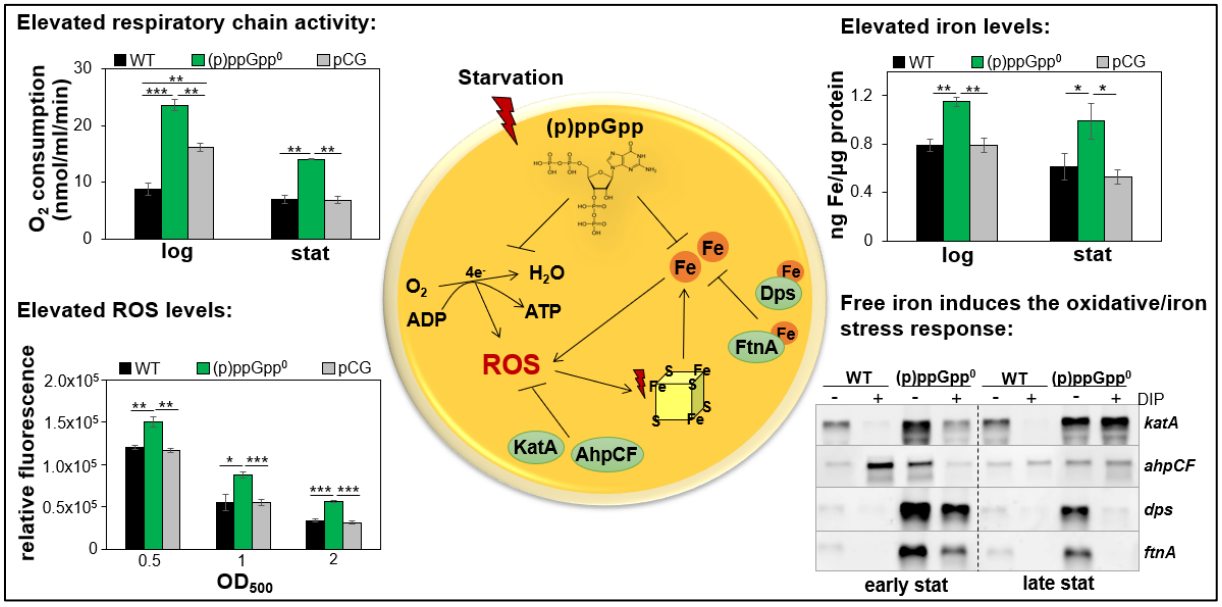

Figure 6: Intracellular (p)ppGpp levels modulate the iron and redox homeostasis in *S. aureus*. Bacterial cells lacking (p)ppGpp showed in the presence of 1 mM glucose as electron donor a higher oxygen consumption rate, indicative of an enhanced respiratory chain activity. Using the $DCFH_2$-DA assay and Northern blot analyses, it was shown, that the (p)ppGpp^0 mutant has increased intracellular ROS levels, which is accompanied by transcriptional induction of ROS detoxifying enzymes, such as *katA* and *ahpCF*. Elevated ROS levels destroy iron-sulfur clusters, increasing the labile iron pool. An elevated transcription of iron storage proteins, such as the (mini)ferritins *dps* and *ftnA,* counteracts the significantly increased intracellular iron levels in the (p)ppGpp^0 mutant compared to the wild type (WT) and the complemented strain expressing Rel_{Syn} (pCG), as determined with ICP-MS analysis. The iron-mediated Fenton reaction contributes to ROS production. Accordingly, the addition of the iron scavenger dipyridyl (DIP) reduced the transcription of *katA*, *ahpCF*, *dps* and *ftnA* in the (p)ppGpp^0 mutant. The figure is adapted from chapter 1 (303), where the experimental procedures are stated. *p<0.05; **p<0.01; ***p>0.001.

By using the $DCFH_2$-DA assay, I could demonstrate that the (p)ppGpp^0 mutant and the strain with a mutated synthetase domain in Rel (Δrel_{syn}) have significantly elevated ROS levels compared to the wild type when grown in RPMI medium **(Fig. 6)**. The determined fluorescence intensities of the mutants were similar to the ones of the strain lacking the catalase KatA ($\Delta katA$), indicating that the (p)ppGpp^0 mutant suffers from increased oxidative stress. Since we detected comparable catalase activities between the wild type and the (p)ppGpp^0 mutant but postponed detoxification of external added H_2O_2 by the (p)ppGpp^0 mutant, we proposed that the antioxidant capacity of the mutant is exhausted by the elevated intracellular ROS amounts (303). In accordance with the two- to sixfold upregulation of the *citCZ*, *sucCD* and *cydAB* operons, implicated in the TCA cycle and respiratory chain, I demonstrated that the (p)ppGpp^0 mutant has an increased oxygen consumption rate compared to the wild type and the

complemented pCG327 strain in the log and stat phase in RPMI and rich medium (303) **(Fig. 6)**. As already described, the respiratory chain represents the main source of endogenous ROS, providing a mechanistic explanation for the elevated ROS levels in the (p)ppGpp^0 mutant in *S. aureus*.

Using the ferene-s assay and in cooperation with Prof. Dr. Roland Lill by ICP-MS analysis, I could confirm the increased intracellular iron levels in the (p)ppGpp^0 mutant **(Fig. 6)**, which were suggested by our transcriptome analyses. Accordingly, the (p)ppGpp^0 mutant was more resistant to the iron scavenger dipyridyl than the wild type. Using streptonigrin, an aminoquinone antibiotic that causes DNA damage through auto-oxidation and ROS generation in the presence of free iron (335), I revealed that the (p)ppGpp^0 mutant not only shows elevated intracellular iron levels but, despite the upregulation of (mini)ferritins, possesses increased free iron levels **(Fig. 5B)**. Elevated total and labile iron levels were also detected in the Δrel_{Syn} mutant in the log and stat phase in RPMI medium. While our analyses demonstrated that *S. aureus* suffers from iron overload, which is enhanced through the addition of iron, the opposite phenomenon was observed in *E. faecalis* (303, 336). Here, the addition of $FeSO_4$ and $MnSO_4$ significantly restored the growth of the (p)ppGpp^0 mutant. It is assumed that these metals would be required as cofactors to counteract the elevated intracellular ROS levels in this strain. Similarly, the addition of various metal ions significantly improved the bacterial growth of the *S. pneumoniae* mutant lacking (p)ppGpp, which showed a growth defect in chemically defined media but not complex media (312). Further evidence of an important role of (p)ppGpp in iron homeostasis is provided by studies, which demonstrated that (p)ppGpp levels rise upon iron limitation in *E. coli* and *E. faecalis* (336, 337). While (p)ppGpp in *E. coli* was found to positively control iron-uptake systems (337), we could demonstrate in collaboration with Prof. Dr. Christiane Wolz that (p)ppGpp in *S. aureus* restricts free intracellular iron levels by down-regulation of uptake systems and induction of iron storage proteins (278, 303). Structural analyses of RelP in *S. aureus* identified two metal-binding sites at the subunit-subunit and dimer-dimer interface (265). While Fe^{3+} binding did not affect the catalytic activity, the researchers observed a biphasic response curve upon Zn^{2+} addition, characterized by an initial activity increase, followed by enzyme inhibition. It will be interesting to investigate whether these *in vitro* findings can be confirmed *in vivo* and, if thereby, RelP acts as a metal sensor to modulate the metal homeostasis in *S. aureus*.

ROS can damage iron-sulfur clusters, leading to the release of $Fe^{2+/3+}$ and an elevated labile iron pool, which can catalyze the Fenton reaction, generating even more ROS **(Fig. 6)** (219). Thus, after the addition of the iron scavenger dipyridyl, I observed a decreased

transcription of ROS detoxifying enzymes and (mini)ferritins in the (p)ppGpp^0 mutant grown in RPMI medium **(Fig. 6)**. Dipyridyl and the ROS scavenger N-acetyl cysteine also improved the growth and survival of the (p)ppGpp^0 and Δrel_{Syn} mutants significantly upon thiol stress and antibiotic treatment, as revealed in growth and survival assays. Without the addition of these compounds, the mutants were significantly more susceptible than the wild type and the pCG327 strain towards HOCl, ciprofloxacin **(Fig. 5B)**, and tetracycline, indicating that (p)ppGpp mediates stress resistance by reduction of iron-induced ROS formation. These findings might explain why we did not observe growth defects or a pronounced oxidative and iron stress response of the (p)ppGpp^0 mutant in LB medium. While in RPMI medium the amount of cysteine, GSH and other ROS scavengers is limited, rich media contain several components that react with ROS and limit the effective concentration of ROS (303).

In conclusion, our data indicate that elevated total and free iron levels, and enhanced respiratory chain activity, caused by an imbalance of the (basal) (p)ppGpp level, lead to increased ROS levels and an enhanced sensitivity towards thiol stress and antibiotics **(Fig. 5B and 6)**. Thereby, our study gave new insights into how (p)ppGpp mediates the oxidative and antibiotic stress resistance of *S. aureus*. Studies by our cooperation partner Prof. Dr. Christiane Wolz confirmed our findings. They demonstrated that increased (p)ppGpp levels indeed lead to an induction of ROS detoxifying enzymes and iron storage proteins, while iron import gets downregulated, likely to protect the bacteria from upcoming stress during infection (278). As outlined above, cumulative evidence in a variety of bacteria indicates that this functional role of (p)ppGpp might be widely conserved and necessary for the stat phase resistance and persistence against various stressors, including redox stress and antibiotics. However, further studies are required to investigate how (p)ppGpp modulates the iron and redox homeostasis in different bacteria.

Simultaneous to our study, the research group from Prof. Dr. Christiane Wolz revealed that the (mini)ferritins and genes implicated in the oxidative stress response are regulated independently from CodY. Furthermore, the (p)ppGpp-dependent transcription of *ftnA* was independent of the main regulators PerR, Fur and SarA (278). Although a direct regulatory function cannot be excluded at this stage, it is conceivable that (p)ppGpp exerts this task via crosstalk with other regulators. (p)ppGpp was shown to regulate RpoS expression and quorum sensing in Gram-negative bacteria (256, 315, 338). Additionally, a crosstalk between (p)ppGpp and the signaling nucleotide cyclic di-adenosine monophosphate (c-di-AMP), which was shown to affect the transcriptional regulation of ROS detoxifying enzymes, was noticed in *S. aureus* and other bacteria (339-341). Of note, higher ROS levels were also determined in cells with

low c-di-AMP levels (342). Thus, most likely the interactions of various signaling systems enable the adaptive adjustment of cellular processes, including ROS and iron homeostasis.

2.6 The HOCl stress response in *S. aureus* and *S. pneumoniae*

In the past, the RCS HOCl has been characterized as the most potent oxidant produced by the respiratory burst, indicating its key role in bacterial killing (54, 67, 343, 344). For example, the inactivation of the MPO increased the intracellular survival of *S. aureus* to 78%, while inhibition of the oxidative burst by diphenyleneiodonium chloride (DPI) elevated the survival of *S. aureus* only by a further 10% (345). Since MPO deficient neutrophils require up to six times longer for pathogen eradication, the MPO-mediated killing is thought to dominate during early post-phagocytosis to enable fast bacterial clearance (66, 346). Owing to its strong antibacterial and biofilm-destructive activity, HOCl represents an ingredient of several FDA-approved wound wash solutions (347-349). The identification of bacterial mechanisms to resist sublethal RCS stress could unveil new, defined targets to design drugs with fewer side effects on human cells to overcome immune deficiencies and treatment failures.

Although studies on the stress response of bacteria towards HOCl have mainly focused on *E. coli* (350-352), a few HOCl stress-specific regulons, such as HypS of *Mycobacterium smegmatis* and HypR of *B. subtilis* and *S. aureus* (353-355), were previously characterized. Except for these HOCl-stress specific defense systems, also transcription factors, primarily known for conferring ROS resistance, such as PerR, were shown to be induced by HOCl (351, 352, 355-357). Common defense strategies against sublethal HOCl concentrations include mechanisms to counteract and repair oxidative protein damage, the induction of ROS detoxifying enzymes and low molecular weight (LMW) thiols, cysteine and methionine biosynthesis genes (343, 358, 359). However, to our knowledge, the HOCl stress response has not been investigated in *S. pneumoniae*. Since *S. pneumoniae* lacks a catalase and the oxidative-stress specific PerR, SoxR and OxyR regulons but has a high H_2O_2 producing capacity (93, 360), the adaptive oxidative stress response of this Gram-positive pathogen is puzzling. Several studies were directed to resolve the resistance mechanisms against endogenous and exogenous H_2O_2 (93, 360-369). These studies characterized the iron-storage protein Dpr, ROS detoxifying enzymes, including the superoxide dismutase (SodA), thiol peroxidase (TpxD) and alkyl hydroperoxidase (AhpD), as well as the NADH oxidase (Nox), which converts O_2 to H_2O, as protective systems in *S. pneumoniae*. Additionally, the two redox sensors SifR and RitR have been characterized. While *in vitro* analyses identified SifR as a monothiol quinone sensor, the peroxide sensing transcription factor RitR was shown to repress the transcription of iron uptake

systems upon dimerization through Cys128 oxidation to intermolecular disulfides (370). However, whether SifR and RitR also function in the HOCl-stress tolerance is unresolved. Thus, the physiological stress response of *S. pneumoniae* D39 after exposure to sublethal HOCl stress, as well as the function and redox-sensing mechanism of the HOCl-sensing MerR-family regulator NmlR were subjects of my doctoral thesis **(chapter 4)**. Moreover, due to the important function of LMW thiols under oxidative stress, parts of my work addressed the role of the bacillithiol redox pathway in the oxidative stress defense of *S. aureus* **(chapter 2)**.

2.6.1 LMW thiols as defense mechanism against reactive species

Reversible protein *S*-thiolations represent an essential post-translational modification that protects thiol groups from proteins against irreversible overoxidation and functions as a redox-regulatory mechanism of transcriptional regulators and redox enzymes (103). For example, the *S*-bacillithiolation of the glyceraldehyde-3-phosphate dehydrogenase (GapDH) and the aldehyde dehydrogenase (AldA) under HOCl stress was identified as a prerequisite to reversibly regulate the functionality of these enzymes under oxidative stress in *S. aureus* (371, 372). Thereby, LMW thiols represent a crucial constituent of the oxidative stress defense **(Fig. 7)**. Despite their critical function in protein-thiol homeostasis, LMW thiols execute as thiol co-factors relevant functions in other cellular processes. The importance of LMW thiols is underlined by the finding that many bacteria encode for more than one LMW thiol and that these can substitute at least partially for each other (105, 373). In the past years, several reviews about the functions of bacterial LMW thiols, such as mycothiol (MSH), BSH and GSH and other LMW thiols, such as ergothioneine, have been published (373-383). The following section will provide a short overview of the characteristics and physiological roles of BSH and GSH as major LMW of *S. aureus* and *S. pneumoniae*, respectively.

The LMW thiol BSH is commonly used in Firmicutes as a substitute for GSH, but phylogenetic analyses indicated that BSH and its derivates, such as N-methyl-bacillithiol, are also produced in other bacterial phyla (384). The α-anomeric glycoside of L-cysteinyl-D-glucosamine with L-malate is synthesized in a three-step process involving the enzymes BshA, BshB and BshC. The intracellular BSH concentration in *S. aureus* under control conditions is dependent on the growth phase and medium and fluctuates according to the literature between 0.1 to 7.2 µmol/g dry weight (102, 385-387). Deletion of one of the three enzymes completely abolished the BSH synthesis in *S. aureus* but did not affect the intracellular cysteine level (385).

The tripeptide GSH (γ-L-glutamyl-L-cysteinyl-glycine) is the major LMW thiol in eukaryotes, Gram-negatives, and a few Gram-positive bacteria. In prokaryotes, GSH is

synthesized in a two-step process by either two enzymes or one multidomain fusion protein (103). Due to the absence of biosynthesis pathways for LMW thiols, *S. pneumoniae* was shown to rely on host-derived GSH, which is imported by the ABC transporter substrate-binding protein GshT to resist HOSCN and paraquat stress (388, 389). Interestingly, also *S. aureus* can import, probably with the ABC transporter system GisABCD, GSH and GSSG, leading to the accumulation of intracellular GSH in stat phase cells. However, the function is barely characterized and might be restricted to the exploitation of an additional sulfur source (390, 391).

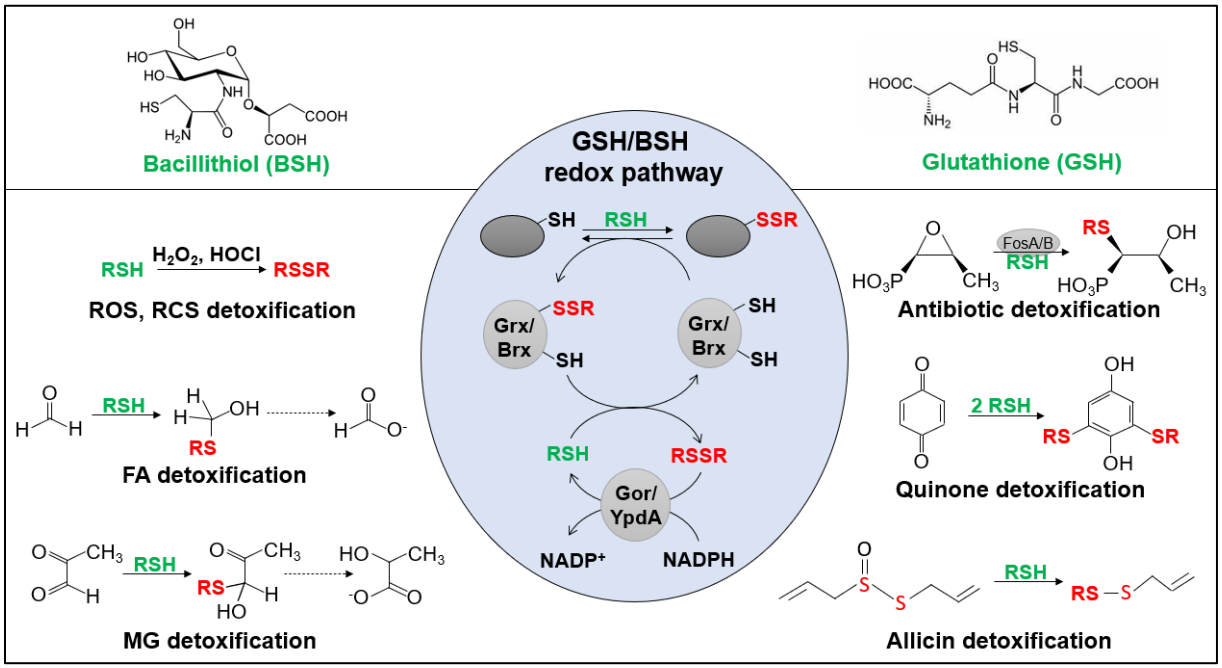

Figure 7: The LMW thiols BSH and GSH and the corresponding redox pathways maintain the bacterial redox homeostasis. GSH and BSH (referred to as RSH) are implicated in the detoxification of reactive oxygen, chlorine, electrophilic and sulfur species (ROS, RCS, RES, RSS). HOCl and H_2O_2 oxidize BSH and GSH to BSSB and GSSG (referred to as RSSR). Allicin reacts with BSH and GSH to *S*-allylmercaptobacillithiol (BSSA) and *S*-allylmercaptoglutathione (GSSA). The reaction of LMW thiols with electrophiles, such as formaldehyde (FA), methylglyoxal (MG) and benzoquinones, generates LMW-thiol adducts, which are further detoxified. The thiol *S*-transferases FosA and FosB catalyze the reaction of GSH and BSH with the epoxide antibiotic fosfomycin for its inactivation. Under oxidative stress, LMW thiols modify protein thiols by *S*-thiolations (e.g., *S*-bacillithiolation and *S*-glutathionylation). *S*-thiolated proteins are reduced by glutaredoxins (Grx) and baciliredoxins (Brx), which are regenerated by GSH and BSH, resulting in GSSG and BSSB formation. These LMW thiol disulfides are reduced by the NADPH-dependent GSSG and BSSB reductases Gor and YpdA, respectively. The figure is adapted from (103, 392) and chapter 3 (105).

While the redox potentials of the main LMW thiols are comparable, a unique characteristic of BSH compared to other LMW thiols, such as GSH, is the low thiol pK_a value of 7.97 compared to 8.93, which is attributed to the L-malate group of BSH. Consequently, at a physiological pH value, the proportion of the bacillithiolate form of BSH is higher, influencing positively thiol-disulfide exchange reactions and increasing, e. g., the reaction rate with H_2O_2 approximately 40-fold (377, 393). However, the precise thiol-disulfide exchange

reactivities depend on various factors, including the relative concentration and steric effects, and should be determined in the cellular context. Nevertheless, both LMW thiols, BSH and GSH, contribute via *S*-thiolations and as cofactors of conserved enzymes and scavengers significantly to the detoxification of ROS, RSS, RNS and RCS and the overall redox homeostasis (103) **(Fig. 7)**. The protective capacity of BSH in *S. aureus* against HOCl stress is emphasized by the finding that the intracellular BSH level decreased five- to sixfold and that the transcription of the BSH synthesis genes upon exposure to a sublethal concentration was increased (102, 355). Recently, the reaction of BSH with HOCl was reported to represent quasi a diffusion-controlled reaction with a second-order rate constant of 6×10^{7} $M^{-1}s^{-1}$ (394). Based on their chemical structure, both LMW thiols can be regarded as cysteine storage, thereby preventing the ROS generation through auto-oxidation of cysteines (376, 377). Additionally, BSH and GSH can form in an enzyme-dependent or independent way *S*-conjugates with various RES, including quinones, xenobiotics, and antibiotics (379, 385, 395-399), leading to their detoxification **(Fig. 7)**. In *S. aureus*, the BSH-dependent (thiol-)*S*-transferases FosB and BstA were shown to be required for the inactivation of the antibiotics fosfomycin and cerulenin, respectively (400, 401). The spontaneous reactions of GSH and BSH with MG and FA generate an LMW-thiol-hemithioacetal adduct and *S*-hydroxymethyl-LMW-thiol, respectively, which represent the substrates for aldehyde detoxification pathways in various bacteria (124, 375, 379, 402-405). While in *S. pneumoniae* the class III alcohol dehydrogenase AdhC was suggested to be implicated in the detoxification of these glutathione-aldehyde adducts, BSH-dependent MG detoxification pathways in *S. aureus* are still unidentified (105, 406).

GSH and BSH increase the bacterial tolerance towards different metal ions, including Zn^{2+}, Fe^{2+}, and Cu^{2+}, either through direct coordination of metal ions via different functional groups or crosstalk with other regulatory systems involved in the metal homeostasis (388, 407-409). Additionally, GSH and BSH might aid in the iron-sulfur cluster biosynthesis by acting alone or in conjunction with other proteins as iron-sulfur cluster carriers (407, 410-412). Due to the diversity of biological functions, BSH and GSH are essential for the virulence and survival of *S. aureus* and *S. pneumoniae* under infections (376, 381, 391, 413). However, the relative importance of BSH might be strain dependent and can be diminished by other (virulence) factors (386).

2.6.2 Reduction of *S*-thiolated proteins and LMW thiol disulfides

To recycle LMW thiols and restore the functionality of *S*-thiolated proteins, bacteria encode for different cellular redox couples that are connected to essential redox pathways. In Gram-

negative bacteria, glutaredoxins (Grx) catalyze the reduction of *S*-glutathionylated proteins and protein disulfides via thiol-disulfide exchange reaction at the expense of GSH **(Fig. 7)**. Thereby, it can be structurally distinguished between dithiol and monothiol Grx, characterized by a thioredoxin (Trx) fold and a CXXC or CXXS motif, respectively (414, 415). While monothiol Grx reduces *S*-glutathionylated proteins through a double displacement reaction, the dithiol oxidoreductases reduce additionally protein disulfides (410). However, studies in yeast demonstrated that also monothiol Grx can catalyze the reduction of disulfide bonds (416). The *S*-glutathionylated Grx (Grx-SSG) is recycled using a second GSH molecule, leading to GSSG, which is reduced by the NADPH-dependent glutathione reductase Gor **(Fig. 7)**. The catalyzed reaction of Gor occurs via a reductive and oxidative half-reaction. First, electrons are transferred from NADPH via the flavin to the proximal cysteine, leading to the protonation of the active site cysteine. In the oxidative half-reaction, a nucleophilic attack of the active site cysteine on bound GSSG finally leads to the regeneration of two GSH molecules (375). *S. pneumoniae* lacks Grx homologs but encodes for the flavoenzyme Gor, which was biochemically characterized and structurally resolved (388, 417). In contempt of high structural similarities with other bacterial Gor, including the NADPH and FAD binding domains with the Rossmann folds, the redox-active cysteines (Cys41 and Cys46) and the dimerization domain, the pneumococcal Gor shows a 3.5-fold weaker affinity for GSSG than the Gor of *E. coli*. The other kinetic parameters of the GSH reductase activity, such as the affinity to NADPH and the maximum velocity of the reaction, were comparable with other Gor homologs (417). Further studies are required to determine the molecular factors contributing to the observed GSSG affinity differences and the physiological implications.

In *S. aureus*, the bacilliredoxins BrxA and BrxB were identified as Trx-like proteins with CGC active sites, while the monothiol BrxC protein contains a TCPIS active motif and resembles the monothiol Grx (374). The three Brx proteins were proposed to function in de-bacillithiolation. In *S. aureus*, BrxA was demonstrated to catalyze the transfer of BSH from the *S*-bacillithiolated protein to its active site Cys54, leading to the Brx-SSB intermediate (371). This was confirmed by crystal structure analyses (418). Similarly, BrxA and BrxB were revealed to function in the de-bacillithiolation of proteins in *B. subtilis* (419) **(Fig. 7)**. Furthermore, the NADPH-dependent flavin disulfide reductase YpdA (Bdr) was proposed as a putative bacillithiol disulfide (BSSB) reductase, which catalyzes analog to Gor the regeneration of the LMW thiol (103, 420). Transcriptome analyses demonstrated that BSH biosynthesis genes as well as *brxA/B* and *ypdA* are upregulated upon various thiol-stress conditions.

However, since experimental evidence for the suggested function of YpdA was missing, our group analyzed the BrxAB/BSH/YpdA/NADPH pathway in more detail (102).

Within my doctoral thesis **(chapter 2)**, I could confirm that the transcription of *brxA*, *brxB* and *ypdA* is induced by HOCl and diamide stress (102). Additionally, they were transcribed under control conditions at a relatively high basal level and appeared to be co-regulated under various stress conditions, pointing towards a common role within one pathway. Biochemical characterizations by colleagues further revealed that the Δ*ypdA* deletion mutant is significantly impaired in its BSH redox balance under control conditions and its ability to regenerate the reduced BSH redox potential under oxidative stress. YpdA was shown to have a strong selectivity for BSSB compared to other LMW thiol disulfides and to act in concert with BrxA and BSH within the BrxA/BSH/YpdA/NADPH redox cycle to restore the redox homeostasis *in vitro* **(Fig. 7)**. Follow-up studies of our group revealed that this pathway also provides protection against allicin by mediating the regeneration of *S*-thioallylated proteins, whereby YpdA catalyzes the regeneration of BSH from *S*-allylmercaptobacillithiol (BSSA) (202). My further work was themed to characterize the role of BrxA, BrxB and YpdA in the oxidative stress defense of *S. aureus in vivo* (102). Together with Dr. Nico Linzner, I could demonstrate that BrxA and YpdA significantly contribute to the stress resistance against HOCl and H_2O_2. In contrast, the complementation of the Δ*brxAB* mutant with *brxB* did not restore the growth and survival rate of the mutant back to the wild type levels in phenotype analyses, indicating that BrxB is probably not essential for the de-bacillithiolation of proteins. Dr. Nico Linzner and Dr. Vu Van Loi could confirm these findings under infection conditions using the murine macrophage cell line J-774A.1. However, follow-up studies of our group demonstrated that BrxA and BrxB catalyze the reduction of *S*-thioallylations under allicin stress (202), indicating functional differences. Importantly, using survival assays, we demonstrated that the Δ*brxAB*Δ*ypdA* triple mutant is as sensitive as the Δ*brxAB* double mutant, suggesting that, in accordance with our other results, BrxA and YpdA function in the same pathway (102) **(chapter 2)**.

In addition, the function of YpdA as BSSB reductase was characterized by the group of Ambrose Cheung in another *S. aureus* strain *in vivo* (387). In agreement with our data, they demonstrated that the expression of *ypdA* is induced upon thiol stress and that the Δ*ypdA* mutant has a significant fitness defect compared to the wild type in a chemically defined medium. By regulating the intracellular BSH/BSSB ratio, YpdA was shown to contribute to the resistance of *S. aureus* against oxidants encountered *in vitro* and during polymorphonuclear leukocyte infections.

In summary, these results established the functionality of the BrxA/BSH/YpdA/NADPH redox pathway **(Fig. 7)** and demonstrated the importance of this pathway under different thiol-stress conditions in *S. aureus*. Since our publication, the BSSB reductase activity of the YpdA homolog in *Bacillus cereus* was also demonstrated and based on the crystal structure, the following catalytic mechanism was suggested (421). Distinct from other flavoprotein disulfide reductases, Cys14 of YpdA was proposed to be not substrate-accessible and positioned 8 Å away from the FAD isoalloxazine ring. BSSB binding was suggested to be mediated by an amino acid gating mechanism, leading to the reduction of BSSB through a thiol-thiolate-pair FAD C4a-cysteine adduct intermediate (421). However, since the structure was resolved in the absence of BSSB as the substrate, this model needs to be validated by further studies. In previous redox proteomics results, the conserved Cys14 was identified as *S*-bacillithiolated upon HOCl stress *in vivo* (371), further supporting its functions in the catalysis of BSSB reduction *in vivo* along with our *in vitro* results. YpdA of *B. subtilis* was also proposed to function as NADPH-dependent bacilliredoxin rather than a BSSB reductase (422). In addition, BrxC of *B. subtilis* was shown to contribute together with YpdA, BrxA and BrxB to the de-bacillithiolation of proteins (422). The redundancy and cross-talk within this pathway also have to be examined as a further research subject (415). Despite the important role of the Brx/BSH/YpdA/NADPH pathway for the oxidative stress resistance in *S. aureus*, alternative LMW thiols, such as coenzyme A (CoASH), might also contribute to the redox homeostasis (386). CoASH is known as an essential thiol cofactor for various metabolic pathways, and numerous proteins were post-translationally modified by *S*-CoAlations upon oxidative stress in *S. aureus*. Consequently, it was suggested that CoASH might substitute for BSH in *S. aureus* (391, 423). Therefore it will be necessary to investigate the interplay and compensatory functions in more detail and to consider potential drug targets and treatment regimens not only in isolation (13) **(chapter 9)**.

2.6.3 The HOCl stress transcriptome signature in *S. pneumoniae*

This part of my thesis aimed to investigate the effect of HOCl on *S. pneumoniae* and to identify potential resistance mechanisms **(chapter 4)** (424). The evaluation of the RNA-seq transcriptome analyses, which I performed in cooperation with Dr. Tobias Busche, uncovered the significant up- and downregulation of 296 and 306 genes, respectively, in response to HOCl stress (424). In general, the transcriptome signature revealed the strong upregulation of the NmlR, SifR, CtsR, HrcA, SczA and CopY regulons and the CTM electron complex, indicating an oxidative, electrophile and metal stress response in *S. pneumoniae* (424) **(Fig. 8)**. This HOCl

stress response is consistent with previous observations in other Gram-positive bacteria, including *S. aureus* (356, 425, 426). Interestingly, similar to *S. aureus* and *P. aeruginosa* (355, 427), we also noted an upregulation of various virulence factors, including PavB in *S. pneumoniae* **(Fig. 8)**. While comparable studies in *S. pneumoniae* are missing, in *S. aureus,* the global virulence regulators MgrA and SarZ were shown to respond to redox stress by a thiol-switch mechanism (105, 428). Thus, the increased expression of virulence factors upon exposure to oxidative stress in different human pathogens is probably reflecting the evolutionary adaptation to the immune system.

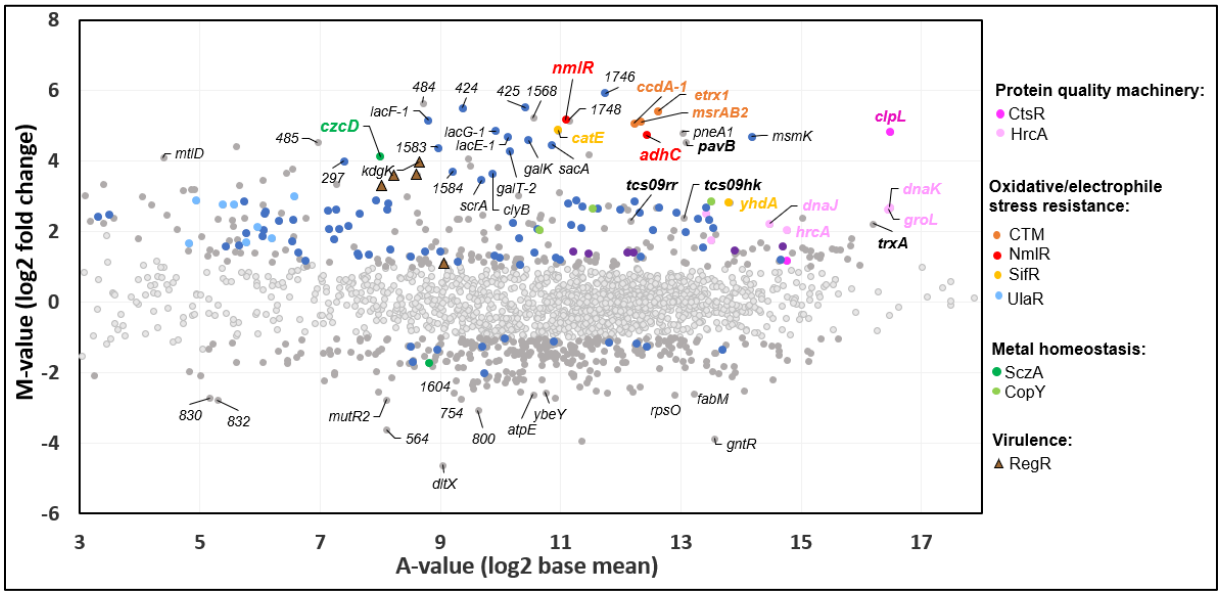

Figure 8: Hypochlorous acid (HOCl) induces an oxidative, electrophile and metal stress response in *S. pneumoniae.* The gene expression profile of our RNA-seq transcriptome analyses is shown as a ratio/intensity scatterplot (M/A-plot), which is based on the differential gene expression reported in (424). Genes belonging to the CtsR, HrcA, NmlR, SifR, SczA and CopY regulons were most strongly induced (M-value ≥1; $p \leq 0.05$). Together with the induction of the CTM operon and the thioredoxin TrxA, functioning in the reduction of oxidized proteins, this transcriptome profile is indicative of protein damage, oxidative, electrophile and metal stress upon HOCl exposure. HOCl also caused the induction of several regulons involved in the catabolism of alternative carbohydrates (denoted in dark blue), including UlaR (light blue). Furthermore, virulence genes, including the pneumococcal adherence and virulence factor B *pavB* and the RegR regulon, were upregulated. A more detailed regulon annotation and the complete transcriptome data are presented in chapter 4 (424).

The oxidation of protein thiol groups, associated with protein unfolding and aggregation is a well-characterized killing mechanism of HOCl (69, 429). Accordingly, Clp proteases and ATP-dependent chaperones, belonging to the CtsR and HrcA regulons, for protein (re)folding and degradation were strongly upregulated upon HOCl stress in *S. pneumoniae* (360, 369, 424). Also, the genes coding for the cytoplasmic thioredoxin/thioredoxin reductase system TrxA/B and the CTM electron complex (CcdA1, Etrx1, MsrAB2), implicated in the reduction of cytoplasmic oxidized protein thiols and methionine residues of oxidized surface proteins, respectively, were highly induced (430-432). Moreover, several metal ion transporters were

differently transcribed after exposure to HOCl stress (424). These transcriptional changes might be induced to counteract the deleterious effects of Fe^{2+} during HOCl stress and could be related to the HOCl-induced oxidative damage of metalloproteins and metalloregulators, such as CopY (433).

Consistent with the previously reported protective function under oxidative stress, we noted an elevated transcription of the GSH importer gene *gshT* and the two-component system 09 (388, 389, 434). Moreover, the transcription of genes involved in the transport and utilization of alternative carbohydrates, including ascorbic acid, was enhanced after HOCl addition (435) **(Fig. 8)**. Ascorbic acid was shown to act as a ROS scavenger and thereby contribute to the adaptive oxidative stress response (109, 436, 437). Other ROS detoxifying enzymes and reducing systems, such as SodA, TpxD, Nox, and Gor, were not differentially expressed or even downregulated upon HOCl stress (424). These results indicate profound differences in the pneumococcal stress response towards ROS, such as H_2O_2, and RCS, like HOCl. This result probably reflects, at least partially, the prevalence of different chemical reactions exerted by these reactive species (438). For example, the reaction of high HOCl levels with the LMW thiol GSH results mainly in the formation of glutathione sulfonamide instead of GSSG, the substrate for Gor (71, 439). Transcriptional differences and strong distinctions in the redox proteome after exposure to HOCl and H_2O_2 were also observed in *S. aureus* and other bacteria (440-444), highlighting the importance of systematic investigation of stress-specific adaptation strategies. In addition, we observed a strong upregulation of the quinone-responsive SifR regulon and the aldehyde stress-specific NmlR regulon (142, 406, 445). SifR and NmlR harbor redox-sensitive Cys residues and might respond to HOCl via thiol switches, which has not been investigated thus far. Since the *nmlR* and *adhC* genes were 36-fold and 26.5-fold induced by HOCl, the NmlR regulon was characterized concerning its function and HOCl-sensing mechanism.

2.6.4 The MerR-family regulator NmlR of *S. pneumoniae*

The MerR-family comprises a diverse class of transcriptional regulators that are widely distributed across different bacterial genera and modulate transcription in response to a variety of environmental stimuli, such as metal ions and antibiotics (446, 447). They bind to palindromic repeats in promoters, characterized by an extended spacing between the -35 and -10 RNA polymerase recognition elements (446). This expanded distance of 19±1 bp instead of the optimal 17±1 bp increases the phase angle between the promoter elements by 72° around the helix axis, preventing optimal promoter recognition (448). A ligand-induced switch of the

MerR-family regulator from the repressor to the activator conformation at the opposite DNA face mediates the required DNA distortion, leading to a realignment of the promoter elements on the same phase plane and transcriptional initiation **(Fig. 9A)** (446, 448-455).

MerR regulators are characterized by conserved structural features, namely the N-terminal winged helix-turn-helix (wHTH) DNA-binding domain, the central antiparallel coiled-coil dimerization domain, and the variable C-terminal ligand-binding domain, which is significantly elongated in members of the multidrug-resistance MerR-subfamily (447, 448, 451). Further subfamilies represent the metal- and the redox-responsive MerR-family transcription factors (448, 456). The first well-characterized MerR-type redox-sensitive regulator is SoxR of *E. coli*, which uses iron-sulfur clusters to sense superoxide and nitrosative stress (446, 457, 458). Protection against oxidative stress, exerted by H_2O_2 and diamide, was also reported for the MerR-family regulators NmlR from *Listeria monocytogenes* and *Neisseria gonorrhoeae* (459, 460). Although the precise regulatory mechanism of NmlR from *N. gonorrhoeae* has not been elucidated, it was proposed that Zn^{2+}-binding by four cysteine residues is involved in the transcriptional regulation (460). In contrast, a metal-independent post-translational modification, such as thiol-(*S*)-alkylation or *S*-nitrosation, of the conserved cysteine residue was suggested as activation mechanism for NmlR of *Haemophilus influenzae* and AdhR of *B. subtilis* (124, 450). Both regulators sense carbonyls and control the expression of genes involved in the thiol-dependent detoxification of aldehydes.

The MerR-family transcriptional regulator NmlR of *S. pneumoniae* shows 44.4% sequence identity to AdhR and activates the transcription of the *nmlR-adhC* operon in response to the aldehydes MG and formaldehyde as well as GSNO (406, 415). Using qRT-PCR analyses, I demonstrated that NmlR responds not only to aldehydes but also to oxidants, such as HOCl, H_2O_2 and diamide (424) **(Fig. 9B) (chapter 4)**. Contradicting the previous annotation of NmlR as a ·NO sensor (445), we observed a <2-fold induction of the *adhC* transcription in the presence of the ·NO donor DEA NONOate (424). This finding suggests that NmlR might not act as a general sensor for RNS but is specific for GSNO. Consistent with our transcriptional analyses, the Δ*nmlR* mutant was sensitive to HOCl and H_2O_2 treatment and significantly impaired in human macrophage infection assays compared to the wild type **(Fig. 9C,D)**. This decreased survival was not attributable to increased phagocytosis rates or differences in adherence (424, 445). Instead, by inhibiting NOX2 and iNOS with DPI (461-463), I could show that the NmlR regulon contributes to the intracellular survival in human macrophages by protecting *S. pneumoniae* against the oxidative burst. Previous studies also identified NmlR as

essential for the colonization and systemic virulence in a murine infection model (445, 464), underscoring the important function of this regulon during host-pathogen interactions.

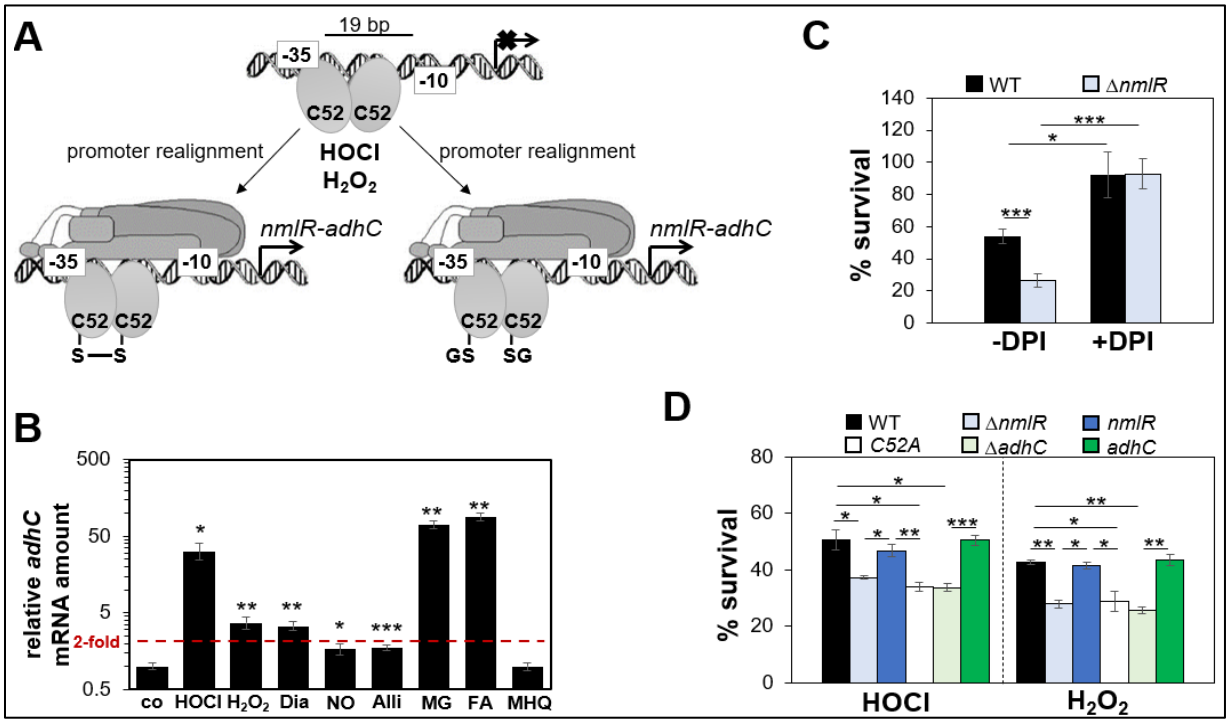

Figure 9: The NmlR regulon protects *S. pneumoniae* against oxidative stress. (A) The transcription factor NmlR binds under control conditions to the 9-9 bp palindromic operator sequence, inhibiting the transcription of the *nmlR-adhC* operon. Upon oxidative stress, the NmlR regulator is *S*-glutathionylated at the conserved Cys52 or forms an intermolecular disulfide. These thiol switches induce a conformational change, which is accompanied by a realignment of the -35 and -10 promoter elements and the transcription of the NmlR regulon from the opposite DNA face. (**B**) A qRT-PCR analysis demonstrated that the NmlR regulon is most strongly induced by aldehydes, such as methylglyoxal (MG) and formaldehyde (FA), and the strong oxidant HOCl. While H_2O_2 and diamide (Dia) cause a more than 2-fold upregulation, the ·NO donor DEA NONOate, allicin (Alli) and methylhydroquinone (MHQ) induce the *adhC* transcription only slightly. (**C**) The NmlR regulon confers resistance against the oxidative burst of the human macrophage cell line THP-1A, as revealed by the addition of the flavoprotein inhibitor diphenyleneiodonium chloride (DPI). (**D**) Survival assays were performed for the *S. pneumoniae* D39 wild type (WT), the Δ*nmlR* and Δ*adhC* deletion mutants and the *nmlR*, *adhC* and *nmlRC52S* complemented strains, showing that the NmlR regulon contributes to the HOCl and H_2O_2 stress resistance. The figure is adapted from (446) and chapter 4 (424), where the experimental procedures are stated. *$p \leq 0.05$, **$p \leq 0.01$ and ***$p \leq 0.001$.

NmlR was shown to solely regulate the *nmlR-adhC* operon (445), recognizing the Zn^{2+}-containing class III alcohol-dehydrogenase AdhC as a major HOCl-defense mechanism of *S. pneumoniae*. Using phenotype analyses, I could confirm that the Δ*adhC* mutant is strongly impaired in its resistance against HOCl and H_2O_2 stress compared to the wild type and the complemented strain. The widespread class III alcohol-dehydrogenase enzymes belong to the medium-chain dehydrogenase/reductase (MDR)-alcohol dehydrogenase (ADH) family and represent important constituents of detoxification and GSH recycling pathways in bacteria (405, 465). It was shown that AdhC homologs have different substrate specificities, leading to different susceptibilities profiles of the Δ*adhC* mutants in *Neisseria meningitidis* and *H. influenzae* (465-467). While class III alcohol-dehydrogenase enzymes have been shown to

catalyze reactions with ω-hydroxy fatty acids, aldehydes, medium-chain alcohols, GSNO and *S*-hydroxymethylglutathione, the detoxification of ROS or the conversion of GSSG to GSH, is not reported for this enzyme class (405). However, oxidants can react with various cellular components, triggering reaction cascades that ultimately lead to the generation of toxic electrophiles, including aldehydes (116-122). Accordingly, we have previously demonstrated that the aldehyde detoxifying enzyme AldA contributes to the HOCl resistance of *S. aureus* (372). Since the Δ*adhC* mutant in *S. pneumoniae* was reported to be as susceptible as the wild type towards MG and formaldehyde stress (406), further studies are required to identify the physiological substrate of AdhC under carbonyl and oxidative stress in *S. pneumoniae*.

Although *S*-nitrosation of NmlR was detected upon GSNO exposure in *in vitro* studies (468), the precise sensing and regulatory mechanism of NmlR remained largely unexplored or ambiguous. While Stroeher *et al*. (2007) characterized NmlR as a "classical" activator, Potter *et al*. (2010) reported that NmlR acts as a repressor and activator under control and stress conditions, respectively. Consistent with the proposed model for MerR-family regulators, I revealed by EMSAs that NmlR binds under reducing and oxidizing conditions specifically to the 9-9 bp palindromic operator sequence CTTGGAGTC-aACTCaAAG (424). Using qRT-PCR to analyze the *adhC* transcription in the wild type, the Δ*nmlR* mutant and the *nmlR* complemented strain, I could show that NmlR activates the *adhC* transcription upon HOCl stress. I could further demonstrate a higher basal *adhC* transcription in the Δ*nmlR* mutant compared to the WT, suggesting that NmlR might act as a repressor under control conditions **(chapter 4)**. Albeit systematic examinations are missing, research on *E. coli* suggested that the repressor phenotype might be caused by the high constitutive activity of the promoter independent of the -35 sequence in the absence of the transcription factor. Only upon MerR binding, this sequence motif would become important for transcription initiation (469). In cooperation with Dr. Nelly Said and Prof. Dr. Markus Wahl, the broccoli-FLAP assay was used to further analyze the *in vitro* transcription with purified NmlR (424, 470). While reduced NmlR repressed the high basal transcription rate of the RNA polymerase at the *nmlR* promoter *in vitro*, oxidized NmlR at least slightly enhanced the transcriptional initiation efficiency, although not statistically significant (424).

Using mutational analysis, I addressed the regulatory mechanism of NmlR in more detail. While the conserved single Cys52 is dispensable for DNA-binding activity *in vitro,* it is important for the redox-sensing mechanism of NmlR and thus for the oxidative stress resistance against H_2O_2 and HOCl *in vivo*. With non-reducing SDS-PAGE analyses and, in cooperation with Dr. Christoph Weise, by matrix-assisted laser desorption ionization-time of flight-mass

spectrometry (MALDI-TOF-MS), I further demonstrated that NmlR is reversibly oxidized by diamide, H_2O_2 and HOCl to Cys52-Cys52' intermolecular disulfides. In the presence of GSH, a proportion of the protein was *S*-glutathionylated, indicating that NmlR senses oxidants by two reversible thiol switches *in vitro* **(Fig. 9A)**. Our ongoing studies are directed to identify through redox-proteomics further redox-sensitive proteins and to determine the extent of different post-translational modifications, such as *S*-glutathionylation and reversible thiol oxidation, and their impact on the gene expression of *S. pneumoniae in vivo*.

Overall, NmlR acts as a major redox-sensing transcriptional regulator of the oxidative and electrophile stress defense in *S. pneumoniae* (406, 415, 424). Similarly, the aldehyde-sensing AdhR regulon of *B. subtilis* was also induced by HOCl stress (356), suggesting that the redox-sensing Cys residue of the MerR/NmlR-family might also respond to oxidative stress in other Firmicutes. Probably due to the tight interconnection of ROS/RCS and RES, several RCS-responsive regulators were found to also sense RES, and to regulate corresponding electrophile-detoxification pathways (343). For example, NemR is regulated by electrophiles through intermolecular disulfide bond formation at Cys21 and Cys116 as well as by reversible HOCl-mediated thiol modification of Cys106, leading to the transcription of the primary MG-detoxifying and the electrophile degrading enzymes *gloA* and *nemA* (351, 471).

2.7 The quinone stress response in Firmicutes

Quinones arouse attention as essential constituents of the electron transport chain, and subsequently, several studies investigated their biosynthesis, properties, and functionality as electron carriers (472, 473). Additionally, different bacteria exploit (the redox state of) quinones inter alia as signal for environmental cues, to modify their membrane fluidity, and as antimicrobials (126, 134, 473, 474). For example, *S. aureus* uses the two-component system SrrAB/SrhSR to adapt to different oxygen levels, ranging from approximately 20% O_2 on the skin and the nasopharyngeal mucus layer to almost anaerobic conditions in the blood (360). Redox-active cysteine residues of the transmembrane histidine kinase SrrB respond to the redox state of the menaquinone pool, affecting the phosphorylation state and hence DNA binding activity of the cognate response regulator SrrA **(chapter 3)** (105, 475). Since reactive species, such as ·NO, can interfere with the redox state of the quinone pool, e.g., by inactivation of heme-containing cytochromes, SrrAB also represents an indirect sensor of elevated reactive species levels (476, 477) and contributes to the nitrosative and oxidative stress resistance (478-482).

Biochemical studies established that quinones can be enzymatically detoxified, either by an oxygen-dependent ring-cleavage or the one- and two-electron reduction pathways **(Fig. 10)**. The ring opening is catalyzed by cofactor-independent dioxygenases belonging to the α/β hydrolase fold superfamily and by metalloenzymes (483-487). Metal-dependent dioxygenases are categorized, depending on the cleavage site at the aromatic ring structure, in intradiol and extradiol dioxygenases, which cleave ortho and meta to the hydroxyl substituents, respectively (488, 489). The enzymatic NAD(P)H-dependent two-electron reduction of quinones is catalyzed by quinone oxidoreductases, nitroreductases and azoreductases, leading in most cases to the formation of the more redox-stable and less cytotoxic hydroquinones as an important quinone detoxification mechanism (490-494). However, the two-electron reduction can also give rise to toxic redox-labile and alkylating hydroquinones, indicating that the success of this reaction is highly dependent on the quinone species (172, 495). Some quinone oxidoreductases, such as QorA from *S. aureus*, also mediate the one-electron reduction, which leads via the semiquinone radical to ROS formation (496). However, whether the one-electron reduction indeed acts as a mediator of high ROS production or mainly leads to the accumulation of the reduced quinone depends on the redox potential of the quinone. Despite their role in quinone detoxification, oxidoreductases and azoreductases might also function in cell signaling by modifying the intracellular quinone redox state (492).

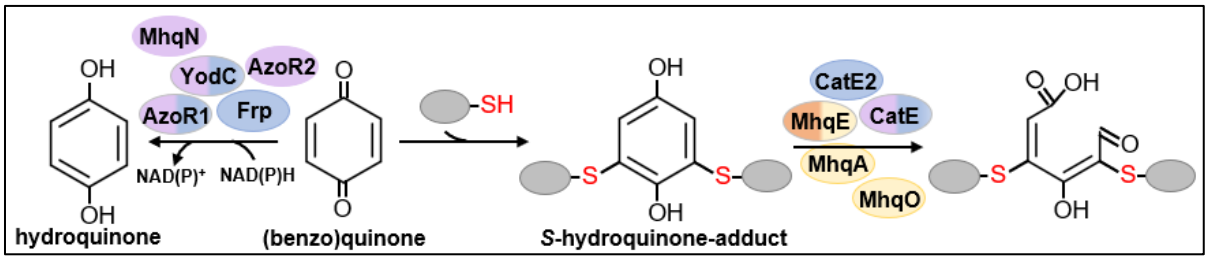

Figure 10: Quinone detoxification in *B. subtilis* and *S. aureus* is mediated by enzymes of the quinone stress-specific MhqR and YodB/QsrR regulons. Enzymes of the MhqR and YodB regulons of *B. subtilis* are colored in yellow and purple, while members of the MhqR and QsrR regulons of *S. aureus* are shown in orange and blue, respectively. The dioxygenases CatE, CatE2, MhqA, MhqE, and MhqO are proposed to catalyze the ring-cleavage of hydroquinones and *S*-hydroquinone-adducts. The two-electron reduction of quinones to the more redox-stable hydroquinone is probably mediated by the azoreductases AzoR1 and AzoR2, the nitroreductases MhqN and YodC, and the oxidoreductase Frp in both bacteria. The figure is adapted from chapter 6 (163).

Global analyses and detailed characterization of resistance mechanisms towards aromatic compounds, such as phenol, catechol, and MHQ, in *B. subtilis* gave first discernments into the bacterial sensing and adaptation strategies to counteract their antimicrobial activity (497). However, although quinones are widely distributed in our environment and pathogens are likely to encounter quinone-like compounds during infections (126, 129-134), in-depth studies on the quinone stress response in pathogenic bacteria are largely missing (473, 498-

501). My doctoral thesis was directed to fill this knowledge gap by studying the quinone stress response of *S. aureus.* This was complemented by the functional and mechanistic characterization of the redox-sensing regulators MhqR, QsrR and GbaA, which were induced to different extents by quinones and other thiol-reactive compounds in *S. aureus* **(chapter 5-8)**.

2.7.1 The quinone-sensing regulators MhqR and YodB of *B. subtilis*

Regulators belonging to the family of multiple antibiotics resistance regulators (MarR) are characterized by a wHTH DNA binding motif. They function in virulence regulation and protection of bacteria against antibiotics, aromatic compounds, organic solvents, ROS, and RES (502, 503). In *B. subtilis*, the MarR-type repressor MhqR was shown to negatively control the expression of the *mhqA*, *azoR2, mhqED* and *mhqNOP* genes and operons. These genes encode for the ring cleavage dioxygenases (MhqA/E/O), the putative azoreductase AzoR2 and nitroreductases (YodC, MhqN) **(Fig. 10)**, which confer resistance against MHQ and catechol but not MG and H_2O_2 stress in *B. subtilis* (504, 505). However, the regulatory mechanism and the structural changes of MhqR upon quinone exposure have not been resolved yet. A thiol-based quinone sensing mechanism by the non-conserved Cys128 could be excluded already (504).

The MarR/DUF24-family repressor YodB autoregulates its expression and controls the transcription of genes encoding a nitroreductase (YodC), an azoreductase (AzoR1) and the redox-sensing regulatory Spx protein (506-508). Thus, the YodB and MhqR regulons control paralogous azoreductases (AzoR1 and AzoR2), which confer resistance to catechol, MHQ and the azocompound diamide (507). YodB was shown to sense quinones and diamide by the intermolecular disulfide formation between Cys6 and one of the non-conserved Cys101' and Cys108' residues of opposing subunits *in vivo*, while the *S*-alkylation of Cys6 by quinones was only identified *in vitro* (507, 508). The intersubunit disulfide formation by diamide was shown to cause, via the reorientation of one monomer, large structural rearrangement, and translocation of the α4 and α4′ helices by 37 Å and 56°. In contrast, the *S*-alkylation at Cys6 is associated with only minor structural changes of YodB, involving a 3 Å movement and 10° rotation of the DNA recognition helices *α*4 and *α*4′ towards each other. Despite the induction of distinct conformational changes of YodB, both post-translational modifications lead to YodB inactivation (509).

MHQ and catechol further up-regulate the transcription of the *catDE* operon, encoding for an oxidoreductase and dioxygenase (505). This operon is controlled by the iron-sensing Fur repressor and the two MarR/DUF24-family repressors YodB and CatR in *B. subtilis* (510, 511).

CatR senses the oxidative mode of quinones by intermolecular disulfide formation between the conserved Cys7 residues of opposing subunits, as shown *in vivo* (510). Since CatE and CatD protect *B. subtilis* not only against exogenously encountered MHQ and catechol stress but also against the degradation products of the catecholate siderophore bacillibactin, the CatR regulon shows a high functional similarity to the SifR regulon of *S. pneumoniae* (142, 505, 511). The SifR regulon encodes inter alia for the Fe^{2+}-dependent catechol-2,3-dioxygenase CatE, the NAD(P)H-dependent quinone reductase YwnB and the NAD(P)H-flavin dependent Fe^{3+}-reductase YhdA, which are implicated in quinone detoxification and processing of Fe^{3+}-catecholate complexes for Fe^{2+} acquisition (142).

Importantly, the CatR, YodB, and MhqR regulons contribute in an additive fashion to the quinone stress resistance of *B. subtilis* (507, 510). However, the regulatory crosstalk between the MhqR and YodB regulons upon thiol stress requires further mechanistic investigations (504, 505).

2.7.2 The mode of action of MHQ and lapachol in *S. aureus*

Structural differences are thought to account for variations in the antimicrobial efficiency and primary mode of action of different quinones (126, 128, 512). However, common parameters to quantitatively describe the structure-toxicity relationship are insufficient to predict the efficiency of quinones, which act via the oxidative and electrophilic modes (170). Previous comparisons of 5-amino-8-hydroxy-1,4-naphthoquinone and the corresponding unsubstituted 1,4-naphthoquinone suggested that the toxicity of quinones decreases with the number of substituted positions (513). This activity decline is probably attributed to the abolished ability of quinones to form *S*-adducts with protein thiols in the absence of unsubstituted positions adjacent to the keto groups of the quinone rings (170, 512, 514). However, detailed analyses revealed that certain quinones have additional, unpredicted modes of action, which affect their toxicity *in vivo*. For example, the 9,10-phenanthrenequinone, which was expected to only act as a redox-cycling agent, was shown to be effective even under anaerobic conditions (169). This ROS-independent antimicrobial activity is attributed to the formation of thiohemiketals at the NAD^+ binding site of the glyceraldehyde 3-phosphate dehydrogenase (515). Although the 2-hydroxy-3-(3-methyl-2-butenyl)-1,4-naphthoquinone lapachol is used since ancient times to cure various diseases in several countries of South America and was proposed more recently as topical wound treatment, due to its antimicrobial activity (135, 516), the principle of operation in bacteria is insufficiently solved. Based on its chemical structure **(Fig. 12A)**, lapachol should be unable to function as an electrophile. *In vitro* studies provided evidence that lapachol can

redox cycle (517, 518), which could account for its microbicidal effect *in vivo*. As part of my doctoral thesis, I investigated together with Dr. Nico Linzner the mode of action of lapachol in *S. aureus* **(chapter 5)**. Additionally, I analyzed the resistance mechanisms of *S. aureus* against lapachol and the hydroquinone MHQ **(chapters 5-7)** (85, 163, 519).

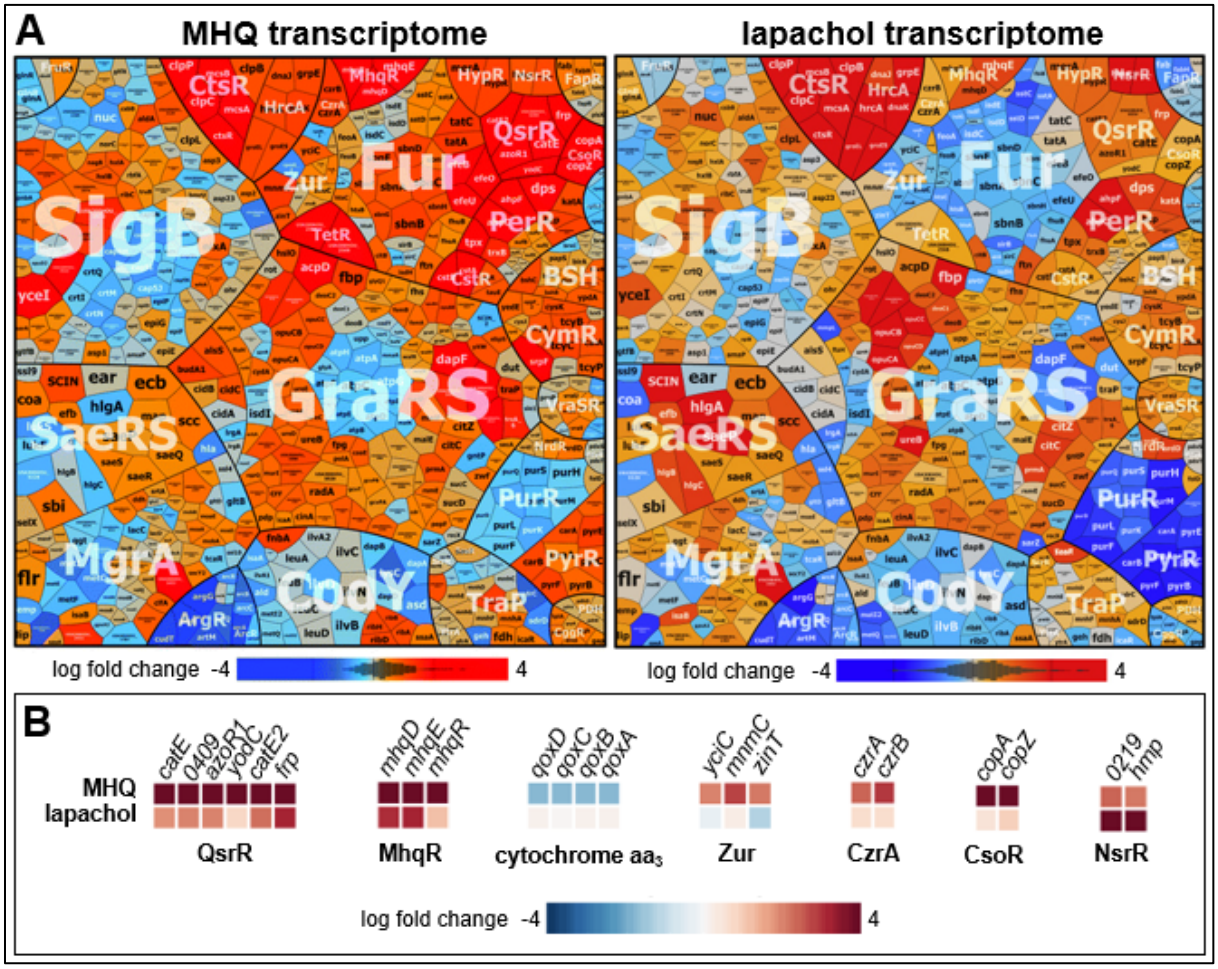

Figure 11: The stress responses of *S. aureus* to lapachol and methylhydroquinone (MHQ). (A) The transcriptome data are shown as Voronoi treemaps constructed by Dr. Jörg Bernhardt (University of Greifswald). Differential gene expression changes are pictured using a color code, where red and blue indicate log2-fold induction and repression of transcription, respectively. The genes are sorted into regulons and clustered accordingly. MHQ and lapachol caused the induction of the MhqR, QsrR, PerR, HypR, GraRS, CtsR and HrcA regulons, indicative of a quinone, oxidative and cell wall stress response and protein damage. (**B)** The log2-fold changes of selected genes are depicted in a heat map created with InstantClue (v0.11.1) by Daniel Bartosik (University of Greifswald) for differentiation of the quinone stress responses. While the QsrR and MhqR regulons are stronger upregulated by MHQ than lapachol, it is the other way around for the ·NO-sensing NsrR regulon. MHQ led to the downregulation of the cytochrome aa_3 terminal oxidase, whereas the Zur, CzrA, and CsoR regulons, implicated in the metal homeostasis, were induced. The figures are adapted from the RNA-seq data presented in chapter 5 and 6 (85, 163).

The transcriptome analyses, which were performed in cooperation with Dr. Tobias Busche, revealed that sublethal MHQ and lapachol stresses caused a thiol-specific oxidative and quinone stress response in *S. aureus* (85, 163) **(Fig. 11A)**. Accordingly, we observed a strong upregulation of the quinone- and oxidative-stress specific MhqR, QsrR, PerR, HypR,

CtsR, and HrcA regulons, and of the enzymes of the Brx/BSH/YpdA/NADPH redox pathway and cysteine metabolism (CymR regulon). Thereby, we could confirm a similar expression profile in response to quinones, as revealed previously for *B. subtilis* upon MHQ addition (497). Moreover, both quinones elicited the downregulation of genes functioning in the amino acid and purine biosynthesis pathways (ArgR, CodY, PurR regulons). Indicated by the induction of the SigB and GraRS regulons, MHQ and lapachol also induced a cell wall stress response in *S. aureus*. Astonishingly, while the pyrimidine biosynthesis PyrR regulon was among the top hits of downregulated genes upon lapachol treatment, MHQ induced these genes. Since quinones were found to form adducts with RNA and DNA bases (520, 521), MHQ might lead to the depletion of pyrimidine nucleotides. Despite the considerable similarities between the stress responses, we noted further transcriptional variations, indicative of distinct modes of action **(Fig. 11)**. For example, the transcription of the cytochrome aa_3 terminal menaquinol oxidase encoding *qoxABCD* operon was downregulated in response to MHQ, suggesting that MHQ might interfere with the respiratory chain activity in *S. aureus*. Moreover, MHQ but not lapachol induces the CstR regulon, which responds to RSS and thiol persulfides (85, 163). While MHQ caused the strong upregulation of the Fur, CsoR, CzrA and Zur regulons, implicated in the Fe^{2+}, Cu^{2+} and Zn^{2+} homeostasis, this metal stress response was not observed in lapachol-treated cells. In contrast, the NsrR regulon, including the *hmp* gene, was 4.8-fold higher induced by lapachol than MHQ. The flavohemoglobin Hmp was shown to act as quinone- and nitroreductase, with high substrate specificity for methyl-1,4-naphthoquinones, and might be involved in the detoxification of lapachol (522).

Further experiments were performed to elucidate the primary mode of action of lapachol *in vivo* (85) **(chapter 5)**. While Dr. Nico Linzner could not detect alkylated and aggregated proteins *in vitro* and *in vivo*, the ability of lapachol to elevate intracellular ROS levels was supported by the detection of *S*-bacillithiolations and HypR oxidation. To further exclude that lapachol exerts its toxicity also independent from ROS production, I performed survival assays under limited oxygen levels. While 1 mM lapachol was highly lethal under normal oxygen conditions (<1 % survival), microaerophilic growth conditions reduced the toxicity of lapachol significantly and increased the survival rate of *S. aureus* to approximately 80% **(Fig. 12B)**. Since anaerobic conditions decrease the redox cycling ability of quinones and hence ROS production but do not interfere with the *S*-adduct formation, the obtained inhibition profiles are in agreement with the mechanistic mode of action (169). Based on our data, it can be concluded that lapachol acts, in accordance with previous *in vitro* results (517, 518), exclusively via the oxidative mode in *S. aureus*.

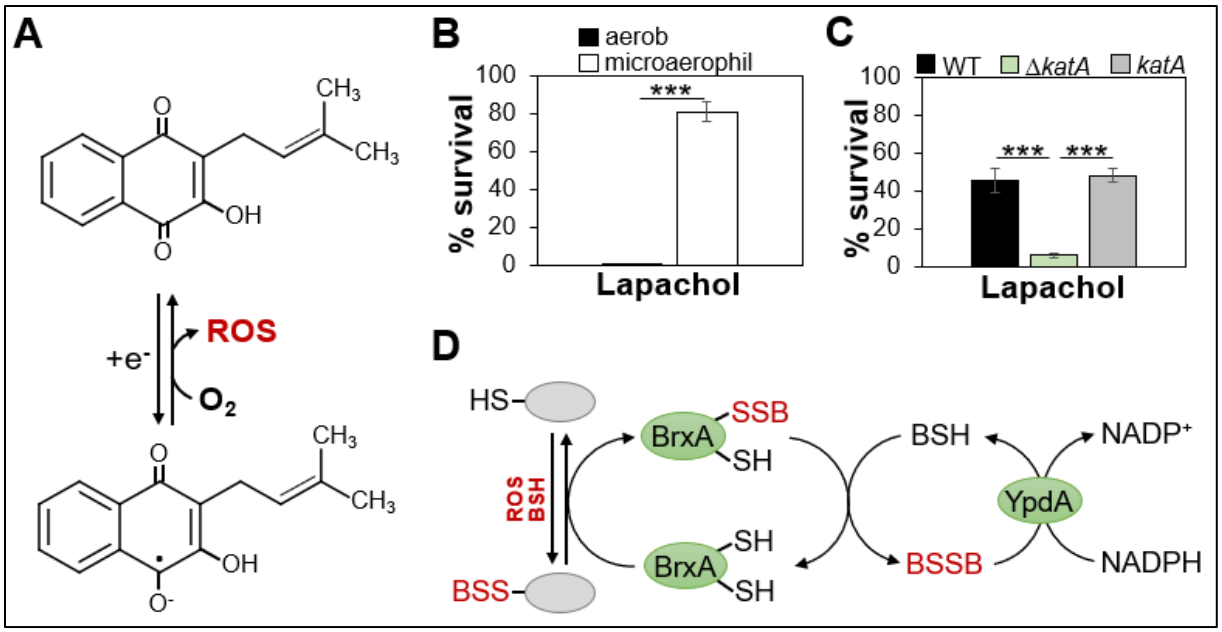

Figure 12: The oxidative stress defense protects *S. aureus* against ROS produced by lapachol. (A) The one-electron reduction of lapachol leads to the semiquinone anion radical and subsequently the formation of reactive oxygen species (ROS). **(B)** Lower oxygen levels limit the redox-cycling of lapachol, as revealed by the increased survival of *S. aureus* during microaerophilic growth conditions. **(C,D)** The catalase (KatA) and the bacilliredoxin (BrxA)/bacillithiol (BSH)/ BSH disulfide reductase (YpdA)/NADPH redox pathway contribute to the resistance of *S. aureus* against lapachol. KatA catalyzes the detoxification of H_2O_2. ROS lead to *S*-bacillithiolated proteins, which are regenerated by the BrxA/BSH/YpdA/NADPH pathway. The figure is adapted from chapter 5 (85), where the experimental procedures are described. ***$p \leq 0.001$.

Even though lapachol induced the quinone-specific MhqR and QsrR regulons of *S. aureus*, I could demonstrate that none of them provides protection (163) (unpublished data). In contrast, both regulons were much stronger induced by MHQ and conferred, in agreement with previous results obtained for the MhqR and YodB regulons in *B. subtilis* (504, 507), resistance against this quinone in *S. aureus* **(Fig. 11 and 13)** (163, 519). Although characterizations of quinone-detoxifying enzymes regulated by the QsrR and MhqR regulons are pending, differences in the rate of reduction and substrate specificities of azo- and nitroreductases were reported previously. These were allocated to the quinone redox potential and structural differences affecting the size of the active site and substrate interactions, respectively (490, 523, 524). For example, while some azoreductases were found to reduce a broad range of quinones with different catalytic efficiencies, others are highly specific for either benzo- or naphthoquinones (490, 525, 526). Likewise, extradiol dioxygenases were reported to differ in their preference for bicyclic and monocyclic substrates (489). Recently, another flavin oxidoreductase, OfrA, was demonstrated to confer resistance against lethal MHQ stress in *S. aureus* (527). While OfrA was 23.3-fold upregulated in our RNA-seq analyses upon MHQ stress, lapachol treatment induced the transcription of this enzyme only 3.6-fold. Further studies are required to investigate whether the weak induction by lapachol is indicative of an absence

of protection mediated by OfrA. Since several enzymes that are implicated in the oxidative stress resistance were highly upregulated in our transcriptome analysis, I investigated whether they confer protection against lapachol. By performing growth and survival assays, I could reveal that *S. aureus* relies on the activity of KatA for H_2O_2 detoxification and the BrxA/BSH/YpdA/NADPH pathway for the reduction of *S*-bacillithiolated proteins and BSSB to counteract the oxidative stress exerted by lapachol **(Fig. 12C,D)**.

2.7.3 The MarR-family regulator MhqR as quinone sensor in *S. aureus*

Since the *mhqRED* operon was strongly induced upon MHQ treatment, we further investigated its function in the quinone-stress resistance in *S. aureus*. The genes of this operon show more than 35% sequence identity to the respective genes in *B. subtilis*. Consequently, I started with the regulatory and functional characterization of the MhqR regulon during my master thesis and continued this work as part of my doctoral thesis (163) **(chapter 6)**. Our transcriptional analyses revealed that the *mhqRED* operon is controlled by MhqR, which acts, like its homolog in *B. subtilis*, as a repressor (504). In contrast to the large MhqR regulon of *B. subtilis* (504), we could not identify further members of the MhqR regulon in *S. aureus*. The MhqR operator was identified as a highly conserved 9-9 bp imperfect inverted repeat in position -6 to +12 relative to the transcriptional start site (TSS) +1 (163). Using EMSAs, I demonstrated that MhqR binds specifically and with a high affinity to this DNA sequence. Interestingly, in contrast to studies in *B. subtilis* and on other MarR-type regulators (504, 528), my EMSA analyses did not reveal the presence of additional MhqR boxes or adjacent secondary direct repeat elements, which could serve for multimeric binding. The presence of multiple binding sites in the promoter region was suggested previously to enable a hierarchical gene expression and a more gradual response depending on the effective concentration of the regulator (529).

While some MarR family regulators, such as the global virulence regulators MgrA and SarZ from *S. aureus*, are regulated by reversible thiol switches (353, 503, 528, 530), my studies demonstrated that the non-conserved cysteine residue Cys95 of MhqR is neither essential for DNA binding nor quinone sensing in *S. aureus in vitro* and *in vivo* (163). Although the purified MhqRC95A mutant protein bound to the DNA with a two-fold lower affinity than the wild type protein in EMSAs *in vitro*, full repression of the *mhqDE* operon was detected under control conditions in the *S. aureus mhqRC95A* mutant *in vivo*. Further, MhqR and the Cys mutant proteins were responsive to MHQ addition, as revealed by the dissociation from the DNA and strong transcriptional induction of the *mhqRED* operon **(Fig. 13B)**. Reducing conditions did not reverse this dissociation, supporting that MhqR inactivation in *S. aureus* is not caused by a

thiol-switch mechanism (163), confirming previous results of MhqR in *B. subtilis* (504). Therefore, we assume that MhqR is regulated by direct ligand binding, like many other MarR-type transcription regulators (503) **(Fig. 13A)**. While most MarR-family regulators possess a ligand-binding pocket between the dimerization domain and the wHTH motif (528), this quinone-binding site still needs to be identified in MhqR (163). Using crystal structure analyses, we aim to identify with cooperation partners the ligand-binding pocket and the ligand-induced conformational changes, leading to the dissociation of MhqR from the DNA. Additionally, I started with mutational analyses of putative ligand coordinating amino acids.

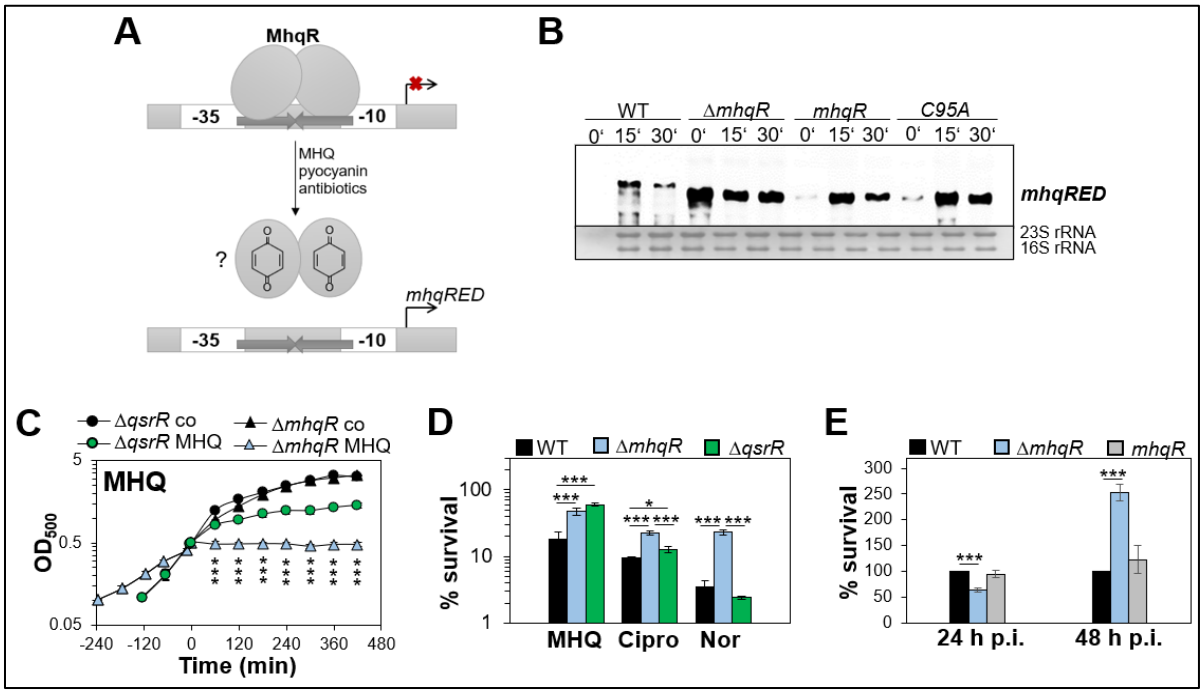

Figure 13: The MhqR regulon contributes to the resistance of *S. aureus* against quinones, antibiotics, and the host-immune defense. (A) The schematic depicts our proposed model of the MhqR regulation by quinone binding to a ligand binding pocket, leading to the derepression of the *mhqRED* operon. **(B)** The transcription of the *mhqRED* operon is shown for the *S. aureus* COL wild type (WT), the Δ*mhqR* mutant, the *mhqR* and *mhqRC95A* complemented strains after 15 and 30 min methylhydroquinone (MHQ) stress. **(C, D)** The QsrR regulon confers higher MHQ resistance, and the MhqR regulon protects *S. aureus* against the quinone-like antibiotics ciprofloxacin (Cipro) and norfloxacin (Nor). **(E)** The increased survival rate of the Δ*mhqR* mutant at 48 hours post-infection (p.i.) indicates that the MhqR regulon contributes to the long-term survival of *S. aureus* inside the murine macrophage cell line J-774A.1. The figure is adapted from chapter 6 (163), where the experimental procedures are stated. *$p \leq 0.05$ and ***$p \leq 0.001$.

Quinones are structural divers and can act as electrophiles and oxidants, raising the question of physiological inducers of the MhqR regulon. Following up on preliminary experiments during my master thesis, I monitored the transcription of the *mhqRED* operon after the addition of different oxidants, electrophiles, and diverse quinone-like compounds, including antibiotics (163). Following the proposed regulatory mechanism via ligand binding, it appeared that the MhqR regulon responds specifically to compounds with quinone-like structures, but not to other substances like HOCl and aldehydes. The high resistance of the Δ*mhqR* mutant to

MHQ and the commonly used antibiotics ciprofloxacin, norfloxacin and rifampicin, established the MhqR regulon as a significant contributor to the quinone and antibiotic tolerance in *S. aureus* **(Fig. 10 and 13C,D)**. This indicates that the MhqR-controlled dioxygenase MhqE and/or the phospholipase/carboxylesterase MhqD might catalyze the antibiotic degradation as newly identified resistance mechanism in *S. aureus* (163, 503, 528, 531, 532).

Increased oxygen consumption rates, which were measured as a proxy for the respiratory chain activity, and the approximately 2.5-fold higher ATP levels in the Δ*mhqR* mutant compared to the wild type suggested that the MhqR regulon could be implicated in the regulation of the electron transport chain by modulating the redox state of the endogenous menaquinone pool (163). Recently, similar conclusions were drawn from studies in *B. subtilis*, showing that the MhqR regulon helps to overcome Mn^{2+} toxicity by reducing the menaquinone pool to alleviate the Mn^{2+}-induced dysfunction of the menaquinol oxidase QoxABCD (225).

Our transcriptome analyses unveiled that most thiol-specific oxidative stress regulons, such as HypR and PerR, are downregulated in the Δ*mhqR* mutant under control conditions (163). Thus, the Δ*mhqR* mutant was significantly impaired in its H_2O_2 detoxification ability and recovery after sublethal stress. However, the survival rates of the mutant were 9.1- and 2.5-fold higher than the ones of the wild type after exposure to lethal amounts of H_2O_2 and HOCl. Moreover, the MhqR regulon was found to be essential under long-term infection conditions (163). While the Δ*mhqR* mutant was more susceptible to killing by the murine macrophage cell line J-774A.1 within 24 hours, the mutant showed a 2.5-fold higher intramacrophage survival rate 48 hours post-infection as compared to the wild type **(Fig. 13E)**. Furthermore, studies in *B. subtilis* associated the MhqR regulon with persistence phenotypes. The MhqR regulon increased the expression of spore coat proteins and promoted the growth of cell wall-deficient L-forms, which are resistant to β-lactam antibiotics and foster persistence (504, 533, 534). Previously, deletions of menaquinone synthesis genes and hence defects in respiration were associated with increased formation of small colony variants (SCV) in *S. aureus* (535). Since the derepression of the MhqR regulon was associated with an enhanced respiratory chain activity (163), subsequent research should be directed to investigate the role of the MhqR regulon in persistence and SCV formation in *S. aureus*.

2.7.4 The MarR/Duf24-family redox and quinone sensor QsrR of *S. aureus*

In previous research, the QsrR regulon was established as an important resistance mechanism against 1,4-benzoquinone, methyl-*p*-benzoquinone and pyocyanin in *S. aureus* (536, 537). QsrR shows 38% sequence identity with YodB of *B. subtilis* and acts by binding to the

palindromic sequence GTATAN$_5$TATAC as a repressor (536). Hereby, the wHTH motif (consisting of α3, the recognition helix α4, β1, β2 and β3) mediates together with the loop region (α1 and α2) the DNA contacts (536). Within my studies, I could demonstrate that this ensures a highly specific DNA binding activity since two base substitutions in each half of the inverted repeat abolished the binding of QsrR completely (519). The DNA binding affinities of QsrR to the *catE2* (K_D=68.3 nM) and *qsrR* (K_D=112.4 nM) promoters were 9- and 15-fold lower compared to the one determined for MhqR, but 19- and 12-fold higher than the one of its close homolog YodB of *B. subtilis* (163, 508, 519).

The QsrR regulon includes genes for the riboflavin biosynthesis, the NAD(P)H-dependent quinone reductases *azoR1* and *frp*, the nitroreductase *yodC*, and the thiol-dependent dioxygenases c*atE* and *catE2*, which are thought to function in quinone detoxification **(Fig. 10)** (536). Of note, while the CatR and SifR regulons in *B. subtilis* and *S. pneumoniae* operate in iron acquisition (142, 511), neither the QsrR nor the MhqR regulons were required for protection under iron starvation caused by the iron scavenger dipyridyl (163). Instead, I could show that the QsrR regulon also participates, although to a lower extent than the MhqR regulon, in the detoxification of the quinone-like antibiotics ciprofloxacin and rifampicin (163). In contrast, the QsrR regulon mediates higher resistance to MHQ stress **(Fig. 13C,D)**. Importantly, like in *B. subtilis*, we observed a crosstalk between both regulons, which was evident by the lower expression of the QsrR regulon in the Δ*mhqR* mutant under MHQ stress conditions. Further studies should investigate the phenotypes in the Δ*qsrR*Δ*mhqR* double mutant to analyze the relative contributions and interactions of both regulons in more detail.

QsrR contains three cysteine residues, which will be referred to, based on the sequence and numbering in the *S. aureus* COL strain, as Cys4, Cys29 and Cys32 (519). In contrast, QsrR of *S. aureus* Newman contains an additional N-terminal methionine, resulting in the numbering of Cys5, Cys30 and Cys33 in the previous study (536). In virtue of the positive dipole of the helix α1, it was proposed that the pK_a value of the thiol group of Cys4 is lowered, making it more nucleophilic (536). Accordingly, the N-terminal cysteine was identified as essential for quinone sensing *in vivo* and *in vitro,* as predicted by its conservation across the MarR/DUF24-family (519, 536). It was further demonstrated that quinones, such as menadione and 1,4-benzoquinone, lead to the thiol-*S*-alkylation of the conserved Cys4, causing conformational changes, by which the distance of the recognition helices increases by 9.2 Å (536). Together with a rotation of 11°, this abolishes the binding to the consecutive major grooves at the operator DNA. However, as these experiments were only performed with the Cys29 and Cys32 mutant protein *in vitro*, the quinone sensing mechanism *in vivo* remains indistinct. Our previous RNA-

seq analyses revealed that the QsrR regulon was not only strongly induced by electrophiles but also by oxidative stress, such as HOCl and AGXX® (105, 163, 202, 355, 538, 539). Therefore, we proposed that QsrR functions as a redox-sensing two-Cys type regulator, like its homolog YodB of *B. subtilis* and other MarR/DUF24-type regulators (508, 509, 528). Thus, I elucidated the regulatory redox-sensing mechanism of QsrR **(Fig. 14A)** as a further subject of my research work **(chapter 7)** (519).

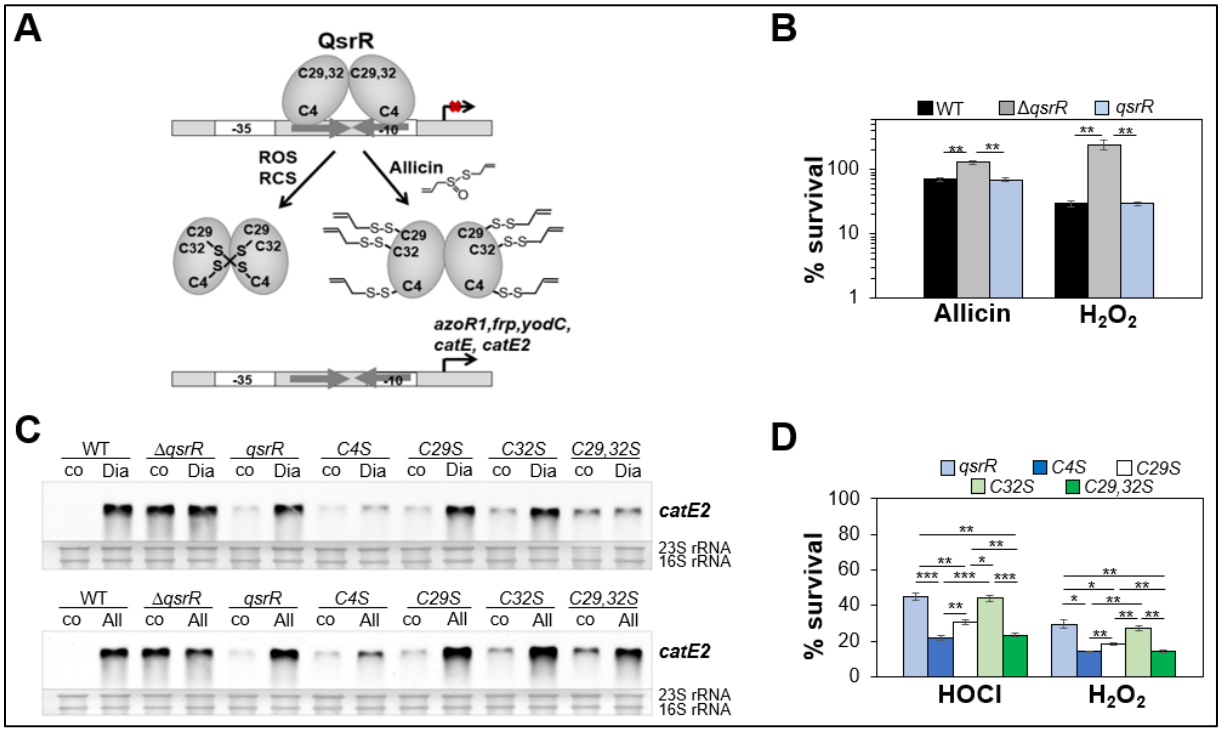

Figure 14: QsrR is regulated by different thiol switches in response to allicin and oxidants in *S. aureus*. (A) QsrR senses disulfide stress by oxidants (HOCl and H_2O_2) or the redox-cycling activity of quinones by intermolecular disulfides between Cys4 and Cys29' or Cys32'. Allicin causes *S*-thioallylations of Cys4, Cys29 and Cys32. These thiol switches inactivate QsrR, causing the derepression of genes, which encode for the dioxygenases (*catE*, *catE2*), the nitroreductase (*yodC*), and the putative azoreductase (*azoR1*) and the oxidoreductase (*frp*). **(C)** The transcription of *catE2* was analyzed in *S. aureus* COL wild type (WT), the Δ*qsrR* mutant and the *qsrR, qsrRC4S, qsrRC29S, qsrRC32S* and *qsrRC29,32S* complemented strains before (co) and after diamide (Dia) and allicin (All) treatment. While Cys4 and either Cys29 or Cys32 are required for diamide sensing, only Cys4 is important for allicin sensing. **(B, D)** Survival assays revealed that the QsrR regulon contributes to the resistance against allicin and H_2O_2. The oxidative stress resistance exerted by QsrR requires Cys4 and either Cys29 or Cys32. The figure is adapted from chapter 7 (519) where the experimental procedures are stated. $*p \leq 0.05$, $**p \leq 0.01$ and $***p \leq 0.001$.

Within my experiments, I could demonstrate that the organosulfur compound allicin and the oxidants HOCl and diamide inhibited the DNA binding ability of QsrR *in vitro* and *in vivo*. Importantly, since the derepression of the QsrR regulon also resulted in increased resistance of *S. aureus* against allicin and the oxidants HOCl and H_2O_2 **(Fig. 14B)**, I used these compounds to study the regulation of QsrR in more detail. By conducting non-reducing Western blots, Northern blot analyses, mass spectrometry, phenotype, and DNA binding assays with QsrR and its Cys mutants, we could reveal the sensing mechanism of QsrR **(Fig. 14A)**. In Northern blot

analyses, the *qsrRC4S* mutant was impaired in the response towards quinones, diamide and allicin *in vivo*, confirming that Cys4 is essential for the redox sensing of QsrR (519), as shown previously (536). While the *qsrRC29S* and *qsrRC32S* mutants were able to sense diamide and allicin stress and to induce the *catE* expression, the *qsrRC29,32S* double mutant did not respond to diamide stress but remained allicin responsive **(Fig. 14C).** These results indicate that Cys4 is sufficient for the inactivation of QsrR by allicin but that Cys4 and either Cys29 or Cys32 are required for diamide sensing *in vivo*.

Likewise, the *qsrRC4S* and *qsrRC29,32S* mutants were equally impaired in their survival upon H_2O_2 and HOCl treatment compared to the resistant phenotype of the Δ*qsrR* mutant **(Fig. 14D)**. Thus, our data demonstrated that Cys4 is essential while Cys29 and Cys32 can substitute for each other under oxidative stress. Nevertheless, we observed that the oxidative stress survival and responsiveness to diamide in DNA binding assays are slightly impaired through the substitution of Cys29 but not Cys32 **(chapter 7) (Fig. 14D)**. With the help of Dr. Benno Kuropka and Dr. Christoph Weise, I analyzed the post-translational thiol modifications of QsrR under diamide and allicin stress to clarify the redox-sensing mechanism further. We demonstrated that the QsrR protein is oxidized to Cys4-Cys29' intermolecular disulfides by diamide *in vitro* (519). In contrast, the organosulfur compound allicin caused the *S*-thioallylation of Cys4 and both other Cys residues *in vitro* **(Fig. 14A)**. Thus, diamide and allicin inactivate QsrR via different thiol-switch mechanisms to induce the QsrR regulon.

Since most quinones, including benzoquinones and MHQ, can act as electrophiles and via ROS production, we assume that both modes can be sensed by QsrR. This is supported by our data, which showed, on the one hand, that MHQ induced less disulfide formation than diamide and, on the other hand, that the DNA binding activity was only incompletely reversible by DTT upon MHQ treatment (519). Thus, MHQ most likely leads to the *S*-alkylation of Cys4, and via ROS production to the intersubunit disulfide formation between Cys4 and Cys29'. Thereby MHQ causes the derepression of the QsrR regulon in two different ways. In previous studies, it was proposed that the *S*-adduct formation abolishes DNA binding completely, whereas the disulfide bond formation only inhibits the DNA binding of YodB to one of the two major grooves, leading to a reduced DNA binding affinity in *B. subtilis* (113, 509). Since our *in vitro* and *in vivo* analyses demonstrated that QsrR is most responsive to quinones and less sensitive to oxidant-based inactivation, a similar mechanism might apply in *S. aureus.* This would allow the differentiation between quinones with different primary modes of action and the translation of two different signals into distinct stress responses. As it was shown previously that lethal but not sublethal quinone levels induce profound protein aggregation (155), this

differentiation would also enable a more gradual response depending on the dosage of the stressor. Of note, the quinone-sensing activity of QsrR was utilized previously to generate a genetically encoded biosensor for dynamic measurements of intracellular quinone levels in mammalian cells (540). However, since our study demonstrated that QsrR also responds strongly to other compounds, such as diamide and allicin (519), the specificity of this biosensor requires further investigations before this tool could be used to study the quinone stress response in various organisms.

Altogether, our results demonstrate that MhqR and QsrR are the main quinone-sensing regulators of *S. aureus*, which control regulons that also confer resistance against a wide range of other antimicrobials, including antibiotics and ROS. Further studies are required to elucidate the enzymatic detoxification mechanisms of these diverse substrates. Based on the substrate range and catalyzed reaction of azoreductases (492), AzoR1 might function in the NAD(P)H-dependent reduction of the azo group of diamide. Moreover, some quinone reductases were shown to be involved in the H_2O_2 resistance of bacteria (526, 541-543). While MhqR most likely senses quinone-ligand compounds through ligand binding, QsrR employs thiol-switch mechanisms to mediate the adaptation of *S. aureus* to oxidative and electrophile stress **(Fig. 13A and 14A)**. The significance of the QsrR regulon is further emphasized by the finding that it protects *S. aureus* against phagocytosis and killing by murine macrophages (536). Another study revealed that the tolerance of *S. aureus* against photodynamic inactivation is mediated by an adaptive genomic *qsrR* mutation, leading to the derepression of the QsrR regulon (544). Photodynamic inactivation, whereby the light-mediated activation of photosensitizers leads to the production of ROS, is currently regarded as an efficient therapeutic option with a low risk of resistance development to treat infectious diseases caused by susceptible and antibiotic-resistant bacteria (545).

2.7.5 The TetR-family repressor GbaA as disulfide and electrophile sensor

Our RNA-Seq analyses revealed that the transcription of the GbaA regulon, including the *SACOL2592-nmrA-90* and *gbaAB-SACOL2595-97* operons **(Fig. 15A)**, was upregulated after exposure to lapachol, MHQ, allicin and AGXX® stress in *S. aureus* (85, 86, 163, 202), suggesting a role of the GbaA regulon under thiol-stress conditions. GbaA was previously characterized as a negative regulator of glucose-induced biofilm formation (546), implying a link between biofilm formation and the disulfide-stress response. We aimed to clarify the role of GbaA in the bacterial stress resistance and to identify the underlying sensing mechanisms. Thereby, I contributed to our understanding of the function of GbaA and its regulon members

under different thiol stress conditions and the involvement of both cysteine residues in the stress response *in vivo* **(chapter 8)** (547).

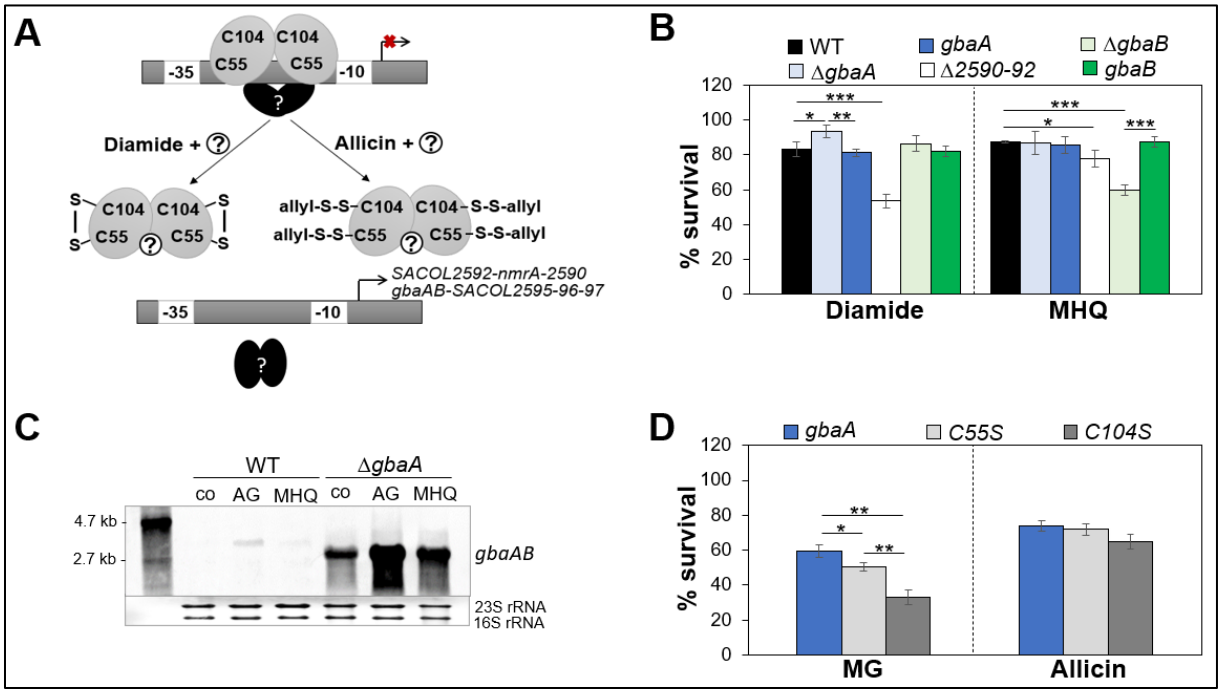

Figure 15: The two-Cys-type TetR repressor GbaA confers resistance against thiol stress in *S. aureus*. (A) GbaA controls the *SACOL2592-nmrA-2590* and *gbaAB-SACOL2595-96-97* operons. GbaA can be oxidized to different thiol switches by diamide and allicin. However, for full derepression of the GbaA regulon, an additional redox-sensing (co)regulator and an unknown ligand are required. **(C)** The transcription of the *gbaAB-SACOL2595-97* operon was analyzed in *S. aureus* COL wild type (WT) and the Δ*gbaA* mutant before (co) and 30 min after the addition of AGXX® (AG) and methylhydroquinone (MHQ). **(B, D)** Survival assays were performed for the *S. aureus* COL WT, the Δ*gbaA,* Δ*gbaB* and *SACOL2592-90* deletion mutants and the *gbaA*, *gbaB*, *gbaAC55S* and *gbaAC104S* complemented strains after exposure to diamide, MHQ **(B)**, MG and allicin **(D)**. The figure is adapted from chapter 8 (547), where the experimental procedures are stated in more detail. *$p \leq 0.05$, **$p \leq 0.01$ and ***$p \leq 0.001$.

In phenotype assays, I could show that, in accordance with our RNA-Seq analysis, the GbaA regulon indeed confers resistance against strong oxidants and electrophiles, such as diamide, NEM and MG. My analyses further revealed the distinct functions of the two divergent operons in the thiol-stress response of *S. aureus*. While the deletion of the upstream *SACOL2592-nmrA-2590* operon was associated with increased sensitivity towards diamide, allicin, NEM and MG, the Δ*gbaB* deletion mutant was solely impaired in survival under MG and MHQ stress **(Fig. 15B)** (547). Since *SACOL2590* encodes a putative glyoxalase-I enzyme, it can be speculated that this enzyme is involved in the BSH-dependent MG detoxification pathway (547). NmrA was suggested previously to function as a regulator of the $NAD(P)^+/NADP(H)$ redox balance (548), while GbaB might catalyze as short-chain dehydrogenase/oxidoreductase oxidation-reduction reactions of aldehydes and quinones (547). However, further studies are required to investigate the enzymatic function of these genes in more detail.

Detailed Northern blot analyses by Dr. Vu Van Loi demonstrated that none of the tested stressors represent the physiological inducer of the GbaA regulon, since full derepression of both operons was only observed in the Δ*gbaA* mutant **(Fig. 15C)** (547). Therefore, it appears that the GbaA regulon is co-regulated by another thiol-redox regulator, indicating a complex regulatory mechanism that is subject to our future studies. In the present work, we aimed to study the redox-sensing mechanism of GbaA in response to thiol-active compounds in more detail. GbaA possesses two conserved cysteine residues, Cys55 and Cys104, suggesting that it could function as a two-Cys-type redox sensor. However, previous studies indicated that GbaA represents a monothiol electrophile sensor, whereby the formation of the intramolecular disulfide has no regulatory function (548). Dr. Vu Van Loi could show that GbaA is oxidized to different thiol switches by diamide and allicin. However, in agreement with the other study (548), these modifications did not affect the DNA-binding activity *in vitro*, further supporting the involvement of an unknown redox-sensitive inducer and secondary regulator (547). My phenotype analyses demonstrated the requirement of both cysteine residues of GbaA for the NEM and MG resistance *in vivo*. However, the deletion of either cysteine did not abrogate the stress resistance towards allicin **(Fig. 15D)**.

In summary, our experiments demonstrated that although the two-Cys-type redox sensor GbaA contributes to the oxidative and electrophile stress response in *S. aureus*, its protective function under quinone stress is limited. Its physiological function and complex regulation remain to be elucidated in future studies **(chapter 8)** (547).

2.8 Thiol targets as prospective treatment options

The previous sections outlined that thiol groups of cysteines are prone to post-translational modifications by reactive species. Thiol oxidations of conserved cysteine residues of redox-sensing transcription factors serve as a signal to induce various pathways for detoxification and regeneration of the redox homeostasis (357). Thereby, mainly reversible thiol-disulfide switches and irreversible thiol-*S*-alkylations lead to conformational changes of redox-sensitive transcriptional regulators to control the gene expression in *S. aureus* **(chapter 3)** (105), and *S. pneumoniae.* Inhibiting the essential bacterial defense mechanisms by targeting these redox regulators, or proteins and LMW thiols involved in the redox homeostasis appears as a promising approach to treat infections caused by multi-drug resistant bacteria. Recently, we have reviewed the current state of antimicrobial drug development concerning thiol-targeting compounds (13) **(chapter 9)**. It turned out that current studies either pursued a global, non-specific approach, for example, by using ROS-generating drugs for thiol depletion, or were

directed to identify specific inhibitors of certain pathways and thiol-containing proteins to interfere with the bacterial redox-homeostasis (13). For instance, several compounds were shown to block the synthesis or recycling of LMW thiols, whereas others specifically target the thiol-containing proteins DsbA and DsbB to inhibit the disulfide bond formation system, which is required for virulence and ROS resistance in Gram-negative pathogens. Importantly (p)ppGpp was also studied as a potential target of adjuvants to render bacteria more sensitive to antibiotic treatment and to interfere with biofilm formation (13, 331, 549-553). However, one of the most promising compounds is disulfiram. It was approved by the U.S. Food and Drug Administration (FDA) for the treatment of alcohol dependence and is assessed in a clinical phase-2 trial for cancer treatment (554). Disulfiram was shown to form mixed disulfides with the β-lactamase active site cysteine residue, causing Zn^{2+} release and enzyme inactivation. Based on its known pharmacological properties and synergistic effect with the β-lactam antibiotic imipenem and other chemicals, it might be used as adjunctive therapy (555, 556). Despite the identification of many promising drug targets and redox-active compounds, most of them have not been examined in clinical trials. The need for further systematic studies is emphasized by the suspected cytotoxicity and non-specific thiol oxidation of human proteins (13).

Interestingly, several redox-active antimicrobials also exert antiviral activity (557-561). For example, ebselen and its derivatives inhibit viral replication by oxidizing thiol-containing viral proteins, leading to selenyl-sulfide linkage and protein inactivation (562). In response to the global pandemic caused by the severe acute respiratory syndrome coronavirus 2 (SARS-CoV-2), I dedicated a part of my doctoral thesis to investigate, together with Dr. Kirstin Friedmann (née Mösbauer), the effect of the redox-active compound allicin on SARS-CoV-2 infected cell cultures (563) **(chapter 10)**.

2.8.1 Allicin as antiviral compound

The thio-2-propene-1-sulfinic acid *S*-allyl ester (or diallyl thiosulfinate) allicin is a natural organosulfur compound of *Allium sativum.* Upon tissue damage of the garlic cloves, the odorous compound allicin is formed by the spontaneous condensation of allyl sulfenic acid, which is produced together with dehydroalanine by alliinase from alliin (564) **(Fig 16A)**. Garlic is used since ancient times to cure different diseases, and since the identification of allicin in 1944, studies demonstrated that this membrane-permeable RSS exhibits antimicrobial, antiparasitic and antifungal activity (564-569). By causing *S*-thioallylations of LMW thiols and protein thiols **(Fig 16A)**, allicin triggers thiol depletion, impairment of the intracellular thiol-

redox balance, protein damage and aggregation, and a strong thiol-specific oxidative and sulfur stress response in most bacteria (200, 570-572). Importantly, allicin also shows potent antiviral activity against several enveloped and non-enveloped DNA and RNA viruses, including influenza and SARS-CoV (573-575), which raised the question of whether it is also effective against SARS-CoV-2.

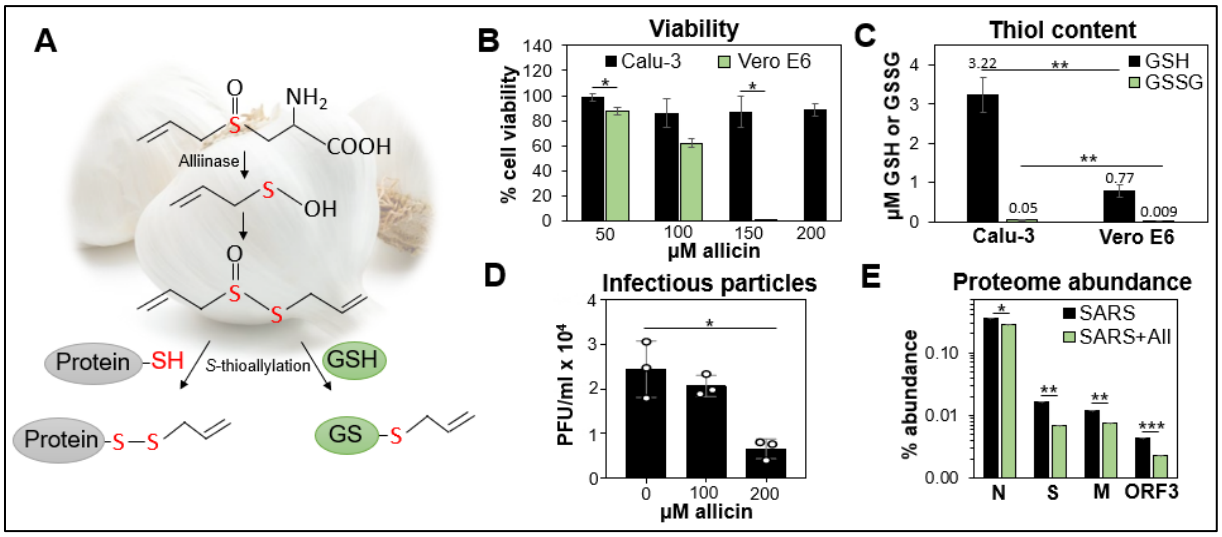

Figure 16: Biocompatible allicin doses exhibit antiviral activity against SARS-CoV-2 in cell cultures. (A) Allicin is produced in *Allium sativum* upon tissue damage by the alliinase. This enzyme hydrolyses alliin to allylsulfenic acid, which reacts with a second allylsulfenic acid molecule to allicin. Allicin causes *S*-thioallylations of proteins and *S*-allylmercaptoglutathione. **(B)** The effect of allicin on the percentual cell viability of Calu-3 and Vero E6 cells was assessed after 24 h exposure to allicin, compared to the untreated control. Calu-3 cells are more tolerant to allicin compared to Vero E6 cells. **(C)** The glutathione (GSH) and glutathione disulfide (GSSG) levels were determined in untreated Calu-3 and Vero E6 cells. **(D)** Allicin treatment of SARS-CoV-2 infected Calu-3 cells leads to decreased infectious viral particles (PFU, plaque forming units) 24 hours post-infection. **(E)** The percentual abundance of the SARS-CoV-2 proteins (N, S, M and ORF3) relative to the total proteome abundance of infected Calu-3 cells 24 hours post-infection was calculated for infected cells without (SARS) and with allicin (SARS+All). After allicin treatment, these viral proteins showed a lower abundance in the proteome. This figure is adapted from (564) and chapter 10 (563), in which the experimental conditions are described in more detail. *$p < 0.05$; **$p < 0.01$; ***$p < 0.001$.

Since the first report of SARS-CoV-2 infection in 2019, the respiratory coronavirus disease 2019 (COVID-19) became a global health threat (576), and still, almost three years later, the consequences are noticeable and affect our daily life. The causative agent of this pandemic, SARS-CoV-2, is a positive-sense, single-stranded RNA virus belonging to the genus *Betacoronavirus*. Although most infected people develop mild to moderate illness, characterized by common symptoms, such as fever and cough, some get viral pneumonia and/or develop the so-called cytokine storm syndrome, characterized by high levels of pro-inflammatory cytokines and hyperinflammation (576, 577). According to the WHO, more than 6.4 million deaths have been reported globally until September 2022 (578). Additionally, there is cumulative evidence of persisting clinical symptoms after the recovery from COVID-19. These health issues are often associated with high morbidity and are summarised by the term

post-acute COVID-19 syndrome, which includes long COVID-19 and (multiorgan) effects due to COVID-19 and/or the treatment procedure (579, 580). When we started our research to examine the antiviral activity of allicin on SARS-CoV-2 **(chapter 10)** (563), the global vaccination campaigns hadn't started yet, and preventive and supportive therapies were demanded to relieve the symptoms and avoid disease progression. Since then, the FDA has approved two drugs, namely remdesivir and baricitinib for the treatment of the zoonotic disease COVID-19. Further ones, such as Paxlovid (nirmatrelvir co-packaged with ritonavir) are authorized under an emergency use authorization (581, 582). Nevertheless, more research is required to develop better preventive and treatment measures to decrease the morbidity, mortality and economic costs associated with COVID-19. Thereby, studies like ours, which investigated the mode of action of natural compounds with antiviral properties against SARS-CoV-2, could represent a starting point to design and test more stable, less cytotoxic, and effective viral inhibitors (583, 584).

Previous reports indicated that high doses of allicin inhibit cell proliferation and induce apoptosis in human cells (564). Differences in the allicin tolerance between various cell lines seem to correlate positively with their intracellular GSH contents (199, 585). GSH reacts with allicin with an apparent bimolecular reaction rate constant of 3.0 M^{-1} s^{-1} and thereby acts as an allicin scavenger (201, 586). Our data confirmed these findings and provided further evidence that the intracellular GSH content is essential for the level of allicin tolerance (563) **(chapter 10)**. My measurements of the intracellular GSH and GSSG levels in two cell lines revealed that the GSH content in the allicin tolerant human lung Calu-3 cells is 4.2-fold higher than in the allicin susceptible primate kidney-derived Vero E6 cells **(Fig 16B, C)**. Using biocompatible allicin concentrations, Dr. Kirstin Friedmann (née Mösbauer) demonstrated that the post-infection treatment of SARS-CoV-2 infected Calu-3 and Vero E6 cells with allicin significantly reduced the number of infectious particles and the viral RNA genome equivalents by ~60-70%. Additionally, allicin decreased the SARS-CoV-2 induced cellular damage, highlighting the antiviral effect of allicin in cell cultures *in vitro* **(Fig 16D)**.

To investigate whether allicin affects host-virus interactions *in vitro*, we used label-free quantitative proteomics performed in cooperation with Prof. Dr. Lorenz Adrian, whereby I was heavily involved in sample preparation and analyses of the changes in the proteome of Calu-3 infected cells (563). In total, we detected 4,243 Calu-3 host proteins and 8 SARS-CoV-2 proteins in the total proteome. SARS-CoV-2 infection resulted in the differential expression of 536 proteins **(Fig 17A)**, accounting for 2.73% of the total proteome abundance. Remarkable is the high abundance of the viral ribonucleocapsid protein (N-protein) 24 hours after infection in

Calu-3 cells. SARS-CoV-2 caused a substantial remodeling of various cellular processes, including gene expression and protein degradation, vesicular trafficking, carbon, lipid and nucleotide metabolism and signal transduction pathways. Importantly, we detected 21 proteins of the interferon (IFN) and interferon-stimulated gene (ISG) response, which were strongly induced upon SARS-CoV-2 infection. Especially the sensor of viral RNA, the cyclic GMP-AMP synthase (cGAS), was 98-fold higher expressed, but also the expression of the dynamin-like GTPase MX1, an inhibitor of viral uncoating and vesicular trafficking, was elevated in infected cells **(Fig. 17)**. We further noticed an upregulation of the 2'-5'-oligoadenylate synthases (OAS1-3, OASL) and the IFN-induced helicase C-domain-containing protein (IFIH), which induce viral RNA degradation and the IFN response, respectively. In agreement with other studies (587-590), our data suggest that host-virus interactions might cause ubiquitination and ISGylation changes, leading to host and virus protein degradation and modulation of the immune response (563).

As indicated by our phenotype analyses, allicin significantly decreased the abundance of four viral proteins by 18% to 59% **(Fig. 16E)**. Additionally, many of the expression changes upon SARS-CoV-2 infections were reverted by allicin treatment in the host proteome, including proteins involved in endocytosis and vesicular trafficking **(Fig. 17)**. It is to be emphasized that this included the IFN-response and ISG signature, which was significantly diminished in allicin-treated cells. Decreased expression levels upon allicin addition compared to the untreated infected cells were, for example, detected for cGAS, MX1, OAS1-3, and proteins involved in ubiquitination (563). Thus, allicin exerts an antiviral and immunomodulatory effect, indicated by the decreased antiviral interferon response in treated SARS-CoV-2 infected cells *in vitro*.

Previous studies showed that eukaryotic and prokaryotic cells can detoxify allicin and express pathways, which catalyze the reversal of protein *S*-thioallylations (202, 586). In our work, we couldn't identify *S*-thioallylated viral or host proteins 24 hours after allicin addition, most likely because these modifications have already been removed by the cellular Grx/GSH/Gor/NADPH system. A proteome analysis in human Jurkat cells revealed that a biocompatible allicin dose leads within ten minutes to *S*-thioallylations of 332 proteins (199). It was proposed that the immune-stimulatory effect of allicin in Jurkat cells is mediated by *S*-thioallylation of Cys118 of $p21^{ras}$, leading to the activation of extracellular signal-regulated kinases 1 and 2 (ERK1/2) (591). Additionally, *S*-thioallylation of Zn^{2+} coordinating Cys thiolates and subsequent Zn^{2+} release was suggested to account for the immunomodulatory activity of allicin in murine EL-4 cells by promoting interleukin (IL)-1β dependent synthesis of

IL-2 (199). Moreover, the allicin-mediated inhibition of the NF-κB signaling pathway contributes to the decreased level of pro-inflammatory cytokines (592, 593). Clinical observations demonstrated that severe COVID-19 illness is mainly mediated by immunopathology and to a lesser extent by virus replication (594, 595). Thus, the extensive immunomodulatory effects of allicin observed in our and previous studies could be exploited to motivate the further development of less toxic and more stable allicin derivates. Additionally, the immunomodulatory effect of allicin might be an integral part of the antiviral effect of allicin to overcome virus-induced immune dysfunctions, which should be further investigated (596).

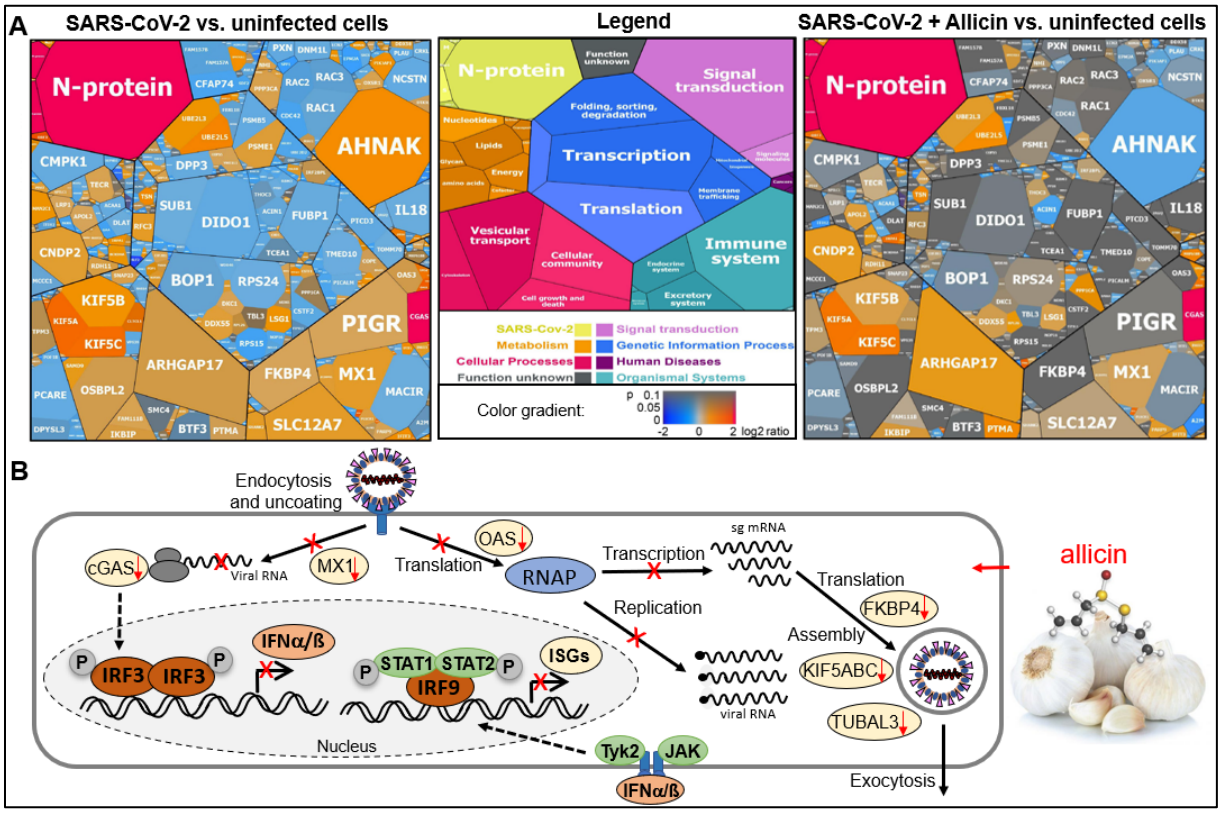

Figure 17: Allicin treatment of infected Calu-3 cells reduced the expression of interferon (IFN) signaling pathways and IFN-stimulated gene (ISG) effectors and reverted several host pathways to levels of uninfected cells. (A) The host-viral proteome treemaps depict the 536 differentially expressed proteins upon SARS-CoV-2 infection versus uninfected cells (left), and after allicin addition versus uninfected cells (right). The cell sizes denote the average abundances of 207 proteins with ≥1.5-fold inductions (red-orange color) and 329 proteins with <0.66-fold decreased (blue color) expression after SARS-CoV-2 infection. The legend indicates the functional KEGG categories (563). **(B)** Schematic representation of the effect of allicin on SARS-CoV-2 infections. Upon endocytosis, the viral RNA is recognized, and ISG effectors, such as cGAS, lead to the activation of a signaling cascade for IFN induction. Binding of Type-I IFN a/ß to the IFNAR receptor leads to the phosphorylation of signal transducers and activators of transcription (STAT1/2) and transcription of ISGs. The ISG effector MX1 inhibits virus endocytosis and uncoating, while the oligoadenylate synthases (OAS) interfere with translation via viral RNA degradation. FKBP4, kinesins (KIFA/B/C) and TUBAL3 promote translation and virus assembly by functioning in protein folding and vesicular transport. Allicin probably interferes with the viral life cycle and reverses most of the SARS-CoV-2 induced proteome changes in Calu-3 cells, leading to a reduced IFN and ISGs response and viral replication. The figure is adapted from (597) and chapter 10 (563).

During the pandemic, many *in silico* molecular docking and screening studies were performed to discover potential antiviral compounds that can be used to target specific SARS-

CoV-2 proteins (598). As a result, allicin was suggested as a putative inhibitor of the main protease M^{pro} and the RNA-dependent RNA polymerase RdRp, which mediate the viral polyprotein processing and viral genome replication (599-601). Recently, the molecular targets and antiviral mechanism of Zn^{2+}-therapy against SARS-CoV-2 were investigated (602). The reversible Zn^{2+} coordination at the catalytic dyad of M^{pro} was found to inhibit the enzymatic activity with nanomolar affinity, leading to diminished viral replication (602). This result suggests that allicin not only directly interferes with the M^{pro} activity but, since Zn^{2+} is released from *S*-thioallylated proteins, also indirectly via elevated Zn^{2+} levels. Although experimental evidence is lacking, it is likely that allicin also targets, like other thiol-reactive compounds, further Cys-containing viral proteins, such as the spike glycoprotein and ORF8 protein (603). The *S*-thioallylation of viral proteins most likely happens analog to the *S*-thioallylation of eukaryotic and prokaryotic proteins (199, 202) within the first 10-30 min of allicin treatment, followed by fast reduction. Therefore, *S*-thioallyations of viral proteins are difficult to investigate due to limited virus particles inside host cells at these early time points post-infection.

Overall, these studies suggest that allicin exerts its antiviral and immunomodulatory activity by a plethora of different targets and interferes with many stages of the viral life cycle. However, our and previous research has shown that allicin also exerts high cytotoxicity on human cells (199, 563, 568). Moreover, the overdosage of raw garlic can cause severe cellular damage, such as garlic burns of the skin and mucosa (604-607). Thus, allicin cannot be applied directly as a therapeutic against viral and bacterial infections. Rather, to exploit the antimicrobial and immunomodulatory activity of allicin, less toxic and more stable allicin derivatives have to be developed. The potential applications of allicin-inspired antibiotics and *A. sativum*-derived carbon dots as antimicrobials and antivirals are currently examined, and first compounds, such as pyridyl disulfides and thiolated fluoroquinolones have been developed (13, 608-610).

3 Conclusion and future perspectives

This doctoral thesis aimed to advance our understanding of the thiol stress response and defense strategies used by *S. aureus* and *S. pneumoniae* to counteract the oxidative burst and microbicidal effects of quinones encountered under infections. The findings resulted in eight original publications and two review articles, which are shown in the following chapters.

Previous research efforts have established the function of various stress-specific regulons in the maintenance of the redox and metal homeostasis of *S. aureus* under changing

environmental conditions. Within this thesis, it was revealed that also the small alarmone (p)ppGpp, the inducer of the stringent response, is involved in these processes. By modulating the respiratory chain activity and free iron levels, (p)ppGpp was found to be essential for the redox homeostasis and acquisition of the non-specific, general oxidative stress and antibiotic resistance of *S. aureus* in the stat phase. Moreover, this thesis contributed to our knowledge about the Brx/BSH/YpdA/NADPH pathway, functioning in the regeneration of *S*-bacillithiolated proteins and BSSB during the recovery from oxidative stress in *S. aureus.* Since (p)ppGpp and enzymes involved in the biosynthesis and recycling of alternative LMW thiols are regarded as promising drug targets, the characterization of their cellular function and regulation, to which this work has added, is essential for a prospective application of effective inhibitors. Triggered by the pandemic, parts of this thesis were also directed to examine the mode of action of the thiol-reactive compound allicin against SARS-CoV-2 infection in cell culture models. Since the interferon response and other host proteome changes in infected Calu-3 lung cells were abrogated upon allicin treatment, our data supported the antiviral and immunomodulatory effect of the RSS allicin. Thus, further studies should be directed to develop less toxic and more stable allicin derivates.

Moreover, the investigation of the physiological responses of *S. pneumoniae* and *S. aureus* to HOCl and quinones, respectively, led to the identification of important resistance mechanisms, and the analysis of four stress-specific regulators, namely NmlR, GbaA, MhqR and QsrR. Thereby, the MerR-family regulator NmlR was characterized as the first HOCl-sensing transcription factor in *S. pneumoniae,* which responds to oxidative stress by intermolecular disulfide formation and *S*-glutathionylation. The NmlR regulon was shown to confer resistance against oxidative stress encountered *in vitro* and after phagocytosis by human macrophages. To further work out the impact of the NmlR regulon under *in vivo* conditions, we are currently elucidating the adaptation strategies of *S. pneumoniae* during human lung tissue infections in cooperation with the research group of Prof. Dr. Andreas Hocke.

The results of the present work also contributed to the functional and regulatory characterization of the GbaA regulon, revealing its involvement in the protection of *S. aureus* against strong oxidants and electrophiles and the role of the Cys residues in the stress defense. Moreover, the oxidative stress defense of *S. aureus* was identified as essential to withstand the microbicidal activity of quinones, which act mainly via ROS production, such as lapachol. In contrast, the resistance against quinones, which function as electrophiles and ROS producers, was dependent on the MhqR and QsrR regulons. The MarR-family regulator MhqR was identified as a novel quinone-sensing repressor in *S. aureus*, which is probably regulated by

direct ligand sensing. On the contrary, the sensing mechanism of QsrR was shown to involve different thiol switches, leading to the derepression of the QsrR regulon. Since my work recognized the MhqR and QsrR regulons as important defense mechanisms of *S. aureus* against oxidants and antibiotics, our current studies are directed to further investigate the crosstalk of both regulators and the underlying enzymatic detoxification mechanisms. Moreover, since the MhqR regulon was shown to be essential for long-term survival in macrophages, the role of MhqR for persistence induction is a topic for follow-up studies.

In conclusion, by coupling global transcriptome analyses with detailed functional and regulatory investigations of general and stress-specific regulators, this doctoral thesis adds to the plethora of known resistance mechanisms employed by the two human pathogens *S. aureus* and *S. pneumoniae* for the successful survival in their niche. The inhibition of these characterized redox-sensing transcription factors and regulons will most likely sensitize these human pathogens and increase the host's own ability to combat bacterial infections and the efficiency of antibiotic treatments.

References

1. Guan N, Li J, Shin HD, Du G, Chen J, Liu L. 2017. Microbial response to environmental stresses: from fundamental mechanisms to practical applications. *Appl Microbiol Biotechnol* 101(10):3991-4008.
2. Kobayashi SD, Malachowa N, DeLeo FR. 2018. Neutrophils and bacterial immune evasion. *J Innate Immun* 10(5-6):432-441.
3. Giacomini E, Perrone V, Alessandrini D, Paoli D, Nappi C, Degli Esposti L. 2021. Evidence of antibiotic resistance from population-based studies: A narrative review. *Infect Drug Resist* 14:849-858.
4. Hutchings MI, Truman AW, Wilkinson B. 2019. Antibiotics: past, present and future. *Curr Opin Microbiol* 51:72-80.
5. Uddin TM, Chakraborty AJ, Khusro A, Zidan BRM, Mitra S, Emran TB, Dhama K, Ripon MKH, Gajdacs M, Sahibzada MUK, Hossain MJ, Koirala N. 2021. Antibiotic resistance in microbes: History, mechanisms, therapeutic strategies and future prospects. *J Infect Public Health* 14(12):1750-1766.
6. WHO. 2020. Fact Sheets - Antibiotic resistance. Available online:https://www.who.int/news-room/fact-sheets/detail/antibiotic-resistance. (accessed on 06/04/2022).
7. Antimicrobial Resistance C. 2022. Global burden of bacterial antimicrobial resistance in 2019: a systematic analysis. *Lancet* 399(10325):629-655.
8. Reynolds MG. 2000. Compensatory evolution in rifampin-resistant *Escherichia coli*. *Genetics* 156(4):1471-81.
9. Smith-Adam HJ, Nichol KA, Hoban DJ, Zhanel GG. 2005. Stability of fluoroquinolone resistance in *Streptococcus pneumoniae* clinical isolates and laboratory-derived mutants. *Antimicrob Agents Chemother* 49(2):846-8.
10. Huemer M, Mairpady Shambat S, Brugger SD, Zinkernagel AS. 2020. Antibiotic resistance and persistence-Implications for human health and treatment perspectives. *EMBO Rep* 21(12):e51034.
11. Levin-Reisman I, Ronin I, Gefen O, Braniss I, Shoresh N, Balaban NQ. 2017. Antibiotic tolerance facilitates the evolution of resistance. *Science* 355(6327):826-830.
12. Windels EM, Michiels JE, Van den Bergh B, Fauvart M, Michiels J. 2019. Antibiotics: Combatting tolerance to stop resistance. *mBio* 10(5).
13. Fritsch VN, Antelmann H. 2022. Chapter 28 - Thiol targets in drug development to combat bacterial infections, p 679-711. Alvarez B, Comini MA, Salinas G, Trujillo M (ed), *In* Redox Chemistry and Biology of Thiols doi:10.1016/B978-0-323-90219-9.00003-0. *Academic Press*
14. Weiser JN, Ferreira DM, Paton JC. 2018. *Streptococcus pneumoniae*: transmission, colonization and invasion. *Nat Rev Microbiol* 16(6):355-367.
15. Henriques-Normark B, Normark S. 2010. Commensal pathogens, with a focus on *Streptococcus pneumoniae*, and interactions with the human host. *Exp Cell Res* 316(8):1408-14.
16. Taylor TA, Unakal CG. 2022. *Staphylococcus aureus*, StatPearls. *StatPearls Publishing*, Treasure Island (FL).Available online: https://www.ncbi.nlm.nih.gov/pubmed/28722898. (accessed on 09/27/2022)
17. Pollitt EJG, Szkuta PT, Burns N, Foster SJ. 2018. *Staphylococcus aureus* infection dynamics. *PLoS Pathog* 14(6):e1007112.
18. Thacker SB. 2019. Antibiotic resistance threats in the United States, 2019, report by Centers for Disease Control and Prevention (CDC). Atlanta, GA. Available online:http://dx.doi.org/10.15620/cdc:82532. (accessed on 09/27/2022).
19. Eriksen KR. 1945. Studies on induced resistance to penicillin in a pneumococcus type I. *Acta Pathol Microbiol Scand* 22(4):398-405.
20. Crespo-Piazuelo D, Lawlor PG. 2021. Livestock-associated methicillin-resistant *Staphylococcus aureus* (LA-MRSA) prevalence in humans in close contact with animals and measures to reduce on-farm colonisation. *Ir Vet J* 74(1):21.
21. Jacobs MR. 1999. Drug-resistant *Streptococcus pneumoniae*: rational antibiotic choices. *The American Journal of Medicine* 106(5, Supplement 1):19-25.

22. Grossman TH. 2016. Tetracycline antibiotics and resistance. *Cold Spring Harb Perspect Med* 6(4):a025387.
23. Lowy FD. 2003. Antimicrobial resistance: the example of *Staphylococcus aureus*. *J Clin Invest* 111(9):1265-73.
24. Reinert RR. 2009. The antimicrobial resistance profile of *Streptococcus pneumoniae*. *Clin Microbiol Infect* 15 Suppl 3:7-11.
25. Miklasinska-Majdanik M. 2021. Mechanisms of resistance to macrolide antibiotics among *Staphylococcus aureus*. *Antibiotics (Basel)* 10(11).
26. Rice LB. 2008. Federal funding for the study of antimicrobial resistance in nosocomial pathogens: no ESKAPE. *J Infect Dis* 197(8):1079-81.
27. Krismer B, Weidenmaier C, Zipperer A, Peschel A. 2017. The commensal lifestyle of *Staphylococcus aureus* and its interactions with the nasal microbiota. *Nat Rev Microbiol* 15(11):675-687.
28. Academy C. 2.7 DNA Replication, transcription and translation.
29. Li JH, H.; Sajid, A.; Zhang, H. and Yuan, Z. 2017. Fluoroquinolone resistance in Salmonella: Mechanisms, fitness, and virulence. Mascellino MT (ed), *In* Salmonella-A re-emerging pathogen doi: 10.5772/intechopen.74699. *IntechOpen, London*.Available online: https://www.intechopen.com/chapters/60197. (accessed on 06/20/2022)
30. Jenul C, Horswill AR. 2019. Regulation of *Staphylococcus aureus* virulence, p 669-686, *In* Gram-Positive Pathogens doi: 10.1128/9781683670131.ch41.Available online: https://onlinelibrary.wiley.com/doi/abs/10.1128/9781683670131.ch41. (accessed on 09/10/2022)
31. Hava DL, LeMieux J, Camilli A. 2003. From nose to lung: the regulation behind *Streptococcus pneumoniae* virulence factors. *Mol Microbiol* 50(4):1103-10.
32. Butrico CE, Cassat JE. 2020. Quorum sensing and toxin production in *Staphylococcus aureus* osteomyelitis: Pathogenesis and paradox. *Toxins (Basel)* 12(8).
33. Foster TJ. 2019. Surface proteins of *Staphylococcus aureus*, p 599-617, *In* Gram-Positive Pathogens doi: 10.1128/9781683670131.ch38.Available online: https://onlinelibrary.wiley.com/doi/abs/10.1128/9781683670131.ch38. (accessed on 09/27/2022)
34. Brooks LRK, Mias GI. 2018. *Streptococcus pneumoniae*'s virulence and host immunity: Aging, diagnostics, and prevention. *Front Immunol* 9:1366.
35. Fischetti VA. 2019. Surface proteins on Gram-positive bacteria, p 19-31. Vincent A. Fischetti RPN, Joseph J. Ferretti,Daniel A. Portnoy,Miriam Braunstein,Julian I. Rood (ed), *In* Gram-Positive Pathogens doi:10.1128/9781683670131.ch2.Available online: https://onlinelibrary.wiley.com/doi/abs/10.1128/9781683670131.ch2. (accessed on 09/27/2022)
36. Jedrzejas MJ. 2001. Pneumococcal virulence factors: structure and function. *Microbiol Mol Biol Rev* 65(2):187-207.
37. Tam K, Torres VJ. 2019. *Staphylococcus aureus* secreted toxins and extracellular enzymes. *Microbiol Spectr* 7(2).
38. Ali MQ, Kohler TP, Burchhardt G, Wust A, Henck N, Bolsmann R, Voss F, Hammerschmidt S. 2020. Extracellular pneumococcal serine proteases affect nasopharyngeal colonization. *Front Cell Infect Microbiol* 10:613467.
39. Marquart ME. 2021. Pathogenicity and virulence of *Streptococcus pneumoniae*: Cutting to the chase on proteases. *Virulence* 12(1):766-787.
40. Jahn K, Kohler TP, Swiatek LS, Wiebe S, Hammerschmidt S. 2022. Platelets, bacterial adhesins and the pneumococcus. *Cells* 11(7).
41. Otto M. 2014. *Staphylococcus aureus* toxins. *Curr Opin Microbiol* 17:32-7.
42. Nishimoto AT, Rosch JW, Tuomanen EI. 2020. Pneumolysin: Pathogenesis and therapeutic target. *Front Microbiol* 11:1543.
43. Marriott HM, Mitchell TJ, Dockrell DH. 2008. Pneumolysin: a double-edged sword during the host-pathogen interaction. *Curr Mol Med* 8(6):497-509.
44. de Jong NWM, van Kessel KPM, van Strijp JAG. 2019. Immune evasion by *Staphylococcus aureus*, p 618-639. Vincent A. Fischetti RPN, Joseph J. Ferretti,Daniel A. Portnoy,Miriam Braunstein,Julian I. Rood (ed), *In* Gram-Positive Pathogens

doi:10.1128/9781683670131.ch39.Available online: https://onlinelibrary.wiley.com/doi/abs/10.1128/9781683670131.ch39. (accessed on 09/27/2022)
45. Tuffs SW, Haeryfar SMM, McCormick JK. 2018. Manipulation of innate and adaptive immunity by Staphylococcal superantigens. *Pathogens* 7(2).
46. Hyams C, Camberlein E, Cohen JM, Bax K, Brown JS. 2010. The *Streptococcus pneumoniae* capsule inhibits complement activity and neutrophil phagocytosis by multiple mechanisms. *Infect Immun* 78(2):704-15.
47. O'Riordan K, Lee JC. 2004. *Staphylococcus aureus* capsular polysaccharides. *Clin Microbiol Rev* 17(1):218-34.
48. Nelson AL, Roche AM, Gould JM, Chim K, Ratner AJ, Weiser JN. 2007. Capsule enhances pneumococcal colonization by limiting mucus-mediated clearance. *Infect Immun* 75(1):83-90.
49. Geno KA, Gilbert GL, Song JY, Skovsted IC, Klugman KP, Jones C, Konradsen HB, Nahm MH. 2015. Pneumococcal capsules and their types: Past, present, and future. *Clin Microbiol Rev* 28(3):871-99.
50. Weinberger DM, Malley R, Lipsitch M. 2011. Serotype replacement in disease after pneumococcal vaccination. *Lancet (London, England)* 378(9807):1962-1973.
51. van der Poll T, Opal SM. 2009. Pathogenesis, treatment, and prevention of pneumococcal pneumonia. *Lancet* 374(9700):1543-56.
52. Masomian M, Ahmad Z, Gew LT, Poh CL. 2020. Development of next generation *Streptococcus pneumoniae* vaccines conferring broad protection. *Vaccines (Basel)* 8(1).
53. Clegg J, Soldaini E, McLoughlin RM, Rittenhouse S, Bagnoli F, Phogat S. 2021. *Staphylococcus aureus* vaccine research and development: The past, present and future, including novel therapeutic strategies. *Front Immunol* 12:705360.
54. Degrossoli A, Muller A, Xie K, Schneider JF, Bader V, Winklhofer KF, Meyer AJ, Leichert LI. 2018. Neutrophil-generated HOCl leads to non-specific thiol oxidation in phagocytized bacteria. *Elife* 7.
55. Roos D. 2016. Chronic granulomatous disease. *Br Med Bull* 118(1):50-63.
56. Rider NL, Jameson MB, Creech CB. 2018. Chronic granulomatous disease: Epidemiology, pathophysiology, and genetic basis of disease. *J Pediatric Infect Dis Soc* 7(suppl_1):S2-S5.
57. Gresham HD, Lowrance JH, Caver TE, Wilson BS, Cheung AL, Lindberg FP. 2000. Survival of *Staphylococcus aureus* inside neutrophils contributes to infection. *J Immunol* 164(7):3713-22.
58. Flannagan RS, Heit B, Heinrichs DE. 2016. Intracellular replication of *Staphylococcus aureus* in mature phagolysosomes in macrophages precedes host cell death, and bacterial escape and dissemination. *Cell Microbiol* 18(4):514-35.
59. Vermot A, Petit-Hartlein I, Smith SME, Fieschi F. 2021. NADPH Oxidases (NOX): An overview from discovery, molecular mechanisms to physiology and pathology. *Antioxidants (Basel)* 10(6).
60. Nguyen GT, Green ER, Mecsas J. 2017. Neutrophils to the ROScue: Mechanisms of NADPH oxidase activation and bacterial resistance. *Front Cell Infect Microbiol* 7:373.
61. Winterbourn CC, Hampton MB, Livesey JH, Kettle AJ. 2006. Modeling the reactions of superoxide and myeloperoxidase in the neutrophil phagosome: implications for microbial killing. *J Biol Chem* 281(52):39860-9.
62. Segal AW. 2005. How neutrophils kill microbes. *Annu Rev Immunol* 23:197-223.
63. Valenta H, Erard M, Dupre-Crochet S, Nubetae O. 2020. The NADPH Oxidase and the Phagosome. *Adv Exp Med Biol* 1246:153-177.
64. Kettle AJ, Anderson RF, Hampton MB, Winterbourn CC. 2007. Reactions of superoxide with myeloperoxidase. *Biochemistry* 46(16):4888-97.
65. Klebanoff SJ. 2005. Myeloperoxidase: friend and foe. *J Leukoc Biol* 77(5):598-625.
66. Ulfig A, Leichert LI. 2021. The effects of neutrophil-generated hypochlorous acid and other hypohalous acids on host and pathogens. *Cell Mol Life Sci* 78(2):385-414.
67. Winterbourn CC, Kettle AJ, Hampton MB. 2016. Reactive oxygen species and neutrophil function. *Annu Rev Biochem* 85:765-92.

68. Rosen H, Klebanoff SJ, Wang Y, Brot N, Heinecke JW, Fu X. 2009. Methionine oxidation contributes to bacterial killing by the myeloperoxidase system of neutrophils. *Proc Natl Acad Sci U S A* 106(44):18686-91.
69. Hawkins CL, Pattison DI, Davies MJ. 2003. Hypochlorite-induced oxidation of amino acids, peptides and proteins. *Amino Acids* 25(3-4):259-74.
70. Yassine E, Rada B. 2021. Microbicidal activity of hypothiocyanite against pneumococcus. *Antibiotics (Basel)* 10(11).
71. Pattison DI, Davies MJ, Hawkins CL. 2012. Reactions and reactivity of myeloperoxidase-derived oxidants: differential biological effects of hypochlorous and hypothiocyanous acids. *Free Radic Res* 46(8):975-95.
72. Ashby MT, Aneetha H. 2004. Reactive sulfur species: aqueous chemistry of sulfenyl thiocyanates. *J Am Chem Soc* 126(33):10216-7.
73. Barrett TJ, Hawkins CL. 2012. Hypothiocyanous acid: benign or deadly? *Chem Res Toxicol* 25(2):263-73.
74. Abuaita BH, Schultz TL, O'Riordan MX. 2018. Mitochondria-derived vesicles deliver antimicrobial reactive oxygen species to control phagosome-localized *Staphylococcus aureus*. *Cell Host Microbe* 24(5):625-636 e5.
75. West AP, Brodsky IE, Rahner C, Woo DK, Erdjument-Bromage H, Tempst P, Walsh MC, Choi Y, Shadel GS, Ghosh S. 2011. TLR signalling augments macrophage bactericidal activity through mitochondrial ROS. *Nature* 472(7344):476-80.
76. Herb M, Schramm M. 2021. Functions of ROS in macrophages and antimicrobial immunity. *Antioxidants (Basel)* 10(2).
77. Kohanski MA, Dwyer DJ, Hayete B, Lawrence CA, Collins JJ. 2007. A common mechanism of cellular death induced by bactericidal antibiotics. *Cell* 130(5):797-810.
78. Li H, Zhou X, Huang Y, Liao B, Cheng L, Ren B. 2020. Reactive oxygen species in pathogen clearance: The killing mechanisms, the adaption response, and the side effects. *Front Microbiol* 11:622534.
79. Dwyer DJ, Belenky PA, Yang JH, MacDonald IC, Martell JD, Takahashi N, Chan CT, Lobritz MA, Braff D, Schwarz EG, Ye JD, Pati M, Vercruysse M, Ralifo PS, Allison KR, Khalil AS, Ting AY, Walker GC, Collins JJ. 2014. Antibiotics induce redox-related physiological alterations as part of their lethality. *Proc Natl Acad Sci U S A* 111(20):E2100-9.
80. Kohanski MA, Dwyer DJ, Collins JJ. 2010. How antibiotics kill bacteria: from targets to networks. *Nat Rev Microbiol* 8(6):423-35.
81. Van Acker H, Coenye T. 2017. The Role of Reactive Oxygen Species in Antibiotic-Mediated Killing of Bacteria. *Trends Microbiol* 25(6):456-466.
82. Dwyer DJ, Collins JJ, Walker GC. 2015. Unraveling the physiological complexities of antibiotic lethality. *Annu Rev Pharmacol Toxicol* 55:313-32.
83. Keren I, Wu Y, Inocencio J, Mulcahy LR, Lewis K. 2013. Killing by bactericidal antibiotics does not depend on reactive oxygen species. *Science* 339(6124):1213-6.
84. Imlay JA. 2015. Diagnosing oxidative stress in bacteria: not as easy as you might think. *Curr Opin Microbiol* 24:124-31.
85. Linzner N, Fritsch VN, Busche T, Tung QN, Loi VV, Bernhardt J, Kalinowski J, Antelmann H. 2020. The plant-derived naphthoquinone lapachol causes an oxidative stress response in *Staphylococcus aureus*. *Free Radic Biol Med* 158:126-136.
86. Loi VV, Busche T, Preuss T, Kalinowski J, Bernhardt J, Antelmann H. 2018. The AGXX$^{(R)}$ antimicrobial coating causes a thiol-specific oxidative stress response and protein *S*-bacillithiolation in *Staphylococcus aureus*. *Front Microbiol* 9:3037.
87. Heiss A, Freisinger B, Held-Fohn E. 2017. Enhanced antibacterial activity of silver-ruthenium coated hollow microparticles. *Biointerphases* 12(5):05G608.
88. Clauss-Lendzian E, Vaishampayan A, de Jong A, Landau U, Meyer C, Kok J, Grohmann E. 2018. Stress response of a clinical *Enterococcus faecalis* isolate subjected to a novel antimicrobial surface coating. *Microbiol Res* 207:53-64.
89. Mourenza A, Gil JA, Mateos LM, Letek M. 2020. Oxidative Stress-Generating Antimicrobials, a Novel Strategy to Overcome Antibacterial Resistance. *Antioxidants (Basel)* 9(5).

90. Winterbourn CC. 2008. Reconciling the chemistry and biology of reactive oxygen species. *Nat Chem Biol* 4(5):278-86.
91. Imlay JA. 2003. Pathways of oxidative damage. *Annu Rev Microbiol* 57:395-418.
92. Imlay JA. 2008. Cellular defenses against superoxide and hydrogen peroxide. *Annu Rev Biochem* 77:755-76.
93. Pericone CD, Park S, Imlay JA, Weiser JN. 2003. Factors contributing to hydrogen peroxide resistance in *Streptococcus pneumoniae* include pyruvate oxidase (SpxB) and avoidance of the toxic effects of the fenton reaction. *J Bacteriol* 185(23):6815-25.
94. Regev-Yochay G, Trzcinski K, Thompson CM, Malley R, Lipsitch M. 2006. Interference between *Streptococcus pneumoniae* and *Staphylococcus aureus*: *In vitro* hydrogen peroxide-mediated killing by *Streptococcus pneumoniae*. *J Bacteriol* 188(13):4996-5001.
95. Pericone CD, Overweg K, Hermans PW, Weiser JN. 2000. Inhibitory and bactericidal effects of hydrogen peroxide production by *Streptococcus pneumoniae* on other inhabitants of the upper respiratory tract. *Infect Immun* 68(7):3990-7.
96. Selva L, Viana D, Regev-Yochay G, Trzcinski K, Corpa JM, Lasa I, Novick RP, Penades JR. 2009. Killing niche competitors by remote-control bacteriophage induction. *Proc Natl Acad Sci U S A* 106(4):1234-8.
97. Murphy MP, Bayir H, Belousov V, Chang CJ, Davies KJA, Davies MJ, Dick TP, Finkel T, Forman HJ, Janssen-Heininger Y, Gems D, Kagan VE, Kalyanaraman B, Larsson NG, Milne GL, Nystrom T, Poulsen HE, Radi R, Van Remmen H, Schumacker PT, Thornalley PJ, Toyokuni S, Winterbourn CC, Yin H, Halliwell B. 2022. Guidelines for measuring reactive oxygen species and oxidative damage in cells and *in vivo*. *Nat Metab* 4(6):651-662.
98. Winterbourn CC, Hampton MB. 2008. Thiol chemistry and specificity in redox signaling. *Free Radic Biol Med* 45(5):549-61.
99. Held JM, Gibson BW. 2012. Regulatory control or oxidative damage? Proteomic approaches to interrogate the role of cysteine oxidation status in biological processes. *Mol Cell Proteomics* 11(4):R111 013037.
100. Halliwell B. 2006. Reactive species and antioxidants. Redox biology is a fundamental theme of aerobic life. *Plant Physiol* 141(2):312-22.
101. Cabiscol E, Tamarit J, Ros J. 2000. Oxidative stress in bacteria and protein damage by reactive oxygen species. *Int Microbiol* 3(1):3-8.
102. Linzner N, Loi VV, Fritsch VN, Tung QN, Stenzel S, Wirtz M, Hell R, Hamilton CJ, Tedin K, Fulde M, Antelmann H. 2019. *Staphylococcus aureus* uses the bacilliredoxin (BrxAB)/bacillithiol disulfide reductase (YpdA) redox pathway to defend against oxidative stress under infections. *Front Microbiol* 10:1355.
103. Loi VV, Rossius M, Antelmann H. 2015. Redox regulation by reversible protein *S*-thiolation in bacteria. *Front Microbiol* 6:187.
104. Sies H. 2020. Oxidative stress: Concept and some practical aspects. *Antioxidants (Basel)* 9(9).
105. Linzner N, Loi VV, Fritsch VN, Antelmann H. 2021. Thiol-based redox switches in the major pathogen *Staphylococcus aureus*. *Biol Chem* 402(3):333-361.
106. Luebke JL, Giedroc DP. 2015. Cysteine sulfur chemistry in transcriptional regulators at the host-bacterial pathogen interface. *Biochemistry* 54(21):3235-49.
107. Netto LES, de Oliveira MA, Monteiro G, Demasi APD, Cussiol JRR, Discola KF, Demasi M, Silva GM, Alves SV, Faria VG, Horta BB. 2007. Reactive cysteine in proteins: protein folding, antioxidant defense, redox signaling and more. *Comp Biochem Physiol C Toxicol Pharmacol* 146(1-2):180-193.
108. Poole LB. 2015. The basics of thiols and cysteines in redox biology and chemistry. *Free Radic Biol Med* 80:148-57.
109. Peskin AV, Winterbourn CC. 2001. Kinetics of the reactions of hypochlorous acid and amino acid chloramines with thiols, methionine, and ascorbate. *Free Radic Biol Med* 30(5):572-9.
110. Storkey C, Davies MJ, Pattison DI. 2014. Reevaluation of the rate constants for the reaction of hypochlorous acid (HOCl) with cysteine, methionine, and peptide derivatives using a new competition kinetic approach. *Free Radic Biol Med* 73:60-6.
111. Winterbourn CC. 2015. Are free radicals involved in thiol-based redox signaling? *Free Radic Biol Med* 80:164-70.
112. Groitl B, Jakob U. 2014. Thiol-based redox switches. *Biochim Biophys Acta* 1844(8):1335-43.

113. Lee IG, Lee BJ. 2021. How bacterial redox sensors transmit redox signals via structural changes. *Antioxidants (Basel)* 10(4).
114. Farmer EE, Davoine C. 2007. Reactive electrophile species. *Curr Opin Plant Biol* 10(4):380-6.
115. Lee C, Park C. 2017. Bacterial responses to glyoxal and methylglyoxal: Reactive electrophilic species. *Int J Mol Sci* 18(1).
116. Okado-Matsumoto A, Fridovich I. 2000. The role of alpha,beta -dicarbonyl compounds in the toxicity of short chain sugars. *J Biol Chem* 275(45):34853-7.
117. Beavers WN, Skaar EP. 2016. Neutrophil-generated oxidative stress and protein damage in Staphylococcus aureus. *Pathog Dis* 74(6).
118. Collin F. 2019. Chemical Basis of Reactive Oxygen Species Reactivity and Involvement in Neurodegenerative Diseases. *Int J Mol Sci* 20(10).
119. Spiteller G. 2008. Peroxyl radicals are essential reagents in the oxidation steps of the Maillard reaction leading to generation of advanced glycation end products. *Ann N Y Acad Sci* 1126:128-33.
120. Marnett LJ, Riggins JN, West JD. 2003. Endogenous generation of reactive oxidants and electrophiles and their reactions with DNA and protein. *J Clin Invest* 111(5):583-93.
121. Anderson MM, Hazen SL, Hsu FF, Heinecke JW. 1997. Human neutrophils employ the myeloperoxidase-hydrogen peroxide-chloride system to convert hydroxy-amino acids into glycolaldehyde, 2-hydroxypropanal, and acrolein. A mechanism for the generation of highly reactive alpha-hydroxy and alpha,beta-unsaturated aldehydes by phagocytes at sites of inflammation. *J Clin Invest* 99(3):424-32.
122. Hazen SL, d'Avignon A, Anderson MM, Hsu FF, Heinecke JW. 1998. Human neutrophils employ the myeloperoxidase-hydrogen peroxide-chloride system to oxidize alpha-amino acids to a family of reactive aldehydes. Mechanistic studies identifying labile intermediates along the reaction pathway. *J Biol Chem* 273(9):4997-5005.
123. LoPachin RM, Gavin T. 2016. Reactions of electrophiles with nucleophilic thiolate sites: relevance to pathophysiological mechanisms and remediation. *Free Radic Res* 50(2):195-205.
124. Nguyen TT, Eiamphungporn W, Mader U, Liebeke M, Lalk M, Hecker M, Helmann JD, Antelmann H. 2009. Genome-wide responses to carbonyl electrophiles in *Bacillus subtilis*: control of the thiol-dependent formaldehyde dehydrogenase AdhA and cysteine proteinase YraA by the MerR-family regulator YraB (AdhR). *Mol Microbiol* 71(4):876-94.
125. LoPachin RM, Gavin T. 2014. Molecular mechanisms of aldehyde toxicity: a chemical perspective. *Chem Res Toxicol* 27(7):1081-91.
126. Morton RA. 1965. Biochemistry of quinones. Acad. Press, London [u.a].
127. Bolton JL, Trush MA, Penning TM, Dryhurst G, Monks TJ. 2000. Role of quinones in toxicology. *Chem Res Toxicol* 13(3):135-60.
128. Hahn FE. 1979. Antibiotics. 5,1, Mechanism of action of antibacterial agents
129. Enguita FJ, Leitao AL. 2013. Hydroquinone: environmental pollution, toxicity, and microbial answers. *Biomed Res Int* 2013:542168.
130. O'Brien PJ. 1991. Molecular mechanisms of quinone cytotoxicity. *Chem Biol Interact* 80(1):1-41.
131. Mothana RA, Jansen R, Julich WD, Lindequist U. 2000. Ganomycins A and B, new antimicrobial farnesyl hydroquinones from the basidiomycete *Ganoderma pfeifferi*. *J Nat Prod* 63(3):416-8.
132. Bittner S. 2006. When quinones meet amino acids: chemical, physical and biological consequences. *Amino Acids* 30(3):205-24.
133. Cory RM, McKnight DM. 2005. Fluorescence spectroscopy reveals ubiquitous presence of oxidized and reduced quinones in dissolved organic matter. *Environ Sci Technol* 39(21):8142-9.
134. Thomson RH. 1991. Distribution of naturally occurring quinones. *Pharm Weekbl Sci* 13(2):70-3.
135. Lira AA, Sester EA, Carvalho AL, Strattmann RR, Albuquerque MM, Wanderley AG, Santana DP. 2008. Development of lapachol topical formulation: anti-inflammatory study of a selected formulation. *AAPS PharmSciTech* 9(1):163-8.

136. Kuang X, Yang T, Zhang C, Peng X, Ju Y, Li C, Zhou X, Luo Y, Xu X. 2020. Repurposing Napabucasin as an antimicrobial agent against oral Streptococcal biofilms. *Biomed Res Int* 2020:8379526.
137. Andrade JC, Morais Braga MF, Guedes GM, Tintino SR, Freitas MA, Quintans LJ, Jr., Menezes IR, Coutinho HD. 2017. Menadione (vitamin K) enhances the antibiotic activity of drugs by cell membrane permeabilization mechanism. *Saudi J Biol Sci* 24(1):59-64.
138. Ahmad T, Suzuki YJ. 2019. Juglone in oxidative stress and cell signaling. *Antioxidants (Basel)* 8(4).
139. Ferreira VF, de Carvalho AS, Ferreira PG, Lima CGS, de CdSF. 2021. Quinone-based drugs: An important class of molecules in medicinal chemistry. *Med Chem* 17(10):1073-1085.
140. Malik EM, Müller CE. 2016. Anthraquinones as pharmacological tools and drugs. *Med Res Rev* 36(4):705-48.
141. Colwell CA, McCall M. 1945. Studies on the mechanism of antibacterial action of 2-methyl-1,4-naphthoquinone. *Science* 101(2632):592-4.
142. Zhang Y, Martin JE, Edmonds KA, Winkler ME, Giedroc DP. 2022. SifR is an Rrf2-family quinone sensor associated with catechol iron uptake in *Streptococcus pneumoniae* D39. *J Biol Chem* 298(7):102046.
143. Conroy BS, Grigg JC, Kolesnikov M, Morales LD, Murphy MEP. 2019. *Staphylococcus aureus* heme and siderophore-iron acquisition pathways. *Biometals* 32(3):409-424.
144. Scott Obach R, Kalgutkar AS. 2010. 1.15 - Reactive electrophiles and metabolic activation, p 309-347. McQueen CA (ed), *In* Comprehensive Toxicology (Second Edition) doi:10.1016/B978-0-08-046884-6.00115-9. *Elsevier*, Oxford.Available online: https://www.sciencedirect.com/science/article/pii/B9780080468846001159. (accessed on 09/01/2022)
145. Alghofaili F, Najmuldeen H, Kareem BO, Shlla B, Fernandes VE, Danielsen M, Ketley JM, Freestone P, Yesilkaya H. 2021. Host stress signals stimulate pneumococcal transition from colonization to dissemination into the lungs. *mBio* 12(6):e0256921.
146. Neal CP, Freestone PP, Maggs AF, Haigh RD, Williams PH, Lyte M. 2001. Catecholamine inotropes as growth factors for *Staphylococcus epidermidis* and other coagulase-negative staphylococci. *FEMS Microbiol Lett* 194(2):163-9.
147. Schweigert N, Zehnder AJ, Eggen RI. 2001. Chemical properties of catechols and their molecular modes of toxic action in cells, from microorganisms to mammals. *Environ Microbiol* 3(2):81-91.
148. Beasley FC, Marolda CL, Cheung J, Buac S, Heinrichs DE. 2011. *Staphylococcus aureus* transporters Hts, Sir, and Sst capture iron liberated from human transferrin by Staphyloferrin A, Staphyloferrin B, and catecholamine stress hormones, respectively, and contribute to virulence. *Infect Immun* 79(6):2345-55.
149. Kalyanaraman B, Felix CC, Sealy RC. 1985. Semiquinone anion radicals of catechol(amine)s, catechol estrogens, and their metal ion complexes. *Environ Health Perspect* 64:185-98.
150. Collins MD, Jones D. 1979. The distribution of isoprenoid quinones in streptococci of serological groups D and N. *J Gen Microbiol* 114(1):27-33.
151. Wakeman CA, Hammer ND, Stauff DL, Attia AS, Anzaldi LL, Dikalov SI, Calcutt MW, Skaar EP. 2012. Menaquinone biosynthesis potentiates haem toxicity in *Staphylococcus aureus*. *Mol Microbiol* 86(6):1376-92.
152. Schurig-Briccio LA, Yano T, Rubin H, Gennis RB. 2014. Characterization of the type 2 NADH:menaquinone oxidoreductases from *Staphylococcus aureus* and the bactericidal action of phenothiazines. *Biochim Biophys Acta* 1837(7):954-63.
153. Schlievert PM, Merriman JA, Salgado-Pabon W, Mueller EA, Spaulding AR, Vu BG, Chuang-Smith ON, Kohler PL, Kirby JR. 2013. Menaquinone analogs inhibit growth of bacterial pathogens. *Antimicrob Agents Chemother* 57(11):5432-7.
154. Mone NS, Kamble EE, Pardesi KR, Satpute SK. 2022. Antibacterial and antibiofilm potency of menadione against multidrug-resistant *S. aureus*. *Current Microbiology* 79(9):282.
155. Liebeke M, Pother DC, van Duy N, Albrecht D, Becher D, Hochgrafe F, Lalk M, Hecker M, Antelmann H. 2008. Depletion of thiol-containing proteins in response to quinones in *Bacillus subtilis*. *Mol Microbiol* 69(6):1513-29.

156. Lown JW. 1983. The mechanism of action of quinone antibiotics. *Mol Cell Biochem* 55(1):17-40.
157. Lin J, Cheng J, Wang Y, Shen X. 2018. The pseudomonas quinolone signal (PQS): Not just for quorum sensing anymore. *Front Cell Infect Microbiol* 8:230.
158. Heeb S, Fletcher MP, Chhabra SR, Diggle SP, Williams P, Camara M. 2011. Quinolones: from antibiotics to autoinducers. *FEMS Microbiol Rev* 35(2):247-74.
159. Abken HJ, Tietze M, Brodersen J, Baumer S, Beifuss U, Deppenmeier U. 1998. Isolation and characterization of methanophenazine and function of phenazines in membrane-bound electron transport of *Methanosarcina mazei* Go1. *J Bacteriol* 180(8):2027-32.
160. Zang W, Li D, Gao L, Gao S, Hao P, Bian H. 2022. The antibacterial potential of ciprofloxacin hybrids against *Staphylococcus aureus*. *Curr Top Med Chem* 22(12):1020-1034.
161. Hassan HM, Fridovich I. 1980. Mechanism of the antibiotic action pyocyanine. *J Bacteriol* 141(1):156-63.
162. Limoli DH, Yang J, Khansaheb MK, Helfman B, Peng L, Stecenko AA, Goldberg JB. 2016. *Staphylococcus aureus* and *Pseudomonas aeruginosa* co-infection is associated with cystic fibrosis-related diabetes and poor clinical outcomes. *European Journal of Clinical Microbiology & Infectious Diseases* 35(6):947-953.
163. Fritsch VN, Loi VV, Busche T, Sommer A, Tedin K, Nurnberg DJ, Kalinowski J, Bernhardt J, Fulde M, Antelmann H. 2019. The MarR-type repressor MhqR confers quinone and antimicrobial resistance in *Staphylococcus aureus*. *Antioxid Redox Signal* 31(16):1235-1252.
164. Hastings J, Owen G, Dekker A, Ennis M, Kale N, Muthukrishnan V, Turner S, Swainston N, Mendes P, Steinbeck C. 2016. ChEBI in 2016: Improved services and an expanding collection of metabolites. *Nucleic acids research* 44(D1):D1214-9.
165. De Haan EJ, Charles R. 1969. The mechanism of uncoupling of oxidative phosphorylation by 2-methyl-1,4-naphthoquinone. *Biochimica et Biophysica Acta (BBA) - Bioenergetics* 180(2):417-419.
166. Brunmark A, Cadenas E. 1989. Redox and addition chemistry of quinoid compounds and its biological implications. *Free Radic Biol Med* 7(4):435-77.
167. Schubert M. 1947. The interaction of thiols and quinones. *J Am Chem Soc* 69(3):712.
168. Klotz LO, Hou X, Jacob C. 2014. 1,4-naphthoquinones: from oxidative damage to cellular and inter-cellular signaling. *Molecules* 19(9):14902-18.
169. Rodriguez CE, Shinyashiki M, Froines J, Yu RC, Fukuto JM, Cho AK. 2004. An examination of quinone toxicity using the yeast *Saccharomyces cerevisiae* model system. *Toxicology* 201(1-3):185-96.
170. Schultz TW, Sinks GD, Cronin MTD. 1997. Quinone-induced toxicity to Tetrahymena: structure-activity relationships. *Aquatic Toxicology* 39(3):267-278.
171. Kumagai Y, Shinkai Y, Miura T, Cho AK. 2012. The chemical biology of naphthoquinones and its environmental implications. *Annu Rev Pharmacol Toxicol* 52:221-47.
172. Taguchi K, Fujii S, Yamano S, Cho AK, Kamisuki S, Nakai Y, Sugawara F, Froines JR, Kumagai Y. 2007. An approach to evaluate two-electron reduction of 9,10-phenanthraquinone and redox activity of the hydroquinone associated with oxidative stress. *Free Radic Biol Med* 43(5):789-99.
173. Snell JM, Weissberger A. 1939. The reaction of thiol compounds with quinones. *Journal of the American Chemical Society* 61:450-453.
174. Braun JS, Novak R, Gao G, Murray PJ, Shenep JL. 1999. Pneumolysin, a protein toxin of *Streptococcus pneumoniae*, induces nitric oxide production from macrophages. *Infect Immun* 67(8):3750-6.
175. Malawista SE, Montgomery RR, van Blaricom G. 1992. Evidence for reactive nitrogen intermediates in killing of staphylococci by human neutrophil cytoplasts. A new microbicidal pathway for polymorphonuclear leukocytes. *J Clin Invest* 90(2):631-6.
176. Kröncke KD, Fehsel K, Kolb-Bachofen V. 1998. Inducible nitric oxide synthase in human diseases. *Clin Exp Immunol* 113(2):147-56.
177. Marriott HM, Ali F, Read RC, Mitchell TJ, Whyte MK, Dockrell DH. 2004. Nitric oxide levels regulate macrophage commitment to apoptosis or necrosis during pneumococcal infection. *FASEB J* 18(10):1126-8.

178. Stamler JS, Lamas S, Fang FC. 2001. Nitrosylation: The prototypic redox-based signaling mechanism. *Cell* 106(6):675-683.
179. Bowman LA, McLean S, Poole RK, Fukuto JM. 2011. The diversity of microbial responses to nitric oxide and agents of nitrosative stress close cousins but not identical twins. *Adv Microb Physiol* 59:135-219.
180. Allan RN, Morgan S, Brito-Mutunayagam S, Skipp P, Feelisch M, Hayes SM, Hellier W, Clarke SC, Stoodley P, Burgess A, Ismail-Koch H, Salib RJ, Webb JS, Faust SN, Hall-Stoodley L. 2016. Low concentrations of nitric oxide modulate *Streptococcus pneumoniae* biofilm metabolism and antibiotic tolerance. *Antimicrob Agents Chemother* 60(4):2456-66.
181. Lancaster JR, Jr. 2015. Nitric oxide: a brief overview of chemical and physical properties relevant to therapeutic applications. *Future Sci OA* 1(1):FSO59.
182. Ferrer-Sueta G, Campolo N, Trujillo M, Bartesaghi S, Carballal S, Romero N, Alvarez B, Radi R. 2018. Biochemistry of peroxynitrite and protein tyrosine nitration. *Chem Rev* 118(3):1338-1408.
183. Reiter TA. 2006. NO* chemistry: a diversity of targets in the cell. *Redox Rep* 11(5):194-206.
184. Radi R, Beckman JS, Bush KM, Freeman BA. 1991. Peroxynitrite oxidation of sulfhydryls. The cytotoxic potential of superoxide and nitric oxide. *J Biol Chem* 266(7):4244-50.
185. Cortese-Krott MM, Fernandez BO, Kelm M, Butler AR, Feelisch M. 2015. On the chemical biology of the nitrite/sulfide interaction. *Nitric Oxide* 46:14-24.
186. Gruhlke MC, Slusarenko AJ. 2012. The biology of reactive sulfur species (RSS). *Plant Physiol Biochem* 59:98-107.
187. Surdel MC, Dutter BF, Sulikowski GA, Skaar EP. 2016. Bacterial nitric oxide synthase is required for the *Staphylococcus aureus* response to heme stress. *ACS Infect Dis* 2(8):572-8.
188. Gusarov I, Nudler E. 2005. NO-mediated cytoprotection: instant adaptation to oxidative stress in bacteria. *Proc Natl Acad Sci U S A* 102(39):13855-60.
189. Gusarov I, Shatalin K, Starodubtseva M, Nudler E. 2009. Endogenous nitric oxide protects bacteria against a wide spectrum of antibiotics. *Science* 325(5946):1380-4.
190. Mogen AB, Carroll RK, James KL, Lima G, Silva D, Culver JA, Petucci C, Shaw LN, Rice KC. 2017. *Staphylococcus aureus* nitric oxide synthase (saNOS) modulates aerobic respiratory metabolism and cell physiology. *Mol Microbiol* 105(1):139-157.
191. Peng H, Zhang Y, Palmer LD, Kehl-Fie TE, Skaar EP, Trinidad JC, Giedroc DP. 2017. Hydrogen sulfide and reactive sulfur species impact proteome *S*-sulfhydration and global virulence regulation in *Staphylococcus aureus*. *ACS Infect Dis* 3(10):744-755.
192. Walsh BJC, Giedroc DP. 2020. H_2S and reactive sulfur signaling at the host-bacterial pathogen interface. *J Biol Chem* 295(38):13150-13168.
193. Toliver-Kinsky T, Cui W, Toro G, Lee SJ, Shatalin K, Nudler E, Szabo C. 2019. H_2S, a bacterial defense mechanism against the host immune response. *Infect Immun* 87(1).
194. Shen J, Keithly ME, Armstrong RN, Higgins KA, Edmonds KA, Giedroc DP. 2015. *Staphylococcus aureus* CstB is a novel multidomain persulfide dioxygenase-sulfurtransferase involved in hydrogen sulfide detoxification. *Biochemistry* 54(29):4542-54.
195. Cuevasanta E, Moller MN, Alvarez B. 2017. Biological chemistry of hydrogen sulfide and persulfides. *Arch Biochem Biophys* 617:9-25.
196. Millikin R, Bianco CL, White C, Saund SS, Henriquez S, Sosa V, Akaike T, Kumagai Y, Soeda S, Toscano JP, Lin J, Fukuto JM. 2016. The chemical biology of protein hydropersulfides: Studies of a possible protective function of biological hydropersulfide generation. *Free Radic Biol Med* 97:136-147.
197. Benchoam D, Cuevasanta E, Moller MN, Alvarez B. 2019. Hydrogen sulfide and persulfides oxidation by biologically relevant oxidizing species. *Antioxidants (Basel)* 8(2).
198. Saund SS, Sosa V, Henriquez S, Nguyen QN, Bianco CL, Soeda S, Millikin R, White C, Le H, Ono K, Tantillo DJ, Kumagai Y, Akaike T, Lin J, Fukuto JM. 2015. The chemical biology of hydropersulfides (RSSH): Chemical stability, reactivity and redox roles. *Arch Biochem Biophys* 588:15-24.
199. Gruhlke MCH, Antelmann H, Bernhardt J, Kloubert V, Rink L, Slusarenko AJ. 2019. The human allicin-proteome: *S*-thioallylation of proteins by the garlic defence substance allicin and its biological effects. *Free Radic Biol Med* 131:144-153.

200. Müller A, Eller J, Albrecht F, Prochnow P, Kuhlmann K, Bandow JE, Slusarenko AJ, Leichert LI. 2016. Allicin induces thiol stress in bacteria through *S*-allylmercapto modification of protein cysteines. *J Biol Chem* 291(22):11477-90.
201. Rabinkov A, Miron T, Mirelman D, Wilchek M, Glozman S, Yavin E, Weiner L. 2000. *S*-Allylmercaptoglutathione: the reaction product of allicin with glutathione possesses SH-modifying and antioxidant properties. *Biochimica et Biophysica Acta (BBA) - Molecular Cell Research* 1499(1):144-153.
202. Loi VV, Huyen NTT, Busche T, Tung QN, Gruhlke MCH, Kalinowski J, Bernhardt J, Slusarenko AJ, Antelmann H. 2019. *Staphylococcus aureus* responds to allicin by global *S*-thioallylation - Role of the Brx/BSH/YpdA pathway and the disulfide reductase MerA to overcome allicin stress. *Free Radic Biol Med* 139:55-69.
203. Fang FC. 2004. Antimicrobial reactive oxygen and nitrogen species: concepts and controversies. *Nat Rev Microbiol* 2(10):820-32.
204. Patel RP, McAndrew J, Sellak H, White CR, Jo H, Freeman BA, Darley-Usmar VM. 1999. Biological aspects of reactive nitrogen species. *Biochim Biophys Acta* 1411(2-3):385-400.
205. Fernando V, Zheng X, Walia Y, Sharma V, Letson J, Furuta S. 2019. *S*-Nitrosylation: An Emerging Paradigm of Redox Signaling. *Antioxidants (Basel)* 8(9).
206. Broniowska KA, Hogg N. 2012. The chemical biology of *S*-nitrosothiols. *Antioxid Redox Signal* 17(7):969-80.
207. Wolhuter K, Whitwell HJ, Switzer CH, Burgoyne JR, Timms JF, Eaton P. 2018. Evidence against stable protein *S*-nitrosylation as a widespread mechanism of post-translational regulation. *Mol Cell* 69(3):438-450 e5.
208. Martinez-Ruiz A, Lamas S. 2007. Signalling by NO-induced protein *S*-nitrosylation and *S*-glutathionylation: convergences and divergences. *Cardiovasc Res* 75(2):220-8.
209. Fukuto JM, Carrington SJ, Tantillo DJ, Harrison JG, Ignarro LJ, Freeman BA, Chen A, Wink DA. 2012. Small molecule signaling agents: the integrated chemistry and biochemistry of nitrogen oxides, oxides of carbon, dioxygen, hydrogen sulfide, and their derived species. *Chem Res Toxicol* 25(4):769-93.
210. Reyes-Caballero H, Campanello GC, Giedroc DP. 2011. Metalloregulatory proteins: metal selectivity and allosteric switching. *Biophys Chem* 156(2-3):103-14.
211. Andreini C, Bertini I, Cavallaro G, Holliday GL, Thornton JM. 2008. Metal ions in biological catalysis: from enzyme databases to general principles. *J Biol Inorg Chem* 13(8):1205-18.
212. Murdoch CC, Skaar EP. 2022. Nutritional immunity: the battle for nutrient metals at the host-pathogen interface. *Nat Rev Microbiol* doi:10.1038/s41579-022-00745-6.
213. Miethke M, Marahiel MA. 2007. Siderophore-based iron acquisition and pathogen control. *Microbiol Mol Biol Rev* 71(3):413-51.
214. Hood MI, Skaar EP. 2012. Nutritional immunity: transition metals at the pathogen-host interface. *Nat Rev Microbiol* 10(8):525-37.
215. Hammer ND, Skaar EP. 2011. Molecular mechanisms of *Staphylococcus aureus* iron acquisition. *Annu Rev Microbiol* 65:129-47.
216. van Dijk MC, de Kruijff RM, Hagedoorn PL. 2022. The role of iron in *Staphylococcus aureus* infection and human disease: A metal tug of war at the host-microbe interface. *Front Cell Dev Biol* 10:857237.
217. Velayudhan J, Castor M, Richardson A, Main-Hester KL, Fang FC. 2007. The role of ferritins in the physiology of *Salmonella enterica* sv. Typhimurium: a unique role for ferritin B in iron-sulphur cluster repair and virulence. *Mol Microbiol* 63(5):1495-507.
218. Dow A, Sule P, O'Donnell TJ, Burger A, Mattila JT, Antonio B, Vergara K, Marcantonio E, Adams LG, James N, Williams PG, Cirillo JD, Prisic S. 2021. Zinc limitation triggers anticipatory adaptations in *Mycobacterium tuberculosis*. *PLoS Pathog* 17(5):e1009570.
219. Imlay JA. 2006. Iron-sulphur clusters and the problem with oxygen. *Mol Microbiol* 59(4):1073-82.
220. Gaballa A, Helmann JD. 2002. A peroxide-induced zinc uptake system plays an important role in protection against oxidative stress in *Bacillus subtilis*. *Mol Microbiol* 45(4):997-1005.
221. Perry JJ, Shin DS, Getzoff ED, Tainer JA. 2010. The structural biochemistry of the superoxide dismutases. *Biochim Biophys Acta* 1804(2):245-62.

222. Imlay JA. 2014. The mismetallation of enzymes during oxidative stress. *J Biol Chem* 289(41):28121-8.
223. Giachino A, Waldron KJ. 2020. Copper tolerance in bacteria requires the activation of multiple accessory pathways. *Mol Microbiol* 114(3):377-390.
224. Tseng HJ, Srikhanta Y, McEwan AG, Jennings MP. 2001. Accumulation of manganese in *Neisseria gonorrhoeae* correlates with resistance to oxidative killing by superoxide anion and is independent of superoxide dismutase activity. *Mol Microbiol* 40(5):1175-86.
225. Sachla AJ, Luo Y, Helmann JD. 2021. Manganese impairs the QoxABCD terminal oxidase leading to respiration-associated toxicity. *Mol Microbiol* 116(3):729-742.
226. Martin JE, Lisher JP, Winkler ME, Giedroc DP. 2017. Perturbation of manganese metabolism disrupts cell division in *Streptococcus pneumoniae*. *Mol Microbiol* 104(2):334-348.
227. von Pein JB, Stocks CJ, Schembri MA, Kapetanovic R, Sweet MJ. 2021. An alloy of zinc and innate immunity: Galvanising host defence against infection. *Cell Microbiol* 23(1):e13268.
228. Sheldon JR, Skaar EP. 2019. Metals as phagocyte antimicrobial effectors. *Curr Opin Immunol* 60:1-9.
229. Keyer K, Imlay JA. 1996. Superoxide accelerates DNA damage by elevating free-iron levels. *Proc Natl Acad Sci U S A* 93(24):13635-40.
230. Hartwig A. 2001. Zinc finger proteins as potential targets for toxic metal ions: differential effects on structure and function. *Antioxid Redox Signal* 3(4):625-34.
231. Sen A, Imlay JA. 2021. How microbes defend themselves from incoming hydrogen peroxide. *Front Immunol* 12:667343.
232. Crack JC, Gaskell AA, Green J, Cheesman MR, Le Brun NE, Thomson AJ. 2008. Influence of the environment on the $[4Fe\text{-}4S]^{2+}$ to $[2Fe\text{-}2S]^{2+}$ cluster switch in the transcriptional regulator FNR. *J Am Chem Soc* 130(5):1749-58.
233. Flint DH, Tuminello JF, Emptage MH. 1993. The inactivation of Fe-S cluster containing hydro-lyases by superoxide. *J Biol Chem* 268(30):22369-76.
234. Crack JC, Green J, Thomson AJ, Le Brun NE. 2014. Iron-sulfur clusters as biological sensors: the chemistry of reactions with molecular oxygen and nitric oxide. *Acc Chem Res* 47(10):3196-205.
235. Green J, Rolfe MD, Smith LJ. 2014. Transcriptional regulation of bacterial virulence gene expression by molecular oxygen and nitric oxide. *Virulence* 5(8):794-809.
236. Repine JE, Fox RB, Berger EM. 1981. Hydrogen peroxide kills *Staphylococcus aureus* by reacting with staphylococcal iron to form hydroxyl radical. *J Biol Chem* 256(14):7094-6.
237. Sambri V, Cevenini R, La Placa M. 1991. Susceptibility of iron-loaded *Borrelia burgdorferi* to killing by hydrogen peroxide and human polymorphonuclear leucocytes. *FEMS Microbiol Lett* 65(1):67-71.
238. Valko M, Morris H, Cronin MT. 2005. Metals, toxicity and oxidative stress. *Curr Med Chem* 12(10):1161-208.
239. Faulkner MJ, Helmann JD. 2011. Peroxide stress elicits adaptive changes in bacterial metal ion homeostasis. *Antioxid Redox Signal* 15(1):175-89.
240. Yamamoto Y, Fukui K, Koujin N, Ohya H, Kimura K, Kamio Y. 2004. Regulation of the intracellular free iron pool by Dpr provides oxygen tolerance to *Streptococcus mutans*. *J Bacteriol* 186(18):5997-6002.
241. Fontenot CR, Tasnim H, Valdes KA, Popescu CV, Ding H. 2020. Ferric uptake regulator (Fur) reversibly binds a [2Fe-2S] cluster to sense intracellular iron homeostasis in *Escherichia coli*. *J Biol Chem* 295(46):15454-15463.
242. Fontenot CR, Ding H. 2022. Ferric uptake regulators (Fur) from *Vibrio cholerae* and *Helicobacter pylori* bind a [2Fe-2S] cluster in response to elevation of intracellular free iron content. *Biometals* 35(3):591-600.
243. Horsburgh MJ, Clements MO, Crossley H, Ingham E, Foster SJ. 2001. PerR controls oxidative stress resistance and iron storage proteins and is required for virulence in *Staphylococcus aureus*. *Infect Immun* 69(6):3744-54.
244. Horsburgh MJ, Wharton SJ, Cox AG, Ingham E, Peacock S, Foster SJ. 2002. MntR modulates expression of the PerR regulon and superoxide resistance in *Staphylococcus aureus* through control of manganese uptake. *Mol Microbiol* 44(5):1269-86.

245. Horsburgh MJ, Ingham E, Foster SJ. 2001. In *Staphylococcus aureus*, Fur is an interactive regulator with PerR, contributes to virulence, and is necessary for oxidative stress resistance through positive regulation of catalase and iron homeostasis. *J Bacteriol* 183(2):468-75.
246. Liochev SI, Fridovich I. 1999. Superoxide and iron: partners in crime. *IUBMB Life* 48(2):157-61.
247. Baker J, Sitthisak S, Sengupta M, Johnson M, Jayaswal RK, Morrissey JA. 2010. Copper stress induces a global stress response in *Staphylococcus aureus* and represses *sae* and *agr* expression and biofilm formation. *Appl Environ Microbiol* 76(1):150-60.
248. Shafeeq S, Yesilkaya H, Kloosterman TG, Narayanan G, Wandel M, Andrew PW, Kuipers OP, Morrissey JA. 2011. The *cop* operon is required for copper homeostasis and contributes to virulence in *Streptococcus pneumoniae*. *Mol Microbiol* 81(5):1255-70.
249. Macomber L, Rensing C, Imlay JA. 2007. Intracellular copper does not catalyze the formation of oxidative DNA damage in *Escherichia coli*. *J Bacteriol* 189(5):1616-26.
250. Johnson MD, Kehl-Fie TE, Rosch JW. 2015. Copper intoxication inhibits aerobic nucleotide synthesis in *Streptococcus pneumoniae*. *Metallomics* 7(5):786-94.
251. Macomber L, Imlay JA. 2009. The iron-sulfur clusters of dehydratases are primary intracellular targets of copper toxicity. *Proc Natl Acad Sci U S A* 106(20):8344-9.
252. Tan G, Yang J, Li T, Zhao J, Sun S, Li X, Lin C, Li J, Zhou H, Lyu J, Ding H. 2017. Anaerobic copper toxicity and iron-sulfur cluster biogenesis in *Escherichia coli*. *Appl Environ Microbiol* 83(16).
253. Liao X, Li H, Guo Y, Yang F, Chen Y, He X, Li H, Xia W, Mao ZW, Sun H. 2022. Regulation of DNA-binding activity of the *Staphylococcus aureus* catabolite control protein A by copper (II)-mediated oxidation. *J Biol Chem* 298(3):101587.
254. Yuan X, Pham AN, Miller CJ, Waite TD. 2013. Copper-catalyzed hydroquinone oxidation and associated redox cycling of copper under conditions typical of natural saline waters. *Environ Sci Technol* 47(15):8355-64.
255. Mancini S, Abicht HK, Gonskikh Y, Solioz M. 2015. A copper-induced quinone degradation pathway provides protection against combined copper/quinone stress in *Lactococcus lactis* IL1403. *Mol Microbiol* 95(4):645-59.
256. Kalia D, Merey G, Nakayama S, Zheng Y, Zhou J, Luo Y, Guo M, Roembke BT, Sintim HO. 2013. Nucleotide, c-di-GMP, c-di-AMP, cGMP, cAMP, (p)ppGpp signaling in bacteria and implications in pathogenesis. *Chemical Society Reviews* 42(1):305-341.
257. Hecker M, Pané-Farré J, Völker U. 2007. SigB-dependent general stress response in *Bacillus subtilis* and related Gram-positive bacteria. *Annual Review of Microbiology* 61(1):215-236.
258. Gaca AO, Colomer-Winter C, Lemos JA. 2015. Many means to a common end: the intricacies of (p)ppGpp metabolism and its control of bacterial homeostasis. *J Bacteriol* 197(7):1146-56.
259. Reiss S, Pane-Farre J, Fuchs S, Francois P, Liebeke M, Schrenzel J, Lindequist U, Lalk M, Wolz C, Hecker M, Engelmann S. 2012. Global analysis of the *Staphylococcus aureus* response to mupirocin. *Antimicrob Agents Chemother* 56(2):787-804.
260. Steinchen W, Zegarra V, Bange G. 2020. (p)ppGpp: Magic modulators of bacterial physiology and metabolism. *Front Microbiol* 11:2072.
261. Atkinson GC, Tenson T, Hauryliuk V. 2011. The RelA/SpoT homolog (RSH) superfamily: distribution and functional evolution of ppGpp synthetases and hydrolases across the tree of life. *PLoS One* 6(8):e23479.
262. Wolz C, Geiger T, Goerke C. 2010. The synthesis and function of the alarmone (p)ppGpp in firmicutes. *Int J Med Microbiol* 300(2-3):142-7.
263. Yang N, Xie S, Tang NY, Choi MY, Wang Y, Watt RM. 2019. The Ps and Qs of alarmone synthesis in *Staphylococcus aureus*. *PLoS One* 14(10):e0213630.
264. Geiger T, Kastle B, Gratani FL, Goerke C, Wolz C. 2014. Two small (p)ppGpp synthases in *Staphylococcus aureus* mediate tolerance against cell envelope stress conditions. *J Bacteriol* 196(4):894-902.
265. Manav MC, Beljantseva J, Bojer MS, Tenson T, Ingmer H, Hauryliuk V, Brodersen DE. 2018. Structural basis for (p)ppGpp synthesis by the *Staphylococcus aureus* small alarmone synthetase RelP. *J Biol Chem* 293(9):3254-3264.

266. Patil PR, Vithani N, Singh V, Kumar A, Prakash B. 2020. A revised mechanism for (p)ppGpp synthesis by Rel proteins: The critical role of the 2'-OH of GTP. *J Biol Chem* 295(37):12851-12867.
267. Steinchen W, Vogt MS, Altegoer F, Giammarinaro PI, Horvatek P, Wolz C, Bange G. 2018. Structural and mechanistic divergence of the small (p)ppGpp synthetases RelP and RelQ. *Sci Rep* 8(1):2195.
268. Nanamiya H, Kasai K, Nozawa A, Yun C-S, Narisawa T, Murakami K, Natori Y, Kawamura F, Tozawa Y. 2008. Identification and functional analysis of novel (p)ppGpp synthetase genes in *Bacillus subtilis*. *Molecular Microbiology* 67(2):291-304.
269. Hauryliuk V, Atkinson GC, Murakami KS, Tenson T, Gerdes K. 2015. Recent functional insights into the role of (p)ppGpp in bacterial physiology. *Nat Rev Microbiol* 13(5):298-309.
270. Geiger T, Goerke C, Fritz M, Schafer T, Ohlsen K, Liebeke M, Lalk M, Wolz C. 2010. Role of the (p)ppGpp synthase RSH, a RelA/SpoT homolog, in stringent response and virulence of *Staphylococcus aureus*. *Infect Immun* 78(5):1873-83.
271. Gratani FL, Horvatek P, Geiger T, Borisova M, Mayer C, Grin I, Wagner S, Steinchen W, Bange G, Velic A, Macek B, Wolz C. 2018. Regulation of the opposing (p)ppGpp synthetase and hydrolase activities in a bifunctional RelA/SpoT homologue from *Staphylococcus aureus*. *PLoS Genet* 14(7):e1007514.
272. Kanjee U, Ogata K, Houry WA. 2012. Direct binding targets of the stringent response alarmone (p)ppGpp. *Mol Microbiol* 85(6):1029-43.
273. Ross W, Vrentas CE, Sanchez-Vazquez P, Gaal T, Gourse RL. 2013. The magic spot: a ppGpp binding site on *E. coli* RNA polymerase responsible for regulation of transcription initiation. *Mol Cell* 50(3):420-9.
274. Anderson BW, Fung DK, Wang JD. 2021. Regulatory themes and variations by the stress-signaling nucleotide alarmones (p)ppGpp in bacteria. *Annu Rev Genet* 55:115-133.
275. Steinchen W, Bange G. 2016. The magic dance of the alarmones (p)ppGpp. *Mol Microbiol* 101(4):531-44.
276. Irving SE, Choudhury NR, Corrigan RM. 2021. The stringent response and physiological roles of (pp)pGpp in bacteria. *Nat Rev Microbiol* 19(4):256-271.
277. Kastle B, Geiger T, Gratani FL, Reisinger R, Goerke C, Borisova M, Mayer C, Wolz C. 2015. rRNA regulation during growth and under stringent conditions in *Staphylococcus aureus*. *Environ Microbiol* 17(11):4394-405.
278. Horvatek P, Salzer A, Hanna AMF, Gratani FL, Keinhorster D, Korn N, Borisova M, Mayer C, Rejman D, Mader U, Wolz C. 2020. Inducible expression of (pp)pGpp synthetases in *Staphylococcus aureus* is associated with activation of stress response genes. *PLoS Genet* 16(12):e1009282.
279. Geiger T, Wolz C. 2014. Intersection of the stringent response and the CodY regulon in low GC Gram-positive bacteria. *Int J Med Microbiol* 304(2):150-5.
280. Kriel A, Bittner AN, Kim SH, Liu K, Tehranchi AK, Zou WY, Rendon S, Chen R, Tu BP, Wang JD. 2012. Direct regulation of GTP homeostasis by (p)ppGpp: a critical component of viability and stress resistance. *Mol Cell* 48(2):231-41.
281. Anderson BW, Hao A, Satyshur KA, Keck JL, Wang JD. 2020. Molecular mechanism of regulation of the purine salvage enzyme XPRT by the alarmones pppGpp, ppGpp, and pGpp. *J Mol Biol* 432(14):4108-4126.
282. Anderson BW, Schumacher MA, Yang J, Turdiev A, Turdiev H, Schroeder JW, He Q, Lee VT, Brennan RG, Wang JD. 2022. The nucleotide messenger (p)ppGpp is an anti-inducer of the purine synthesis transcription regulator PurR in Bacillus. *Nucleic Acids Res* 50(2):847-866.
283. Gourse RL, Chen AY, Gopalkrishnan S, Sanchez-Vazquez P, Myers A, Ross W. 2018. Transcriptional Responses to ppGpp and DksA. *Annu Rev Microbiol* 72:163-184.
284. Tojo S, Kumamoto K, Hirooka K, Fujita Y. 2010. Heavy involvement of stringent transcription control depending on the adenine or guanine species of the transcription initiation site in glucose and pyruvate metabolism in *Bacillus subtilis*. *J Bacteriol* 192(6):1573-85.
285. Krásny L, Gourse RL. 2004. An alternative strategy for bacterial ribosome synthesis: *Bacillus subtilis* rRNA transcription regulation. *EMBO J* 23(22):4473-83.

286. Krasny L, Tiserova H, Jonak J, Rejman D, Sanderova H. 2008. The identity of the transcription +1 position is crucial for changes in gene expression in response to amino acid starvation in *Bacillus subtilis*. *Mol Microbiol* 69(1):42-54.
287. Brinsmade SR. 2017. CodY, a master integrator of metabolism and virulence in Gram-positive bacteria. *Curr Genet* 63(3):417-425.
288. Majerczyk CD, Dunman PM, Luong TT, Lee CY, Sadykov MR, Somerville GA, Bodi K, Sonenshein AL. 2010. Direct targets of CodY in *Staphylococcus aureus*. *J Bacteriol* 192(11):2861-77.
289. Geiger T, Francois P, Liebeke M, Fraunholz M, Goerke C, Krismer B, Schrenzel J, Lalk M, Wolz C. 2012. The stringent response of *Staphylococcus aureus* and its impact on survival after phagocytosis through the induction of intracellular PSMs expression. *PLoS Pathog* 8(11):e1003016.
290. Milon P, Tischenko E, Tomsic J, Caserta E, Folkers G, La Teana A, Rodnina MV, Pon CL, Boelens R, Gualerzi CO. 2006. The nucleotide-binding site of bacterial translation initiation factor 2 (IF2) as a metabolic sensor. *Proc Natl Acad Sci U S A* 103(38):13962-7.
291. Mitkevich VA, Ermakov A, Kulikova AA, Tankov S, Shyp V, Soosaar A, Tenson T, Makarov AA, Ehrenberg M, Hauryliuk V. 2010. Thermodynamic characterization of ppGpp binding to EF-G or IF2 and of initiator tRNA binding to free IF2 in the presence of GDP, GTP, or ppGpp. *J Mol Biol* 402(5):838-46.
292. Diez S, Ryu J, Caban K, Gonzalez RL, Jr., Dworkin J. 2020. The alarmones (p)ppGpp directly regulate translation initiation during entry into quiescence. *Proc Natl Acad Sci U S A* 117(27):15565-15572.
293. Bennison DJ, Irving SE, Corrigan RM. 2019. The impact of the stringent response on TRAFAC GTPases and prokaryotic ribosome assembly. *Cells* 8(11).
294. Vinogradova DS, Zegarra V, Maksimova E, Nakamoto JA, Kasatsky P, Paleskava A, Konevega AL, Milon P. 2020. How the initiating ribosome copes with ppGpp to translate mRNAs. *PLoS Biol* 18(1):e3000593.
295. Corrigan RM, Bellows LE, Wood A, Grundling A. 2016. ppGpp negatively impacts ribosome assembly affecting growth and antimicrobial tolerance in Gram-positive bacteria. *Proc Natl Acad Sci U S A* 113(12):E1710-9.
296. Pausch P, Steinchen W, Wieland M, Klaus T, Freibert SA, Altegoer F, Wilson DN, Bange G. 2018. Structural basis for (p)ppGpp-mediated inhibition of the GTPase RbgA. *J Biol Chem* 293(51):19699-19709.
297. Basu A, Yap MN. 2017. Disassembly of the *Staphylococcus aureus* hibernating 100S ribosome by an evolutionarily conserved GTPase. *Proc Natl Acad Sci U S A* 114(39):E8165-E8173.
298. Bennison DJ, Nakamoto JA, Craggs TD, Milon P, Rafferty JB, Corrigan RM. 2021. The stringent response inhibits 70S ribosome formation in *Staphylococcus aureus* by impeding GTPase-ribosome interactions. *mBio* 12(6):e0267921.
299. Yang J, Anderson BW, Turdiev A, Turdiev H, Stevenson DM, Amador-Noguez D, Lee VT, Wang JD. 2020. The nucleotide pGpp acts as a third alarmone in Bacillus, with functions distinct from those of (p) ppGpp. *Nat Commun* 11(1):5388.
300. Petchiappan A, Naik SY, Chatterji D. 2020. RelZ-mediated stress response in *Mycobacterium smegmatis*: pGpp synthesis and its regulation. *J Bacteriol* 202(2).
301. Poudel A, Pokhrel A, Oludiran A, Coronado EJ, Alleyne K, Gilfus MM, Gurung RK, Adhikari SB, Purcell EB. 2022. Unique features of alarmone metabolism in *Clostridioides difficile*. *J Bacteriol* 204(4):e0057521.
302. Ooga T, Ohashi Y, Kuramitsu S, Koyama Y, Tomita M, Soga T, Masui R. 2009. Degradation of ppGpp by nudix pyrophosphatase modulates the transition of growth phase in the bacterium *Thermus thermophilus*. *J Biol Chem* 284(23):15549-56.
303. Fritsch VN, Loi VV, Busche T, Tung QN, Lill R, Horvatek P, Wolz C, Kalinowski J, Antelmann H. 2020. The alarmone (p)ppGpp confers tolerance to oxidative stress during the stationary phase by maintenance of redox and iron homeostasis in *Staphylococcus aureus*. *Free Radic Biol Med* 161:351-364.
304. Dalebroux ZD, Svensson SL, Gaynor EC, Swanson MS. 2010. ppGpp conjures bacterial virulence. *Microbiol Mol Biol Rev* 74(2):171-99.

305. Boehm A, Steiner S, Zaehringer F, Casanova A, Hamburger F, Ritz D, Keck W, Ackermann M, Schirmer T, Jenal U. 2009. Second messenger signalling governs *Escherichia coli* biofilm induction upon ribosomal stress. *Mol Microbiol* 72(6):1500-16.
306. Gao W, Cameron DR, Davies JK, Kostoulias X, Stepnell J, Tuck KL, Yeaman MR, Peleg AY, Stinear TP, Howden BP. 2013. The RpoB $H_{481}Y$ rifampicin resistance mutation and an active stringent response reduce virulence and increase resistance to innate immune responses in *Staphylococcus aureus*. *J Infect Dis* 207(6):929-39.
307. Pacios O, Blasco L, Bleriot I, Fernandez-Garcia L, Ambroa A, Lopez M, Bou G, Canton R, Garcia-Contreras R, Wood TK, Tomas M. 2020. (p)ppGpp and its role in bacterial persistence: New challenges. *Antimicrob Agents Chemother* 64(10).
308. Kundra S, Colomer-Winter C, Lemos JA. 2020. Survival of the fittest: The relationship of (p)ppGpp with bacterial virulence. *Front Microbiol* 11:601417.
309. Salzer A, Keinhorster D, Kastle C, Kastle B, Wolz C. 2020. Small alarmone synthetases RelP and RelQ of *Staphylococcus aureus* are involved in biofilm formation and maintenance under cell wall stress conditions. *Front Microbiol* 11:575882.
310. Li Y, Croucher NJ, Thompson CM, Trzcinski K, Hanage WP, Lipsitch M. 2015. Identification of pneumococcal colonization determinants in the stringent response pathway facilitated by genomic diversity. *BMC Genomics* 16:369.
311. Aggarwal SD, Lloyd AJ, Yerneni SS, Narciso AR, Shepherd J, Roper DI, Dowson CG, Filipe SR, Hiller NL. 2021. A molecular link between cell wall biosynthesis, translation fidelity, and stringent response in *Streptococcus pneumoniae*. *Proc Natl Acad Sci U S A* 118(14).
312. Kazmierczak KM, Wayne KJ, Rechtsteiner A, Winkler ME. 2009. Roles of $rel_{(Spn)}$ in stringent response, global regulation and virulence of serotype 2 *Streptococcus pneumoniae* D39. *Mol Microbiol* 72(3):590-611.
313. Hava DL, Camilli A. 2002. Large-scale identification of serotype 4 *Streptococcus pneumoniae* virulence factors. *Mol Microbiol* 45(5):1389-406.
314. Kim HY, Go J, Lee KM, Oh YT, Yoon SS. 2018. Guanosine tetra- and pentaphosphate increase antibiotic tolerance by reducing reactive oxygen species production in *Vibrio cholerae*. *J Biol Chem* 293(15):5679-5694.
315. Khakimova M, Ahlgren HG, Harrison JJ, English AM, Nguyen D. 2013. The stringent response controls catalases in *Pseudomonas aeruginosa* and is required for hydrogen peroxide and antibiotic tolerance. *J Bacteriol* 195(9):2011-20.
316. Martins D, McKay G, Sampathkumar G, Khakimova M, English AM, Nguyen D. 2018. Superoxide dismutase activity confers (p)ppGpp-mediated antibiotic tolerance to stationary-phase *Pseudomonas aeruginosa*. *Proc Natl Acad Sci U S A* 115(39):9797-9802.
317. Ma Z, King K, Alqahtani M, Worden M, Muthuraman P, Cioffi CL, Bakshi CS, Malik M. 2019. Stringent response governs the oxidative stress resistance and virulence of *Francisella tularensis*. *PLoS One* 14(10):e0224094.
318. Wu J, Long Q, Xie J. 2010. (p)ppGpp and drug resistance. *J Cell Physiol* 224(2):300-4.
319. Spira B, Ospino K. 2020. Diversity in *E. coli* (p)ppGpp levels and its consequences. *Front Microbiol* 11:1759.
320. Kim C, Mwangi M, Chung M, Milheirico C, de Lencastre H, Tomasz A. 2013. The mechanism of heterogeneous beta-lactam resistance in MRSA: key role of the stringent stress response. *PLoS One* 8(12):e82814.
321. Mwangi MM, Kim C, Chung M, Tsai J, Vijayadamodar G, Benitez M, Jarvie TP, Du L, Tomasz A. 2013. Whole-genome sequencing reveals a link between beta-lactam resistance and synthetases of the alarmone (p)ppGpp in *Staphylococcus aureus*. *Microb Drug Resist* 19(3):153-9.
322. Bryson D, Hettle AG, Boraston AB, Hobbs JK. 2020. Clinical mutations that partially activate the stringent response confer multidrug tolerance in *Staphylococcus aureus*. *Antimicrob Agents Chemother* 64(3).
323. Bhawini A, Pandey P, Dubey AP, Zehra A, Nath G, Mishra MN. 2019. RelQ mediates the expression of beta-lactam resistance in methicillin-resistant *Staphylococcus aureus*. *Front Microbiol* 10:339.

324. Aedo S, Tomasz A. 2016. Role of the stringent stress response in the antibiotic resistance phenotype of methicillin-resistant *Staphylococcus aureus*. *Antimicrob Agents Chemother* 60(4):2311-7.
325. Schäfer H, Beckert B, Frese CK, Steinchen W, Nuss AM, Beckstette M, Hantke I, Driller K, Sudzinova P, Krasny L, Kaever V, Dersch P, Bange G, Wilson DN, Turgay K. 2020. The alarmones (p)ppGpp are part of the heat shock response of *Bacillus subtilis*. *PLoS Genet* 16(3):e1008275.
326. Fitzsimmons LF, Liu L, Kim JS, Jones-Carson J, Vazquez-Torres A. 2018. Salmonella reprograms nucleotide metabolism in its adaptation to nitrosative stress. *mBio* 9(1).
327. VanBogelen RA, Kelley PM, Neidhardt FC. 1987. Differential induction of heat shock, SOS, and oxidation stress regulons and accumulation of nucleotides in *Escherichia coli*. *J Bacteriol* 169(1):26-32.
328. Hanna N, Ouahrani-Bettache S, Drake KL, Adams LG, Kohler S, Occhialini A. 2013. Global Rsh-dependent transcription profile of *Brucella suis* during stringent response unravels adaptation to nutrient starvation and cross-talk with other stress responses. *BMC Genomics* 14:459.
329. Gaca AO, Kajfasz JK, Miller JH, Liu K, Wang JD, Abranches J, Lemos JA. 2013. Basal levels of (p)ppGpp in *Enterococcus faecalis*: the magic beyond the stringent response. *mBio* 4(5):e00646-13.
330. Nguyen D, Joshi-Datar A, Lepine F, Bauerle E, Olakanmi O, Beer K, McKay G, Siehnel R, Schafhauser J, Wang Y, Britigan BE, Singh PK. 2011. Active starvation responses mediate antibiotic tolerance in biofilms and nutrient-limited bacteria. *Science* 334(6058):982-6.
331. Pulschen AA, Fernandes AZN, Cunha AF, Sastre DE, Matsuguma BE, Gueiros-Filho FJ. 2021. Many birds with one stone: targeting the (p)ppGpp signaling pathway of bacteria to improve antimicrobial therapy. *Biophys Rev* 13(6):1039-1051.
332. Boutte CC, Crosson S. 2013. Bacterial lifestyle shapes stringent response activation. *Trends Microbiol* 21(4):174-80.
333. Mäder U, Nicolas P, Depke M, Pané-Farré J, Debarbouille M, van der Kooi-Pol MM, Guérin C, Dérozier S, Hiron A, Jarmer H, Leduc A, Michalik S, Reilman E, Schaffer M, Schmidt F, Bessières P, Noirot P, Hecker M, Msadek T, Völker U, van Dijl JM. 2016. *Staphylococcus aureus* transcriptome architecture: From laboratory to infection-mimicking conditions. *PLoS Genet* 12(4):e1005962.
334. Kriel A, Brinsmade SR, Tse JL, Tehranchi AK, Bittner AN, Sonenshein AL, Wang JD. 2014. GTP dysregulation in *Bacillus subtilis* cells lacking (p)ppGpp results in phenotypic amino acid auxotrophy and failure to adapt to nutrient downshift and regulate biosynthesis genes. *J Bacteriol* 196(1):189-201.
335. Bolzán AD, Bianchi MS. 2001. Genotoxicity of streptonigrin: a review. *Mutat Res* 488(1):25-37.
336. Colomer-Winter C, Gaca AO, Lemos JA. 2017. Association of metal homeostasis and (p)ppGpp regulation in the pathophysiology of *Enterococcus faecalis*. *Infect Immun* 85(7).
337. Vinella D, Albrecht C, Cashel M, D'Ari R. 2005. Iron limitation induces SpoT-dependent accumulation of ppGpp in *Escherichia coli*. *Mol Microbiol* 56(4):958-70.
338. Brown L, Gentry D, Elliott T, Cashel M. 2002. DksA affects ppGpp induction of RpoS at a translational level. *J Bacteriol* 184(16):4455-65.
339. Corrigan RM, Bowman L, Willis AR, Kaever V, Grundling A. 2015. Cross-talk between two nucleotide-signaling pathways in *Staphylococcus aureus*. *J Biol Chem* 290(9):5826-39.
340. Rao F, See RY, Zhang D, Toh DC, Ji Q, Liang ZX. 2010. YybT is a signaling protein that contains a cyclic dinucleotide phosphodiesterase domain and a GGDEF domain with ATPase activity. *J Biol Chem* 285(1):473-82.
341. Peterson BN, Young MKM, Luo S, Wang J, Whiteley AT, Woodward JJ, Tong L, Wang JD, Portnoy DA. 2020. (p)ppGpp and c-di-AMP homeostasis is controlled by CbpB in *Listeria monocytogenes*. *mBio* 11(4).
342. Zeden MS, Schuster CF, Bowman L, Zhong Q, Williams HD, Grundling A. 2018. Cyclic di-adenosine monophosphate (c-di-AMP) is required for osmotic regulation in *Staphylococcus aureus* but dispensable for viability in anaerobic conditions. *J Biol Chem* 293(9):3180-3200.

343. Gray MJ, Wholey WY, Jakob U. 2013. Bacterial responses to reactive chlorine species. *Annu Rev Microbiol* 67:141-60.
344. Xiang Y, Jin C, Wang W, Wang Z, Huang Y, Fan F, Ma Y, Zhang X, Xu W, Yin Y, He Y. 2017. The critical role of myeloperoxidase in *Streptococcus pneumoniae* clearance and tissue damage during mouse acute otitis media. *Innate Immun* 23(3):296-306.
345. Green JN, Kettle AJ, Winterbourn CC. 2014. Protein chlorination in neutrophil phagosomes and correlation with bacterial killing. *Free Radic Biol Med* 77:49-56.
346. Klebanoff SJ, Kettle AJ, Rosen H, Winterbourn CC, Nauseef WM. 2013. Myeloperoxidase: a front-line defender against phagocytosed microorganisms. *J Leukoc Biol* 93(2):185-98.
347. FDA. 2016. FDA (U.S. Food and Drug Administration) executive summary - Classification of wound dressings combined with drugs. Available online:https://www.fda.gov/media/100005/download. (accessed on 07/11/2022).
348. Nedelea AG, Plant RL, Robins LI, Maddocks SE. 2022. Testing the efficacy of topical antimicrobial treatments using a two- and five-species chronic wound biofilm model. *J Appl Microbiol* 132(1):715-724.
349. Kiamco MM, Zmuda HM, Mohamed A, Call DR, Raval YS, Patel R, Beyenal H. 2019. Hypochlorous-acid-generating electrochemical scaffold for treatment of wound biofilms. *Sci Rep* 9(1):2683.
350. Sultana S, Foti A, Dahl JU. 2020. Bacterial defense systems against the neutrophilic oxidant hypochlorous acid. *Infect Immun* 88(7).
351. da Cruz Nizer WS, Inkovskiy V, Overhage J. 2020. Surviving reactive chlorine stress: Responses of Gram-negative bacteria to hypochlorous acid. *Microorganisms* 8(8).
352. Varatnitskaya M, Degrossoli A, Leichert LI. 2021. Redox regulation in host-pathogen interactions: thiol switches and beyond. *Biol Chem* 402(3):299-316.
353. Tung QN, Busche T, Van Loi V, Kalinowski J, Antelmann H. 2020. The redox-sensing MarR-type repressor HypS controls hypochlorite and antimicrobial resistance in *Mycobacterium smegmatis*. *Free Radic Biol Med* 147:252-261.
354. Palm GJ, Khanh Chi B, Waack P, Gronau K, Becher D, Albrecht D, Hinrichs W, Read RJ, Antelmann H. 2012. Structural insights into the redox-switch mechanism of the MarR/DUF24-type regulator HypR. *Nucleic Acids Res* 40(9):4178-92.
355. Loi VV, Busche T, Tedin K, Bernhardt J, Wollenhaupt J, Huyen NTT, Weise C, Kalinowski J, Wahl MC, Fulde M, Antelmann H. 2018. Redox-sensing under hypochlorite stress and infection conditions by the Rrf2-family repressor HypR in *Staphylococcus aureus*. *Antioxid Redox Signal* 29(7):615-636.
356. Chi BK, Gronau K, Mader U, Hessling B, Becher D, Antelmann H. 2011. *S*-bacillithiolation protects against hypochlorite stress in *Bacillus subtilis* as revealed by transcriptomics and redox proteomics. *Mol Cell Proteomics* 10(11):M111 009506.
357. Hillion M, Antelmann H. 2015. Thiol-based redox switches in prokaryotes. *Biol Chem* 396(5):415-44.
358. Wang S, Phillippy AM, Deng K, Rui X, Li Z, Tortorello ML, Zhang W. 2010. Transcriptomic responses of *Salmonella enterica* serovars Enteritidis and Typhimurium to chlorine-based oxidative stress. *Appl Environ Microbiol* 76(15):5013-24.
359. Beavers WN, DuMont AL, Monteith AJ, Maloney KN, Tallman KA, Weiss A, Christian AH, Toste FD, Chang CJ, Porter NA, Torres VJ, Skaar EP. 2021. *Staphylococcus aureus* peptide methionine sulfoxide reductases protect from human whole-blood killing. *Infect Immun* 89(8):e0014621.
360. Yesilkaya H, Andisi VF, Andrew PW, Bijlsma JJ. 2013. *Streptococcus pneumoniae* and reactive oxygen species: an unusual approach to living with radicals. *Trends Microbiol* 21(4):187-95.
361. Tseng HJ, McEwan AG, Paton JC, Jennings MP. 2002. Virulence of *Streptococcus pneumoniae*: PsaA mutants are hypersensitive to oxidative stress. *Infect Immun* 70(3):1635-9.
362. Yesilkaya H, Kadioglu A, Gingles N, Alexander JE, Mitchell TJ, Andrew PW. 2000. Role of manganese-containing superoxide dismutase in oxidative stress and virulence of *Streptococcus pneumoniae*. *Infection and immunity* 68(5):2819-2826.
363. Hua CZ, Howard A, Malley R, Lu YJ. 2014. Effect of nonheme iron-containing ferritin Dpr in the stress response and virulence of pneumococci. *Infect Immun* 82(9):3939-47.

364. Pesakhov S, Benisty R, Sikron N, Cohen Z, Gomelsky P, Khozin-Goldberg I, Dagan R, Porat N. 2007. Effect of hydrogen peroxide production and the Fenton reaction on membrane composition of *Streptococcus pneumoniae*. *Biochim Biophys Acta* 1768(3):590-7.
365. Lisher JP, Tsui HT, Ramos-Montañez S, Hentchel KL, Martin JE, Trinidad JC, Winkler ME, Giedroc DP. 2017. Biological and chemical adaptation to endogenous hydrogen peroxide production in *Streptococcus pneumoniae* D39. *mSphere* 2(1).
366. Hajaj B, Yesilkaya H, Benisty R, David M, Andrew PW, Porat N. 2012. Thiol peroxidase is an important component of *Streptococcus pneumoniae* in oxygenated environments. *Infect Immun* 80(12):4333-43.
367. Auzat I, Chapuy-Regaud S, Le Bras G, Dos Santos D, Ogunniyi AD, Le Thomas I, Garel JR, Paton JC, Trombe MC. 1999. The NADH oxidase of *Streptococcus pneumoniae*: its involvement in competence and virulence. *Mol Microbiol* 34(5):1018-28.
368. Paterson GK, Blue CE, Mitchell TJ. 2006. An operon in *Streptococcus pneumoniae* containing a putative alkylhydroperoxidase D homologue contributes to virulence and the response to oxidative stress. *Microb Pathog* 40(4):152-60.
369. Mraheil MA, Toque HA, La Pietra L, Hamacher J, Phanthok T, Verin A, Gonzales J, Su Y, Fulton D, Eaton DC, Chakraborty T, Lucas R. 2021. Dual role of hydrogen peroxide as an oxidant in pneumococcal pneumonia. *Antioxid Redox Signal* 34(12):962-978.
370. Glanville DG, Han L, Maule AF, Woodacre A, Thanki D, Abdullah IT, Morrissey JA, Clarke TB, Yesilkaya H, Silvaggi NR, Ulijasz AT. 2018. RitR is an archetype for a novel family of redox sensors in the streptococci that has evolved from two-component response regulators and is required for pneumococcal colonization. *PLoS Pathog* 14(5):e1007052.
371. Imber M, Huyen NTT, Pietrzyk-Brzezinska AJ, Loi VV, Hillion M, Bernhardt J, Thärichen L, Kolsek K, Saleh M, Hamilton CJ, Adrian L, Gräter F, Wahl MC, Antelmann H. 2018. Protein *S*-Bacillithiolation functions in thiol protection and redox regulation of the glyceraldehyde-3-phosphate dehydrogenase Gap in *Staphylococcus aureus* under hypochlorite stress. *Antioxid Redox Signal* 28(6):410-430.
372. Imber M, Loi VV, Reznikov S, Fritsch VN, Pietrzyk-Brzezinska AJ, Prehn J, Hamilton C, Wahl MC, Bronowska AK, Antelmann H. 2018. The aldehyde dehydrogenase AldA contributes to the hypochlorite defense and is redox-controlled by protein *S*-bacillithiolation in *Staphylococcus aureus*. *Redox Biol* 15:557-568.
373. Cumming BM, Chinta KC, Reddy VP, Steyn AJC. 2018. Role of ergothioneine in microbial physiology and pathogenesis. *Antioxid Redox Signal* 28(6):431-444.
374. Imber M, Pietrzyk-Brzezinska AJ, Antelmann H. 2019. Redox regulation by reversible protein *S*-thiolation in Gram-positive bacteria. *Redox Biol* 20:130-145.
375. Deponte M. 2013. Glutathione catalysis and the reaction mechanisms of glutathione-dependent enzymes. *Biochim Biophys Acta* 1830(5):3217-66.
376. Tung QN, Linzner N, Loi VV, Antelmann H. 2018. Application of genetically encoded redox biosensors to measure dynamic changes in the glutathione, bacillithiol and mycothiol redox potentials in pathogenic bacteria. *Free Radic Biol Med* 128:84-96.
377. Ezeriņa D, Messens J. 2022. Chapter 23 - Sugar-based cysteine thiols recruited for oxidative stress defense and redox regulation, p 533-554. Alvarez B, Comini MA, Salinas G, Trujillo M (ed), *In* Redox Chemistry and Biology of Thiols doi:10.1016/B978-0-323-90219-9.00013-3. *Academic Press*
378. Couto N, Wood J, Barber J. 2016. The role of glutathione reductase and related enzymes on cellular redox homoeostasis network. *Free Radic Biol Med* 95:27-42.
379. Chandrangsu P, Loi VV, Antelmann H, Helmann JD. 2018. The role of bacillithiol in Gram-positive Firmicutes. *Antioxid Redox Signal* 28(6):445-462.
380. Van Laer K, Hamilton CJ, Messens J. 2013. Low-molecular-weight thiols in thiol-disulfide exchange. *Antioxid Redox Signal* 18(13):1642-53.
381. Ku JWK, Gan YH. 2021. New roles for glutathione: Modulators of bacterial virulence and pathogenesis. *Redox Biol* 44:102012.
382. Ulrich K, Jakob U. 2019. The role of thiols in antioxidant systems. *Free Radic Biol Med* 140:14-27.
383. Reyes AM, Pedre B, De Armas MI, Tossounian MA, Radi R, Messens J, Trujillo M. 2018. Chemistry and redox biology of mycothiol. *Antioxid Redox Signal* 28(6):487-504.

384. Hiras J, Sharma SV, Raman V, Tinson RAJ, Arbach M, Rodrigues DF, Norambuena J, Hamilton CJ, Hanson TE. 2018. Physiological studies of *Chlorobiaceae* suggest that bacillithiol derivatives are the most widespread thiols in bacteria. *mBio* 9(6).
385. Rajkarnikar A, Strankman A, Duran S, Vargas D, Roberts AA, Barretto K, Upton H, Hamilton CJ, Rawat M. 2013. Analysis of mutants disrupted in bacillithiol metabolism in Staphylococcus aureus. *Biochem Biophys Res Commun* 436(2):128-33.
386. Ashby LV, Springer R, Loi VV, Antelmann H, Hampton MB, Kettle AJ, Dickerhof N. 2022. Oxidation of bacillithiol during killing of *Staphylococcus aureus* USA300 inside neutrophil phagosomes. *J Leukoc Biol* doi:10.1002/JLB.4HI1021-538RR.
387. Mikheyeva IV, Thomas JM, Kolar SL, Corvaglia A-R, Gaïa N, Leo S, Francois P, Liu GY, Rawat M, Cheung AL. 2019. YpdA, a putative bacillithiol disulfide reductase, contributes to cellular redox homeostasis and virulence in *Staphylococcus aureus*. *Molecular Microbiology* 111(4):1039-1056.
388. Potter AJ, Trappetti C, Paton JC. 2012. *Streptococcus pneumoniae* uses glutathione to defend against oxidative stress and metal ion toxicity. *J Bacteriol* 194(22):6248-54.
389. Shearer HL, Paton JC, Hampton MB, Dickerhof N. 2022. Glutathione utilization protects *Streptococcus pneumoniae* against lactoperoxidase-derived hypothiocyanous acid. *Free Radic Biol Med* 179:24-33.
390. Lensmire JM, Wischer MR, Sosinski LM, Ensink E, Dodson JP, Shook JC, Delekta PC, Cooper CC, Havlichek D, Mulks MH, Lunt SY, Ravi J, Hammer ND. 2021. The glutathione import system satisfies the *Staphylococcus aureus* nutrient sulfur requirement and promotes interspecies competition. *bioRxiv* doi:10.1101/2021.10.26.465763:2021.10.26.465763.
391. Pöther DC, Gierok P, Harms M, Mostertz J, Hochgräfe F, Antelmann H, Hamilton CJ, Borovok I, Lalk M, Aharonowitz Y, Hecker M. 2013. Distribution and infection-related functions of bacillithiol in *Staphylococcus aureus*. *Int J Med Microbiol* 303(3):114-23.
392. Helmann JD. 2011. Bacillithiol, a new player in bacterial redox homeostasis. *Antioxid Redox Signal* 15(1):123-33.
393. Sharma SV, Arbach M, Roberts AA, Macdonald CJ, Groom M, Hamilton CJ. 2013. Biophysical features of bacillithiol, the glutathione surrogate of *Bacillus subtilis* and other firmicutes. *Chembiochem* 14(16):2160-8.
394. Dickerhof N, Paton L, Kettle AJ. 2020. Oxidation of bacillithiol by myeloperoxidase-derived oxidants. *Free Radic Biol Med* 158:74-83.
395. Kelly RA, Leedale J, Calleja D, Enoch SJ, Harrell A, Chadwick AE, Webb S. 2019. Modelling changes in glutathione homeostasis as a function of quinone redox metabolism. *Sci Rep* 9(1):6333.
396. Bolton JL, Dunlap T. 2017. Formation and biological targets of quinones: Cytotoxic versus cytoprotective effects. *Chem Res Toxicol* 30(1):13-37.
397. Newton GL, Fahey RC, Rawat M. 2012. Detoxification of toxins by bacillithiol in *Staphylococcus aureus*. *Microbiology (Reading)* 158(Pt 4):1117-1126.
398. Allocati N, Federici L, Masulli M, Di Ilio C. 2009. Glutathione transferases in bacteria. *FEBS J* 276(1):58-75.
399. Newton GL, Leung SS, Wakabayashi JI, Rawat M, Fahey RC. 2011. The DinB superfamily includes novel mycothiol, bacillithiol, and glutathione *S*-transferases. *Biochemistry* 50(49):10751-60.
400. Sharma SV, Jothivasan VK, Newton GL, Upton H, Wakabayashi JI, Kane MG, Roberts AA, Rawat M, La Clair JJ, Hamilton CJ. 2011. Chemical and chemoenzymatic syntheses of bacillithiol: a unique low-molecular-weight thiol amongst low G +C Gram-positive bacteria. *Angew Chem Int Ed Engl* 50(31):7101-4.
401. Perera VR, Newton GL, Parnell JM, Komives EA, Pogliano K. 2014. Purification and characterization of the *Staphylococcus aureus* bacillithiol transferase BstA. *Biochim Biophys Acta* 1840(9):2851-61.
402. Chandrangsu P, Dusi R, Hamilton CJ, Helmann JD. 2014. Methylglyoxal resistance in *Bacillus subtilis*: contributions of bacillithiol-dependent and independent pathways. *Mol Microbiol* 91(4):706-15.

403. Klein VJ, Irla M, Gil Lopez M, Brautaset T, Fernandes Brito L. 2022. Unravelling formaldehyde metabolism in bacteria: Road towards synthetic methylotrophy. *Microorganisms* 10(2).
404. Chen NH, Djoko KY, Veyrier FJ, McEwan AG. 2016. Formaldehyde stress responses in bacterial pathogens. *Front Microbiol* 7:257.
405. Staab CA, Hellgren M, Hoog JO. 2008. Medium- and short-chain dehydrogenase/reductase gene and protein families : Dual functions of alcohol dehydrogenase 3: implications with focus on formaldehyde dehydrogenase and *S*-nitrosoglutathione reductase activities. *Cell Mol Life Sci* 65(24):3950-60.
406. Potter AJ, Kidd SP, McEwan AG, Paton JC. 2010. The MerR/NmlR family transcription factor of *Streptococcus pneumoniae* responds to carbonyl stress and modulates hydrogen peroxide production. *J Bacteriol* 192(15):4063-6.
407. Rosario-Cruz Z, Boyd JM. 2016. Physiological roles of bacillithiol in intracellular metal processing. *Curr Genet* 62(1):59-65.
408. Helbig K, Bleuel C, Krauss GJ, Nies DH. 2008. Glutathione and transition-metal homeostasis in *Escherichia coli*. *J Bacteriol* 190(15):5431-8.
409. Ma Z, Chandrangsu P, Helmann TC, Romsang A, Gaballa A, Helmann JD. 2014. Bacillithiol is a major buffer of the labile zinc pool in *Bacillus subtilis*. *Mol Microbiol* 94(4):756-70.
410. Lillig CH, Berndt C. 2013. Glutaredoxins in thiol/disulfide exchange. *Antioxid Redox Signal* 18(13):1654-65.
411. Talib EA, Outten CE. 2021. Iron-sulfur cluster biogenesis, trafficking, and signaling: Roles for CGFS glutaredoxins and BolA proteins. *Biochim Biophys Acta Mol Cell Res* 1868(1):118847.
412. Rosario-Cruz Z, Chahal HK, Mike LA, Skaar EP, Boyd JM. 2015. Bacillithiol has a role in Fe-S cluster biogenesis in *Staphylococcus aureus*. *Mol Microbiol* 98(2):218-42.
413. Posada AC, Kolar SL, Dusi RG, Francois P, Roberts AA, Hamilton CJ, Liu GY, Cheung A. 2014. Importance of bacillithiol in the oxidative stress response of *Staphylococcus aureus*. *Infect Immun* 82(1):316-32.
414. Fernandes AP, Holmgren A. 2004. Glutaredoxins: glutathione-dependent redox enzymes with functions far beyond a simple thioredoxin backup system. *Antioxid Redox Signal* 6(1):63-74.
415. Ströher E, Millar AH. 2012. The biological roles of glutaredoxins. *Biochem J* 446(3):333-48.
416. Zimmermann J, Oestreicher J, Hess S, Herrmann JM, Deponte M, Morgan B. 2020. One cysteine is enough: A monothiol Grx can functionally replace all cytosolic Trx and dithiol Grx. *Redox Biol* 36:101598.
417. Sikanyika M, Aragao D, McDevitt CA, Maher MJ. 2019. The structure and activity of the glutathione reductase from *Streptococcus pneumoniae*. *Acta Crystallogr F Struct Biol Commun* 75(Pt 1):54-61.
418. McHugh CS, Cook PD. 2022. Structure of BrxA from *Staphylococcus aureus*, a bacilliredoxin involved in redox homeostasis in Firmicutes. *Acta Crystallogr F Struct Biol Commun* 78(Pt 4):144-149.
419. Gaballa A, Chi BK, Roberts AA, Becher D, Hamilton CJ, Antelmann H, Helmann JD. 2014. Redox regulation in *Bacillus subtilis*: The bacilliredoxins BrxA(YphP) and BrxB(YqiW) function in de-bacillithiolation of *S*-bacillithiolated OhrR and MetE. *Antioxid Redox Signal* 21(3):357-67.
420. Gaballa A, Newton GL, Antelmann H, Parsonage D, Upton H, Rawat M, Claiborne A, Fahey RC, Helmann JD. 2010. Biosynthesis and functions of bacillithiol, a major low-molecular-weight thiol in Bacilli. *Proc Natl Acad Sci U S A* 107(14):6482-6.
421. Hammerstad M, Gudim I, Hersleth HP. 2020. The crystal structures of bacillithiol disulfide reductase Bdr (YpdA) provide structural and functional insight into a new type of FAD-containing NADPH-dependent oxidoreductase. *Biochemistry* 59(51):4793-4798.
422. Gaballa A, Su TT, Helmann JD. 2021. The *Bacillus subtilis* monothiol bacilliredoxin BrxC (YtxJ) and the Bdr (YpdA) disulfide reductase reduce *S*-bacillithiolated proteins. *Redox Biol* 42:101935.
423. Tsuchiya Y, Zhyvoloup A, Baković J, Thomas N, Yu BYK, Das S, Orengo C, Newell C, Ward J, Saladino G, Comitani F, Gervasio FL, Malanchuk OM, Khoruzhenko AI, Filonenko

V, Peak-Chew SY, Skehel M, Gout I. 2018. Protein CoAlation and antioxidant function of coenzyme A in prokaryotic cells. *Biochem J* 475(11):1909-1937.
424. Fritsch VN, Linzner N, Busche T, Said N, Weise C, Kalinowski J, Wahl MC, Antelmann H. 2022. The MerR-family regulator NmlR is involved in the defense against HOCl stress in *Streptococcus pneumoniae*. *Mol Microbiol* Under major revision.
425. Ceragioli M, Mols M, Moezelaar R, Ghelardi E, Senesi S, Abee T. 2010. Comparative transcriptomic and phenotypic analysis of the responses of *Bacillus cereus* to various disinfectant treatments. *Appl Environ Microbiol* 76(10):3352-60.
426. Jang HJ, Nde C, Toghrol F, Bentley WE. 2009. Global transcriptome analysis of the *Mycobacterium bovis* BCG response to sodium hypochlorite. *Appl Microbiol Biotechnol* 85(1):127-40.
427. Farrant KV, Spiga L, Davies JC, Williams HD. 2020. Response of *Pseudomonas aeruginosa* to the innate immune system-derived oxidants hypochlorous acid and hypothiocyanous acid. *J Bacteriol* 203(2).
428. Bakovic J, Yu BYK, Silva D, Baczynska M, Peak-Chew SY, Switzer A, Burchell L, Wigneshweraraj S, Vandanashree M, Gopal B, Filonenko V, Skehel M, Gout I. 2021. Redox regulation of the quorum-sensing transcription factor AgrA by coenzyme A. *Antioxidants (Basel)* 10(6).
429. Winter J, Ilbert M, Graf PC, Ozcelik D, Jakob U. 2008. Bleach activates a redox-regulated chaperone by oxidative protein unfolding. *Cell* 135(4):691-701.
430. Gennaris A, Collet JF. 2013. The 'captain of the men of death', *Streptococcus pneumoniae,* fights oxidative stress outside the 'city wall'. *EMBO Mol Med* 5(12):1798-800.
431. Saleh M, Bartual SG, Abdullah MR, Jensch I, Asmat TM, Petruschka L, Pribyl T, Gellert M, Lillig CH, Antelmann H, Hermoso JA, Hammerschmidt S. 2013. Molecular architecture of *Streptococcus pneumoniae* surface thioredoxin-fold lipoproteins crucial for extracellular oxidative stress resistance and maintenance of virulence. *EMBO molecular medicine* 5(12):1852-1870.
432. Collet JF, Messens J. 2010. Structure, function, and mechanism of thioredoxin proteins. *Antioxid Redox Signal* 13(8):1205-16.
433. Glauninger H, Zhang Y, Higgins KA, Jacobs AD, Martin JE, Fu Y, Coyne Rd HJ, Bruce KE, Maroney MJ, Clemmer DE, Capdevila DA, Giedroc DP. 2018. Metal-dependent allosteric activation and inhibition on the same molecular scaffold: the copper sensor CopY from *Streptococcus pneumoniae*. *Chem Sci* 9(1):105-118.
434. Hirschmann S, Gomez-Mejia A, Mader U, Karsunke J, Driesch D, Rohde M, Haussler S, Burchhardt G, Hammerschmidt S. 2021. The Two-Component System 09 Regulates Pneumococcal Carbohydrate Metabolism and Capsule Expression. *Microorganisms* 9(3).
435. Afzal M, Shafeeq S, Henriques-Normark B, Kuipers OP. 2015. UlaR activates expression of the *ula* operon in *Streptococcus pneumoniae* in the presence of ascorbic acid. *Microbiology (Reading)* 161(Pt 1):41-49.
436. Manjula Rao Y, Sureshkumar GK. 2000. Direct biosynthesis of ascorbic acid from glucose by *Xanthomonas campestris* through induced free-radicals. *Biotechnology Letters* 22(5):407-411.
437. Vissers MC, Lee WG, Hampton MB. 2001. Regulation of apoptosis by vitamin C. Specific protection of the apoptotic machinery against exposure to chlorinated oxidants. *J Biol Chem* 276(50):46835-40.
438. Dukan S, Touati D. 1996. Hypochlorous acid stress in *Escherichia coli*: resistance, DNA damage, and comparison with hydrogen peroxide stress. *J Bacteriol* 178(21):6145-50.
439. Harwood DT, Kettle AJ, Winterbourn CC. 2006. Production of glutathione sulfonamide and dehydroglutathione from GSH by myeloperoxidase-derived oxidants and detection using a novel LC-MS/MS method. *Biochem J* 399(1):161-8.
440. Wang S, Deng K, Zaremba S, Deng X, Lin C, Wang Q, Tortorello ML, Zhang W. 2009. Transcriptomic response of *Escherichia coli* O157:H7 to oxidative stress. *Applied and environmental microbiology* 75(19):6110-6123.
441. Basu Thakur P, Long AR, Nelson BJ, Kumar R, Rosenberg AF, Gray MJ. 2019. Complex responses to hydrogen peroxide and hypochlorous acid by the probiotic bacterium *Lactobacillus reuteri*. *mSystems* 4(5).

442. Leichert LI, Gehrke F, Gudiseva HV, Blackwell T, Ilbert M, Walker AK, Strahler JR, Andrews PC, Jakob U. 2008. Quantifying changes in the thiol redox proteome upon oxidative stress *in vivo*. *Proc Natl Acad Sci U S A* 105(24):8197-202.
443. Small DA, Chang W, Toghrol F, Bentley WE. 2007. Comparative global transcription analysis of sodium hypochlorite, peracetic acid, and hydrogen peroxide on *Pseudomonas aeruginosa*. *Appl Microbiol Biotechnol* 76(5):1093-105.
444. Palazzolo-Ballance AM, Reniere ML, Braughton KR, Sturdevant DE, Otto M, Kreiswirth BN, Skaar EP, DeLeo FR. 2008. Neutrophil microbicides induce a pathogen survival response in community-associated methicillin-resistant *Staphylococcus aureus*. *J Immunol* 180(1):500-9.
445. Stroeher UH, Kidd SP, Stafford SL, Jennings MP, Paton JC, McEwan AG. 2007. A pneumococcal MerR-like regulator and *S*-nitrosoglutathione reductase are required for systemic virulence. *J Infect Dis* 196(12):1820-6.
446. Brown NL, Stoyanov JV, Kidd SP, Hobman JL. 2003. The MerR family of transcriptional regulators. *FEMS Microbiol Rev* 27(2-3):145-63.
447. McEwan AG, Djoko KY, Chen NH, Counago RL, Kidd SP, Potter AJ, Jennings MP. 2011. Novel bacterial MerR-like regulators their role in the response to carbonyl and nitrosative stress. *Adv Microb Physiol* 58:1-22.
448. Fang C, Zhang Y. 2022. Bacterial MerR family transcription regulators: activation by distortion. *Acta Biochim Biophys Sin (Shanghai)* 54(1):25-36.
449. Yang Y, Liu C, Zhou W, Shi W, Chen M, Zhang B, Schatz DG, Hu Y, Liu B. 2021. Structural visualization of transcription activated by a multidrug-sensing MerR family regulator. *Nat Commun* 12(1):2702.
450. Counago RM, Chen NH, Chang CW, Djoko KY, McEwan AG, Kobe B. 2016. Structural basis of thiol-based regulation of formaldehyde detoxification in H. influenzae by a MerR regulator with no sensor region. *Nucleic Acids Res* 44(14):6981-93.
451. Schumacher MA, Brennan RG. 2002. Structural mechanisms of multidrug recognition and regulation by bacterial multidrug transcription factors. *Mol Microbiol* 45(4):885-93.
452. Chang CC, Lin LY, Zou XW, Huang CC, Chan NL. 2015. Structural basis of the mercury(II)-mediated conformational switching of the dual-function transcriptional regulator MerR. *Nucleic Acids Res* 43(15):7612-23.
453. Fang C, Zhang Y. 2022. Bacterial MerR family transcription regulators: activationby distortion. *Acta Biochim Biophys Sin (Shanghai)* 54(1):1-12.
454. Shi W, Zhang B, Jiang Y, Liu C, Zhou W, Chen M, Yang Y, Hu Y, Liu B. 2021. Structural basis of copper-efflux-regulator-dependent transcription activation. *iScience* 24(5):102449.
455. Fang C, Li L, Zhao Y, Wu X, Philips SJ, You L, Zhong M, Shi X, O'Halloran TV, Li Q, Zhang Y. 2020. The bacterial multidrug resistance regulator BmrR distorts promoter DNA to activate transcription. *Nat Commun* 11(1):6284.
456. Hobman JL, Wilkie J, Brown NL. 2005. A design for life: prokaryotic metal-binding MerR family regulators. *Biometals* 18(4):429-36.
457. Pomposiello PJ, Demple B. 2001. Redox-operated genetic switches: the SoxR and OxyR transcription factors. *Trends Biotechnol* 19(3):109-14.
458. Crack JC, Le Brun NE. 2017. Redox-sensing iron-sulfur cluster regulators. *Antioxid Redox Signal* doi:10.1089/ars.2017.7369.
459. Supa-Amornkul S, Chantratita W, Srichunrusami C, Janchompoo P, Chaturongakul S. 2016. Listeria monocytogenes MerR-Like Regulator NmlRlm: Its Transcriptome and Role in Stress Response. *Foodborne Pathog Dis* 13(7):369-78.
460. Kidd SP, Potter AJ, Apicella MA, Jennings MP, McEwan AG. 2005. NmlR of *Neisseria gonorrhoeae*: a novel redox responsive transcription factor from the MerR family. *Mol Microbiol* 57(6):1676-89.
461. Stuehr DJ, Fasehun OA, Kwon NS, Gross SS, Gonzalez JA, Levi R, Nathan CF. 1991. Inhibition of macrophage and endothelial cell nitric oxide synthase by diphenyleneiodonium and its analogs. *FASEB J* 5(1):98-103.
462. Altenhofer S, Radermacher KA, Kleikers PW, Wingler K, Schmidt HH. 2015. Evolution of NADPH Oxidase Inhibitors: Selectivity and Mechanisms for Target Engagement. *Antioxid Redox Signal* 23(5):406-27.

463. O'Donnell BV, Tew DG, Jones OT, England PJ. 1993. Studies on the inhibitory mechanism of iodonium compounds with special reference to neutrophil NADPH oxidase. *Biochem J* 290 (Pt 1):41-9.
464. van Opijnen T, Camilli A. 2012. A fine scale phenotype-genotype virulence map of a bacterial pathogen. *Genome Res* 22(12):2541-51.
465. Chen NH, Couñago RM, Djoko KY, Jennings MP, Apicella MA, Kobe B, McEwan AG. 2013. A glutathione-dependent detoxification system is required for formaldehyde resistance and optimal survival of *Neisseria meningitidis* in biofilms. *Antioxid Redox Signal* 18(7):743-55.
466. Kidd SP, Jiang D, Tikhomirova A, Jennings MP, McEwan AG. 2012. A glutathione-based system for defense against carbonyl stress in *Haemophilus influenzae*. *BMC Microbiol* 12:159.
467. Kidd SP, Jiang D, Jennings MP, McEwan AG. 2007. Glutathione-dependent alcohol dehydrogenase AdhC is required for defense against nitrosative stress in *Haemophilus influenzae*. *Infect Immun* 75(9):4506-13.
468. Reeves BD, Joshi N, Campanello GC, Hilmer JK, Chetia L, Vance JA, Reinschmidt JN, Miller CG, Giedroc DP, Dratz EA, Singel DJ, Grieco PA. 2014. Conversion of *S*-phenylsulfonylcysteine residues to mixed disulfides at pH 4.0: utility in protein thiol blocking and in protein-*S*-nitrosothiol detection. *Org Biomol Chem* 12(40):7942-56.
469. Lund PA, Brown NL. 1989. Regulation of transcription in *Escherichia coli* from the *mer* and *merR* promoters in the transposon Tn501. *J Mol Biol* 205(2):343-53.
470. Huang Y-H, Trapp V, Puro O, Mäkinen JJ, Metsä-Ketelä M, Wahl MC, Belogurov GA. 2022. Fluorogenic RNA aptamers to probe transcription initiation and co-transcriptional RNA folding by multi-subunit RNA polymerases. *Methods in Enzymology* doi:10.1016/bs.mie.2022.07.010.
471. Gray MJ, Wholey WY, Parker BW, Kim M, Jakob U. 2013. NemR is a bleach-sensing transcription factor. *J Biol Chem* 288(19):13789-98.
472. Lemma E, Hagerhall C, Geisler V, Brandt U, von Jagow G, Kroger A. 1991. Reactivity of the *Bacillus subtilis* succinate dehydrogenase complex with quinones. *Biochim Biophys Acta* 1059(3):281-5.
473. Franza T, Gaudu P. 2022. Quinones: more than electron shuttles. *Res Microbiol* 173(6-7):103953.
474. Seel W, Flegler A, Zunabovic-Pichler M, Lipski A. 2018. Increased isoprenoid quinone concentration modulates membrane fluidity in *Listeria monocytogenes* at low growth temperatures. *J Bacteriol* 200(13).
475. Tiwari N, Lopez-Redondo M, Miguel-Romero L, Kulhankova K, Cahill MP, Tran PM, Kinney KJ, Kilgore SH, Al-Tameemi H, Herfst CA, Tuffs SW, Kirby JR, Boyd JM, McCormick JK, Salgado-Pabon W, Marina A, Schlievert PM, Fuentes EJ. 2020. The SrrAB two-component system regulates *Staphylococcus aureus* pathogenicity through redox sensitive cysteines. *Proc Natl Acad Sci U S A* 117(20):10989-10999.
476. Price EE, Roman-Rodriguez F, Boyd JM. 2021. Bacterial approaches to sensing and responding to respiration and respiration metabolites. *Mol Microbiol* 116(4):1009-1021.
477. Giuffre A, Borisov VB, Mastronicola D, Sarti P, Forte E. 2012. Cytochrome bd oxidase and nitric oxide: from reaction mechanisms to bacterial physiology. *FEBS Lett* 586(5):622-9.
478. Richardson AR, Dunman PM, Fang FC. 2006. The nitrosative stress response of *Staphylococcus aureus* is required for resistance to innate immunity. *Mol Microbiol* 61(4):927-39.
479. Kinkel TL, Roux CM, Dunman PM, Fang FC. 2013. The *Staphylococcus aureus* SrrAB two-component system promotes resistance to nitrosative stress and hypoxia. *mBio* 4(6):e00696-13.
480. Lewis AM, Matzdorf SS, Endres JL, Windham IH, Bayles KW, Rice KC. 2015. Examination of the *Staphylococcus aureus* nitric oxide reductase (saNOR) reveals its contribution to modulating intracellular NO levels and cellular respiration. *Mol Microbiol* 96(3):651-69.
481. Mashruwala AA, Boyd JM. 2017. The *Staphylococcus aureus* SrrAB regulatory system modulates hydrogen peroxide resistance factors, which imparts protection to aconitase during aerobic growth. *PLoS One* 12(1):e0170283.

482. Oogai Y, Kawada-Matsuo M, Komatsuzawa H. 2016. *Staphylococcus aureus* SrrAB affects susceptibility to hydrogen peroxide and co-existence with *Streptococcus sanguinis*. *PLoS One* 11(7):e0159768.
483. Frerichs-Deeken U, Ranguelova K, Kappl R, Huttermann J, Fetzner S. 2004. Dioxygenases without requirement for cofactors and their chemical model reaction: compulsory order ternary complex mechanism of 1*H*-3-hydroxy-4-oxoquinaldine 2,4-dioxygenase involving general base catalysis by histidine 251 and single-electron oxidation of the substrate dianion. *Biochemistry* 43(45):14485-99.
484. Fetzner S. 2002. Oxygenases without requirement for cofactors or metal ions. *Appl Microbiol Biotechnol* 60(3):243-57.
485. Lipscomb JD. 2008. Mechanism of extradiol aromatic ring-cleaving dioxygenases. *Curr Opin Struct Biol* 18(6):644-9.
486. Bugg TDH. 2003. Dioxygenase enzymes: Catalytic mechanisms and chemical models. *ChemInform* 34.
487. Qi F, Zhang W, Xue Y, Geng C, Huang X, Sun J, Lu X. 2021. Bienzyme-catalytic and dioxygenation-mediated anthraquinone ring opening. *Journal of the American Chemical Society* 143(40):16326-16331.
488. Eltis LD, Bolin JT. 1996. Evolutionary relationships among extradiol dioxygenases. *J Bacteriol* 178(20):5930-7.
489. Vaillancourt FH, Bolin JT, Eltis LD. 2006. The ins and outs of ring-cleaving dioxygenases. *Crit Rev Biochem Mol Biol* 41(4):241-67.
490. Ryan A, Kaplan E, Nebel JC, Polycarpou E, Crescente V, Lowe E, Preston GM, Sim E. 2014. Identification of NAD(P)H quinone oxidoreductase activity in azoreductases from *P. aeruginosa*: azoreductases and NAD(P)H quinone oxidoreductases belong to the same FMN-dependent superfamily of enzymes. *PLoS One* 9(6):e98551.
491. Binter A, Staunig N, Jelesarov I, Lohner K, Palfey BA, Deller S, Gruber K, Macheroux P. 2009. A single intersubunit salt bridge affects oligomerization and catalytic activity in a bacterial quinone reductase. *FEBS J* 276(18):5263-74.
492. Deller S, Macheroux P, Sollner S. 2008. Flavin-dependent quinone reductases. *Cell Mol Life Sci* 65(1):141-60.
493. Crescente V, Holland SM, Kashyap S, Polycarpou E, Sim E, Ryan A. 2016. Identification of novel members of the bacterial azoreductase family in *Pseudomonas aeruginosa*. *Biochem J* 473(5):549-58.
494. Nivinskas H, Staskeviciene S, Sarlauskas J, Koder RL, Miller AF, Cenas N. 2002. Two-electron reduction of quinones by *Enterobacter cloacae* NAD(P)H:nitroreductase: quantitative structure-activity relationships. *Arch Biochem Biophys* 403(2):249-58.
495. Cadenas E. 1995. Antioxidant and prooxidant functions of DT-diaphorase in quinone metabolism. *Biochem Pharmacol* 49(2):127-40.
496. Maruyama A, Kumagai Y, Morikawa K, Taguchi K, Hayashi H, Ohta T. 2003. Oxidative-stress-inducible *qorA* encodes an NADPH-dependent quinone oxidoreductase catalysing a one-electron reduction in *Staphylococcus aureus*. *Microbiology (Reading)* 149(Pt 2):389-398.
497. Antelmann H, Hecker M, Zuber P. 2008. Proteomic signatures uncover thiol-specific electrophile resistance mechanisms in *Bacillus subtilis*. *Expert Rev Proteomics* 5(1):77-90.
498. Tropel D, van der Meer JR. 2004. Bacterial transcriptional regulators for degradation pathways of aromatic compounds. *Microbiol Mol Biol Rev* 68(3):474-500.
499. Suzuki H. 2019. Remarkable diversification of bacterial azoreductases: primary sequences, structures, substrates, physiological roles, and biotechnological applications. *Appl Microbiol Biotechnol* 103(10):3965-3978.
500. Wang J, Cheng Y, Wu R, Jiang D, Bai B, Tan D, Yan T, Sun X, Zhang Q, Wu Z. 2016. Antibacterial activity of juglone against *Staphylococcus aureus*: From apparent to proteomic. *Int J Mol Sci* 17(6).
501. Nasher F, Taylor AJ, Elmi A, Lehri B, Ijaz UZ, Baker D, Goram R, Lynham S, Singh D, Stabler R, Kelly DJ, Gundogdu O, Wren BW. 2022. MdaB and NfrA, two novel reductases important in the survival and persistence of the major enteropathogen *Campylobacter jejuni*. *J Bacteriol* 204(1):e0042121.

502. Wilkinson SP, Grove A. 2006. Ligand-responsive transcriptional regulation by members of the MarR family of winged helix proteins. *Curr Issues Mol Biol* 8(1):51-62.
503. Perera IC, Grove A. 2010. Molecular mechanisms of ligand-mediated attenuation of DNA binding by MarR family transcriptional regulators. *J Mol Cell Biol* 2(5):243-54.
504. Töwe S, Leelakriangsak M, Kobayashi K, Van Duy N, Hecker M, Zuber P, Antelmann H. 2007. The MarR-type repressor MhqR (YkvE) regulates multiple dioxygenases/glyoxalases and an azoreductase which confer resistance to 2-methylhydroquinone and catechol in *Bacillus subtilis*. *Mol Microbiol* 66(1):40-54.
505. Duy NV, Wolf C, Mäder U, Lalk M, Langer P, Lindequist U, Hecker M, Antelmann H. 2007. Transcriptome and proteome analyses in response to 2-methylhydroquinone and 6-brom-2-vinyl-chroman-4-on reveal different degradation systems involved in the catabolism of aromatic compounds in *Bacillus subtilis*. *Proteomics* 7(9):1391-408.
506. Leelakriangsak M, Kobayashi K, Zuber P. 2007. Dual negative control of *spx* transcription initiation from the P3 promoter by repressors PerR and YodB in *Bacillus subtilis*. *J Bacteriol* 189(5):1736-44.
507. Leelakriangsak M, Huyen NT, Töwe S, van Duy N, Becher D, Hecker M, Antelmann H, Zuber P. 2008. Regulation of quinone detoxification by the thiol stress sensing DUF24/MarR-like repressor, YodB in *Bacillus subtilis*. *Mol Microbiol* 67(5):1108-24.
508. Chi BK, Albrecht D, Gronau K, Becher D, Hecker M, Antelmann H. 2010. The redox-sensing regulator YodB senses quinones and diamide via a thiol-disulfide switch in *Bacillus subtilis*. *Proteomics* 10(17):3155-64.
509. Lee SJ, Lee IG, Lee KY, Kim DG, Eun HJ, Yoon HJ, Chae S, Song SH, Kang SO, Seo MD, Kim HS, Park SJ, Lee BJ. 2016. Two distinct mechanisms of transcriptional regulation by the redox sensor YodB. *Proc Natl Acad Sci U S A* 113(35):E5202-11.
510. Chi BK, Kobayashi K, Albrecht D, Hecker M, Antelmann H. 2010. The paralogous MarR/DUF24-family repressors YodB and CatR control expression of the catechol dioxygenase CatE in *Bacillus subtilis*. *J Bacteriol* 192(18):4571-81.
511. Pi H, Helmann JD. 2018. Genome-wide characterization of the Fur regulatory network reveals a link between catechol degradation and bacillibactin metabolism in *Bacillus subtilis*. *mBio* 9(5).
512. Smith MT. 1985. Quinones as mutagens, carcinogens, and anticancer agents: introduction and overview. *J Toxicol Environ Health* 16(5):665-72.
513. Medina LF, Hertz PF, Stefani V, Henriques JA, Zanotto-Filho A, Brandelli A. 2006. Aminonaphthoquinone induces oxidative stress in *Staphylococcus aureus*. *Biochem Cell Biol* 84(5):720-7.
514. Hoffmann-Ostenhof O. Chapter 22 – Enzyme inhibition by quinones, p. *In* (ed),
515. Rodriguez CE, Fukuto JM, Taguchi K, Froines J, Cho AK. 2005. The interactions of 9,10-phenanthrenequinone with glyceraldehyde-3-phosphate dehydrogenase (GAPDH), a potential site for toxic actions. *Chem Biol Interact* 155(1-2):97-110.
516. Ravelo ÁG, Estévez-Braun A, Pérez-Sacau E. 2003. The chemistry and biology of lapachol and related natural products α and β-lapachones. *Studies in Natural Products Chemistry* 29:719-760.
517. Kumagai Y, Tsurutani Y, Shinyashiki M, Homma-Takeda S, Nakai Y, Yoshikawa T, Shimojo N. 1997. Bioactivation of lapachol responsible for DNA scission by NADPH-cytochrome P450 reductase. *Environ Toxicol Pharmacol* 3(4):245-50.
518. Goulart MlOF, Falkowski P, Ossowski T, Liwo A. 2003. Electrochemical study of oxygen interaction with lapachol and its radical anions. *Bioelectrochemistry* 59(1):85-87.
519. Fritsch VN, Loi VV, Kuropka B, H. GMC, Weise C, Antelmann H. 2022. The MarR/DUF24-family QsrR repressor senses quinones and oxidants by thiol switch mechanisms in *Staphylococcus aureus Antioxid Redox Signal* accepted on September 24th, 2022.
520. Bose A, Basu S. 2009. Interaction of quinones with three pyrimidine bases: A laser flash photolysis study. *Journal of Luminescence* 129:1385-1389.
521. Wang X, Guodong C, Zhiyi Y, Zongwei C. 2021. DNA and RNA adducts formation from 3,4-quinone metabolites of Bisphenol F. *Environmental Science & Technology Letters* 8.

522. Moussaoui M, Miseviciene L, Anusevicius Z, Maroziene A, Lederer F, Baciou L, Cenas N. 2018. Quinones and nitroaromatic compounds as subversive substrates of *Staphylococcus aureus* flavohemoglobin. *Free Radic Biol Med* 123:107-115.
523. Ito K, Nakanishi M, Lee WC, Zhi Y, Sasaki H, Zenno S, Saigo K, Kitade Y, Tanokura M. 2008. Expansion of substrate specificity and catalytic mechanism of azoreductase by X-ray crystallography and site-directed mutagenesis. *J Biol Chem* 283(20):13889-96.
524. Rau J, Stolz A. 2003. Oxygen-insensitive nitroreductases NfsA and NfsB of *Escherichia coli* function under anaerobic conditions as lawsone-dependent Azo reductases. *Appl Environ Microbiol* 69(6):3448-55.
525. Liu G, Zhou J, Fu QS, Wang J. 2009. The *Escherichia coli* azoreductase AzoR Is involved in resistance to thiol-specific stress caused by electrophilic quinones. *J Bacteriol* 191(20):6394-400.
526. Liu G, Zhou J, Jin R, Zhou M, Wang J, Lu H, Qu Y. 2008. Enhancing survival of *Escherichia coli* by expression of azoreductase AZR possessing quinone reductase activity. *Appl Microbiol Biotechnol* 80(3):409-16.
527. Ibrahim ES, Ohlsen K. 2022. The old yellow enzyme OfrA fosters *Staphylococcus aureus* survival via affecting thiol-dependent redox homeostasis. *Front Microbiol* 13:888140.
528. Deochand DK, Grove A. 2017. MarR family transcription factors: dynamic variations on a common scaffold. *Crit Rev Biochem Mol Biol* 52(6):595-613.
529. Belitsky BR, Sonenshein AL. 2011. Contributions of multiple binding sites and effector-independent binding to CodY-mediated regulation in *Bacillus subtilis*. *J Bacteriol* 193(2):473-84.
530. Will WR, Fang FC. 2020. The evolution of MarR family transcription factors as counter-silencers in regulatory networks. *Curr Opin Microbiol* 55:1-8.
531. Beggs GA, Brennan RG, Arshad M. 2020. MarR family proteins are important regulators of clinically relevant antibiotic resistance. *Protein Sci* 29(3):647-653.
532. Truong-Bolduc QC, Zhang X, Hooper DC. 2003. Characterization of NorR protein, a multifunctional regulator of *norA* expression in *Staphylococcus aureus*. *J Bacteriol* 185(10):3127-38.
533. Zou J, Peng B, Qu J, Zheng J. 2021. Are bacterial persisters dormant cells only? *Front Microbiol* 12:708580.
534. Kawai Y, Mercier R, Wu LJ, Dominguez-Cuevas P, Oshima T, Errington J. 2015. Cell growth of wall-free L-form bacteria is limited by oxidative damage. *Curr Biol* 25(12):1613-8.
535. Proctor RA, von Eiff C, Kahl BC, Becker K, McNamara P, Herrmann M, Peters G. 2006. Small colony variants: a pathogenic form of bacteria that facilitates persistent and recurrent infections. *Nature Reviews Microbiology* 4(4):295-305.
536. Ji Q, Zhang L, Jones MB, Sun F, Deng X, Liang H, Cho H, Brugarolas P, Gao YN, Peterson SN, Lan L, Bae T, He C. 2013. Molecular mechanism of quinone signaling mediated through *S*-quinonization of a YodB family repressor QsrR. *Proc Natl Acad Sci U S A* 110(13):5010-5.
537. Noto MJ, Burns WJ, Beavers WN, Skaar EP. 2017. Mechanisms of pyocyanin toxicity and genetic determinants of resistance in *Staphylococcus aureus*. *J Bacteriol* 199(17).
538. Linzner N, Fritsch VN, Busche T, Tung QN, Van Loi V, Bernhardt J, Kalinowski J, Antelmann H. 2020. The plant-derived naphthoquinone lapachol causes an oxidative stress response in *Staphylococcus aureus*. *Free Radic Biol Med* 158:126-136.
539. Loi VV, Busche T, Preuss T, Kalinowski J, Bernhardt J, Antelmann H. 2018. The AGXX antimicrobial coating causes a thiol-specific oxidative stress response and protein *S*-bacillithiolation in *Staphylococcus aureus*. *Front Microbiol* 9:3037.
540. Ji Q, Zhao BS, He C. 2013. A highly sensitive and genetically encoded fluorescent reporter for ratiometric monitoring of quinones in living cells. *Chem Commun (Camb)* 49(73):8027-9.
541. Wang G, Maier RJ. 2004. An NADPH quinone reductase of *Helicobacter pylori* plays an important role in oxidative stress resistance and host colonization. *Infect Immun* 72(3):1391-6.
542. Gonzalez CF, Ackerley DF, Lynch SV, Matin A. 2005. ChrR, a soluble quinone reductase of *Pseudomonas putida* that defends against H_2O_2. *J Biol Chem* 280(24):22590-5.
543. Hong Y, Wang G, Maier RJ. 2008. The NADPH quinone reductase MdaB confers oxidative stress resistance to *Helicobacter hepaticus*. *Microb Pathog* 44(2):169-74.

544. Snell SB, Gill AL, Haidaris CG, Foster TH, Baran TM, Gill SR. 2021. *Staphylococcus aureus* tolerance and genomic response to photodynamic inactivation. *mSphere* 6(1).
545. Rapacka-Zdonczyk A, Wozniak A, Michalska K, Pieranski M, Ogonowska P, Grinholc M, Nakonieczna J. 2021. Factors Determining the Susceptibility of Bacteria to Antibacterial Photodynamic Inactivation. *Front Med (Lausanne)* 8:642609.
546. You Y, Xue T, Cao L, Zhao L, Sun H, Sun B. 2014. *Staphylococcus aureus* glucose-induced biofilm accessory proteins, GbaAB, influence biofilm formation in a PIA-dependent manner. *Int J Med Microbiol* 304(5-6):603-12.
547. Loi VV, Busche T, Fritsch VN, Weise C, Gruhlke MCH, Slusarenko AJ, Kalinowski J, Antelmann H. 2021. The two-Cys-type TetR repressor GbaA confers resistance under disulfide and electrophile stress in *Staphylococcus aureus*. *Free Radic Biol Med* 177:120-131.
548. Ray A, Edmonds KA, Palmer LD, Skaar EP, Giedroc DP. 2020. *Staphylococcus aureus* glucose-induced biofilm accessory protein A (GbaA) is a monothiol-dependent electrophile sensor. *Biochemistry* 59(31):2882-2895.
549. Jiale Z, Jian J, Xinyi T, Haoji X, Xueqin H, Xiao W. 2021. Design of a novel antimicrobial peptide 1018M targeted ppGpp to inhibit MRSA biofilm formation. *AMB Express* 11(1):49.
550. Hall DC, Jr., Krol JE, Cahill JP, Ji HF, Ehrlich GD. 2020. The Development of a pipeline for the identification and validation of small-molecule RelA inhibitors for use as anti-biofilm drugs. *Microorganisms* 8(9).
551. Kushwaha GS, Oyeyemi BF, Bhavesh NS. 2019. Stringent response protein as a potential target to intervene persistent bacterial infection. *Biochimie* 165:67-75.
552. Wexselblatt E, Oppenheimer-Shaanan Y, Kaspy I, London N, Schueler-Furman O, Yavin E, Glaser G, Katzhendler J, Ben-Yehuda S. 2012. Relacin, a novel antibacterial agent targeting the stringent response. *PLoS Pathog* 8(9):e1002925.
553. Syal K, Flentie K, Bhardwaj N, Maiti K, Jayaraman N, Stallings CL, Chatterji D. 2017. Synthetic (p)ppGpp analogue is an inhibitor of stringent response in Mycobacteria. *Antimicrob Agents Chemother* 61(6).
554. Lu C, Li X, Ren Y, Zhang X. 2021. Disulfiram: a novel repurposed drug for cancer therapy. *Cancer Chemother Pharmacol* 87(2):159-172.
555. Meneguello JE, Murase LS, de Souza JVP, de Oliveira CG, Ghiraldi-Lopes LD, Teixeira JJV, Scodro RBL, Ferracioli KRC, Siqueira VLD, Campanerut-Sa PAZ, Cardoso RF. 2022. Systematic review of disulfiram as an antibacterial agent: what is the evidence? *Int J Antimicrob Agents* 59(5):106578.
556. Chen C, Yang KW, Wu LY, Li JQ, Sun LY. 2020. Disulfiram as a potent metallo-beta-lactamase inhibitor with dual functional mechanisms. *Chem Commun (Camb)* 56(18):2755-2758.
557. Brogi S, Ibba R, Rossi S, Butini S, Calderone V, Gemma S, Campiani G. 2022. Covalent reversible inhibitors of cysteine proteases containing the nitrile warhead: Recent advancement in the field of viral and parasitic diseases. *Molecules* 27(8).
558. Adrover JM, Carrau L, Dassler-Plenker J, Bram Y, Chandar V, Houghton S, Redmond D, Merrill JR, Shevik M, tenOever BR, Lyons SK, Schwartz RE, Egeblad M. 2022. Disulfiram inhibits neutrophil extracellular trap formation and protects rodents from acute lung injury and SARS-CoV-2 infection. *JCI Insight* 7(5).
559. Koyama J. 2006. Anti-infective quinone derivatives of recent patents. *Recent Pat Antiinfect Drug Discov* 1(1):113-25.
560. Wang YQ, Li QS, Zheng XQ, Lu JL, Liang YR. 2021. Antiviral effects of green tea EGCG and its potential application against COVID-19. *Molecules* 26(13).
561. Lin N, Verma D, Saini N, Arbi R, Munir M, Jovic M, Turak A. 2021. Antiviral nanoparticles for sanitizing surfaces: A roadmap to self-sterilizing against COVID-19. *Nano Today* 40:101267.
562. Nogara PA, Oliveira CS, Pereira ME, Bortoli M, Orian L, Aschner M, Rocha JBT. 2022. Chapter 27 - Therapeutic applications of low-molecular-weight thiols and selenocompounds, p 643-677. Alvarez B, Comini MA, Salinas G, Trujillo M (ed), *In* Redox Chemistry and Biology of Thiols doi:10.1016/B978-0-323-90219-9.00005-4. *Academic Press*

563. Mösbauer K, Fritsch VN, Adrian L, Bernhardt J, Gruhlke MCH, Slusarenko AJ, Niemeyer D, Antelmann H. 2021. The Effect of Allicin on the Proteome of SARS-CoV-2 Infected Calu-3 Cells. *Front Microbiol* 12:746795.
564. Borlinghaus J, Albrecht F, Gruhlke MC, Nwachukwu ID, Slusarenko AJ. 2014. Allicin: chemistry and biological properties. *Molecules* 19(8):12591-618.
565. Schier C, Foerster J, Heupel M, Dörner P, Klaas M, Schröder W, Rink L, Slusarenko AJ, Gruhlke MCH. 2022. Allicin as a volatile or nebulisable antimycotic for the treatment of pulmonary mycoses: *In vitro* studies using a lung flow test rig. *International Journal of Molecular Sciences* 23(12).
566. Miron T, Rabinkov A, Mirelman D, Wilchek M, Weiner L. 2000. The mode of action of allicin: its ready permeability through phospholipid membranes may contribute to its biological activity. *Biochimica et Biophysica Acta (BBA) - Biomembranes* 1463(1):20-30.
567. Ankri S, Mirelman D. 1999. Antimicrobial properties of allicin from garlic. *Microbes Infect* 1(2):125-9.
568. El-Saber Batiha G, Magdy Beshbishy A, L GW, Elewa YHA, A AA-S, Abd El-Hack ME, Taha AE, Y MA-E, Prasad Devkota H. 2020. Chemical constituents and pharmacological activities of Garlic (*Allium sativum* L.): A review. *Nutrients* 12(3).
569. Rivlin RS. 2001. Historical perspective on the use of garlic. *J Nutr* 131(3s):951S-4S.
570. Reiter J, Hubbers AM, Albrecht F, Leichert LIO, Slusarenko AJ. 2020. Allicin, a natural antimicrobial defence substance from garlic, inhibits DNA gyrase activity in bacteria. *Int J Med Microbiol* 310(1):151359.
571. Chi BK, Huyen NTT, Loi VV, Gruhlke MCH, Schaffer M, Mäder U, Maass S, Becher D, Bernhardt J, Arbach M, Hamilton CJ, Slusarenko AJ, Antelmann H. 2019. The disulfide stress response and protein *S*-thioallylation caused by allicin and diallyl polysulfanes in *Bacillus subtilis* as revealed by transcriptomics and proteomics. *Antioxidants (Basel)* 8(12).
572. Wüllner D, Haupt A, Prochnow P, Leontiev R, Slusarenko AJ, Bandow JE. 2019. Interspecies comparison of the bacterial response to allicin reveals species-specific defense strategies. *Proteomics* 19(24):e1900064.
573. Weber ND, Andersen DO, North JA, Murray BK, Lawson LD, Hughes BG. 1992. *In vitro* virucidal effects of *Allium sativum* (garlic) extract and compounds. *Planta Med* 58(5):417-23.
574. Tsai Y, Cole LL, Davis LE, Lockwood SJ, Simmons V, Wild GC. 1985. Antiviral properties of garlic: *in vitro* effects on influenza B, herpes simplex and coxsackie viruses. *Planta Med*(5):460-1.
575. Rouf R, Uddin SJ, Sarker DK, Islam MT, Ali ES, Shilpi JA, Nahar L, Tiralongo E, Sarker SD. 2020. Antiviral potential of garlic (*Allium sativum*) and its organosulfur compounds: A systematic update of pre-clinical and clinical data. *Trends Food Sci Technol* 104:219-234.
576. Montazersaheb S, Hosseiniyan Khatibi SM, Hejazi MS, Tarhriz V, Farjami A, Ghasemian Sorbeni F, Farahzadi R, Ghasemnejad T. 2022. COVID-19 infection: an overview on cytokine storm and related interventions. *Virol J* 19(1):92.
577. Fara A, Mitrev Z, Rosalia RA, Assas BM. 2020. Cytokine storm and COVID-19: a chronicle of pro-inflammatory cytokines. *Open Biol* 10(9):200160.
578. WHO. 2022. COVID-19 weekly epidemiological update. Available online: https://www.who.int/docs/default-source/coronaviruse/situation-reports/20220615_weekly_epi_update_96.pdf?sfvrsn=4c68273c_3&download=true. (accessed on 06/21/2022).
579. Chippa V, Aleem A, Anjum F. 2022. Post acute coronavirus (COVID-19) syndrome, *In* StatPearls. *StatPearls Publishing*, Treasure Island (FL).Available online: https://pubmed.ncbi.nlm.nih.gov/34033370/. (accessed on 09/27/2022)
580. Yong SJ. 2021. Long COVID or post-COVID-19 syndrome: putative pathophysiology, risk factors, and treatments. *Infect Dis (Lond)* 53(10):737-754.
581. FDA. 2022. Coronavirus (COVID-19) drugs. Available online: https://www.fda.gov/drugs/emergency-preparedness-drugs/coronavirus-covid-19-drugs. (accessed on 09/26/2022).
582. Anonymous. 2022. Paxlovid for treatment of COVID-19. *Med Lett Drugs Ther* 64(1642):9-10.

583. Adhikari B, Marasini BP, Rayamajhee B, Bhattarai BR, Lamichhane G, Khadayat K, Adhikari A, Khanal S, Parajuli N. 2021. Potential roles of medicinal plants for the treatment of viral diseases focusing on COVID-19: A review. *Phytother Res* 35(3):1298-1312.
584. Anonymous. 2020. Redeploying plant defences. *Nat Plants* 6(3):177.
585. Gruhlke MC, Nicco C, Batteux F, Slusarenko AJ. 2016. The effects of allicin, a reactive sulfur species from garlic, on a selection of mammalian cell lines. *Antioxidants (Basel)* 6(1).
586. Borlinghaus J, Foerster Nee Reiter J, Kappler U, Antelmann H, Noll U, Gruhlke MCH, Slusarenko AJ. 2021. Allicin, the Odor of Freshly Crushed Garlic: A Review of Recent Progress in Understanding Allicin's Effects on Cells. *Molecules* 26(6).
587. Stukalov A, Girault V, Grass V, Karayel O, Bergant V, Urban C, Haas DA, Huang Y, Oubraham L, Wang A, Hamad MS, Piras A, Hansen FM, Tanzer MC, Paron I, Zinzula L, Engleitner T, Reinecke M, Lavacca TM, Ehmann R, Wolfel R, Jores J, Kuster B, Protzer U, Rad R, Ziebuhr J, Thiel V, Scaturro P, Mann M, Pichlmair A. 2021. Multilevel proteomics reveals host perturbations by SARS-CoV-2 and SARS-CoV. *Nature* 594(7862):246-252.
588. Tecalco Cruz AC. 2022. Free ISG15 and protein ISGylation emerging in SARS-CoV-2 infection. *Curr Drug Targets* 23(7):686-691.
589. Zhang H, Zheng H, Zhu J, Dong Q, Wang J, Fan H, Chen Y, Zhang X, Han X, Li Q, Lu J, Tong Y, Chen Z. 2021. Ubiquitin-modified proteome of SARS-CoV-2-infected host cells reveals insights into virus-host interaction and pathogenesis. *J Proteome Res* 20(5):2224-2239.
590. Cao X. 2021. ISG15 secretion exacerbates inflammation in SARS-CoV-2 infection. *Nat Immunol* 22(11):1360-1362.
591. Patya M, Zahalka MA, Vanichkin A, Rabinkov A, Miron T, Mirelman D, Wilchek M, Lander HM, Novogrodsky A. 2004. Allicin stimulates lymphocytes and elicits an antitumor effect: a possible role of p21ras. *Int Immunol* 16(2):275-81.
592. Lang A, Lahav M, Sakhnini E, Barshack I, Fidder HH, Avidan B, Bardan E, Hershkoviz R, Bar-Meir S, Chowers Y. 2004. Allicin inhibits spontaneous and TNF-alpha induced secretion of proinflammatory cytokines and chemokines from intestinal epithelial cells. *Clin Nutr* 23(5):1199-208.
593. Li C, Lun W, Zhao X, Lei S, Guo Y, Ma J, Zhi F. 2015. Allicin alleviates inflammation of trinitrobenzenesulfonic acid-induced rats and suppresses P38 and JNK pathways in Caco-2 cells. *Mediators Inflamm* 2015:434692.
594. Lamers MM, Haagmans BL. 2022. SARS-CoV-2 pathogenesis. *Nat Rev Microbiol* 20(5):270-284.
595. Costela-Ruiz VJ, Illescas-Montes R, Puerta-Puerta JM, Ruiz C, Melguizo-Rodriguez L. 2020. SARS-CoV-2 infection: The role of cytokines in COVID-19 disease. *Cytokine Growth Factor Rev* 54:62-75.
596. Wang L, Jiao H, Zhao J, Wang X, Sun S, Lin H. 2017. Allicin alleviates reticuloendotheliosis virus-induced immunosuppression via ERK/Mitogen-activated protein kinase pathway in specific pathogen-free chickens. *Front Immunol* 8:1856.
597. Anonymous. 2020. Allicin: The natural sulfur compound from garlic with many uses. Cundell DR (ed), Nutrition and Diet Research Progress. *Nova Science Publishers, Inc.*
598. Banerjee R, Perera L, Tillekeratne LMV. 2021. Potential SARS-CoV-2 main protease inhibitors. *Drug Discov Today* 26(3):804-816.
599. Bastikar V, Bastikar A, Chhajed SS. 2020. Understanding the role of natural medicinal compounds such as curcumin and allicin against SARS-CoV-2 proteins as potential treatment against COVID-19: An *in silico* approach. *Journal of Proteomics & Bioinformatics*:1-14.
600. Shekh S, Reddy KKA, Gowd KH. 2021. *In silico* allicin induced *S*-thioallylation of SARS-CoV-2 main protease. *Journal of Sulfur Chemistry* 42(1):109-120.
601. Oso BJ, Adeoye AO, Olaoye IF. 2022. Pharmacoinformatics and hypothetical studies on allicin, curcumin, and gingerol as potential candidates against COVID-19-associated proteases. *J Biomol Struct Dyn* 40(1):389-400.
602. Panchariya L, Khan WA, Kuila S, Sonkar K, Sahoo S, Ghoshal A, Kumar A, Verma DK, Hasan A, Khan MA, Jain N, Mohapatra AK, Das S, Thakur JK, Maiti S, Nanda RK, Halder R, Sunil S, Arockiasamy A. 2021. Zinc^{2+} ion inhibits SARS-CoV-2 main protease and viral replication *in vitro*. *Chemical Communications* 57(78):10083-10086.

603. Shi Y, Zeida A, Edwards CE, Mallory ML, Sastre S, Machado MR, Pickles RJ, Fu L, Liu K, Yang J, Baric RS, Boucher RC, Radi R, Carroll KS. 2022. Thiol-based chemical probes exhibit antiviral activity against SARS-CoV-2 via allosteric disulfide disruption in the spike glycoprotein. *Proc Natl Acad Sci U S A* 119(6).
604. Al-Qattan MM. 2009. Garlic burns: Case reports with an emphasis on associated and underlying pathology. *Burns* 35(2):300-302.
605. Vargo RJ, Warner BM, Potluri A, Prasad JL. 2017. Garlic burn of the oral mucosa: A case report and review of self-treatment chemical burns. *The Journal of the American Dental Association* 148(10):767-771.
606. Hitl M, Kladar N, Gavarić N, Srđenović Čonić B, Božin B. 2021. Garlic burn injuries- a systematic review of reported cases. *The American Journal of Emergency Medicine* 44:5-10.
607. Muniz IAF, Campos DES, Shinkai RSA, Trindade TGD, Cosme-Trindade DC. 2021. Case report of oral mucosa garlic burn during COVID-19 pandemic outbreak and role of teledentistry to manage oral health in an older adult woman. *Spec Care Dentist* 41(5):639-643.
608. Sheppard JG, Long TE. 2016. Allicin-inspired thiolated fluoroquinolones as antibacterials against ESKAPE pathogens. *Bioorg Med Chem Lett* 26(22):5545-5549.
609. Miron T, Listowsky I, Wilchek M. 2010. Reaction mechanisms of allicin and allyl-mixed disulfides with proteins and small thiol molecules. *Eur J Med Chem* 45(5):1912-8.
610. Kalkal A, Allawadhi P, Pradhan R, Khurana A, Bharani KK, Packirisamy G. 2021. *Allium sativum* derived carbon dots as a potential theranostic agent to combat the COVID-19 crisis. *Sens Int* 2:100102.

Chapter 1

The alarmone (p)ppGpp confers tolerance to oxidative stress during the stationary phase by maintenance of redox and iron homeostasis in *Staphylococcus aureus*

Verena Nadin Fritsch[1], Vu Van Loi[1], Tobias Busche[1,2], Quach Ngoc Tung[1], Roland Lill[3], Petra Horvatek[4], Christiane Wolz[4], Jörn Kalinowski[2], and Haike Antelmann[1]*

[1]Freie Universität Berlin, Institute for Biology-Microbiology, D-14195, Berlin, Germany

[2]Center for Biotechnology, Bielefeld University, D-33594, Bielefeld, Germany

[3]Institute of Cytobiology, Philipps-University of Marburg, D-35037, Marburg, Germany

Research Center for Synthetic Microbiology SynMikro, Hans-Meerwein-Str., D-35043, Marburg, Germany

[4]Interfaculty Institute of Microbiology and Infection Medicine, University of Tübingen, D-72076, Tübingen, Germany

*Corresponding author: haike.antelmann@fu-berlin.de

Published in:
Free Radical Biology and Medicine 161:351-364, 2020
DOI: https://doi.org/10.1016/j.freeradbiomed.2020.10.322

Personal contribution:

As the first author, I conducted most of the experiments. Thereby I was involved in phenotype analyses to investigate the ability of *S. aureus* to acquire a non-specific stress tolerance during the stationary phase and the role of (p)ppGpp (Fig. 1). Together with Dr. Quach Ngoc Tung, Dr. Tobias Busche and Prof. Dr. Haike Antelmann, I was responsible for the transcriptome data analysis and the further research design. I helped to characterize the function of (p)ppGpp in the iron and redox homeostasis by measuring the catalase activity and the intracellular amount of reactive oxygen species using the DCFH2-DA dye (Fig. 5D,F). Additionally, I determined oxygen consumption rates (Fig. 6) and performed the Northern blots in Fig. 8A and S3. For quantification of intracellular iron levels, I applied the ferene-s assay and prepared the samples for ICP-MS analysis (Fig. 7C,D). Moreover, I performed phenotype analyses to characterize the susceptibility of the *S. aureus* strains to iron limitation, different antibiotics, and reactive oxygen species (ROS) in dependence on the endogenous iron and ROS levels (Fig. 7E,F; 9; 10; S4; S5). I drafted the initial manuscript and prepared with the co-authors the figures for publication.

Free Radical Biology and Medicine 161 (2020) 351–364

Contents lists available at ScienceDirect

Free Radical Biology and Medicine

journal homepage: www.elsevier.com/locate/freeradbiomed

Original article

The alarmone (p)ppGpp confers tolerance to oxidative stress during the stationary phase by maintenance of redox and iron homeostasis in *Staphylococcus aureus*

Verena Nadin Fritsch [a], Vu Van Loi [a], Tobias Busche [a,b], Quach Ngoc Tung [a], Roland Lill [c,d], Petra Horvatek [e], Christiane Wolz [e], Jörn Kalinowski [b], Haike Antelmann [a,*]

[a] Freie Universität Berlin, Institute of Biology-Microbiology, D-14195, Berlin, Germany
[b] Center for Biotechnology, Bielefeld University, D-33594, Bielefeld, Germany
[c] Institute of Cytobiology, Philipps-University of Marburg, D-35037, Marburg, Germany
[d] Research Center for Synthetic Microbiology SynMikro, Hans-Meerwein-Str., D-35043, Marburg, Germany
[e] Interfaculty Institute of Microbiology and Infection Medicine, University of Tübingen, D-72076, Tübingen, Germany

ARTICLE INFO

Keywords:
Staphylococcus aureus
(p)ppGpp
Stringent response
ROS
HOCl
Antibiotics

ABSTRACT

Slow growing stationary phase bacteria are often tolerant to multiple stressors and antimicrobials. Here, we show that the pathogen *Staphylococcus aureus* develops a non-specific tolerance towards oxidative stress during the stationary phase, which is mediated by the nucleotide second messenger (p)ppGpp. The (p)ppGpp^0 mutant was highly susceptible to HOCl stress during the stationary phase. Transcriptome analysis of the (p)ppGpp^0 mutant revealed an increased expression of the PerR, SigB, QsrR, CtsR and HrcA regulons during the stationary phase, indicating an oxidative stress response. The (p)ppGpp^0 mutant showed a slight oxidative shift in the bacillithiol (BSH) redox potential (E_{BSH}) and an impaired H_2O_2 detoxification due to higher endogenous ROS levels. The increased ROS levels in the (p)ppGpp^0 mutant were shown to be caused by higher respiratory chain activity and elevated total and free iron levels. Consistent with these results, N-acetyl cysteine and the iron-chelator dipyridyl improved the growth and survival of the (p)ppGpp^0 mutant under oxidative stress. Elevated free iron levels caused 8 to 31-fold increased transcription of Fe-storage proteins ferritin (*ftnA*) and miniferritin (*dps*) in the (p)ppGpp^0 mutant, while Fur-regulated uptake systems for iron, heme or siderophores (*efeOBU*, *isdABCDEFG*, *sirABC* and *sstADBCD*) were repressed. Finally, the susceptibility of the (p)ppGpp^0 mutant towards the bactericidal action of the antibiotics ciprofloxacin and tetracycline was abrogated with N-acetyl cysteine and dipyridyl. Taken together, (p)ppGpp confers tolerance to ROS and antibiotics by down-regulation of respiratory chain activity and free iron levels, lowering ROS formation to ensure redox homeostasis in *S. aureus*.

1. Introduction

Staphylococcus aureus is an opportunistic pathogen, which colonizes the nose and the skin of one quarter of the human population, but can also cause severe life-threatening infections [1–5]. The success of *S. aureus* as major human pathogen is further caused by the increasing prevalence of multiple antibiotic-resistant strains with limited treatment options, such as methicillin-resistant *S. aureus* isolates (MRSA) [6,7]. During acute and chronic infections, *S. aureus* has to combat with the oxidative burst of the host innate immune defense. Activated macrophages and neutrophils produce large amounts of reactive oxygen and chlorine species (ROS, RCS), such as H_2O_2 and HOCl as the first line defense to kill invading pathogens [8–11]. In addition, *S. aureus* has to adapt to antimicrobial compounds and reactive electrophilic species (RES), such as quinones during host-pathogen interactions. Thus, it is of utmost importance to study the defense and resistance mechanisms of *S. aureus* under ROS, RCS, RES and antibiotics for identification of new drug targets and development of alternative therapy strategies to combat infections with multi-resistant *S. aureus* isolates [12].

During infections, *S. aureus* produces an arsenal of different virulence factors, such as toxins and extracellular enzymes that are secreted during the stationary phase to damage host tissues [13]. In addition,

* Corresponding author. Institute for Biology-Microbiology, Freie Universität Berlin, Königin-Luise-Strasse 12-16, D-14195, Berlin, Germany.
E-mail address: haike.antelmann@fu-berlin.de (H. Antelmann).

https://doi.org/10.1016/j.freeradbiomed.2020.10.322
Received 12 August 2020; Received in revised form 18 October 2020; Accepted 28 October 2020
Available online 1 November 2020

S. aureus encodes several stressor-specific defense mechanisms to cope with ROS, RCS, RES and antibiotics treatment [10,14–16]. The low molecular weight thiol bacillithiol (BSH) and its associated bacilliredoxin (Brx)/BSH/bacillithiol disulfide reductase (YpdA) pathway play important roles to maintain redox homeostasis during recovery from oxidative stress [17–19]. Moreover, several redox regulators, including PerR, HypR, MgrA, SarZ, QsrR and MhqR sense ROS, RCS and RES to control specific detoxification pathways for degradation of redox-active compounds or to repair the resulting damage in *S. aureus* [17,18,20–23]. Such mechanisms provide protection against the respective reactive species and contribute to virulence and survival of the pathogen.

Apart from specific stress responses, many bacteria acquire a non-specific prospective resistance to multiple stressors and antibiotics during the stationary phase, which can be provoked by nutrient starvation, physical and chemical stressors [24,25]. In *Bacillus subtilis*, the alternative sigma factor SigmaB was shown to control a large general stress and starvation regulon which confers resistance and cross-protection to multiple stimuli, such as heat, salt and oxidative stress during the stationary phase [26]. However, the mechanisms of starvation-induced stationary phase resistance to stress and antibiotics are not fully understood in *S. aureus*.

In bacteria, the small alarmone (p)ppGpp accumulates during entry into the stationary phase by amino acid or carbon source limitation leading to the stringent response (SR) [26–29]. The SR is characterized by down-regulation of processes required for active growth, such as cell division, replication, transcription and translation, mediated by the repression of genes for rRNAs, ribosomal proteins and translation factors [30]. The main goal of the SR is to save energy and cellular resources during the non-growing state [29,31]. In addition, stress defense mechanisms and amino acid biosynthesis pathways are induced under SR conditions to ensure continued synthesis of stress proteins that are required for bacterial survival [24,25]. In *S. aureus*, the bifunctional synthase/hydrolase Rel (RelA/SpoT homolog) and two truncated (p)ppGpp synthases (RelP and RelQ) catalyze the pyrophosphate transfer from ATP to GTP or GDP to synthesize (p)ppGpp [32–35]. Compared to the many targets discovered for (p)ppGpp in Gram-negative bacteria, little is known about (p)ppGpp targets in Gram-positive firmicutes. In many bacteria, GTPases can be competitively inhibited by (p)ppGpp, including the ribosomal translation factors EF-Tu, EF-G, RF3 and IF2 [28,36–39]. In *S. aureus*, (p)ppGpp was shown to inhibit two enzymes needed for GTP synthesis (HprT and Gmk) and five GTPases (RsgA, RbgA, Era, HflX and ObgE) that are implicated in ribosome assembly [40,41]. The lack of GTP synthesis leads to inhibition of transcription of ribosomal RNAs that require GTP as initiating NTP [42,43]. In firmicutes, the decreased GTP pool upon (p)ppGpp synthesis causes inactivation of the CodY repressor, resulting in derepression of amino acid biosynthesis genes as part of the SR [40].

In addition, the SR is associated with virulence, biofilm formation, persister formation and involved in stationary phase-induced antibiotics tolerance [44–50]. The *S. aureus* (p)ppGpp^0 mutant which lacks all three (p)ppGpp synthases showed increased sensitivity to cell wall-active antibiotics, such as vancomycin and ampicillin and was impaired in survival in phagocytosis assay [51,52]. In addition, (p)ppGpp conferred high level of beta lactam resistance in MRSA strains *via* increased expression of penicillin-binding proteins, encoded by *mecA* and *pbpD* [47,48]. Overproduction of (p)ppGpp due to *rel* mutations in clinical isolates resulted in increased tolerance to five different antibiotic classes [53].

In *Vibrio cholerae*, (p)ppGpp was shown to reduce endogenous ROS formation possibly by inhibition of the iron-uptake transporter FbpA, which promotes tolerance to the antibiotic tetracycline [54]. Furthermore, (p)ppGpp down-regulates TCA cycle enzymes of central carbon metabolism and aerobic respiration to decrease ROS levels [54]. The *Pseudomonas aeruginosa* SR mutant suffered from increased ROS levels due to reduced activities of catalases and superoxide dismutases resulting in decreased multidrug tolerance [54–56]. Thus, several studies provide a link between (p)ppGpp and increased antibiotic tolerance via ROS levels. Moreover, ROS were shown to be involved in the killing mode of different antibiotic classes, which involves cellular respiration, metabolic pathways and the redox state [57–59]. Thus, factors that regulate the redox balance of bacteria play an important role in virulence and antibiotic susceptibility.

In this study, we found that *S. aureus* acquires a non-specific resistance towards oxidative stress during the stationary phase, which was dependent on the SR mediated by (p)ppGpp. We therefore investigated the mechanisms of underlying ROS susceptibility in the (p)ppGpp^0 mutant. Expression of the antioxidant stress response and iron-storage ferritins was induced in the (p)ppGpp^0 mutant during the stationary phase due to elevated ROS and free iron levels leading to decreased tolerance to HOCl, tetracycline and ciprofloxacin. In addition, higher respiratory chain activity contributed to ROS increase in the absence of (p)ppGpp. Thus, (p)ppGpp impacts aerobic respiration, iron and redox homeostasis in *S. aureus* to promote tolerance to antibiotics and oxidative stress during the stationary phase, which could be particularly important during long-term and chronic infections with MRSA strains.

2. Materials and methods

2.1. Bacterial strains, growth and survival assays

Bacterial strains and primers are listed in Tables S1 and S2. The *S. aureus* strains used in this study were *S. aureus* COL and USA300JE2 wild types (WT) and the USA300JE2 derivative with mutations in the *rel* synthetase domain (Δrel_{syn}), which was transduced from the restriction-negative intermediate RN4220 Δrel_{syn} into strain USA300JE2 as previously described [52]. The USA300JE2 (p)ppGpp^0 strain contained mutations in the active sites of each of the three (p)ppGpp synthetases, *relP, relQ* and *rel* [60]. The (p)ppGpp^0 strain was complemented with plasmid pCG327, which expresses the Rel synthetase (Rel_{syn}) under the control of an anhydrotetracycline (AHT) inducible promotor [61] (Table S1). The Brx-roGFP2 biosensor expressing strains USA300JE2 pRB473-*brx-roGFP2* and USA300JE2 (p)ppGpp^0 pRB473-*brx-roGFP2* were constructed by phage transduction from RN4220 pRB473-*brx-roGFP2* into USA300JE2 and the isogenic (p)ppGpp^0 mutant as previously described [62]. Construction of the *katA* mutant was described previously [63]. For growth and survival assays, *S. aureus* strains were cultivated in RPMI 1640 cell culture medium (Bioscience Lonza, Catalog No. BE12-918F) containing 0.75 μM $FeCl_3$. Survival was determined by plating 100 μl of serial dilutions of *S. aureus* strains after 1–2 h of stress exposure onto LB agar plates for CFUs counting. Brx-roGFP2 biosensor measurements were conducted by cultivation of *S. aureus* WT and (p)ppGpp^0 mutant strains with plasmid pRB473-*brx-roGFP2* in LB and Belitsky minimal medium as described previously [62,64]. Statistical analysis was performed using the Student's unpaired two-tailed *t*-test by the graph prism software. The chemicals and antibiotics methylhydroquinone (MHQ), NaOCl, 2, 2′−dipyridyl, N-acetyl cysteine, $FeCl_3$, ciprofloxacin, tetracycline and streptonigrin were purchased from Sigma Aldrich and Merck, respectively. NaOCl dissociates in aqueous solution to hypochlorous acid (HOCl) and hypochlorite (OCl^-) [65]. Thus, the concentration of HOCl was determined by absorbance measurements as reported previously [66].

2.2. RNA isolation, northern blot analysis, transcriptome sequencing and bioinformatics

For RNA isolation, *S. aureus* strains were cultivated in RPMI and LB medium and harvested during the log and stationary phases as indicated in the figure and table legends. Northern blot hybridizations were performed as described [67,68] with the digoxigenin-labeled antisense RNA probes specific for the transcripts RNAIII, *katA*, *ahpC*, *ftnA*, *dps, ohr*, *clpB* and *asp23,* which were synthesized *in vitro* using T7 RNA

polymerase and the specific primer pairs as described previously [20,69] and in Table S2.

Transcriptome sequencing was performed using RNA of *S. aureus* USA300JE2 and the (p)ppGpp^0 mutant grown in RPMI medium and harvested at an OD_{500} of 0.5 and 1.2 for log and stationary phases, respectively, as described [21]. Differential gene expression analysis of 3 biological replicates was performed using DESeq2 [70] with ReadXplorer v2.2 [71] as described previously [21] using an adjusted *p*-value cutoff of ≤0.05 and a signal intensity ratio (*M*-value) cutoff of ≥0.6 or ≤ −0.6 (fold-change of ±1.5). Genes were sorted into regulons based on the RegPrecise database as in previous studies [21]. Whole transcriptome RNA-seq raw data files are available in the ArrayExpress database under accession number E-MTAB-9368.

2.3. Determination of intracellular iron levels using ferene-s assay and ICP-mass spectrometry

The intracellular iron concentrations of *S. aureus* USA300JE2 WT, (p)ppGpp^0 and *rel*$_{syn}$ mutants as well as the complemented (p)ppGpp^0 pCG327 strain were determined with ferene-s (3-(2-pyridyl)-5,6-di (2-furyl)-1,2,4-triazine-5′,5″-disulfonic acid disodium salt) assay purchased from Sigma-Aldrich according to the instructions of the manufacturer with some modifications. In brief, *S. aureus* strains grown in RPMI were harvested during the log and stationary phases at an OD_{500} of 0.5, 1 and 2, respectively. Cell pellets were lysed with 1% hydrochloric acid (HCl) and heated at 80 °C for 10 min. Excess acid was neutralized with 7.5% ammonium acetate. Next, ferric iron (Fe^{3+}) was reduced to ferrous iron (Fe^{2+}) with 4% ascorbic acid. Precipitated protein was complexed with 2.5% sodium dodecyl sulfate. About 1.5% of the iron chelator ferene-s was added leading to the formation of a blue iron-ferene-s complex (Fe^{2+}: ferene-s). Samples were centrifuged at 9000 rpm for 7 min and the absorbance was measured at 593 nm. Ammonium iron (II) sulfate hexahydrate (Sigma Aldrich) was used to prepare the iron standard curve.

Iron levels were further determined using inductively coupled plasma (ICP) mass spectrometry. *S. aureus* cell cultures of ~70–280 ml, containing total protein amounts of ~6–10 mg were harvested by centrifugation. The dried cell pellets were mixed with an excess of concentrated nitric acid (69%) and incubated at 60 °C for at least 2 h to destroy any organic content. Samples were diluted with water to a final nitric acid concentration of 10%. For metal detection, samples were further diluted 1:10, and 1 ppb rhodium was added as an internal standard. Elements of interest were quantified using an Element 2 ICP-MS system (Thermo Scientific™, Bremen). For ionization of analytes, a plasma was generated with a power of 1200 W. For quantitation, the standard addition method was utilized. A matrix sample was used as blank and subtracted.

2.4. Measurements of BSH redox potential (E_{BSH}) changes using the Brx-roGFP2 biosensor

S. aureus USA300JE2 WT and (p)ppGpp^0 mutant strains expressing the Brx-roGFP2 biosensor were cultivated in LB and used for measurements of the biosensor oxidation degree (OxD) along the growth curves and after injection of H_2O_2 and HOCl into the microplate well as described [62,64]. Fully reduced and oxidized controls were prepared with 10 mM DTT and 20 mM cumene hydroperoxide, respectively. Brx-roGFP2 biosensor fluorescence emission was measured at 510 nm after excitation at 405 and 488 nm using the CLARIOstar microplate reader (BMG Labtech). The OxD of the Brx-roGFP2 biosensor was determined for each sample and normalized to fully reduced and oxidized controls. Based on the OxD and $E^{0'}_{roGFP2}$ = - 280 mV [72], the BSH redox potential (E_{BSH}) was calculated according to the Nernst equation [62]. The E_{BSH} results are presented in Table S3.

2.5. FOX assay for determination of H_2O_2 detoxification capacity of cell extracts

The FOX assay was used to determine the H_2O_2 consumption capacity of cytoplasmic extracts of *S. aureus* USA300JE2 WT, (p)ppGpp^0 mutant and complemented (p)ppGpp^0 pCG327 cells, which were harvested in RPMI at OD_{500} of 1.2 as described previously [73]. FOX reagent was prepared by adding 100 ml FOX I (100 mM sorbitol, 125 μM xylenol orange) to 1 ml FOX II (25 mM ammonium ferrous (II)sulfate in 2.5 M H_2SO_4). To prepare cytoplasmic extracts, cells were washed twice with 83 mM phosphate buffer (pH 7.05) and disrupted using the ribolyzer. Next, 100 μl cell lysate containing 10 μg protein was added to 500 μl of 10 mM H_2O_2 solution. After different times (1–5 min), 2 μl of the samples were added to 200 μl FOX reagent and incubated for 30 min at room temperature. The absorbance was measured at 560 nm using the CLARIOstar microplate reader. H_2O_2 standard curves were measured with 20 μl H_2O_2 (0–18 μM final concentrations) and 200 μl FOX reagent as above.

2.6. ROS measurements using 2′,7′-dichlorodihydrofluorescein diacetate ($DCFH_2$-DA)

Endogenous ROS levels were measured using the 2′,7′-dichlorodihydrofluorescein diacetate ($DCFH_2$-DA) dye (Th. Geyer) [74]. $DCFH_2$-DA is de-acetylated by alkaline hydrolysis by NaOH to generate $DCFH_2$, which is oxidized by ROS to the fluorescent dye 2′,7′-dichlorofluorescein (DCF) using the previous protocol [75]. Briefly, *S. aureus* USA300JE2 wild type, the (p)ppGpp^0, *rel*$_{syn}$ and *katA* mutants as well as the complemented (p)ppGpp^0 pCG327 strain were cultivated in RPMI medium to an OD_{500} of 0.5, 1 and 2. The cells were harvested at an OD_{600} equivalent of 5×10^8 cells by centrifugation. Cell pellets were incubated with $DCFH_2$ for 40 min as described [75]. Relative DCF fluorescence was measured using the CLARIOstar microplate reader at an excitation and emission wavelength of 488 and 515 nm, respectively.

2.7. Determination of catalase activity using native PAGE and diaminobenzidine staining

S. aureus strains were grown in RPMI and cytoplasmic extracts prepared as above for the FOX assay. Cytoplasmic extracts were separated using native PAGE and stained for catalase activity using the diaminobenzidine staining method as described previously [76,77].

2.8. Determination of oxygen consumption rates

For measurements of respiratory chain activity by oxygen consumption rates in *S. aureus* strains, the Clark-type electrode (Oxygraph, Hansatech) was used as described previously [21,78,79]. In brief, *S. aureus* strains were grown in RPMI to an OD_{500} of 0.5 and 1 or in TSB to an OD_{600} of 0.6 and 3. Cells were harvested by centrifugation, washed in 33 mM potassium phosphate buffer (pH 7.0) and adjusted to an OD_{578} of 5. Oxygen consumption rates were determined after addition of 1 mM glucose as electron donor in 3 biological replicates. The values were corrected for basal oxygen consumption without electron donors.

3. Results

3.1. S. aureus acquires a non-specific tolerance to oxidative stress during the stationary phase, which is mediated by the alarmone (p)ppGpp

Previously, we characterized various stressor-specific resistance mechanisms that conferred protection of *S. aureus* to the thiol-reactive compounds HOCl and quinones during the exponential growth, including the redox-sensing HypR and MhqR repressors [18,21]. In this study, we were interested if *S. aureus* is able to develop non-specific tolerance to HOCl and MHQ during the stationary phase. Thus,

survival rates of the *S. aureus* COL and USA300JE2 isolates were determined after exposure to 3.5 mM HOCl and 400 μM MHQ during the log and stationary phases at OD_{500} of 0.5 and 2–3, respectively (Fig. 1). These doses reduced the survival of log phase bacteria, but stationary phase cells displayed an enhanced survival rate upon HOCl and MHQ treatment (Fig. 1). Specifically, the survival of stationary phase cells was 40-fold increased after 400 μM MHQ treatment compared to log phase cells, while only <2-fold elevated survival rates were determined in stationary phase cells in response to 3.5 mM HOCl challenge (Fig. 1).

Next, we analyzed the survival of the USA300JE2 (p)ppGpp^0 mutant, which cannot synthesize (p)ppGpp, after exposure to 3.5 mM HOCl and 400 μM MHQ during the log or stationary phases (Fig. 1C and D). While the survival of HOCl-treated log phase cells of the (p)ppGpp^0 mutant was only slightly different from the WT, strong killing of mutant cells was observed with only 2% survivors during the stationary phase (Fig. 1C). In contrast, the absence of (p)ppGpp resulted in a similar enhanced stationary phase-induced tolerance to MHQ stress compared to the WT (Fig. 1D). However, the (p)ppGpp^0 mutant was more sensitive to MHQ treatment during the log and stationary phases relative to its parent strain. Plasmid-borne expression of the (p)ppGpp synthetase Rel_{syn} (pCG327) restored the stationary phase tolerance of the (p)ppGpp^0 mutant under HOCl and MHQ stress (Fig. 1C and D). These results indicate that (p)ppGpp protects from oxidative and quinone stress provoked by HOCl and MHQ during the log and stationary phases.

3.2. The absence of (p)ppGpp induces an oxidative and iron stress response in S. aureus during the stationary phase in the transcriptome

To understand the mechanisms of impaired stationary phase tolerance to HOCl stress in the (p)ppGpp^0 mutant, we analyzed the gene expression changes in the (p)ppGpp^0 mutant versus WT cells during the log and stationary phases using transcriptomics (Fig. 2, S1-S2, Tables S4–S9). Significant changes were determined by an M-value cut-off (log2-fold change (p)ppGpp^0 mutant/WT, $p \leq 0.05$) of ≥0.6 and ≤-0.6 (fold-change of ± 1.5, P ≤ 0.05). In total, 282 and 190 genes were significantly >1.5-fold up- and down-regulated, respectively in the (p)ppGpp^0 mutant compared to the WT during the stationary phase (Fig. 2, Tables S4–S9). The most interesting stress and starvation-induced or repressed regulons in the (p)ppGpp^0 mutant are labeled in the ratio/intensity scatter plots (M/A-plots) (Fig. 2, S1-S2, Tables S4–S6).

Among the top scorers are the oxidative stress responsive PerR, CstR, QsrR, CtsR and HrcA regulons, which were highly elevated in the (p)ppGpp^0 mutant during the stationary phase (Fig. 2, Tables S4–S6). However, this oxidative stress response was not induced in log phase cells (Fig. S2, Tables S7–S9). The peroxide sensing PerR repressor controls genes for H_2O_2 detoxification, heme and iron sulfur cluster biogenesis [80], including the catalase *katA* (3.4-fold induced), the peroxidase *ahpCF* (2.7–3.6-fold), the miniferritin *dps* (31-fold), the *hemEHY* operon (2–2.8-fold) and the *sufCDSUB* operon (4.7-8-fold) (Fig. 2, Tables S4–S6). The induction of the oxidative stress response could point to increased ROS levels in the absence of (p)ppGpp. In addition, the genes and operons of the CtsR and HrcA regulons for proteases and chaperones displayed the highest fold-changes, including *clpB* (15.6-fold), *clpP* (2.3-fold), *ctsR-mcsA-mcsB-clpC* (6.8-9-fold), *hrcA-grpE-dnaKJ* (6.9–11-fold) and *groESL* (5.5–6.4-fold). These protein quality control machineries facilitate protein folding and degradation of oxidatively damaged proteins and are associated with the thiol stress response as shown previously under HOCl, AGXX® and allicin stress [18,21,81–85].

Of note, the transcriptome results further revealed a very strong iron stress response in the (p)ppGpp^0 mutant since Fe-storage ferritin (*ftnA*) and miniferritin (*dps*) were most strongly 8-31-fold up-regulated [23,80,86] (Fig. 2, Tables S4–S6). Elevated iron storage is further supported by the increased transcription of *sufCDSUB* operon for enhanced iron-sulfur

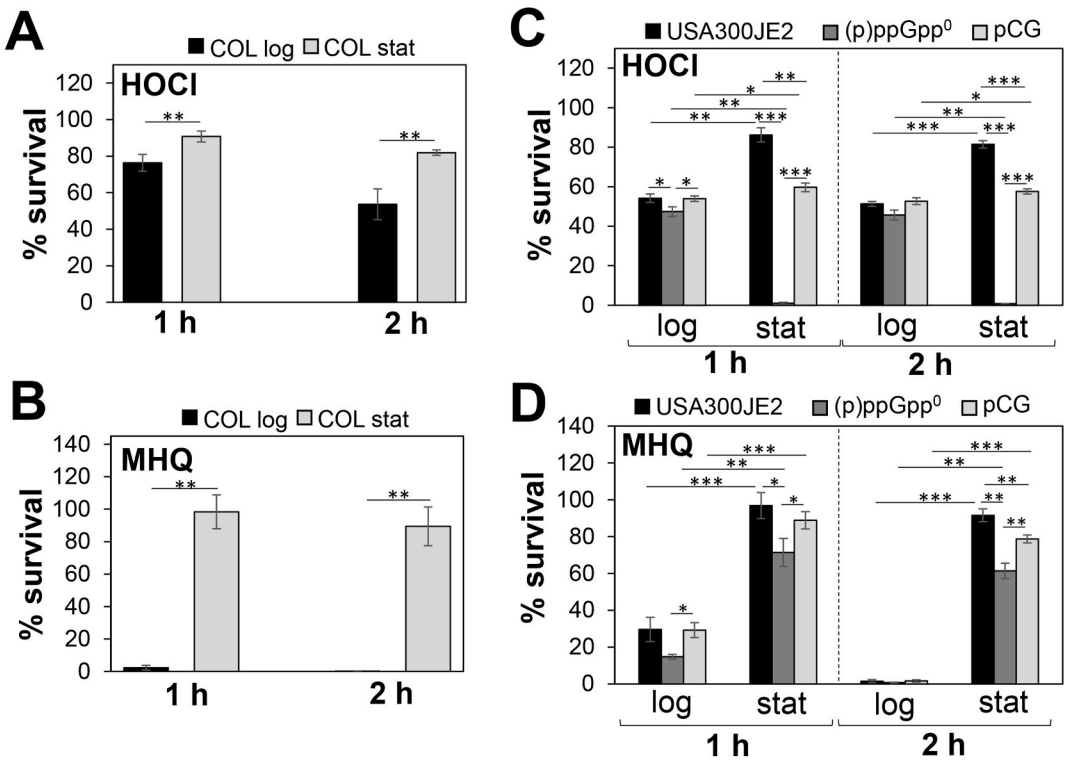

Fig. 1. The alarmone (p)ppGpp confers tolerance to oxidative stress in *S. aureus* during the stationary phase. For survival assays, *S. aureus* COL and USA300JE2 wild type, the (p)ppGpp^0 mutant and complemented strain (pCG) were exposed to 3.5 mM HOCl **(A,C)** and 400 μM MHQ **(B,D)** during the log and stationary phases at OD_{500} of 0.5 and 2–3, respectively. The CFUs after 1 and 2 h stress exposure were calculated as survival rates relative to the untreated control, which was set to 100%. The (p)ppGpp^0 mutant was more sensitive to HOCl and MHQ stress, and impaired to acquire the stationary phase-induced tolerance towards HOCl. The results are from four biological replicates. Error bars represent the standard deviation. $^*p < 0.05$; $^{**}p < 0.01$; $^{***}p < 0.001$.

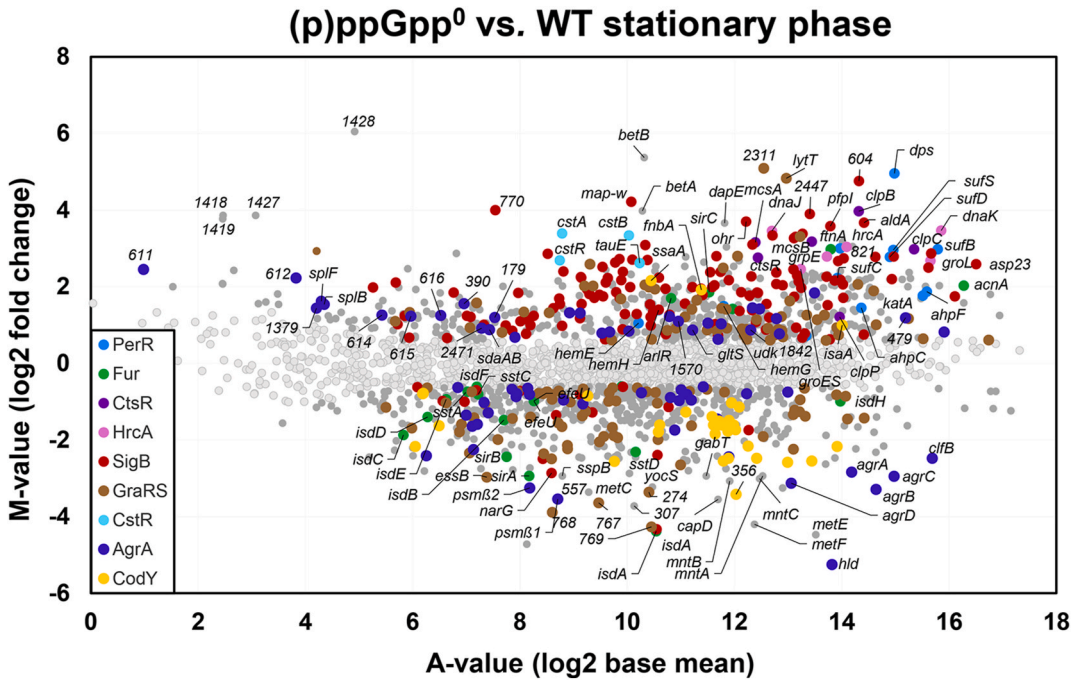

Fig. 2. Transcriptome analysis reveals an oxidative and iron stress response in the (p)ppGpp^0 mutant during the stationary phase. *S. aureus* USA300JE2 and the (p)ppGpp^0 mutant were grown in RPMI medium and RNA was isolated from cells harvested at an OD_{500} of 1.2. The gene expression profile of the (p)ppGpp^0 mutant versus the WT is shown as ratio/intensity scatterplot (M/A-plot), which is based on the differential gene expression analysis using DeSeq2. Colored symbols indicate significantly induced and repressed transcripts (M-value ≥0.6 or ≤ −0.6; $p \leq 0.05$), which could be allocated to the PerR (blue), Fur (green), CtsR (magenta), HrcA (pink), SigB (red), GraRS (brown), CstR (light blue), Agr (dark blue) and CodY regulons (yellow). Light gray symbols denote transcripts with no fold-changes ($p > 0.05$). The complete transcriptome data and regulon classifications are listed in Tables S4–S7. (For interpretation of the references to colour in this figure legend, the reader is referred to the Web version of this article.)

cluster biosynthesis, suggesting increased iron levels in the (p)ppGpp^0 mutant. In contrast, the majority of Fur-controlled uptake systems for iron, heme and siderophores were strongly down-regulated in the (p)ppGpp^0 mutant. The repressed iron transporters include the iron-dependent peroxidase *efeOBU* operon (0.5–0.7-fold), the Fe(III)-staphyloferrin-B *sirAB* uptake system (0.13–0.18-fold), the catechol-type Fe(III) siderophore importer *sstABC* operons and the iron-regulated surface determinant *isdABCDEFG* operon for uptake of heme iron (0.05–0.5-fold) [87,88]. In addition, down-regulation of the Mn(II) uptake *mntABC* operon (0.12–0.13-fold) further denotes metal ion dysregulation in the (p)ppGpp^0 mutant. Thus, the up-regulation of the PerR regulon, the increased iron-storage and the repressed iron transport together support the hypothesis of a prevailing internal iron excess, which may lead to ROS formation via Fenton chemistry [54,80].

Moreover, the sulfur-stress specific CstR regulon (6.1–10.5-fold) and the quinone stress responsive QsrR regulon (2.5–5.3-fold) were both strongly upregulated in the mutant. The CstR and QsrR repressors harbour redox-sensing Cys residues and were previously shown to respond to disulfide stress, such as HOCl, AGXX® and allicin stress in *S. aureus* [18,22,84–86,89]. Additionally, genes for cysteine and BSH biosynthesis (*cysK, bshB, bshC*) displayed 2-4-fold higher expression levels in the (p)ppGpp^0 mutant, indicating an impaired redox homeostasis in the (p)ppGpp^0 mutant. Furthermore, the majority of genes of the SigB general stress regulon were strongly up-regulated in the (p)ppGpp^0 mutant during the stationary phase (Fig. 2, Tables S4–S6). These include the *sigB-rsbW-rsbV-rsbU*-operon (3.6–4.1-fold), the *asp23-SA-COL2174-amaP-opuD2* operon (6–9.7-fold), the multi-drug transporter *bmrU* (10.1-fold), the capsule biosynthesis *cap* operon (2-4-fold), the staphyloxanthin biosynthesis *crtNMQIO* operon (2.3–6.5-fold), the aldehyde dehydrogenase *aldA* (12.7-fold), the *ohr* peroxiredoxin (13-fold) and several genes that code for hypothetical proteins.

In addition, the cell wall stress-responsive GraRS regulon [90,91] was partially up- or down-regulated in the (p)ppGpp^0 mutant (Tables S4–S6). Among the GraRS regulon were highly induced the flavodoxin *acpD* gene (7-fold), the TCA cycle enzymes *citCZ* and *sucCD* operons (2-4-fold), the cytochrome D ubiquinol oxidase *cydAB* operon (4-6-fold), the glycine-betaine transporter *opuCA-CB-CC-CD* operon (3.2-4-fold) and the *SAUSA300_2310/2311* operon (28-34-fold) of unknown functions. Elevated expression of the *citCZ, sucCD and cydAB* operons could indicate an enhanced TCA cycle activity and higher respiratory chain activity in the (p)ppGpp^0 mutant, which might contribute to ROS formation. Apart from the *opuC* operon, we found a strong up-regulation of the *betAB* operon that codes for a glycine betaine synthetase (15.8–41-fold), pointing to an enhanced synthesis and uptake of compatible solutes in the (p)ppGpp^0 mutant.

As expected, the CodY regulon genes for amino acid biosynthesis were strongly down-regulated in the absence of (p)ppGpp due to increased GTP-levels resulting in stronger CodY repression [51]. The main role of (p)ppGpp is to downregulate genes for active growth and to stop protein translation [31]. Thus, the majority of genes encoding ribosomal proteins, translation elongation factors and aminoacyl-tRNA synthetases were 2-10-fold induced in the absence of (p)ppGpp (Fig. 2, S1, Tables S4–S9). Altogether, the transcriptome signature of the (p)ppGpp^0 mutant supports the hypothesis of an oxidative and iron stress response due to enhanced respiration and iron overload leading to ROS production and an impaired redox balance.

3.3. The oxidative and iron stress response is elevated in the (p)ppGpp^0 mutant only in RPMI medium during the stationary phase

Previous studies revealed no growth defects of the (p)ppGpp^0 mutant in complex LB or TSB medium [33], which was confirmed in our study (Fig. 3A and B). However, the (p)ppGpp^0 and rel_{syn} mutants revealed a strong growth delay when cultivated in RPMI (Fig. 3C). Thus, we were interested to unravel the underlying mechanism of the growth delay of the (p)ppGpp^0 mutant in RPMI medium. Based on the transcriptome

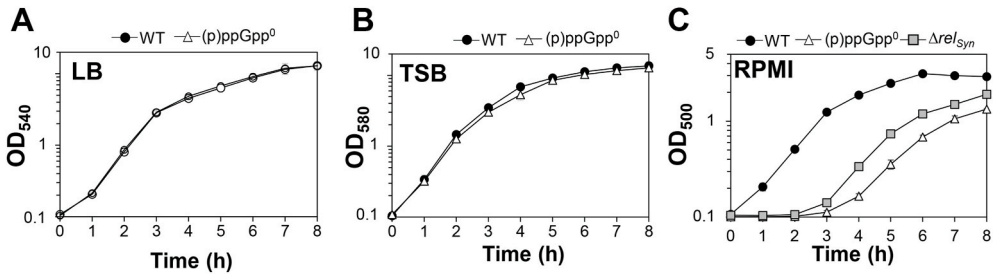

Fig. 3. The (p)ppGpp^0 mutant shows a growth defect in RPMI medium. Growth curves were monitored of the *S. aureus* USA300JE2 wild type (WT), the (p)ppGpp^0 and Δ*rel*$_{syn}$ mutants in LB **(A)**, TSB **(B)** and RPMI medium **(C)**.

data, the (p)ppGpp^0 mutant showed an enhanced oxidative and iron stress response in RPMI during the stationary phase (Fig. 2, Tables S4–S6). Thus, we used Northern blots to investigate whether the oxidative and iron stress response is responsible for the growth defect of the (p)ppGpp^0 mutant in RPMI during the stationary phase (Fig. 4). The Northern blot results of the (p)ppGpp^0 mutant in LB did not reveal differences in transcription of oxidative stress genes controlled by PerR (*katA*, *ahpCF*, *dps*), CtsR (*clpB*), SigB (*asp23, ohr*) and Agr (RNAIII). Only slightly increased transcription in the (p)ppGpp^0 mutant versus WT cells was observed for the peroxiredoxin (*ohr*) and the ferritin (*ftnA*) genes in LB during the stationary phase (Fig. 4). These data support that WT and (p)ppGpp^0 mutant cells do not show growth differences in rich LB medium. In contrast, cultivation in RPMI medium resulted in up-regulation of genes encoding antioxidant enzymes (*katA*, *ahpCF, ohr*), the Clp protease (*clpB*) and iron storage proteins (*dps*, *ftnA*) in the (p)ppGpp^0 mutant during the stationary phase compared to the WT (Fig. 4). This induction of the oxidative and iron stress responses in the (p)ppGpp^0 mutant was abrogated in the (p)ppGpp complemented *rel*$_{syn}$ strain (Fig. S3). Furthermore, transcription of the Agr-controlled RNAIII was down-regulated in the (p)ppGpp^0 mutant in RPMI, which is consistent with the strong repression of the *agrABCD* operon in the transcriptome and might be related to the slower growth rate (Figs. 2 and 4). Overall, these transcriptional results support the hypothesis that the (p)ppGpp^0 mutant suffers from oxidative and iron stress in RPMI medium during the stationary phase, which might be responsible for its growth delay in RPMI (Fig. 3C).

3.4. The (p)ppGpp^0 mutant shows a slight oxidative shift in the BSH redox potential, an increased ROS level and delayed H_2O_2 detoxification

Transcriptional studies revealed an increased oxidative stress response in the absence of (p)ppGpp. Hence, we hypothesized that the (p)ppGpp^0 mutant might have an impaired redox balance. The Brx-roGFP2 biosensor was applied to monitor the changes in the BSH redox potential (E_{BSH}) inside WT and (p)ppGpp^0 mutant cells during different growth phases and after oxidative stress (Fig. 5A–C). However, E_{BSH} changes could not be measured upon growth in RPMI medium due to low expression of the Brx-roGFP2 biosensor resulting in low fluorescence intensities, which did not allow ratiometric quantification of the fluorescence changes. Consequently, the oxidation degree (OxD) of the Brx-roGFP2 was measured along the growth in LB based on the ratiometric changes of the 405 nm and 488 nm excitation maxima upon roGFP2 oxidation as described previously (Fig. 5A) [62,64]. The corresponding E_{BSH} values were calculated from the OxD using the Nernst equation (Table S3). The biosensor results showed that WT cells maintained a highly reduced E_{BSH} of ~ -290 mV with little fluctuations during the log and stationary phases. However, a slight but significant oxidative shift in E_{BSH} to ~ -280 mV was determined throughout the growth in the

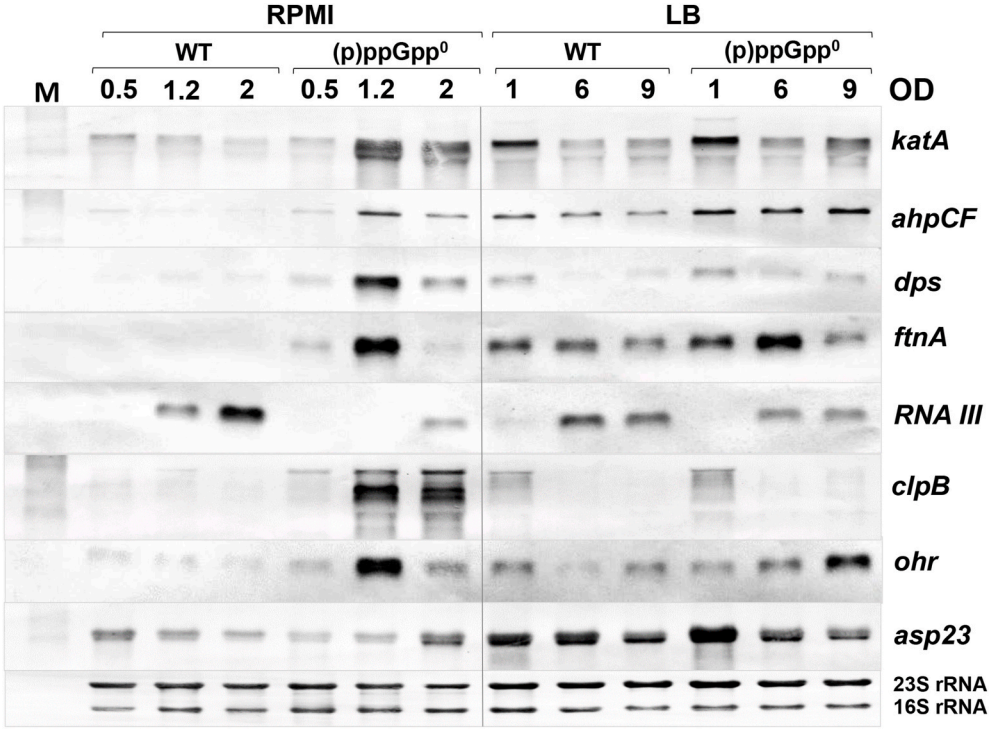

Fig. 4. The oxidative and iron stress response is elevated in the (p)ppGpp^0 mutant only in RPMI during the stationary phase. Northern blot transcriptional analysis was performed for the PerR (*katA, ahpCF*), SigB (*asp23, ohr*), CtsR (*clpB*) and Agr (RNAIII) regulons and the iron storage ferritins (*dps, ftnA*) in *S. aureus* USA300JE2 WT and the (p)ppGpp^0 mutant in RPMI and LB during the log and stationary phases. The (p)ppGpp^0 mutant showed increased transcription of genes for iron storage (*dps*, *ftnA*), ROS detoxification (*katA, ahpCF*) and protein quality control (*clpB*) in RPMI. The methylene blue stain is the RNA loading control indicating the 16S and 23S rRNAs.

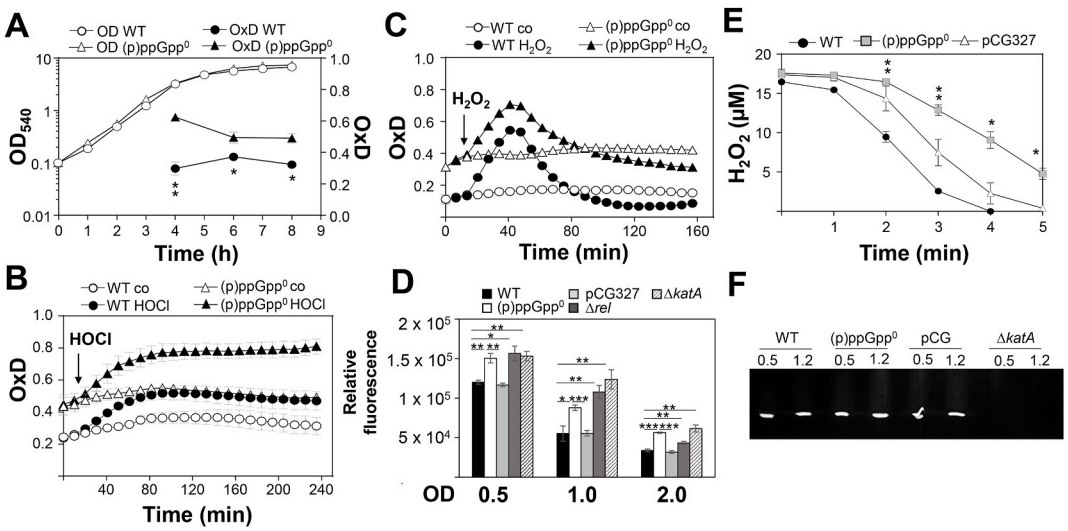

Fig. 5. The (p)ppGpp^0 mutant shows an oxidized basal BSH redox potential (E_{BSH}) (A, B, C), an elevated endogenous ROS level (D) and is delayed in H_2O_2 detoxification (E). (A) The basal level of E_{BSH} was measured in LB medium using the Brx-roGFP2 biosensor along the growth curve in *S. aureus* USA300JE2 WT and the (p)ppGpp^0 mutant. **(B, C)** Oxidation of the Brx-roGFP2 biosensor was monitored in *S. aureus* USA300JE2 and the (p)ppGpp^0 mutant after exposure to 150 μM HOCl **(B)** and 100 mM H_2O_2 **(C)**. The (p)ppGpp^0 mutant showed a slight oxidative shift of the basal E_{BSH}, but is not impaired in the response to H_2O_2 and HOCl stress. The Brx-roGFP2 biosensor responses are shown as OxD values which were calculated based on 405/488 nm excitation ratios with emission at 510 nm and related to the fully oxidized and reduced controls. The E_{BSH} changes were calculated using the Nernst equation and presented in Table S3. **(D)** Intracellular ROS levels were quantified in the *S. aureus* USA300JE2 WT, the (p)ppGpp^0 mutant, the complemented strain (pCG327), the rel_{syn} mutant and the *katA* mutant using the DCFH$_2$-DA dye, which is oxidized to DCF by ROS. DCF fluorescence is measured after excitation at 488 nm and emission at 515 nm. **(E)** The FOX assay was used to determine the H_2O_2 detoxification ability in *S. aureus* WT, the (p)ppGpp^0 mutant and the complemented strain (pCG327) during the stationary phase at OD_{500} of 1.2 in RPMI. H_2O_2 detoxification was slower in the (p)ppGpp^0 mutant compared to the WT. The results are from 3 biological replicates. Error bars represent the standard deviation. *$p < 0.05$; **$p < 0.01$; ***$p < 0.001$. **(F)** The catalase activity was determined in cell extracts of *S. aureus* USA300JE2 WT, the (p)ppGpp^0 mutant, the complemented strain (pCG) and the *katA* mutant during growth in RPMI using native PAGE and diamidobenzidine staining as described [76].

(p)ppGpp^0 mutant (Fig. 5A, Table S3). This higher basal level oxidation of Brx-roGFP2 in the (p)ppGpp^0 mutant was most evident at an OD_{540} of 3 with an increased OxD of 0.63 compared to 0.3 in the WT (Fig. 5A). This oxidative shift of the basal OxD could be verified in the oxidant injection assays before treatment with H_2O_2 and HOCl, supporting an impaired basal redox state of the (p)ppGpp^0 mutant (Fig. 5B and C). However, the biosensor response to 150 μM HOCl and 100 mM H_2O_2 was similar in both WT and (p)ppGpp^0 mutant cells. While both strains were able to regenerate the reduced E_{BSH} within 80 min during recovery from H_2O_2 stress, regeneration of reduced E_{BSH} was not possible after HOCl stress (Fig. 5B and C). Thus, the (p)ppGpp^0 mutant showed a slight oxidative shift in its basal E_{BSH} observed during the transition to stationary phase when grown in LB.

Next, we used the previously established DCFH$_2$-DA assay to determine endogenous ROS levels in the *S. aureus* strains grown in RPMI medium [75]. The results showed an ~1.3-2-fold elevated fluorescence of the oxidized DCF dye in the (p)ppGpp^0 and rel_{syn} mutants during the log and stationary phases as detected by excitation at 488 nm and emission at 515 nm (Fig. 5D). Thus, ROS levels are significantly increased in the (p)ppGpp^0 and rel_{syn} mutants when grown in RPMI medium. Complementation of the (p)ppGpp^0 mutant with the Rel synthetase on plasmid pCG327 resulted in ROS decrease (Fig. 5D). Of note, the ppGpp^0 mutant showed a similar internal ROS level as the *katA* mutant, which is deficient in H_2O_2 detoxification and was used as positive control.

In addition, the FOX assay was used to determine the activities for detoxification of external H_2O_2 in cell extracts. The results revealed fast H_2O_2 detoxification within 4 min in stationary phase WT cells, but a delayed removal of external H_2O_2 in (p)ppGpp^0 mutant cells (Fig. 5E). This points to an increased endogenous ROS level in the (p)ppGpp^0 mutant, exceeding the ROS detoxification capacity of antioxidant enzymes. To exclude that the slower H_2O_2 detoxification ability in the (p)ppGpp^0 mutant is caused by decreased translation of KatA, the *S. aureus* cell extracts were subjected to native PAGE and diaminobenzidine staining assay for visualization of catalase activity [76,77]. However, similar strong KatA activities were observed in WT and (p)ppGpp^0 mutant cells (Fig. 5F), indicating that increased endogenous ROS levels in the (p)ppGpp^0 mutant must overwhelm the antioxidant systems causing the delay in external H_2O_2 detoxification in the FOX assay (Fig. 5E). Together, our results confirm the hypothesis of higher ROS levels in the absence of (p)ppGpp. Increased ROS disturb the cellular redox balance, leading to an increased expression of the antioxidant response in the transcriptome.

3.5. Respiratory chain activity is elevated in the (p)ppGpp^0 mutant

Transcription of TCA cycle enzymes (*citCZ* and *sucCD*) and the terminal oxidases (*cydAB*) was 2-6-fold enhanced in the (p)ppGpp^0 mutant. Thus, we hypothesized that higher respiratory chain activity could contribute to elevated ROS levels in the (p)ppGpp^0 mutant. Oxygen consumption was measured in the WT, (p)ppGpp^0 mutant and pCG327 complemented strain in RPMI and TSB medium with 1 mM glucose as electron donor (Fig. 6A and B). Indeed, the (p)ppGpp^0 mutant showed significantly 1.5-3-fold increased oxygen reduction rates compared to the WT and complemented strain during the log and stationary phases in RPMI and TSB medium (Fig. 6A and B). These results confirmed that respiratory chain activity is elevated in the absence of (p)ppGpp, leading to enhanced ROS production.

3.6. The (p)ppGpp^0 mutant is susceptible to iron excess due to elevated total intracellular iron levels, including the labile iron pool

The transcriptome analysis revealed an oxidative and iron stress response with the highest fold-changes for *dps* and *ftnA* encoding iron storage ferritins in the (p)ppGpp^0 mutant in RPMI during the stationary phase (Fig. 2, Tables S4–S5). This could point to higher iron levels in the (p)ppGpp^0 mutant, which might be responsible for the growth delay in RPMI (Fig. 3C). Growth in RPMI medium was shown to mimic infection

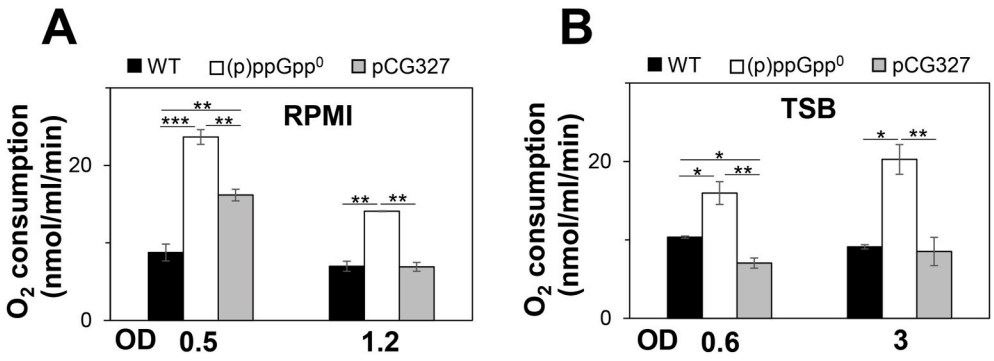

Fig. 6. The (p)ppGpp^0 mutant exhibits an elevated respiratory chain activity, contributing to ROS formation. (A,B) The *S. aureus* USA300JE2 WT, (p)ppGpp^0 mutant and pCG327 complemented strain were grown in RPMI **(A)** and TSB **(B)** and harvested at an OD_{500} of 0.5 and 1.2 in RPMI and at an OD_{600} of 0.6 and 3 in TSB. The oxygen consumption rates were determined with 1 mM glucose as electron donor using the Clark-type electrode in three biological replicates. Error bars represent the standard deviation. $*p < 0.05$; $**p < 0.01$; $***p < 0.001$.

conditions of *S. aureus* in human plasma resulting in higher expression levels of iron-regulated genes [92]. To test the hypothesis of increased endogenous iron levels, we analyzed the growth of the (p)ppGpp^0 and *rel$_{syn}$* mutants under iron excess with 120 μM $FeCl_3$. The (p)ppGpp^0 and *rel$_{syn}$* mutants were both more sensitive in growth under iron excess relative to the WT (Fig. 7A and B), which could point to internal iron overload.

Thus, the total intracellular iron levels of the *S. aureus* WT, (p)ppGpp^0 and *rel$_{syn}$* mutants as well as the Rel_{Syn} complemented strains were determined during the log and stationary phases using ferene-s assay and ICP-MS analysis (Fig. 7C and D). In agreement with our hypothesis, the (p)ppGpp^0 mutant showed significantly increased internal total iron levels during the log and stationary phases. The iron concentrations could be reversed to WT level in the Rel_{syn} complemented strain. In addition, the (p)ppGpp^0 mutant was not impaired in growth under iron starvation with dipyridyl in contrast to the WT, further supporting that the (p)ppGpp^0 mutant suffers from internal iron overload (Fig. 7E).

Previous studies showed that increased ROS levels destroy FeS clusters leading to the release of free iron as labile iron pool [93,94]. To determine whether the increased total iron level in the (p)ppGpp^0 mutant is caused by an elevated labile iron pool, we determined the sensitivity of the strains to the aminoquinone antibiotic streptonigrin using survival assays. The toxic effect of streptonigrin involves DNA damage by complexing the labile iron pool and autoxidation leading to ROS formation [95]. In fact, both (p)ppGpp^0 and *rel$_{syn}$* mutants showed 1.7-3-fold decreased survival after streptonigrin intoxication compared to the WT and pCG327 complemented strain, supporting that higher free iron levels accumulate in the (p)ppGpp^0 mutant in RPMI (Fig. 7F). To verify that the streptonigrin sensitivity depends on the internal iron level, *S. aureus* strains were exposed to dipyridyl prior to streptonigrin treatment. The survival of the (p)ppGpp^0 and *rel$_{syn}$* mutants was strongly improved and restored to WT level after dipyridyl pre-treatment (Fig. 7F). These results indicate that FeS-cluster damage by ROS might contribute to the elevated total and free iron level in the (p)ppGpp^0 mutant. Together, our data suggest that physiological (p)ppGpp levels lead to reduction of cellular free iron levels due to decreased respiratory chain activity in *S. aureus* during the stationary phase to prevent ROS generation and ensure long-term survival.

3.7. Elevated free iron levels contribute to ROS production and an oxidative stress response in the (p)ppGpp^0 mutant during the stationary phase

To investigate whether elevated free iron levels induce ROS

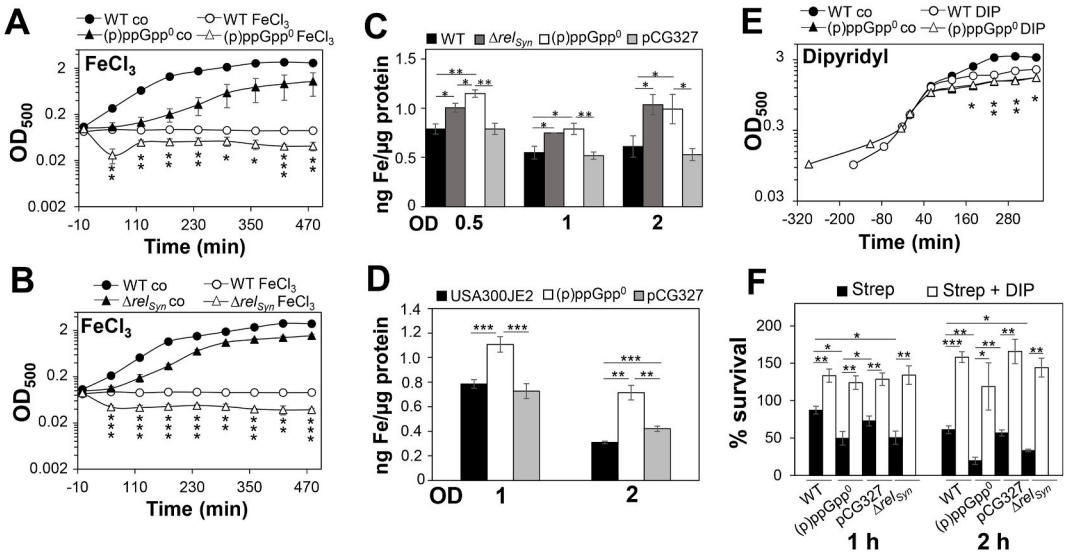

Fig. 7. The (p)ppGpp^0 mutant is sensitive to iron excess due to increased intracellular total and free iron levels. (A, B) The growth curves of the *S. aureus* USA300JE2 WT, (p)ppGpp^0 and *rel$_{syn}$* mutants were monitored in RPMI with and without 120 μM $FeCl_3$. **(C, D)** The total cellular iron levels were determined with ferene-s assay **(C)** and ICP-MS analysis **(D)**. Total intracellular iron levels are significantly increased in the (p)ppGpp^0 and *rel$_{syn}$* mutants as compared to the WT and the complemented strain pCG327 during the log and stationary phases. **(E)** The (p)ppGpp^0 mutant was not impaired in growth after addition of 10 mM dipyridyl (DIP) at an OD_{500} of 0.5 as compared to the WT. **(F)** In addition, survival assays of *S. aureus* strains were performed after 1 and 2 h of treatment with the antibiotic streptonigrin at an OD_{500} of 0.5 in the presence or absence of dipyridyl (DIP). The (p)ppGpp^0 and *rel$_{syn}$* mutants showed increased sensitivity to streptonigrin, indicating an elevated labile iron pool. The addition of DIP restored the survival of all strains. The results are from 3 to 4 biological replicates. Error bars represent the standard deviation. Statistical tests in A, B and E are shown for "WT $FeCl_3$/DIP" vs. "ppGpp^0/Δ*rel$_{syn}$* $FeCl_3$/DIP ": $*p < 0.05$; $**p < 0.01$; $***p < 0.001$.

formation and the oxidative stress response in the (p)ppGpp^0 mutant, transcription of PerR regulon genes was analyzed after dipyridyl addition (Fig. 8A). The Northern blot results showed that dipyridyl decreased transcription of the antioxidant genes *ahpCF* and *katA* during the stationary phase at an OD_{500} of 1.2, but not at an OD_{500} of 2. In addition, transcription of genes encoding iron storage ferritins *dps* and *ftnA* was decreased by dipyridyl in the (p)ppGpp^0 mutant, especially during the later stationary phase (Fig. 8A). However, no difference in transcription was observed for the CtsR-regulated *clpB* gene after dipyridyl addition. These results support that elevated iron levels in the (p)ppGpp^0 mutant partly lead to the induction of the oxidative and iron stress response as a consequence of Fenton-induced ROS formation. To verify that iron-induced ROS levels cause disturbance of the cellular redox potential in the (p)ppGpp^0 mutant, we monitored the E_{BSH} changes using the Brx-roGFP2 biosensor along the growth in the presence of dipyridyl. The addition of dipyridyl resulted in a reductive shift of E_{BSH} in the (p)ppGpp^0 mutant, with no significant difference to the dipyridyl-treated WT (Fig. 8B, Table S3). These data support that iron-induced ROS formation results in an impaired redox balance in the absence of (p)ppGpp.

3.8. (p)ppGpp confers tolerance to HOCl stress during the stationary phase by limiting endogenous ROS formation

We hypothesized that enhanced ROS levels contribute to the impaired redox balance in the (p)ppGpp^0 mutant, which confers the HOCl-sensitive phenotype during the stationary phase. To investigate the role of iron-induced ROS in terms of HOCl susceptibility, growth and survival assays were performed with the ROS scavenger N-acetyl cysteine added prior to HOCl exposure. The (p)ppGpp^0 and rel_{syn} mutants were strongly impaired in growth and survival under HOCl stress without ROS scavengers during stationary phase (Fig. 9A–F). Pretreatment with N-acetyl cysteine strongly improved the growth and survival of stationary phase (p)ppGpp^0 and rel_{syn} mutants under HOCl stress (Fig. 9A–E). The protective effect of dipyridyl in HOCl stress survival was less significant in the mutants (Fig. 9F). While survival of stationary phase (p)ppGpp^0 and rel_{syn} mutants under HOCl was increased by 20% with N-acetyl cysteine, dipyridyl-exposed mutant cells showed only 2–5% elevated viability (Fig. 9E and F). However, while growth of the (p)ppGpp^0 and rel_{syn} mutants could be fully restored with N-acetyl cysteine, the survival could not be fully restored to WT level (Fig. 9A–E). These results indicate that the HOCl susceptibility of the (p)ppGpp^0 and rel_{syn} mutants is caused by ROS formation, which can be limited by ROS scavengers. Apart from the reduction of iron and ROS levels, additional mechanisms account for the increased tolerance of *S. aureus* towards HOCl stress by (p)ppGpp during the stationary phase.

3.9. (p)ppGpp contributes to antibiotics tolerance towards ciprofloxacin and tetracycline during the log and stationary phase by reduction of iron-induced ROS formation

The alarmone (p)ppGpp has been shown to contribute to the tolerance to various antibiotics in *S. aureus*, including vancomycin, ampicillin and other β-lactam antibiotics [47,48,51,52]. Due to the involvement of ROS in the killing mode of different antibiotic classes [59,96], we were interested whether (p)ppGpp confers tolerance to antibiotics by limiting ROS formation during the stationary phase. In survival assays, we could confirm that the *S. aureus* USA300JE2 WT acquires a 2–3 fold increased tolerance to the antibiotics ciprofloxacin and tetracycline during the stationary phase (Fig. 10). Both (p)ppGpp^0 and rel_{syn} mutants are more sensitive in growth to sub-lethal concentrations of 5.19 mM tetracycline and 90.5 μM ciprofloxacin as compared to the WT (Figs. S4 and S5). In addition, both mutants displayed a 5–15% decreased survival after exposure to 90.5 μM ciprofloxacin and 62.38 mM tetracycline during the log and stationary phases relative to its parent (Fig. 10). The growth and survival phenotype of the (p)ppGpp^0 mutant could be restored in the (p)ppGpp complemented strain (Fig. 10, Fig. S4DH and Fig. S5DH). Treatment of the (p)ppGpp^0 and rel_{syn} mutants with N-acetyl cysteine or dipyridyl prior to antibiotics exposure significantly improved the growth and survival and restored their tolerance to the antibiotics to WT levels (Fig. 10, Fig. S4BCFG and Fig. S5BCFG). Of note, the protection of the (p)ppGpp^0 mutant against ciprofloxacin-induced ROS formation was stronger with ROS scavengers, while dipyridyl showed a smaller protective effect (Fig. 10A,B). In addition, the (p)ppGpp^0 mutant was still able to acquire an enhanced tolerance to antibiotics during the stationary phase (Fig. 10), indicating that other stationary phase mechanisms must contribute to antibiotics tolerance. Taken together, our results support that (p)ppGpp contributes to oxidative stress protection and antibiotics tolerance in *S. aureus* during the stationary phase by reducing cellular free iron-levels and aerobic respiration to limit ROS formation and to regenerate redox homeostasis.

4. Discussion

In this study, we have shown that *S. aureus* cells can acquire an improved tolerance towards HOCl and MHQ during the stationary phase, which was dependent on the small alarmone (p)ppGpp. Transcriptome analyses of stationary phase (p)ppGpp^0 mutant cells revealed high expression of genes for iron-storage ferritins and miniferritin (*dps, ftnA*) as well as the induction of the PerR, QsrR, CstR, CtsR and HrcA regulons, indicating an oxidative and iron stress response. Of note, this starvation-induced oxidative stress response was only observed in cell

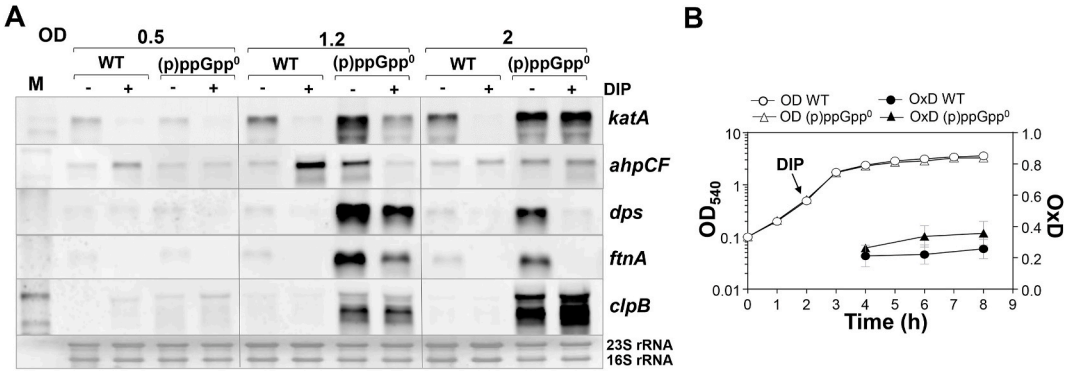

Fig. 8. Increased free cellular iron levels induce an oxidative stress response in the (p)ppGpp^0 mutant. (A) Northern blot analysis was used to analyze transcription of PerR and CtsR regulon genes in *S. aureus* USA300JE2 WT and the (p)ppGpp^0 mutant in RPMI medium with and without 10 mM dipyridyl (DIP), which was added at an OD_{500} of 0.5. Dipyridyl partially decreased transcription of genes for iron storage (*dps* and *ftnA*) and H_2O_2 detoxification (*katA*, *ahpCF*) in the (p)ppGpp^0 mutant. The methylene blue stain is the RNA loading control indicating the bands of the 16S and 23S rRNAs. **(B)** The basal level of E_{BSH} was determined using Brx-roGFP2 biosensor along the growth curve in *S. aureus* USA300JE2 WT and the (p)ppGpp^0 mutant after addition of dipyridyl.

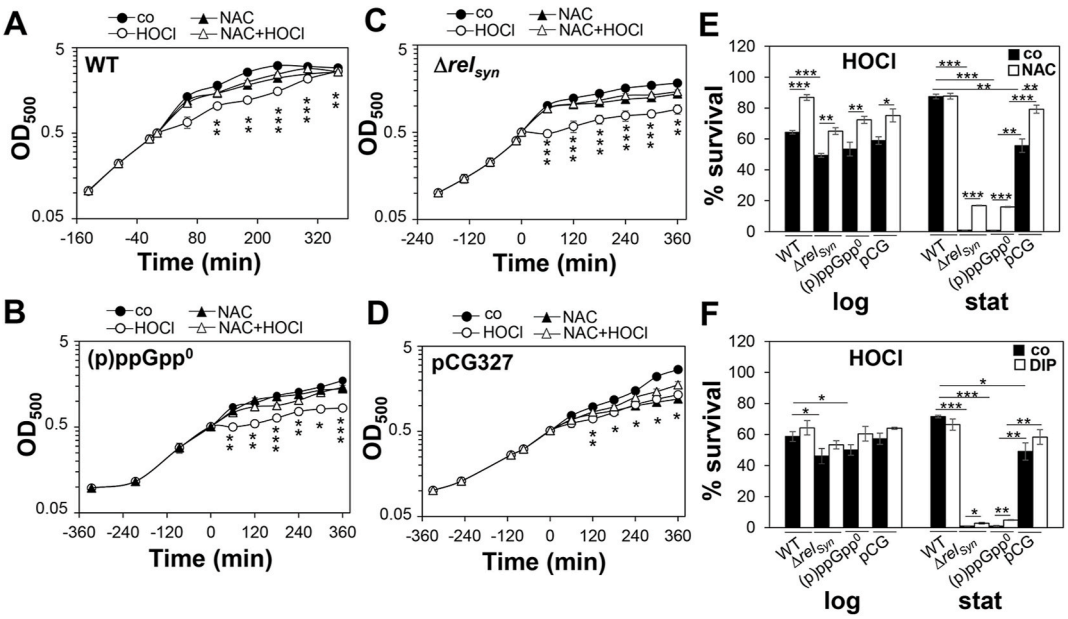

Fig. 9. ROS and iron scavengers protect the (p)ppGpp^0 mutant against oxidative stress. (A–D) For the growth curves, *S. aureus* USA300JE2 WT, (p)ppGpp^0 and Δ*rel*$_{syn}$ mutants as well as the complemented strain (pCG327) were grown in RPMI until an OD_{500} of 0.5 and treated with sub-lethal concentrations of 1.25 mM N-acetyl cysteine (NAC) and 1.5 mM HOCl. **(E, F)** Survival assays were performed by treatment of the *S. aureus* strains with 3.5 mM HOCl and 1.25 mM N-acetyl cysteine (NAC) **(E)** or 10 mM dipyridyl (DIP) **(F)** at OD_{500} of 0.5 and 2. The CFUs were determined after 1 h stress exposure and survival rates calculated relative to the control, which was set to 100%. The addition of N-acetyl cysteine and dipyridyl significantly improved the resistance against HOCl of the (p)ppGpp^0 and *rel*$_{syn}$ mutants. The HOCl sensitivity of the stationary phase (p)ppGpp^0 mutant could be restored partially to wild-type levels in the pCG327 complemented strain. The results are from three biological replicates. Error bars represent the standard deviation. Statistical test for the growth curves in A–D: "HOCl" vs "NAC + HOCl": *p < 0.05; **p < 0.01; ***p < 0.001.

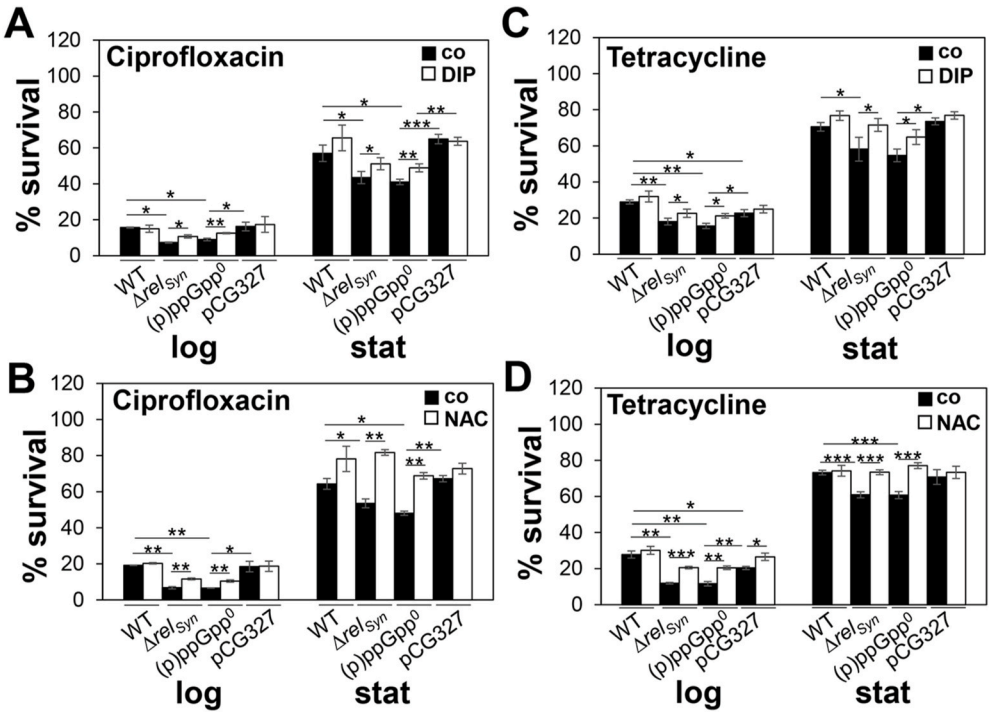

Fig. 10. ROS and iron scavengers enhance survival of the (p)ppGpp^0 and Δ*rel*$_{syn}$ mutants under ciprofloxacin and tetracycline stress. (A–D) For survival assays, *S. aureus* USA300JE2 WT, (p)ppGpp^0 and Δ*rel*$_{syn}$ mutants as well as the complemented strain (pCG327) were grown in RPMI until an OD_{500} of 0.5 and 2 for log and stationary phase. Cells were treated with 90.5 μM ciprofloxacin **(A,B)** or 62.38 mM tetracycline **(C,D)** in the presence or absence of 10 mM dipyridyl (DIP) **(A,C)** or 1.25 mM N-acetyl cysteine (NAC) **(B,D)**, respectively. The CFUs were determined after 2 h stress exposure and survival rates calculated relative to the untreated control, which was set to 100%. The addition of N-acetyl cysteine and dipyridyl significantly improved the survival of the (p)ppGpp^0 and Δ*rel*$_{syn}$ mutants under antibiotics stress. The results are from 3 to 4 biological replicates. Error bars represent the standard deviation. *p < 0.05; **p < 0.01; ***p < 0.001.

culture RPMI medium, resulting in a growth delay of the (p)ppGpp^0 mutant. We anticipate that the oxidative stress phenotype of the (p)ppGpp^0 mutant in RPMI is related to its lower amounts of ROS scavenging components, retaining higher levels of oxidizing equivalents of HOCl and H_2O_2 [97]. In contrast, nutrient-rich LB and TSB contain high amounts of ROS-quenching amino acids, peptides and the antioxidant tripeptide glutathione (GSH), which scavenge ROS and thereby decrease oxidant toxicity [97]. Since RPMI resembles infection conditions in human plasma [92], this could be relevant for long-term and chronic *S. aureus* infections and highlights the crucial role of (p)ppGpp for survival of starved bacteria [52,98].

Based on the transcriptome signature, we hypothesized that ROS

levels are increased in the absence of (p)ppGpp during the stationary phase. Indeed, the (p)ppGpp^0 mutant revealed a slightly impaired redox state, higher endogenous ROS levels and apparently overloaded antioxidant enzymes, which were delayed in H_2O_2 detoxification. ROS increase in the (p)ppGpp^0 mutant could be attributed to elevated intracellular iron levels and higher respiratory chain activities, resulting in an oxidative and iron stress response. In support of iron-induced ROS formation, the PerR-dependent oxidative stress response was partly abolished by the iron chelator dipyridyl. Moreover, the impaired redox balance and iron excess are responsible for the susceptibility of the (p)ppGpp^0 mutant towards HOCl stress, since ROS and iron scavengers improved the growth and survival of the mutant.

Elevated iron levels in the (p)ppGpp^0 mutant resulted in induction of iron storage ferritins and strong Fur-dependent repression of uptake systems for iron, heme and siderophores to prevent further iron intoxication. Increased ROS and iron levels were previously shown to induce the PerR regulon in *S. aureus*, supporting the connection between iron excess and oxidative stress [23,99]. However, it seems counterintuitive, that despite the growth-limiting effects of increased iron levels, FeS cluster synthesis is still increased in the (p)ppGpp^0 mutant. The enhanced need for FeS cluster synthesis might be explained by ROS poisoning of exposed FeS clusters of dehydratases, such as the TCA cycle enzymes aconitase and fumarase or the isopropylmalate dehydratase LeuCD [100,101]. This is supported by an elevated transcription of TCA cycle genes in the absence of (p)ppGpp. The release of free iron from oxidized FeS-clusters [93,94] could be responsible for elevated endogenous iron levels, potentiating ROS formation in the (p)ppGpp^0 mutant. In agreement with this hypothesis, the (p)ppGpp^0 mutant showed an increased pool of labile iron as indicated by its sensitivity to the antibiotic streptonigrin. Thus, respiratory ROS increase might be the first event leading to an increased internal iron level that further potentiates ROS formation through the Fenton chemistry.

Strikingly, we previously showed that overproduction of (p)ppGpp during the log phase also results in the activation of genes involved in oxidative stress and iron-storage (*ftnA, dps*) independently of the global regulators PerR, Fur, SarA or CodY [60]. We hypothesize that the iron and oxidative stress response induced by (p)ppGpp during the log phase protects *S. aureus* from anticipated future stress and to inhibit toxic iron accumulation, whereas the (p)ppGpp^0 mutant responds to ROS increase due to elevated respiration via the classical PerR-dependent oxidative stress response. These findings suggest that physiological (p)ppGpp levels are intimately linked to redox and iron homeostasis of the cells.

Similar connections between iron, aerobic respiratory chain activity, ROS and the stringent response have been demonstrated in other bacteria. In *E. coli,* (p)ppGpp accumulated in response to iron starvation, leading to induction of Fur-controlled iron uptake systems [102]. In this case, SpoT has been proposed to act as direct sensor for Fe^{2+} or Fe^{3+} inside the cell [102]. Similar to *S. aureus,* (p)ppGpp has been proposed to decrease iron and ROS levels in *V. cholerae*, which promotes tolerance to the antibiotic tetracycline [54]. Increased free iron levels were measured in the (p)ppGpp^0 mutant in *V. cholerae*, which resulted in 10-fold elevated expression of the Fe(III) ABC transporter substrate-binding protein FbpA [54]. In contrast, (p)ppGpp accumulation led to repression of FbpA and reduced iron levels to prevent Fenton chemistry and ROS generation. Furthermore, expression of several TCA cycle enzymes, such as *acnB, icd, sucCD, sdhABC* and *mdh* was increased in the absence of (p)ppGpp suggesting enhanced TCA cycle activity and central carbon catabolism as another source of ROS in *V. cholerae* [54]. Similarly, transcription of *acnA (citB), citC, citZ, sucCD, sdhABCD* and *cydAB* was 2-4-fold enhanced in the *S. aureus* (p)ppGpp^0 mutant, supporting higher TCA cycle and respiratory chain activity, leading to increased ROS levels. Thus, in *S. aureus* the induction of the SR represses respiratory chain activity and endogenous iron levels to lower ROS levels, contributing to the tolerance towards oxidative stress and antibiotics (Fig. 11).

In *Pseudomonas aeruginosa*, decreased activities of the antioxidant enzymes catalase and superoxide dismutase have been determined in

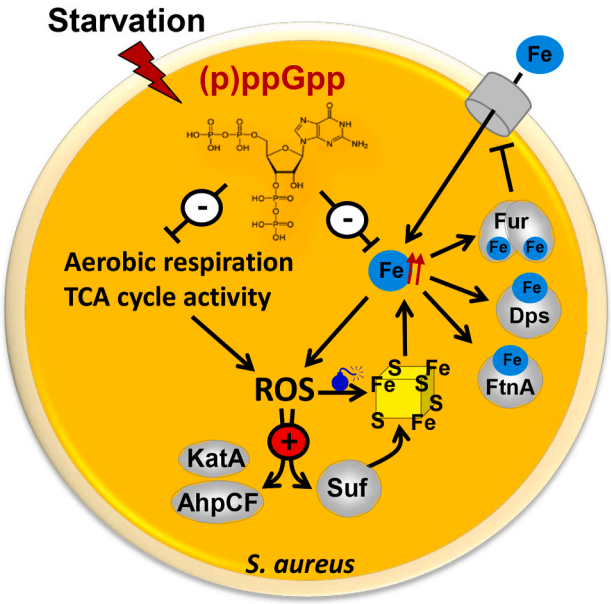

Fig. 11. Schematics of (p)ppGpp regulated tolerance to oxidants and antibiotics in *S. aureus*. (p)ppGpp down-regulates internal iron levels and respiratory chain activity leading to decreased ROS levels. In the (p)ppGpp^0 mutant, increased iron levels cause induction of iron storage proteins (Dps, FtnA) and Fur-mediated repression of iron-uptake systems. Increased ROS levels in the (p)ppGpp^0 mutant cause derepression of the PerR-controlled antioxidant systems (KatA, AhpCF) for ROS detoxification and the Suf machinery for FeS-cluster biosynthesis, since ROS destroy FeS clusters potentiating the release of free iron and in turn ROS levels. These ROS and iron-mediated responses are repressed by (p)ppGpp leading to a reductive shift in E_{BSH}, which promotes tolerance to HOCl and ROS produced by the antibiotics tetracycline and ciprofloxacin in *S. aureus*.

the (p)ppGpp^0 mutant, leading to decreased detoxification of superoxide anion and H_2O_2 [55,56]. Increased ROS levels in SR mutants have been associated with enhanced susceptibility to H_2O_2 stress and antibiotics during the stationary phase [55,56]. Similarly, the *S. aureus* (p)ppGpp^0 mutant was more susceptible to H_2O_2 [60] and HOCl stress during the stationary phase. While the *S. aureus* (p)ppGpp^0 mutant showed decreased H_2O_2 detoxification ability, the catalase activity was not affected. Instead, the antioxidant systems seem to be busy with removal of internal ROS in the (p)ppGpp^0 mutant, resulting in delayed detoxification of external H_2O_2. The (p)ppGpp^0 mutant further showed a slight oxidized shift in the E_{BSH}, explaining its susceptibility to survive HOCl stress exposure during the stationary phase.

Another study showed a protective effect of (p)ppGpp under nitrosative (NO) stress in the intestinal pathogen *Salmonella* Typhimurium [103]. Specifically, (p)ppGpp was shown to activate transcription of biosynthesis genes for branched chain amino acids to restore translation of flavohemoglobin Hmp, which is involved in NO detoxification [103]. Altogether, (p)ppGpp contributes in bacteria to ROS and RNS tolerance via different mechanisms, affecting iron and redox homeostasis, ROS levels, activities of antioxidant enzymes, central carbon catabolism and amino acid biosynthesis to facilitate translation of antioxidant and anti-nitrosative defense mechanisms.

In addition, we found that the *S. aureus* (p)ppGpp^0 mutant is more susceptible to ROS generated by the antibiotics tetracycline and ciprofloxacin. The involvement of ROS in the bactericidal mode of action of various antibiotic classes is well established [59,61,96,104]. Our results revealed that ROS and iron scavengers increased the tolerance of the (p)ppGpp^0 mutant towards tetracycline and ciprofloxacin, supporting that ROS and iron contributed to the antibiotics susceptibility. Thus, (p)ppGpp promotes tolerance to ROS-producing antibiotics by regulation of iron and redox homeostasis in *S. aureus*.

Altogether, we propose a model that (p)ppGpp down-regulates respiratory chain activity and free iron levels in *S. aureus*, leading to decreased internal ROS levels, which renders the cells tolerant to oxidative stress and antibiotics during the stationary phase (Fig. 11). Future studies will be directed to elucidate the molecular mechanisms of how (p)ppGpp modulates iron and redox homeostasis in *S. aureus*.

Declaration of competing interest

No competing financial interests exist.

Acknowledgements

We thank Franziska Kiele for excellent technical assistance and Florian Melerowicz for help with growth and survival assays of the (p)ppGpp^0 mutant. We gratefully acknowledge the work of Jan Bamberger from the Core Facility 'Mass spectrometry and Elemental analysis' of Philipps-Universität Marburg. We are further grateful to Dennis Nürnberg and Prof. Holger Dau (Freie Universität Berlin, Department of Physics) for providing the Clark electrode for measurements of oxygen consumption rates. This work was supported by an ERC Consolidator grant (GA 615585) MYCOTHIOLOME and grants from the Deutsche Forschungsgemeinschaft (AN746/4-1 and AN746/4-2) within the SPP1710, by the SFB973 project C08 and by the SFB/TR84 project B06 to H.A. We further acknowledge funding from the Deutsche Forschungsgemeinschaft by grants LI 415/4-2 within the SPP1710 and LI 415/7-2 within SPP1927 to R.L. as well as by the SPP1879 to C.W.

Appendix A. Supplementary data

Supplementary data to this article can be found online at https://doi.org/10.1016/j.freeradbiomed.2020.10.322.

List of abbreviations

BSH	bacillithiol
DTT	dithiothreitol
H_2O_2	hydrogen peroxide
HOCl	hypochlorous acid
LB	Luria Bertani
MHQ	methylhydroquinone
MRSA	methicillin-resistant *Staphylococcus aureus*
(p)ppGpp	guanosine tetra- and pentaphosphate
OD_{500}	optical density at 500 nm
RCS	reactive chlorine species
RES	reactive electrophilic species
ROS	reactive oxygen species
SR	stringent response

References

[1] G.L. Archer, *Staphylococcus aureus*: a well-armed pathogen, Clin. Infect. Dis. 26 (5) (1998) 1179–1181.
[2] H.W. Boucher, G.R. Corey, Epidemiology of methicillin-resistant *Staphylococcus aureus*, Clin. Infect. Dis. 46 (Suppl 5) (2008) S344–S349.
[3] F.D. Lowy, *Staphylococcus aureus* infections, N. Engl. J. Med. 339 (8) (1998) 520–532.
[4] T.J. Foster, The *Staphylococcus aureus* "superbug, J. Clin. Invest. 114 (12) (2004) 1693–1696.
[5] H.F. Wertheim, D.C. Melles, M.C. Vos, W. van Leeuwen, A. van Belkum, H. A. Verbrugh, J.L. Nouwen, The role of nasal carriage in *Staphylococcus aureus* infections, Lancet Infect. Dis. 5 (12) (2005) 751–762.
[6] H.F. Chambers, F.R. Deleo, Waves of resistance: *Staphylococcus aureus* in the antibiotic era, Nat. Rev. Microbiol. 7 (9) (2009) 629–641.
[7] M. Vestergaard, D. Frees, H. Ingmer, Antibiotic resistance and the MRSA problem, Microbiol. Spectr. 7 (2) (2019), https://doi.org/10.1128/microbiolspec.GPP3-0057-2018.
[8] C.C. Winterbourn, A.J. Kettle, Redox reactions and microbial killing in the neutrophil phagosome, Antioxidants Redox Signal. 18 (6) (2013) 642–660.
[9] C.C. Winterbourn, A.J. Kettle, M.B. Hampton, Reactive oxygen species and neutrophil function, Annu. Rev. Biochem. 85 (2016) 765–792.
[10] W.N. Beavers, E.P. Skaar, Neutrophil-generated oxidative stress and protein damage in *Staphylococcus aureus*, Pathogens and disease 74 (6) (2016) ftw060.
[11] A. Ulfig, L.I. Leichert, The effects of neutrophil-generated hypochlorous acid and other hypohalous acids on host and pathogens, Cell. Mol. Life Sci. (2020), https://doi.org/10.1007/s00018-020-03591-y.
[12] C.M. Grunenwald, M.R. Bennett, E.P. Skaar, Nonconventional therapeutics against *Staphylococcus aureus*, Microbiol. Spectr. 6 (6) (2018), https://doi.org/10.1128/microbiolspec.GPP3-0047-2018.
[13] K. Tam, V.J. Torres, *Staphylococcus aureus* secreted toxins and extracellular enzymes, Microbiol. Spectr. 7 (2) (2019), https://doi.org/10.1128/microbiolspec.GPP3-0039-2018.
[14] R. Gaupp, N. Ledala, G.A. Somerville, Staphylococcal response to oxidative stress, Front Cell Infect Microbiol 2 (2012) 33.
[15] V.V. Loi, M. Rossius, H. Antelmann, Redox regulation by reversible protein *S*-thiolation in bacteria, Front. Microbiol. 6 (2015) 187.
[16] M. Hillion, H. Antelmann, Thiol-based redox switches in prokaryotes, Biol. Chem. 396 (5) (2015) 415–444.
[17] N. Linzner, V.V. Loi, V.N. Fritsch, Q.N. Tung, S. Stenzel, M. Wirtz, R. Hell, C. J. Hamilton, K. Tedin, M. Fulde, H. Antelmann, *Staphylococcus aureus* uses the bacilliredoxin (BrxAB)/bacillithiol disulfide reductase (YpdA) redox pathway to defend against oxidative stress under infections, Front. Microbiol. 10 (2019) 1355.
[18] P. Chandrangsu, V.V. Loi, H. Antelmann, J.D. Helmann, The role of bacillithiol in Gram-positive firmicutes, Antioxidants Redox Signal. 28 (6) (2018) 445–462.
[19] I.V. Mikheyeva, J.M. Thomas, S.L. Kolar, A.R. Corvaglia, N. Gaiotaa, S. Leo, P. Francois, G.Y. Liu, M. Rawat, A.L. Cheung, YpdA, a putative bacillithiol disulfide reductase, contributes to cellular redox homeostasis and virulence in *Staphylococcus aureus*, Mol. Microbiol. 111 (4) (2019) 1039–1056.
[20] M. Imber, V.V. Loi, S. Reznikov, V.N. Fritsch, A.J. Pietrzyk-Brzezinska, J. Prehn, C. Hamilton, M.C. Wahl, A.K. Bronowska, H. Antelmann, The aldehyde dehydrogenase AldA contributes to the hypochlorite defense and is redox-controlled by protein *S*-bacillithiolation in *Staphylococcus aureus*, Redox Biol 15 (2018) 557–568.
[21] V.N. Fritsch, V.V. Loi, T. Busche, A. Sommer, K. Tedin, D.J. Nürnberg, J. Kalinowski, J. Bernhardt, M. Fulde, H. Antelmann, The MarR-type repressor MhqR confers quinone and antimicrobial resistance in *Staphylococcus aureus*, Antioxidants Redox Signal. 31 (16) (2019) 1235–1252.
[22] Q. Ji, L. Zhang, M.B. Jones, F. Sun, X. Deng, H. Liang, H. Cho, P. Brugarolas, Y. N. Gao, S.N. Peterson, L. Lan, T. Bae, C. He, Molecular mechanism of quinone signaling mediated through *S*-quinonization of a YodB family repressor QsrR, Proc. Natl. Acad. Sci. U. S. A. 110 (13) (2013) 5010–5015.
[23] M.J. Horsburgh, M.O. Clements, H. Crossley, E. Ingham, S.J. Foster, PerR controls oxidative stress resistance and iron storage proteins and is required for virulence in *Staphylococcus aureus*, Infect. Immun. 69 (6) (2001) 3744–3754.
[24] J. Jaishankar, P. Srivastava, Molecular basis of stationary phase survival and applications, Front. Microbiol. 8 (2017) 2000.
[25] A. Ishihama, Adaptation of gene expression in stationary phase bacteria, Curr. Opin. Genet. Dev. 7 (5) (1997) 582–588.
[26] M. Hecker, J. Pane-Farre, U. Völker, SigB-dependent general stress response in *Bacillus subtilis* and related gram-positive bacteria, Annu. Rev. Microbiol. 61 (2007) 215–236.
[27] J. Pane-Farre, B. Jonas, K. Förstner, S. Engelmann, M. Hecker, The sigmaB regulon in *Staphylococcus aureus* and its regulation, Int J Med Microbiol 296 (4–5) (2006) 237–258.
[28] Z.D. Dalebroux, M.S. Swanson, ppGpp: magic beyond RNA polymerase, Nat. Rev. Microbiol. 10 (3) (2012) 203–212.
[29] M. Cashel, The control of ribonucleic acid synthesis in *Escherichia coli*. IV. Relevance of unusual phosphorylated compounds from amino acid-starved stringent strains, J. Biol. Chem. 244 (12) (1969) 3133–3141.
[30] A.O. Gaca, C. Colomer-Winter, J.A. Lemos, Many means to a common end: the intricacies of (p)ppGpp metabolism and its control of bacterial homeostasis, J. Bacteriol. 197 (7) (2015) 1146–1156.
[31] K. Potrykus, M. Cashel, (p)ppGpp: still magical? Annu. Rev. Microbiol. 62 (2008) 35–51.
[32] G.C. Atkinson, T. Tenson, V. Hauryliuk, The RelA/SpoT homolog (RSH) superfamily: distribution and functional evolution of ppGpp synthetases and hydrolases across the tree of life, PloS One 6 (8) (2011), e23479.
[33] T. Geiger, B. Kastle, F.L. Gratani, C. Goerke, C. Wolz, Two small (p)ppGpp synthases in *Staphylococcus aureus* mediate tolerance against cell envelope stress conditions, J. Bacteriol. 196 (4) (2014) 894–902.
[34] H. Nanamiya, K. Kasai, A. Nozawa, C.S. Yun, T. Narisawa, K. Murakami, Y. Natori, F. Kawamura, Y. Tozawa, Identification and functional analysis of novel (p)ppGpp synthetase genes in *Bacillus subtilis*, Mol. Microbiol. 67 (2) (2008) 291–304.
[35] C. Wolz, T. Geiger, C. Goerke, The synthesis and function of the alarmone (p)ppGpp in firmicutes, Int J Med Microbiol 300 (2–3) (2010) 142–147.
[36] A.M. Rojas, M. Ehrenberg, S.G. Andersson, C.G. Kurland, ppGpp inhibition of elongation factors Tu, G and Ts during polypeptide synthesis, Mol. Gen. Genet. 197 (1) (1984) 36–45.
[37] K. Kihira, Y. Shimizu, Y. Shomura, N. Shibata, M. Kitamura, A. Nakagawa, T. Ueda, K. Ochi, Y. Higuchi, Crystal structure analysis of the translation factor RF3 (release factor 3), FEBS Lett. 586 (20) (2012) 3705–3709.
[38] V.A. Mitkevich, A. Ermakov, A.A. Kulikova, S. Tankov, V. Shyp, A. Soosaar, T. Tenson, A.A. Makarov, M. Ehrenberg, V. Hauryliuk, Thermodynamic

characterization of ppGpp binding to EF-G or IF2 and of initiator tRNA binding to free IF2 in the presence of GDP, GTP, or ppGpp, J. Mol. Biol. 402 (5) (2010) 838–846.
[39] S. Diez, J. Ryu, K. Caban, R.L. Gonzalez Jr., J. Dworkin, The alarmones (p)ppGpp directly regulate translation initiation during entry into quiescence, Proc. Natl. Acad. Sci. U. S. A. 117 (27) (2020) 15565–15572.
[40] T. Geiger, C. Wolz, Intersection of the stringent response and the CodY regulon in low GC Gram-positive bacteria, Int J Med Microbiol 304 (2) (2014) 150–155.
[41] A. Kriel, A.N. Bittner, S.H. Kim, K. Liu, A.K. Tehranchi, W.Y. Zou, S. Rendon, R. Chen, B.P. Tu, J.D. Wang, Direct regulation of GTP homeostasis by (p)ppGpp: a critical component of viability and stress resistance, Mol. Cell. 48 (2) (2012) 231–241.
[42] R.L. Gourse, A.Y. Chen, S. Gopalkrishnan, P. Sanchez-Vazquez, A. Myers, W. Ross, Transcriptional responses to ppGpp and DksA, Annu. Rev. Microbiol. 72 (2018) 163–184.
[43] S. Tojo, K. Kumamoto, K. Hirooka, Y. Fujita, Heavy involvement of stringent transcription control depending on the adenine or guanine species of the transcription initiation site in glucose and pyruvate metabolism in *Bacillus subtilis*, J. Bacteriol. 192 (6) (2010) 1573–1585.
[44] W. Gao, K. Chua, J.K. Davies, H.J. Newton, T. Seemann, P.F. Harrison, N. E. Holmes, H.W. Rhee, J.I. Hong, E.L. Hartland, T.P. Stinear, B.P. Howden, Two novel point mutations in clinical *Staphylococcus aureus* reduce linezolid susceptibility and switch on the stringent response to promote persistent infection, PLoS Pathog. 6 (6) (2010), e1000944.
[45] T.P. Primm, S.J. Andersen, V. Mizrahi, D. Avarbock, H. Rubin, C.E. Barry 3rd, The stringent response of *Mycobacterium tuberculosis* is required for long-term survival, J. Bacteriol. 182 (17) (2000) 4889–4898.
[46] V. Hauryliuk, G.C. Atkinson, K.S. Murakami, T. Tenson, K. Gerdes, Recent functional insights into the role of (p)ppGpp in bacterial physiology, Nat. Rev. Microbiol. 13 (5) (2015) 298–309.
[47] S. Aedo, A. Tomasz, Role of the stringent stress response in the antibiotic resistance phenotype of methicillin-resistant *Staphylococcus aureus*, Antimicrob. Agents Chemother. 60 (4) (2016) 2311–2317.
[48] C. Kim, M. Mwangi, M. Chung, C. Milheirico, H. de Lencastre, A. Tomasz, The mechanism of heterogeneous beta-lactam resistance in MRSA: key role of the stringent stress response, PloS One 8 (12) (2013), e82814.
[49] J. Abranches, A.R. Martinez, J.K. Kajfasz, V. Chavez, D.A. Garsin, J.A. Lemos, The molecular alarmone (p)ppGpp mediates stress responses, vancomycin tolerance, and virulence in *Enterococcus faecalis*, J. Bacteriol. 191 (7) (2009) 2248–2256.
[50] J. Wu, Q. Long, J. Xie, (p)ppGpp and drug resistance, J. Cell. Physiol. 224 (2) (2010) 300–304.
[51] T. Geiger, P. Francois, M. Liebeke, M. Fraunholz, C. Goerke, B. Krismer, J. Schrenzel, M. Lalk, C. Wolz, The stringent response of *Staphylococcus aureus* and its impact on survival after phagocytosis through the induction of intracellular PSMs expression, PLoS Pathog. 8 (11) (2012), e1003016.
[52] T. Geiger, C. Goerke, M. Fritz, T. Schafer, K. Ohlsen, M. Liebeke, M. Lalk, C. Wolz, Role of the (p)ppGpp synthase RSH, a RelA/SpoT homolog, in stringent response and virulence of *Staphylococcus aureus*, Infect. Immun. 78 (5) (2010) 1873–1883.
[53] D. Bryson, A.G. Hettle, A.B. Boraston, J.K. Hobbs, Clinical mutations that partially activate the stringent response confer multidrug tolerance in *Staphylococcus aureus*, Antimicrob. Agents Chemother. 64 (3) (2020).
[54] H.Y. Kim, J. Go, K.M. Lee, Y.T. Oh, S.S. Yoon, Guanosine tetra- and pentaphosphate increase antibiotic tolerance by reducing reactive oxygen species production in *Vibrio cholerae*, J. Biol. Chem. 293 (15) (2018) 5679–5694.
[55] M. Khakimova, H.G. Ahlgren, J.J. Harrison, A.M. English, D. Nguyen, The stringent response controls catalases in *Pseudomonas aeruginosa* and is required for hydrogen peroxide and antibiotic tolerance, J. Bacteriol. 195 (9) (2013) 2011–2020.
[56] D. Martins, G. McKay, G. Sampathkumar, M. Khakimova, A.M. English, D. Nguyen, Superoxide dismutase activity confers (p)ppGpp-mediated antibiotic tolerance to stationary-phase *Pseudomonas aeruginosa*, Proc. Natl. Acad. Sci. U. S. A. 115 (39) (2018) 9797–9802.
[57] D.J. Dwyer, P.A. Belenky, J.H. Yang, I.C. MacDonald, J.D. Martell, N. Takahashi, C.T. Chan, M.A. Lobritz, D. Braff, E.G. Schwarz, J.D. Ye, M. Pati, M. Vercruysse, P. S. Ralifo, K.R. Allison, A.S. Khalil, A.Y. Ting, G.C. Walker, J.J. Collins, Antibiotics induce redox-related physiological alterations as part of their lethality, Proc. Natl. Acad. Sci. U. S. A. 111 (20) (2014) E2100–E2109.
[58] M.A. Kohanski, D.J. Dwyer, J.J. Collins, How antibiotics kill bacteria: from targets to networks, Nat. Rev. Microbiol. 8 (6) (2010) 423–435.
[59] M.A. Kohanski, D.J. Dwyer, B. Hayete, C.A. Lawrence, J.J. Collins, A common mechanism of cellular death induced by bactericidal antibiotics, Cell 130 (5) (2007) 797–810.
[60] P. Horvatek, A.M.F. Hanna, F.L. Gratani, D. Keinhörster, N. Korn, M. Borisova, C. Mayer, D. Rejman, U. Mäder, C. Wolz, Inducible expression of (p)ppGpp synthetases in *Staphylococcus aureus* is associated with activation of stress response genes, bioRxiv (2020), https://doi.org/10.1101/2020.04.25.059725, 2020.04.25.059725.
[61] F.L. Gratani, P. Horvatek, T. Geiger, M. Borisova, C. Mayer, I. Grin, S. Wagner, W. Steinchen, G. Bange, A. Velic, B. Macek, C. Wolz, Regulation of the opposing (p)ppGpp synthetase and hydrolase activities in a bifunctional RelA/SpoT homologue from *Staphylococcus aureus*, PLoS Genet. 14 (7) (2018), e1007514.
[62] V.V. Loi, M. Harms, M. Müller, N.T.T. Huyen, C.J. Hamilton, F. Hochgräfe, J. Pane-Farre, H. Antelmann, Real-time imaging of the bacillithiol redox potential in the human pathogen *Staphylococcus aureus* using a genetically encoded bacilliredoxin-fused redox biosensor, Antioxidants Redox Signal. 26 (15) (2017) 835–848.
[63] N. Linzner, V.N. Fritsch, T. Busche, Q.N. Tung, V.V. Loi, J. Bernhardt, J. Kalinowski, H. Antelmann, The plant-derived naphthoquinone lapachol causes an oxidative stress response in *Staphylococcus aureus*, Free Radic. Biol. Med. 158 (2020) 126–136.
[64] V. Van Loi, H. Antelmann, Method for measurement of bacillithiol redox potential changes using the Brx-roGFP2 redox biosensor in *Staphylococcus aureus*, Methods (Orlando) 7 (2020) 100900.
[65] C. Estrela, C.R.A. Estrela, E.L. Barbin, J.C.E. Spanó, M.A. Marchesan, J.D. Pécora, Mechanism of action of sodium hypochlorite, Braz. Dent. J. 13 (2) (2002) 113–117.
[66] J. Winter, M. Ilbert, P.C. Graf, D. Ozcelik, U. Jakob, Bleach activates a redox-regulated chaperone by oxidative protein unfolding, Cell 135 (4) (2008) 691–701.
[67] M. Wetzstein, U. Völker, J. Dedio, S. Lobau, U. Zuber, M. Schiesswohl, C. Herget, M. Hecker, W. Schumann, Cloning, sequencing, and molecular analysis of the dnaK locus from *Bacillus subtilis*, J. Bacteriol. 174 (10) (1992) 3300–3310.
[68] T. Tam le, C. Eymann, D. Albrecht, R. Sietmann, F. Schauer, M. Hecker, H. Antelmann, Differential gene expression in response to phenol and catechol reveals different metabolic activities for the degradation of aromatic compounds in *Bacillus subtilis*, Environ. Microbiol. 8 (8) (2006) 1408–1427.
[69] T. Busche, M. Hillion, V. Van Loi, D. Berg, B. Walther, T. Semmler, B. Strommenger, W. Witte, C. Cuny, A. Mellmann, M.A. Holmes, J. Kalinowski, L. Adrian, J. Bernhardt, H. Antelmann, Comparative secretome analyses of human and zoonotic *Staphylococcus aureus* isolates CC8, CC22, and CC398, Mol. Cell. Proteomics 17 (12) (2018) 2412–2433.
[70] M.I. Love, W. Huber, S. Anders, Moderated estimation of fold change and dispersion for RNA-seq data with DESeq2, Genome Biol. 15 (12) (2014) 550.
[71] R. Hilker, K.B. Stadermann, O. Schwengers, E. Anisiforov, S. Jaenicke, B. Weisshaar, T. Zimmermann, A. Goesmann, ReadXplorer 2-detailed read mapping analysis and visualization from one single source, Bioinformatics 32 (24) (2016) 3702–3708.
[72] C.T. Dooley, T.M. Dore, G.T. Hanson, W.C. Jackson, S.J. Remington, R.Y. Tsien, Imaging dynamic redox changes in mammalian cells with green fluorescent protein indicators, J. Biol. Chem. 279 (21) (2004) 22284–22293.
[73] J. Nourooz-Zadeh, J. Tajaddini-Sarmadi, S.P. Wolff, Measurement of plasma hydroperoxide concentrations by the ferrous oxidation-xylenol orange assay in conjunction with triphenylphosphine, Anal. Biochem. 220 (2) (1994) 403–409.
[74] M.J. Reiniers, R.F. van Golen, S. Bonnet, M. Broekgaarden, T.M. van Gulik, M. R. Egmond, M. Heger, Preparation and practical applications of 2',7'-dichlorodihydrofluorescein in redox assays, Anal. Chem. 89 (7) (2017) 3853–3857.
[75] S.E. George, J. Hrubesch, I. Breuing, N. Vetter, N. Korn, K. Hennemann, L. Bleul, M. Willmann, P. Ebner, F. Gotz, C. Wolz, Oxidative stress drives the selection of quorum sensing mutants in the *Staphylococcus aureus* population, Proc. Natl. Acad. Sci. U. S. A. 116 (38) (2019) 19145–19154.
[76] D.A. Clare, M.N. Duong, D. Darr, F. Archibald, I. Fridovich, Effects of molecular oxygen on detection of superoxide radical with nitroblue tetrazolium and on activity stains for catalase, Anal. Biochem. 140 (2) (1984) 532–537.
[77] P.C. Loewen, J. Switala, Multiple catalases in *Bacillus subtilis*, J. Bacteriol. 169 (8) (1987) 3601–3607.
[78] M.S. Zeden, C.F. Schuster, L. Bowman, Q. Zhong, H.D. Williams, A. Grundling, Cyclic di-adenosine monophosphate (c-di-AMP) is required for osmotic regulation in *Staphylococcus aureus* but dispensable for viability in anaerobic conditions, J. Biol. Chem. 293 (9) (2018) 3180–3200.
[79] S. Mayer, W. Steffen, J. Steuber, F. Götz, The *Staphylococcus aureus* NuoL-like protein MpsA contributes to the generation of membrane potential, J. Bacteriol. 197 (5) (2015) 794–806.
[80] M.J. Horsburgh, E. Ingham, S.J. Foster, In *Staphylococcus aureus*, Fur is an interactive regulator with PerR, contributes to virulence, and Is necessary for oxidative stress resistance through positive regulation of catalase and iron homeostasis, J. Bacteriol. 183 (2) (2001) 468–475.
[81] H. Antelmann, M. Hecker, P. Zuber, Proteomic signatures uncover thiol-specific electrophile resistance mechanisms in *Bacillus subtilis*, Expert Rev. Proteomics 5 (1) (2008) 77–90.
[82] D. Frees, U. Gerth, H. Ingmer, Clp chaperones and proteases are central in stress survival, virulence and antibiotic resistance of *Staphylococcus aureus*, Int J Med Microbiol 304 (2) (2014) 142–149.
[83] D. Frees, K. Savijoki, P. Varmanen, H. Ingmer, Clp ATPases and ClpP proteolytic complexes regulate vital biological processes in low GC, Gram-positive bacteria, Mol. Microbiol. 63 (5) (2007) 1285–1295.
[84] V.V. Loi, T. Busche, T. Preuss, J. Kalinowski, J. Bernhardt, H. Antelmann, The AGXX(R) antimicrobial coating causes a thiol-specific oxidative stress response and protein *S*-bacillithiolation in *Staphylococcus aureus*, Front. Microbiol. 9 (2018) 3037.
[85] V.V. Loi, N.T.T. Huyen, T. Busche, Q.N. Tung, M.C.H. Gruhlke, J. Kalinowski, J. Bernhardt, A.J. Slusarenko, H. Antelmann, *Staphylococcus aureus* responds to allicin by global *S*-thioallylation - role of the Brx/BSH/YpdA pathway and the disulfide reductase MerA to overcome allicin stress, Free Radic. Biol. Med. 139 (2019) 55–69.
[86] J.L. Luebke, J. Shen, K.E. Bruce, T.E. Kehl-Fie, H. Peng, E.P. Skaar, D.P. Giedroc, The CsoR-like sulfurtransferase repressor (CstR) is a persulfide sensor in *Staphylococcus aureus*, Mol. Microbiol. 94 (6) (2014) 1343–1360.
[87] A.W. Maresso, O. Schneewind, Iron acquisition and transport in *Staphylococcus aureus*, Biometals 19 (2) (2006) 193–203.
[88] M. Marchetti, O. De Bei, S. Bettati, B. Campanini, S. Kovachka, E. Gianquinto, F. Spyrakis, L. Ronda, Iron metabolism at the interface between host and

pathogen: from nutritional immunity to antibacterial development, Int. J. Mol. Sci. 21 (6) (2020).
[89] H. Peng, J. Shen, K.A. Edmonds, J.L. Luebke, A.K. Hickey, L.D. Palmer, F. J. Chang, K.A. Bruce, T.E. Kehl-Fie, E.P. Skaar, D.P. Giedroc, Sulfide homeostasis and nitroxyl intersect via formation of reactive sulfur species in *Staphylococcus aureus*, mSphere 2 (3) (2017).
[90] M. Falord, U. Mäder, A. Hiron, M. Debarbouille, T. Msadek, Investigation of the *Staphylococcus aureus* GraSR regulon reveals novel links to virulence, stress response and cell wall signal transduction pathways, PloS One 6 (7) (2011), e21323.
[91] L. Kubistova, L. Dvoracek, J. Tkadlec, O. Melter, I. Licha, Environmental stress affects the formation of *Staphylococcus aureus* persisters tolerant to antibiotics, Microb. Drug Resist. 24 (5) (2018) 547–555.
[92] U. Mäder, P. Nicolas, M. Depke, J. Pane-Farre, M. Debarbouille, M.M. van der Kooi-Pol, C. Guerin, S. Derozier, A. Hiron, H. Jarmer, A. Leduc, S. Michalik, E. Reilman, M. Schaffer, F. Schmidt, P. Bessieres, P. Noirot, M. Hecker, T. Msadek, U. Völker, J.M. van Dijl, *Staphylococcus aureus* transcriptome architecture: from laboratory to infection-mimicking conditions, PLoS Genet. 12 (4) (2016), e1005962.
[93] J.A. Imlay, Pathways of oxidative damage, Annu. Rev. Microbiol. 57 (2003) 395–418.
[94] J.A. Imlay, Cellular defenses against superoxide and hydrogen peroxide, Annu. Rev. Biochem. 77 (2008) 755–776.
[95] A.D. Bolzan, M.S. Bianchi, Genotoxicity of streptonigrin: a review, Mutat. Res. 488 (1) (2001) 25–37.
[96] M. Goswami, S.H. Mangoli, N. Jawali, Involvement of reactive oxygen species in the action of ciprofloxacin against *Escherichia coli*, Antimicrob. Agents Chemother. 50 (3) (2006) 949–954.
[97] L.V. Ashby, R. Springer, M.B. Hampton, A.J. Kettle, C.C. Winterbourn, Evaluating the bactericidal action of hypochlorous acid in culture media, Free Radic. Biol. Med. 159 (2020) 119–124.
[98] W.B. Schofield, M. Zimmermann-Kogadeeva, M. Zimmermann, N.A. Barry, A. L. Goodman, The stringent response determines the ability of a commensal bacterium to survive starvation and to persist in the gut, Cell Host Microbe 24 (1) (2018) 120–132 e6.
[99] J.A. Morrissey, A. Cockayne, K. Brummell, P. Williams, The staphylococcal ferritins are differentially regulated in response to iron and manganese and via PerR and Fur, Infect. Immun. 72 (2) (2004) 972–979.
[100] S. Jang, J.A. Imlay, Micromolar intracellular hydrogen peroxide disrupts metabolism by damaging iron-sulfur enzymes, J. Biol. Chem. 282 (2) (2007) 929–937.
[101] K. Keyer, J.A. Imlay, Superoxide accelerates DNA damage by elevating free-iron levels, Proc. Natl. Acad. Sci. U. S. A. 93 (24) (1996) 13635–13640.
[102] D. Vinella, C. Albrecht, M. Cashel, R. D'Ari, Iron limitation induces SpoT-dependent accumulation of ppGpp in *Escherichia coli*, Mol. Microbiol. 56 (4) (2005) 958–970.
[103] L.F. Fitzsimmons, L. Liu, J.S. Kim, J. Jones-Carson, A. Vazquez-Torres, *Salmonella* reprograms nucleotide metabolism in its adaptation to nitrosative stress, mBio 9 (1) (2018).
[104] D.J. Dwyer, M.A. Kohanski, B. Hayete, J.J. Collins, Gyrase inhibitors induce an oxidative damage cellular death pathway in *Escherichia coli*, Mol. Syst. Biol. 3 (2007) 91.

Chapter 2

Staphylococcus aureus uses the bacilliredoxin (BrxAB)/ bacillithiol disulfide reductase (YpdA) redox pathway to defend against oxidative stress under infections

Nico Linzner[1], Vu Van Loi[1], Verena Nadin Fritsch[1], Quach Ngoc Tung[1], Saskia Stenzel[1], Markus Wirtz[2], Rüdiger Hell[2], Chris J. Hamilton[3], Karsten Tedin[4], Marcus Fulde[4], and Haike Antelmann[1]*

[1]Institute for Biology-Microbiology, Freie Universität Berlin, Berlin, Germany

[2]Plant Molecular Biology, Centre for Organismal Studies Heidelberg, Heidelberg University, Heidelberg, Germany

[3]School of Pharmacy, University of East Anglia, Norwich, United Kingdom

[4]Institute of Microbiology and Epizootics, Centre for Infection Medicine, Freie Universität Berlin, Berlin, Germany

*Corresponding author: haike.antelmann@fu-berlin.de

Published in:
Frontiers in Microbiology 10: 1355, 2019
DOI: https://doi.org/10.3389/fmicb.2019.01355

Personal contribution:

I carried out the RNA isolation and Northern blot analyses to study the transcriptional regulation of *brxA*, *brxB*, and *ypdA* under control and thiol-specific stress conditions (Fig. 2). Together with Dr. Nico Linzner, I performed phenotype analyses to investigate the role of BrxAB and YpdA under HOCl and H_2O_2. I did the data analysis of these experiments and drafted the corresponding figures (Fig. 6 and 7).

frontiers in Microbiology

ORIGINAL RESEARCH
published: 18 June 2019
doi: 10.3389/fmicb.2019.01355

Staphylococcus aureus Uses the Bacilliredoxin (BrxAB)/Bacillithiol Disulfide Reductase (YpdA) Redox Pathway to Defend Against Oxidative Stress Under Infections

Nico Linzner[1], Vu Van Loi[1], Verena Nadin Fritsch[1], Quach Ngoc Tung[1], Saskia Stenzel[1], Markus Wirtz[2], Rüdiger Hell[2], Chris J. Hamilton[3], Karsten Tedin[4], Marcus Fulde[4] and Haike Antelmann[1]*

[1] Institute for Biology – Microbiology, Freie Universität Berlin, Berlin, Germany, [2] Plant Molecular Biology, Centre for Organismal Studies Heidelberg, Heidelberg University, Heidelberg, Germany, [3] School of Pharmacy, University of East Anglia, Norwich, United Kingdom, [4] Institute of Microbiology and Epizootics, Centre for Infection Medicine, Freie Universität Berlin, Berlin, Germany

OPEN ACCESS

Edited by:
Boris Macek,
University of Tübingen, Germany

Reviewed by:
Alberto A. Iglesias,
National University of the Littoral, Argentina
Ivan Mijakovic,
Chalmers University of Technology, Sweden
Bruno Manta,
New England Biolabs, United States

***Correspondence:**
Haike Antelmann
haike.antelmann@fu-berlin.de

Specialty section:
This article was submitted to Microbial Physiology and Metabolism, a section of the journal Frontiers in Microbiology

Received: 03 February 2019
Accepted: 31 May 2019
Published: 18 June 2019

Citation:
Linzner N, Loi VV, Fritsch VN, Tung QN, Stenzel S, Wirtz M, Hell R, Hamilton CJ, Tedin K, Fulde M and Antelmann H (2019) Staphylococcus aureus Uses the Bacilliredoxin (BrxAB)/Bacillithiol Disulfide Reductase (YpdA) Redox Pathway to Defend Against Oxidative Stress Under Infections. Front. Microbiol. 10:1355. doi: 10.3389/fmicb.2019.01355

Staphylococcus aureus is a major human pathogen and has to cope with reactive oxygen and chlorine species (ROS, RCS) during infections. The low molecular weight thiol bacillithiol (BSH) is an important defense mechanism of *S. aureus* for detoxification of ROS and HOCl stress to maintain the reduced state of the cytoplasm. Under HOCl stress, BSH forms mixed disulfides with proteins, termed as *S*-bacillithiolations, which are reduced by bacilliredoxins (BrxA and BrxB). The NADPH-dependent flavin disulfide reductase YpdA is phylogenetically associated with the BSH synthesis and BrxA/B enzymes and was recently suggested to function as BSSB reductase (Mikheyeva et al., 2019). Here, we investigated the role of the complete bacilliredoxin BrxAB/BSH/YpdA pathway in *S. aureus* COL under oxidative stress and macrophage infection conditions *in vivo* and in biochemical assays *in vitro*. Using HPLC thiol metabolomics, a strongly enhanced BSSB level and a decreased BSH/BSSB ratio were measured in the *S. aureus* COL Δ*ypdA* deletion mutant under control and NaOCl stress. Monitoring the oxidation degree (OxD) of the Brx-roGFP2 biosensor revealed that YpdA is required for regeneration of the reduced BSH redox potential (E_{BSH}) upon recovery from oxidative stress. In addition, the Δ*ypdA* mutant was impaired in H_2O_2 detoxification as measured with the novel H_2O_2-specific Tpx-roGFP2 biosensor. Phenotype analyses further showed that BrxA and YpdA are required for survival under NaOCl and H_2O_2 stress *in vitro* and inside murine J-774A.1 macrophages in infection assays *in vivo*. Finally, NADPH-coupled electron transfer assays provide evidence for the function of YpdA in BSSB reduction, which depends on the conserved Cys14 residue. YpdA acts together with BrxA and BSH in de-bacillithiolation of *S*-bacillithiolated GapDH. In conclusion, our results point to a major role of the BrxA/BSH/YpdA pathway in BSH redox homeostasis in *S. aureus* during recovery from oxidative stress and under infections.

Keywords: *Staphylococcus aureus*, oxidative stress, bacillithiol, bacilliredoxin, bacillithiol disulfide reductase, YpdA, roGFP2

INTRODUCTION

Staphylococcus aureus is an important human pathogen, which can cause many diseases, ranging from local soft-tissue and wound infections to life-threatening systemic and chronic infections, such as endocarditis, septicaemia, bacteraemia, pneumonia or osteomyelitis (Archer, 1998; Lowy, 1998; Boucher and Corey, 2008). Due to the prevalence of methicillin-resistant *S. aureus* isolates, which are often resistant to multiple antibiotics, treatment options are limited to combat *S. aureus* infections (Livermore, 2000). Therefore, the "European Center of Disease Prevention and Control" has classified *S. aureus* as one out of six ESKAPE pathogens which are the leading causes of nosocomial infections worldwide (Pendleton et al., 2013). During infections, activated macrophages and neutrophils produce reactive oxygen and chlorine species (ROS, RCS) in large quantities, including H_2O_2 and HOCl with the aim to kill invading pathogens (Winterbourn and Kettle, 2013; Hillion and Antelmann, 2015; Beavers and Skaar, 2016; Winterbourn et al., 2016).

Low molecular weight thiols play important roles in the defense against ROS and HOCl in bacterial pathogens and are required for survival, host colonization, and pathogenicity (Loi et al., 2015; Tung et al., 2018). Gram-negative bacteria produce GSH as major LMW thiol, which is absent in most Gram-positive bacteria (Fahey, 2013). Instead, many firmicutes utilize BSH as alternative LMW thiol (**Figure 1A**), which is essential for virulence of *S. aureus* in macrophage infection assays (Newton et al., 2012; Pöther et al., 2013; Posada et al., 2014; Chandrangsu et al., 2018). A recent study identified a BSH derivative with an *N*-methylated cysteine as *N*-methyl-BSH in anaerobic phototrophic *Chlorobiaceae*, suggesting that BSH derivatives are more widely distributed and not restricted to Gram-positive firmicutes (Hiras et al., 2018). In *S. aureus* and *Bacillus subtilis*, BSH was characterized as cofactor of thiol-*S*-transferases (e.g., FosB), glyoxalases, peroxidases, and other redox enzymes that are involved in detoxification of ROS, HOCl, methylglyoxal, toxins, and antibiotics (Chandrangsu et al., 2018). In addition, BSH participates in post-translational thiol-modifications under HOCl stress by formation of BSH mixed protein disulfides, termed as protein *S*-bacillithiolations (Chi et al., 2011, 2013; Imber et al., 2018a,c).

Protein *S*-bacillithiolation functions in thiol-protection and redox regulation of redox-sensing regulators, metabolic enzymes and antioxidant enzymes (Chi et al., 2011, 2013; Loi et al., 2015; Imber et al., 2018a,b,c). In *S. aureus*, the glycolytic glyceraldehyde-3-phosphate dehydrogenase (GapDH) and the aldehyde dehydrogenase AldA were identified as most abundant *S*-bacillithiolated proteins that are inactivated under HOCl stress (Imber et al., 2018a,b). In *B. subtilis*, the methionine synthase MetE and the OhrR repressor are *S*-bacillithiolated under HOCl stress leading to methionine auxotrophy and derepression of the OhrR-controlled *ohrA* peroxiredoxin gene, respectively (Fuangthong et al., 2001; Lee et al., 2007; Chi et al., 2011).

Reduction of *S*-bacillithiolated OhrR, MetE, and GapDH proteins is catalyzed by the bacilliredoxins (BrxA/B) in *B. subtilis* and *S. aureus in vitro* (Gaballa et al., 2014; Chandrangsu et al., 2018). BrxA (YphP) and BrxB (YqiW) are paralogous thioredoxin-fold proteins of the UPF0403 family with an unusual CGC active site that are conserved in BSH-producing firmicutes (**Supplementary Figure S1**). Upon de-bacillithiolation, the BSH moiety is transferred to the Brx active site, resulting in BrxA-SSB formation (**Figure 1B**). However, the Brx associated thiol-disulfide reductase involved in regeneration of Brx activity is not known. In GSH-producing bacteria, Grx catalyze the reduction of *S*-glutathionylated proteins, which requires GSH for regeneration of Grx, resulting in GSSG formation (Lillig et al., 2008; Allen and Mieyal, 2012). The regeneration of GSH is catalyzed by the flavoenzyme Gor, which belongs to the pyridine nucleotide disulfide reductases and recycles GSSG on expense of NADPH (Argyrou and Blanchard, 2004; Deponte, 2013).

Phylogenomic profiling of protein interaction networks using EMBL STRING search has suggested the flavoenzyme YpdA (SACOL1520) as putative NADPH-dependent BSSB reductase (**Supplementary Figure S1**), since YpdA co-occurs together with BrxA/B and the BSH biosynthesis enzymes (BshA/B/C) only in BSH-producing bacteria, such as *B. subtilis* and *S. aureus* (**Supplementary Figure S2**; Gaballa et al., 2010). While our work was in progress, a recent study provides first evidence for the function of YpdA as putative BSSB reductase in *S. aureus in vivo* since an increased BSSB level and a decreased BSH/BSSB ratio was measured in the Δ*ypdA* mutant under control and H_2O_2 stress conditions (Mikheyeva et al., 2019). YpdA overproduction was shown to increase the BSH level and contributes to

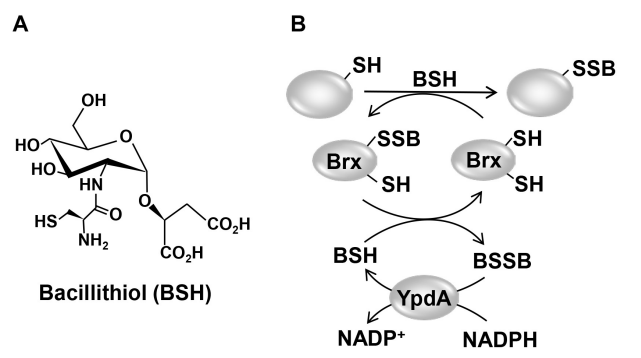

FIGURE 1 | Structure of the LMW thiol bacillithiol (BSH) **(A)** and mechanism of the bacilliredoxin (Brx)/BSH/YpdA de-bacillithiolation pathway **(B)**. **(A)** Bacillithiol is composed of glucosamine, malate, and cysteine. **(B)** Under HOCl stress, BSH leads to *S*-bacillithiolation of proteins which are reduced by bacilliredoxins (BrxA/B), resulting in the transfer of BSH to the Brx active site (Brx-SSB). BSH functions in Brx-SSB reduction to restore Brx activity, leading to BSSB formation. The BSSB reductase YpdA (SACOL1520) regenerates BSH on expense of NADPH.

Abbreviations: BSH, bacillithiol; BSSB, bacillithiol disulfide; BrxA/B, bacilliredoxin A (YphP)/bacilliredoxin B (YqiW); CFUs, colony forming units; DTT, dithiothreitol; E_{BSH}, bacillithiol redox potential; GapDH, glyceraldehyde 3-phosphate dehydrogenase; GSH, glutathione; GSSG, glutathione disulfide; Gor, glutathione disulfide reductase; Grx, glutaredoxins; HOCl, hypochlorous acid; LMW, low molecular weight; Mtr, mycothiol disulfide reductase; NaOCl, sodium hypochlorite; OD_{500}, optical density at 500 nm; rdw, raw dry weight; RCS, reactive chlorine species; ROS, reactive oxygen species; YpdA, bacillithiol disulfide reductase.

oxidative stress resistance, fitness, and virulence of *S. aureus* (Mikheyeva et al., 2019). However, biochemical evidence for the function of YpdA as BSSB reductase and the association of YpdA to the BrxA/B enzymes have not been demonstrated in *B. subtilis* or *S. aureus*.

In this work, we aimed to investigate the role of the complete BrxAB/BSH/YpdA pathway in *S. aureus in vivo* and *in vitro*. We used phenotype and biochemical analyses, HPLC metabolomics and redox biosensor measurements to study the physiological role of the Brx/BSH/YpdA redox pathway in *S. aureus* under oxidative stress and macrophage infection assays. Our data point to important roles of both BrxA and YpdA in the oxidative stress defense for regeneration of reduced E_{BSH} and de-bacillithiolation upon recovery from oxidative stress. Biochemical assays further provide evidence for the function of YpdA as BSSB reductase *in vitro*, which acts in the BrxA/BSH/YpdA electron pathway in de-bacillithiolation of GapDH-SSB.

MATERIALS AND METHODS

Bacterial Strains, Growth, and Survival Assays

Bacterial strains, plasmids and primers used in this study are listed in **Supplementary Tables S1, S2, S3**. For cloning and genetic manipulation, *Escherichia coli* was cultivated in LB medium. For stress experiments, *S. aureus* COL wild type and mutant strains were cultivated in LB, RPMI, or Belitsky minimal medium and exposed to the different compounds during the exponential growth as described previously (Loi et al., 2017, 2018b). NaOCl, methylglyoxal, diamide, methylhydroquinone, DTT, cumene hydroperoxide (80% w/v), H_2O_2 (35% w/v), and monobromobimane were purchased from Sigma Aldrich.

Cloning, Expression, and Purification of His-Tagged Brx-roGFP2, Tpx-roGFP2, GapDH, BrxA, YpdA, and YpdAC14A Proteins in *E. coli*

Construction of plasmids pET11b-*brx-roGFP2* for expression of the Brx-roGFP2 biosensor was described previously (Loi et al., 2017). The pET11b-derived plasmids for overexpression of the His-tagged GapDH and BrxA (SACOL1321) proteins were generated previously (Imber et al., 2018a). The plasmid pET11b-*brx-roGFP2* was used as a template for construction of the Tpx-roGFP2 biosensor to replace *brx* by the *tpx* gene of *S. aureus*. The *tpx* gene (*SACOL1762*) was PCR-amplified from chromosomal DNA of *S. aureus* COL using primers pET-tpx-for-NheI and pET-tpx-rev-SpeI (**Supplementary Table S3**), digested with *Nhe*I and *Bam*HI and cloned into plasmid pET11b-*brx-roGFP2* to generate pET11b-*tpx-roGFP2*. To construct plasmids pET11b-*ypdA* or pET11b-*ypdAC14A*, the *ypdA* gene (*SACOL1520*) was PCR-amplified from chromosomal DNA of *S. aureus* COL with pET-ypdA-for-NdeI or pET-ypdAC14A-for-NdeI as forward primers and pET-ypdA-rev-BamHI as reverse primer (**Supplementary Table S3**), digested with *Nde*I and *Bam*HI and inserted into plasmid pET11b (Novagen). For expression of His-tagged proteins (GapDH, BrxA, YpdA, YpdAC14A, Tpx-roGFP2), *E. coli* BL21(DE3) *plys*S carrying plasmids pET11b-*gap,* pET11b-*brxA,* pET11b-*ypdA*, pET11b-*ypdAC14A* and pET11b-*tpx-roGFP2* was cultivated in 1 l LB medium until an OD_{600} of 0.8 followed by addition of 1 mM IPTG (isopropyl-β-D-thiogalactopyranoside) for 16 h at 25°C. His_6-tagged GapDH, BrxA, YpdA, YpdAC14A, and Tpx-roGFP2 proteins were purified using His Trap™ HP Ni-NTA columns (5 ml; GE Healthcare, Chalfont St Giles, United Kingdom) and the ÄKTA purifier liquid chromatography system (GE Healthcare) as described (Loi et al., 2018b).

Construction of *S. aureus* COL Δ*ypdA*, Δ*brxAB* and Δ*brxAB*Δ*ypdA* Clean Deletion Mutants and Complemented Mutant Strains

Staphylococcus aureus COL Δ*ypdA* (*SACOL1520*), Δ*brxA* (*SACOL1464*), and Δ*brxB* (*SACOL1558*) single deletion mutants as well as the Δ*brxAB* double and Δ*brxAB*Δ*ypdA* triple mutants were constructed using pMAD as described (Arnaud et al., 2004; Loi et al., 2018b). Briefly, the 500 bp up- and downstream regions of *ypdA*, *brxA,* and *brxB* were amplified using gene-specific primers (**Supplementary Table S3**), fused by overlap extension PCR and ligated into the *Bgl*II and *Sal*I sites of plasmid pMAD. The pMAD constructs were electroporated into *S. aureus* RN4220 and further transduced into *S. aureus* COL using phage 81 (Rosenblum and Tyrone, 1964). The clean marker-less deletions of *ypdA*, *brxA,* or *brxB* were selected after plasmid excision as described (Loi et al., 2018b). All mutants were clean deletions of internal gene regions with no genetic changes in the up- and downstream encoding genes. The deletions of the internal gene regions were verified by PCR and DNA sequencing. The Δ*brxAB* and Δ*brxAB*Δ*ypdA* double and triple mutants were obtained by transduction and excision of pMAD-Δ*brxB* into the Δ*brxA* mutant, leading to the Δ*brxAB* deletion and of plasmid pMAD-Δ*ypdA* into the Δ*brxAB* mutant, resulting in the Δ*brxAB*Δ*ypdA* knockout. For construction of *ypdA, brxA,* and *brxB* complemented strains, the xylose-inducible ectopic *E. coli/S. aureus* shuttle vector pRB473 was applied (Brückner et al., 1993). Primers pRB-ypdA, pRB-brxA, and pRB-brxB (**Supplementary Table S3**) were used for amplification of the genes, which were cloned into pRB473 after digestion with *Bam*HI and *Kpn*I to generate plasmids pRB473-*ypdA*, pRB473-*brxA,* and pRB473-*brxB,* respectively. The pRB473 constructs were confirmed by PCR and DNA sequencing and transduced into the Δ*ypdA* and Δ*brxAB* deletion mutants as described (Loi et al., 2017).

Construction of Tpx-roGFP2 and Brx-roGFP2 Biosensor Fusions in *S. aureus* COL

The *tpx-roGFP2* fusion was amplified from plasmid pET11b-*tpx-roGFP2* with primers pRB-tpx-roGFP2-for-BamHI and pRB-tpx-roGFP2-rev-SacI and digested with *Bam*HI and *Sac*I (**Supplementary Table S3**). The PCR product was cloned into

pRB473 generating plasmid pRB473-*tpx-roGFP2*, which was confirmed by DNA sequencing. The biosensor plasmids pRB473-*tpx-roGFP2* and pRB473-*brx-roGFP2* were electroporated into *S. aureus* RN4220 and further transferred to the *S. aureus* COL Δ*ypdA*, Δ*brxAB* and Δ*brxAB*Δ*ypdA* mutants by phage transduction as described (Loi et al., 2017).

Northern Blot Experiments

Northern blot analyses were performed using RNA isolated from *S. aureus* COL before and 15 min after exposure to 0.5 mM methylglyoxal, 0.75 mM formaldehyde, 1 mM NaOCl, 10 mM H_2O_2, 2 mM diamide, and 45 μM methylhydroquinone as described (Wetzstein et al., 1992). Hybridizations were conducted using digoxigenin-labeled antisense RNA probes for *ypdA, brxA,* and *brxB* that were synthesized *in vitro* using T7 RNA polymerase and primers ypdA-NB-for/rev, brxA-NB-for/rev, or brxB-NB-for/rev (**Supplementary Table S3**) as in previous studies (Tam le et al., 2006).

HPLC Thiol Metabolomics for Quantification of LMW Thiols and Disulfides

For preparation of thiol metabolomics samples, *S. aureus* COL WT, Δ*ypdA* and Δ*brxAB* mutants as well as the *ypdA* complemented strains were grown in RPMI medium to an OD_{500} of 0.9 and exposed to 2 mM NaOCl stress for 30 min. The intracellular amounts of reduced and oxidized LMW thiols and disulfides (BSH, BSSB, cysteine and cystine) were extracted from the *S. aureus* cells, labeled with monobromobimane and measured by HPLC thiol metabolomics as described (Chi et al., 2013).

Western Blot Analysis

Staphylococcus aureus strains were grown in LB until an OD_{540} of 2, transferred to Belitsky minimal medium and treated with 100 μM NaOCl for 60 and 90 min. Cytoplasmic proteins were prepared and subjected to non-reducing BSH-specific Western blot analysis using the polyclonal rabbit anti-BSH antiserum as described previously (Chi et al., 2013). The de-bacillithiolation reactions with purified GapDH-SSB and the BrxA/BSH/YpdA/NADPH pathway were also subjected to non-reducing BSH-specific Western blots.

Brx-roGFP2 and Tpx-roGFP2 Biosensor Measurements

Staphylococcus aureus COL, Δ*ypdA* and Δ*brxAB* mutant strains expressing the Brx-roGFP2 and Tpx-roGFP2 biosensor plasmids were grown in LB and used for measurements of the biosensor oxidation degree (OxD) along the growth curves and after injection of the oxidants H_2O_2 and NaOCl as described previously (Loi et al., 2017). The fully reduced and oxidized control samples of Tpx-roGFP2 expression strains were treated with 15 mM DTT and 20 mM cumene hydroperoxide, respectively. The Brx-roGFP2 and Tpx-roGFP2 biosensor fluorescence emission was measured at 510 nm after excitation at 405 and 488 nm using the CLARIOstar microplate reader (BMG Labtech). The OxD of the Brx-roGFP2 and Tpx-roGFP2 biosensors was determined for each sample and normalized to fully reduced and oxidized controls as described (Loi et al., 2017) according to the Eq. (1):

$$\mathrm{O{\times}D} = \frac{I405_{\mathrm{sample}} \times I488_{\mathrm{red}} - I405_{\mathrm{red}} \times I488_{\mathrm{sample}}}{I405_{\mathrm{sample}} \times I488_{\mathrm{red}} - I405_{\mathrm{sample}} \times I488_{\mathrm{ox}} + I405_{\mathrm{ox}} \times I488_{\mathrm{sample}} - I405_{\mathrm{red}} \times I488_{\mathrm{sample}}} \quad (1)$$

The values of $I405_{\mathrm{sample}}$ and $I488_{\mathrm{sample}}$ are the observed fluorescence excitation intensities at 405 and 488 nm, respectively. The values of $I405_{\mathrm{red}}$, $I488_{\mathrm{red}}$, $I405_{\mathrm{ox}}$, and $I488_{\mathrm{ox}}$ represent the fluorescence intensities of fully reduced and oxidized controls, respectively.

Based on the OxD values and the previously determined $E^{o'}_{\mathrm{roGFP2}} = -280$ mV (Dooley et al., 2004), the BSH redox potential (E_{BSH}) can be calculated using to the Nernst equation (2):

$$E_{\mathrm{BSH}} = E_{\mathrm{roGFP2}} = E^{o'}_{\mathrm{roGFP2}} - \left(\frac{\mathrm{RT}}{2\mathrm{F}}\right) \times \mathrm{In}\left(\frac{1-\mathrm{OxD}}{\mathrm{OxD}}\right) \quad (2)$$

Biochemical Assays for NADPH-Dependent BSSB Reduction by YpdA and De-Bacillithiolation of GapDH-SSB Using the BrxA/BSH/YpdA Electron Pathway *in vitro*

Before the activity assays, the purified BrxA, YpdA, and YpdAC14A proteins were prereduced with 10 mM DTT followed by DTT removal with Micro Biospin 6 columns (Biorad). For the biochemical activity assays of the specific BSSB reductase activity, 12.5 μM of purified YpdA and YpdAC14A proteins were incubated with 40 μM BSSB, 40 μM GSSG, or 40 μM coenzyme A disulfide and 500 μM NADPH in 20 mM Tris, 1.25 mM EDTA, pH 8.0. NADPH consumption of YpdA and YpdAC14A was measured immediately after the start of the reaction as absorbance change at 340 nm using the Clariostar microplate reader. The NADPH-dependent BrxA/BSH/YpdA electron pathway was reconstituted *in vitro* for de-bacillithiolation of GapDH-SSB. About 60 μM of purified GapDH was *S*-bacillithiolated with 600 μM BSH in the presence of 6 mM H_2O_2 for 5 min. Excess of BSH and H_2O_2 were removed with Micro Biospin 6 columns, which were equilibrated with 20 mM Tris, 1.25 mM EDTA, pH 8.0. Before starting the de-bacillithiolation assay using the BrxA/BSH/YpdA electron pathway, 2.5 μM GapDH-SSB was incubated with 12.5 μM BrxA, 40 μM BSH, and 500 μM NADPH in 20 mM Tris, 1.25 mM EDTA, pH 8.0 at room temperature for 30 min. Next, 12.5 μM YpdA or YpdAC14A proteins were added to the reaction mix at 30°C for 8 min and NADPH consumption was measured at 340 mm. The biochemical activity assays were performed in four replicate experiments.

Infection Assays With Murine Macrophage Cell Line J-774A.1

The murine cell line J774A.1 was cultivated in Iscove's modified Dulbecco MEM medium (Biochrom) with 10% heat inactivated

fetal bovine serum (FBS) and used for *S. aureus* infection assays as described (Loi et al., 2018b). Macrophages were infected with *S. aureus* cells at a multiplicity of infection (MOI) of 1:25. One hour after infection, the cell culture medium was replaced and 150 μg/ml gentamycin was added for 1 h to kill extracellular bacteria and to stop the uptake of *S. aureus*. The *S. aureus* cells were harvested at 2, 4, and 24 h post infection. To determine the percentage of surviving *S. aureus* cells, infected macrophages were lysed with 0.1% Triton X-100 and the supernatant of internalized bacteria was plated on brain heart infusion (BHI) agar plates. The CFUs were counted after incubation for 24–36 h at 37°C (Loi et al., 2018b).

Statistical Analyses

Statistical analysis of growth and survival assays was performed using the Student's unpaired two-tailed *t*-test by the graph prism software. The statistics of the J-774.1 macrophage infection assays was calculated using the one-way ANOVA and Tukey's multiple comparisons *post hoc* test by the graph prism software. The results of the statistical tests are included in the figure legends.

RESULTS

Transcription of *ypdA*, *brxA,* and *brxB* Is Induced Under Disulfide Stress by Diamide and NaOCl in *S. aureus* COL

The bacilliredoxins BrxA (SACOL1464) and BrxB (SACOL1558) of *S. aureus* share an unusual CGC active site and are highly conserved in BSH-producing firmicutes (**Supplementary Figure S1**; Gaballa et al., 2014). The pyridine nucleotide disulfide oxidoreductase YpdA (SACOL1520) belongs to the FAD/NAD(P)-binding domain superfamily (IPR036188) and was annotated as putative BSSB reductase due to its phylogenetic co-occurence with the BSH biosynthesis enzymes and BrxA/B in BSH-producing firmicutes (**Supplementary Figure S2**; Gaballa et al., 2010). We used Northern blot analysis to investigate whether transcription of *brxA*, *brxB,* and *ypdA* is co-regulated and up-regulated under thiol-specific stress conditions, such as 0.5 mM methylglyoxal, 0.75 mM formaldehyde, 1 mM NaOCl, 10 mM H_2O_2, 2 mM diamide and 45 μM methylhydroquinone (**Figure 2**). The *brxA* gene is co-transcribed with *SACOL1465-66-67* in a 2 kb operon and *brxB* is located in the 1.6 kb *SACOL1557-brxB-SACOL1559* operon. The genes co-transcribed together with *brxA* and *brxB* encode proteins of unknown functions. The Northern blot results revealed significant basal transcription of the *brxA, brxB,* and *ypdA* genes and operons in the control, and strong induction under disulfide stress provoked by NaOCl and diamide. Of note, the *brxB* operon was stronger induced under disulfide stress compared to the *brxA* operon (**Figure 2**). No up-regulation of the *brxA, brxB,* and *ypdA* specific mRNAs was detected upon H_2O_2, aldehyde and quinone stress. The co-regulation of BrxA/B and YpdA under disulfide stress suggests that they act in the same pathway to regenerate *S*-bacillithiolated proteins under NaOCl stress upon recovery from oxidative stress.

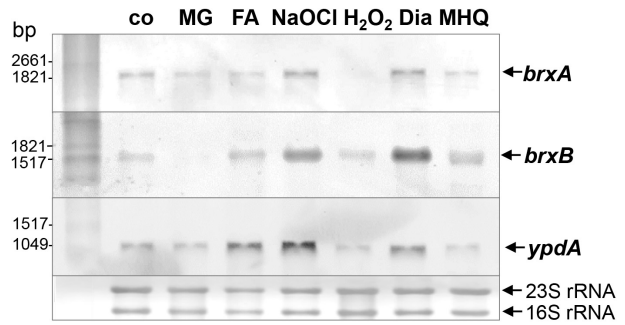

FIGURE 2 | Transcription of *brxA*, *brxB,* and *ypdA* is induced by disulfide stress in *S. aureus*. Northern blot analysis was used to analyze transcription of *brxA*, *brxB,* and *ypdA* in *S. aureus* COL wild type before (co) and 15 min after exposure to 0.5 mM methylglyoxal (MG), 0.75 mM formaldehyde (FA), 1 mM NaOCl, 10 mM H_2O_2, 2 mM diamide (Dia), and 45 μM methylhydroquinone (MHQ) stress at an OD_{500} of 0.5. The arrows point toward the transcript sizes of the *brxA*, *brxB,* and *ypdA* specific genes and operons. The methylene blue-stained bands of the 16S and 23S rRNAs are shown as RNA loading control at the bottom.

The BSSB Level Is Significantly Increased and the BSH/BSSB Ratio Is Decreased in the *S. aureus* Δ*ypdA* Mutant

To investigate the physiological role of BrxA/B and YpdA under oxidative stress and in BSH redox homeostasis, we constructed Δ*brxAB* and Δ*ypdA* deletion mutants. Using HPLC thiol metabolomics, the intracellular levels of BSH and BSSB were determined in the Δ*brxAB* and Δ*ypdA* mutants under control and NaOCl stress after monobromobimane derivatisation of LMW thiols and disulfides. In the *S. aureus* COL wild type, a BSH level of 1.6–1.9 μmol/g rdw was determined, which was not significantly different in the Δ*ypdA* and Δ*brxAB* mutants (**Figure 3A**). Exposure of *S. aureus* to 2 mM NaOCl stress caused a five to sixfold decreased intracellular BSH level in the wild type, Δ*ypdA* and Δ*brxAB* mutants (**Figure 3A**). The level of BSSB was similar in control and NaOCl-treated cells of the wild type and Δ*brxAB* mutant (∼0.05 μmol/g rdw) (**Figure 3B**). Most interestingly, the Δ*ypdA* mutant showed a significantly twofold increased BSSB level under control and NaOCl stress compared to the wild type (**Figure 3B**), confirming previous data (Mikheyeva et al., 2019). Thus, the BSH/BSSB ratio is ∼2–3-fold decreased in the Δ*ypdA* mutant under control and NaOCl relative to the parent (**Figure 3C**). The increased BSSB levels and the decreased BSH/BSSB redox ratio in the Δ*ypdA* mutant could be restored to wild type levels in the *ypdA* complemented strain. In addition, a significantly 1.5-fold increased cysteine level was measured in the Δ*ypdA* mutant under NaOCl stress, but no changes in the level of cystine (**Supplementary Figures S3A–C**). The cysteine levels could be also restored to wild type level in the *ypdA* complemented

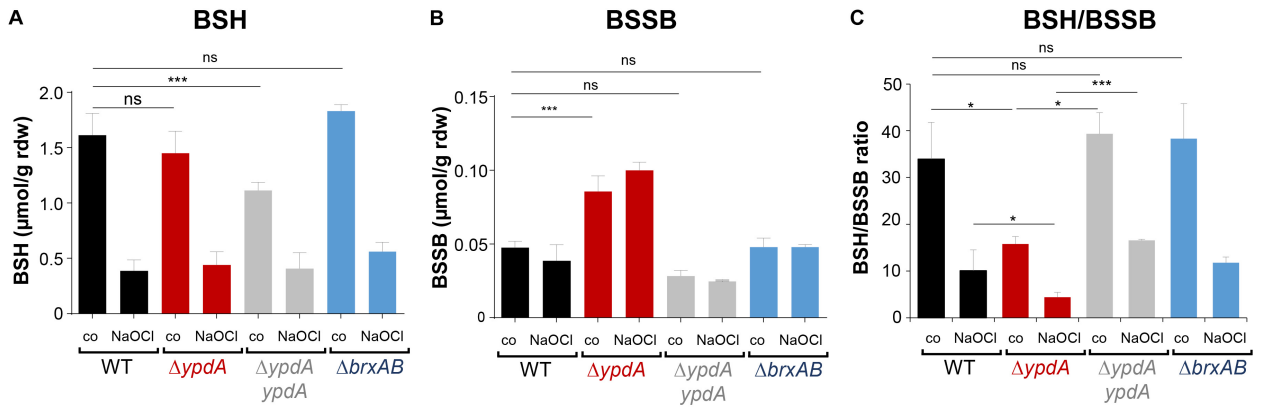

FIGURE 3 | The BSSB level is strongly increased and the BSH/BSSB redox ratio is decreased in the *S. aureus* COL Δ*ypdA* mutant under control and NaOCl stress. The levels of BSH **(A)**, BSSB **(B)** and the BSH/BSSB redox ratio **(C)** were determined in *S. aureus* COL wild type (WT), the Δ*ypdA* and Δ*brxAB* mutants as well as in the *ypdA* complemented strain before (co) and 30 min after treatment with 2 mM NaOCl stress. LMW thiols and disulfides were labeled with monobromobimane and measured using HPLC-thiol-metabolomics. Mean values and standard deviations (SD) of four biological replicates are shown. $^{ns}p > 0.05$; $^{*}p \leq 0.01$, and $^{***}p \leq 0.001$.

strain. These results indicate that YpdA is important to maintain the reduced level of BSH under control and NaOCl stress, supporting previous results (Mikheyeva et al., 2019), while the bacilliredoxins BrxA/B are dispensible for the cellular BSH/BSSB redox balance during the growth and under oxidative stress in *S. aureus*.

The *S. aureus* Δ*ypdA* Mutant Is Impaired to Regenerate the Reduced BSH Redox Potential and to Detoxify H_2O_2 Under Oxidative Stress

Next, we applied the Brx-roGFP2 biosensor to monitor the changes of its OxD in *S. aureus* COL wild type, the Δ*ypdA* and Δ*brxAB* mutants during the growth and under oxidative stress (Loi et al., 2017). Using the Nernst equation the OxD values were used to calculate the changes in the BSH redox potential (E_{BSH}) in wild type and mutant strains (see section "Materials and Methods" for details). Measurements of the Brx-roGFP2 OxD in LB medium along the growth did not reveal notable differences in the basal level of E_{BSH} between wild type, Δ*ypdA* and Δ*brxAB* mutant strains (**Supplementary Figures S4A,B, S5A,B** and **Supplementary Table S4**). The basal level of E_{BSH} varied from −282 to −295 mV in the wild type and from −286 to −299 mV in the Δ*ypdA* and Δ*brxAB* mutants in different growth phases (**Supplementary Figures S5A,B** and **Supplementary Table S4**). Thus, we monitored the biosensor OxD and calculated the E_{BSH} changes in Δ*ypdA* and Δ*brxAB* mutants after exposure to sub-lethal doses of 100 µM NaOCl and 100 mM H_2O_2 to identify functions for BrxAB or YpdA under oxidative stress. The Brx-roGFP2 biosensor was strongly oxidized under NaOCl and H_2O_2 stress in the wild type, the Δ*ypdA* and Δ*brxAB* mutants (**Figures 4A–D**). The calculated E_{BSH} increased upon NaOCl stress from −286 to −254 mV in the wild type, from −285 to −247 mV in the Δ*ypdA* mutant and from −288 to −259 mV in the Δ*brxAB* mutant (**Supplementary Figures S5C,D** and **Supplementary Table S5**). This indicates a stronger increase of E_{BSH} by NaOCl stress in the Δ*ypdA* mutant compared to the wild type. Regeneration of the reduced basal level E_{BSH} occurred already after 2 h reaching values of −269 mV in the wild type and −274 mV in the Δ*brxAB* mutant (**Figure 4B**, **Supplementary Figure S5D**, and **Supplementary Table S5**). However, the Δ*ypdA* mutant was significantly impaired to recover the reduced state and E_{BSH} values remained high with −252 mV after 2 h of NaOCl stress (**Figure 4A**, **Supplementary Figure S5C**, and **Supplementary Table S5**). Of note, the defect of the Δ*ypdA* mutant to restore the reduced state of E_{BSH} was reproducible with both oxidants, H_2O_2 and NaOCl (**Figures 4A,C**, **Supplementary Figures S5C,E**, and **Supplementary Table S6**). While recovery of reduced E_{BSH} after H_2O_2 stress was fast in the wild type and Δ*brxAB* mutant reaching E_{BSH} values of −280 and −283 mV already after 60 min, the Δ*ypdA* mutant was still oxidized after 2 h with high E_{BSH} values of −264 mV (**Supplementary Figures S5E,F** and **Supplementary Table S6**). These Brx-roGFP2 measurements document the important role of YpdA to reduce BSSB and to regenerate the reduced E_{BSH} during the recovery phase of cells from oxidative stress.

We further hypothesized that the Δ*ypdA* mutant is defective in H_2O_2 detoxification due to its increased BSSB levels. To analyse the kinetics of H_2O_2 detoxification in the Δ*ypdA* mutant, we constructed a genetically encoded H_2O_2-specific Tpx-roGFP2 biosensor. First, we verified that Tpx-roGFP2 showed the same ratiometric changes of the excitation spectrum in the fully reduced and oxidized state *in vitro* and *in vivo* as previously measured for Brx-roGFP2 (**Supplementary Figures S6A,B**). Tpx-roGFP2 was shown to respond strongly to low levels of 0.5–1 µM H_2O_2 *in vitro* and was fully oxidized with 100 mM H_2O_2 inside *S. aureus* COL wild type cells indicating the utility of the probe to measure H_2O_2 detoxification kinetics in *S. aureus* (**Supplementary Figures S6C,D**). Measurements of Tpx-roGFP2 oxidation along the growth in LB medium

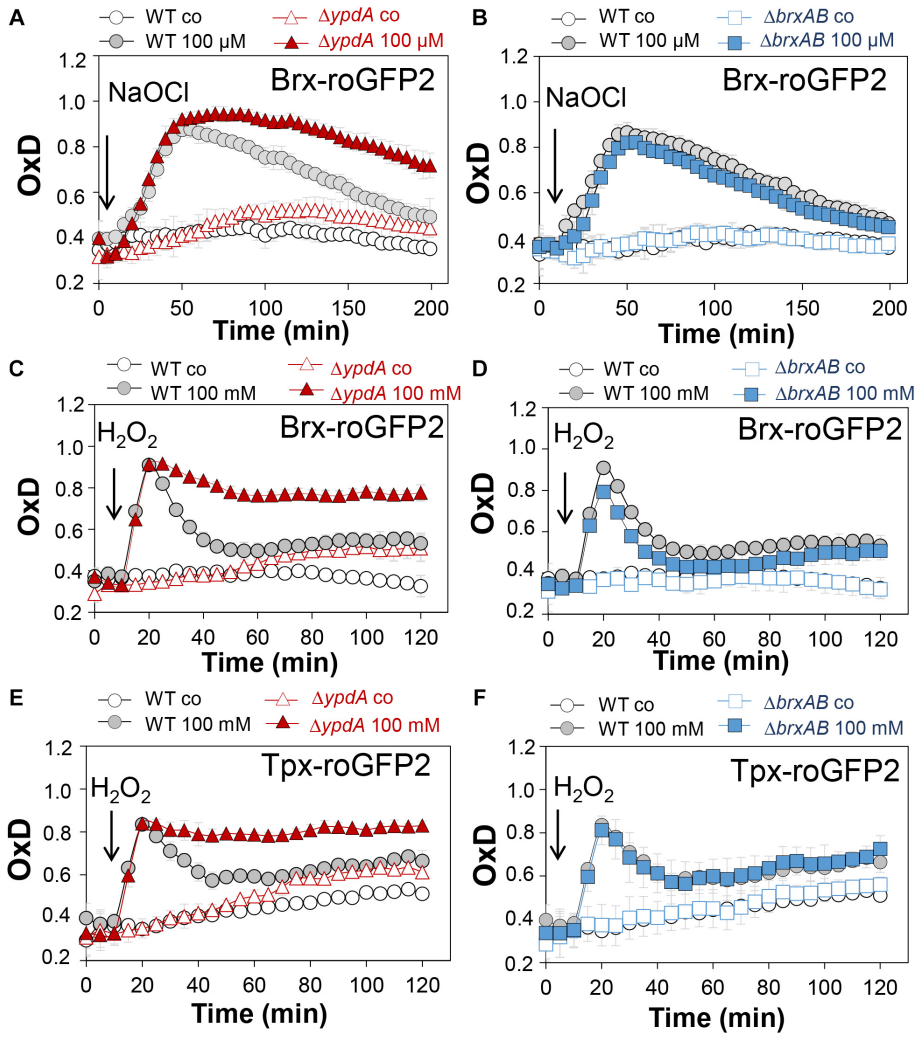

FIGURE 4 | Brx-roGFP2 and Tpx-roGFP2 biosensors measurements of the OxD indicate that the *S. aureus* Δ*ypdA* mutant is impaired to regenerate the reduced state of E_{BSH} and to detoxify H_2O_2 during recovery from oxidative stress. **(A–D)** Response of the Brx-roGFP2 biosensor to 100 µM NaOCl and 100 mM H_2O_2 stress in *S. aureus* COL WT, the Δ*ypdA* **(A,C)** and Δ*brxAB* **(B,D)** mutants. **(E,F)** Response of the Tpx-roGFP2 biosensor under 100 mM H_2O_2 stress in the *S. aureus* COL WT, the Δ*ypdA* and Δ*brxAB* mutants. The Brx-roGFP2 biosensor responses are shown as OxD values and the corresponding E_{BSH} changes were calculated using the Nernst equation and presented in **Supplementary Figure S5** and **Supplementary Tables S5, S6**. Mean values and SD of three biological replicates are shown.

revealed a similar high OxD of ∼0.5–0.6 in the wild type, Δ*brxAB* and Δ*ypdA* mutant strains (**Supplementary Figures S4C,D**). The absence of BrxA/B or YpdA did not affect the biosensor OxD under non-stress conditions, which further provides evidence for roles under oxidative stress. Thus, we monitored the H_2O_2 response of Tpx-roGFP2 and the kinetics of H_2O_2 detoxification in the Δ*ypdA* and Δ*brxAB* mutants. Interestingly, Tpx-roGFP2 showed a similar response to 100 mM H_2O_2 in all strains, but the Δ*ypdA* mutant was significantly impaired in H_2O_2 detoxification compared to the wild type (**Figures 4E,F**). These results clearly confirmed that the Δ*ypdA* mutant is defective to recover from oxidative stress due to its higher BSSB level resulting in an oxidized E_{BSH} as revealed using Brx-roGFP2 and thiol-metabolomics studies.

S-Bacillithiolation of GapDH Is Not Affected in Δ*ypdA* and Δ*brxAB* Mutants or in *ypdA*, *brxA*, and *brxB* Complemented Strains

In *S. aureus*, the glyceraldehyde-3 phosphate dehydrogenase GapDH was previously identified as most abundant *S*-bacillithiolated protein under NaOCl stress that is visible as major band in BSH-specific non-reducing Western blots (Imber et al., 2018a). Since GapDH activity could be recovered with purified BrxA *in vitro* previously (Imber et al., 2018a), we analyzed the pattern of GapDH *S*-bacillithiolation in the Δ*brxAB* and Δ*ypdA* mutants as well as in *ypdA*, *brxA* and *brxB* complemented strains *in vivo*. However, the amount of *S*-bacillithiolated GapDH was similar after

100 μM NaOCl stress between wild type, Δ*brxAB* and Δ*ypdA* mutants and complemented strains (**Figures 5A,B**). This indicates that the absence of the BrxAB/YpdA pathway does not affect the level of *S*-bacillithiolation of GapDH under NaOCl stress.

The Bacilliredoxins BrxA/B and the Putative BSSB Reductase YpdA Are Important for Growth and Survival Under Oxidative Stress and Macrophage Infections

Next, we analyzed the physiological role of the BrxA/B/YpdA pathway for growth and survival of *S. aureus* under H_2O_2 and NaOCl stress. The growth of the Δ*ypdA* and Δ*brxAB* mutants in RPMI medium without stress exposure was comparable to the wild type (**Figures 6A,C**). Interestingly, both Δ*brxAB* and Δ*ypdA* mutants displayed a small, but statistically significant growth delay after exposure to sub-lethal amounts of 1.5 mM NaOCl compared to the wild type, while no growth delay was observed with sub-lethal 10 mM H_2O_2 (**Figures 6A,C**, **7A,B**). This might indicate that BrxAB and YpdA function in the same pathway as already suggested by phylogenomic profiling using STRING search (**Supplementary Figure S2**). Determination of viable counts revealed significantly ∼2-fold decreased survival rates of both Δ*brxAB* and Δ*ypdA* mutants after exposure to lethal doses of 3.5 mM NaOCl and 40 mM H_2O_2 relative to the wild type (**Figures 6F,G**, **7C,D**). These oxidant sensitive growth and survival phenotypes of the Δ*brxAB* and Δ*ypdA* mutants could be restored back to wild type levels by complementation with *brxA* and *ypdA,* respectively (**Figures 6B,D,F,G**, **7C,D**). However, complementation of the Δ*brxAB* mutant with *brxB* did not restore the growth and viability of the wild type under NaOCl stress (**Figures 6E,G**), although xylose-inducible *brxB* expression of plasmid pRB473-*brxB* could be verified in Northern blots (**Supplementary Figure S7**). Moreover, the Δ*brxAB*Δ*ypdA* triple mutant displayed the same sensitivity as the Δ*brxAB* mutant to 40 mM H_2O_2 and 3 mM NaOCl indicating that BrxA and YpdA function in the same pathway for reduction of *S*-bacillithiolated proteins (**Figures 7D** and **Supplementary Figure S8C**).

To investigate the function of the BrxA/B/YpdA pathway under infection-relevant conditions, we measured the intracellular survival of the Δ*brxAB* and Δ*ypdA* mutants in phagocytosis assays inside murine macrophages of the cell line J-774A.1, as previously (Loi et al., 2018b). The viable counts (CFUs) of internalized *S. aureus* cells were determined at 2, 4, and 24 h post infection of the macrophages. The number of surviving cells decreased to 21.3% at 24 h post infection for the *S. aureus* COL wild type, but more strongly to 11.4 and 10.2% for the Δ*ypdA* and Δ*brxAB* mutants (**Figures 8A,C**). Thus, the number of viable counts was significantly ∼2-fold lower for both Δ*brxAB* and Δ*ypdA* mutants at 24 h post infection compared to the wild type. These sensitive phenotypes of the Δ*ypdA* and Δ*brxAB* mutants under macrophage infections could be restored to 80% of wild type levels after complementation with plasmid-encoded *ypdA* or *brxA*, respectively (**Figures 8B,D**). However, complementation with *brxB* did not restore the survival defect of the Δ*brxAB* mutant, pointing again to the major role of BrxA in this pathway.

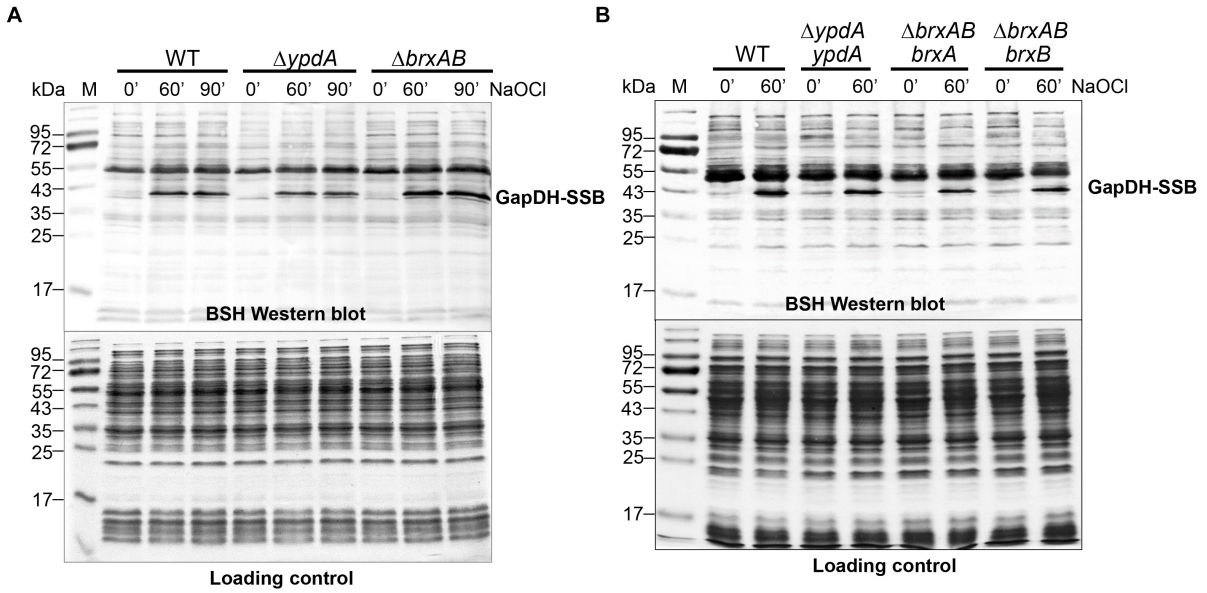

FIGURE 5 | Protein *S*-bacillithiolation of GapDH is not affected in the Δ*ypdA* and Δ*brxAB* mutants **(A)** or in the *ypdA*, *brxA,* and *brxB* complemented strains **(B)** as revealed by non-reducing BSH Western blots. The prominent GapDH-SSB band is visible in the cell extracts of NaOCl-treated *S. aureus* cells using non-reducing BSH Western blots. Other bands visible under control and stress conditions are proteins cross-reactive with the polyclonal rabbit anti-BSH antibodies. The amount of GapDH-SSB is similar in the WT, Δ*ypdA* and Δ*brxAB* mutants **(A)** as well as in the *ypdA*, *brxA,* and *brxB* complemented strains **(B)**. The SDS PAGE loading control is shown at the bottom for comparison.

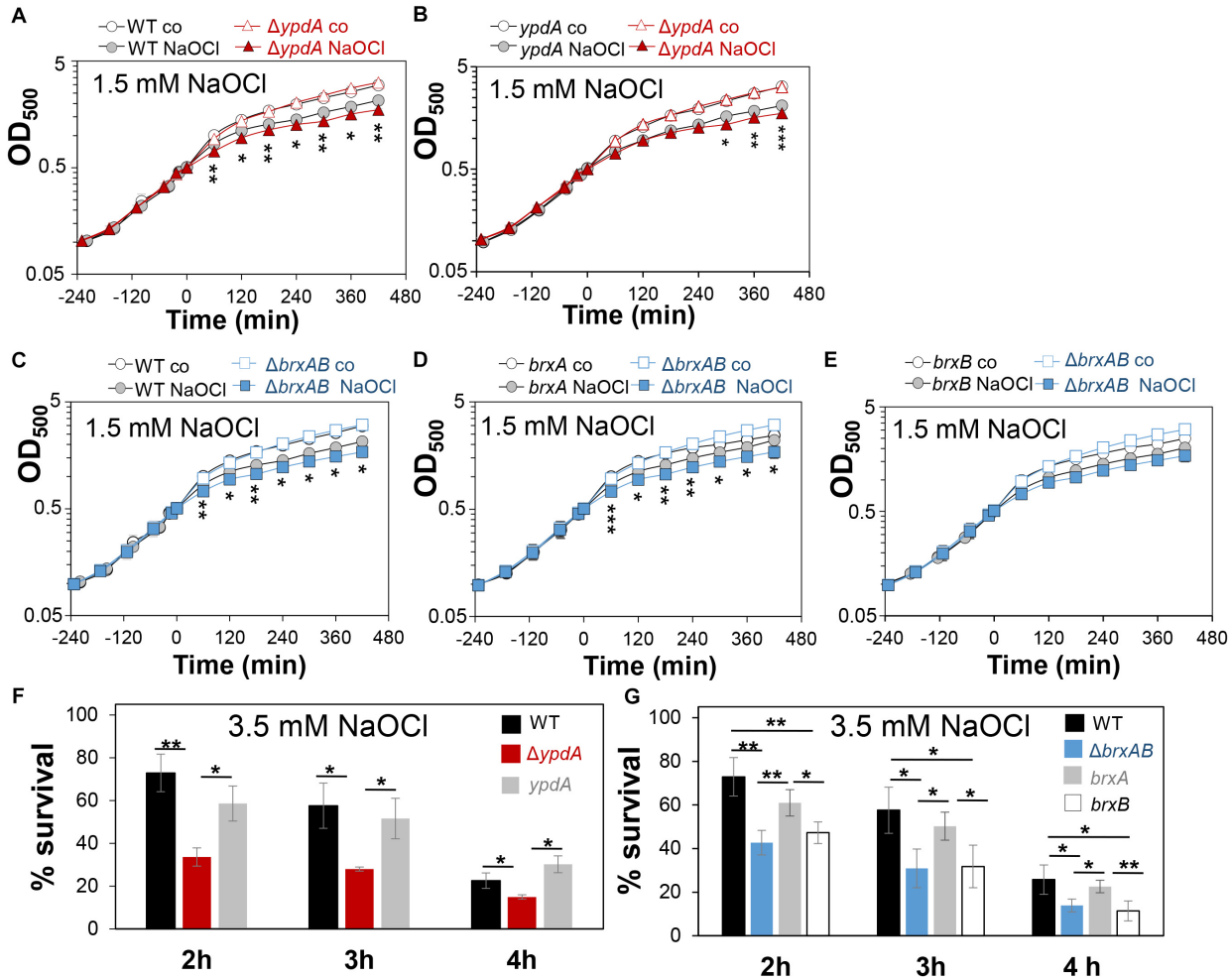

FIGURE 6 | The *S. aureus* Δ*ypdA* and Δ*brxAB* mutants are more sensitive under NaOCl stress. **(A–E)** Growth curves of *S. aureus* COL WT, Δ*ypdA* and Δ*brxAB* mutants as well as *ypdA*, *brxA,* and *brxB* complemented strains in RPMI medium after exposure to 1.5 mM NaOCl stress at an OD_{500} of 0.5. **(F,G)** Survival rates were determined as CFUs for *S. aureus* COL WT, Δ*ypdA* and Δ*brxAB* mutants as well as *ypdA*, *brxA,* and *brxB* complemented strains at 2, 3, and 4 h after treatment with 3.5 mM NaOCl. Survival of the untreated control was set to 100%. Mean values and SD of 3–4 biological replicates are presented. The statistics was calculated using a Student's unpaired two-tailed *t*-test by the graph prism software. Symbols are: $^{ns}p > 0.05$, $^{*}p \leq 0.05$, and $^{**}p \leq 0.01$.

Taken together, our results revealed that the bacilliredoxin BrxA and the putative BSSB reductase YpdA are required for improved survival of *S. aureus* inside macrophages to resist the oxidative burst. Our data suggest that BrxA and YpdA act together in the BrxA/BSH/YpdA pathway to regenerate *S*-bacillithiolated proteins and to restore the BSH redox potential upon recovery from oxidative stress during infections.

The Flavin Disulfide Reductase YpdA Functions in BSSB Reduction and De-Bacillithiolation of GapDH-SSB in the BrxA/BSH/YpdA Electron Transfer Assay *in vitro*

Next, we aimed to analyze the catalytic activity of purified YpdA in a NADPH-coupled assay with BSSB as substrate *in vitro,* since biochemical evidence for the function of YpdA as BSSB reductase activity *in vitro* is still missing (Mikheyeva et al., 2019). The His-tagged YpdA protein was purified as yellow colored enzyme and the UV-visible spectrum revealed the presence of the FAD co-factor indicated by the two absorbance peaks at 375 and 450 nm (**Supplementary Figure S9**). Incubation of YpdA protein with BSSB resulted in significant and fast consumption of NADPH as measured by a rapid absorbance decrease at 340 nm (**Figure 9A**). Only little NADPH consumption was measured with YpdA alone in the absence of the BSSB substrate supporting previous finding that YpdA consumes NADPH alone (Mikheyeva et al., 2019). However, in our assays, BSSB significantly enhanced NADPH consumption by YpdA compared to the control reaction without BSSB. No increased NADPH consumption was measured with coenzyme A disulphide ($CoAS_2$) or GSSG as substrate indicating the specificity of YpdA for BSSB (**Figure 9A**). In addition, we investigated the role of the conserved Cys14 of YpdA for the BSSB reductase activity in the NADPH-coupled assay.

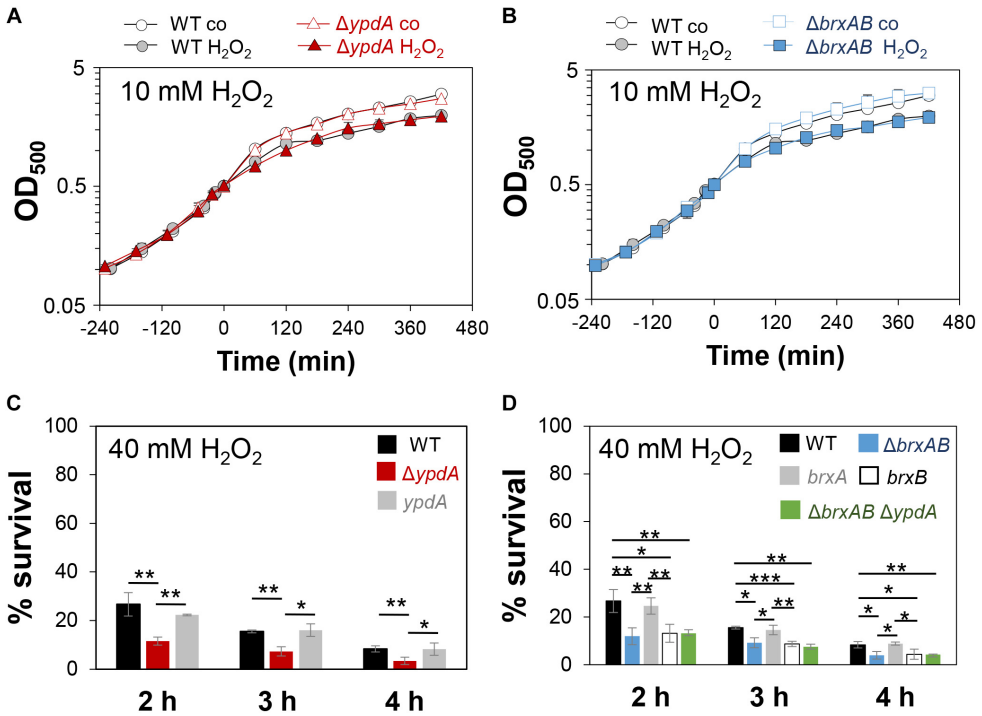

FIGURE 7 | The *S. aureus* Δ*ypdA* and Δ*brxAB* mutants show increased sensitivities to H_2O_2 stress. **(A,B)** Growth curves of *S. aureus* COL WT, the Δ*ypdA* and Δ*brxAB* mutants in RPMI after exposure to 10 mM H_2O_2 stress at an OD_{500} of 0.5. **(C,D)** Survival rates were determined as CFUs for *S. aureus* COL WT, Δ*ypdA*, Δ*brxAB* and Δ*brxAB*Δ*ypdA* mutants as well as *ypdA*, *brxA*, *brxB* complemented strains at 2, 3, and 4 h after treatment with 40 mM H_2O_2. Survival of the untreated control was set to 100%. Mean values and SD of 3–5 biological replicates are presented. The statistics was calculated using a Student's unpaired two-tailed *t*-test by the graph prism software. Symbols are: $^{ns}p > 0.05$, $^{*}p \leq 0.05$, and $^{**}p \leq 0.01$.

NADPH-consumption of YpdAC14A upon BSSB reduction was much slower and similar to the control reaction of YpdA and YpdAC14A without BSSB (**Figure 9B**).

Our *in vivo* data support that YpdA and BrxA act together in the BrxA/BSH/YpdA de-bacillithiolation pathway. Thus, we analyzed NADPH-consumption by the BrxA/BSH/YpdA electron pathway in de-bacillithiolation of GapDH-SSB *in vitro*. The de-bacillithiolation assays revealed fast NADPH consumption in the complete BrxA/BSH/YpdA coupled assays (**Figure 9C**). NADPH consumption by YpdA was slower in the absence of BrxA and might be caused by residual BSSB in the BSH samples. The control reaction of GapDH-SSB with BrxA did not consume NADPH and only little NADPH consumption was measured with BrxA, BSH and the YpdAC14A mutant protein in de-bacillithiolation of GapDH-SSB (**Figure 9D**).

In addition, BSH-specific non-reducing Western blots were used to investigate if BrxA and the complete BrxA/BSH/YpdA pathway catalyze de-bacillithiolation of GapDH-SSB (**Figure 9E**). The BSH-blots showed that BrxA is sufficient for de-bacillithiolation of GapDH-SSB, since all reactions of GapDH-SSB with BrxA lead to complete de-bacillithiolation with and without YpdA or YpdAC14A plus NADPH. However, the reactions of GapDH-SSB with YpdA/NADPH alone did not lead to reduction of GapDH-SSB, indicating the main role of BrxA in de-bacillithiolation while YpdA functions in regeneration of BSH in the BrxA/BSH/YpdA/NADPH redox cycle.

In conclusion, our biochemical assays revealed that YpdA functions as BSSB reductase in an NADPH coupled assay. Cys14 of YpdA is important for the BSSB reductase activity *in vitro*. Thus, YpdA facilitates together with BrxA the reduction of *S*-bacillithiolated GapDH in the BrxA/BSH/YpdA redox pathway upon recovery from oxidative stress.

DISCUSSION

The putative disulfide reductase YpdA was previously shown to be phylogenetically associated with the BSH biosynthesis enzymes and bacilliredoxins (**Supplementary Figure S2**), providing evidence for a functional Brx/BSH/YpdA pathway in BSH-producing bacteria (Gaballa et al., 2010). Recent work confirmed the importance of YpdA for the BSH/BSSB redox balance and survival under oxidative stress and neutrophil infections in *S. aureus in vivo* (Mikheyeva et al., 2019). Here, we have studied the role of the bacilliredoxins BrxA/B and the BSSB reductase YpdA in the defense of *S. aureus* against oxidative stress *in vivo* and their biochemical function in the de-bacillithiolation pathway *in vitro*. Transcription of *brxA*, *brxB* and *ypdA* is strongly upregulated under disulfide stress, provoked by diamide and NaOCl. About two to fourfold increased transcription of *ypdA*, *brxA*, and *brxB* was previously found under H_2O_2, diamide and NaOCl stress, by the antimicrobial surface coating

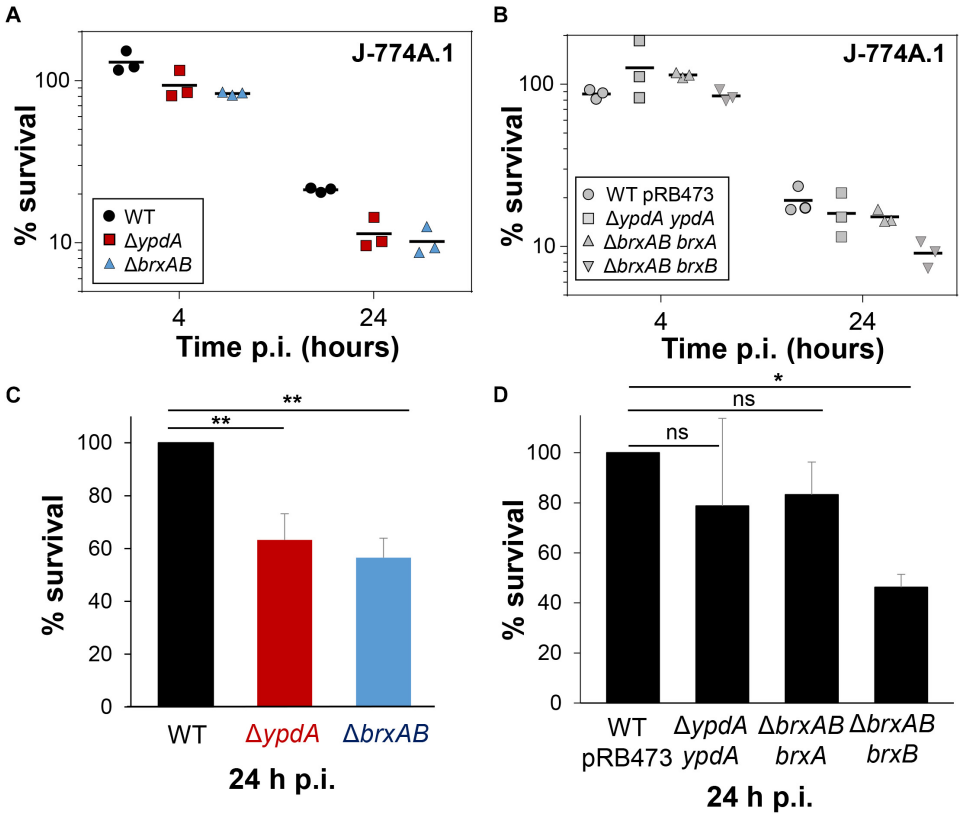

FIGURE 8 | YpdA and BrxA/B promote the intracellular survival of *S. aureus* inside murine macrophages during infections. **(A,B)** The survival of *S. aureus* WT, Δ*ypdA* and Δ*brxAB* mutants and complemented strains was analyzed 2, 4 and 24 h post infection (p.i.) of the murine macrophage cell line J-774A.1 by CFU counting. The percentages in survival of the Δ*ypdA* and Δ*brxAB* mutants and complemented strains were calculated after 4 and 24 h in relation to the 2 h time point, which was set to 100%. **(C,D)** The average percentage in survival was calculated for Δ*ypdA* and Δ*brxAB* mutants **(C)** and complemented strain **(D)** in relation to the WT and WT with empty plasmid pRB473, which were set to 100%. Error bars represent the SEM and the statistics were calculated using one-way ANOVA and Tukey's multiple comparisons *post hoc* test using the graph prism software ($p = 0.0050$ for WT/Δ*ypdA*, $p = 0.0022$ for WT/Δ*brxAB* and $p = 0.026$ for WT pRB473/Δ*brxAB brxB*). Symbols: $^{ns}p > 0.05$; $^{*}p \leq 0.05$, and $^{**}p \leq 0.01$.

composed of Ag^+ and Ru^+ (AGXX®) and after exposure to azurophilic granule proteins in *S. aureus* (Palazzolo-Ballance et al., 2008; Posada et al., 2014; Mäder et al., 2016; Loi et al., 2018a,b; Mikheyeva et al., 2019). The elevated transcription of *brxA, brxB,* and *ypdA* under disulfide stress correlated with the up-regulation of the *bshA*, *bshB,* and *bshC* genes for BSH biosynthesis in *S. aureus* and *B. subtilis* (Chi et al., 2011; Nicolas et al., 2012; Loi et al., 2018a,b). The *bshA, bshB,* and *bshC* genes and operons are under control of the disulfide stress-specific Spx regulator in *B. subtilis,* which controls a large regulon for thiol-redox homeostasis (Gaballa et al., 2013). Thus, genes for BSH biosynthesis and the BrxA/B/YpdA pathway might be also regulated by Spx in *S. aureus*.

The co-regulation of BrxA/B and YpdA under disulfide stress points to their function in the same pathway in *S. aureus*. HOCl, diamide and AGXX® were shown to cause a strong disulfide stress response in the transcriptome and protein *S*-bacillithiolation in the proteome of *S. aureus* (Imber et al., 2018a; Loi et al., 2018a,b). Thus, the BrxA/B and YpdA redox enzymes are up-regulated under conditions of protein *S*-bacillithiolations, connecting their functions to the de-bacillithiolation pathway. We could show here that NaOCl stress leads to five to sixfold depletion of the cellular pool of reduced BSH in the *S. aureus* COL wild type, which was not accompanied by an enhanced BSSB level. In the previous study, 20 mM H_2O_2 resulted in twofold reduction of BSH and threefold increase of BSSB in the *S. aureus* wild type (Mikheyeva et al., 2019). Most probably, the increased BSSB level under NaOCl stress was used for protein *S*-bacillithiolation in our study (Imber et al., 2018a), while sub-lethal 20 mM H_2O_2 might not lead to an increase in *S*-bacillithiolation in the previous study (Mikheyeva et al., 2019).

The BSH/BSSB redox ratio of *S. aureus* wild type cells was determined as ∼35:1 under control conditions and decreased threefold to 10:1 under NaOCl. Of note, this basal BSH/BSSB ratio in *S. aureus* COL wild type was higher compared to the basal BSH/BSSB ratio of ∼17:1 as determined previously in the *bshC* repaired SH1000 strain (Mikheyeva et al., 2019). In *E. coli*, the GSH/GSSG redox ratio was determined in the range between 30:1 and 100:1 (Hwang et al., 1995; Van Laer et al., 2013), which is similar as measured for the basal BSH/BSSB ratio in *S. aureus* COL. The differences in the BSH/BSSB ratios might be related to different *S. aureus* strain

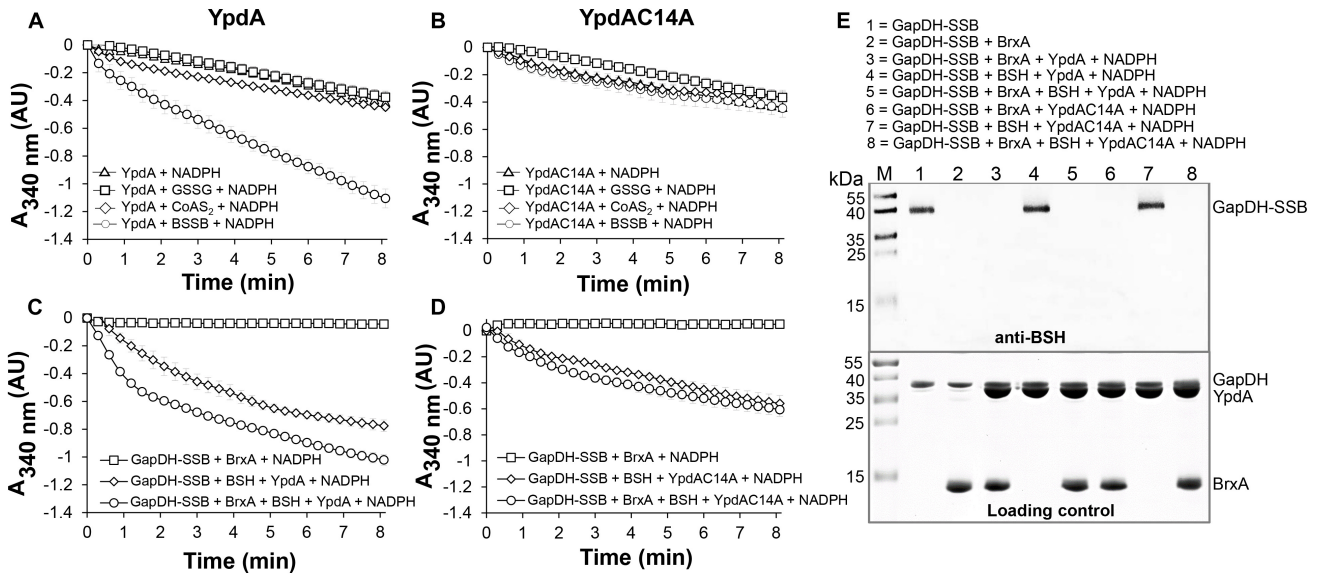

FIGURE 9 | YpdA functions as BSSB reductase in the NADPH-coupled BrxA/BSH/YpdA electron pathway for de-bacillithiolation of GapDH-SSB *in vitro*. **(A)** Purified YpdA is able to reduce BSSB back to BSH with electrons from NADPH as measured by the absorbance change at 340 nm. Only little NADPH consumption was measured with YpdA alone in the absence of BSSB, with coenzymeA disulfide (CoAS2) or glutathione disulfide (GSSG) **(A)** and in the YpdAC14A mutant **(B)** indicating the function of the conserved Cys14 as active site of YpdA for BSSB reduction. **(C)** NADPH consumption of YpdA was measured in the coupled BrxA/BSH/YpdA de-bacillithiolation assay for reduction of GapDH-SSB. While fast NADPH consumption was measured upon de-bacillithiolation of GapDH-SSB with purified YpdA **(C)**, the reaction was much slower with the YpdAC14A mutant **(D)**. The coupled assays were conducted with 2.5 μM Gap-SSB, 12.5 μM BrxA, 40 μM BSH, 500 μM NADPH in 20 mM Tris, 1.25 mM EDTA, pH 8.0. After 30-min incubation, 12.5 μM YpdA or YpdAC14A proteins were added to the reaction mix and NADPH consumption was monitored at 340 nm as a function of time. Mean values and SEM of four independent experiments are shown. **(E)** The de-bacillithiolation of GapDH-SSB is catalyzed by BrxA or the complete BrxA/BSH/YpdA pathway, but not by YpdA alone as shown by non-reducing BSH-specific Western blots. The loading controls are shown below as Coomassie-stained SDS-PAGE with the same de-bacillithiolation reactions of GapDH-SSB as in the BSH-blot.

backgrounds or growth conditions. Nevertheless, NaOCl and H_2O_2 decreased the BSH/BSSB ratio in our and the previous study (Mikheyeva et al., 2019). In the *S. aureus* Δ*brxAB* mutant, we also measured a threefold decrease of the BSH/BSSB ratio from control conditions (38:1) to NaOCl (12:1). However, the Δ*ypdA* mutant showed a twofold enhanced BSSB level in control and NaOCl-treated cells, leading to a significantly decreased BSH/BSSB ratio under control (17:1) and NaOCl stress (5:1). These results support previous results of the *bshC* repaired SH1000, showing a decreased BSH/BSSB ratio under control (6:1) to H_2O_2 stress (2:1) (Mikheyeva et al., 2019), although both ratios were again much lower as in our study. Taken together, our data indicate that BrxAB are dispensable for the BSH redox homeostasis, while YpdA is essential for BSSB reduction to maintain the reduced pool of BSH and a high BSH/BSSB ratio in *S. aureus*.

Brx-roGFP2 biosensor measurements provide further support that YpdA is the candidate BSSB reductase. The Δ*ypdA* mutant was significantly impaired to restore reduced E_{BSH} during recovery from NaOCl and H_2O_2 stress as calculated using the Nernst equation based on the OxD values of the Brx-roGFP2 biosensor measurements (**Supplementary Tables S5, S6**). Moreover, application of the Tpx-roGFP2 biosensor revealed a delay in H_2O_2 detoxification in Δ*ypdA* mutant cells during the recovery phase. These results clearly support the important role of YpdA as BSSB reductase particularly under oxidative stress to recover reduced E_{BSH} required for detoxification of ROS.

These *in vivo* data were further corroborated by biochemical activity assays of YpdA for BSSB reduction in a NADPH-coupled assay. While little NADPH consumption was measured in the presence of YpdA alone, BSSB significantly enhanced NADPH consumption, supporting the crucial role of YpdA as BSSB reductase *in vitro*. Further electron transfer assays revealed that YpdA functions together with BrxA and BSH in reduction of GapDH-SSB *in vitro*. Previous de-bacillithiolation assays have revealed regeneration of GapDH activity by BrxA *in vitro* (Imber et al., 2018a). Here, we confirmed that BrxA activity is sufficient for complete de-bacillithiolation of GapDH-SSB *in vitro*, while YpdA alone had no effect on the GapDH-SSB reduction. Thus, BrxA catalyzes reduction of *S*-bacillithiolated proteins and YpdA is involved in BSH regeneration in the complete BrxA/BSH/YpdA redox cycle.

The BSSB reductase activity of YpdA was shown to be dependent on the conserved Cys14, which is located in the glycine-rich Rossmann-fold NAD(P)H binding domain ($GGGPC_{14}G$) (Bragg et al., 1997; Mikheyeva et al., 2019). Cys14 might be *S*-bacillithiolated by BSSB and reduced by electron transfer from NADPH via the FAD co-factor. Cys14 was previously identified as oxidized under NaOCl stress in the *S. aureus* redox proteome using the OxICAT method, further supporting its role as active site Cys and its *S*-bacillithiolation

during the BrxA/BSH/YpdA catalytic cycle (Imber et al., 2018a). The catalytic mechanism of BSSB reduction via Cys14 of YpdA is an interesting subject of future studies.

Previous phenotype results of the Δ*ypdA* mutant revealed that YpdA is important for survival of *S. aureus* in infection assays with human neutrophils (Mikheyeva et al., 2019). Our phenotype analyses further showed protective functions of the complete BrxA/BSH/YpdA redox pathway for growth and survival of *S. aureus* under oxidative stress *in vitro* and in macrophage infections *in vivo*. The Δ*ypdA* and Δ*brxAB* mutants were significantly impaired in growth and survival after exposure to sub-lethal and lethal doses of NaOCl and displayed survival defects under lethal H_2O_2. Moreover, the H_2O_2 and NaOCl-sensitivity and the defect to recover reduced E_{BSH} in the Δ*brxAB*Δ*ypdA* triple mutant was comparable with that of the Δ*ypdA* mutant (**Figure 7D** and **Supplementary Figure S8**). These results clearly indicate that BrxA/B and YpdA function in the same de-bacillithiolation pathway, which is an important defense mechanism of *S. aureus* against oxidative stress.

Based on previous bacilliredoxin activity assays *in vitro*, both BrxA and BrxB should use a monothiol mechanism to reduce *S*-bacillithiolated client proteins, such as OhrR, GapDH and MetE in *B. subtilis* and *S. aureus* (Gaballa et al., 2014; Imber et al., 2018a). Most di-thiol Grx of *E. coli* (Grx1, Grx2, and Grx3) use the monothiol mechanism for de-glutathionylation of proteins (Lillig et al., 2008; Allen and Mieyal, 2012; Loi et al., 2015). In the monothiol mechanism, the nucleophilic thiolate of the Brx CGC motif attacks the *S*-bacillithiolated protein, resulting in reduction of the protein substrate and Brx-SSB formation. Brx-SSB is then recycled by BSH, leading to increased BSSB formation. YpdA reduces BSSB back to BSH with electrons from NADPH (**Figure 1B**). The oxidation-sensitive phenotypes of Δ*ypdA* and Δ*brxAB* mutants could be complemented by plasmid-encoded *ypdA* and *brxA*, but not *brxB*, respectively. These results provide evidence for the function of the BrxA/BSH/YpdA de-bacillithiolation pathway using the monothiol-Brx mechanism in *S. aureus*.

Similar phenotypes were found for mutants lacking related redox enzymes of the GSH and mycothiol pathways in other bacteria. In *E. coli*, strains lacking the Gor and Grx are more sensitive under diamide and cumene hydroperoxide stress (Alonso-Moraga et al., 1987; Vlamis-Gardikas et al., 2002; Lillig et al., 2008). In *Mycobacterium smegmatis*, the mycoredoxin-1 mutant displayed an oxidative stress-sensitive phenotype (Van Laer et al., 2012). In *Corynebacterium glutamicum*, deficiency of the Mtr resulted in an oxidized mycothiol redox potential (Tung et al., 2019), and Mtr overexpression contributed to improved oxidative stress resistance (Si et al., 2016). Taken together, our results revealed that not only BSH, but also BrxA and YpdA are required for virulence and promote survival in infection assays inside murine macrophages.

In several human pathogens, such as *Streptococcus pneumoniae, Listeria monocytogenes, Salmonella Typhimurium*, and *Pseudomonas aeruginosa*, LMW thiols or the Gor are required for virulence, colonization and to resist host-derived oxidative or nitrosative stress (Potter et al., 2012; Song et al., 2013; Reniere et al., 2015; Tung et al., 2018; Wongsaroj et al., 2018). *S. aureus* BSH deficient mutants showed decreased survival in murine macrophages and in human whole blood infections (Pöther et al., 2013; Posada et al., 2014). The virulence mechanisms might be related to a lack of BSH regeneration and decreased recovery of inactivated *S*-bacillithiolated proteins inside macrophages. Future studies should elucidate the targets for *S*-bacillithiolations that are reduced by the BrxA/BSH/YpdA pathway inside macrophages, increasing survival, metabolism or persistence under infections.

In summary, our results showed the importance of the BrxA/BSH/YpdA redox pathway to resist oxidative stress and macrophage infection in *S. aureus*. Through measurements of the BSH/BSSB redox ratio and E_{BSH}, we provide evidence that the NADPH-dependent disulfide reductase YpdA regenerates BSH and restores reduced E_{BSH} upon recovery from oxidative stress in *S. aureus*. Finally, biochemical evidence for YpdA as BSSB reductase and for the role of BrxA/BSH/YpdA pathway in de-bacillithiolation was provided *in vitro*. The detailed biochemical mechanism of YpdA and the cross-talk of the Trx and Brx systems in de-bacillithiolation under oxidative stress and infections are subject of our future studies.

AUTHOR CONTRIBUTIONS

HA and NL designed the experiments of this study. NL, VVL, VNF, QNT and SS constructed the mutants, performed the experiments and analyzed the data of this manuscript. MW and RH performed the HPLC thiol metabolomics analyses and analyzed the data. KT and MF contributed with the infection assays to this work. CH synthesized BSH and BSSB for the biochemical assays of the manuscript. NL and HA wrote the manuscript. All authors contributed with corrections of the manuscript.

FUNDING

In this work, HA was supported by an ERC Consolidator Grant (GA 615585) MYCOTHIOLOME and grants from the Deutsche Forschungsgemeinschaft (AN746/4-1 and AN746/4-2) within the SPP1710, by the SFB973 project C08N, and by the SFB/TR84 project B06. We further thank funding by the SPP1710 grants HE1848/16-1 and WI3560/2-1 to RH and MW.

ACKNOWLEDGMENTS

We acknowledge support by the Open Access Publication Initiative of Freie Universität Berlin.

SUPPLEMENTARY MATERIAL

The Supplementary Material for this article can be found online at: https://www.frontiersin.org/articles/10.3389/fmicb.2019.01355/full#supplementary-material

REFERENCES

Allen, E. M., and Mieyal, J. J. (2012). Protein-thiol oxidation and cell death: regulatory role of glutaredoxins. *Antioxid. Redox Signal*. 17, 1748–1763. doi: 10.1089/ars.2012.4644

Alonso-Moraga, A., Bocanegra, A., Torres, J. M., Lopez-Barea, J., and Pueyo, C. (1987). Glutathione status and sensitivity to GSH-reacting compounds of *Escherichia coli* strains deficient in glutathione metabolism and/or catalase activity. *Mol. Cell Biochem.* 73, 61–68.

Archer, G. L. (1998). *Staphylococcus aureus*: a well-armed pathogen. *Clin. Infect. Dis.* 26, 1179–1181. doi: 10.1086/520289

Argyrou, A., and Blanchard, J. S. (2004). Flavoprotein disulfide reductases: advances in chemistry and function. *Progr. Nucleic Acid Res. Mol. Biol.* 78, 89–142. doi: 10.1016/s0079-6603(04)78003-4

Arnaud, M., Chastanet, A., and Débarbouillé, M. (2004). New vector for efficient allelic replacement in naturally nontransformable, low-GC-content, gram-positive bacteria. *Appl. Environ. Microbiol.* 70, 6887–6891. doi: 10.1128/aem.70.11.6887-6891.2004

Beavers, W. N., and Skaar, E. P. (2016). Neutrophil-generated oxidative stress and protein damage in *Staphylococcus aureus*. *Pathog. Dis.* 74:ftw060. doi: 10.1093/femspd/ftw060

Boucher, H. W., and Corey, G. R. (2008). Epidemiology of methicillin-resistant *Staphylococcus aureus*. *Clin. Infect Dis.* 46(Suppl. 5), S344–S349. doi: 10.1086/533590

Bragg, P. D., Glavas, N. A., and Hou, C. (1997). Mutation of conserved residues in the NADP(H)-binding domain of the proton translocating pyridine nucleotide transhydrogenase of *Escherichia coli*. *Arch. Biochem. Biophys.* 338, 57–66. doi: 10.1006/abbi.1996.9797

Brückner, R., Wagner, E., and Götz, F. (1993). Characterization of a sucrase gene from *Staphylococcus xylosus*. *J. Bacteriol.* 175, 851–857. doi: 10.1128/jb.175.3.851-857.1993

Chandrangsu, P., Loi, V. V., Antelmann, H., and Helmann, J. D. (2018). The role of bacillithiol in Gram-positive *Firmicutes*. *Antioxid. Redox Signal.* 28, 445–462. doi: 10.1089/ars.2017.7057

Chi, B. K., Gronau, K., Mäder, U., Hessling, B., Becher, D., and Antelmann, H. (2011). *S*-bacillithiolation protects against hypochlorite stress in *Bacillus subtilis* as revealed by transcriptomics and redox proteomics. *Mol. Cell Proteo.* 10:M111009506. doi: 10.1074/mcp.M111.009506

Chi, B. K., Roberts, A. A., Huyen, T. T., Bäsell, K., Becher, D., Albrecht, D., et al. (2013). *S*-bacillithiolation protects conserved and essential proteins against hypochlorite stress in *Firmicutes* bacteria. *Antioxid. Redox Signal.* 18, 1273–1295. doi: 10.1089/ars.2012.4686

Deponte, M. (2013). Glutathione catalysis and the reaction mechanisms of glutathione-dependent enzymes. *Biochim. Biophys. Acta* 1830, 3217–3266. doi: 10.1016/j.bbagen.2012.09.018

Dooley, C. T., Dore, T. M., Hanson, G. T., Jackson, W. C., Remington, S. J., and Tsien, R. Y. (2004). Imaging dynamic redox changes in mammalian cells with green fluorescent protein indicators. *J. Biol. Chem.* 279, 22284–22293. doi: 10.1074/jbc.m312847200

Fahey, R. C. (2013). Glutathione analogs in prokaryotes. *Biochim. Biophys. Acta* 1830, 3182–3198. doi: 10.1016/j.bbagen.2012.10.006

Fuangthong, M., Atichartpongkul, S., Mongkolsuk, S., and Helmann, J. D. (2001). OhrR is a repressor of *ohrA*, a key organic hydroperoxide resistance determinant in *Bacillus subtilis*. *J. Bacteriol.* 183, 4134–4141. doi: 10.1128/jb.183.14.4134-4141.2001

Gaballa, A., Antelmann, H., Hamilton, C. J., and Helmann, J. D. (2013). Regulation of *Bacillus subtilis* bacillithiol biosynthesis operons by Spx. *Microbiology* 159, 2025–2035. doi: 10.1099/mic.0.070482-0

Gaballa, A., Chi, B. K., Roberts, A. A., Becher, D., Hamilton, C. J., Antelmann, H., et al. (2014). Redox regulation in *Bacillus subtilis*: The bacilliredoxins BrxA(YphP) and BrxB(YqiW) function in de-bacillithiolation of S-bacillithiolated OhrR and MetE. *Antioxid. Redox Signal.* 21, 357–367. doi: 10.1089/ars.2013.5327

Gaballa, A., Newton, G. L., Antelmann, H., Parsonage, D., Upton, H., Rawat, M., et al. (2010). Biosynthesis and functions of bacillithiol, a major low-molecular-weight thiol in Bacilli. *Proc. Natl. Acad. Sci. U.S.A.* 107, 6482–6486. doi: 10.1073/pnas.1000928107

Hillion, M., and Antelmann, H. (2015). Thiol-based redox switches in prokaryotes. *Biol. Chem.* 396, 415–444. doi: 10.1515/hsz-2015-0102

Hiras, J., Sharma, S. V., Raman, V., Tinson, R. A. J., Arbach, M., Rodrigues, D. F., et al. (2018). Physiological studies of *Chlorobiaceae* suggest that bacillithiol derivatives are the most widespread thiols in bacteria. *MBio* 9:e01603-18. doi: 10.1128/mBio.01603-18

Hwang, C., Lodish, H. F., and Sinskey, A. J. (1995). Measurement of glutathione redox state in cytosol and secretory pathway of cultured cells. *Methods Enzymol.* 251, 212–221. doi: 10.1016/0076-6879(95)51123-7

Imber, M., Huyen, N. T. T., Pietrzyk-Brzezinska, A. J., Loi, V. V., Hillion, M., Bernhardt, J., et al. (2018a). Protein *S*-bacillithiolation functions in thiol protection and redox regulation of the glyceraldehyde-3-phosphate dehydrogenase Gap in *Staphylococcus aureus* under hypochlorite stress. *Antioxid. Redox Signal.* 28, 410–430. doi: 10.1089/ars.2016.6897

Imber, M., Loi, V. V., Reznikov, S., Fritsch, V. N., Pietrzyk-Brzezinska, A. J., Prehn, J., et al. (2018b). The aldehyde dehydrogenase AldA contributes to the hypochlorite defense and is redox-controlled by protein *S*-bacillithiolation in *Staphylococcus aureus*. *Redox. Biol.* 15, 557–568. doi: 10.1016/j.redox.2018.02.001

Imber, M., Pietrzyk-Brzezinska, A. J., and Antelmann, H. (2018c). Redox regulation by reversible protein *S*-thiolation in Gram-positive bacteria. *Redox. Biol.* 20, 130–145. doi: 10.1016/j.redox.2018.08.017

Lee, J. W., Soonsanga, S., and Helmann, J. D. (2007). A complex thiolate switch regulates the *Bacillus subtilis* organic peroxide sensor OhrR. *Proc. Natl. Acad. Sci. U.S.A.* 104, 8743–8748. doi: 10.1073/pnas.0702081104

Lillig, C. H., Berndt, C., and Holmgren, A. (2008). Glutaredoxin systems. *Biochim. Biophys. Acta* 1780, 1304–1317. doi: 10.1016/j.bbagen.2008.06.003

Livermore, D. M. (2000). Antibiotic resistance in staphylococci. *Int. J. Antimicrob. Agents* 16(Suppl. 1), S3–S10.

Loi, V. V., Busche, T., Preuss, T., Kalinowski, J., Bernhardt, J., and Antelmann, H. (2018a). The AGXX antimicrobial coating causes a thiol-specific oxidative stress response and protein S-bacillithiolation in *Staphylococcus aureus*. *Front. Microbiol.* 9:3037. doi: 10.3389/fmicb.2018.03037

Loi, V. V., Busche, T., Tedin, K., Bernhardt, J., Wollenhaupt, J., Huyen, N. T. T., et al. (2018b). Redox-sensing under hypochlorite stress and infection conditions by the Rrf2-family repressor HypR in *Staphylococcus aureus*. *Antioxid. Redox Signal.* 29, 615–636. doi: 10.1089/ars.2017.7354

Loi, V. V., Harms, M., Müller, M., Huyen, N. T. T., Hamilton, C. J., Hochgräfe, F., et al. (2017). Real-time imaging of the bacillithiol redox potential in the human pathogen *Staphylococcus aureus* using a genetically encoded bacilliredoxin-fused redox biosensor. *Antioxid. Redox Signal.* 26, 835–848. doi: 10.1089/ars.2016.6733

Loi, V. V., Rossius, M., and Antelmann, H. (2015). Redox regulation by reversible protein *S*-thiolation in bacteria. *Front. Microbiol.* 6:187. doi: 10.3389/fmicb.2015.00187

Lowy, F. D. (1998). *Staphylococcus aureus* infections. *N. Engl. J. Med.* 339, 520–532.

Mäder, U., Nicolas, P., Depke, M., Pane-Farre, J., Debarbouille, M., Van Der Kooi-Pol, M. M., et al. (2016). *Staphylococcus aureus* transcriptome architecture: from laboratory to infection-mimicking conditions. *PLoS Genet.* 12:e1005962. doi: 10.1371/journal.pgen.1005962

Mikheyeva, I. V., Thomas, J. M., Kolar, S. L., Corvaglia, A. R., Gaiotaa, N., Leo, S., et al. (2019). YpdA, a putative bacillithiol disulfide reductase, contributes to cellular redox homeostasis and virulence in *Staphylococcus aureus*. *Mol. Microbiol.* 111, 1039–1056. doi: 10.1111/mmi.14207

Newton, G. L., Fahey, R. C., and Rawat, M. (2012). Detoxification of toxins by bacillithiol in *Staphylococcus aureus*. *Microbiology* 158, 1117–1126. doi: 10.1099/mic.0.055715-0

Nicolas, P., Mäder, U., Dervyn, E., Rochat, T., Leduc, A., Pigeonneau, N., et al. (2012). Condition-dependent transcriptome reveals high-level regulatory architecture in *Bacillus subtilis*. *Science* 335, 1103–1106. doi: 10.1126/science.1206848

Palazzolo-Ballance, A. M., Reniere, M. L., Braughton, K. R., Sturdevant, D. E., Otto, M., Kreiswirth, B. N., et al. (2008). Neutrophil microbicides induce a pathogen survival response in community-associated methicillin-resistant *Staphylococcus aureus*. *J. Immunol.* 180, 500–509. doi: 10.4049/jimmunol.180.1.500

Pendleton, J. N., Gorman, S. P., and Gilmore, B. F. (2013). Clinical relevance of the ESKAPE pathogens. *Expert Rev. Anti. Infect. Ther.* 11, 297–308. doi: 10.1586/eri.13.12

Posada, A. C., Kolar, S. L., Dusi, R. G., Francois, P., Roberts, A. A., Hamilton, C. J., et al. (2014). Importance of bacillithiol in the oxidative stress response of *Staphylococcus aureus*. *Infect. Immun.* 82, 316–332. doi: 10.1128/IAI.01074-13

Pöther, D. C., Gierok, P., Harms, M., Mostertz, J., Hochgräfe, F., Antelmann, H., et al. (2013). Distribution and infection-related functions of bacillithiol in *Staphylococcus aureus*. *Int. J. Med. Microbiol.* 303, 114–123. doi: 10.1016/j.ijmm.2013.01.003

Potter, A. J., Trappetti, C., and Paton, J. C. (2012). *Streptococcus pneumoniae* uses glutathione to defend against oxidative stress and metal ion toxicity. *J. Bacteriol.* 194, 6248–6254. doi: 10.1128/JB.01393-12

Reniere, M. L., Whiteley, A. T., Hamilton, K. L., John, S. M., Lauer, P., Brennan, R. G., et al. (2015). Glutathione activates virulence gene expression of an intracellular pathogen. *Nature* 517, 170–173. doi: 10.1038/nature14029

Rosenblum, E. D., and Tyrone, S. (1964). Serology, density, and morphology of staphylococcal phages. *J. Bacteriol.* 88, 1737–1742.

Si, M., Zhao, C., Zhang, B., Wei, D., Chen, K., Yang, X., et al. (2016). Overexpression of mycothiol disulfide reductase enhances *Corynebacterium glutamicum* robustness by modulating cellular redox homeostasis and antioxidant proteins under oxidative stress. *Sci. Rep.* 6:29491. doi: 10.1038/srep29491

Song, M., Husain, M., Jones-Carson, J., Liu, L., Henard, C. A., and Vazquez-Torres, A. (2013). Low-molecular-weight thiol-dependent antioxidant and antinitrosative defences in *Salmonella* pathogenesis. *Mol. Microbiol.* 87, 609–622. doi: 10.1111/mmi.12119

Tam le, T., Eymann, C., Albrecht, D., Sietmann, R., Schauer, F., Hecker, M., et al. (2006). Differential gene expression in response to phenol and catechol reveals different metabolic activities for the degradation of aromatic compounds in *Bacillus subtilis*. *Environ. Microbiol.* 8, 1408–1427. doi: 10.1111/j.1462-2920.2006.01034.x

Tung, Q. N., Linzner, N., Loi, V. V., and Antelmann, H. (2018). Application of genetically encoded redox biosensors to measure dynamic changes in the glutathione, bacillithiol and mycothiol redox potentials in pathogenic bacteria. *Free Radic. Biol. Med.* 128, 84–96. doi: 10.1016/j.freeradbiomed.2018.02.018

Tung, Q. N., Loi, V. V., Busche, T., Nerlich, A., Mieth, M., Milse, J., et al. (2019). Stable integration of the Mrx1-roGFP2 biosensor to monitor dynamic changes of the mycothiol redox potential in *Corynebacterium glutamicum*. *Redox. Biol.* 20, 514–525. doi: 10.1016/j.redox.2018.11.012

Van Laer, K., Buts, L., Foloppe, N., Vertommen, D., Van Belle, K., Wahni, K., et al. (2012). Mycoredoxin-1 is one of the missing links in the oxidative stress defence mechanism of Mycobacteria. *Mol. Microbiol.* 86, 787–804. doi: 10.1111/mmi.12030

Van Laer, K., Hamilton, C. J., and Messens, J. (2013). Low-molecular-weight thiols in thiol-disulfide exchange. *Antioxid. Redox Signal.* 18, 1642–1653. doi: 10.1089/ars.2012.4964

Vlamis-Gardikas, A., Potamitou, A., Zarivach, R., Hochman, A., and Holmgren, A. (2002). Characterization of *Escherichia coli* null mutants for glutaredoxin 2. *J. Biol. Chem.* 277, 10861–10868.

Wetzstein, M., Völker, U., Dedio, J., Löbau, S., Zuber, U., Schiesswohl, M., et al. (1992). Cloning, sequencing, and molecular analysis of the *dnaK* locus from *Bacillus subtilis*. *J. Bacteriol.* 174, 3300–3310. doi: 10.1128/jb.174.10.3300-3310.1992

Winterbourn, C. C., and Kettle, A. J. (2013). Redox reactions and microbial killing in the neutrophil phagosome. *Antioxid. Redox Signal.* 18, 642–660. doi: 10.1089/ars.2012.4827

Winterbourn, C. C., Kettle, A. J., and Hampton, M. B. (2016). Reactive oxygen species and neutrophil function. *Annu. Rev. Biochem.* 85, 765–792. doi: 10.1146/annurev-biochem-060815-014442

Wongsaroj, L., Saninjuk, K., Romsang, A., Duang-Nkern, J., Trinachartvanit, W., Vattanaviboon, P., et al. (2018). *Pseudomonas aeruginosa* glutathione biosynthesis genes play multiple roles in stress protection, bacterial virulence and biofilm formation. *PLoS One* 13:e0205815. doi: 10.1371/journal.pone.0205815

Conflict of Interest Statement: The authors declare that the research was conducted in the absence of any commercial or financial relationships that could be construed as a potential conflict of interest.

Chapter 3

Thiol-based redox switches in the major pathogen *Staphylococcus aureus*

Nico Linzner[1], Vu Van Loi[1], Verena Nadin Fritsch[1], and Haike Antelmann[1]*

[1]Freie Universität Berlin, Institute of Biology-Microbiology, D-14195, Berlin, Germany

*Corresponding author: haike.antelmann@fu-berlin.de

Published in:
Biological Chemistry 402(3): 333–361, 2021
DOI: https://doi.org/10.1515/hsz-2020-0272

Personal contribution:

Together with all other authors, I was involved in the literature search and writing of initial manuscript sections. My focus was on the sections about the quinone sensing and stress resistance mechanisms, the SrrAB two-component system, and the defense mechanism of *S. aureus* against reactive nitrogen and sulfur species (RNS, RSS).

Review

Nico Linzner, Vu Van Loi, Verena Nadin Fritsch and Haike Antelmann*

Thiol-based redox switches in the major pathogen *Staphylococcus aureus*

https://doi.org/10.1515/hsz-2020-0272
Received August 4, 2020; accepted November 5, 2020;
published online November 23, 2020

Abstract: *Staphylococcus aureus* is a major human pathogen, which encounters reactive oxygen, nitrogen, chlorine, electrophile and sulfur species (ROS, RNS, RCS, RES and RSS) by the host immune system, during cellular metabolism or antibiotics treatments. To defend against redox active species and antibiotics, *S. aureus* is equipped with redox sensing regulators that often use thiol switches to control the expression of specific detoxification pathways. In addition, the maintenance of the redox balance is crucial for survival of *S. aureus* under redox stress during infections, which is accomplished by the low molecular weight (LMW) thiol bacillithiol (BSH) and the associated bacilliredoxin (Brx)/BSH/bacillithiol disulfide reductase (YpdA)/NADPH pathway. Here, we present an overview of thiol-based redox sensors, its associated enzymatic detoxification systems and BSH-related regulatory mechanisms in *S. aureus*, which are important for the defense under redox stress conditions. Application of the novel Brx-roGFP2 biosensor provides new insights on the impact of these systems on the BSH redox potential. These thiol switches of *S. aureus* function in protection against redox active desinfectants and antimicrobials, including HOCl, the AGXX® antimicrobial surface coating, allicin from garlic and the naphthoquinone lapachol. Thus, thiol switches could be novel drug targets for the development of alternative redox-based therapies to combat multi-drug resistant *S. aureus* isolates.

Keywords: bacillithiol; electrophiles; HOCl; ROS; *Staphylococcus aureus*; thiol switches.

***Corresponding author: Haike Antelmann**, Freie Universität Berlin, Institute of Biology-Microbiology, Königin-Luise-Straße 12–16, D-14195 Berlin, Germany, E-mail: haike.antelmann@fu-berlin.de. https://orcid.org/0000-0002-1766-4386
Nico Linzner, Vu Van Loi and Verena Nadin Fritsch, Freie Universität Berlin, Institute of Biology-Microbiology, Königin-Luise-Straße 12–16, D-14195 Berlin, Germany

General introduction into redox stress and thiol switches in *Staphylococcus aureus*

Staphylococcus aureus is an opportunistic human pathogen, which asymptomatically colonizes one quarter of the human population (Foster 2004). However, in the hospital setting and in immunocompromised persons the pathogen can cause many serious diseases, ranging from local skin abscesses to life threatening systemic and chronic infections, such as septicemia, endocarditis and pneumonia (Archer 1998; Boucher and Corey 2008; Lowy 1998). During infections, *S. aureus* has to cope with the oxidative burst of activated macrophages and neutrophils, which is a hallmark of the host innate immune defense (Winterbourn and Kettle 2013; Winterbourn et al. 2016; Ulfig and Leichert 2020). The successful infection with *S. aureus* is enabled by an arsenal of secreted and surface-bound virulence factors to damage host tissues and to evade the host immune defense (Tam and Torres 2019). The increasing prevalence of multiple antibiotic resistant isolates, such as methicillin resistant *S. aureus* (MRSA) poses another health burden since treatment options are limited (Chambers and Deleo 2009; Vestergaard et al. 2019).

During host-pathogen interactions, cellular metabolism, aerobic respiration and antibiotics treatment, *S. aureus* is exposed to various redox active species, including reactive oxygen, electrophile, nitrogen, chlorine and sulfur species (ROS, RES, RNS, RCS, RSS) (Loi et al. 2015). These redox active species affect the cellular redox balance and lead to damages of cellular macromolecules, including proteins, lipids and carbohydrates. As defense mechanism against redox active species, *S. aureus* encodes specific detoxification systems, low molecular weight (LMW) thiols, such as bacillithiol (BSH) and coenzyme A (CoASH) and associated thiol-disulfide oxidoreductases, including the Trx/TrxR/NADPH and Brx/BSH/YpdA/NADPH pathways. These defense mechanisms are directed to neutralize the reactive species or to regenerate oxidized proteins and redox homeostasis and often contribute to resistance and virulence properties of the pathogen.

In addition, specific transcriptional regulators are involved in redox sensing of reactive species, which control defense mechanisms to restore the reduced state of the cytoplasm (Antelmann and Helmann 2011; Chen et al. 2011; Hillion and Antelmann 2015). Redox sensing transcription factors often utilize conserved cysteine residues to sense and respond to redox stress conditions via post-translational thiol modifications, including thiol-disulfide switches as the most common theme (Antelmann and Helmann 2011; Chen et al. 2011; Hillion and Antelmann 2015; Vazquez-Torres 2012). Through innovative mass spectrometry-based redox proteomics approaches, many new thiol switches have been discovered over the past years, which are present in metabolic and redox enzymes, transcription and translation factors. Thiol switches are important regulatory devices from bacteria to men, which alter structure and functions of proteins, often leading to their inactivation and reprogramming of cellular metabolism. Thiol oxidation of redox sensing transcription factors controls specific regulons involved in detoxification pathways or regeneration of redox homeostasis (Antelmann and Helmann 2011; Hillion and Antelmann 2015). Here, we provide an overview of thiol-based redox sensing regulators, the associated detoxification pathways and BSH-related thiol-disulfide reducing systems in the human pathogen *S. aureus*. These defense mechanisms provide resistance and enable survival and efficient adaptation to the host environment contributing to the virulence of this major pathogen.

Sources and thiol chemistry of reactive oxygen, electrophile, chlorine, nitrogen and sulfur species (ROS, RES, RCS, RNS and RSS)

In all organisms, the reduced state of protein thiols in the cytoplasm is maintained by LMW thiols and enzymatic thiol-disulfide reducing systems (Van Laer et al. 2013). *S. aureus* encounters various redox active species during infections by the host immune defense, antibiotic treatment or cellular metabolism, which affects the cellular redox balance, including ROS, RES, RNS, RCS and RSS (Hillion and Antelmann 2015). The most frequent source of ROS is the aerobic respiratory chain, when O_2 is incompletely reduced by stepwise one-electron transfer reactions, generating superoxide anion ($O_2^{\bullet -}$), hydrogen peroxide (H_2O_2) and hydroxyl radicals (OH•) (Figure 1) (Imlay, 2003, 2008). Furthermore, autoxidation of flavin cofactors in redox enzymes contributes to ROS production. In the Fenton reaction, Fe^{2+} and H_2O_2 produce the highly toxic OH•, which can oxidize proteins, lipids and DNA (Forman and Torres 2001; Imlay, 2003, 2008).

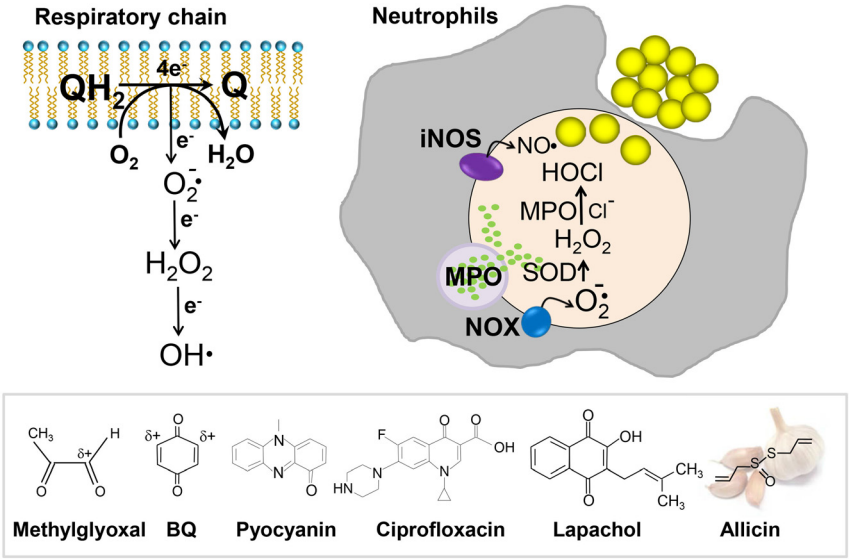

Figure 1: Generation of reactive oxygen, chlorine, nitrogen and electrophile species (ROS, RCS, RNS, RES) during aerobic respiration, infections and antibiotics treatment in *Staphylococcus aureus*. ROS are generated in the respiratory chain by one-electron transfer to O_2, including $O_2\bullet^-$ and H_2O_2. The OH• is produced by reaction of H_2O_2 and Fe^{2+} in the Fenton reaction (Imlay 2003). In activated neutrophils, NOX produces $O_2\bullet^-$, which is dismutated by SOD to H_2O_2. MPO converts H_2O_2 and Cl^- to the bactericidal HOCl (Winterbourn and Kettle 2013). In neutrophils, iNOS synthesizes NO• from arginine. RES include quinones, such as benzoquinone (BQ), which are electron carriers of the respiratory chain (menaquinone) and structural elements of catechol-type siderophores and antibiotics (e.g. pyocyanin, naphthoquinone and ciprofloxacin). Methylglyoxal is produced as toxic aldehyde in the glycolysis. Allicin is an organosulfur compound that acts as antimicrobial.

In addition, pathogens encounter ROS, RCS and RNS generated during the oxidative burst of activated macrophages and neutrophils as the first line defense of the innate immune system, including $O_2^{\bullet-}$, H_2O_2, nitric oxide (NO), and hypochlorous acid (HOCl) (Winterbourn and Kettle 2013; Winterbourn et al. 2016; Ulfig and Leichert 2020). While $O_2^{\bullet-}$ is produced by the membrane-bound NADPH oxidase (NOX) in neutrophils, superoxide dismutase (SOD) dismutates $O_2^{\bullet-}$ to H_2O_2. The myeloperoxidase (MPO) produces the strong oxidant HOCl from H_2O_2 and chloride anion (Cl^-) in neutrophils after degranulation of azurophilic granules (Figure 1) (Winterbourn and Kettle 2013; Winterbourn et al. 2016; Ulfig and Leichert 2020). While low concentrations of 25 µM $O_2^{\bullet-}$ and 2 µM H_2O_2 are produced in the neutrophil phagosome, MPO generates millimolar levels of HOCl, which are released during infections to kill pathogens (Winterbourn et al. 2006).

ROS react with Cys thiols to form unstable sulfenic acids (R-SOH), which are further oxidized to intramolecular or intermolecular protein disulfides or *S*-thiolations of proteins with LMW thiols, such as *S*-bacillithiolations or *S*-CoAlations in *S. aureus* (Figure 2) (Antelmann and Helmann 2011; Imber et al. 2019; Tsuchiya et al. 2018). In the absence of proximal thiols, ROS can irreversibly oxidize Cys thiols to sulfinic (R-SO_2H) or sulfonic acids (R-SO_3H) (Antelmann and Helmann 2011). While H_2O_2 reacts slowly with biological thiols according to second-order rate constants in the range of k = 18–26 $M^{-1}s^{-1}$ (Winterbourn and Metodiewa 1999), the reaction of HOCl with thiols is several orders of magnitude faster and occurs with rate constants of $k > 10^8$ $M^{-1}s^{-1}$ (Storkey et al. 2014). HOCl chlorinates Cys thiols to generate unstable sulfenylchloride (R-SCl), which is further oxidized to form reversible or irreversible thiol oxidation products (Davies 2011; Hawkins et al. 2003). Apart from Cys thiols, HOCl reacts with methionine residues to methionine sulfoxides (Davies 2011; Rosen et al. 2009). The reaction of HOCl with primary amines leads to chloramine formation (Green et al. 2017). Chloramines formed with free amino acids can further decompose to electrophiles, such as glyoxal, acrolein and *p*-hydroxyphenylacetaldehyde, which react with thiols via *S*-alkylation (Beavers and Skaar 2016; Hazen et al. 1998). HOCl can modify proteins by *N*-chlorination as another reversible modification, which activates chaperone functions of proteins (Davies 2011; Hawkins et al. 2003; Müller et al. 2014; Ulfig and Leichert 2020). In *S. aureus* and *Bacillus* species, we have shown that HOCl causes widespread *S*-bacillithiolations of redox sensing regulators and metabolic enzymes, which function in redox regulation of protein activities and protection against overoxidation to Cys sulfonic acids (Chi et al., 2011,2013; Imber et al. 2019).

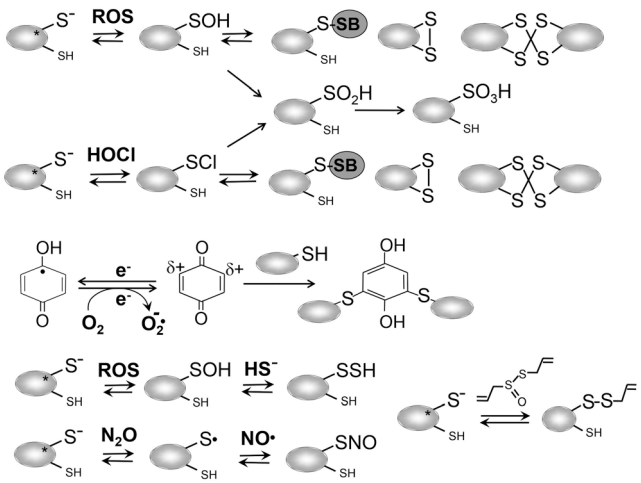

Figure 2: Post-translational thiol modifications of proteins by ROS, RCS, RES, RNS, RSS in *S. aureus*. H_2O_2 causes thiol oxidation of Cys to the Cys-SOH intermediate, which reacts further to protein disulfides or *S*-thiolations, such as *S*-bacillithiolations and *S*-CoAlations. Overoxidation of Cys-SOH leads to Cys-SO_2H or Cys-SO_3H. HOCl causes Cys chlorination to the unstable Cys-SCl, resulting in thiol oxidation to protein disulfides, such as *S*-thiolations (Hawkins et al. 2003). Additionally, Cys-SCl can be overoxidized to Cys-SO_2H or Cys-SO_3H. Quinones modify Cys residues by thiol-*S*-alkylation as electrophiles or by thiol oxidation as oxidants. As oxidants, quinones are reduced to semiquinone anions, leading to ROS generation. HS^- reacts with Cys-SOH or protein disulfides (not shown here) leading to persulfidations (Cys-SSH) (Walsh and Giedroc 2020). Allicin leads to *S*-thioallylation of thiols. NO• reacts with oxygen to generate dinitrogen oxide and trioxide (N_2O and N_2O_3). N_2O activates Cys thiols to thiyl radicals, which react with NO• leading to *S*-nitrosylation (Cys-SNO). N_2O_3 can directly react with Cys thiolates to Cys-SNO (not shown here) (Fernando et al. 2019; Foster et al. 2003; Stomberski et al. 2019). The star (*) indicates the active site Cys of the protein.

Moreover, neutrophils use the inducible nitric oxide synthase (iNOS) to produce nitric oxide (NO•) from arginine as bactericidal RNS. In bacteria, endogenous NO• is generated by the nitrate reductase from nitrate, which is used as anaerobic electron acceptor (Foster et al. 2003; Stomberski et al. 2019). NO• is a weak oxidant and can further react with $O_2^{\bullet-}$ to generate peroxynitrite ($ONOO^-$) as highly reactive intermediate between ROS and RNS (Radi 2018). NO• was shown to interact with H_2S to form nitroxyl (HNO) (Peng et al. 2017a; Walsh and Giedroc 2020). Thus, this crosstalk between ROS, RNS and RSS yields new reactive species that could partly explain the broad specificity of certain redox sensors. RNS can lead to post-translational thiol modifications of proteins and LMW thiols resulting in *S*-nitrosylation (Cys-SNO), which occurs via different chemical routes (Fernando et al. 2019; Foster et al. 2003; Stomberski et al. 2019). NO• autoxidation by oxygen yields dinitrogen oxide and trioxide (N_2O and

N_2O_3). N_2O activates Cys thiols to thiyl radicals (Cys-S•), which react with NO• to Cys-SNO (Figure 2). N_2O_3 directly reacts with Cys thiolates to form Cys-SNO (Fernando et al. 2019; Foster et al. 2003; Stomberski et al. 2019). In addition, the NO group can be transferred from metal-NO complexes or LMW-SNOs to protein Cys thiolates via *trans-S*-nitrosylation (Stomberski et al. 2019). Thus, *S. aureus* must be equipped with effective protection systems against ROS, RCS and RNS encountered endogenously and during interaction with host immune cells.

Additionally, *S. aureus* is exposed to antibiotics, xenosiderophores and metabolites, which have electron-deficient centers and are termed as reactive electrophilic species (RES). In *S. aureus*, endogenous RES are present as menaquinones in the electron chain, catechol-type siderophores and glycolytic aldehydes, such as methylglyoxal. Host-derived electrophiles are generated during macrophage and neutrophil infections by RNS and ROS as secondary reactive metabolites from oxidation of amino acids, unsaturated fatty acids and carbohydrates (Marnett et al. 2003). Electrophilic fatty acids accumulate especially during inflammation and can exert anti-inflammatory signaling effects (Delmastro-Greenwood et al. 2014). Electrophilic quinones have two modes of actions, an oxidative and an alkylating mode (Monks et al. 1992; O'Brien 1991). In the oxidative mode, quinones are reduced by one-electron transfer reactions to the highly reactive semiquinone anion radicals, leading to $O_2^{\bullet -}$ generation (Figure 2). In the alkylation mode, quinones react irreversibly with thiol groups via thiol-*S*-alkylation, resulting in protein aggregation and thiol depletion in the proteome and thiol metabolome (O'Brien, 1991,Monks et al., 1992,Liebeke et al., 2008). In general, the ability of quinones to alkylate protein thiols decreases with the number of substitutions of the quinone ring adjacent to the keto groups (O'Brien 1991; Smith 1985). Unsubstituted quinones, such as benzoquinones have a high ability to alkylate and aggregate protein thiols (Brunmark and Cadenas 1989; Liebeke et al. 2008). However, the fully substituted naphthoquinone lapachol was recently shown to act only via the oxidative mode in *S. aureus* (Linzner et al. 2020). In addition, the electrophile methylglyoxal is produced as toxic byproduct during glycolysis from dihydroxyacetone phosphate in many organisms (Booth et al. 2003; Ferguson et al. 1998; Kalapos 2008). Methylglyoxal conjugates nucleophilic thiols and amino groups of amino acids, DNA and RNA bases, leading to glycation end products (Kalapos 2008).

In addition, host and bacterial cells produce reactive sulfur species (RSS), such as H_2S, HS^- and S^{2-}, which have important signaling functions and act as gasotransmitters (Walsh and Giedroc 2020). RSS can lead to persulfidations of protein thiols and LMW thiols (RSSH). Persulfides have nucleophilic and electrophilic properties (Benchoam et al. 2020). While host phagocytes generate ROS and HOCl as microbicidal killing agents, RSS have beneficial properties as antioxidants to provide protection of bacterial pathogens against oxidative stress and antibiotics during infections (Shatalin et al. 2011; Walsh and Giedroc 2020). H_2S has been shown to confer tolerance to antibiotics by counteracting ROS production in many bacteria (Mironov et al. 2017; Shatalin et al. 2011). Mechanistically, H_2S has been proposed to sequester free iron to protect bacteria against oxidative stress elicited by antibiotics by inhibition of the Fenton reaction (Mironov et al. 2017). In *S. aureus*, endogenous H_2S is generated by the enzymes cystathionine-β-synthase (CBS) and cystathionine-γ-lyase (CSE) in the transsulfuration pathway from cysteine and homocysteine (Walsh and Giedroc 2020). The *S. aureus cbs/cbe* mutant, deficient in H_2S biogenesis, was impaired in survival under macrophage and neutrophil infections, indicating that RSS are important antioxidants and defense mechanisms during host-pathogen interactions (Toliver-Kinsky et al. 2019; Walsh and Giedroc 2020). HS^- reacts with Cys-SOH or protein disulfides leading to widespread persulfidations of proteins in the proteome of *S. aureus* (Figure 2). Persulfidation of the major virulence regulator MgrA inhibits its DNA binding activity resulting in lower secretion of cytotoxins in the secretome (Peng et al. 2017bPeng et al. 2017). Furthermore, *S. aureus* encounters RSS in the form of the antimicrobial organosulfur compound and common foodstuff allicin from garlic, which is composed of the diallylthiosulfinate (Borlinghaus et al. 2014). In *S. aureus*, allicin reacts with redox sensitive protein thiols and LMW thiols via *S*-thioallylation, leading to inactivation of protein functions (Loi et al. 2019).

Defense mechanisms of *S. aureus* against ROS, RES, RCS, RNS and RSS

Enzymatic detoxification systems

Superoxide anion and H_2O_2 detoxification

S. aureus encodes several antioxidant enzymes, including superoxide dismutases (SODs), catalases and peroxiredoxins, which are involved in detoxification of $O_2^{\bullet -}$ and H_2O_2 and provide protection under infection conditions (Imlay 2008; Mishra and Imlay 2012). Two superoxide dismutases (SodA and SodM) are present in *S. aureus* that

catalyze the dismutation of $O_2^{\bullet-}$ to H_2O_2 (Clements et al. 1999; Valderas and Hart 2001; Valderas et al. 2002). While other bacteria possess Fe^{2+}- and Mn^{2+}-containing SODs, SodA and SodM of *S. aureus* are both Mn-dependent enzymes. Both SODs are induced by the redox cycling agents paraquat and methyl viologen as well as during the post-exponential growth phase in *S. aureus* (Clements et al. 1999; Karavolos et al. 2003; Valderas and Hart 2001; Valderas et al. 2002). We have recently shown that transcription of *sodA* and *sodM* is strongly enhanced under lapachol stress, which exerts its toxicity via redox cycling in *S. aureus*, leading to $O_2^{\bullet-}$ and H_2O_2 production (Linzner et al. 2020). In addition, SodM expression was upregulated in *S. aureus* in airway environments of cystic fibrosis patients (Treffon et al. 2018).

Both SodA and SodM are important for virulence in a murine abscess model and required for nutritional immunity in *S. aureus*, when Mn^{2+} is restricted in the host due to sequestering by calprotectin during infections (Garcia et al. 2017; Gaupp et al. 2012; Karavolos et al. 2003; Kehl-Fie et al. 2011). SodA is required for oxidative stress resistance and virulence in a murine infection model in the presence of Mn^{2+}, while SodM is more important under Mn^{2+}-starvation and provides resistance to nutritional immunity (Garcia et al. 2017). The cambialistic nature of SodM has been demonstrated *in vitro*, showing similar activity with Mn^{2+} and Fe^{2+} as metal cofactor. Thus, SodA is strictly Mn-dependent and SodM can switch from a Mn^{2+}- to a Fe^{2+}-dependent enzyme under conditions of Mn^{2+} depletion during infections (Garcia et al. 2017). Interestingly, expression of *sodA* is regulated by the MntR-dependent small non-coding RNA RsaC, which is induced under Mn^{2+}-starvation and basepairs with the *sodA* mRNA, thereby inhibiting translation of SodA under conditions of nutritional immunity, when expression of the cambialistic SodM is favored to combat oxidative stress (Lalaouna et al. 2019). The altered metal specificity of SodM is caused by two mutations, which evolved in close proximity to the active site, but without direct contacts of the sidechains to the metal or metal-coordinating ligands (Barwinska-Sendra et al. 2020).

Catalases (Kat) and peroxiredoxins (Prx) are the primary antioxidant enzymes for detoxification of H_2O_2 in most aerobic bacteria (Imlay, 2003, 2008; Mishra and Imlay 2012). While catalases operate at high H_2O_2 levels under oxidative stress, peroxiredoxins scavenge physiological levels of H_2O_2 produced during aerobic respiration (Imlay, 2003, 2008; Mishra and Imlay 2012). H_2O_2 detoxification by the major vegetative catalase involves heme iron for disproportionation of H_2O_2 to H_2O and O_2. In contrast, peroxiredoxins use a peroxidative Cys (C_P) for reduction of H_2O_2, leading to Prx-SOH and subsequent disulfide formation between C_P and the resolving Cys (C_R) (Poole et al. 2011). Recycling of oxidized Prx requires electron donors, such as the Trx/TrxR/NADPH pathway (Mishra and Imlay 2012).

S. aureus exhibits a remarkable H_2O_2 resistance and can survive 100 mM H_2O_2 (Weber et al. 2004), which depends on the major catalase KatA. KatA is peroxide-inducible, mediates resistance to oxidative stress and is controlled by the metalloregulatory Fur-family PerR repressor (Horsburgh et al. 2001a,b). While PerR was required for full virulence in a murine skin abscess model of infection, KatA was not essential for pathogenicity (Horsburgh et al. 2001a). However, KatA is important for survival under glucose starvation and desiccation conditions and promotes nasal colonization in *S. aureus* (Cosgrove et al. 2007; Horsburgh et al. 2001a). In addition, transcription of *katA* was strongly enhanced under oxidative and electrophile stress in *S. aureus*, including HOCl, AGXX®, MHQ, allicin and lapachol (Fritsch et al. 2019; Loi et al., 2018a,b, 2019; Linzner et al. 2020). Moreover, the *katA* mutant was sensitive to lapachol-induced ROS generation, indicating that KatA provides protection under quinone stress (Linzner et al. 2020).

The peroxiredoxins of *S. aureus* include the alkyl hydroperoxide reductase (AhpCF), the thiol peroxidase (Tpx), the bacterioferritin comigratory protein (Bcp) and two thiol-dependent peroxidases (GpxA1 and GpxA2). As a typical 2-Cys peroxiredoxin, bacterial AhpC reacts with peroxides to the C_P-SOH, resulting in intersubunit disulfide formation between C_P and C_R in the AhpC dimer and oligomerization to an inactive AhpC decamer complex (Parsonage et al., 2008,2015). Oxidized AhpC is regenerated by the flavin disulfide oxidoreductase AhpF, which uses NADPH or NADH as electron donors (Mishra and Imlay 2012; Poole and Ellis 1996). In *S. aureus*, the *ahpCF* and *bcp* peroxiredoxins are both PerR-controlled and H_2O_2-inducible (Horsburgh et al. 2001a). KatA and AhpCF have compensatory roles in H_2O_2 resistance, persistence and nasal colonization (Cosgrove et al. 2007). In the *katA* mutant, the *ahpCF* operon showed increased expression, contributing to H_2O_2 detoxification. *Vice versa*, expression of *katA* was elevated in the *ahpCF* mutant, providing H_2O_2 resistance (Cosgrove et al. 2007). The *katA ahpCF* double mutant exhibits growth defects during aerobic cultivations due to elevated endogenous ROS levels leading to DNA damage and cell death (Cosgrove et al. 2007).

In addition, *S. aureus* encodes two homologs of the thiol-dependent peroxidase Ohr, which are involved in detoxification of organic hydroperoxides, originating from lipid peroxidation (Dubbs and Mongkolsuk 2007; Mongkolsuk and Helmann 2002). The Ohr paralogs are redox-controlled by the thiol-based MarR/OhrR-family repressors MgrA and SarZ as well as by MsaB in *S. aureus* (Chen et al.

2011; Pandey et al. 2019). However, many other peroxiredoxins respond to oxidative stress, such as Tpx, Bcp or GpxA1 and GpxA2, which remain to be, characterized in future studies.

HOCl detoxification

While the functions of KatA and AhpCF in peroxide detoxification are widely studied, the enzymatic pathways for removal of HOCl are only beginning to emerge. We have recently identified the NADPH-dependent flavin disulfide oxidoreductase MerA, which responds most strongly to HOCl and is controlled by the Rrf2-family HypR repressor in *S. aureus* (Loi et al. 2018b). MerA conferred protection under oxidative stress provoked by HOCl, AGXX® and allicin in *S. aureus*. In addition, the *merA* mutant was impaired in survival under macrophage infections, indicating important roles of MerA in the virulence of *S. aureus* (Loi et al., 2018a,b, 2019). Thus, we hypothesize that the physiological function of MerA could be the reduction of strong oxidants, such as HOCl or OH•, which are generated under infection, aerobic growth or by ROS-producing antimicrobials.

The MerA flavin disulfide reductase harbors a $C_{43}XXXXC_{48}$ active site, which forms a disulfide during catalysis to transfer electrons from NADPH via a FAD cofactor to the substrate, such as allicin and possibly HOCl (Argyrou and Blanchard 2004). Accordingly, Cys43 was required for survival under HOCl stress and infections in *S. aureus* (Loi et al. 2018b). Moreover, MerA is a homolog of the RclA flavin disulfide reductase of *Escherichia coli* and *Salmonella* Typhimurium, which is controlled by the HOCl specific RclR regulator and was shown to promote survival of *S.* Typhimurium inside the phagosome (Baek et al. 2020; Parker et al. 2013). The crystal structure of RclA of *S.* Typhimurium revealed the typical flavin disulfide reductase-fold with two Cys in the active site and a FAD cofactor (Baek et al. 2020). Interestingly, Cu^{2+} enhanced the RclA-mediated oxidation of NADH, resulting in decreased oxygen levels, which might inhibit the oxidative burst of macrophages (Baek et al. 2020). In *Pseudomonas aeruginosa*, an alkyl hydroperoxidase D-like protein PA0565 (RcsA) was shown to reduce HOCl via its catalytic $C_{60}XXC_{63}$ motif and provides resistance under HOCl and infections (Nontaleerak et al. 2020). Thus, AhpD-like peroxiredoxins, MerA and RclA flavoenzymes could be responsible for HOCl removal in different bacterial pathogens.

Quinone and aldehyde detoxification

Furthermore, *S. aureus* encodes enzymes for detoxification of quinones, including quinone reductases (Frp, AzoR1), a nitroreductase (YodC), an FMN-linked monooxygenase, thiol-dependent dioxygenases (CatE, CatE2, MhqE) and a phospholipase/carboxylesterase (MhqD) (Fritsch et al. 2019; Ji et al. 2013). The quinone and nitroreductases catalyze reduction of quinones to hydroquinones. The thiol-dependent dioxygenases function in ring cleavage of quinones for their detoxification (Leelakriangsak et al. 2008). These quinone detoxification enzymes confer resistance to quinones and quinone-like antimicrobials and are controlled by the quinone-sensing MarR-type repressors QsrR and MhqR in *S. aureus* (Fritsch et al. 2019; Ji et al. 2013).

In addition, several uncharacterized thiol-dependent glyoxalases and aldehyde dehydrogenases are present in *S. aureus*, which might be involved in the detoxification of methylglyoxal and other aldehyde substrates. We have recently characterized the aldehyde dehydrogenase AldA, which showed broad-spectrum activity for oxidation of various aldehyde substrates, including methylglyoxal (Imber et al. 2018b). However, AldA was shown to confer resistance to HOCl stress and could be involved in methylglyoxal detoxification, which is elevated under HOCl stress (Imber et al. 2018b). In *E. coli*, methylglyoxal detoxification involved the GSH-dependent glyoxalase pathway, converting methylglyoxal to lactate (Booth et al. 2003; Ferguson et al. 1998). While there are structural and biochemical studies on putative glyoxalase enzymes in *S. aureus* (Chirgadze et al. 2018; Kim et al. 2017), a functional glyoxalase pathway has not been characterized. Of particular interest for future studies should be the DJ-1/ThiJ/PfpI superfamily protein HchA, which is induced under oxidative and electrophile stress conditions in *S. aureus*, such as AGXX®, HOCl, MHQ, allicin and lapachol (Fritsch et al. 2019; Loi et al., 2018a,b, 2019; Linzner et al. 2020). Purified HchA showed glyoxalase III and chaperone holdase activity in biochemical assays *in vitro* (Kim et al. 2017). However, the role of HchA in *S. aureus* cells under various stress conditions remains to be investigated.

H_2S and NO• detoxification

S. aureus cells possess detoxification enzymes for removal of toxic H_2S, which are encoded by the CstR-controlled *cstAB-sqr* operon and provide protection against RSS (Luebke et al. 2014). The sulfide:quinone oxidoreductase SQR catalyzes the two-electron oxidation of HS^-, leading to formation of LMW persulfides. CstA functions as sulfurtransferase reacting with inorganic polysulfides and persulfides of the cysteine desulfurase SufS. The persulfide dioxygenase CstB oxidizes LMW persulfides, such as

bacillithiol persulfides (BSSH) and coenzyme A persulfides (CoASSH) to produce thiosulfate and LMW thiols (Higgins et al. 2015; Shen et al., 2015,2016; Walsh and Giedroc 2020).

S. aureus adapts to NO• stress by expression of the lactate dehydrogenases *ddh*, *ldh1* and *lqo* and two terminal oxidases *qoxABCD* and *cydAB* for maintenance of the redox balance (Fuller et al. 2011). The flavohemoglobin Hmp catalyzes the oxidation of NO• to NO_3^-, representing the main enzymatic mechanism of RNS detoxification in *S. aureus* (Goncalves et al. 2006). NO• leads to activation of the SrrAB two-component system, which controls expression of *hmp*, *qoxABCD* and *cydAB* (Grosser et al. 2016; Kinkel et al. 2013). Apart from Hmp, the flavodiiron NO• reductase Nor contributes to NO• detoxification, which is induced under anaerobic conditions and important for the virulence in *S. aureus* (Favazzo et al. 2019; Lewis et al. 2015).

Functions of bacillithiol in detoxification and antibiotics resistance

LMW thiols are non-proteinogenous thiol compounds that are present in millimolar concentrations in the bacterial cytoplasm and function in maintenance of redox homeostasis (Chandrangsu et al. 2018; Loi et al. 2015; Van Laer et al. 2013). While the tripeptide glutathione (GSH) is utilized as LMW thiol by most Gram-negative bacteria, *Staphylococcus* species and other firmicutes produce bacillithiol (BSH) as alternative LMW thiol, which functions as GSH surrogate to maintain redox homeostasis (Chandrangsu et al. 2018). BSH derivatives are present in *Thermus thermophiles* and in phototrophic *Chlorobiaceae* (Hiras et al. 2018; Newton and Rawat 2019; Norambuena et al. 2018) and widely distributed in archaea (Rawat and Maupin-Furlow 2020). In addition, *S. aureus* uses coenzyme A (CoASH) as alternative LMW thiol, which is maintained in its reduced state by the CoASH disulfide reductase Cdr (delCardayre and Davies 1998; delCardayré et al. 1998).

Bacillithiol (BSH, Cys-GlcN-malate) is an α-anomeric glycoside of L-cysteinyl-D-glucosamine with L-malic acid of 398 Da (Figure 3), which is synthesized by the glycosyltransferase BshA, the deacetylase BshB and the Cys ligase BshC in *S. aureus* (Chandrangsu et al. 2018; Gaballa et al. 2010; Newton et al. 2009). Using biophysical methods, the BSH standard redox potential was determined as $E^{0'}$(BSSB/BSH) of −221mV (Sharma et al. 2013). However, Brx-roGFP2 measurements inside *S. aureus* revealed a more negative BSH redox potential (E_{BSH}) ranging from −282 to −295 mV during the growth (Loi et al. 2017). Under oxidative stress provoked by H_2O_2 and HOCl stress, BSH is oxidized to BSH disulfide (BSSB) as shown *in vitro* and *in vivo* in *S. aureus* (Dickerhof et al. 2020). At higher levels, HOCl leads to BSH sulfonamide formation and overoxidation to BSH sulfonic acids (Dickerhof et al. 2020). The reaction of HOCl with BSH is very fast and occurs with second order rate constants of 6 x 10^7 $M^{-1}s^{-1}$ (Dickerhof et al. 2020).

The reduced state of BSH is maintained by the NADPH-dependent flavin disulfide reductase YpdA in *S. aureus*, which functions as a BSSB reductase (Figure 3) (Linzner et al. 2019; Mikheyeva et al. 2019). YpdA acts in the Brx/BSH/YpdA/NADPH redox pathway to regenerate *S*-bacillithiolated proteins under oxidative stress in *S. aureus* as outlined in the next sections (Linzner et al. 2019).

Importantly, BSH was identified as virulence factor in clinical MRSA isolates, such as COL and the highly virulent USA300 strain. BSH promotes survival inside murine macrophages and neutrophils in human whole-blood infection assays (Posada et al. 2014; Pöther et al. 2013; Rajkarnikar et al. 2013). Moreover, *S. aureus* isolates of the NCTC8325-4 lineage evolved mutations in the *bshC* gene, leading to the lack of BSH synthesis (Newton et al. 2012;

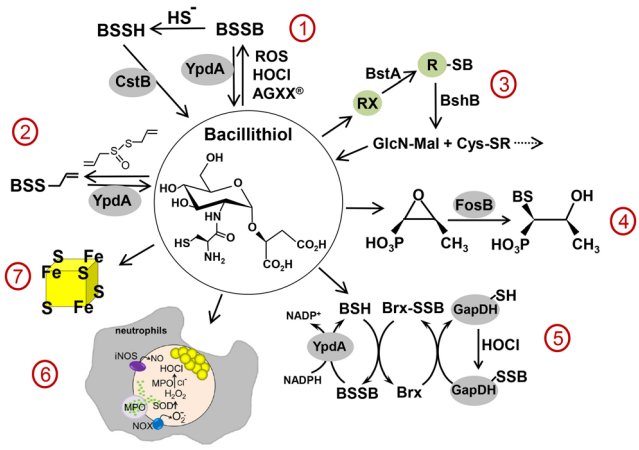

Figure 3: Bacillithiol functions in detoxification, antibiotics resistance and virulence in *S. aureus*. BSH is involved in detoxification of ROS, RES, HOCl, RSS and confers resistance to the redox active antibiotics fosfomycin, allicin, lapachol and AGXX® in *S. aureus*. (1) ROS, HOCl and AGXX® oxidize BSH to bacillithiol disulfide (BSSB), which is recycled by the BSSB reductase YpdA. BSSB could further react with HS^- generating BSH persulfides (BSSH), which are regenerated by the dioxygenase CstB. (2) Allicin reacts with BSH to *S*-allylmercaptobacillithiol (BSSA) as another substrate of YpdA. (3) The *S*-transferase BstA conjugates RES to BSH, forming BS-electrophiles (BS-R), which are cleaved by the amidase BshB to GlcN-Mal and mercapturic acids (Cys-SR), followed by their export. (4) The *S*-transferase FosB conjugates BSH to fosfomycin for its inactivation. (5) HOCl leads to *S*-bacillithiolations of proteins, which are reversed by the Brx/BSH/YpdA/NADPH pathway. (6) The Brx/BSH/YpdA/NADPH pathway is important under infections in *S. aureus*. (7) BSH functions in FeS cluster assembly in *S. aureus*.

Pöther et al. 2013). Thus, the *S. aureus* strain SH1000 of the NCTC8325-4 lineage was impaired in survival in infection assays compared to the SH1000 *bshC* repaired strain (Pöther et al. 2013). Interestingly, the *S. aureus bshA, ypdA* and *brxAB* mutants showed similar defects in survival inside J774.1 macrophages and neutrophils, indicating that the Brx/BSH/YpdA/NADPH system is essential under infections to regenerate BSH and protein thiols (Linzner et al. 2019; Mikheyeva et al. 2019; Pöther et al. 2013; Posada et al. 2014). Future studies should investigate the physiological role of BSH and the Brx/BSH/YpdA/NADPH redox pathway in *S. aureus* in murine infection models with defects in the NADPH oxidase and myeloperoxidase to elucidate if BSH homeostasis provides protection against the oxidative burst of neutrophils and macrophages.

Phenotype analyses of BSH-deficient mutants revealed important functions of BSH in the defense against ROS, HOCl, electrophiles, metals, xenobiotics, fosfomycin, rifampicin, AGXX®, allicin and lapachol in *S. aureus* (Figure 3)(Chandrangsu et al. 2018; Linzner et al. 2020; Loi et al., 2018a, 2019).

BSH is an important cofactor for the thiol-*S*-transferase FosB, which confers fosfomycin resistance. FosB catalyzes the ring cleavage of fosfomycin leading to formation of the BS-fosfomycin-conjugate (Figure 3) (Chandrangsu et al. 2018; Roberts et al. 2013). Both *fosB* and *bshA* mutants were similarly susceptible under fosfomycin stress in *S. aureus*, supporting the function of FosB as a BSH-dependent thiol-*S*-transferase (Posada et al. 2014; Rajkarnikar et al. 2013). In addition, the BSH-dependent *S*-transferase BstA was shown to conjugate BSH to electrophiles, such as 1-chloro-2,4-dinitrobenzene, monobromobimane and the antibiotic cerulenin in *S. aureus* (Newton et al., 2011,2012; Perera et al. 2014). BstA belongs to the widely conserved DinB/YfiT superfamily of *S*-transferases in BSH-, MSH- and GSH-producing bacteria (Newton et al. 2011; Perera et al. 2014). The resulting BS-electrophile conjugates are cleaved by the BSH *S*-conjugate amidase BshB to GlcN-Mal and mercapturic acids (CysSR), which are subsequently exported (Figure 3) (Newton et al. 2011). Thus, the thiol-*S*-transferases FosB and BstA are important determinants of antibiotics resistance in *S. aureus*.

Additionally, BSH and the Brx/BSH/YpdA/NADPH pathway were shown to confer protection against the naphthoquinone lapachol in *S. aureus* (Linzner et al. 2020). Lapachol acts via the oxidative mode, resulting in ROS formation, which leads to increased thiol oxidations and an oxidative shift in the E_{BSH} in *S. aureus*. Thus, the *bshA, brxAB* and *ypdA* mutants were more sensitive in growth and survival assays under lapachol treatment, indicating that the Brx/BSH/YpdA/NADPH pathway is essential to restore thiol homeostasis under lapachol stress (Linzner et al. 2020).

Similarly, BSH was shown to promote resistance to the antimicrobial surface coating AGXX® (Largentech GmbH, Berlin), which is composed of Ag^+ and Ru^+ ions and can be electroplated on medical devices and implants (Clauss-Lendzian et al. 2018; Gupta et al. 1999; Guridi et al. 2015; Heiss et al. 2017; Loi et al. 2018a; Vaishampayan et al. 2018). The Ag^+ and Ru^+ ions form a micro-galvanic cell, resulting in H_2O_2 and OH• generation due to the electric field. In support of ROS production, AGXX® caused strong oxidative, quinone and metal stress responses in the *S. aureus* transcriptome (Loi et al. 2018a). AGXX® induced an oxidative shift in the E_{BSH} and protein *S*-bacillithiolation of GapDH. The *bshA* mutant was strongly impaired in growth and survival under AGXX® stress, indicating an important role of BSH in protection against ROS generated by AGXX® (Loi et al. 2018a). Thus, BSH is a beneficial antioxidant in *S. aureus*, to ensure survival during host-pathogen interactions and under ROS-producing antimicrobials.

Furthermore, BSH functions in detoxification of RSS and RNS in *S. aureus*, such as H_2S and nitroxyl (HNO), the latter being an intermediate of NO• and H_2S (Peng et al. 2017a,b). H_2S caused widespread persulfidations in the proteome and thiol metabolome of *S. aureus* as revealed by elevated amounts of BSH persulfide (BSSH), CoASH persulfide (CoASSH) and cysteine persulfide (CysSSH) after exposure to Na_2S and HNO (Figure 3) (Peng et al. 2017a,b). Among the targets for persulfidations are the glycolytic GapDH and the major virulence regulator MgrA, which both were redox-controlled and inactivated by persulfidations of the active site Cys residues. The reversal of persulfidations was controlled by the novel thioredoxins TrxP and TrxQ (Peng et al. 2017bPeng et al. 2017).

In addition, BSH is crucial for resistance towards allicin and polysulfanes from garlic in *S. aureus* and *Bacillus subtilis* (Borlinghaus et al. 2014; Chi et al. 2019; Loi et al. 2019). The diallylthiosulfinate allicin decomposes upon heating to diallyl polysulfanes with up to seven sulfur chains (Münchberg et al. 2007; Tocmo et al. 2017). Allicin and diallyl tetrasulfane (DAS4) caused a strong oxidative and sulfur stress response in the transcriptome and widespread *S*-thioallylations of redox sensitive enzymes and transcriptional regulators in the proteome (Figure 2) (Chi et al. 2019; Loi et al. 2019). BSH-deficient mutants of *S. aureus* and *B. subtilis* are strongly impaired in growth and survival under allicin and DAS4 treatment (Arbach et al. 2019; Chi et al. 2019; Loi et al. 2019). In *S. aureus*, allicin caused a strong oxidative shift in the E_{BSH}, which is caused by BSH depletion and formation of *S*-allylmercaptobacillithiol (BSSA) (Figure 3). BSSA was identified as

substrate of the BSSB reductase YpdA to regenerate BSH by production of allyl thiol (Loi et al. 2019). In addition, the disulfide reductase MerA was shown to function in reduction of allicin to allyl thiols and the Brx/BSH/YpdA/NADPH pathway was important for regeneration of *S*-thioallylated proteins in *S. aureus*. Consistent with their biochemical functions in allicin detoxification, the *bshA*, *brxAB* and *ypdA* mutants were susceptible to allicin stress in *S. aureus* (Loi et al. 2019). In *B. subtilis*, the toxicity of polysulfanes was increased with longer sulfur chains (Arbach et al. 2019). Exposure to DAS3 and DAS4 caused strong depletion of BSH and cysteine, which was accompanied by increased formation of allyl thiols (Arbach et al. 2019), suggesting detoxification of polysulfanes in *B. subtilis* via related pathways as revealed in *S. aureus* (Loi et al. 2019).

During host-pathogen interactions, *S. aureus* has to cope with nutritional immunity caused by restriction of iron and other metal ions by host proteins (Maresso and Schneewind 2006; Marchetti et al. 2020). Thus, *S. aureus* must develop strategies to maintain Fe^{2+} homeostasis to ensure the biosynthesis of FeS clusters and Fe^{2+}-containing enzymes, such as catalase and superoxide dismutase (Maresso and Schneewind 2006; Marchetti et al. 2020). BSH plays an important role in FeS-cluster biogenesis in *S. aureus* (Figure 3). Specifically, BSH-deficient mutants were impaired in growth under iron starvation (Rosario-Cruz and Boyd 2016; Rosario-Cruz et al. 2015). BSH mutants showed growth defects in the absence of branched chain amino acids due to decreased synthesis of FeS cluster-containing enzymes, involved in leucine or isoleucine biosynthesis (Rosario-Cruz and Boyd 2016; Rosario-Cruz et al. 2015). It was suggested that BSH functions in FeS cluster assembly and transport to target proteins independently of the SufA and Nfu carrier proteins (Rosario-Cruz and Boyd 2016; Rosario-Cruz et al. 2015). However, the role of BSH in FeS cluster assembly is still unknown. It might be possible that BSH coordinates FeS cluster biogenesis together with the bacilliredoxins BrxAB as shown for GSH and glutaredoxins in eukaryotes (Lill 2020).

Redox regulation of proteins by protein *S*-bacillithiolation

During infections, *S. aureus* encounters the highly bactericidal HOCl as part of the oxidative burst by activated neutrophils (Winterbourn and Kettle 2013; Winterbourn et al. 2016). HOCl stress leads to formation of BSH mixed protein disulfides, termed as protein *S*-bacillithiolations, which are widespread across *Bacillus* and *Staphylococcus* species (Chi et al., 2011, 2013; Lee et al. 2007). These *S*-bacillithiolated proteins include metabolic and antioxidant enzymes, translation factors and redox sensing regulators, which respond to oxidative stress (Figure 4) (Chi et al., 2011,2013; Imber et al., 2018a, 2019). *S*-bacillithiolation was proposed to function in redox regulation of HOCl-specific transcription factors and to prevent irreversible overoxidation of vulnerable Cys thiols to sulfonic acids (Imber et al. 2019). In *B. subtilis*, the OhrR repressor was shown to sense HOCl and organic hydroperoxides (OHP) by *S*-bacillithiolation at its lone Cys15 residue, resulting in expression of the OhrA peroxidredoxin, which confers OHP and HOCl resistance (Chi et al. 2011; Lee et al. 2007).

In *S. aureus*, two OhrR homologs SarZ and MgrA are important virulence and antibiotics resistance regulators and share the conserved N-terminal Cys residue of the OhrR family, which senses oxidative stress via thiol oxidation (Figure 4) (Chen et al. 2011; Hillion and Antelmann 2015). The crystal structure of SarZ was resolved with Cys13 in the reduced, Cys-SOH and *S*-thiolated form with benzene thiol (Poor et al. 2009). Only the *S*-thiolated SarZ resulted in conformational changes in the DNA-binding helix-turn-helix motif, resulting in dissociation of SarZ from the target gene promoter (Poor et al. 2009). Increased thiol oxidation of MgrA and SarZ was found under HOCl stress in the redox proteome of *S. aureus*, supporting the hypothesis that both might be redox-controlled by *S*-bacillithiolation *in vivo* (Imber et al. 2018a). Furthermore, MgrA was regulated by persulfidation under sulfide stress, which impacts virulence factor secretion in the secretome of *S. aureus* (Peng et al. 2017bPeng et al. 2017).

Additionally, conserved *S*-bacillithiolated proteins were identified as metabolic enzymes with redox active catalytic centers, such as the methionine synthase MetE, the inosine monophosphate (IMP) dehydrogenase GuaB, the glyceraldehyde 3-phosphate dehydrogenase GapDH and the aldehyde dehydrogenase AldA (Figure 4) (Chi et al. 2011; Imber et al., 2018a, 2019). MetE represents the most abundant *S*-bacillithiolated protein in *B. subtilis* cells, which forms the BSH mixed disulfide at Cys730 in the active site Zn^{2+} center, resulting in inactivation of the enzyme and methionine auxotropy under HOCl stress. Moreover, the enzymes SerA, PpaC, MetI and YxjG were *S*-bacillithiolated under HOCl stress, which act in the same pathway as MetE (Chi et al. 2011; Imber et al., 2018a, 2019).

The glycolytic GapDH displayed 29% increased thiol oxidation under HOCl stress and was the most abundant *S*-bacillithiolated protein in *S. aureus* cells, representing 4% of the total Cys proteome (Imber et al., 2018a). GapDH *S*-bacillithiolation occurs under oxidative stress at the active site Cys151, resulting in enzyme inactivation and metabolic switching from glycolysis to the pentose phosphate

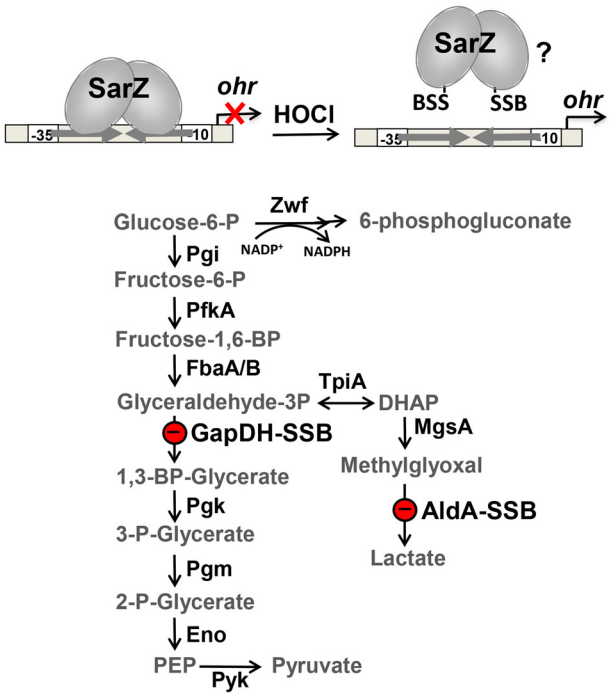

Figure 4: Physiological roles of *S*-bacillithiolations of GapDH, AldA and SarZ under HOCl stress in *S. aureus*. The OhrR-type repressors MgrA and SarZ were identified as HOCl-sensitive using OxICAT and *S*-thioallylated at Cys13 by allicin in *S. aureus*, indicating their possible redox regulation by *S*-bacillithiolation under HOCl stress (Imber et al. 2018a; Loi et al. 2019). SarZ controls the *ohr* peroxiredoxin, efflux pumps for antibiotics (*norB, tet38*), virulence factors and metabolic genes. SarZ confers resistance to OHP and antibiotics and contributes to virulence (Chen et al. 2011). HOCl stress causes *S*-bacillithiolation of the glycolytic GapDH and the aldehyde dehydrogenase AldA in *S. aureus,* resulting in the switch from glycolysis to the pentose phosphate pathway for NADPH regeneration (Deng et al. 2013; Imber et al. 2018a). AldA might be involved in methylglyoxal detoxification under HOCl stress. Abbreviations are: Pgi, glucose 6 phosphate isomerase; Pfk, phosphofructokinase; FbaA/B, fructose-1,6-bisphosphate aldolase; GapDH, glyceraldehyde 3-phosphate dehydrogenase; Pgk, phosphoglycerate kinase; Pgm, phosphoglycerate mutase; Eno, enolase; Pyk, pyruvate kinase; Zwf, glucose 6 phosphate dehydrogenase; TpiA, triose phosphate isomerase; MgsA, methylglyoxal synthase.

pathway (Deng et al. 2013; Imber et al. 2018a). Interestingly, GapDH inactivation by *S*-bacillithiolation proceeds faster compared to its inhibition by overoxidation in the absence of BSH *in vitro* (Imber et al. 2018a). Thus, *S*-bacillithiolation functions in redox regulation of GapDH activity and can prevent overoxidation of the active site (Imber et al. 2018a). Using molecular docking, BSH was modeled into the Cys151 active site of the apo- and holoenzymes. Interestingly, BSH occupies two different positions in the GapDH active site depending on the NAD^+ cofactor. While the BSH moiety is located in the active site with Cys151 in the attacking state position in the holoenzyme, *S*-bacillithiolation of the apoenzyme occurs with Cys151 in the resting state in the absence of the NAD^+ cofactor (Imber et al., 2018a,2019). However, *S*-bacillithiolation of GapDH did not cause major structural changes.

Similarly, the NAD^+-dependent aldehyde dehydrogenase AldA showed 29% increased thiol oxidation at its active site Cys279 and was inactivated by *S*-bacillithiolation under HOCl stress in *S. aureus* (Imber et al. 2018a,b). Computational chemistry revealed similar attacking and resting state positions of Cys279 upon *S*-bacillithiolation of the AldA holo- and apoenzymes, respectively, as shown for GapDH. In addition, *S*-bacillithiolation of AldA elicits no major structural and conformational changes (Imber et al., 2018b,2019). AldA was shown to catalyze oxidation of formaldehyde, methylglyoxal, acetaldehyde and glycolaldehyde *in vitro*, but its physiological substrate *in vivo* is unknown. Transcription of *aldA* is elevated under oxidative and electrophile stress, such as formaldehyde, methylglyoxal, HOCl, allicin and AGXX®, and depends of an unknown redox regulator. Phenotype analyses revealed that AldA is required for survival under HOCl stress, but dispensable under aldehyde stress. Thus, the physiological role of AldA under HOCl stress and its regulation remain to be elucidated in future studies (Imber et al. 2018b).

Apart from GapDH and AldA, GuaB is another NAD^+-containing enzyme with a highly conserved Cys308 active site that forms an adduct with the IMP substrate. GuaB is the most conserved target for *S*-glutathionylation, *S*-bacillithiolation and *S*-mycothiolation across prokaryotes and eukaryotes (Imber et al. 2019; Loi et al. 2015). Based on the different conformations of Cys308 in the substrate bound enzyme or in the apoenzyme structures, the BSH moiety may adopt a similar position in the GuaB active site with Cys308 in the attacking or resting state, respectively, as shown for GapDH and AldA (Imber et al., 2018a,b,2019). Altogether, *S*-bacillithiolations were shown to occur at accessible active site Cys residues of redox sensitive metabolic enzymes or transcriptional regulators. While *S*-bacillithiolation of GapDH and AldA does not lead to conformational changes, major structural rearrangements in the DNA binding HTH motif are required to accommodate redox regulation of the 1-Cys type OhrR-family repressors.

Reversal of protein *S*-bacillithiolation by the Brx/BSH/YpdA/NADPH pathway

The bacilliredoxins BrxA, BrxB and BrxC were previously identified as *S*-bacillithiolated in *B. subtilis* and *Staphylococcus carnosus* under HOCl stress, which suggested their role in the reversal of protein *S*-bacillithiolations (Chi et al. 2013).

BrxA and BrxB are paralogs of the DUF1094 family with a Trx fold and a CGC active site motif, which co-occur together with the BSH synthesis enzymes in BSH-producing bacteria (Gaballa et al. 2014). However, the redox potential of BrxA is relatively positive with −130 mV, and rather in the range of disulfide isomerases (Derewenda et al. 2009). BrxC has a TCPIS active site motif suggesting its possible function as monothiol Brx.

The functions of BrxA and BrxB as bacilliredoxins in reduction of *S*-bacillithiolated proteins have been first demonstrated for the *S*-bacillithiolated OhrR and MetE proteins in *B. subtilis* (Gaballa et al. 2014). DNA binding assays revealed the reactivation of OhrR after de-bacillithiolation of OhrR-SSB with the BrxB resolving Cys mutant protein, but not with the BrxB active site mutant. The removal of BSH from *S*-bacillithiolated MetE in *B. subtilis* cell extracts was shown with both BrxA and BrxB using BSH specific Western blots and mass spectrometry (Gaballa et al. 2014). In *S. aureus*, Brx activity assays were conducted with purified GapDH as most abundant *S*-bacillithiolated protein *in vivo* (Imber et al. 2018a). The *S. aureus* BrxA homolog catalyzed the de-bacillithiolation of GapDH, as shown by reactivation of the glycolytic activity of GapDH to oxidize the glyceraldehyde 3-phosphate substrate to 1,3-bis-phoshoglycerate with generation of NADH. While the BrxA resolving Cys mutant could restore GapDH activity, the BrxA active site mutant did not. The de-bacillithiolation reaction could be monitored using non-reducing BSH specific Western blots (Imber et al. 2018a). These results established the function of BrxA and BrxB in reversal of *S*-bacillithiolations *in vitro*.

Furthermore, the flavin disulfide reductase YpdA was phylogenetically associated with the BSH biosynthesis enzymes and bacilliredoxins (Gaballa et al. 2010). Transcriptome analyses revealed increased transcription of *ypdA, brxA, brxB, bshA*, *bshB* and *bshC* under oxidative and electrophile stress, such as H_2O_2, HOCl, diamide, AGXX®, lapachol, allicin and azurophilic granule proteins in *S. aureus* (Linzner et al. 2020; Loi et al., 2018a,b,2019; Palazzolo-Ballance et al. 2008). These data provide evidence for a functional Brx/BSH/YpdA/NADPH redox cycle in *S. aureus* (Figure 3), which is co-regulated under redox stress conditions. YpdA was characterized as a NADPH-dependent BSSB reductase in *S. aureus* to regenerate BSH homeostasis during recovery from oxidative stress and under infections (Linzner et al. 2019; Mikheyeva et al. 2019). Moreover, the *S. aureus brxAB*, *bshA* and *ypdA* mutants were more sensitive in growth and survival under HOCl stress and in macrophage infection assays *in vivo* (Linzner et al. 2019; Mikheyeva et al. 2019; Pöther et al. 2013; Posada et al. 2014). In addition, the *ypdA* mutant showed a 2-fold increased basal level of BSSB compared to the wild type (WT). Overproduction of YpdA, in turn, resulted in higher BSH levels (Mikheyeva et al. 2019). While the basal BSH levels of the *S. aureus* COL WT and the *ypdA* mutant were determined in a similar range of 1.5–1.9 µmol/g raw dry weight (rdw), the basal BSSB levels were measured as ~0.05 µmol/g and ~0.09 µg rdw in WT and *ypdA* mutant cells, respectively (Linzner et al. 2019). Thus, the BSH/BSSB ratio was determined as 35:1 for the WT and decreased to 17:1 in the *ypdA* mutant under non-stress conditions. Based on the high BSH levels in both WT and *ypdA* mutant strains, the basal E_{BSH} was not affected under non-stress conditions along the growth curve as measured using the Brx-roGFP2 biosensor, which is described in more detail in the following section (Linzner et al. 2019). However, due to the increased BSSB levels, the *ypdA* mutant was impaired to regenerate the reduced E_{BSH} upon recovery from oxidative stress, supporting the function of YpdA as BSSB reductase especially under oxidative stress in *S. aureus* (Linzner et al. 2019; Mikheyeva et al. 2019).

These results confirm previous findings, which revealed unchanged cytosolic GSH levels, but increased GSSG amounts in a yeast mutant deficient for the glutathione disulfide reductase Glr (Morgan et al., 2011,2013). Grx-roGFP2 biosensor measurements showed that the basal GSH redox potential (E_{GSH}) was only slightly increased by ~20 mV in the yeast *glr* mutant, whereas the H_2O_2 response was much stronger in the *glr* mutant with an impaired recovery of the reduced state (Morgan et al. 2011). It was further shown that Grx2 and Trx2 can compensate for GSSG reduction in the absence of Glr (Morgan et al. 2013). However, in *S. aureus* BrxA did not show BSSB reductase activity *in vitro* and the BSSB levels were not affected in the *brxAB* mutant, indicating that BrxAB cannot replace YpdA in regeneration of BSH (Linzner et al. 2019; Mikheyeva et al. 2019).

YpdA is a flavin disulfide reductase, which contains a conserved Cys14 residue in the glycine-rich Rossmann-fold NADPH binding domain ($GGGPC_{14}G$) (Bragg et al. 1997; Mikheyeva et al. 2019). Using NADPH coupled electron transfer assays, we demonstrated that YpdA consumes NADPH in the presence of BSSB, but not with other LMW thiol disulfides, such as GSSG, cystine or $CoAS_2$, confirming its function as BSSB reductase in *S. aureus in vitro* (Linzner et al. 2019). The BSSB reductase activity of YpdA was dependent on the conserved Cys14, which is unique in YpdA homologs and represents a novel active site. In support of its active site function, Cys14 of YpdA was identified as HOCl-sensitive with >10% increased oxidation using the redox proteomics approach OxICAT in *S. aureus* (Imber et al. 2018a). Thus, Cys14 might be *S*-bacillithiolated by BSSB, and regenerated by electron transfer from NADPH

via the FAD co-factor. Moreover, YpdA works in concert with BrxA and BSH to establish a functional Brx/BSH/YpdA/NADPH redox pathway for reduction of *S*-bacillithiolated proteins in *S. aureus*. In biochemical assays with the complete Brx/BSH/YpdA/NADPH pathway, BrxA was sufficient for the complete de-bacillithiolation of GapDH. In contrast, YpdA cannot regenerate *S*-bacillithiolated proteins, but functions instead in BSSB reduction to complete the Brx/BSH/YpdA/NADPH cycle (Linzner et al. 2019). In this redox cycle, the BrxA active site Cys attacks the *S*-bacilithiolated protein, resulting in Brx-SSB formation (Gaballa et al. 2014). Brx-SSB is resolved with BSH, leading to BSSB formation, which is recycled by YpdA to BSH (Linzner et al. 2019). However, structural analyses are required to resolve the detailed catalytic mechanism of YpdA in BSSB reduction. Future studies should be directed to identify the substrates of the Brx/BSH/YpdA/NADPH pathway under infection conditions inside host cells, which promote virulence, survival and persistence of *S. aureus* inside the host.

Monitoring the changes in the E_{BSH} using the Brx-roGFP2 biosensor

To monitor E_{BSH} changes inside *S. aureus*, BrxA were fused to the redox sensitive green fluorescent protein (roGFP2), generating a genetically encoded Brx-roGFP2 biosensor (Loi et al. 2017; Loi and Antelmann 2020). Upon oxidation, the two Cys residues in roGFP2 form a disulfide, influencing the spectral properties of roGFP2 (Meyer and Dick 2010; Schwarzländer et al. 2016). Specifically, the 488 nm excitation maximum is decreased and the 405 nm maximum increased, resulting in ratiometric changes in the 405/488 excitation ratio, which is quantified as oxidation degree (OxD). The fusion of Brx to roGFP2 facilitates the equilibration of roGFP2 with the BSH/BSSB redox pair enabling specific measurements of the E_{BSH} in *S. aureus* (Loi and Antelmann 2020; Loi et al. 2017; Meyer and Dick 2010; Schwarzländer et al. 2016). ROS exposure causes oxidation of cellular BSH to BSSB, which reacts with the Brx active site Cys of the Brx-roGFP2 probe, leading to Brx-SSB formation. The BSH moiety of Brx-SSB is transfered to the coupled roGFP2, which rearranges to the roGFP2 disulfide resulting in ratiometric changes of the excitation spectrum (Figure 5). Assuming that roGFP2 and the BSH/BSSB pair are in equilibrium, E_{BSH} is equal to the calculated E_{roGFP2}. Consequently, E_{BSH} can be calculated based on the OxD values of the Brx-roGFP2 biosensor and the previously determined $E^{o'}_{roGFP2}$ of −280 mV (Dooley et al. 2004), according to the Nernst equation as described (Loi et al. 2017; Morgan et al. 2011).

We have used the Brx-roGFP2 biosensor to monitor the changes in the E_{BSH} during the growth, under oxidative stress and antbiotics treatments in *S. aureus* isolates and in different mutant backgrounds (Loi and Antelmann 2020; Loi et al. 2017). First, purified Brx-roGFP2 was shown to respond fast and specific to low levels of 10–100 µM BSSB, but not to other LMW disulfides *in vitro*. The changes in E_{BSH} were determined in *S. aureus* COL *bshA*, *brxAB* and *ypdA* mutants along the growth and under oxidative stress to investigate the impact of the Brx/BSH/YpdA/NADPH pathway on the basal E_{BSH} and in response to oxidative stress (Linzner et al. 2019; Loi et al. 2017). Brx-roGFP2 measurements along the growth revealed a highly reducing basal level E_{BSH} in the range from −282 to −295 mV in the *S. aureus* COL WT, which was similar in the *ypdA* and *brxAB* mutants (Linzner et al. 2019; Loi et al. 2017). However, in the *bshA* mutant the biosensor was fully oxidized (Figure 5) (Loi et al. 2017). This indicates an impaired redox balance in the BSH-deficient strain, which might be caused by ROS increase. Interestingly, the *ypdA* mutant showed a strong Brx-roGFP2 oxidation after exposure to HOCl and H_2O_2, but was unable to regenerate the reduced state of E_{BSH} during recovery from oxidative stress due to its higher BSSB levels (Figure 5) (Linzner et al. 2019). In addition, the *ypdA* mutant was impaired in H_2O_2 detoxification as measured using the Tpx-roGFP2 biosensor (Linzner et al. 2019). These results confirmed the function of YpdA to regenerate reduced BSH after oxidative stress.

In addition, Brx-roGFP2 oxidation was analyzed after treatment of *S. aureus* COL WT with oxidants, different antibiotics and ROS-producing antimicrobials to investigate E_{BSH} changes (Loi et al., 2017,2018a, 2019). Brx-roGFP2 responds very fast to low levels of 50–100 µM HOCl, resulting in complete oxidation and slow recovery of the reduced E_{BSH} in *S. aureus* COL. Due to the high level of H_2O_2 resistance, Brx-roGFP2 was less reactive to 100 mM H_2O_2 and the *S. aureus* cells were able to recover faster their reduced E_{BSH} (Loi et al. 2017). Determination of the E_{BSH} changes of *S. aureus* COL after infection inside THP-1 macrophages revealed about 87% oxidation after 1 h, supporting that *S. aureus* experiences the oxidative burst (Loi et al. 2017). However, Brx-roGFP2 did not respond to sub-lethal concentrations of different antibiotics classes, such as rifampicin, fosfomycin, ampicillin, oxacillin, vancomycin, aminoglycosides and fluoroquinolones in *S. aureus* log phase cells (Loi et al. 2017).

In contrast, the Brx-roGFP2 biosensor was highly oxidized by the redox active antimicrobials AGXX®, allicin and lapachol resulting in an oxidative shift of E_{BSH} in *S. aureus* (Loi et al., 2018a, 2019, Linzner et al. 2020). Exposure of *S. aureus* COL to sub-lethal concentrations of

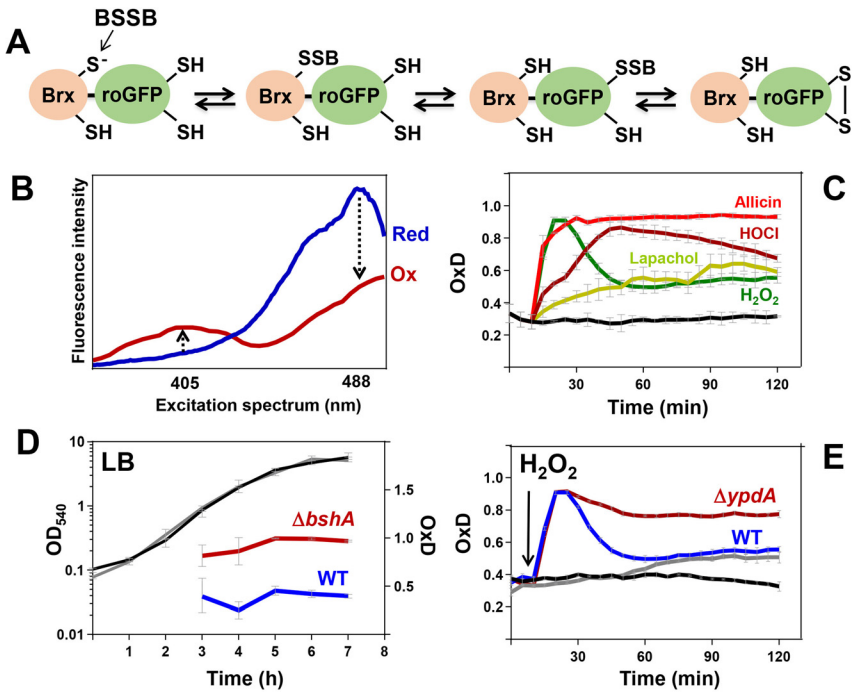

Figure 5: Principle, ratiometric changes and results of the Brx-roGFP2 biosensor in *S. aureus*. (A) The Brx active site thiolate of the Brx-roGFP2 biosensor reacts with BSSB, resulting in Brx-SSB formation, transfer of BSH to roGFP2, and re-arrangement to the roGFP2 disulfide (Loi et al. 2017). (B) Brx-roGFP2 oxidation results in ratiometric changes at the 405 and 488 nm maxima of the excitation spectrum, shown reduced (blue) and oxidized (red). The 405/488 excitation ratio is used for calculation of the biosensor oxidation degree (OxD). (C) *S. aureus* cells respond differentially to 100 mM H_2O_2, 100 µM HOCl, 50 µM allicin and 100 µM lapachol (Linzner et al. 2020; Loi et al. 2017; Loi et al. 2019). (D) The *bshA* mutant showed a fully oxidized basal redox state and (E) the *ypdA* mutant was impaired in recovery of the reduced E_{BSH} under oxidative stress (Linzner et al. 2019; Loi et al. 2017).

AGXX® leads to strong biosensor oxidation, which is caused by OH• and other ROS generated by AGXX® (Clauss-Lendzian et al. 2018; Loi et al. 2018a). Allicin causes *S*-thioallylations of BSH, resulting in BSSA formation, which oxidizes Brx-roGFP2 similar as BSSB (Loi et al. 2019). Thus, 50–100 µM allicin lead to fast and complete biosensor oxidation within 10 min in *S. aureus*, which was reversible with DTT, supporting the strong thiol reactivity of allicin (Figure 5) (Loi et al. 2019). The response of the Brx-roGFP2 biosensor was different for the naphthoquinone lapachol, which acts via the redox cycling mode in *S. aureus* (Linzner et al. 2020). Upon exposure to 100 µM lapachol, Brx-roGFP2 oxidation was slowly increased within 2 h with no recovery of reduced E_{BSH} (Linzner et al. 2020). This indicates constant generation of H_2O_2 by lapachol as measured with the Tpx-roGFP2 biosensor. In conclusion, Brx-roGFP2 is a valuable tool to screen for ROS-production and intracellular redox potential changes by redox active antibiotics in *S. aureus*.

Redox regulation of proteins by protein *S*-CoAlation

S. aureus produces millimolar CoASH and encodes a CoASH disulfide reductase Cdr, which reduces CoASH disulfide ($CoAS_2$) back to CoASH *in vitro* (delCardayre and Davies 1998,1998). Thus, before the discovery of BSH, CoASH was proposed to function as LMW thiol in *S. aureus* (delCardayre and Davies 1998; Tsuchiya et al. 2018). CoASH is an important thiol cofactor, which activates sugar metabolites of the central carbon catabolism by formation of energy-rich CoA thioesters, such as acetyl-CoA and succinyl-CoA to ensure ATP generation (Jackowski and Rock 1986). Recently, evidence was provided that CoASH can function in redox modification of proteins via *S*-CoAlations, which may substitute for *S*-bacillithiolation in the absence of BSH in *S. aureus* (Gout 2019; Tsuchiya et al. 2018). *S*-CoAlated proteins were enriched using pulldown with monoclonal anti-CoASH antibodies and identified by mass spectrometry (Gout 2019; Tsuchiya et al. 2018). In *S. aureus*, about 356 *S*-CoAlated proteins were identified under diamide stress, including conserved redox sensitive metabolic and antioxidant enzymes (GapDH, AldA, GuaB, Trx, AhpC, Tpx) and transcriptional regulators (SarR, CtsR, AgrA, PerR, SarS), which harbor active site Cys residues and overlap with *S*-bacillithiolated proteins under HOCl stress (Gout 2019; Tsuchiya et al. 2018).

Furthermore, protein *S*-CoAlation of the active site Cys151 of GapDH resulted in enzyme inactivation, which was reversible by DTT reduction (Tsuchiya et al. 2018). Computational chemistry proposed that the ADP moiety of CoASH occupies the NAD^+ binding pocket in the apoenzyme, facilitating *S*-CoAlation of Cys151 of GapDH (Tsuchiya et al. 2018). However, the physiological role of *S*-CoAlation in relation to sugar catabolism remains to be elucidated in *S. aureus*. Based on its metabolic role, enzymes involved in the activation of pyruvate and succinate by CoASH, such as pyruvate dehydrogenase (Pdh) and

succinyl-CoA-synthetase (SucCD) could be redox-controlled by *S*-CoAlation, which may impact the metabolic flux through the TCA cycle. Similarly, the pathways for reversal of *S*-CoAlations and the physiological role of Cdr under oxidative stress and infections are important subjects of future studies in *S. aureus*.

Thiol-based and other redox switches in *S. aureus*

PerR as Fur-family metal-based peroxide sensor

The peroxide specific PerR repressor belongs to the Fur family of metalloregulators and was characterized in *B. subtilis* and *S. aureus* (Faulkner and Helmann 2011; Pinochet-Barros and Helmann 2018). PerR negatively controls the adaptive response to H_2O_2 and confers H_2O_2 resistance in both bacteria (Faulkner and Helmann 2011; Horsburgh et al. 2001a; Ji et al. 2015; Mongkolsuk and Helmann 2002). The members of the PerR regulon function in ROS detoxification and iron storage, including genes for catalase, peroxiredoxins and thioredoxin reductase (*katA, ahpCF, bcp, trxB*), the iron storage ferritin and miniferritin (*ftnA, dps*), the ferric uptake (*fur*) repressor and the FeS cluster machinery (*sufCDSUB*) in *S. aureus* (Figure 6) (Horsburgh et al. 2001a). PerR binds to a conserved inverted repeat sequence ATTATAATTATTATAAT in the promoter region of the PerR regulon genes (Horsburgh et al. 2001a). In *S. aureus*, PerR is required for virulence in murine skin abscess and *Caenorhabditis elegans* infection models. In contrast, the catalase KatA is dispensable for pathogenicity (Ji et al. 2015; Horsburgh et al. 2001a).

The structures of *B. subtilis* and *S. aureus* PerR proteins contain two metal binding sites each, a structural Zn^{2+} site coordinated by four Cys residues and the regulatory Fe^{2+} or Mn^{2+} site, which includes His and Asp residues (Faulkner and Helmann 2011; Pinochet-Barros and Helmann 2018). The PerR repressors sense H_2O_2 by metal-catalyzed histidine oxidation in the regulatory Fe^{2+} binding sites, leading to their inactivation and derepression of transcription of the PerR regulons in *B. subtilis* and *S. aureus* (Ji et al. 2015; Lee and Helmann 2006; Pinochet-Barros and Helmann 2018). While the His and Asp residues in the regulatory site can bind both Fe^{2+} or Mn^{2+} as corepressors, only the Fe^{2+}-bound PerR can sense H_2O_2 by iron-catalyzed His oxidation. Specifically, Fe^{2+} in the regulatory site is oxidized by H_2O_2 in a Fenton reaction to generate OH•, leading to oxidation of His37 or His91 to form 2-oxo-histidine in the

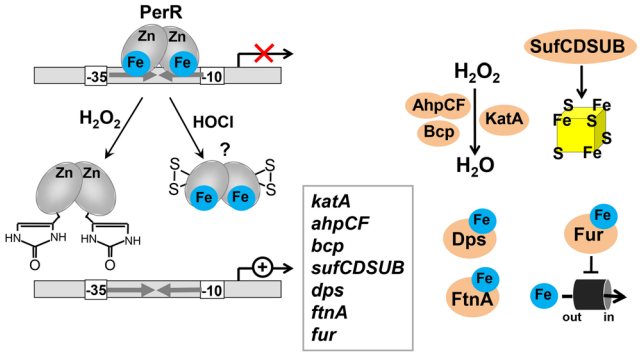

Figure 6: Redox regulation of the PerR repressor by iron-catalyzed His oxidation in response to H_2O_2 and by a putative thiol switch under HOCl stress in *S. aureus*. PerR senses H_2O_2 by Fe^{2+} catalyzed oxidation in the regulatory Asp/His site, leading to HO• formation and His37/His91 oxidation to 2-oxo-histidines, resulting in derepression of the PerR regulon (Ji et al. 2015; Lee and Helmann 2006). HOCl treatment leads most likely to PerR inactivation by a thiol switch in the structural Zn^{2+} site as identified in *Bacillus subtilis* cells using mass spectrometry *in vivo* (Chi et al. 2011). PerR controls genes encoding catalase, peroxiredoxins and thioredoxin reductase (*katA, ahpCF, bcp, trxB*), Fe-storage ferritin and miniferritin (*ftnA, dps*), the FeS cluster machinery (*sufCDSUB*) and the ferric uptake (*fur*) repressor in *S. aureus*. This figure is adapted from (Hillion and Antelmann 2015).

B. subtilis and *S. aureus* PerR proteins (Duarte and Latour 2010; Ji et al. 2015; Lee and Helmann 2006). However, the PerR repressor of *S. aureus* was hypersensitive to low H_2O_2 levels, which might explain its predominant Mn^{2+}-dependent repressor activity under aerobic conditions (Ji et al. 2015). This hypersensitivity of PerR towards H_2O_2 could be responsible for the higher basal expression of the PerR regulon genes, resulting in a high level of H_2O_2 resistance in *S. aureus*.

However, the PerR regulon was strongly induced under oxidative and electrophile stress, such as HOCl, diamide, MHQ, lapachol, allicin and AGXX® in *S. aureus* (Fritsch et al. 2019; Loi et al., 2018a,b, 2019; Linzner et al. 2020). Thus, PerR might sense various redox active compounds by a thiol switch mechanism in its structural Zn^{2+} site. In support of this hypothesis, a PerR intramolecular disulfide was identified by mass spectrometry in HOCl-treated *B. subtilis* cells (Chi et al. 2011). Thus, PerR might employ different redox sensing mechanisms to respond to H_2O_2 and other redox active compounds, that induce oxidative and electrophile stress responses.

The MgrA/SarZ/SarA-family of virulence and antibiotic regulators

S. aureus encodes several global MarR-type transcription factors, which control virulence, antibiotics and oxidative

stress resistance, including the Multiple gene regulator MgrA, SarZ and the Staphylococcal accessory regulator SarA (Ballal et al. 2009; Chen et al. 2009; Kaito et al. 2006; Poor et al. 2009; Truong-Bolduc et al. 2005, 2008). MgrA and SarZ belong to the MarR/OhrR-family, which sense ROS by thiol switch mechanisms via a conserved single Cys residue (Chen et al. 2011). MgrA is a global virulence regulator, which controls expression of >300 genes, involved in virulence, autolysis, antibiotics resistance, capsule and biofilm formation (Luong et al. 2006). Among the MgrA regulon genes are α–toxin (*hla*), coagulase (*coa*), protein A (*spa*), large surface proteins (*ebh, sraP* and *sasG*), fibrinogen-binding protein (*fnb*), extracellular protease, nuclease (*nuc*), autolysins (*lytM* and *lytN)*, multidrug efflux pumps (*norA*, *norB* and *tetAB)*, virulence regulators (*agr*, *lytRS*, *arlRS*, *sarS* and *sarV*) and capsule biosynthesis (*cap5*) (Ingavale et al. 2005; Kaatz et al. 2005; Luong et al. 2006; Truong-Bolduc et al. 2005, 2008). In DNase-I footprinting experiments, purified MgrA protein was shown to protect the conserved nucleotide sequence (A/T)GTTGT, which was repeated thrice upstream of the *sarV* promoter (Crosby et al. 2016; Manna et al. 2004). MgrA is important for virulence of *S. aureus* as shown in several infection models, including murine abscess, septic arthritis, sepsis, murine bacteremia and endocarditis models (Chen et al. 2006; Jonsson et al. 2008; Li et al. 2019).

The second MarR/OhrR-type regulator SarZ regulates a large regulon involved in virulence, antibiotic resistance, cellular metabolism and the *ohr* peroxiredoxin as main target gene (Kaito et al. 2006). Purified SarZ was shown to bind rather non-specific to the promoter regions of *hla*, *asp23* and *agr*, since a specific SarZ recognition motif could not be identified (Kaito et al. 2006). Both MgrA and SarZ sense oxidative stress by thiol switches, which involve the conserved redox sensing Cys13 residues. Thiol oxidation of MgrA and SarZ by organic hydroperoxides and H_2O_2 leads to formation of the Cys13-SOH (Chen et al., 2006,2009; Poor et al. 2009). Further oxidation of SarZ with the synthetic benzene thiol resulted in *S*-thiolated SarZ, which causes conformational changes in the HTH motif, leading to dissociation of SarZ from the promoter DNA as resolved in the crystal structure (Figure 4) (Poor et al. 2009).

The third redox sensing MarR-type regulator SarA controls genes involved in the oxidative stress defense (*sodB, trxB*) and virulence, including α- and ß-hemolysins (*hla, hlb*), toxic shock syndrome toxin 1 (*tst*), staphylococcal enterotoxin B (*entB*), protein A (*spa*) and fibronectin binding protein (*fnb*) (Chan and Foster 1998). SarA binds to a conserved operator sequence ATTTGTATTTAATATTTA-TATAATTG located upstream of the –35 promoter region of several SarA-regulated virulence genes (Chien et al. 1999). SarA contains a redox sensing Cys9 in its dimer interface and may use a thiol switch for regulation (Ballal and Manna 2009, 2010).

Furthermore, MgrA, SarZ and SarA were shown to be reversibly redox-controlled by Cys phosphorylation by the serine/threonine kinase (Stk1) and phosphatase (Stp1) (Sun et al. 2012). However, we identified the Cys13 peptides of MgrA and SarZ as HOCl-sensitive with >10% increased thiol oxidation under HOCl stress in *S. aureus* (Imber et al. 2018a). Furthermore, SarZ and MgrA were *S*-thioallylated under allicin stress in *S. aureus* (Loi et al. 2019). Thus, SarZ and MgrA might be redox-controlled by *S*-bacillithiolation under HOCl stress in *S. aureus*.

HypR as Rrf2-family redox sensor of HOCl stress

The Rrf2-family HypR repressor was identified as a novel redox sensor of HOCl stress in *S. aureus*, which uses a thiol switch mechanism (Loi et al. 2018b). Rrf2-family transcription factors are widespread in prokaryotes and regulate diverse functions, such as FeS cluster biogenesis (IscR), cysteine biosynthesis (CymR) and NO• detoxification (NsrR, RsrR) (Karlinsey et al. 2012; Mettert and Kiley 2015; Nakano et al. 2014; Partridge et al. 2009; Remes et al. 2015; Soutourina et al. 2009, 2010). HypR senses strong oxidants, such as HOCl, diamide, AGXX® and allicin stress (Loi et al. 2018a,b, 2019). HypR negatively controls expression of the *hypR-merA* operon, which was most strongly upregulated under HOCl stress in the transcriptome (Loi et al. 2018b) (Figure 7). In addition, the *hypR-merA* operon was highly induced in *S. aureus* during phagocytosis assays with neutrophils (Voyich et al. 2005), suggesting important functions as HOCl defense mechanism. The HypR repressor was shown to bind to a 12-3-12 bp inverted repeat sequence TAATTGTAACTA-N_3-CAGTTACAATTA in the *hypR-merA* promoter region, which is conserved across staphylococci.

HypR controls the NADPH-dependent flavin disulfide reductase MerA, which confers resistance towards HOCl, allicin and AGXX® stress as well as under infection conditions inside murine macrophages J774A.1 (Loi et al. 2018a,b, 2019). We hypothesize that MerA could be involved in HOCl reduction to promote survival under infections inside macrophages and neutrophils. In addition, the coupled transcription in the *hypR-merA* operon suggests that MerA could be the redox partner of HypR to recycle oxidized HypR during recovery from oxidative stress. The detailed functional analyses of MerA in terms of HOCl resistance are important goals of our current research.

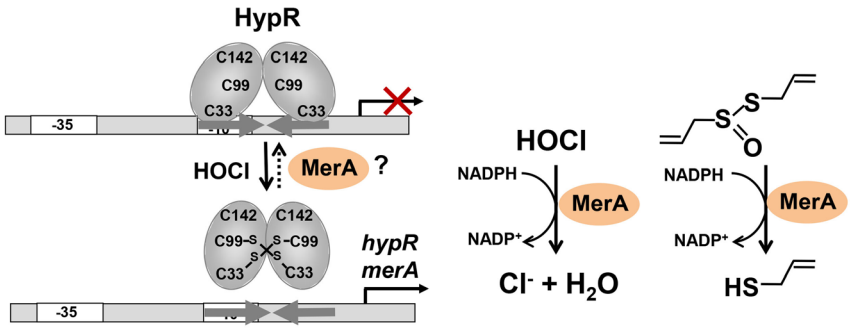

Figure 7: Redox regulation of the Rrf2-family repressor HypR under HOCl stress in *S. aureus*. HypR of *S. aureus* resembles a 2-Cys type redox regulator, which senses HOCl stress by intersubunit disulfide formation between Cys33 and Cys99′, leading to its inactivation and derepression of transcription of the *hypR-merA* operon (Loi et al. 2018b). The flavin disulfide reductase MerA is involved in HOCl and allicin detoxification and confers resistance to HOCl, allicin and infection conditions.

The HypR structure contains three Cys residues, including Cys33, Cys99 and Cys142, but only Cys99 is conserved in Rrf2 homologs (Loi et al. 2018b). While Cys33 is essential for redox sensing of HOCl stress, Cys99 is required for DNA binding activity of HypR in *S. aureus*. Under HOCl stress, HypR is oxidized to intersubunit disulfides between Cys33 and Cys99′ of opposing subunits in the HypR dimer, resulting in inhibition of its repressor activity and derepression of transcription of the *hypR-merA* operon (Loi et al. 2018b). Thus, the thiol switch model of HypR resembles that of a typical 2-Cys type redox sensing regulator. Future studies are directed to elucidate the structural changes of HypR upon oxidation, leading to its inactivation.

The MarR-family regulators QsrR and MhqR sense quinones

S. aureus and *B. subtilis* both encode two quinone-sensing MarR-type repressors, including the redox sensing MarR/DUF24-family regulator QsrR (or YodB) and the MarR-type repressor MhqR (Figure 8) (Chi et al. 2010; Fritsch et al. 2019; Ji et al. 2013; Leelakriangsak et al. 2008; Töwe et al. 2007). QsrR controls genes involved in the detoxification of quinones, such as ring-cleavage dioxygenases (*catE*, *catE2*), quinone and nitro reductases (*azoR1*, *frp*, and *yodC*) (Fritsch et al. 2019; Ji et al. 2013). A conserved inverted repeat with the consensus GTATAN$_5$TATAC was identified as the QsrR operator in the promoter region of the QsrR regulon genes (Ji et al. 2013). The MhqR repressor negatively controls transcription of the *mhqRED* operon, encoding the dioxygenase MhqE and the phospholipase/carboxylesterase MhqD. MhqR was shown to bind to a 9-9 bp inverted repeat sequence TATCTCGAA-aTCGAaATA in the promoter region upstream of *mhqR* (Fritsch et al. 2019). The quinone and nitroreductases (AzoR1, Frp, YodC) function in quinone reduction to redox stable hydroquinones (Figure 8) (Antelmann et al. 2008). Since benzoquinone alkylates protein and LMW thiols (Liebeke et al. 2008), the dioxygenases CatE, CatE2 and MhqE might catalyze ring cleavage of hydroquinones and quinone-*S*-adducts (Tam le et al. 2006).

In *S. aureus* and *B. subtilis*, the MhqR and QsrR regulons are most strongly upregulated by methylhydroquinone (MHQ) in the transcriptomes and contribute independently to quinone resistance (Fritsch et al. 2019; Ji et al. 2013; Leelakriangsak et al. 2008; Töwe et al. 2007). Interestingly, the MhqR and QsrR regulons of *S. aureus* confer resistance to antimicrobials with quinone elements, such as pyocyanin, rifampicin and ciprofloxacin (Fritsch et al. 2019; Ji et al. 2013). Pyocyanin is a toxic pigment produced by *P. aeruginosa*. Thus, MhqR and QsrR provide resistance of *S. aureus* towards pyocyanin to survive respiratory co-infections with *P. aeruginosa* in cystic fibrosis patients (Noto et al. 2017).

Furthermore, the MhqR regulon conferred tolerance to lethal H_2O_2 stress and was important for long-term survival of *S. aureus* inside macrophages (Fritsch et al. 2019). Similarly, the QsrR regulon mediates resistance to killing by macrophages in infection assays, indicating a crucial role of quinone detoxification pathways for virulence and survival of *S. aureus* inside host cells (Ji et al. 2013). During infections, the QsrR and MhqR regulons could be involved in detoxification of host-derived catecholamines, which are produced in macrophages and neutrophils to enhance the inflammatory response (Flierl et al. 2007). Infection-relevant electrophilic quinones could further arise in neutrophils from MPO-catalyzed serotonin oxidation to tryptamine-4,5-dione, which might be detoxified by the QsrR and MhqR regulons to enhance survival of *S. aureus* (Ximenes et al. 2009). Phenotype analyses further revealed an increased respiratory chain activity and higher ATP levels in the *S. aureus mhqR* mutant, pointing to the physiological role of the MhqR regulon to maintain the respiratory menaquinones in their reduced state (Fritsch

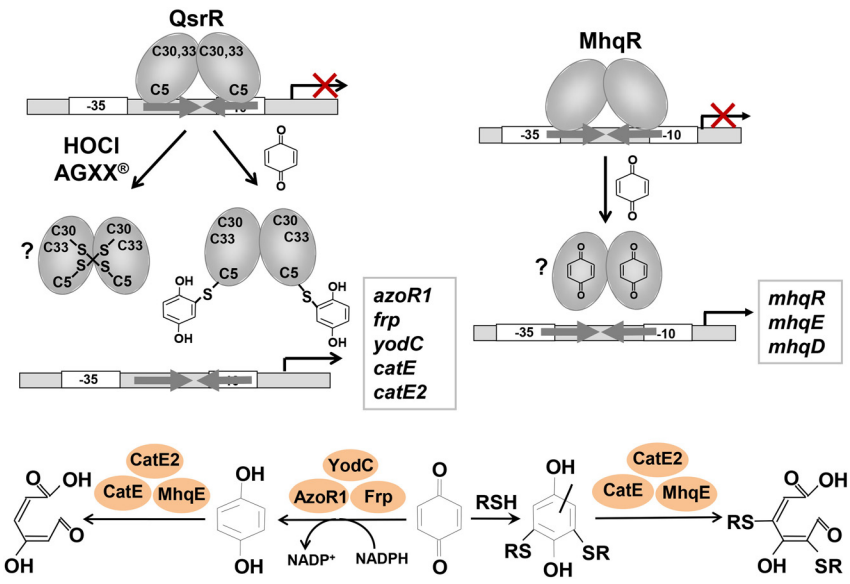

Figure 8: Redox sensing of quinones and antibiotics by the MarR-type repressors QsrR and MhqR in *S. aureus*. QsrR senses quinones by thiol-*S*-alkylation of Cys5, leading to derepression of dioxygenases (*catE, catE2*) and quinone reductases (*frp, azoR1, yodC*) (Ji et al. 2013). In addition, QsrR might sense oxidative stress by a thiol switch *via* intersubunit disulfide formation in *S. aureus* as revealed for the homologous YodB repressor in *B. subtilis* (Chi et al. 2010; Lee et al. 2016). Quinone sensing by MhqR involves most likely quinone binding to the conserved ligand pocket, resulting in upregulation of the *mhqRED* operon, which codes for the phospholipase/carboxylesterase MhqD and the dioxygenase MhqE (Fritsch et al. 2019). Since benzoquinone alkylates protein and LMW thiols in *B. subtilis* (Liebeke et al. 2008), we hypothesize that dioxygenases catalyze ring cleavage of hydroquinones and quinone-*S*-adducts. Both QsrR and MhqR confer independently resistance to quinones and the antimicrobials pyocyanin, ciprofloxacin and rifampicin.

et al. 2019). In support of this notion, the MhqR regulon of *B. subtilis* was important for the formation of cell-wall free L-forms, which requires reduced quinones for continued respiration and contributes to survival and resistance (Kawai et al. 2015).

The MhqR repressors of *B. subtilis* and *S. aureus* do not use thiol-based mechanisms for redox sensing of quinones (Fritsch et al. 2019; Töwe et al. 2007). Since many MarR--type regulators harbor conserved ligand binding pockets, MhqR might sense quinones by direct binding to a ligand pocket, leading to derepression of the *mhqRED* operon in *S. aureus* (Grove 2017; Perera and Grove 2010; Wilkinson and Grove 2006).

In contrast to MhqR, QsrR contains a conserved redox sensing Cys5 and two non-conserved Cys30 and Cys33 residues (Ji et al. 2013). The redox sensing mechanism of QsrR was shown to involve thiol-*S*-alkylation of the Cys5 residue, resulting in QsrR inactivation (Figure 8) (Ji et al. 2013). The detailed mechanism and structural changes of QsrR upon *S*-alkylation have been resolved for reduced and menadione-bound QsrR. QsrR alkylation leads to movement and rotation of the $\alpha4$ and $\alpha4'$ DNA binding helices from 106 to 117°, which is incompatible with DNA binding and causes dissociation of QsrR from the promoter (Ji et al. 2013). However, this Cys-alkylation model has been resolved with the QsrR Cys30,33 double mutant protein. The *B. subtilis* YodB repressor was previously shown to sense diamide and quinones via intersubunit disulfide bond formation between the conserved Cys6 and the C-terminal Cys101′ or Cys108′ of opposing subunits in the YodB dimer *in vivo* (Chi et al. 2010).

Recent crystal structure analyses have resolved two mechanisms for YodB inactivation, the *S*-alkylation of Cys6 by methyl-*p*-benzoquinone and the thiol switch between Cys6 and Cys101′ under diamide stress (Lee et al. 2016). Quinones cause *S*-alkylation at Cys6 with minor structural changes by 3 Å rotations of the $\alpha4$ and $\alpha4'$ domains, similar as shown for QsrR (Lee et al. 2016). In contrast, diamide leads to Cys6-Cys101′ intersubunit disulfide formation with large structural rearrangement, leading to complete dissociation from the DNA (Lee et al. 2016). Transcriptome analyses revealed that the QsrR regulon is strongly upregulated by quinones and other redox active compounds, such as MHQ, HOCl, AGXX®, allicin and lapachol in *S. aureus* (Fritsch et al. 2019; Linzner et al. 2020; Loi et al. 2018a,b, 2019). Thus, the two Cys QsrR repressor most likely senses quinones and strong oxidants by *S*-alkylation and disulfide formation, respectively, which remains to be elucidated.

It is possible that QsrR/YodB and MhqR sense different quinone-related redox signals, controlling the detoxification/reduction of oxidized quinones and ROS by QsrR/YodB as overarching thiol-based regulator, while MhqR could be additionally involved in trapping and regulation of ring cleavage of reduced and oxidized quinones. QsrR/YodB uses a thiol switch mechanism to respond to ROS,

which oxidize respiratory menaquinones and require quinone detoxification/reduction pathways to restore respiration. MhqR could rather sense accumulating quinones to induce additional quinone detoxification pathways when the QsrR/YodB regulon is overwhelmed.The crosstalk of both systems was confirmed by lower expression of QsrR/YodB regulons in the *mhqR* mutants and *vice versa* in *B. subtilis* and *S. aureus* (Fritsch et al. 2019; Leelakriangsak et al. 2008; Töwe et al. 2007). The investigation of the kinetics, specificities, crosstalks and reversibilities of both systems are interesting goals of future mechanistic studies.

The thiol-based redox sensor Spx and its YjbH adapter

The thiol-based redox sensor Spx belongs to the arsenate reductase (ArsC) family, representing an unusual transcriptional activator lacking the HTH motif (Nakano et al. 2003, 2005; Zuber 2009). In *S. aureus*, transcription of *spx* is positively regulated by the ArlRS two-component system (Crosby et al. 2020). Spx is activated in response to oxidative stress by thiol oxidation of its CXXC redox switch motif to an intramolecular disulfide (Nakano et al. 2005). The Spx disulfide interacts with the *α*-C-terminal domain of the RNA polymerase and activates transcription of the Spx regulon, which is involved in the thiol redox homeostasis and oxidative stress resistance, including thioredoxin and thioredoxin reductase (*trxA, trxB*) (Figure 9) (Nakano et al. 2003, 2005; Zuber 2004, 2009). Thus, the *spx* mutant shows increased susceptibility to oxidative, heat and salt stress in *S. aureus* (Pamp et al. 2006; Wang et al. 2010). Furthermore, Spx is involved in *pia*-dependent biofilm formation and controls expression of the *icaABCD* operon. Spx represses *cspA* transcription, which inhibits the activation of SigB leading indirectly to downregulation of aureolysin (*aur*) and staphyloxanthin biosynthesis (*crtOPQMN* operon) (Austin et al. 2019; Donegan et al. 2019).

The post-translational control involves the proteolytic degradation of Spx by the ClpXP system with the help of the YjbH adapter. Under control conditions, YjbH binds Spx, which is targeted to the ClpXP machinery resulting in Spx degradation (Engman et al. 2012; Garg et al. 2009; Pamp et al. 2006). Oxidative stress causes YjbH self-aggregation possibly due to thiol oxidation of its Zn^{2+} redox switch motif leading to Spx stabilization and increased Spx protein levels (Figure 9) (Engman and von Wachenfeldt 2015). Apart from proteolysis, YjbH controls antibiotic resistance in *S. aureus*. The *yjbH* mutant was resistant to *ß*-lactam antibiotics due to increased PBP4 expression and

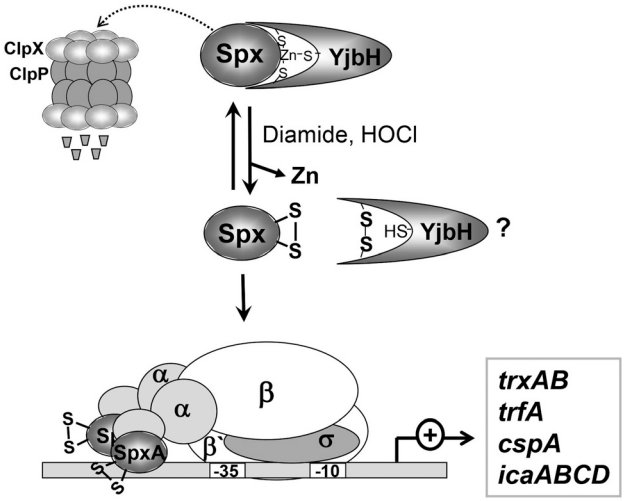

Figure 9: Redox control of the oxidative stress regulator Spx in *S. aureus*. Under control conditions, Spx is complexed by the YjbH adapter and targeted to the ClpXP machinery for proteolytic degradation. Oxidative stress causes possibly thiol oxidation and self-aggregation of YjbH, resulting in Spx stabilization (Engman and von Wachenfeldt 2015). Spx is activated by thiol oxidation to an intramolecular disulfide. Oxidized Spx binds to the αCTD of RNAP leading to activation of transcription of *trxA, trxB*, *trfA*, *cspA* and *icaABCD* in *S. aureus*, which impacts redox homeostasis, virulence factor expression, antibiotics resistance and biofilm formation. This figure is adapted from (Hillion and Antelmann 2015).

peptidoglycan cross-linking (Gohring et al. 2011). Spx controls the *mecA* homolog *trfA* in *S. aureus*. While the *trfA* mutant was susceptible to oxacillin and glycopeptide antibiotics, *trfA* upregulation in the *yjbH* mutant conferred antibiotics resistance (Jousselin et al. 2013). In addition, Spx activates the MazEF toxin-antitoxin system, which promotes dormancy and antibiotic tolerance (Panasenko et al. 2020). The lack of the extracellular proteases, such as aureolysin in the *yjbH* mutant led to hypervirulence in a systemic mouse infection model and enhanced colonization of the kidney and the spleen in a murine sepsis model (Austin et al. 2019; Kolar et al. 2013).

The TetR-family regulator and electrophile sensor GbaA

The TetR-family regulator GbaA (Glucose-induced biofilm accessory protein A) was characterized as a novel thiol switch and monothiol electrophile sensor (Ray et al. 2020). GbaA controls glucose-induced biofilm formation by the polysaccharide intracellular adhesion (PIA), which is composed of poly-*N*-acetyl glucosamine (PNAG) as biofilm matrix in *S. aureus* (Ray et al. 2020; You et al. 2014; Yu et al.

2017). GbaA negatively controls two operons of unknown functions, encoding a putative glyoxalase, the NAD^+ dependent epimerase/dehydratase NmrA, the short chain dehydrogenase/oxidoreductase GbaB, an amidohydrolase and an α, *β*-fold hydrolase (Figure 10) (Ray et al. 2020; You et al. 2014; Yu et al. 2017). The GbaA repressor was shown to bind to a palindromic sequence AAACGGAGAGTTATCCGTTT in the upstream promoter region of *gbaA*. The *gbaA* mutant showed strongly enhanced biofilm formation in a super-biofilm elaborating clinical isolate *S. aureus* TF2758 (Yu et al. 2017), and biofilm formation was dependent on GbaB (Ray et al. 2020). GbaB was suggested to catalyze the oxidation of an alcohol to a sugar aldehyde in the PNAG biosynthesis pathway, but the physiological role and the inducer of the GbaA regulon are unknown (You et al. 2014; Yu et al. 2017).

Interestingly, the GbaA regulon was induced by different redox active compounds and antibiotics, including RNS, AGXX®, allicin, erythromycin, colistin, vancomycin and most strongly by the electrophiles methylglyoxal and N-ethylmaleimide (NEM) (Loi et al. 2018a, 2019; Mäder et al. 2016; Ray et al. 2020; Schlag et al. 2007Loi et al. 2018, 2019; Mäder et al. 2016; Ray et al. 2020; Schlag et al. 2007). GbaA was shown to function as a thiol switch and an electrophile sensor *in vitro*, which involves the conserved Cys55 and Cys104 residues in the DNA binding and regulatory domains (Ray et al. 2020). GbaA is oxidized to an intramolecular disulfide in response to diamide, BSSB, GSSG and GSNO *in vitro*, which does not affect its DNA binding activity (Figure 10). However, treatment of the single Cys55A or Cys104A mutant proteins with NEM and BSSB resulted in NEM-alkylation and *S*-bacillithiolation of the remaining Cys leading to inactivation of the GbaA repressor (Figure 10) (Ray et al. 2020). In addition, Cys104 was found more reactive and accessible towards electrophiles, indicating that Cys104 is the redox sensing Cys and most likely modified by electrophiles or BSSB *in vivo* (Ray et al. 2020). Thus, the redox sensing mechanism of GbaA differs from other electrophile sensors, such as YodB, which senses diamide and quinones via thiol switch and *S*-alkylation mechanisms, both leading to structural changes and inhibition of its DNA binding activity (Chi et al. 2010; Lee et al. 2016; Leelakriangsak et al. 2008). While GbaA resembles a 2-Cys type regulator, only *S*-thiolation or *S*-alkylation causes structural changes (Ray et al. 2020). However, the physiological electrophile and functions of the GbaA regulon members under oxidative and electrophile stress and biofilm formation are unknown.

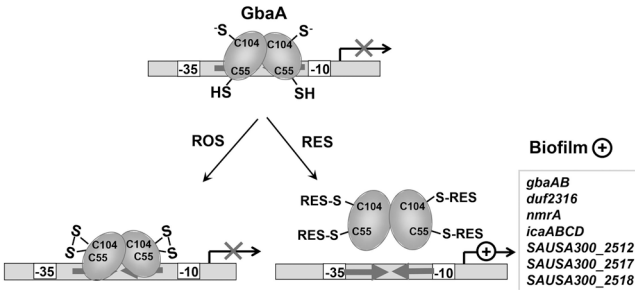

Figure 10: Redox sensing of electrophiles by the TetR-family biofilm regulator GbaA. The GbaA repressor is oxidized by different oxidants to the Cys55-Cys104 intramolecular disulfide, which does not affect the structure and DNA binding activity of GbaA. Alkylation of GbaA by electrophiles causes structural changes and loss of DNA binding, resulting in derepression of transcription of the GbaA regulon (Ray et al. 2020). GbaA controls two operons involved in biofilm formation, including a glyoxalase, the NAD^+-dependent epimerase/dehydratase NmrA, DUF2316, the short chain dehydrogenase/oxidoreductase GbaB, the GbaA repressor, an amidohydrolase and an *α*, *β*-fold hydrolase.

Since the GbaA regulon is required for glucose-induced biofilm formation, host-derived oxidation products of glucose, such as the *α*,*β*-dicarbonyls glucosone, glyoxal, methylglyoxal, glycolaldehydes, or other reactive glycolytic intermediates could be physiological electrophiles sensed by GbaA. These glucose oxidation products accumulate in human tissues, blood and activated neutrophils causing glycation of lysine, arginine and cysteine in proteins (Vetter 2015). In neutrophils, the MPO reaction product HOCl causes formation of chloramines, which are degraded to acrolein and *p*-hydroxyphenylacetaldehyde as further infection-related electrophiles (Hazen et al. 1998). Reactive aldehydes might increase in *S. aureus* during the switch to biofilm formation and anaerobic fermentation, which relies on high glycolytic activity for ATP production. In the next section, we discuss the SrrAB system, which senses oxygen levels and controls the switch to anaerobiose and biofilm formation via the SrrB redox switch (Tiwari et al. 2020; Yarwood and Schlievert 2000). Thus, GbaA and SrrAB might be responsible to sense different signals during biofilm formation and the switch from aerobic to anaerobic conditions to allow biofilm matrix synthesis, removal of toxic aldehydes and metabolic adaptation.

Another infection-relevant electrophile could be the major immunoregulatory metabolite itaconate, which inhibits the succinate dehydrogenase resulting in metabolic rewiring during inflammatory macrophage activation (Lampropoulou et al. 2016). Itaconate reacts as electrophile with GSH and induces electrophile stress in host cells (Bambouskova et al. 2018). In *P. aeruginosa* lung infections, host-derived itaconate reprograms bacterial metabolism and induces biofilm formation via enhanced exopolysaccharide matrix biosynthesis (Riquelme et al.

2020). Thus, itaconate could be a candidate electrophile to inactivate the GbaA repressor to promote PNAG synthesis and biofilm formation in *S. aureus*, which remains to be investigated.

Furthermore, GbaA belongs to the TetR-family regulators, which are often inactivated by direct binding of antibiotics as ligands to the C-terminal regulatory domain (Cuthbertson and Nodwell 2013). Since GbaA responds to various antibiotics and allicin (Loi et al. 2019; Mäder et al. 2016), a direct binding of antibiotics and electrophiles coupled with ROS-induced *S*-thiolation or *S*-alkylation of Cys104 could possibly inactivate GbaA *in vivo*. In summary, *S. aureus* can be exposed to a plethora of oxidants and electrophiles present during host-pathogen interactions that might be sensed by GbaA and other redox sensors, which enable host adaptation. Thus, future studies should shed light on the signals and redox chemistry of host-pathogen interactions.

The SrrAB two-component system as redox sensor of oxygen levels

The Staphylococcal respiratory regulator (SrrAB) two-component system consists of the sensor histidine kinase SrrB and the DNA-binding response regulator SrrA (Yarwood and Schlievert 2000). The SrrAB regulon is implicated in long-term biofilm stability, anaerobic growth, oxidative and nitrosative stress resistance and contributes to the virulence and protection against neutrophil killing in *S. aureus* (Kinkel et al. 2013; Mashruwala and Boyd 2017; Pragman et al. 2004; Ulrich et al. 2007). SrrAB regulon members include genes for the biogenesis of cytochromes and terminal oxidases (*ctaB*, *cydAB*, *qoxABCD*), heme biosynthesis (*hemACDX*), anaerobic fermentation (*pflAB*, *adhE*, *nrdDG*), and RNS resistance (*hmp*, *scdA*) (Figure 11) (Kinkel et al. 2013; Mashruwala and Boyd 2017; Oogai et al. 2016; Yarwood and Schlievert 2000). In addition, the SrrA response regulator binds to the *agr*, *spa*, *srrAB*, *icaA*, *RNAIII* and *tst* promoters and is involved in virulence regulation, directly and indirectly via Agr (Pragman et al. 2004; Ulrich et al. 2007). However, no consensus sequence of a potential SrrA recognition motif could be identified in the promoter regions of the target genes. Furthermore, SrrAB positively influences expression of *dps*, *scdA*, *ahpCF* and *katA*, which function in iron storage, FeS-cluster repair and H_2O_2 detoxification leading to an oxidative stress resistance (Mashruwala and Boyd 2017). The crosstalk between Nos and SrrAB mediates the switch from aerobic to anaerobic energy metabolism, since SrrAB co-regulates

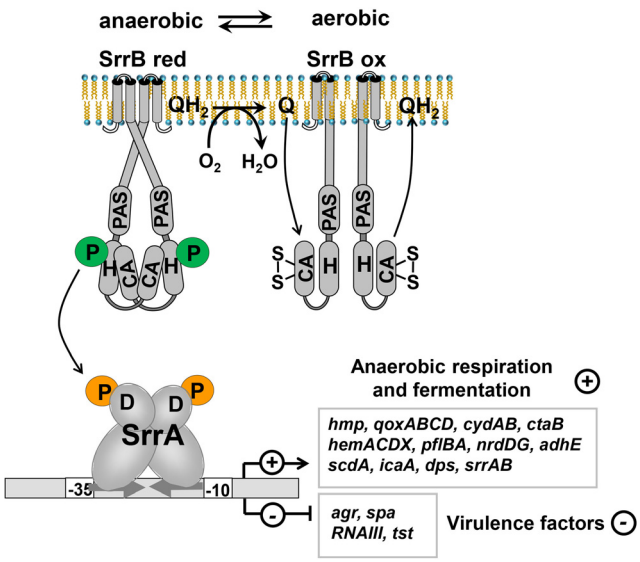

Figure 11: Sensing of oxygen by the SrrAB two-component system. SrrAB senses oxygen availability *via* the redox state of respiratory menaquinones and by a thiol switch in its sensor kinase SrrB (Tiwari et al. 2020). Aerobic conditions lead to menaquinone oxidation and intramolecular disulfide formation between Cys464 and Cys501 in SrrB, resulting in SrrB inactivation. During anaerobiosis, the two Cys residues in SrrB are reduced directly by reduced menaquinones or indirectly by a ligand binding to the PAS domain of SrrB. Reduced SrrB is active as kinase, leading to autophosphorylation and phosphorylation of the response regulator SrrA. SrrA-P positively controls biofilm formation *via* the *icaABCD* operon and represses *tst* gene transcription. Anaerobic respiration and fermentation are activated by SrrAB, while virulence factors are repressed as indicated.

narG and *nirB*, which are involved in nitrate respiration and nitrite transport (James et al. 2019).

S. aureus utilizes SrrAB for adaptation to lower oxygen availability during anaerobiosis and changes in the respiratory flux (Yarwood and Schlievert 2000). SrrB senses the reduced state of the respiratory menaquinone pool and acts as kinase and phosphatase via the PAS domain to regulate the phosphorylation state of the response regulator SrrA (Kinkel et al. 2013; Mashruwala et al. 2017; Tiwari et al. 2020). Two cysteines (Cys464 and Cys501) are present in the ATP-binding catalytic domain of SrrB, which are oxidized to an intramolecular disulfide under aerobic conditions inhibiting the autokinase activity of SrrB (Figure 11) (Tiwari et al. 2020). Under anaerobic conditions, the reduced menaquinone pool leads to reduction of the disulfide in SrrB, directly or indirectly via a PAS domain/ligand complex, leading to a 40% increase in autophosphorylation of SrrB, which activates SrrA, affecting biofilm formation and *tst* toxin expression (Tiwari et al. 2020). SrrAB senses indirectly increasing ROS levels during

aerobic growth and induces the oxidative stress response. Thus, SrrAB contributes to the protection of FeS cluster enzymes, such as aconitase and facilitates the growth under aerobic conditions in *S. aureus* (Mashruwala and Boyd 2017). In support of this notion, the SrrB disulfide under aerobic conditions was important for pathogenesis of *S. aureus* in an endocarditis model of infection (Tiwari et al. 2020).

Outlook for future research

In this review, we present an overview of thiol-based redox switches in the pathogen *S. aureus*, which sense different reactive species via conserved Cys residues and control specific enzymatic detoxification pathways. We provide new insights into the role of BSH and the Brx/BSH/YpdA/NADPH pathway for redox homeostasis under oxidative stress, infection conditions and redox active antimicrobials in *S. aureus*. Significant progress occurred in the physiological and biochemical characterization of the NADPH-dependent flavin disulfide reductase YpdA as a BSSB reductase, which established a functional Brx/BSH/YpdA/NADPH electron pathway for regeneration of *S*-bacillithiolated proteins. BSH and the Brx/BSH/YpdA/NADPH redox pathway are crucial for redox homeostasis in *S. aureus* during host-pathogen interactions and contribute to antibiotic resistance towards redox active antimicrobials. The novel Brx-roGFP2 biosensor revealed the impact of BSH and YpdA on redox homeostasis and the oxidative mode of action of the antimicrobials allicin, lapachol and AGXX®.

However, the functions of BSH as cofactor of redox enzymes for detoxification of electrophiles and oxidants are only beginning to emerge. While BSH-dependent und BSH-independent glyoxalases for methylglyoxal removal have been characterized in *B. subtilis* (Chandrangsu et al. 2014), nothing is known about related mechanisms in *S. aureus*, although methylglyoxal is the most conserved toxic electrophile in all organisms. In addition, *S. aureus* encodes so many peroxiredoxins, such as Tpx, Bcp, GpxA1 and GpxA2, but their functions, substrates and the roles of the Brx/BSH/YpdA/NADPH and Trx/TrxR/NADPH pathways for their recycling are completely unknown. These peroxiredoxins might be particularly important to prevent accumulation of host-derived fatty acid electrophiles during infections.

While BSH plays an important role in FeS cluster assembly in *S. aureus*, the detailed mechanism awaits further studies. Similarly, the role of BSH in metal storage or buffering under conditions of nutritional immunity, such as Fe^{2+}, Cu^{2+} or Zn^{2+} starvation are important subjects in terms of host-pathogen interactions in *S. aureus*. Through mass spectrometry-based redox proteomics approaches, many new thiol switches, including *S*-bacillithiolated and *S*-CoAlated proteins have been discovered recently. While the role of *S*-bacillithiolation in thiol protection and redox regulation has been studied for GapDH in *S. aureus*, the implication of this redox modification and its reversal by the Brx/BSH/YpdA/NADPH pathway for cellular physiology during *S. aureus* infections are important tasks of future research. Furthermore, the physiological role of *S*-CoAlation and its reversal in *S. aureus* remain further subjects of investigations.

The described thiol-based redox regulators of *S. aureus* cover a wide spectrum of bacterial transcription factor families, including Fur (PerR), MarR (SarZ/MgrA/SarA/QsrR/MhqR), Rrf2 (HypR), ArsC (Spx), TetR (GbaA) and two-component systems (SrrAB). These redox regulators sense oxygen, ROS, HOCl, NEM, quinones, methylglyoxal or antibiotics and often promote survival during infections. The thiol switch mechanisms can be divided into 1-Cys type and 2-Cys type models, including intra- or intersubunit disulfide formation of the 2-Cys type regulators (e.g. QsrR, HypR, Spx, SrrAB) and *S*-thiolation, *S*-alkylation or *S*-phosphorylation of the 1-Cys type redox sensors (e.g. SarZ, MgrA, SarA, GbaA). Specific redox regulators may employ different regulatory mechanisms to sense different reactive species (e.g. PerR, QsrR, GbaA), which has yet to be explored mechanistically and for cellular physiology or pathophysiology.

Finally, future studies should be directed to investigate structural determinants of the specificity (or non-specificity) of regulatory thiol switches towards sensing of ROS, RES or HOCl. While there is evidence for an extensive cross reactivity of thiol switches towards various ROS, RES or HOCl (e.g. QsrR, MhqR, HypR, Spx, GbaA), the structural changes might be similar for some, but different for other redox sensors depending on the signals. The challenge is to find the physiological important signal and to dissect whether primary or secondary signals lead to inactivation or activation of the redox regulator. The functions of the specific regulon members might help to deduce the specific signals important for physiology or pathophysiology. For example, the HypR repressor responds to neutrophil infections, HOCl and the redox active antimicrobials AGXX®, allicin and lapachol by intersubunit disulfide formation leading to upregulation of the disulfide reductase MerA. However, in terms of pathophysiology, HOCl is the most important signal, since MerA provides protection during infections. Similar cross reactivities to RES and antimicrobials are observed for QsrR/YodB and MhqR, but their functions in quinone detoxification have been clearly established. Thus, the specificity

of the primary or secondary redox signal has to be revealed in concert with the functions of the regulon members in the physiology or pathophysiology of *S. aureus*. The discovery and characterization of thiol switches, which sense novel biochemical signals during host-pathogen interactions, remain exciting future challenges in the field of redox biology in microbial pathogens.

Acknowledgments: This work was supported by an ERC Consolidator grant (GA 615585) MYCOTHIOLOME and grants from the Deutsche Forschungsgemeinschaft (AN746/4-1 and AN746/4-2) within the priority program on "Thiol-based Redox switches in Cellular Physiology SPP1710", by the SFB973 project C08 and by the SFB/TR84 project B06 to H.A.
Author contribution: All the authors have accepted responsibility for the entire content of this submitted manuscript and approved submission.
Research funding: Deutsche Forschungsgemeinschaft SPP1710 grants AN746/4-1 and AN746/4-2; SFB973 project C08; TR84 project B06; ERC Consolidator Grant MYCOTHIOLOME GA615585.
Conflict of interest statement: The authors declare no conflicts of interest regarding this article.

References

Antelmann, H., Hecker, M., and Zuber, P. (2008). Proteomic signatures uncover thiol-specific electrophile resistance mechanisms in *Bacillus subtilis*. Expert Rev. Proteomics 5: 77–90.

Antelmann, H. and Helmann, J.D. (2011). Thiol-based redox switches and gene regulation. Antioxid. Redox. Signal 14: 1049–1063.

Arbach, M., Santana, T.M., Moxham, H., Tinson, R., Anwar, A., Groom, M., and Hamilton, C.J. (2019). Antimicrobial garlic-derived diallyl polysulfanes: interactions with biological thiols in *Bacillus subtilis*. Biochim. Biophys. Acta 1863: 1050–1058.

Archer, G.L. (1998). *Staphylococcus aureus*: a well-armed pathogen. Clin. Infect. Dis. 26: 1179–1181.

Argyrou, A. and Blanchard, J.S. (2004). Flavoprotein disulfide reductases: advances in chemistry and function. Prog. Nucleic Acid Res. Mol. Biol. 78: 89–142.

Austin, C.M., Garabaglu, S., Krute, C.N., Ridder, M.J., Seawell, N.A., Markiewicz, M.A., Boyd, J.M., and Bose, J.L. (2019). Contribution of YjbIH to virulence factor expression and host colonization in *Staphylococcus aureus*. Infect. Immun. 87: e00155-19.

Baek, Y., Kim, J., Ahn, J., Jo, I., Hong, S., Ryu, S., and Ha, N.C. (2020). Structure and function of the hypochlorous acid-induced flavoprotein RclA from *Escherichia coli*. J. Biol. Chem. 295: 3202–3212.

Ballal, A. and Manna, A.C. (2009). Regulation of superoxide dismutase (sod) genes by SarA in *Staphylococcus aureus*. J. Bacteriol. 191: 3301–3310.

Ballal, A., and Manna, A.C. (2010). Control of thioredoxin reductase gene (*trxB*) transcription by SarA in *Staphylococcus aureus*. J. Bacteriol. 192: 336–345.

Ballal, A., Ray, B., and Manna, A.C. (2009). *sarZ*, a SarA family gene, is transcriptionally activated by MgrA and is involved in the regulation of genes encoding exoproteins in *Staphylococcus aureus*. J. Bacteriol. 191: 1656–1665.

Bambouskova, M., Gorvel, L., Lampropoulou, V., Sergushichev, A., Loginicheva, E., Johnson, K., Korenfeld, D., Mathyer, M.E., Kim, H., Huang, L.H., et al. (2018). Electrophilic properties of itaconate and derivatives regulate the IkappaBzeta-ATF3 inflammatory axis. Nature 556: 501–504.

Barwinska-Sendra, A., Garcia, Y.M., Sendra, K.M., Basle, A., Mackenzie, E.S., Tarrant, E., Card, P., Tabares, L.C., Bicep, C., Un, S., et al. (2020). An evolutionary path to altered cofactor specificity in a metalloenzyme. Nat. Commun. 11: 2738.

Beavers, W.N., and Skaar, E.P. (2016). Neutrophil-generated oxidative stress and protein damage in *Staphylococcus aureus*. Pathog. Dis. 74: ftw060, https://doi.org/10.1093/femspd/ftw060.

Benchoam, D., Cuevasanta, E., Moller, M.N., and Alvarez, B. (2020). Persulfides, at the crossroads between hydrogen sulfide and thiols. Essays Biochem. 64: 155–168.

Booth, I.R., Ferguson, G.P., Miller, S., Li, C., Gunasekera, B., and Kinghorn, S. (2003). Bacterial production of methylglyoxal: a survival strategy or death by misadventure? Biochem. Soc. Trans. 31: 1406–1408.

Borlinghaus, J., Albrecht, F., Gruhlke, M.C., Nwachukwu, I.D., and Slusarenko, A.J. (2014). Allicin: chemistry and biological properties. Molecules 19: 12591–12618.

Boucher, H.W. and Corey, G.R. (2008). Epidemiology of methicillin-resistant *Staphylococcus aureus*. Clin. Infect. Dis. 46(Suppl. 5): S344–S349.

Bragg, P.D., Glavas, N.A., and Hou, C. (1997). Mutation of conserved residues in the NADP(H)-binding domain of the proton translocating pyridine nucleotide transhydrogenase of *Escherichia coli*. Arch. Biochem. Biophys. 338: 57–66.

Brunmark, A. and Cadenas, E. (1989). Redox and addition chemistry of quinoid compounds and its biological implications. Free Radic. Biol. Med. 7: 435–477.

Chambers, H.F. and Deleo, F.R. (2009). Waves of resistance: *Staphylococcus aureus* in the antibiotic era. Nat. Rev. Microbiol. 7: 629–641.

Chan, P.F. and Foster, S.J. (1998). Role of SarA in virulence determinant production and environmental signal transduction in *Staphylococcus aureus*. J. Bacteriol. 180: 6232–6241.

Chandrangsu, P., Dusi, R., Hamilton, C.J., and Helmann, J.D. (2014). Methylglyoxal resistance in *Bacillus subtilis*: contributions of bacillithiol-dependent and independent pathways. Mol. Microbiol. 91: 706–715.

Chandrangsu, P., Loi, V.V., Antelmann, H., and Helmann, J.D. (2018). The role of bacillithiol in Gram-positive firmicutes. Antioxid. Redox. Signal 28: 445–462.

Chen, P.R., Bae, T., Williams, W.A., Duguid, E.M., Rice, P.A., Schneewind, O., and He, C. (2006). An oxidation-sensing mechanism is used by the global regulator MgrA in *Staphylococcus aureus*. Nat. Chem. Biol. 2: 591–595.

Chen, P.R., Brugarolas, P., and He, C. (2011). Redox signaling in human pathogens. Antioxid. Redox. Signal 14: 1107–1118.

Chen, P.R., Nishida, S., Poor, C.B., Cheng, A., Bae, T., Kuechenmeister, L., Dunman, P.M., Missiakas, D., and He, C. (2009). A new oxidative sensing and regulation pathway mediated by the MgrA homologue SarZ in *Staphylococcus aureus*. Mol. Microbiol. 71: 198–211.

Chi, B.K., Albrecht, D., Gronau, K., Becher, D., Hecker, M., and Antelmann, H. (2010). The redox-sensing regulator YodB senses quinones and diamide via a thiol-disulfide switch in *Bacillus subtilis*. Proteomics 10: 3155–3164.

Chi, B.K., Gronau, K., Mäder, U., Hessling, B., Becher, D., and Antelmann, H. (2011). *S*-bacillithiolation protects against hypochlorite stress in *Bacillus subtilis* as revealed by transcriptomics and redox proteomics. Mol. Cell. Proteomics 10: M111–009506.

Chi, B.K., Huyen, N.T.T., Loi, V.V., Gruhlke, M.C.H., Schaffer, M., Mäder, U., Maass, S., Becher, D., Bernhardt, J., and Arbach, M., et al (2019). The disulfide stress response and protein S-thioallylation caused by allicin and diallyl polysulfanes in *Bacillus subtilis* as revealed by transcriptomics and proteomics. Antioxidants 8: 605.

Chi, B.K., Roberts, A.A., Huyen, T.T., Basell, K., Becher, D., Albrecht, D., Hamilton, C.J., and Antelmann, H. (2013). *S*-bacillithiolation protects conserved and essential proteins against hypochlorite stress in firmicutes bacteria. Antioxid. Redox. Signal 18: 1273–1295.

Chien, Y., Manna, A.C., Projan, S.J., and Cheung, A.L. (1999). SarA, a global regulator of virulence determinants in *Staphylococcus aureus*, binds to a conserved motif essential for *sar*-dependent gene regulation. J. Biol. Chem. 274: 37169–37176.

Chirgadze, Y.N., Boshkova, E.A., Battaile, K.P., Mendes, V.G., Lam, R., Chan, T.S.Y., Romanov, V., Pai, E.F., and Chirgadze, N.Y. (2018). Crystal structure of *Staphylococcus aureus* Zn-glyoxalase I: new subfamily of glyoxalase I family. J. Biomol. Struct. Dyn. 36: 376–386.

Clauss-Lendzian, E., Vaishampayan, A., de Jong, A., Landau, U., Meyer, C., Kok, J., and Grohmann, E. (2018). Stress response of a clinical *Enterococcus faecalis* isolate subjected to a novel antimicrobial surface coating. Microbiol. Res. 207: 53–64.

Clements, M.O., Watson, S.P., and Foster, S.J. (1999). Characterization of the major superoxide dismutase of *Staphylococcus aureus* and its role in starvation survival, stress resistance, and pathogenicity. J. Bacteriol. 181: 3898–3903.

Cosgrove, K., Coutts, G., Jonsson, I.M., Tarkowski, A., Kokai-Kun, J.F., Mond, J.J., and Foster, S.J. (2007). Catalase (KatA) and alkyl hydroperoxide reductase (AhpC) have compensatory roles in peroxide stress resistance and are required for survival, persistence, and nasal colonization in *Staphylococcus aureus*. J. Bacteriol. 189: 1025–1035.

Crosby, H.A., Schlievert, P.M., Merriman, J.A., King, J.M., Salgado-Pabon, W., and Horswill, A.R. (2016). The *Staphylococcus aureus* global regulator MgrA modulates clumping and virulence by controlling surface protein expression. PloS Pathog. 12: e1005604.

Crosby, H.A., Tiwari, N., Kwiecinski, J.M., Xu, Z., Dykstra, A., Jenul, C., Fuentes, E.J., and Horswill, A.R. (2020). The *Staphylococcus aureus* ArlRS two-component system regulates virulence factor expression through MgrA. Mol. Microbiol. 113: 103–122.

Cuthbertson, L. and Nodwell, J.R. (2013). The TetR family of regulators. Microbiol. Mol. Biol. Rev. 77: 440–475.

Davies, M.J. (2011). Myeloperoxidase-derived oxidation: mechanisms of biological damage and its prevention. J. Clin. Biochem. Nutr. 48: 8–19.

delCardayre, S.B. and Davies, J.E. (1998). *Staphylococcus aureus* coenzyme A disulfide reductase, a new subfamily of pyridine nucleotide-disulfide oxidoreductase. Sequence, expression, and analysis of cdr. J. Biol. Chem. 273: 5752–5757.

delCardayré, S.B., Stock, K.P., Newton, G.L., Fahey, R.C., and Davies, J.E. (1998). Coenzyme A disulfide reductase, the primary low molecular weight disulfide reductase from *Staphylococcus aureus*. Purification and characterization of the native enzyme. J. Biol. Chem. 273: 5744–5751.

Delmastro-Greenwood, M., Freeman, B.A., and Wendell, S.G. (2014). Redox-dependent anti-inflammatory signaling actions of unsaturated fatty acids. Annu. Rev. Physiol. 76: 79–105.

Deng, X., Weerapana, E., Ulanovskaya, O., Sun, F., Liang, H., Ji, Q., Ye, Y., Fu, Y., Zhou, L., Li, J., et al. (2013). Proteome-wide quantification and characterization of oxidation-sensitive cysteines in pathogenic bacteria. Cell Host Microbe. 13: 358–370.

Derewenda, U., Boczek, T., Gorres, K.L., Yu, M., Hung, L.W., Cooper, D., Joachimiak, A., Raines, R.T., and Derewenda, Z.S. (2009). Structure and function of *Bacillus subtilis* YphP, a prokaryotic disulfide isomerase with a CXC catalytic motif. Biochemistry 48: 8664–8671.

Dickerhof, N., Paton, L., and Kettle, A.J. (2020). Oxidation of bacillithiol by myeloperoxidase-derived oxidants. Free Radic. Biol. Med. 158: 74–83.

Donegan, N.P., Manna, A.C., Tseng, C.W., Liu, G.Y., and Cheung, A.L. (2019). CspA regulation of *Staphylococcus aureus* carotenoid levels and sigma (B) activity is controlled by YjbH and Spx. Mol. Microbiol. 112: 532–551.

Dooley, C.T., Dore, T.M., Hanson, G.T., Jackson, W.C., Remington, S.J., and Tsien, R.Y. (2004). Imaging dynamic redox changes in mammalian cells with green fluorescent protein indicators. J. Biol. Chem. 279: 22284–22293.

Duarte, V. and Latour, J.M. (2010). PerR versus OhrR: selective peroxide sensing in *Bacillus subtilis*. Mol. Biosyst. 6: 316–323.

Dubbs, J.M. and Mongkolsuk, S. (2007). Peroxiredoxins in bacterial antioxidant defense. Subcell. Biochem. 44: 143–193.

Engman, J., Rogstam, A., Frees, D., Ingmer, H., and von Wachenfeldt, C. (2012). The YjbH adaptor protein enhances proteolysis of the transcriptional regulator Spx in *Staphylococcus aureus*. J. Bacteriol. 194: 1186–1194.

Engman, J. and von Wachenfeldt, C. (2015). Regulated protein aggregation: a mechanism to control the activity of the ClpXP adaptor protein YjbH. Mol. Microbiol. 95: 51–63.

Faulkner, M.J. and Helmann, J.D. (2011). Peroxide stress elicits adaptive changes in bacterial metal ion homeostasis. Antioxid. Redox. Signal 15: 175–189.

Favazzo, L.J., Gill, A.L., Farnsworth, C.W., Mooney, R.A., and Gill, S.R. (2019). The response of *nor* and *nos* contributes to *Staphylococcus aureus* virulence and metabolism. J. Bacteriol. 201: e00107-19.

Ferguson, G.P., Totemeyer, S., MacLean, M.J., and Booth, I.R. (1998). Methylglyoxal production in bacteria: suicide or survival? Arch. Microbiol. 170: 209–218.

Fernando, V., Zheng, X., Walia, Y., Sharma, V., Letson, J., and Furuta, S. (2019). *S-nitrosylation: an emerging paradigm of redox signaling*-nitrosylation: an emerging paradigm of redox signaling. Antioxidants 8: 404.

Flierl, M.A., Rittirsch, D., Nadeau, B.A., Chen, A.J., Sarma, J.V., Zetoune, F.S., McGuire, S.R., List, R.P., Day, D.E., Hoesel, L.M., et al. (2007). Phagocyte-derived catecholamines enhance acute inflammatory injury. Nature 449: 721–725.

Forman, H.J., and Torres, M. (2001). Redox signaling in macrophages. Mol. Aspect. Med. 22: 189–216.

Foster, M.W., McMahon, T.J., and Stamler, J.S. (2003). *S*-nitrosylation in health and disease. Trends Mol. Med. 9: 160–168.

Foster, T.J. (2004). The *Staphylococcus aureus* "superbug". J. Clin. Invest. 114: 1693–1696.

Fritsch, V.N., Loi, V.V., Busche, T., Sommer, A., Tedin, K., Nürnberg, D.J., Kalinowski, J., Bernhardt, J., Fulde, M., and Antelmann, H. (2019). The MarR-type repressor MhqR confers quinone and antimicrobial resistance in *Staphylococcus aureus*. Antioxid. Redox. Signal 31: 1235–1252.

Fuller, J.R., Vitko, N.P., Perkowski, E.F., Scott, E., Khatri, D., Spontak, J.S., Thurlow, L.R., and Richardson, A.R. (2011). Identification of a lactate-quinone oxidoreductase in *Staphylococcus aureus* that is essential for virulence. Front. Cell Infect. Microbiol. 1: 19.

Gaballa, A., Chi, B.K., Roberts, A.A., Becher, D., Hamilton, C.J., Antelmann, H., and Helmann, J.D. (2014). Redox regulation in *Bacillus subtilis*: the bacilliredoxins BrxA(YphP) and BrxB(YqiW) function in de-bacillithiolation of *S*-bacillithiolated OhrR and MetE. Antioxid. Redox. Signal 21: 357–367.

Gaballa, A., Newton, G.L., Antelmann, H., Parsonage, D., Upton, H., Rawat, M., Claiborne, A., Fahey, R.C., and Helmann, J.D. (2010). Biosynthesis and functions of bacillithiol, a major low-molecular-weight thiol in Bacilli. Proc. Natl. Acad. Sci. USA 107: 6482–6486.

Garcia, Y.M., Barwinska-Sendra, A., Tarrant, E., Skaar, E.P., Waldron, K.J., and Kehl-Fie, T.E. (2017). A superoxide dismutase capable of functioning with iron or manganese promotes the resistance of *Staphylococcus aureus* to calprotectin and nutritional immunity. PloS Pathog. 13: e1006125.

Garg, S.K., Kommineni, S., Henslee, L., Zhang, Y., and Zuber, P. (2009). The YjbH protein of *Bacillus subtilis* enhances ClpXP-catalyzed proteolysis of Spx. J. Bacteriol. 191: 1268–1277.

Gaupp, R., Ledala, N., and Somerville, G.A. (2012). Staphylococcal response to oxidative stress. Front. Cell Infect. Microbiol. 2: 33.

Gohring, N., Fedtke, I., Xia, G., Jorge, A.M., Pinho, M.G., Bertsche, U., and Peschel, A. (2011). New role of the disulfide stress effector YjbH in beta-lactam susceptibility of *Staphylococcus aureus*. Antimicrob. Agents Chemother. 55: 5452–5458.

Goncalves, V.L., Nobre, L.S., Vicente, J.B., Teixeira, M., and Saraiva, L.M. (2006). Flavohemoglobin requires microaerophilic conditions for nitrosative protection of *Staphylococcus aureus*. FEBS Lett. 580: 1817–1821.

Gout, I. (2019). Coenzyme A: a protective thiol in bacterial antioxidant defence. Biochem. Soc. Trans. 47: 469–476.

Green, J.N., Chapman, A.L.P., Bishop, C.J., Winterbourn, C.C., and Kettle, A.J. (2017). Neutrophil granule proteins generate bactericidal ammonia chloramine on reaction with hydrogen peroxide. Free Radic. Biol. Med. 113: 363–371.

Grosser, M.R., Weiss, A., Shaw, L.N., and Richardson, A.R. (2016). Regulatory requirements for *Staphylococcus aureus* nitric oxide resistance. J. Bacteriol. 198: 2043–2055.

Grove, A. (2017). Regulation of metabolic pathways by MarR family transcription factors. Comput. Struct. Biotechnol. J. 15: 366–371.

Gupta, A., Matsui, K., Lo, J.F., and Silver, S. (1999). Molecular basis for resistance to silver cations in *Salmonella*. Nat. Med. 5: 183–188.

Guridi, A., Diederich, A.K., Aguila-Arcos, S., Garcia-Moreno, M., Blasi, R., Broszat, M., Schmieder, W., Clauss-Lendzian, E., Sakinc-Gueler, T., Andrade, R., et al. (2015). New antimicrobial contact catalyst killing antibiotic resistant clinical and waterborne pathogens. Mater. Sci. Eng. C Mater. Biol. Appl. 50: 1–11.

Hawkins, C.L., Pattison, D.I., and Davies, M.J. (2003). Hypochlorite-induced oxidation of amino acids, peptides and proteins. Amino acids 25: 259–274.

Hazen, S.L., d'Avignon, A., Anderson, M.M., Hsu, F.F., and Heinecke, J.W. (1998). Human neutrophils employ the myeloperoxidase-hydrogen peroxide-chloride system to oxidize alpha-amino acids to a family of reactive aldehydes. Mechanistic studies identifying labile intermediates along the reaction pathway. J. Biol. Chem. 273: 4997–5005.

Heiss, A., Freisinger, B., and Held-Fohn, E. (2017). Enhanced antibacterial activity of silver-ruthenium coated hollow microparticles. Biointerphases 12: 05G608.

Higgins, K.A., Peng, H., Luebke, J.L., Chang, F.M., and Giedroc, D.P. (2015). Conformational analysis and chemical reactivity of the multidomain sulfurtransferase, *Staphylococcus aureus* CstA. Biochemistry 54: 2385–2398.

Hillion, M. and Antelmann, H. (2015). Thiol-based redox switches in prokaryotes. Biol. Chem. 396: 415–444.

Hiras, J., Sharma, S.V., Raman, V., Tinson, R.A.J., Arbach, M., Rodrigues, D.F., Norambuena, J., Hamilton, C.J., and Hanson, T.E. (2018). Physiological studies of *Chlorobiaceae* suggest that bacillithiol derivatives are the most widespread thiols in bacteria. mBio. 9: e01603-18.

Horsburgh, M.J., Clements, M.O., Crossley, H., Ingham, E., and Foster, S.J. (2001a). PerR controls oxidative stress resistance and iron storage proteins and is required for virulence in *Staphylococcus aureus*. Infect. Immun. 69: 3744–3754.

Horsburgh, M.J., Ingham, E., and Foster, S.J. (2001b). In *Staphylococcus aureus, Fur* is an interactive regulator with PerR, contributes to virulence, and is necessary for oxidative stress resistance through positive regulation of catalase and iron homeostasis. J. Bacteriol. 183: 468–475.

Imber, M., Huyen, N.T.T., Pietrzyk-Brzezinska, A.J., Loi, V.V., Hillion, M., Bernhardt, J., Thärichen, L., Kolsek, K., Saleh, M., Hamilton, C.J., et al. (2018a). Protein S-bacillithiolation functions in thiol protection and redox regulation of the glyceraldehyde-3-phosphate dehydrogenase gap in *Staphylococcus aureus* under hypochlorite stress. Antioxid. Redox. Signal 28: 410–430.

Imber, M., Loi, V.V., Reznikov, S., Fritsch, V.N., Pietrzyk-Brzezinska, A.J., Prehn, J., Hamilton, C., Wahl, M.C., Bronowska, A.K., and Antelmann, H. (2018b). The aldehyde dehydrogenase AldA contributes to the hypochlorite defense and is redox-controlled by protein S-bacillithiolation in *Staphylococcus aureus*. Redox. Biol. 15: 557–568.

Imber, M., Pietrzyk-Brzezinska, A.J., and Antelmann, H. (2019). Redox regulation by reversible protein *S*-thiolation in Gram-positive bacteria. Redox. Biol. 20: 130–145.

Imlay, J.A. (2003). Pathways of oxidative damage. Annu. Rev. Microbiol. 57: 395–418.

Imlay, J.A. (2008). Cellular defenses against superoxide and hydrogen peroxide. Annu. Rev. Biochem. 77: 755–776.

Ingavale, S., van Wamel, W., Luong, T.T., Lee, C.Y., and Cheung, A.L. (2005). Rat/MgrA, a regulator of autolysis, is a regulator of virulence genes in *Staphylococcus aureus*. Infect. Immun. 73: 1423–1431.

Jackowski, S. and Rock, C.O. (1986). Consequences of reduced intracellular coenzyme A content in *Escherichia coli*. J. Bacteriol. 166: 866–871.

James, K.L., Mogen, A.B., Brandwein, J.N., Orsini, S.S., Ridder, M.J., Markiewicz, M.A., Bose, J.L., and Rice, K.C. (2019). Interplay of

nitric oxide synthase (NOS) and SrrAB in modulation of *Staphylococcus aureus* metabolism and virulence. Infect. Immun. 87: e00570-18.

Ji, C.J., Kim, J.H., Won, Y.B., Lee, Y.E., Choi, T.W., Ju, S.Y., Youn, H., Helmann, J.D., and Lee, J.W. (2015). *Staphylococcus aureus* PerR is a hypersensitive hydrogen peroxide sensor using iron-mediated histidine oxidation. J. Biol. Chem. 290: 20374–20386.

Ji, Q., Zhang, L., Jones, M.B., Sun, F., Deng, X., Liang, H., Cho, H., Brugarolas, P., Gao, Y.N., Peterson, S.N., et al. (2013). Molecular mechanism of quinone signaling mediated through *S*-quinonization of a YodB family repressor QsrR. Proc. Natl. Acad. Sci. USA 110: 5010–5015.

Jonsson, I.M., Lindholm, C., Luong, T.T., Lee, C.Y., and Tarkowski, A. (2008). MgrA regulates staphylococcal virulence important for induction and progression of septic arthritis and sepsis. Microb. Infect. 10: 1229–1235.

Jousselin, A., Kelley, W.L., Barras, C., Lew, D.P., and Renzoni, A. (2013). The *Staphylococcus aureus* thiol/oxidative stress global regulator Spx controls *trfA*, a gene implicated in cell wall antibiotic resistance. Antimicrob. Agents Chemother. 57: 3283–3292.

Kaatz, G.W., Thyagarajan, R.V., and Seo, S.M. (2005). Effect of promoter region mutations and *mgrA* overexpression on transcription of *norA*, which encodes a *Staphylococcus aureus* multidrug efflux transporter. Antimicrob. Agents Chemother. 49: 161–169.

Kaito, C., Morishita, D., Matsumoto, Y., Kurokawa, K., and Sekimizu, K. (2006). Novel DNA binding protein SarZ contributes to virulence in *Staphylococcus aureus*. Mol. Microbiol. 62: 1601–1617.

Kalapos, M.P. (2008). The tandem of free radicals and methylglyoxal. Chem. Biol. Interact. 171: 251–271.

Karavolos, M.H., Horsburgh, M.J., Ingham, E., and Foster, S.J. (2003). Role and regulation of the superoxide dismutases of *Staphylococcus aureus*. Microbiology 149: 2749–2758.

Karlinsey, J.E., Bang, I.S., Becker, L.A., Frawley, E.R., Porwollik, S., Robbins, H.F., Thomas, V.C., Urbano, R., McClelland, M., and Fang, F.C. (2012). The NsrR regulon in nitrosative stress resistance of *Salmonella enterica* serovar Typhimurium. Mol. Microbiol. 85: 1179–1193.

Kawai, Y., Mercier, R., Wu, L.J., Dominguez-Cuevas, P., Oshima, T., and Errington, J. (2015). Cell growth of wall-free L-form bacteria is limited by oxidative damage. Curr. Biol. 25: 1613–1618.

Kehl-Fie, T.E., Chitayat, S., Hood, M.I., Damo, S., Restrepo, N., Garcia, C., Munro, K.A., Chazin, W.J., and Skaar, E.P. (2011). Nutrient metal sequestration by calprotectin inhibits bacterial superoxide defense, enhancing neutrophil killing of *Staphylococcus aureus*. Cell Host Microbe. 10: 158–164.

Kim, H.J., Lee, K.Y., Kwon, A.R., and Lee, B.J. (2017). Structural and functional studies of SAV0551 from *Staphylococcus aureus* as a chaperone and glyoxalase III. Biosci. Rep. 37: BSR20171106.

Kinkel, T.L., Roux, C.M., Dunman, P.M., and Fang, F.C. (2013). The *Staphylococcus aureus* SrrAB two-component system promotes resistance to nitrosative stress and hypoxia. mBio. 4: e00696–e00613.

Kolar, S.L., Ibarra, J.A., Rivera, F.E., Mootz, J.M., Davenport, J.E., Stevens, S.M., Horswill, A.R., and Shaw, L.N. (2013). Extracellular proteases are key mediators of *Staphylococcus aureus* virulence via the global modulation of virulence-determinant stability. Microbiologyopen 2: 18–34.

Lalaouna, D., Baude, J., Wu, Z., Tomasini, A., Chicher, J., Marzi, S., Vandenesch, F., Romby, P., Caldelari, I., and Moreau, K. (2019). RsaC sRNA modulates the oxidative stress response of *Staphylococcus aureus* during manganese starvation. Nucleic Acids Res. 47: 9871–9887.

Lampropoulou, V., Sergushichev, A., Bambouskova, M., Nair, S., Vincent, E.E., Loginicheva, E., Cervantes-Barragan, L., Ma, X., Huang, S.C., Griss, T., et al. (2016). Itaconate links inhibition of succinate dehydrogenase with macrophage metabolic remodeling and regulation of inflammation. Cell Metabol. 24: 158–166.

Lee, J.W. and Helmann, J.D. (2006). The PerR transcription factor senses H_2O_2 by metal-catalysed histidine oxidation. Nature 440: 363–367.

Lee, J.W., Soonsanga, S., and Helmann, J.D. (2007). A complex thiolate switch regulates the *Bacillus subtilis* organic peroxide sensor. OhrR. Proc Natl Acad Sci USA 104: 8743–8748.

Lee, S.J., Lee, I.G., Lee, K.Y., Kim, D.G., Eun, H.J., Yoon, H.J., Chae, S., Song, S.H., Kang, S.O., Seo, M.D., et al. (2016). Two distinct mechanisms of transcriptional regulation by the redox sensor YodB. Proc. Natl. Acad. Sci. USA. 113: E5202–E5211.

Leelakriangsak, M., Huyen, N.T., Towe, S., van Duy, N., Becher, D., Hecker, M., Antelmann, H., and Zuber, P. (2008). Regulation of quinone detoxification by the thiol stress sensing DUF24/MarR-like repressor, YodB in *Bacillus subtilis*. Mol. Microbiol. 67: 1108–1124.

Lewis, A.M., Matzdorf, S.S., Endres, J.L., Windham, I.H., Bayles, K.W., and Rice, K.C. (2015). Examination of the *Staphylococcus aureus* nitric oxide reductase (saNOR) reveals its contribution to modulating intracellular NO levels and cellular respiration. Mol. Microbiol. 96: 651–669.

Li, L., Wang, G., Cheung, A., Abdelhady, W., Seidl, K., and Xiong, Y.Q. (2019). MgrA governs adherence, host cell interaction, and virulence in a murine model of bacteremia due to *Staphylococcus aureus*. J. Infect. Dis. 220: 1019–1028.

Liebeke, M., Pöther, D.C., van Duy, N., Albrecht, D., Becher, D., Hochgräfe, F., Lalk, M., Hecker, M., and Antelmann, H. (2008). Depletion of thiol-containing proteins in response to quinones in *Bacillus subtilis*. Mol. Microbiol. 69: 1513–1529.

Lill, R. (2020). From the discovery to molecular understanding of cellular iron-sulfur protein biogenesis. Biol. Chem. 401: 855–876.

Linzner, N., Fritsch, V.N., Busche, T., Tung, Q.N., Van Loi, V., Bernhardt, J., Kalinowski, J., and Antelmann, H. (2020). The plant-derived naphthoquinone lapachol causes an oxidative stress response in *Staphylococcus aureus*. Free Radic. Biol. Med. 158: 126–136.

Linzner, N., Loi, V.V., Fritsch, V.N., Tung, Q.N., Stenzel, S., Wirtz, M., Hell, R., Hamilton, C.J., Tedin, K., Fulde, M., et al. (2019). *Staphylococcus aureus* uses the bacilliredoxin (BrxAB)/bacillithiol disulfide reductase (YpdA) redox pathway to defend against oxidative stress under infections. Front. Microbiol. 10: 1355.

Loi, V.V., and Antelmann, H. (2020). Method for measurement of bacillithiol redox potential changes using the Brx-roGFP2 redox biosensor in *Staphylococcus aureus*. MethodsX 7: 100900.

Loi, V.V., Busche, T., Preuss, T., Kalinowski, J., Bernhardt, J., and Antelmann, H. (2018a). The AGXX antimicrobial coating causes a thiol-specific oxidative stress response and protein *S*-bacillithiolation in *Staphylococcus aureus*. Front. Microbiol. 9: 3037.

Loi, V.V., Busche, T., Tedin, K., Bernhardt, J., Wollenhaupt, J., Huyen, N.T.T., Weise, C., Kalinowski, J., Wahl, M.C., Fulde, M., et al. (2018b). Redox-sensing under hypochlorite stress and infection conditions by the Rrf2-family repressor HypR in *Staphylococcus aureus*. Antioxid. Redox. Signal 29: 615–636.

Loi, V.V., Harms, M., Müller, M., Huyen, N.T.T., Hamilton, C.J., Hochgräfe, F., Pane-Farre, J., and Antelmann, H. (2017). Real-time imaging of the bacillithiol redox potential in the human pathogen *Staphylococcus aureus* using a genetically encoded bacilliredoxin-fused redox biosensor. Antioxid. Redox. Signal 26: 835–848.

Loi, V.V., Huyen, N.T.T., Busche, T., Tung, Q.N., Gruhlke, M.C.H., Kalinowski, J., Bernhardt, J., Slusarenko, A.J., and Antelmann, H. (2019). *Staphylococcus aureus* responds to allicin by global *S*-thioallylation – role of the Brx/BSH/YpdA pathway and the disulfide reductase MerA to overcome allicin stress. Free Radic. Biol. Med. 139: 55–69.

Loi, V.V., Rossius, M., and Antelmann, H. (2015). Redox regulation by reversible protein *S*-thiolation in bacteria. Front. Microbiol. 6: 187.

Lowy, F.D. (1998). *Staphylococcus aureus* infections. N. Engl. J. Med. 339: 520–532.

Luebke, J.L., Shen, J., Bruce, K.E., Kehl-Fie, T.E., Peng, H., Skaar, E.P., and Giedroc, D.P. (2014). The CsoR-like sulfurtransferase repressor (CstR) is a persulfide sensor in *Staphylococcus aureus*. Mol. Microbiol. 94: 1343–1360.

Luong, T.T., Dunman, P.M., Murphy, E., Projan, S.J., and Lee, C.Y. (2006). Transcription profiling of the *mgrA* regulon in *Staphylococcus aureus*. J. Bacteriol. 188: 1899–1910.

Mäder, U., Nicolas, P., Depke, M., Pane-Farre, J., Debarbouille, M., van der Kooi-Pol, M.M., Guerin, C., Derozier, S., Hiron, A., Jarmer, H., et al. (2016). *Staphylococcus aureus* transcriptome architecture: from laboratory to infection-mimicking conditions. PloS Genet. 12: e1005962.

Manna, A.C., Ingavale, S.S., Maloney, M., van Wamel, W., and Cheung, A.L. (2004). Identification of sarV (SA2062), a new transcriptional regulator, is repressed by SarA and MgrA (SA0641) and involved in the regulation of autolysis in *Staphylococcus aureus*. J. Bacteriol. 186: 5267–5280.

Marchetti, M., De Bei, O., Bettati, S., Campanini, B., Kovachka, S., Gianquinto, E., Spyrakis, F., and Ronda, L. (2020). Iron metabolism at the interface between host and pathogen: from nutritional immunity to antibacterial development. Int. J. Mol. Sci. 21: 2145.

Maresso, A.W. and Schneewind, O. (2006). Iron acquisition and transport in *Staphylococcus aureus*. Biometals 19: 193–203.

Marnett, L.J., Riggins, J.N., and West, J.D. (2003). Endogenous generation of reactive oxidants and electrophiles and their reactions with DNA and protein. J. Clin. Invest. 111: 583–593.

Mashruwala, A.A. and Boyd, J.M. (2017). The *Staphylococcus aureus* SrrAB regulatory system modulates hydrogen peroxide resistance factors, which imparts protection to aconitase during aerobic growth. PloS One 12: e0170283.

Mashruwala, A.A., Guchte, A.V., and Boyd, J.M. (2017). Impaired respiration elicits SrrAB-dependent programmed cell lysis and biofilm formation in *Staphylococcus aureus*. Elife 6: e23845.

Mettert, E.L. and Kiley, P.J. (2015). Fe-S proteins that regulate gene expression. Biochim. Biophys. Acta 1853: 1284–1293.

Meyer, A.J. and Dick, T.P. (2010). Fluorescent protein-based redox probes. Antioxid. Redox. Signal 13: 621–650.

Mikheyeva, I.V., Thomas, J.M., Kolar, S.L., Corvaglia, A.R., Gaiotaa, N., Leo, S., Francois, P., Liu, G.Y., Rawat, M., and Cheung, A.L. (2019). YpdA, a putative bacillithiol disulfide reductase, contributes to cellular redox homeostasis and virulence in *Staphylococcus aureus*. Mol. Microbiol. 111: 1039–1056.

Mironov, A., Seregina, T., Nagornykh, M., Luhachack, L.G., Korolkova, N., Lopes, L.E., Kotova, V., Zavilgelsky, G., Shakulov, R., Shatalin, K., et al. (2017). Mechanism of H_2S-mediated protection against oxidative stress in *Escherichia coli*. Proc. Natl. Acad. Sci. USA 114: 6022–6027.

Mishra, S. and Imlay, J. (2012). Why do bacteria use so many enzymes to scavenge hydrogen peroxide? Arch. Biochem. Biophys. 525: 145–160.

Mongkolsuk, S. and Helmann, J.D. (2002). Regulation of inducible peroxide stress responses. Mol. Microbiol. 45: 9–15.

Monks, T.J., Hanzlik, R.P., Cohen, G.M., Ross, D., and Graham, D.G. (1992). Quinone chemistry and toxicity. Toxicol. Appl. Pharmacol. 112: 2–16.

Morgan, B., Ezerina, D., Amoako, T.N., Riemer, J., Seedorf, M., and Dick, T.P. (2013). Multiple glutathione disulfide removal pathways mediate cytosolic redox homeostasis. Nat. Chem. Biol. 9: 119–125.

Morgan, B., Sobotta, M.C., and Dick, T.P. (2011). Measuring E(GSH) and H_2O_2 with roGFP2-based redox probes. Free Radic. Biol. Med. 51: 1943–1951.

Müller, A., Langklotz, S., Lupilova, N., Kuhlmann, K., Bandow, J.E., and Leichert, L.I. (2014). Activation of RidA chaperone function by N-chlorination. Nat. Commun. 5: 5804.

Münchberg, U., Anwar, A., Mecklenburg, S., and Jacob, C. (2007). Polysulfides as biologically active ingredients of garlic. Org. Biomol. Chem. 5: 1505–1518.

Nakano, M.M., Kominos-Marvell, W., Sane, B., Nader, Y.M., Barendt, S.M., Jones, M.B., and Zuber, P. (2014). *spxA2*, encoding a regulator of stress resistance in *Bacillus anthracis*, is controlled by SaiR, a new member of the Rrf2 protein family. Mol. Microbiol. 94: 815–827.

Nakano, S., Erwin, K.N., Ralle, M., and Zuber, P. (2005). Redox-sensitive transcriptional control by a thiol/disulphide switch in the global regulator, Spx. Mol. Microbiol. 55: 498–510.

Nakano, S., Kuster-Schock, E., Grossman, A.D., and Zuber, P. (2003). Spx-dependent global transcriptional control is induced by thiol-specific oxidative stress in *Bacillus subtilis*. Proc. Natl. Acad. Sci. USA 100: 13603–13608.

Newton, G.L., Fahey, R.C., and Rawat, M. (2012). Detoxification of toxins by bacillithiol in *Staphylococcus aureus*. Microbiology 158: 1117–1126.

Newton, G.L., Leung, S.S., Wakabayashi, J.I., Rawat, M., and Fahey, R.C. (2011). The DinB superfamily includes novel mycothiol, bacillithiol, and glutathione *S*-transferases. Biochemistry 50: 10751–10760.

Newton, G.L., and Rawat, M. (2019). N-methyl-bacillithiol, a novel thiol from anaerobic bacteria. mBio. 10: e02634-18.

Newton, G.L., Rawat, M., La Clair, J.J., Jothivasan, V.K., Budiarto, T., Hamilton, C.J., Claiborne, A., Helmann, J.D., and Fahey, R.C. (2009). Bacillithiol is an antioxidant thiol produced in bacilli. Nat. Chem. Biol. 5: 625–627.

Nontaleerak, B., Duang-Nkern, J., Wongsaroj, L., Trinachartvanit, W., Romsang, A., and Mongkolsuk, S. (2020). Roles of the AhpD-family protein RcsA in reactive chlorine stress resistance and

virulence in *Pseudomonas aeruginosa*. Appl. Environ. Microbiol 86: e01480-20.

Norambuena, J., Wang, Y., Hanson, T., Boyd, J.M., and Barkay, T. (2018). Low-molecular-weight thiols and thioredoxins are important players in Hg(II) resistance in *Thermus thermophilus* HB27. Appl. Environ. Microbiol. 84: e01931-17.

Noto, M.J., Burns, W.J., Beavers, W.N., and Skaar, E.P. (2017). Mechanisms of pyocyanin toxicity and genetic determinants of resistance in *Staphylococcus aureus*. J. Bacteriol. 199: e00221-17.

O'Brien, P.J. (1991). Molecular mechanisms of quinone cytotoxicity. Chem. Biol. Interact. 80: 1–41.

Oogai, Y., Kawada-Matsuo, M., and Komatsuzawa, H. (2016). *Staphylococcus aureus* SrrAB affects susceptibility to hydrogen peroxide and co-existence with *Streptococcus sanguinis*. PloS One 11: e0159768.

Palazzolo-Ballance, A.M., Reniere, M.L., Braughton, K.R., Sturdevant, D.E., Otto, M., Kreiswirth, B.N., Skaar, E.P., and DeLeo, F.R. (2008). Neutrophil microbicides induce a pathogen survival response in community-associated methicillin-resistant *Staphylococcus aureus*. J. Immunol. 180: 500–509.

Pamp, S.J., Frees, D., Engelmann, S., Hecker, M., and Ingmer, H. (2006). Spx is a global effector impacting stress tolerance and biofilm formation in *Staphylococcus aureus*. J. Bacteriol. 188: 4861–4870.

Panasenko, O.O., Bezrukov, F., Komarynets, O., and Renzoni, A. (2020). YjbH solubility controls Spx in *Staphylococcus aureus*: implication for MazEF toxin-antitoxin system regulation. Front. Microbiol. 11: 113.

Pandey, S., Sahukhal, G.S., and Elasri, M.O. (2019). The *msaABCR* operon regulates the response to oxidative stress in *Staphylococcus aureus*. J. Bacteriol. 201: e00417-19.

Parker, B.W., Schwessinger, E.A., Jakob, U., and Gray, M.J. (2013). The RclR protein is a reactive chlorine-specific transcription factor in *Escherichia coli*. J. Biol. Chem. 288: 32574–32584.

Parsonage, D., Karplus, P.A., and Poole, L.B. (2008). Substrate specificity and redox potential of AhpC, a bacterial peroxiredoxin. Proc. Natl. Acad. Sci. USA 105: 8209–8214.

Parsonage, D., Nelson, K.J., Ferrer-Sueta, G., Alley, S., Karplus, P.A., Furdui, C.M., and Poole, L.B. (2015). Dissecting peroxiredoxin catalysis: separating binding, peroxidation, and resolution for a bacterial AhpC. Biochemistry 54: 1567–1575.

Partridge, J.D., Bodenmiller, D.M., Humphrys, M.S., and Spiro, S. (2009). NsrR targets in the *Escherichia coli* genome: new insights into DNA sequence requirements for binding and a role for NsrR in the regulation of motility. Mol. Microbiol. 73: 680–694.

Peng, H., Shen, J., Edmonds, K.A., Luebke, J.L., Hickey, A.K., Palmer, L.D., Chang, F.J., Bruce, K.A., Kehl-Fie, T.E., and Skaar, E.P., et al (2017a). Sulfide homeostasis and nitroxyl intersect via formation of reactive sulfur species in *Staphylococcus aureus*. mSphere 2: e00082-17.

Peng, H., Zhang, Y., Palmer, L.D., Kehl-Fie, T.E., Skaar, E.P., Trinidad, J.C., and Giedroc, D.P. (2017b). Hydrogen sulfide and reactive sulfur species impact proteome *S*-sulfhydration and global virulence regulation in *Staphylococcus aureus*. ACS Infect. Dis. 3: 744–755.

Perera, I.C. and Grove, A. (2010). Molecular mechanisms of ligand-mediated attenuation of DNA binding by MarR family transcriptional regulators. J. Mol. Cell Biol. 2: 243–254.

Perera, V.R., Newton, G.L., Parnell, J.M., Komives, E.A., and Pogliano, K. (2014). Purification and characterization of the *Staphylococcus aureus* bacillithiol transferase BstA. Biochim. Biophys. Acta 1840: 2851–2861.

Pinochet-Barros, A. and Helmann, J.D. (2018). Redox sensing by Fe(2+) in bacterial fur family metalloregulators. Antioxid. Redox. Signal 29: 1858–1871.

Poole, L.B. and Ellis, H.R. (1996). Flavin-dependent alkyl hydroperoxide reductase from *Salmonella typhimurium*. 1. Purification and enzymatic activities of overexpressed AhpF and AhpC proteins. Biochemistry 35: 56–64.

Poole, L.B., Hall, A., and Nelson, K.J. (2011). Overview of peroxiredoxins in oxidant defense and redox regulation. Curr. Protoc. Toxicol., Chapter 7: Unit7.9, https://doi.org/10.1002/0471140856.tx0709s49.

Poor, C.B., Chen, P.R., Duguid, E., Rice, P.A., and He, C. (2009). Crystal structures of the reduced, sulfenic acid, and mixed disulfide forms of SarZ, a redox active global regulator in *Staphylococcus aureus*. J. Biol. Chem. 284: 23517–23524.

Posada, A.C., Kolar, S.L., Dusi, R.G., Francois, P., Roberts, A.A., Hamilton, C.J., Liu, G.Y., and Cheung, A. (2014). Importance of bacillithiol in the oxidative stress response of *Staphylococcus aureus*. Infect. Immun. 82: 316–332.

Pöther, D.C., Gierok, P., Harms, M., Mostertz, J., Hochgräfe, F., Antelmann, H., Hamilton, C.J., Borovok, I., Lalk, M., Aharonowitz, Y., et al. (2013). Distribution and infection-related functions of bacillithiol in *Staphylococcus aureus*. Int. J. Med. Microbiol. 303: 114–123.

Pragman, A.A., Yarwood, J.M., Tripp, T.J., and Schlievert, P.M. (2004). Characterization of virulence factor regulation by SrrAB, a two-component system in *Staphylococcus aureus*. J. Bacteriol. 186: 2430–2438.

Radi, R. (2018). Oxygen radicals, nitric oxide, and peroxynitrite: redox pathways in molecular medicine. Proc. Natl. Acad. Sci. USA 115: 5839–5848.

Rajkarnikar, A., Strankman, A., Duran, S., Vargas, D., Roberts, A.A., Barretto, K., Upton, H., Hamilton, C.J., and Rawat, M. (2013). Analysis of mutants disrupted in bacillithiol metabolism in *Staphylococcus aureus*. Biochem. Biophys. Res. Commun. 436: 128–133.

Rawat, M., and Maupin-Furlow, J.A. (2020). Redox and thiols in archaea. Antioxidants 9: 381, https://doi.org/10.3390/antiox9050381.

Ray, A., Edmonds, K.A., Palmer, L.D., Skaar, E.P., and Giedroc, D.P. (2020). *Staphylococcus aureus* glucose-induced biofilm accessory protein A (GbaA) is a monothiol-dependent electrophile sensor. Biochemistry 59: 2882–2895.

Remes, B., Eisenhardt, B.D., Srinivasan, V., and Klug, G. (2015). IscR of *Rhodobacter sphaeroides* functions as repressor of genes for iron-sulfur metabolism and represents a new type of iron-sulfur-binding protein. Microbiologyopen 4: 790–802.

Riquelme, S.A., Liimatta, K., Wong Fok Lung, T., Fields, B., Ahn, D., Chen, D., Lozano, C., Saenz, Y., Uhlemann, A.C., Kahl, B.C., et al. (2020). *Pseudomonas aeruginosa* utilizes host-derived itaconate to redirect its metabolism to promote biofilm formation. Cell Metabol. 31: 1091–1106, e1096.

Roberts, A.A., Sharma, S.V., Strankman, A.W., Duran, S.R., Rawat, M., and Hamilton, C.J. (2013). Mechanistic studies of FosB: a divalent-metal-dependent bacillithiol-*S*-transferase that mediates fosfomycin resistance in *Staphylococcus aureus*. Biochem. J. 451: 69–79.

Rosario-Cruz, Z. and Boyd, J.M. (2016). Physiological roles of bacillithiol in intracellular metal processing. Curr. Genet. 62: 59–65.

Rosario-Cruz, Z., Chahal, H.K., Mike, L.A., Skaar, E.P., and Boyd, J.M. (2015). Bacillithiol has a role in Fe-S cluster biogenesis in *Staphylococcus aureus*. Mol. Microbiol. 98: 218–242.

Rosen, H., Klebanoff, S.J., Wang, Y., Brot, N., Heinecke, J.W., and Fu, X. (2009). Methionine oxidation contributes to bacterial killing by the myeloperoxidase system of neutrophils. Proc. Natl. Acad. Sci. USA 106: 18686–18691.

Schlag, S., Nerz, C., Birkenstock, T.A., Altenberend, F., and Gotz, F. (2007). Inhibition of staphylococcal biofilm formation by nitrite. J. Bacteriol. 189: 7911–7919.

Schwarzländer, M., Dick, T.P., Meyer, A.J., and Morgan, B. (2016). Dissecting redox biology using fluorescent protein sensors. Antioxid. Redox. Signal 24: 680–712.

Sharma, S.V., Arbach, M., Roberts, A.A., Macdonald, C.J., Groom, M., and Hamilton, C.J. (2013). Biophysical features of bacillithiol, the glutathione surrogate of *Bacillus subtilis* and other firmicutes. Chembiochem 14: 2160–2168.

Shatalin, K., Shatalina, E., Mironov, A., and Nudler, E. (2011). H_2S: a universal defense against antibiotics in bacteria. Science 334: 986–990.

Shen, J., Keithly, M.E., Armstrong, R.N., Higgins, K.A., Edmonds, K.A., and Giedroc, D.P. (2015). *Staphylococcus aureus* CstB is a novel multidomain persulfide dioxygenase-sulfurtransferase involved in hydrogen sulfide detoxification. Biochemistry 54: 4542–4554.

Shen, J., Peng, H., Zhang, Y., Trinidad, J.C., and Giedroc, D.P. (2016). *Staphylococcus aureus sqr* encodes a type II sulfide: quinone oxidoreductase and impacts reactive sulfur speciation in cells. Biochemistry 55: 6524–6534.

Smith, M.T. (1985). Quinones as mutagens, carcinogens, and anticancer agents: introduction and overview. J. Toxicol. Environ. Health 16: 665–672.

Soutourina, O., Dubrac, S., Poupel, O., Msadek, T., and Martin-Verstraete, I. (2010). The pleiotropic CymR regulator of *Staphylococcus aureus* plays an important role in virulence and stress response. PLoS Pathog. 6: e1000894.

Soutourina, O., Poupel, O., Coppee, J.Y., Danchin, A., Msadek, T., and Martin-Verstraete, I. (2009). CymR, the master regulator of cysteine metabolism in *Staphylococcus aureus*, controls host sulphur source utilization and plays a role in biofilm formation. Mol. Microbiol. 73: 194–211.

Stomberski, C.T., Hess, D.T., and Stamler, J.S. (2019). Protein S-nitrosylation: determinants of specificity and enzymatic regulation of S-nitrosothiol-based signaling. Antioxid. Redox. Signal 30: 1331–1351.

Storkey, C., Davies, M.J., and Pattison, D.I. (2014). Reevaluation of the rate constants for the reaction of hypochlorous acid (HOCl) with cysteine, methionine, and peptide derivatives using a new competition kinetic approach. Free Radic. Biol. Med. 73: 60–66.

Sun, F., Ding, Y., Ji, Q., Liang, Z., Deng, X., Wong, C.C., Yi, C., Zhang, L., Xie, S., Alvarez, S., et al. (2012). Protein cysteine phosphorylation of SarA/MgrA family transcriptional regulators mediates bacterial virulence and antibiotic resistance. Proc. Natl. Acad. Sci. USA 109: 15461–15466.

Tam, K. and Torres, V.J. (2019). *Staphylococcus aureus* secreted toxins and extracellular enzymes. Microbiol. Spectr. 7, https://doi.org/10.1128/microbiolspec.gpp3-0039-2018.

Tam le, T., Eymann, C., Albrecht, D., Sietmann, R., Schauer, F., Hecker, M., and Antelmann, H. (2006). Differential gene expression in response to phenol and catechol reveals different metabolic activities for the degradation of aromatic compounds in *Bacillus subtilis*. Environ. Microbiol. 8: 1408–1427.

Tiwari, N., Lopez-Redondo, M., Miguel-Romero, L., Kulhankova, K., Cahill, M.P., Tran, P.M., Kinney, K.J., Kilgore, S.H., Al-Tameemi, H., Herfst, C.A., et al. (2020). The SrrAB two-component system regulates *Staphylococcus aureus* pathogenicity through redox sensitive cysteines. Proc. Natl. Acad. Sci. USA 117: 10989–10999.

Tocmo, R., Wu, Y., Liang, D., Fogliano, V., and Huang, D. (2017). Boiling enriches the linear polysulfides and the hydrogen sulfide-releasing activity of garlic. Food Chem. 221: 1867–1873.

Toliver-Kinsky, T., Cui, W., Toro, G., Lee, S.J., Shatalin, K., Nudler, E., and Szabo, C. (2019). H_2S, a bacterial defense mechanism against the host immune response. Infect. Immun. 87: e00272-18.

Töwe, S., Leelakriangsak, M., Kobayashi, K., Van Duy, N., Hecker, M., Zuber, P., and Antelmann, H. (2007). The MarR-type repressor MhqR (YkvE) regulates multiple dioxygenases/glyoxalases and an azoreductase which confer resistance to 2-methylhydroquinone and catechol in *Bacillus subtilis*. Mol. Microbiol. 66: 40–54.

Treffon, J., Block, D., Moche, M., Reiss, S., Fuchs, S., Engelmann, S., Becher, D., Langhanki, L., Mellmann, A., Peters, G., et al. (2018). Adaptation of *Staphylococcus aureus* to airway environments in patients with cystic fibrosis by upregulation of superoxide dismutase M and iron-scavenging proteins. J. Infect. Dis. 217: 1453–1461.

Truong-Bolduc, Q.C., Ding, Y., and Hooper, D.C. (2008). Posttranslational modification influences the effects of MgrA on *norA* expression in *Staphylococcus aureus*. J. Bacteriol. 190: 7375–7381.

Truong-Bolduc, Q.C., Dunman, P.M., Strahilevitz, J., Projan, S.J., and Hooper, D.C. (2005). MgrA is a multiple regulator of two new efflux pumps in *Staphylococcus aureus*. J. Bacteriol. 187: 2395–2405.

Tsuchiya, Y., Zhyvoloup, A., Bakovic, J., Thomas, N., Yu, B.Y.K., Das, S., Orengo, C., Newell, C., Ward, J., and Saladino, G., et al (2018). Protein CoAlation and antioxidant function of coenzyme A in prokaryotic cells. Biochem. J. 475: 1909–1937.

Ulfig, A. and Leichert, L.I. (2020). The effects of neutrophil-generated hypochlorous acid and other hypohalous acids on host and pathogens. Cell. Mol. Life Sci., https://doi.org/10.1007/s00018-020-03591-y.

Ulrich, M., Bastian, M., Cramton, S.E., Ziegler, K., Pragman, A.A., Bragonzi, A., Memmi, G., Wolz, C., Schlievert, P.M., Cheung, A., et al. (2007). The staphylococcal respiratory response regulator SrrAB induces ica gene transcription and polysaccharide intercellular adhesin expression, protecting *Staphylococcus aureus* from neutrophil killing under anaerobic growth conditions. Mol. Microbiol. 65: 1276–1287.

Vaishampayan, A., de Jong, A., Wight, D.J., Kok, J., and Grohmann, E. (2018). A novel antimicrobial coating represses biofilm and virulence-related genes in methicillin-resistant *Staphylococcus aureus*. Front. Microbiol. 9: 221.

Valderas, M.W., Gatson, J.W., Wreyford, N., and Hart, M.E. (2002). The superoxide dismutase gene *sodM* is unique to *Staphylococcus aureus*: absence of *sodM* in coagulase-negative staphylococci. J. Bacteriol. 184: 2465–2472.

Valderas, M.W. and Hart, M.E. (2001). Identification and characterization of a second superoxide dismutase gene (*sodM*) from *Staphylococcus aureus*. J. Bacteriol. 183: 3399–3407.

Van Laer, K., Hamilton, C.J., and Messens, J. (2013). Low-molecular-weight thiols in thiol-disulfide exchange. Antioxid. Redox. Signal 18: 1642–1653.

Vazquez-Torres, A. (2012). Redox active thiol sensors of oxidative and nitrosative stress. Antioxid. Redox. Signal 17: 1201–1214.

Vestergaard, M., Frees, D., and Ingmer, H. (2019). Antibiotic resistance and the MRSA problem. Microbiol. Spectr. 7, https://doi.org/10.1128/microbiolspec.gpp3-0057-2018.

Vetter, S.W. (2015). Glycated serum albumin and AGE receptors. Adv. Clin. Chem. 72: 205–275.

Voyich, J.M., Braughton, K.R., Sturdevant, D.E., Whitney, A.R., Said-Salim, B., Porcella, S.F., Long, R.D., Dorward, D.W., Gardner, D.J., Kreiswirth, B.N., et al. (2005). Insights into mechanisms used by *Staphylococcus aureus* to avoid destruction by human neutrophils. J. Immunol. 175: 3907–3919.

Walsh, B.J.C. and Giedroc, D.P. (2020). H_2S and reactive sulfur signaling at the host-bacterial pathogen interface. J. Biol. Chem. 295: 13150–13168.

Wang, C., Fan, J., Niu, C., Wang, C., Villaruz, A.E., Otto, M., and Gao, Q. (2010). Role of spx in biofilm formation of *Staphylococcus epidermidis*. FEMS Immunol. Med. Microbiol. 59: 152–160.

Weber, H., Engelmann, S., Becher, D., and Hecker, M. (2004). Oxidative stress triggers thiol oxidation in the glyceraldehyde-3-phosphate dehydrogenase of *Staphylococcus aureus*. Mol. Microbiol. 52: 133–140.

Wilkinson, S.P. and Grove, A. (2006). Ligand-responsive transcriptional regulation by members of the MarR family of winged helix proteins. Curr. Issues Mol. Biol. 8: 51–62.

Winterbourn, C.C., Hampton, M.B., Livesey, J.H., and Kettle, A.J. (2006). Modeling the reactions of superoxide and myeloperoxidase in the neutrophil phagosome: implications for microbial killing. J. Biol. Chem. 281: 39860–39869.

Winterbourn, C.C. and Kettle, A.J. (2013). Redox reactions and microbial killing in the neutrophil phagosome. Antioxid. Redox. Signal 18: 642–660.

Winterbourn, C.C., Kettle, A.J., and Hampton, M.B. (2016). Reactive oxygen species and neutrophil function. Annu. Rev. Biochem. 85: 765–792.

Winterbourn, C.C. and Metodiewa, D. (1999). Reactivity of biologically important thiol compounds with superoxide and hydrogen peroxide. Free Radic. Biol. Med. 27: 322–328.

Ximenes, V.F., Maghzal, G.J., Turner, R., Kato, Y., Winterbourn, C.C., and Kettle, A.J. (2009). Serotonin as a physiological substrate for myeloperoxidase and its superoxide-dependent oxidation to cytotoxic tryptamine-4,5-dione. Biochem. J. 425: 285–293.

Yarwood, J.M. and Schlievert, P.M. (2000). Oxygen and carbon dioxide regulation of toxic shock syndrome toxin 1 production by *Staphylococcus aureus* MN8. J. Clin. Microbiol. 38: 1797–1803.

You, Y., Xue, T., Cao, L., Zhao, L., Sun, H., and Sun, B. (2014). *Staphylococcus aureus* glucose-induced biofilm accessory proteins, GbaAB, influence biofilm formation in a PIA-dependent manner. Int. J. Med. Microbiol. 304: 603–612.

Yu, L., Hisatsune, J., Hayashi, I., Tatsukawa, N., Sato'o, Y., Mizumachi, E., Kato, F., Hirakawa, H., Pier, G.B., and Sugai, M. (2017). A novel repressor of the *ica* Locus discovered in clinically isolated super-biofilm-elaborating *Staphylococcus aureus*. mBio. 8: e02282-16.

Zuber, P. (2004). Spx-RNA polymerase interaction and global transcriptional control during oxidative stress. J. Bacteriol. 186: 1911–1918.

Zuber, P. (2009). Management of oxidative stress in *Bacillus*. Annu. Rev. Microbiol. 63: 575–597.

Chapter 4

The MerR-family regulator NmlR is involved in the defense against HOCl stress in *Streptococcus pneumoniae*

Verena Nadin Fritsch[1], Nico Linzner[1], Tobias Busche[2,3], Nelly Said[4], Christoph Weise[5], Jörn Kalinowski[2], Markus C. Wahl[4,6] and Haike Antelmann[1]*

[1]Freie Universität Berlin, Institute of Biology-Microbiology, D-14195 Berlin, Germany

[2]Center for Biotechnology, University Bielefeld, D-33615 Bielefeld, Germany

[3]NGS Core Facility, Medical School OWL, Bielefeld University, D-33615 Bielefeld, Germany

[4]Freie Universität Berlin, Laboratory of Structural Biochemistry, D-14195 Berlin, Germany

[5]Freie Universität Berlin, Institute of Chemistry and Biochemistry, D-14195, Berlin, Germany

[6]Helmholtz-Zentrum Berlin für Materialien und Energie, Macromolecular Crystallography, D-12489 Berlin, Germany

*Corresponding author: haike.antelmann@fu-berlin.de

submitted to*:*
Molecular Microbiology on 15-Jul-2022, currently under major revision

Personal contribution:

To assess the HOCl-stress response of *S. pneumoniae*, I prepared the RNA for the RNA-seq analysis performed by Dr. Tobias Busche. After I analyzed the obtained data, I developed together with Prof. Dr. Haike Antelmann the concept of this research project. Together with Dr. Nico Linzner, I performed the murine macrophage infection assays and assisted him with the mutant constructions. To investigate the function of the NmlR regulon and elucidate the redox-sensing mechanism, I used phenotype analyses, qRT-PCR, EMSAs and (non-)reducing SDS-PAGE analyses (Fig. 2; 3; 5; 7; 8; S1 and S2). Additionally, I performed the structural modeling shown in Fig. S3, the data analysis, and created the figures for the experiments I conducted. Additionally, I drafted the initial manuscript.

The MerR-family regulator NmlR is involved in the defense against HOCl stress in *Streptococcus pneumoniae*

Verena Nadin Fritsch[1], Nico Linzner[1], Tobias Busche[2,3], Nelly Said[4], Christoph Weise[5], Jörn Kalinowski[2], Markus C. Wahl[4,6] and Haike Antelmann[1]*

Departments & Institutions:

[1]Freie Universität Berlin, Institute of Biology-Microbiology, D-14195 Berlin, Germany

[2]Center for Biotechnology, University Bielefeld, D-33615 Bielefeld, Germany

[3]NGS Core Facility, Medical School OWL, Bielefeld University, D-33615 Bielefeld, Germany

[4]Freie Universität Berlin, Laboratory of Structural Biochemistry, D-14195 Berlin, Germany

[5]Freie Universität Berlin, Institute of Chemistry and Biochemistry, D-14195, Berlin, Germany

[6]Helmholtz-Zentrum Berlin für Materialien und Energie, Macromolecular Crystallography, D-12489 Berlin, Germany

Running title: NmlR protects against oxidative stress in *S. pneumoniae*

***Corresponding author:**

Haike Antelmann, Institute for Biology-Microbiology, Freie Universität Berlin,

Königin-Luise-Straße 12-16, D-14195 Berlin, Germany,

Tel: +49-(0)30-838-51221, Fax: +49-(0)30-838-451221

E-mail: haike.antelmann@fu-berlin.de

Key words: *Streptococcus pneumoniae*/ NmlR/ thiol switches/ HOCl/ H_2O_2

ABSTRACT

Streptococcus pneumoniae has to cope with the strong oxidant hypochlorous acid (HOCl), during host–pathogen interactions. Thus, we analysed the global gene expression profile of *S. pneumoniae* D39 towards HOCl stress. In the RNA-seq transcriptome, the NmlR, SifR, CtsR, HrcA, SczA and CopY regulons and the *etrx1-ccdA1-msrAB2* operon were most strongly induced under HOCl stress, which participate in the oxidative, electrophile and metal stress response in *S. pneumoniae*. The MerR-family regulator NmlR harbors a conserved Cys52 and controls the alcohol dehydrogenase-encoding *adhC* gene under carbonyl and NO stress. We demonstrated that NmlR senses also HOCl stress to activate transcription of the *nmlR-adhC* operon. Transcriptional induction of *adhC* under HOCl was dependent on Cys52 of NmlR. Using mass spectrometry, NmlR was shown to be oxidized to intersubunit disulfides or *S*-glutathionylated under oxidative stress in vitro. A broccoli-FLAP-based assay further showed that oxidized NmlR increased transcription initiation at the *nmlR* promoter by RNAP in vitro. Phenotype analyses revealed that NmlR functions in the defense against oxidative stress and promotes survival of *S. pneumoniae* during macrophage infections. In conclusion, NmlR was characterized as HOCl-sensing transcriptional regulator, which activates transcription of *adhC* under oxidative stress by thiol switches in *S. pneumoniae*.

GRAPHICAL ABSTRACT

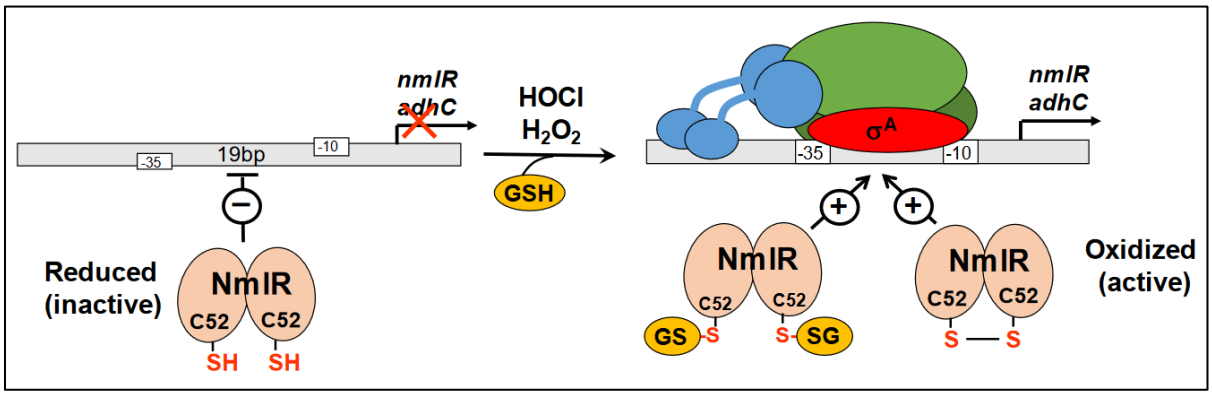

INTRODUCTION

The human pathogen *Streptococcus pneumoniae* (also called the pneumococcus) is a major cause of bacterial pneumonia and meningitis worldwide, which often occurs in young children, older people or immunocompromised persons (CDC, 2020). During infections, *S. pneumoniae* is phagocytosed by immune cells, such as macrophages and neutrophils, which produce a cocktail of reactive oxygen species (ROS) and hypohalous acids, such as hypochlorous and hypobromous acids (HOCl, HOBr) and hypothiocyanite (HOSCN) to kill the invading bacteria (Winterbourn & Kettle, 2013, Winterbourn *et al.*, 2016, Ulfig & Leichert, 2021, Gray *et al.*, 2013). The NADPH oxidase (NOX) in the phagosomal membrane generates superoxide anions, which dismutate to hydrogen peroxide (H_2O_2) either spontaneously or by the superoxide dismutase. The myeloperoxidase (MPO) is released in the phagosomal lumen to convert H_2O_2 and halides or pseudohalides to hypohalous acids (Ulfig & Leichert, 2021). The highly reactive HOCl is the most potent oxidant produced by the respiratory burst, which leads to oxidative damage of proteins, DNA and carbohydrates (Winterbourn *et al.*, 2016, Gray *et al.*, 2013). The most susceptible targets for oxidation by HOCl are the sulfur-containing amino acids cysteine and methionine. Thus, the pathogen *S. pneumoniae* requires efficient defense mechanisms for detoxification of HOCl or to repair the resulting oxidative protein damage.

To cope with oxidative stress, *S. pneumoniae* utilizes the low molecular weight (LMW) thiol glutathione (GSH) as well as enzymatic ROS detoxification enzymes and thiol-disulfide oxidoreductases for the maintenance of the redox homeostasis (Mraheil *et al.*, 2021, Yesilkaya *et al.*, 2013). However, as facultative anaerobic bacterium, *S. pneumoniae* lacks the catalase and produces high amounts of endogenous H_2O_2 by the pyruvate oxidase SpxB and lactate oxidase LctO as unique defense mechanism to promote bacterial colonization and to kill competing bacteria in the microbial community (Pericone *et al.*, 2003, Mraheil *et al.*, 2021). For detoxification of oxygen, superoxide anion and H_2O_2, the pneumococcus uses the NADH oxidase (Nox), the superoxide dismutase (SodA), the thiol peroxidase (TpxD) and the alkyl hydroperoxidase (AhpD), which contribute to the oxidative stress resistance and virulence (Mraheil *et al.*, 2021, Yesilkaya *et al.*, 2013). In related firmicutes, exposure to ROS and HOCl

causes strongly increased reversible protein thiol-oxidation, including protein *S*-thiolations, which function in redox regulation and protect vulnerable Cys residues against overoxidation (Loi *et al.*, 2015, Imber *et al.*, 2019). Similarly, endogenous H_2O_2 induces cysteine sulfenylation of >50 cytoplasmic proteins, including the glyceraldehyde-3-phosphate dehydrogenase (GapA) and SpxB in *S. pneumoniae* (Lisher *et al.*, 2017). To repair oxidized Met residues under H_2O_2 stress at the bacterial surface, *S. pneumoniae* encodes the CTM electron transfer complex, composed the CcdA electron shuttle, extracellular thioredoxins (Etrx1/2) and the methionine sulfoxide reductase (MsrAB2), which are important for virulence and survival during host–pathogen interactions (Saleh *et al.*, 2013). In addition, the ATP-dependent Clp protease and the chaperones DnaK and GroESL are involved in the protein quality control and contribute to the degradation and refolding of oxidatively damaged proteins (Yesilkaya *et al.*, 2013, Mraheil *et al.*, 2021). H_2O_2 can also react with ferrous iron (Fe^{2+}) to generate the highly toxic hydroxyl radical, which causes DNA damage (Imlay, 2003). To avoid poisoning by the Fenton chemistry, *S. pneumoniae* contains only few FeS cluster proteins and the iron-storage Dpr protein (Pericone *et al.*, 2003).

Furthermore, common bacterial redox regulators of the peroxide stress response, such as PerR and OxyR, are absent in the pneumococcus (Hillion & Antelmann, 2015, Mraheil *et al.*, 2021). Instead, the pneumococcus encodes alternative transcriptional regulators, such as SpxR, Rgg, RitR, NmlR, CodY and SifR, which control enzymes involved in ROS generation and detoxification as well as other defense mechanisms required for bacterial survival during host–pathogen interactions (Yesilkaya *et al.*, 2013, Mraheil *et al.*, 2021, Zhang *et al.*, 2022). The MerR-family regulator NmlR has been characterized as transcriptional activator, which controls the expression of the *nmlR-adhC* operon under formaldehyde, methylglyoxal and *S*-nitrosoglutathione (GSNO) stress in *S. pneumoniae* (Potter *et al.*, 2010, Stroeher *et al.*, 2007). The *adhC* gene encodes a class 3 alcohol dehydrogenase, which catalyzes the reduction of GSNO and contributes to H_2O_2 and GSNO resistance. While AdhC is not essential for the carbonyl stress resistance, the Δ*nmlR* mutant was resistant to aerobic growth due to lower endogenous H_2O_2 levels, providing a link between NmlR and H_2O_2 resistance (Potter *et al.*,

2010). Additionally, AdhC was required for systemic virulence of *S. pneumoniae* in a mouse model by promoting the survival in the blood (Stroeher *et al.*, 2007). Similarly, other MerR/NmlR homologs were characterized in *Haemophilus influenzae*, *Bacillus subtilis*, *Listeria monocytogenes*, *Neisseria gonorrhoeae* and *Neisseria meningitidis* and shown to control the expression of conserved *adhC* genes, which conferred resistance under GSNO, H_2O_2 and carbonyl stress and during infections (Counago *et al.*, 2016, Nguyen *et al.*, 2009, Supa-Amornkul *et al.*, 2016, Kidd *et al.*, 2005, Chen *et al.*, 2013).

While the role of AdhC in GSNO and carbonyl detoxification is well understood (Staab *et al.*, 2008), the regulatory mechanisms of MerR/NmlR-family regulators still remain to be elucidated. MerR-family regulators often function as transcriptional activators, which bind to palindromic repeats in promoters with overlong spacers of 19–20 bp between the −35 and −10 elements, which usually cannot be recognized by the RNA polymerase (RNAP) alone (Brown *et al.*, 2003, Hobman *et al.*, 2005, McEwan *et al.*, 2011). Activation of the MerR-family transcription factor leads to conformational changes of the promoter, resulting in realignment of the promoter elements allowing recognition and initiation of transcription by the RNAP (Brown *et al.*, 2003, Hobman *et al.*, 2005, McEwan *et al.*, 2011). In addition, MerR/NmlR-family regulators share a conserved Cys residue, which is required for redox-sensing of aldehyde and nitric oxide (NO) stress in *B. subtilis* AdhR and *N. gonorrhoeae* NmlR, respectively (McEwan *et al.*, 2011, Kidd *et al.*, 2005, Nguyen *et al.*, 2009). The activation mechanism of NmlR might involve post-translational thiol-modification of the conserved Cys by thiol-*S*-alkylation upon aldehyde exposure or by *S*-nitrosylation in response to NO stress (McEwan *et al.*, 2011, Chen *et al.*, 2013).

In this study, we were interested in the transcriptome response of *S. pneumoniae* D39 under HOCl stress to identify novel redox-sensing regulators, which might control protection mechanisms against the oxidative burst of immune cells. The NmlR-controlled *adhC* gene was strongly upregulated under HOCl stress, suggesting an additional role of the NmlR regulon in the HOCl stress response. Thus, we further characterized the redox regulation of NmlR and the role of AdhC in the defense against HOCl and ROS stress in *S. pneumoniae*. Our results

demonstrate that NmlR is oxidized by HOCl and ROS to intersubunit disulfides or *S*-glutathionylations in vitro. Using the broccoli-FLAP assay (Filonov *et al.*, 2014), oxidized NmlR was shown to activate transcription of *adhC* by the σ^{70}-RNAP holoenzyme in vitro. AdhC is further important to protect *S. pneumoniae* against ROS, HOCl and under macrophage infections, suggesting its high potential as future drug target to combat pneumococcal disease.

RESULTS

HOCl stress causes an oxidative and metal stress response and protein damage in the transcriptome of *S. pneumoniae* D39. To investigate the transcriptional response of *S. pneumoniae* D39 under HOCl stress, we analyzed the changes in the RNA-seq transcriptome after 30 min of exposure to sub-lethal doses of 800 µM HOCl stress during the log phase of microaerophilic bacteria **(Fig. 1; Tables S1 and S2; Fig. S1)**. For significant fold-changes (FC) of induced or repressed genes, the M-value cutoff (log2 FC HOCl vs. control) of m≥1.0 and m≤-1.0 was chosen (adjusted p-value ≤0.01). Accordingly, 296 and 306 genes were significantly ≥2-fold up- and downregulated, respectively, in *S. pneumoniae* D39 under HOCl stress. These HOCl-responsive genes were classified into known regulons and visualized by color codes in the M/A ratio intensity scatter plot **(Fig. 1; Tables S1 and S2)**.

First, we were interested to reveal the redox-controlled regulons, which respond most strongly to HOCl stress in the pneumococcus. Among the top-scorers was the CTM electron complex, encoded by the *ccdA1-etrxA1-msrAB2* operon (33.4–42.5-fold), which is involved in the oxidative stress response and functions in reduction of oxidized methionine residues of cell envelope proteins in *S. pneumoniae* (Gennaris & Collet, 2013, Saleh *et al.*, 2013). In addition, the *trxA* and *trxB* genes (4.7- and 3.8-fold) encoding the cytoplasmic thioredoxin (Trx)/ thioredoxin reductase system, were upregulated by HOCl stress, indicating an increased protein thiol-oxidation in *S. pneumoniae*. Interestingly, the *nmlR* (36-fold) and *adhC* (26.5-fold) genes were among the most strongly HOCl-induced transcripts in the pneumococcal transcriptome **(Fig. 1; Tables S1 and S2)**. This suggests an important role of AdhC in the HOCl stress defense, which was investigated in this work in more detail (see next sections).

Furthermore, HOCl stress caused the strong induction of the quinone-responsive SifR regulon, including the *catE* (29.2-fold) and *yhdA* (7.1-fold) genes, which encode the catechol-2,3-dioxygenase and NAD(P)H-dependent FMN ferric reductase, respectively (Zhang *et al.*, 2022).

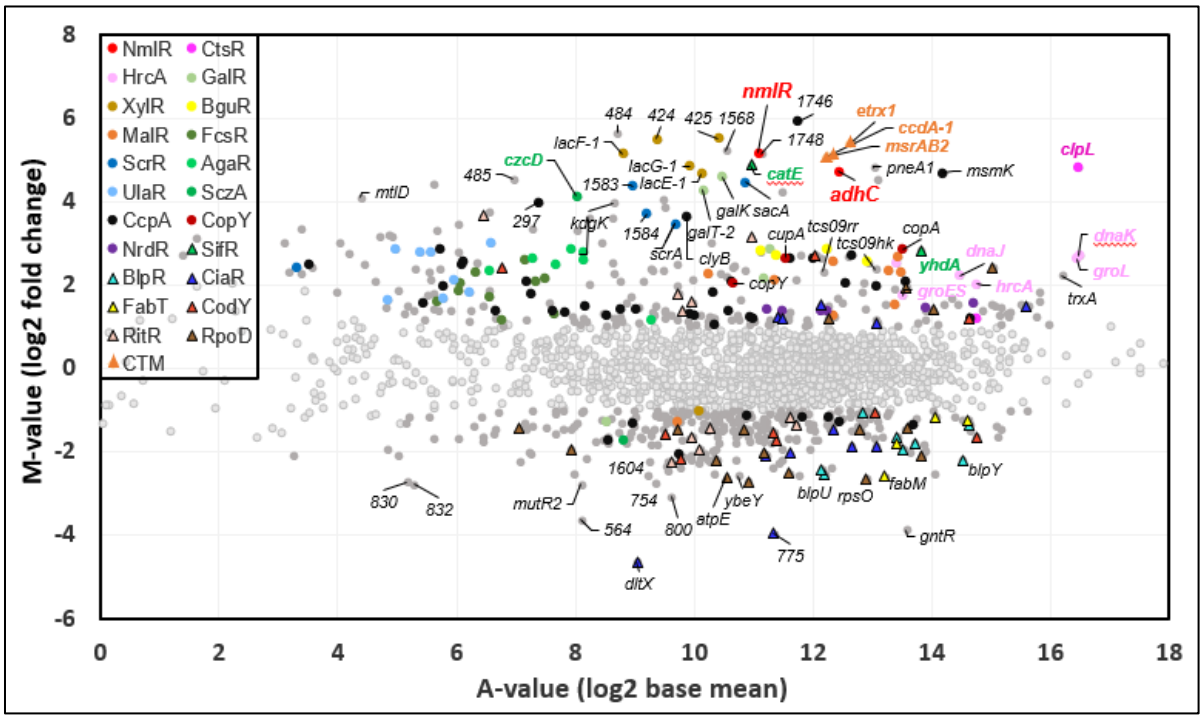

Fig. 1: The RNA-seq transcriptome of *S. pneumoniae* D39 after HOCl stress. For RNA-seq transcriptomics, *S. pneumoniae* D39 was grown in supplemented RPMI medium and treated with 800 µM HOCl stress for 30 min. The gene expression profile of control versus HOCl stress is shown as ratio/intensity scatterplot (M/A-plot), which is based on the differential gene expression analysis using DeSeq2 as previously described (Love *et al.*, 2014). Colored symbols indicate significantly induced and repressed transcripts (*M*-value ≥1 or ≤−1; $p \leq 0.05$). Most strongly induced are the NmlR, SifR, CtsR, HrcA, SczA and CopY regulons and the CTM operon, indicating oxidative and metal stress and protein damage. The derepression of the CcpA regulon and induction of regulons for catabolism of alternative carbohydrates, including GalR (Leloir, galactose), XylR (lactose), BguR (ß-glucosides), MalR (maltose), FcsR (fucose), ScrR (sucrose), AgaR (N-acetylgalactosamine) and UlaR (ascorbic acid) are further visualized using specific color codes. Downregulated transcription after HOCl stress are indicated for the BlpR, CiaR, FabT, CodY, RitR, and RpoD regulons. Light gray symbols denote transcripts with no fold-changes after HOCl stress ($p > 0.05$). The complete transcriptome data and regulon classifications are listed in **Tables S1 and S2**.

Due to increased protein thiol-oxidation and aggregation, the CtsR-controlled Clp proteases, such as *clpL* (28.6-fold) and *clpE* (2.3-fold), and the HrcA-regulated chaperones encoded by the *hrcA-grpE-dnaK-dnaJ* (3.4–6.2-fold) and *groL-groES* (4.1–6.5-fold) operons were highly upregulated under HOCl stress in the *S. pneumoniae* transcriptome **(Fig. 1; Tables S1 and S2)**. This protein quality control machinery of proteases and chaperones is required for protein folding and degradation of oxidatively damaged proteins under HOCl stress (Yesilkaya *et al.*, 2013, Mraheil *et al.*, 2021)

Among the top hits was further the Zn^{2+} efflux pump-encoding *czcD* gene (17.4-fold), which is transcribed upstream of the *nmlR-adhC* operon and controlled by the TetR-family regulator SczA (Kloosterman *et al.*, 2007). HOCl also caused the induction of the copper-controlled CopY regulon (4.1–7.2-fold), including *cupA* and the copper-transport ATPase-encoding *copA* gene (Shafeeq *et al.*, 2011). In addition, the RegR regulon required for virulence, adherence and competence of *S. pneumoniae*, was strongly induced by HOCl stress (2.1–15.7-fold) (Chapuy-Regaud *et al.*, 2003). As another virulence factor, the pneumococcal adherence and virulence factor B *pavB* was strongly (23.3-fold) induced by HOCl stress.

Interestingly, HOCl stress also caused the induction of several regulons involved in the uptake and utilization of alternative carbohydrates, which serve as energy and carbon sources in the absence of glucose and are important for virulence in *S. pneumoniae* (Minhas et al., 2021). The induction of these sugar catabolic regulons was accompanied by the derepression of 76 genes of the CcpA regulon (2–50.5-fold), indicating that CcpA is partially inactivated after HOCl exposure in the pneumococcus **(Fig. 1; Tables S1 and S2)**. The most strongly induced disaccharide utilization systems were the XylR (25.5-45.9-fold) and ScrR regulons (5.4–22-fold), which include the ABC and PTS transporters and catabolic enzymes for the hydrolysis of lactose and sucrose, respectively (Minhas *et al.*, 2021). Among the HOCl-induced regulons were further GalR (19.4–24.1-fold) and LacR (4.5–7.4-fold), comprising the enzymes of the Leloir and tagatose 6-phosphate pathways for catabolism of galactose and lactose (Minhas *et al.*, 2021). Furthermore, the BguR, FcsR, RafR, MalR, AgaR and UlaR regulons required for the acquisition and catabolism of ß-glucosides, fucose, raffinose, maltose, *N*-acetylgalactosamine and ascorbic acid, respectively (Minhas *et al.*, 2021), were upregulated at lower levels (2.2–8.1-fold) upon HOCl stress. Taken together, the upregulation of many utilization systems for alternative carbohydrates suggests that HOCl stress might affect either directly or indirectly the regulation of carbon catabolite repression.

In other bacteria, HOCl stress was shown to cause strong ATP depletion, which correlated with the loss of viability (Barrette *et al.*, 1989, Ulfig & Leichert, 2021). Since HOCl exposure affected also the growth in the pneumococcus **(Fig. S1H)**, the ATP synthase

subunits-encoding genes (*atpF* and *atpE*) and genes for ribosomal proteins were downregulated in the HOCl stress transcriptome **(Fig. 1, Table S1 and S2)**. Furthermore, the *fabT*, *fabM*, *fabH* and *acpP* genes required for fatty acid biosynthesis showed decreased transcription (2.3–6-fold) in HOCl-treated cells.

The NmlR regulon responds most strongly to methylglyoxal, formaldehyde and HOCl stress in *S. pneumoniae*. Due to its strong induction under HOCl stress, the NmlR regulon was selected to study in more detail the redox-sensing mechanism of NmlR and the role of AdhC under oxidative stress in the pneumococcus. The *nmlR-adhC* operon was previously shown to respond strongly to formaldehyde, methylglyoxal and GSNO stress in *S. pneumoniae* (Potter *et al.*, 2010, Stroeher *et al.*, 2007). qRT-PCR analysis was used to monitor the expression profile of *adhC* in *S. pneumoniae* D39 after exposure to sub-lethal doses of different thiol-reactive compounds, such as 800 µM HOCl, 0.45 mM H_2O_2, 4 mM diamide, 0.167 mM diethylamine (DEA)-NONOate, 0.4 mM allicin, 325 µM methylglyoxal, 0.3 mM formaldehyde and 10 mM methylhydroquinone (MHQ) **(Fig. 2; Fig. S1).** The qRT-PCR results confirmed the strongest induction of the *nmlR-adhC* operon under aldehyde stress (70.4-89.6-fold) (Potter *et al.*, 2010). Consistent with the transcriptome data, *adhC* transcription was strongly increased after HOCl treatment (31.4-fold). Exposure to the NO donor, allicin, H_2O_2 and diamide resulted in a much weaker induction of *adhC* (1.7-3.7-fold). In addition, *adhC* transcription was not upregulated by MHQ. These results indicate that the NmlR regulon responds most strongly to reactive aldehydes and the strong oxidant HOCl in *S. pneumoniae* D39.

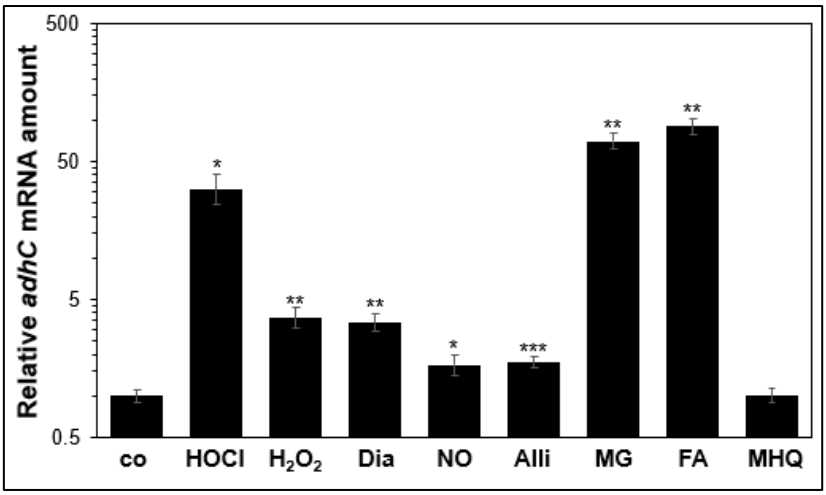

Fig. 2: Transcription of *adhC* is most strongly induced after aldehyde and HOCl stress in *S. pneumoniae* D39. RNA was isolated from S. pneumoniae D39 before (co) and 30 min after exposure to 800 µM HOCl, 0.45 mM H_2O_2, 4 mM diamide, 0.167 mM DEA-NONOate as NO donor (NO), 0.4 mM allicin (Alli), 325 µM methylglyoxal (MG), 0.3 mM formaldehyde (FA) and 10 mM methylhydroquinone (MHQ). Transcription of *adhC* was analyzed by qRT-PCR after the different stress conditions and the transcript levels were normalized to the mRNA level of untreated cells (co), which was set to 1. Error bars represent the standard deviation of 3 biological replicates with 2 technical replicates each. Statistical differences to the control were determined using a Student's unpaired two-tailed t-test. *$p \leq 0.05$; **$p \leq 0.01$ and ***$p \leq 0.001$.

The conserved Cys52 of NmlR is essential for redox-sensing of HOCl stress in vivo. To study the function of the conserved Cys52 of NmlR for redox sensing of HOCl stress, we analyzed transcriptional activation of *adhC* in the Δ*nmlR* mutant and in the *nmlR*-and *nmlRC52A*-complemented strains under control and HOCl stress conditions by qRT-PCR **(Fig. 3A)**. While *adhC* transcription was strongly (17.6-fold) upregulated in the wild type (WT) under HOCl stress, the transcript level of *adhC* was decreased in the Δ*nmlR* mutant under HOCl stress. These results support that NmlR acts as transcriptional activator of the *nmlR-adhC* operon under HOCl stress. In agreement with previous studies (Potter *et al.*, 2010), *adhC* transcription was 5.1-fold enhanced in the untreated Δ*nmlR* mutant, suggesting that NmlR might repress *adhC* transcription under control conditions. In contrast, decreased *adhC* levels were found in the untreated Δ*nmlR* mutant in another study (Stroeher *et al.*, 2007). Surprisingly, *adhC* transcription was further increased in the *nmlR*-complemented strain under control conditions, suggesting that constitutive overproduction of NmlR might also lead to activation of *adhC* transcription **(Fig. 3A)**. Upon HOCl stress, the expression level of *adhC* was further elevated in the *nmlR*-complemented strain, supporting that NmlR activates *adhC* transcription upon HOCl exposure. In contrast, the transcriptional level of *adhC* was low in the HOCl-treated

nmlRC52A mutant, indicating that Cys52 is required for redox-sensing and transcriptional activation by NmlR. These results revealed that NmlR acts as redox-sensing activator of *adhC* transcription under HOCl stress, depending on the conserved Cys52 in vivo.

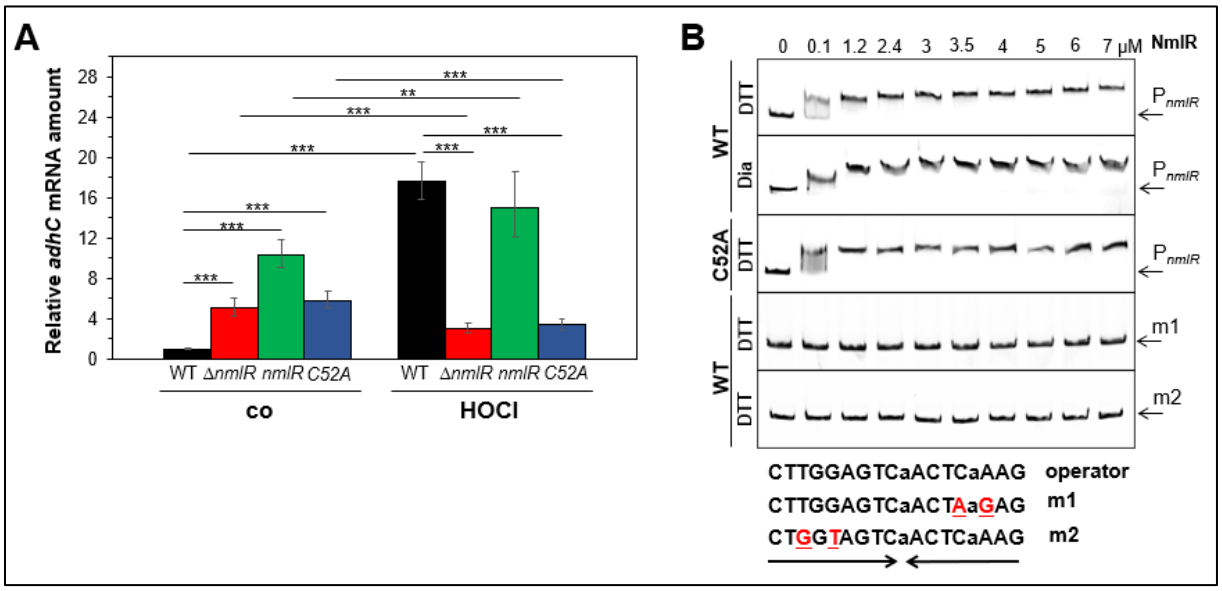

Fig. 3: NmlR activates *adhC* transcription under HOCl stress in vivo (A) and binds to the *nmlR-adhC* promoter in vitro (B). (A) Transcription of *adhC* was analyzed using qRT-PCR in the *S. pneumoniae* D39 WT, the Δ*nmlR* mutant, the *nmlR*-complemented strain and the *nmlRC52A* mutant before (co) and 30 min after exposure to 800 µM HOCl stress. The transcript levels were normalized to the mRNA level of the WT under control conditions, which was set to 1. Error bars represent the standard deviation of 3 biological replicates with 2-4 technical replicates each. The statistics was determined using a Student's unpaired two-tailed t-test **p ≤ 0.01 and ***p ≤ 0.001. **(B)** NmlR binds to the palindromic sequence upstream of the *nmlR-adhC* operon under reducing and oxidizing conditions. EMSAs were used to analyze the DNA-binding activity of increasing amounts (0.1–7 µM) of NmlR and NmlRC52A to the *nmlR* promoter (P_{nmlR}) in vitro. To analyze the specific binding to the palindrome, two base substitutions were introduced in each half of the inverted repeat, denoted in red (m1 and m2). The arrows denote the free DNA probe and the shifted band indicates the DNA-NmlR promoter complex.

NmlR binds specifically to the *nmlR-adhC* operator in the reduced and oxidized state. NmlR was proposed to bind to the 9-9 bp palindromic operator sequence CTTGGAGTC-aACTCaAAG, located between the –35 and –10 promoter elements (Stroeher *et al.*, 2007). However, experimental evidence for the specific binding of NmlR to the operator is still missing. Thus, gel electrophoretic mobility shift assays (EMSAs) were used to investigate the DNA-binding activity of purified NmlR protein to the *nmlR-adhC* operon promoter in vitro. The gel-shift results showed that purified reduced NmlR protein binds to the *nmlR* promoter probe, which is indicated by the band shift in the NmlR-DNA-binding reactions **(Fig. 3B)**. To analyze the specific binding of NmlR to the predicted operator sequence, we exchanged two nucleotides in each half of the inverted repeat (m1: C to A and A to G; m2: T to G and G to T)

and analyzed the DNA-binding activity of NmlR to these mutated promoter probes **(Fig. 3B)**. NmlR was unable to bind to the mutated palindromic sequences m1 and m2 in vitro, supporting the specific binding of NmlR to the 9-9 bp palindromic sequence.

Next, the effect of thiol-oxidation on the DNA-binding activity of NmlR was assessed using the EMSAs. Treatment of NmlR with increasing concentrations of diamide did not affect the DNA-binding activity **(Fig. 3B)**. Similarly, the DNA-binding activity was not impaired under HOCl stress (data not shown). These results are in accordance with previous data, demonstrating that MerR-family regulators interact with their cognate DNA both in the presence and absence of the specific inducers. In response to specific signals, MerR proteins undergo a conformational change, leading to a DNA distortion and reorientation of the –35 and –10 elements for RNAP recognition (Brown *et al.*, 2003, Fang & Zhang, 2022).

Since Cys52 of NmlR was identified as essential for activation of *adhC* transcription upon HOCl stress, we analyzed the role of Cys52 for the DNA-binding activity of NmlR in gel shift assays. The reduced NmlRC52A mutant protein showed a similar DNA-binding affinity compared to NmlR **(Fig. 3B)**, indicating that Cys52 is not required for the DNA-binding of NmlR.

NmlR activates transcription of the *nmlR* promoter by the *Escherichia coli* σ^{70}-RNAP in vitro. To test the activation of transcription initiation by NmlR at the *nmlR-adhC* operon promoter, in vitro transcription by *E. coli* σ^{70}-RNAP was monitored on a DNA template that harbors the broccoli fluorescent light-up RNA aptamer (broccoli-FLAP), an RNA mimic of green fluorescent protein (GFP) (Filonov *et al.*, 2014), downstream of the *nmlR* promoter **(Fig. 4)**. Upon transcription, the broccoli aptamer adopts a defined three-dimensional fold that provides the binding platform for the fluorogen DFHBI-1T, a mimic of the GFP fluorophore (Filonov *et al.*, 2014). By binding to broccoli-FLAP, DFHBI-1T emits fluorescence (emission = 507 nm), which serves as a readout for transcription. An initial lag phase (t_0) determines the time in which a first complete broccoli-FLAP is transcribed, folded and bound by DFBHI-T1. T The lag phase is followed by a linear increase in fluorescence and the slope corresponds to the initial

transcription rate or relative transcription initiation rate, respectively. Multi-round transcription showed that broccoli-FLAP production by RNAP in the presence of NmlR in a reduced state ($NmlR_{red}$) with DTT decreases the relative initiation rate to 0.72 compared to 1 by RNAP alone. In contrast, relative initiation rates are increased to 1.4 through oxidation of NmlR ($NmlR_{ox}$) upon H_2O_2 treatment. These data support the model that NmlR is activated by oxidation leading to enhanced transcription of the *nmlR-adhC* operon by the RNAP.

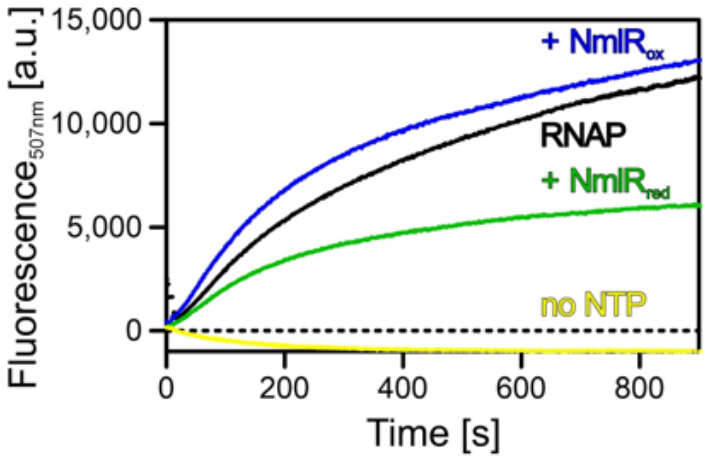

Sample	t_0 [s]	Initial rate [s^{-1}]	Relative initiation rate
RNAP	19.4	28.8 ± 2.5	1.00 ± 0.09
+ $NmlR_{ox}$	16.4	40.9 ± 0.9	1.42 ± 0.03
+ $NmlR_{red}$	24.4	20.7 ± 4.2	0.72 ± 0.14

Fig. 4: Oxidized NmlR activates *adhC* transcription by *E. coli* σ^{70}-RNAP in vitro. To compare transcriptional initiation efficiencies at the *nmlR-adhC* operon promoter by the *E. coli* σ^{70}-RNAP and reduced or oxidized NmlR ($NmlR_{red}$ and $NmlR_{ox}$), the broccoli-FLAP assay was used (see Experimental Procedures). Transcription of complete broccoli-FLAP is reported by binding of a pro-fluorophore to the aptamer, leading to an increase in fluorescence emission at 507 nm. The initial slopes in the curves represent the relative initiation rates of transcription. The table shows the calculated values of linear fits of the initial increases in fluorescence as determined after time offset t_0 for the reaction of RNAP without or with NmlR proteins, which were oxidized with 2.5% H_2O_2 ($NmlR_{ox}$) or reduced with 10 mM DTT($NmlR_{red}$).

NmlR is oxidized to intermolecular disulfides or *S*-glutathionylated at the redox-sensing Cys52 in vitro. To investigate the redox-sensing mechanism, the post-translational thiol modifications of NmlR were analyzed in response to different oxidants, such as diamide, H_2O_2 and HOCl. Using non-reducing SDS-PAGE, NmlR was shown to be completely oxidized to form Cys52–Cys52' intersubunit disulfides after treatment with the oxidants **(Fig. 5A-C)**. As expected, the intermolecular disulfides could be reversed in the reducing SDS-PAGE analysis

(Fig. 5A-C). Since NmlR represents a one-Cys-type redox-sensing regulator, it could also sense HOCl and H_2O_2 stress by formation of mixed disulfides at Cys52 with the LMW thiol GSH, termed as *S*-glutathionylation. While treatment of NmlR with H_2O_2 in the presence of GSH resulted in the formation of intersubunit disulfides, NmlR was not fully oxidized in this NmlR sample, suggesting its partial *S*-glutathionylation **(Fig. 5C)**.

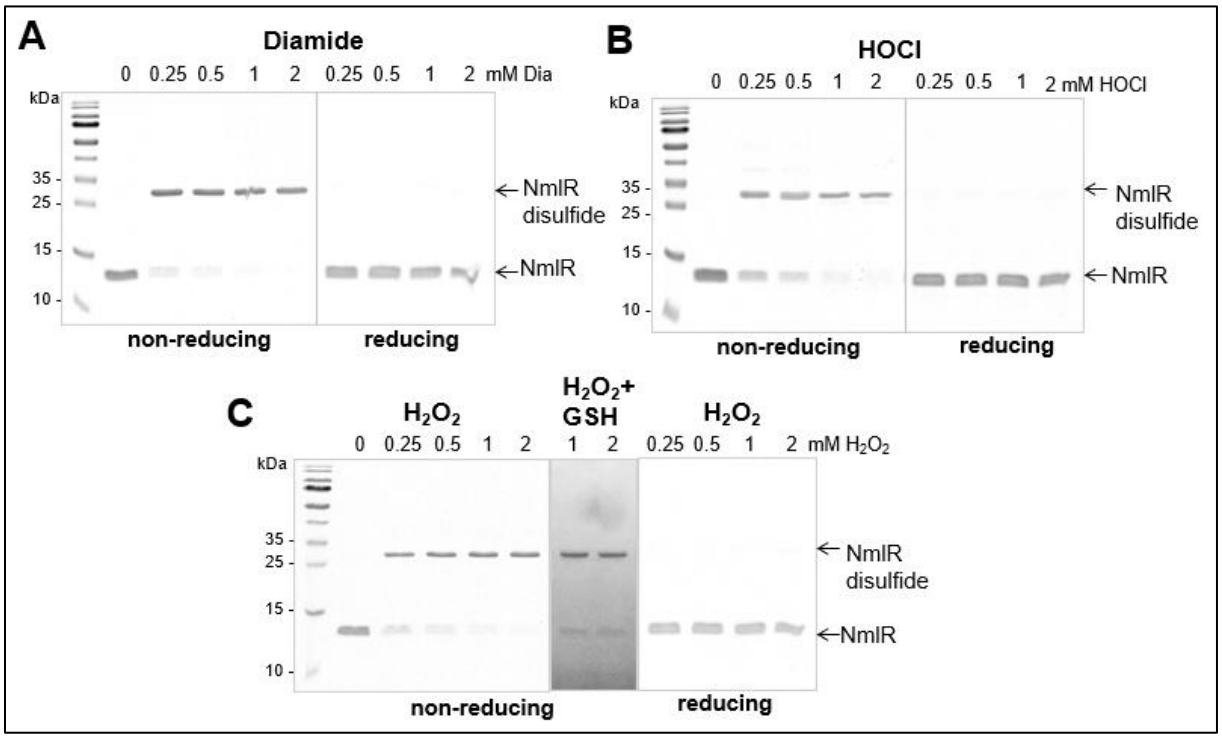

Fig. 5: NmlR can be oxidized to intermolecular disulfides in the presence of H_2O_2 in vitro. (A-C) The purified NmlR protein was treated with increasing amounts (0.25-2 mM) of diamide **(A)**, HOCl **(B)** and H_2O_2 **(C)** for 15 min in vitro and subjected to non-reducing SDS-PAGE analysis. **(C)** NmlR was oxidized either with H_2O_2 alone or with 1 and 2 mM H_2O_2 in the presence of 100 and 200 µM GSH. The reduction of the NmlR disulfides is shown in the reducing SDS-PAGE analyses.

Matrix-assisted laser desorption ionization-time of flight-mass spectrometry (MALDI-TOF-MS) was used to identify the post-translational thiol-modifications of reduced and oxidized NmlR after tryptic digestion. In the MS1 scan of the peptides of the reduced NmlR sample, a peptide was identified with the m/z of 482.19 Da, corresponding to the carbamidomethylated CFR peptide **(Fig. 6A)**. In the H_2O_2-oxidized samples of the disulfide-linked dimer without or with GSH, this CFR-CAM peptide was absent and instead a peptide with the m/z of 847.43 Da was detected, confirming the oxidation of NmlR to the Cys52–Cys52' intermolecular disulfide **(Fig. 6B, C)**. In addition, the *S*-glutathionylated CFR peptide was detected as peak at m/z of 730.30 Da in the lower gel band of the oxidized NmlR sample, which was treated with H_2O_2 in

the presence of GSH **(Fig. 6D)**. In conclusion, our data support that NmlR functions as redox-sensing transcriptional activator of the *nmlR-adhC* operon that senses oxidants by reversible thiol switches, including intersubunit disulfides or *S*-glutathionylations in vitro.

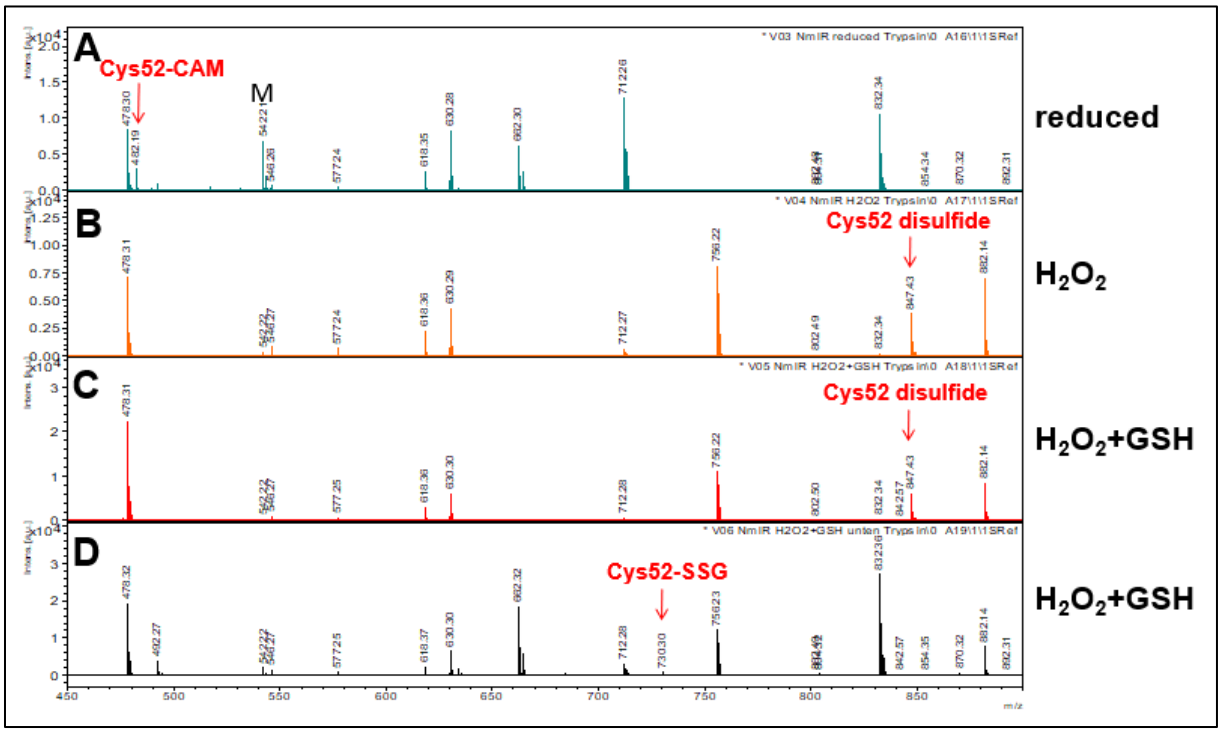

Fig. 6: NmlR can be oxidized by H_2O_2 to intermolecular disulfides and *S*-glutathionylated in the presence of GSH in vitro as revealed by MALDI-TOF MS. The bands of the reduced NmlR and the oxidized NmlR intermolecular disulfide-linked dimer were tryptic digested and the peptides analyzed by MALDI-TOF MS. The MS1 spectra are displayed in the m/z range of 450–900 showing the mass peaks of the small C_{52}FR peptide in the **(A)** reduced and **(B-D)** H_2O_2-oxidized NmlR samples without or with GSH. **(A)** Cys52 is fully carbamidomethylated (m/z 482.19 Da) in reduced NmlR. **(B)** Treatment of NmlR with H_2O_2 alone leads to oxidation to the C52–C52' intersubunit disulfide peptide (m/z 847.43 Da). **(C)** Oxidation with H_2O_2 in the presence of GSH leads to the formation of the C52–-C52' intersubunit disulfide-linked dimer and **(D)** the *S*-glutathionylated Cys52 peptide (m/z 730.3 Da) as labelled in the non-reducing SDS-PAGE analysis in **Fig. 5**.

The alcohol dehydrogenase AdhC functions in the defense against HOCl and H_2O_2 stress in *S. pneumoniae* D39. To investigate the role of AdhC in the protection against oxidative stress in *S. pneumoniae*, growth and survival analyses of the Δ*nmlR* and Δ*adhC* mutants were performed under HOCl and H_2O_2 stress **(Fig. 7).** The growth of both mutants was significantly impaired after treatment with sub-lethal doses of 800 µM HOCl as compared to the WT **(Fig. 7A, C)**. In addition, the Δ*nmlR* and Δ*adhC* mutants displayed 13.4–17% decreased survival rates after 3 h and 4 h exposure to the lethal dose of 1.1 mM HOCl **(Fig. 7E)**. While the growth of the Δ*nmlR* mutant was not affected by sub-lethal H_2O_2 stress, treatment with lethal 1 mM H_2O_2 resulted in decreased survival rates of the Δ*nmlR* mutant

compared to the WT **(Fig. 7D, F)**. Similarly, the Δ*adhC* mutant showed a higher sensitivity towards lethal H_2O_2 stress, indicated by the 1.7–2.3-fold lower survival rates than the WT. The growth and survival defects of both mutants could be restored back to the WT level in the *nmlR* and *adhC*-complemented strains, respectively **(Fig. 7E, F and Fig. S2)**. In contrast, the *nmlRC52A* mutation was unable to complement the HOCl- and H_2O_2-sensitive phenotypes of the Δ*nmlR* mutant **(Fig 7B, E, F)**. These results indicate that Cys52 is important for activation of *adhC* expression and that AdhC confers resistance towards HOCl and ROS stress in *S. pneumoniae* D39.

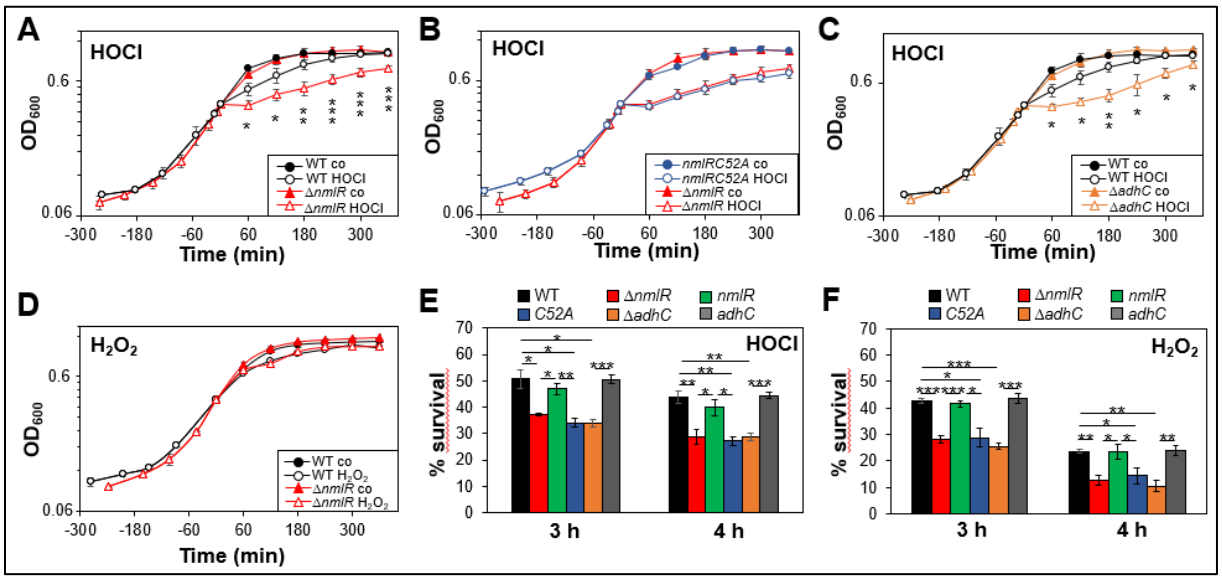

Fig. 7: The NmlR regulon confers resistance to HOCl and H_2O_2. Growth curves **(A-D)** and survival assays **(E,F)** were performed with *S. pneumoniae* D39 WT, the Δ*nmlR* and Δ*adhC* mutants as well as the *nmlR-, nmlRC52A-* and *adhC*-complemented strains in RPMI medium. At an OD_{600} of 0.4, bacteria were treated with sublethal doses of 800 µM HOCl and 0.45 mM H_2O_2 for growth phenotypes and survival data, which were acquired 3 and 4 h after exposure to 1.1 mM HOCl and 1 mM H_2O_2. The survival rates of CFUs for the treated samples were calculated relative to the control, which was set to 100%. Growth curves of the *nmlR*- and *adhC*-complemented strains are shown in **Fig. S2**. The results are from three to five biological replicates. Error bars represent the standard deviation. The statistics was calculated using a Student's unpaired two-tailed *t*-test. $^*p < 0.05$; $^{**}p < 0.01$; $^{***}p < 0.001$.

The NmlR regulon confers protection against the oxidative burst of human macrophages. To analyze the role of the NmlR regulon in the defense of macrophage-derived ROS production under infection conditions, we determined the intracellular survival of the Δ*nmlR* mutant in the human macrophage cell line THP-1A **(Fig. 8A)**. The colony-forming units (CFUs) of intracellular *S. pneumoniae* were determined 2 to 5 h post-infection (p.i.) **(Fig. 8A)**. The results revealed that the Δ*nmlR* mutant was significantly impaired in survival inside human macrophages. Specifically, at 3 h p.i., the number of viable bacteria decreased to 53.9% for

the WT and to 26.7% for the Δ*nmlR* mutant **(Fig. 8A)**. Thus, the Δ*nmlR* mutant showed a 50% reduced survival rate compared with the WT after 3 h p.i.. This sensitivity of the Δ*nmlR* mutant could be abolished by the addition of the flavoprotein inhibitor diphenyleneiodonium (DPI) **(Fig. 8A)**. DPI was previously shown to inhibit NOX2 and the macrophage NO synthase to prevent ROS and NO generation (Stuehr *et al.*, 1991, Altenhofer *et al.*, 2015, O'Donnell *et al.*, 1993). Thus, DPI treatment increased the survival rate of both *S. pneumoniae* strains to >90% after 3 h p.i. **(Fig. 8A)**. Interestingly, the protective effect of DPI was less pronounced after 4 and 5 h p.i., probably indicating the onset of other killing mechanisms. Nevertheless, also at these later time points, the survival of the Δ*nmlR* mutant was significantly improved through inhibition of the oxidative burst. Under control conditions, the Δ*nmlR* mutant showed a 2.4–2.5-fold lower survival than the WT, whereas the viability rate was only 1.5–1.8-fold decreased after DPI addition.

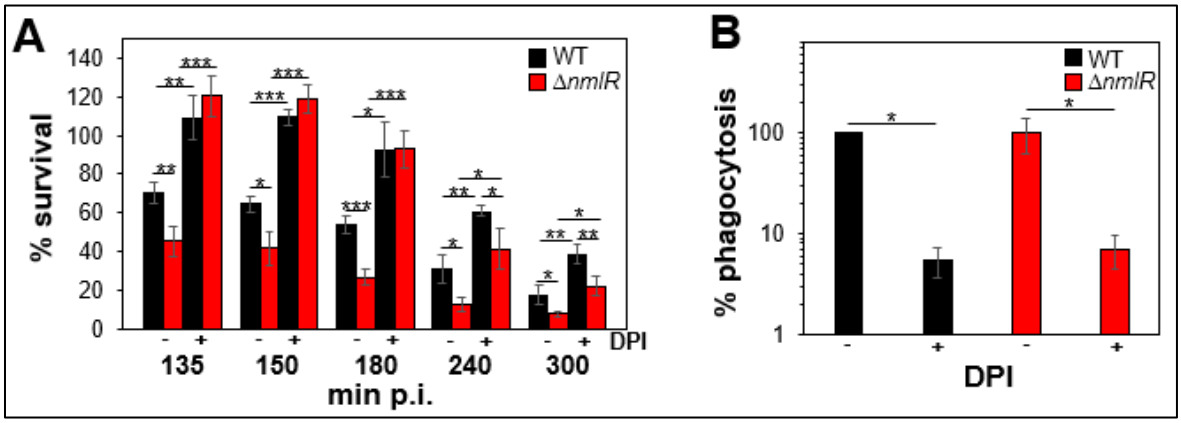

Fig. 8: The Δ*nmlR* mutant is impaired in survival inside THP-1A human macrophages. (A) The survival of S. pneumoniae D39 WT and the Δ*nmlR* mutant was analyzed without or with diphenyleneiodonium chloride (DPI) at 135, 150, 180, 240 and 300 min post-infection (p.i.) of the human macrophage cell line THP-1A. The percentage of survival was calculated and normalized to the 2 h time point, which was set to 100%. **(B)** The relative phagocytosis rate was determined for S. pneumoniae D39 WT and the Δ*nmlR* mutant by analysing the CFUs 2 h after infection relative to the input values and displayed in relation to the WT without DPI treatment, which was set to 100%. The results are from four biological replicates and the error bars represent the standard deviation. The statistics was calculated using a Student's unpaired two-tailed t-test. *$p < 0.05$; **$p < 0.01$; ***$p < 0.001$.

Since DPI was shown to affect the phagocytosis rate (Lv *et al.*, 2017, Zhu *et al.*, 2017), phagocytosis assays were performed to exclude differences in the internalization of the WT and the Δ*nmlR* mutant. DPI significantly decreased the phagocytosis rate of THP-1A cells ~16.5-fold **(Fig. 8B)**. However, the phagocytosis rate of both strains by THP-1A cells was comparable in the absence and presence of DPI **(Fig. 8B)**. These results indicate that the

NmlR-controlled AdhC is important for the defense against oxidative stress and contributes to the resistance of *S. pneumoniae* D39 against the respiratory burst during macrophage infections.

DISCUSSION

In this work, we have used RNA-seq transcriptome analysis to study the expression profile of *S. pneumoniae* in response to the strong oxidant HOCl. The transcriptome signature revealed that HOCl stress caused the most prominent induction of the thiol-specific oxidative stress response, indicated by the extracellular CTM complex for repair of oxidized Met residues (Saleh *et al.*, 2013, Gennaris & Collet, 2013), the NmlR-controlled *adhC* gene (Potter *et al.*, 2010, Stroeher *et al.*, 2007) and the CtsR and HrcA regulons for repair or degradation of oxidatively damaged proteins (Yesilkaya *et al.*, 2013, Mraheil *et al.*, 2021). In addition, the quinone-responsive SifR regulon (Zhang *et al.*, 2022) and the CopY and SczA regulons controlling metal efflux systems (Kloosterman *et al.*, 2007, Shafeeq *et al.*, 2011) were strongly induced by HOCl stress. The upregulation of these metal efflux systems is related to the HOCl-induced oxidation of metal-coordinating Cys residues of metal regulators (Fliss & Menard, 1991), accounting also for the pneumococcal SczA and CopY and the related ArsR and CopR repressors of *B. subtilis* (Chi et al., 2011). Thus, similar thiol-specific oxidative, electrophile and metal stress responses were previously reported under HOCl stress in other Gram-positive bacteria, such as *Staphylococcus aureus* and *B. subtilis* (Loi *et al.*, 2018, Chi *et al.*, 2011). Due to its high reactivity with thiols (Storkey *et al.*, 2014), HOCl generally induced most known regulons controlled by redox-sensing regulators in the different bacteria. The prominent induction of the HrcA- and CtsR-controlled proteases and chaperones under HOCl stress is conserved throughout firmicutes, supporting that HOCl causes increased protein thiol-oxidation and protein aggregation.

In addition, HOCl caused derepression of the CcpA regulon in *S. pneumoniae*, accompanied by induction of many regulons for the uptake and utilization of alternative carbohydrates, including the ScrR, FcsR, RafR, MalR, RegR, AgaR, XylR, BguR, GalR and LacR regulons (Minhas *et al.*, 2021). While the basis for the CcpA derepression under HOCl

in the pneumococcus is unknown, this study provides insights into the usage of alternative carbon sources under the growth conditions in supplemented RPMI medium. The XylR, GalR and LacR regulons for utilization and catabolism of lactose and galactose responded most strongly to HOCl stress, suggesting the switch from utilization of glucose to lactose (and the released galactose) via the Leloir and tagatose 6-phosphate pathways (Minhas *et al.*, 2021). Galactose was shown to be the key sugar for niche adaptation to the nasopharynx and important for pneumococcal colonization (Paixao *et al.*, 2015). However, whether this glucose-lactose/galactose switch is physiologically important to mediate protection against the oxidative burst during infections remains to be investigated in future studies.

Since the *nmlR-adhC* operon was most strongly upregulated under HOCl stress, the redox-sensing mechanism and functions of the MerR-family regulator NmlR were investigated in the pneumococcus. qRT-PCR analysis revealed that *adhC* transcription is most strongly elevated by aldehydes (Potter *et al.*, 2010), HOCl, diamide and H_2O_2 stress in the pneumococcus. However, *adhC* was only weakly induced by the NO donor DEA-NONOate. Treatment of bacteria with the NO donor might cause a lower intracellular GSNO level compared to the external GSNO amount applied directly in the previous study (Stroeher *et al.*, 2007). Transcriptional studies further showed that NmlR acts as activator of *adhC* transcription under HOCl stress, depending on the conserved Cys52 in vivo. The role of Cys52 of NmlR in redox-sensing was further confirmed in growth and survival assays under HOCl and H_2O_2 stress, since the *nmlRC52A* mutant was unable to restore the sensitive phenotypes of the Δ*nmlR* mutant back to the WT levels. Similarly, the conserved Cys was essential for aldehyde sensing in other MerR/NmlR homologs, including AdhR of *B. subtilis* (Nguyen *et al.*, 2009) and NmlR of *H. influenzae* (Counago *et al.*, 2016). In contrast, all four Cys residues were involved in transcriptional regulation of NmlR of *N. gonorrhoeae*, probably reflecting their role in Zn^{2+}-binding (Kidd *et al.*, 2005).

Using non-reducing SDS-PAGE and mass spectrometry, NmlR was shown to undergo a reversible thiol switch by formation of intersubunit disulfides or *S*-glutathionylation at Cys52 under oxidative stress in vitro. To estimate the position of Cys52, the structure of NmlR was

modelled based on the template of the structure of the *L. monocytogenes* MerR homolog LMOf2365_2715 (PDB: 3gp4.1). In this NmlR model, the N-terminal α1 and α2 helices form the DNA-binding helix-turn-helix (HTH) motifs in each subunit, while the dimer interface is formed by the α5 helices. The Cys52 residues are located in the α3 helices and are ~27.8 Å apart in the dimeric structure, which is quite far away for disulfide bond formation **(Fig. S3)**. Thus, the *S*-glutathionylation model would be the more realistic redox-sensing mechanism under in vivo conditions, in agreement with the model for typical one-Cys-type redox-sensing regulators (Lee *et al.*, 2007, Hillion & Antelmann, 2015).

Many MerR-type regulators were shown to be activated by conformational changes upon binding of inducers, resulting in re-orientation of the DNA-binding HTH motifs (Yang *et al.*, 2021, Counago *et al.*, 2016). The structural rearrangements of MerR-type regulators lead to realignments of the –35 and –10 promoter elements by introducing a kink in the DNA molecule to compensate for the overlong spacer of 19–20 bp, allowing the recognition by the RNAP to initiate transcription. Based on this overlong spacer, most MerR-family transcription factors, including pneumococcal NmlR, were shown to function as transcriptional activators in response to specific signals (Brown *et al.*, 2003). However, NmlR might also function as repressor of *adhC* under control conditions, since transcription of *adhC* was upregulated in the Δ*nmlR* mutant. Similarly, other MerR-family transcription factors were postulated to switch from the repressor to the activator conformation in the presence of an inducer (Brown *et al.*, 2003, Chang *et al.*, 2015, Fang & Zhang, 2022). However, the higher transcriptional activity without the MerR-type transcription factor might be also caused by the high promoter activity independent of the –35 element. Only upon MerR binding, this element was shown to be important for transcriptional initiation by the RNAP (Lund & Brown, 1989). Using the broccoli-FLAP assay, we were able to demonstrate for the first time that oxidized NmlR activates transcription initiation of the *nmlR-adhC* operon promoter by the *E. coli* σ^{70}-RNAP in vitro, while reduced NmlR rather inhibited transcription. The high basal transcription rate of the *nmlR* promoter by the *E: coli* σ^{70}-RNAP alone and the decreased transcription upon binding of reduced NmlR might indicate its function as repressor under control conditions. Thus, our in

vivo and in vitro transcriptional results support that reduced NmlR acts as repressor under non-stress conditions, whereas NmlR is oxidized upon H_2O_2 and HOCl stress and functions as activator to induce the transcription of *adhC* by the RNAP.

Overall, NmlR was identified as major redox-sensing regulator of the oxidative stress defense in *S. pneumonia*e. NmlR significantly improved the survival of *S. pneumoniae* D39 in the human macrophage cell line THP-1A. Decreased ROS and NO levels due to the addition of the flavoprotein inhibitor diphenyleneiodonium (DPI) significantly enhanced the intracellular survival of the Δ*nmlR* mutant (Stuehr *et al.*, 1991, Altenhofer *et al.*, 2015, O'Donnell *et al.*, 1993). Thus, NmlR plays an important role in the virulence of *S. pneumoniae* by conferring resistance against the oxidative burst of activated immune cells during infections. The observed bacterial killing of the WT and the Δ*nmlR* mutant over time, even in the presence of DPI, is in agreement with previous findings that *S. pneumoniae* contributes to its cell death in the phagosome by endogenous H_2O_2 production (Mandell & Hook, 1969, Pitt & Bernheimer, 1974). Additionally, ROS and RNS production is thought to act in concert with changes in ion flux, pH decrease and hydrolytic enzymes in human macrophages to promote killing of the pathogen (Nüsse, 2011, Haas, 2007).

The NmlR-controlled alcohol dehydrogenase AdhC was identified as major defense mechanism against HOCl and H_2O_2 stress encountered during infections in *S. pneumoniae*. Alcohol-dehydrogenase 3 enzymes are widespread in bacteria and have been shown to catalyze detoxification of ω-hydroxy fatty acids, various aldehydes, medium-chain alcohols, GSNO and *S*-hydroxymethylglutathione (HMGSH) (Staab *et al.*, 2008). In *N. meningitidis,* AdhC conferred protection against formaldehyde, but the Δ*adhC* mutant was not sensitive to methylglyoxal (Chen *et al.*, 2013). The Δ*adhC* mutant of *H. influenzae* was unable to grow with high oxygen levels and displayed increased susceptibilities towards GSNO, methylglyoxal, glyceraldehyde and glycolaldehyde (Kidd *et al.*, 2012, Kidd *et al.*, 2007), indicating also roles of other AdhC homologs in the oxidative and aldehyde stress defense. However, the Δ*adhC* mutant of *S. pneumoniae* did not show sensitive phenotypes under methylglyoxal and

formaldehyde stress (Potter *et al.*, 2010), raising the question of the physiological substrate of AdhC in *S. pneumonia*e.

Our results have shown that AdhC protects *S. pneumoniae* against HOCl and H_2O_2 stress, suggesting a direct or indirect role of AdhC in detoxification of these oxidants, which remains to be elucidated. Oxidants can react with various cellular macromolecules, resulting in reactive electrophilic species as secondary reactive species, such as quinones and aldehydes. Especially lipid peroxidation, DNA and sugar oxidation were shown to generate various aldehydes, including glyoxal, formaldehyde, and glycerine aldehyde (Okado-Matsumoto & Fridovich, 2000, Beavers & Skaar, 2016, Spiteller, 2008, Marnett *et al.*, 2003). Activated neutrophils contribute indirectly via HOCl production to the production of α-hydroxy and α,β-unsaturated aldehydes and other reactive species, highlighting the relevance of the redox sensor NmlR and the AdhC enzyme under infection conditions. Thus, our future analyses are directed to further investigate the redox-sensing and defense mechanisms of *S. pneumoniae* to mediate survival, replication and adaptation inside infected immune cells.

EXPERIMENTAL PROCEDURES

Bacterial strains, growth and survival assays. Bacterial strains and primers are listed in **Tables S3 and S4**. *E. coli* strains were cultivated in Luria broth (LB) medium for plasmid construction and protein expression. For growth and survival assays, *S. pneumoniae* strains were cultivated in supplemented RPMI medium as described previously (Schulz *et al.*, 2014). At an optical density at 600 nm (OD_{600}) of 0.4, the bacteria were exposed to different thiol-reactive compounds to monitor the growth and survival. Survival assays were performed by plating 100 µl of serial dilutions of *S. pneumoniae* strains onto Columbia blood agar plates for CFUs counting. Statistical analysis was performed using the Student's unpaired two-tailed t-test. The chemicals methylhydroquinone (MHQ), NaOCl, H_2O_2, diamide, methylglyoxal, formaldehyde and DEA-NONOate were purchased from Sigma Aldrich, Roth and Cayman Chemical Company, respectively. NaOCl dissociates in aqueous solution to hypochlorous acid (HOCl) and hypochlorite (OCl^-) (Estrela *et al.*, 2002). Thus, the concentration of HOCl was

determined by absorbance measurements as described previously (Winter *et al.*, 2008). DEA-NONOate was reported to dissociate to generate 1.5 M NO per 1 M of the parent compound (Keefer *et al.*, 1996). Allicin was kindly provided by Martin Gruhlke and synthesized as described (Loi *et al.*, 2019).

Construction of the *S. pneumoniae* D39 Δ*nmlR* and Δ*adhC* mutant as well as the *nmlR-, nmlRC52A*- and *adhC*-complemented strains. The *S. pneumoniae* D39 *nmlR* (SPD_1637) and *adhC* (SPD_1636) deletion mutants were constructed by insertion-deletion mutagenesis as described previously (Hirschmann *et al.*, 2021). For generation of the pSP72-Δ*nmlR*::*ermB* and pSP72-Δ*adhC*::*ermB* plasmids, the 5′ and 3′ flanking regions of both genes were amplified by PCR using primers nmlR_fl_HindIII_for and nmlR_fl_BglII_rev or adhC_fl_HindIII_for and adhC_fl_BglII_rev, respectively **(Table S4)**. The PCR products were digested with *Hind*III and *Bgl*II and cloned into plasmid pSP72. The recombinant plasmids were used as a template for an inverse PCR with primers nmlR_in_SalI_for and nmlR_in_BamHI_rev or adhC_in_SalI_for and adhC_in_BamHI_rev, respectively **(Table S4)**. The resulting PCR products were digested with *BamH*I and *Sal*I and ligated with the erm^R cassette, which was amplified with the primers Ery_BamHI_for and Ery_SalI_rev from the plasmid pTP1. The generated plasmids were transferred into *S. pneumoniae* D39 WT as described previously (Gomez-Mejia *et al.*, 2018). Briefly, the bacteria were cultivated in THY-medium until an OD_{600} of 0.1. The transformation was induced by addition of the competence-stimulating peptide 1 (CSP1) and the pSP72-Δ*nmlR*::*ermB* and pSP72-Δ*adhC*::*ermB* plasmids. The bacteria were exposed to a cold shock for 10 min, followed by 30 min incubation at 30°C. Bacteria were grown for 2 h at 37°C and plated onto Columbia blood agar plates containing erythromycin for selection.

For construction of the *S. pneumoniae* D39 *nmlR* and *adhC*-complemented strains the coding sequences were amplified from chromosomal DNA using the primers nmlR_pBAV_for_NcoI and nmlR_pBAV_rev_HindIII or adhC_pBAV_for_NcoI and adhC_pBAV_rev_HindIII **(Table S4)**. To generate the plasmid for construction of the *nmlRC52A*-complemented strain, two first-round PCR products, obtained with the primer pairs

NmlRC52A_f2_for and nmlR_pBAV_rev_HindIII as well as NmlRC52A_f1_rev and nmlR_pBAV_for_NcoI, were hybridized and amplified by a second round of PCR using the primers nmlR_pBAV_for_NcoI and nmlR_pBAV_rev_HindIII, as described previously (Loi *et al.*, 2018). The purified PCR products were digested with *Nco*I and *Hind*III and ligated into plasmid pBAV (Hess *et al.*, 2017), which was kindly provided by Sven Hammerschmidt (University of Greifswald). The resulting plasmids pBAV-*nmlR,* pBAV-*nmlRC52A* and pBAV-*adhC* **(Table S3)** were introduced into the corresponding *S. pneumoniae* D39 Δ*nmlR* and Δ*adhC* mutants as described above. Transformants were selected on Columbia blood agar plates containing erythromycin and chloramphenicol.

RNA isolation, RNA-seq transcriptomics and qRT-PCR analysis. *S. pneumoniae* strains were cultivated in RPMI medium and treated with various thiol-reactive compounds at an OD_{600} of 0.4 for 30 min. Bacteria were harvested in ice-cold killing buffer (50 mM Tris pH 7.5, 5 mM $MgCl_2$, 20 mM NaN_3), centrifuged at 4,750 rpm for 10 min at 4°C and the pellets were immediately frozen in liquid nitrogen and stored at -80°C. RNA isolation was performed using an acidic phenol-chloroform extraction protocol (Wetzstein *et al.*, 1992). After DNase-I treatment (Zymo Research, Germany), the RNA quality was checked by Trinean Xpose (Gentbrugge, Belgium) and the Agilent RNA Nano 6,000 kit using an Agilent 2,100 Bioanalyzer (Agilent Technologies, Böblingen, Germany). For RNA-seq transcriptomics, Ribo-Zero rRNA Removal Kit (Bacteria) from Illumina (San Diego, CA, USA) was used to remove the rRNA. TruSeq Stranded mRNA Library Prep Kit from Illumina (San Diego, CA, United States) was applied to prepare the cDNA libraries. The cDNAs were sequenced paired end on an Illumina HiSeq 1,500 (San Diego, CA, United States) using 70 and 75 bp read length and a minimum sequencing depth of 10 million reads per library. The transcriptome sequencing raw data files are available in the ArrayExpress database (www.ebi.ac.uk/arrayexpress) under accession number E-MTAB-11968.

For quantitative Real-Time PCR (qRT-PCR) analysis, the purified total RNA was reverse-transcribed into cDNA using the High-capacity cDNA reverse transcription kit (Applied

Biosystems, USA) according to the recommendations of the manufacturer. SYBR™ GreenER™ (Applied Biosystems, USA) intercalation in double-stranded DNA was measured using a 7300 Real-Time PCR System (Applied Biosystems, USA) according to the manufacturer's instructions. The amplification primer pair is listed in **Table S4**. The verification of the resulting RT-PCR products was performed by melting curve analysis. The crossing points were determined using the Sequence Detection Software Version 1.4 (Applied Biosystems, USA) and the differences in gene expression were analysed by comparing the crossing points of the samples measured in duplicate as described previously (Busche *et al.*, 2012).

Cloning, expression and purification of His-tagged NmlR and NmlRC52A proteins in *E. coli.* To generate the plasmids pET11b-*nmlR* and pET11b-*nmlRC52A*, the *nmlR* gene (SPD_1637) was amplified from chromosomal DNA of *S. pneumoniae* D39 or from the pBAV-*nmlRC52A* plasmid, respectively, using primers nmlR_pET_NheI_for and nmlR_pET_BamHI_rev **(Table S4)**. The PCR products were digested with *Nhe*I and *BamH*I and inserted into plasmid pET11b (Novagen) **(Table S3)**. For expression and purification of His-tagged NmlR and NmlRC52A, *E. coli* BL21(DE3)*plysS* with plasmids pET11b-*nmlR* and pET11b-*nmlRC52A* were cultivated in 1.5 l LB medium until the exponential growth phase at an OD_{600} of 0.7, followed by addition of 1 mM iso-propyl-β-D-thiogalactopyranoside (IPTG) for 5 h at 30°C. Recombinant His-tagged proteins were purified using His Trap™ HP Ni-NTA columns and the ÄKTA purifier liquid chromatography system as described (Loi *et al.*, 2018).

Electrophoretic mobility shift assays (EMSAs) of NmlR and NmlRC52A proteins. For EMSAs, the 274 bp DNA fragment containing the upstream region of *nmlR* was amplified by PCR **(Table S4)**. The DNA-binding reactions were performed with 15 ng of the promoter region and purified His-tagged NmlR and NmlRC52A proteins for 45 min, as described previously (Loi *et al.*, 2018). Diamide was added to the DNA-NmlR-complex for 30 min to observe the dissociation of NmlR from the DNA. To generate two base substitutions in each half of the

inverted repeat, two first-round PCRs were performed using the primer pairs EMSA_nmlR_m1_for, Emsa_nmlR_rev and EMSA_nmlR_m1_rev, EMSA_nmlR_for or EMSA_nmlR_m2_for, Emsa_nmlR_rev and EMSA_nmlR_m2_rev, EMSA_nmlR_for, respectively **(Table S4)**. The first round PCR products were hybridized and amplified by a second round of PCR using the primers EMSA_nmlR_for and Emsa_nmlR_rev.

Multiround in vitro transcription assay to monitor transcription initiation rates using broccoli-FLAP assay. To determine regulatory effects of NmlR on transcription initiation of σ^{70}-RNAP, broccoli-FLAP assay was performed as described (Huang et al., 2022, submitted) with slight variations. In short, the broccoli gene was placed under control of the *S. pneumoniae nmlR* promoter region (CTTGACTTGGAGTCAACTCAAAGTTATATAATAAGATAA) (Stroeher *et al.*, 2007) in pOP005 (https://benchling.com/s/seq-5bEIoESV96X1uEPcEWOw). *E. coli* RNAP and *E. coli* σ^{70} were purified as described before (Said *et al.*, 2017). To monitor transcription, *E. coli* RNAP and σ^{70} were incubated for 30 min at 30°C to form the holoenzyme. 3 µM holoenzyme were mixed with 150 nM DNA template and 20 µM DFHBI-1T in transcription buffer (10 mM Tris pH 7.9, 10 mM $MgCl_2$, 100 mM KCl) and transcription was started by adding an equal volume of 1 mM rNTPs to the reaction and quick mixing. The sample was placed in an OptiPlateTM 384-well plate (PerkinElmer) and fluorescence was measured using a Spark Multimode Microplate reader (Tecan). Fluorescence was monitored every second for a total duration of 15 min using an excitation wavelength of 472 nm and an emission wavelength of 507 nm. Where indicated, 20 µM of NmlR was added to the transcription reaction prior to rNTP addition and incubated for 15 min at room temperature. $NmlR_{red}$ was reduced with 10 mM DTT. $NmlR_{ox}$ was oxidized by first reducing the protein with 10 mM DTT, followed by buffer exchange, and oxidation with 2.5% H_2O_2 (w/v). All measurements were performed in triplicates. Initial transcription rates were calculated from the slope of the initial linear increase in fluorescence after the corresponding lag phases (t_0, determined from the graph) using Prism software (GraphPad; RRID: SCR_002798). Relative initiation rates were determined by correlating initial transcription rates to the rates of RNAP, which was set to 1.

Identification of thiol-modifications of the NmlR protein in vitro. To study thiol-oxidation of the NmlR protein in vitro, the purified protein was reduced with 10 mM DTT for 15 min and oxidised with increasing amounts of diamide, HOCl and H_2O_2 for 15 min. Free thiols were alkylated with 50 mM iodoacetamide (IAM) for 30 min in the dark before samples were subjected to non-reducing SDS-PAGE analyses. The post-translational thiol-modifications of oxidized NmlR (with or without GSH) were determined by matrix-assisted laser desorption ionization-time of flight mass spectrometry (MALDI-TOF-MS) using an Ultraflex-II TOF/TOF instrument (Bruker Daltonics, Bremen, Germany) equipped with a 200 Hz solid-state Smart beam™ laser. The bands of reduced and oxidized NmlR from the non-reducing SDS–PAGE were in-gel tryptic digested as described previously (Chi *et al.*, 2011). Alpha-Cyano-4-hydroxycinnamic acid was used as matrix substance and the mass spectrometer was operated in the positive reflector mode. Mass spectra were acquired over an m/z range of 400–4,000.

Macrophage infection assays. The infection assays were performed as reported previously (Kohler *et al.*, 2016), using the human macrophage cell line THP-1A, an adherent derivative of the THP-1 cell line (Van Immerseel *et al.*, 2003). The cells were cultivated in Iscove's modified Dulbecco's medium (Biochrom) with 10% heat-inactivated fetal bovine serum (FBS) at 37°C and 5% CO_2. Two days before the infection experiment, the cells were seeded at densities of $1x10^5$ cells/ml in 48-well TC-plates (Sarstedt, Germany). If indicated, 5 µM of the flavoprotein inhibitor diphenyleneiodonium (DPI) was added 16 hours prior infection. On the day of infection, *S. pneumoniae* strains were grown in supplemented RPMI medium to an OD_{600} of 0.35. Macrophages were infected with log phase bacteria at a multiplicity of infection (MOI) of 1:50. One hour after infection, the cell culture medium was replaced and 100 µg/ml gentamicin and 100 U/ml penicillin G were added for 1 h to kill extracellular bacteria. The intracellular survival was determined at different time points after phagocytosis. Infected macrophages were lysed with 1% saponin and the supernatant with internalized intracellular bacteria was plated on Columbia blood agar plates for determination of CFUs.

ACKNOWLEDGEMENTS

This work was supported by grants from the Deutsche Forschungsgemeinschaft (DFG) (AN746/4-1 and AN746/4-2) within the SPP1710 on “Thiol-based Redox switches”, by the SFB973 project C08 and TR84 project B06 to H.A. This experiments related to the in vitro transcription assay at the *nmlR* promoter were further supported by the DFG grant WA 1126/11-1 (project number 433623608) to M.C.W. For mass spectrometry performed by C.W., we would like to acknowledge the assistance of the Core Facility BioSupraMol supported by the DFG. We are grateful to Sven Hammerschmidt (University of Greifswald) for providing the pBAV plasmid and to Doris Frey (Charité-Universitätsmedizin, Berlin) for the technical assistance with the qRT-PCR analyses. We further would like to thank Martin Clemens Horst Gruhlke and Alan John Slusarenko (RWTH Aachen University, Department of Plant Physiology) for providing allicin.

AUTHOR DISCLOSURE STATEMENT

No competing financial interests exist.

AUTHOR CONTRIBUTIONS

V.N.F. and H.A. designed the concept of this project. V.N.F performed the majority of the experiments and analyzed the data. N.L. contributed to mutant constructions and infection assays. T.B. and J.K. performed the RNA-seq analysis and bioinformatics of the transcriptome data. N.S. and M.C.W. performed the broccoli-FLAP assay, analyzed the data and contributed to writing. C.W. performed the mass spectrometry and analyzed the data. H.A. and V.N.F. wrote the manuscript. H.A. and M.C.W. provided funding for the project. All authors have read, edited and approved the final manuscript.

ABBREVIATED SUMMARY

In this work, we have studied the transcriptome of *Streptococcus pneumoniae* under HOCl stress and characterized the MerR family regulator NmlR as HOCl-sensing transcriptional activator of the alcohol dehydrogenase-encoding *adhC* gene. NmlR was oxidized by HOCl to intersubunit disulfides and *S*-glutathionylated in vitro, resulting in transcriptional activation of the *nmlR-adhC* operon by the RNAP. The NmlR regulon was shown to be important for the defense against oxidative stress and macrophage infections in *S. pneumoniae*.

REFERENCES

Altenhofer, S., Radermacher, K.A., Kleikers, P.W., Wingler, K., and Schmidt, H.H. (2015) Evolution of NADPH oxidase inhibitors: selectivity and mechanisms for target engagement. *Antioxid Redox Signal* **23**: 406-427.

Barrette, W.C., Jr., Hannum, D.M., Wheeler, W.D., and Hurst, J.K. (1989) General mechanism for the bacterial toxicity of hypochlorous acid: abolition of ATP production. *Biochemistry* **28**: 9172-9178.

Beavers, W.N., and Skaar, E.P. (2016) Neutrophil-generated oxidative stress and protein damage in *Staphylococcus aureus*. *Pathogens and disease* **74**.

Biasini, M., Bienert, S., Waterhouse, A., Arnold, K., Studer, G., Schmidt, T., Kiefer, F., Gallo Cassarino, T., Bertoni, M., Bordoli, L., and Schwede, T. (2014) SWISS-MODEL: modelling protein tertiary and quaternary structure using evolutionary information. *Nucleic Acids Res* **42**: W252-258.

Brown, N.L., Stoyanov, J.V., Kidd, S.P., and Hobman, J.L. (2003) The MerR family of transcriptional regulators. *FEMS Microbiol Rev* **27**: 145-163.

Busche, T., Silar, R., Picmanova, M., Patek, M., and Kalinowski, J. (2012) Transcriptional regulation of the operon encoding stress-responsive ECF sigma factor SigH and its anti-sigma factor RshA, and control of its regulatory network in *Corynebacterium glutamicum*. *BMC Genomics* **13**: 445.

CDC (2020) Pneumococcal Disease.

Chang, C.C., Lin, L.Y., Zou, X.W., Huang, C.C., and Chan, N.L. (2015) Structural basis of the mercury(II)-mediated conformational switching of the dual-function transcriptional regulator MerR. *Nucleic Acids Res* **43**: 7612-7623.

Chapuy-Regaud, S., Ogunniyi, A.D., Diallo, N., Huet, Y., Desnottes, J.F., Paton, J.C., Escaich, S., and Trombe, M.C. (2003) RegR, a global LacI/GalR family regulator, modulates virulence and competence in *Streptococcus pneumoniae*. *Infect Immun* **71**: 2615-2625.

Chen, N.H., Counago, R.M., Djoko, K.Y., Jennings, M.P., Apicella, M.A., Kobe, B., and McEwan, A.G. (2013) A glutathione-dependent detoxification system is required for formaldehyde resistance and optimal survival of *Neisseria meningitidis* in biofilms. *Antioxid Redox Signal* **18**: 743-755.

Chi, B.K., Gronau, K., Mäder, U., Hessling, B., Becher, D., and Antelmann, H. (2011) *S*-bacillithiolation protects against hypochlorite stress in *Bacillus subtilis* as revealed by transcriptomics and redox proteomics. *Mol Cell Proteomics* **10**: M111 009506.

Counago, R.M., Chen, N.H., Chang, C.W., Djoko, K.Y., McEwan, A.G., and Kobe, B. (2016) Structural basis of thiol-based regulation of formaldehyde detoxification in *H. influenzae* by a MerR regulator with no sensor region. *Nucleic Acids Res* **44**: 6981-6993.

Estrela, C., Estrela, C.R.A., Barbin, E.L., Spanó, J.C.E., Marchesan, M.A., and Pécora, J.D. (2002) Mechanism of action of sodium hypochlorite. *Brazilian Dental Journal* **13**: 113-117.

Fang, C., and Zhang, Y. (2022) Bacterial MerR family transcription regulators: activation by distortion. *Acta Biochim Biophys Sin (Shanghai)* **54**: 25-36.

Filonov, G.S., Moon, J.D., Svensen, N., and Jaffrey, S.R. (2014) Broccoli: rapid selection of an RNA mimic of green fluorescent protein by fluorescence-based selection and directed evolution. *J Am Chem Soc* **136**: 16299-16308.

Fliss, H., and Menard, M. (1991) Hypochlorous acid-induced mobilization of zinc from metalloproteins. *Arch Biochem Biophys* **287**: 175-179.

Gennaris, A., and Collet, J.F. (2013) The 'captain of the men of death', *Streptococcus pneumoniae*, fights oxidative stress outside the 'city wall'. *EMBO Mol Med* **5**: 1798-1800.

Gomez-Mejia, A., Gamez, G., Hirschmann, S., Kluger, V., Rath, H., Bohm, S., Voss, F., Kakar, N., Petruschka, L., Volker, U., Bruckner, R., Mader, U., and Hammerschmidt, S. (2018) Pneumococcal metabolic adaptation and colonization are regulated by the two-component regulatory system 08. *mSphere* **3**.

Gray, M.J., Wholey, W.Y., and Jakob, U. (2013) Bacterial responses to reactive chlorine species. *Annu Rev Microbiol*.

Haas, A. (2007) The phagosome: compartment with a license to kill. *Traffic* **8**: 311-330.

Hess, N., Waldow, F., Kohler, T.P., Rohde, M., Kreikemeyer, B., Gomez-Mejia, A., Hain, T., Schwudke, D., Vollmer, W., Hammerschmidt, S., and Gisch, N. (2017) Lipoteichoic acid deficiency permits normal growth but impairs virulence of *Streptococcus pneumoniae*. *Nat Commun* **8**: 2093.

Hillion, M., and Antelmann, H. (2015) Thiol-based redox switches in prokaryotes. *Biol Chem* **396**: 415-444.

Hirschmann, S., Gomez-Mejia, A., Mäder, U., Karsunke, J., Driesch, D., Rohde, M., Häussler, S., Burchhardt, G., and Hammerschmidt, S. (2021) The two-component system 09 regulates pneumococcal carbohydrate metabolism and capsule expression. *Microorganisms* **9**.

Hobman, J.L., Wilkie, J., and Brown, N.L. (2005) A design for life: prokaryotic metal-binding MerR family regulators. *Biometals* **18**: 429-436.

Imber, M., Pietrzyk-Brzezinska, A.J., and Antelmann, H. (2019) Redox regulation by reversible protein *S*-thiolation in Gram-positive bacteria. *Redox Biol* **20**: 130-145.

Imlay, J.A. (2003) Pathways of oxidative damage. *Annu Rev Microbiol* **57**: 395-418.

Keefer, L.K., Nims, R.W., Davies, K.M., and Wink, D.A. (1996) "NONOates" (1-substituted diazen-1-ium-1,2-diolates) as nitric oxide donors: convenient nitric oxide dosage forms. *Methods Enzymol* **268**: 281-293.

Kidd, S.P., Jiang, D., Jennings, M.P., and McEwan, A.G. (2007) Glutathione-dependent alcohol dehydrogenase AdhC is required for defense against nitrosative stress in *Haemophilus influenzae*. *Infect Immun* **75**: 4506-4513.

Kidd, S.P., Jiang, D., Tikhomirova, A., Jennings, M.P., and McEwan, A.G. (2012) A glutathione-based system for defense against carbonyl stress in *Haemophilus influenzae*. *BMC Microbiol* **12**: 159.

Kidd, S.P., Potter, A.J., Apicella, M.A., Jennings, M.P., and McEwan, A.G. (2005) NmlR of *Neisseria gonorrhoeae*: a novel redox responsive transcription factor from the MerR family. *Mol Microbiol* **57**: 1676-1689.

Kloosterman, T.G., van der Kooi-Pol, M.M., Bijlsma, J.J., and Kuipers, O.P. (2007) The novel transcriptional regulator SczA mediates protection against Zn^{2+} stress by activation of the Zn^{2+}-resistance gene *czcD* in *Streptococcus pneumoniae*. *Mol Microbiol* **65**: 1049-1063.

Kohler, T.P., Scholz, A., Kiachludis, D., and Hammerschmidt, S. (2016) Induction of central host signaling kinases during pneumococcal infection of human THP-1 cells. *Front Cell Infect Microbiol* **6**: 48.

Lee, J.W., Soonsanga, S., and Helmann, J.D. (2007) A complex thiolate switch regulates the *Bacillus subtilis* organic peroxide sensor OhrR. *Proc Natl Acad Sci U S A* **104**: 8743-8748.

Lisher, J.P., Tsui, H.T., Ramos-Montanez, S., Hentchel, K.L., Martin, J.E., Trinidad, J.C., Winkler, M.E., and Giedroc, D.P. (2017) Biological and chemical adaptation to endogenous hydrogen peroxide production in *Streptococcus pneumoniae* D39. *mSphere* **2**.

Loi, V.V., Busche, T., Tedin, K., Bernhardt, J., Wollenhaupt, J., Huyen, N.T.T., Weise, C., Kalinowski, J., Wahl, M.C., Fulde, M., and Antelmann, H. (2018) Redox-sensing under hypochlorite stress and

infection conditions by the Rrf2-family repressor HypR in *Staphylococcus aureus*. *Antioxid Redox Signal* **29**: 615-636.

Loi, V.V., Huyen, N.T.T., Busche, T., Tung, Q.N., Gruhlke, M.C.H., Kalinowski, J., Bernhardt, J., Slusarenko, A.J., and Antelmann, H. (2019) *Staphylococcus aureus* responds to allicin by global *S*-thioallylation - role of the Brx/BSH/YpdA pathway and the disulfide reductase MerA to overcome allicin stress. *Free Radic Biol Med* **139**: 55-69.

Loi, V.V., Rossius, M., and Antelmann, H. (2015) Redox regulation by reversible protein *S*-thiolation in bacteria. *Front Microbiol* **6**: 187.

Love, M.I., Huber, W., and Anders, S. (2014) Moderated estimation of fold change and dispersion for RNA-seq data with DESeq2. *Genome Biol* **15**: 550.

Lund, P.A., and Brown, N.L. (1989) Regulation of transcription in *Escherichia coli* from the *mer* and *merR* promoters in the transposon Tn501. *J Mol Biol* **205**: 343-353.

Lv, J., He, X., Wang, H., Wang, Z., Kelly, G.T., Wang, X., Chen, Y., Wang, T., and Qian, Z. (2017) TLR4-NOX2 axis regulates the phagocytosis and killing of Mycobacterium tuberculosis by macrophages. *BMC Pulm Med* **17**: 194.

Mandell, G.L., and Hook, E.W. (1969) Leukocyte bactericidal activity in chronic granulomatous disease: correlation of bacterial hydrogen peroxide production and susceptibility to intracellular killing. *J Bacteriol* **100**: 531-532.

Marnett, L.J., Riggins, J.N., and West, J.D. (2003) Endogenous generation of reactive oxidants and electrophiles and their reactions with DNA and protein. *J Clin Invest* **111**: 583-593.

McEwan, A.G., Djoko, K.Y., Chen, N.H., Counago, R.L., Kidd, S.P., Potter, A.J., and Jennings, M.P. (2011) Novel bacterial MerR-like regulators their role in the response to carbonyl and nitrosative stress. *Adv Microb Physiol* **58**: 1-22.

Minhas, V., Paton, J.C., and Trappetti, C. (2021) Sickly sweet - How sugar utilization impacts pneumococcal disease progression. *Trends Microbiol* **29**: 768-771.

Mraheil, M.A., Toque, H.A., La Pietra, L., Hamacher, J., Phanthok, T., Verin, A., Gonzales, J., Su, Y., Fulton, D., Eaton, D.C., Chakraborty, T., and Lucas, R. (2021) Dual role of hydrogen peroxide as an oxidant in pneumococcal pneumonia. *Antioxid Redox Signal* **34**: 962-978.

Nguyen, T.T., Eiamphungporn, W., Mäder, U., Liebeke, M., Lalk, M., Hecker, M., Helmann, J.D., and Antelmann, H. (2009) Genome-wide responses to carbonyl electrophiles in *Bacillus subtilis*: control of the thiol-dependent formaldehyde dehydrogenase AdhA and cysteine proteinase YraA by the MerR-family regulator YraB (AdhR). *Mol Microbiol* **71**: 876-894.

Nüsse, O. (2011) Biochemistry of the Phagosome: The Challenge to Study a Transient Organelle. *TheScientificWorldJOURNAL* **11**: 741046.

O'Donnell, B.V., Tew, D.G., Jones, O.T., and England, P.J. (1993) Studies on the inhibitory mechanism of iodonium compounds with special reference to neutrophil NADPH oxidase. *Biochem J* **290 (Pt 1)**: 41-49.

Okado-Matsumoto, A., and Fridovich, I. (2000) The role of alpha,beta -dicarbonyl compounds in the toxicity of short chain sugars. *J Biol Chem* **275**: 34853-34857.

Paixao, L., Oliveira, J., Verissimo, A., Vinga, S., Lourenco, E.C., Ventura, M.R., Kjos, M., Veening, J.W., Fernandes, V.E., Andrew, P.W., Yesilkaya, H., and Neves, A.R. (2015) Host glycan sugar-specific pathways in *Streptococcus pneumoniae*: galactose as a key sugar in colonisation and infection [corrected]. *PLoS One* **10**: e0121042.

Pericone, C.D., Park, S., Imlay, J.A., and Weiser, J.N. (2003) Factors contributing to hydrogen peroxide resistance in *Streptococcus pneumoniae* include pyruvate oxidase (SpxB) and avoidance of the toxic effects of the fenton reaction. *J Bacteriol* **185**: 6815-6825.

Pitt, J., and Bernheimer, H.P. (1974) Role of peroxide in phagocytic killing of pneumococci. *Infect Immun* **9**: 48-52.

Potter, A.J., Kidd, S.P., McEwan, A.G., and Paton, J.C. (2010) The MerR/NmlR family transcription factor of *Streptococcus pneumoniae* responds to carbonyl stress and modulates hydrogen peroxide production. *J Bacteriol* **192**: 4063-4066.

Said, N., Krupp, F., Anedchenko, E., Santos, K.F., Dybkov, O., Huang, Y.H., Lee, C.T., Loll, B., Behrmann, E., Burger, J., Mielke, T., Loerke, J., Urlaub, H., Spahn, C.M.T., Weber, G., and Wahl, M.C. (2017) Structural basis for lambdaN-dependent processive transcription antitermination. *Nature microbiology* **2**: 17062.

Saleh, M., Bartual, S.G., Abdullah, M.R., Jensch, I., Asmat, T.M., Petruschka, L., Pribyl, T., Gellert, M., Lillig, C.H., Antelmann, H., Hermoso, J.A., and Hammerschmidt, S. (2013) Molecular architecture of *Streptococcus pneumoniae* surface thioredoxin-fold lipoproteins crucial for extracellular oxidative stress resistance and maintenance of virulence. *EMBO Mol Med* **5**: 1852-1870.

Schulz, C., Gierok, P., Petruschka, L., Lalk, M., Mader, U., and Hammerschmidt, S. (2014) Regulation of the arginine deiminase system by ArgR2 interferes with arginine metabolism and fitness of *Streptococcus pneumoniae*. *mBio* **5**.

Shafeeq, S., Yesilkaya, H., Kloosterman, T.G., Narayanan, G., Wandel, M., Andrew, P.W., Kuipers, O.P., and Morrissey, J.A. (2011) The *cop* operon is required for copper homeostasis and contributes to virulence in *Streptococcus pneumoniae*. *Mol Microbiol* **81**: 1255-1270.

Spiteller, G. (2008) Peroxyl radicals are essential reagents in the oxidation steps of the Maillard reaction leading to generation of advanced glycation end products. *Ann N Y Acad Sci* **1126**: 128-133.

Staab, C.A., Hellgren, M., and Hoog, J.O. (2008) Medium- and short-chain dehydrogenase/reductase gene and protein families : Dual functions of alcohol dehydrogenase 3: implications with focus on formaldehyde dehydrogenase and S-nitrosoglutathione reductase activities. *Cell Mol Life Sci* **65**: 3950-3960.

Storkey, C., Davies, M.J., and Pattison, D.I. (2014) Reevaluation of the rate constants for the reaction of hypochlorous acid (HOCl) with cysteine, methionine, and peptide derivatives using a new competition kinetic approach. *Free Radic Biol Med* **73**: 60-66.

Stroeher, U.H., Kidd, S.P., Stafford, S.L., Jennings, M.P., Paton, J.C., and McEwan, A.G. (2007) A pneumococcal MerR-like regulator and S-nitrosoglutathione reductase are required for systemic virulence. *J Infect Dis* **196**: 1820-1826.

Stuehr, D.J., Fasehun, O.A., Kwon, N.S., Gross, S.S., Gonzalez, J.A., Levi, R., and Nathan, C.F. (1991) Inhibition of macrophage and endothelial cell nitric oxide synthase by diphenyleneiodonium and its analogs. *FASEB J* **5**: 98-103.

Supa-Amornkul, S., Chantratita, W., Srichunrusami, C., Janchompoo, P., and Chaturongakul, S. (2016) *Listeria monocytogenes* MerR-Like Regulator NmlRlm: Its Transcriptome and Role in Stress Response. *Foodborne Pathog Dis* **13**: 369-378.

Ulfig, A., and Leichert, L.I. (2021) The effects of neutrophil-generated hypochlorous acid and other hypohalous acids on host and pathogens. *Cell Mol Life Sci* **78**: 385-414.

Van Immerseel, F., De Buck, J., Pasmans, F., Velge, P., Bottreau, E., Fievez, V., Haesebrouck, F., and Ducatelle, R. (2003) Invasion of *Salmonella enteritidis* in avian intestinal epithelial cells in vitro is influenced by short-chain fatty acids. *Int J Food Microbiol* **85**: 237-248.

Wetzstein, M., Volker, U., Dedio, J., Lobau, S., Zuber, U., Schiesswohl, M., Herget, C., Hecker, M., and Schumann, W. (1992) Cloning, sequencing, and molecular analysis of the *dnaK* locus from *Bacillus subtilis*. *J Bacteriol* **174**: 3300-3310.

Winter, J., Ilbert, M., Graf, P.C., Ozcelik, D., and Jakob, U. (2008) Bleach activates a redox-regulated chaperone by oxidative protein unfolding. *Cell* **135**: 691-701.

Winterbourn, C.C., and Kettle, A.J. (2013) Redox reactions and microbial killing in the neutrophil phagosome. *Antioxid Redox Signal* **18**: 642-660.

Winterbourn, C.C., Kettle, A.J., and Hampton, M.B. (2016) Reactive oxygen species and neutrophil function. *Annu Rev Biochem* **85**: 765-792.

Yang, Y., Liu, C., Zhou, W., Shi, W., Chen, M., Zhang, B., Schatz, D.G., Hu, Y., and Liu, B. (2021) Structural visualization of transcription activated by a multidrug-sensing MerR family regulator. *Nat Commun* **12**: 2702.

Yesilkaya, H., Andisi, V.F., Andrew, P.W., and Bijlsma, J.J. (2013) *Streptococcus pneumoniae* and reactive oxygen species: an unusual approach to living with radicals. *Trends Microbiol* **21**: 187-195.

Zhang, Y., Martin, J.E., Edmonds, K.A., Winkler, M.E., and Giedroc, D.P. (2022) SifR is an Rrf2-family quinone sensor associated with catechol iron uptake in *Streptococcus pneumoniae* D39. *J Biol Chem*: 102046.

Zhu, Y., Fan, S., Wang, N., Chen, X., Yang, Y., Lu, Y., Chen, Q., Zheng, J., and Liu, X. (2017) NADPH oxidase 2 inhibitor diphenyleneiodonium enhances ROS-independent bacterial phagocytosis in murine macrophages via activation of the calcium-mediated p38 MAPK signaling pathway. *Am J Transl Res* **9**: 3422-3432.

SUPPLEMENTAL FIGURES

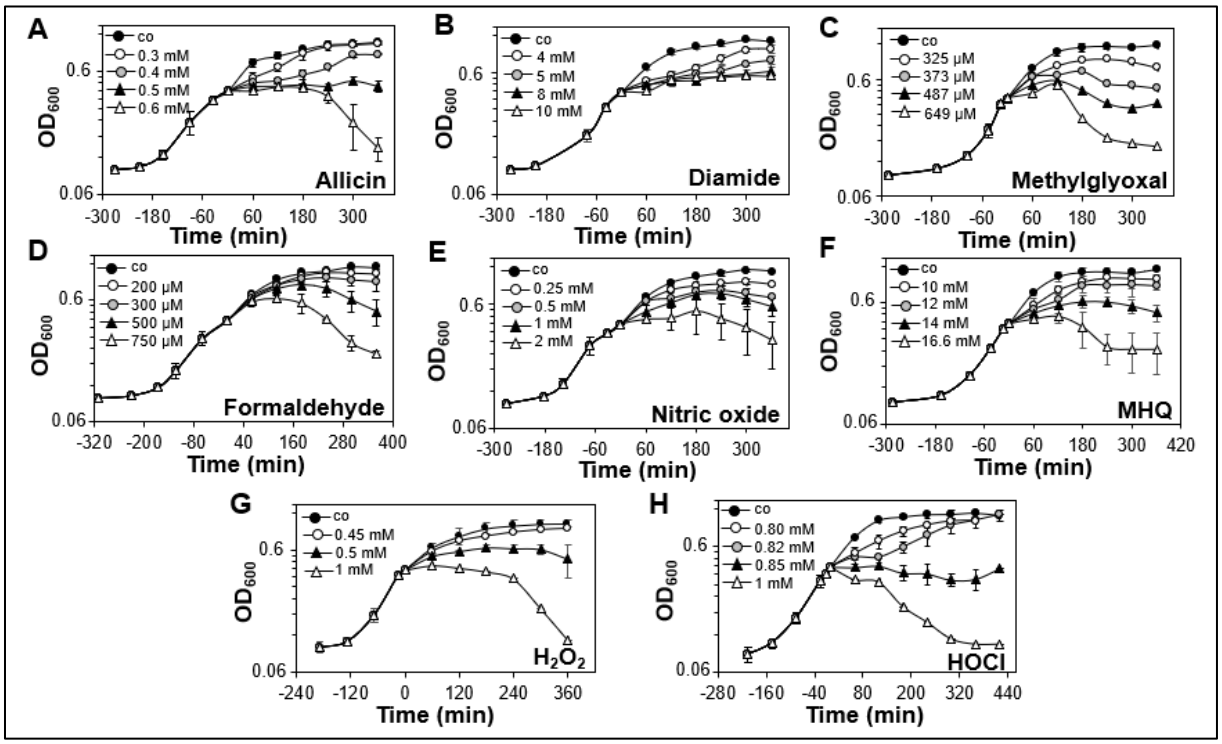

Fig. S1. Growth of *S. pneumoniae* D39 after treatment with thiol-reactive compounds. To monitor the effect of different redox-active compounds on the growth of *S. pneumoniae* D39, the WT was cultivated in RPMI medium until an OD_{600} of 0.4 and subjected to 0.3–0.6 mM allicin, 4–10 mM diamide, 325–649 µM methylglyoxal, 200–750 µM formaldehyde, 0.167–1,33 mM of the NO donor DEA-NONOate, 10–16.6 mM methylhydroquinone (MHQ), 0.45–1 mM H_2O_2 and 0.8–1 mM HOCl. The results are from 1–3 biological replicates, error bars represent the standard deviation.

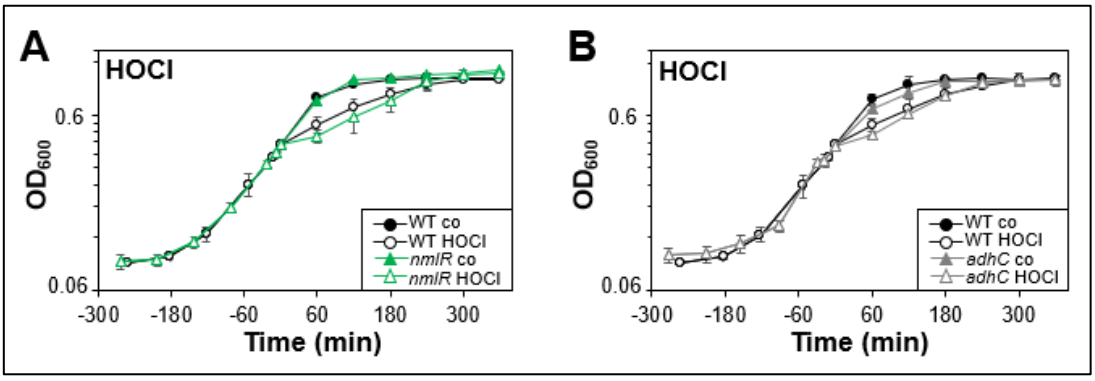

Fig. S2. The phenotype of the Δ*nmlR and* Δ*adhC* mutants can be restored to the WT level in the *nmlR*- and *adhC*-complemented strains. For the growth curves, *S. pneumoniae* D39 WT, the *nmlR*- and *adhC*-complemented strains were grown in RPMI medium. At an OD_{600} of 0.4 the strains were exposed to 800 µM HOCl. The results are from three to four biological replicates. Error bars represent the standard deviation. The statistics was calculated using a Student's unpaired two-tailed *t*-test. $p > 0.05$.

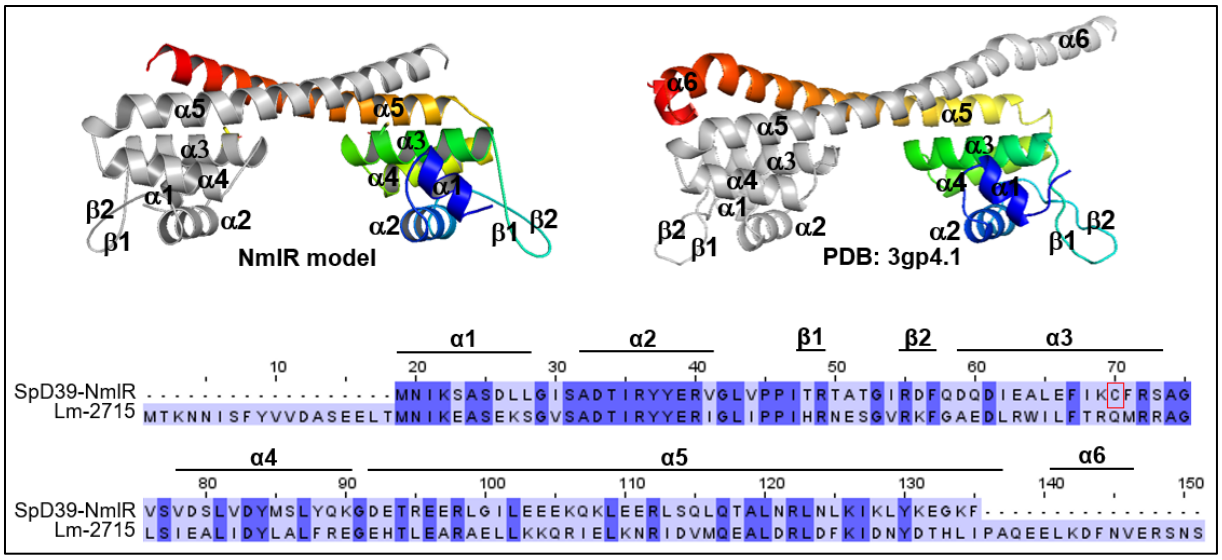

Fig. S3. Structural modeling of NmlR based on the structure of the MerR family transcriptional regulator LMOf2365_2715 of *Listeria monocytogenes.* The structural model of NmlR was generated using SWISS-MODEL (Biasini *et al.*, 2014), and visualized with PyMOL using the template of the structure of *Listeria monocytogenes* LMOf2365_2715 (PDB: 3gp4.1) with 43.59% sequence identity to NmlR. The protein sequence alignment was performed with ClustalΩ2 and is presented in Jalview. The Cys52 of NmlR is labeled in red.

Table S1. DESeq2 differential gene expression analysis of *Streptococcus pneumoniae* D39 wild type after HOCl treatment

						WT HOCl vs control							
Locus	Gene Symbol	Regulon	Further Regulon	Function	Base-Mean	A-value	M-value	Fold-change	Standard error	Wald statistic	P-value	Adjusted P-value
SPD_1746	SPD_1746	CcpA		hypothetical protein	3415.28	11.74	5.92	60.55	0.21	27.83684507	1.5543E-170	1.4852E-167
SPD_0484	SPD_0484			hypothetical protein	417.88	8.71	5.64	49.87	0.27	20.97450464	1.12128E-97	1.07138E-95
SPD_0425	SPD_0425	XylR	CcpA	hypothetical protein	1362.47	10.41	5.52	45.89	0.26	21.29847732	1.1727E-100	1.40066E-98
SPD_0424	SPD_0424	XylR	CcpA	PTS system, cellobiose-specific IIC component	662.16	9.37	5.50	45.25	0.25	21.59761476	1.8913E-103	2.4095E-101
SPD_0572	etrx1			thioredoxin family protein	6321.53	12.63	5.41	42.52	0.22	24.48002239	2.4113E-132	7.68E-130
SPD_1568	queF			GTP cyclohydrolase, putative	1485.15	10.54	5.22	37.27	0.21	24.96881031	1.3343E-137	5.0996E-135
SPD_1637	nmlR	NmlR	SczA	transcriptional MerR/NmlR regulator	2174.97	11.09	5.17	36.00	0.22	23.83889835	1.3201E-125	3.604E-123
SPD_1748	pneA2			Class II two-component lantibiotic peptide PneA2	2246.91	11.13	5.15	35.51	0.23	21.91297585	1.9539E-106	2.6671E-104
SPD_0426	lacF-1	XylR	CcpA	PTS system, lactose-specific IIA component	446.06	8.80	5.15	35.51	0.24	21.27389703	1.9812E-100	2.22708E-98
SPD_0573	msrAB2			peptide methionine sulfoxide reductase msrA/msrB 2	5155.11	12.33	5.11	34.54	0.22	23.75019579	1.0936E-124	2.6124E-122
SPD_0571	ccdA-1			cytochrome c-type biogenesis protein CcdA	4769.85	12.22	5.06	33.36	0.26	19.17577394	5.89842E-82	4.50875E-80
SPD_0072	catE	SlfR	RpoD	carechol-2,3-dioxygenase	1986.80	10.96	4.87	29.24	0.21	23.25156272	1.3717E-119	2.6213E-117
SPD_0427	lacG-1	XylR	CcpA	6-phospho-beta-galactosidase	969.32	9.92	4.85	28.84	0.18	27.02696297	7.1267E-161	3.4048E-158
SPD_0308	clpL	CtsR		ATP-dependent Clp protease, ATP-binding subunit	90861.08	16.47	4.84	28.64	0.22	22.09477048	3.5487E-108	5.6513E-106
SPD_1747	pneA1			Class II two-component lantibiotic peptide PneA1	8320.67	13.02	4.80	27.86	0.23	20.88991933	6.6131E-97	6.01792E-95
SPD_1636	adhC	NmlR	SczA	alcohol dehydrogenase, zinc-containing	5520.11	12.43	4.73	26.54	0.16	29.49776944	3.075E-191	5.8763E-188
SPD_1409	msmK	CcpA	RpoD	sugar ABC transporter, ATP-binding protein	18559.88	14.18	4.69	25.81	0.17	27.3670663	6.7661E-165	4.31E-162
SPD_0428	lacE-1	XylR	CcpA	PTS system, lactose-specific IIBC components	1113.22	10.12	4.67	25.46	0.22	21.15560447	2.4503E-99	2.60139E-97
SPD_1634	galK	GalR	CcpA	galactokinase	1415.82	10.47	4.59	24.08	0.21	21.95272271	8.1567E-107	1.199E-104
SPD_0080	pavB			cell wall surface anchor family protein	8674.17	13.08	4.54	23.26	0.60	7.59651323	3.04216E-14	1.83393E-13
SPD_0485	SPD_0485			hypothetical protein	124.02	6.95	4.53	23.10	0.36	12.51703458	6.02441E-36	1.25138E-34
SPD_1582	sacA	ScrR	RpoD	sucrose-6-phosphate hydrolase, putative	1854.71	10.86	4.46	22.01	0.34	12.97834974	1.62341E-38	3.97735E-37
SPD_0486	SPD_0486			hypothetical protein	48.16	5.59	4.43	21.56	0.45	9.899443245	4.18599E-23	4.67803E-22
SPD_1583	SPD_1583	ScrR	RpoD	ABC transporter, permease protein	499.13	8.96	4.37	20.68	0.34	12.7069229	5.41225E-37	1.20265E-35
SPD_1633	galT-2	GalR	RitR, CcpA	galactose-1-phosphate uridyltransferase	1137.32	10.15	4.28	19.43	0.20	21.09623879	8.612E-99	8.66187E-97
SPD_1749	lanM			Lanthionine biosynthesis protein LanM	2837.35	11.47	4.20	18.38	0.18	23.34210239	1.6578E-120	3.52E-118
SPD_1638	czcD	SczA		cation efflux system protein	256.49	8.00	4.12	17.39	0.28	14.85182858	6.76966E-50	2.75252E-48
SPD_0363	mtlD			mannitol-1-phosphate 5-dehydrogenase	20.92	4.39	4.09	17.03	0.59	6.898659632	5.24955E-12	2.59222E-11
SPD_0662	SPD_0662			endonuclease/exonuclease/phosphatase family protein	705.24	9.46	4.07	16.80	0.18	23.04674259	1.5858E-117	2.755E-115
SPD_0297	SPD_0297	CcpA		PTS system, IID component	167.97	7.39	3.99	15.89	0.30	13.47207226	2.28366E-41	6.51353E-40
SPD_0290	kdgK	RegR	CcpA, RpoD	carbohydrate kinase, PfkB family protein	400.18	8.64	3.97	15.67	0.21	19.05916934	5.51433E-81	4.05303E-79
SPD_1750	wrbA			multimeric flavodoxin WrbA (general function prediction only)	715.67	9.48	3.86	14.52	0.24	15.80410116	2.91518E-56	1.39273E-54
SPD_0294	ugl			glucuronyl hydrolase	92.36	6.53	3.78	13.74	0.35	10.80345523	3.31489E-27	4.62392E-26
SPD_1584	SPD_1584	ScrR	RpoD	ABC transporter, permease protein	588.87	9.20	3.70	13.00	0.63	5.831127109	5.50542E-09	2.09579E-08
SPD_0296	SPD_0296	RitR	CcpA	PTS system, IIC component	86.13	6.43	3.66	12.64	0.34	10.89382366	1.2335E-27	1.78577E-26
SPD_1752	clyB	CcpA		toxin secretion ABC transporter, ATP-binding/permease protei	935.74	9.87	3.65	12.55	0.22	16.3656776	3.36264E-60	1.836E-58
SPD_0289	eda	RegR	CcpA, RpoD	4-hydroxy-2-oxoglutarate aldolase/2-deydro-3-deoxyphosphogl	389.58	8.61	3.61	12.21	0.20	17.80298906	6.69957E-71	4.41479E-69
SPD_0291	SPD_0291	RegR	CcpA, RpoD	ribose 5-phosphate isomerase, putative	298.28	8.22	3.59	12.04	0.21	17.48449001	1.88088E-68	1.12324E-66
SPD_1532	scrA	ScrR	CcpA, RpoD	PTS system IIABC components	819.16	9.68	3.46	11.00	0.22	15.79351802	3.44802E-56	1.60711E-54
SPD_0295	SPD_0295			PTS system, IIB component	65.74	6.04	3.45	10.93	0.33	10.45926133	1.32888E-25	1.68178E-24
SPD_1751	SPD_1751			membrane protein, putative	152.98	7.26	3.34	10.13	0.35	9.482760043	2.47644E-21	2.42692E-20
SPD_1983	SPD_1983			hypothetical protein	10.51	3.39	3.34	10.13	0.74	4.53717178	5.70137E-06	1.51745E-05
SPD_0164	SPD_0164			hypothetical protein	50.29	5.65	3.32	9.99	0.37	9.006286671	2.13152E-19	1.8858E-18
SPD_0292	gno	RegR	CcpA, RpoD	oxidoreductase, short chain dehydrogenase/reductase family p	258.78	8.02	3.29	9.78	0.23	14.49118444	1.37747E-47	5.16146E-46
SPD_0293	SPD_0293			PTS system, IIA component	28.97	4.86	3.21	9.25	0.55	5.78201387	7.38116E-09	2.77665E-08
SPD_1501	yejO			ABC transporter, permease protein	30.05	4.91	3.19	9.13	0.48	6.621931546	3.54535E-11	1.65248E-10
SPD_0298	yajC-1			preprotein translocase, YajC subunit	26.14	4.71	3.18	9.06	0.53	5.977286623	2.26885E-09	8.99537E-09
SPD_1114	SPD_1114			hypothetical protein	3.03	1.60	3.13	8.75	0.90	3.476039697	0.000508877	0.001058909
SPD_1585	ABC-SBP	RitR	ScrR, RpoD	ABC transporter, sugar-binding protein	2015.96	10.98	3.12	8.69	0.17	17.84318886	3.26519E-71	2.22849E-69
SPD_1753	nisP			serine protease, subtilase family protein	1249.22	10.29	3.02	8.11	0.25	11.88770094	1.37129E-32	2.51975E-31
SPD_0362	mtlA2			PTS system, mannitol-specific enzyme IIA	8.50	3.09	3.02	8.11	0.70	4.311525463	1.62132E-05	4.10921E-05
SPD_0313	SPD_0313			hypothetical protein	348.05	8.44	3.01	8.06	0.25	11.89267083	1.29208E-32	2.39724E-31
SPD_1847	ulaA	UlaR		PTS system, membrane component, putative	95.11	6.57	3.01	8.06	0.31	9.722093797	2.42738E-22	2.57707E-21
SPD_0936	SPD_0936			Tn5252-family relaxase	16.33	4.03	2.99	7.94	0.57	5.223758932	1.75327E-07	5.72735E-07
SPD_1050	lacD	GalR	CcpA, LacR	tagatose 1,6-diphosphate aldolase	2453.66	11.26	2.89	7.41	0.20	14.54298137	6.47117E-48	2.52376E-46
SPD_0071	galM	AgaR	CcpA, RpoD	aldose 1-epimerase	242.34	7.92	2.89	7.41	0.20	14.47149879	1.83431E-47	6.6139E-46
SPD_1845	ulaC	UlaR		PTS system, IIA component	30.69	4.94	2.89	7.41	0.48	5.976136979	2.28491E-09	9.04029E-09
SPD_1830	bguA	BguR		glycosyl hydrolase, family protein 1	4823.43	12.24	2.86	7.26	0.18	15.75377501	6.47009E-56	2.94389E-54
SPD_0088	SPD_0088	CcpA		ABC transporter, permease protein	52.95	5.73	2.86	7.26	0.34	8.437138112	3.25202E-17	2.42758E-16
SPD_0635	copA	CopY	RpoD	copper-transporting ATPase, E1-E2 family protein	11616.68	13.50	2.84	7.16	0.19	14.86823388	5.29929E-50	2.20151E-48
SPD_1375	yhdA	SlfR		NADPH-dependent FMN reductase, putative	14271.29	13.80	2.82	7.06	0.18	15.96872337	2.11062E-57	1.06142E-55
SPD_1833	bguC	BguR		PTS system, IIA component	2223.67	11.12	2.80	6.96	0.25	11.07592963	1.64167E-28	2.50979E-27
SPD_0070	agaS	AgaR	CcpA, RpoD	sugar isomerase domain protein AgaS	279.18	8.13	2.80	6.96	0.26	10.81342826	2.97346E-27	4.17815E-26
SPD_2038	SPD_2038			hypothetical protein	65.46	6.03	2.78	6.87	0.34	8.229318809	1.88281E-16	1.33261E-15
SPD_1846	ulaB	UlaR		PTS system, IIB component	47.29	5.56	2.78	6.87	0.36	7.69471109	1.41814E-14	8.77045E-14
SPD_1844	ulaD	UlaR		hexulose-6-phosphate synthase, putative	41.50	5.37	2.78	6.87	0.46	5.978208862	2.25604E-09	8.9632E-09
SPD_0934	SPD_0934			Tn5252- family protein	18.13	4.18	2.77	6.82	0.57	4.873443278	1.0967E-06	3.23924E-06
SPD_1051	lacC	LacR	CcpA, RpoD	tagatose-6-phosphate kinase	3540.77	11.79	2.74	6.68	0.19	14.31550092	1.75098E-46	5.97522E-45
SPD_0413	SPD_0413			hypothetical protein	2.63	1.40	2.73	6.63	0.92	2.983589772	0.002848884	0.00540101
SPD_1832	bguB	BguR		PTS system, IIB component	2634.35	11.36	2.72	6.59	0.19	13.93374049	3.95109E-44	1.27975E-42
SPD_1408	SPD_1408	CodY		hypothetical protein	4236.51	12.05	2.72	6.59	0.28	9.789435239	1.24992E-22	1.35716E-21
SPD_0158	SPD_0158	CcpA	RpoD	DNA-binding response regulator	6397.01	12.64	2.69	6.45	0.13	19.97991739	8.236E-89	7.15409E-87
SPD_0460	dnaK	HrcA	VraR, CcpA	chaperone protein DnaK	91101.19	16.48	2.69	6.45	0.22	12.15364316	5.48651E-34	1.04847E-32
SPD_0311	dexB	MalR	CcpA	glucan 1,6-alpha-glucosidase	10953.31	13.42	2.68	6.41	0.19	13.83255531	1.62156E-43	4.99807E-42
SPD_0152	dapE			peptidase, M20/M25/M40 family protein	6138.56	12.58	2.67	6.36	0.20	13.24759924	4.65869E-40	1.21956E-38
SPD_0634	cupA	CopY	RpoD	hypothetical protein	2972.32	11.54	2.65	6.28	0.17	15.85633966	1.27088E-56	6.22733E-55
SPD_1977	arcC	CcpA		carbamate kinase	3131.94	11.61	2.64	6.23	0.15	17.76969992	1.21338E-70	7.72924E-69
SPD_1978	arcD	ArgR	CcpA	membrane protein, putative	4048.05	11.98	2.63	6.19	0.14	18.78380091	1.02475E-78	7.25295E-77
SPD_1979	SPD_1979	ArgR	CcpA	peptidase, M20/M25/M40 family protein	4399.70	12.10	2.63	6.19	0.15	17.70025488	4.17414E-70	2.57315E-68
SPD_1709	groL	HrcA	CtsR	chaperonin GroEL	89485.75	16.45	2.63	6.19	0.19	13.60592858	3.69249E-42	1.08559E-40
SPD_0069	gadF	AgaR	CcpA, RpoD	PTS system, IIA component	153.31	7.26	2.63	6.19	0.29	8.998569462	2.28678E-19	2.01384E-18
SPD_0068	gadE	AgaR	CcpA, RpoD	PTS system, IID component	277.16	8.11	2.62	6.15	0.28	9.297674757	1.43551E-20	1.35136E-19
SPD_1988	fucY	FcsR		hypothetical protein	139.66	7.13	2.60	6.06	0.26	10.02552915	1.17727E-23	1.38023E-22
SPD_0090	SPD_0090	CcpA		ABC transporter, substrate-binding protein	67.88	6.08	2.56	5.90	0.30	8.428269888	3.50813E-17	2.59847E-16
SPD_0661	ptsG	MalR	CcpA	PTS system, IIABC components	5106.38	12.32	2.54	5.82	0.17	14.51882678	9.20726E-48	3.51902E-46
SPD_1831	bguD	BguR		PTS system, IIC component	7748.39	12.92	2.53	5.78	0.24	10.62673594	2.23809E-26	3.03332E-25
SPD_1377	mga1			hypothetical protein	391.41	8.61	2.53	5.78	0.30	8.528909823	1.47733E-17	1.13381E-16
SPD_1499	nanB			sialidase B precursor	81.20	6.34	2.53	5.78	0.34	7.437596832	1.02533E-13	5.90185E-13
SPD_0459	grpE	HrcA	VraR, CodY	heat shock protein GrpE	10913.23	13.41	2.52	5.74	0.20	12.87636583	6.11477E-38	1.47916E-36
SPD_0067	gadW	AgaR	CcpA, RpoD	PTS system, IIC component	200.86	7.65	2.50	5.66	0.30	8.353140931	6.64713E-17	4.82991E-16
SPD_0089	SPD_0089	CcpA		ABC transporter, permease protein	67.50	6.08	2.50	5.66	0.35	7.11349094	1.13144E-12	5.95642E-12
SPD_0630	thiM			hydroxyethylthiazole kinase, putative	824.90	9.69	2.49	5.62	0.15	16.11340626	2.05391E-58	1.09029E-56
SPD_1500	SPD_1500			ABC transporter, permease protein	21.65	4.44	2.48	5.58	0.49	5.107472599	3.26496E-07	1.05897E-06
SPD_2010	SPD_2010	CcpA		hypothetical protein	11.23	3.49	2.48	5.58	0.63	3.914234518	9.06915E-05	0.000211098
SPD_1052	lacB	LacR	CcpA, RpoD	galactose-6-phosphate isomerase, LacB subunit	1626.38	10.67	2.47	5.54	0.15	16.01018676	1.08484E-57	5.60304E-56
SPD_1533	SPD_1533	ScrR		hypothetical protein	9.85	3.30	2.43	5.39	0.66	3.700082858	0.000215529	0.000475059
SPD_1642	proWX	RpoD		choline transporter (glycine betaine transport system permease	33189.87	15.02	2.40	5.28	0.24	9.871729214	5.52046E-23	6.13349E-22
SPD_0614	SPD_0614			ABC transporter, ATP-binding protein	1601.77	10.65	2.40	5.28	0.26	9.238556822	2.49844E-20	2.28446E-19
SPD_0935	SPD_0935			Tn5252-family protein	11.82	3.56	2.40	5.28	0.64	3.740019037	0.000184006	0.000408404
SPD_1498	SPD_1498			putative oxidoreductase	53.04	5.73	2.39	5.24	0.33	7.166465309	7.69589E-13	4.13114E-12
SPD_0575	tcs09hk			sensor histidine kinase, putative	8456.09	13.05	2.38	5.21	0.24	10.00107865	1.50746E-23	1.74591E-22
SPD_1011	glxK	CodY	CcpA	glycerate kinase	107.87	6.75	2.38	5.21	0.29	8.187173389	2.67433E-16	1.8652E-15
SPD_0631	thiE			thiamine-phosphate pyrophosphorylase	617.19	9.27	2.37	5.17	0.17	13.88533538	7.7519E-44	2.4285E-42
SPD_0361	mtlR			transcriptional regulator, putative	39.32	5.30	2.37	5.17	0.37	6.427862535	1.29411E-10	5.67211E-10
SPD_1934	malX	MalR	RpoD, CcpA	maltose/maltodextrin ABC transporter, maltose/maltodextrin-bi	9938.52	13.28	2.36	5.13	0.14	17.23286904	1.50498E-66	8.7152E-65
SPD_0629	thiW			thiW protein	706.37	9.46	2.36	5.13	0.18	12.80095497	1.61947E-37	3.82076E-36
SPD_0628	tenA			transcriptional activator TenA, TENA/THI-4 family protein	634.55	9.31	2.36	5.13	0.20	11.69565002	1.34156E-31	2.26878E-30
SPD_0613	SPD_0613			membrane protein, putative	1841.03	10.85	2.34	5.06	0.25	9.362610583	7.77904E-21	7.47023E-20
SPD_0066	gadV	AgaR	CcpA, RpoD	PTS system, IIB component	93.27	6.54	2.34	5.06	0.30	7.894957498	2.90414E-15	1.89413E-14
SPD_1932	malP	MalR	CiaR, CcpA	maltodextrin phosphorylase	11394.37	13.48	2.32	4.99	0.20	11.33156125	9.1558E-30	1.48277E-28
SPD_1045	SPD_1045			hypothetical protein	46.26	5.53	2.32	4.99	0.42	5.490164483	4.0156E-08	1.40804E-07
SPD_0574	tcs09rr			DNA-binding response regulator	4591.32	12.16	2.31	4.96	0.22	10.58007259	3.68672E-26	4.92681E-25
SPD_1994	fucA	FcsR		L-fuculose phosphate aldolase	79.15	6.31	2.31	4.96	0.35	6.680623919	2.37927E-11	1.1199E-10
SPD_1174	SPD_1174			hypothetical protein	8.96	3.16	2.31	4.96	0.69	3.353741246	0.000797269	0.00162602
SPD_0627	ykoC			membrane protein, putative	400.00	8.64	2.26	4.79	0.19	12.06123507	1.69226E-33	3.1705E-32
SPD_0626	ykoD			ABC transporter, ATP-binding protein	1402.82	10.45	2.25	4.76	0.13	17.17853523	3.84498E-66	2.1611E-64
SPD_1936	malD	MalR	RpoD	maltodextrin ABC transporter, permease protein	1184.58	10.21	2.25	4.76	0.16	14.40303115	4.9523E-47	1.7207E-45
SPD_0938	SPD_0938			hypothetical protein	10.47	3.39	2.25	4.76	0.63	3.552657496	0.000381361	0.000817935
SPD_1567	trxA			thioredoxin	74692.24	16.19	2.23	4.69	0.34	6.666057545	2.62766E-11	1.23075E-10
SPD_0461	dnaJ	HrcA	VraR	chaperone protein DnaJ	22712.82	14.47	2.22	4.66	0.23	9.569603682	1.07316E-21	1.07938E-20
SPD_1801	SPD_1801			ABC transporter, ATP-binding protein	1471.30	10.52	2.21	4.63	0.20	10.82999075	2.4818E-27	3.51313E-26
SPD_1053	lacA	GalR	LacR	galactose-6-phosphate isomerase, LacA subunit	2323.24	11.18	2.18	4.53	0.18	12.36047015	4.27648E-35	8.33914E-34
SPD_1989	SPD_1989	FcsR		PTS system, IID component	177.05	7.47	2.16	4.47	0.25	8.660094102	4.71375E-18	3.81694E-17
SPD_0360	mtlA			PTS system, mannitol-specific IIBC components	46.68	5.54	2.15	4.44	0.34	6.30735703	2.83841E-10	1.21892E-09
SPD_0612	SPD_0612			lipoprotein, putative	994.44	9.96	2.14	4.41	0.31	6.868586481	6.48412E-12	3.17722E-11
SPD_1843	ulaE	UlaR		hexulose-6-phosphate isomerase, putative	61.86	5.95	2.12	4.35	0.34	6.253850876	4.00453E-10	1.68561E-09
SPD_0154	metP			ABC transporter, permease protein, putative	3381.18	11.72	2.11	4.32	0.17	12.65184881	1.09273E-36	2.40023E-35
SPD_1935	malC	MalR	RpoD	maltodextrin ABC transporter, permease protein	2606.33	11.35	2.10	4.29	0.15	14.10921135	3.33284E-45	1.09811E-43
SPD_0562	bgaA	CcpA	RpoD	beta-galactosidase precursor, putative	11935.36	13.54	2.09	4.26	0.16	13.29092854	2.61315E-40	7.1339E-39
SPD_1795	ansB			hypothetical protein	24.49	4.61	2.08	4.23	0.45	4.636920516	3.53638E-06	9.64055E-06
SPD_0561	gatC	CcpA		PTS system, IIC component, putative	1560.22	10.61	2.07	4.20	0.14	14.63927168	1.57749E-48	6.28038E-47
SPD_0073	SPD_0073			hypothetical protein	564.32	9.14	2.07	4.20	0.20	10.61356536	2.57723E-26	3.46837E-25
SPD_1632	paaI			hypothetical protein	428.46	8.74	2.07	4.20	0.20	10.07551193	7.08907E-24	8.41441E-23
SPD_1987	fucL	FcsR		fucolectin-related protein	159.44	7.32	2.07	4.20	0.24	8.76696858	1.83541E-18	1.53165E-17
SPD_2012	glpO	CcpA		alpha-glycerophosphate oxidase	141.78	7.15	2.07	4.20	0.24	8.763195337	1.89792E-18	1.57693E-17
SPD_0157	SPD_0157	CcpA	RpoD	sensor histidine kinase, putative	5957.28	12.54	2.05	4.14	0.18	11.67716022	1.66774E-31	2.79567E-30
SPD_0633	copY	CopY	RpoD	transcriptional copper regulator	1612.13	10.65	2.04	4.11	0.13	15.46440378	6.03293E-54	2.68114E-52
SPD_0153	metN			ABC transporter, ATP-binding protein	7465.40	12.87	2.04	4.11	0.20	10.40955599	2.24265E-25	2.80112E-24
SPD_1990	SPD_1990	FcsR		PTS system, IIC component	66.71	6.06	2.04	4.11	0.29	7.082789989	1.41281E-12	7.39692E-12
SPD_0458	hrcA	HrcA	VraR	heat-inducible transcription repressor HrcA	27616.33	14.75	2.03	4.08	0.20	9.970607971	2.0497E-23	2.3455E-22

Table S1 continued

					WT HOCl vs control							
Locus	Gene Symbol	Regulon	Further Regulon	Function	Base-Mean	A-value	M-value	Fold-change	Standard error	Wald statistic	P-value	Adjusted P-value
SPD_0625	ykoE			membrane protein, putative	302.43	8.24	2.02	4.06	0.19	10.84807279	2.03674E-27	2.90464E-26
SPD_1976	argF	CcpA		ornithine carbamoyltransferase	8631.86	13.08	1.98	3.94	0.16	12.57645709	2.84506E-36	6.04101E-35
SPD_0611	SPD_0611			membrane protein, putative	841.06	9.72	1.97	3.92	0.25	7.954917155	1.79251E-15	1.18529E-14
SPD_1502	SPD_1502	CcpA		ABC transporter, substrate-binding protein	54.48	5.77	1.95	3.86	0.39	5.04273732	4.58919E-07	1.433E-06
SPD_1643	proV	RpoD		choline transporter	12143.46	13.57	1.92	3.78	0.23	8.317129938	9.01189E-17	6.49877E-16
SPD_1287	trxB			thioredoxin-disulfide reductase	10517.58	13.36	1.91	3.76	0.18	10.51628075	7.26864E-26	9.38539E-25
SPD_1993	fucU	FcsR		RbsD/FucU transport protein family protein	65.59	6.04	1.88	3.68	0.32	5.934468226	2.94799E-09	1.14738E-08
SPD_0300	SPD_0300			oligohyaluronate lyase	93.36	6.54	1.86	3.63	0.25	7.388504011	1.4849E-13	8.32153E-13
SPD_1770	SPD_1770			hypothetical protein	32.44	5.02	1.86	3.63	0.39	4.79833632	1.59989E-06	4.57693E-06
SPD_0151	metQ	CmhR		lipoprotein	7237.37	12.82	1.85	3.61	0.14	13.41759825	4.7692E-41	1.34029E-39
SPD_1906	SPD_1906			IS1381, transposase OrfB	15.58	3.96	1.82	3.53	0.63	2.900930242	0.003720567	0.006943363
SPD_0156	SPD_0156	CcpA		membrane protein, putative	1260.04	10.30	1.81	3.51	0.21	8.598230346	8.09547E-18	6.36644E-17
SPD_1842	araD	UlaR		L-ribulose-5-phosphate 4-epimerase	73.02	6.19	1.81	3.51	0.29	6.198718809	5.69246E-10	2.35461E-09
SPD_1566	SPD_1566			hypothetical protein	57957.97	15.82	1.80	3.48	0.57	3.168513536	0.001532206	0.003015495
SPD_2013	glpK	CcpA		glycerol kinase	150.21	7.23	1.79	3.46	0.24	7.496567937	6.55105E-14	3.85202E-13
SPD_1054	SPD_1054			hypothetical protein	49.07	5.62	1.79	3.46	0.32	5.628989302	1.81269E-08	6.54829E-08
SPD_1800	SPD_1800	RitR	RpoD	membrane protein, putative	852.80	9.74	1.78	3.43	0.18	9.918900272	3.44531E-23	3.87294E-22
SPD_1710	groES	HrcA	CtsR	chaperonin, 10 kDa	11653.01	13.51	1.75	3.36	0.21	8.153621842	3.53184E-16	2.43659E-15
SPD_1057	SPD_1057			PTS system, IIB component, putative	44.78	5.48	1.74	3.34	0.35	4.987985822	6.1012E-07	1.88055E-06
SPD_1802	SPD_1802			hypothetical protein	483.51	8.92	1.71	3.27	0.24	7.13274227	9.83887E-13	5.23735E-12
SPD_1991	SPD_1991	FcsR		PTS system, IIB component	92.15	6.53	1.71	3.27	0.28	6.040514139	1.53624E-09	6.16755E-09
SPD_0211	rpmD			ribosomal protein L30	20326.12	14.31	1.69	3.23	0.15	11.15130161	7.05665E-29	1.09636E-27
SPD_1841	ulaR	UlaR		transcriptional regulator, BglG family protein	54.52	5.77	1.69	3.23	0.34	5.044172719	4.55488E-07	1.42461E-06
SPD_1449	SPD_1449			hypothetical protein	5446.56	12.41	1.68	3.20	0.14	11.76061988	6.22754E-32	1.09182E-30
SPD_1840	ulaG	UlaR	RitR	hypothetical protein	28.31	4.82	1.65	3.14	0.41	4.06270284	4.85078E-05	0.000116602
SPD_0773	fruA			PTS system, fructose specific IIABC components	1753.55	10.78	1.63	3.10	0.16	9.998896789	1.54104E-23	1.77406E-22
SPD_0210	rpsE			ribosomal protein S5	57900.05	15.82	1.61	3.05	0.24	6.750948203	1.46882E-11	7.01729E-11
SPD_1992	SPD_1992	FcsR	CcpA	PTS system, IIA component	50.48	5.66	1.60	3.03	0.33	4.903751335	9.40235E-07	2.80748E-06
SPD_0187	nrdD	NrdR	ScrA, RpoD	anaerobic ribonucleoside-triphosphate reductase	26423.00	14.69	1.59	3.01	0.13	12.38614575	3.10617E-35	6.2483E-34
SPD_1448	sifR			Rrf2 family protein	5746.09	12.49	1.59	3.01	0.16	9.732581565	2.18964E-22	2.35079E-21
SPD_1268	SPD_1268			hypothetical protein	188.16	7.56	1.59	3.01	0.28	5.701674752	1.18636E-08	4.38517E-08
SPD_0560	gatB	RitR	CcpA, RpoD	PTS system, IIB component, putative	995.80	9.96	1.58	2.99	0.22	7.114548024	1.1228E-12	5.9437E-12
SPD_2011	glpF	CcpA		glycerol uptake facilitator protein	43.12	5.43	1.58	2.99	0.39	4.035598695	5.44632E-05	0.000129613
SPD_1803	SPD_1803			hypothetical protein	462.41	8.85	1.57	2.97	0.25	6.215152222	5.12749E-10	2.12552E-09
SPD_0202	rpsQ			ribosomal protein S17	21899.15	14.42	1.56	2.95	0.12	12.60973827	1.86612E-36	4.00691E-35
SPD_0442	pyrG			CTP synthase	9476.60	13.21	1.56	2.95	0.14	11.45563248	2.20349E-30	3.59903E-29
SPD_1933	malM	MalR	CiaR, CcpA, RpoD	4-alpha-glucanotransferase	10543.12	13.36	1.55	2.93	0.26	5.981045261	2.2171E-09	8.84527E-09
SPD_0205	rplE			ribosomal protein L5	32933.24	15.01	1.54	2.91	0.13	11.86815581	1.73245E-32	3.15305E-31
SPD_0212	rplO			ribosomal protein L15	18661.98	14.19	1.53	2.89	0.12	13.25988869	3.95482E-40	1.06446E-38
SPD_0204	rplX			ribosomal protein L24	46797.46	15.51	1.51	2.85	0.14	10.7258297	7.6993E-27	1.05851E-25
SPD_0483	rbfA	CiaR		ribosome-binding factor A	4455.04	12.12	1.49	2.81	0.12	12.37567528	3.53905E-35	6.9723E-34
SPD_0149	azlC			hypothetical protein	4900.96	12.26	1.49	2.81	0.16	9.308366304	1.29814E-20	1.22809E-19
SPD_0208	rplF			ribosomal protein L6	34381.83	15.07	1.48	2.79	0.13	11.5305328	9.2569E-31	1.525E-29
SPD_0213	secY			preprotein translocase, SecY subunit	51100.63	15.64	1.48	2.79	0.13	11.33006301	9.31377E-30	1.49568E-28
SPD_0482	infB	CiaR		initiation factor IF-2	48639.28	15.57	1.48	2.79	0.15	9.817051159	9.50843E-23	1.03832E-21
SPD_0925	SPD_0925			hydrolase, putative	645.46	9.33	1.48	2.79	0.17	8.623223208	6.01187E-18	4.82718E-17
SPD_1673	gtfA	RafR	CcpA	sucrose phosphorylase	287.02	8.17	1.48	2.79	0.19	7.589230675	3.2181E-14	1.92784E-13
SPD_1756	SPD_1756			hypothetical protein	85.56	6.42	1.48	2.79	0.35	4.258056726	2.06212E-05	5.19197E-05
SPD_0715	SPD_0715			MutT/nudix family protein	35.69	5.16	1.48	2.79	0.40	3.678040472	0.000235033	0.000515669
SPD_0199	rpsC			ribosomal protein S3	36331.74	15.15	1.47	2.77	0.15	9.866040399	5.84256E-23	6.41674E-22
SPD_0932	SPD_0932			hypothetical protein	532.95	9.06	1.46	2.75	0.27	5.420706388	5.9364E-08	2.05144E-07
SPD_1579	SPD_1579			hypothetical protein	27.74	4.79	1.46	2.75	0.41	3.557667847	0.000374162	0.000803397
SPD_1043	nrdF	NrdR	RpoD	ribonucleoside-diphosphate reductase, beta subunit	15196.94	13.89	1.45	2.73	0.17	8.495868975	1.96458E-17	1.50172E-16
SPD_1180	SPD_1180			CAAX amino terminal protease family protein	48.12	5.59	1.44	2.71	0.41	3.509584262	0.000448808	0.000945614
SPD_0209	rplR			ribosomal protein L18	15501.85	13.92	1.43	2.69	0.15	9.574534422	1.02317E-21	1.03454E-20
SPD_2009	SPD_2009	CcpA		hypothetical protein	430.58	8.75	1.43	2.69	0.18	7.934744	2.1093E-15	1.38996E-14
SPD_0092	SPD_0092	CcpA		hypothetical protein	511.92	9.00	1.43	2.69	0.18	7.821491097	5.22013E-15	3.32522E-14
SPD_0188	SPD_0188	NrdR	RpoD	hypothetical protein	2365.72	11.21	1.42	2.68	0.17	8.24594466	1.6386E-16	1.16408E-15
SPD_2033	yfiA	ComX	CcpA	ribosomal subunit interface protein	7517.14	12.88	1.42	2.68	0.22	6.333350622	2.39894E-10	1.03954E-09
SPD_1644	SPD_1644	RpoD		hypothetical protein	16702.25	14.03	1.41	2.66	0.24	5.911024992	3.39985E-09	1.31255E-08
SPD_1676	rafF	RafR	CcpA	sugar ABC transporter, permease protein	98.95	6.63	1.41	2.66	0.26	5.488406946	4.05575E-08	1.41951E-07
SPD_0772	fruB	CcpA		1-phosphofructokinase, putative	1511.64	10.56	1.40	2.64	0.14	10.23417891	1.39372E-24	1.66463E-23
SPD_0203	rplN			ribosomal protein L14	29290.49	14.84	1.40	2.64	0.14	9.919568776	3.42232E-23	3.86985E-22
SPD_0191	SPD_0191	NrdR	RpoD	hypothetical protein	4397.19	12.10	1.40	2.64	0.17	8.40815438	4.16513E-17	3.04964E-16
SPD_0190	nrdG	NrdR	ScrA, RpoD	anaerobic ribonucleoside-triphosphate reductase activating pr	4750.93	12.21	1.40	2.64	0.19	7.54948384	4.36987E-14	2.59342E-13
SPD_1182	SPD_1182			hypothetical protein	38.17	5.25	1.40	2.64	0.38	3.699632578	0.000215912	0.000475354
SPD_1183	SPD_1183			hypothetical protein	50.86	5.67	1.39	2.62	0.31	4.443945543	8.8324E-06	2.30583E-05
SPD_1916	SPD_1916			transcriptional regulator	59.56	5.90	1.39	2.62	0.33	4.250380929	2.13407E-05	5.35199E-05
SPD_1046	lacG-2	LacT	CcpA	6-phospho-beta-galactosidase	724.76	9.50	1.38	2.60	0.28	4.944003375	7.64178E-07	2.30338E-06
SPD_1677	rafE	RafR	CcpA	sugar ABC transporter, sugar-binding protein	195.99	7.61	1.37	2.58	0.21	6.533610288	6.50663E-11	2.93259E-10
SPD_0206	rpsN			ribosomal protein S14	15132.78	13.89	1.36	2.57	0.15	9.146151491	5.89979E-20	5.34337E-19
SPD_0189	SPD_0189	NrdR	RpoD	acetyltransferase, GNAT family protein	2832.98	11.47	1.36	2.57	0.15	9.11118366	8.1488E-20	7.31097E-19
SPD_0553	SPD_0553			hypothetical protein	75.95	6.25	1.36	2.57	0.29	4.619922651	3.83883E-06	1.04502E-05
SPD_0730	deoD			purine nucleoside phosphorylase	3069.27	11.58	1.35	2.55	0.16	8.588350602	8.82267E-18	6.85371E-17
SPD_1675	rafG	RafR	CcpA	sugar ABC transporter, permease protein	224.99	7.81	1.35	2.55	0.19	7.313048406	2.61149E-13	1.44654E-12
SPD_0201	rpmC			ribosomal protein L29	40929.50	15.32	1.34	2.53	0.15	8.72591933	2.64027E-18	2.16547E-17
SPD_1175	SPD_1175	RitR		membrane protein, putative	886.77	9.79	1.34	2.53	0.18	7.595809075	3.05875E-14	1.83814E-13
SPD_0924	SPD_0924			hypothetical protein	731.08	9.51	1.34	2.53	0.19	7.199390567	6.04823E-13	3.26502E-12
SPD_0933	SPD_0933			hypothetical protein	630.16	9.30	1.34	2.53	0.27	4.934947927	8.01721E-07	2.41274E-06
SPD_0207	rpsH			ribosomal protein S8	38971.23	15.25	1.32	2.50	0.16	8.190549373	2.60036E-16	1.82026E-15
SPD_0734	SPD_0734			membrane protein, putative	34.67	5.12	1.32	2.50	0.38	3.487097318	0.000488294	0.001022047
SPD_1008	glgA	CcpA	RpoD	glycogen/starch synthase, ADP-glucose type	960.00	9.91	1.31	2.48	0.15	8.599441149	8.01052E-18	6.32566E-17
SPD_1986	fucI	FcsR		L-fucose isomerase	198.48	7.63	1.31	2.48	0.21	6.280850446	3.36726E-10	1.42996E-09
SPD_0155	SPD_0155			membrane protein, putative	354.90	8.47	1.31	2.48	0.23	5.760173993	8.40273E-09	3.15474E-08
SPD_0523	vex3			ABC transporter, transmembrane protein Vexp3	789.19	9.62	1.29	2.45	0.16	8.18374625	2.75153E-16	1.90514E-15
SPD_1755	SPD_1755			ABC transporter, ATP-binding protein	641.85	9.33	1.29	2.45	0.18	7.154165028	8.41837E-13	4.50631E-12
SPD_0197	rpsS			ribosomal protein S19	36095.20	15.14	1.29	2.45	0.20	6.315935179	2.68533E-10	1.15839E-09
SPD_1678	aga	RafR	CcpA	alpha-galactosidase AgaN	362.83	8.50	1.29	2.45	0.21	6.248293709	4.14961E-10	1.74284E-09
SPD_0580	rokB	MalR	CcpA	glucokinase	5117.73	12.32	1.28	2.43	0.15	8.582011928	9.3228E-18	7.18382E-17
SPD_0610	SPD_0610			hypothetical protein	1086.54	10.09	1.28	2.43	0.26	4.963859179	6.91061E-07	2.10289E-06
SPD_0931	pezT	PezA		hypothetical protein	1676.73	10.71	1.27	2.41	0.20	6.235074541	4.51563E-10	1.88414E-09
SPD_0559	gatA	CcpA		PTS system IIA component, putative	1014.71	9.99	1.27	2.41	0.24	5.29507529	1.18967E-07	3.95386E-07
SPD_1007	glgD	CcpA	RpoD	glucose-1-phosphate adenylyltransferase, GlgD subunit	1937.79	10.92	1.26	2.39	0.13	9.948338854	2.56428E-23	2.91698E-22
SPD_0200	rplP			ribosomal protein L16	40269.54	15.30	1.26	2.39	0.14	8.989592872	2.48148E-19	2.17528E-18
SPD_2024	thiZ	ComX		ABC transporter, ATP-binding protein	3064.29	11.58	1.25	2.38	0.13	9.753865582	1.77575E-22	1.91721E-21
SPD_0002	dnaN			DNA polymerase III, beta subunit	5260.25	12.36	1.25	2.38	0.17	7.30996461	2.67213E-13	1.47585E-12
SPD_1504	nanA	NanR	CcpA	sialidase A precursor	1217.56	10.25	1.24	2.36	0.14	8.880753486	6.6409E-19	5.69092E-18
SPD_0480	SPD_0480	CiaR		Putative nucleic-acid-binding protein implicated in transcriptio	2745.52	11.42	1.24	2.36	0.15	8.259649597	1.46101E-16	1.04179E-15
SPD_1163	SPD_1163			N-acetyleuraminate lyase, putative	246.21	7.94	1.24	2.36	0.19	6.527859284	6.67163E-11	2.99988E-10
SPD_0198	rplV			ribosomal protein L22	55636.68	15.76	1.24	2.36	0.20	6.334994125	2.3735E-10	1.03086E-09
SPD_0166	ribH			6,7-dimethyl-8-ribityllumazine synthase	428.75	8.74	1.24	2.36	0.22	5.526555323	3.26579E-08	1.16653E-07
SPD_0444	endoD			endo-beta-N-acetylglucosaminidase, putative	1255.70	10.29	1.23	2.35	0.15	8.280518966	1.2264E-16	8.77769E-16
SPD_1608	SPD_1608			ABC transporter ATP-binding protein	400.77	8.65	1.23	2.35	0.18	6.778731351	1.21236E-11	5.85054E-11
SPD_0712	SPD_0712			transposase family protein	101.12	6.66	1.23	2.35	0.26	4.696061617	2.65226E-06	7.36695E-06
SPD_1757	ndk			nucleoside diphosphate kinase	1285.99	10.33	1.22	2.33	0.14	8.616986807	6.87391E-18	5.47335E-17
SPD_1245	rpsU	RpoD		ribosomal protein S21	4900.06	12.26	1.22	2.33	0.17	7.027349045	2.10494E-12	1.07843E-11
SPD_0522	vex2			ABC transporter, ATP-binding protein Vexp2	279.71	8.13	1.20	2.30	0.19	6.452622324	1.09931E-10	4.84051E-10
SPD_1944	SPD_1944			CAAX amino terminal protease family protein	727.82	9.51	1.20	2.30	0.20	6.107682356	1.01088E-09	4.11897E-09
SPD_1018	iga			immunoglobulin A1 protease precursor	25742.36	14.65	1.19	2.28	0.13	9.377315373	6.76738E-21	6.56471E-20
SPD_1006	glgC	CcpA	RpoD	glucose-1-phosphate adenylyltransferase	2026.13	10.98	1.19	2.28	0.16	7.510583914	5.88642E-14	3.48265E-13
SPD_0262	manN	CcpA	CiaR	PTS system, mannose/fructose/sorbose family protein, IID com	25936.32	14.66	1.19	2.28	0.16	7.498510903	6.45469E-14	3.80707E-13
SPD_1246	nagB	CodY	CcpA, NagR	glucosamine-6-phosphate isomerase	25309.91	14.63	1.18	2.27	0.15	7.906814937	2.64058E-15	1.72813E-14
SPD_0481	SPD_0481	CiaR		ribosomal protein L7A family protein	2849.04	11.48	1.18	2.27	0.15	7.824498255	5.09686E-15	3.25756E-14
SPD_0717	clpE	CtsR		ATP-dependent Clp protease ATP-binding subunit ClpE	27705.97	14.76	1.18	2.27	0.17	6.843767419	7.71371E-12	3.75087E-11
SPD_0959	SPD_0959			Putative aromatic ring hydroxylating enzyme	3756.94	11.88	1.17	2.25	0.15	7.729520147	1.07953E-14	6.76386E-14
SPD_1609	SPD_1609			ABC transporter, substrate-binding protein	422.50	8.72	1.17	2.25	0.18	6.484354045	8.91127E-11	3.96034E-10
SPD_1799	SPD_1799			sensor histidine kinase, putative	1696.45	10.73	1.17	2.25	0.21	5.650537491	1.59947E-08	5.85553E-08
SPD_2017	cbpA			choline binding protein A	15076.10	13.88	1.16	2.23	0.15	7.842192145	4.42748E-15	2.86811E-14
SPD_1303	SPD_1303			hypothetical protein	1559.85	10.61	1.16	2.23	0.21	5.459739634	4.76833E-08	1.65678E-07
SPD_1162	SPD_1162			hypothetical protein	43.52	5.44	1.16	2.23	0.32	3.591662727	0.000328575	0.000710302
SPD_1995	fucK	FcsR	CcpA	L-fuculose kinase FucK, putative	107.61	6.75	1.16	2.23	0.33	3.471330287	0.000517887	0.00107574
SPD_0129	gidA			tRNA uridine 5-carboxymethylaminomethyl modification enzym	8448.94	13.04	1.15	2.22	0.16	7.078790901	1.45418E-12	7.59271E-12
SPD_1176	SPD_1176			ABC transporter, ATP-binding protein	834.29	9.70	1.15	2.22	0.17	6.850037506	7.38306E-12	3.59924E-11
SPD_1865	adhB2	Rex	AdcR, CcpA	alcohol dehydrogenase, zinc-containing	2500.83	11.29	1.15	2.22	0.20	5.739290927	9.50738E-09	3.56247E-08
SPD_0214	adk			adenylate kinase	3037.10	11.57	1.15	2.22	0.20	5.710401811	1.1271E-08	4.1823E-08
SPD_1164	cdd-2			cytidine deaminase	142.28	7.15	1.15	2.22	0.28	4.123558763	3.73063E-05	9.09342E-05
SPD_0065	bgaC	AgaR	CcpA, RpoD	Beta-galactosidase 3	624.46	9.29	1.15	2.22	0.29	3.940094398	8.14496E-05	0.000190514
SPD_1024	lplA			lipoate-protein ligase, putative	1970.40	10.94	1.14	2.20	0.17	6.62108406	3.56574E-11	1.65794E-10
SPD_1606	mgtC			MgtC/SapB family protein	289.95	8.18	1.14	2.20	0.19	6.127653533	8.91845E-10	3.65733E-09
SPD_1721	SPD_1721			ABC transporter, ATP-binding protein	73.02	6.19	1.14	2.20	0.28	4.058907922	4.93027E-05	0.000118215
SPD_1376	pclA			G5 domain family protein	1208.48	10.24	1.13	2.19	0.21	5.378105613	7.52737E-08	2.55503E-07
SPD_0333	SPD_0333			hypothetical protein	2075.63	11.02	1.13	2.19	0.24	4.638051932	3.51708E-06	9.60164E-06
SPD_1607	sfuB			ABC transporter, permease protein	441.36	8.79	1.12	2.17	0.17	6.479065517	9.22924E-11	4.09213E-10
SPD_0057	purH			bifunctional purine biosynthesis protein PurH	942.73	9.88	1.12	2.17	0.22	5.18703331	2.13671E-07	6.9325E-07
SPD_0884	SPD_0884			hypothetical protein	249.53	7.96	1.12	2.17	0.26	4.37835034	1.19581E-05	3.07563E-05
SPD_0479	nusA	CiaR		transcription termination factor NusA	8688.63	13.08	1.10	2.14	0.16	7.026273835	2.12122E-12	1.08386E-11
SPD_0287	spnHL	RegR		hyaluronate lyase precursor	530.36	9.05	1.10	2.14	0.19	5.698039379	1.21193E-08	4.47104E-08
SPD_1216	alaS			alanyl-tRNA synthetase	13932.76	13.77	1.09	2.13	0.13	8.183765274	2.7511E-16	1.90514E-15
SPD_0087	SPD_0087			hypothetical protein	1932.15	10.92	1.08	2.11	0.20	5.387256303	7.15414E-08	2.437E-07
SPD_0150	gshT	CmbR	CmhR	ABC transporter, substrate-binding protein	17567.69	14.10	1.07	2.10	0.14	7.4475321	9.51024E-14	5.49066E-13

Table S1 continued

					WT HOCl vs control							
Locus	Gene Symbol	Regulon	Further Regulon	Function	Base-Mean	A-value	M-value	Fold-change	Standard error	Wald statistic	P-value	Adjusted P-value
SPD_0174	SPD_0174			membrnae protein, putative	3859.75	11.91	1.07	2.10	0.15	6.956692822	3.48353E-12	1.74268E-11
SPD_2025	thiY	ComX		ABC transporter, substrate-binding protein, putative	2485.83	11.28	1.07	2.10	0.15	6.953216443	3.5705E-12	1.78152E-11
SPD_0237	gldA			glycerol dehydrogenase	409.81	8.68	1.07	2.10	0.19	5.554123932	2.79007E-08	1.00222E-07
SPD_1754	SPD_1754			Putative immunity protein	1270.01	10.31	1.07	2.10	0.20	5.418155984	6.02169E-08	2.07341E-07
SPD_1758	rpoC			DNA-directed RNA polymerase, beta' subunit	63965.93	15.97	1.06	2.08	0.16	6.578996446	4.73634E-11	2.17054E-10
SPD_0335	eng	CcpA		cell wall surface anchor family protein	1287.82	10.33	1.05	2.07	0.21	4.954838397	7.23904E-07	2.19584E-06
SPD_0160	nrdI			nrdI protein, putative	2429.04	11.25	1.04	2.06	0.13	8.104175574	5.31044E-16	3.63736E-15
SPD_2041	tsf			translation elongation factor Ts	36442.50	15.15	1.04	2.06	0.15	6.768357289	1.30253E-11	6.26985E-11
SPD_0637	SPD_0637			glyoxalase family protein	1026.42	10.00	1.04	2.06	0.16	6.687296062	2.27332E-11	1.07267E-10
SPD_0055	purN			phosphoribosylglycinamide formyltransferase	269.42	8.07	1.03	2.04	0.32	3.228014356	0.001246527	0.002484268
SPD_0958	rpoD			RNA polymerase sigma-70 factor	11069.69	13.43	1.02	2.03	0.16	6.289763381	3.1795E-10	1.35382E-09
SPD_1025	lpdA			dihydrolipoamide dehydrogenase	3717.51	11.86	1.02	2.03	0.17	6.017074898	1.77597E-09	7.11505E-09
SPD_1664	treP	TreR	CcpA	PTS system, trehalose-specific IIABC components	109.48	6.77	1.02	2.03	0.30	3.399014578	0.000676291	0.001392664
SPD_1491	SPD_1491	NanR	CcpA, NiaR	hypothetical protein	366.24	8.52	1.01	2.01	0.20	5.151604472	2.58267E-07	8.3089E-07
SPD_1495	satA	NanR	CcpA, RitR, NiaR	sugar ABC transporter, sugar-binding protein	955.23	9.90	1.00	2.00	0.15	6.595136929	4.24864E-11	1.95642E-10
SPD_0167	ribB			3,4-dihydroxy-2-butanone 4-phosphate synthase/GTP cyclohyd	1194.16	10.22	1.00	2.00	0.16	6.110423277	9.93672E-10	4.0575E-09
SPD_2006	dltX	CiaR		D-alanyl-lipoteichoic acid biosynthesis protein DltX	524.47	9.03	-4.63	0.04	0.24	-19.472368	1.88359E-84	1.56502E-82
SPD_0775	SPD_0775	CiaR		Acetyltransferase	2586.77	11.34	-3.95	0.06	0.28	-13.89405525	6.88256E-44	2.1921E-42
SPD_1524	gntR	GntR	RpoD	transcriptional regulator, GntR family protein	12079.68	13.56	-3.87	0.07	0.20	-19.3414972	2.40393E-83	1.91413E-81
SPD_0564	SPD_0564			hypothetical protein	274.53	8.10	-3.63	0.08	0.26	-13.77379278	3.66458E-43	1.11159E-41
SPD_0800	SPD_0800			capsular polysaccharide biosynthesis protein, putative	786.42	9.62	-3.07	0.12	0.22	-13.75208919	4.94798E-43	1.47743E-41
SPD_0832	SPD_0832			IS1381, transposase OrfA	39.13	5.29	-2.78	0.15	0.44	-6.272498282	3.553E-10	1.5055E-09
SPD_0939	mutR2			transcriptional activator, Rgg/GadR/MutR family protein	274.19	8.10	-2.77	0.15	0.29	-9.710770378	2.71279E-22	2.86417E-21
SPD_0754	SPD_0754			hypothetical protein	649.32	9.34	-2.75	0.15	0.29	-9.507615329	1.95083E-21	1.95185E-20
SPD_0303	yorfE	RpoD		transcriptional regulator, putative	1919.44	10.91	-2.73	0.15	0.32	-8.433368034	3.35856E-17	2.49736E-16
SPD_0830	SPD_0830			IS1381, transposase OrfB	35.75	5.16	-2.73	0.15	0.45	-6.05780136	1.37995E-09	5.56346E-09
SPD_1439	rpsO	RpoD		ribosomal protein S15	7611.50	12.89	-2.63	0.16	0.21	-12.52695435	5.31654E-36	1.11647E-34
SPD_1341	atpE	RpoD	CcpA	ATP synthase F0, C subunit	1490.16	10.54	-2.62	0.16	0.24	-10.97699631	4.93046E-28	7.41898E-27
SPD_0378	fabM	FabT		enoyl-CoA hydratase/isomerase family protein	9461.29	13.21	-2.59	0.17	0.19	-13.31555333	1.87975E-40	5.20608E-39
SPD_1604	SPD_1604			hypothetical protein	592.75	9.21	-2.58	0.17	0.21	-12.38362386	3.20536E-35	6.38067E-34
SPD_0855	ybeY			conserved hypothetical protein TIGR00043	1712.17	10.74	-2.57	0.17	0.17	-15.0995311	1.63089E-51	6.92585E-50
SPD_0447	glnR	GlnR	CcpA	transcriptional regulator, MerR family protein	3486.82	11.77	-2.57	0.17	0.20	-12.72469342	4.31164E-37	9.69358E-36
SPD_0046	blpU	BlpR		bacteriocin BlpU	4679.02	12.19	-2.55	0.17	0.55	-4.667807425	3.04431E-06	8.37076E-06
SPD_1262	SPD_1262			transcriptional regulator, AraC family protein	1276.95	10.32	-2.54	0.17	0.24	-10.55906493	4.61233E-26	6.12095E-25
SPD_2007	SPD_2007			transporter, major facilitator family protein	250.59	7.97	-2.53	0.17	0.32	-7.870658295	3.5278E-15	2.29307E-14
SPD_1525	SPD_1525	GntR	RpoD, CcpA	ABC transporter, ATP-binding protein	16925.28	14.05	-2.52	0.17	0.23	-10.9312705	8.16965E-28	1.19177E-26
SPD_0622	SPD_0622	RpoD		transcriptional regulator, TENA/THI-4 family protein, putative	3072.27	11.59	-2.51	0.18	0.16	-15.3719312	2.52528E-53	1.09678E-51
SPD_0904	tdk			thymidine kinase	745.62	9.54	-2.45	0.18	0.18	-13.25714973	4.10192E-40	1.08872E-38
SPD_0467	blpS	BlpR	ComE	BlpS protein	4546.53	12.15	-2.43	0.19	0.19	-13.08245105	4.14844E-39	1.05702E-37
SPD_0273	SPD_0273			hypothetical protein	2545.56	11.31	-2.40	0.19	0.17	-14.47792753	1.67059E-47	6.13941E-46
SPD_1851	rnpA			ribonuclease P protein component	5067.44	12.31	-2.40	0.19	0.22	-11.02180413	2.99985E-28	4.54978E-27
SPD_0302	SPD_0302			hypothetical protein	864.58	9.76	-2.38	0.19	0.36	-6.612334388	3.78306E-11	1.75047E-10
SPD_0703	SPD_0703	WalR		hypothetical protein	736.96	9.53	-2.33	0.20	0.25	-9.277314508	1.73804E-20	1.61233E-19
SPD_1442	SPD_1442			hypothetical protein	1071.86	10.07	-2.27	0.21	0.18	-12.78376389	2.0205E-37	4.65201E-36
SPD_0674	rpsP			ribosomal protein S16	2762.33	11.43	-2.27	0.21	0.21	-10.97299991	5.15337E-28	7.69382E-27
SPD_0676	SPD_0676			hypothetical protein	1225.13	10.26	-2.25	0.21	0.17	-13.14768654	1.75461E-39	4.53116E-38
SPD_0398	gatC			glutamyl-tRNA(Gln) amidotransferase, C subunit	748.06	9.55	-2.25	0.21	0.18	-12.79850046	1.67148E-37	3.89536E-36
SPD_0856	dgkA	RitR		diacylglycerol kinase	782.44	9.61	-2.25	0.21	0.23	-9.710095793	2.7308E-22	2.86734E-21
SPD_1256	SPD_1256			peptidase, U32 family protein	608.68	9.25	-2.23	0.21	0.20	-10.94490498	7.02914E-28	1.03328E-26
SPD_1454	SPD_1454			hypothetical protein	132.84	7.05	-2.22	0.21	0.29	-7.706202642	1.29617E-14	8.06833E-14
SPD_1374	SPD_1374			hypothetical protein	1649.08	10.69	-2.20	0.22	0.17	-13.02489574	8.83216E-39	2.19198E-37
SPD_0473	blpY	BlpR	ComE	immunity protein BlpY	23417.45	14.52	-2.20	0.22	0.19	-11.63364639	2.77965E-31	4.61905E-30
SPD_1088	coaB			phosphopantothenate--cysteine ligase	981.62	9.94	-2.20	0.22	0.20	-10.86665386	1.66184E-27	2.38781E-26
SPD_0801	SPD_0801			hypothetical protein	1215.05	10.25	-2.20	0.22	0.20	-10.75647901	5.52406E-27	7.64963E-26
SPD_1864	SPD_1864	RpoD		DNA-binding protein	1333.20	10.38	-2.20	0.22	0.21	-10.2498483	1.18529E-24	1.42459E-23
SPD_0677	SPD_0677			hypothetical protein	2825.74	11.46	-2.18	0.22	0.18	-12.40926745	2.32773E-35	4.73222E-34
SPD_0778	SPD_0778	CodY		hypothetical protein	869.17	9.76	-2.18	0.22	0.21	-10.5423936	5.50789E-26	7.2093E-25
SPD_0987	SPD_0987			conserved hypothetical protein TIGR00103	1271.33	10.31	-2.17	0.22	0.17	-12.77936851	2.17681E-37	4.95225E-36
SPD_0905	bltD			acetyltransferase, GNAT family protein	1097.63	10.10	-2.17	0.22	0.18	-12.09957105	1.06164E-33	2.00872E-32
SPD_2067	rlmH			hypothetical protein	288.99	8.17	-2.15	0.23	0.19	-11.15378451	6.86242E-29	1.07493E-27
SPD_1603	SPD_1603			hypothetical protein	894.06	9.80	-2.12	0.23	0.27	-7.989072246	1.35958E-15	9.05281E-15
SPD_0098	SPD_0098	CiaR	CcpA	glycosyl transferase, group 2 family protein	2378.43	11.22	-2.11	0.23	0.16	-13.49009856	1.78861E-41	5.17885E-40
SPD_1340	atpB	RpoD	CodY	ATP synthase F0, A subunit	14648.83	13.84	-2.10	0.23	0.17	-12.31266123	7.74273E-35	1.49458E-33
SPD_0552	SPD_0552			hypothetical protein	9.41	3.23	-2.08	0.24	0.65	-3.229338215	0.001240771	0.002477652
SPD_1140	gidB			methyltransferase GidB	990.56	9.95	-2.07	0.24	0.18	-11.8029416	3.76902E-32	6.73139E-31
SPD_0897	mesH			GtrA family protein	32.11	5.00	-2.07	0.24	0.43	-4.803107374	1.56222E-06	4.48259E-06
SPD_0997	hlpA			DNA-binding protein HU	2363.61	11.21	-2.05	0.24	0.23	-8.902828512	5.44413E-19	4.72897E-18
SPD_1705	recX			regulatory protein RecX	150.62	7.23	-2.05	0.24	0.23	-8.773629764	1.72997E-18	1.44999E-17
SPD_1829	bguR			transcriptional regulator, GntR family protein	1160.78	10.18	-2.03	0.24	0.14	-14.17730866	1.2661E-45	4.24476E-44
SPD_0446	SPD_0446	CcpA		membrane protein, putative	852.63	9.74	-2.03	0.24	0.16	-12.47218803	1.05878E-35	2.17563E-34
SPD_1127	ispD	CiaR		2-C-methyl-D-erythritol 4-phosphate cytidylyltransferase	3088.34	11.59	-2.03	0.24	0.17	-11.84458966	2.29539E-32	4.1382E-31
SPD_0284	SPD_0284	RpoD		hypothetical protein	2303.07	11.17	-2.03	0.24	0.27	-7.406481155	1.29695E-13	7.33274E-13
SPD_0967	murA-1			UDP-N-acetylglucosamine 1-carboxyvinyltransferase	12672.70	13.63	-2.01	0.25	0.14	-14.41027668	4.4592E-47	1.57806E-45
SPD_1587	mga2			transcriptional activator, putative	149.62	7.23	-2.00	0.25	0.27	-7.421744995	1.15587E-13	6.57915E-13
SPD_1963	rpmF			ribosomal protein L32	15190.99	13.89	-1.99	0.25	0.22	-9.269679722	1.86706E-20	1.72365E-19
SPD_0896	mscL			large conductance mechanosensitive channel protein MscL	1266.99	10.31	-1.99	0.25	0.27	-7.381883304	1.56066E-13	8.72053E-13
SPD_0474	blpZ	BlpR	ComE	immunity protein BlpZ	11759.97	13.52	-1.95	0.26	0.17	-11.74466201	7.52226E-32	1.29505E-30
SPD_0491	SPD_0491			hypothetical protein	1315.76	10.36	-1.95	0.26	0.19	-10.26663585	9.96181E-25	1.21255E-23
SPD_1822	rluD2	RitR		ribosomal large subunit pseudouridine synthase, RluD subfam	1085.34	10.08	-1.95	0.26	0.21	-9.416965693	4.64312E-21	4.52704E-20
SPD_0647	SPD_0647	RpoD		transcriptional regulator, TetR family protein	243.13	7.93	-1.95	0.26	0.28	-7.049214017	1.79931E-12	9.2932E-12
SPD_0941	SPD_0941			hypothetical protein	28.30	4.82	-1.95	0.26	0.48	-4.059758465	4.91235E-05	0.000117933
SPD_0632	thiD			phosphomethylpyrimidine kinase	2848.84	11.48	-1.92	0.26	0.19	-10.25716192	1.09889E-24	1.3291E-23
SPD_0718	SPD_0718			hypothetical protein	3933.82	11.94	-1.91	0.27	0.18	-10.50612373	8.09528E-26	1.03826E-24
SPD_0913	SPD_0913	CiaR		Extracellular protein	6391.83	12.64	-1.87	0.27	0.28	-6.610452689	3.83147E-11	1.76858E-10
SPD_2068	htrA	CiaR		serine protease	8532.67	13.06	-1.86	0.28	0.29	-6.460226598	1.04546E-10	4.61404E-10
SPD_1625	SPD_1625			hypothetical protein	622.74	9.28	-1.84	0.28	0.20	-9.289009787	1.5573E-20	1.45171E-19
SPD_0096	ptvR	PtvR	RpoD, CcpA	transcriptional regulator, PadR family protein	665.99	9.38	-1.84	0.28	0.25	-7.303464303	2.80451E-13	1.5445E-12
SPD_1154	rpmE			ribosomal protein L31	14981.34	13.87	-1.83	0.28	0.21	-8.858591582	8.10317E-19	6.88229E-18
SPD_0468	blpR	BlpR		response regulator BlpR	13310.13	13.70	-1.81	0.29	0.20	-8.87515398	6.98367E-19	5.95795E-18
SPD_1443	SPD_1443			hypothetical protein	463.62	8.86	-1.81	0.29	0.21	-8.586485868	8.96698E-18	6.93761E-17
SPD_0565	SPD_0565			hypothetical protein	377.47	8.56	-1.81	0.29	0.26	-6.978217425	2.98949E-12	1.51135E-11
SPD_0381	acpP	FabT	WalR	acyl carrier protein	10947.35	13.42	-1.80	0.29	0.17	-10.41348701	2.15192E-25	2.70547E-24
SPD_1704	rumA-2			23S rRNA (uracil-5-)-methyltransferase RumA	1647.81	10.69	-1.79	0.29	0.17	-10.54580067	5.31185E-26	7.00065E-25
SPD_0952	ftsW			cell division protein FtsW, putative	2535.43	11.31	-1.78	0.29	0.16	-11.0990491	1.26786E-28	1.95393E-27
SPD_0759	SPD_0759			hypothetical protein	1349.76	10.40	-1.77	0.29	0.17	-10.64915064	1.75963E-26	2.4019E-25
SPD_1586	bfrR			sugar-binding transcriptional regulator, LacI family protein	1932.10	10.92	-1.75	0.30	0.17	-10.28772516	8.00451E-25	9.80552E-24
SPD_2000	adcR	AdcR		adc operon repressor AdcR	2279.93	11.15	-1.74	0.30	0.20	-8.895838976	5.79796E-19	4.99095E-18
SPD_2053	SPD_2053			hypothetical protein	320.78	8.33	-1.74	0.30	0.21	-8.197805202	2.44816E-16	1.72001E-15
SPD_1081	relE2			mRNA interferase RelE2	455.92	8.83	-1.73	0.30	0.17	-10.05996499	8.30279E-24	9.79421E-23
SPD_0501	licT			transcription antiterminator LicT	87.73	6.45	-1.73	0.30	0.27	-6.511487462	7.44102E-11	3.33798E-10
SPD_0138	epsF			glycosyl transferase, group 1 family protein	355.12	8.47	-1.72	0.30	0.18	-9.294610155	1.47747E-20	1.38404E-19
SPD_1563	SPD_1563	CodY	RpoD	dicarboxylate/amino acid:cation (Na+ or H+) symporter (DAACS	2687.66	11.39	-1.72	0.30	0.20	-8.470889242	2.43527E-17	1.84674E-16
SPD_1639	sczA	SczA		transcriptional regulator, TetR family protein	447.65	8.81	-1.72	0.30	0.21	-8.209054199	2.22938E-16	1.57208E-15
SPD_0430	trkA			potassium uptake protein, Trk family protein	2198.68	11.10	-1.71	0.31	0.15	-11.71419428	1.07811E-31	1.83953E-30
SPD_1838	yajC-2			preprotein translocase, YajC subunit	4295.97	12.07	-1.71	0.31	0.17	-9.871132393	5.55341E-22	6.13443E-22
SPD_0803	SPD_0803	VraR	HrcA	Putative phage shock protein C	4160.65	12.02	-1.71	0.31	0.21	-7.967026374	1.62538E-15	1.07851E-14
SPD_0492	SPD_0492			acetyltransferase, GNAT family protein	884.46	9.79	-1.71	0.31	0.23	-7.564601486	3.89055E-14	2.31615E-13
SPD_1818	comX2	ComE		transcriptional regulator ComX2	3345.55	11.71	-1.71	0.31	0.24	-7.053798731	1.74098E-12	9.0163E-12
SPD_1010	SPD_1010	CcpA		hypothetical protein	370.91	8.53	-1.70	0.31	0.24	-7.232763879	4.73262E-13	2.56278E-12
SPD_1157	SPD_1157			hypothetical protein	65.49	6.03	-1.69	0.31	0.32	-5.224629353	1.74504E-07	5.71023E-07
SPD_0281	celC	CelR	CcpA, RpoD	PTS system, IIA component	48.51	5.60	-1.69	0.31	0.40	-4.225730039	2.38167E-05	5.94951E-05
SPD_1909	pnpS			sensor histidine kinase PnpS	8304.57	13.02	-1.68	0.31	0.13	-13.0314469	8.10559E-39	2.03813E-37
SPD_1577	hicB			hypothetical protein	3061.78	11.58	-1.67	0.31	0.13	-12.85180103	8.40308E-38	2.00729E-36
SPD_1119	SPD_1119			hypothetical protein	551.26	9.11	-1.67	0.31	0.20	-8.460008065	2.67359E-17	2.01946E-16
SPD_0799	SPD_0799			hypothetical protein	964.93	9.91	-1.67	0.31	0.20	-8.424381216	3.62662E-17	2.66556E-16
SPD_0014	comX1	ComE		transcriptional regulator ComX1	3325.96	11.70	-1.67	0.31	0.24	-6.912586414	4.75896E-12	2.35605E-11
SPD_0315	cps2A	CpsR	RpoD, VncR	integral membrane regulatory protein Cps2A	35452.41	15.11	-1.66	0.32	0.15	-11.27899922	1.66631E-29	2.63166E-28
SPD_0466	blpT	BlpR	ComE	BlpT protein	10969.81	13.42	-1.66	0.32	0.26	-6.295223165	3.06958E-10	1.31524E-09
SPD_0903	xylH			4-oxalocrotonate tautomerase	545.00	9.09	-1.66	0.32	0.26	-6.289696614	3.18087E-10	1.35382E-09
SPD_0476	SPD_0476			phosphotransferase enzyme family protein	9125.03	13.16	-1.64	0.32	0.13	-12.62416432	1.55382E-36	3.37427E-35
SPD_0120	SPD_0120	RitR		membrane protein, putative	1000.73	9.97	-1.64	0.32	0.17	-9.637883773	5.53166E-22	5.74511E-21
SPD_0075	SPD_0075			hypothetical protein	86.99	6.44	-1.64	0.32	0.32	-5.109929012	3.2228E-07	1.02818E-06
SPD_0266	SPD_0266			Cof family protein	2349.96	11.20	-1.63	0.32	0.15	-10.94604339	6.94139E-28	1.02829E-26
SPD_1671	amiA	CodY		oligopeptide ABC transporter, oligopeptide-binding protein Am	27638.97	14.75	-1.63	0.32	0.19	-8.613989777	7.0561E-18	5.59511E-17
SPD_0112	SPD_0112			hypothetical protein	477.82	8.90	-1.63	0.32	0.20	-8.300235896	1.03905E-16	7.46474E-16
SPD_1707	SPD_1707			hypothetical protein	370.90	8.53	-1.63	0.32	0.26	-6.374860863	1.83129E-10	7.98995E-10
SPD_0872	SPD_0872			membrane protein, putative	1332.51	10.38	-1.62	0.33	0.17	-9.595261711	8.37044E-22	8.50846E-21
SPD_1118	cutC			copper homeostasis protein CutC	1907.05	10.90	-1.62	0.33	0.18	-8.949537666	3.56974E-19	3.11497E-18
SPD_0493	SPD_0493			hypothetical protein	1669.64	10.71	-1.61	0.33	0.23	-7.06441746	1.61291E-12	8.39857E-12
SPD_0847	infC			translation initiation factor IF-3	7702.14	12.91	-1.60	0.33	0.32	-5.064811636	4.08804E-07	1.2807E-06
SPD_1481	SPD_1481			membrane protein, putative	2109.23	11.04	-1.59	0.33	0.15	-10.46845787	1.20591E-25	1.53634E-24
SPD_1954	SPD_1954	CodY		hypothetical protein	721.08	9.49	-1.59	0.33	0.18	-8.759503264	1.96113E-18	1.62239E-17
SPD_0816	SPD_0816			Cof family protein	609.10	9.25	-1.59	0.33	0.20	-7.781933902	7.14242E-15	4.51959E-14
SPD_0495	SPD_0495			hypothetical protein	201.77	7.66	-1.57	0.34	0.25	-6.240783257	4.35385E-10	1.82461E-09
SPD_0463	SPD_0463			Hit-like protein involved in cell-cycle regulation, putative	1723.38	10.75	-1.56	0.34	0.22	-7.087800139	1.36261E-12	7.15368E-12
SPD_1430	fer			ferredoxin	97.53	6.61	-1.55	0.34	0.32	-4.891571021	1.00034E-06	2.97766E-06
SPD_1258	SPD_1258	CodY		peptidase, U32 family protein	2584.97	11.34	-1.54	0.34	0.17	-8.784076159	1.57655E-18	1.32722E-17
SPD_0118	SPD_0118			hypothetical protein	422.43	8.72	-1.54	0.34	0.18	-8.596056789	8.2502E-18	6.46153E-17
SPD_0121	SPD_0121			hypothetical protein	1761.73	10.78	-1.53	0.35	0.17	-9.132883944	6.66983E-20	6.01229E-19
SPD_0684	bioY			biotin synthase (BioY family protein), putative	1836.84	10.84	-1.53	0.35	0.21	-7.148545253	8.77023E-13	4.68154E-12

Table S1 continued

					WT HOCl vs control							
Locus	Gene Symbol	Regulon	Further Regulon	Function	Base-Mean	A-value	M-value	Fold-change	Standard error	Wald statistic	P-value	Adjusted P-value
SPD_0731	flaR			DNA topology modulation protein FlaR, putative	483.58	8.92	-1.52	0.35	0.19	-8.025236518	1.01331E-15	6.8425E-15
SPD_1248	cbpM			hypothetical protein	616.45	9.27	-1.52	0.35	0.24	-6.448205199	1.13182E-10	4.97222E-10
SPD_0909	SPD_0909			acetyltransferase, GNAT family protein	4139.94	12.02	-1.51	0.35	0.13	-11.2877708	1.50813E-29	2.4017E-28
SPD_0023	comW	ComE		hypothetical protein	6449.76	12.66	-1.51	0.35	0.27	-5.645536948	1.64667E-08	6.01678E-08
SPD_0537	SPD_0537			matrixin family protein	1321.46	10.37	-1.50	0.35	0.17	-8.745325523	2.22374E-18	1.83171E-17
SPD_0047	SPD_0047			hypothetical protein	1414.95	10.47	-1.50	0.35	0.29	-5.239748725	1.60795E-07	5.27972E-07
SPD_0554	SPD_0554			ABC transporter, ATP-binding protein	25332.72	14.63	-1.49	0.36	0.16	-9.503255019	2.03443E-21	2.02476E-20
SPD_0589	SPD_0589			hypothetical protein	1954.21	10.93	-1.49	0.36	0.16	-9.169213704	4.76482E-20	4.33598E-19
SPD_2005	dltA	CiaR		D-alanine--poly(phosphoribitol) ligase subunit 1	5225.04	12.35	-1.49	0.36	0.17	-8.896174671	5.78046E-19	4.99095E-18
SPD_1624	SPD_1624			hypothetical protein	1188.19	10.21	-1.49	0.36	0.18	-8.484933218	2.15843E-17	1.64333E-16
SPD_0074	SPD_0074			phosphorylase, Pnp/Udp family protein, putative	1614.03	10.66	-1.49	0.36	0.22	-6.744646977	1.534E-11	7.31039E-11
SPD_1761	hlyX			CBS domain membrane protein	3926.83	11.94	-1.48	0.36	0.13	-11.75373065	6.75685E-32	1.17385E-30
SPD_0861	secG			preprotein translocase, SecG subunit	712.11	9.48	-1.48	0.36	0.16	-9.332133921	1.0376E-20	9.86499E-20
SPD_1605	SPD_1605			sugar-binding transcriptional regulator, LacI family protein	567.62	9.15	-1.48	0.36	0.20	-7.35877964	1.85599E-13	1.03405E-12
SPD_1144	SPD_1144			hypothetical protein	240.56	7.91	-1.48	0.36	0.20	-7.232724902	4.73398E-13	2.56278E-12
SPD_1949	SPD_1949			hypothetical protein	142.77	7.16	-1.48	0.36	0.26	-5.715536826	1.09358E-08	4.06583E-08
SPD_0667	sodA	RpoD	CcpA	superoxide dismutase, manganese-dependent	7115.71	12.80	-1.47	0.36	0.14	-10.52463701	6.65173E-26	8.64725E-25
SPD_1530	SPD_1530			membrane protein, putative	1252.37	10.29	-1.47	0.36	0.15	-9.488083912	2.3532E-21	2.33003E-20
SPD_1201	licD3			phosphotransferase LicD3	1740.38	10.77	-1.47	0.36	0.17	-8.807904697	1.27507E-18	1.07817E-17
SPD_1767	SPD_1767			type II DNA modification methyltransferase, putative	2214.45	11.11	-1.47	0.36	0.21	-7.059670653	1.66898E-12	8.66689E-12
SPD_0974	SPD_0974			class I glutamine amidotransferase, putative	1823.39	10.83	-1.46	0.36	0.19	-7.604308754	2.86431E-14	1.74321E-13
SPD_1294	SPD_1294	RpoD	RitR	hypothetical protein	843.53	9.72	-1.46	0.36	0.29	-5.078551744	3.80323E-07	1.19736E-06
SPD_0908	tsaC			Sua5/YciO/YrdC/YwlC family protein	11998.49	13.55	-1.45	0.37	0.15	-9.68449828	3.50927E-22	3.6646E-21
SPD_1427	phnA			PhnA protein	1920.01	10.91	-1.45	0.37	0.17	-8.683545506	3.83619E-18	3.11956E-17
SPD_1424	truA			tRNA pseudouridine synthase A	644.68	9.33	-1.45	0.37	0.21	-7.032477141	2.02899E-12	1.04512E-11
SPD_1982	SPD_1982			hypothetical protein	221.20	7.79	-1.45	0.37	0.21	-6.928306733	4.25908E-12	2.11956E-11
SPD_0675	khpA			hypothetical protein	1102.78	10.11	-1.45	0.37	0.21	-6.914945438	4.68043E-12	2.3232E-11
SPD_0623	thiM	RpoD		hydroxyethylthiazole kinase	1823.83	10.83	-1.45	0.37	0.21	-6.866095555	6.59829E-12	3.22489E-11
SPD_1461	psaB	PsaR		manganese ABC transporter, ATP-binding protein	36440.91	15.15	-1.44	0.37	0.12	-11.79976674	3.91395E-32	6.92552E-31
SPD_1293	SPD_1293			acetyltransferase, GNAT family protein	1432.47	10.48	-1.44	0.37	0.15	-9.487523423	2.36588E-21	2.33052E-20
SPD_1339	atpF	RpoD		ATP synthase F0, B subunit	12217.91	13.58	-1.44	0.37	0.21	-6.965225641	3.27878E-12	1.65323E-11
SPD_0668	SPD_0668			hypothetical protein	1412.43	10.46	-1.43	0.37	0.15	-9.633139917	5.79317E-22	5.98418E-21
SPD_0907	hemK			HemK protein	4995.68	12.29	-1.43	0.37	0.16	-9.03873538	1.58495E-19	1.40876E-18
SPD_1548	gmk			guanylate kinase	2453.08	11.26	-1.43	0.37	0.19	-7.603611745	2.87978E-14	1.74707E-13
SPD_1869	SPD_1869			membrane protein, putative	2324.77	11.18	-1.43	0.37	0.19	-7.421641701	1.15677E-13	6.57915E-13
SPD_1319	SPD_1319			hypothetical protein	101.33	6.66	-1.43	0.37	0.29	-4.858737736	1.18136E-06	3.47321E-06
SPD_0648	comEB	RpoD		cytidine and deoxycytidylate deaminase family protein	132.26	7.05	-1.43	0.37	0.30	-4.748255653	2.05179E-06	5.76612E-06
SPD_0119	SPD_0119	RitR		membrane protein, putative	1230.96	10.27	-1.42	0.37	0.18	-7.834698912	4.69968E-15	3.01378E-14
SPD_1438	cadD			cadmium resistance transporter, putative	8913.28	13.12	-1.42	0.37	0.20	-7.01443267	2.30884E-12	1.17658E-11
SPD_1080	SPD_1080			type II restriction endonuclease, putative	2373.35	11.21	-1.41	0.38	0.15	-9.267937799	1.8978E-20	1.7436E-19
SPD_1156	efeB			Dyp-type peroxidase family protein	181.57	7.50	-1.41	0.38	0.27	-5.161185092	2.45391E-07	7.92133E-07
SPD_1128	tacF			polysaccharide biosynthesis protein, putative	1438.34	10.49	-1.40	0.38	0.17	-8.066797197	7.21663E-16	4.90782E-15
SPD_1981	SPD_1981			IgA1 protease	508.09	8.99	-1.40	0.38	0.21	-6.577475332	4.78503E-11	2.18761E-10
SPD_0576	ywlG			conserved hypothetical protein TIGR01440	6787.37	12.73	-1.39	0.38	0.13	-10.40263529	2.41169E-25	2.99269E-24
SPD_0280	celR	CelR	CcpA, RpoD	transcriptional regulator, putative	156.24	7.29	-1.39	0.38	0.27	-5.093127436	3.52205E-07	1.11067E-06
SPD_0338	SPD_0338			hypothetical protein	249.01	7.96	-1.38	0.38	0.20	-6.839488747	7.94763E-12	3.8548E-11
SPD_2065	comC1	ComE		competence-stimulating peptide type 1	35124.02	15.10	-1.38	0.38	0.23	-5.949345849	2.69216E-09	1.05209E-08
SPD_1452	SPD_1452			membrane protein, putative	78.20	6.29	-1.38	0.38	0.31	-4.434813053	9.21522E-06	2.39596E-05
SPD_0649	upp			uracil phosphoribosyltransferase	4057.92	11.99	-1.37	0.39	0.17	-8.027580663	9.94136E-16	6.73686E-15
SPD_0678	rimM	RitR		16S rRNA processing protein RimM	3361.61	11.71	-1.37	0.39	0.17	-7.998186867	1.26265E-15	8.43677E-15
SPD_0475	pncP	BlpR		CAAX amino terminal protease family protein	25334.29	14.63	-1.37	0.39	0.17	-7.837405457	4.59951E-15	2.95948E-14
SPD_1260	SPD_1260			type II DNA modification methyltransferase, putative	1290.63	10.33	-1.37	0.39	0.32	-4.247199592	2.16459E-05	5.42141E-05
SPD_0789	pfkA	CcpA		6-phosphofructokinase	13150.53	13.68	-1.36	0.39	0.16	-8.723319166	2.70163E-18	2.20633E-17
SPD_0976	rex			Redox-sensitive transcriptional regulator Rex	1186.52	10.21	-1.36	0.39	0.21	-6.325404408	2.5257E-10	1.09199E-09
SPD_1964	rpmG			ribosomal protein L33	4794.57	12.23	-1.36	0.39	0.28	-4.885512158	1.0316E-06	3.06593E-06
SPD_1384	mntE			cation efflux family protein	2101.62	11.04	-1.35	0.39	0.13	-10.0227928	1.21034E-23	1.41034E-22
SPD_1908	pnpR			response regulator	5221.24	12.35	-1.35	0.39	0.14	-9.726948783	2.31431E-21	2.47075E-21
SPD_1450	mntR			iron-dependent transcriptional regulator	1145.65	10.16	-1.34	0.40	0.19	-7.128865694	1.01199E-12	5.372E-12
SPD_0733	coaA	CcpA		pantothenate kinase	493.94	8.95	-1.34	0.40	0.22	-6.118665713	9.43621E-10	3.86137E-09
SPD_0566	SPD_0566			hypothetical protein	443.07	8.79	-1.34	0.40	0.22	-5.952380655	2.6427E-09	1.03569E-08
SPD_0139	SPD_0139			glycosyl transferase, group 2 family protein	141.56	7.15	-1.34	0.40	0.25	-5.467071014	4.57533E-08	1.59261E-07
SPD_1850	yidC2			SpoIIIJ family protein	2932.12	11.52	-1.33	0.40	0.16	-8.445607176	3.02469E-17	2.26674E-16
SPD_0103	sdhB			L-serine dehydratase, iron-sulfur-dependent, beta subunit	2335.85	11.19	-1.33	0.40	0.18	-7.477640371	7.56689E-14	4.42212E-13
SPD_1943	SPD_1943			hypothetical protein	1612.43	10.66	-1.33	0.40	0.30	-4.432884819	9.29805E-06	2.41421E-05
SPD_0944	SPD_0944			hypothetical protein	35.18	5.14	-1.33	0.40	0.46	-2.902677984	0.003699869	0.006911485
SPD_0095	ptvA	PtvR	CcpA, RpoD	hypothetical protein	2315.08	11.18	-1.32	0.40	0.18	-7.185628411	6.68988E-13	3.60123E-12
SPD_0873	SPD_0873			hypothetical protein	1719.07	10.75	-1.32	0.40	0.20	-6.731543326	1.67873E-11	7.98022E-11
SPD_0807	SPD_0807			IS1239, transposase, putative	257.60	8.01	-1.32	0.40	0.21	-6.228583593	4.70671E-10	1.95959E-09
SPD_0760	dnaX			DNA polymerase III, gamma and tau subunits	7304.39	12.83	-1.30	0.41	0.13	-9.617709056	6.73136E-22	6.87895E-21
SPD_1796	SPD_1796			L-asparaginase, putative	808.92	9.66	-1.30	0.41	0.16	-8.073807223	6.81394E-16	4.65052E-15
SPD_0532	recJ			single-stranded-DNA-specific exonuclease RecJ	3888.36	11.92	-1.30	0.41	0.17	-7.781980938	7.13976E-15	4.51959E-14
SPD_1068	udk			uridine kinase	739.59	9.53	-1.29	0.41	0.17	-7.69796529	1.38253E-14	8.57796E-14
SPD_0645	SPD_0645			hypothetical protein	993.61	9.96	-1.27	0.41	0.14	-9.054114394	1.3768E-19	1.22947E-18
SPD_1215	amyA2	MalR		alpha-amylase	824.82	9.69	-1.27	0.41	0.22	-5.695024064	1.23355E-08	4.53328E-08
SPD_0745	plsY			membrane protein, putative	1359.16	10.41	-1.27	0.41	0.23	-5.614044375	1.97651E-08	7.12664E-08
SPD_1342	SPD_1342			IS1239, transposase, putative	864.33	9.76	-1.26	0.42	0.15	-8.655580368	4.9041E-18	3.95432E-17
SPD_0719	glnP4	ArgR	RpoD	amino acid ABC transporter, permease protein	2380.32	11.22	-1.26	0.42	0.15	-8.318529166	8.90616E-17	6.44684E-16
SPD_1126	tarJ	CcpA		alcohol dehydrogenase, zinc-containing	5519.79	12.43	-1.26	0.42	0.16	-8.123640083	4.52406E-16	3.10988E-15
SPD_1635	galR	GalR		galactose operon repressor	362.67	8.50	-1.26	0.42	0.17	-7.301557615	2.84455E-13	1.56205E-12
SPD_0732	rpsT			ribosomal protein S20	1644.46	10.68	-1.26	0.42	0.18	-6.985802667	2.75273E-12	1.39906E-11
SPD_1526	SPD_1526	GntR	RpoD	membrane protein, putative	8675.66	13.08	-1.26	0.42	0.29	-4.275744379	1.905E-05	4.8027E-05
SPD_1716	SPD_1716			hypothetical protein	348.83	8.45	-1.25	0.42	0.17	-7.397586402	1.38682E-13	7.81774E-13
SPD_1263	SPD_1263			ABC transporter, ATP-binding/permease protein	2284.50	11.16	-1.25	0.42	0.21	-5.865102248	4.48856E-09	1.71553E-08
SPD_0885	ccdA-2			cytochrome c-type biogenesis protein CcdA	4942.93	12.27	-1.25	0.42	0.29	-4.339998398	1.42484E-05	3.62565E-05
SPD_0380	fabH	FabT	WalR	3-oxoacyl-(acyl-carrier-protein) synthase III	24978.26	14.61	-1.24	0.42	0.12	-10.35992271	3.77267E-25	4.65133E-24
SPD_1672	tacL	RafR	RpoD	membrane protein, putative	2299.48	11.17	-1.24	0.42	0.13	-9.346976533	9.0189E-21	8.61755E-20
SPD_1623	SPD_1623			hypothetical protein	1754.62	10.78	-1.24	0.42	0.15	-8.405704465	4.25301E-17	3.1021E-16
SPD_0402	asp23			hypothetical protein	2314.13	11.18	-1.24	0.42	0.16	-7.839918337	4.5084E-15	2.91066E-14
SPD_1249	SPD_1249			putative acetyltransferase	753.31	9.56	-1.24	0.42	0.18	-6.88752693	5.67706E-12	2.7961E-11
SPD_0251	rpsL			ribosomal protein S12	23380.79	14.51	-1.23	0.43	0.18	-6.963016808	3.33062E-12	1.67495E-11
SPD_0761	SPD_0761			hypothetical protein	497.06	8.96	-1.23	0.43	0.21	-5.73096435	9.98613E-09	3.73454E-08
SPD_0012	hpt			hypoxanthine phosphoribosyltransferase	2846.28	11.47	-1.23	0.43	0.22	-5.500876785	3.77907E-08	1.33244E-07
SPD_0988	SPD_0988			integral membrane protein	766.74	9.58	-1.22	0.43	0.16	-7.688792769	1.4853E-14	9.15614E-14
SPD_0339	gpsB			hypothetical protein	2290.25	11.16	-1.22	0.43	0.16	-7.421897638	1.15454E-13	6.57915E-13
SPD_1297	pdxS			pyridoxine biosynthesis protein	13692.46	13.74	-1.21	0.43	0.15	-8.016308554	1.08971E-15	7.33249E-15
SPD_0243	uppS			undecaprenyl diphosphate synthase	5719.76	12.48	-1.21	0.43	0.16	-7.349290362	1.99262E-13	1.10695E-12
SPD_1224	budA			alpha-acetolactate decarboxylase	1846.13	10.85	-1.21	0.43	0.18	-6.679808815	2.39254E-11	1.12338E-10
SPD_0114	SPD_0114			hypothetical protein	1304.73	10.35	-1.21	0.43	0.20	-5.980002528	2.23134E-09	8.88353E-09
SPD_1381	def2	ComE		polypeptide deformylase	4784.25	12.22	-1.21	0.43	0.25	-4.878710779	1.06782E-06	3.16371E-06
SPD_1278	cppA			C3-degrading proteinase	1538.31	10.59	-1.20	0.44	0.15	-7.743981644	9.63509E-15	6.0568E-14
SPD_0076	trkH			potassium uptake protein, Trk family protein	8010.67	12.97	-1.20	0.44	0.16	-7.613587837	2.6659E-14	1.62765E-13
SPD_0477	trmB			tRNA (guanine-N(7)-)-methyltransferase	7053.70	12.78	-1.20	0.44	0.16	-7.455825425	8.93069E-14	5.1874E-13
SPD_0124	SPD_0124			membrane protein, putative	387.86	8.60	-1.20	0.44	0.18	-6.572747947	4.9395E-11	2.25284E-10
SPD_2052	SPD_2052	CcpA		hypothetical protein	4911.34	12.26	-1.19	0.44	0.14	-8.595368953	8.29977E-18	6.47382E-17
SPD_1089	coaC			phosphopantothenoylcysteine decarboxylase	1923.81	10.91	-1.19	0.44	0.18	-6.612848179	3.76995E-11	1.74863E-10
SPD_0379	fabT	FabT	WalR	transcriptional regulator, MarR family protein	17170.15	14.07	-1.18	0.44	0.12	-9.631813696	5.86844E-22	6.02935E-21
SPD_1086	mutY	RitR	RpoD	A/G-specific adenine glycosylase	3098.90	11.60	-1.18	0.44	0.14	-8.629212056	6.17761E-18	4.9395E-17
SPD_0123	SPD_0123			hypothetical protein	674.57	9.40	-1.18	0.44	0.16	-7.44943903	9.37379E-14	5.42828E-13
SPD_1837	SPD_1837			phosphotyrosine protein phosphatase	1360.63	10.41	-1.18	0.44	0.17	-7.11358422	1.13067E-12	5.95642E-12
SPD_0011	tilS			tRNA(Ile)-lysidine synthetase	6283.50	12.62	-1.18	0.44	0.25	-4.681994184	2.84098E-06	7.85688E-06
SPD_0806	SPD_0806			hypothetical protein	85.02	6.41	-1.18	0.44	0.34	-3.510314991	0.000447576	0.00094406
SPD_0945	SPD_0945			AMP-binding enzyme, putative	36.96	5.21	-1.18	0.44	0.38	-3.079645243	0.002072473	0.003984402
SPD_1766	coaD			pantetheine-phosphate adenylyltransferase	2710.80	11.40	-1.17	0.44	0.20	-5.941794239	2.81919E-09	1.09948E-08
SPD_0316	cps2B	CpsR	RpoD, VncR	tyrosine-protein phosphatase CpsB	21281.41	14.38	-1.17	0.44	0.20	-5.926347577	3.09747E-09	1.2031E-08
SPD_1255	SPD_1255			ABC transporter, ATP-binding protein	511.92	9.00	-1.17	0.44	0.33	-3.524396528	0.000424449	0.000901284
SPD_1715	SPD_1715			hypothetical protein	710.55	9.47	-1.15	0.45	0.15	-7.725409267	1.11495E-14	6.96294E-14
SPD_0582	SPD_0582			hypothetical protein	1704.46	10.74	-1.15	0.45	0.15	-7.585279337	3.31772E-14	1.9813E-13
SPD_1401	folA	CcpA		dihydrofolate reductase	3588.95	11.81	-1.15	0.45	0.17	-6.752297977	1.45522E-11	6.96972E-11
SPD_1160	SPD_1160			ABC transporter, ATP-binding protein	2012.66	10.97	-1.15	0.45	0.24	-4.752624929	2.00793E-06	5.66787E-06
SPD_1942	SPD_1942			hypothetical protein	46.03	5.52	-1.15	0.45	0.35	-3.269685312	0.001076672	0.002163533
SPD_0911	SPD_0911			hypothetical protein	9714.08	13.25	-1.13	0.46	0.12	-9.364873976	7.61411E-21	7.34877E-20
SPD_0980	prs2			ribose-phosphate pyrophosphokinase	2917.09	11.51	-1.13	0.46	0.13	-8.42627614	3.5684E-17	2.6329E-16
SPD_1343	SPD_1343			acetyltransferase, GNAT family protein	1543.21	10.59	-1.13	0.46	0.14	-8.003262456	1.21165E-15	8.12445E-15
SPD_0767	dacC			penicillin-binding protein 3/D-alanyl-D-alanine carboxypeptidas	1513.76	10.56	-1.13	0.46	0.15	-7.62627535	2.41633E-14	1.48E-13
SPD_0982	SPD_0982	CcpA	RpoD	pyrophosphokinase family protein	1891.45	10.89	-1.13	0.46	0.21	-5.364378386	8.12285E-08	2.7377E-07
SPD_1143	SPD_1143			hypothetical protein	694.38	9.44	-1.13	0.46	0.22	-5.107848901	3.25847E-07	1.03697E-06
SPD_0122	SPD_0122			hypothetical protein	645.00	9.33	-1.12	0.46	0.19	-5.967198147	2.41362E-09	9.5107E-09
SPD_1898	SPD_1898			hypothetical protein	649.43	9.34	-1.12	0.46	0.23	-4.956753874	7.16807E-07	2.17777E-06
SPD_1286	trmH			TrmH family RNA methyltransferase group 3	1530.60	10.58	-1.11	0.46	0.15	-7.597051004	3.02955E-14	1.83211E-13
SPD_0871	ebsC			regulatory protein, putative	732.01	9.52	-1.11	0.46	0.15	-7.49372276	6.69471E-14	3.92441E-13
SPD_0239	SPD_0239			acetyltransferase, GNAT family protein	911.01	9.83	-1.11	0.46	0.15	-7.249420726	4.18558E-13	2.27881E-12
SPD_0431	SPD_0431	CmhR		hypothetical protein	1075.73	10.07	-1.11	0.46	0.16	-6.872018654	6.32997E-12	3.10966E-11
SPD_0374	shetA	ComE	CcpA	exfoliative toxin, putative	1787.24	10.80	-1.11	0.46	0.19	-5.869378571	4.37432E-09	1.67521E-08
SPD_1310	SPD_1310			hypothetical protein	1175.63	10.20	-1.11	0.46	0.23	-4.791881517	1.65224E-06	4.7126E-06
SPD_0590	SPD_0590			rhodanese-like domain	1452.53	10.50	-1.10	0.47	0.14	-7.664914391	1.78951E-14	1.0996E-13
SPD_1950	hisS			histidyl-tRNA synthetase	3142.11	11.62	-1.10	0.47	0.15	-7.420196594	1.16947E-13	6.6316E-13
SPD_1306	SPD_1306			hypothetical protein	941.80	9.88	-1.10	0.47	0.15	-7.394343945	1.42108E-13	7.98731E-13
SPD_1484	ddlA			D-alanine-D-alanine ligase	2502.67	11.29	-1.10	0.47	0.16	-6.764859444	1.33439E-11	6.40707E-11
SPD_1338	atpH	RpoD		ATP synthase F1, delta subunit	6785.59	12.73	-1.10	0.47	0.16	-6.255332833	3.96669E-10	1.67337E-09
SPD_1049	lacT	LacT	CcpA	transcription antiterminator LacT	1422.93	10.47	-1.10	0.47	0.19	-5.802860582	6.5193E-09	2.46213E-08

Table S1 continued

					WT HOCl vs control							
Locus	Gene Symbol	Regulon	Further Regulon	Function	Base-Mean	A-value	M-value	Fold-change	Standard error	Wald statistic	P-value	Adjusted P-value
SPD_2069	**parB**	**CiaR**		**SpoJ protein**	**3376.69**	**11.72**	**-1.10**	**0.47**	**0.32**	**-3.475853956**	**0.00050923**	**0.001058909**
SPD_1999	**adcC**	**AdcR**		**zinc ABC transporter, ATP-binding protein**	**3914.01**	**11.93**	**-1.09**	**0.47**	**0.17**	**-6.419288629**	**1.36913E-10**	**5.98719E-10**
SPD_1487	**nanR**			**phosphosugar-binding transcriptional regulator, putative**	**5006.16**	**12.29**	**-1.09**	**0.47**	**0.20**	**-5.39200796**	**6.96747E-08**	**2.37765E-07**
SPD_1523	**nrdR**	**RpoD**		**transcriptional regulator, NrdR family protein**	**1292.19**	**10.34**	**-1.08**	**0.47**	**0.15**	**-7.28091922**	**3.31553E-13**	**1.81028E-12**
SPD_2032	**pde1**			**DHH subfamily 1 protein**	**7105.97**	**12.79**	**-1.08**	**0.47**	**0.16**	**-6.80787697**	**9.90495E-12**	**4.79199E-11**
SPD_0749	**livE**	**CodY**		**branched-chain amino acid aminotransferase**	**8433.49**	**13.04**	**-1.08**	**0.47**	**0.17**	**-6.194747798**	**5.83784E-10**	**2.40953E-09**
SPD_0346	**mvk**			**mevalonate kinase**	**838.85**	**9.71**	**-1.08**	**0.47**	**0.18**	**-5.887579662**	**3.91892E-09**	**1.50685E-08**
SPD_1718	**SPD_1718**			**hypothetical protein**	**1955.91**	**10.93**	**-1.08**	**0.47**	**0.20**	**-5.537951611**	**3.0603E-08**	**1.09517E-07**
SPD_0694	**SPD_0694**			**hypothetical protein**	**201.59**	**7.66**	**-1.08**	**0.47**	**0.20**	**-5.510021931**	**3.58789E-08**	**1.26737E-07**
SPD_1307	**SPD_1307**			**hypothetical protein**	**874.79**	**9.77**	**-1.07**	**0.48**	**0.16**	**-6.632611696**	**3.29799E-11**	**1.54094E-10**
SPD_1953	**SPD_1953**			**hypothetical protein**	**103.19**	**6.69**	**-1.07**	**0.48**	**0.25**	**-4.239577369**	**2.23941E-05**	**5.60146E-05**
SPD_1965	**pcpA**	**PsaR**	**CodY**	**choline binding protein PcpA**	**8130.15**	**12.99**	**-1.07**	**0.48**	**0.28**	**-3.860939882**	**0.000112952**	**0.000259748**
SPD_0230	**deoR**			**transcriptional regulator, DeoR family protein**	**273.08**	**8.09**	**-1.07**	**0.48**	**0.30**	**-3.603164038**	**0.000314367**	**0.000681128**
SPD_0469	**blpH**	**BlpR**		**histidine kinase BlpH, putative**	**7293.02**	**12.83**	**-1.06**	**0.48**	**0.20**	**-5.197733676**	**2.01733E-07**	**6.57869E-07**
SPD_0117	**SPD_0117**			**hypothetical protein**	**949.82**	**9.89**	**-1.06**	**0.48**	**0.21**	**-5.077573437**	**3.82286E-07**	**1.20156E-06**
SPD_0704	**SPD_0704**			**hypothetical protein**	**3629.44**	**11.83**	**-1.05**	**0.48**	**0.13**	**-7.9294305**	**2.20153E-15**	**1.44575E-14**
SPD_0115	**SPD_0115**			**hypothetical protein**	**9832.28**	**13.26**	**-1.05**	**0.48**	**0.16**	**-6.704457759**	**2.02156E-11**	**9.58609E-11**
SPD_1907	**SPD_1907**			**hypothetical protein**	**3069.75**	**11.58**	**-1.04**	**0.49**	**0.17**	**-6.24037454**	**4.36524E-10**	**1.82538E-09**
SPD_1462	**psaC**	**PsaR**		**manganese ABC transporter, permease protein, putative**	**41036.73**	**15.32**	**-1.04**	**0.49**	**0.17**	**-6.171913414**	**6.74684E-10**	**2.77274E-09**
SPD_1836	**SPD_1836**			**hypothetical protein**	**1586.45**	**10.63**	**-1.04**	**0.49**	**0.22**	**-4.807453525**	**1.52865E-06**	**4.40611E-06**
SPD_0423	**xylR**	**XylR**	**CcpA**	**ROK family protein**	**1070.65**	**10.06**	**-1.04**	**0.49**	**0.24**	**-4.420073444**	**9.86674E-06**	**2.55147E-05**
SPD_0651	**pyrK**	**PyrR**		**dihydroorotate dehydrogenase electron transfer subunit**	**412.71**	**8.69**	**-1.04**	**0.49**	**0.24**	**-4.384275138**	**1.16373E-05**	**2.99714E-05**
SPD_0848	**rpmI**			**ribosomal protein L35**	**6282.29**	**12.62**	**-1.04**	**0.49**	**0.26**	**-3.942757371**	**8.05501E-05**	**0.000188641**
SPD_0968	**SPD_0968**			**acetyltransferase, GNAT family protein**	**3586.86**	**11.81**	**-1.03**	**0.49**	**0.12**	**-8.451478713**	**2.87636E-17**	**2.16407E-16**
SPD_1032	**ung**			**uracil-DNA glycosylase**	**1696.06**	**10.73**	**-1.03**	**0.49**	**0.18**	**-5.830675587**	**5.52034E-09**	**2.09729E-08**
SPD_1706	**SPD_1706**			**hypothetical protein**	**5431.77**	**12.41**	**-1.03**	**0.49**	**0.18**	**-5.632633311**	**1.77479E-08**	**6.4357E-08**
SPD_0567	**ytqB**			**rRNA methylase, putative**	**654.26**	**9.35**	**-1.03**	**0.49**	**0.19**	**-5.525642367**	**3.28282E-08**	**1.17042E-07**
SPD_1717	**SPD_1717**			**membrane protein, putative**	**1108.08**	**10.11**	**-1.03**	**0.49**	**0.19**	**-5.524751516**	**3.29952E-08**	**1.17419E-07**
SPD_0215	**infA**			**translation initiation factor IF-1**	**50204.70**	**15.62**	**-1.03**	**0.49**	**0.20**	**-5.072406096**	**3.92817E-07**	**1.23263E-06**
SPD_2054	**recF**			**recF protein**	**873.65**	**9.77**	**-1.03**	**0.49**	**0.24**	**-4.350003811**	**1.36135E-05**	**3.478E-05**
SPD_1665	**treR**	**TreR**	**CcpA**	**trehalose operon repressor**	**153.22**	**7.26**	**-1.03**	**0.49**	**0.26**	**-3.893926827**	**9.86344E-05**	**0.00022875**
SPD_0857	**era**			**GTP-binding protein Era**	**2777.22**	**11.44**	**-1.02**	**0.49**	**0.16**	**-6.505395128**	**7.74894E-11**	**3.46797E-10**
SPD_1082	**relB2**			**Replicon stabilization protein RelB2**	**276.85**	**8.11**	**-1.02**	**0.49**	**0.20**	**-5.155898766**	**2.52417E-07**	**8.13439E-07**
SPD_1344	**SPD_1344**			**hypothetical protein**	**201.49**	**7.65**	**-1.02**	**0.49**	**0.25**	**-4.073542745**	**4.63033E-05**	**0.000111443**
SPD_0310	**SPD_0310**			**hypothetical protein**	**7240.64**	**12.82**	**-1.01**	**0.50**	**0.20**	**-4.981182808**	**6.31968E-07**	**1.93851E-06**
SPD_0646	**SPD_0646**			**hypothetical protein**	**3147.18**	**11.62**	**-1.01**	**0.50**	**0.22**	**-4.507298254**	**6.56583E-06**	**1.73785E-05**
SPD_0910	**glyA**			**serine hydroxymethyltransferase**	**16449.38**	**14.01**	**-1.00**	**0.50**	**0.14**	**-7.427141754**	**1.10969E-13**	**6.36825E-13**
SPD_1769	**SPD_1769**	**CiaR**		**membrane protein, putative**	**7633.34**	**12.90**	**-1.00**	**0.50**	**0.16**	**-6.361372487**	**1.99959E-10**	**8.70436E-10**
SPD_1617	**pfbA**			**cell wall surface anchor family protein**	**508.71**	**8.99**	**-1.00**	**0.50**	**0.20**	**-5.015561811**	**5.28787E-07**	**1.64044E-06**
SPD_1236	**spx**			**regulatory protein Spx**	**1035.77**	**10.02**	**-1.00**	**0.50**	**0.21**	**-4.740645905**	**2.13038E-06**	**5.96944E-06**
SPD_0061	**SPD_0061**			**hypothetical protein**	**797.87**	**9.64**	**-1.00**	**0.50**	**0.22**	**-4.551109177**	**5.33638E-06**	**1.43027E-05**
SPD_1451	**SPD_1451**			**hypothetical protein**	**220.15**	**7.78**	**-1.00**	**0.50**	**0.25**	**-4.039007317**	**5.36779E-05**	**0.000127903**
SPD_0196	rplB			ribosomal protein L2	35355.89	15.11	0.96	1.95	0.12	7.774774607	7.55819E-15	4.7669E-14
SPD_0030	SPD_0030	ComX		Carbonic anhydrase	1507.16	10.56	-0.97	0.51	0.13	-7.471963844	7.90067E-14	4.6031E-13
SPD_0705	yoaA			DnaQ family exonuclease/DinG family helicase, putative	5592.13	12.45	-0.99	0.50	0.14	-7.296329388	2.95724E-13	1.61928E-12
SPD_1552	SPD_1552			hypothetical protein	4926.62	12.27	0.96	1.95	0.14	7.030328081	2.06048E-12	1.05849E-11
SPD_1823	gap	Rex	CodY	glyceraldehyde-3-phosphate dehydrogenase, type I	132500.19	17.02	0.99	1.99	0.14	6.987274976	2.80277E-12	1.42071E-11
SPD_0621	lctO	CcpA	RpoD	lactate oxidase	16656.30	14.02	0.92	1.89	0.13	6.962066472	3.35317E-12	1.68187E-11
SPD_0784	SPD_0784			type I restriction-modification system, R subunit, putative	9117.38	13.15	-0.84	0.56	0.13	-6.697424403	2.12125E-11	1.00339E-10
SPD_1212	ywbD			hypothetical protein	4206.25	12.04	-0.87	0.55	0.13	-6.59342982	4.2978E-11	1.9743E-10
SPD_1005	glgB	CcpA		1,4-alpha-glucan branching enzyme	1379.70	10.43	0.91	1.88	0.14	6.563184962	5.26704E-11	2.39651E-10
SPD_1794	SPD_1794			Cof family protein	3017.54	11.56	-0.89	0.54	0.14	-6.559461726	5.40024E-11	2.45127E-10
SPD_0669	rlmN			radical SAM enzyme, Cfr family protein	2973.89	11.54	-0.83	0.56	0.13	-6.556789361	5.49786E-11	2.48967E-10
SPD_0331	rfbD	VncR		dTDP-4-dehydrorhamnose reductase	25513.82	14.64	0.84	1.79	0.13	6.535425919	6.34288E-11	2.86554E-10
SPD_1152	fld			flavodoxin	1339.96	10.39	-0.95	0.52	0.15	-6.490480972	8.55628E-11	3.81303E-10
SPD_0330	rfbB	CpsR	RpoD, RitR, VncR	dTDP-glucose 4,6-dehydratase	31627.49	14.95	0.83	1.78	0.13	6.490417872	8.55986E-11	3.81303E-10
SPD_0006	mfd			transcription-repair coupling factor	4958.36	12.28	0.93	1.91	0.14	6.46303622	1.02623E-10	4.53963E-10
SPD_2004	dltB	CiaR		protein DltB	3008.01	11.55	-0.89	0.54	0.14	-6.313094093	2.73511E-10	1.17721E-09
SPD_1382	SPD_1382			glutathione S-transferase family protein	3607.57	11.82	0.79	1.73	0.13	6.290037002	3.1739E-10	1.35382E-09
SPD_1541	SPD_1541			membrane protein, putative	832.44	9.70	-0.96	0.51	0.15	-6.268123781	3.65424E-10	1.54497E-09
SPD_1085	vicR	WalR	RpoD	DNA-binding response regulator	3209.46	11.65	-0.83	0.56	0.13	-6.217383982	5.05512E-10	2.10007E-09
SPD_1714	SPD_1714			thioredoxin family protein	1645.97	10.68	-0.90	0.54	0.15	-6.172123058	6.7379E-10	2.77274E-09
SPD_0860	pmrA			multi-drug resistance efflux pump	1641.21	10.68	-0.87	0.55	0.14	-6.106297848	1.01969E-09	4.146E-09
SPD_1400	SPD_1400			hypothetical protein	981.34	9.94	-0.95	0.52	0.16	-6.07771664	1.21906E-09	4.94612E-09
SPD_1958	tktN			transketolase N-terminal subunit	558.85	9.13	0.96	1.95	0.16	6.073875152	1.2486E-09	5.05524E-09
SPD_0246	proS			prolyl-tRNA synthetase	17965.20	14.13	0.81	1.75	0.13	6.058454789	1.37435E-09	5.55262E-09
SPD_0329	rfbC	CpsR	VncR	dTDP-4-dehydrorhamnose 3,5-epimerase, putative	9077.50	13.15	0.72	1.65	0.12	6.046986612	1.4758E-09	5.93738E-09
SPD_1771	yjfA			SpoU rRNA Methylase family protein	2216.05	11.11	-0.89	0.54	0.15	-5.993271979	2.05666E-09	8.22212E-09
SPD_1195	hom			homoserine dehydrogenase	8793.29	13.10	-0.77	0.59	0.13	-5.969171402	2.38461E-09	9.41529E-09
SPD_0858	mutM			formamidopyrimidine-DNA glycosylase	2967.52	11.54	-0.83	0.56	0.14	-5.963148991	2.47423E-09	9.7289E-09
SPD_0269	folP			dihydropteroate synthase	2341.90	11.19	-0.99	0.50	0.17	-5.95225151	2.64479E-09	1.03569E-08
SPD_1079	SPD_1079			type II restriction endonuclease, putative	7855.73	12.94	-0.80	0.57	0.14	-5.925375575	3.11584E-09	1.20778E-08
SPD_0998	SPD_0998			ABC transporter, ATP-binding protein	6253.18	12.61	-0.85	0.55	0.14	-5.92346773	3.15223E-09	1.21941E-08
SPD_0818	cmbR			transcriptional regulator, LysR family protein	1682.20	10.72	-0.94	0.52	0.16	-5.893479995	3.78146E-09	1.45693E-08
SPD_0887	yfnA	ArgR	RpoD	amino acid permease family protein	2263.00	11.14	-0.89	0.54	0.15	-5.879233552	4.1217E-09	1.58164E-08
SPD_0028	SPD_0028	ComX		phosphoglycerate mutase family protein	1746.55	10.77	0.82	1.77	0.14	5.837501594	5.29894E-09	2.02121E-08
SPD_0031	SPD_0031			membrane protein, putative	2604.93	11.35	-0.83	0.56	0.14	-5.82510125	5.7078E-09	2.16421E-08
SPD_0782	SPD_0782			type I restriction-modification system, M subunit, putative	1875.53	10.87	-0.92	0.53	0.16	-5.824355613	5.73334E-09	2.16959E-08
SPD_1362	SPD_1362			hypothetical protein	1838.57	10.84	0.92	1.89	0.16	5.79613271	6.78616E-09	2.55786E-08
SPD_1798	SPD_1798	RitR	RpoD	DNA-binding response regulator	878.52	9.78	0.89	1.85	0.15	5.720332221	1.06316E-08	3.96816E-08
SPD_0798	SPD_0798			membrane protein, putative	8057.47	12.98	-0.96	0.51	0.17	-5.717555159	1.08258E-08	4.03279E-08
SPD_0077	cabP			potassium uptake protein, Trk family protein	5168.73	12.34	-0.72	0.61	0.13	-5.708371933	1.14062E-08	4.22427E-08
SPD_0511	metF	CmhR	CmbR	5,10-methylenetetrahydrofolate reductase	649.76	9.34	0.86	1.82	0.15	5.695957455	1.22681E-08	4.51723E-08
SPD_0776	SPD_0776			aminotransferase, class V	3313.91	11.69	-0.73	0.60	0.13	-5.65652333	1.5447E-08	5.66588E-08
SPD_1200	SPD_1200			glycosyl transferase, group 1 family protein	1955.62	10.93	-0.87	0.55	0.15	-5.641351313	1.68721E-08	6.15315E-08
SPD_0382	fabK	FabT	RpoD, WalR	trans-2-enoyl-ACP reductase II	20808.78	14.34	-0.96	0.51	0.17	-5.638825423	1.71214E-08	6.23219E-08
SPD_0108	SPD_0108			amino acid ABC transporter, ATP-binding protein, putative	1190.62	10.22	0.85	1.80	0.15	5.633266195	1.76828E-08	6.42431E-08
SPD_1333	SPD_1333			hypothetical protein	6657.23	12.70	-0.84	0.56	0.15	-5.632079707	1.78049E-08	6.44417E-08
SPD_0965	SPD_0965			hypothetical protein	651.08	9.35	0.89	1.85	0.16	5.5593729	2.70746E-08	9.74379E-08
SPD_0218	rpoA	CodY		DNA-directed RNA polymerase, alpha subunit	47245.84	15.53	-0.80	0.57	0.14	-5.544091249	2.95485E-08	1.05942E-07
SPD_0815	SPD_0815			hydrolase, carbon-nitrogen family protein	2489.33	11.28	0.82	1.77	0.15	5.515940554	3.39114E-08	1.20325E-07
SPD_0263	manM	CcpA	CiaR	PTS system, mannose-specific IIC component	10281.92	13.33	0.87	1.83	0.16	5.519803543	3.39379E-08	1.20325E-07
SPD_0247	bglA			glycosyl hydrolase, family protein 1	1075.59	10.07	0.90	1.87	0.16	5.515260267	3.48264E-08	1.23247E-07
SPD_1197	tarQ			hypothetical protein	5715.65	12.48	0.65	1.57	0.12	5.500529883	3.78652E-08	1.3326E-07
SPD_0465	ecsB			ABC transporter, permease protein, putative	4568.37	12.16	0.78	1.72	0.14	5.490803741	4.00109E-08	1.40553E-07
SPD_0854	pavA			adherence and virulence protein A	2656.99	11.38	-0.99	0.50	0.18	-5.48249565	4.19367E-08	1.4651E-07
SPD_1060	lepA			GTP-binding protein LepA	13528.12	13.72	0.93	1.91	0.17	5.480430942	4.24291E-08	1.4796E-07
SPD_1292	ogt			methylated-DNA--protein-cysteine S-methyltransferase	1211.33	10.24	-0.78	0.58	0.14	-5.434405081	5.49796E-08	1.90682E-07
SPD_0309	luxS			S-ribosylhomocysteine lyase (autoinducer-2 production protein luxS	3385.14	11.73	-0.82	0.57	0.15	-5.425733122	5.77171E-08	1.99814E-07
SPD_1493	satC	NanR	CcpA, NiaR	sugar ABC transporter, permease protein	574.84	9.17	0.88	1.84	0.16	5.418266206	6.01798E-08	2.07341E-07
SPD_1247	queA	CcpA		S-adenosylmethionine:tRNA ribosyltransferase-isomerase	2249.62	11.14	-0.98	0.51	0.18	-5.415882605	6.09871E-08	2.09616E-07
SPD_1390	glmM			phosphoglucomutase/phosphomannomutase family protein	6240.01	12.61	0.76	1.69	0.14	5.415506138	6.11156E-08	2.0968E-07
SPD_1570	SPD_1570			hypothetical protein	1589.17	10.63	0.73	1.66	0.13	5.412374913	6.21943E-08	2.12999E-07
SPD_0969	SPD_0969			hypothetical protein	7898.65	12.95	-0.66	0.63	0.12	-5.40399779	6.51717E-08	2.22796E-07
SPD_0853	lytB	WalR	RpoD	endo-beta-N-acetylglucosaminidase precursor, putative	4399.33	12.10	-0.85	0.55	0.16	-5.385535004	7.22295E-08	2.45606E-07
SPD_1223	SPD_1223			membrane protein, putative	1189.93	10.22	-0.79	0.58	0.15	-5.372651835	7.7587E-08	2.62888E-07
SPD_1146	yidA			Cof family protein	1985.51	10.96	0.68	1.60	0.13	5.371122455	7.8248E-08	2.64658E-07
SPD_1662	SPD_1662	RpoD		hypothetical protein	1125.18	10.14	-0.78	0.58	0.15	-5.370740479	7.8414E-08	2.64751E-07
SPD_1250	nadE			NAD+ synthetase	3052.66	11.58	-0.87	0.55	0.16	-5.355069816	8.55234E-08	2.87738E-07
SPD_1096	uvrB			excinuclease ABC, B subunit	1994.49	10.96	-0.83	0.56	0.16	-5.346173059	8.98333E-08	3.01707E-07
SPD_0825	tmk			thymidylate kinase	616.17	9.27	-0.87	0.55	0.16	-5.343306501	9.12662E-08	3.05982E-07
SPD_0128	SPD_0128			MutT/nudix family protein	3778.34	11.88	0.72	1.65	0.14	5.33865748	9.36374E-08	3.13382E-07
SPD_0874	glmU			UDP-N-acetylglucosamine pyrophosphorylase	6626.66	12.69	-0.67	0.63	0.12	-5.334106781	9.6016E-08	3.20781E-07
SPD_0900	asd	CodY		aspartate-semialdehyde dehydrogenase	6750.60	12.72	-0.84	0.56	0.16	-5.331188639	9.7572E-08	3.2541E-07
SPD_1475	ylmH			YlmH protein	12708.38	13.63	-0.76	0.59	0.14	-5.330103591	9.81568E-08	3.2679E-07
SPD_0437	ribU			membrane protein, putative	2727.59	11.41	-0.77	0.59	0.15	-5.291533896	1.21295E-07	4.0242E-07
SPD_1522	dnaB			hypothetical protein	5072.22	12.31	-0.83	0.56	0.16	-5.289752093	1.22482E-07	4.05656E-07
SPD_1914	phoU	PnpR		phosphate transport system regulatory protein PhoU	271.17	8.08	0.96	1.95	0.18	5.262727618	1.41934E-07	4.69265E-07
SPD_1136	SPD_1136			putative ACR	2036.68	10.99	-0.72	0.61	0.14	-5.254917748	1.48091E-07	4.88403E-07
SPD_1913	pstB	PnpR		phosphate ABC transporter, ATP-binding protein	363.51	8.51	0.89	1.85	0.17	5.254740508	1.48233E-07	4.88403E-07
SPD_0720	glnQ4	ArgR	RpoD	amino acid ABC transporter, ATP-binding protein	3159.24	11.63	-0.72	0.61	0.14	-5.25282645	1.49783E-07	4.92659E-07
SPD_0788	dnaE			DNA polymerase III, alpha subunit	7277.26	12.83	-0.65	0.64	0.12	-5.237100722	1.63119E-07	5.34682E-07
SPD_2002	dltD	CiaR		undecaprenol-phosphate-poly(glycerophosphate subunit) D-alanine	4542.40	12.15	-0.74	0.60	0.14	-5.19514058	2.04565E-07	6.65969E-07
SPD_0859	coaE			dephospho-CoA kinase	1599.64	10.64	-0.81	0.57	0.16	-5.192698958	2.07267E-07	6.73618E-07
SPD_0814	aguA			agmatine deiminase	3305.04	11.69	0.80	1.74	0.15	5.175793852	2.26944E-07	7.35068E-07
SPD_2036	SPD_2036			conserved hypothetical protein TIGR00257	657.48	9.36	-0.92	0.53	0.18	-5.173452803	2.29807E-07	7.43082E-07
SPD_0762	sufC			FeS assembly ATPase SufC	14211.55	13.79	-0.69	0.62	0.13	-5.138527541	2.769E-07	8.89336E-07
SPD_1241	SPD_1241			hypothetical protein	3678.90	11.85	0.80	1.74	0.16	5.136258795	2.80262E-07	8.98624E-07
SPD_1125	pck	CcpA	RpoD	choline kinase	4136.93	12.01	-0.85	0.55	0.17	-5.115003779	3.13735E-07	1.00427E-06
SPD_1145	SPD_1145			hypothetical protein	2591.08	11.34	-0.88	0.54	0.17	-5.112444446	3.18017E-07	1.01627E-06
SPD_0729	SPD_0729			hemolysin-related protein	5100.69	12.32	0.85	1.80	0.17	5.107376114	3.26663E-07	1.03697E-06
SPD_1957	tktC			transketolase, C-terminal subunit	461.35	8.85	0.96	1.95	0.19	5.103687223	3.33099E-07	1.05564E-06
SPD_0579	cbpL			pneumococcal surface protein, putative	3391.24	11.73	0.63	1.55	0.12	5.100544071	3.38679E-07	1.07155E-06
SPD_0517	SPD_0517			hypothetical protein	8213.07	13.00	0.74	1.67	0.15	5.094150256	3.50309E-07	1.10651E-06
SPD_1121	SPD_1121			membrane protein, putative	1250.75	10.29	-0.76	0.59	0.15	-5.026265948	5.00122E-07	1.55911E-06
SPD_1416	murT			hypothetical protein	8381.79	13.03	-0.78	0.58	0.16	-5.021298589	5.13233E-07	1.59738E-06
SPD_1042	nrdE	NrdR	RpoD	ribonucleoside-diphosphate reductase, alpha subunit	24098.21	14.56	0.84	1.79	0.17	5.02023424	5.16085E-07	1.60364E-06
SPD_0598	murD			UDP-N-acetylmuramoylalanine--D-glutamate ligase	3378.00	11.72	-0.67	0.63	0.13	-5.000406018	5.72097E-07	1.77192E-06
SPD_1107	guaC			guanosine monophosphate reductase	1702.23	10.73	-0.92	0.53	0.18	-4.993455659	5.93084E-07	1.83395E-06
SPD_0220	SPD_0220			hypothetical protein	907.16	9.83	-0.93	0.52	0.19	-4.988370226	6.08908E-07	1.87984E-06

Table S1 continued

					WT HOCl vs control							
Locus	Gene Symbol	Regulon	Further Regulon	Function	Base-Mean	A-value	M-value	Fold-change	Standard error	Wald statistic	P-value	Adjusted P-value
SPD_1282	SPD_1282			hypothetical protein	661.83	9.37	-0.81	0.57	0.16	-4.985934274	6.16631E-07	1.89756E-06
SPD_1017	SPD_1017			hypothetical protein	1873.60	10.87	0.73	1.66	0.15	4.982623366	6.2728E-07	1.92722E-06
SPD_0771	lacR1	CcpA		lactose phosphotransferase system repressor	655.06	9.36	0.72	1.65	0.14	4.980059775	6.35646E-07	1.94667E-06
SPD_0916	piaB			iron-compound ABC transporter, permease protein	3429.34	11.74	-0.94	0.52	0.19	-4.973273442	6.58317E-07	2.01287E-06
SPD_1919	galU			UTP-glucose-1-phosphate uridylyltransferase	7272.99	12.83	0.81	1.75	0.16	4.971581335	6.6409E-07	2.02728E-06
SPD_1426	SPD_1426			membrane protein, putative	1952.99	10.93	-0.65	0.64	0.13	-4.968948836	6.73168E-07	2.05171E-06
SPD_1207	tyrA			prephenate dehydrogenase	8118.20	12.99	0.61	1.53	0.12	4.951471642	7.36544E-07	2.23064E-06
SPD_1540	SPD_1540			membrane protein, putative	992.84	9.96	-0.74	0.60	0.15	-4.950753104	7.39268E-07	2.23535E-06
SPD_0728	SPD_0728			hypothetical protein	1918.48	10.91	0.78	1.72	0.16	4.949464107	7.44181E-07	2.24665E-06
SPD_1564	SPD_1564	CodY		hypothetical protein	4489.69	12.13	-0.91	0.53	0.19	-4.925445736	8.41683E-07	2.52902E-06
SPD_0241	ruvB			Holliday junction DNA helicase RuvB	1360.27	10.41	-0.77	0.59	0.16	-4.922838338	8.52979E-07	2.55894E-06
SPD_0544	SPD_0544			hypothetical protein	232.68	7.86	0.95	1.93	0.19	4.917770005	8.75357E-07	2.62195E-06
SPD_0328	cps2L	CpsR	RpoD, VncR	glucose-1-phosphate thymidylyltransferase	17090.30	14.06	0.67	1.59	0.14	4.905086025	9.33864E-07	2.79282E-06
SPD_1735	SPD_1735			hypothetical protein	560.19	9.13	0.86	1.82	0.18	4.901915132	9.49068E-07	2.82944E-06
SPD_1465	SPD_1465			efflux ABC transporter, permease protein	2621.14	11.36	0.72	1.65	0.15	4.882779138	1.04601E-06	3.10392E-06
SPD_1528	qsrA	ComE	CcpA	ABC transporter, ATP-binding protein	19739.32	14.27	-0.87	0.55	0.18	-4.874209905	1.09245E-06	3.23168E-06
SPD_0708	SPD_0708			hydrolase, haloacid dehalogenase-like family protein	1106.33	10.11	-0.74	0.60	0.15	-4.867419621	1.13065E-06	3.33436E-06
SPD_0727	SPD_0727			hypothetical protein	3690.57	11.85	0.74	1.67	0.15	4.859466096	1.17703E-06	3.46579E-06
SPD_1061	pphA			serine/threonine protein phosphatase	5105.47	12.32	0.63	1.55	0.13	4.856496392	1.19481E-06	3.50734E-06
SPD_1478	ylmE			YlmE protein	10255.94	13.32	-0.57	0.67	0.12	-4.855897513	1.19843E-06	3.50836E-06
SPD_0448	glnA	GlnR		glutamine synthetase, type I	10131.29	13.31	-0.98	0.51	0.20	-4.855831467	1.19883E-06	3.50836E-06
SPD_0411	glnQ1			amino acid ABC transporter, ATP-binding protein	2525.60	11.30	0.84	1.79	0.17	4.855005716	1.20383E-06	3.51762E-06
SPD_1129	licD1			phosphotransferase LicD1	1054.68	10.04	-0.99	0.50	0.20	-4.85091205	1.22895E-06	3.58553E-06
SPD_1538	SPD_1538			hypothetical protein	664.13	9.38	-0.70	0.62	0.14	-4.848723827	1.24258E-06	3.61978E-06
SPD_0834	pyrH			uridylate kinase	4872.21	12.25	-0.64	0.64	0.13	-4.845575406	1.26245E-06	3.67207E-06
SPD_1472	ileS			isoleucyl-tRNA synthetase	9341.91	13.19	0.87	1.83	0.18	4.827292427	1.38402E-06	4.01954E-06
SPD_0336	pbp1A	CodY		penicillin-binding protein 1A	41623.59	15.35	0.81	1.75	0.17	4.815741632	1.46654E-06	4.24666E-06
SPD_1553	SPD_1553			hypothetical protein	3259.78	11.67	0.64	1.56	0.13	4.81572478	1.46667E-06	4.24666E-06
SPD_0864	tehB			tellurite resistance protein TehB	6278.87	12.62	0.66	1.58	0.14	4.813141466	1.48576E-06	4.29544E-06
SPD_0651	SPD_0651			hypothetical protein	997.30	9.96	-0.81	0.57	0.17	-4.807719082	1.52662E-06	4.40611E-06
SPD_1084	vicK	WalR	RpoD	sensory box sensor histidine kinase	14815.27	13.85	-0.63	0.65	0.13	-4.806774754	1.53385E-06	4.41443E-06
SPD_1044	lacR2			lactose phosphotransferase system repressor	5017.04	12.29	0.92	1.89	0.19	4.805750669	1.54172E-06	4.43041E-06
SPD_0926	SPD_0926			conserved hypothetical protein TIGR00147	1848.90	10.85	-0.82	0.57	0.17	-4.802041043	1.57056E-06	4.49977E-06
SPD_1984	ybbK	ComE		hypersensitive-induced reaction protein 4	6907.47	12.75	-0.84	0.56	0.18	-4.792106993	1.65039E-06	4.7126E-06
SPD_1667	amiF	CodY		oligopeptide ABC transporter, ATP-binding protein AmiF	11680.98	13.51	0.66	1.58	0.14	4.786596896	1.69633E-06	4.83113E-06
SPD_0961	lafA			glycosyl transferase, group 1	5620.17	12.46	0.67	1.59	0.14	4.779194868	1.75999E-06	5.00496E-06
SPD_1488	nanK	NanR	CcpA, NiaR	ROK family protein	299.35	8.23	0.97	1.96	0.20	4.77100158	1.83312E-06	5.20519E-06
SPD_1206	SPD_1206			hypothetical protein	1926.97	10.91	0.76	1.69	0.16	4.769832109	1.8438E-06	5.22773E-06
SPD_1531	scrK			fructokinase	386.78	8.60	0.87	1.83	0.18	4.763054079	1.90685E-06	5.3985E-06
SPD_1602	trpE			anthranilate synthase component I	1599.35	10.64	-0.86	0.55	0.18	-4.757814957	1.957E-06	5.53228E-06
SPD_1309	pgdA	ComX		peptidoglycan GlcNAc deacetylase	11000.98	13.43	-0.77	0.59	0.16	-4.751367288	2.02046E-06	5.69483E-06
SPD_1288	SPD_1288			hypothetical protein	1042.93	10.03	-0.81	0.57	0.17	-4.74957788	2.03842E-06	5.73699E-06
SPD_1385	SPD_1385			ABC transporter, ATP-binding protein	10503.42	13.36	0.76	1.69	0.16	4.744641587	2.08876E-06	5.86141E-06
SPD_1848	SPD_1848			hypothetical protein	623.70	9.28	0.67	1.59	0.14	4.739584948	2.14156E-06	5.99199E-06
SPD_1895	SPD_1895			cytidine/deoxycytidylate deaminase family protein	1649.12	10.69	-0.83	0.56	0.18	-4.726731847	2.28162E-06	6.37453E-06
SPD_1905	argS			arginyl-tRNA synthetase	5282.20	12.37	-0.72	0.61	0.15	-4.726020466	2.28963E-06	6.38755E-06
SPD_1363	ppaC			manganese-dependent inorganic pyrophosphatase, putative	5508.10	12.43	0.71	1.64	0.15	4.71387918	2.43045E-06	6.77053E-06
SPD_1304	glyS			glycyl-tRNA synthetase, beta subunit	8088.29	12.98	0.68	1.60	0.15	4.699207734	2.61173E-06	7.26493E-06
SPD_1225	SPD_1225			hypothetical protein	850.09	9.73	-0.90	0.54	0.19	-4.695617111	2.65803E-06	7.37227E-06
SPD_1661	murI	RitR		glutamate racemase	3643.83	11.83	-0.70	0.62	0.15	-4.694807452	2.66858E-06	7.39081E-06
SPD_0170	ruvA			Holliday junction DNA helicase RuvA	962.49	9.91	-0.82	0.57	0.18	-4.678557032	2.88901E-06	7.97817E-06
SPD_0443	nptA			Na/Pi-cotransporter II-related protein	3231.96	11.66	-0.84	0.56	0.18	-4.676593888	2.91679E-06	8.04327E-06
SPD_0005	pth			peptidyl-tRNA hydrolase	2354.07	11.20	0.74	1.67	0.16	4.673425445	2.96217E-06	8.15665E-06
SPD_1139	lemA			LemA protein	4092.27	12.00	-0.72	0.61	0.15	-4.657264582	3.20439E-06	8.79825E-06
SPD_1596	trpA			tryptophan synthase, alpha subunit	2897.18	11.50	0.78	1.72	0.17	4.655272558	3.23552E-06	8.871E-06
SPD_2003	dltC	CiaR		D-alanine--poly(phosphoribitol) ligase subunit 2	1243.51	10.28	-0.69	0.62	0.15	-4.653626959	3.26147E-06	8.92932E-06
SPD_1555	SPD_1555			isochorismatase family protein	3622.52	11.82	0.63	1.55	0.14	4.652691984	3.27629E-06	8.95708E-06
SPD_0478	rimP	CiaR		Bacterial ribosome SSU maturation protein RimP	2912.09	11.51	0.87	1.83	0.19	4.619215783	3.85193E-06	1.04709E-05
SPD_1646	SPD_1646			hypothetical protein	2593.04	11.34	0.86	1.82	0.19	4.616857958	3.89594E-06	1.05755E-05
SPD_1998	adcB	AdcR		zinc ABC transporter, permease protein	5314.67	12.38	-0.68	0.62	0.15	-4.603718442	4.15013E-06	1.12495E-05
SPD_0445	pgk			phosphoglycerate kinase	29099.57	14.83	0.89	1.85	0.19	4.600590312	4.21295E-06	1.14036E-05
SPD_0583	miaA			tRNA delta(2)-isopentenylpyrophosphate transferase	2617.69	11.35	-0.63	0.65	0.14	-4.598828833	4.24873E-06	1.14842E-05
SPD_1407	apt			adenine phosphoribosyltransferase	5546.99	12.44	0.76	1.69	0.17	4.59027273	4.42667E-06	1.19483E-05
SPD_1130	licD2			phosphotransferase LicD2	1313.66	10.36	-0.94	0.52	0.20	-4.584578786	4.54903E-06	1.22612E-05
SPD_0515	cysS			cysteinyl-tRNA synthetase	12151.32	13.57	0.60	1.52	0.13	4.572865139	4.811E-06	1.2949E-05
SPD_1328	aatB	RafR		amino acid ABC transporter, amino acid-binding protein	7772.13	12.92	0.71	1.64	0.15	4.554671975	5.24674E-06	1.4102E-05
SPD_0304	mraW			S-adenosyl-methyltransferase MraW	1657.36	10.69	-0.86	0.55	0.19	-4.553686555	5.27139E-06	1.41483E-05
SPD_0494	valS			valyl-tRNA synthetase	20538.44	14.33	0.80	1.74	0.17	4.550671667	5.34749E-06	1.43124E-05
SPD_1039	ptsI			phosphoenolpyruvate-protein phosphotransferase	36772.06	15.17	0.71	1.64	0.16	4.545943647	5.46897E-06	1.46171E-05
SPD_1405	dnaD			hypothetical protein	2623.30	11.36	0.96	1.95	0.21	4.540952823	5.60006E-06	1.49465E-05
SPD_1072	SPD_1072			hypothetical protein	863.43	9.75	-0.70	0.62	0.15	-4.538070329	5.67713E-06	1.51311E-05
SPD_0813	nspC			carboxynorspermidine decarboxylase	2640.58	11.37	0.67	1.59	0.15	4.531617313	5.85338E-06	1.55575E-05
SPD_0453	hsdS			type I restriction-modification system, S subunit	4658.16	12.19	0.64	1.56	0.14	4.527826384	5.95935E-06	1.58171E-05
SPD_1554	rsfA			iojap-related protein	1230.50	10.27	0.78	1.72	0.17	4.525089645	6.03699E-06	1.6001E-05
SPD_1773	yidC1			SpoIIIJ family protein	3135.80	11.61	-0.72	0.61	0.16	-4.497845814	6.86454E-06	1.8144E-05
SPD_0368	rnhC			ribonuclease HIII	2748.64	11.42	-0.81	0.57	0.18	-4.495146297	6.95221E-06	1.83504E-05
SPD_1403	lytC			1,4-beta-N-acetylmuramidase, putative	30948.31	14.92	0.56	1.47	0.12	4.491276023	7.07977E-06	1.86613E-05
SPD_1026	acoC	CcpA		acetoin dehydrogenase complex, E2 component, dihydrolipoamide	1633.82	10.67	0.64	1.56	0.14	4.489933339	7.12455E-06	1.87535E-05
SPD_0957	dnaG			DNA primase	11114.66	13.44	0.62	1.54	0.14	4.479051502	7.49754E-06	1.97081E-05
SPD_0350	vraT	VraR		hypothetical protein	1504.23	10.55	-0.92	0.53	0.20	-4.469589561	7.83698E-06	2.05721E-05
SPD_1394	SPD_1394			putative BCR	10008.97	13.29	0.62	1.54	0.14	4.466926213	7.93515E-06	2.08012E-05
SPD_1352	patB2			aminotransferase, class II	689.52	9.43	0.67	1.59	0.15	4.462325632	8.10749E-06	2.12239E-05
SPD_0318	cps2D	CpsR	VncR	tyrosine-protein kinase Cps2D cytosolic ATPase domain	21940.74	14.42	-0.71	0.61	0.16	-4.445647214	8.76276E-06	2.29079E-05
SPD_1547	rpoZ			DNA-directed RNA polymerase omega chain, putative	2149.92	11.07	-0.70	0.62	0.16	-4.438357789	9.06478E-06	2.36327E-05
SPD_0894	pepT			peptidase T	3891.47	11.93	0.80	1.74	0.18	4.437357958	9.10698E-06	2.37104E-05
SPD_1925	pbp1B			penicillin-binding protein 1B	14924.69	13.87	0.54	1.45	0.12	4.431044722	9.37776E-06	2.4316E-05
SPD_1597	trpB	ComX		tryptophan synthase, beta subunit	3060.51	11.58	0.83	1.78	0.19	4.422112131	9.77407E-06	2.53093E-05
SPD_0587	SPD_0587			oxidoreductase, short chain dehydrogenase/reductase family protei	3941.80	11.94	0.62	1.54	0.14	4.40628245	1.0516E-05	2.71568E-05
SPD_1151	SPD_1151			chorismate mutase	544.23	9.09	-0.97	0.51	0.22	-4.403573067	1.06482E-05	2.74612E-05
SPD_0027	dut	ComX		deoxyuridine 5'-triphosphate nucleotidohydrolase	1141.03	10.16	0.70	1.62	0.16	4.377613088	1.19986E-05	3.07899E-05
SPD_0270	sulB			folylpolyglutamate synthase	4754.90	12.22	-0.61	0.66	0.14	-4.377526284	1.20034E-05	3.07899E-05
SPD_0144	mutR1	CodY	RpoD	transcriptional regulator	2175.73	11.09	-0.61	0.66	0.14	-4.375906403	1.20929E-05	3.09779E-05
SPD_0434	mtsB	CodY		ABC transporter, ATP-binding protein	3466.17	11.76	-0.57	0.67	0.13	-4.372921557	1.22595E-05	3.13626E-05
SPD_1896	gltX			glutamyl-tRNA synthetase	3558.72	11.80	-0.58	0.67	0.13	-4.348516707	1.37061E-05	3.49699E-05
SPD_1395	SPD_1395			hypothetical protein	7121.71	12.80	0.61	1.53	0.14	4.347026786	1.37995E-05	3.51612E-05
SPD_0056	vanZ			vanZ protein, putative	410.29	8.68	0.79	1.73	0.18	4.331643121	1.48001E-05	3.76103E-05
SPD_0464	ecsA			ABC transporter, ATP-binding protein	1990.46	10.96	0.75	1.68	0.17	4.314780979	1.59761E-05	4.0545E-05
SPD_0454	hsdM			type I restriction-modification system, M subunit	2529.81	11.30	0.60	1.52	0.14	4.293838434	1.7561E-05	4.44492E-05
SPD_1067	xseA			exodeoxyribonuclease VII, large subunit	3196.65	11.64	-0.68	0.62	0.16	-4.288607104	1.79797E-05	4.54487E-05
SPD_1281	SPD_1281			hypothetical protein	388.31	8.60	-0.80	0.57	0.19	-4.281155362	1.85925E-05	4.69357E-05
SPD_1069	SPD_1069			hypothetical protein	895.79	9.81	-0.69	0.62	0.16	-4.257150422	2.07049E-05	5.20619E-05
SPD_0177	ypdF			peptidase M24 family protein	4569.66	12.16	0.62	1.54	0.15	4.255238663	2.08826E-05	5.24398E-05
SPD_1028	acoA			TPP-dependent acetoin dehydrogenase alpha-subunit	1606.80	10.65	-0.67	0.63	0.16	-4.221534198	2.42645E-05	6.05346E-05
SPD_0524	vncR			DNA-binding response regulator VncR	878.44	9.78	-0.90	0.54	0.21	-4.217755213	2.46746E-05	6.14775E-05
SPD_2026	thiX	ComX		ABC transporter, permease protein	955.00	9.90	0.64	1.56	0.15	4.207037216	2.58741E-05	6.43819E-05
SPD_0695	fabG2			oxidoreductase, short chain dehydrogenase/reductase family protei	823.79	9.69	-0.63	0.65	0.15	-4.205657671	2.60324E-05	6.46917E-05
SPD_0721	folD	CmhR	ArgR, MtaR, RpoD	methylenetetrahydrofolate dehydrogenase/methenyltetrahydrofolate	3289.26	11.68	-0.55	0.68	0.13	-4.205076684	2.60994E-05	6.47739E-05
SPD_0244	cdsA			phosphatidate cytidylyltransferase	5424.83	12.41	-0.72	0.61	0.17	-4.191393007	2.77247E-05	6.87184E-05
SPD_0355	SPD_0355	VraR		hypothetical protein	604.38	9.24	-0.86	0.55	0.21	-4.181113949	2.90084E-05	7.18072E-05
SPD_1093	niaR			transcriptional regulator, biotin repressor family protein	1300.61	10.34	-0.70	0.62	0.17	-4.177880342	2.94238E-05	7.27412E-05
SPD_0686	SPD_0686	GntR		efflux transporter, RND family protein, MFP subunit	3783.01	11.89	-0.84	0.56	0.20	-4.159153629	3.19429E-05	7.88668E-05
SPD_0543	SPD_0543			hypothetical protein	948.28	9.89	0.70	1.62	0.17	4.157141464	3.22254E-05	7.94617E-05
SPD_0178	spxA2	VraR		hypothetical protein	7002.31	12.77	-0.83	0.56	0.20	-4.156181342	3.23611E-05	7.96934E-05
SPD_0195	rplW			ribosomal protein L23	48374.46	15.56	0.64	1.56	0.15	4.149648122	3.32987E-05	8.18967E-05
SPD_0779	SPD_0779			hypothetical protein	222.95	7.80	-0.97	0.51	0.23	-4.146857288	3.3707E-05	8.27022E-05
SPD_1904	argR			arginine repressor	1924.75	10.91	-0.80	0.57	0.19	-4.146818302	3.37127E-05	8.27022E-05
SPD_0701	ciaR	CiaR		DNA-binding response regulator CiaR	3746.18	11.87	-0.98	0.51	0.24	-4.144669807	3.40304E-05	8.33744E-05
SPD_0995	SPD_0995			membrane protein, putative	739.95	9.53	-0.69	0.62	0.17	-4.14416998	3.41047E-05	8.34495E-05
SPD_2046	cbiQ			cobalt ABC transporter, permease protein	1728.59	10.76	0.68	1.60	0.17	4.128116934	3.65746E-05	8.93786E-05
SPD_0545	SPD_0545			hypothetical protein	106.16	6.73	0.97	1.96	0.23	4.127795367	3.66258E-05	8.93894E-05
SPD_0724	deoB			phosphopentomutase	7275.25	12.83	0.76	1.69	0.18	4.117782929	3.82535E-05	9.31241E-05
SPD_1291	SPD_1291	RitR		ArsC family protein	1835.00	10.84	-0.58	0.67	0.14	-4.100553719	4.12163E-05	0.000100209
SPD_0542	pepV	CodY		dipeptidase PepV	12881.63	13.65	0.53	1.44	0.13	4.093529701	4.24856E-05	0.000103164
SPD_1199	cps23FU			glycosyl transferase, group 2 family protein	2381.39	11.22	-0.60	0.66	0.15	-4.085299026	4.40201E-05	0.000106754
SPD_2029	SPD_2029			hypothetical protein	1621.91	10.66	0.65	1.57	0.16	4.082985492	4.44608E-05	0.000107686
SPD_0740	SPD_0740			sugar ABC transporter, ATP-binding protein	6365.66	12.64	-0.57	0.67	0.14	-4.081469297	4.47519E-05	0.000108254
SPD_1777	cbf1	ComX		cmp-binding-factor 1	3548.90	11.79	0.67	1.59	0.16	4.080991548	4.4844E-05	0.00010834
SPD_0507	SPD_0507			hypothetical protein	2827.02	11.47	-0.85	0.55	0.21	-4.079881644	4.50586E-05	0.000108721
SPD_1742	SPD_1742	ComE		acetyltransferase, GNAT family protein	4901.60	12.26	-0.67	0.63	0.16	-4.073542845	4.63033E-05	0.000111443
SPD_0194	rplD			ribosomal protein L4	14762.38	13.85	0.70	1.62	0.17	4.05610431	4.98898E-05	0.000119367
SPD_1414	oxlT			oxalate:formate antiporter	2497.28	11.29	-0.77	0.59	0.19	-4.05605723	4.99008E-05	0.000119367
SPD_0656	livF	CodY		branched-chain amino acid ABC transporter, ATP-binding protein	3580.45	11.81	0.50	1.41	0.12	4.046915273	5.1897E-05	0.000123969
SPD_0250	spuA	MalR	CcpA	pullulanase, extracellular	1600.02	10.64	0.54	1.45	0.13	4.040422968	5.33549E-05	0.000127292
SPD_0451	SPD_0451			type I restriction-modification system, S subunit, putative	1371.09	10.42	0.76	1.69	0.19	4.034834013	5.46409E-05	0.000129874
SPD_1217	SPD_1217			hypothetical protein	2374.25	11.21	-0.53	0.69	0.13	-4.017336765	5.88596E-05	0.000139728
SPD_1489	SPD_1489	NanR	CcpA, NiaR	N-acetylneuraminate lyase, putative	322.02	8.33	0.69	1.61	0.17	4.013324506	5.98695E-05	0.000141949
SPD_0168	ribE			riboflavin synthase, alpha subunit	584.62	9.19	0.72	1.65	0.18	3.996026144	6.44146E-05	0.000152536
SPD_1177	SPD_1177			drug efflux ABC transporter, ATP-binding/permease protein	866.27	9.76	0.78	1.72	0.19	3.992723993	6.53186E-05	0.000154485
SPD_1496	nanP	NanR	CcpA, NiaR	PTS system, IIBC components	824.31	9.69	0.59	1.51	0.15	3.991815702	6.55693E-05	0.000154842
SPD_0449	SPD_0449			hypothetical protein	218.57	7.77	-0.91	0.53	0.23	-3.991591201	6.56314E-05	0.000154842

Table S1 continued

					WT HOCI vs control							
Locus	Gene Symbol	Regulon	Further Regulon	Function	Base-Mean	A-value	M-value	Fold-change	Standard error	Wald statistic	P-value	Adjusted P-value
SPD_1571	pepF2			oligoendopeptidase F, putative	7076.60	12.79	0.70	1.62	0.18	3.98441237	6.76473E-05	0.000159401
SPD_0506	pheT			phenylalanyl-tRNA synthetase, beta subunit	4171.23	12.03	0.68	1.60	0.17	3.973279271	7.08899E-05	0.000166836
SPD_1776	purR			pur operon repressor PurR	2797.54	11.45	-0.57	0.67	0.14	-3.966531078	7.29263E-05	0.000171417
SPD_0588	mtaR			transcriptional regulator, putative	1130.05	10.14	-0.68	0.62	0.17	-3.956157543	7.61649E-05	0.00017881
SPD_0086	SPD_0086			hypothetical protein	7915.56	12.95	0.72	1.65	0.18	3.944090917	8.01033E-05	0.000187825
SPD_1002	pulA	RpoD		pullulanase, type I	8475.87	13.05	0.62	1.54	0.16	3.929198356	8.52295E-05	0.000199112
SPD_0620	lysS			lysyl-tRNA synthetase	9575.50	13.23	-0.66	0.63	0.17	-3.927025914	8.60027E-05	0.000200673
SPD_0826	holB			DNA polymerase III, delta prime subunit	1520.50	10.57	-0.67	0.63	0.17	-3.923120127	8.74095E-05	0.000203707
SPD_0393	nusB			transcription antitermination factor NusB	9218.43	13.17	0.52	1.43	0.13	3.908251288	9.29666E-05	0.00021613
SPD_1330	glnP6			amino acid ABC transporter, permease protein	1759.68	10.78	-0.74	0.60	0.19	-3.904675052	9.43521E-05	0.000219085
SPD_0912	pvaA			pneumococcal vaccine antigen A	2017.76	10.98	-0.75	0.59	0.19	-3.888179763	0.000100999	0.00023395
SPD_1332	SPD_1332			membrane protein, putative	4032.44	11.98	-0.78	0.58	0.20	-3.876409627	0.000106009	0.000245258
SPD_0692	SPD_0692	RitR		membrane protein, putative	2205.94	11.11	0.91	1.88	0.23	3.864367155	0.000111378	0.000257367
SPD_1580	SPD_1580			ATPase, AAA family protein	2251.13	11.14	-0.56	0.68	0.14	-3.863458779	0.000111793	0.000258014
SPD_1436	ctpE			cation-transporting ATPase, E1-E2 family protein	17326.59	14.08	0.64	1.56	0.17	3.862613019	0.000112181	0.000258597
SPD_1105	rnc			ribonuclease III	464.00	8.86	-0.79	0.58	0.20	-3.862126662	0.000112404	0.000258801
SPD_0742	SPD_0742	RitR		sugar ABC transporter, permease protein, putative	5551.64	12.44	0.50	1.41	0.13	3.86012215	0.00011333	0.000260306
SPD_0670	SPD_0670			conserved hypothetical, predicted membrane protein	1217.39	10.25	-0.58	0.67	0.15	-3.85611406	0.000115204	0.000264291
SPD_1782	ksgA			dimethyladenosine transferase	2378.65	11.22	-0.68	0.62	0.18	-3.855359318	0.00011556	0.00026479
SPD_1235	SPD_1235			hypothetical protein	471.19	8.88	-0.58	0.67	0.15	-3.851230928	0.000117526	0.000268972
SPD_1494	satB	NanR	CcpA, NiaR	sugar ABC transporter, permease protein	637.66	9.32	0.63	1.55	0.16	3.832135295	0.000127036	0.000290389
SPD_0766	sufB			FeS assembly protein SufB	48530.05	15.57	0.62	1.54	0.16	3.831422486	0.000127405	0.000290884
SPD_0812	lys1			saccharopine dehydrogenase	1988.43	10.96	0.70	1.62	0.18	3.830136523	0.000128072	0.00029206
SPD_0679	trmD			tRNA (guanine-N1)-methyltransferase	4417.42	12.11	-0.53	0.69	0.14	-3.82427906	0.000131155	0.000298734
SPD_0317	cps2C	CpsR	RpoD, VncR	chain length determinant protein/polysaccharide export protein, MPA	17495.81	14.09	-0.78	0.58	0.20	-3.821746965	0.00013251	0.000301459
SPD_1473	SPD_1473			hypothetical protein	4409.67	12.11	0.58	1.49	0.15	3.815439443	0.000135941	0.000308898
SPD_0054	purM			phosphoribosylformylglycinamidine cyclo-ligase	640.79	9.32	0.98	1.97	0.26	3.81432772	0.000136554	0.000309923
SPD_0555	SPD_0555			membrane protein, putative	10141.29	13.31	-0.58	0.67	0.15	-3.793054516	0.000148805	0.000337328
SPD_0906	prfA			peptide chain release factor 1	1887.76	10.88	-0.69	0.62	0.18	-3.789908849	0.000150703	0.000341223
SPD_1900	patB			ABC transporter, ATP-binding/permease protein	7530.96	12.88	0.48	1.39	0.13	3.786846109	0.000152572	0.000345046
SPD_1729	SPD_1729			hypothetical protein	6392.65	12.64	-0.59	0.66	0.16	-3.783309895	0.000154757	0.000349574
SPD_1459	SPD_1459			metallo-beta-lactamase superfamily protein	2932.38	11.52	-0.76	0.59	0.20	-3.782435742	0.000155301	0.00035039
SPD_1178	ptrB			prolyl oligopeptidase family protein	1572.31	10.62	0.64	1.56	0.17	3.780494396	0.000156517	0.000352718
SPD_1251	pncB	Rex		nicotinate phosphoribosyltransferase, putative	3516.54	11.78	-0.64	0.64	0.17	-3.77468471	0.000160021	0.000360614
SPD_0914	rumA-1	CiaR		23S rRNA (uracil-5-)-methyltransferase RumA	1067.86	10.06	-0.56	0.68	0.15	-3.773650913	0.000160876	0.000361687
SPD_0660	ftsX			cell division ABC transporter, permease protein FtsX	7390.64	12.85	0.68	1.60	0.18	3.770357646	0.000163014	0.000366063
SPD_1959	ulaA2			PTS system, IIC component, putative	553.15	9.11	0.67	1.59	0.18	3.765692444	0.000166088	0.000372529
SPD_0870	gpmB2			phosphoglycerate mutase family protein	1237.47	10.27	-0.71	0.61	0.19	-3.76376502	0.000167374	0.000374973
SPD_1653	yidD			conserved hypothetical protein TIGR00278	1265.52	10.31	0.62	1.54	0.17	3.762103397	0.00016849	0.000377032
SPD_0351	vraS	VraR		sensor histidine kinase, putative	2145.92	11.07	-0.78	0.58	0.21	-3.761093584	0.000169172	0.000378115
SPD_2045	mreC			rod shape-determining protein MreC	3909.18	11.93	0.50	1.41	0.13	3.75670542	0.000172165	0.000384354
SPD_0490	SPD_0490			hypothetical protein	688.24	9.43	-0.77	0.59	0.21	-3.743710295	0.000181323	0.000404326
SPD_1839	tkt	UlaR		transketolase	10615.34	13.37	0.57	1.48	0.15	3.742653203	0.000182087	0.000405558
SPD_0235	pfl			pyruvate formate-lyase	550.56	9.10	0.75	1.68	0.20	3.74143804	0.00018297	0.00040705
SPD_0063	strH	SpxR	CcpA	beta-N-acetylhexosaminidase	1059.06	10.05	0.66	1.58	0.18	3.740409452	0.000183721	0.000408245
SPD_0111	argH	ArgR		argininosuccinate lyase	615.50	9.27	0.53	1.44	0.14	3.734346187	0.000188203	0.000417235
SPD_0783	SPD_0783			type I restriction-modification system, S subunit, putative	2589.02	11.34	-0.64	0.64	0.17	-3.733302518	0.000188985	0.000418483
SPD_0307	mraY			phospho-N-acetylmuramoyl-pentapeptide- transferase	2292.51	11.16	0.55	1.46	0.15	3.730877737	0.000190814	0.000422043
SPD_0700	pepN			aminopeptidase N	25156.64	14.62	0.64	1.56	0.17	3.723570935	0.000196425	0.000433951
SPD_1228	pstB2-2			phosphate ABC transporter, ATP-binding protein, putative	3947.81	11.95	0.47	1.39	0.13	3.713510359	0.000204404	0.000451058
SPD_1389	SPD_1389			hypothetical protein	2431.84	11.25	0.50	1.41	0.14	3.6900521	0.000224208	0.000493051
SPD_0697	SPD_0697			acetyltransferase, GNAT family protein	1810.10	10.82	-0.62	0.65	0.17	-3.679545749	0.00023365	0.000513224
SPD_0586	rnz			ribonuclease Z	3957.56	11.95	0.47	1.39	0.13	3.673279267	0.000239458	0.000524774
SPD_0396	gatB			glu-trnaGln amidotransferase subunit b	8508.15	13.05	0.58	1.49	0.16	3.657337745	0.000254848	0.000557864
SPD_2023	ctsR	CtsR		transcriptional regulator CtsR	1936.35	10.92	-0.61	0.66	0.17	-3.653077629	0.000259116	0.000566557
SPD_0962	SPD_0962			hypothetical protein	1569.55	10.62	0.82	1.77	0.23	3.642849611	0.000269636	0.000588886
SPD_0219	rplQ			ribosomal protein L17	5286.29	12.37	-0.64	0.64	0.18	-3.64245972	0.000270045	0.000589106
SPD_1038	phpA	AdcR		pneumococcal histidine triad protein A precursor	16407.08	14.00	-0.69	0.62	0.19	-3.636273867	0.00027661	0.000602739
SPD_1490	SPD_1490	NanR	CcpA, NiaR	hypothetical protein	207.27	7.70	0.73	1.66	0.20	3.627639568	0.000286024	0.000622542
SPD_0979	nifS			aminotransferase, class V	5822.29	12.51	-0.61	0.66	0.17	-3.615805886	0.000299415	0.000650946
SPD_0301	regR			sugar binding transcriptional regulator RegR	3790.36	11.89	-0.51	0.70	0.14	-3.611126083	0.00030487	0.000662054
SPD_1172	nanE-2			N-acetylmannosamine-6-phosphate 2-epimerase 2, putative	437.22	8.77	-0.66	0.63	0.18	-3.608536899	0.000307929	0.000667936
SPD_1302	SPD_1302	CcpA	RpoD	oxidoreductase, putative	376.27	8.56	0.76	1.69	0.21	3.601879187	0.000315925	0.000683729
SPD_0785	SPD_0785			hypothetical protein	537.83	9.07	-0.74	0.60	0.21	-3.586857608	0.000334687	0.000722697
SPD_0726	SPD_0726	CodY		purine nucleoside phosphorylase, family protein 2	7133.80	12.80	0.53	1.44	0.15	3.565464143	0.000363213	0.000783408
SPD_0644	SPD_0644			MutT/nudix family protein	546.86	9.10	-0.61	0.66	0.17	-3.564785305	0.000364154	0.000784553
SPD_2042	rpsB			ribosomal protein S2	47583.01	15.54	0.50	1.41	0.14	3.562199775	0.00036776	0.00079143
SPD_1285	def			peptide deformylase	3083.81	11.59	-0.47	0.72	0.13	-3.558105607	0.000373534	0.00080295
SPD_1101	ftsY			signal recognition particle-docking protein FtsY	3094.08	11.60	0.56	1.47	0.16	3.549929676	0.000385334	0.000825533
SPD_0377	lysC			aspartate kinase	3555.27	11.80	-0.61	0.66	0.17	-3.54369505	0.000394561	0.000844352
SPD_0410	SPD_0410			hypothetical protein	4673.15	12.19	-0.77	0.59	0.22	-3.541084608	0.000398486	0.000851797
SPD_0521	vex1			ABC transporter, transmembrane protein Vexp1	461.61	8.85	0.73	1.66	0.21	3.53462977	0.000408347	0.00087154
SPD_0516	mrnC			hypothetical protein	4784.12	12.22	0.73	1.66	0.21	3.534444	0.000408634	0.00087154
SPD_0780	SPD_0780	CodY		hypothetical protein	306.46	8.26	-0.72	0.61	0.20	-3.533362113	0.00041031	0.000874139
SPD_1277	SPD_1277			hypothetical protein	2034.27	10.99	-0.51	0.70	0.14	-3.526803031	0.00042061	0.000895083
SPD_0902	trmE			tRNA modification GTPase TrmE	3993.16	11.96	-0.53	0.69	0.15	-3.524345639	0.00042453	0.000901284
SPD_0765	sufE2			SUF system FeS assembly protein, NifU family protein	18990.69	14.21	0.53	1.44	0.15	3.524091035	0.000424938	0.000901284
SPD_1556	yqeK			conserved hypothetical protein TIGR00488	4153.73	12.02	0.46	1.38	0.13	3.519554706	0.000432272	0.000915822
SPD_0216	rpsM			ribosomal protein S13	26319.63	14.68	-0.79	0.58	0.23	-3.516730393	0.000436897	0.000924597
SPD_0169	ribD			riboflavin biosynthesis protein RibD	520.95	9.02	0.56	1.47	0.16	3.513991958	0.000441426	0.000933148
SPD_0236	talC			transaldolase, putative	211.58	7.73	0.75	1.68	0.21	3.512060135	0.000444647	0.000939891
SPD_0370	zapB			CvpA family protein	5323.00	12.38	0.56	1.47	0.16	3.5084558	0.000450716	0.000948589
SPD_0229	pflE			glycyl-radical enzyme activating protein family protein	107.57	6.75	-0.84	0.56	0.24	-3.506936099	0.000453298	0.000952973
SPD_0824	proC			pyrroline-5-carboxylate reductase	2434.90	11.25	0.50	1.41	0.14	3.498517574	0.000467852	0.00098249
SPD_0641	manA			mannose-6-phosphate isomerase, class I	988.58	9.95	0.52	1.43	0.15	3.496670276	0.000471104	0.000988232
SPD_1476	ylmG			YlmG protein	1276.21	10.32	-0.64	0.64	0.18	-3.491236083	0.000480791	0.001007447
SPD_0737	deoC			deoxyribose-phosphate aldolase	3735.56	11.87	-0.52	0.70	0.15	-3.484730899	0.000492632	0.00103
SPD_1373	aspC			aspartate aminotransferase	2935.86	11.52	-0.59	0.66	0.17	-3.482236893	0.000497244	0.001038505
SPD_0689	metG			methionyl-tRNA synthetase	6776.35	12.73	0.44	1.36	0.13	3.481459764	0.000498689	0.001040387
SPD_1660	rdgB			non-canonical purine NTP pyrophosphatase, rdgB/HAM1 family pro	6473.87	12.66	-0.49	0.71	0.14	-3.477768381	0.000505607	0.001053669
SPD_0596	SPD_0596			membrane protein, putative	348.83	8.45	0.70	1.62	0.20	3.451221335	0.000558056	0.00115792
SPD_0539	SPD_0539			Ser/Thr protein phosphatase family protein	2174.10	11.09	-0.44	0.74	0.13	-3.448798137	0.000563087	0.001167059
SPD_1940	SPD_1940			membrane protein, putative	4316.41	12.08	0.43	1.35	0.13	3.43263991	0.000597735	0.001237565
SPD_1651	piuD	RitR	RpoD, CodY, SifR	iron-compound ABC transporter, ATP-binding protein	250.92	7.97	0.73	1.66	0.21	3.417763414	0.00063138	0.001305808
SPD_1645	SPD_1645	RpoD		transcriptional regulator, MarR family protein	5736.78	12.49	0.73	1.66	0.21	3.412008007	0.000644862	0.00133225
SPD_0518	SPD_0518			hypothetical protein	325.88	8.35	0.67	1.59	0.20	3.411640799	0.000645731	0.001332606
SPD_1537	mvaS			hydroxymethylglutaryl-CoA synthase	3079.76	11.59	-0.47	0.72	0.14	-3.400537434	0.000672535	0.001386424
SPD_1952	rgg			transcriptional activator, Rgg/GadR/MutR family protein, C-terminal	867.43	9.76	-0.63	0.65	0.19	-3.392248738	0.000693215	0.001424499
SPD_1226	glnH	ArgR	RpoD	amino acid ABC transporter, amino acid-binding protein	922.51	9.85	0.58	1.49	0.17	3.392238311	0.000693241	0.001424499
SPD_0714	SPD_0714	CcpA		hypothetical protein	3688.11	11.85	-0.91	0.53	0.27	-3.391228326	0.000695801	0.001428223
SPD_2044	mreD			rod shpae-determining protein MreD, putative	1072.37	10.07	0.64	1.56	0.19	3.390502237	0.000697647	0.001430475
SPD_0983	ppnK	CcpA	RpoD	inorganic polyphosphate/ATP-NAD kinase, putative	2253.47	11.14	-0.74	0.60	0.22	-3.383121501	0.000716669	0.001467904
SPD_0990	SPD_0990			hypothetical protein	78630.34	16.26	-0.83	0.56	0.24	-3.377803408	0.000730673	0.001494985
SPD_0538	uvrC			excinuclease ABC, C subunit	2683.93	11.39	-0.68	0.62	0.20	-3.375262131	0.000737454	0.001507246
SPD_2047	cbiO1			cobalt ABC transporter, ATP-binding protein CbiO1	4298.35	12.07	0.55	1.46	0.16	3.370809766	0.000749476	0.00153018
SPD_1912	pstA	RitR		phosphate ABC transporter, permease protein PstA	212.67	7.73	0.66	1.58	0.20	3.349563339	0.00080939	0.001648982
SPD_1924	SPD_1924	PnpR		membrane protein, putative	2113.47	11.05	0.49	1.40	0.15	3.345851755	0.000820302	0.001669433
SPD_1359	murE			UDP-N-acetylmuramoylalanyl-D-glutamate--2, 6-diaminopimelate lig	2879.48	11.49	-0.54	0.69	0.16	-3.344418778	0.000824552	0.001676296
SPD_1938	malR	MalR		maltose operon transcriptional repressor	2472.62	11.27	0.58	1.49	0.17	3.343109755	0.000828451	0.001682434
SPD_0996	SPD_0996			DegV family protein	4324.34	12.08	-0.70	0.62	0.21	-3.341832473	0.000832273	0.0016884
SPD_0462	SPD_0462			hypothetical protein	1152.95	10.17	-0.79	0.58	0.24	-3.339293855	0.000839917	0.0017021
SPD_0960	cpoA			glycosyl transferase CpoA	3565.03	11.80	0.45	1.37	0.13	3.327135148	0.000877438	0.001776254
SPD_0140	SPD_0140			ABC transporter, ATP-binding protein	444.98	8.80	-0.72	0.61	0.22	-3.311944995	0.000926498	0.001873584
SPD_1985	adh2	CcpA		alcohol dehydrogenase, iron-containing	98.28	6.62	0.90	1.87	0.27	3.30880094	0.000936964	0.001891561
SPD_0341	rlmL			RNA methylase family protein UPF0020, putative	4252.50	12.05	-0.58	0.67	0.17	-3.308680674	0.000937367	0.001891561
SPD_1296	pdxT			glutamine amidotransferase, SNO family protein, putative	8189.40	13.00	-0.50	0.71	0.15	-3.307901211	0.00093998	0.001894832
SPD_1091	niaX	NiaR		membrane protein, putative	799.60	9.64	-0.67	0.63	0.20	-3.298121291	0.000973341	0.001960015
SPD_0053	purF			amidophosphoribosyltransferase	983.28	9.94	0.84	1.79	0.26	3.280896827	0.001034776	0.002081533
SPD_0666	holA			DNA polymerase III, delta subunit	7199.13	12.81	0.42	1.34	0.13	3.262562998	0.001104096	0.002216311
SPD_0319	cps2E	CpsR	VncR	undecaprenylphosphate glucosephosphotransferase Cps2E	35719.61	15.12	-0.48	0.72	0.15	-3.261883004	0.001106748	0.002219303
SPD_0764	sufS			cysteine desulfurase, SufS subfamily protein	36910.78	15.17	0.40	1.32	0.12	3.257699495	0.001123193	0.002249918
SPD_1227	phoU2			phosphate transport system regulatory protein PhoU, putative	12367.42	13.59	0.44	1.36	0.13	3.253084945	0.001141594	0.002284383
SPD_1396	SPD_1396			hypothetical protein	5796.64	12.50	0.57	1.48	0.18	3.242651329	0.00118423	0.002367222
SPD_0930	pezA	PezA		transcriptional regulator, putative	223.22	7.80	0.89	1.85	0.27	3.227978367	0.001246684	0.002484268
SPD_1047	lacE-2	LacT	CcpA	PTS system, lactose-specific IIBC components	1623.72	10.67	0.67	1.59	0.21	3.215318376	0.001302999	0.002593783
SPD_0488	SPD_0488			hypothetical protein	2574.66	11.33	-0.46	0.73	0.14	-3.209367998	0.001330271	0.002645315
SPD_0510	metE	CmhR	CmbR	5-methyltetrahydropteroyltriglutamate-- homocysteine S-methyltrans	867.13	9.76	0.61	1.53	0.19	3.2041455	0.00135464	0.002690974
SPD_1117	SPD_1117			hypothetical protein	541.90	9.08	-0.66	0.63	0.21	-3.195472143	0.001396023	0.0027703
SPD_0253	fusA			translation elongation factor G	43698.97	15.42	0.50	1.41	0.16	3.191449797	0.001415607	0.002806625
SPD_0029	radA	ComX		DNA repair protein RadA	2429.61	11.25	0.85	1.80	0.27	3.189847557	0.001423479	0.00281893
SPD_1786	plcR			transcriptional regulator PlcR, putative	1333.98	10.38	0.70	1.62	0.22	3.180198704	0.001471741	0.002911488
SPD_2048	cbiO2			cobalt ABC transporter, ATP-binding protein CbiO2	4703.52	12.20	0.49	1.40	0.15	3.179756154	0.00147399	0.002912922
SPD_0131	SPD_0131			hypothetical protein	4011.27	11.97	-0.59	0.66	0.19	-3.175051714	0.001498098	0.002957505
SPD_1652	piuA	RitR	RpoD, CodY, SifR	iron-compound ABC transporter, iron-compound-binding protein	367.80	8.52	0.59	1.51	0.19	3.173970347	0.001503691	0.002965483
SPD_1612	galE-2			UDP-glucose 4-epimerase	130.21	7.02	0.67	1.59	0.21	3.172364464	0.001512031	0.002978857
SPD_1477	ylmF			YlmF protein	6529.55	12.67	-0.42	0.75	0.13	-3.161271893	0.001570818	0.003087815
SPD_0706	rodA			rod shape-determining protein RodA, putative	2382.00	11.22	-0.44	0.74	0.14	-3.161018681	0.001572184	0.003087815
SPD_1211	aroD			3-dehydroquinate dehydratase, type I	2320.30	11.18	-0.40	0.76	0.13	-3.160202452	0.001576595	0.0030933
SPD_0433	SPD_0433			hypothetical protein	220.20	7.78	0.70	1.62	0.22	3.159169692	0.001582119	0.003101099
SPD_1875	SPD_1875			hydrolase, haloacid dehalogenase-like family protein	1196.46	10.22	0.63	1.55	0.20	3.155615616	0.001601598	0.003135915

Table S1 continued

					WT HOCl vs control							
Locus	Gene Symbol	Regulon	Further Regulon	Function	Base-Mean	A-value	M-value	Fold-change	Standard error	Wald statistic	P-value	Adjusted P-value
SPD_0033	prsA	CiaR		ribose-phosphate pyrophosphokinase	2038.72	10.99	-0.58	0.67	0.18	-3.152375196	0.00161948	0.003167684
SPD_1521	dnaI			primosomal protein DnaI	2770.29	11.44	-0.44	0.74	0.14	-3.148501368	0.0016411	0.003206688
SPD_1480	ftsA			cell division protein FtsA	23805.22	14.54	-0.46	0.73	0.15	-3.148181005	0.001642899	0.003206926
SPD_0004	ychF	RpoD		GTP-binding protein	3379.47	11.72	0.51	1.42	0.16	3.144041151	0.00166632	0.003249324
SPD_0746	parE			DNA topoisomerase IV, B subunit	2739.16	11.42	-0.62	0.65	0.20	-3.13883241	0.001696224	0.003304266
SPD_0503	bglA-2			6-phospho-beta-glucosidase	874.93	9.77	0.53	1.44	0.17	3.135747597	0.001714167	0.003335817
SPD_1335	atpD	RpoD		ATP synthase F1, beta subunit	26748.24	14.71	0.47	1.39	0.15	3.125717059	0.001773721	0.003448201
SPD_1779	SPD_1779			thiamine pyrophosphokinase	2815.17	11.46	0.45	1.37	0.15	3.117320682	0.001825029	0.003544341
SPD_1561	corA2			magnesium transporter, CorA family protein, putative	4418.68	12.11	-0.46	0.73	0.15	-3.115353375	0.001837247	0.003564445
SPD_0650	clpP	CtsR		ATP-dependent Clp protease, proteolytic subunit ClpP	4863.50	12.25	-0.38	0.77	0.12	-3.111494495	0.001859193	0.003602515
SPD_0231	SPD_0231			transcriptional activator	365.90	8.52	-0.83	0.56	0.27	-3.111619802	0.00186064	0.003602515
SPD_0037	SPD_0037			hypothetical protein	1732.60	10.76	-0.66	0.63	0.21	-3.101496611	0.001925451	0.003724227
SPD_1545	fmt			methionyl-tRNA formyltransferase	3131.03	11.61	0.51	1.42	0.16	3.09644397	0.001958569	0.003782732
SPD_1095	SPD_1095			hypothetical protein	832.00	9.70	-0.52	0.70	0.17	-3.096279232	0.001959657	0.003782732
SPD_1876	SPD_1876			MATE efflux family protein	2653.32	11.37	0.70	1.62	0.23	3.087694948	0.002017154	0.00388979
SPD_1576	SPD_1576			hypothetical protein	1161.34	10.18	-0.99	0.50	0.32	-3.08472928	0.002037375	0.003924822
SPD_0722	nnrD			YjeF-like protein	1859.64	10.86	-0.53	0.69	0.17	-3.083844316	0.002043445	0.003932551
SPD_1549	rny			KH domain protein	14400.37	13.81	-0.48	0.72	0.16	-3.072949899	0.002119541	0.004070796
SPD_0126	pspA	WalR	RpoD	pneumococcal surface protein A	18318.81	14.16	0.50	1.41	0.16	3.063224804	0.002189655	0.004201236
SPD_0496	SPD_0496			cell filamentation protein Fic-related protein	660.92	9.37	-0.57	0.67	0.19	-3.054217948	0.002256481	0.00432511
SPD_1276	SPD_1276			membrane protein, putative	1049.54	10.04	-0.46	0.73	0.15	-3.04358042	0.002337809	0.004476507
SPD_1492	yjgK	NanR	CcpA, NiaR	hypothetical protein	214.60	7.75	0.64	1.56	0.21	3.03931307	0.002371183	0.004535867
SPD_1668	amiE	CodY		oligopeptide ABC transporter, ATP-binding protein AmiE	15854.81	13.95	0.37	1.29	0.12	3.032241302	0.002427451	0.004638858
SPD_1945	SPD_1945			membrane protein, putative	825.17	9.69	0.71	1.64	0.23	3.029197612	0.002452042	0.004681172
SPD_1650	piuC	RitR	RpoD, CodY, SifR	iron-compound ABC transporter, permease protein	355.37	8.47	0.68	1.60	0.23	3.026228865	0.002476248	0.004722664
SPD_1242	SPD_1242			hypothetical protein	1591.47	10.64	0.47	1.39	0.16	3.020147007	0.00252652	0.004813739
SPD_0036	SPD_0036			hypothetical protein	1044.87	10.03	-0.60	0.66	0.20	-3.008385463	0.002626398	0.00499905
SPD_0604	SPD_0604			HesA/MoeB/ThiF family protein	535.60	9.07	-0.76	0.59	0.25	-3.002559493	0.002677196	0.005090669
SPD_1835	SPD_1835			hypothetical protein	192.86	7.59	-0.85	0.55	0.28	-3.001110293	0.002689971	0.005109876
SPD_0833	gid			tRNA uridine 5-carboxymethylaminomethyl modification enzyme gid	1249.37	10.29	-0.47	0.72	0.16	-2.989081222	0.002798177	0.005310146
SPD_1165	SPD_1165			hypothetical protein	363.26	8.50	0.79	1.73	0.27	2.97980304	0.002884338	0.005462804
SPD_0344	ritR	RitR		DNA-binding response regulator	15516.86	13.92	0.40	1.32	0.13	2.977354631	0.002907475	0.005501173
SPD_0435	mtsC			membrane protein, putative	879.67	9.78	-0.67	0.63	0.23	-2.976371965	0.002916808	0.005513374
SPD_1745	plcR			transcriptional regulator PlcR, putative	982.91	9.94	0.79	1.73	0.26	2.975406549	0.002926005	0.005525292
SPD_0258	pepS			aminopeptidase PepS	7340.97	12.84	0.55	1.46	0.19	2.970426192	0.002973869	0.005610131
SPD_1821	pbp2A			penicillin-binding protein 2A	6773.37	12.73	0.47	1.39	0.16	2.960002414	0.003076366	0.005797767
SPD_0505	paiA			acetyltransferase, GNAT family protein	1026.17	10.00	0.50	1.41	0.17	2.955220234	0.003124459	0.005882603
SPD_1188	rplJ	CodY		ribosomal protein L10	19048.17	14.22	-0.88	0.54	0.30	-2.929402424	0.003396144	0.006387826
SPD_1626	xth			exodeoxyribonuclease III	7999.37	12.97	-0.39	0.76	0.13	-2.924781215	0.003446985	0.006477078
SPD_0366	yrrC	RitR		helicase, RecD/TraA family protein	5739.83	12.49	0.42	1.34	0.14	2.923561345	0.00346052	0.006492101
SPD_1300	apbE	RitR	CcpA	thiamine biosynthesis protein ApbE, putative	211.32	7.72	-0.73	0.60	0.25	-2.923448528	0.003461775	0.006492101
SPD_0082	SPD_0082			sensor histidine kinase	3582.77	11.81	0.74	1.67	0.25	2.918167858	0.003520948	0.006592729
SPD_0217	rpsK			ribosomal protein S11	7513.39	12.88	-0.65	0.64	0.22	-2.918045278	0.003522332	0.006592729
SPD_0750	SPD_0750	CodY		hypothetical protein	5776.03	12.50	-0.55	0.68	0.19	-2.914080101	0.003567384	0.006670519
SPD_0696	SPD_0696			MutT/nudix family protein	802.31	9.65	-0.57	0.67	0.20	-2.897983027	0.003755709	0.006999447
SPD_0989	rplU			ribosomal protein L21	17393.79	14.09	-0.63	0.56	0.29	-2.897796364	0.003757945	0.006999447
SPD_1334	atpC	RpoD		ATP synthase F1, epsilon subunit	6131.76	12.58	0.53	1.44	0.19	2.885180967	0.003911887	0.007279081
SPD_0274	rplM			ribosomal protein L13	13640.25	13.74	-0.59	0.66	0.20	-2.883684899	0.003930518	0.007305187
SPD_0672	ppiA			peptidyl-prolyl cis-trans isomerase, cyclophilin-type	2494.81	11.28	-0.47	0.72	0.16	-2.883441081	0.003933562	0.007305187
SPD_0438	SPD_0438			PAP2 family protein	2326.27	11.18	-0.46	0.73	0.16	-2.878514154	0.003995534	0.007413072
SPD_1406	metA	CmbR		homoserine O-succinyltransferase	8156.13	12.99	0.40	1.32	0.14	2.873379473	0.00406106	0.007527338
SPD_1279	SPD_1279			GDSL-like lipase/acylhydrolase, putative	658.27	9.36	-0.46	0.73	0.16	-2.86792904	0.004131682	0.007650515
SPD_0470	blpC	BlpR	ComE, RitR	peptide pheromone BlpC	495.50	8.95	-0.61	0.66	0.21	-2.86763512	0.004135522	0.007650515
SPD_0592	rsuA-2	RitR		ribosomal small subunit pseudouridine synthase A	62.58	5.97	-0.90	0.54	0.31	-2.86303681	0.004196018	0.007754923
SPD_0852	pyrDb	RitR	RpoD, PyrR	dihydroorotate dehydrogenase, catalytic subunit	450.07	8.81	-0.54	0.69	0.19	-2.860842522	0.004225169	0.007801253
SPD_1357	aliB	ArgR	RpoD	oligopeptide ABC transporter, oligopeptide-binding protein AliB	4170.91	12.03	0.53	1.44	0.19	2.858235448	0.004260042	0.00785805
SPD_0569	nha2			sodium/hydrogen exchanger family protein	2124.63	11.05	-0.37	0.77	0.13	-2.841037723	0.004496699	0.008286589
SPD_1929	rrmA			rRNA (guanine-N1-)-methyltransferase	906.31	9.82	-0.46	0.73	0.16	-2.836865618	0.004555878	0.008387556
SPD_1153	pde2			DHH subfamily 1 protein	1583.42	10.63	-0.47	0.72	0.17	-2.830876776	0.00464206	0.008537995
SPD_1391	SPD_1391			YbbR-like lipoprotein, putative	2771.25	11.44	0.40	1.32	0.14	2.824808887	0.004730882	0.008692996
SPD_1679	msmR	RafR	CcpA	msm operon regulatory protein MsmR	865.85	9.76	-0.64	0.64	0.23	-2.824493855	0.004735536	0.008693188
SPD_0921	ccrB			site-specific recombinase, resolvase family protein	826.95	9.69	-0.45	0.73	0.16	-2.822106684	0.00477093	0.008749758
SPD_1222	murB			UDP-N-acetylenolpyruvoylglucosamine reductase	972.17	9.93	-0.45	0.73	0.16	-2.815654811	0.004867794	0.008918844
SPD_1280	SPD_1280			Cof family protein	1087.80	10.09	-0.47	0.72	0.17	-2.809349586	0.004964171	0.009082941
SPD_0595	SPD_0595			hypothetical protein	171.38	7.42	0.63	1.55	0.23	2.80917512 8	0.004966862	0.009082941
SPD_2064	comD	ComE		putative sensor histidine kinase ComD	28973.06	14.82	-0.93	0.52	0.33	-2.808664225	0.00497475	0.009088669
SPD_1062	recN			DNA repair protein RecN	9395.40	13.20	0.43	1.35	0.15	2.807570773	0.004991671	0.009110872
SPD_1240	hemN			oxygen-independent coproporphyrinogen III oxidase, putative	8388.82	13.03	-0.43	0.74	0.15	-2.804904229	0.005033153	0.00917782
SPD_0883	SPD_0883			hypothetical protein	91.53	6.52	0.88	1.84	0.31	2.801629843	0.005084518	0.009262644
SPD_0757	rpsA			ribosomal protein S1	32124.72	14.97	-0.51	0.70	0.18	-2.797245252	0.005154039	0.009380352
SPD_1326	pgm	CodY		phosphoglucomutase/phosphomannomutase family protein	13076.38	13.67	0.43	1.35	0.15	2.796616028	0.005164086	0.009389695
SPD_1640	pnuC	NiaR	RitR	nicotinamide mononucleotide transporter PnuC, putative	133.40	7.06	0.74	1.67	0.27	2.794788216	0.005193372	0.009433968
SPD_0320	cps2T	CpsR	RpoD	glycosyl transferase, group 1 family protein, putative	27425.71	14.74	-0.46	0.73	0.16	-2.790274602	0.005266335	0.009557424
SPD_1654	rluB			ribosomal large subunit pseudouridine synthase B	3705.26	11.86	0.45	1.37	0.16	2.786855986	0.005322213	0.009649666
SPD_1819	nusG			transcription termination/antitermination factor NusG	2638.42	11.37	0.41	1.33	0.15	2.78263775	0.005391897	0.009766744
SPD_0371	mutS2			MutS2 family protein	5105.79	12.32	0.40	1.32	0.14	2.771943812	0.005572265	0.010083901
SPD_1828	SPD_1828	ComX		hypothetical protein	5798.75	12.50	-0.55	0.68	0.20	-2.768172185	0.005637166	0.010191698
SPD_1518	SPD_1518			transcriptional activator, Rgg/GadR/MutR family protein	822.13	9.68	-0.79	0.58	0.29	-2.767206894	0.005653886	0.010207326
SPD_0487	SPD_0487			hypothetical protein	365.68	8.51	-0.55	0.68	0.20	-2.767056611	0.005656493	0.010207326
SPD_1023	xerS			integrase/recombinase, phage integrase family protein	1013.16	9.98	0.47	1.39	0.17	2.765494943	0.005683649	0.010246186
SPD_1098	glnHP5	GlnR		amino acid ABC transporter, amino acid-binding protein/permease p	10546.03	13.36	-0.56	0.68	0.20	-2.765202248	0.005688751	0.010246186
SPD_1663	treC	TreR	CcpA	alpha,alpha-phosphotrehalase	186.81	7.55	0.55	1.46	0.20	2.761899584	0.005746615	0.01034066
SPD_1918	gpsA			(NAD(P)+) glycerol-3-phosphate dehydrogenase	9680.34	13.24	-0.48	0.72	0.18	-2.754059028	0.005886115	0.010581718
SPD_0568	SPD_0568			hypothetical protein	299.41	8.23	-0.47	0.72	0.17	-2.74910768	0.005975775	0.010732807
SPD_0044	SPD_0044			acyl carrier protein, putative	737.73	9.53	0.63	1.55	0.23	2.748749307	0.005982312	0.010734459
SPD_1202	psr			Psr protein	10251.75	13.32	0.36	1.28	0.13	2.747994258	0.005996106	0.010749117
SPD_1166	SPD_1166			hypothetical protein	1702.43	10.73	0.51	1.42	0.19	2.741594145	0.006114184	0.01095052
SPD_1383	pacL			cation-transporting ATPase, E1-E2 family protein	7425.47	12.86	0.43	1.35	0.16	2.74081088	0.006128777	0.01096638
SPD_1283	SPD_1283			hypothetical protein	132.12	7.05	-0.60	0.66	0.22	-2.73330044	0.006270311	0.011200251
SPD_1731	SPD_1731			hypothetical protein	56.08	5.81	0.85	1.80	0.31	2.733253584	0.006271203	0.011200251
SPD_2037	cysK			cysteine synthase A	844.12	9.72	0.47	1.39	0.17	2.728961686	0.006353409	0.011336474
SPD_1457	dtd			D-tyrosyl-tRNA(Tyr) deacylase	2355.02	11.20	0.47	1.39	0.17	2.728148912	0.006369085	0.011353844
SPD_1614	phoU3			phosphate transport system regulatory protein PhoU, putative	48.65	5.60	-0.97	0.51	0.35	-2.723412199	0.006461139	0.011509723
SPD_1428	cmk			cytidylate kinase	1745.42	10.77	0.59	1.51	0.22	2.716794873	0.006591745	0.011728887
SPD_0863	smpB			SsrA-binding protein	3594.53	11.81	0.47	1.39	0.17	2.714336963	0.006640858	0.011805283
SPD_1299	SPD_1299			hypothetical protein	32.96	5.04	-1.33	0.40	0.49	-2.712997461	0.006667762	0.011842094
SPD_1354	SPD_1354			hypothetical protein	130.28	7.03	0.69	1.61	0.25	2.711566743	0.006696606	0.011882278
SPD_0106	SPD_0106			bacteriocin, putative	640.23	9.32	0.46	1.38	0.17	2.705519564	0.006819763	0.01208958
SPD_0035	SPD_0035			hypothetical protein	1391.24	10.44	-0.45	0.73	0.17	-2.7044438	0.006841884	0.012117554
SPD_1034	SPD_1034			hydrolase, haloacid dehalogenase-like family protein	753.72	9.56	-0.54	0.69	0.20	-2.703955659	0.006851943	0.012124133
SPD_0624	thiE-1	RpoD		thiamine-phosphate pyrophosphorylase	578.91	9.18	-0.53	0.69	0.20	-2.702116321	0.006889965	0.012180133
SPD_0664	metK			S-adenosylmethionine synthetase	8071.21	12.98	-0.39	0.76	0.14	-2.699387361	0.006946727	0.012269126
SPD_1411	entB			isochorismatase family protein	4265.85	12.06	0.46	1.38	0.17	2.698178372	0.006972007	0.012294512
SPD_1787	rnmV			primase-related protein	2108.51	11.04	0.42	1.34	0.16	2.698084822	0.006973967	0.012294512
SPD_0404	ilvB	CodY	CcpA, RpoD	acetolactate synthase, large subunit, biosynthetic type	7953.43	12.96	-0.63	0.65	0.23	-2.696683585	0.007003378	0.012334982
SPD_1422	pdxU2			membrane protein, putative	587.20	9.20	0.46	1.38	0.17	2.691046176	0.007122834	0.012533826
SPD_0577	zmpB			zinc metalloprotease ZmpB	168129.28	17.36	0.39	1.31	0.14	2.687411157	0.007200826	0.012659409
SPD_0052	purL			phosphoribosylformylglycinamidine synthase, putative	905.22	9.82	0.59	1.51	0.22	2.682271899	0.0073124	0.012843747
SPD_1014	SPD_1014			IS630-Spn1, transposase Orf1	5048.45	12.30	-0.67	0.63	0.25	-2.678123712	0.007403587	0.012991969
SPD_1967	SPD_1967			IS1381, transposase OrfB	10.91	3.45	1.87	3.66	0.70	2.666430348	0.007666149	0.013440377
SPD_2060	pipR			transcriptional regulator, TetR family protein	116.18	6.86	1.04	2.06	0.39	2.644031412	0.008192505	0.014350025
SPD_1534	scrB	ScrR		sucrose-6-phosphate hydrolase	717.36	9.49	-0.48	0.72	0.18	-2.630147314	0.008534788	0.014935878
SPD_1616	SPD_1616			hypothetical protein	49.24	5.62	-0.91	0.53	0.34	-2.626823128	0.008618612	0.015068772
SPD_0489	SPD_0489			hypothetical protein	245.86	7.94	-0.53	0.69	0.20	-2.624237836	0.008684312	0.015169762
SPD_1486	penA			penicillin-binding protein 2B	5381.11	12.39	-0.36	0.78	0.14	-2.613300653	0.008967238	0.015649673
SPD_1159	SPD_1159			hypothetical protein	360.00	8.49	-0.71	0.61	0.27	-2.608895771	0.00908349	0.015838093
SPD_0519	SPD_0519			hypothetical protein	92.87	6.54	0.88	1.84	0.34	2.596701855	0.009412358	0.016396551
SPD_1208	aroC			chorismate synthase	6841.90	12.74	0.46	1.38	0.18	2.586476069	0.00969629	0.016875784
SPD_1939	SPD_1939			hypothetical protein	4.63	2.21	2.04	4.11	0.79	2.580401345	0.009868555	0.017159971
SPD_0305	ftsL			cell division protein FtsL	1637.22	10.68	-0.38	0.77	0.15	-2.577081379	0.009963849	0.017309923
SPD_0867	SPD_0867	ComX		O-methyltransferase	1545.99	10.59	0.51	1.42	0.20	2.576088549	0.009992505	0.01734394
SPD_1232	pstS2			phosphate ABC transporter, phosphate-binding protein, putative	5105.93	12.32	-0.49	0.71	0.19	-2.574295088	0.010044456	0.017418291
SPD_1120	topA			DNA topoisomerase I	6396.64	12.64	-0.47	0.72	0.18	-2.571099903	0.010137608	0.017563888
SPD_0180	SPD_0180			hypothetical protein	4220.82	12.04	-0.67	0.63	0.26	-2.569042462	0.010197996	0.01765251
SPD_2018	SPD_2018			isoprenylcysteine carboxyl methyltransferase (ICMT) family protein	1316.73	10.36	0.42	1.34	0.16	2.561795836	0.010413251	0.018008799
SPD_1784	SPD_1784			ABC transporter, ATP-binding protein	760.93	9.57	0.54	1.45	0.21	2.556274864	0.010579951	0.018280548
SPD_0599	murG			UDP-N-acetylglucosamine--N-acetylmuramyl- (pentapeptide) pyroph	2385.61	11.22	-0.37	0.77	0.14	-2.555572189	0.010601337	0.01829827
SPD_0603	SPD_0603			peptidase, M50 family protein	359.39	8.49	-0.71	0.61	0.28	-2.555130001	0.010614815	0.01829827
SPD_0963	SPD_0963			hypothetical protein	438.09	8.78	0.61	1.53	0.24	2.554989244	0.010619108	0.01829827
SPD_0127	trmU			tRNA (5-methylaminomethyl-2-thiouridylate)-methyltransferase	4963.81	12.28	0.38	1.30	0.15	2.554681236	0.010628508	0.01829827
SPD_0375	serS			seryl-tRNA synthetase	6356.64	12.63	0.37	1.29	0.14	2.553606663	0.010661362	0.01833831
SPD_1713	SPD_1713			hypothetical protein	2904.24	11.50	-0.32	0.80	0.13	-2.550555212	0.010755149	0.018482994
SPD_0260	rsuA-1			ribosomal small subunit pseudouridine synthase A	1244.41	10.28	-0.42	0.75	0.17	-2.55016635	0.010767153	0.018486999
SPD_0091	SPD_0091	CodY		hypothetical protein	6523.46	12.67	0.33	1.26	0.13	2.548900904	0.0108063	0.018537558
SPD_1397	aldR			endoribonuclease L-PSP	5789.72	12.50	0.36	1.28	0.14	2.546639948	0.010876559	0.018641349
SPD_1071	SPD_1071			hypothetical protein	1559.78	10.61	-0.48	0.72	0.19	-2.527567688	0.011485568	0.019667492
SPD_1402	dpr	RitR	CodY	non-heme iron-containing ferritin	91028.41	16.47	-0.37	0.77	0.15	-2.521910939	0.011671926	0.019968711
SPD_0809	cad			lysine decarboxylase	1171.22	10.19	-0.48	0.72	0.19	-2.519938847	0.011737522	0.020062974
SPD_1469	SPD_1469			hypothetical protein	19.44	4.28	1.15	2.22	0.46	2.518569387	0.011783267	0.020123166
SPD_1386	cca			polyA polymerase family protein	7620.88	12.90	0.39	1.31	0.16	2.517945256	0.011804167	0.020140859

Table S1 continued

					WT HOCl vs control							
Locus	Gene Symbol	Regulon	Further Regulon	Function	Base-Mean	A-value	M-value	Fold-change	Standard error	Wald statistic	P-value	Adjusted P-value
SPD_0259	SPD_0259			Transglycosylase associated protein	2358.38	11.20	0.45	1.37	0.18	2.516901373	0.011839197	0.020182609
SPD_0110	argG	ArgR		argininosuccinate synthase	536.95	9.07	0.41	1.33	0.16	2.512879189	0.011975034	0.02039598
SPD_1973	SPD_1973			alpha-1,2-mannosidase, putative	702.17	9.46	0.45	1.37	0.18	2.510688306	0.012049604	0.020504713
SPD_1783	SPD_1783			hypothetical protein	212.33	7.73	0.46	1.38	0.18	2.500306492	0.01240859	0.021096811
SPD_1170	appA			oligopeptide ABC transporter,oligopeptide-binding protein	543.25	9.09	0.64	1.56	0.26	2.497081607	0.012522014	0.021270727
SPD_0819	lspA			signal peptidase II	895.12	9.81	-0.39	0.76	0.16	-2.49402812	0.012630254	0.021435537
SPD_0777	thil			thiamine biosynthesis/tRNA modification protein Thil	4329.35	12.08	-0.38	0.77	0.15	-2.493428581	0.012651603	0.021452719
SPD_0345	cbpC			choline binding protein C	3356.58	11.71	0.38	1.30	0.15	2.488144753	0.012841146	0.021754813
SPD_1920	SPD_1920			peptidase, S54 (rhomboid) family protein	2035.20	10.99	0.42	1.34	0.17	2.485866283	0.012923652	0.021875198
SPD_1759	rpoB			DNA-directed RNA polymerase, beta subunit	33220.82	15.02	0.43	1.35	0.17	2.484934586	0.012957524	0.021913123
SPD_0827	yabA			hypothetical protein	595.25	9.22	-0.42	0.75	0.17	-2.483289336	0.013017531	0.021995138
SPD_1193	msrAB1			peptide methionine sulfoxide reductase msrA/msrB 1	13500.70	13.72	0.33	1.26	0.13	2.479959079	0.013139746	0.022182027
SPD_1031	mutX			Mutator mutT protein (7,8-dihydro-8-oxoguanine-triphosphatase) (8-	938.14	9.87	-0.50	0.71	0.20	-2.47908876	0.013171852	0.022216602
SPD_0781	SPD_0781	CodY		hypothetical protein	740.41	9.53	-0.42	0.75	0.17	-2.471374908	0.013459463	0.022681688
SPD_1437	plsC			acyltransferase domain protein	1115.62	10.12	-0.47	0.72	0.19	-2.466412831	0.013647394	0.022978124
SPD_1412	codY	CodY		GTP-sensing transcriptional pleiotropic repressor CodY	3677.42	11.84	0.36	1.28	0.15	2.465030951	0.013700142	0.02302745
SPD_1852	SPD_1852			hypothetical protein	70.12	6.13	0.71	1.64	0.29	2.465013985	0.01370079	0.02302745
SPD_1115	leuB			3-isopropylmalate dehydrogenase	1013.52	9.99	-0.44	0.74	0.18	-2.463893366	0.013743699	0.02307927
SPD_1482	mutT			MutT/nudix family protein	1395.68	10.45	-0.32	0.80	0.13	-2.461773878	0.01382518	0.023195714
SPD_1387	dapB			dihydrodipicolinate reductase	6358.86	12.63	0.50	1.41	0.20	2.460970355	0.013856181	0.023227336
SPD_1479	ftsZ			cell division protein FtsZ	16932.01	14.05	0.35	1.27	0.14	2.456256651	0.014039285	0.023513649
SPD_0514	SPD_0514			acetyltransferase, GNAT family protein	6107.26	12.58	0.36	1.28	0.15	2.454943463	0.014090675	0.023579054
SPD_1737	lytA	ComX		autolysin/N-acetylmuramoyl-L-alanine amidase	42887.42	15.39	0.43	1.35	0.18	2.45318547	0.014159731	0.023673881
SPD_0994	ribF	ComE		riboflavin biosynthesis protein RibF	11131.49	13.44	-0.80	0.57	0.33	-2.448164199	0.01435862	0.023985423
SPD_1460	pepO			endopeptidase O	24028.78	14.55	0.40	1.32	0.16	2.443690617	0.014537887	0.024263671
SPD_1560	SPD_1560			HAD superfamily protein (subfamily IIIA) phosphatase	2633.98	11.36	-0.36	0.78	0.15	-2.438291418	0.014756872	0.024607664
SPD_1610	SPD_1610	CcpA		hypothetical protein	89.45	6.48	0.71	1.64	0.29	2.43714659	0.014803677	0.02466419
SPD_0175	corA1			magnesium transporter, CorA family protein	5295.44	12.37	0.39	1.31	0.16	2.431121278	0.015052175	0.025056365
SPD_2051	SPD_2051			peptidase, M16 family protein	5405.79	12.40	-0.43	0.74	0.18	-2.430805494	0.0150653	0.025056386
SPD_0286	basA	CcpA		glutathione peroxidase	264.92	8.05	-0.54	0.69	0.22	-2.424892325	0.015312928	0.025446091
SPD_1440	ywnB	SifR		NAD(P)H-dependent quinone reductase	41.47	5.37	0.96	1.95	0.40	2.422288789	0.015423088	0.025606883
SPD_1736	SPD_1736			Putative toxin	234.51	7.87	0.45	1.37	0.19	2.421125927	0.015472516	0.025666648
SPD_1378	yaaA	ComE		UPF0246 protein YaaA	1632.70	10.67	-0.38	0.78	0.15	-2.418110251	0.015601349	0.025857917
SPD_0898	queT			membrane protein, putative	917.23	9.84	-0.48	0.54	0.36	-2.415971031	0.01569331	0.025987795
SPD_0145	SPD_0145	CodY	RpoD	hypothetical protein	183911.41	17.49	0.58	1.49	0.24	2.413907058	0.015782488	0.026112843
SPD_0795	SPD_0795			hypothetical protein	184.27	7.53	0.53	1.44	0.22	2.412718895	0.015834026	0.026175454
SPD_0942	SPD_0942			hypothetical protein	23.54	4.56	-1.14	0.45	0.47	-2.412268332	0.015853609	0.026185174
SPD_1167	appD			ABC transporter, ATP-binding protein	1491.58	10.54	0.41	1.33	0.17	2.397302015	0.016516304	0.02725618
SPD_1926	tyrS			tyrosyl-tRNA synthetase	7059.14	12.79	0.33	1.26	0.14	2.387343504	0.016970626	0.027981766
SPD_1113	SPD_1113			3-isopropylmalate dehydratase small subunit, putative	312.72	8.29	-0.43	0.74	0.18	-2.384978671	0.017080112	0.028138011
SPD_0452	creX	FabT		integrase/recombinase, phage integrase family protein	740.42	9.53	0.37	1.29	0.15	2.384171994	0.0171176	0.028175481
SPD_1004	gapN	Rex	CodY	glyceraldehyde-3-phosphate dehydrogenase, NADP-dependent	12033.96	13.55	0.43	1.35	0.18	2.383140437	0.017165644	0.028230247
SPD_0234	celD			PTS system, IIC component	219.37	7.78	0.48	1.39	0.20	2.38273697	0.017184468	0.028236903
SPD_0597	SPD_0597			ABC transporter, ATP-binding protein	130.41	7.03	0.58	1.49	0.24	2.38172738	0.017231649	0.028290104
SPD_0738	cdd-1			cytidine deaminase	3280.45	11.68	-0.34	0.79	0.14	-2.378900297	0.017364372	0.028483532
SPD_0163	SPD_0163			hypothetical protein	147.35	7.20	-0.59	0.66	0.25	-2.377788706	0.017416803	0.028545034
SPD_1797	ccpA	CcpA	GlnR	catabolite control protein A	4577.47	12.16	0.36	1.28	0.15	2.374379028	0.017578495	0.028785351
SPD_0585	SPD_0585			hypothetical protein	2158.13	11.08	0.33	1.26	0.14	2.369399034	0.017817019	0.029150962
SPD_1592	SPD_1592			acetyltransferase, GNAT family protein	77.72	6.28	-0.80	0.57	0.34	-2.363060677	0.018124702	0.029629004
SPD_1148	rplS			ribosomal protein L19	8177.93	13.00	-0.49	0.71	0.21	-2.360214442	0.018264374	0.029829414
SPD_0890	phtE	AdcR		pneumococcal histidine triad protein E precursor	15537.16	13.92	-0.47	0.72	0.20	-2.359927315	0.018278516	0.029829414
SPD_0353	SPD_0353			hypothetical protein	303.95	8.25	-0.47	0.72	0.20	-2.357355455	0.018405619	0.03001121
SPD_0399	prfC			peptide chain release factor 3	10761.76	13.39	-0.31	0.81	0.13	-2.356363891	0.018454829	0.030065796
SPD_0417	bacA			bacitracin resistance protein/undecaprenol kinase, putative	5542.22	12.44	0.42	1.34	0.18	2.35430681	0.018557287	0.030206964
SPD_1124	licB	CiaR	CcpA, RpoD	protein LicB	4068.82	11.99	-0.37	0.77	0.16	-2.351424612	0.018701679	0.030404784
SPD_1867	adr			membrane protein, putative	9557.46	13.22	-0.31	0.81	0.13	-2.351246457	0.018710636	0.030404784
SPD_1016	rexA			exonuclease RexA	6394.92	12.64	0.34	1.27	0.14	2.349709069	0.018788809	0.030504706
SPD_1937	malA	MalR		maltodextrose utilization protein MalA	1483.56	10.53	0.43	1.35	0.18	2.347339472	0.018908019	0.030673365
SPD_1550	yoeB			addiction module toxin, Txe/YoeB family protein	60.87	5.93	0.73	1.66	0.31	2.340407415	0.019262714	0.031222261
SPD_1012	eno	RpoD		phosphopyruvate hydratase	58720.25	15.84	0.38	1.30	0.16	2.3320021	0.019700581	0.031904923
SPD_0050	comB	ComE		competence factor transport protein ComB	17398.49	14.09	0.57	1.48	0.24	2.327619633	0.01993231	0.032252874
SPD_1187	rplL	CodY		ribosomal protein L7/L12	8918.33	13.12	-0.37	0.77	0.16	-2.321978008	0.02023412	0.032690673
SPD_1456	SPD_1456			hypothetical protein	6.17	2.63	-1.66	0.32	0.72	-2.321922984	0.020237083	0.032690673
SPD_1104	smc			chromosome segregation protein SMC	6071.02	12.57	-0.38	0.77	0.16	-2.320113104	0.02033476	0.032820714
SPD_1003	SPD_1003			hypothetical protein	3.08	1.62	1.98	3.94	0.86	2.319274221	0.020380172	0.032866253
SPD_0964	obgE			GTP1/Obg family GTP-binding protein	6569.83	12.68	0.40	1.32	0.17	2.31617545	0.020548691	0.033110075
SPD_0222	gpmB1			phosphoglycerate mutase family protein	5363.83	12.39	-0.32	0.80	0.14	-2.30833253	0.020980648	0.033777607
SPD_0535	murM			serine/alanine-adding enzyme MurM	5430.37	12.41	-0.32	0.80	0.14	-2.307122515	0.021047991	0.033857501
SPD_1572	SPD_1572			conserved hypothetical protein TIGR00046	1949.02	10.93	0.63	1.55	0.27	2.306803721	0.021065765	0.033857592
SPD_0975	radC	ComX		DNA repair protein RadC	1729.83	10.76	-0.77	0.59	0.33	-2.305585933	0.02113378	0.033938364
SPD_1670	amiC	RitR	CodY	oligopeptide ABC transporter, permease protein AmiC	8313.36	13.02	-0.40	0.76	0.17	-2.296236195	0.02166238	0.034758025
SPD_1557	nadD			nicotinate (nicotinamide) nucleotide adenylyltransferase	3486.53	11.77	0.38	1.30	0.17	2.29345075	0.021822068	0.034984875
SPD_0805	SPD_0805			transporter, permease protein, putative	529.21	9.05	0.53	1.44	0.23	2.292579214	0.021872242	0.035035922
SPD_1237	SPD_1237			membrane protein, putative	2003.78	10.97	0.32	1.25	0.14	2.291827637	0.021915591	0.035075959
SPD_1213	SPD_1213			membrane protein, putative	177.68	7.47	0.59	1.51	0.26	2.284669232	0.02233223	0.03571288
SPD_0321	cps2F	CpsR	RpoD, VncR	glycosyl transferase, group 2 family protein	10770.33	13.39	-0.31	0.81	0.14	-2.279346961	0.022646448	0.036185086
SPD_0999	rggD			transcriptional regulator MutR, putative	1951.27	10.93	-0.33	0.80	0.15	-2.277423016	0.022760977	0.036317483
SPD_0104	SPD_0104	WalR		LysM domain protein	12342.56	13.59	-0.59	0.66	0.26	-2.277316746	0.022767318	0.036317483
SPD_1184	SPD_1184			hypothetical protein	51.59	5.69	0.83	1.78	0.37	2.269524497	0.023236449	0.037034908
SPD_2050	rodZ			hypothetical protein	3463.36	11.76	0.38	1.30	0.17	2.262788511	0.023648729	0.037660602
SPD_0917	piaC			iron-compound ABC transporter, permease protein	1549.65	10.60	-0.44	0.74	0.20	-2.253909329	0.024201873	0.038509393
SPD_1542	stkP			serine/threonine protein kinase	23776.53	14.54	0.33	1.26	0.15	2.251385252	0.024361147	0.038730576
SPD_1102	SPD_1102			Cof family protein	2049.90	11.00	0.33	1.26	0.15	2.247628399	0.024599895	0.039077639
SPD_1137	SPD_1137			ABC transporter, ATP-binding protein	390.79	8.61	-0.42	0.75	0.19	-2.246060534	0.024700131	0.039204277
SPD_0278	SPD_0278	CelR	CcpA	hypothetical protein	8.27	3.05	-1.55	0.34	0.69	-2.241628191	0.024985412	0.039624169
SPD_1946	SPD_1946	RitR		hypothetical protein	430.15	8.75	0.46	1.38	0.21	2.232262667	0.025597608	0.040561383
SPD_1931	SPD_1931	CcpA		hypothetical protein	865.99	9.76	0.62	1.54	0.28	2.231643002	0.025638567	0.040592628
SPD_1969	SPD_1969			glycosyl hydrolase-related protein	34.67	5.12	0.84	1.79	0.37	2.22952872	0.025778747	0.040780782
SPD_1877	thrC			threonine synthase	8667.05	13.08	0.35	1.27	0.16	2.222405194	0.026255935	0.041501316
SPD_1311	mocA			oxidoreductase, Gfo/Idh/MocA family protein	4351.18	12.09	-0.54	0.69	0.25	-2.21363791	0.026853697	0.042411087
SPD_1834	adhE	Rex	CcpA, RpoD, RitR	alcohol dehydrogenase, iron-containing	12706.47	13.63	0.46	1.38	0.21	2.198346315	0.027924436	0.044065729
SPD_0134	SPD_0134			hypothetical protein	639.54	9.32	-0.38	0.77	0.17	-2.192329156	0.028355748	0.044709434
SPD_0408	SPD_0408	CodY	RpoD	hypothetical protein	1163.05	10.18	0.37	1.29	0.17	2.191365488	0.028425354	0.044782236
SPD_1290	tcyB	CmbR		amino acid ABC transporter, permease protein	2364.89	11.21	-0.31	0.81	0.14	-2.189695862	0.028546301	0.044935735
SPD_0747	SPD_0747			hypothetical protein	313.80	8.29	-0.53	0.69	0.24	-2.1889418	0.02860107	0.044984893
SPD_0327	cps2P	CpsR	RpoD	UDP-galactopyranose mutase	7748.85	12.92	0.32	1.25	0.15	2.188074773	0.028664156	0.045047041
SPD_1419	SPD_1419			hypothetical protein	247.43	7.95	0.59	1.51	0.27	2.176770597	0.029497688	0.046318884
SPD_1264	SPD_1264			ABC transporter, ATP-binding protein	2213.53	11.11	-0.36	0.78	0.17	-2.174751452	0.029648747	0.046517862
SPD_0658	prfB			peptide chain release factor 2	5556.24	12.44	-0.31	0.81	0.14	-2.172643754	0.02980714	0.04672801
SPD_1181	SPD_1181			hypothetical protein	21.23	4.41	0.98	1.97	0.45	2.171944147	0.029859876	0.046772314
SPD_1298	nox			NADH oxidase	10265.56	13.33	0.36	1.28	0.17	2.160161153	0.030760196	0.048143108
SPD_0094	ptvB	PtvR	RitR, RpoD, CcpA	hypothetical protein	5554.95	12.44	-0.48	0.72	0.22	-2.159318655	0.030825454	0.048205763
SPD_1506	axe1			acetyl xylan esterase, putative	2844.35	11.47	-0.56	0.68	0.26	-2.156199685	0.031068076	0.048530193
SPD_0846	SPD_0846	ComX		membrane protein, putative	9812.79	13.26	0.51	1.42	0.24	2.155995519	0.031083703	0.048530193
SPD_2049	pgsA	CodY		CDP-diacylglycerol--glycerol-3-phosphate 3-phosphatidyltransferase	1591.88	10.64	0.43	1.35	0.20	2.153372111	0.031289446	0.048811535
SPD_1090	panT			membrane protein, putative	3662.00	11.84	-0.40	0.76	0.19	-2.152210594	0.031380772	0.048914074
SPD_0254	polC			DNA polymerase III, alpha subunit, Gram-positive type	9095.42	13.15	0.39	1.31	0.18	2.148926507	0.031640226	0.049278299
SPD_1551	yefM			prevent-host-death family protein	99.28	6.63	0.62	1.54	0.29	2.148416911	0.031680651	0.049301078
SPD_1455	SPD_1455			hypothetical protein	7.51	2.91	-1.43	0.37	0.66	-2.145382787	0.031922254	0.049636638
SPD_0711	SPD_0711			hypothetical protein	74.69	6.22	0.59	1.51	0.27	2.14401419	0.03203175	0.049766402
SPD_0041	araT			aromatic amino acid aminotransferase	3083.00	11.59	-0.39	0.76	0.18	-2.142613346	0.032144159	0.049900477
SPD_1346	mltG			putative BCR, putative	13433.23	13.71	-0.29	0.82	0.14	-2.141126316	0.032263853	0.050045636
SPD_1372	SPD_1372			glyoxalase family protein	1646.04	10.68	-0.45	0.73	0.21	-2.13960005	0.032387103	0.050196069
SPD_1734	SPD_1734			hypothetical protein	258.44	8.01	0.47	1.39	0.22	2.135889338	0.032688435	0.050622041
SPD_2022	clpC	CtsR		ATP-dependent Clp protease, ATP-binding subunit	11328.50	13.47	-0.35	0.78	0.16	-2.129030279	0.033251755	0.051452716
SPD_0593	typA			elongation factor Tu family protein	1663.16	14.05	-0.29	0.82	0.14	-2.116570091	0.034296351	0.053026154
SPD_1100	zwf	GlnR		glucose-6-phosphate 1-dehydrogenase	11863.97	13.53	0.43	1.35	0.20	2.106773071	0.035137255	0.054282372
SPD_0849	rplT			ribosomal protein L20	3956.57	11.95	-0.39	0.76	0.19	-2.103294077	0.035440071	0.054705958
SPD_0796	SPD_0796			hypothetical protein	463.78	8.86	0.45	1.37	0.22	2.094064518	0.036254233	0.055917546
SPD_1470	SPD_1470			hypothetical protein	41.95	5.39	0.67	1.59	0.32	2.081197255	0.037415855	0.05766266
SPD_0526	fba	MgrA	Rex, CodY, CcpA	fructose-1,6-bisphosphate aldolase, class II	20831.64	14.35	0.30	1.23	0.15	2.077266959	0.037776927	0.058172206
SPD_1168	appC			oligopeptide ABC transporter, pemease protein	462.25	8.85	0.33	1.26	0.16	2.069093835	0.038537282	0.059295287
SPD_1466	SPD_1466			ABC transporter, ATP-binding protein	638.04	9.32	0.34	1.27	0.17	2.065952698	0.038832946	0.05970214
SPD_0365	tig			trigger factor	24848.22	14.60	0.36	1.28	0.18	2.059114008	0.039483318	0.060653232
SPD_0282	SPD_0282	CelR	CcpA, RpoD	membrane protein, putative	24.84	4.63	-1.09	0.47	0.53	-2.053379756	0.040035761	0.061443712
SPD_1179	lanL			Lanthionine biosynthesis protein LanL	1984.31	10.95	0.37	1.29	0.18	2.053107005	0.040062201	0.061443712
SPD_1649	piuB	RitR	RpoD, CodY, SifR	iron-compound ABC transporter, permease protein	184.14	7.52	0.68	1.60	0.33	2.052244292	0.040145927	0.061522748
SPD_1360	SPD_1360	CcpA		hypothetical protein	2343.22	11.19	-0.61	0.66	0.30	-2.0381654	0.041533394	0.063598801
SPD_1192	SPD_1192			ABC transporter, ATP-binding/permease protein	6557.03	12.68	0.30	1.23	0.15	2.037802256	0.041569713	0.063602659
SPD_0172	SPD_0172			CAAX amino terminal protease family protein	688.02	9.43	-0.39	0.76	0.19	-2.027079327	0.042654301	0.065209895
SPD_1229	pstB2-1			phosphate ABC transporter, ATP-binding protein, putative	4296.76	12.07	0.25	1.19	0.12	2.021279282	0.043250863	0.066069063
SPD_0836	SPD_0836			hypothetical protein	3323.69	11.70	-0.29	0.82	0.14	-2.013848299	0.044025463	0.06719861
SPD_0264	manL	CcpA	CiaR	PTS system, mannose-specific IIAB components	6834.74	12.74	0.39	1.31	0.19	2.011030859	0.044322197	0.067597541
SPD_1921	SPD_1921			5-formyltetrahydrofolate cyclo-ligase family protein	2000.17	10.97	0.29	1.22	0.14	2.007514133	0.044694947	0.068111678
SPD_0928	SPD_0928			hypothetical protein	359.52	8.49	-0.36	0.78	0.18	-2.001794197	0.04530687	0.068989187
SPD_1955	SPD_1955			hypothetical protein	10.87	3.44	-1.18	0.44	0.59	-1.998098761	0.045705954	0.069541464
SPD_1723	SPD_1723			hypothetical protein	54.77	5.78	0.71	1.64	0.36	1.99511164	0.046030705	0.069979855
SPD_1611	SPD_1611			hypothetical protein	11.09	3.47	1.14	2.20	0.57	1.994161275	0.046134433	0.070081797
SPD_0886	etrx2			thioredoxin family protein	2520.75	11.30	-0.49	0.71	0.24	-1.988097149	0.046800947	0.071037815
SPD_0078	SPD_0078			glycosyl transferase, group 2 family protein	725.97	9.50	-0.36	0.78	0.18	-1.981355241	0.047551449	0.072119698

Table S1 continued

					WT HOCl vs control							
Locus	Gene Symbol	Regulon	Further Regulon	Function	Base-Mean	A-value	M-value	Fold-change	Standard error	Wald statistic	P-value	Adjusted P-value
SPD_0790	pyk	CcpA		pyruvate kinase	18075.64	14.14	-0.30	0.81	0.15	-1.978326387	0.047891898	0.072578444
SPD_1191	SPD_1191			ABC transporter, ATP-binding/permease protein	7536.18	12.88	0.26	1.20	0.13	1.976292957	0.048121607	0.072868772
SPD_1244	hprK	CcpA		Hpr(Ser) kinase/phosphatase	5930.44	12.53	-0.35	0.78	0.18	-1.973236679	0.048468603	0.073336105
SPD_0062	purB			adenylosuccinate lyase	4534.33	12.15	0.31	1.24	0.15	1.972865113	0.048510932	0.073342082
SPD_1599	trpC			indole-3-glycerol phosphate synthase	1617.25	10.66	0.40	1.32	0.20	1.972301423	0.048575207	0.073349305
SPD_1544	sun			ribosomal RNA small subunit methyltransferase B	6134.05	12.58	0.29	1.22	0.15	1.97215009	0.048592475	0.073349305
SPD_2030	dnaB			replicative DNA helicase	10734.87	13.39	0.33	1.26	0.17	1.971195765	0.048701488	0.073414042
SPD_1388	SPD_1388			DegV family protein	7443.54	12.86	0.24	1.18	0.12	1.971102128	0.048712195	0.073414042
SPD_0245	eep			zinc metalloprotease Eep	7996.10	12.97	0.31	1.24	0.16	1.962323382	0.049724847	0.074881152
SPD_1337	atpA	RpoD		ATP synthase F1, alpha subunit	20616.84	14.33	-0.29	0.82	0.15	-1.961427068	0.049829225	0.074979251
SPD_0391	briC	ComE		hypothetical protein	3038.48	11.57	-0.43	0.74	0.22	-1.960539146	0.049932807	0.075030175
SPD_1674	SPD_1674	RafR		hypothetical protein	16.68	4.06	1.04	2.06	0.53	1.960463913	0.049941592	0.075030175
SPD_0267	SPD_0267	RpoD		xanthine/uracil permease family protein	2199.78	11.10	-0.41	0.75	0.21	-1.957882586	0.050243792	0.075424891
SPD_0255	relB1			addiction module antitoxin, RelB/DinJ family protein, putative	818.63	9.68	0.35	1.27	0.18	1.956543891	0.050401117	0.075583727
SPD_0655	livG	CodY		branched-chain amino acid ABC transporter, ATP-binding protein	4269.79	12.06	0.31	1.24	0.16	1.956309521	0.050428703	0.075583727
SPD_0991	rpmA			ribosomal protein L27	13908.46	13.76	-0.36	0.78	0.18	-1.955951656	0.050470849	0.075587612
SPD_0322	cps2G	CpsR	RpoD, VncR	glycosyl transferase, group 1 family protein	32743.75	15.00	-0.36	0.78	0.19	-1.949521004	0.051233237	0.076669315
SPD_1194	thrB			homoserine kinase	7248.62	12.82	-0.25	0.84	0.13	-1.941677334	0.052176174	0.078019303
SPD_1853	ackA	CcpA		acetate kinase	5225.86	12.35	0.24	1.18	0.13	1.93167527	0.053399599	0.079781406
SPD_0753	pcp	CodY		pyrrolidone-carboxylate peptidase	6417.57	12.65	0.34	1.27	0.17	1.931363664	0.053438095	0.079781406
SPD_0680	SPD_0680			hypothetical protein	2307.06	11.17	-0.35	0.78	0.18	-1.917856802	0.055129171	0.082239563
SPD_1169	appB			oligopeptide ABC transporter, permease protein	289.42	8.18	0.34	1.27	0.17	1.917529841	0.055170654	0.082239563
SPD_1768	asnA			aspartate--ammonia ligase	12065.39	13.56	-0.28	0.82	0.14	-1.916617738	0.055286513	0.082348033
SPD_1351	snf			Snf2 family protein	7740.70	12.92	0.28	1.21	0.15	1.913999168	0.055620262	0.082780624
SPD_1019	rbgA			GTP-binding protein	2337.93	11.19	-0.33	0.80	0.17	-1.91243317	0.055820657	0.083014222
SPD_1774	pflA	CcpA	GlnR	pyruvate formate-lyase activating enzyme	5513.40	12.43	-0.23	0.85	0.12	-1.89960723	0.057484683	0.085422417
SPD_1077	gyrA			DNA gyrase, A subunit	14925.26	13.87	-0.24	0.85	0.13	-1.897284973	0.057790337	0.085809895
SPD_0973	pcrA			ATP-dependent DNA helicase PcrA	4846.37	12.24	0.30	1.23	0.16	1.896727835	0.057863868	0.085852369
SPD_1273	SPD_1273			IS66 family element, Orf1	11.46	3.52	-1.06	0.48	0.56	-1.896077187	0.057949839	0.08590658
SPD_2015	hslO			chaperonin, 33 kDa	3524.44	11.78	-0.31	0.81	0.16	-1.895771144	0.057990313	0.08590658
SPD_0739	SPD_0739			putative membrane lipoprotein TmpC precursor	15030.40	13.88	0.27	1.21	0.14	1.895159901	0.058071221	0.085959801
SPD_0326	cps2K	CpsR	RpoD, CodY, VncR	UDP-glucose 6-dehydrogenase, putative	20140.84	14.30	0.28	1.21	0.15	1.894387109	0.058173646	0.086044766
SPD_0349	fni			isopentenyl-diphosphate delta-isomerase, type 2	2081.49	11.02	0.28	1.21	0.15	1.892859317	0.058376581	0.086278148
SPD_1732	SPD_1732			hypothetical protein	244.98	7.94	0.40	1.32	0.21	1.890566106	0.058682288	0.086662947
SPD_0165	hexB			DNA mismatch repair protein HexB	5586.52	12.45	0.29	1.22	0.16	1.884555053	0.059489935	0.087787851
SPD_0735	SPD_0735			methyltransferase small domain, putative	1360.65	10.41	-0.36	0.78	0.19	-1.881425297	0.059914088	0.088345542
SPD_1593	comA	ComX		type IV prepilin peptidase, putative	1019.58	9.99	0.60	1.52	0.32	1.878086377	0.06036935	0.088948209
SPD_0043	plsX			fatty acid/phospholipid synthesis protein PlsX	2234.67	11.13	0.42	1.34	0.23	1.876978876	0.060520989	0.089102935
SPD_0357	cbpF	VraR		choline binding protein F	3598.95	11.81	-0.28	0.82	0.15	-1.875367245	0.060742218	0.089359799
SPD_0093	ptvC	PtvR	RpoD, CcpA	membrane protein, putative	2858.09	11.48	0.39	1.31	0.21	1.874190309	0.060904199	0.089529173
SPD_1029	pdrM			MATE efflux family protein	3371.19	11.72	0.28	1.21	0.15	1.872654546	0.061116104	0.089771618
SPD_1772	acyP			acylphosphatase, putative	160.75	7.33	0.40	1.32	0.21	1.869716219	0.061523236	0.090300234
SPD_1348	SPD_1348			acetyltransferase, GNAT family protein	1890.47	10.88	0.26	1.20	0.14	1.867565601	0.061822645	0.09067005
SPD_1171	SPD_1171			hypothetical protein	541.46	9.08	-0.45	0.73	0.24	-1.866406856	0.061984465	0.090814665
SPD_0039	SPD_0039			hypothetical protein	1198.35	10.23	0.41	1.33	0.22	1.866179232	0.062016294	0.090814665
SPD_1087	fhs	CmhR		formate--tetrahydrofolate ligase	4341.32	12.08	-0.33	0.80	0.17	-1.86443358	0.062260529	0.091102505
SPD_1897	pgi			glucose-6-phosphate isomerase	15228.69	13.89	0.25	1.19	0.14	1.863756529	0.062355903	0.09117225
SPD_1951	SPD_1951			transporter, major facilitator family protein	100.87	6.66	-0.49	0.71	0.26	-1.862502556	0.062532286	0.091360243
SPD_1349	murC			UDP-N-acetylmuramate--alanine ligase	9559.01	13.22	0.23	1.17	0.13	1.861578402	0.06266254	0.091480607
SPD_1728	SPD_1728			hypothetical protein	15707.60	13.94	-0.31	0.81	0.17	-1.850389349	0.064257453	0.093737399
SPD_1780	rpe			ribulose-phosphate 3-epimerase	2459.72	11.26	0.26	1.20	0.14	1.846678631	0.064793731	0.094447612
SPD_0414	SPD_0414			membrane protein, putative	2849.84	11.48	-0.29	0.82	0.16	-1.844097135	0.065168985	0.094922203
SPD_0838	phoH			PhoH family protein	3210.76	11.65	-0.30	0.81	0.16	-1.825680218	0.067898445	0.098822489
SPD_1150	crcB2			CrcB protein	1270.67	10.31	-0.31	0.81	0.17	-1.825209066	0.067969486	0.0988506
SPD_1655	scpB			segregation and condensation protein B	4283.10	12.06	0.26	1.20	0.14	1.823802115	0.068181994	0.099084251
SPD_1629	pbuX			xanthine permease	752.11	9.55	0.47	1.39	0.26	1.81933942	0.068859663	0.099993021
SPD_1350	SPD_1350			hypothetical protein	7036.66	12.78	-0.45	0.73	0.25	-1.815560991	0.069437742	0.100755904
SPD_0352	vraR	VraR		DNA-binding response regulator	570.32	9.16	-0.46	0.73	0.25	-1.81498529	0.06952617	0.100807672
SPD_0064	cpsR	CpsR	CcpA	transcriptional regulator, GntR family protein	33595.18	15.04	-0.36	0.78	0.20	-1.809865769	0.070316606	0.101876447
SPD_0265	adhA			alcohol dehydrogenase, zinc-containing	1348.52	10.40	0.25	1.19	0.14	1.800533897	0.071776376	0.103912617
SPD_0013	ftsH			cell division protein FtsH	18306.83	14.16	0.35	1.27	0.19	1.797683427	0.072227189	0.104486116
SPD_0376	manO			hypothetical protein	2334.71	11.19	-0.38	0.77	0.21	-1.795633687	0.072552795	0.104877754
SPD_0673	SPD_0673			hypothetical protein	13.42	3.75	-0.96	0.51	0.53	-1.794973022	0.072657998	0.104950442
SPD_1511	aroG			phospho-2-dehydro-3-deoxyheptonate aldolase	7970.50	12.96	-0.25	0.84	0.14	-1.788179857	0.073746995	0.10637438
SPD_1474	divIVA			cell division protein DivIVA	9443.91	13.21	0.25	1.19	0.14	1.788129419	0.07375513	0.10637438
SPD_1744	comM	ComE		lipoprotein, putative	1440.10	10.49	-0.35	0.78	0.20	-1.777834135	0.0754311	0.108709527
SPD_0948	nikS			hypothetical protein	43.43	5.44	0.59	1.51	0.34	1.77376849	0.076101452	0.109513624
SPD_1076	srtA			sortase	4085.45	12.00	0.26	1.20	0.15	1.773755152	0.076103659	0.109513624
SPD_2043	pcsB	WalR		secreted 45 kDa protein precursor	15498.03	13.92	-0.34	0.79	0.19	-1.772377608	0.076331896	0.109759408
SPD_0915	piaA			iron-compound ABC transporter, iron compound-binding protein	4845.31	12.24	-0.39	0.76	0.22	-1.769895602	0.076744534	0.110269777
SPD_1364	SPD_1364			hypothetical protein	2913.92	11.51	0.30	1.23	0.17	1.769037104	0.076887683	0.110392458
SPD_0136	tsaD			glycoprotease family protein	2687.24	11.39	0.27	1.21	0.15	1.768526787	0.076972878	0.110431809
SPD_1185	SPD_1185			hypothetical protein	45.79	5.52	0.57	1.48	0.33	1.763304663	0.077849119	0.111605151
SPD_0418	SPD_0418			hypothetical protein	137.04	7.10	0.41	1.33	0.23	1.762379852	0.07800514	0.111744995
SPD_1322	SPD_1322			hypothetical protein	20.32	4.34	0.97	1.96	0.55	1.761526734	0.078149292	0.111867639
SPD_1520	frp			nitroreductase family protein	3280.10	11.68	-0.28	0.82	0.16	-1.759527723	0.078487916	0.112268269
SPD_0364	SPD_0364			ABC-type polar amino acid transport system, ATPase component	4.82	2.27	1.39	2.62	0.79	1.758827931	0.078606739	0.112354135
SPD_1778	rmuC	ComX		hypothetical protein	9032.57	13.14	0.35	1.27	0.20	1.756668673	0.0789743	0.112795133
SPD_0394	SPD_0394			hypothetical protein	8772.82	13.10	0.28	1.21	0.16	1.753084662	0.079587476	0.113586009
SPD_1312	yfmL			ATP-dependent RNA helicase, DEAD/DEAH box family protein	5237.85	12.35	0.26	1.20	0.15	1.743549854	0.081237614	0.115854537
SPD_1743	TsaE	ComE		TsaE protein, required for threonylcarbamoyladenosine t(6)A37 form	1658.98	10.70	-0.35	0.78	0.20	-1.742101322	0.081490716	0.116128828
SPD_0636	spxB	SpxR		pyruvate oxidase	79348.83	16.28	0.28	1.21	0.16	1.739486476	0.081949229	0.116695214
SPD_1196	mecA			adapter protein mecA	4154.96	12.02	-0.29	0.82	0.17	-1.739028133	0.082029814	0.11672299
SPD_1123	licC	CiaR	RpoD	CTP:phosphocholine cytidylyltransferase	3029.11	11.56	-0.25	0.84	0.15	-1.724185264	0.084674404	0.120396418
SPD_1158	gdhA	GlnR	CodY	NADP-specific glutamate dehydrogenase	17148.82	14.07	-0.29	0.82	0.17	-1.720630764	0.085317847	0.12122112
SPD_0707	thiJ			4-methyl-5(b-hydroxyethyl)-thiazole monophosphate biosynthesis pr	1956.56	10.93	0.21	1.16	0.12	1.718666985	0.085675027	0.12163817
SPD_1911	pstC	PnpR		phosphate ABC transporter, permease protein PstC	228.53	7.84	0.31	1.24	0.18	1.715846201	0.086190196	0.122278741
SPD_0822	proB			glutamate 5-kinase	2409.89	11.23	-0.25	0.84	0.14	-1.712998466	0.086712822	0.122928934
SPD_2035	comFA	ComX		helicase, putative	1998.70	10.96	-0.46	0.73	0.27	-1.710865677	0.087105912	0.123394661
SPD_2063	comE	ComE		response regulator	15000.16	13.87	-0.60	0.66	0.35	-1.7097329	0.087315276	0.123599624
SPD_1619	aatB			capsular polysaccharide biosynthesis protein, putative	13694.05	13.74	0.33	1.26	0.19	1.709262144	0.087402402	0.123631377
SPD_1719	SPD_1719			PAP2 family protein	74.73	6.22	-0.53	0.69	0.31	-1.705107381	0.088174399	0.124631122
SPD_0763	sufD			FeS assembly protein SufD	40447.27	15.30	0.22	1.16	0.13	1.701641156	0.088822657	0.125454618
SPD_1447	SPD_1447			hypothetical protein	372.32	8.54	-0.33	0.80	0.20	-1.701178087	0.088909551	0.125484603
SPD_0125	SPD_0125			hypothetical protein	17.07	4.09	-0.91	0.53	0.54	-1.694058618	0.090254145	0.127279677
SPD_1856	SPD_1856			hypothetical protein	4319.02	12.08	0.43	1.35	0.25	1.693740412	0.090314622	0.127279677
SPD_1510	aroF			phospho-2-dehydro-3-deoxyheptonate aldolase	11177.94	13.45	0.23	1.17	0.14	1.687002072	0.091602954	0.12900018
SPD_1647	pepA			glutamyl aminopeptidase PepA	4972.54	12.28	0.30	1.23	0.18	1.686412673	0.091716342	0.12906475
SPD_1015	rexB			ATP-dependent exonuclease RexB	3844.41	11.91	-0.26	0.84	0.15	-1.684244215	0.092134481	0.129557759
SPD_0828	SPD_0828			conserved hypothetical protein TIGR00096	1041.91	10.03	-0.26	0.84	0.15	-1.682106597	0.092548171	0.130043791
SPD_0869	SPD_0869			hypothetical protein	2.30	1.20	-1.51	0.35	0.90	-1.68076126	0.092809296	0.13031489
SPD_0786	argR2			transcriptional regulator of arginine metabolism expression, putative	406.14	8.67	0.38	1.30	0.23	1.680362377	0.092886831	0.130327999
SPD_0256	relE1			conserved hypothetical protein TIGR00053	1540.44	10.59	0.38	1.30	0.23	1.672449973	0.094435625	0.13233725
SPD_1483	murF			UDP-N-acetylmuramoylalanyl-D-glutamyl-2, 6-diaminopimelate--D-a	1215.64	10.25	-0.29	0.82	0.17	-1.672339691	0.094457357	0.13233725
SPD_2027	SPD_2027	ComX		Cytoplasmic thiamin-binding component of thiamin ABC transporter	764.57	9.58	0.24	1.18	0.14	1.666049443	0.095703567	0.133984994
SPD_0578	pabB			para-aminobenzoate synthase, component I	7278.78	12.83	0.32	1.25	0.19	1.659089824	0.097097693	0.135837256
SPD_0797	SPD_0797			hypothetical protein	6113.25	12.58	-0.32	0.80	0.19	-1.657129748	0.097493246	0.136290851
SPD_0657	acuB	CodY	CcpA	acetoin utilization protein AcuB, putative	266.88	8.06	0.30	1.23	0.18	1.655348705	0.097853785	0.13669487
SPD_1997	adcA	AdcR		zinc ABC transporter, zinc-binding lipoprotein	10975.68	13.42	-0.24	0.85	0.14	-1.652817916	0.098367927	0.137254133
SPD_1353	metB	CmhR		Cys/Met metabolism PLP-dependent enzyme, putative	736.71	9.52	0.28	1.21	0.17	1.652671279	0.098397783	0.137254133
SPD_0845	SPD_0845			ABC transporter, ATP-binding protein	2828.29	11.47	0.34	1.27	0.21	1.650588634	0.098822601	0.137746164
SPD_1970	SPD_1970			ROK family protein	19.70	4.30	0.72	1.65	0.43	1.648905335	0.09916703	0.137827561
SPD_0600	divIB			cell division protein DivIB	4229.43	12.05	-0.23	0.85	0.14	-1.648684112	0.099212367	0.137827561
SPD_1733	SPD_1733			hypothetical protein	123.96	6.95	0.38	1.30	0.23	1.648670201	0.099215218	0.137827561
SPD_0978	SPD_0978			hypothetical protein	3020.22	11.56	-0.33	0.80	0.20	-1.648544175	0.099241053	0.137827561
SPD_1097	SPD_1097			CAAX amino terminal protease family protein	745.47	9.54	-0.38	0.77	0.23	-1.648541441	0.099241614	0.137827561
SPD_1657	xerD			integrase/recombinase, phage integrase family protein	3886.46	11.92	0.25	1.19	0.15	1.642205254	0.100547474	0.139539741
SPD_0181	yqgF			conserved hypothetical protein TIGR00250	10153.31	13.31	-0.37	0.77	0.22	-1.637043997	0.101621277	0.14092762
SPD_0984	rluD3	CcpA	RpoD	ribosomal large subunit pseudouridine synthase, RluD subfamily pro	1640.74	10.68	-0.34	0.79	0.21	-1.634952083	0.102059093	0.141432144
SPD_0109	SPD_0109			amino acid ABC transporter, periplasmic amino acid-binding protein	177.74	7.47	0.41	1.33	0.25	1.63038129	0.103020936	0.142661601
SPD_0943	SPD_0943			hypothetical protein	49.77	5.64	-0.57	0.67	0.35	-1.628272024	0.103467219	0.143175855
SPD_1962	SPD_1962			hypothetical protein	3318.85	11.70	0.30	1.23	0.19	1.620692939	0.105083509	0.145307225
SPD_1040	ptsH	RpoD		phosphocarrier protein HPr	6575.09	12.68	0.27	1.21	0.17	1.616876602	0.10590492	0.146337167
SPD_1974	SPD_1974			hypothetical protein	160.38	7.33	0.62	1.54	0.39	1.611041396	0.1071707	0.147979196
SPD_1142	ffh			signal recognition particle protein	4682.99	12.19	0.21	1.16	0.13	1.606680684	0.108124433	0.149188297
SPD_0741	SPD_0741			sugar ABC transporter, permease protein, putative	3111.54	11.60	0.21	1.16	0.13	1.603786335	0.108761158	0.149910561
SPD_0601	SPD_0601			hypothetical protein	777.94	9.60	-0.29	0.82	0.18	-1.603588502	0.108804787	0.149910561
SPD_1254	SPD_1254			membrane protein, putative	120.96	6.92	-0.61	0.66	0.38	-1.601789975	0.109202061	0.150349523
SPD_1720	SPD_1720			hypothetical protein	47.27	5.56	-0.61	0.66	0.38	-1.593992133	0.110937797	0.152629323
SPD_1793	SPD_1793	CcpA		universal stress protein family protein	478.04	8.90	-0.29	0.82	0.18	-1.590771926	0.111660913	0.153513673
SPD_0049	comA	ComE		competence factor transporting ATP-binding/permease protein Com	22789.23	14.48	-0.34	0.79	0.21	-1.585179316	0.112925599	0.155085347
SPD_1628	xpt			xanthine phosphoribosyltransferase	297.60	8.22	0.45	1.37	0.28	1.584999681	0.112966407	0.155085347
SPD_0877	mtnN			MTA/SAH nucleosidase	3931.65	11.94	0.21	1.16	0.13	1.581237077	0.113823841	0.156150294
SPD_0862	rnr			ribonuclease R	8442.95	13.04	0.19	1.14	0.12	1.578722421	0.11439974	0.156827764
SPD_1631	dpnC			Dam-replacing family protein	331.66	8.37	-0.31	0.81	0.20	-1.577064237	0.114780745	0.157237279
SPD_0716	SPD_0716			IS630-Spn1, transposase Orf1	2058.06	11.01	-0.34	0.79	0.22	-1.574640183	0.115339522	0.157889561
SPD_0866	pepF	ComX		oligoendopeptidase F	4387.70	12.10	0.28	1.21	0.18	1.574055907	0.115474525	0.157961215
SPD_0895	hemH	RitR		ferrochelatase	61.79	5.95	0.55	1.46	0.35	1.572904168	0.11574101	0.158212496
SPD_1336	atpG	RpoD		ATP synthase F1, gamma subunit	20132.32	14.30	0.23	1.17	0.15	1.571996492	0.116044159	0.158513501
SPD_0919	SPD_0919			hypothetical protein	167.35	7.39	0.57	1.48	0.36	1.570048475	0.116403834	0.158891234

Table S1 continued

					WT HOCl vs control							
Locus	Gene Symbol	Regulon	Further Regulon	Function	Base-Mean	A-value	M-value	Fold-change	Standard error	Wald statistic	P-value	Adjusted P-value
SPD_1726	ply			pneumolysin	50151.50	15.61	0.23	1.17	0.15	1.569374714	0.116560652	0.158991725
SPD_0395	efp			translation elongation factor P	4716.44	12.20	-0.21	0.86	0.14	-1.568147639	0.116846681	0.159268193
SPD_1855	SPD_1855			hypothetical protein	6937.65	12.76	0.41	1.33	0.26	1.565925658	0.117366022	0.159862059
SPD_0257	SPD_0257			hypothetical protein	448.66	8.81	0.36	1.28	0.23	1.561954733	0.118298653	0.161017611
SPD_1190	trzA			Atz/Trz family protein	4686.83	12.19	0.23	1.17	0.15	1.561479682	0.118410614	0.161055291
SPD_1792	SPD_1792			hypothetical protein	142.57	7.16	-0.42	0.75	0.27	-1.561048698	0.118512261	0.161078898
SPD_1598	trpF			N-(5'phosphoribosyl)anthranilate isomerase	2329.90	11.19	0.24	1.18	0.15	1.559075285	0.118978562	0.161497731
SPD_0439	SPD_0439			hypothetical protein	2137.03	11.06	-0.24	0.85	0.16	-1.559029356	0.118989432	0.161497731
SPD_0359	SPD_0359			hypothetical protein	24.32	4.60	0.70	1.62	0.45	1.555727281	0.119772957	0.162338789
SPD_0024	purA	ComE		adenylosuccinate synthetase	9790.35	13.26	0.29	1.22	0.19	1.555701825	0.119779012	0.162338789
SPD_1355	SPD_1355			hypothetical protein	744.26	9.54	0.37	1.29	0.24	1.550431097	0.121038086	0.163928974
SPD_0530	glnH2			amino acid ABC transporter, amino acid-binding protein	510.45	9.00	-0.34	0.79	0.22	-1.548679062	0.12145889	0.164382392
SPD_0179	SPD_0179	VraR		lipoprotein, putative	8632.59	13.08	-0.36	0.78	0.23	-1.545225051	0.122291837	0.165392569
SPD_1204	aroK			shikimate kinase	3038.83	11.57	0.28	1.21	0.18	1.54464018	0.122433322	0.165466816
SPD_1267	SPD_1267			ABC transporter, ATP-binding protein	1711.00	10.74	-0.25	0.84	0.16	-1.543506579	0.122707912	0.165720721
SPD_0793	SPD_0793			hypothetical protein	84.02	6.39	0.42	1.34	0.27	1.541829602	0.123115007	0.166153091
SPD_1827	SPD_1827			membrane protein, putative	2781.90	11.44	0.29	1.22	0.19	1.541424228	0.123213571	0.166168761
SPD_1463	psaA	PsaR		ABC transporter, substrate binding lipoprotein	61523.27	15.91	-0.28	0.82	0.18	-1.53418336	0.12498455	0.168406614
SPD_1790	rpmH	RpoD		ribosomal protein L34	1880.69	10.88	-0.38	0.77	0.25	-1.533920627	0.125049181	0.168406614
SPD_0457	SPD_0457			hypothetical protein	61.60	5.94	0.47	1.39	0.31	1.531528035	0.125638943	0.169081704
SPD_1037	SPD_1037			histidine triad protein	36211.92	15.14	0.24	1.18	0.16	1.530859736	0.125804062	0.169184773
SPD_1020	rnhB			ribonuclease HII	2594.06	11.34	-0.26	0.84	0.17	-1.518993853	0.128764043	0.172972082
SPD_0681	SPD_0681			hypothetical protein	2453.87	11.26	0.46	1.38	0.31	1.51884588	0.128801294	0.172972082
SPD_0736	pdp			pyrimidine-nucleoside phosphorylase	1694.57	10.73	0.24	1.18	0.16	1.515655191	0.129606564	0.17393128
SPD_0227	SPD_0227			iron(III) ABC transporter, iron-binding protein	9.32	3.22	-0.97	0.51	0.64	-1.515019878	0.12976737	0.174024873
SPD_0879	dnaQ			exonuclease	651.49	9.35	-0.24	0.85	0.16	-1.511520063	0.130656001	0.175093701
SPD_0185	cls			cardiolipin synthetase	1490.04	10.54	0.23	1.17	0.16	1.509997514	0.131044058	0.175393676
SPD_1221	potA			spermidine/putrescine ABC transporter, ATP-binding protein	2590.03	11.34	-0.27	0.83	0.18	-1.509921695	0.131063406	0.175393676
SPD_0455	hsdR			type I restriction-modification system, R subunit	5269.38	12.36	-0.26	0.84	0.17	-1.509039338	0.13128873	0.175572263
SPD_0804	SPD_0804			ABC transporter, ATP-binding protein	200.64	7.65	-0.35	0.78	0.23	-1.505381477	0.132226029	0.176623745
SPD_0920	SPD_0920			hypothetical protein	80.13	6.32	-0.47	0.72	0.31	-1.505249851	0.132259853	0.176623745
SPD_1971	SPD_1971			glycosyl hydrolase-related protein	78.88	6.30	0.48	1.39	0.32	1.50339881	0.132736233	0.177136133
SPD_0271	folE			GTP cyclohydrolase I	2354.66	11.20	-0.26	0.84	0.17	-1.496834954	0.134436209	0.17927955
SPD_0102	sdhA			L-serine dehydratase, iron-sulfur-dependent, alpha subunit	1214.38	10.25	-0.25	0.84	0.17	-1.496283358	0.13457983	0.179345924
SPD_0450	SPD_0450			type I restriction-modification system, S subunit, putative	74.03	6.21	0.45	1.37	0.30	1.492035141	0.135689933	0.180699277
SPD_0992	SPD_0992			hypothetical protein	1.01	0.02	-1.31	0.40	0.88	-1.485868981	0.13731378	0.182734424
SPD_0422	SPD_0422			hypothetical protein	338.93	8.40	-0.41	0.75	0.28	-1.484006192	0.137807278	0.183263541
SPD_1270	SPD_1270			hypothetical protein	20.67	4.37	0.68	1.60	0.46	1.480299216	0.138793412	0.1844466
SPD_0369	zapA			hypothetical protein	2118.25	11.05	0.28	1.21	0.19	1.479624425	0.138973505	0.184557587
SPD_1392	disA			conserved hypothetical protein TIGR00159	3460.67	11.76	-0.25	0.84	0.17	-1.468639583	0.141930573	0.188353697
SPD_1503	SPD_1503	CcpA		hypothetical protein	7.33	2.87	0.95	1.93	0.65	1.461541471	0.143866903	0.190790876
SPD_0663	yqfR			ATP-dependent RNA helicase, DEAD/DEAH box family protein	3907.42	11.93	-0.19	0.88	0.13	-1.460851598	0.144056172	0.190909393
SPD_0751	SPD_0751	CodY		membrane protein, putative	12925.20	13.66	-0.28	0.82	0.20	-1.457745168	0.144910797	0.191908893
SPD_1320	SPD_1320	CcpA		glycerol uptake facilitator protein, putative	5374.09	12.39	-0.22	0.86	0.15	-1.450652285	0.146876708	0.194377693
SPD_0584	hflX			GTP-binding protein HflX	3997.14	11.96	-0.22	0.86	0.15	-1.445471584	0.148325469	0.19615915
SPD_0602	SPD_0602			hypothetical protein	205.54	7.68	-0.27	0.83	0.19	-1.442773455	0.149084299	0.197026346
SPD_1083	vicX	RpoD		vicX protein	4715.11	12.20	-0.24	0.85	0.17	-1.441917974	0.149325515	0.197208749
SPD_0105	SPD_0105			hypothetical protein	127.89	7.00	-0.38	0.77	0.27	-1.441181121	0.149533521	0.19734707
SPD_0184	SPD_0184	RpoD		lipoprotein, putative	3349.91	11.71	0.30	1.23	0.21	1.440340227	0.149771166	0.197524291
SPD_0981	SPD_0981			adenylate cyclase, putative	250.47	7.97	-0.35	0.78	0.24	-1.438413019	0.150316901	0.198107308
SPD_1622	SPD_1622			ABC transporter, ATP-binding/permease protein	12416.89	13.60	-0.28	0.82	0.19	-1.437806141	0.150489066	0.198197523
SPD_0642	SPD_0642			sodium-dependent transporter	137.31	7.10	0.29	1.22	0.20	1.434692778	0.151374663	0.199226571
SPD_1266	SPD_1266			membrane protein, putative	701.07	9.45	-0.23	0.85	0.16	-1.432232799	0.152077208	0.200013451
SPD_0051	purC	ComE		phosphoribosylaminoimidazole-succinocarboxamide synthase	82.35	6.36	0.54	1.45	0.38	1.429910807	0.15274262	0.200625097
SPD_1573	prmA			ribosomal protein L11 methyltransferase	2677.13	11.39	0.38	1.30	0.27	1.429877319	0.152752233	0.200625097
SPD_1393	SPD_1393			pyridine nucleotide-disulfide oxidoreductase family protein	977.64	9.93	0.27	1.21	0.19	1.427606615	0.153405118	0.201344218
SPD_0347	mvaD			diphosphomevalonate decarboxylase	1780.09	10.80	-0.22	0.86	0.16	-1.425646054	0.153970535	0.201947627
SPD_1041	nrdH	NrdR	RpoD	glutaredoxin-like protein NrdH	2356.30	11.20	-0.45	0.73	0.32	-1.422258861	0.154951117	0.203094365
SPD_0970	map	RitR		methionine aminopeptidase, type I	4814.71	12.23	0.19	1.14	0.13	1.412893984	0.157686898	0.206538494
SPD_1923	dapD			2,3,4,5-tetrahydropyridine-2-carboxylate N-succinyltransferase, puta	3489.38	11.77	-0.21	0.86	0.15	-1.411927224	0.157971391	0.206769403
SPD_0698	SPD_0698			hypothetical protein	1683.72	10.72	-0.19	0.88	0.13	-1.4037756	0.160385682	0.209785789
SPD_1725	yeeN			conserved hypothetical protein TIGR01033	10749.45	13.39	0.22	1.16	0.16	1.398320348	0.16201689	0.211774471
SPD_1595	SPD_1595	NrdR		hypothetical protein	1559.52	10.61	-0.27	0.83	0.19	-1.394379128	0.163203148	0.213179231
SPD_0272	sulD			bifunctional folate synthesis protein	2216.72	11.11	0.27	1.21	0.19	1.393129706	0.163580572	0.213526279
SPD_0268	SPD_0268	RpoD		CAAX amino terminal protease family protein	528.56	9.05	-0.25	0.84	0.18	-1.392536575	0.163759974	0.213614546
SPD_0868	prsA	CiaR		protease maturation protein, putative	5998.21	12.55	0.32	1.25	0.23	1.392054369	0.163905935	0.2136591
SPD_1109	SPD_1109			endonuclease, putative	904.03	9.82	-0.19	0.88	0.14	-1.390866807	0.16426582	0.213982264
SPD_0821	cbpE			choline binding protein E	6199.20	12.60	0.18	1.13	0.13	1.388197375	0.16477274	0.214496394
SPD_1209	aroB			3-dehydroquinate synthase	5625.07	12.46	0.25	1.19	0.18	1.385866934	0.165787539	0.215670516
SPD_1295	SPD_1295	RpoD		hemolysin	1586.56	10.63	-0.32	0.80	0.23	-1.383468115	0.166521378	0.216477791
SPD_1656	scpA	MgrA		segregation and condensation protein A	6377.52	12.64	0.17	1.13	0.12	1.382644883	0.16677378	0.216658527
SPD_0829	SPD_0829			hypothetical protein	895.93	9.81	0.25	1.19	0.18	1.381746046	0.167049691	0.216869537
SPD_1866	nagA	NagR	RpoD	N-acetylglucosamine-6-phosphate deacetylase	16561.17	14.02	-0.27	0.83	0.20	-1.377760114	0.168277364	0.218315033
SPD_0581	thyA			thymidylate synthase	2078.37	11.02	-0.27	0.83	0.19	-1.376222398	0.16875279	0.21869806
SPD_0436	cspR			TrmH family RNA methyltransferase	130.93	7.03	-0.37	0.77	0.27	-1.376065082	0.168801485	0.21869806
SPD_1331	SPD_1331			TPR domain protein	3775.60	11.88	-0.22	0.86	0.16	-1.37277043	0.169823726	0.219873402
SPD_1966	SPD_1966			IS1381, transposase OrfA	17.57	4.13	0.70	1.62	0.51	1.361571208	0.173333247	0.224265291
SPD_1239	SPD_1239			acyl-ACP thioesterase, putative	5402.67	12.40	-0.23	0.85	0.17	-1.36088961	0.173548577	0.22439197
SPD_0682	SPD_0682			hypothetical protein	12.44	3.64	-0.79	0.58	0.58	-1.357474297	0.174630555	0.225638263
SPD_1956	ilvD			dihydroxy-acid dehydratase	19876.31	14.28	-0.20	0.87	0.15	-1.355995553	0.175100583	0.226092712
SPD_0192	rpsJ			ribosomal protein S10	20368.21	14.31	-0.25	0.84	0.19	-1.34254608	0.179419	0.231512295
SPD_2019	SPD_2019			sensor histidine kinase	3146.12	11.62	0.21	1.16	0.16	1.340432015	0.180104933	0.232240572
SPD_1324	SPD_1324			IS630-Spn1, transposase Orf2	2.32	1.21	1.20	2.30	0.90	1.339441909	0.180426854	0.232498798
SPD_0802	tex			S1 RNA binding domain	4525.60	12.14	-0.20	0.87	0.15	-1.338610287	0.180695756	0.232690746
SPD_0550	rplK			ribosomal protein L11	13102.94	13.68	-0.33	0.80	0.25	-1.336828959	0.181278474	0.233281592
SPD_0279	celB	CelR	CcpA, RpoD	PTS system, IIB component	26.35	4.72	-0.60	0.66	0.45	-1.335680275	0.181653799	0.233603992
SPD_1321	mucB			cell wall surface anchor family protein	23.37	4.55	0.55	1.46	0.41	1.335314338	0.181773488	0.233603992
SPD_0171	tag			DNA-3-methyladenine glycosylase I	1665.44	10.70	-0.26	0.84	0.19	-1.33237923	0.182735604	0.23468262
SPD_1507	recG			ATP-dependent DNA helicase RecG	6058.96	12.56	0.24	1.18	0.18	1.323202831	0.185767935	0.238416739
SPD_1203	pheA			prephenate dehydratase	5169.50	12.34	0.20	1.15	0.15	1.317668103	0.187614777	0.240625395
SPD_0401	rpmB			ribosomal protein L28	6694.15	12.71	0.31	1.24	0.24	1.311147316	0.189807998	0.243275039
SPD_1253	SPD_1253			transcriptional repressor, putative	431.76	8.75	-0.38	0.77	0.30	-1.29385748	0.195714654	0.250677415
SPD_1857	comGG	ComX		Late competence protein ComGG	16052.32	13.97	0.35	1.27	0.27	1.292830849	0.196069568	0.250963794
SPD_0147	SPD_0147	CodY	RpoD	CAAX amino terminal protease family protein	101059.73	16.62	-0.16	0.90	0.13	-1.290302811	0.196945541	0.251916285
SPD_0709	gyrB			DNA gyrase, B subunit	9411.84	13.20	-0.18	0.88	0.14	-1.288407696	0.197604081	0.252589565
SPD_0009	SPD_0009			hypothetical protein	278.92	8.12	0.25	1.19	0.20	1.285722444	0.198539945	0.2536162
SPD_1826	nadC	NiaR	ComX	nicotinate-nucleotide pyrophosphorylase	3877.36	11.92	-0.24	0.85	0.19	-1.283995091	0.199143673	0.254217475
SPD_1711	ssbB	ComX		single-strand binding protein family protein	15985.63	13.96	-0.67	0.63	0.52	-1.282639924	0.199618256	0.254653196
SPD_0040	yeiH	RpoD		membrane protein, putative	10400.69	13.34	-0.16	0.90	0.13	-1.277157733	0.201546566	0.256860821
SPD_0432	mtsA			membrane protein, putative	522.67	9.03	0.20	1.15	0.16	1.27691919	0.201630779	0.256860821
SPD_1615	SPD_1615			hypothetical protein	47.16	5.56	-0.50	0.71	0.39	-1.276575913	0.20175201	0.256860821
SPD_1562	SPD_1562			small conductance mechanosensitive ion channel (MscS) family pro	2423.11	11.24	-0.26	0.84	0.20	-1.27316956	0.20295788	0.25822404
SPD_1565	SPD_1565			transcriptional regulator, putative	2204.29	11.11	0.20	1.15	0.15	1.271300716	0.203621688	0.258896238
SPD_1013	SPD_1013			integrase/recombinase, phage integrase family protein	2111.17	11.04	-0.30	0.81	0.23	-1.269171064	0.204380059	0.259574359
SPD_1858	comGF	ComX		Late competence protein ComGF	9361.01	13.19	0.35	1.27	0.28	1.269040294	0.204426693	0.259574359
SPD_0383	fabD	FabT	WalR, RpoD	malonyl CoA-acyl carrier protein transacylase	13997.79	13.77	-0.23	0.85	0.18	-1.259783479	0.207747481	0.263615828
SPD_2016	SPD_2016			TIM-barrel protein, nifR3 family protein, putative	4552.66	12.15	0.21	1.16	0.17	1.255281436	0.209376612	0.265506772
SPD_0817	SPD_0817	BlpR	ComE	CAAX amino terminal protease family protein	5228.30	12.35	-0.38	0.77	0.30	-1.249537347	0.211468603	0.267945109
SPD_1329	glnQ6			amino acid ABC transporter, ATP-binding protein	4759.28	12.22	0.19	1.14	0.15	1.249232934	0.21157989	0.267945109
SPD_0107	SPD_0107			membrane protein, putative	3600.56	11.81	0.18	1.13	0.15	1.247423621	0.21224221	0.26860587
SPD_0608	pyrF	PyrR	RpoD	orotidine 5'-phosphate decarboxylase	284.85	8.15	-0.33	0.80	0.27	-1.243876963	0.213544849	0.270004581
SPD_0276	SPD_0276			hypothetical protein	1.56	0.65	1.14	2.20	0.92	1.243645674	0.213629998	0.270004581
SPD_0927	nplT			Neopullulanase	621.54	9.28	-0.23	0.85	0.18	-1.24098023	0.214613052	0.271067775
SPD_0058	purD			phosphoribosylamine--glycine ligase	525.91	9.04	0.30	1.23	0.24	1.240294608	0.214866446	0.271208572
SPD_0551	rplA			ribosomal protein L1	17551.02	14.10	0.25	1.19	0.20	1.239655099	0.215102992	0.271327932
SPD_1379	SPD_1379	ComE		hypothetical protein	492.40	8.94	0.35	1.27	0.29	1.237868054	0.215764989	0.27198344
SPD_1099	glnQ5	GlnR		amino acid ABC transporter, ATP-binding protein	6265.15	12.61	0.26	1.20	0.21	1.236956899	0.216103084	0.272230055
SPD_1591	SPD_1591	RpoD		hypothetical protein	4997.55	12.29	0.66	1.58	0.54	1.23521644	0.216749963	0.272865071
SPD_0546	brnQ	RpoD		branched-chain amino acid transport system II carrier protein	2142.88	11.07	0.22	1.16	0.18	1.232923641	0.217604254	0.273760191
SPD_0791	SPD_0791			hypothetical protein	19.64	4.30	-0.72	0.61	0.58	-1.227608242	0.219594066	0.27608175
SPD_1594	SPD_1594	NrdR		transcriptional regulator	2666.48	11.38	0.31	1.24	0.25	1.226280805	0.220093022	0.27652713
SPD_1271	SPD_1271			hypothetical protein	8.41	3.07	0.83	1.78	0.68	1.219778968	0.222548676	0.279428726
SPD_1205	aroA			3-phosphoshikimate 1-carboxyvinyltransferase	5820.01	12.51	0.23	1.17	0.19	1.218881033	0.222889349	0.279672716
SPD_0547	SPD_0547			hypothetical protein	1733.95	10.76	-0.20	0.87	0.17	-1.218234736	0.223134783	0.279796962
SPD_1941	aspS			aspartyl-tRNA synthetase	6165.26	12.59	0.16	1.12	0.13	1.214134007	0.224696556	0.281570569
SPD_1218	potD			spermidine/putrescine ABC transporter, spermidine/putrescine-bindi	2814.11	11.46	0.16	1.12	0.13	1.207646804	0.227183148	0.284499997
SPD_1027	acoB			acetoin dehydrogenase, E1 component, beta subunit, putative	1069.31	10.06	0.19	1.14	0.16	1.206986084	0.227437503	0.284632003
SPD_1112	SPD_1112			hypothetical protein	143.85	7.17	-0.25	0.84	0.21	-1.201626392	0.229508312	0.287035593
SPD_1763	epuA			hypothetical protein	1838.94	10.84	0.18	1.13	0.15	1.198220542	0.23083117	0.288501221
SPD_1873	SPD_1873			hypothetical protein	68.30	6.09	-0.34	0.79	0.28	-1.196223345	0.231609413	0.289284698
SPD_0277	bglA-1	CelR	CcpA	6- phospho-beta-glucosidase	226.80	7.83	-0.27	0.83	0.23	-1.187629411	0.234979445	0.293302234
SPD_0878	orfX			hypothetical protein	4111.65	12.01	-0.26	0.84	0.22	-1.185343011	0.235881854	0.294236438
SPD_0835	frr			ribosome recycling factor	3196.06	11.64	-0.20	0.87	0.17	-1.179889733	0.238044074	0.296739873
SPD_0159	SPD_0159	CcpA		membrane protein putative	3349.16	11.71	0.23	1.17	0.19	1.178164123	0.238731183	0.297402405
SPD_1648	SPD_1648			NAD-dependent epimerase/dehydratase family protein	13.25	3.73	-0.66	0.63	0.56	-1.173288393	0.240680175	0.299635059
SPD_0248	glmS	NagR	RpoD	glucosamine--fructose-6-phosphate aminotransferase, isomerizing	8525.83	13.06	-0.16	0.90	0.14	-1.170216733	0.241913761	0.300974737
SPD_1927	ctpC			cation-transporting ATPase, E1-E2 family protein	7009.60	12.78	-0.20	0.87	0.17	-1.168883443	0.242450595	0.301446381
SPD_0865	coiA	ComX		competence protein CoiA	182.57	7.51	0.35	1.27	0.30	1.168066436	0.242779968	0.301659635
SPD_0405	ilvN	CodY	CcpA, RpoD	acetolactate synthase, small subunit	2719.88	11.41	-0.25	0.84	0.21	-1.166875796	0.243260532	0.302060348
SPD_1220	potH			spermidine/putrescine ABC transporter, permease protein	1140.45	10.16	-0.20	0.87	0.17	-1.166370423	0.243464712	0.302117574

Table S1 continued

					WT HOCl vs control							
Locus	Gene Symbol	Regulon	Further Regulon	Function	Base-Mean	A-value	M-value	Fold-change	Standard error	Wald statistic	P-value	Adjusted P-value
SPD_1928	SPD_1928			hypothetical protein	2758.67	11.43	-0.22	0.86	0.19	-1.164313118	0.244297142	0.302953822
SPD_2055	guaB			inosine-5'-monophosphate dehydrogenase	6709.40	12.71	-0.16	0.90	0.14	-1.16311473	0.244782957	0.303359423
SPD_1601	trpG			anthranilate synthase component II	1158.11	10.18	-0.21	0.86	0.18	-1.158605456	0.246617044	0.30543433
SPD_0831	SPD_0831			hypothetical protein	5.19	2.37	0.89	1.85	0.77	1.157011323	0.247267734	0.306041866
SPD_0985	pta	CcpA	RpoD	phosphate acetyltransferase	2008.08	10.97	0.20	1.15	0.17	1.155711829	0.247799048	0.306500959
SPD_1961	ulaR2			transcriptional regulator, BglG family protein	307.13	8.26	-0.25	0.84	0.22	-1.151441732	0.249550554	0.308467729
SPD_2028	cbpD	ComX		choline binding protein D	4520.95	12.14	-0.28	0.82	0.25	-1.149239749	0.250457135	0.309388225
SPD_1289	SPD_1289			amino acid ABC transporter, ATP-binding protein	3057.64	11.58	0.15	1.11	0.13	1.14491705	0.25224352	0.311196299
SPD_0977	SPD_0977			hypothetical protein	1669.13	10.70	-0.18	0.88	0.16	-1.14490985	0.252246503	0.311196299
SPD_1444	thrS			threonyl-tRNA synthetase	9153.37	13.16	0.20	1.15	0.18	1.136542009	0.255729794	0.315290089
SPD_1512	secA			preprotein translocase, SecA subunit	19172.44	14.23	-0.16	0.90	0.14	-1.135180611	0.256299652	0.315788933
SPD_0143	ugd	RitR		UDP-glucose 6-dehydrogenase, putative	21.77	4.44	0.50	1.41	0.44	1.134734268	0.256486675	0.315815744
SPD_1917	SPD_1917			hypothetical protein	15.74	3.98	0.64	1.56	0.57	1.131594073	0.257805133	0.317143373
SPD_0003	SPD_0003			hypothetical protein	641.65	9.33	0.28	1.21	0.24	1.131376142	0.257896809	0.317143373
SPD_1155	efeU			hypothetical protein	38.04	5.25	-0.38	0.77	0.34	-1.128102803	0.259276505	0.318634985
SPD_1066	xseB			exodeoxyribonuclease VII, small subunit	1772.13	10.79	-0.23	0.85	0.20	-1.126006511	0.260162763	0.319518664
SPD_0808	SPD_0808			hypothetical protein	0.62	-0.68	-0.92	0.53	0.82	-1.123946699	0.261035639	0.320384782
SPD_1103	SPD_1103			Cof family protein	1788.89	10.80	-0.17	0.89	0.15	-1.11985906	0.262773827	0.322311157
SPD_0527	SPD_0527	SifR	RpoD	oxidoreductase, putative	317.47	8.31	0.28	1.21	0.25	1.117776201	0.263662588	0.323193846
SPD_0285	SPD_0285			glycosyl hydrolase, family protein 31	4985.74	12.28	-0.21	0.86	0.19	-1.113771748	0.26537712	0.325086972
SPD_0839	SPD_0839			acetyltransferase, GNAT family protein	2400.31	11.23	-0.16	0.90	0.14	-1.112426987	0.265954607	0.325571601
SPD_1108	SPD_1108			hypothetical protein	415.10	8.70	0.18	1.13	0.17	1.112057403	0.26611347	0.325571601
SPD_1600	trpD			anthranilate phosphoribosyltransferase	2454.22	11.26	0.19	1.14	0.17	1.108188487	0.267780422	0.327401399
SPD_0001	dnaA			chromosomal replication initiator protein DnaA	5042.16	12.30	0.18	1.13	0.16	1.106147813	0.268662547	0.328269902
SPD_1418	pepQ			proline dipeptidase PepQ	2679.44	11.39	-0.18	0.88	0.17	-1.104086983	0.269555407	0.329150405
SPD_1558	SPD_1558			conserved hypothetical protein TIGR00253	4384.60	12.10	0.18	1.13	0.16	1.102030572	0.270448381	0.330029921
SPD_0570	yihY			ribonuclease BN, putative	630.70	9.30	-0.20	0.87	0.18	-1.100253253	0.271221794	0.330762507
SPD_0787	pepX			Xaa-Pro dipeptidyl-peptidase PepX	716.57	9.48	-0.21	0.86	0.19	-1.099670856	0.271475557	0.330860833
SPD_1189	SPD_1189			hypothetical protein	3.80	1.93	-0.97	0.51	0.89	-1.091180227	0.275193587	0.335178422
SPD_2014	SPD_2014	CcpA		Trans-acting positive regulator	1846.07	10.85	-0.15	0.90	0.13	-1.089912463	0.275751706	0.335644274
SPD_1327	bta	RafR		bacterocin transport accessory protein	2740.62	11.42	-0.27	0.83	0.25	-1.087643527	0.276752508	0.336648022
SPD_0133	cibA	ComX		hypothetical protein	15079.61	13.88	-0.60	0.66	0.55	-1.083842045	0.27843484	0.338478994
SPD_0079	SPD_0079			hypothetical protein	495.20	8.95	-0.17	0.89	0.15	-1.079122557	0.280533097	0.340812936
SPD_1272	SPD_1272			IS66 family element, Orf2	26.37	4.72	-0.43	0.74	0.40	-1.077851826	0.281099887	0.341284553
SPD_1727	SPD_1727			hypothetical protein	12849.88	13.65	-0.16	0.90	0.15	-1.06462471	0.287045793	0.348282229
SPD_0059	purE			phosphoribosylaminoimidazole carboxylase, catalytic subunit	204.01	7.67	0.27	1.21	0.26	1.060119708	0.289090143	0.350540141
SPD_0409	ilvA	CodY	RpoD	threonine dehydratase	3595.05	11.81	-0.16	0.90	0.15	-1.054372936	0.291712208	0.353495263
SPD_1063	ahrC			transcriptional regulator of arginine metabolism expression, putative	1803.45	10.82	0.14	1.10	0.14	1.049905748	0.293761449	0.355752933
SPD_2021	SPD_2021			hypothetical protein	333.19	8.38	-0.23	0.85	0.22	-1.04784	0.29471233	0.356678444
SPD_0224	SPD_0224			iron(III) ABC transporter, permease protein	9.90	3.31	0.62	1.54	0.59	1.046536099	0.295313587	0.357179915
SPD_1948	SPD_1948			hypothetical protein	676.14	9.40	-0.34	0.79	0.33	-1.04527975	0.295893694	0.357655186
SPD_1078	ldh	CcpA		L-lactate dehydrogenase	17010.09	14.05	-0.15	0.90	0.15	-1.041983479	0.297419339	0.359272033
SPD_0342	mapZ			hypothetical protein	6811.01	12.73	-0.14	0.91	0.13	-1.040415336	0.29814698	0.359923486
SPD_0671	SPD_0671			ABC transporter, ATP-binding protein	5552.88	12.44	0.14	1.10	0.13	1.0361244	0.30014411	0.362105678
SPD_1485	recR			recombination protein RecR	2255.88	11.14	0.20	1.15	0.19	1.035197112	0.300576867	0.362398986
SPD_0233	celC	CelR	CcpA, RpoD	PTS system, IIB component	66.58	6.06	0.33	1.26	0.33	1.01263517	0.311234454	0.375012007
SPD_0693	SPD_0693			oxidoreductase, aldo/keto reductase family protein	1009.42	9.98	0.15	1.11	0.15	1.003710193	0.315518322	0.379934161
SPD_0922	SPD_0922			hypothetical protein	259.92	8.02	-0.22	0.86	0.22	-0.99854696	0.318014205	0.382516651
SPD_0007	SPD_0007			S4 domain protein	1362.79	10.41	-0.16	0.90	0.16	-0.998445672	0.318063296	0.382516651
SPD_0323	csp2H	CpsR	RpoD, VncR	Polysaccharide polymerase	9036.13	13.14	-0.21	0.86	0.22	-0.990790574	0.321787853	0.38675257
SPD_1257	SPD_1257			hypothetical protein	1.09	0.13	-0.90	0.54	0.91	-0.981303913	0.326442894	0.392100798
SPD_0182	SPD_0182			hypothetical protein	14687.92	13.84	-0.21	0.86	0.21	-0.98004174	0.327065515	0.392601884
SPD_0146	SPD_0146	CodY	RpoD	CAAX amino terminal protease family protein	140926.92	17.10	0.13	1.09	0.13	0.978362485	0.327895076	0.393136282
SPD_0441	rpoE			DNA-directed RNA polymerase, delta subunit, putative	9785.08	13.26	-0.14	0.91	0.14	-0.97830772	0.327922153	0.393136282
SPD_0993	SPD_0993			hypothetical protein	1.07	0.10	-0.89	0.54	0.92	-0.97355487	0.330277604	0.395711912
SPD_1588	SPD_1588	RpoD		hypothetical protein	6607.00	12.69	-0.30	0.81	0.31	-0.971192439	0.331452458	0.396870707
SPD_1441	SPD_1441			hypothetical protein	1.44	0.53	0.88	1.84	0.91	0.967634943	0.333226719	0.39874533
SPD_0690	SPD_0690			hypothetical protein	29.51	4.88	-0.37	0.77	0.38	-0.966288061	0.333900058	0.399301008
SPD_1901	SPD_1901			transposase, putative	12.00	3.59	-0.60	0.66	0.63	-0.965055971	0.334516778	0.399788345
SPD_1788	tatD			hydrolase, TatD family protein	906.98	9.82	0.16	1.12	0.17	0.960751887	0.336676935	0.402118514
SPD_0556	SPD_0556			membrane protein, putative	12276.81	13.58	-0.14	0.91	0.15	-0.953424501	0.340375033	0.406281504
SPD_0135	riml			ribosomal-protein-alanine acetyltransferase	1113.04	10.12	-0.13	0.91	0.14	-0.952911809	0.340634756	0.406337715
SPD_0232	celB			PTS system, IIA component	60.70	5.92	-0.34	0.79	0.35	-0.95122574	0.341489795	0.407103554
SPD_1030	pyrC			dihydroorotase	2791.93	11.45	0.13	1.09	0.14	0.949900548	0.342162788	0.407250421
SPD_1275	nagR			transcriptional regulator, GntR family protein	1.11	0.14	0.86	1.82	0.91	0.949811745	0.342207917	0.407250421
SPD_0955	trpY			amino acid or sugar ABC transport system permease protein	715.54	9.48	-0.17	0.89	0.17	-0.949724384	0.342252316	0.407250421
SPD_0421	SPD_0421			hypothetical protein	415.49	8.70	-0.26	0.84	0.27	-0.948781319	0.342731845	0.407567241
SPD_0594	SPD_0594			hypothetical protein	5522.49	12.43	0.20	1.15	0.22	0.931447721	0.351622015	0.417879149
SPD_1613	galT-1			galactose-1-phosphate uridylyltransferase	382.95	8.58	-0.21	0.86	0.22	-0.920225324	0.357455023	0.424547265
SPD_1345	greA			transcription elongation factor GreA	5106.50	12.32	0.16	1.12	0.17	0.918685283	0.35826021	0.425239292
SPD_0429	trkH			potassium uptake protein, Trk family protein	2459.64	11.26	-0.15	0.90	0.16	-0.91823128	0.358497796	0.425257162
SPD_1317	SPD_1317			hypothetical protein	61.51	5.94	-0.29	0.82	0.32	-0.916142008	0.359592417	0.426291011
SPD_1972	SPD_1972			hypothetical protein	18.96	4.24	0.48	1.39	0.53	0.912071927	0.361730855	0.428560238
SPD_1508	alr			alanine racemase	3701.31	11.85	0.16	1.12	0.18	0.904276725	0.365848685	0.433170284
SPD_1618	SPD_1618			hypothetical protein	1.47	0.56	-0.83	0.56	0.92	-0.900655494	0.367771519	0.435177321
SPD_1094	SPD_1094			acetyltransferase, GNAT family protein	325.09	8.34	-0.18	0.88	0.20	-0.893430268	0.3716268	0.439467088
SPD_0525	vncS	RitR		sensor histidine kinase VncS	1609.03	10.65	-0.17	0.89	0.19	-0.892331633	0.372215204	0.439890696
SPD_1859	comGE	ComX		Late competence protein ComGE	6365.69	12.64	0.25	1.19	0.28	0.890051533	0.373438216	0.440795682
SPD_1092	SPD_1092			MutT/nudix family protein	584.88	9.19	0.15	1.11	0.17	0.890043951	0.373442287	0.440795682
SPD_1347	SPD_1347			acetyltransferase, GNAT family protein	1721.33	10.75	0.13	1.09	0.14	0.889518603	0.37372443	0.440856411
SPD_0617	glnP3b			amino acid ABC transporter, permease protein	30.09	4.91	-0.34	0.79	0.38	-0.887329274	0.374901649	0.441972273
SPD_1446	SPD_1446			DNA-binding response regulator	310.07	8.28	-0.18	0.88	0.21	-0.886186422	0.375517079	0.44424487
SPD_1075	nirC	RitR	CcpA	transporter, FNT family protein, putative	406.61	8.67	-0.16	0.90	0.18	-0.885173892	0.376062851	0.442794891
SPD_0918	piaD			iron-compound ABC transporter, ATP-binding protein	1362.38	10.41	-0.16	0.90	0.19	-0.882371206	0.377576102	0.444302913
SPD_1070	truB			tRNA pseudouridine synthase B	1993.93	10.96	-0.12	0.92	0.14	-0.87993653	0.378893694	0.445578984
SPD_2034	comF	ComX		competence protein ComF, putative	711.00	9.47	-0.25	0.84	0.28	-0.879096716	0.379348838	0.44583987
SPD_0652	livJ	CodY	RpoD	branched-chain amino acid ABC transporter, amino acid-binding prc	3652.10	11.83	0.12	1.09	0.14	0.877688808	0.38011262	0.446462948
SPD_0950	mefE			transporter, major facilitator family protein	77.36	6.27	-0.25	0.84	0.28	-0.876257982	0.380889802	0.447012613
SPD_1122	dprA	ComX		DNA processing protein DprA, putative	7769.00	12.92	0.21	1.16	0.24	0.875267018	0.381428636	0.447012613
SPD_1134	pyrR	PyrR		pyrimidine operon regulatory protein/uracil phosphoribosyltransferas	512.00	9.00	-0.15	0.90	0.17	-0.875175029	0.381478678	0.447012613
SPD_0509	higA			hypothetical protein	18.06	4.17	0.46	1.38	0.53	0.875026753	0.381559349	0.447012613
SPD_0687	SPD_0687	GntR		ABC transporter ATP-binding protein	1484.16	10.54	-0.15	0.90	0.17	-0.874676087	0.381750175	0.447012613
SPD_0792	SPD_0792			lipoprotein, putative	982.12	9.94	0.14	1.10	0.16	0.874166699	0.382027478	0.447063387
SPD_0183	folC			folylpolyglutamate synthase	4432.84	12.11	0.15	1.11	0.17	0.871120639	0.383688286	0.448732139
SPD_0101	gph			hydrolase, haloacid dehalogenase-like family protein	3532.91	11.79	0.14	1.10	0.16	0.870196061	0.384193268	0.449047912
SPD_0084	SPD_0084			IS630-Spn1, transposase Orf1	842.97	9.72	0.30	1.23	0.35	0.869446639	0.384602882	0.4492519
SPD_0823	proA			gamma-glutamyl phosphate reductase	3705.58	11.86	0.11	1.08	0.12	0.865045287	0.387013933	0.451792075
SPD_1505	SPD_1505	CcpA		hypothetical protein	35.53	5.15	-0.33	0.80	0.38	-0.862602915	0.388355827	0.453081798
SPD_1878	SPD_1878			hypothetical protein	5687.38	12.47	0.13	1.09	0.15	0.860315003	0.389615425	0.454273999
SPD_1762	endA			DNA-entry nuclease	4051.45	11.98	0.14	1.10	0.16	0.856708525	0.391605993	0.456316493
SPD_0929	SPD_0929			hypothetical protein	236.59	7.89	-0.19	0.88	0.23	-0.853841333	0.393192909	0.45788267
SPD_1515	SPD_1515	CcpA		membrane protein, putative	248.52	7.96	-0.20	0.87	0.23	-0.853414877	0.393429275	0.45788267
SPD_1516	SPD_1516			membrane protein, putative	161.30	7.33	0.20	1.15	0.23	0.851255955	0.394627186	0.458997293
SPD_0654	livM	CodY		branched-chain amino acid ABC transporter, permease protein	2805.17	11.45	0.13	1.09	0.15	0.850609245	0.394986452	0.459135712
SPD_0946	SPD_0946			hypothetical protein	43.55	5.44	-0.31	0.81	0.36	-0.845987478	0.39755973	0.461845984
SPD_1399	clpX			ATP-dependent Clp protease, ATP-binding subunit ClpX	10269.17	13.33	-0.12	0.92	0.14	-0.844809559	0.398217177	0.462328691
SPD_1231	pstC2			phosphate ABC transporter, permease protein, putative	4784.55	12.22	-0.13	0.91	0.15	-0.843677376	0.398849713	0.462721211
SPD_0972	SPD_0972			IS1381, transposase OrfB	400.64	8.65	0.17	1.13	0.20	0.843337819	0.399039537	0.462721211
SPD_1791	aspC			aminotransferase, class I	7653.73	12.90	0.11	1.08	0.13	0.841051704	0.400318969	0.463923317
SPD_1922	hipO			peptidase, M20/M25/M40 family protein	4561.15	12.16	0.16	1.12	0.19	0.836776586	0.40271816	0.466420851
SPD_1863	cglA	ComX		competence protein CglA	20740.59	14.34	0.16	1.12	0.19	0.835914606	0.403202945	0.466699471
SPD_0373	mip			hypothetical protein	670.86	9.39	-0.16	0.90	0.20	-0.835231743	0.40358724	0.466861511
SPD_0173	SPD_0173			MccC family protein	1185.63	10.21	-0.12	0.92	0.14	-0.83387708	0.404350254	0.467461183
SPD_0768	cozE	RitR		membrane protein, putative	5014.49	12.29	-0.16	0.90	0.20	-0.823153124	0.410420922	0.474192492
SPD_1429	SPD_1429			hypothetical protein	2869.58	11.49	-0.16	0.90	0.20	-0.812949725	0.416246883	0.480633108
SPD_0710	ezrA			septation ring formation regulator EzrA	14356.82	13.81	0.13	1.09	0.16	0.809907634	0.417993264	0.482358169
SPD_0403	SPD_0403			hypothetical protein	16013.20	13.97	-0.11	0.93	0.15	-0.781022469	0.43478928	0.501437727
SPD_1658	SPD_1658			CBS domain protein	3620.13	11.82	0.17	1.13	0.22	0.77828006	0.436403928	0.502996325
SPD_0116	SPD_0116			hypothetical protein	10439.11	13.35	0.17	1.13	0.21	0.777638422	0.436782204	0.503128868
SPD_0010	SPD_0010			hypothetical protein	4134.49	12.01	0.12	1.09	0.16	0.775198042	0.438222645	0.504484021
SPD_1871	SPD_1871	WalR		hypothetical protein	120.17	6.91	0.24	1.18	0.31	0.772520276	0.439806343	0.506002361
SPD_1141	uraA	PyrR		uracil-xanthine permease	1038.02	10.02	0.13	1.09	0.16	0.771231661	0.440569631	0.506302533
SPD_0702	ciaH	CiaR		sensor histidine kinase CiaH	5768.26	12.49	-0.18	0.88	0.23	-0.771185262	0.440597128	0.506302533
SPD_1861	cglC	ComX		competence protein CglC	7690.07	12.91	0.21	1.16	0.28	0.76557653	0.443928314	0.509823923
SPD_0083	rpsD			ribosomal protein S4	17223.92	14.07	0.16	1.12	0.21	0.763448504	0.445195962	0.510972663
SPD_0397	gatA			glutamyl-tRNA(Gln) amidotransferase subunit A	7215.64	12.82	-0.12	0.92	0.16	-0.75692015	0.449097702	0.514869562
SPD_1036	SPD_1036			hypothetical protein	22.46	4.49	0.35	1.27	0.47	0.756866132	0.449130068	0.514869562
SPD_0540	SPD_0540			amino acid ABC transporter, amino acid-binding protein, putative	184.28	7.53	0.22	1.16	0.29	0.753157492	0.45135528	0.517110276
SPD_0534	estA			tributyrin esterase	3463.51	11.76	-0.09	0.94	0.12	-0.750934979	0.452691788	0.518330741
SPD_1781	rsgA			ribosome small subunit-dependent GTPase A	3450.02	11.75	-0.14	0.91	0.18	-0.748393123	0.45422307	0.519772626
SPD_1368	rpsR			ribosomal protein S18	9343.35	13.19	0.11	1.08	0.15	0.746861068	0.455147428	0.520518693
SPD_1621	SPD_1621			ABC transporter, ATP-binding/permease protein	14373.89	13.81	0.11	1.08	0.15	0.745557554	0.455934732	0.52110722
SPD_0419	dinP			DNA-damage inducible protein P	358.57	8.49	0.14	1.10	0.18	0.743181098	0.457372045	0.522437525
SPD_0685	gor			glutathione-disulfide reductase	13380.42	13.71	-0.20	0.87	0.27	-0.727848902	0.466706086	0.532780962
SPD_0337	recU			recombination protein U	7139.45	12.80	0.10	1.07	0.13	0.722981901	0.469691004	0.535868363
SPD_1575	SPD_1575			lipoprotein, putative	1624.60	10.67	0.24	1.18	0.33	0.72207919	0.470245792	0.53618121
SPD_1535	scrR			sucrose operon repressor	748.41	9.55	0.12	1.09	0.16	0.721598575	0.470541315	0.536198243
SPD_1214	SPD_1214			ABC transporter, ATP-binding protein	192.61	7.59	0.25	1.19	0.35	0.720577886	0.471169264	0.53659384
SPD_1367	SPD_1367	CcpA		Cof family protein/peptidyl-prolyl cis-trans isomerase, cyclophilin typ	13858.93	13.76	-0.09	0.94	0.12	-0.719461002	0.471856918	0.537056922
SPD_1284	SPD_1284			hypothetical protein	1.27	0.35	-0.66	0.63	0.92	-0.716025417	0.473975654	0.539147307

Table S1 continued

					WT HOCl vs control							
Locus	Gene Symbol	Regulon	Further Regulon	Function	Base-Mean	A-value	M-value	Fold-change	Standard error	Wald statistic	P-value	Adjusted P-value
SPD_1574	mutT			MutT/nudix family protein	439.99	8.78	0.17	1.13	0.24	0.714359967	0.47500462	0.539879934
SPD_0420	pflB	CcpA	RpoD, GlnR, GntR	formate acetyltransferase	18392.40	14.17	0.16	1.12	0.22	0.714068625	0.475184746	0.539879934
SPD_1423	pdxK			phosphomethylpyrimidine kinase, putative	1139.47	10.15	-0.13	0.91	0.18	-0.706341238	0.479975954	0.544999435
SPD_1738	dinF	ComX		MATE efflux family protein DinF	26273.49	14.68	-0.13	0.91	0.19	-0.703915621	0.481485323	0.54638863
SPD_0042	recO			DNA repair protein RecO	1852.05	10.85	0.14	1.10	0.20	0.700791421	0.483433193	0.54827349
SPD_0148	SPD_0148	CodY	RpoD	transporter, major facilitator family protein	184476.63	17.49	-0.09	0.94	0.13	-0.699631124	0.4841577	0.548769493
SPD_0653	livH	CodY		branched-chain amino acid ABC transporter, permease protein	2698.40	11.40	-0.10	0.93	0.15	-0.687911759	0.491508351	0.556770871
SPD_0186	SPD_0186	ComX		competence-induced protein Ccs4	5734.60	12.49	0.13	1.09	0.20	0.681906395	0.495298141	0.560731486
SPD_2020	SPD_2020			DNA-binding response regulator	2423.12	11.24	0.12	1.09	0.18	0.678401724	0.497517016	0.562910017
SPD_0951	SPD_0951			hypothetical protein	0.25	-1.98	-0.45	0.73	0.67	-0.673146429	0.500854138	0.566350449
SPD_0412	glnHP1			amino acid ABC transporter, amino acid-binding protein/permease p	4372.28	12.09	0.10	1.07	0.15	0.670516503	0.50252859	0.567907827
SPD_1415	merA	CcpA		oxidoreductase, pyridine nucleotide-disulfide, class I	5446.22	12.41	-0.18	0.88	0.27	-0.66729917	0.504581057	0.569890307
SPD_0252	rpsG			ribosomal protein S7	9078.10	13.15	-0.12	0.92	0.18	-0.660158533	0.5091521	0.574713327
SPD_1765	SPD_1765			hypothetical protein	2914.54	11.51	-0.14	0.91	0.22	-0.656644389	0.5114096	0.576663811
SPD_1301	SPD_1301	CcpA	RpoD	NADPH-dependent FMN reductase	158.84	7.31	0.18	1.13	0.27	0.656129625	0.511740724	0.576663811
SPD_1712	ydfG			oxidoreductase, short chain dehydrogenase/reductase family protein	1791.94	10.81	0.09	1.06	0.14	0.656060248	0.51178536	0.576663811
SPD_0025	SPD_0025			cytidine/deoxycytidylate deaminase family protein	391.27	8.61	0.12	1.09	0.18	0.654731302	0.512640768	0.577152392
SPD_1365	SPD_1365			hypothetical protein	8760.21	13.10	0.08	1.06	0.13	0.654448332	0.512823005	0.577152392
SPD_1265	SPD_1265			membrane protein, putative	480.35	8.91	-0.12	0.92	0.18	-0.651059486	0.515008088	0.579270428
SPD_1775	lysA			diaminopimelate decarboxylase	5359.88	12.39	0.10	1.07	0.15	0.646025098	0.518263102	0.582588699
SPD_0953	ppc			phosphoenolpyruvate carboxylase	15462.82	13.92	-0.09	0.94	0.15	-0.629593564	0.528960536	0.594264305
SPD_1669	amiD	CodY		oligopeptide ABC transporter, permease protein AmiD	8081.35	12.98	0.09	1.06	0.15	0.626533759	0.530964901	0.596165644
SPD_0261	pepC			aminopeptidase C	9333.58	13.19	0.08	1.06	0.13	0.623507363	0.532951165	0.597931687
SPD_0504	pheS			phenylalanyl-tRNA synthetase, alpha subunit	935.92	9.87	-0.14	0.91	0.22	-0.623184058	0.533163577	0.597931687
SPD_0691	SPD_0691			transcriptional regulator, PadR family protein	2325.62	11.18	0.16	1.12	0.27	0.621134644	0.534511037	0.599091256
SPD_1930	SPD_1930			hypothetical protein	12.84	3.68	-0.36	0.78	0.59	-0.616538196	0.537539371	0.60213232
SPD_0384	fabG	FabT	WalR, RpoD	3-oxoacyl-(acyl-carrier-protein) reductase	17733.76	14.11	-0.11	0.93	0.18	-0.613334375	0.539655268	0.604148341
SPD_0141	SPD_0141			hypothetical protein	18.87	4.24	0.27	1.21	0.43	0.612470299	0.540226643	0.604433908
SPD_1519	engA			phosphoglycerate dehydrogenase-related protein	11850.40	13.53	-0.08	0.95	0.13	-0.610884052	0.541276343	0.605254003
SPD_1318	tuf			translation elongation factor Tu	241936.11	17.88	0.11	1.08	0.18	0.609870399	0.541947662	0.605650282
SPD_0334	aliA	CodY		oligopeptide ABC transporter, oligopeptide-binding protein AliA	30699.78	14.91	0.12	1.09	0.19	0.6075803	0.54346587	0.606991979
SPD_0842	SPD_0842			acetyltransferase, GNAT family protein	679.25	9.41	-0.09	0.94	0.15	-0.606464472	0.544206367	0.607464
SPD_1417	gatD			hypothetical protein	6309.03	12.62	-0.09	0.94	0.15	-0.605305465	0.544976051	0.607968029
SPD_0099	capD			capsular polysaccharide biosynthesis protein	4575.87	12.16	-0.08	0.95	0.14	-0.602573265	0.54679261	0.609597534
SPD_0616	glnQ3			amino acid ABC transporter, ATP-binding protein	30.95	4.95	0.22	1.16	0.36	0.602149376	0.54707471	0.609597534
SPD_0275	rpsI			ribosomal protein S9	13234.77	13.69	0.09	1.06	0.16	0.600594114	0.548110359	0.610395627
SPD_0193	rplC			ribosomal protein L3	40804.18	15.32	0.13	1.09	0.21	0.597407871	0.5502351	0.612404936
SPD_0638	SPD_0638			transposase family protein	0.98	-0.03	-0.54	0.69	0.91	-0.592088898	0.553791061	0.61600391
SPD_0097	SPD_0097	CcpA		transporter, putative	1187.26	10.21	-0.11	0.93	0.18	-0.591602672	0.554116684	0.616007553
SPD_0240	SPD_0240			acetyltransferase, GNAT family protein	324.15	8.34	0.12	1.09	0.20	0.582422518	0.560282117	0.622499492
SPD_0619	SPD_0619			hypothetical protein	89.86	6.49	0.14	1.10	0.24	0.581491039	0.560909556	0.622834492
SPD_1369	ssb	ComX		single-strand binding protein	32739.48	15.00	-0.10	0.93	0.18	-0.573100629	0.566576561	0.628761793
SPD_1854	SPD_1854			hypothetical protein	1407.44	10.46	-0.13	0.91	0.23	-0.566656668	0.570947466	0.633244694
SPD_0406	ilvC	CodY	CcpA, RpoD	ketol-acid reductoisomerase	6416.55	12.65	0.10	1.07	0.17	0.555098636	0.578827196	0.641611816
SPD_0225	SPD_0225			ABC transporter, ATP-binding protein	30.75	4.94	0.21	1.16	0.37	0.554333068	0.579350923	0.641820066
SPD_1527	qsrB	ComE		ABC transporter membrane-spanning permease - Na+ export	18045.78	14.14	-0.10	0.93	0.17	-0.548913368	0.583064904	0.645560273
SPD_1432	galE-1			UDP-glucose 4-epimerase	10450.07	13.35	-0.10	0.93	0.18	-0.54140897	0.588225726	0.650878655
SPD_0400	SPD_0400			Glycosyl transferase family protein 8, putative	2655.42	11.37	-0.09	0.94	0.17	-0.540939019	0.588549615	0.650878655
SPD_0956	SPD_0956			ABC transporter, ATP-binding protein	793.83	9.63	-0.10	0.93	0.19	-0.534092691	0.593277407	0.65572766
SPD_0591	SPD_0591			hypothetical protein	190.15	7.57	-0.13	0.91	0.24	-0.52789264	0.597573853	0.660094586
SPD_2001	SPD_2001			hypothetical protein	0.49	-1.02	0.40	1.32	0.78	0.517339781	0.604918989	0.667822177
SPD_1022	SPD_1022			hypothetical protein	0.90	-0.16	0.44	1.36	0.86	0.513773301	0.607410496	0.6701856
SPD_1543	phpP			phosphatase, putative	7333.79	12.84	-0.08	0.95	0.15	-0.508487137	0.611111758	0.673880305
SPD_1138	htpX			heat shock protein HtpX	3961.80	11.95	-0.07	0.95	0.15	-0.507399265	0.611874701	0.674332499
SPD_1590	gls24	RpoD		general stress protein 24, putative	16523.98	14.01	0.28	1.21	0.54	0.504861088	0.613656406	0.675906278
SPD_1471	SPD_1471			hypothetical protein	18.73	4.23	-0.27	0.83	0.55	-0.497138089	0.619091677	0.681500112
SPD_0038	polA			DNA polymerase I	10945.99	13.42	-0.06	0.96	0.13	-0.495943296	0.619934418	0.682034929
SPD_1234	SPD_1234			inositol monophosphatase family protein	790.28	9.63	-0.09	0.94	0.19	-0.491907621	0.622784651	0.684776449
SPD_0324	cps2I	CpsR	RpoD, VncR	glycosyl transferase, group 1 family protein, putative	14027.37	13.78	0.08	1.06	0.17	0.490536792	0.623754101	0.685448009
SPD_1064	SPD_1064			hemolysin A, putative	5970.23	12.54	-0.06	0.96	0.12	-0.486067624	0.626919221	0.688530248
SPD_1589	SPD_1589	RpoD		lipoprotein, putative	2872.26	11.49	-0.25	0.84	0.52	-0.482759015	0.629266855	0.690711637
SPD_0940	rffD			UDP-N-acetyl-D-mannosaminuronic acid dehydrogenase, putative	19.76	4.30	0.22	1.16	0.46	0.480562965	0.630827142	0.69202679
SPD_1902	patA			ABC transporter, ATP-binding/permease protein	8423.74	13.04	-0.07	0.95	0.15	-0.478931891	0.631987082	0.6929015
SPD_0512	pnp			polyribonucleotide nucleotidyltransferase	12227.42	13.58	-0.08	0.95	0.17	-0.477558558	0.632964433	0.693575133
SPD_0683	SPD_0683	ComX		hypothetical protein	2145.91	11.07	0.07	1.05	0.16	0.476991972	0.633367838	0.693619449
SPD_1210	aroE			shikimate 5-dehydrogenase	2353.47	11.20	-0.08	0.95	0.18	-0.472735205	0.636402107	0.696543199
SPD_1860	clgD	ComX		competence protein ClgD	10322.01	13.33	0.13	1.09	0.28	0.471244486	0.637466154	0.697308426
SPD_0541	nrd			nitroreductase family protein	4337.91	12.08	-0.06	0.96	0.13	-0.466424286	0.640911831	0.700676493
SPD_0947	SPD_0947			membrane protein, putative	32.33	5.01	0.19	1.14	0.42	0.464718359	0.642133159	0.701610103
SPD_1233	SPD_1233			NOL1/NOP2/sun family protein	762.18	9.57	0.08	1.06	0.18	0.459878893	0.645603151	0.704756552
SPD_0499	SPD_0499			hypothetical protein	11.77	3.56	0.25	1.19	0.53	0.459321818	0.646003082	0.704756552
SPD_1862	cglB	ComX		competence protein CglB	27900.24	14.77	0.13	1.09	0.29	0.459160328	0.646119037	0.704756552
SPD_0242	SPD_0242			hypothetical protein	830.64	9.70	0.10	1.07	0.23	0.458023029	0.646935897	0.705245008
SPD_0456	SPD_0456	RitR		hypothetical protein	22.03	4.46	-0.19	0.88	0.43	-0.455713912	0.648595717	0.706651319
SPD_1305	glyQ			glycyl-tRNA synthetase, alpha subunit	2951.74	11.53	-0.07	0.95	0.16	-0.453712638	0.650035669	0.707816618
SPD_1899	yvdE	CmbR		glutamine amidotransferase, class 1	460.20	8.85	0.08	1.06	0.18	0.453075711	0.650494225	0.707912564
SPD_1467	SPD_1467			hypothetical protein	913.98	9.84	-0.07	0.95	0.17	-0.448536369	0.653766144	0.711068356
SPD_1370	rpsF			ribosomal protein S6	9545.59	13.22	-0.08	0.95	0.18	-0.443084898	0.657704328	0.714944807
SPD_1464	psaD	CodY		thiol peroxidase	6238.71	12.61	0.08	1.06	0.19	0.440181516	0.659805646	0.716627082
SPD_1252	SPD_1252			membrane protein, putative	398.49	8.64	-0.11	0.93	0.26	-0.439689488	0.660162017	0.716627082
SPD_0130	mjA			metallo-beta-lactamase superfamily protein domain protein	2974.64	14.86	0.07	1.05	0.15	0.439392834	0.660376918	0.716627082
SPD_1960	ulaB2			PTS system, IIB component, putative	72.58	6.18	0.13	1.09	0.30	0.437453722	0.661782331	0.717744628
SPD_0226	SPD_0226			iron ABC transporter, iron-binding protein	11.89	3.57	0.23	1.17	0.52	0.436880777	0.662197814	0.717787874
SPD_0893	SPD_0893			hypothetical protein	245.03	7.94	-0.11	0.93	0.26	-0.433897644	0.66436277	0.719726335
SPD_1371	asnS			asparaginyl-tRNA synthetase	7936.60	12.95	0.06	1.04	0.15	0.433161424	0.664897502	0.719897522
SPD_1425	SPD_1425			transporter, major facilitator family protein	1393.72	10.44	0.07	1.05	0.17	0.432306936	0.665518347	0.720161699
SPD_2057	SPD_2057			ABC transporter, ATP-binding protein	5318.10	12.38	0.07	1.05	0.16	0.429972972	0.667215302	0.721589384
SPD_1517	SPD_1517			hypothetical protein	225.70	7.82	0.09	1.06	0.20	0.428810585	0.668061075	0.722095427
SPD_0249	SPD_0249			hypothetical protein	6006.87	12.55	-0.08	0.95	0.18	-0.425922956	0.670163987	0.723958948
SPD_1413	cshA			ATP-dependent RNA helicase, putative	5754.60	12.49	-0.08	0.95	0.18	-0.424784057	0.670994101	0.724446174
SPD_0665	pyrDa	CcpA		dihydroorotate dehydrogenase A	6507.41	12.67	-0.06	0.96	0.13	-0.422010892	0.673017067	0.726199731
SPD_1680	birA	RafR	CcpA	biotin--acetyl-CoA-carboxylase ligase	632.42	9.30	-0.10	0.93	0.23	-0.421342252	0.673505181	0.726199731
SPD_1308	SPD_1308	ComX		oxidoreductase, aldo/keto reductase family protein	3286.16	11.68	0.05	1.04	0.12	0.420995584	0.673758307	0.726199731
SPD_1243	lgt			prolipoprotein diacylglyceryl transferase	7674.42	12.91	0.07	1.05	0.18	0.416045896	0.677376419	0.729687901
SPD_1996	fucR	FcsR	CcpA, RpoD	fucose operon repressor, putative	713.78	9.48	0.14	1.10	0.34	0.414293816	0.678658942	0.730657599
SPD_0536	fibB			beta-lactam resistance factor	4925.72	12.27	0.05	1.04	0.13	0.413391388	0.679319883	0.730957375
SPD_0387	fabZ	FabT	RpoD	beta-hydroxyacyl-(acyl-carrier-protein) dehydratase FabZ	9506.68	13.21	0.10	1.07	0.24	0.412207353	0.680187448	0.731479017
SPD_0142	SPD_0142			hypothetical protein	17.09	4.09	0.21	1.16	0.52	0.403711252	0.686425065	0.737627597
SPD_0954	SPD_0954			hypothetical protein	803.17	9.65	0.09	1.06	0.22	0.402930509	0.686999346	0.737627597
SPD_1740	cinA	ComX		competence-damage protein (Exported protein 10), putative	39877.49	15.28	-0.10	0.93	0.24	-0.402844179	0.687062858	0.737627597
SPD_0723	rpiA			ribose 5-phosphate isomerase A	4677.52	12.19	0.07	1.05	0.17	0.400800223	0.688567215	0.738827595
SPD_0513	cysE			serine O-acetyltransferase	8183.39	13.00	0.07	1.05	0.17	0.400222598	0.688992572	0.738869138
SPD_0060	purK			phosphoribosylaminoimidazole carboxylase, ATPase subunit	809.84	9.66	0.10	1.07	0.24	0.395421808	0.692531618	0.742247853
SPD_0609	pyrE	PyrR		orotate phosphoribosyltransferase	266.25	8.06	-0.10	0.93	0.24	-0.393489382	0.693958065	0.743359788
SPD_0752	SPD_0752	CodY		membrane protein, putative	4710.29	12.20	0.06	1.04	0.15	0.391786165	0.695216218	0.744091159
SPD_0844	celB	ComX		competence protein CelB	14200.64	13.79	0.10	1.07	0.26	0.390821711	0.695929026	0.744091159
SPD_1048	lacF-2	LacT	CcpA	PTS system, lactose-specific IIA component	322.56	8.33	0.09	1.06	0.22	0.390763466	0.695972082	0.744091159
SPD_1132	carA	PyrR		carbamoyl-phosphate synthase, small subunit	3226.15	11.66	0.07	1.05	0.17	0.390457439	0.696198321	0.744091159
SPD_1033	SPD_1033			hypothetical protein	270.53	8.08	0.08	1.06	0.20	0.384955365	0.700270486	0.748025097
SPD_1785	SPD_1785			immunity protein, putative	598.33	9.22	0.06	1.04	0.16	0.38412817	0.700883453	0.748261608
SPD_1358	ytgP			polysaccharide biosynthesis protein, putative	4168.31	12.03	-0.05	0.97	0.14	-0.383332442	0.701473288	0.748473173
SPD_1230	pstA2			phosphate ABC transporter, permease protein, putative	5281.60	12.37	0.05	1.04	0.13	0.382367969	0.702188446	0.748818147
SPD_1849	eloR			protein jag (SpoIIJ-associated protein), putative	4111.49	12.01	-0.06	0.96	0.15	-0.379098511	0.704614712	0.750986456
SPD_1404	tpiA			triosephosphate isomerase	9680.69	13.24	0.05	1.04	0.13	0.377813311	0.705569285	0.751584673
SPD_1578	SPD_1578			hypothetical protein	4.25	2.09	-0.29	0.82	0.77	-0.376371331	0.706640856	0.752306784
SPD_1110	SPD_1110			hypothetical protein	174.76	7.45	-0.08	0.95	0.22	-0.368490482	0.712507541	0.75813024
SPD_1569	aqpZ	RpoD		aquaporin	4538.86	12.15	-0.06	0.96	0.16	-0.36752458	0.71322776	0.758474263
SPD_0888	lmb	AdcR	ArgR, RpoD	adhesion lipoprotein	6845.60	12.74	0.06	1.04	0.16	0.360772347	0.718269637	0.763411166
SPD_1261	SPD_1261			hypothetical protein	9.87	3.30	-0.22	0.86	0.62	-0.355127953	0.722493736	0.767473891
SPD_1219	potC			spermidine/putrescine ABC transporter, permease protein	1148.68	10.17	-0.06	0.96	0.16	-0.353634091	0.723613122	0.767959005
SPD_1434	ybgI			conserved hypothetical protein TIGR00486	1154.78	10.17	-0.06	0.96	0.17	-0.353445949	0.723754143	0.767959005
SPD_1035	SPD_1035			hypothetical protein	12.02	3.59	0.20	1.15	0.56	0.349276794	0.726881518	0.770849379
SPD_1445	SPD_1445			sensor histidine kinase	482.91	8.92	-0.05	0.97	0.15	-0.340440856	0.733524556	0.777462799
SPD_1238	nagD			hydrolase, haloacid dehalogenase-like family protein	5257.71	12.36	-0.05	0.97	0.14	-0.338137395	0.735259652	0.778869842
SPD_1874	SPD_1874	WalR		LysM domain protein	14803.74	13.85	-0.06	0.96	0.17	-0.333617661	0.738668089	0.781756019
SPD_1001	ligA			DNA ligase, NAD-dependent	3486.01	11.77	0.06	1.04	0.17	0.333439711	0.738802391	0.781756019
SPD_0639	SPD_0639			hypothetical protein	1.65	0.72	-0.29	0.82	0.90	-0.326987314	0.74367748	0.786479062
SPD_1198	tarP			membrane protein, putative	3309.32	11.69	-0.06	0.96	0.17	-0.321637919	0.747727014	0.790324294
SPD_0811	speE			spermidine synthase	1290.22	10.33	0.05	1.04	0.17	0.317418419	0.750926133	0.79326691
SPD_0389	accD	FabT	RpoD	acetyl-CoA carboxylase, carboxyl transferase, beta subunit	20724.74	14.34	0.07	1.05	0.23	0.307303582	0.75861231	0.800943715
SPD_1161	SPD_1161			hypothetical protein	78.33	6.29	-0.10	0.93	0.32	-0.301956949	0.762684882	0.8047989
SPD_0367	lepB			signal peptidase I	4107.25	12.00	0.04	1.03	0.14	0.300296438	0.76395105	0.805690097
SPD_0528	glnP2b			amino acid ABC transporter, permease protein	575.17	9.17	-0.06	0.96	0.20	-0.292915025	0.769587104	0.810893675
SPD_1708	SPD_1708			IS1167, transposase	29.44	4.88	-0.12	0.92	0.41	-0.292723228	0.769733714	0.810893675
SPD_0820	rluD	RitR		ribosomal large subunit pseudouridine synthase D	1064.94	10.06	-0.04	0.97	0.13	-0.29178634	0.77044999	0.811201064
SPD_1630	dpnD			hypothetical protein	326.98	8.35	-0.07	0.95	0.23	-0.287802838	0.773497665	0.813961474
SPD_0875	SPD_0875			hydrolase, NUDIX family protein	3744.66	11.87	-0.04	0.97	0.14	-0.285239921	0.775460337	0.815577713
SPD_1509	acpS			holo-(acyl-carrier-protein) synthase	2647.88	11.37	0.06	1.04	0.21	0.281029907	0.778687461	0.818521308
SPD_0843	celA	CelR	CcpA, ComX	competence protein CelA	1907.46	10.90	-0.07	0.95	0.24	-0.278418037	0.780691475	0.820176695
SPD_0085	SPD_0085			hypothetical protein	0.87	-0.20	0.25	1.19	0.91	0.277041799	0.781748011	0.820835411

Table S1 continued

					WT HOCl vs control							
Locus	Gene Symbol	Regulon	Further Regulon	Function	Base-Mean	A-value	M-value	Fold-change	Standard error	Wald statistic	P-value	Adjusted P-value
SPD_1073	SPD_1073			O-acetylhomoserine aminocarboxypropyltransferase/cysteine synth	209.37	7.71	0.06	1.04	0.21	0.272367978	0.785339092	0.824153215
SPD_1536	mvaA			hydroxymethylglutaryl-CoA reductase, degradative	4117.81	12.01	-0.04	0.97	0.15	-0.270372744	0.786873507	0.825310248
SPD_0971	SPD_0971			IS1381, transposase OrfA	468.63	8.87	-0.05	0.97	0.20	-0.268325764	0.788448576	0.826508628
SPD_0032	SPD_0032			hypothetical protein	308.28	8.27	-0.08	0.95	0.32	-0.264385786	0.791482663	0.828791074
SPD_0388	accC	FabT	WalR, RpoD	acetyl-CoA carboxylase, biotin carboxylase	31138.34	14.93	-0.05	0.97	0.21	-0.264371971	0.791493307	0.828791074
SPD_1910	pstS	PnpR	CcpA	phosphate ABC transporter, phosphate-binding protein	547.47	9.10	0.04	1.03	0.16	0.26253672	0.792907679	0.829817401
SPD_1559	yqeH			GTP-binding protein	6059.14	12.56	-0.04	0.97	0.16	-0.261889776	0.793406422	0.829884878
SPD_0529	glnP2a			amino acid ABC transporter, permease protein	236.57	7.89	0.05	1.04	0.21	0.256424686	0.797622928	0.833390523
SPD_0880	SPD_0880			glycerophosphoryl diester phosphodiesterase family protein	1485.05	10.54	-0.04	0.97	0.17	-0.256415299	0.797630176	0.833390523
SPD_2058	SPD_2058			ABC transporter, permease protein, putative	2604.36	11.35	-0.06	0.96	0.25	-0.254465704	0.799135796	0.834507381
SPD_0161	SPD_0161	CodY		membrane protein, putative	2454.12	11.26	-0.04	0.97	0.15	-0.252078736	0.800980205	0.83597663
SPD_0008	divIC			septum formation initiator, putative	2366.66	11.21	0.03	1.02	0.14	0.247701195	0.804365607	0.839051679
SPD_0238	leuS			leucyl-tRNA synthetase	11269.31	13.46	0.03	1.02	0.13	0.243488643	0.807626882	0.841993984
SPD_0606	SPD_0606			membrane protein, putative	449.48	8.81	0.05	1.04	0.19	0.242215935	0.808612848	0.842512233
SPD_1149	crcB1			CrcB protein	369.82	8.53	-0.05	0.97	0.20	-0.241668339	0.809037164	0.842512233
SPD_1497	nanE-1	NanR	CcpA, NiaR	N-acetylmannosamine-6-phosphate 2-epimerase 2, putative	504.52	8.98	0.04	1.03	0.16	0.24114001	0.809446604	0.842512233
SPD_1820	secE			preprotein translocase, SecE subunit	823.82	9.69	0.04	1.03	0.18	0.239196571	0.810953162	0.843620845
SPD_1468	gpmA			phosphoglycerate mutase	4447.77	12.12	0.04	1.03	0.16	0.23305344	0.815719909	0.848117925
SPD_0889	phtD	AdcR	ArgR, RpoD	pneumococcal histidine triad protein D precursor	30309.32	14.89	0.04	1.03	0.16	0.231933615	0.816589575	0.848560456
SPD_0223	SPD_0223			iron(III) ABC transporter, permease protein	14.48	3.86	0.13	1.09	0.56	0.226030713	0.821177533	0.852864275
SPD_0348	mvaK2			phosphomevalonate kinase	3816.87	11.90	0.03	1.02	0.14	0.212744317	0.831526398	0.862891119
SPD_1316	SPD_1316			hypothetical protein	118.84	6.89	0.06	1.04	0.27	0.212476993	0.831734925	0.862891119
SPD_1433	SPD_1433			FAD dependent oxidoreductase	1082.50	10.08	0.04	1.03	0.19	0.209924665	0.833726471	0.864487947
SPD_0228	SPD_0228			transcriptional regulator, AraC family protein	39.65	5.31	-0.10	0.93	0.48	-0.207766267	0.835411473	0.865706231
SPD_1947	SPD_1947			transcriptional regulator, putative	196.41	7.62	0.05	1.04	0.26	0.206992117	0.836016015	0.865706231
SPD_0949	SPD_0949			bacterial transferase hexapeptide (three repeats), putative	35.48	5.15	0.08	1.06	0.39	0.206679151	0.836260441	0.865706231
SPD_1764	murA-2			UDP-N-acetylglucosamine 1-carboxyvinyltransferase	9208.72	13.17	0.04	1.03	0.18	0.203098596	0.839057969	0.868131987
SPD_1435	SPD_1435			hypothetical protein	480.01	8.91	0.04	1.03	0.21	0.201562572	0.840258708	0.868903891
SPD_1021	SPD_1021			voltage-gated chloride channel family protein	5343.00	12.38	0.04	1.03	0.18	0.198572833	0.842596906	0.870850562
SPD_1903	mutS			DNA mismatch repair protein MutS	7438.58	12.86	0.03	1.02	0.13	0.191504344	0.848130478	0.875966943
SPD_0699	SPD_0699			hypothetical protein	603.72	9.24	0.03	1.02	0.16	0.191078545	0.848464057	0.875966943
SPD_1620	SPD_1620			glycosyl transferase, putative	7956.28	12.96	-0.03	0.98	0.14	-0.184404415	0.853696206	0.880892792
SPD_0502	bglF			PTS system, beta-glucosides-specific IIABC components	884.03	9.79	0.04	1.03	0.20	0.183513899	0.854394814	0.881137879
SPD_1739	recA	ComX		DNA recombination/repair protein RecA	36128.78	15.14	0.04	1.03	0.23	0.182236376	0.855397227	0.881695847
SPD_0548	SPD_0548			HIT family protein	1422.32	10.47	-0.03	0.98	0.18	-0.181616813	0.855883453	0.881721444
SPD_1133	pyrB	PyrR		aspartate carbamoyltransferase	2163.71	11.08	0.03	1.02	0.16	0.176172786	0.8601582	0.885647802
SPD_1546	priA			primosomal protein N'	4298.21	12.07	0.03	1.02	0.18	0.171428025	0.86388722	0.889008335
SPD_0923	SPD_0923			hypothetical protein	383.90	8.58	-0.03	0.98	0.21	-0.166726246	0.867585453	0.892005297
SPD_1323	SPD_1323			hypothetical protein	1.34	0.42	0.15	1.11	0.92	0.166538682	0.867733044	0.892005297
SPD_1514	SPD_1514			ABC transporter, ATP-binding protein	442.45	8.79	0.03	1.02	0.19	0.162483698	0.870924965	0.894805165
SPD_0901	dapA	CodY		dihydrodipicolinate synthase	7931.81	12.95	0.02	1.01	0.14	0.161597474	0.871622847	0.895040978
SPD_0837	SPD_0837			hypothetical protein	617.88	9.27	0.03	1.02	0.18	0.155187106	0.876673813	0.899744177
SPD_1968	SPD_1968			hypothetical protein	0.90	-0.16	-0.13	0.91	0.89	-0.144422754	0.88516665	0.907972876
SPD_1059	SPD_1059			hypothetical protein	0.65	-0.63	-0.12	0.92	0.86	-0.141946465	0.887122292	0.909490719
SPD_0748	parC	RitR		DNA topoisomerase IV, A subunit	6715.53	12.71	-0.03	0.98	0.20	-0.140419985	0.888328169	0.910238678
SPD_0533	mjB			metallo-beta-lactamase superfamily protein	18945.36	14.21	0.02	1.01	0.13	0.1380763	0.890180117	0.911647483
SPD_0385	fabF	FabT	WalR, RpoD	3-oxoacyl-[acyl-carrier-protein] synthase II	29918.89	14.87	-0.03	0.98	0.19	-0.136539816	0.891394551	0.912402242
SPD_0774	ftsK			SpoE family protein	4862.30	12.25	-0.02	0.99	0.14	-0.133012156	0.894183766	0.914767226
SPD_0390	accA	FabT	WalR, RpoD	acetyl-CoA carboxylase, carboxyl transferase, alpha subunit	12221.58	13.58	0.03	1.02	0.22	0.131682903	0.895235109	0.915025223
SPD_0343	gnd			6-phosphogluconate dehydrogenase, decarboxylating	22209.09	14.44	0.02	1.01	0.14	0.131482539	0.895393598	0.915025223
SPD_1659	SPD_1659			phosphodiesterase, MJ0936 family protein	2963.17	11.53	0.02	1.01	0.18	0.126020478	0.899715715	0.918950685
SPD_0081	SPD_0081			DNA-binding response regulator	2547.77	11.32	-0.04	0.97	0.28	-0.124641999	0.900806978	0.91957379
SPD_1065	ispA			geranyltranstransferase	3638.25	11.83	-0.02	0.99	0.19	-0.12231518	0.902649411	0.920962639
SPD_0558	prtA	PsaR		cell wall-associated serine protease PrtA	183566.82	17.49	0.02	1.01	0.17	0.121130377	0.903587769	0.921361511
SPD_1074	SPD_1074			hypothetical protein	15.82	3.98	-0.07	0.95	0.56	-0.120604099	0.904004622	0.921361511
SPD_0386	accB	FabT	WalR, RpoD	acetyl-CoA carboxylase, biotin carboxyl carrier protein	14004.00	13.77	0.03	1.02	0.22	0.119480642	0.904894576	0.921776937
SPD_0407	SPD_0407	CodY	RpoD	hypothetical protein	1908.34	10.90	0.03	1.02	0.24	0.116545309	0.90722038	0.92365378
SPD_1111	SPD_1111			hypothetical protein	214.38	7.74	0.02	1.01	0.21	0.114053475	0.909195403	0.92517168
SPD_1000	SPD_1000			transporter, major facilitator family protein	782.60	9.61	0.02	1.01	0.14	0.112290883	0.91059277	0.925954046
SPD_0392	SPD_0392			hypothetical protein	3436.33	11.75	-0.02	0.99	0.20	-0.111859704	0.910934648	0.925954046
SPD_1274	guaA			GMP synthase, C-terminal domain	9744.41	13.25	0.02	1.01	0.14	0.111181246	0.911472623	0.925954046
SPD_0440	SPD_0440			hypothetical protein	4009.60	11.97	0.02	1.01	0.16	0.110639258	0.911902415	0.925954046
SPD_0176	uvrA			excinuclease ABC, A subunit	7576.34	12.89	0.02	1.01	0.18	0.107244421	0.914595076	0.928195002
SPD_0840	SPD_0840			hypothetical protein	2323.45	11.18	-0.02	0.99	0.15	-0.101496189	0.919156583	0.932329209
SPD_2056	trpS			tryptophanyl-tRNA synthetase	1711.81	10.74	0.02	1.01	0.17	0.100202555	0.920183517	0.932875704
SPD_0132	cibB	ComX		Two-peptide bacteriocin peptide CibB	4252.89	12.05	-0.06	0.96	0.60	-0.095614455	0.923826784	0.935609263
SPD_1789	dlA			cell wall surface anchor family protein	526.26	9.04	-0.02	0.99	0.20	-0.095573808	0.923859068	0.935609263
SPD_1398	engB			GTP-binding protein	9272.06	13.18	0.01	1.01	0.15	0.093315285	0.92565309	0.936929584
SPD_0306	pbpX			penicillin-binding protein 2X	8544.59	13.06	0.01	1.01	0.14	0.092644214	0.926186217	0.936972928
SPD_1186	SPD_1186			hypothetical protein	0.50	-1.00	0.07	1.05	0.83	0.089203716	0.928920012	0.939241346
SPD_0372	glyP			sodium:alanine symporter family protein	1846.39	10.85	0.01	1.01	0.17	0.086835702	0.930802109	0.940646658
SPD_0549	ldcB			lipoprotein, putative	2280.39	11.16	-0.01	0.99	0.15	-0.078895534	0.937115716	0.946526497
SPD_0283	celD	CelR	CcpA, RpoD	PTS system, IIC component	140.88	7.14	-0.02	0.99	0.30	-0.076423799	0.939081936	0.9480114
SPD_1269	SPD_1269			hypothetical protein	3.28	1.71	-0.06	0.96	0.81	-0.071022425	0.943379908	0.951582471
SPD_2031	rplI			ribosomal protein L9	3056.54	11.58	-0.01	0.99	0.19	-0.0707267	0.943615271	0.951582471
SPD_0688	SPD_0688	GntR		efflux ABC transporter, permease protein	5199.24	12.34	0.01	1.01	0.15	0.066742269	0.946786883	0.954277286
SPD_0876	macP	RitR		hypothetical protein	2208.71	11.11	0.01	1.01	0.13	0.063406161	0.949443081	0.956450041
SPD_0659	ftsE			cell division ATP-binding protein FtsE	9240.87	13.17	0.01	1.01	0.15	0.061657929	0.950835244	0.957347814
SPD_1868	tgt			queuine tRNA-ribosyltransferase	5032.76	12.30	0.01	1.01	0.15	0.05294873	0.957772758	0.963533998
SPD_1431	gtrB			glycosyl transferase, group 2 family protein	1993.62	10.96	0.01	1.01	0.21	0.052678897	0.957987753	0.963533998
SPD_1380	SPD_1380	ComE		Cell shape-determining protein	12411.09	13.60	0.01	1.01	0.24	0.047919099	0.961780718	0.966840059
SPD_1135	nth			endonuclease III	2767.44	11.43	0.01	1.01	0.13	0.042305054	0.966255516	0.970827703
SPD_1131	carB			carbamoyl-phosphate synthase, large subunit	5416.02	12.40	0.01	1.01	0.19	0.028024802	0.97764237	0.981752269
SPD_0618	glnP3a	CmbR		amino acid ABC transporter, permease protein	15.35	3.94	0.01	1.01	0.58	0.025530721	0.979631645	0.983233232
SPD_0850	gloA			lactoylglutathione lyase	1742.30	10.77	0.00	1.00	0.17	-0.020603845	0.983561674	0.986505227
SPD_1741	lytR	ComE		transcriptional regulator, putative	6024.97	12.56	0.00	1.00	0.16	0.020149511	0.983924104	0.986505227
SPD_0162	SPD_0162			membrane protein, putative	154.13	7.27	0.01	1.01	0.30	0.019191572	0.984688281	0.9867537
SPD_1824	SPD_1824	ComX		ABC transporter, permease protein	3966.03	11.95	0.00	1.00	0.18	-0.01326977	0.989412566	0.990968246
SPD_1366	SPD_1366			general stress protein 13, putative	7215.28	12.82	0.00	1.00	0.15	-0.009339633	0.992548159	0.993588021
SPD_0325	cps2J	CpsR	RpoD, VncR	membrane protein, putative	7589.39	12.89	0.00	1.00	0.19	-0.004546791	0.996372198	0.996893859
SPD_1458	relA			GTP pyrophosphokinase	7471.41	12.87	0.00	1.00	0.20	-0.001739159	0.998612352	0.998612352

Table S1: DESeq2 differential gene expression analysis of *Streptococcus pneumoniae* D39 wild type after HOCl treatment in three biological replicates. *S. pneumoniae* wild type and deletion mutant cells were grown in 3 biological replicates and harvested before and after exposure to HOCl stress. The RNA-isolation, library preparation, sequencing and mapping was performed as described in the methods section. Transcripts were analyzed for differential gene expression using the software DEseq2 included in the ReadXplorer v2.2 software. The signal intensity value (A-value) was calculated by log2 base mean of normalized read counts and the signal intensity ratio (M-value) by log2 fold change. The evaluation of the differential RNAseq data was performed using an adjusted p-value cut-off of ≤ 0.05 and a signal intensity ratio (M-value) cut-off of ≥ 1 or ≤ - 1 (printed in bold). Genes were classified into regulons according to PneumoBrowse and previous publications (Slager et al., 2018).

Table S2: RNA-Seq transcriptome analysis of *Streptococcus pneumoniae* D39 wild type after HOCl treatment

FunCat	Regulon	Locus	Gene Symbol	Function	M-value	Fold-change
Amino acid metabolism	**CodY**	**SPD_1408**	**SPD_1408**	**hypothetical protein**	**2.72**	**6.59**
Amino acid metabolism	**CodY**	**SPD_1011**	**glxK**	**glycerate kinase**	**2.38**	**5.21**
Amino acid metabolism	**CodY**	**SPD_1246**	**nagB**	**glucosamine-6-phosphate isomerase**	**1.18**	**2.27**
Amino acid metabolism	**CodY**	**SPD_0778**	**SPD_0778**	**hypothetical protein**	**-2.18**	**0.22**
Amino acid metabolism	**CodY**	**SPD_1563**	**SPD_1563**	**dicarboxylate/amino acid:cation (Na+ or H+) symporter**	**-1.72**	**0.30**
Amino acid metabolism	**CodY**	**SPD_1671**	**amiA**	**oligopeptide ABC transporter, oligopeptide-binding pr**	**-1.63**	**0.32**
Amino acid metabolism	**CodY**	**SPD_1954**	**SPD_1954**	**hypothetical protein**	**-1.59**	**0.33**
Amino acid metabolism	**CodY**	**SPD_1258**	**SPD_1258**	**peptidase, U32 family protein**	**-1.54**	**0.34**
Amino acid metabolism	**CodY**	**SPD_0749**	**ilvE**	**branched-chain amino acid aminotransferase**	**-1.08**	**0.47**
Amino acid metabolism	CodY	SPD_0218	rpoA	DNA-directed RNA polymerase, alpha subunit	-0.80	0.57
Amino acid metabolism	CodY	SPD_0900	asd	aspartate-semialdehyde dehydrogenase	-0.84	0.56
Amino acid metabolism	CodY	SPD_1564	SPD_1564	hypothetical protein	-0.91	0.53
Amino acid metabolism	CodY	SPD_0336	pbp1A	penicillin-binding protein 1A	0.81	1.75
Amino acid metabolism	CodY	SPD_1667	amiF	oligopeptide ABC transporter, ATP-binding protein AmiF	0.66	1.58
Amino acid metabolism	CodY	SPD_0144	mutR1	transcriptional regulator	-0.61	0.66
Amino acid metabolism	CodY	SPD_0434	mtsB	ABC transporter, ATP-binding protein	-0.57	0.67
Amino acid metabolism	CodY	SPD_0542	pepV	dipeptidase PepV	0.53	1.44
Amino acid metabolism	CodY	SPD_0656	livF	branched-chain amino acid ABC transporter, ATP-binding	0.50	1.41
Amino acid metabolism	CodY	SPD_0726	SPD_0726	purine nucleoside phosphorylase, family protein 2	0.53	1.44
Amino acid metabolism	CodY	SPD_0780	SPD_0780	hypothetical protein	-0.72	0.61
Amino acid metabolism	CodY	SPD_1668	amiE	oligopeptide ABC transporter, ATP-binding protein AmiE	0.37	1.29
Amino acid metabolism	CodY	SPD_1188	rplJ	ribosomal protein L10	-0.88	0.54
Amino acid metabolism	CodY	SPD_0750	SPD_0750	hypothetical protein	-0.55	0.68
Amino acid metabolism	CodY	SPD_1326	pgm	phosphoglucomutase/phosphomannomutase family protein	0.43	1.35
Amino acid metabolism	CodY	SPD_0404	ilvB	acetolactate synthase, large subunit, biosynthetic type	-0.63	0.65
Amino acid metabolism	CodY	SPD_0091	SPD_0091	hypothetical protein	0.33	1.26
Amino acid metabolism	CodY	SPD_0781	SPD_0781	hypothetical protein	-0.42	0.75
Amino acid metabolism	CodY	SPD_1412	codY	GTP-sensing transcriptional pleiotropic repressor CodY	0.36	1.28
Amino acid metabolism	CodY	SPD_0145	SPD_0145	hypothetical protein	0.58	1.49
Amino acid metabolism	CodY	SPD_1187	rplL	ribosomal protein L7/L12	-0.37	0.77
Amino acid metabolism	CodY	SPD_0408	SPD_0408	hypothetical protein	0.37	1.29
Amino acid metabolism	CodY	SPD_2049	pgsA	CDP-diacylglycerol--glycerol-3-phosphate 3-phosphatidyltr	0.43	1.35
Amino acid metabolism	CodY	SPD_0655	livG	branched-chain amino acid ABC transporter, ATP-binding	0.31	1.24
Amino acid metabolism	CodY	SPD_0753	pcp	pyrrolidone-carboxylate peptidase	0.34	1.27
Amino acid metabolism	CodY	SPD_0657	acuB	acetoin utilization protein AcuB, putative	0.30	1.23
Amino acid metabolism	CodY	SPD_0751	SPD_0751	membrane protein, putative	-0.28	0.82
Amino acid metabolism	CodY	SPD_0147	SPD_0147	CAAX amino terminal protease family protein	-0.16	0.90
Amino acid metabolism	CodY	SPD_0405	ilvN	acetolactate synthase, small subunit	-0.25	0.84
Amino acid metabolism	CodY	SPD_0409	ilvA	threonine dehydratase	-0.16	0.90
Amino acid metabolism	CodY	SPD_0146	SPD_0146	CAAX amino terminal protease family protein	0.13	1.09
Amino acid metabolism	CodY	SPD_0652	livJ	branched-chain amino acid ABC transporter, amino acid-bi	0.12	1.09
Amino acid metabolism	CodY	SPD_0654	livM	branched-chain amino acid ABC transporter, permease pr	0.13	1.09
Amino acid metabolism	CodY	SPD_0148	SPD_0148	transporter, major facilitator family protein	-0.09	0.94
Amino acid metabolism	CodY	SPD_0653	livH	branched-chain amino acid ABC transporter, permease pr	-0.10	0.93
Amino acid metabolism	CodY	SPD_1669	amiD	oligopeptide ABC transporter, permease protein AmiD	0.09	1.06
Amino acid metabolism	CodY	SPD_0334	aliA	oligopeptide ABC transporter, oligopeptide-binding protein	0.12	1.09
Amino acid metabolism	CodY	SPD_0406	ilvC	ketol-acid reductoisomerase	0.10	1.07
Amino acid metabolism	CodY	SPD_1464	psaD	thiol peroxidase	0.08	1.06
Amino acid metabolism	CodY	SPD_0752	SPD_0752	membrane protein, putative	0.06	1.04
Amino acid metabolism	CodY	SPD_0161	SPD_0161	membrane protein, putative	-0.04	0.97
Amino acid metabolism	CodY	SPD_0901	dapA	dihydrodipicolinate synthase	0.02	1.01
Amino acid metabolism	CodY	SPD_0407	SPD_0407	hypothetical protein	0.03	1.02
Amino acid metabolism	**GlnR**	**SPD_0447**	**glnR**	**transcriptional regulator, MerR family protein**	**-2.57**	**0.17**
Amino acid metabolism	GlnR	SPD_0448	glnA	glutamine synthetase, type I	-0.98	0.51
Amino acid metabolism	GlnR	SPD_1098	glnHP5	amino acid ABC transporter, amino acid-binding protein/pe	-0.56	0.68
Amino acid metabolism	GlnR	SPD_1100	zwf	glucose-6-phosphate 1-dehydrogenase	0.43	1.35
Amino acid metabolism	GlnR	SPD_1158	gdhA	NADP-specific glutamate dehydrogenase	-0.29	0.82
Amino acid metabolism	GlnR	SPD_1099	glnQ5	amino acid ABC transporter, ATP-binding protein	0.26	1.20
Amino acid transport	**ArgR**	**SPD_1978**	**arcD**	**membrane protein, putative**	**2.63**	**6.19**
Amino acid transport	**ArgR**	**SPD_1979**	**SPD_1979**	**peptidase, M20/M25/M40 family protein**	**2.63**	**6.19**
Amino acid transport	**ArgR**	**SPD_0719**	**glnP4**	**amino acid ABC transporter, permease protein**	**-1.26**	**0.42**
Amino acid transport	ArgR	SPD_0887	yfnA	amino acid permease family protein	-0.89	0.54
Amino acid transport	ArgR	SPD_0720	glnQ4	amino acid ABC transporter, ATP-binding protein	-0.72	0.61
Amino acid transport	ArgR	SPD_0111	argH	argininosuccinate lyase	0.53	1.44
Amino acid transport	ArgR	SPD_1226	glnH	amino acid ABC transporter, amino acid-binding protein	0.58	1.49
Amino acid transport	ArgR	SPD_1357	aliB	oligopeptide ABC transporter, oligopeptide-binding protein	0.53	1.44
Amino acid transport	ArgR	SPD_0110	argG	argininosuccinate synthase	0.41	1.33
Amino acid transport	**CmhR**	**SPD_0151**	**metQ**	**lipoprotein**	**1.85**	**3.61**
Amino acid transport	**CmhR**	**SPD_0431**	**SPD_0431**	**hypothetical protein**	**-1.11**	**0.46**
Amino acid transport	CmhR	SPD_0511	metF	5,10-methylenetetrahydrofolate reductase	0.86	1.82
Amino acid transport	CmhR	SPD_0721	folD	methylenetetrahydrofolate dehydrogenase/methenyltetrahy	-0.55	0.68
Amino acid transport	CmhR	SPD_0510	metE	5-methyltetrahydropteroyltriglutamate-- homocysteine S-m	0.61	1.53
Amino acid transport	CmhR	SPD_1087	fhs	formate--tetrahydrofolate ligase	-0.33	0.80
Amino acid transport	CmhR	SPD_1353	metB	Cys/Met metabolism PLP-dependent enzyme, putative	0.28	1.21
Antibiotic resistance	**CiaR**	**SPD_0483**	**rbfA**	**ribosome-binding factor A**	**1.49**	**2.81**
Antibiotic resistance	**CiaR**	**SPD_0482**	**infB**	**initiation factor IF-2**	**1.48**	**2.79**
Antibiotic resistance	**CiaR**	**SPD_0480**	**SPD_0480**	**Putative nucleic-acid-binding protein implicated in tran**	**1.24**	**2.36**
Antibiotic resistance	**CiaR**	**SPD_0481**	**SPD_0481**	**ribosomal protein L7A family protein**	**1.18**	**2.27**
Antibiotic resistance	**CiaR**	**SPD_0479**	**nusA**	**transcription termination factor NusA**	**1.10**	**2.14**
Antibiotic resistance	**CiaR**	**SPD_2006**	**dltX**	**D-alanyl-lipoteichoic acid biosynthesis protein DltX**	**-4.63**	**0.04**
Antibiotic resistance	**CiaR**	**SPD_0775**	**SPD_0775**	**Acetyltransferase**	**-3.95**	**0.06**
Antibiotic resistance	**CiaR**	**SPD_0098**	**SPD_0098**	**glycosyl transferase, group 2 family protein**	**-2.11**	**0.23**
Antibiotic resistance	**CiaR**	**SPD_1127**	**ispD**	**2-C-methyl-D-erythritol 4-phosphate cytidylyltransferas**	**-2.03**	**0.24**
Antibiotic resistance	**CiaR**	**SPD_0913**	**SPD_0913**	**Extracellular protein**	**-1.87**	**0.27**
Antibiotic resistance	**CiaR**	**SPD_2068**	**htrA**	**serine protease**	**-1.86**	**0.28**
Antibiotic resistance	**CiaR**	**SPD_2005**	**dltA**	**D-alanine--poly(phosphoribitol) ligase subunit 1**	**-1.49**	**0.36**
Antibiotic resistance	**CiaR**	**SPD_2069**	**parB**	**SpoJ protein**	**-1.10**	**0.47**

Table S2: continued

FunCat	Regulon	Locus	Gene Symbol	Function	M-value	Fold-change
Antibiotic resistance	**CiaR**	**SPD_1769**	**SPD_1769**	**membrane protein, putative**	**-1.00**	**0.50**
Antibiotic resistance	CiaR	SPD_2004	dltB	protein DltB	-0.89	0.54
Antibiotic resistance	CiaR	SPD_2002	dltD	undecaprenol-phosphate-poly(glycerophosphate subunit) D	-0.74	0.60
Antibiotic resistance	CiaR	SPD_2003	dltC	D-alanine--poly(phosphoribitol) ligase subunit 2	-0.69	0.62
Antibiotic resistance	CiaR	SPD_0478	rimP	Bacterial ribosome SSU maturation protein RimP	0.87	1.83
Antibiotic resistance	CiaR	SPD_0701	ciaR	DNA-binding response regulator CiaR	-0.98	0.51
Antibiotic resistance	CiaR	SPD_0914	rumA-1	23S rRNA (uracil-5-)-methyltransferase RumA	-0.56	0.68
Antibiotic resistance	CiaR	SPD_0033	prsA	ribose-phosphate pyrophosphokinase	-0.58	0.67
Antibiotic resistance	CiaR	SPD_1124	licB	protein LicB	-0.37	0.77
Antibiotic resistance	CiaR	SPD_1123	licC	CTP:phosphocholine cytidylyltransferase	-0.25	0.84
Antibiotic resistance	CiaR	SPD_0868	prsA	protease maturation protein, putative	0.32	1.25
Antibiotic resistance	CiaR	SPD_0702	ciaH	sensor histidine kinase CiaH	-0.18	0.88
Antibiotic resistance	**PtvR**	**SPD_0096**	**ptvR**	**transcriptional regulator, PadR family protein**	**-1.84**	**0.28**
Antibiotic resistance	**PtvR**	**SPD_0095**	**ptvA**	**hypothetical protein**	**-1.32**	**0.40**
Antibiotic resistance	PtvR	SPD_0094	ptvB	hypothetical protein	-0.48	0.72
Antibiotic resistance	PtvR	SPD_0093	ptvC	membrane protein, putative	0.39	1.31
bacteriocin production	**BlpR**	**SPD_0046**	**blpU**	**bacteriocin BlpU**	**-2.55**	**0.17**
bacteriocin production	**BlpR**	**SPD_0467**	**blpS**	**BlpS protein**	**-2.43**	**0.19**
bacteriocin production	**BlpR**	**SPD_0473**	**blpY**	**immunity protein BlpY**	**-2.20**	**0.22**
bacteriocin production	**BlpR**	**SPD_0474**	**blpZ**	**Immunity protein BlpZ**	**-1.95**	**0.26**
bacteriocin production	**BlpR**	**SPD_0468**	**blpR**	**response regulator BlpR**	**-1.81**	**0.29**
bacteriocin production	**BlpR**	**SPD_0466**	**blpT**	**BlpT protein**	**-1.66**	**0.32**
bacteriocin production	**BlpR**	**SPD_0475**	**pncP**	**CAAX amino terminal protease family protein**	**-1.37**	**0.39**
bacteriocin production	**BlpR**	**SPD_0469**	**blpH**	**histidine kinase BlpH, putative**	**-1.06**	**0.48**
bacteriocin production	BlpR	SPD_0470	blpC	peptide pheromone BlpC	-0.61	0.66
bacteriocin production	BlpR	SPD_0817	SPD_0817	CAAX amino terminal protease family protein	-0.38	0.77
capsular polysaccharide biosynthesis	**CpsR**	**SPD_0315**	**cps2A**	**integral membrane regulatory protein Cps2A**	**-1.66**	**0.32**
capsular polysaccharide biosynthesis	**CpsR**	**SPD_0316**	**cps2B**	**tyrosine-protein phosphatase CpsB**	**-1.17**	**0.44**
capsular polysaccharide biosynthesis	CpsR	SPD_0330	rfbB	dTDP-glucose 4,6-dehydratase	0.83	1.78
capsular polysaccharide biosynthesis	CpsR	SPD_0329	rfbC	dTDP-4-dehydrorhamnose 3,5-epimerase, putative	0.72	1.65
capsular polysaccharide biosynthesis	CpsR	SPD_0328	cps2L	glucose-1-phosphate thymidylyltransferase	0.67	1.59
capsular polysaccharide biosynthesis	CpsR	SPD_0318	cps2D	tyrosine-protein kinase Cps2D cytosolic ATPase domain	-0.71	0.61
capsular polysaccharide biosynthesis	CpsR	SPD_0317	cps2C	chain length determinant protein/polysaccharide export pro	-0.78	0.58
capsular polysaccharide biosynthesis	CpsR	SPD_0319	cps2E	undecaprenylphosphate glucosephosphotransferase Cps2	-0.48	0.72
capsular polysaccharide biosynthesis	CpsR	SPD_0320	cps2T	glycosyl transferase, group 1 family protein, putative	-0.46	0.73
capsular polysaccharide biosynthesis	CpsR	SPD_0321	cps2F	glycosyl transferase, group 2 family protein	-0.31	0.81
capsular polysaccharide biosynthesis	CpsR	SPD_0327	cps2P	UDP-galactopyranose mutase	0.32	1.25
capsular polysaccharide biosynthesis	CpsR	SPD_0322	cps2G	glycosyl transferase, group 1 family protein	-0.36	0.78
capsular polysaccharide biosynthesis	CpsR	SPD_0326	cps2K	UDP-glucose 6-dehydrogenase, putative	0.28	1.21
capsular polysaccharide biosynthesis	CpsR	SPD_0064	cpsR	transcriptional regulator, GntR family protein	-0.36	0.78
capsular polysaccharide biosynthesis	CpsR	SPD_0323	csp2H	Polysaccharide polymerase	-0.21	0.86
capsular polysaccharide biosynthesis	CpsR	SPD_0324	cps2I	glycosyl transferase, group 1 family protein, putative	0.08	1.06
capsular polysaccharide biosynthesis	CpsR	SPD_0325	cps2J	membrane protein, putative	0.00	1.00
capsular polysaccharide biosynthesis	VncR	SPD_0331	rfbD	dTDP-4-dehydrorhamnose reductase	0.84	1.79
competence	**ComE**	**SPD_1818**	**comX2**	**transcriptional regulator ComX2**	**-1.71**	**0.31**
competence	**ComE**	**SPD_0014**	**comX1**	**transcriptional regulator ComX1**	**-1.67**	**0.31**
competence	**ComE**	**SPD_0023**	**comW**	**hypothetical protein**	**-1.51**	**0.35**
competence	**ComE**	**SPD_2065**	**comC1**	**competence-stimulating peptide type 1**	**-1.38**	**0.38**
competence	**ComE**	**SPD_1381**	**def2**	**polypeptide deformylase**	**-1.21**	**0.43**
competence	**ComE**	**SPD_0374**	**shetA**	**exfoliative toxin, putative**	**-1.11**	**0.46**
competence	ComE	SPD_1528	qsrA	ABC transporter, ATP-binding protein	-0.87	0.55
competence	ComE	SPD_1984	ybbK	hypersensitive-induced reaction protein 4	-0.84	0.56
competence	ComE	SPD_1742	SPD_1742	acetyltransferase, GNAT family protein	-0.67	0.63
competence	ComE	SPD_2064	comD	putative sensor histidine kinase ComD	-0.93	0.52
competence	ComE	SPD_0994	ribF	riboflavin biosynthesis protein RibF	-0.80	0.57
competence	ComE	SPD_1378	yaaA	UPF0246 protein YaaA	-0.36	0.78
competence	ComE	SPD_0050	comB	competence factor transport protein ComB	0.57	1.48
competence	ComE	SPD_0391	briC	hypothetical protein	-0.43	0.74
competence	ComE	SPD_1744	comM	lipoprotein, putative	-0.35	0.78
competence	ComE	SPD_1743	tsaE	TsaE protein, required for threonylcarbamoyladenosine t(6	-0.35	0.78
competence	ComE	SPD_2063	comE	response regulator	-0.60	0.66
competence	ComE	SPD_0049	comA	competence factor transporting ATP-binding/permease pro	-0.34	0.79
competence	ComE	SPD_0024	purA	adenylosuccinate synthetase	0.29	1.22
competence	ComE	SPD_0051	purC	phosphoribosylaminoimidazole-succinocarboxamide synth	0.54	1.45
competence	ComE	SPD_1379	SPD_1379	hypothetical protein	0.35	1.27
competence	ComE	SPD_1527	qsrB	ABC transporter membrane-spanning permease - Na+ exp	-0.10	0.93
competence	ComE	SPD_1380	SPD_1380	Cell shape-determining protein	0.01	1.01
competence	ComE	SPD_1741	lytR	transcriptional regulator, putative	0.00	1.00
competence	**ComX**	**SPD_2033**	**yfiA**	**ribosomal subunit interface protein**	**1.42**	**2.68**
competence	**ComX**	**SPD_2024**	**thiZ**	**ABC transporter, ATP-binding protein**	**1.25**	**2.38**
competence	**ComX**	**SPD_2025**	**thiY**	**ABC transporter, substrate-binding protein, putative**	**1.07**	**2.10**
competence	ComX	SPD_0030	SPD_0030	Carbonic anhydrase	-0.97	0.51
competence	ComX	SPD_0028	SPD_0028	phosphoglycerate mutase family protein	0.82	1.77
competence	ComX	SPD_1309	pgdA	peptidoglycan GlcNAc deacetylase	-0.77	0.59
competence	ComX	SPD_1597	trpB	tryptophan synthase, beta subunit	0.83	1.78
competence	ComX	SPD_0027	dut	deoxyuridine 5'-triphosphate nucleotidohydrolase	0.70	1.62
competence	ComX	SPD_2026	thiX	ABC transporter, permease protein	0.64	1.56
competence	ComX	SPD_1777	cbf1	cmp-binding-factor 1	0.67	1.59
competence	ComX	SPD_0029	radA	DNA repair protein RadA	0.85	1.80
competence	ComX	SPD_1828	SPD_1828	hypothetical protein	-0.55	0.68
competence	ComX	SPD_0867	SPD_0867	O-methyltransferase	0.51	1.42
competence	ComX	SPD_1737	lytA	autolysin/N-acetylmuramoyl-L-alanine amidase	0.43	1.35
competence	ComX	SPD_0975	radC	DNA repair protein RadC	-0.77	0.59
competence	ComX	SPD_0846	SPD_0846	membrane protein, putative	0.51	1.42
competence	ComX	SPD_1593	cclA	type IV prepilin peptidase, putative	0.60	1.52
competence	ComX	SPD_1778	rmuC	hypothetical protein	0.35	1.27
competence	ComX	SPD_2035	comFA	helicase, putative	-0.46	0.73

Table S2: continued

FunCat	Regulon	Locus	Gene Symbol	Function	M-value	Fold-change
competence	ComX	SPD_2027	SPD_2027	Cytoplasmic thiamin-binding component of thiamin ABC tra	0.24	1.18
competence	ComX	SPD_0866	pepF	oligoendopeptidase F	0.28	1.21
competence	ComX	SPD_1857	comGG	Late competence protein ComGG	0.35	1.27
competence	ComX	SPD_1711	ssbB	single-strand binding protein family protein	-0.67	0.63
competence	ComX	SPD_1858	comGF	Late competence protein ComGF	0.35	1.27
competence	ComX	SPD_0865	coiA	competence protein CoiA	0.35	1.27
competence	ComX	SPD_2028	cbpD	choline binding protein D	-0.28	0.82
competence	ComX	SPD_0133	cibA	hypothetical protein	-0.60	0.66
competence	ComX	SPD_1859	comGE	Late competence protein ComGE	0.25	1.19
competence	ComX	SPD_2034	comF	competence protein ComF, putative	-0.25	0.84
competence	ComX	SPD_1122	dprA	DNA processing protein DprA, putative	0.21	1.16
competence	ComX	SPD_1863	cglA	competence protein CglA	0.16	1.12
competence	ComX	SPD_1861	cglC	competence protein CglC	0.21	1.16
competence	ComX	SPD_1738	dinF	MATE efflux family protein DinF	-0.13	0.91
competence	ComX	SPD_0186	SPD_0186	competence-induced protein Ccs4	0.13	1.09
competence	ComX	SPD_1369	ssb	single-strand binding protein	-0.10	0.93
competence	ComX	SPD_0683	SPD_0683	hypothetical protein	0.07	1.05
competence	ComX	SPD_1860	clgD	competence protein CglD	0.13	1.09
competence	ComX	SPD_1862	cglB	competence protein CglB	0.13	1.09
competence	ComX	SPD_1308	SPD_1308	oxidoreductase, aldo/keto reductase family protein	0.05	1.04
competence	ComX	SPD_1740	cinA	competence-damage protein (Exported protein 10), putativ	-0.10	0.93
competence	ComX	SPD_0844	celB	competence protein CelB	0.10	1.07
competence	ComX	SPD_1739	recA	DNA recombination/repair protein RecA	0.04	1.03
competence	ComX	SPD_0132	cibB	Two-peptide bacteriocin peptide CibB	-0.06	0.96
competence	ComX	SPD_1824	SPD_1824	ABC transporter, permease protein	0.00	1.00
cysteine uptake	**CmbR**	**SPD_0150**	**gshT**	**ABC transporter, substrate-binding protein**	**1.07**	**2.10**
cysteine uptake	CmbR	SPD_1406	metA	homoserine O-succinyltransferase	0.40	1.32
cysteine uptake	CmbR	SPD_1290	tcyB	amino acid ABC transporter, permease protein	-0.31	0.81
cysteine uptake	CmbR	SPD_1899	yvdE	glutamine amidotransferase, class 1	0.08	1.06
cysteine uptake	CmbR	SPD_0618	glnP3a	amino acid ABC transporter, permease protein	0.01	1.01
N-acetylgalactosamine utilization	**AgaR**	**SPD_0071**	**galM**	**aldose 1-epimerase**	**2.89**	**7.41**
N-acetylgalactosamine utilization	**AgaR**	**SPD_0070**	**agaS**	**sugar isomerase domain protein AgaS**	**2.80**	**6.96**
N-acetylgalactosamine utilization	**AgaR**	**SPD_0069**	**gadF**	**PTS system, IIA component**	**2.63**	**6.19**
N-acetylgalactosamine utilization	**AgaR**	**SPD_0068**	**gadE**	**PTS system, IID component**	**2.62**	**6.15**
N-acetylgalactosamine utilization	**AgaR**	**SPD_0067**	**gadW**	**PTS system, IIC component**	**2.50**	**5.66**
N-acetylgalactosamine utilization	**AgaR**	**SPD_0066**	**gadV**	**PTS system, IIB component**	**2.34**	**5.06**
N-acetylgalactosamine utilization	**AgaR**	**SPD_0065**	**bgaC**	**Beta-galactosidase 3**	**1.15**	**2.22**
Cellobiose utilization	**BguR**	**SPD_1830**	**bguA**	**glycosyl hydrolase, family protein 1**	**2.86**	**7.26**
Cellobiose utilization	**BguR**	**SPD_1833**	**bguC**	**PTS system, IIA component**	**2.80**	**6.96**
Cellobiose utilization	**BguR**	**SPD_1832**	**bguB**	**PTS system, IIB component**	**2.72**	**6.59**
Cellobiose utilization	**BguR**	**SPD_1831**	**bguD**	**PTS system, IIC component**	**2.53**	**5.78**
C-catabolite Repression	**CcpA**	**SPD_1746**	**SPD_1746**	**hypothetical protein**	**5.92**	**60.55**
C-catabolite Repression	**CcpA**	**SPD_1409**	**msmK**	**sugar ABC transporter, ATP-binding protein**	**4.69**	**25.81**
C-catabolite Repression	**CcpA**	**SPD_0297**	**SPD_0297**	**PTS system, IID component**	**3.99**	**15.89**
C-catabolite Repression	**CcpA**	**SPD_1752**	**clyB**	**toxin secretion ABC transporter, ATP-binding/permeas**	**3.65**	**12.55**
C-catabolite Repression	**CcpA**	**SPD_0088**	**SPD_0088**	**ABC transporter, permease protein**	**2.86**	**7.26**
C-catabolite Repression	**CcpA**	**SPD_0158**	**SPD_0158**	**DNA-binding response regulator**	**2.69**	**6.45**
C-catabolite Repression	**CcpA**	**SPD_1977**	**arcC**	**carbamate kinase**	**2.64**	**6.23**
C-catabolite Repression	**CcpA**	**SPD_0090**	**SPD_0090**	**ABC transporter, substrate-binding protein**	**2.56**	**5.90**
C-catabolite Repression	**CcpA**	**SPD_0089**	**SPD_0089**	**ABC transporter, permease protein**	**2.50**	**5.66**
C-catabolite Repression	**CcpA**	**SPD_2010**	**SPD_2010**	**hypothetical protein**	**2.48**	**5.58**
C-catabolite Repression	**CcpA**	**SPD_0562**	**bgaA**	**beta-galactosidase precursor, putative**	**2.09**	**4.26**
C-catabolite Repression	**CcpA**	**SPD_0561**	**gatC**	**PTS system, IIC component, putative**	**2.07**	**4.20**
C-catabolite Repression	**CcpA**	**SPD_2012**	**glpO**	**alpha-glycerophosphate oxidase**	**2.07**	**4.20**
C-catabolite Repression	**CcpA**	**SPD_0157**	**SPD_0157**	**sensor histidine kinase, putative**	**2.05**	**4.14**
C-catabolite Repression	**CcpA**	**SPD_1976**	**argF**	**ornithine carbamoyltransferase**	**1.98**	**3.94**
C-catabolite Repression	**CcpA**	**SPD_1502**	**SPD_1502**	**ABC transporter, substrate-binding protein**	**1.95**	**3.86**
C-catabolite Repression	**CcpA**	**SPD_0156**	**SPD_0156**	**membrane protein, putative**	**1.81**	**3.51**
C-catabolite Repression	**CcpA**	**SPD_2013**	**glpK**	**glycerol kinase**	**1.79**	**3.46**
C-catabolite Repression	**CcpA**	**SPD_2011**	**glpF**	**glycerol uptake facilitator protein**	**1.58**	**2.99**
C-catabolite Repression	**CcpA**	**SPD_2009**	**SPD_2009**	**hypothetical protein**	**1.43**	**2.69**
C-catabolite Repression	**CcpA**	**SPD_0092**	**SPD_0092**	**hypothetical protein**	**1.43**	**2.69**
C-catabolite Repression	**CcpA**	**SPD_0772**	**fruB**	**1-phosphofructokinase, putative**	**1.40**	**2.64**
C-catabolite Repression	**CcpA**	**SPD_1008**	**glgA**	**glycogen/starch synthase, ADP-glucose type**	**1.31**	**2.48**
C-catabolite Repression	**CcpA**	**SPD_0559**	**gatA**	**PTS system IIA component, putative**	**1.27**	**2.41**
C-catabolite Repression	**CcpA**	**SPD_1007**	**glgD**	**glucose-1-phosphate adenylyltransferase, GlgD subun**	**1.26**	**2.39**
C-catabolite Repression	**CcpA**	**SPD_1006**	**glgC**	**glucose-1-phosphate adenylyltransferase**	**1.19**	**2.28**
C-catabolite Repression	**CcpA**	**SPD_0262**	**manN**	**PTS system, mannose/fructose/sorbose family protein**	**1.19**	**2.28**
C-catabolite Repression	**CcpA**	**SPD_0335**	**eng**	**cell wall surface anchor family protein**	**1.05**	**2.07**
C-catabolite Repression	**CcpA**	**SPD_0446**	**SPD_0446**	**membrane protein, putative**	**-2.03**	**0.24**
C-catabolite Repression	**CcpA**	**SPD_1010**	**SPD_1010**	**hypothetical protein**	**-1.70**	**0.31**
C-catabolite Repression	**CcpA**	**SPD_0789**	**pfkA**	**6-phosphofructokinase**	**-1.36**	**0.39**
C-catabolite Repression	**CcpA**	**SPD_0733**	**coaA**	**pantothenate kinase**	**-1.34**	**0.40**
C-catabolite Repression	**CcpA**	**SPD_1126**	**tarJ**	**alcohol dehydrogenase, zinc-containing**	**-1.26**	**0.42**
C-catabolite Repression	**CcpA**	**SPD_2052**	**SPD_2052**	**hypothetical protein**	**-1.19**	**0.44**
C-catabolite Repression	**CcpA**	**SPD_1401**	**folA**	**dihydrofolate reductase**	**-1.15**	**0.45**
C-catabolite Repression	**CcpA**	**SPD_0982**	**SPD_0982**	**pyrophosphokinase family protein**	**-1.13**	**0.46**
C-catabolite Repression	CcpA	SPD_0621	lctO	lactate oxidase	0.92	1.89
C-catabolite Repression	CcpA	SPD_1005	glgB	1,4-alpha-glucan branching enzyme	0.91	1.88
C-catabolite Repression	CcpA	SPD_0263	manM	PTS system, mannose-specific IIC component	0.87	1.83
C-catabolite Repression	CcpA	SPD_1247	queA	S-adenosylmethionine:tRNA ribosyltransferase-isomerase	-0.98	0.51
C-catabolite Repression	CcpA	SPD_1125	pck	choline kinase	-0.85	0.55
C-catabolite Repression	CcpA	SPD_0771	lacR1	lactose phosphotransferase system repressor	0.72	1.65
C-catabolite Repression	CcpA	SPD_1026	acoC	acetoin dehydrogenase complex, E2 component, dihydrolip	0.64	1.56
C-catabolite Repression	CcpA	SPD_1302	SPD_1302	oxidoreductase, putative	0.76	1.69
C-catabolite Repression	CcpA	SPD_0714	SPD_0714	hypothetical protein	-0.91	0.53
C-catabolite Repression	CcpA	SPD_0983	ppnK	inorganic polyphosphate/ATP-NAD kinase, putative	-0.74	0.60

Table S2: continued

FunCat	Regulon	Locus	Gene Symbol	Function	M-value	Fold-change
C-catabolite Repression	CcpA	SPD_1985	adh2	alcohol dehydrogenase, iron-containing	0.90	1.87
C-catabolite Repression	CcpA	SPD_1610	SPD_1610	hypothetical protein	0.71	1.64
C-catabolite Repression	CcpA	SPD_0286	basA	glutathione peroxidase	-0.54	0.69
C-catabolite Repression	CcpA	SPD_1797	ccpA	catabolite control protein A	0.36	1.28
C-catabolite Repression	CcpA	SPD_1931	SPD_1931	hypothetical protein	0.62	1.54
C-catabolite Repression	CcpA	SPD_1360	SPD_1360	hypothetical protein	-0.61	0.66
C-catabolite Repression	CcpA	SPD_0264	manL	PTS system, mannose-specific IIAB components	0.39	1.31
C-catabolite Repression	CcpA	SPD_0790	pyk	pyruvate kinase	-0.30	0.81
C-catabolite Repression	CcpA	SPD_1244	hprK	Hpr(Ser) kinase/phosphatase	-0.35	0.78
C-catabolite Repression	CcpA	SPD_1853	ackA	acetate kinase	0.24	1.18
C-catabolite Repression	CcpA	SPD_1774	pflA	pyruvate formate-lyase activating enzyme	-0.23	0.85
C-catabolite Repression	CcpA	SPD_0984	rluD3	ribosomal large subunit pseudouridine synthase, RluD sub	-0.34	0.79
C-catabolite Repression	CcpA	SPD_1793	SPD_1793	universal stress protein family protein	-0.29	0.82
C-catabolite Repression	CcpA	SPD_1503	SPD_1503	hypothetical protein	0.95	1.93
C-catabolite Repression	CcpA	SPD_1320	SPD_1320	glycerol uptake facilitator protein, putative	-0.22	0.86
C-catabolite Repression	CcpA	SPD_0159	SPD_0159	membrane protein putative	0.23	1.17
C-catabolite Repression	CcpA	SPD_0985	pta	phosphate acetyltransferase	0.20	1.15
C-catabolite Repression	CcpA	SPD_2014	SPD_2014	Trans-acting positive regulator	-0.15	0.90
C-catabolite Repression	CcpA	SPD_1078	ldh	L-lactate dehydrogenase	-0.15	0.90
C-catabolite Repression	CcpA	SPD_1505	SPD_1505	hypothetical protein	-0.33	0.80
C-catabolite Repression	CcpA	SPD_1515	SPD_1515	membrane protein, putative	-0.20	0.87
C-catabolite Repression	CcpA	SPD_1367	SPD_1367	Cof family protein/peptidyl-prolyl cis-trans isomerase, cyclo	-0.09	0.94
C-catabolite Repression	CcpA	SPD_0420	pflB	formate acetyltransferase	0.16	1.12
C-catabolite Repression	CcpA	SPD_1415	merA	oxidoreductase, pyridine nucleotide-disulfide, class I	-0.18	0.88
C-catabolite Repression	CcpA	SPD_1301	SPD_1301	NADPH-dependent FMN reductase	0.18	1.13
C-catabolite Repression	CcpA	SPD_0097	SPD_0097	transporter, putative	-0.11	0.93
C-catabolite Repression	CcpA	SPD_0665	pyrDa	dihydroorotate dehydrogenase A	-0.06	0.96
Cellobiose utilization	**CelR**	**SPD_0281**	**celC**	**PTS system, IIA component**	**-1.69**	**0.31**
Cellobiose utilization	**CelR**	**SPD_0280**	**celR**	**transcriptional regulator, putative**	**-1.39**	**0.38**
Cellobiose utilization	**CelR**	**SPD_0278**	**SPD_0278**	**hypothetical protein**	**-1.55**	**0.34**
Cellobiose utilization	**CelR**	**SPD_0282**	**SPD_0282**	**membrane protein, putative**	**-1.09**	**0.47**
Cellobiose utilization	CelR	SPD_0279	celB	PTS system, IIB component	-0.60	0.66
Cellobiose utilization	CelR	SPD_0277	bglA-1	6- phospho-beta-glucosidase	-0.27	0.83
Cellobiose utilization	CelR	SPD_0233	celC	PTS system, IIB component	0.33	1.26
Cellobiose utilization	CelR	SPD_0843	celA	competence protein CelA	-0.07	0.95
Cellobiose utilization	CelR	SPD_0283	celD	PTS system, IIC component	-0.02	0.99
Fucose utilization	**FcsR**	**SPD_1988**	**fucY**	**hypothetical protein**	**2.60**	**6.06**
Fucose utilization	**FcsR**	**SPD_1994**	**fucA**	**L-fuculose phosphate aldolase**	**2.31**	**4.96**
Fucose utilization	**FcsR**	**SPD_1989**	**SPD_1989**	**PTS system, IID component**	**2.16**	**4.47**
Fucose utilization	**FcsR**	**SPD_1987**	**fucL**	**fucolectin-related protein**	**2.07**	**4.20**
Fucose utilization	**FcsR**	**SPD_1990**	**SPD_1990**	**PTS system, IIC component**	**2.04**	**4.11**
Fucose utilization	**FcsR**	**SPD_1993**	**fucU**	**RbsD/FucU transport protein family protein**	**1.88**	**3.68**
Fucose utilization	**FcsR**	**SPD_1991**	**SPD_1991**	**PTS system, IIB component**	**1.71**	**3.27**
Fucose utilization	**FcsR**	**SPD_1992**	**SPD_1992**	**PTS system, IIA component**	**1.60**	**3.03**
Fucose utilization	**FcsR**	**SPD_1986**	**fucI**	**L-fucose isomerase**	**1.31**	**2.48**
Fucose utilization	**FcsR**	**SPD_1995**	**fucK**	**L-fuculose kinase FucK, putative**	**1.16**	**2.23**
Fucose utilization	FcsR	SPD_1996	fucR	fucose operon repressor, putative	0.14	1.10
Leloir pathway	**GalR**	**SPD_1635**	**galR**	**galactose operon repressor**	**-1.26**	**0.42**
Leloir pathway	**GalR**	**SPD_1634**	**galK**	**galactokinase**	**4.59**	**24.08**
Leloir pathway	**GalR**	**SPD_1633**	**galT-2**	**galactose-1-phosphate uridylyltransferase**	**4.28**	**19.43**
Tagatose-6P-pathway	**LacR**	**SPD_1053**	**lacA**	**galactose-6-phosphate isomerase, LacA subunit**	**2.18**	**4.53**
Tagatose-6P-pathway	**LacR**	**SPD_1052**	**lacB**	**galactose-6-phosphate isomerase, LacB subunit**	**2.47**	**5.54**
Tagatose-6P-pathway	**LacR**	**SPD_1051**	**lacC**	**tagatose-6-phosphate kinase**	**2.74**	**6.68**
Tagatose-6P-pathway	**LacR**	**SPD_1050**	**lacD**	**tagatose 1,6-diphosphate aldolase**	**2.89**	**7.41**
Lactose utilization	**LacT**	**SPD_1046**	**lacG-2**	**6-phospho-beta-galactosidase**	**1.38**	**2.60**
Lactose utilization	**LacT**	**SPD_1049**	**lacT**	**transcription antiterminator LacT**	**-1.10**	**0.47**
Lactose utilization	LacT	SPD_1047	lacE-2	PTS system, lactose-specific IIBC components	0.67	1.59
Lactose utilization	LacT	SPD_1048	lacF-2	PTS system, lactose-specific IIA component	0.09	1.06
Maltose utilization	**MalR**	**SPD_0311**	**dexB**	**glucan 1,6-alpha-glucosidase**	**2.68**	**6.41**
Maltose utilization	**MalR**	**SPD_0661**	**ptsG**	**PTS system, IIABC components**	**2.54**	**5.82**
Maltose utilization	**MalR**	**SPD_1934**	**malX**	**maltose/maltodextrin ABC transporter, maltose/maltod**	**2.36**	**5.13**
Maltose utilization	**MalR**	**SPD_1932**	**malP**	**maltodextrin phosphorylase**	**2.32**	**4.99**
Maltose utilization	**MalR**	**SPD_1936**	**malD**	**maltodextrin ABC transporter, permease protein**	**2.25**	**4.76**
Maltose utilization	**MalR**	**SPD_1935**	**malC**	**maltodextrin ABC transporter, permease protein**	**2.10**	**4.29**
Maltose utilization	**MalR**	**SPD_1933**	**malM**	**4-alpha-glucanotransferase**	**1.55**	**2.93**
Maltose utilization	**MalR**	**SPD_0580**	**rokB**	**glucokinase**	**1.28**	**2.43**
Maltose utilization	**MalR**	**SPD_1215**	**amyA2**	**alpha-amylase**	**-1.27**	**0.41**
Maltose utilization	MalR	SPD_0250	spuA	pullulanase, extracellular	0.54	1.45
Maltose utilization	MalR	SPD_1938	malR	maltose operon transcriptional repressor	0.58	1.49
Maltose utilization	MalR	SPD_1937	malA	maltodextrose utilization protein MalA	0.43	1.35
N-acetylglucosamine utilization	NagR	SPD_1866	nagA	N-acetylglucosamine-6-phosphate deacetylase	-0.27	0.83
N-acetylglucosamine utilization	NagR	SPD_0248	glmS	glucosamine--fructose-6-phosphate aminotransferase, isor	-0.16	0.90
Raffinose utilization	**RafR**	**SPD_1673**	**gtfA**	**sucrose phosphorylase**	**1.48**	**2.79**
Raffinose utilization	**RafR**	**SPD_1676**	**rafF**	**sugar ABC transporter, permease protein**	**1.41**	**2.66**
Raffinose utilization	**RafR**	**SPD_1677**	**rafE**	**sugar ABC transporter, sugar-binding protein**	**1.37**	**2.58**
Raffinose utilization	**RafR**	**SPD_1675**	**rafG**	**sugar ABC transporter, permease protein**	**1.35**	**2.55**
Raffinose utilization	**RafR**	**SPD_1678**	**aga**	**alpha-galactosidase AgaN**	**1.29**	**2.45**
Raffinose utilization	**RafR**	**SPD_1672**	**tacL**	**membrane protein, putative**	**-1.24**	**0.42**
Raffinose utilization	RafR	SPD_1328	aatB	amino acid ABC transporter, amino acid-binding protein	0.71	1.64
Raffinose utilization	RafR	SPD_1679	msmR	msm operon regulatory protein MsmR	-0.64	0.64
Raffinose utilization	**RafR**	**SPD_1674**	**SPD_1674**	**hypothetical protein**	**1.04**	**2.06**
Raffinose utilization	RafR	SPD_1327	bta	bacterocin transport accessory protein	-0.27	0.83
Raffinose utilization	RafR	SPD_1680	birA	biotin--acetyl-CoA-carboxylase ligase	-0.10	0.93
Sucrose utilization	**ScrR**	**SPD_1582**	**sacA**	**sucrose-6-phosphate hydrolase, putative**	**4.46**	**22.01**
Sucrose utilization	**ScrR**	**SPD_1583**	**SPD_1583**	**ABC transporter, permease protein**	**4.37**	**20.68**
Sucrose utilization	**ScrR**	**SPD_1584**	**SPD_1584**	**ABC transporter, permease protein**	**3.70**	**13.00**
Sucrose utilization	**ScrR**	**SPD_1532**	**scrA**	**PTS system IIABC components**	**3.46**	**11.00**

Table S2: continued

FunCat	Regulon	Locus	Gene Symbol	Function	M-value	Fold-change
Sucrose utilization	**ScrR**	**SPD_1533**	**SPD_1533**	**hypothetical protein**	**2.43**	**5.39**
Sucrose utilization	ScrR	SPD_1534	scrB	sucrose-6-phosphate hydrolase	-0.48	0.72
Pyruvate oxidase regulation	SpxR	SPD_0063	strH	beta-N-acetylhexosaminidase	0.66	1.58
Pyruvate oxidase regulation	SpxR	SPD_0636	spxB	pyruvate oxidase	0.28	1.21
Trehalose utilization	**TreR**	**SPD_1664**	**treP**	**PTS system, trehalose-specific IIABC components**	**1.02**	**2.03**
Trehalose utilization	**TreR**	**SPD_1665**	**treR**	**trehalose operon repressor**	**-1.03**	**0.49**
Trehalose utilization	TreR	SPD_1663	treC	alpha,alpha-phosphotrehalase	0.55	1.46
Ascorbic acid utilization	**UlaR**	**SPD_1847**	**ulaA**	**PTS system, membrane component, putative**	**3.01**	**8.06**
Ascorbic acid utilization	**UlaR**	**SPD_1845**	**ulaC**	**PTS system, IIA component**	**2.89**	**7.41**
Ascorbic acid utilization	**UlaR**	**SPD_1846**	**ulaB**	**PTS system, IIB component**	**2.78**	**6.87**
Ascorbic acid utilization	**UlaR**	**SPD_1844**	**ulaD**	**hexulose-6-phosphate synthase, putative**	**2.78**	**6.87**
Ascorbic acid utilization	**UlaR**	**SPD_1843**	**ulaE**	**hexulose-6-phosphate isomerase, putative**	**2.12**	**4.35**
Ascorbic acid utilization	**UlaR**	**SPD_1842**	**araD**	**L-ribulose-5-phosphate 4-epimerase**	**1.81**	**3.51**
Ascorbic acid utilization	**UlaR**	**SPD_1841**	**ulaR**	**transcriptional regulator, BglG family protein**	**1.69**	**3.23**
Ascorbic acid utilization	**UlaR**	**SPD_1840**	**ulaG**	**hypothetical protein**	**1.65**	**3.14**
Ascorbic acid utilization	UlaR	SPD_1839	tkt	transketolase	0.57	1.48
Lactose utilization	**XylR**	**SPD_0425**	**SPD_0425**	**hypothetical protein**	**5.52**	**45.89**
Lactose utilization	**XylR**	**SPD_0424**	**SPD_0424**	**PTS system, cellobiose-specific IIC component**	**5.50**	**45.25**
Lactose utilization	**XylR**	**SPD_0426**	**lacF-1**	**PTS system, lactose-specific IIA component**	**5.15**	**35.51**
Lactose utilization	**XylR**	**SPD_0427**	**lacG-1**	**6-phospho-beta-galactosidase**	**4.85**	**28.84**
Lactose utilization	**XylR**	**SPD_0428**	**lacE-1**	**PTS system, lactose-specific IIBC components**	**4.67**	**25.46**
Lactose utilization	**XylR**	**SPD_0423**	**xylR**	**ROK family protein**	**-1.04**	**0.49**
Envelope stress	**VraR**	**SPD_0803**	**SPD_0803**	**Putative phage shock protein C**	**-1.71**	**0.31**
Envelope stress	VraR	SPD_0350	vraT	hypothetical protein	-0.92	0.53
Envelope stress	VraR	SPD_0355	SPD_0355	hypothetical protein	-0.86	0.55
Envelope stress	VraR	SPD_0178	spxA2	hypothetical protein	-0.83	0.56
Envelope stress	VraR	SPD_0351	vraS	sensor histidine kinase, putative	-0.78	0.58
Envelope stress	VraR	SPD_0357	cbpF	choline binding protein F	-0.28	0.82
Envelope stress	VraR	SPD_0352	vraR	DNA-binding response regulator	-0.46	0.73
Envelope stress	VraR	SPD_0179	SPD_0179	lipoprotein, putative	-0.36	0.78
Envelope stress	**WalR**	**SPD_0703**	**SPD_0703**	**hypothetical protein**	**-2.33**	**0.20**
Envelope stress	WalR	SPD_1085	vicR	DNA-binding response regulator	-0.83	0.56
Envelope stress	WalR	SPD_0853	lytB	endo-beta-N-acetylglucosaminidase precursor, putative	-0.85	0.55
Envelope stress	WalR	SPD_1084	vicK	sensory box sensor histidine kinase	-0.63	0.65
Envelope stress	WalR	SPD_0126	pspA	pneumococcal surface protein A	0.50	1.41
Envelope stress	WalR	SPD_0104	SPD_0104	LysM domain protein	-0.59	0.66
Envelope stress	WalR	SPD_2043	pcsB	secreted 45 kDa protein precursor	-0.34	0.79
Envelope stress	WalR	SPD_1871	SPD_1871	hypothetical protein	0.24	1.18
Envelope stress	WalR	SPD_1874	SPD_1874	LysM domain protein	-0.06	0.96
exponential growth	**RpoD**	**SPD_1642**	**proWX**	**choline transporter (glycine betaine transport system p**	**2.40**	**5.28**
exponential growth	**RpoD**	**SPD_1643**	**proV**	**choline transporter**	**1.92**	**3.78**
exponential growth	**RpoD**	**SPD_1644**	**SPD_1644**	**hypothetical protein**	**1.41**	**2.66**
exponential growth	**RpoD**	**SPD_1245**	**rpsU**	**ribosomal protein S21**	**1.22**	**2.33**
exponential growth	**RpoD**	**SPD_0303**	**yorfE**	**transcriptional regulator, putative**	**-2.73**	**0.15**
exponential growth	**RpoD**	**SPD_1439**	**rpsO**	**ribosomal protein S15**	**-2.63**	**0.16**
exponential growth	**RpoD**	**SPD_1341**	**atpE**	**ATP synthase F0, C subunit**	**-2.62**	**0.16**
exponential growth	**RpoD**	**SPD_0622**	**SPD_0622**	**transcriptional regulator, TENA/THI-4 family protein, pu**	**-2.51**	**0.18**
exponential growth	**RpoD**	**SPD_1864**	**SPD_1864**	**DNA-binding protein**	**-2.20**	**0.22**
exponential growth	**RpoD**	**SPD_1340**	**atpB**	**ATP synthase F0, A subunit**	**-2.10**	**0.23**
exponential growth	**RpoD**	**SPD_0284**	**SPD_0284**	**hypothetical protein**	**-2.03**	**0.24**
exponential growth	**RpoD**	**SPD_0647**	**SPD_0647**	**transcriptional regulator, TetR family protein**	**-1.95**	**0.26**
exponential growth	**RpoD**	**SPD_0667**	**sodA**	**superoxide dismutase, manganese-dependent**	**-1.47**	**0.36**
exponential growth	**RpoD**	**SPD_1294**	**SPD_1294**	**hypothetical protein**	**-1.46**	**0.36**
exponential growth	**RpoD**	**SPD_0623**	**thiM**	**hydroxyethylthiazole kinase**	**-1.45**	**0.37**
exponential growth	**RpoD**	**SPD_1339**	**atpF**	**ATP synthase F0, B subunit**	**-1.44**	**0.37**
exponential growth	**RpoD**	**SPD_0648**	**comEB**	**cytidine and deoxycytidylate deaminase family protein**	**-1.43**	**0.37**
exponential growth	**RpoD**	**SPD_1338**	**atpH**	**ATP synthase F1, delta subunit**	**-1.10**	**0.47**
exponential growth	**RpoD**	**SPD_1523**	**nrdR**	**transcriptional regulator, NrdR family protein**	**-1.08**	**0.47**
exponential growth	RpoD	SPD_1662	SPD_1662	hypothetical protein	-0.78	0.58
exponential growth	RpoD	SPD_1002	pulA	pullulanase, type I	0.62	1.54
exponential growth	RpoD	SPD_1645	SPD_1645	transcriptional regulator, MarR family protein	0.73	1.66
exponential growth	RpoD	SPD_0004	ychF	GTP-binding protein	0.51	1.42
exponential growth	RpoD	SPD_1335	atpD	ATP synthase F1, beta subunit	0.47	1.39
exponential growth	RpoD	SPD_1334	atpC	ATP synthase F1, epsilon subunit	0.53	1.44
exponential growth	RpoD	SPD_0624	thiE-1	thiamine-phosphate pyrophosphorylase	-0.53	0.69
exponential growth	RpoD	SPD_1012	eno	phosphopyruvate hydratase	0.38	1.30
exponential growth	RpoD	SPD_1337	atpA	ATP synthase F1, alpha subunit	-0.29	0.82
exponential growth	RpoD	SPD_0267	SPD_0267	xanthine/uracil permease family protein	-0.41	0.75
exponential growth	RpoD	SPD_1040	ptsH	phosphocarrier protein HPr	0.27	1.21
exponential growth	RpoD	SPD_1336	atpG	ATP synthase F1, gamma subunit	0.23	1.17
exponential growth	RpoD	SPD_1790	rpmH	ribosomal protein L34	-0.38	0.77
exponential growth	RpoD	SPD_1083	vicX	vicX protein	-0.24	0.85
exponential growth	RpoD	SPD_0184	SPD_0184	lipoprotein, putative	0.30	1.23
exponential growth	RpoD	SPD_0268	SPD_0268	CAAX amino terminal protease family protein	-0.25	0.84
exponential growth	RpoD	SPD_1295	SPD_1295	hemolysin	-0.32	0.80
exponential growth	RpoD	SPD_0040	yeiH	membrane protein, putative	-0.16	0.90
exponential growth	RpoD	SPD_1591	SPD_1591	hypothetical protein	0.66	1.58
exponential growth	RpoD	SPD_0546	brnQ	branched-chain amino acid transport system II carrier prote	0.22	1.16
exponential growth	RpoD	SPD_1588	SPD_1588	hypothetical protein	-0.30	0.81
exponential growth	RpoD	SPD_1590	gls24	general stress protein 24, putative	0.28	1.21
exponential growth	RpoD	SPD_1589	SPD_1589	lipoprotein, putative	-0.25	0.84
exponential growth	RpoD	SPD_1569	aqpZ	aquaporin	-0.06	0.96
fatty acid biosynthesis	**FabT**	**SPD_0378**	**fabM**	**enoyl-CoA hydratase/isomerase family protein**	**-2.59**	**0.17**
fatty acid biosynthesis	**FabT**	**SPD_0381**	**acpP**	**acyl carrier protein**	**-1.80**	**0.29**
fatty acid biosynthesis	**FabT**	**SPD_0380**	**fabH**	**3-oxoacyl-(acyl-carrier-protein) synthase III**	**-1.24**	**0.42**
fatty acid biosynthesis	**FabT**	**SPD_0379**	**fabT**	**transcriptional regulator, MarR family protein**	**-1.18**	**0.44**
fatty acid biosynthesis	FabT	SPD_0382	fabK	trans-2-enoyl-ACP reductase II	-0.96	0.51

Table S2: continued

FunCat	Regulon	Locus	Gene Symbol	Function	M-value	Fold-change
fatty acid biosynthesis	FabT	SPD_0452	creX	integrase/recombinase, phage integrase family protein	0.37	1.29
fatty acid biosynthesis	FabT	SPD_0383	fabD	malonyl CoA-acyl carrier protein transacylase	-0.23	0.85
fatty acid biosynthesis	FabT	SPD_0384	fabG	3-oxoacyl-(acyl-carrier-protein) reductase	-0.11	0.93
fatty acid biosynthesis	FabT	SPD_0387	fabZ	beta-hydroxyacyl-(acyl-carrier-protein) dehydratase FabZ	0.10	1.07
fatty acid biosynthesis	FabT	SPD_0389	accD	acetyl-CoA carboxylase, carboxyl transferase, beta subunit	0.07	1.05
fatty acid biosynthesis	FabT	SPD_0388	accC	acetyl-CoA carboxylase, biotin carboxylase	-0.05	0.97
fatty acid biosynthesis	FabT	SPD_0385	fabF	3-oxoacyl-[acyl-carrier-protein] synthase II	-0.03	0.98
fatty acid biosynthesis	FabT	SPD_0390	accA	acetyl-CoA carboxylase, carboxyl transferase, alpha subun	0.03	1.02
fatty acid biosynthesis	FabT	SPD_0386	accB	acetyl-CoA carboxylase, biotin carboxyl carrier protein	0.03	1.02
Metal homeostasis	**AdcR**	**SPD_2000**	**adcR**	**adc operon repressor AdcR**	**-1.74**	**0.30**
Metal homeostasis	**AdcR**	**SPD_1999**	**adcC**	**zinc ABC transporter, ATP-binding protein**	**-1.09**	**0.47**
Metal homeostasis	AdcR	SPD_1998	adcB	zinc ABC transporter, permease protein	-0.68	0.62
Metal homeostasis	AdcR	SPD_1038	phpA	pneumococcal histidine triad protein A precursor	-0.69	0.62
Metal homeostasis	AdcR	SPD_0890	phtE	pneumococcal histidine triad protein E precursor	-0.47	0.72
Metal homeostasis	AdcR	SPD_1997	adcA	zinc ABC transporter, zinc-binding lipoprotein	-0.24	0.85
Metal homeostasis	AdcR	SPD_0888	lmb	adhesion lipoprotein	0.06	1.04
Metal homeostasis	AdcR	SPD_0889	phtD	pneumococcal histidine triad protein D precursor	0.04	1.03
Metal homeostasis	**CopY**	**SPD_0635**	**copA**	**copper-transporting ATPase, E1-E2 family protein**	**2.84**	**7.16**
Metal homeostasis	**CopY**	**SPD_0634**	**cupA**	**hypothetical protein**	**2.65**	**6.28**
Metal homeostasis	**CopY**	**SPD_0633**	**copY**	**transcriptional copper regulator**	**2.04**	**4.11**
Metal homeostasis	**RitR**	**SPD_0296**	**SPD_0296**	**PTS system, IIC component**	**3.66**	**12.64**
Metal homeostasis	**RitR**	**SPD_1585**	**ABC-SBP**	**ABC transporter, sugar-binding protein**	**3.12**	**8.69**
Metal homeostasis	**RitR**	**SPD_1800**	**SPD_1800**	**membrane protein, putative**	**1.78**	**3.43**
Metal homeostasis	**RitR**	**SPD_0560**	**gatB**	**PTS system, IIB component, putative**	**1.58**	**2.99**
Metal homeostasis	**RitR**	**SPD_1175**	**SPD_1175**	**membrane protein, putative**	**1.34**	**2.53**
Metal homeostasis	**RitR**	**SPD_0856**	**dgkA**	**diacylglycerol kinase**	**-2.25**	**0.21**
Metal homeostasis	**RitR**	**SPD_1822**	**rluD2**	**ribosomal large subunit pseudouridine synthase, RluD**	**-1.95**	**0.26**
Metal homeostasis	**RitR**	**SPD_0120**	**SPD_0120**	**membrane protein, putative**	**-1.64**	**0.32**
Metal homeostasis	**RitR**	**SPD_0119**	**SPD_0119**	**membrane protein, putative**	**-1.42**	**0.37**
Metal homeostasis	**RitR**	**SPD_0678**	**rimM**	**16S rRNA processing protein RimM**	**-1.37**	**0.39**
Metal homeostasis	**RitR**	**SPD_1086**	**mutY**	**A/G-specific adenine glycosylase**	**-1.18**	**0.44**
Metal homeostasis	RitR	SPD_1798	SPD_1798	DNA-binding response regulator	0.89	1.85
Metal homeostasis	RitR	SPD_1661	murI	glutamate racemase	-0.70	0.62
Metal homeostasis	RitR	SPD_1291	SPD_1291	ArsC family protein	-0.58	0.67
Metal homeostasis	RitR	SPD_0692	SPD_0692	membrane protein, putative	0.91	1.88
Metal homeostasis	RitR	SPD_0742	SPD_0742	sugar ABC transporter, permease protein, putative	0.50	1.41
Metal homeostasis	RitR	SPD_1651	piuD	iron-compound ABC transporter, ATP-binding protein	0.73	1.66
Metal homeostasis	RitR	SPD_1912	pstA	phosphate ABC transporter, permease protein PstA	0.66	1.58
Metal homeostasis	RitR	SPD_1652	piuA	iron-compound ABC transporter, iron-compound-binding pr	0.59	1.51
Metal homeostasis	RitR	SPD_1650	piuC	iron-compound ABC transporter, permease protein	0.68	1.60
Metal homeostasis	RitR	SPD_0344	ritR	DNA-binding response regulator	0.40	1.32
Metal homeostasis	RitR	SPD_0366	yrrC	helicase, RecD/TraA family protein	0.42	1.34
Metal homeostasis	RitR	SPD_1300	apbE	thiamine biosynthesis protein ApbE, putative	-0.73	0.60
Metal homeostasis	RitR	SPD_0592	rsuA-2	ribosomal small subunit pseudouridine synthase A	-0.90	0.54
Metal homeostasis	RitR	SPD_0852	pyrDb	dihydroorotate dehydrogenase, catalytic subunit	-0.54	0.69
Metal homeostasis	RitR	SPD_1402	dpr	non-heme iron-containing ferritin	-0.37	0.77
Metal homeostasis	RitR	SPD_1670	amiC	oligopeptide ABC transporter, permease protein AmiC	-0.40	0.76
Metal homeostasis	RitR	SPD_1946	SPD_1946	hypothetical protein	0.46	1.38
Metal homeostasis	RitR	SPD_1649	piuB	iron-compound ABC transporter, permease protein	0.68	1.60
Metal homeostasis	RitR	SPD_0895	hemH	ferrochelatase	0.55	1.46
Metal homeostasis	RitR	SPD_0970	map	methionine aminopeptidase, type I	0.19	1.14
Metal homeostasis	RitR	SPD_0143	ugd	UDP-glucose 6-dehydrogenase, putative	0.50	1.41
Metal homeostasis	RitR	SPD_0525	vncS	sensor histidine kinase VncS	-0.17	0.89
Metal homeostasis	RitR	SPD_1075	nirC	transporter, FNT family protein, putative	-0.16	0.90
Metal homeostasis	RitR	SPD_0768	cozE	membrane protein, putative	-0.16	0.90
Metal homeostasis	RitR	SPD_0456	SPD_0456	hypothetical protein	-0.19	0.88
Metal homeostasis	RitR	SPD_0820	rluD	ribosomal large subunit pseudouridine synthase D	-0.04	0.97
Metal homeostasis	RitR	SPD_0748	parC	DNA topoisomerase IV, A subunit	-0.03	0.98
Metal homeostasis	RitR	SPD_0876	macP	hypothetical protein	0.01	1.01
Metal homeostasis	**SczA**	**SPD_1638**	**czcD**	**cation efflux system protein**	**4.12**	**17.39**
Metal homeostasis	**SczA**	**SPD_1639**	**sczA**	**transcriptional regulator, TetR family protein**	**-1.72**	**0.30**
niacin transport and biosynthesis	**Rex**	**SPD_1865**	**adhB2**	**alcohol dehydrogenase, zinc-containing**	**1.15**	**2.22**
niacin transport and biosynthesis	Rex	SPD_1823	gap	glyceraldehyde-3-phosphate dehydrogenase, type I	0.99	1.99
niacin transport and biosynthesis	Rex	SPD_1251	pncB	nicotinate phosphoribosyltransferase, putative	-0.64	0.64
niacin transport and biosynthesis	Rex	SPD_1004	gapN	glyceraldehyde-3-phosphate dehydrogenase, NADP-deper	0.43	1.35
niacin transport and biosynthesis	Rex	SPD_1834	adhE	alcohol dehydrogenase, iron-containing	0.46	1.38
nucleotide biosynthesis	**NrdR**	**SPD_0187**	**nrdD**	**anaerobic ribonucleoside-triphosphate reductase**	**1.59**	**3.01**
nucleotide biosynthesis	**NrdR**	**SPD_1043**	**nrdF**	**ribonucleoside-diphosphate reductase, beta subunit**	**1.45**	**2.73**
nucleotide biosynthesis	**NrdR**	**SPD_0188**	**SPD_0188**	**hypothetical protein**	**1.42**	**2.68**
nucleotide biosynthesis	**NrdR**	**SPD_0191**	**SPD_0191**	**hypothetical protein**	**1.40**	**2.64**
nucleotide biosynthesis	**NrdR**	**SPD_0190**	**nrdG**	**anaerobic ribonucleoside-triphosphate reductase activ**	**1.40**	**2.64**
nucleotide biosynthesis	**NrdR**	**SPD_0189**	**SPD_0189**	**acetyltransferase, GNAT family protein**	**1.36**	**2.57**
nucleotide biosynthesis	NrdR	SPD_1042	nrdE	ribonucleoside-diphosphate reductase, alpha subunit	0.84	1.79
nucleotide biosynthesis	NrdR	SPD_1041	nrdH	glutaredoxin-like protein NrdH	-0.45	0.73
nucleotide biosynthesis	NrdR	SPD_1595	SPD_1595	hypothetical protein	-0.27	0.83
nucleotide biosynthesis	NrdR	SPD_1594	SPD_1594	transcriptional regulator	0.31	1.24
nucleotide biosynthesis	**PyrR**	**SPD_0851**	**pyrK**	**dihydroorotate dehydrogenase electron transfer subur**	**-1.04**	**0.49**
nucleotide biosynthesis	PyrR	SPD_0608	pyrF	orotidine 5'-phosphate decarboxylase	-0.33	0.80
nucleotide biosynthesis	PyrR	SPD_1134	pyrR	pyrimidine operon regulatory protein/uracil phosphoribosylt	-0.15	0.90
nucleotide biosynthesis	PyrR	SPD_1141	uraA	uracil-xanthine permease	0.13	1.09
nucleotide biosynthesis	PyrR	SPD_0609	pyrE	orotate phosphoribosyltransferase	-0.10	0.93
nucleotide biosynthesis	PyrR	SPD_1132	carA	carbamoyl-phosphate synthase, small subunit	0.07	1.05
nucleotide biosynthesis	PyrR	SPD_1133	pyrB	aspartate carbamoyltransferase	0.03	1.02
Protein folding	**CtsR**	**SPD_0308**	**clpL**	**ATP-dependent Clp protease, ATP-binding subunit**	**4.84**	**28.64**
Protein folding	**CtsR**	**SPD_0717**	**clpE**	**ATP-dependent Clp protease ATP-binding subunit ClpI**	**1.18**	**2.27**
Protein folding	CtsR	SPD_2023	ctsR	transcriptional regulator CtsR	-0.61	0.66
Protein folding	CtsR	SPD_0650	clpP	ATP-dependent Clp protease, proteolytic subunit ClpP	-0.38	0.77

Table S2: continued

FunCat	Regulon	Locus	Gene Symbol	Function	M-value	Fold-change
Protein folding	CtsR	SPD_2022	clpC	ATP-dependent Clp protease, ATP-binding subunit	-0.35	0.78
Protein folding	**HrcA**	**SPD_0460**	**dnaK**	**chaperone protein DnaK**	**2.69**	**6.45**
Protein folding	**HrcA**	**SPD_1709**	**groL**	**chaperonin GroEL**	**2.63**	**6.19**
Protein folding	**HrcA**	**SPD_0459**	**grpE**	**heat shock protein GrpE**	**2.52**	**5.74**
Protein folding	**HrcA**	**SPD_0461**	**dnaJ**	**chaperone protein DnaJ**	**2.22**	**4.66**
Protein folding	**HrcA**	**SPD_0458**	**hrcA**	**heat-inducible transcription repressor HrcA**	**2.03**	**4.08**
Protein folding	**HrcA**	**SPD_1710**	**groES**	**chaperonin, 10 kDa**	**1.75**	**3.36**
Redox regulons	**NmlR**	**SPD_1637**	**nmlR**	**transcriptional MerR/NmlR regulator**	**5.17**	**36.00**
Redox regulons	**NmlR**	**SPD_1636**	**adhC**	**alcohol dehydrogenase, zinc-containing**	**4.73**	**26.54**
Redox regulons	**SifR**	**SPD_0072**	**catE**	**carechol-2,3-dioxygenase**	**4.87**	**29.24**
Redox regulons	**SifR**	**SPD_1375**	**yhdA**	**NADPH-dependent FMN reductase, putative**	**2.82**	**7.06**
Redox regulons	SifR	SPD_1440	ywnB	NAD(P)H-dependent quinone reductase	0.96	1.95
Redox regulons	SifR	SPD_0527	SPD_0527	oxidoreductase, putative	0.28	1.21
Transport	**GntR**	**SPD_1524**	**gntR**	**transcriptional regulator, GntR family protein**	**-3.87**	**0.07**
Transport	**GntR**	**SPD_1525**	**SPD_1525**	**ABC transporter, ATP-binding protein**	**-2.52**	**0.17**
Transport	**GntR**	**SPD_1526**	**SPD_1526**	**membrane protein, putative**	**-1.26**	**0.42**
Transport	GntR	SPD_0686	SPD_0686	efflux transporter, RND family protein, MFP subunit	-0.84	0.56
Transport	GntR	SPD_0687	SPD_0687	ABC transporter ATP-binding protein	-0.15	0.90
Transport	GntR	SPD_0688	SPD_0688	efflux ABC transporter, permease protein	0.01	1.01
Transport	NiaR	SPD_1091	niaX	membrane protein, putative	-0.67	0.63
Transport	NiaR	SPD_1640	pnuC	nicotinamide mononucleotide transporter PnuC, putative	0.74	1.67
Transport	NiaR	SPD_1826	nadC	nicotinate-nucleotide pyrophosphorylase	-0.24	0.85
Transport	PnpR	SPD_1914	phoU	phosphate transport system regulatory protein PhoU	0.96	1.95
Transport	PnpR	SPD_1913	pstB	phosphate ABC transporter, ATP-binding protein	0.89	1.85
Transport	PnpR	SPD_1924	SPD_1924	membrane protein, putative	0.49	1.40
Transport	PnpR	SPD_1911	pstC	phosphate ABC transporter, permease protein PstC	0.31	1.24
Transport	PnpR	SPD_1910	pstS	phosphate ABC transporter, phosphate-binding protein	0.04	1.03
Virulence	MgrA	SPD_0526	fba	fructose-1,6-bisphosphate aldolase, class II	0.30	1.23
Virulence	MgrA	SPD_1656	scpA	segregation and condensation protein A	0.17	1.13
Virulence	**NanR**	**SPD_1504**	**nanA**	**sialidase A precursor**	**1.24**	**2.36**
Virulence	**NanR**	**SPD_1491**	**SPD_1491**	**hypothetical protein**	**1.01**	**2.01**
Virulence	**NanR**	**SPD_1495**	**satA**	**sugar ABC transporter, sugar-binding protein**	**1.00**	**2.00**
Virulence	NanR	SPD_1493	satC	sugar ABC transporter, permease protein	0.88	1.84
Virulence	NanR	SPD_1488	nanK	ROK family protein	0.97	1.96
Virulence	NanR	SPD_1489	SPD_1489	N-acetylneuraminate lyase, putative	0.69	1.61
Virulence	NanR	SPD_1496	nanP	PTS system, IIBC components	0.59	1.51
Virulence	NanR	SPD_1494	satB	sugar ABC transporter, permease protein	0.63	1.55
Virulence	NanR	SPD_1490	SPD_1490	hypothetical protein	0.73	1.66
Virulence	NanR	SPD_1492	yjgK	hypothetical protein	0.64	1.56
Virulence	NanR	SPD_1497	nanE-1	N-acetylmannosamine-6-phosphate 2-epimerase 2, putativ	0.04	1.03
Virulence	**PezA**	**SPD_0931**	**pezT**	**hypothetical protein**	**1.27**	**2.41**
Virulence	PezA	SPD_0930	pezA	transcriptional regulator, putative	0.89	1.85
Virulence	**PsaR**	**SPD_1461**	**psaB**	**manganese ABC transporter, ATP-binding protein**	**-1.44**	**0.37**
Virulence	**PsaR**	**SPD_1965**	**pcpA**	**choline binding protein PcpA**	**-1.07**	**0.48**
Virulence	**PsaR**	**SPD_1462**	**psaC**	**manganese ABC transporter, permease protein, putati**	**-1.04**	**0.49**
Virulence	PsaR	SPD_1463	psaA	ABC transporter, substrate binding lipoprotein	-0.28	0.82
Virulence	PsaR	SPD_0558	prtA	cell wall-associated serine protease PrtA	0.02	1.01
Virulence	**RegR**	**SPD_0290**	**kdgK**	**carbohydrate kinase, PfkB family protein**	**3.97**	**15.67**
Virulence	**RegR**	**SPD_0289**	**eda**	**4-hydroxy-2-oxoglutarate aldolase/2-deydro-3-deoxyph**	**3.61**	**12.21**
Virulence	**RegR**	**SPD_0291**	**SPD_0291**	**ribose 5-phosphate isomerase, putative**	**3.59**	**12.04**
Virulence	**RegR**	**SPD_0292**	**gno**	**oxidoreductase, short chain dehydrogenase/reductase**	**3.29**	**9.78**
Virulence	**RegR**	**SPD_0287**	**spnHL**	**hyaluronate lyase precursor**	**1.10**	**2.14**

Table S2: RNA-Seq transcriptome analysis of *S. pneumoniae* D39 wild type after exposure to HOCl stress. *S. pneumoniae* D39 wild type cells were grown in 3 biological replicates and harvested before and after exposure to HOCl stress. The RNA-isolation and RNA-Seq transcriptome analysis was performed as described in the Methods section. Transcripts were analyzed for differential expression using the software DEseq2 included in the ReadXplorer v2.2 software. The signal intensity value (A-value) was calculated by log2 mean of normalized read counts and the signal intensity ratio (M-value) by log2 fold change. The evaluation of the differential RNAseq data was performed using an adjusted p-value cut-off of $P \leq 0.05$ and a signal intensity ratio (m-value) cut-off of ≥ 1 or ≤ -1. Genes were classified into regulons according to PneumoBrowse and previous publications (Slager et al., 2018). Significantly induced or repressed genes under HOCl-treatment are printed bold.

Table S3. Bacterial strains and plasmids.

Strain	Description	Reference
Streptococcus pneumoniae		
D39	Serotype 2	(1)
D39-Δ*nmlR*	D39 *nmlR* deletion mutant, Ery^R	This study
D39-Δ*nmlR*-pBAV-*nmlR*	D39 *nmlR* deletion mutant complemented with pBAV-*nmlR,* Ery^R; Cm^R	This study
D39-Δ*nmlR*-pBAV-*nmlRC52A*	D39 *nmlR* deletion mutant complemented with pBAV-*nmlRC52A,* Ery^R; Cm^R	This study
D39-Δ*adhC*	D39 *adhC* deletion mutant, Ery^R	This study
D39-Δ*adhC*-pBAV-*adhC*	D39 *adhC* deletion mutant complemented with pBAV-*adhC,* Ery^R; Cm^R	This study
Escherichia coli		
DH5α	F-φ80dlacZ Δ(lacZYA-argF) U169 deoRsupE44ΔlacU169 (f80lacZDM15) hsdR17 recA1 endA1 (rk- mk+) supE44gyrA96 thi-1 gyrA69 relA1	(2)
BL21(DE3)*plysS*	F- ompT hsdS gal (rb- mb+) DE3(Sam7 Δnin5 lacUV5-T7 Gen1)	(2)
BL21(DE3)*plysS* pET11b-*nmlR*	For overexpression of NmlR	This study
BL21(DE3)*plysS* pET11b-*nmlRC52A*	For overexpression of NmlRC52A	This study
plasmids		
pBAV	pBAV1K-T5-gfp-derivative, P_{Ery} promoter, Cm^R	(3)
pBAV-*nmlR*	pBAV-derivative expressing *nmlR* under P_{Ery}	This study
pBAV-*nmlRC52A*	pBAV-derivative expressing *nmlRC52A* under P_{Ery}	This study
pBAV-*adhC*	pBAV-derivative expressing *adhC* under P_{Ery}	This study
pET11b	*E. coli* expression plasmid	Novagen
pET11b-*nmlR*	pET11b-derivative for overexpression of His-tagged NmlR	This study
pET11b-*nmlRC52A*	pET11b-derivative for overexpression of His-tagged NmlRC52A	This study
pTP1	pET28 expression vector with a TEV protease cleavage site	(4)
pSP72	Cloning vector, Amp^R	(5)

^{R}: resistant, Ery: erythromycin, Cm: chloramphenicol, Amp: ampicillin

Table S4. Oligonucleotide (primer) sequences

Primer name	Sequence (5’ to 3’)
qRT-adhC-for	TGACTCTTGCAGATGTCATGCC
qRT-adhC-rev	GTCGCACCTGACTCCATAGC
nmlR_pBAV_for_NcoI	CGCGCCATGGTTAATATTAAATCTGCCAGTG
nmlR_pBAV_rev_HindIII	GCGCAAGCTTTTAAAATTTTCCTTCCTTAT
adhC_pBAV_for_NcoI	CGCGCCATGGTTAAATCAGCAGTATATACAAAGG
adhC_pBAV_rev_HindIII	GCGCAAGCTTTTATTCGATTACAATCATAG
EMSA_nmlR_for	ATGAGCATCAACATTAGA
EMSA_nmlR_rev	GATTTAATATTCACACGCTAACC
EMSA_nmlR_m1_for	GACTTGGAGTCAACT**A**A**G**AG
EMSA_nmlR_m1_rev	CT**C**T**T**AGTTGACTCCAAGTC
EMSA_nmlR_m2_for	GACT**G**G**T**AGTCAACTCAAAG
EMSA_nmlR_m2_rev	CTTTGAGTTGACT**A**C**C**AGTC
nmlR_fl_HindIII_for	GCGCAAGCTTGTGCCAGAAGGTCTTGATATC
nmlR_fl_BglII_rev	GCGCAGATCTCATCACCGATAACAACAACC
nmlR_in_SalI_for	GCGCGTCGACCTTGTCTCAGCTACAGACAG
nmlR_in_BamHI_rev	GCGCGGATCCTCGTATCCGCTGAAATTCC
NmlRC52A_f1_rev	GACACCCGCCGAACGAAA**CGC**CTTAATAAATTCCAGCGC
NmlRC52A_f2_for	GCGCTGGAATTTATTAAG**GCG**TTTCGTTCGGCGGGTGTC
adhC_fl_HindIII_for	GCGCAAGCTTGGTAAGAGAAGAGCATTGTAT
adhC_fl_BglII_rev	GCGCAGATCTGGCTTGAGGAAACAACAGAC
adhC_in_SalI_for	GCGCGTCGACGGAAGATATCGACCAAGCCT
adhC_in_BamHI_rev	GCGCGGATCCATGCTAGCAAGTCCAACCTG
Ery_BamHI_for	CCCGGGGAAATTTTGATATCGATGGATCCGGAGCTCGAATTCACGGTT
Ery_SalI_rev	CCCGGGGAAATTTTGATATCGATGTCGACGAATTCGTAGGCGCTAGGGACCT
nmlR_pET_NheI_for	GCGCGCTAGCGTGAATATTAAATCTGCCAG
nmlR_pET_BamHI_rev	GCGCGGATCCTTAAAATTTTCCTTCCTTAT

Supplementary References

1. Jensch I, Gamez G, Rothe M, Ebert S, Fulde M, Somplatzki D, Bergmann S, Petruschka L, Rohde M, Nau R, Hammerschmidt S. 2010. PavB is a surface-exposed adhesin of *Streptococcus pneumoniae* contributing to nasopharyngeal colonization and airways infections. Mol Microbiol 77:22-43.

2. Studier FW, Moffatt BA. 1986. Use of bacteriophage T7 RNA polymerase to direct selective high-level expression of cloned genes. J Mol Biol 189:113-30.

3. Heß N, Waldow F, Kohler TP, Rohde M, Kreikemeyer B, Gomez-Mejia A, Hain T, Schwudke D, Vollmer W, Hammerschmidt S, Gisch N. 2017. Lipoteichoic acid deficiency permits normal growth but impairs virulence of *Streptococcus pneumoniae*. Nat Commun 8:2093.

4. Saleh M, Bartual SG, Abdullah MR, Jensch I, Asmat TM, Petruschka L, Pribyl T, Gellert M, Lillig CH, Antelmann H, Hermoso JA, Hammerschmidt S. 2013. Molecular architecture of *Streptococcus pneumoniae* surface thioredoxin-fold lipoproteins crucial for extracellular oxidative stress resistance and maintenance of virulence. EMBO Mol Med 5:1852-70.

5. Krieg PA, Melton DA. 1987. In vitro RNA synthesis with SP6 RNA polymerase. Methods Enzymol 155:397-415.

Chapter 5

The plant-derived naphthoquinone lapachol causes an oxidative stress response in *Staphylococcus aureus*

Nico Linzner[1#], Verena Nadin Fritsch[1#], Tobias Busche[1,2], Quach Ngoc Tung[1], Vu Van Loi[1], Jörg Bernhardt[3], Jörn Kalinowski[2], and Haike Antelmann[1]*

[1]Freie Universität Berlin, Institute of Biology-Microbiology, 14195, Berlin, Germany

[2]Center for Biotechnology, University Bielefeld, Bielefeld, 33615, Germany

[3]Institute for Microbiology, University of Greifswald, 17489, Greifswald, Germany

*Corresponding author: haike.antelmann@fu-berlin.de
#Both authors contributed equally to this work.

Published in:
Free Radical Biology and Medicine 158:126-136, 2020
DOI: https://doi.org/10.1016/j.freeradbiomed.2020.07.025

Personal contribution:

Together with Prof. Dr. Haike Antelmann, I developed the idea to compare the stress response of *S. aureus* against different quinones, including lapachol. My contribution to this paper included the first assessment of the antimicrobial activity of lapachol against *S. aureus* (Fig. 1A). Further, I was involved in the analysis of the mode of action of lapachol by performing survival assays under different oxygen conditions and ROS levels (Fig. 5). To characterize the resistance mechanisms of *S. aureus* in more detail, I prepared the RNA-seq samples (Fig. 2) and performed phenotype analyses of different mutant strains (Fig. 7; S3). I did the data analysis and figure drafts for the experiments I executed, and together with all other authors, I participated in the literature review and correction of the manuscript.

Free Radical Biology and Medicine 158 (2020) 126–136

Contents lists available at ScienceDirect

Free Radical Biology and Medicine

journal homepage: www.elsevier.com/locate/freeradbiomed

Original article

The plant-derived naphthoquinone lapachol causes an oxidative stress response in *Staphylococcus aureus*

Nico Linzner[a,1], Verena Nadin Fritsch[a,1], Tobias Busche[a,b], Quach Ngoc Tung[a], Vu Van Loi[a], Jörg Bernhardt[c], Jörn Kalinowski[b], Haike Antelmann[a,*]

[a] Freie Universität Berlin, Institute of Biology-Microbiology, 14195, Berlin, Germany
[b] Center for Biotechnology, University Bielefeld, 33615, Bielefeld, Germany
[c] Institute for Microbiology, University of Greifswald, 17489, Greifswald, Germany

ARTICLE INFO

Keywords:
Staphylococcus aureus
Lapachol
Quinone
ROS
Bacillithiol
Bacilliredoxin
YpdA

ABSTRACT

Staphylococcus aureus is a major human pathogen, which causes life-threatening systemic and chronic infections and rapidly acquires resistance to multiple antibiotics. Thus, new antimicrobial compounds are required to combat infections with drug resistant *S. aureus* isolates. The 2-hydroxy-3-(3-methyl-2-butenyl)-1,4-naphthoquinone lapachol was previously shown to exert antimicrobial effects. In this study, we investigated the antimicrobial mode of action of lapachol in *S. aureus* using RNAseq transcriptomics, redox biosensor measurements, *S*-bacillithiolation assays and phenotype analyses of mutants. In the RNA-seq transcriptome, lapachol caused an oxidative and quinone stress response as well as protein damage as revealed by induction of the PerR, HypR, QsrR, MhqR, CtsR and HrcA regulons. Lapachol treatment further resulted in up-regulation of the SigB and GraRS regulons, which is indicative for cell wall and general stress responses. The redox-cycling mode of action of lapachol was supported by an elevated bacillithiol (BSH) redox potential (E_{BSH}), higher endogenous ROS levels, a faster H_2O_2 detoxification capacity and increased thiol-oxidation of GapDH and the HypR repressor *in vivo*. The ROS scavenger N-acetyl cysteine and microaerophilic growth conditions improved the survival of lapachol-treated *S. aureus* cells. Phenotype analyses revealed an involvement of the catalase KatA and the Brx/BSH/YpdA pathway in protection against lapachol-induced ROS-formation in *S. aureus*. However, no evidence for irreversible protein alkylation and aggregation was found in lapachol-treated *S. aureus* cells. Thus, the antimicrobial mode of action of lapachol in *S. aureus* is mainly caused by ROS formation resulting in an oxidative stress response, an oxidative shift of the E_{BSH} and increased protein thiol-oxidation. As ROS-generating compound, lapachol is an attractive alternative antimicrobial to combat multi-resistant *S. aureus* isolates.

1. Introduction

Staphylococcus aureus is an important human pathogen, which can cause acute skin and soft tissue infections, but also life-threatening systemic and chronic diseases, such as sepsis, endocarditis, pneumonia and osteomyelitis [1–4]. Moreover, the prevalence of multiple antibiotic resistant strains, such as methicillin-resistant *S. aureus* (MRSA) imposes a major health burden [5,6]. Thus, the discovery of new antimicrobial compounds from natural sources is an urgent need to combat infections with multi-resistant *S. aureus* isolates.

Many natural antimicrobial compounds contain quinone-like structures, such as the fungal 6-brom-2-vinyl-chroman-4-on [7]. Recently, two novel quinone compounds with cytostatic properties were discovered from the fungus *Septofusidium berolinense,* including 3,6-dihydroxy-2-propylbenzaldehyde (GE-1) and 2-hydroxymethyl-3-propylcyclohexa-2,5-diene-1,4-dione (GE-2), which act as topoisomerase-II inhibitors [8,9]. In addition, the 2-hydroxy-3-(3-methyl-2-butenyl)-1,4-naphthoquinone lapachol of the lapacho tree *Tabebuia impetiginosa* was shown to exert antimicrobial, antiparasitic and cytostatic effects [10–15]. Lapachol showed strong killing effects against various Gram-positive bacteria, such as *Bacillus subtilis*, *Enterococcus faecalis*, *Clostridium perfringens* and *S. aureus*, but was less effective against Gram-negative *Escherichia coli*, *Pseudomonas aeruginosa* and *Salmonella* Typhimurium [16–20]. Furthermore, lapachol was antiproliferative in WHCO1 oesophageal and promyelocytic leukemia HL-60 cancer cell lines with 50% growth inhibition at concentrations of 24.1 μM and

* Corresponding author. Institute of Biology-Microbiology, Freie Universität Berlin, Königin-Luise-Strasse 12-16, D-14195 Berlin, Germany.
E-mail address: haike.antelmann@fu-berlin.de (H. Antelmann).
[1] Both authors contributed equally to this work.

https://doi.org/10.1016/j.freeradbiomed.2020.07.025
Received 24 January 2020; Received in revised form 28 June 2020; Accepted 18 July 2020
Available online 24 July 2020

3.18 μM, respectively [21,22]. Cytotoxic lapachol concentrations were determined as 185 μg/ml, which kill 50% Balb/c murine peritoneal macrophages [23]. While ROS formation has been demonstrated by lapachol *in vitro* [24,25], its antimicrobial mode of action in pathogenic bacteria has not been studied in detail.

The antimicrobial and toxic effect of quinones can be attributed to their mode of actions as electrophiles and oxidants [26–31]. In the electrophilic mode, quinones lead to alkylation and aggregation of thiols via the irreversible *S*-alkylation chemistry, resulting in thiol depletion in the proteome and thiol-metabolome [29,31]. As oxidants, quinones can be reduced to semiquinone anion radicals that transfer electrons to molecular oxygen, leading to ROS formation, such as superoxide anion [24,25,27,28,32,33]. The mode of action of quinones is dependent on the physicochemical features, the chemical structure and the availability of oxygen [34–36]. In general, the toxicity and thiol-alkylation ability of quinones increases when the positions adjacent to the keto groups are unsubstituted in the quinone ring (e.g. benzoquinone) [27,34]. Fully substituted quinone rings cannot alkylate protein thiols, but retain redox-cycling activity, including ubiquinone and tetramethyl-*p*-benzoquinone [36]. Since the quinone ring is fully substituted, lapachol may act mainly via the oxidative mode as antimicrobial in *S. aureus*, which was subject of this study [27,34].

We have previously investigated the transcriptome signature in response to 2-methylhydroquinone (MHQ) in *S. aureus* [26]. MHQ was shown to induce a strong thiol-specific oxidative and quinone stress response in the *S. aureus* transcriptome [26]. The quinone-responsive QsrR and MhqR regulons were most strongly induced by MHQ and conferred independent resistance to quinones and quinone-like antimicrobials, including ciprofloxacin, pyocyanin, norfloxacin and rifampicin [26,37]. The MhqR repressor controls the *mhqRED* operon, which encodes for the predicted phospholipase/carboxylesterase MhqD and ring-cleavage dioxygenase MhqE involved in quinone detoxification [26]. The redox-sensing QsrR repressor senses quinones by thiol-*S*-alkylation and regulates paralogous dioxygenases and quinone reductases in *S. aureus* [37].

The oxidative mode of action of MHQ was revealed by induction of the peroxide-specific PerR regulon, which controls antioxidant enzymes, such as catalase and peroxidases (KatA, Tpx, Bcp), Fe-binding miniferritin (Dps) and the FeS-cluster machinery (Suf) [38–40]. Moreover, the disulfide-stress-specific HypR regulon was upregulated by MHQ, including the NADPH-dependent flavin disulfide reductase MerA [41]. In addition to ROS detoxification enzymes, *S. aureus* uses the low molecular weight thiol bacillithiol (BSH) for protection against ROS [42]. BSH is an important thiol cofactor that functions in detoxification of various redox-active compounds, electrophiles and antibiotics and contributes to survival of *S. aureus* in macrophage infection assays [42–45]. BSH also participates in redox modifications of proteins and forms protein *S*-bacillithiolation under disulfide stress, such as HOCl and the ROS-producing antimicrobial surface coating AGXX® [46–48]. Protein *S*-bacillithiolations are involved in thiol-protection and regulate protein activities as shown for the glycolytic glyceraldehyde-3-phosphate dehydrogenase (GapDH) in *S. aureus* [31,46–50]. The removal of protein *S*-bacillithiolation is controlled by bacilliredoxins (Brx), which are regenerated by BSH and the bacillithiol disulfide (BSSB) reductase YpdA [48,51–53]. Moreover, the Brx/BSH/YpdA pathway is important for protection of *S. aureus* under oxidative stress and infection conditions [51,52].

In this study, we analyzed the molecular stress responses and mode of action of lapachol in *S. aureus*. Using RNA-seq transcriptomics, lapachol induced an oxidative and quinone stress response as well as strong protein damage in *S. aureus*. This signature was revealed by the induction of the QsrR, MhqR, PerR, HypR, CtsR and HrcA regulons and of the enzymes of the Brx/BSH/YpdA redox pathway. The oxidative mode of action of lapachol was demonstrated by an oxidative shift of the BSH redox potential, elevated ROS formation and faster H_2O_2 detoxification capacity, increased protein *S*-bacillithiolation of GapDH and thiol-oxidation of the HypR repressor *in vivo*. However, no evidence for protein alkylation and aggregation was revealed. In support of the oxidative mode, the ROS scavenger N-acetyl cysteine and microaerophilic growth conditions improved the survival of *S. aureus* under lapachol stress. Phenotype analyses revealed that KatA and the Brx/BSH/YpdA pathway are important for the defense of *S. aureus* against lapachol-induced ROS. Overall, our results indicate that the antimicrobial effect of lapachol is mainly caused by ROS-formation, resulting in an impaired redox homeostasis and increased protein thiol-oxidation in *S. aureus*.

2. Experimental procedures

Bacterial strains, growth and survival assays. For cloning and genetic manipulation, *E. coli* was cultivated in Luria broth (LB) medium. The His-tagged GapDH protein of *S. aureus* was expressed and purified in *E. coli* BL21(DE3) *plys*S with plasmid pET11b-*gapDH* as previously described [48]. For lapachol stress experiments, we used *S. aureus* COL *katA*, *bshA*, *brxAB* and *ypdA* deletion mutants and the *katA, bshA*, *ypdA, brxA* and *brxB* complemented strains as described in Tables S1 and S2 [51]. *S. aureus* strains were cultivated in LB, RPMI or Belitsky minimal medium (BMM) depending on the specific experiments and treated with lapachol during the exponential growth as described [41,54]. Specifically, biosensor experiments, *S*-bacillithiolation and HypR oxidation assays were performed in BMM medium due to high expression of the biosensor and low ROS quenching effects as described [54,55]. All growth and survival assays as well as RNA-seq experiments were performed in rich RPMI medium, which resembles infection conditions and allows fast growth. Survival assays were performed by plating 100 μl of serial dilutions of *S. aureus* onto LB agar plates and determination of colony forming units (CFUs). Statistical analysis was performed using Student's unpaired two-tailed *t*-test by the graph prism software. Lapachol, diamide, sodium hypochlorite (NaOCl), N-acetyl cysteine, dithiothreitol (DTT) and cumene hydroperoxide (CHP, 80% w/v) were purchased from Sigma Aldrich.

Determination of the minimal inhibitory concentration (MIC) of lapachol. MIC assays were performed in 96-well plates with 200 μl of serial two-fold dilutions of the 40 mM lapachol stock in RPMI medium. The *S. aureus* overnight culture was inoculated to an OD_{500} of 0.03 into the microplate wells. After 24 h shaking at 37 °C, the OD_{500} was measured using the CLARIOstar microplate reader (BMG Labtech).

Construction of *S. aureus* COL *katA* and *bshA* mutants as well as complemented strains. The construction of the *S. aureus katA* and *bshA* deletion mutants was performed using the pMAD *E. coli/S. aureus* shuttle vector as described [41,56]. Briefly, the 500 bp up- and downstream regions of *katA* and *bshA* were amplified using primers pMAD-katA-for-BglII, pMAD-katA-f1-rev, pMAD-katA-f2-for, pMAD-katA-rev-SalI for *katA* and pMAD-bshA-f1-rev, pMAD-bshA-for-BglII, pMAD-bshA-rev-SalI, pMAD-bshA-f2-for for *bshA* (Table S3), fused by overlap extension PCR and ligated into the *Bgl*II and *Sal*I sites of plasmid pMAD. The pMAD constructs were electroporated into *S. aureus* RN4220 and further transduced into *S. aureus* COL using phage 81 [57]. The clean deletions of *katA* and *bshA* were selected after plasmid excision as described [41].

For construction of the *katA* and *bshA* complemented strains, the xylose-inducible ectopic *E. coli/S. aureus* shuttle vector pRB473 was applied [58]. Primer pairs pRB-katA-for-*Bam*HI and pRB-katA-rev-*Kpn*I as well as pRB-bshA-for-*Bam*HI and pRB-bshA-rev-*Kpn*I (Table S3) were used for amplification of *katA* and *bshA*, respectively. The PCR products were cloned into pRB473 after digestion with *Bam*HI and *Kpn*I to generate plasmids pRB473-*katA* and pRB473-*bshA*. The pRB473-*katA* and pRB473-*bshA* plasmids were transduced into the *katA* and *bshA* deletion mutants, respectively, to construct the complemented strains as described [54].

For construction of *S. aureus* COL WT expressing His-tagged HypR, *hypR*-His was amplified from the *S. aureus* COL genome by PCR using

primer pRB-hypR-for-BamHI and primer pRB-hypR-His-rev-KpnI (Table S3), which included the codons for 6 His residues at the C-terminus. The PCR product was cloned into plasmid pRB473 after digestion with *Bam*HI and *Kpn*I to generate plasmid pRB473-*hypR*-His, which was introduced into *S. aureus* COL WT via phage transduction as described [41].

Live/Dead viability assay. The viability assay of *S. aureus* COL WT was conducted after treatment with sub-lethal and lethal concentrations of 0.3–1 mM lapachol at an OD_{500} of 0.5 using the LIVE/DEAD™ BacLight™ bacterial viability kit (Thermo Fisher) as described [59]. In brief, *S. aureus* COL was stained with SYTO9 or propidium iodide for live or dead cells, respectively. Fluorescence was analyzed after excitation at 488 and 555 nm using a fluorescence microscope (Nikon, Eclipse, T*i*2) (SYTO9 Ex: 488 nm, propidium iodide Ex: 555 nm). Live and dead cells were false-colored in green and red, respectively.

RNA isolation, library preparation, next generation cDNA sequencing and differential gene expression analysis after lapachol stress. RNA-seq transcriptomics was performed using RNA of *S. aureus* COL, which was grown in RPMI medium and subjected to 0.3 mM lapachol for 30 min as described [59]. Differential gene expression analysis of 3 biological replicates was performed using DESeq2 [60] with ReadXplorer v2.2 [61] using an adjusted p-value cut-off of $P \leq 0.05$ and a signal intensity ratio (M-value) cut-off of ≥1 or ≤ -1 (fold-change of ± 2) as described previously [59]. The RNA-seq raw data files for the whole transcriptome are available in the ArrayExpress database (www.ebi.ac.uk/arrayexpress) under E-MTAB-8691.

Construction of the Voronoi transcriptome treemap. The lapachol transcriptome treemap was constructed using the Paver software (DECODON GmbH, Greifswald, Germany) as described [59]. The red-blue color gradient indicates log2-fold changes (M-values) of selected genes, operons and regulons that are up- or down-regulated under lapachol stress. The cell sizes denote absolute log2-fold changes in the transcriptome under lapachol versus the control.

Brx-roGFP2 and Tpx-roGFP2 biosensor measurements. *S. aureus* COL expressing the biosensor plasmids pRB473-*tpx-roGFP2* and pRB473-*brx-roGFP2* were grown in LB overnight and used for measurements of the biosensor oxidation degree (OxD) after treatment with 100 μM lapachol as described [51,54]. The fully reduced and oxidized controls of *S. aureus* cells expressing Tpx-roGFP2 were treated with 15 mM DTT and 20 mM cumene hydroperoxide, respectively. The Brx-roGFP2 and Tpx-roGFP2 biosensor fluorescence emission was measured at 510 nm after excitation at 405 and 488 nm using the CLARIOstar microplate reader (BMG Labtech). The OxD of the Brx-roGFP2 and Tpx-roGFP2 biosensors was determined for each sample and normalized to fully reduced and oxidized controls as described [51,54].

Analyses of GapDH *S*-bacillithiolation and thiol-oxidation of the HypR repressor after lapachol stress. For GapDH *S*-bacillithiolation assay *in vivo*, *S. aureus* cells were grown in LB until an OD_{540} of 2, harvested by centrifugation and transferred to Belitsky minimal medium (BMM) as described [47]. The cells were treated with 100 μM lapachol and harvested after 30, 60, 120 and 180 min in TE buffer (pH 8.0) with 50 mM N-ethylmaleimide (NEM). Protein extracts were prepared and analyzed by BSH-specific Western blot analysis for *S*-bacillithiolated proteins using polyclonal rabbit anti-BSH antiserum as described [47]. To analyze *S*-bacillithiolation of purified GapDH with lapachol *in vitro*, 60 μM of GapDH was *S*-bacillithiolated with 600 μM BSH in the presence of 10-fold excess of 6 mM lapachol for 5 min. As control, GapDH was incubated with BSH in the absence of lapachol. Excess of BSH and lapachol were removed with Micro Biospin 6 columns (Biorad). *S*-bacillithiolation of GapDH was analyzed using non-reducing BSH-specific Western blots. To study thiol-oxidation of the HypR repressor *in vivo*, *S. aureus* COL WT strain expressing His-tagged HypR (Table S1) was cultivated as described for the *in vivo S*-bacillithiolation assay above. Cell extracts were alkylated with 50 mM NEM and HypR oxidation analyzed using non-reducing SDS-PAGE and Western blot analysis with His-tag specific monoclonal antibodies (Thermo Fisher).

Analysis of H_2O_2 detoxification capacity in cell extracts by the FOX assay. The FOX assay was performed with cytoplasmic cell extracts as described previously [62]. FOX reagent was prepared by adding 100 ml FOX I (100 mM sorbitol, 125 μM xylenol orange) to 1 ml FOX II (25 mM ammonium ferrous(II)sulfate in 2.5 M H_2SO_4). To prepare cytoplasmic extracts, *S. aureus* COL WT was cultivated in RPMI to an OD_{500} of 0.5, exposed to 0.3 mM lapachol and harvested after 1 h and 2 h. Cells were washed in 83 mM phosphate buffer (pH 7.05), disrupted using the ribolyzer and 100 μl cell lysate was added to 500 μl of 10 mM H_2O_2 solution. After different times (1–5 min), 2 μl of the samples were added to 200 μl FOX reagent and incubated for 30 min at room temperature. The absorbance was measured at 560 nm using the CLARIOstar microplate reader. H_2O_2 standard curves were measured with 20 μl H_2O_2 (0–18 μM final concentrations) and 200 μl FOX reagent as above.

Protein aggregation assays after lapachol stress *in vitro* and *in vivo*. For *in vitro* aggregation analyses, purified GapDH was pre-reduced with 10 mM DTT for 30 min at RT and DTT was removed with spin columns. Subsequently, 5 μM GapDH was incubated with different concentrations of lapachol for 30 min at RT and subjected to SDS-PAGE. For isolation of insoluble protein aggregates of cell extracts *in vivo*, *S. aureus* COL WT was cultivated in RPMI to an OD_{500} of 0.5 and treated with 0.3 and 1.0 mM lapachol for 30 min. Cell extracts were harvested and protein aggregates isolated as insoluble protein fraction as described previously [59,63,64].

3. Results

Lapachol has a strong antimicrobial and killing effect in *S. aureus* COL. To determine the growth-inhibitory and lethal lapachol concentrations, *S. aureus* COL was grown in RPMI medium and exposed to increasing doses 0.3–1 mM lapachol during the exponential growth (Fig. 1A,B). Cell viability was analyzed using CFU counting and the LIVE/DEAD™ Bacterial Viability Kit (Fig. 1B,C). Sub-lethal doses of 0.3 mM lapachol resulted in a decreased growth rate, but cells were able to recover in growth and the survival rate was not affected (Fig. 1A,B). This result was confirmed using live/dead staining since only few red cells were observed after treatment with sub-lethal 0.3 mM lapachol similar as in the untreated control (Fig. 1C). Increasing concentrations of 0.4–1 mM lapachol were lethal for *S. aureus* COL as shown by decreased growth and viability rates (Fig. 1A,B). Only few SYTO9-labelled cells could be observed using the LIVE/DEAD™ assay after exposure to 0.7–1 mM lapachol, indicating that lapachol exerts a strong antimicrobial and killing effect in *S. aureus* (Fig. 1C). However, the MIC of lapachol was determined as 1.25 mM in *S. aureus* (Table S4), which was higher compared to the growth-inhibitory amount. The higher MIC is probably caused by inactivation of lapachol over the long time of incubation for 24 h in the microplate assay.

Lapachol induces a quinone and oxidative stress response in the *S. aureus* COL transcriptome. In previous transcriptome studies, we monitored physiological stress responses by treatment of *S. aureus* with sub-lethal doses of antimicrobial compounds [41,59,65]. Thus, the changes in the transcriptome were analyzed after exposure of *S. aureus* COL to sub-lethal 0.3 mM lapachol stress for 30 min in 3 biological replicates using the RNA-seq method as described earlier [41]. Significant differential gene expression is indicated by the M-value cut-off (log2-fold change lapachol/control) of ≥1 and ≤-1 (fold-change of ± 2, $P \leq 0.05$) which includes most known redox regulons up-regulated under lapachol stress (Fig. 2). In total, 564 genes were significantly > 2-fold up-regulated and 515 genes were < -2-fold down-regulated in the lapachol transcriptome of *S. aureus* COL (Fig. 2, Tables S5 and S6). Overall, the significantly and most strongly induced regulons in the lapachol transcriptome include the CtsR, HrcA, PerR, HypR, NsrR, MhqR, QsrR, CymR, SaeRS, GraRS and SigB regulons. These regulons indicate that lapachol causes an oxidative and quinone

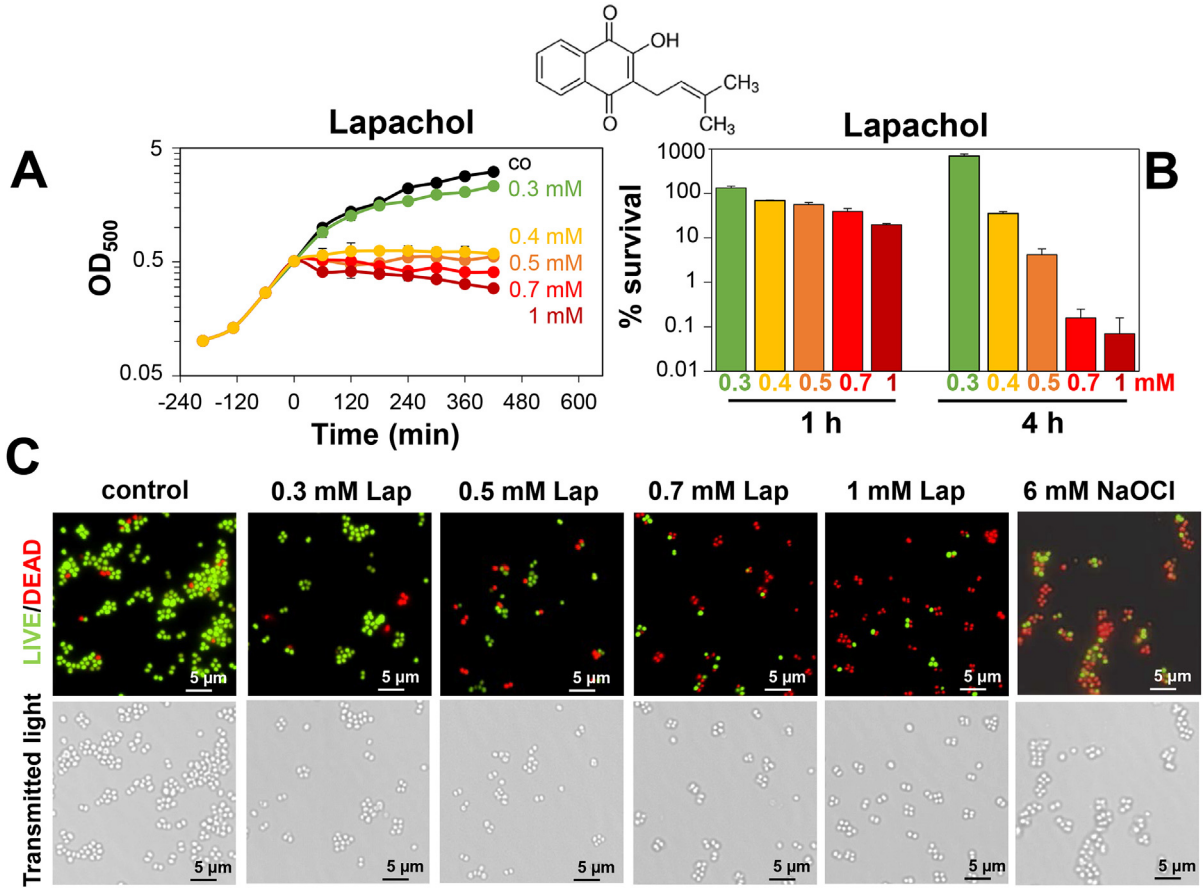

Fig. 1. Lapachol has a strong antimicrobial effect in *S. aureus*. (A–C) The structure of the 2-hydroxy-3-(3-methyl-2-butenyl)-1,4-naphthoquinone lapachol is shown above the figures **(A)** and **(B)**. *S. aureus* COL was grown in RPMI medium to an OD_{500} of 0.5 and exposed to sub-lethal (300 µM) and lethal (0.4, 0.5, 0.7 and 1 mM) doses lapachol. **(A)** Growth curves and **(B)** survival assays were performed to determine sub-lethal and lethal lapachol concentrations. The cells were plated for CFUs after 1 and 4 h of lapachol stress. **(C)** Cell viability was also analyzed after 1 h of lapachol stress using the Live/Dead™ BacLight™ Bacterial Viability Kit and visualized with a fluorescence microscope (Nikon, Eclipse, Ti2). Live and dead cells show green and red fluorescence, respectively. As control for dead cells, the toxic concentration of 6 mM NaOCl was applied.

stress transcriptome signature and protein damage. Up-regulated genes and regulons are labelled with different color codes in the ratio/intensity scatter plot (M/A-plot) and are also displayed in the Voronoi transcriptomics treemap (Figs. 2 and 3, Tables S5 and S6).

Lapachol stress leads to strong induction of the CtsR and HrcA regulons, which control the protein quality control machinery, including Clp proteases and the DnaK-GrpE, GroESL chaperones [66,67]. The heat-shock specific CtsR controlled *ctsR-mcsA-mcsB-clpC* operon and the HrcA-regulated *hrcA-grpE-dnaKJ* operon are 46-62-fold and 44-50-fold up-regulated, respectively, under lapachol stress (Figs. 2 and 3, Tables S5 and S6). Thus, lapachol induces strong protein damage, which might be caused by oxidative or electrophilic protein modifications, such as thiol-oxidation or *S*-alkylations. Among the top scorers was further the peroxide specific PerR regulon with fold-changes of 5–26. The PerR-regulon genes encode for peroxidases *ahpCF* (20-26-fold), *bcp* (11-fold), *tpx* (5-fold), the catalase *katA* (11-fold), the mini-ferritin *dps* (11-fold) and the thioredoxin reductase *trxB* (5-fold) (Figs. 2 and 3, Tables S5 and S6). The induction of the PerR-regulon confirms that lapachol acts via the oxidative mode leading to ROS formation, such as H_2O_2 inside *S. aureus*. Furthermore, both genes encoding superoxide dismutases (*sodA1* and *sodA2*) were highly expressed (11-12-fold) under lapachol stress (Fig. 2, Tables S5 and S6). This supports the generation of superoxide anions in the oxidative mode of lapachol as has been measured previously *in vitro* [24].

In addition, lapachol resulted in 23-26-fold induction of the NsrR-controlled *hmp* gene encoding a flavohemoglobin, which is predominantly involved in nitric oxide detoxification [68]. Interestingly, Hmp of *S. aureus* was shown to function in quinone and nitrocompound detoxification using mixed one- and two electron reduction mechanisms [69]. Hmp exhibits a strong substrate preference for 2-methyl-1,4-naphthoquinones [69], which are related to lapachol. Thus, Hmp might be involved in lapachol detoxification in *S. aureus*. Furthermore, the HypR regulon, including the disulfide reductase encoding *merA* gene was 5-fold induced by lapachol, which is indicative for disulfide stress caused by lapachol [41].

The RNA-seq transcriptome data further suggest an electrophilic mode of action of lapachol, as revealed by the significant induction of both quinone-specific MhqR and QsrR regulons. The MhqR-regulated *mhqRED* operon was 10-fold induced under lapachol treatment. The QsrR regulon genes encoding quinone reductases and dioxygenases are 3.7-9-fold up-regulated by lapachol, including *catE, catE2*, *azoR1*, *frp* and *yodC* (Figs. 2 and 3, Tables S5 and S6). Thus, the main transcriptome signature suggests that lapachol exerts its toxicity as oxidant and electrophile in *S. aureus*. In addition, lapachol leads to strong up-regulation of the SaeRS, GraRS and SigB regulons. Among the virulence factor controlling SaeRS regulon, the myeloperoxidase inhibitor SPIN was most strongly 123-fold induced, while the γ-hemolysin operon *hlgABC* was 8-10-fold up-regulated by lapachol. Several GraRS regulon members were 3-60-fold up-regulated. The large GraRS regulon responds to cell wall-active antibiotics and is involved in the oxidative stress defense in *S. aureus* [70]. Finally, the genes encoding enzymes for biosynthesis of BSH and the Brx/YpdA pathway, such as *bshA*, *bshB*,

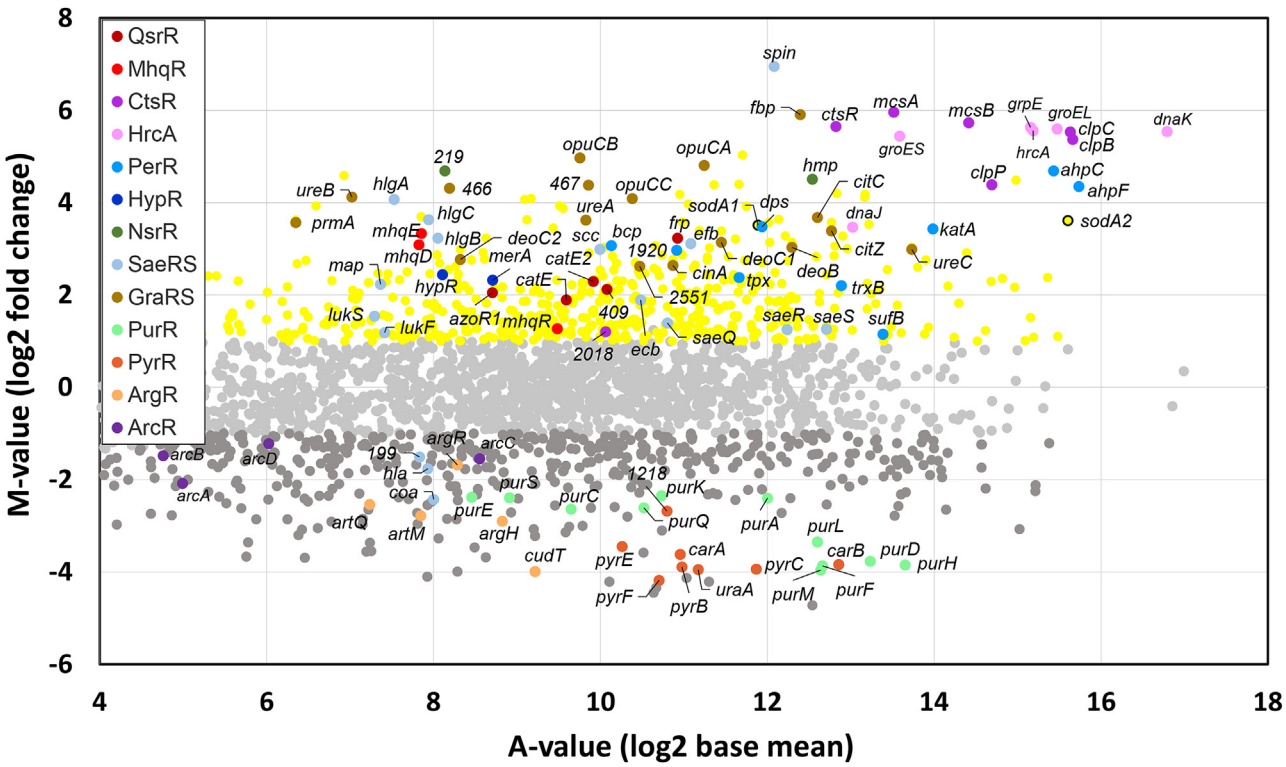

Fig. 2. RNA-seq transcriptomics after lapachol stress in *S. aureus* COL. For RNA-seq transcriptomics, *S. aureus* COL was grown in RPMI medium and treated with 300 μM lapachol for 30 min. The gene expression profile is shown as ratio/intensity scatter plot (M/A-plot) which is based on differential gene expression analysis using DeSeq2. Colored symbols indicate subsets of the significantly induced regulons QsrR, MhqR, CtsR, HrcA, PerR, HypR, SaeRS, NsrR (dark red, red, magenta, light magenta, blue, dark blue, light blue, green). The significantly down-regulated regulons PurR, PyrR, ArgR, ArcR are labelled in light green, orange, light orange and dark violet. All other significantly induced (yellow) or repressed (dark grey) transcripts were defined with an M-value ≥ 1 or ≤ -1; P-value ≤ 0.05. Light grey symbols denote transcripts with no fold-changes after lapachol stress (P > 0.05). The transcriptome analysis was performed from three biological replicates. The RNA-seq expression data of all genes after lapachol stress and their regulon classifications are listed in Tables S5 and S6.

bshC, brxB and *ypdA* were 2-4-fold up-regulated by lapachol in *S. aureus*. This further points to the generation of ROS in the oxidative mode of lapachol resulting in an impaired redox homeostasis in *S. aureus*.

Among the down-regulated regulons, the CodY and ArgR regulons involved in the biosynthesis of branched chain amino acids (lysine, isoleucine and leucine) and arginine, respectively, were strongly repressed in the lapachol transcriptome. The PyrR and PurR regulons, which control purine and pyrimidine biosynthesis operons were further down-regulated under lapachol. The shut-down of amino acid and nucleotide biosynthesis enzymes might be caused by decreased ATP levels since the ATP synthase operon was further down-regulated under lapachol stress (Figs. 2 and 3, Tables S5 and S6).

Altogether, the RNA-seq transcriptome signature indicates that lapachol causes an oxidative, quinone and cell wall stress response as well as protein damage, suggesting its mode of action as oxidant and electrophile.

Lapachol stress leads to an increased BSH redox potential, elevated endogenous ROS levels and enhanced H_2O_2 detoxification in *S. aureus*. Previous studies revealed that lapachol is reduced to its semiquinone anion radical, leading to reduction of O_2 and formation of reactive oxygen species (ROS), such as superoxide anions and hydroxyperoxyl radicals [24,25]. Our transcriptome data further support the oxidative mode of lapachol and an impaired redox balance (Figs. 2 and 3). Thus, we applied the recently constructed genetically encoded Brx-roGFP2 and Tpx-roGFP2 biosensors to measure intracellular redox changes in *S. aureus* after sub-lethal doses of 100 μM lapachol [51,54]. The coupled Brx-roGFP2 biosensor is specific for BSSB leading to *S*-bacillithiolation of the Brx active site Cys and transfer of BSH to the roGFP2 moiety, which finally rearranges to the roGFP2 disulfide [54]. Oxidation of roGFP2 results in a ratiometric change of the 405 and 488 nm excitation maxima. The 405/488 nm excitation ratio of Brx-roGFP2 after lapachol stress reflects the oxidation degree (OxD) of the biosensor and the changes in the BSH redox potential (E_{BSH}) in *S. aureus* [54]. The Brx-roGFP2 biosensor showed an increased OxD of 0.65 after 100 μM lapachol stress compared to the untreated control (OxD ~ 0.3) (Fig. 4A). However, cells were unable to regenerate the reduced basal level of E_{BSH} within 3 h of lapachol stress. These results indicate that lapachol causes a constant oxidative shift in E_{BSH} in *S. aureus* probably due to its redox-cycling action.

Next, we monitored endogenous H_2O_2 levels using the Tpx-roGFP2 biosensor in *S. aureus* after lapachol stress [51]. The Tpx-roGFP2 biosensor is specific for low levels of H_2O_2 [51]. H_2O_2 reacts with the Tpx active site to Cys sulfenic acid (SOH), which is transferred to roGFP2 leading to roGFP2 disulfide formation and the ratiometric changes in the roGFP2 excitation spectrum. The Tpx-roGFP2 biosensor was shown to respond very fast to 100 μM lapachol leading to an increased OxD of ~0.7 (Fig. 4B). These results confirm that lapachol treatment leads to increased endogenous H_2O_2 levels resulting in an increased E_{BSH} supporting the oxidative mode of action. In addition, the FOX assay was performed to investigate the H_2O_2 detoxification capacity of cellular extracts of *S. aureus* after lapachol stress. H_2O_2 detoxification occurred much faster in lapachol-treated cell extracts, compared to that of untreated control cells (Fig. 4C). Thus, *S. aureus* has an enhanced H_2O_2 detoxification capacity after lapachol stress due to a higher catalase activity, which is consistent with the increased expression of the PerR controlled *katA* and *ahpCF* antioxidant genes.

The ROS scavenger N-acetyl cysteine and microaerophilic growth conditions improve the survival of *S. aureus* under lapachol stress. Since ROS generation by lapachol depends on oxygen

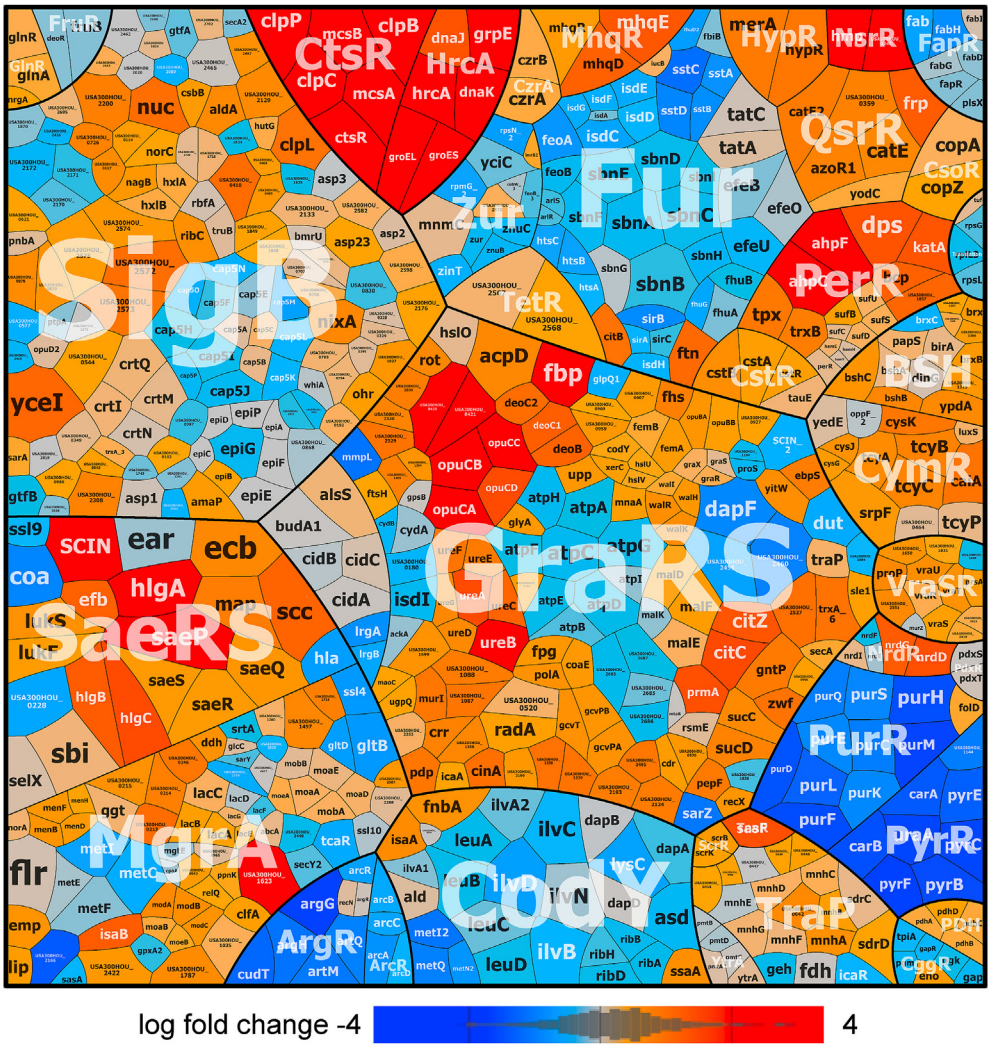

Fig. 3. The transcriptome treemap after lapachol indicates an oxidative and quinone stress response in *S. aureus* COL. The treemap shows the log2-fold changes (M-values) using the red-blue color code where red indicates log2-fold induction and blue repression of selected regulons after exposure to 300 μM lapachol in the RNA-seq transcriptome of *S. aureus* COL. The genes, operons and regulons are based on RegPrecise (http://regprecise.lbl.gov/RegPrecise/index.jsp) and previous classifications. Lapachol caused a strong quinone and oxidative stress response as well as protein damage as revealed by induction of the PerR, HypR, QsrR, MhqR, CtsR, HrcA regulons in *S. aureus*. The induction of the SigmaB and GraRS regulons further indicates cell wall and general stress responses in *S. aureus*. The detailed transcriptome data of all genes differentially expressed in response to lapachol are presented in Tables S5 and S6.

availability, we compared the survival of *S. aureus* under aerobic and microaerophilic growth conditions. The results showed that the survival of *S. aureus* was strongly improved after 0.4 and 1 mM lapachol stress under microaerophilic conditions (Fig. 5A). Both concentrations were lethal under aerobic conditions (Fig. 1B; Fig. 5A). While microaerophilic growth resulted in ~80% survival of cells exposed to 1 mM lapachol, only less than 1% of cells survived with 1 mM lapachol under aerobic conditions (Fig. 5A). This result was supported by the ROS scavenger N-acetyl cysteine, which was added to the aerobic culture before the exposure to 0.4 mM lapachol (Fig. 5B). The aerobic *S. aureus* culture treated with N-acetyl cysteine showed significantly improved survival after 0.4 mM lapachol stress (Fig. 5B). Together, our results revealed that the antimicrobial effect of lapachol is based on ROS formation, since decreased ROS levels lead to an enhanced survival of lapachol-treated cells.

Lapachol causes increased *S*-bacillithiolation of GapDH and thiol-oxidation of the HypR repressor in *S. aureus*. Previously, we used BSH-specific Western blots to analyze the extent of protein *S*-bacillithiolation in *S. aureus* under HOCl stress [48]. The glyceraldehyde-3-phosphate dehydrogenase GapDH was the most abundant *S*-bacillithiolated protein under HOCl stress that could be visualized as major band in non-reducing BSH-specific Western blots [48]. Thus, we investigated the oxidative mode of action of lapachol by analysis of the pattern of *S*-bacillithiolation in *S. aureus*. The BSH specific Western blots revealed an increased *S*-bacillithiolation of the GapDH band after 30–120 min of lapachol stress, which was absent in the *bshA* mutant (Fig. 6A). These results confirm the oxidative mode of action to induce thiol-oxidation of GapDH in *S. aureus in vivo*.

Next, we used BSH-specific non-reducing Western blots to investigate whether lapachol-induced ROS can also lead to *S*-bacillithiolation of purified GapDH *in vitro*. Pre-reduced GapDH was treated with lapachol in the presence of BSH. While no *S*-bacillithiolated GapDH band was visible in the control reaction of GapDH with BSH alone, the presence of lapachol strongly induced *S*-bacillithiolation of GapDH *in vitro* (Fig. 6B). However, we did not find evidence for protein alkylation or aggregation of purified GapDH after treatment with increasing doses 0.5–7.5 mM lapachol alone as revealed by SDS-PAGE (Fig. S1A). In addition, we isolated the insoluble protein fraction of protein aggregates from lapachol-treated cells using the protocol as established previously [63,64]. However, the results did not reveal increased protein aggregates after lapachol stress (Fig. S1B).

To further support the oxidative mode of lapachol, we investigated the redox state of the redox-sensing HypR repressor, which senses disulfide stress by intersubunit disulfide formation in *S. aureus* [41]. *S. aureus* cells expressing His-tagged HypR protein were subjected to different concentrations of 0.1–1 mM lapachol stress. The redox state of HypR was analyzed using non-reducing Western blots with anti-His-tag specific monoclonal antibodies. The results revealed that lapachol leads to oxidation of HypR to the intermolecular disulfide-linked dimer after lapachol stress (Fig. S2AB). Thiol-oxidation of HypR was reversible with DTT, supporting the oxidative mode of lapachol. However, we could not detect irreversible protein alkylation and aggregation of

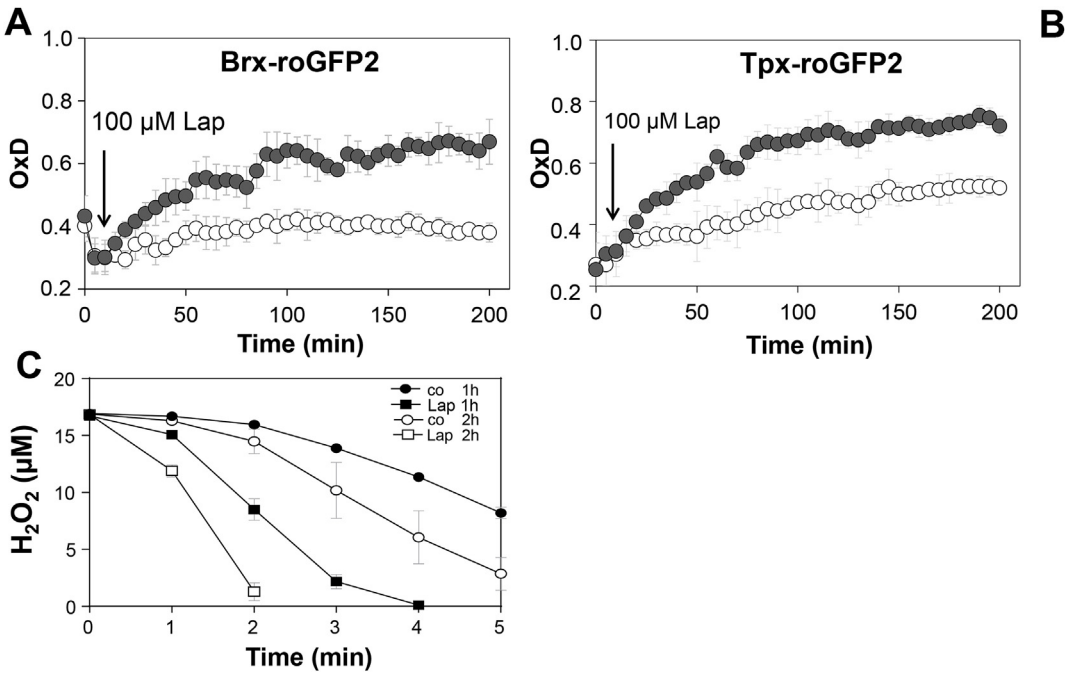

Fig. 4. Lapachol causes an increased BSH redox potential, elevated endogenous H_2O_2 levels and faster H_2O_2 detoxification in *S. aureus* COL. Responses of the Brx-roGFP2 **(A)** and Tpx-roGFP2 **(B)** biosensors to 100 µM lapachol stress in *S. aureus* COL. The oxidation degrees (OxD) of the Brx-roGFP2 and Tpx-roGFP2 biosensors were calculated for untreated control cells (white symbols) and after lapachol stress (grey symbols). OxD values were calibrated to fully reduced and oxidized controls. **(C)** Lapachol-treated *S. aureus* cells showed faster H_2O_2 detoxification in the FOX assay indicating higher catalase activity. *S. aureus* was exposed to 0.3 mM lapachol for 1–2 h and cell extracts were analyzed for H_2O_2 decomposition using the FOX-Assay. Mean values and SD of 3–4 biological replicates are shown.

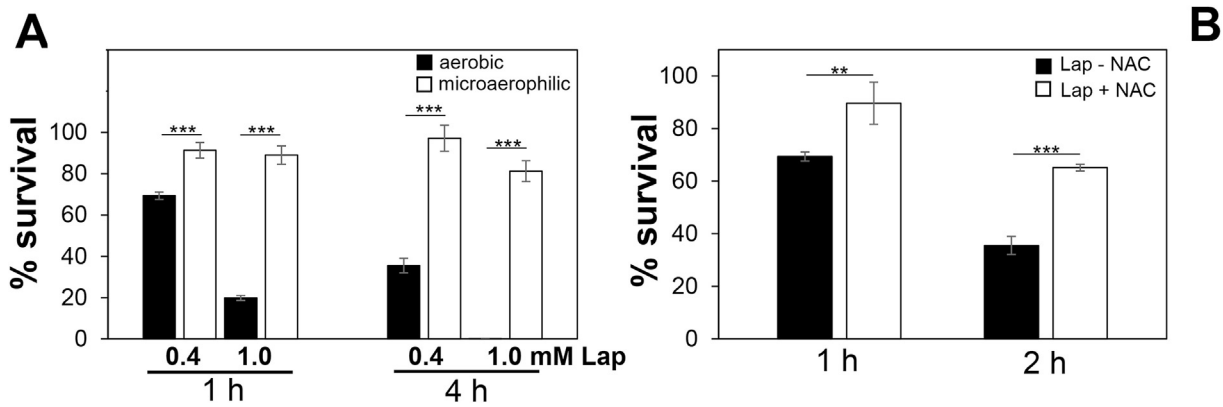

Fig. 5. Microaerophilic growth and the ROS-scavenger N-acetyl cysteine improve survival of *S. aureus* under lapachol stress. (A) Survival assays were performed of *S. aureus* COL WT grown in RPMI under aerobic or microaerophilic conditions after exposure to 0.4 and 1 mM lapachol at an OD_{500} of 0.5. The aerobic survival rates are the same shown in Fig. 1B. **(B)** Survival rates were determined under aerobic growth conditions after 0.4 mM lapachol stress in the absence or presence of 1.25 mM N-acetyl cysteine (NAC). CFUs were determined after 1 or 4 h of stress exposure and the survival of the untreated control was set to 100%. Mean values and SD of three to four biological replicates are presented. The statistics was calculated using a Student's unpaired two-tailed *t*-test by the graph prism software. Symbols are: $^{**}p \leq 0.01$ and $^{***}p \leq 0.001$.

proteins in the Western blot or SDS-PAGE loading control. Together, our results support the oxidative mode of lapachol to induce protein *S*-bacillithiolation of GapDH *in vitro* and *in vivo* as well as reversible thiol-oxidation of the redox-sensing HypR repressor in *S. aureus*.

The catalase KatA and the Brx/BSH/YpdA pathway confer tolerance of *S. aureus* towards lapachol treatment. To confirm the oxidative mode of lapachol by ROS generation, we analyzed the phenotype of the *katA* mutant deficient for the major catalase. The *katA* mutant displayed a growth delay under lapachol stress and was strongly impaired in survival compared to the parent (Fig. 7A,B). These results clearly confirm the production of H_2O_2 and increased catalase activity by lapachol as shown with the Tpx-roGFP2 biosensor and FOX assay, since the *katA* mutant is very sensitive to oxidative stress. In addition, we showed previously that the BrxA/BSH/YpdA redox pathway is important for de-bacillithiolation of proteins during recovery from oxidative stress and infection conditions [51]. Here, we have shown that lapachol causes an oxidative shift in E_{BSH} and increased *S*-bacillithiolation of GapDH (Figs. 4 and 6). Thus, we investigated the phenotypes of the *bshA*, *brxAB* and *ypdA* deletion mutants during growth and survival of *S. aureus* under lapachol stress. The growth of mutants deficient for BSH, bacilliredoxins BrxA/B and the BSSB reductase YpdA was significantly impaired after exposure to sub-lethal 0.3 mM lapachol (Fig. 7C,E,G). Furthermore, all mutants showed a significantly decreased survival after lethal 0.4 mM lapachol stress (Fig. 7D,F,H). These lapachol-sensitive phenotypes could be restored back to WT level after complementation with *katA*, *bshA*, *brxA* and *ypdA*, respectively (Fig. 7B,D,F,H; Fig. S3A,B,C,E). However, the complementation of the *brxAB* mutant with *brxB* did not restore the

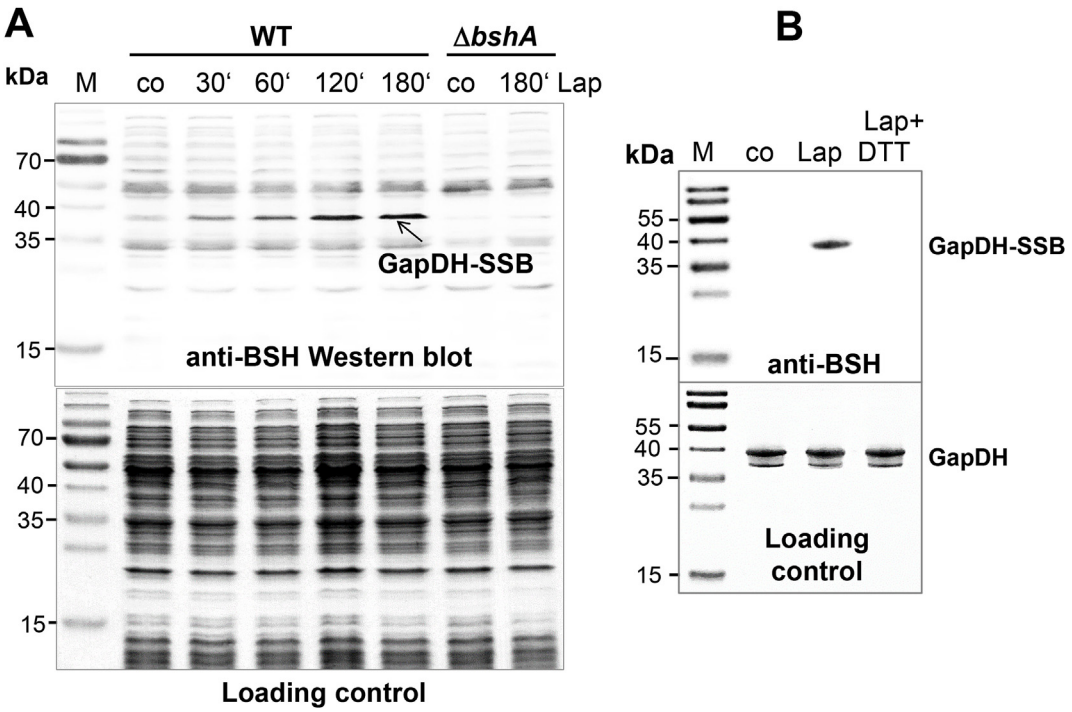

Fig. 6. Lapachol leads to *S*-bacillithiolation of GapDH *in vivo* and *in vitro*. (A) *S. aureus* COL WT and the *bshA* mutant were exposed to 100 μM lapachol for different times and the *S*-bacillithiolated GapDH (GapDH-SSB) is visualized in BSH-specific Western blot as most abundant *S*-bacillithiolated protein as shown previously under NaOCl stress [48]. **(B)** Purified GapDH is treated with 6 mM lapachol in the presence of 600 μM BSH resulting in *S*-bacillithiolation of GapDH *in vitro* as revealed in BSH-specific Western blots. As control, GapDH was treated with BSH alone (co). The Coomassie-stained SDS-PAGE loading controls are shown below the BSH Western blots.

phenotype back to wild type level (Fig. 7H; Fig.S3D). Taken together, these results revealed that the catalase KatA and the BrxA/BSH/YpdA redox pathway provide protection against lapachol-induced ROS formation in *S. aureus*.

4. Discussion

In this study, we have analyzed the antimicrobial mode of action of the naphthoquinone lapachol in the major pathogen *S. aureus*. Using growth and survival assays, the sub-lethal lapachol concentration was determined as 0.3 mM, while higher doses of 0.4–1.0 mM were toxic for *S. aureus* and strongly decreased the survival. Previously, the MIC of lapachol in *S. aureus* has been determined as 128–256 μg/ml (~0.53–1.06 mM) [71], which is in agreement with the MIC determined in this work. Since low doses of 0.4 mM lapachol are toxic for exponentially growing *S. aureus* cells, lapachol could be suited as redox-active antimicrobial to treat MRSA strains in wound infections.

In this work, we combined RNA-seq transcriptomics, redox biosensor measurements, protein thiol-oxidation assays and phenotype analyses of mutants to investigate the antimicrobial mode of action and stress responses caused by lapachol in *S. aureus*. The transcriptome results showed that lapachol caused an oxidative and quinone stress response and protein damage in *S. aureus*. The oxidative stress-specific PerR and HypR regulons, which control catalases, peroxidases and disulfide reductases, and the superoxide dismutases *sodA1* and *sodA2* are most strongly up-regulated by lapachol, which are indicative for the oxidative mode of action of lapachol. This antioxidant response induced by lapachol supports the generation of ROS by the redox cycling action of lapachol, such as superoxide anions, which are converted to H_2O_2 by SodA1/2.

Thus, our results are in agreement with previous studies of the bioactivation of lapachol using NADPH-dependent cytochrome P450 reductase and the interaction of lapachol with oxygen *in vitro* [24,25]. The naphthoquinone lapachol was shown to be bioactivated via reduction by P450 reductase to semiquinone anion radical, which leads to electron transfer to molecular oxygen, resulting in superoxide anion generation [25]. In an electrochemical study, the semiquinone anion radical was demonstrated to interact with oxygen in an electron-chain mechanism, resulting in the deprotonated lapachol and hydroxyperoxyl radicals [24].

To investigate the oxidative stress response caused by lapachol-induced ROS, we studied the changes of the BSH redox potential and endogenous H_2O_2 formation by lapachol using the Brx-roGFP2 and Tpx-roGFP2 biosensors in *S. aureus*. Our results showed an oxidative shift of E_{BSH} after lapachol stress in *S. aureus*. Increased H_2O_2 production was measured in *S. aureus* with the Tpx-roGFP2 biosensor after lapachol exposure. However, both biosensors could not be regenerated after 3 h of stress, which is probably caused by the constant redox-cyclic action of lapachol in *S. aureus*. In addition, we used the FOX assay to demonstrate an enhanced H_2O_2 detoxification capacity of *S. aureus* cells after lapachol stress, which supports an increased catalase activity in lapachol-treated cells. Survival assays under aerobic and microaerophilic conditions could further link lapachol toxicity to increased ROS formation under aerobic conditions in *S. aureus*. The survival of lapachol-treated *S. aureus* cells was strongly increased under microaerophilic conditions, while the aerobic culture was protected against lapachol toxicity by the ROS scavenger N-acetyl cysteine. These combined results of an oxidative shift in E_{BSH}, elevated H_2O_2 levels with the Tpx-roGFP2 biosensor, faster H_2O_2 detoxification and increased survival with decreased ROS levels indicate that the redox-cycling mode is the main antimicrobial mode of action of lapachol in *S. aureus* cells.

In agreement with the oxidative mode, growth and survival assays revealed an increased sensitivity of the *katA* mutant to lapachol, which is compromised in H_2O_2 detoxification [72]. Apart from *katA*, the peroxidase *ahpCF* operon is very strongly 20-26-fold induced by lapachol. Both KatA and AhpCF have compensatory roles in peroxide detoxification, since the absence of KatA resulted in elevated AhpCF expression and *vice versa* [72]. Our transcriptome results indicate that

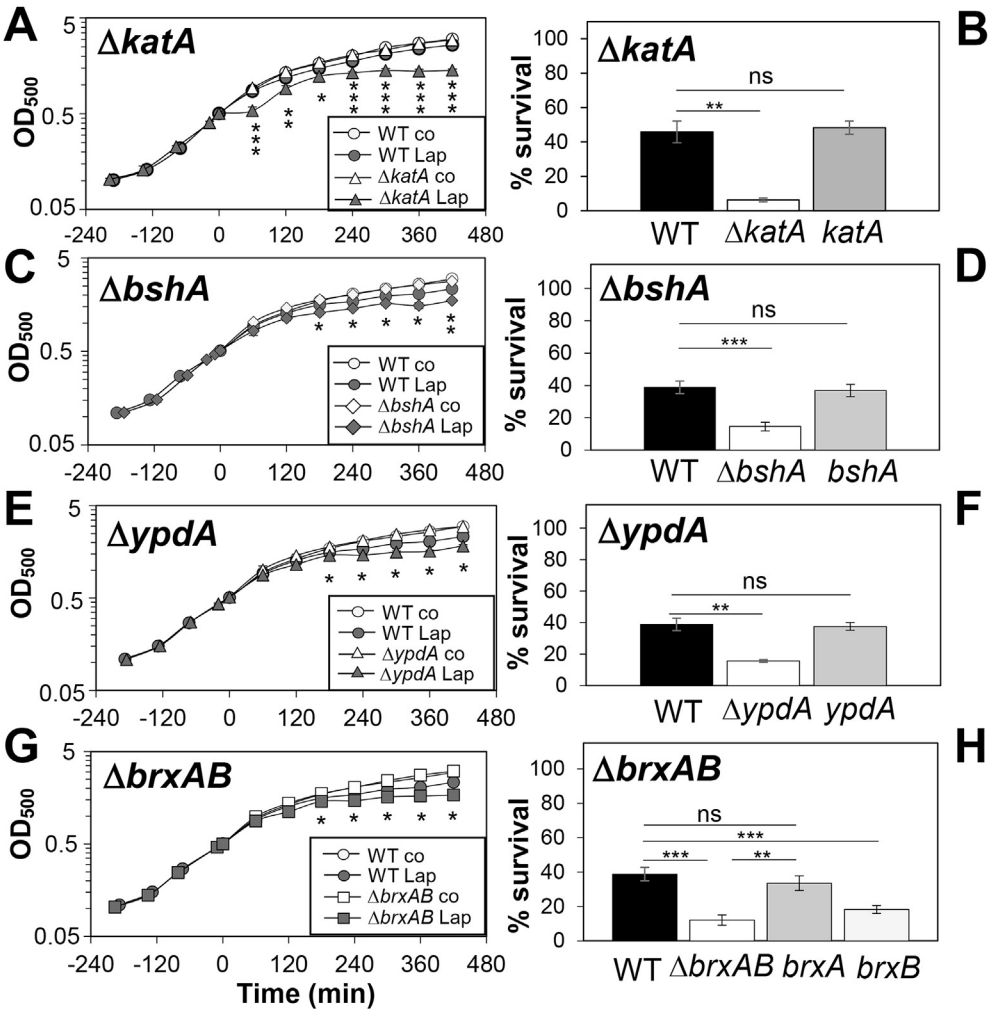

Fig. 7. The *S. aureus katA, bshA, ypdA* and *brxAB* deletion mutants are more sensitive under lapachol stress as shown in growth and survival assays. (A–H) Growth curves **(A, C, E, G)** and survival assays **(B,D,F,H)** were performed of *S. aureus* COL WT, *katA*, *bshA*, *brxAB*, and *ypdA* mutants and complemented strains (*katA*, *bshA, ypdA, brxA, brxB*) in RPMI medium after exposure to lapachol stress at an OD_{500} of 0.5. Growth phenotypes were determined after 300 μM lapachol and survival rates were calculated 4 h after exposure to 400 μM lapachol and determination of CFUs. Growth curves of the *bshA, katA, ypdA, brxA* and *brxB* complemented strains are shown in Fig. S3. Survival of the untreated control was set to 100%. Mean values and SD of four biological replicates are presented. The statistics was calculated using a Student's unpaired two-tailed *t*-test by the graph prism software. Symbols are: $^{ns}p > 0.05$, $^{*}p \leq 0.05$, $^{**}p \leq 0.01$ and $^{***}p \leq 0.001$.

both KatA and AhpCF are highly induced by lapachol to remove H_2O_2. The increased catalase activity was confirmed using the FOX assay in extracts of lapachol-treated cells. In the *katA* mutant, the *ahpCF* operon might compensate for detoxification of H_2O_2 which is produced by lapachol.

In addition, we analyzed the thiol-oxidation of GapDH and the HypR repressor in the proteome of *S. aureus*. Lapachol induced *S*-bacillithiolation of GapDH both *in vivo* and *in vitro*, supporting further ROS generation. *S*-bacillithiolation of GapDH was previously observed in response to strong oxidants, such as HOCl and by the antimicrobial coating AGXX®, which causes hydroxyl radical formation [48,59]. Thus, the previously measured hydroxyperxoxyl radical under lapachol stress might provoke *S*-bacillithiolation of GapDH [24]. Regeneration of *S*-bacillithiolated proteins and BSSB was shown to require the BrxA/BSH/YpdA pathway in *S. aureus*, which is important under oxidative stress and infections [48,51,52]. Consistent with these results, the *bshA*, *brxAB* and *ypdA* mutants showed significant growth and survival defects under lapachol stress. This confirms the importance of the BrxA/BSH/YpdA pathway for recovery of *S. aureus* from lapachol stress by reduction of oxidized proteins and BSSB.

The HypR repressor was previously shown to sense strong disulfide stress, such as HOCl, AGXX® and allicin [41,59,65]. The redox-sensing mechanism of HypR involves intermolecular disulfide formation under HOCl stress. Here, we confirmed that HypR is oxidized to the HypR disulfide-linked dimer leading to its inactivation and derepression of transcription of the disulfide reductase-encoding *merA* gene. Consistent with these results, the *hypR-merA* operon was 5-fold induced in the transcriptome under lapachol stress. The increased protein thiol-oxidation by lapachol is further in agreement with the strong induction of the CtsR and HrcA regulons, controlling Clp proteases and the DnaK-GrpE, GroESL chaperones to degrade and refold oxidatively damaged proteins. Altogether, our results indicate that lapachol provokes mainly an oxidative stress response in the transcriptome, which was confirmed by an oxidized E_{BSH}, elevated H_2O_2 levels, increased catalase activity and protein thiol-oxidation during aerobic growth in *S. aureus*.

However, quinones have been described to exert their cytotoxicity via oxidative and electrophilic mechanisms [13,27,28]. In the electrophilic mode, quinones lead to *S*-alkylation of nucleophilic Cys residues, resulting in irreversible protein aggregation and depletion of Cys proteins in the proteome [29]. Thus, the question arises whether the naphthoquinone lapachol could lead to thiol-*S*-alkylation and aggregation of protein thiols. Previous studies on diesel exhaust phenanthraquinone revealed the oxidation of proximal protein thiols and oxidative modification of Cu, Zn superoxide dismutase through the redox cycling mode of action [33,73]. Our transcriptome signature revealed the induction of the quinone-specific MhqR and QsrR regulons under lapachol stress, which could point to the alkylation mode. However, these quinone-specific regulons were induced at lower levels (~10-fold) compared to the oxidant-induced PerR-regulated *ahpCF* and *katA* genes. This might indicate that the naphthoquinone lapachol does not lead to alkylation and aggregation of protein thiols as shown for benzoquinones previously [29]. In contrast, the MhqR and QsrR regulons responded much stronger to the hydroquinone MHQ in previous transcriptome studies [26]. Specifically, MHQ leads to 34-67-fold induction of the MhqR regulon and up-to 280-fold induction of the QsrR regulon in *S. aureus* [26]. The *S*-alkylation and oxidation modes of

action were both previously demonstrated for benzoquinones in *B. subtilis* [29].

To exclude the alkylation mode of lapachol, we treated the GapDH protein with increasing concentrations of lapachol up-to 7.5 mM *in vitro*, but did not observe any aggregation in the higher molecular range (Fig. S1A) compared to previous studies with benzoquinones [29]. The isolation of the insoluble protein fraction in cell extracts *in vivo* did not reveal increased protein aggregates after treatment of cells with 0.3 and 1 mM lapachol (Fig. S1B). In addition, no irreversible protein aggregation could be observed for the HypR repressor, which was oxidized to the reversible HypR intermolecular disulfides indicative for the oxidative mode (Fig. S2AB). We did not find any evidence for protein alkylation and aggregation since cellular proteins could be well separated using SDS-PAGE. No alkylated aggregates migrated in the upper range of the SDS gel or remained in the stacking gel (see loading controls of Fig. 6A and Fig. S2AB) as observed previously for benzoquinones [29]. These results were expected since the quinone ring is fully substituted in lapachol, which prevents thiol-*S*-alkylation and aggregation of protein thiols [27,34]. In general, the toxicity and alkylation activity increases with the number of unsubstituted positions adjacent to the keto groups of the quinone rings [27,34]. In conclusion, our results demonstrate that lapachol leads to ROS formation and acts mainly via its redox-cycling oxidative mode as antimicrobial mechanism in *S. aureus*.

Finally, the question arises if *S. aureus* is able to detoxify lapachol. Lapachol metabolic pathways have been studied in fungi and streptomycetes, which involve monooxygenases or dioxygenases [74,75]. Our transcriptome data identified the flavohemoglobin *hmp* as strongly induced under lapachol stress in *S. aureus*. Hmp was characterized as NO dioxygenase, which converts NO and O_2 to NO_3^- via the haem-Fe^{2+} active center using NADPH and FAD as cofactors for electron transfer [68]. Recently, *S. aureus* Hmp was revealed to function in detoxification of quinones by mixed single and two-electron reduction mechanisms with preference for 1,4-naphthoquinones as best electron acceptors [69]. Quinone reduction required electrons from NADH and reduced FAD, but not from haem-$Fe^{2+}O_2$, indicating that quinones are subverse substrates for Hmp using different mechanisms for detoxification compared to NO [69]. These results indicate that lapachol detoxification could involve various NADPH-dependent flavoenzymes in *S. aureus*, which are upregulated in the transcriptome under lapachol stress and remain to be subjects of future studies.

Acknowledgements

This work was supported by an ERC Consolidator grant (GA 615585) MYCOTHIOLOME and grants from the Deutsche Forschungsgemeinschaft (AN746/4-1 and AN746/4-2) within the SPP1710, by the SFB973 project C08N and by the SFB/TR84 project B06 to H.A.

Appendix A. Supplementary data

Supplementary data to this article can be found online at https://doi.org/10.1016/j.freeradbiomed.2020.07.025.

References

[1] F.D. Lowy, *Staphylococcus aureus* infections, N. Engl. J. Med. 339 (8) (1998) 520–532.
[2] H.W. Boucher, G.R. Corey, Epidemiology of methicillin-resistant *Staphylococcus aureus*, Clin. Infect. Dis. 46 (Suppl 5) (2008) S344–S349.
[3] G.L. Archer, *Staphylococcus aureus*: a well-armed pathogen, Clin. Infect. Dis. 26 (5) (1998) 1179–1181.
[4] S.Y. Tong, J.S. Davis, E. Eichenberger, T.L. Holland, V.G. Fowler Jr., *Staphylococcus aureus* infections: epidemiology, pathophysiology, clinical manifestations, and management, Clin. Microbiol. Rev. 28 (3) (2015) 603–661.
[5] D.M. Livermore, Antibiotic resistance in staphylococci, Int. J. Antimicrob. Agents 16 (Suppl 1) (2000) S3–S10.
[6] S. Lakhundi, K. Zhang, Methicillin-Resistant *Staphylococcus aureus*: molecular characterization, evolution, and epidemiology, Clin. Microbiol. Rev. 31 (4) (2018).
[7] V.D. Nguyen, C. Wolf, U. Mäder, M. Lalk, P. Langer, U. Lindequist, M. Hecker, H. Antelmann, Transcriptome and proteome analyses in response to 2-methylhydroquinone and 6-brom-2-vinyl-chroman-4-on reveal different degradation systems involved in the catabolism of aromatic compounds in *Bacillus subtilis*, Proteomics 7 (9) (2007) 1391–1408.
[8] K.R. Vann, G. Ekiz, S. Zencir, E. Bedir, Z. Topcu, N. Osheroff, Effects of secondary metabolites from the fungus *Septofusidium berolinense* on DNA cleavage mediated by human topoisomerase II alpha, Chem. Res. Toxicol. 29 (3) (2016) 415–420.
[9] G. Ekiz, E.E. Hames, A. Nalbantsoy, E. Bedir, Two rare quinone-type metabolites from the fungus *Septofusidium berolinense* and their biological activities, J. Antibiot. (Tokyo) 69 (2) (2016) 111–113.
[10] H. Hussain, I.R. Green, Lapachol and lapachone analogs: a journey of two decades of patent research(1997-2016), Expert Opin. Ther. Pat. 27 (10) (2017) 1111–1121.
[11] C.A. Colwell, M. McCall, Studies on the mechanism of antibacterial action of 2-methyl-1,4-naphthoquinone, Science 101 (2632) (1945) 592–594.
[12] H. Schildknecht, Die Wehrchemie von Land- und Wasserkäfern, Angew. Chem. 82 (1) (1970) 17–25.
[13] R.A. Morton, Biochemistry of Quinones, Academic Press, 1965.
[14] Á. Ravelo, A. Estévez-Braun, E. Pérez-Sacau, The Chemistry and Biology of Lapachol and Related Natural Products α and β-lapachones, Studies in Natural Products Chemistry, Elsevier, 2003, pp. 719–760.
[15] F. Epifano, S. Genovese, S. Fiorito, V. Mathieu, R. Kiss, Lapachol and its congeners as anticancer agents: a review, Phytochemistry Rev. 13 (1) (2014) 37–49.
[16] O.A. Binutu, K.E. Adesogan, J.I. Okogun, Antibacterial and antifungal compounds from *Kigelia pinnata*, Planta Med. 62 (4) (1996) 352–353.
[17] R.M. Ali, P.J. Houghton, A. Raman, J.R.S. Hoult, Antimicrobial and antiinflammatory activities of extracts and constituents of *Oroxylum indicum* (L.) Vent, Phytomedicine 5 (5) (1998) 375–381.
[18] B.S. Park, J.R. Kim, S.E. Lee, K.S. Kim, G.R. Takeoka, Y.J. Ahn, J.H. Kim, Selective growth-inhibiting effects of compounds identified in *Tabebuia impetiginosa* inner bark on human intestinal bacteria, J. Agric. Food Chem. 53 (4) (2005) 1152–1157.
[19] E.M. Pereira, B. Machado Tde, I.C. Leal, D.M. Jesus, C.R. Damaso, A.V. Pinto, M. Giambiagi-deMarval, R.M. Kuster, K.R. Santos, *Tabebuia avellanedae* naphthoquinones: activity against methicillin-resistant staphylococcal strains, cytotoxic activity and in vivo dermal irritability analysis, Ann. Clin. Microbiol. Antimicrob. 5 (2006) 5.
[20] M.A. Souza, S. Johann, L.A. Lima, F.F. Campos, I.C. Mendes, H. Beraldo, E.M. Souza-Fagundes, P.S. Cisalpino, C.A. Rosa, T.M. Alves, N.P. de Sa, C.L. Zani, The antimicrobial activity of lapachol and its thiosemicarbazone and semicarbazone derivatives, Mem. Inst. Oswaldo Cruz 108 (3) (2013).
[21] E. Perez-Sacau, R.G. Diaz-Penate, A. Estevez-Braun, A.G. Ravelo, J.M. Garcia-Castellano, L. Pardo, M. Campillo, Synthesis and pharmacophore modeling of naphthoquinone derivatives with cytotoxic activity in human promyelocytic leukemia HL-60 cell line, J. Med. Chem. 50 (4) (2007) 696–706.
[22] S.N. Sunassee, C.G. Veale, N. Shunmoogam-Gounden, O. Osoniyi, D.T. Hendricks, M.R. Caira, J.A. de la Mare, A.L. Edkins, A.V. Pinto, E.N. da Silva Junior, M.T. Davies-Coleman, Cytotoxicity of lapachol, beta-lapachone and related synthetic 1,4-naphthoquinones against oesophageal cancer cells, Eur. J. Med. Chem. 62 (2013) 98–110.
[23] M.N. Rocha, P.M. Nogueira, C. Demicheli, L.G. de Oliveira, M.M. da Silva, F. Frezard, M.N. Melo, R.P. Soares, Cytotoxicity and in vitro antileishmanial activity of antimony (V), bismuth (V), and tin (IV) complexes of lapachol, Bioinorgan. Chem. Appl. 2013 (2013) 961783.
[24] M.O. Goulart, P. Falkowski, T. Ossowski, A. Liwo, Electrochemical study of oxygen interaction with lapachol and its radical anions, Bioelectrochemistry 59 (1–2) (2003) 85–87.
[25] Y. Kumagai, Y. Tsurutani, M. Shinyashiki, S. Homma-Takeda, Y. Nakai, T. Yoshikawa, N. Shimojo, Bioactivation of lapachol responsible for DNA scission by NADPH-cytochrome P450 reductase, Environ. Toxicol. Pharmacol. 3 (4) (1997) 245–250.
[26] V.N. Fritsch, V.V. Loi, T. Busche, A. Sommer, K. Tedin, D.J. Nürnberg, J. Kalinowski, J. Bernhardt, M. Fulde, H. Antelmann, The MarR-type repressor MhqR confers quinone and antimicrobial resistance in *Staphylococcus aureus*, Antioxidants Redox Signal. 31 (16) (2019) 1235–1252.
[27] P.J. O'Brien, Molecular mechanisms of quinone cytotoxicity, Chem. Biol. Interact. 80 (1) (1991) 1–41.
[28] T.J. Monks, R.P. Hanzlik, G.M. Cohen, D. Ross, D.G. Graham, Quinone chemistry and toxicity, Toxicol. Appl. Pharmacol. 112 (1) (1992) 2–16.
[29] M. Liebeke, D.C. Pöther, N. van Duy, D. Albrecht, D. Becher, F. Hochgräfe, M. Lalk, M. Hecker, H. Antelmann, Depletion of thiol-containing proteins in response to quinones in *Bacillus subtilis*, Mol. Microbiol. 69 (6) (2008) 1513–1529.
[30] H. Antelmann, J.D. Helmann, Thiol-based redox switches and gene regulation, Antioxidants Redox Signal. 14 (6) (2011) 1049–1063.
[31] V.V. Loi, M. Rossius, H. Antelmann, Redox regulation by reversible protein S-thiolation in bacteria, Front. Microbiol. 6 (2015) 187.
[32] S. Bittner, When quinones meet amino acids: chemical, physical and biological consequences, Amino Acids 30 (3) (2006) 205–224.
[33] Y. Kumagai, S. Koide, K. Taguchi, A. Endo, Y. Nakai, T. Yoshikawa, N. Shimojo, Oxidation of proximal protein sulfhydryls by phenanthraquinone, a component of diesel exhaust particles, Chem. Res. Toxicol. 15 (4) (2002) 483–489.
[34] M.T. Smith, Quinones as mutagens, carcinogens, and anticancer agents: introduction and overview, J. Toxicol. Environ. Health 16 (5) (1985) 665–672.
[35] T.W. Schultz, G.D. Sinks, M.T.D. Cronin, Quinone-induced toxicity to Tetrahymena: structure-activity relationships, Aquat. Toxicol. 39 (3–4) (1997) 267–278.

[36] A. Brunmark, E. Cadenas, Redox and addition chemistry of quinoid compounds and its biological implications, Free Radic. Biol. Med. 7 (4) (1989) 435–477.
[37] Q. Ji, L. Zhang, M.B. Jones, F. Sun, X. Deng, H. Liang, H. Cho, P. Brugarolas, Y.N. Gao, S.N. Peterson, Molecular mechanism of quinone signaling mediated through S-quinonization of a YodB family repressor QsrR, Proc. Natl. Acad. Sci. Unit. States Am. 110 (13) (2013) 5010–5015.
[38] C.J. Ji, J.H. Kim, Y.B. Won, Y.E. Lee, T.W. Choi, S.Y. Ju, H. Youn, J.D. Helmann, J.W. Lee, *Staphylococcus aureus* PerR is a hypersensitive hydrogen peroxide sensor using iron-mediated histidine oxidation, J. Biol. Chem. 290 (33) (2015) 20374–20386.
[39] A. Pinochet-Barros, J.D. Helmann, Redox sensing by Fe(2+) in bacterial Fur family metalloregulators, Antioxidants Redox Signal. 29 (18) (2018) 1858–1871.
[40] M.J. Horsburgh, M.O. Clements, H. Crossley, E. Ingham, S.J. Foster, PerR controls oxidative stress resistance and iron storage proteins and is required for virulence in *Staphylococcus aureus*, Infect. Immun. 69 (6) (2001) 3744–3754.
[41] V.V. Loi, T. Busche, K. Tedin, J. Bernhardt, J. Wollenhaupt, N.T.T. Huyen, C. Weise, J. Kalinowski, M.C. Wahl, M. Fulde, H. Antelmann, Redox-sensing under hypochlorite stress and infection conditions by the Rrf2-family repressor HypR in *Staphylococcus aureus*, Antioxidants Redox Signal. 29 (7) (2018) 615–636.
[42] P. Chandrangsu, V.V. Loi, H. Antelmann, J.D. Helmann, The role of bacillithiol in Gram-positive firmicutes, Antioxidants Redox Signal. 28 (6) (2018) 445–462.
[43] G.L. Newton, R.C. Fahey, M. Rawat, Detoxification of toxins by bacillithiol in *Staphylococcus aureus*, Microbiology 158 (Pt 4) (2012) 1117–1126.
[44] D.C. Pöther, P. Gierok, M. Harms, J. Mostertz, F. Hochgräfe, H. Antelmann, C.J. Hamilton, I. Borovok, M. Lalk, Y. Aharonowitz, M. Hecker, Distribution and infection-related functions of bacillithiol in *Staphylococcus aureus*, Int J Med Microbiol 303 (3) (2013) 114–123.
[45] A.C. Posada, S.L. Kolar, R.G. Dusi, P. Francois, A.A. Roberts, C.J. Hamilton, G.Y. Liu, A. Cheung, Importance of bacillithiol in the oxidative stress response of *Staphylococcus aureus*, Infect. Immun. 82 (1) (2014) 316–332.
[46] B.K. Chi, K. Gronau, U. Mäder, B. Hessling, D. Becher, H. Antelmann, S-bacillithiolation protects against hypochlorite stress in *Bacillus subtilis* as revealed by transcriptomics and redox proteomics, Mol. Cell. Proteomics 10 (11) (2011) M111 009506.
[47] B.K. Chi, A.A. Roberts, N.T.T. Huyen, K. Bäsell, D. Becher, D. Albrecht, C.J. Hamilton, H. Antelmann, S-bacillithiolation protects conserved and essential proteins against hypochlorite stress in firmicutes bacteria, Antioxidants Redox Signal. 18 (11) (2013) 1273–1295.
[48] M. Imber, N.T.T. Huyen, A.J. Pietrzyk-Brzezinska, V.V. Loi, M. Hillion, J. Bernhardt, L. Thärichen, K. Kolsek, M. Saleh, C.J. Hamilton, L. Adrian, F. Gräter, M.C. Wahl, H. Antelmann, Protein S-bacillithiolation functions in thiol protection and redox regulation of the glyceraldehyde-3-phosphate dehydrogenase Gap in *Staphylococcus aureus* under hypochlorite stress, Antioxidants Redox Signal. 28 (6) (2018) 410–430.
[49] M. Imber, V.V. Loi, S. Reznikov, V.N. Fritsch, A.J. Pietrzyk-Brzezinska, J. Prehn, C. Hamilton, M.C. Wahl, A.K. Bronowska, H. Antelmann, The aldehyde dehydrogenase AldA contributes to the hypochlorite defense and is redox-controlled by protein S-bacillithiolation in *Staphylococcus aureus*, Redox Biol 15 (2018) 557–568.
[50] M. Imber, A.J. Pietrzyk-Brzezinska, H. Antelmann, Redox regulation by reversible protein S-thiolation in Gram-positive bacteria, Redox Biol 20 (2018) 130–145.
[51] N. Linzner, V.V. Loi, V.N. Fritsch, Q.N. Tung, S. Stenzel, M. Wirtz, R. Hell, C.J. Hamilton, K. Tedin, M. Fulde, H. Antelmann, *Staphylococcus aureus* uses the bacilliredoxin (BrxAB)/bacillithiol disulfide reductase (YpdA) redox pathway to defend against oxidative stress under infections, Front. Microbiol. 10 (2019) 1355.
[52] I.V. Mikheyeva, J.M. Thomas, S.L. Kolar, A.R. Corvaglia, N. Gaiotaa, S. Leo, P. Francois, G.Y. Liu, M. Rawat, A.L. Cheung, YpdA, a putative bacillithiol disulfide reductase, contributes to cellular redox homeostasis and virulence in *Staphylococcus aureus*, Mol. Microbiol. 111 (4) (2019) 1039–1056.
[53] A. Gaballa, B.K. Chi, A.A. Roberts, D. Becher, C.J. Hamilton, H. Antelmann, J.D. Helmann, Redox regulation in *Bacillus subtilis*: the bacilliredoxins BrxA(YphP) and BrxB(YqiW) function in de-bacillithiolation of S-bacillithiolated OhrR and MetE, Antioxidants Redox Signal. 21 (3) (2014) 357–367.
[54] V.V. Loi, M. Harms, M. Müller, N.T.T. Huyen, C.J. Hamilton, F. Hochgräfe, J. Pane-Farre, H. Antelmann, Real-time imaging of the bacillithiol redox potential in the human pathogen *Staphylococcus aureus* using a genetically encoded bacilliredoxin-fused redox biosensor, Antioxidants Redox Signal. 26 (15) (2017) 835–848.
[55] V. Van Loi, H. Antelmann, Method for measurement of bacillithiol redox potential changes using the Brx-roGFP2 redox biosensor in *Staphylococcus aureus*, Methods (Orlando) 7 (2020) 100900.
[56] M. Arnaud, A. Chastanet, M. Debarbouille, New vector for efficient allelic replacement in naturally nontransformable, low-GC-content, gram-positive bacteria, Appl. Environ. Microbiol. 70 (11) (2004) 6887–6891.
[57] E.D. Rosenblum, S. Tyrone, Serology, density, and morphology of staphylococcal phages, J. Bacteriol. 88 (6) (1964) 1737–1742.
[58] R. Brückner, E. Wagner, F. Götz, Characterization of a sucrase gene from *Staphylococcus xylosus*, J. Bacteriol. 175 (3) (1993) 851–857.
[59] V.V. Loi, T. Busche, T. Preuss, J. Kalinowski, J. Bernhardt, H. Antelmann, The AGXX® antimicrobial coating causes a thiol-specific oxidative stress response and protein S-bacillithiolation in *Staphylococcus aureus*, Front. Microbiol. 9 (2018) 3037.
[60] M.I. Love, W. Huber, S. Anders, Moderated estimation of fold change and dispersion for RNA-seq data with DESeq2, Genome Biol. 15 (12) (2014) 550.
[61] R. Hilker, K.B. Stadermann, O. Schwengers, E. Anisiforov, S. Jaenicke, B. Weisshaar, T. Zimmermann, A. Goesmann, ReadXplorer 2-detailed read mapping analysis and visualization from one single source, Bioinformatics 32 (24) (2016) 3702–3708.
[62] J. Nourooz-Zadeh, J. Tajaddini-Sarmadi, S.P. Wolff, Measurement of plasma hydroperoxide concentrations by the ferrous oxidation-xylenol orange assay in conjunction with triphenylphosphine, Anal. Biochem. 220 (2) (1994) 403–409.
[63] B. Groitl, J.U. Dahl, J.W. Schroeder, U. Jakob, *Pseudomonas aeruginosa* defense systems against microbicidal oxidants, Mol. Microbiol. 106 (3) (2017) 335–350.
[64] T. Tomoyasu, F. Arsene, T. Ogura, B. Bukau, The C terminus of sigma(32) is not essential for degradation by FtsH, J. Bacteriol. 183 (20) (2001) 5911–5917.
[65] V.V. Loi, N.T.T. Huyen, T. Busche, Q.N. Tung, M.C.H. Gruhlke, J. Kalinowski, J. Bernhardt, A.J. Slusarenko, H. Antelmann, *Staphylococcus aureus* responds to allicin by global S-thioallylation - role of the Brx/BSH/YpdA pathway and the disulfide reductase MerA to overcome allicin stress, Free Radic. Biol. Med. 139 (2019) 55–69.
[66] D. Frees, U. Gerth, H. Ingmer, Clp chaperones and proteases are central in stress survival, virulence and antibiotic resistance of *Staphylococcus aureus*, Int J Med Microbiol 304 (2) (2014) 142–149.
[67] D. Frees, K. Savijoki, P. Varmanen, H. Ingmer, Clp ATPases and ClpP proteolytic complexes regulate vital biological processes in low GC, Gram-positive bacteria, Mol. Microbiol. 63 (5) (2007) 1285–1295.
[68] R.K. Poole, Flavohaemoglobin: the Pre-eminent Nitric Oxide-Detoxifying Machine of Microorganisms vol. 9, (2020), p. F1000Res.
[69] M. Moussaoui, L. Miseviciene, Z. Anusevicius, A. Maroziene, F. Lederer, L. Baciou, N. Cenas, Quinones and nitroaromatic compounds as subversive substrates of *Staphylococcus aureus* flavohemoglobin, Free Radic. Biol. Med. 123 (2018) 107–115.
[70] M. Falord, U. Mäder, A. Hiron, M. Debarbouille, T. Msadek, Investigation of the *Staphylococcus aureus* GraSR regulon reveals novel links to virulence, stress response and cell wall signal transduction pathways, PloS One 6 (7) (2011) e21323.
[71] C.G. Oliveira, F.F. Miranda, V.F. Ferreira, C.C. Freitas, R.F. Rabello, J.M. Carballido, L.C. Corrêa, Synthesis and antimicrobial evaluation of 3-hydrazino-naphthoquinones as analogs of lapachol, J. Braz. Chem. Soc. 12 (3) (2001) 339–345.
[72] K. Cosgrove, G. Coutts, I.M. Jonsson, A. Tarkowski, J.F. Kokai-Kun, J.J. Mond, S.J. Foster, Catalase (KatA) and alkyl hydroperoxide reductase (AhpC) have compensatory roles in peroxide stress resistance and are required for survival, persistence, and nasal colonization in *Staphylococcus aureus*, J. Bacteriol. 189 (3) (2007) 1025–1035.
[73] R. Koizumi, K. Taguchi, M. Hisamori, Y. Kumagai, Interaction of 9,10-phenanthraquinone with dithiol causes oxidative modification of Cu,Zn-superoxide dismutase (SOD) through redox cycling, J. Toxicol. Sci. 38 (3) (2013) 317–324.
[74] S. Otten, J.P. Rosazza, Microbial transformations of natural antitumor agents: oxidation of lapachol by *Penicillium notatum*, Appl. Environ. Microbiol. 35 (3) (1978) 554–557.
[75] S.L. Otten, J.P. Rosazza, Oxidative ring fission of the naphthoquinones lapachol and dichloroallyl lawsone by *Penicillium notatum*, J. Biol. Chem. 258 (3) (1983) 1610–1613.

Chapter 6

The MarR-type repressor MhqR confers quinone and antimicrobial resistance in *Staphylococcus aureus*

Verena Nadin Fritsch[1], Vu Van Loi[1], Tobias Busche[1,2], Anna Sommer[1], Karsten Tedin[3], Dennis J. Nürnberg[4], Jörn Kalinowski[2], Jörg Bernhardt[5], Marcus Fulde[3], and Haike Antelmann[1]*

[1]Institute for Biology-Microbiology, Freie Universität Berlin, Berlin, Germany

[2]Center for Biotechnology, University Bielefeld, Bielefeld, Germany

[3]Institute of Microbiology and Epizootics, Freie Universität Berlin, Berlin, Germany

[4]Institute of Experimental Physics, Freie Universität Berlin, Berlin, Germany

[5]Institute for Microbiology, University of Greifswald, Greifswald, Germany

*Corresponding author: haike.antelmann@fu-berlin.de

Published in:
Antioxidants & Redox Signaling 31(16): 1235-1252, 2019
DOI: https://doi.org/10.1089/ars.2019.7750

Personal contribution:

I contributed to the concept of this paper, performed most of the experiments, and created the corresponding figures. Parts of the experiments were performed within my master thesis. This included the construction of the Δ*qsrR* deletion mutant and *mhqR* complemented strain, Fig. 4B,D,E; Fig. S7A and to some extent Fig. 4C. My experimental work during my doctoral thesis included the Northern blot analyses under different stress conditions and electrophoretic mobility shift assays (EMSAs) to the mutated inverted repeat (Fig. 4A,C), murine macrophage infection assays (Fig. 8A,B), ATP measurements, determination of the oxygen consumption rates with methylene blue and with the help of Dr. Dennis Nürnberg by using a Clark-type electrode (Fig. 9). Preliminary growth and survival assays during my master thesis were finalised and extended (Fig. 6-8; S1; S6; S8). I also measured the Brx-roGFP2 biosensor oxidation after H2O2 addition (Fig. S7B). Alongside the protein sequence alignments (Fig. S3), I designed figure S4 and wrote the manuscript together with Prof. Dr. Haike Antelmann.

ANTIOXIDANTS & REDOX SIGNALING
Volume 31, Number 16, 2019
Mary Ann Liebert, Inc.
DOI: 10.1089/ars.2019.7750

ORIGINAL RESEARCH COMMUNICATION

The MarR-Type Repressor MhqR Confers Quinone and Antimicrobial Resistance in *Staphylococcus aureus*

Verena Nadin Fritsch,[1] Vu Van Loi,[1] Tobias Busche,[1,2] Anna Sommer,[1] Karsten Tedin,[3] Dennis J. Nürnberg,[4] Jörn Kalinowski,[2] Jörg Bernhardt,[5] Marcus Fulde,[3] and Haike Antelmann[1]

Abstract

Aims: Quinone compounds are electron carriers and have antimicrobial and toxic properties due to their mode of actions as electrophiles and oxidants. However, the regulatory mechanism of quinone resistance is less well understood in the pathogen *Staphylococcus aureus*.

Results: Methylhydroquinone (MHQ) caused a thiol-specific oxidative and electrophile stress response in the *S. aureus* transcriptome as revealed by the induction of the PerR, QsrR, CstR, CtsR, and HrcA regulons. The *SACOL2531-29* operon was most strongly upregulated by MHQ and was renamed as *mhqRED* operon based on its homology to the *Bacillus subtilis* locus. Here, we characterized the MarR-type regulator MhqR (SACOL2531) as quinone-sensing repressor of the *mhqRED* operon, which confers quinone and antimicrobial resistance in *S. aureus*. The *mhqRED* operon responds specifically to MHQ and less pronounced to pyocyanin and ciprofloxacin, but not to reactive oxygen species (ROS), hypochlorous acid, or aldehydes. The MhqR repressor binds specifically to a 9–9 bp inverted repeat (MhqR operator) upstream of the *mhqRED* operon and is inactivated by MHQ *in vitro*, which does not involve a thiol-based mechanism. In phenotypic assays, the *mhqR* deletion mutant was resistant to MHQ and quinone-like antimicrobial compounds, including pyocyanin, ciprofloxacin, norfloxacin, and rifampicin. In addition, the *mhqR* mutant was sensitive to sublethal ROS and 24 h post-macrophage infections but acquired an improved survival under lethal ROS stress and after long-term infections.

Innovation: Our results provide a link between quinone and antimicrobial resistance *via* the MhqR regulon of *S. aureus*.

Conclusion: The MhqR regulon was identified as a novel resistance mechanism towards quinone-like antimicrobials and contributes to virulence of *S. aureus* under long-term infections. *Antioxid. Redox Signal.* 31, 1235–1252.

Keywords: *Staphylococcus aureus*, MhqR, QsrR, quinones, antimicrobial resistance

Introduction

Staphylococcus aureus is a major human pathogen, which can cause several diseases including life-threatening systemic and chronic infections, such as sepsis, necrotizing pneumonia, or endocarditis (3, 8, 47).The increasing prevalence of multiple antibiotic resistant strains, such as methicillin-resistant *S. aureus*, leads to treatment failure and high mortality rates (15, 54). Understanding the defense and resistance mechanisms of *S. aureus* to antibiotics and the host immune response, including reactive oxygen species (ROS) and reactive electrophilic species, will lead to the discovery of novel resistance mechanisms and potential new drug targets to combat multiple antimicrobial resistance.

[1]Institute of Biology–Microbiology, Freie Universität Berlin, Berlin, Germany.
[2]Center for Biotechnology, Bielefeld University, Bielefeld, Germany.
[3]Institute of Microbiology and Epizootics, Freie Universität Berlin, Berlin, Germany.
[4]Institute of Experimental Physics, Freie Universität Berlin, Berlin, Germany.
[5]Institute for Microbiology, University of Greifswald, Greifswald, Germany.

Innovation

The adaptation strategies of *Staphylococcus aureus* toward reactive oxygen species and reactive electrophilic species are not fully understood, which are required for the successful infection and establishment of antibiotics resistance. In this work, we characterized the novel MhqR repressor as important quinone-sensing and regulatory mechanism in *S. aureus*, which controls quinone detoxification genes and conferred resistance to quinones and quinone-like antimicrobial compounds, including fluoroquinolones (ciprofloxacin, norfloxacin), rifampicin, and pyocyanin. The *mhqR* mutation further caused an increased survival of *S. aureus* during long-term macrophage infections, and thus, the enzymes of MhqR regulon could be possible drug targets.

Quinones are essential lipid electron carriers of the aerobic and anaerobic respiratory chain in bacteria (*e.g.*, ubiquinone and menaquinone) (31, 39, 71). However, many natural antimicrobial compounds contain quinone-like structures that are encountered as exogenous sources of quinone stress in pathogenic bacteria, such as the fungal 6-brom-2-vinyl-chroman-4-on (55) or the plant-derived 1,4-naphthoquinone lapachol (32). The toxic effect of quinones is caused by their electrophilic and oxidative modes of actions (35, 52, 57). Quinones have electron-deficient carbon centers and react as electrophiles with the nucleophilic thiol groups of cysteines *via* irreversible thiol-*S*-alkylations, leading to aggregation and depletion of thiol-containing proteins in the proteome (43). As oxidants, quinones can form highly reactive semiquinone radicals that subsequently promote ROS generation, such as superoxide anions, which in turn cause reversible thiol oxidations in proteins (7, 35, 52, 57).

In *Bacillus subtilis*, two MarR/DUF24 family regulators YodB and CatR as well as the MarR-type repressor MhqR respond to quinones and the azo compound diamide and control together paralogous quinone or azo compound reductases (AzoR1, AzoR2), nitroreductases (YodC, MhqN), and ring-cleavage dioxygenases (MhqA, MhqE, MhqO, CatE) for quinone detoxification (1, 2, 13, 29, 42, 69). The YodB- and MhqR-regulated quinone reductases have been shown to confer additive resistance to quinones and diamide in *B. subtilis* and function in quinone and diamide reduction to hydroquinones and dimethylurea, respectively. The thiol-dependent dioxygenases catalyze the ring cleavage of quinone-*S*-adducts formed by reaction with low-molecular-weight thiols, such as bacillithiol (BSH) (9). Apart from its role in detoxification of exogenous quinones, the catechol 2,3-dioxygenase CatE was recently shown to function in recycling of the endogenous catecholate siderophore bacillibactin under iron limitation in *B. subtilis* (65).

Furthermore, the *mhqR* mutant supported the growth of cell wall-deficient L-forms in *B. subtilis*, which are resistant to β-lactam antibiotics and promote persister formation (17, 34). The constitutive expression of quinone detoxification genes in the *mhqR* mutant was suggested to decrease respiratory chain activity and to limit ROS production as mechanism of L-form growth (34).

YodB and CatR are redox-sensing repressors that sense and respond directly to quinones by a redox-switch mechanism involving thiol oxidation at the conserved Cys6 and Cys7 residues, respectively (12, 13). The YodB repressor forms intermolecular disulfides between Cys6 and the C-terminal Cys101 or Cys108 in the opposing subunits of the YodB dimer under quinone and diamide stress *in vitro* and *in vivo* (12, 41). However, the mechanism of MhqR regulation under quinone stress is unknown thus far and may not involve a thiol-switch mechanism (69).

In *S. aureus*, the YodB homologue QsrR has been ascribed to be implicated in quinone detoxification, which controls related quinone reductases and a nitroreductase, an flavin mononucleotide-linked monooxygenase, and thiol-dependent dioxygenases (33). The crystal structure of quinone-modified QsrR has been resolved, and the redox-regulatory mechanism was shown to involve thiol-*S*-alkylation of the conserved Cys5 by quinones *in vitro* (33). Importantly, the QsrR regulon was essential for the pathogenicity of *S. aureus* leading to reduced phagocytosis and increased resistance against killing by bone marrow-derived macrophages (33).

In this work, we aimed to further investigate the quinone-stress-specific response in *S. aureus* to elucidate novel mechanisms of redox signaling and antimicrobial resistance. Using RNA-seq transcriptomics, we identified the *mhqRED* operon as most strongly induced by methylhydroquinone (MHQ) in *S. aureus*, which is controlled by SACOL2531 (MhqR), a close homolog to MhqR of *B. subtilis* (69). Our results demonstrate that the *mhqRED* operon confers resistance to quinones and quinone-like antimicrobials, including pyocyanin, ciprofloxacin, norfloxacin, and rifampicin. Due to the increasing prevalence of multiple antibiotic resistant *S. aureus* isolates, these results are important to understand the underlying mechanisms of antimicrobial resistance.

Results

MHQ elicits a thiol-specific oxidative, electrophile, and metal stress response in the RNA-seq transcriptome of S. aureus

To investigate the quinone-stress-specific response of *S. aureus* COL, we analyzed the changes in the RNA-seq transcriptome after exposure to sublethal MHQ stress (45 μM) (Supplementary Fig. S1) (30, 44). For significant fold-changes, the *M*-value cutoff (log2-fold-change MHQ *vs.* control) of ± 0.6 was chosen (adjusted *p*-value ≤ 0.05). In total, 730 transcripts were significantly >1.5-fold upregulated and 675 were >1.5-fold downregulated in the transcriptome of *S. aureus* under MHQ stress (Supplementary Tables S1 and S2). A subset of the most strongly upregulated regulons is displayed in the Voronoi transcriptome treemap (Fig. 1). About 70 genes displayed the highest fold-changes under MHQ stress ranging from 10 to 536 (*M*-values of 3.3–9), which could be mainly allocated to the TetR, QsrR, PerR, Fur, CtsR, CstR, CsoR, SigB, and GraRS regulons (Figs. 1 and 2 and Supplementary Fig. S2; Supplementary Tables S1 and S2). This indicates that MHQ leads generally to a strong thiol-specific oxidative (PerR), electrophile (QsrR), metal (Fur, CsoR), and cell wall stress response (GraRS, SigB) in *S. aureus*.

Among the top hits was the *SACOL2588-89* operon of hypothetical functions (510- to 536-fold) and the QsrR regulon, including *SACOL2533* (*catE2*), *SACOL0408-09-10* (*catE-SACOL0409-azoR1*), *SACOL2534* (*frp*), and *SACOL2020* (*yodC*) (25- to 121-fold induced). Interestingly, our transcriptome data revealed also a strong (35- to 67-fold) upregulation of the *SACOL2531-30-29* operon that encodes

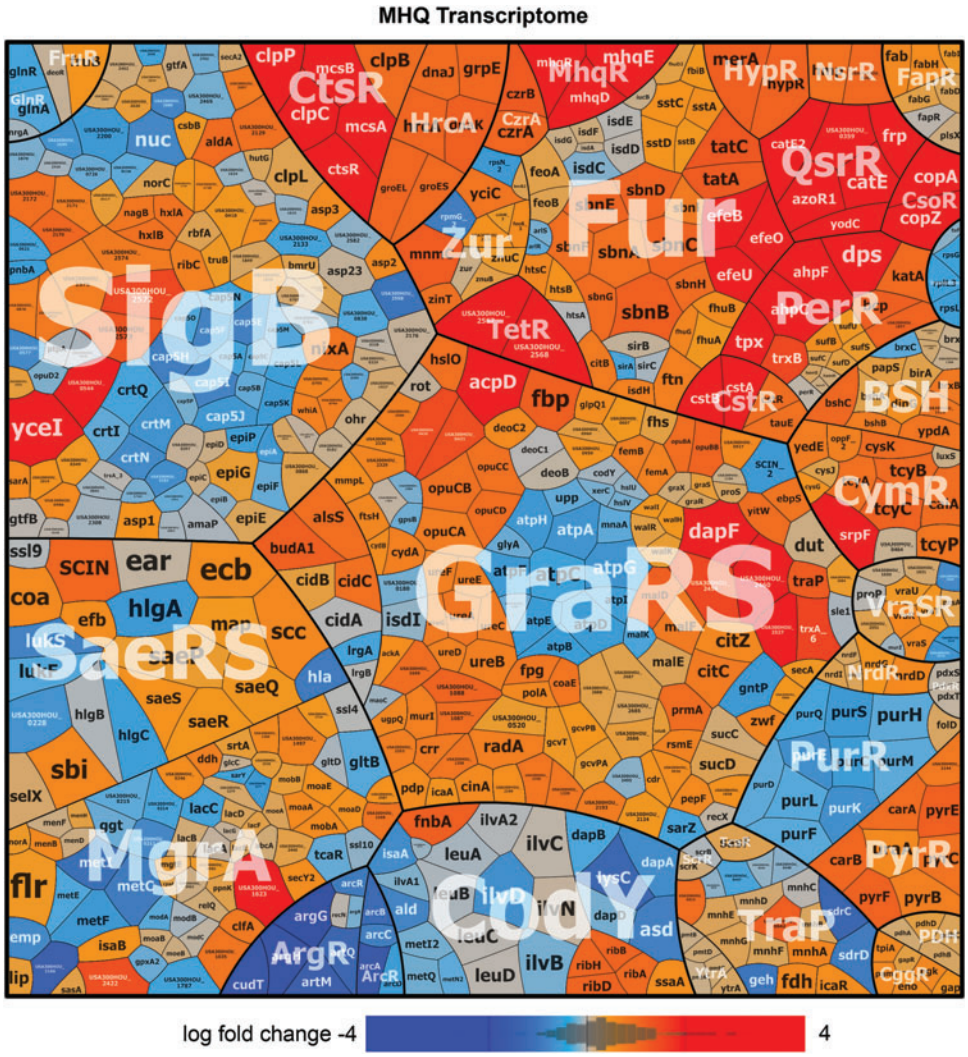

FIG. 1. The transcriptome treemap of *Staphylococcus aureus* COL under MHQ stress indicates a strong upregulation of the MhqR and QsrR regulons. The transcriptome treemap shows the differential gene expression of *S. aureus* after exposure to 45 μM MHQ as log2-fold-changes (M-values). The genes are classified into operons and regulons based on the RegPrecise database and previous publications (44, 49, 72). Differential gene expression is visualized using a *red–blue color code* where *red* indicates log2-fold induction and *blue* indicates repression of transcription under MHQ stress. The quinone-stress-specific regulons MhqR and QsrR are most strongly upregulated under MHQ stress in *S. aureus* COL. The induction of the PerR, CsoR, Fur, HrcA, CtsR, and GraRS regulons reveals an oxidative, electrophile, metal, and cell wall stress response and protein damage in *S. aureus*. The RNA-seq expression data of the selected highly transcribed genes after MHQ stress and their regulon classifications are listed in Supplementary Table S2. MHQ, methylhydroquinone. Color images are available online.

for the phospholipase/carboxylesterase SACOL2529 (MhqD), the dioxygenase SACOL2530 (MhqE), and the unknown MarR-type regulator SACOL2531. SACOL2531 showed striking homology (39.4% sequence identity) to the quinone-specific MhqR repressor of *B. subtilis* (69) and was renamed MhqR in *S. aureus* (Supplementary Fig. S3A). Thus, the transcriptome results identified QsrR and MhqR as most responsive to MHQ in *S. aureus*, which resembles the quinone stress response in *B. subtilis* (1, 18, 29, 42, 55, 68, 69).

We have previously analyzed the transcriptome signature of *S. aureus* USA300 in response to the strong oxidant sodium hypochlorite (NaOCl) and the antimicrobial surface coating AgXX®, which causes ROS formation, such as hydroxyl radicals (44, 72). Our RNA-seq data after MHQ treatment showed a similar expression profile by the strong induction of the PerR, QsrR, Fur, CsoR, HrcA, CtsR, and GraRS regulons, as observed under NaOCl and AGXX stress (44, 72). This signature is indicative for a thiol-specific oxidative, electrophile, metal, and cell wall stress response as well as protein damage.

Specifically, MHQ leads to induction of the CtsR-controlled Clp proteases, including *clpP* (17-fold) and the *ctsR-mcsA-mcsB-clpC* operon (16- to 21-fold) involved in protein quality control and proteolytic degradation of quinone-aggregated proteins (1). The PerR, Fur, and CsoR regulons function in ROS detoxification, iron or copper homeostasis, and these metallo-regulatory proteins have oxidation-sensitive metal binding sites (5, 23). The CstR regulon responds to reactive sulfur species and thiol persulfides (48). Transcription of the genes for cysteine and bacillithiol metabolism (*cysK*, *bshA* operon, *bshB*, *bshC*, *brxB*, and *ypdA*) was 1.6- to 5.6-fold elevated by MHQ in *S. aureus* supporting the thiol-reactive mode of action of quinones, which affects the cellular thiol-redox homeostasis (67). About 87 genes

of the GraRS regulon and parts of the SigB regulon were upregulated by MHQ, which function in the cell wall and general stress response as well as in the oxidative stress defense (21).

However, the SigB-dependent *crtNMQIO* operon for staphyloxanthin biosynthesis and the capsule biosynthesis *cap5ABCDEFGHIJKLMNOP* operon were strongly repressed by MHQ (Fig. 1 and Supplementary Tables S1 and S2). Among the downregulated regulons were further the arginine biosynthesis ArgR regulon, including the *argBJCD*, *argHG*, and *artQM* operons, as well as the arginine catabolic ArcR regulon, controlling the arginine deiminase *arcCDBA* operon. In addition, the purine biosynthesis PurR regulon was downregulated by MHQ, which might be attributed to the reduced growth rate under sublethal MHQ (Supplementary Fig. S1). Altogether, the transcriptome signature of MHQ resembles the thiol-specific oxidative, electrophile, and metal stress response and identified the *mhqRED* operon as novel quinone-regulatory system that was selected for further study.

The MhqR repressor senses quinones and controls the specific expression of the mhqRED *operon in* S. aureus

We conducted RNA-Seq transcriptomics of a *mhqR* deletion mutant to identify the genes of the MhqR regulon. The *mhqE and mhqD* genes were most strongly upregulated (206.5- to 891.4-fold) under control conditions in the *mhqR* mutant transcriptome, indicating that MhqR represses transcription of the *mhqRED* operon in the wild type (Figs. 2 and 3 and Supplementary Fig. S2; Supplementary Table S2). MhqE and MhqD showed 35.4% and 38.8% sequence identity to the homologous dioxygenase MhqE and phospholipase/carboxylesterase MhqD of *B. subtilis*, respectively (Supplementary Fig. S3B). In contrast to *B. subtilis*, MhqR only controls the *mhqRED* operon in *S. aureus* (Fig. 2 and Supplementary Fig. S2; Supplementary Table S2) (69).

The transcriptome results of the *mhqR* mutant further revealed that most thiol-specific oxidative and electrophile stress regulons (*e.g.*, HypR, QsrR, and PerR) are expressed at a lower basal level under control conditions in the *mhqR* mutant compared with the wild type. For example, peroxide scavenging peroxiredoxins and catalases (*ahpCF* and *katA*) showed twofold lower basal level expression in the *mhqR* mutant compared with the wild type (Fig. 2 and Supplementary Fig. S2; Supplementary Table S2). This lower basal expression of antioxidant and quinone detoxification regulons might be due to the quinone-resistant phenotype of the *mhqR* mutant enabling faster quinone detoxification, which leads to lower basal levels of ROS. Consequently, the

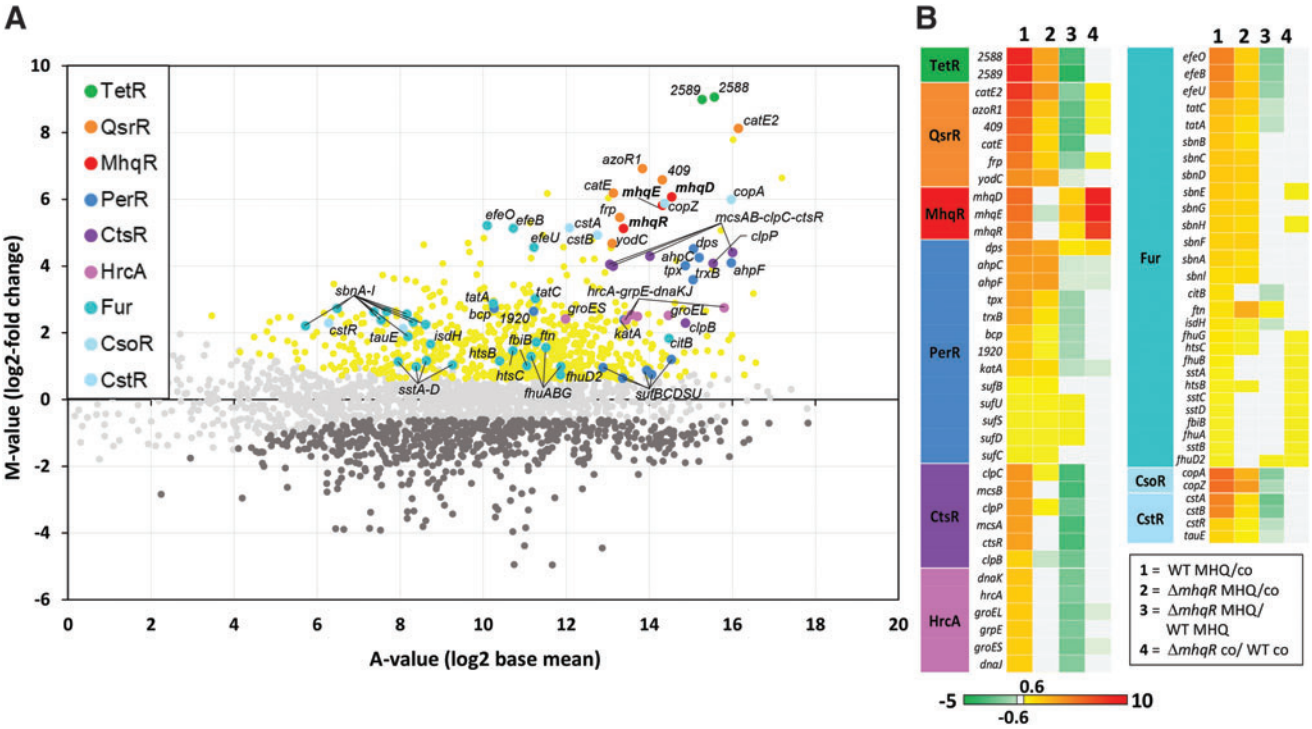

FIG. 2. RNA-seq transcriptomics of *S. aureus* COL wild type and the *mhqR* mutant under MHQ stress. For RNA-seq transcriptomics, *S. aureus* COL and the *mhqR* mutant were grown in RPMI1640 medium and treated with 45 μM MHQ stress for 30 min. **(A)** The gene expression profile of the wild type under MHQ stress is shown as ratio/intensity scatterplot (M/A-plot), which is based on the differential gene expression analysis using DeSeq2 (46). *Colored symbols* indicate significantly induced (*red*, *orange*, *yellow*, *blue*, *cyan*, *violet*, *green*) or repressed (*dark gray*) transcripts (M-value ≥0.6 or ≤–0.6; $p \leq 0.05$). *Light gray symbols* denote transcripts with no fold-changes after MHQ stress ($p > 0.05$). The TetR, QsrR, MhqR, PerR, CtsR, HrcA, Fur, CsoR, and CstR regulons are most strongly upregulated under MHQ stress. **(B)** The *color-coded heat map* displays log2-fold-changes of gene expression between the wild type and the *mhqR* mutant under control and MHQ. *Red* and *green* indicate significantly induced and repressed transcripts (M-value ≥0.6 or ≤ –0.6; $p \leq 0.05$) in three biological replicates, respectively. The RNA-seq expression data of all genes under MHQ stress and their regulon classifications are listed in Supplementary Tables S1 and S2. Color images are available online.

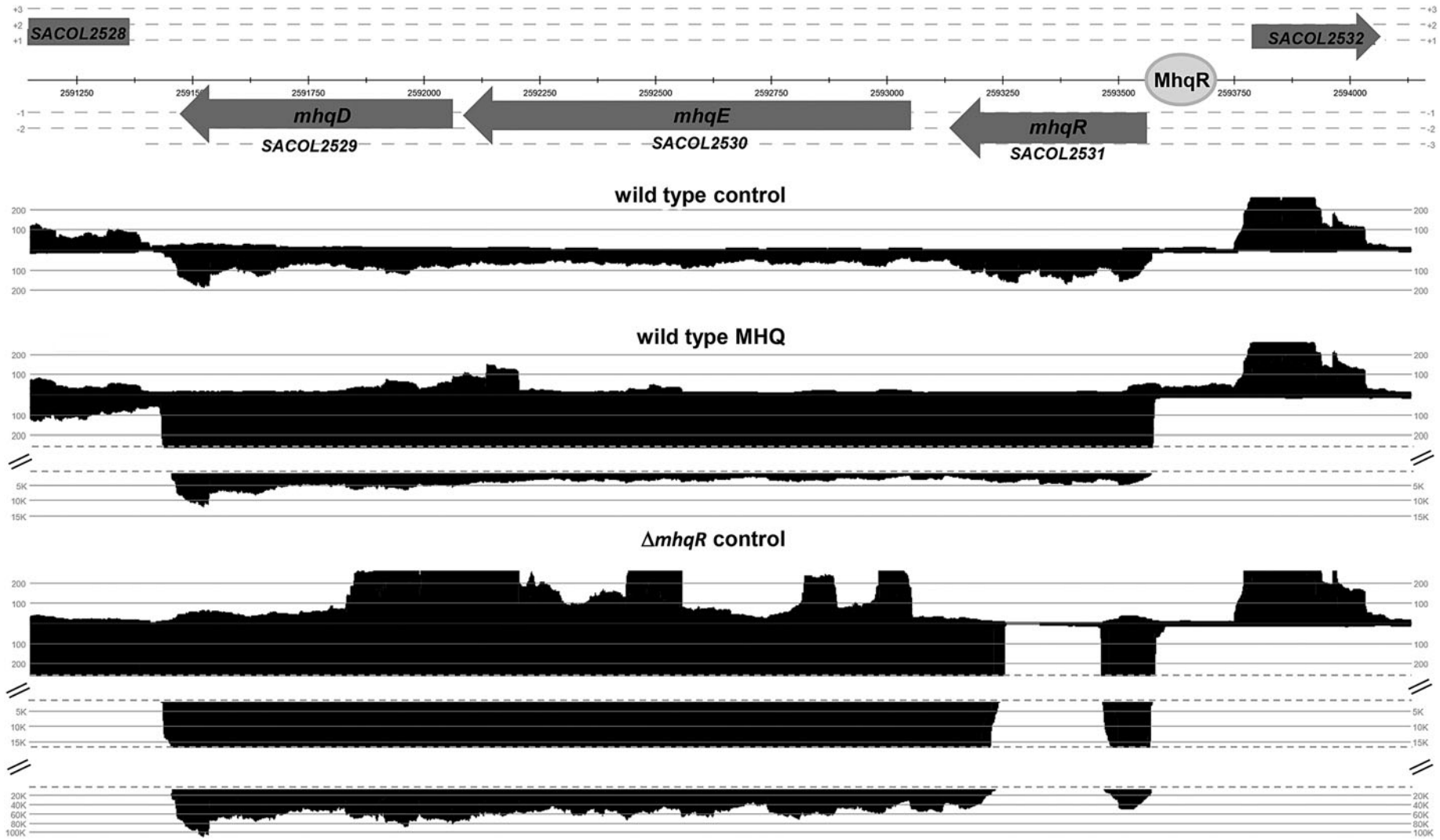

FIG. 3. The *mhqRED* operon (SACOL2531-2529) is strongly upregulated in the RNA-seq transcriptome of *S. aureus* COL under MHQ stress and fully derepressed in the *mhqR* mutant. The mapped cDNA reads for the transcription profile of the *mhqRED* locus under control and MHQ stress are shown as displayed in Read Explorer (28). Transcription of the *mhqRED* operon is 35- to 67-fold induced under MHQ stress in *S. aureus* COL and most strongly derepressed in the *mhqR* mutant under control conditions (206- to 891-fold). Thus, *mhqR* encodes for a MarR-type transcriptional repressor of the *mhqE* and *mhqD* genes that encode for a dioxygenase and phospholipase/carboxylesterase, respectively.

quinone and oxidative stress responsive HypR, QsrR, and PerR regulons and genes required for low molecular weight thiol biosynthesis (Cys, BSH) were only weakly upregulated in the *mhqR* mutant under MHQ treatment due to its higher tolerance for quinones. Similarly, the *mhqR* mutant displayed decreased fold-changes under MHQ for the majority of members of the cell wall, sulfide, and metal stress-sensing SigB, GraRS, CsoR, and CstR regulons (Fig. 2 and Supplementary Fig. S2; Supplementary Table S2). Moreover, the expression of the CtsR- and HrcA-controlled protein quality control machinery was >5-fold decreased under MHQ stress in the *mhqR* mutant. In conclusion, constitutive derepression of the MhqR regulon in the *mhqR* mutant leads to higher quinone detoxification capability, which limits ROS generation and the resulting protein oxidation and damage.

The mhqRED *operon responds specifically to quinones and the antimicrobials ciprofloxacin, pyocyanin, and lapachol in* S. aureus

Next, we conducted Northern blot analysis to study *mhqRED* transcription in *S. aureus* COL under different stress conditions and antibiotic treatment, including 45 μM MHQ, 1 mM NaOCl, 2 mM diamide, 0.75 mM formaldehyde, 0.5 mM methylglyoxal, 300 μM lapachol, 76 μM pyocyanin, and 90.5 μM ciprofloxacin (Fig. 4A). The Northern blot results

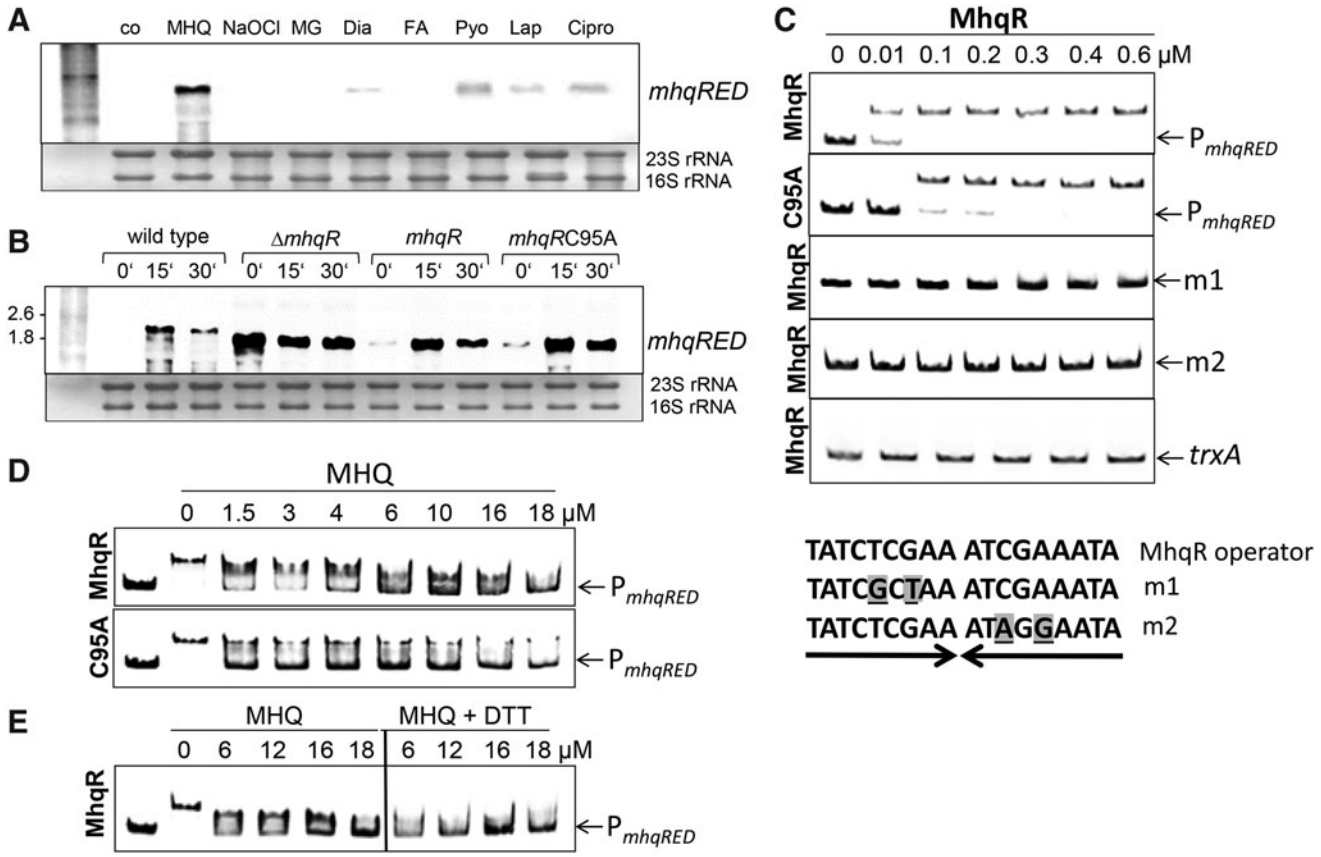

FIG. 4. Transcriptional induction of the MhqR regulon under quinones, aldehydes, and antimicrobials and the quinone response of MhqR in DNA binding assays *in vitro*. (A) Transcription of the *mhqRED* operon was analyzed using the Northern blots in *S. aureus* COL wild type 30 min after exposure to 45 μM MHQ, 1 mM NaOCl, 0.5 mM methylglyoxal (MG), 2 mM diamide (Dia), 0.75 mM formaldehyde (FA), 300 μM lapachol (Lap), 90.5 μM ciprofloxacin (Cipro), and 76 μM pyocyanin (Pyo). The compounds were added at an OD_{500} of 0.5. The *mhqRED* operon responds most strongly to MHQ and less strongly to lapachol, pyocyanin, and ciprofloxacin. **(B)** The Northern blot analysis was performed with RNA of the wild type, the *mhqR* mutant, and the *mhqR* and *mhqRC95A* complemented strains before (0 min) and 15 and 30 min after MHQ stress. Cys95 is not required for DNA binding and quinone sensing of MhqR *in vivo*. The methylene blue stain is the RNA loading control indicating the 16S and 23S rRNAs. **(C)** MhqR binds specifically to the *mhqRED* promoter *in vitro*. EMSAs were used to analyze the DNA binding activity of increasing amounts (0.01–0.6 μM) of MhqR and MhqRC95A proteins to the *mhqRED* promoter (P_{mhqRED}) *in vitro*. To test the specificity of binding, two base substitutions were introduced in each half of the inverted repeat, denoted in *gray* and *underlined* (m1 and m2). As nonspecific control DNA probe we used the *trxA* gene. The *arrows* denote the free DNA probe and the *shifted band* indicates the DNA-MhqR promoter complex. **(D)** EMSAs of MhqR and MhqRC95A proteins (0.6 μM) to the *mhqRED* promoter were performed to study the inactivation of MhqR by increasing amounts of MHQ (1.5–18 μM) leading to the loss of DNA binding. The *arrows* denote the free *mhqRED* promoter probe and the *shifted band* indicates the DNA-MhqR promoter complex. **(E)** MhqR inactivation by quinones could not be reversed with 1 mM DTT, which was added to the MhqR-DNA binding reaction 30 min after MHQ addition. Cys95 is not important for MHQ sensing or DNA binding of MhqR *in vitro*. DTT, dithiothreitol; EMSA, electrophoretic mobility shift assay; NaOCl, sodium hypochlorite.

revealed that the *mhqRED* operon is most strongly induced by MHQ stress but does not respond to NaOCl and aldehydes. Interestingly, increased transcription of *mhqRED* operon was also found by the quinone-like antimicrobials, such as ciprofloxacin, pyocyanin, and the 1,4-naphthoquinone lapachol (Fig. 4A; Supplementary Fig. S4). Thus, the MhqR regulon responds specifically to quinones and diverse quinone-like antimicrobials in *S. aureus*, suggesting a function in antimicrobial resistance.

The DNA binding activity of MhqR is inhibited by quinones in vivo *and* in vitro*, which does not involve a thiol-based mechanism*

S. aureus MhqR harbors a nonconserved Cys at position 95. To examine the role of Cys95 for DNA binding and quinone sensing, we complemented the *mhqR* mutant with plasmid-encoded *mhqR* and the *mhqRC95A* mutant allele. The Northern blot analyses confirmed the constitutive expression of the 1.7 kb truncated *mhqRED*-specific mRNA in the *mhqR* mutant. Complementation of the *mhqR* mutant with *mhqR* restored repression of transcription of the *mhqRED* operon under control conditions and the strong quinone response to wild-type level (Fig. 4B). However, the *mhqRC95A* mutant also showed the same low basal level transcription and strong responsiveness to MHQ of the *mhqRED* operon compared with the wild type and *mhqR* complemented strain. Thus, the Northern blot data revealed that Cys95 is neither required for DNA binding nor for quinone sensing *in vivo*.

Electrophoretic mobility shift assays (EMSAs) were used to investigate the DNA binding activity of purified MhqR protein to the *mhqRED* promoter *in vitro*. The *mhqRED*-specific promoter probe covered the region from +32 to −192 relative to the transcription start site (TSS). The gel shift results showed that purified MhqR binds to the *mhqRED* promoter probe, which is indicated by the band shift in the DNA binding reactions with MhqR (Fig. 4C).

Inspection of the *mhqRED* promoter region identified a 9–9 bp imperfect inverted repeat with the sequence TATCTCGAA-aTCGAaATA in position −6 to +12 relative to the TSS +1 (Fig. 5). The inverted repeat overlapping with the TSS was termed as MhqR operator based on its conservation with the MhqR operator upstream of *azoR2*, *mhqNOP*, *mhqED*, and *mhqA* in *B. subtilis* (69). To analyze the specific binding of MhqR to the MhqR operator, we exchanged two nucleotides in each half of the inverted repeat (m1: T to G and G to T; m2: C to A and A to G) and analyzed the DNA binding activity of MhqR to these mutated promoter probes (Fig. 4C). MhqR was unable to bind to the mutated inverted repeats m1 and m2 *in vitro*. In addition, no band shift was observed in the reaction of MhqR with the nonspecific *trxA* DNA probe, further supporting the specific binding of MhqR to the identified operator sequence (Fig. 4C).

Next, we investigated DNA binding and quinone-sensing of MhqR and MhqRC95A proteins. The MhqRC95A protein was able to bind with slightly decreased affinity to the *mhqRED* promoter probe compared with MhqR (Fig. 4C). Based on the EMSA results, the dissociation constants (K_d) were calculated as 7.38 and 14.25 n*M* for MhqR and MhqRC95A mutant proteins, respectively. Treatment with increasing concentrations of MHQ resulted in complete dissociation of the MhqR and MhqRC95A proteins from the *mhqRED* promoter probe with 16–18 μM MHQ, respectively (Fig. 4D). The addition of dithiothreitol (DTT) to the reaction of quinone-treated MhqR did not restore the DNA binding ability of MhqR, supporting that MhqR inactivation by quinones is not caused by a reversible thiol-switch (Fig. 4E). Thus, the nonconserved Cys95 of MhqR is not required for DNA binding and redox sensing of quinones *in vitro*, confirming our *in vivo* Northern blot results. This indicates that inactivation of the MhqR repressor by quinones does not involve a thiol-based mechanism. We speculate that MHQ binds to a specific ligand binding pocket in MhqR as revealed for other ligand binding MarR-type regulators (24), leading to its inactivation and derepression of the *mhqRED* operon.

Since no crystal structure of MhqR is available, the structure of *S. aureus* MhqR was modeled based on the template of the crystal structure of the MarR-family regulator ST1710 from *Sulfolobus tokodaii* (3GFI) using SWISS MODEL (6, 38) (Supplementary Fig. S5). MhqR of *S. aureus* shares 18.2% sequence identity with ST1710. The crystal structure of the ST1710 dimer was resolved in complex with its promoter DNA and with its ligand sodium salicylate, which is a common inhibitor of MarR proteins (38) (Supplementary Fig. S5A).

Similar to other MarR-type transcription factors, each subunit of the MhqR dimer is composed of six α-helices and two β-sheets, arranged as $\alpha1$–$\alpha2$–$\alpha3$–$\alpha4$–$\beta1$–$\beta2$–$\alpha5$–$\alpha6$ (Supplementary Fig. S5B). The $\alpha1$, $\alpha5$, and $\alpha6$ helices form the dimer interface of the two MhqR subunits, and the DNA binding domain is composed of the $\alpha2$, $\alpha3$, $\alpha4$ helices and the $\beta1$, $\beta2$ wing, known as winged helix-turn-helix (wHTH) DNA binding motif (16, 24). In the ST1710 structure complexed with salicylate, the ligand was coordinated by Y37 and Y111 of one subunit and A16, K17, and R20 of the opposing subunit of the dimer. This ligand binding pocket is located at the interface between the dimerization domains and the wHTH motif as described for other MarR-type regulators (24, 38). However, none of the salicylate coordinating tyrosine, lysine, or arginine residues of ST1710 is conserved in MhqR (Supplementary Fig. S5B). Thus, the mechanism of quinone binding in MhqR and the resulting conformational changes remain to be elucidated.

The MhqR regulon confers resistance to MHQ and quinone-like antimicrobials in S. aureus

Next, we were interested whether the MhqR regulon is involved in quinone and antimicrobial resistance mechanisms. The growth and survival phenotypes of the *mhqR* mutant were analyzed under MHQ stress and after treatment with different antimicrobial compounds, including pyocyanin, ciprofloxacin, norfloxacin, rifampicin, and lapachol (Figs. 6 and 7). The *mhqR* mutant showed high resistance to 50 μM MHQ and was not inhibited in growth compared with the wild type and *mhqR* complemented strain (Fig. 6A and Supplementary Fig. S6A). In addition, the *mhqR* mutant displayed two- to threefold increased survival in killing assays with lethal doses of 100–250 μM MHQ (Fig. 6C).

Treatment of the *mhqR* mutant with the antimicrobials pyocyanin, ciprofloxacin, norfloxacin, and rifampicin resulted in slightly improved growth at sublethal doses and significantly enhanced survival in killing assays with lethal concentrations of the antimicrobial compounds (Figs. 6D–I

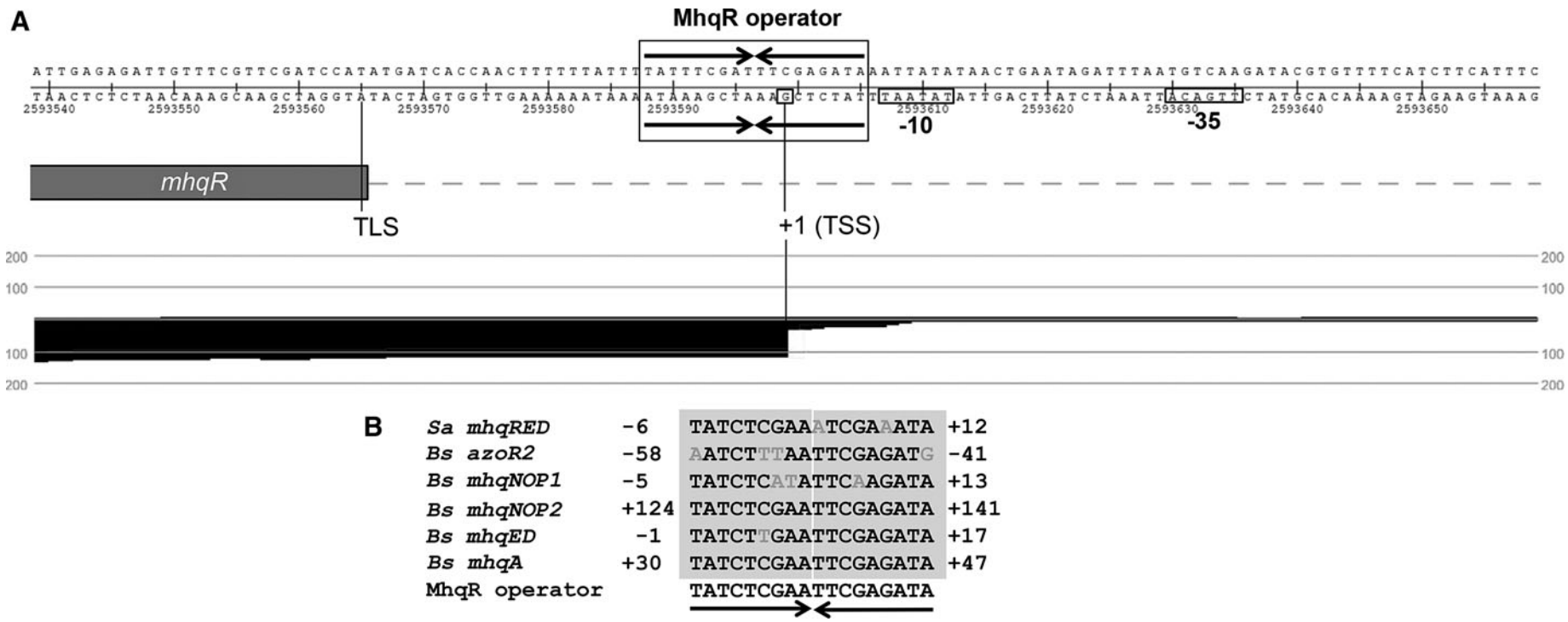

FIG. 5. TSS annotation of the *mhqRED* mRNA with the 9–9 bp inverted repeat as operator site for the MhqR repressor in *S. aureus*. (**A**) The upstream promoter region of the *mhqRED* operon of *S. aureus* contains a 9–9 bp palindrome as MhqR operator (denoted with *boxes*) in position −6 to +12 relative to the TSS that is highly conserved upstream of *azoR2*, *mhqNOP*, *mhqED*, and *mhqA* of the MhqR regulon in *Bacillus subtilis* (69). The mapped reads enriched for primary 5′-transcripts of *S. aureus* USA300 transcriptome under control conditions are displayed for the 5′-end of *mhqRED* operon using Read Explorer as described in the Experimental Procedures section. The −10 and −35 promoter sequences, the TSS, and the TLS are indicated, and the MhqR operator is marked with *arrows*. **(B)** All 9–9 bp MhqR operator sites in front of genes of the MhqR regulons of *S. aureus* and *B. subtilis* (69) were aligned (denoted by *gray letters*), and the MhqR consensus sequence is indicated. TLS, translation start site; TSS, transcription start site.

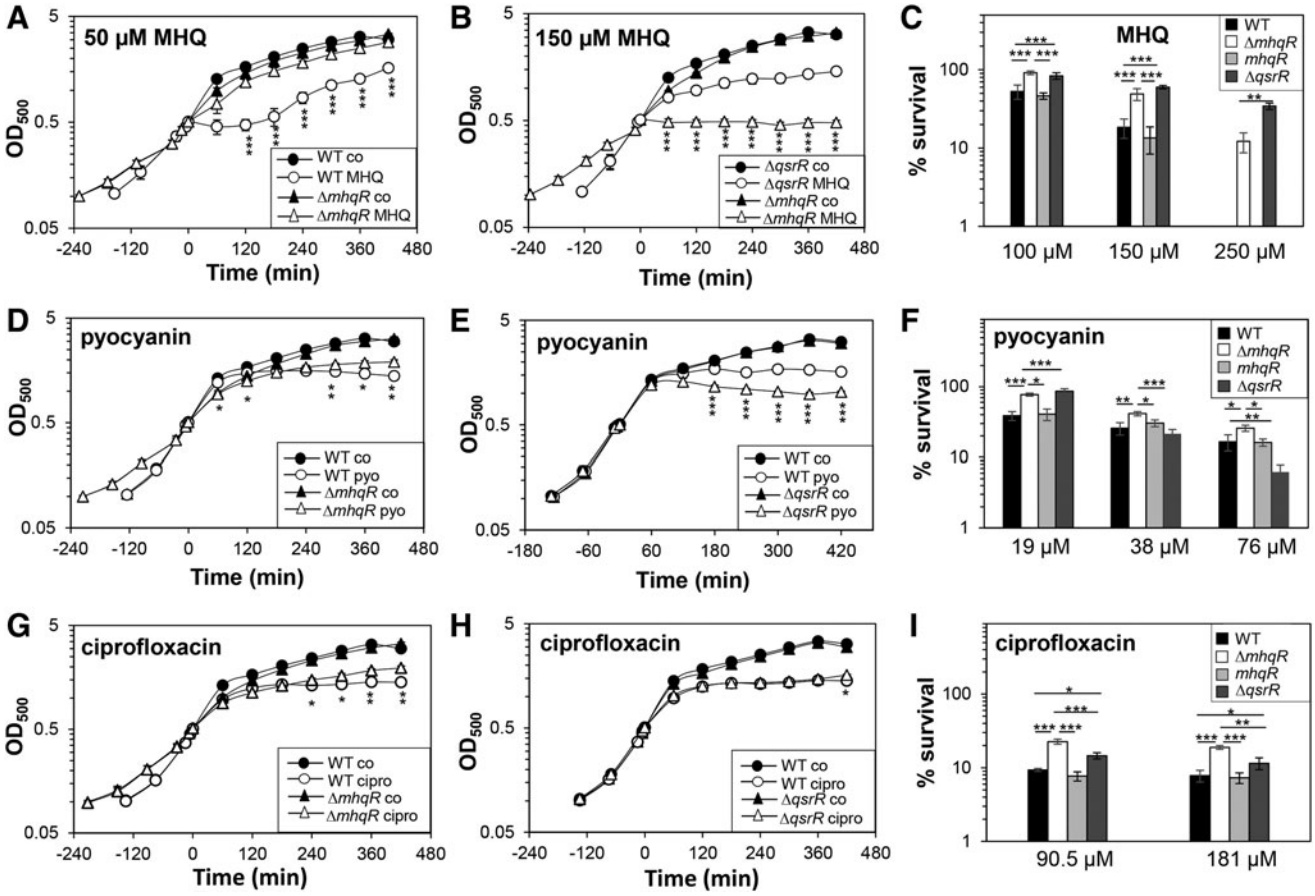

FIG. 6. The MhqR and QsrR regulons confer resistance to MHQ and the antimicrobials pyocyanin and ciprofloxacin. (A, B, D, E, G, and H) For the growth curves, *S. aureus* COL wild type, *mhqR* and *qsrR* mutants, as well as the *mhqR* complemented strain (*mhqR*) were grown in RPMI until an OD_{500} of 0.5 and treated with 50 and 150 μM MHQ, 76 μM pyocyanin, and 90.5 μM ciprofloxacin. **(C, F, and I)** Survival assays were performed by treatment with sublethal and lethal doses and plating 100 μL of serial dilutions onto LB agar plates after 4 h of stress exposure. The survival rates of CFUs for the treated samples were calculated relative to the control, which was set to 100%. The *mhqR* and *qsrR* mutants are significantly more resistant to MHQ, pyocyanin, and ciprofloxacin, which could be restored to wild-type levels in the *mhqR* complemented strain. The results are from four biological replicates. Error bars represent the standard deviation. $*p<0.05$; $**p<0.01$; $***p<0.001$. CFU, colony-forming unit; LB, Luria–Bertani.

and 7A–D). These antibiotic resistant phenotypes of the *mhqR* mutant could be restored back to wild-type level in the *mhqR* complemented strain (Supplementary Fig. S6B–E). However, the *mhqR* mutant was significantly impaired in growth and survival after treatment with the 1,4-naphthoquinone lapachol (Fig. 7E, F). These results indicate that the MhqR regulon protects *S. aureus* against benzoquinones, and many other antimicrobials that contain quinone-like structures, but not against naphthoquinones.

The MhqR and QsrR regulons contribute independently to quinone and antimicrobial resistance

Apart from MhqR, the MarR/DUF24-type regulator QsrR was shown to mediate resistance to quinones and pyocyanin in *S. aureus* (33, 56). Thus, we compared the growth and survival phenotypes of the *mhqR* and *qsrR* mutants in response to MHQ, ciprofloxacin, norfloxacin, rifampicin, and pyocyanin (Figs. 6 and 7). The MhqR and QsrR regulons conferred significant resistance to MHQ, rifampicin, and the fluoroquinolone ciprofloxacin, but not to the same extent. The *qsrR* mutant was able to grow even with lethal doses of 150 μM MHQ, which resulted in growth inhibition of the *mhqR* mutant (Fig. 6B). In survival assays, both mutants exhibited the same level of approximately two- to threefold increased resistance toward MHQ relative to the parent (Fig. 6C). Thus, the QsrR regulon conferred higher resistance to quinones than the *mhqR* mutant.

In contrast, the *mhqR* mutant showed higher ciprofloxacin resistance in growth assays and improved survival under ciprofloxacin, norfloxacin, and rifampicin treatment compared with the *qsrR* mutant (Figs. 6G–I and 7A–D).The MhqR and QsrR regulons contributed to a significant protection under low doses of 19 μM pyocyanin (Fig. 6D–F). However, only the MhqR regulon protected against high pyocyanin concentrations (38–76 μM) in killing assays. In contrast, the *qsrR* mutant was significantly more susceptible than the wild type at higher pyocyanin doses (Fig. 6E, F). These results point to independent roles of MhqR and QsrR as players in the quinone stress response. While the QsrR regulon

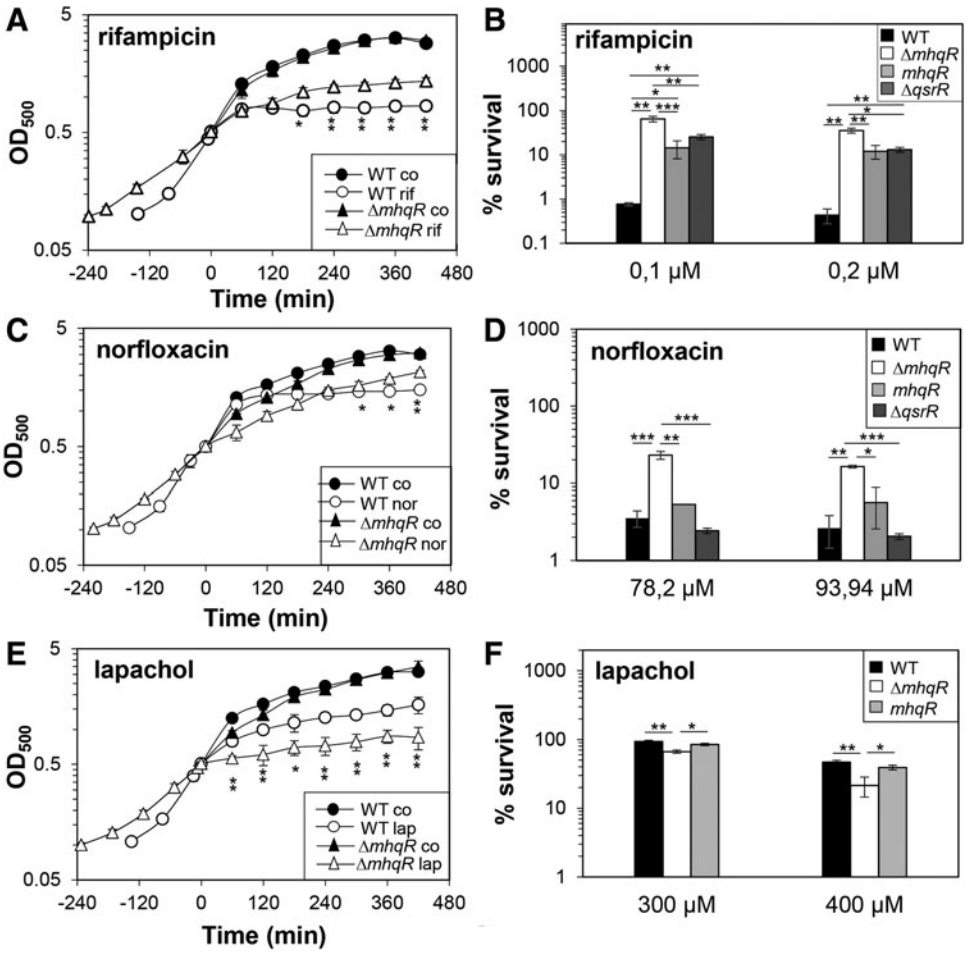

FIG. 7. The *mhqR* mutant is resistant to rifampicin and norfloxacin but impaired in survival after lapachol stress. (A, C, E) For the growth curves, *S. aureus* COL wild type, the *mhqR* and *qsrR* mutants, and the *mhqR* complemented strain (*mhqR*) were grown in RPMI until an OD_{500} of 0.5 and treated with 0.05 μM rifampicin, 62.6 μM norfloxacin, and 300 μM lapachol. **(B, D, F)** Survival assays were performed by treatment with sublethal and lethal doses and plating 100 μL of serial dilutions onto LB agar plates after 4 h of stress exposure. The survival rates of CFUs for the treated samples were calculated relative to the control, which was set to 100%. The *mhqR* mutant is significantly more resistant to rifampicin and norfloxacin, which could be restored in the *mhqR* complemented strain back to wild-type level. However, the *mhqR* mutant is significantly more susceptible to the naphthoquinone lapachol than the wild type. The results are from four biological replicates. Error bars represent the standard deviation. $*p<0.05$; $**p<0.01$; $***p<0.001$.

mediates higher resistance to quinones, the MhqR regulon functions in resistance mechanisms against quinone-derived antimicrobials.

The mhqR *mutant shows differential susceptibilities to killing by murine macrophage* in vivo *and under oxidative stress* in vitro

To analyze the role of the MhqR regulon under infection conditions, we determined the survival of the *mhqR* mutant in phagocytosis assays using the murine macrophage cell line J-774A.1, as previously described (44) (Fig. 8A, B). The colony-forming units (CFUs) of intracellular *S. aureus* were determined 2, 4, 24, and 48 h postinfection. At 24 h postinfection, the number of viable bacteria decreased to ~20% for the wild type and 10% for the *mhqR* mutant (Fig. 8A). Thus, the *mhqR* mutant showed a 50% reduced survival rate compared with the wild type. This sensitive survival phenotype of the *mhqR* mutant could be restored to >90% in the *mhqR* complemented strain (Fig. 8B). Interestingly, 48 h postinfection, the number of surviving bacteria increased to ~20% for the *mhqR* mutant and decreased to 6% for the wild type and *mhqR* complemented strain (Fig. 8A, B). Thus, the intramacrophage survival of the *mhqR* mutant was 2.5-fold higher compared with the wild type after 48 h of infections (Fig. 8B). This indicates that the *mhqR* mutation sensitizes *S. aureus* during early stages of macrophage infections, whereas improved survival of the *mhqR* mutant is acquired during long-term infection inside macrophages.

Transcriptome analysis revealed that the peroxide-specific PerR regulon was downregulated in the *mhqR* mutant under control and MHQ stress (Fig. 2 and Supplementary Fig. S2; Supplementary Table S2). Thus, we investigated the ROS susceptibility of the *mhqR* mutant *in vitro*. Growth phenotype analyses revealed an increased susceptibility of the *mhqR* deletion mutant under sublethal 1.5 m*M* NaOCl and 10 m*M* hydrogen peroxide (H_2O_2) stress (Fig. 8C, D). However, the *mhqR* mutant showed an improved survival upon lethal NaOCl

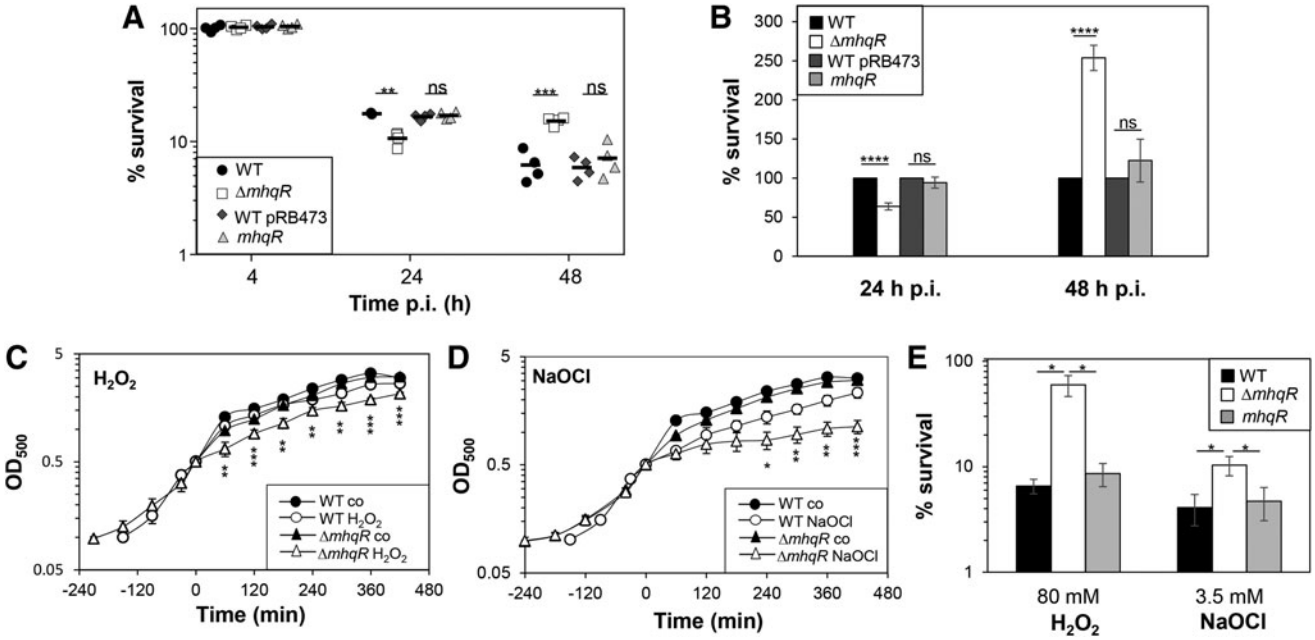

FIG. 8. The *mhqR* mutant is impaired in survival inside J-774.1 murine macrophages after 24 h and growth sensitive under sublethal ROS and NaOCl but resistant to long-term infections and toxic ROS and NaOCl. (A, B) The survival of *S. aureus* strains was analyzed 2, 4, 24, and 48 h postinfection (p.i.) of the murine macrophage cell line J-774A.1 and the CFUs were determined. **(A)** The percentages in survival of the wild type (WT), WT pRB473, *mhqR* deletion mutant, and the *mhqR* complemented strain (*mhqR*) were calculated, and the survival at the 2 h time point was set to 100%. **(B)** The average percentage in survival was calculated for each mutant and complemented strains in relation to the WT or WT pRB473, which was set to 100%. Results of four biological replicates are presented as *scatter dots* in **(A)** and mean values **(B)**. **(C, D)** For growth curves, *S. aureus* COL wild type, the *mhqR* deletion mutant, and the *mhqR* complemented strain were grown in RPMI until an OD_{500} of 0.5 and treated with sublethal 10 m*M* H_2O_2 and 1.5 m*M* NaOCl. **(E)** Survival assays were performed by treatment with lethal 80 m*M* H_2O_2 and 3.5 m*M* NaOCl and plating serial dilutions onto LB agar plates after 4 h of stress exposure. The survival rates of CFUs for the treated samples were calculated relative to the control, which was set to 100%. The results are from three biological replicates. Error bars represent the standard deviation. ns, $p > 0.05$; $*p < 0.05$; $**p < 0.01$; $***p < 0.001$; $****p \leq 0.0001$. H_2O_2, hydrogen peroxide; ROS, reactive oxygen species.

and H_2O_2 stress compared with the wild type (Fig. 8E). The genetically encoded Brx-roGFP2 biosensor was applied to measure the changes in the BSH redox potential in the *mhqR* mutant during the growth and under H_2O_2 stress (Supplementary Fig. S7). The basal level oxidation of the Brx-roGFP2 was similar between the wild type and the *mhqR* mutant. However, the *mhqR* mutant showed a slightly higher oxidation increase and delayed recovery of the BSH redox potential compared with the wild type. Altogether, these results indicate that the *mhqR* mutant is sensitive in growth to sublethal ROS and to the host immune defense during the first 24 h of macrophage infections. However, under long-term infection conditions (48 h) and lethal ROS concentrations, the MhqR regulon is an important defense mechanism and required for *S. aureus* survival, providing an attractive drug target.

The mhqR *mutant shows enhanced respiratory chain activity and increased ATP levels*

Quinones, such as menaquinone, are important electron carriers of the respiratory chain in *S. aureus*. Previous studies have shown that the quinone-sensing QsrR repressor responds also to menadione, the precursor of menaquinone in *S. aureus* (33). Thus, we investigated whether the upregulation of quinone degradation enzymes MhqD and MhqE in the *mhqR* mutant affects the electron transport to reduce molecular oxygen in the respiratory chain. Oxygen consumption rates were measured using a Clark-type electrode for the *mhqR* and *qsrR* mutants during the exponential growth and stationary phases with 1 m*M* glucose or 100 m*M* succinate as electron donors (Fig. 9A).

During the exponential growth phase, all strains showed high oxygen consumption rates of 55–70 nmol/mL/min with glucose as electron donor. The *mhqR* mutant had a significantly increased oxygen consumption rate with glucose compared with the wild type, but no differences were observed with succinate. During the stationary phase, the oxygen consumption rate of the wild type was ~35 nmol/mL/min with glucose, significantly increased in the *mhqR* mutant (48 nmol/mL/min), but decreased in the *qsrR* mutant (Fig. 9A). Similarly, stationary phase *mhqR* mutant cells showed higher oxygen reduction rates with succinate (28 nmol/mL/min). These results of the higher respiratory chain activity in the *mhqR* mutant were also confirmed under microaerophilic conditions with methylene blue as indicator of oxygen consumption (Fig. 9B).

Due to the increased electron transport, elevated ATP levels could be determined in the *mhqR* mutant compared with the wild type (Fig. 9C). Thus, we speculate that quinones are more reduced in the *mhqR* mutant leading to an increased electron transport and higher ATP levels, which is supported

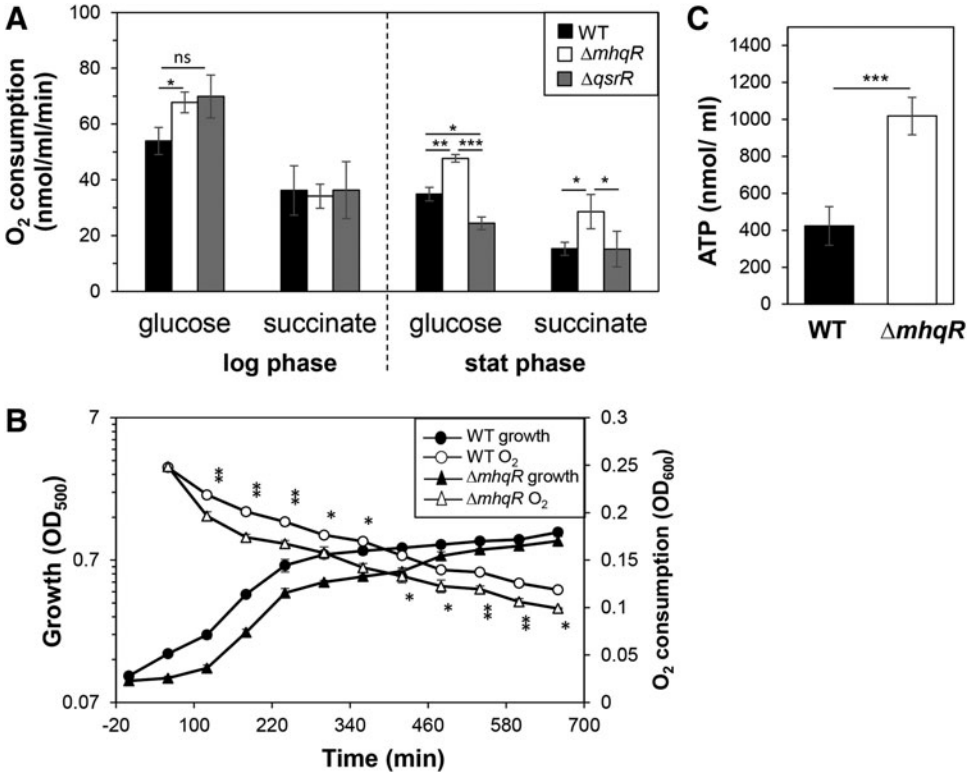

FIG. 9. The *mhqR* mutant shows a higher respiratory chain activity and increased ATP level. (A) Oxygen consumption rates of the wild type and *mhqR* and *qsrR* mutants were determined during the exponential growth and stationary phases with glucose or succinate as electron donor using a Clark-type electrode. The results are presented as average values of three biological replicates with standard deviations. **(B)** To measure oxygen consumption under microaerophilic conditions, discoloration of methylene blue was measured as absorbance change at OD_{600} together with the OD_{500} as bacterial growth. **(C)** The ATP levels of the wild type and the *mhqR* mutant were determined during the exponential growth phrase with the ATP Bioluminescence Assay Kit CLS II (Sigma–Aldrich) according to the manufacturer's instructions. The results are from four biological replicates. Error bars represent the standard deviation. ns, $p > 0.05$; $*p < 0.05$; $**p < 0.01$; $***p < 0.001$.

by reduced expression of oxidative stress-specific genes in the transcriptome of the *mhqR* mutant.

Discussion

In this study, we characterized the novel quinone-sensing MhqR repressor of *S. aureus* as an important component of the global response of *S. aureus* to quinones and antimicrobials. Transcriptome analysis in response to MHQ revealed the global signature of a thiol-specific oxidative and electrophile stress response, which is evident by the induction of the PerR, QsrR, MhqR, CtsR, and HrcA regulons. In addition, quinones caused a metal, sulfide, and cell wall stress response by upregulation of the Fur, CsoR, CstR, and GraRS regulons. This transcriptome profile overlaps strongly with the response to quinones in *B. subtilis* as shown by the inductions of the PerR, Spx, YodB, MhqR, HrcA, and CtsR regulons (1, 29, 42, 55, 68, 69).

The MhqR and QsrR regulons represent the quinone stress signature in *S. aureus*. The QsrR regulon includes genes encoding ring-cleavage dioxygenases (*catE*, *catE2*), quinone reductases (*azoR1*, *frp*), and nitroreductases (*yodC*) (33). The MhqR regulon consists only of the *mhqRED* operon in *S. aureus* (Fig. 10). MhqD is annotated as phospholipase/carboxylesterase of the widespread alpha/beta fold hydrolase family (59). These enzymes cleave carboxylate esters to acids and alcohols and might be involved in the catabolism of quinone compounds. MhqE encodes a ring-cleavage dioxygenase in *S. aureus*. Thus, paralogous ring-cleavage dioxygenases and the nitro- and quinone reductases confer additive resistance to MHQ in *S. aureus*. Homologous dioxygenases (CatE, MhqA, MhqE, MhqO), quinone, and nitroreductases (AzoR1, AzoR2, YodC) have been shown to function in detoxification of exogenous quinones and catecholic compounds (Fig. 10) (12, 13, 42, 55, 68, 69), as well as the endogenous catecholate siderophore bacillibactin in *B. subtilis* (65). Thus, the QsrR and MhqR regulons have a similar composition of detoxification genes in both bacteria and confer resistance to quinones.

The catechol-2,3-dioxygenases CatE of *B. subtilis* was previously shown to cleave catechol to produce 2-hydroxymuconic semialdehyde (55, 68), whereas the dioxygenase MhqE of the MhqR regulon shares strong homology to hydroquinone-type 1,2-dioxygenase LinE of *Sphingomonas paucimobilis* that is involved in degradation of the xenobiotic insecticide hexachlorocyclohexane (51). Catechol-2,3-dioxygenases are iron-containing enzymes (51), and CatE was shown to respond also to iron limitation in *B. subtilis* through control by the Fur repressor (65). Thus, the *S. aureus* dioxygenases could be also involved in the decomposition of siderophores. *S. aureus* utilizes carboxylate siderophores

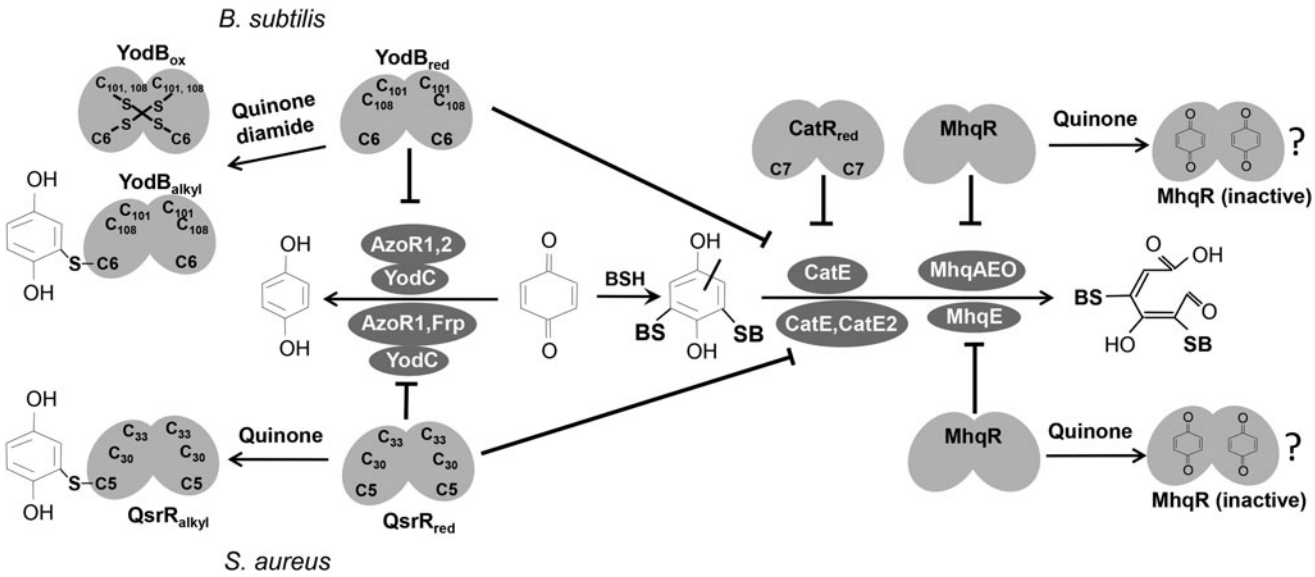

FIG. 10. The roles of the quinone-sensing MhqR, CatR, and YodB/QsrR regulons in *B. subtilis* and *S. aureus*. Exposure of *B. subtilis* and *S. aureus* to quinones induces the quinone detoxification regulons controlled by the homologous MarR-type repressors MhqR, YodB/QsrR, and CatR. The redox-sensing MarR/DUF24-family repressors YodB and CatR of *B. subtilis* are inactivated by intersubunit disulfide formation *in vivo* that involves the conserved Cys6 or Cys7 (1, 2, 12, 13, 69). The YodB and QsrR repressor mutant proteins with single Cys6 and Cys5 sense quinones also by thiol-*S*-alkylation *in vitro* (33, 41). The MhqR repressors might be inactivated by direct binding of quinones to a specific pocket. The MhqR and YodB/QsrR regulon include homologous quinone reductases, nitroreductases, and dioxygenases for quinone and diamide detoxification. The thiol-dependent dioxygenases MhqA, MhqE, CatE, and MhqO of *B. subtilis* and their respective homologs CatE, MhqE, and CatE2 of *S. aureus* (Supplementary Fig. S3B) are involved in ring cleavage of quinone-*S*-adducts. The quinone reductases AzoR1 and AzoR2 of *B. subtilis* and AzoR1 and Frp of *S. aureus* and the nitroreductases YodC and MhqN of *B. subtilis* and YodC of *S. aureus* catalyze the reduction of quinones to redox stable hydroquinones.

staphyloferrin A and B but can also import xenosiderophores of other bacteria (25). However, the *S. aureus mhqR* and *qsrR* mutants showed no growth and survival phenotype upon treatment with the iron-scavenger 2,2′-dipyridyl compared with the wild type, indicating no function under iron limitation (Supplementary Fig. S8). More detailed studies are required to define the precise functions of the many detoxification enzymes of the MhqR and QsrR regulons in *S. aureus*.

MhqR belongs to the widespread MarR family of transcriptional regulators harboring wHTH DNA binding motifs that bind to 16–20 bp (pseudo) palindromic double-stranded DNA in adjacent major grooves (16). In previous studies, we identified a conserved 9–9 bp inverted repeat sequence as MhqR operator site for *B. subtilis* MhqR (69). This palindromic operator sequence was conserved in the *S. aureus mhqRED* upstream promoter region.

DNA binding assays revealed specific binding of MhqR to its operator with a high affinity ($K_d = 7.38$ n*M*). Comparative studies have shown that the dissociation constants vary across MarR type regulators (37, 75). However, the K_d value of MhqR is in the range of other MarR-type regulators, such as OhrR of *B. subtilis* ($K_d = 5$ n*M*) and MepR of *S. aureus* ($K_d = 6.3$ n*M*) (22, 36).

DNA binding assays further revealed that quinones lead to inhibition of the DNA binding activity of MhqR, which does not involve a thiol-based mechanism. Cys95 of MhqR is also not conserved in other MhqR homologs and dispensable for quinone regulation and DNA binding *in vivo* and *in vitro*. No involvement of the nonconserved Cys126 in quinone regulation was also shown for the *B. subtilis* MhqR protein (69). Thus, the regulatory mechanism of MhqR is different compared with redox-sensing MarR-type or Rrf2-family regulators, which sense directly redox-active compounds, such as ROS, hypochlorous acid (HOCl), or quinones by specific conserved redox-sensitive Cys residues (2, 29, 44). These redox-sensing regulators include YodB, CatR, HypR, and OhrR of *B. subtilis* and their homologs QsrR, SarZ, and MgrA of *S. aureus* (11, 12, 29, 33, 41, 42,44, 60, 61).

We speculate that the quinone-sensing mechanism of MhqR occurs *via* a direct binding of the quinone as ligand to a specific pocket. The DNA binding activity of many MarR-type regulators is altered by chemical ligands, such as phenolic or aromatic compounds (*e.g.*, salicylate, urate, protocatechuate, hydroxyphenylacetate, *p*-hydroxycinnamate-CoA) (24, 62, 75). Structural and biochemical studies of ligand-binding MarR-family proteins suggest a shared ligand-binding pocket between dimerization and DNA binding regions (16). This common ligand-binding pocket was also identified between the dimer interface and the wHTH motif in the structure of the MarR-type regulator ST1710 of *Sulfolobus tokodaii* in complex with its inhibitor salicylate (38).

The structure of the ST1710-salicylate complex was used as template to model the MhqR structure of *S. aureus* using SWISS-MODEL (Supplementary Fig. S5A). However, the salicylate contact residues Tyr37 and Tyr111 of one subunit and Ala16, Lys17, and Arg20 of the opposing subunit in the ST1710 dimer are not conserved in MhqR of *S. aureus*. Thus, the specific interactions of the putative ligand-binding pocket of MhqR with quinones and the resulting conformational changes in the wHTH motifs remain to be elucidated.

Apart from quinone resistance, the MhqR regulon also confers broad-spectrum antimicrobial resistance to quinone-like compounds in *S. aureus*, such as pyocyanin, ciprofloxacin, norfloxacin, and rifampicin. The fluoroquinolones ciprofloxacin and norfloxacin are priority class antibiotics to combat *S. aureus* infections, which act as DNA gyrase and topoisomerase inhibitors, causing superoxide anions and hydroxyl radicals through gyrase poisoning (19, 64). Pyocyanin is produced by *Pseudomonas aeruginosa*, a pathogen often co-isolated with *S. aureus* in cystic fibrosis patients. Pyocyanin blocks the electron transport chain by trapping electrons from NADH (26, 58). Mutations in *qsrR* have been previously selected as pyocyanin resistance mechanism (56). Rifampicin inhibits the RNA polymerase resulting in frequent *rpoB* mutations as resistance mechanism in *S. aureus* (74).

Our study revealed an involvement of the MhqR and QsrR regulons in antimicrobial resistance toward quinone-like antimicrobials in *S. aureus*. Similarly, the MarR-type regulators MarR of *Escherichia coli*, MgrA and MepR of *S. aureus*, as well as MexR in *P. aeruginosa* have been shown to confer resistance to multiple antibiotics by controlling efflux pumps (10, 14, 64, 70). We hypothesize that the MhqR- and QsrR-controlled dioxygenases and quinone reductases contribute to detoxification of the antimicrobial compounds with quinone structures as new resistance mechanism. There is also the controversial debate about the involvement of ROS generation in the killing mode of antibiotics. Thus, the antibiotic resistant phenotypes of the *mhqR* mutant could be connected to its ROS resistance in survival assays.

However, the MhqR regulon did not confer resistance to the naphthoquinone lapachol. Differences in the detoxification of benzoquinones and naphthoquinones have been described in *E. coli* (77). In *S. aureus*, flavohemoglobin has high substrate specificity for 2-hydroxy-1,4-naphthoquinones and might be more specific for naphthoquinone detoxification (53).

While the MhqR regulon plays an important role in antibiotic resistance, the *mhqR* mutant showed increased sensitivity at early time points of 24 h after macrophage infections and under sublethal ROS and HOCl exposure *in vitro*. We hypothesize that the lower basal transcription of PerR regulon genes in the *mhqR* mutant could contribute to the H_2O_2- and NaOCl-sensitive phenotypes as well as to decreased survival in infection assays. Surprisingly, the *mhqR* was delayed in growth after sublethal HOCl and H_2O_2 but acquired resistance to lethal doses of NaOCl and H_2O_2 in killing assays. In addition, at a later time point, 48 h postinfection of macrophages, the *mhqR* mutant showed a higher survival rate than the wild type.

It could be possible that the respiratory chain activity is decreased in the *S. aureus mhqR* mutant, as has been proposed in the *B. subtilis mhqR* mutant (34). Decreased respiratory chain activity was linked to lower ROS levels and facilitated growth of antibiotic resistant cell wall-deficient L-forms in *B. subtilis* (34). The *qsrR* mutant indeed showed decreased oxygen consumption with glucose, but only during the stationary phase. However, the *mhqR* mutant had a higher respiratory chain activity and increased ATP levels than the wild type. Thus, it might be possible that quinones are more reduced in the *mhqR* mutant, leading to enhanced electron transport. Our future analyses are directed to further investigate the functions and redox-sensing mechanisms of MhqR and QsrR in response to quinones and related antimicrobials.

Experimental Procedures

Bacterial strains, growth, and survival assays

Bacterial strains, plasmids, and primers are listed in Supplementary Tables S3 and S4. *E. coli* was cultivated in Luria–Bertani (LB) broth medium and *S. aureus* in RPMI medium. Survival assays were performed by plating 100 μL of serial dilutions of *S. aureus* onto LB agar plates and determination of CFUs. Statistical analysis was performed using Student's unpaired two-tailed *t*-test by the graph prism software. The compounds used for growth and survival assays (*e.g.*, MHQ, ciprofloxacin, norfloxacin, lapachol, pyocyanin, H_2O_2, NaOCl) were purchased from Sigma–Aldrich. NaOCl dissociates in aqueous solution to HOCl and hypochlorite (OCl^-) (20). The concentration of HOCl was determined by absorbance measurements, as reported previously (76).

Construction of the S. aureus *COL* mhqR *and* qsrR *deletion mutants and the complemented* mhqR *and* mhqRC95A *mutant strains*

The *S. aureus* COL *mhqR* (SACOL2531) and *qsrR* (SACOL2115) deletion mutants were constructed by allelic replacement *via* pMAD, as described previously (4, 44). The 500 bp upstream and downstream regions of *mhqR* and *qsrR* were each fused by overlap extension PCR and ligated into the *Bgl*II and *Sal*I sites of plasmid pMAD. The pMAD constructs were electroporated into *S. aureus* RN4220, transferred to *S. aureus* COL by phage transduction, and selected for plasmid excision leading to clean deletions of *mhqR* and *qsrR*, as described previously (44, 66).

The complemented *mhqR* and *mhqRC95A* mutant strains were constructed using the pRB473 plasmid, as described previously (44). The *mhqR* and *mhqRC95A* sequences were amplified from plasmids pET11b-*mhqR* and pET11b-*mhqRC95A*, digested with *Bam*HI and *Kpn*I, and inserted into pRB473 resulting in plasmids pRB473-*mhqR* and pRB473-*mhqRC95A* (Supplementary Table S3). The plasmids were introduced into the *mhqR* mutant *via* phage transduction, as described previously (44).

RNA isolation, Northern blot analysis, RNA-seq transcriptomics, and bioinformatics

For RNA isolation, *S. aureus* COL was cultivated in RPMI medium and treated with 45 μM MHQ, 300 μM lapachol, 90.5 μM ciprofloxacin, 76 μM pyocyanin, 1 mM NaOCl, 0.5 mM methylglyoxal, 2 mM diamide, and 0.75 mM formaldehyde for 15 and 30 min, as described previously (73). Northern blot hybridizations were performed with the digoxigenin-labeled *mhqD*-specific antisense RNA probe synthesized *in vitro* using T7 RNA polymerase and the primer pairs SACOL2529-for/rev (Supplementary Table S4), as described previously (68, 73).

RNA-seq transcriptomics was performed using RNA of *S. aureus* COL and the *mhqR* deletion mutant isolated before and 30 min after 45 μM MHQ, as described in previous studies (72). Differential gene expression analysis of three biological replicates was performed using DESeq2 (46) with ReadXplorer v2.2 (28) as described previously (72) using an adjusted *p*-value cutoff of ≤ 0.05 and a signal intensity ratio (*M*-value) cutoff of ≥ 0.6 or ≤ -0.6 (fold-change of ± 1.5).

The cDNAs enriched for primary 5′-transcripts were prepared according to the method described previously (63). cDNAs were sequenced paired end on an Illumina MiSeq System (San Diego, CA) using 75 bp read length. The R1 cDNA reads were mapped to the *S. aureus* USA300_TCH1516 genome (27) with bowtie2 v2.2.7 (40) using the default settings for single-end read mapping and visualized with Read Explorer v.2.2 (28). The whole transcriptome and 5′ enriched RNA-seq raw data files are available in the ArrayExpress database under E-MTAB-7074 and E-MTAB-7385.

Cloning, expression, and purification of His-tagged MhqR and MhqRC95A mutant protein in E. coli

The *mhqR* gene (SACOL2531) was amplified from chromosomal DNA of *S. aureus* COL by PCR using primers SACOL2531-pET-for-NheI and SACOL2531-pET-rev-BamHI (Supplementary Table S4), digested with *Nhe*I and *Bam*HI, and inserted into plasmid pET11b (Novagen) to generate plasmid pET11b-*mhqR*. For the construction of *mhqRC95A* mutant, two first-round PCRs were performed using primer pairs SACOL2531-pET-for-NheI and SACOL2531-pET-C95A-Rev as well as primer pairs SACOL2531-pET-C95A-for and SACOL2531-pET-rev-BamHI (Supplementary Table S4). The two first-round PCR products were hybridized and amplified by a second round of PCR using primers SACOL2531-pET-for-NheI and SACOL2531-pET-rev-BamHI. The second-round PCR products were digested with *Nhe*I and *Bam*HI and inserted into plasmid pET11b to generate plasmid pET11b-*mhqRC95A*. For expression and purification of His-tagged MhqR and MhqRC95A proteins, *E. coli* BL21(DE3) p*lysS* was used with the plasmids pET11b-*mhqR* and pET11b-*mhqRC95A*, as described previously (44). Cultivation of the *E. coli* expression strains was performed in 1 L LB medium until the exponential growth phase at OD_{600} of 0.8, followed by the addition of 1 m*M* isopropyl-β-D-thiogalactopyranoside for 5 h at 30°C. Recombinant His-tagged MhqR and the MhqRC95A mutant proteins were purified, as described previously (44).

EMSAs of MhqR and MhqRC95A proteins

For EMSAs, the DNA fragment containing the *mhqR* upstream region was amplified by PCR with the primer set emsa2531-for and emsa2531-rev (Supplementary Table S4). The DNA-binding reactions were performed with 15 ng/μL PCR product and purified His-MhqR and His-MhqRC95A proteins for 45 min, as described previously (44). MHQ was added to the DNA-MhqR-complex for 30 min to observe the dissociation of MhqR from the DNA. To analyze the reversibility of inhibition of MhqR by quinones, DTT was added 30 min after MHQ addition to the MhqR-DNA reaction. Thus, MHQ and DTT were added subsequently to the DNA-MhqR-complex for each 30 min. EMSAs were carried out as described previously (44).

Brx-roGFP2 biosensor measurements

S. aureus COL and *mhqR* mutant strains with the Brx-roGFP2 biosensor plasmids were cultivated in LB and used for measurements of the biosensor oxidation degree along the growth curves and after injection of H_2O_2, as described previously (45). Fully reduced and oxidized controls were treated with 10 m*M* DTT and 5 m*M* diamide or 20 m*M* cumene hydroperoxide, respectively. Brx-roGFP2 biosensor fluorescence emission was measured at 510 nm after excitation at 405 and 488 nm using the CLARIOstar Microplate Reader (BMG Labtech), as described previously (45).

Macrophage infection assays

The infection assays were performed using the murine macrophage cell line J-774A.1, as described previously (44). Intracellular survival of phagocytosed *S. aureus* was measured after 2, 4, 24, and 48 h postinfection by determination of CFUs, as described previously (44).

Determination of oxygen consumption rates

The oxygen consumption rates of *S. aureus* strains were determined with a Clark-type electrode (Oxygraph; Hansatech) at 25°C according to a modified protocol, as described previously (50, 78). For determination of the respiratory chain activity during the exponential growth and stationary phases, cells were grown in tryptic soy broth medium to an OD_{600} of 0.6 and for 24 h. Cells were harvested by centrifugation, washed in 33 m*M* potassium phosphate buffer (pH 7.0), and adjusted to an OD_{578} of 5. Oxygen consumption was measured upon addition of 100 m*M* disodium succinate or 1 m*M* glucose as electron donors in three bioreplicates. Measurements were corrected for basal oxygen consumption without electron donors.

In addition, colorimetric determination of the oxygen consumption rates was performed by discoloration of methylene blue. Methylene blue was added at a final concentration of 0.004 mg/mL to 40 mL of *S. aureus* cells that were cultivated under microaerophilic conditions. The discoloration of methylene blue was determined as absorbance change at OD_{600} together with the optical density of the culture at OD_{500}.

ATP measurements

The ATP levels of *S. aureus* strains were determined with the ATP Bioluminescence Assay Kit CLS II (Sigma–Aldrich) according to the manufacturer's instructions. Briefly, 1 mL of exponentially growing cells was harvested, resuspended in 100 μL dilution buffer, and disrupted by boiling in 900 μL of 100 m*M* Tris, 4 m*M* ethylenediaminetetraacetic acid, pH 7.75, for 2 min. After centrifugation of the lysate, 50 μL of the supernatant was incubated with 50 μL luciferase and the luminescence was measured using the CLARIOstar Microplate Reader (BMG Labtech). The values were corrected for the autoluminescence of the cells, and the ATP level was determined based on the ATP standard curve.

Acknowledgments

We thank Prof. Holger Dau (Department of Physics, Freie Universität Berlin) for providing the Clark electrode. This work was supported by an ERC Consolidator grant (GA 615585) MYCOTHIOLOME and grants from the Deutsche Forschungsgemeinschaft (AN746/4-1 and AN746/4-2) within the SPP1710, by the SFB973 project C08N, and by the SFB/TR84 project B06 to H.A.

Author Disclosure Statement

No competing financial interests exist.

Supplementary Material

Supplementary Table S1
Supplementary Table S2
Supplementary Table S3
Supplementary Table S4
Supplementary Figure S1
Supplementary Figure S2
Supplementary Figure S3
Supplementary Figure S4
Supplementary Figure S5
Supplementary Figure S6
Supplementary Figure S7
Supplementary Figure S8

References

1. Antelmann H, Hecker M, and Zuber P. Proteomic signatures uncover thiol-specific electrophile resistance mechanisms in *Bacillus subtilis*. *Expert Rev Proteomics* 5: 77–90, 2008.
2. Antelmann H and Helmann JD. Thiol-based redox switches and gene regulation. *Antioxid Redox Signal* 14: 1049–1063, 2011.
3. Archer GL. *Staphylococcus aureus*: a well-armed pathogen. *Clin Infect Dis* 26: 1179–1181, 1998.
4. Arnaud M, Chastanet A, and Débarbouillé M. New vector for efficient allelic replacement in naturally nontransformable, low-GC-content, gram-positive bacteria. *Appl Environ Microbiol* 70: 6887–6891, 2004.
5. Baker J, Sengupta M, Jayaswal RK, and Morrissey JA. The *Staphylococcus aureus* CsoR regulates both chromosomal and plasmid-encoded copper resistance mechanisms. *Environ Microbiol* 13: 2495–2507, 2011.
6. Biasini M, Bienert S, Waterhouse A, Arnold K, Studer G, Schmidt T, Kiefer F, Gallo Cassarino T, Bertoni M, Bordoli L, and Schwede T. SWISS-MODEL: modelling protein tertiary and quaternary structure using evolutionary information. *Nucleic Acids Res* 42: W252–W258, 2014.
7. Bittner S. When quinones meet amino acids: chemical, physical and biological consequences. *Amino Acids* 30: 205–224, 2006.
8. Boucher HW and Corey GR. Epidemiology of methicillin-resistant *Staphylococcus aureus*. *Clin Infect Dis* 46 Suppl 5: S344–S349, 2008.
9. Chandrangsu P, Loi VV, Antelmann H, and Helmann JD. The role of bacillithiol in Gram-positive *Firmicutes*. *Antioxid Redox Signal* 28: 445–462, 2018.
10. Chen H, Hu J, Chen PR, Lan L, Li Z, Hicks LM, Dinner AR, and He C. The *Pseudomonas aeruginosa* multidrug efflux regulator MexR uses an oxidation-sensing mechanism. *Proc Natl Acad Sci U S A* 105: 13586–13591, 2008.
11. Chen PR, Nishida S, Poor CB, Cheng A, Bae T, Kuechenmeister L, Dunman PM, Missiakas D, and He C. A new oxidative sensing and regulation pathway mediated by the MgrA homologue SarZ in *Staphylococcus aureus*. *Mol Microbiol* 71: 198–211, 2009.
12. Chi BK, Albrecht D, Gronau K, Becher D, Hecker M, and Antelmann H. The redox-sensing regulator YodB senses quinones and diamide via a thiol-disulfide switch in *Bacillus subtilis*. *Proteomics* 10: 3155–3164, 2010.
13. Chi BK, Kobayashi K, Albrecht D, Hecker M, and Antelmann H. The paralogous MarR/DUF24-family repressors YodB and CatR control expression of the catechol dioxygenase CatE in *Bacillus subtilis*. *J Bacteriol* 192: 4571–4581, 2010.
14. Cohen SP, McMurry LM, Hooper DC, Wolfson JS, and Levy SB. Cross-resistance to fluoroquinolones in multiple-antibiotic-resistant (Mar) *Escherichia coli* selected by tetracycline or chloramphenicol: decreased drug accumulation associated with membrane changes in addition to OmpF reduction. *Antimicrob Agents Chemother* 33: 1318–1325, 1989.
15. Cosgrove SE, Sakoulas G, Perencevich EN, Schwaber MJ, Karchmer AW, and Carmeli Y. Comparison of mortality associated with methicillin-resistant and methicillin-susceptible *Staphylococcus aureus* bacteremia: a meta-analysis. *Clin Infect Dis* 36: 53–59, 2003.
16. Deochand DK and Grove A. MarR family transcription factors: dynamic variations on a common scaffold. *Crit Rev Biochem Mol Biol* 52: 595–613, 2017.
17. Domingue GJ, Sr., and Woody HB. Bacterial persistence and expression of disease. *Clin Microbiol Rev* 10: 320–344, 1997.
18. Duy NV, Mäder U, Tran NP, Cavin JF, Tam le T, Albrecht D, Hecker M, and Antelmann H. The proteome and transcriptome analysis of *Bacillus subtilis* in response to salicylic acid. *Proteomics* 7: 698–710, 2007.
19. Dwyer DJ, Kohanski MA, Hayete B, and Collins JJ. Gyrase inhibitors induce an oxidative damage cellular death pathway in *Escherichia coli*. *Mol Syst Biol* 3: 91, 2007.
20. Estrela C, Estrela CRA, Barbin EL, Spanó JCE, Marchesan MA, and Pécora JD. Mechanism of action of sodium hypochlorite. *Braz Dent J* 13: 113–117, 2002.
21. Falord M, Mäder U, Hiron A, Debarbouille M, and Msadek T. Investigation of the *Staphylococcus aureus* GraSR regulon reveals novel links to virulence, stress response and cell wall signal transduction pathways. *PLoS One* 6: e21323, 2011.
22. Fuangthong M and Helmann JD. The OhrR repressor senses organic hydroperoxides by reversible formation of a cysteine-sulfenic acid derivative. *Proc Natl Acad Sci U S A* 99: 6690–6695, 2002.
23. Gaupp R, Ledala N, and Somerville GA. Staphylococcal response to oxidative stress. *Front Cell Infect Microbiol* 2: 33, 2012.
24. Grove A. Regulation of metabolic pathways by MarR family transcription factors. *Comput Struct Biotechnol J* 15: 366–371, 2017.
25. Hammer ND and Skaar EP. Molecular mechanisms of *Staphylococcus aureus* iron acquisition. *Annu Rev Microbiol* 65: 129–147, 2011.
26. Hassan HM and Fridovich I. Mechanism of the antibiotic action pyocyanine. *J Bacteriol* 141: 156–163, 1980.
27. Highlander SK, Hulten KG, Qin X, Jiang H, Yerrapragada S, Mason EO, Jr., Shang Y, Williams TM, Fortunov RM, Liu Y, Igboeli O, Petrosino J, Tirumalai M, Uzman A, Fox GE, Cardenas AM, Muzny DM, Hemphill L, Ding Y, Dugan S, Blyth PR, Buhay CJ, Dinh HH, Hawes AC, Holder M, Kovar CL, Lee SL, Liu W, Nazareth LV, Wang Q, Zhou J, Kaplan SL, and Weinstock GM. Subtle genetic changes enhance virulence of methicillin resistant and sensitive *Staphylococcus aureus*. *BMC Microbiol* 7: 99, 2007.
28. Hilker R, Stadermann KB, Schwengers O, Anisiforov E, Jaenicke S, Weisshaar B, Zimmermann T, and Goesmann

A. ReadXplorer 2-detailed read mapping analysis and visualization from one single source. *Bioinformatics* 32: 3702–3708, 2016.
29. Hillion M and Antelmann H. Thiol-based redox switches in prokaryotes. *Biol Chem* 396: 415–444, 2015.
30. Hillion M, Bernhardt J, Busche T, Rossius M, Maass S, Becher D, Rawat M, Wirtz M, Hell R, Rückert C, Kalinowski J, and Antelmann H. Monitoring global protein thiol-oxidation and protein S-mycothiolation in *Mycobacterium smegmatis* under hypochlorite stress. *Sci Rep* 7: 1195, 2017.
31. Hoffmann-Ostenhof O. *Enzyme Inhibition by Quinones Metabolic Inhibitors V2: A Comprehensive Treatise*. Burlington, VT: Elsevier Science, 1963.
32. Hussain H and Green IR. Lapachol and lapachone analogs: a journey of two decades of patent research(1997–2016). *Expert Opin Ther Pat* 27: 1111–1121, 2017.
33. Ji Q, Zhang L, Jones MB, Sun F, Deng X, Liang H, Cho H, Brugarolas P, Gao YN, Peterson SN, Lan L, Bae T, and He C. Molecular mechanism of quinone signaling mediated through S-quinonization of a YodB family repressor QsrR. *Proc Natl Acad Sci U S A* 110: 5010–5015, 2013.
34. Kawai Y, Mercier R, Wu LJ, Dominguez-Cuevas P, Oshima T, and Errington J. Cell growth of wall-free L-form bacteria is limited by oxidative damage. *Curr Biol* 25: 1613–1618, 2015.
35. Kumagai Y, Koide S, Taguchi K, Endo A, Nakai Y, Yoshikawa T, and Shimojo N. Oxidation of proximal protein sulfhydryls by phenanthraquinone, a component of diesel exhaust particles. *Chem Res Toxicol* 15: 483–489, 2002.
36. Kumaraswami M, Schuman JT, Seo SM, Kaatz GW, and Brennan RG. Structural and biochemical characterization of MepR, a multidrug binding transcription regulator of the *Staphylococcus aureus* multidrug efflux pump MepA. *Nucleic Acids Res* 37: 1211–1224, 2009.
37. Kumarevel T. The MarR family of transcriptional regulators—a structural perspective. In: Pana M (ed.). *Antibiotic Resistant Bacteria—A Continuous Challenge in the New Millennium.* London, United Kingdom: IntechOpen, 2012, pp. 403–418.
38. Kumarevel T, Tanaka T, Umehara T, and Yokoyama S. ST1710-DNA complex crystal structure reveals the DNA binding mechanism of the MarR family of regulators. *Nucleic Acids Res* 37: 4723–4735, 2009.
39. Kurosu M, Begari E. Vitamin K2 in electron transport system: are enzymes involved in vitamin K2 biosynthesis promising drug targets? *Molecules* 15: 1531–1553, 2010.
40. Langmead B and Salzberg SL. Fast gapped-read alignment with Bowtie 2. *Nat Methods* 9: 357–359, 2012.
41. Lee SJ, Lee IG, Lee KY, Kim DG, Eun HJ, Yoon HJ, Chae S, Song SH, Kang SO, Seo MD, Kim HS, Park SJ, and Lee BJ. Two distinct mechanisms of transcriptional regulation by the redox sensor YodB. *Proc Natl Acad Sci U S A* 113: E5202–E5211, 2016.
42. Leelakriangsak M, Huyen NT, Töwe S, van Duy N, Becher D, Hecker M, Antelmann H, and Zuber P. Regulation of quinone detoxification by the thiol stress sensing DUF24/MarR-like repressor, YodB in *Bacillus subtilis*. *Mol Microbiol* 67: 1108–1124, 2008.
43. Liebeke M, Pöther DC, van Duy N, Albrecht D, Becher D, Hochgräfe F, Lalk M, Hecker M, and Antelmann H. Depletion of thiol-containing proteins in response to quinones in *Bacillus subtilis*. *Mol Microbiol* 69: 1513–1529, 2008.
44. Loi VV, Busche T, Tedin K, Bernhardt J, Wollenhaupt J, Huyen NTT, Weise C, Kalinowski J, Wahl MC, Fulde M, and Antelmann H. Redox-sensing under hypochlorite stress and infection conditions by the Rrf2-family repressor HypR in *Staphylococcus aureus*. *Antioxid Redox Signal* 29: 615–636, 2018.
45. Loi VV, Harms M, Müller M, Huyen NTT, Hamilton CJ, Hochgräfe F, Pane-Farre J, and Antelmann H. Real-time imaging of the bacillithiol redox potential in the human pathogen *Staphylococcus aureus* using a genetically encoded bacilliredoxin-fused redox biosensor. *Antioxid Redox Signal* 26: 835–848, 2017.
46. Love MI, Huber W, and Anders S. Moderated estimation of fold change and dispersion for RNA-seq data with DESeq2. *Genome Biol* 15: 550, 2014.
47. Lowy FD. *Staphylococcus aureus* infections. *N Engl J Med* 339: 520–532, 1998.
48. Luebke JL, Shen J, Bruce KE, Kehl-Fie TE, Peng H, Skaar EP, and Giedroc DP. The CsoR-like sulfurtransferase repressor (CstR) is a persulfide sensor in *Staphylococcus aureus*. *Mol Microbiol* 94: 1343–1360, 2014.
49. Mäder U, Nicolas P, Depke M, Pane-Farre J, Debarbouille M, van der Kooi-Pol MM, Guerin C, Derozier S, Hiron A, Jarmer H, Leduc A, Michalik S, Reilman E, Schaffer M, Schmidt F, Bessieres P, Noirot P, Hecker M, Msadek T, Völker U, and van Dijl JM. *Staphylococcus aureus* transcriptome architecture: from laboratory to infection-mimicking conditions. *PLoS Genet* 12: e1005962, 2016.
50. Mayer S, Steffen W, Steuber J, and Gotz F. The *Staphylococcus aureus* NuoL-like protein MpsA contributes to the generation of membrane potential. *J Bacteriol* 197: 794–806, 2015.
51. Miyauchi K, Adachi Y, Nagata Y, and Takagi M. Cloning and sequencing of a novel meta-cleavage dioxygenase gene whose product is involved in degradation of gamma-hexachlorocyclohexane in *Sphingomonas paucimobilis*. *J Bacteriol* 181: 6712–6719, 1999.
52. Monks TJ, Hanzlik RP, Cohen GM, Ross D, and Graham DG. Quinone chemistry and toxicity. *Toxicol Appl Pharmacol* 112: 2–16, 1992.
53. Moussaoui M, Miseviciene L, Anusevicius Z, Maroziene A, Lederer F, Baciou L, and Cenas N. Quinones and nitroaromatic compounds as subversive substrates of *Staphylococcus aureus* flavohemoglobin. *Free Radic Biol Med* 123: 107–115, 2018.
54. National Nosocomial Infections Surveillance System Report. National Nosocomial Infections Surveillance (NNIS) System Report, data summary from January 1992 through June 2004, issued October 2004. *Am J Infect Control* 32: 470–485, 2004.
55. Nguyen VD, Wolf C, Mäder U, Lalk M, Langer P, Lindequist U, Hecker M, and Antelmann H. Transcriptome and proteome analyses in response to 2-methylhydroquinone and 6-brom-2-vinyl-chroman-4-on reveal different degradation systems involved in the catabolism of aromatic compounds in *Bacillus subtilis*. *Proteomics* 7: 1391–1408, 2007.
56. Noto MJ, Burns WJ, Beavers WN, and Skaar EP. Mechanisms of pyocyanin toxicity and genetic determinants of resistance in *Staphylococcus aureus*. *J Bacteriol* 199: e00221-17, 2017.
57. O'Brien PJ. Molecular mechanisms of quinone cytotoxicity. *Chem Biol Interact* 80: 1–41, 1991.
58. O'Malley YQ, Reszka KJ, Spitz DR, Denning GM, and Britigan BE. *Pseudomonas aeruginosa* pyocyanin directly oxidizes glutathione and decreases its levels in airway

epithelial cells. *Am J Physiol Lung Cell Mol Physiol* 287: L94–L103, 2004.
59. Ollis DL, Cheah E, Cygler M, Dijkstra B, Frolow F, Franken SM, Harel M, Remington SJ, Silman I, Schrag J, Sussman JL, Verschueren KHG, and Goldman A. The alpha/beta hydrolase fold. *Protein Eng* 5: 197–211, 1992.
60. Palm GJ, Khanh Chi B, Waack P, Gronau K, Becher D, Albrecht D, Hinrichs W, Read RJ, and Antelmann H. Structural insights into the redox-switch mechanism of the MarR/DUF24-type regulator HypR. *Nucleic Acids Res* 40: 4178–4192, 2012.
61. Panmanee W, Vattanaviboon P, Poole LB, and Mongkolsuk S. Novel organic hydroperoxide-sensing and responding mechanisms for OhrR, a major bacterial sensor and regulator of organic hydroperoxide stress. *J Bacteriol* 188: 1389–1395, 2006.
62. Perera IC and Grove A. Molecular mechanisms of ligand-mediated attenuation of DNA binding by MarR family transcriptional regulators. *J Mol Cell Biol* 2: 243–254, 2010.
63. Pfeifer-Sancar K, Mentz A, Ruckert C, and Kalinowski J. Comprehensive analysis of the *Corynebacterium glutamicum* transcriptome using an improved RNAseq technique. *BMC Genomics* 14: 888, 2013.
64. Phillips-Jones MK and Harding SE. Antimicrobial resistance (AMR) nanomachines-mechanisms for fluoroquinolone and glycopeptide recognition, efflux and/or deactivation. *Biophys Rev* 10: 347–362, 2018.
65. Pi H and Helmann JD. Genome-wide characterization of the Fur regulatory network reveals a link between catechol degradation and bacillibactin metabolism in *Bacillus subtilis*. *mBio* 9: pii:e01451-18, 2018.
66. Rosenblum ED and Tyrone S. Serology, density, and morphology of staphylococcal phages. *J Bacteriol* 88: 1737–1742, 1964.
67. Soutourina O, Dubrac S, Poupel O, Msadek T, and Martin-Verstraete I. The pleiotropic CymR regulator of *Staphylococcus aureus* plays an important role in virulence and stress response. *PLoS Pathog* 6: e1000894, 2010.
68. Tam le T, Eymann C, Albrecht D, Sietmann R, Schauer F, Hecker M, and Antelmann H. Differential gene expression in response to phenol and catechol reveals different metabolic activities for the degradation of aromatic compounds in *Bacillus subtilis*. *Environ Microbiol* 8: 1408–1427, 2006.
69. Töwe S, Leelakriangsak M, Kobayashi K, Van Duy N, Hecker M, Zuber P, and Antelmann H. The MarR-type repressor MhqR (YkvE) regulates multiple dioxygenases/glyoxalases and an azoreductase which confer resistance to 2-methylhydroquinone and catechol in *Bacillus subtilis*. *Mol Microbiol* 66: 40–54, 2007.
70. Truong-Bolduc QC, Dunman PM, Strahilevitz J, Projan SJ, and Hooper DC. MgrA is a multiple regulator of two new efflux pumps in *Staphylococcus aureus*. *J Bacteriol* 187: 2395–2405, 2005.
71. Unden G and Bongaerts J. Alternative respiratory pathways of *Escherichia coli:* energetics and transcriptional regulation in response to electron acceptors. *Biochim Biophys Acta* 1320: 217–234, 1997.
72. Van Loi V, Busche T, Preuss T, Kalinowski J, Bernhardt J, and Antelmann H. The AGXX antimicrobial coating causes a thiol-specific oxidative stress response and protein *S*-bacillithiolation in *Staphylococcus aureus*. *Front Microbiol* 9: 3037, 2018.
73. Wetzstein M, Völker U, Dedio J, Löbau S, Zuber U, Schiesswohl M, Herget C, Hecker M, and Schumann W. Cloning, sequencing, and molecular analysis of the *dnaK* locus from *Bacillus subtilis*. *J Bacteriol* 174: 3300–3310, 1992.
74. Wichelhaus TA, Boddinghaus B, Besier S, Schafer V, Brade V, and Ludwig A. Biological cost of rifampin resistance from the perspective of *Staphylococcus aureus*. *Antimicrob Agents Chemother* 46: 3381–3385, 2002.
75. Wilkinson SP and Grove A. Ligand-responsive transcriptional regulation by members of the MarR family of winged helix proteins. *Curr Issues Mol Biol* 8: 51–62, 2006.
76. Winter J, Ilbert M, Graf PC, Ozcelik D, and Jakob U. Bleach activates a redox-regulated chaperone by oxidative protein unfolding. *Cell* 135: 691–701, 2008.
77. Wosilait WD and Nason A. Pyridine nucleotide-menadione reductase from *Escherichia coli*. *J Biol Chem* 208: 785–798, 1954.
78. Zeden MS, Schuster CF, Bowman L, Zhong Q, Williams HD, and Grundling A. Cyclic di-adenosine monophosphate (c-di-AMP) is required for osmotic regulation in Staphylococcus aureus but dispensable for viability in anaerobic conditions. *J Biol Chem* 293: 3180–3200, 2018.

Address correspondence to:
Prof. Haike Antelmann
Institute for Biology–Microbiology
Freie Universität Berlin
Königin-Luise-Strasse 12–16
Berlin D-14195
Germany

E-mail: haike.antelmann@fu-berlin.de

Date of first submission to ARS Central, February 5, 2019; date of final revised submission, June 18, 2019; date of acceptance, July 5, 2019.

Abbreviations Used

BSH = bacillithiol
CFU = colony-forming unit
DTT = dithiothreitol
EMSA = electrophoretic mobility shift assay
H_2O_2 = hydrogen peroxide
HOCl = hypochlorous acid
LB = Luria–Bertani
MHQ = methylhydroquinone
NaOCl = sodium hypochlorite
ROS = reactive oxygen species
TSS = transcription start site
wHTH = winged helix-turn-helix

Chapter 7

The MarR/DUF24-family QsrR repressor senses quinones and oxidants by thiol switch mechanisms in *Staphylococcus aureus*

Verena Nadin Fritsch[1], Vu Van Loi[1], Benno Kuropka[2], Martin Gruhlke[3], Christoph Weise[2], and Haike Antelmann[1]*

[1]Freie Universität Berlin, Institute of Biology-Microbiology, D-14195 Berlin, Germany

[2]Freie Universität Berlin, Institute of Chemistry and Biochemistry, D-14195 Berlin, Germany

[3]Department of Plant Physiology, RWTH Aachen University, D-52056 Aachen, Germany

*Corresponding author: haike.antelmann@fu-berlin.de

Published in:
Antioxidants & Redox Signaling
The manuscript was accepted by the journal on September 24th, 2022.
DOI: https://doi.org/10.1089/ars.2022.0090

Personal contribution:

Together with Prof. Dr. Haike Antelmann, I designed the concept of this study, wrote the methods section, and edited the manuscript. Furthermore, I performed most of the experiments. Thereby, I created together with Dr. Vu Van Loi the mutant strains and performed the Northern blot analyses of Fig. 1A. I analyzed the function of the QsrR regulon in the thiol-stress resistance and the role of the three cysteine residues for DNA binding and redox sensing by conducting phenotype analyses, Northern and Western blots, EMSAs and (non-)reducing SDS-PAGEs (Fig. 1C,E,G; 2-7; 9A,B; S1; S2). I made the quantitative and statistical evaluation of the experimental data, including Fig. 1B,D,F,H, and created all figures corresponding to the mentioned experiments.

The MarR/DUF24-family QsrR repressor senses quinones and oxidants by thiol switch mechanisms in *Staphylococcus aureus*

Verena Nadin Fritsch[1], Vu Van Loi[1], Benno Kuropka[2], Martin Gruhlke[3], Christoph Weise[2] and Haike Antelmann[1]*

Departments & Institutions:

[1]Freie Universität Berlin, Institute of Biology-Microbiology, D-14195 Berlin, Germany

[2]Freie Universität Berlin, Institute of Chemistry and Biochemistry, D-14195, Berlin, Germany

[3]Department of Plant Physiology, RWTH Aachen University, D-52056 Aachen, Germany

Running title: QsrR functions as thiol switch in *S. aureus*

***Corresponding author:**

Haike Antelmann, Institute for Biology-Microbiology, Freie Universität Berlin,

Königin-Luise-Straße 12-16, D-14195 Berlin, Germany,

Tel: +49-(0)30-838-51221, Fax: +49-(0)30-838-451221

E-mail: haike.antelmann@fu-berlin.de

Key words: *Staphylococcus aureus*/ QsrR/ thiol-switch / quinones/ ROS/ RES/ HOCl

Word count: 6586
Number of references: 64
Number of greyscale images: 8
Number of colour images: 2

ABSTRACT

Aims: The MarR/DUF24-family QsrR and YodB repressors control quinone detoxification pathways in *Staphylococcus aureus* and *Bacillus subtilis*. In *S. aureus*, the QsrR regulon confers also resistance to antimicrobial compounds with quinone-like elements, such as rifampicin, ciprofloxacin and pyocyanin. While QsrR was shown to be inhibited by thiol-*S*-alkylation of its conserved Cys4 residue by 1,4-benzoquinone, YodB senses quinones and diamide by formation of reversible intermolecular disulfides. In this study, we aimed to further investigate the redox-regulation of QsrR and the role of its Cys4, Cys29 and Cys32 residues under quinone and oxidative stress in *S. aureus*.

Results: The QsrR regulon was strongly induced by quinones and oxidants, such as diamide, allicin, HOCl and AGXX® in *S. aureus*. Transcriptional induction of *catE2* by quinones and oxidants required Cys4 and either Cys29' or Cys32' of QsrR for redox sensing *in vivo*. DNA-binding assays revealed that QsrR is reversibly inactivated by quinones and oxidants, depending on Cys4. Using mass spectrometry, QsrR was shown to sense diamide by an intermolecular thiol-disulfide switch, involving Cys4 and Cys29' of opposing subunits *in vitro*. In contrast, allicin caused *S*-thioallylation of all three Cys residues in QsrR, leading to its dissociation from the operator sequence. Furthermore, the QsrR regulon confers resistance against quinones and oxidants, depending on Cys4 and either Cys29' or Cys32'.

Conclusion and Innovation: QsrR was characterized as a two-Cys-type redox-sensing regulator, which senses the oxidative mode of quinones and strong oxidants, such as diamide, HOCl and the antimicrobial compound allicin via different thiol switch mechanisms.

INTRODUCTION

Staphylococcus aureus is an important human pathogen, which can cause many life-threatening diseases in human, such as septic shock syndrome, endocarditis, pneumonia and osteomyelitis (Archer 1998). Due to the fast evolution of multi-drug-resistant *S. aureus* isolates, the treatment options are very limited, posing a major threat to the healthcare systems (Vestergaard et al, 2019). Thus, the investigation of the virulence and adaptation mechanisms of *S. aureus* under host infections represents an important research topic to identify new drug targets to combat this major pathogen.

During infections, cellular metabolism and antibiotic treatments, *S. aureus* has to cope with reactive oxygen, electrophile and chlorine species (ROS, RES, RCS) (Linzner et al, 2021; Loi et al, 2015). *S. aureus* encounters endogenous ROS, such as superoxide anions, H_2O_2 and hydroxyl radicals, which are produced as byproducts in the aerobic respiratory chain (Imlay 2008). After phagocytosis of *S. aureus* cells, activated macrophages and neutrophils release the strong oxidant hypochlorous acid (HOCl) as most potent killing agent against the invading bacteria (Ulfig and Leichert 2021). ROS and HOCl can damage all cellular macromolecules, including proteins, DNA bases and carbohydrates, leading to bacterial killing by the immune cells. The Cys thiol group is the most susceptible target for oxidation by ROS and RES, leading to reversible thiol switches or irreversible thiol-oxidation products (Linzner et al, 2021). The oxidation of cellular metabolites, such as glucose, unsaturated fatty acids and amino acids by ROS further generates RES as secondary reactive species (Jacobs and Marnett 2010; Marnett et al, 2003).

RES include quinones and aldehydes, which have electron-deficient carbon centers and can react with the nucleophilic Cys thiol group (Linzner et al, 2021). *S. aureus* synthesizes endogenous menaquinone as an electron carrier but has also to cope with external quinone-like antimicrobial compounds, such as pyocyanin, ciprofloxacin and the naphthoquinone lapachol. Many fully substituted quinones, such as lapachol act via the oxidative mode to generate semiquinone radicals, resulting in ROS formation and protein thiol-oxidation (Linzner et al, 2020; Monks et al, 1992; O'Brien 1991). In addition, unsubstituted quinones, such as 1,4-

benzoquinone (BQ) act as oxidants and electrophiles via the thiol-*S*-alkylation chemistry with protein thiols, resulting in aggregation and depletion of thiol-containing proteins in the proteome, especially at toxic concentrations (Liebeke et al, 2008; Loi et al, 2015; Monks et al, 1992; O'Brien 1991). Apart from ROS and RES, *S. aureus* encounters other redox-active antimicrobials, such as the natural organosulfur compound allicin from garlic, which are used as alternative treatment option to combat methicillin-resistant *S. aureus* (MRSA). Allicin has been shown to act as strong antimicrobial against bacteria, fungi and parasites, including multi-drug-resistant strains. The killing effect of allicin is mediated by *S*-thioallylation of low molecular weight thiols and protein thiols as revealed in several bacteria (Borlinghaus et al, 2014; Borlinghaus et al, 2021; Loi et al, 2019; Müller et al, 2016).

In *Bacillus subtilis* and *S. aureus*, the MarR-type repressors MhqR and YodB (QsrR) sense and respond directly to quinones and regulate quinone detoxification pathways, including quinone reductases (AzoR1, YodC) and ring-cleavage dioxygenases (CatE, CatE2, MhqE), which confer resistance to quinones (Chi et al, 2010a; Fritsch et al, 2019; Ji et al, 2013; Leelakriangsak et al, 2008; Töwe et al, 2007). The quinone reductase (AzoR1) and nitroreductase (YodC) might function as NADPH-dependent flavoenzymes in the reduction of quinones to redox-stable hydroquinones. The thiol-dependent dioxygenases (CatE, CatE2, MhqE) are involved in the ring cleavage of quinones and catechol to the γ-hydroxymuconic semialdehyde as demonstrated for CatE in *B. subtilis* (Leelakriangsak et al, 2008; Tam le et al, 2006). In *S. aureus*, the QsrR and MhqR regulons confer independent resistance to MHQ, BQ and quinone-like antimicrobials, such as pyocyanin, ciprofloxacin and rifampicin (Fritsch et al, 2019; Ji et al, 2013; Noto et al, 2017). QsrR also mediates tolerance of *S. aureus* to photodynamic inactivation by the photosensitizer methylene blue (Snell et al, 2021). Thus, the dioxygenases and quinone reductases might function in the detoxification of phenolic antimicrobials and dyes as mechanisms of antimicrobial resistance.

Recently, the quinone-sensing Rrf2-family SifR repressor was characterized in *Streptococcus pneumoniae* (Zhang et al, 2022). SifR controls the Fe^{2+}-dependent catechol-2,3-dioxygenase CatE and the NAD(P)H-dependent quinone reductase YwnB, which was

capable to reduce the host-derived catecholamines norepinephrine and adrenochrome (Zhang et al, 2022). Thus, SifR is postulated to make iron available from catecholate-Fe^{3+} complexes, taken up via the PiuBCDA transporter. While the DNA-binding activity of SifR was inhibited by *S*-alkylation of the redox-sensing Cys102 *in vitro*, the redox-sensing mechanism of SifR remains to be investigated *in vivo* (Zhang et al, 2022). Interestingly, the *catDE* operon of *B. subtilis* was shown to be controlled by two MarR/DUF24-type repressors (YodB, CatR) and the iron-sensing Fur repressor, providing a link between iron limitation and catechol degradation (Chi et al, 2010b; Pi and Helmann 2018). CatE was shown to be involved in the degradation of the endogenously produced catecholate siderophore bacillibactin to avoid accumulation of toxic catechol derivatives during iron starvation in *B. subtilis* (Pi and Helmann 2018). Thus, the quinone response is also important for removal and reduction of endogenous catecholate siderophores and utilization of host-derived catecholamine hormones in bacteria (Alghofaili et al, 2021; Pi and Helmann 2018; Zhang et al, 2022).

In *S. aureus*, MhqR controls the *mhqRED* operon, encoding the dioxygenase MhqE and phospholipase/carboxylesterase MhqD (Fritsch et al, 2019). MhqR does not sense quinones via thiol-based redox switches or *S*-alkylation mechanisms. We hypothesize that quinones bind to a specific ligand-binding pocket, which is conserved in MarR-type regulators (Grove 2017; Perera and Grove 2010; Wilkinson and Grove 2006), resulting in conformational changes of the DNA-binding helix-turn-helix (HTH) motifs and dissociation of MhqR from the promoter DNA (Linzner et al, 2021). The MarR/DUF24-family QsrR repressor of *S. aureus* resembles a two-Cys-type redox-sensing regulator, which has three Cys residues in positions 4, 29 and 32 (numbering based on the *S. aureus* COL QsrR sequence). Of note, the QsrR protein of *S. aureus* Newman (NWMN_2027) is annotated with an additional N-terminal Met residue, leading to the renumbering of Cys5, Cys30 and Cys33 in the previous study (Ji et al, 2013). For unification, we refer to the *S. aureus* COL numbering of Cys4, Cys29 and Cys32 regarding QsrR regulation throughout the manuscript. The N-terminal redox-sensing Cys is conserved across the MarR/DUF24-family of regulators, including YodB, CatR and HypR of *B. subtilis* and QsrR of *S. aureus* (Antelmann and Helmann 2011; Ji et al, 2013; Linzner et al,

2021; Yurimoto et al, 2005). These MarR/DUF24 proteins harbor the HxlR-type winged HTH domain (IPR002577) of 90-100 aa (https://www.ebi.ac.uk/interpro/), first described for the formaldehyde-sensing HxlR regulator of *B. subtilis* (Yurimoto et al, 2005). QsrR has been shown to sense quinones by thiol-*S*-alkylation of the conserved Cys4 *in vitro*, leading to structural changes and derepression of the transcription of the QsrR-controlled dioxygenases (CatE, CatE2) and quinone reductases (AzoR1, YodC) (Ji et al, 2013). However, this thiol-*S*-alkylation model and the structural changes were shown for the single Cys QsrR protein lacking the Cys29 and Cys32 residues *in vitro* (Ji et al, 2013). According to our previous RNA-seq analyses, the QsrR regulon was strongly induced under oxidative and electrophile stress, such as MHQ, lapachol, HOCl, allicin and AGXX® stress in *S. aureus* (Fritsch et al, 2019; Linzner et al, 2020; Linzner et al, 2021; Loi et al, 2018a; Loi et al, 2018b; Loi et al, 2019). Thus, we hypothesize that QsrR might sense ROS, generated in the oxidative mode of quinones, and disulfide stress by strong oxidants and antimicrobials due to intersubunit disulfide formation between the conserved Cys4 and the Cys29' or Cys32' residues of opposing subunits, as revealed for the homologous YodB repressor of *B. subtilis* (Chi et al, 2010a; Linzner et al, 2021).

In this work, we have investigated the regulatory mechanisms of the QsrR repressor and the role of its three Cys residues for DNA-binding activity and redox sensing under quinone and oxidative stress in *S. aureus*. Using transcriptional analyses of the QsrR Cys4, Cys29 and Cys32 mutants, we showed that Cys4 and either Cys29 or Cys32 residues are involved in redox sensing of quinones and oxidants in *S. aureus*. Mass spectrometry revealed that QsrR senses diamide stress by intermolecular disulfides between Cys4 and Cys29', while allicin resulted in *S*-thioallylation of all three Cys residues of QsrR. Mutational phenotype analyses further supported that Cys4 and either Cys29' or Cys32' are required for redox regulation to confer resistance towards MHQ, HOCl and H_2O_2 stress in *S. aureus*. Altogether, this work has unraveled the thiol switch mechanisms of QsrR for adaptation towards oxidative and electrophile stress as well as redox-active antimicrobials in *S. aureus*.

RESULTS

1. Transcriptional induction of the QsrR regulon by quinone and oxidants requires the redox-sensing Cys4 and either Cys29 or Cys32 in *S. aureus*. Previous RNAseq analyses showed a strong up-regulation of the QsrR regulon by quinones (MHQ, lapachol) and strong oxidants (HOCl, AGXX® and allicin) in the transcriptome of *S. aureus* (Fritsch et al, 2019; Linzner et al, 2020; Loi et al, 2018a; Loi et al, 2018b; Loi et al, 2019). The QsrR regulon genes *azoR1, catE, catE2, yodC* and *SACOL0409* were most strongly induced (14-278-fold) under allicin, AGXX® and methylhydroquinone (MHQ) stress **(Table S1)**. In addition, the MhqR and QsrR regulons were previously shown to confer independent resistance to antimicrobials with quinone-like elements, such as ciprofloxacin, rifampicin and pyocyanin (Fritsch et al, 2019; Noto et al, 2017). Thus, we analyzed transcription of the *catE2* and *qsrR* genes upon exposure to different thiol-reactive compounds and antibiotics. Northern blot analyses verified the strong transcriptional induction of *catE2* (25-48-fold) and *qsrR* (3-10-fold) under MHQ, diamide, AGXX® and allicin stress in *S. aureus* **(Fig. 1A, B)**. The *catE2* gene was only weakly ~2-fold upregulated by different antibiotics, formaldehyde and methylglyoxal stress in *S. aureus*, while erythromycin and rifampicin caused a 10.7 and 4.1-fold transcriptional induction of the *qsrR* gene **(Fig. 1A, B)**. These data suggest that QsrR might potentially sense and respond to quinones and strong oxidants, which cause disulfide stress in *S. aureus*.

Next, we used quantitative Northern blot analyses to investigate the roles of the three Cys residues (Cys4, Cys29 and Cys32) of QsrR for redox sensing and DNA-binding activity under quinone and disulfide stress *in vivo* **(Fig. 1C-H)**. Transcription of *catE2* was analyzed in the *qsrR* mutant complemented with *qsrR* and the *qsrR C4S*, *C29S* and *C32S* mutant alleles. We further confirmed that QsrR and the QsrR Cys mutant proteins are expressed in *S. aureus* **(Fig. S1)**. The Northern blot analysis revealed that *catE2* is fully >80-fold derepressed in the *qsrR* mutant, and repression could be restored in the *qsrR* complemented strain **(Fig. 1C-H)**. Due to the strong autoregulation of *qsrR* expression in the WT after thiol stress, the basal level of *catE2* transcription was higher in the *qsrR* complemented strain **(Fig. 1C-H)**. While *catE2* transcription was fully inducible in the *qsrR* complemented strain after MHQ, diamide and allicin

stress, the C4S mutant failed to respond significantly to MHQ and diamide stress **(Fig. 2C-F)**. There was only a weak 3-fold induction of *catE2* transcription in the C4S mutant under allicin stress **(Fig. 1G, H)**. Thus, Cys4 was clearly identified as redox-sensing Cys, which is required for the responsiveness of QsrR to quinones and disulfide stress in *S. aureus in vivo* **(Fig. 1C-F)**. However, while both C29S and C32S mutants showed a similar strong response to MHQ and diamide as the WT protein, the C29,32S double mutant was unresponsive and did not show increased *catE2* transcription under thiol-stress **(Fig. 1C-F)**. This indicates that Cys4 and either Cys29 or Cys32 are required for redox sensing of QsrR and transcriptional induction of the QsrR regulon under MHQ and diamide stress *in vivo*. In contrast, a significant induction of *catE2* transcription was measured in the C29S, C32S and C29,32S mutants after allicin stress, supporting that the allicin response requires only Cys4 **(Fig. 1G, H)**. Thus, the redox-sensing mechanisms of QsrR differ between MHQ, diamide and allicin stress. In addition, the C29S, Cys32S and C29,32S mutants were slightly impaired in DNA binding as revealed by the higher basal level of *catE2* transcription **(Fig. 1C-H)**.

2. The Cys residues do not affect the DNA-binding activity of QsrR to the specific QsrR operator sequence *in vitro*. Gel shift assays were used to investigate the DNA-binding activity of QsrR and the single C4S, C29S and C32S mutant proteins to the palindromic QsrR operator in the *catE2* and *qsrR* promoter regions as previously defined with the consensus sequence GTATA-N_5-TATAC (Ji et al, 2013). QsrR was shown to bind with high affinity to the *catE2* and *qsrR* upstream promoter regions **(Fig. 2A, B)**. The dissociation constants (K_D) of QsrR were calculated as 68.3 nM for the *catE2* promoter and as 112.4 nM for the *qsrR* promoter **(Fig. 2C, D)**. The C4S, C29S and C32S mutant proteins showed similar DNA-binding affinities and their K_D values for the *catE2* promoter were determined as 61.5 nM, 66.5 nM and 61.1 nM and for the *qsrR* promoter as 103.7 nM, 105.4 nM and 105.5 nM, respectively. Thus, the single Cys mutations do not affect the DNA-binding activity of QsrR *in vitro* **(Fig. 2A-D)**. However, the Cys29,32S double mutant might reveal the role of the Cys residues in DNA binding *in vitro* as was shown by the transcriptional assays *in vivo* **(Fig. 1C-H)**.

The specificity of QsrR binding to the *catE2* and *qsrR* promoter regions was verified using the upstream promoter region of the unrelated *trxA* and *yceI* genes and mutated *qsrR* promoter probes (m1, m2) with two base substitutions in each half of the inverted repeat sequence **(Fig. 2E)**. QsrR was unable to bind to the *trxA* and *yceI* promoters or to the mutated *qsrR* promoter probes, supporting the specific DNA-binding activity to the QsrR operator sequence.

3. Quinones, diamide and HOCl lead to reversible inhibition of the DNA-binding activity of QsrR *in vitro*, which depends on Cys4 and Cys29. Next, we used EMSAs to study the role of the three Cys residues of QsrR for redox sensing of quinones, diamide and HOCl stress *in vitro*. Previously, BQ was shown to inhibit the DNA-binding activity of the QsrRC29,32S mutant protein *in vitro* due to thiol-*S*-alkylation of the redox-sensing Cys4 (Ji et al, 2013). However, the reversibility of the effect of quinones on the DNA-binding activity of the QsrR WT protein and the three Cys mutants has not been analyzed in the previous study (Ji et al, 2013). Treatment of QsrR with increasing concentrations of MHQ (0.25–20 μM) resulted in dissociation of QsrR from the *catE2* and *qsrR* promoter regions **(Fig. 3A, B)**. DNA binding of MHQ-treated QsrR could be almost restored after treatment with 10 mM DTT, indicating that MHQ acts mainly via the oxidative mode, leading to reversible thiol-oxidation and inactivation of QsrR **(Fig. 3C, D)**. DNA-binding assays of the three Cys mutants in the presence of MHQ revealed that Cys4 is essential for redox sensing of QsrR, since the DNA-binding activity of the C4S mutant to the *catE2* and *qsrR* operators was not inhibited by MHQ **(Fig. 3A, B)**. While the C32S mutant showed a similar response to quinones as the QsrR WT protein, the C29S mutant was less sensitive to inactivation by MHQ, indicating that Cys29 is partly involved in quinone sensing **(Fig. 3A, B)**. Furthermore, the DNA-binding activities of the quinone-treated C29S and C32S mutant proteins could be almost restored after DTT reduction, supporting that QsrR, the C29S and C32S mutants are reversibly oxidized by MHQ *in vitro* **(Fig. 3C, D)**. In conclusion, while Cys4 is essential for MHQ sensing, the non-conserved Cys29 functions also in redox regulation of QsrR *in vitro*, involving a reversible thiol switch mechanism.

Since the QsrR regulon was strongly induced under disulfide stress **(Fig. 1A, B)**, we analyzed the effect of diamide and HOCl on the DNA-binding activity of QsrR and its Cys mutants. Treatment of QsrR with 25-50 μM diamide resulted in its partial release from the *catE2* promoter region **(Fig. 4A)**. DNA-binding activity of diamide-treated QsrR could be restored by DTT reduction, indicating that QsrR is reversibly oxidized and inactivated by a thiol switch mechanism in response to diamide stress **(Fig. 4A)**. The comparison of the DNA-binding activities of QsrR and the three Cys mutants to the *catE2* and *qsrR* promoters after diamide treatment revealed that Cys4 is required for redox sensing of diamide, since the C4S mutant did not respond to disulfide stress **(Fig. 4B-E)**. However, the DNA-binding activities of the C29S and C32S mutants were inhibited by diamide stress, indicating that both Cys residues are not essential or can replace each other for redox sensing of disulfide stress **(Fig. 4B-E)**. The unresponsiveness of the C4S mutant to diamide was reflected by the K_D values, which were determined for the *catE* and *qsrR* promoters as 61.1 nM and 102.9 nM, respectively. These K_D were similar under oxidized and reduced conditions **(Fig. 2C, D and Fig. 4D, E)**. In contrast, the K_D values of QsrR and the QsrRC32S mutant protein increased after diamide treatment to a similar extent for the *catE2* (337.5 nM and 325.5 nM) and *qsrR* promoters (291.9 nM and 295.6 nM), respectively, indicating that Cys32 is not involved in diamide sensing **(Fig. 4D, E)**. A slightly decreased K_D value of the QsrRC29S mutant protein was estimated for the *catE2* (296.3 nM) and *qsrR* promoters (266.2 nM) in response to diamide treatment **(Fig. 4D, E)**. These results support that Cys4 and Cys29 of QsrR are involved in redox sensing of strong oxidants, such as diamide stress *in vitro*.

Similarly, HOCl treatment resulted in decreased DNA-binding activity of QsrR and the C29S and C32S mutant proteins to the *catE2* and *qsrR* promoters, indicating that Cys29 and Cys32 are dispensable or can replace each other for redox sensing of HOCl stress *in vitro* **(Fig. 5A, B)**. The DNA-binding activities of the diamide-treated QsrR, the C29S and C32S mutants could be restored with DTT, supporting that QsrR responds via thiol switch mechanisms **(Fig. 5C, D)**. In contrast, the C4S mutant was impaired in redox sensing and did not respond to HOCl stress in the DNA-binding assays *in vitro* **(Fig. 5A, B)**. The

unresponsiveness of the C4S mutant towards HOCl stress was evident also by the low K_D values, which were determined as 63.3 nM and 103 nM for the *catE2* and *qsrR* promoters, respectively **(Fig. 5E, F)**. In contrast, the K_D values of the QsrR, QsrRC29S and QsrRC32S proteins were increased after HOCl treatment at similar levels for the *catE2* (176.3 nM, 167.8 nM and 175.5 nM) and the *qsrR* promoters (239.9 nM, 222 nM and 221 nM), respectively **(Fig. 5E, F)**. Altogether, these results revealed that QsrR is reversibly inactivated under quinone and disulfide stress *in vitro*, which requires Cys4 and in part Cys29 for redox sensing *in vitro*.

4. QsrR senses disulfide stress and quinones by intermolecular disulfides between Cys4 and Cys29' *in vitro* and *in vivo*. To reveal the redox-sensing mechanism of QsrR under quinone and disulfide stress *in vitro*, thiol-oxidations of QsrR and the QsrR Cys mutant proteins were analyzed by non-reducing SDS-PAGE **(Fig. 6)**. Exposure to diamide and HOCl resulted in QsrR oxidation and formation of an intermolecular disulfide band with the size of ~30 kDa, which was reversible with DTT **(Fig. 6A, B)**. These QsrR intermolecular disulfides were also visible after MHQ treatment, although less pronounced compared to diamide-treated QsrR **(Fig. 6A, C)**. The oxidation to intermolecular disulfides was observed also in the C29S and C32S mutants after diamide and HOCl treatment, but not in the C4S mutant, supporting that Cys4 is the redox-sensing Cys and involved in intersubunit disulfide formation *in vitro* **(Fig. 6D, E)**. To monitor QsrR oxidation to intermolecular disulfides *in vivo*, we performed non-reducing Western blot analyses of *S. aureus* complemented strains expressing the His-tagged QsrR, C4S, C29S, C32S and C29,32S proteins. The protein extracts were harvested after alkylation with IAM in the dark to block reduced thiols in *S. aureus* cells. While the Western blot results revealed the oxidation of the QsrR WT and C29S, C32S and C29,32S mutant proteins to the intersubunit disulfides upon diamide stress in *S. aureus* cells, the C4S mutant was unable to form intermolecular disulfides upon diamide stress *in vivo* **(Fig. 7A)**. The intermolecular QsrR disulfides were reversible in the reducing SDS-PAGE analysis **(Fig. 7B)**. These results support the critical role of Cys4 in redox sensing of disulfide stress by an intersubunit thiol switch mechanism in *S. aureus*.

Next, we were interested to identify the cross-linked Cys residues in the QsrR disulfide after diamide stress *in vitro*. The reduced QsrR and oxidized QsrR intermolecular disulfide bands were tryptic in-gel digested and the peptides subjected to LC-MS/MS analysis **(Fig. 8)**. The Mascot search results identified two main disulfide cross-linked peptides **(Fig. 8A, B)**, which were present in the oxidized QsrR disulfide band but not in the reduced QsrR sample as revealed by the extracted ion chromatogram **(Fig. 8C, D)**. These oxidized disulfide peptides include the Cys4-Cys29' disulfide with the monoisotopic mass of 3089.221 Da **(Fig. 8A)** and the Cys4-Cys4' intermolecular disulfide with the monoisotopic mass of 3321.4477 Da **(Fig. 8B)** as revealed by the MS/MS spectra. The Cys4-Cys32' disulfide peptide was not detected in the diamide-treated QsrR sample. According to the previously characterized YodB mechanism (Chi et al, 2010a; Lee et al, 2016), QsrR is most likely oxidized to Cys4-Cys29' intermolecular disulfides, which have been reshuffled to Cys4-Cys4' disulfides *in vitro* due to the high reactivity of the redox-sensing Cys4. These results are in agreement with our Northern blots, indicating that Cys4 and either Cys29' or Cys32' are required for redox sensing of diamide and MHQ *in vivo* **(Fig. 1C-F)**. Thus, QsrR senses quinones and oxidants by Cys4-Cys29' intersubunit disulfide formation, leading to the derepression of transcription of the QsrR regulon.

5. Allicin causes *S*-thioallylation of QsrR, leading to inhibition of DNA binding *in vitro*. Transcription of the QsrR regulon was strongly upregulated by the organosulfur compound allicin **(Fig. 1A, B; Table S1)**. The mode of action of allicin involves widespread *S*-thioallylations of protein and low molecular weight thiols in bacteria and human cells (Chi et al, 2019; Gruhlke et al, 2019; Loi et al, 2019). Thus, we were interested whether QsrR is redox-controlled by formation of intersubunit disulfides or *S*-thioallylations after allicin treatment. In gel-shift assays, the DNA-binding activity of QsrR to the *catE2* and *qsrR* promoters was reversibly inhibited after allicin treatment **(Fig. 9A)**. The non-reducing SDS-PAGE analyses revealed no formation of the intermolecular disulfide in the QsrR protein after exposure to allicin **(Fig. 9B)**. Thus, we hypothesized that allicin might cause *S*-thioallylation of the Cys residues of QsrR, leading to its inactivation and relief of repression. The thiol-modifications of untreated

and allicin-treated QsrR bands were investigated by MALDI-TOF MS analysis after in-gel tryptic digestion. The MS1 scans of the peptides in the reduced QsrR sample showed the carbamidomethylated Cys4 peptide with the mass of 1703.85 Da and the carbamidomethylated Cys29,32 peptide with the mass of 1471.64 Da, indicating that Cys4, Cys29 and Cys32 are reduced in the QsrR control sample **(Fig. 9C, D, upper panel)**. In the allicin-treated QsrR protein sample, all three Cys residues were found to be *S*-thioallylated as revealed by the mass shift of 72 Da for $C_3H_5S_1$ at Cys residues. In the MS1 spectra, the *S*-thioallylated Cys4 peptide was identified with the mass of 1718.82 Da (1646.7440+72 Da) and the Cys29,32 peptide with the mass of 1501.58 Da (1357.4970+144 Da) **(Fig. 9C, D, lower panel)**. Of note, the Cys4 peptide was also identified with a dethiomethylated methionine sulfoxide in the reduced and *S*-thioallylated samples, as labelled in the MS1 spectra with the mass peaks of 1655.85 Da and 1670.83 Da, respectively. Overall, these data clearly confirm that allicin causes *S*-thioallylation of all three Cys residues in QsrR, leading to its inactivation and the strong induction of the QsrR regulon in allicin-treated *S. aureus* cells **(Fig. 1A, B)**. Moreover, the *S*-thioallylation at Cys4 alone in the C29,32S mutant might be sufficient to cause conformational and structural changes, leading to derepression of *catE2* transcription (**Fig. 1G, H)**.

6. The QsrR regulon confers resistance towards quinones and oxidants, which depends on Cys4 and either Cys29' or Cys32'. Previously, the *qsrR* deletion mutant has been shown to confer resistance towards quinone stress in *S. aureus* (Fritsch et al, 2019; Ji et al, 2013). Since QsrR responds to quinone and disulfide stress by different thiol switches, we investigated the growth and survival phenotypes of the *qsrR* mutant and Cys mutant strains under MHQ, H_2O_2, HOCl and allicin stress in *S. aureus*. Consistent with previous data (Fritsch et al, 2019; Ji et al, 2013), the *qsrR* mutant was not affected in growth after 100 µM MHQ stress and showed a 3-17-fold increased survival after treatment with 250 µM MHQ, supporting that the QsrR regulon contributes most strongly to the quinone resistance in *S. aureus* **(Fig. 10A, E)**. In growth curves, the *qsrR* mutant was only slightly more resistant after exposure to

sublethal doses of 10 mM H_2O_2, 1.5 mM HOCl and 0.3 mM allicin stress as compared to the WT **(Fig. 10B-D)**. However, in survival assays the *qsrR* mutant was significantly more resistant to the oxidants than the WT and showed an increased survival after treatment with lethal doses of 40 mM H_2O_2, 2 mM HOCl and 0.5 mM allicin **(Fig. 10F-H)**. All growth and survival phenotypes could be reversed to WT levels in the *qsrR* complemented strain **(Fig. 10E-H; Fig. S3A-D)**.

The phenotypes of the QsrR Cys mutants were analyzed regarding the resistance against MHQ, H_2O_2 and HOCl stress in comparison to the *qsrR* complemented strain **(Fig. 10I-K; Fig. S4)**. The QsrRC4S mutant showed a significantly decreased survival after MHQ, H_2O_2 and HOCl exposure as compared the *qsrR* complemented strain, supporting its redox-sensing function under quinone and oxidative stress. In addition, the C32S mutant showed similar survival rates as the *qsrR* complemented strain after exposure to these stressors, indicating that Cys32 is not involved in redox sensing. While the C29S mutant showed a slightly reduced survival after MHQ, H_2O_2 and HOCl stress than the *qsrR* complemented strain, the Cys29,32S double mutant was similarly sensitive as the C4S mutant to the oxidants **(Fig. 10I-K)**. These data support that both Cys4 and Cys29 residues are required for redox-regulation of QsrR by Cys4-Cys29' intersubunit disulfide formation *in vivo*.

DISCUSSION

In this manuscript, we have shown that the quinone-sensing QsrR repressor is redox-controlled by different thiol switch mechanisms to sense quinones and disulfide stress in *S. aureus*. QsrR belongs to the MarR/DUF24 family of winged HTH transcriptional regulators, which possess the highly conserved HxlR-type HTH domain (IPR002577) and are widely distributed across firmicutes, actinobacteria, bacteroidetes, proteobacteria and euryarchaeota **(Figure S6)**. All HxlR-type HTH domain proteins share the conserved N-terminal Cys4 residue of QsrR, which was shown to be essential for redox-sensing in the MarR/DUF24-homologs HxlR, YodB, CatR and HypR of *B. subtilis* and QsrR of *S. aureus* **(Figure S7)** (Chi et al, 2010a; Chi et al, 2010b; Ji et al, 2013; Leelakriangsak et al, 2008; Palm et al, 2012; Yurimoto et al, 2005). Additionally, most MarR/DUF24-family regulators have one or two Cys residues at non-conserved positions, suggesting that these could also function as two-Cys regulators. Interestingly, while Cys29 of QsrR was found widely conserved in homologs across *Staphylococcus* species, Cys101 of YodB showed some conservation in homologs of *Bacillus* species, supporting the common regulatory model of QsrR and YodB by intersubunit disulfide formation in response to oxidative stress **(Figure S7)**. However, there are other MarR/DUF24 homologs, such as HxlR, which harbor only the conserved Cys and might use monothiol mechanisms for redox sensing (Yurimoto et al, 2005).

QsrR was previously shown to respond to BQ by thiol-*S*-alkylation of the redox-sensing Cys4 to control the ring-cleavage dioxygenases (CatE, CatE2) and quinone reductases (AzoR1, YodC) in *S. aureus* (Ji et al, 2013). However, the *S*-alkylation model has been shown for the C29,32S mutant protein *in vitro*, but not for the QsrR WT protein containing three Cys residues *in vivo* (Ji et al, 2013). In addition, the reversibility of the QsrR response to quinones and other thiol-reactive compounds was not investigated in the previous study (Ji et al, 2013). In our earlier RNAseq transcriptome data and the Northern blot results of this manuscript, the QsrR regulon was found to respond most strongly to MHQ and strong oxidants, including diamide, HOCl, allicin and AGXX®, which cause disulfide stress in *S. aureus* (Fritsch et al, 2019; Loi et al, 2018a; Loi et al, 2018b; Loi et al, 2019). Similarly, the QsrR-homologue YodB

was shown to sense and respond to quinones and diamide by a thiol switch mechanism in *B. subtilis* (Chi et al, 2010a; Chi et al, 2010b), indicating that QsrR might be not directly alkylated by quinones, but rather senses the oxidative mode of quinones *in vivo*. While the YodB-regulated CatE was active as catechol-2,3-dioxygenase in catechol detoxification to generate 2-hydroxymuconic semialdehyde, the azoreductases AzoR1 and AzoR2 were involved in quinone and diamide reduction in *B. subtilis* (Antelmann et al, 2008; Tam le et al, 2006). Additionally, the SifR-controlled catechol-2,3-dioxygenase CatE and NAD(P)H-dependent quinone reductase YwnB were shown to catalyze detoxification of catechol iron complexes and catecholamine stress hormones in *S. pneumoniae* (Zhang et al, 2022). Based on their induction by strong oxidants, the QsrR-controlled enzymes CatE, CatE2, YodC and AzoR1 might function in quinone, diamide and allicin detoxification in *S. aureus*.

Phenotype assays revealed that the QsrR regulon conferred the strongest protection against quinones, but also mediated significant resistance under H_2O_2, HOCl and allicin stress. Our data further revealed that QsrR responds rather to the oxidative mode of quinones as well as strong oxidants, which cause disulfide stress in *S. aureus*. The toxicity of BQ was previously shown to be related to its *S*-alkylation and oxidative mode (Kumagai et al, 2002; Monks et al, 1992; O'Brien 1991). In *B. subtilis*, we could confirm that BQ can act via both the alkylation and oxidative mode, depending on the quinone concentration and the capacity of cells for detoxification and reduction of quinones (Liebeke et al, 2008). While sublethal doses of BQ caused the reversible thiol-oxidation of GapDH in the redox proteome of *B. subtilis,* supporting the oxidative mode of BQ, higher lethal doses resulted in aggregation and depletion of thiol-containing proteins by the thiol-*S*-alkylation chemistry (Liebeke et al, 2008). However, the alkylation mode was always accompanied by cell death due to the irreversible protein damage and depletion of thiol-containing proteins and LMW thiols (Liebeke et al, 2008). Thus, under physiological conditions, QsrR should sense rather the oxidative mode of sublethal doses of quinones to induce the quinone detoxification enzymes, which enables the recovery of the cells from quinone stress. In the alkylation mode, the quinone response would not be reversible since the *S*-alkylated proteins cannot be repaired, indicating no shutdown of the quinone

response and no recovery of the cells from quinone stress, which would not be favored under *in vivo* conditions.

In this study, QsrR was shown to function as typical two-Cys-type redox-sensing regulator, which uses different thiol switch mechanisms for redox sensing of quinones and disulfide stress. The transcriptional data showed that Cys4 and either Cys29 or Cys32 are important for redox sensing of MHQ and diamide, whereas only Cys4 is required for allicin sensing. This is in agreement with the different thiol switch models of QsrR as revealed by non-reducing SDS-PAGE, mass spectrometry and Western blot analysis. While diamide and HOCl stress lead to Cys4-Cys29' intermolecular disulfide formation, allicin causes *S*-thioallylations of all three Cys residues to inhibit the repressor activity of QsrR. The DNA-binding assays confirmed that Cys4 is most important for redox sensing of QsrR upon quinone, diamide and HOCl stress *in vitro*. The K_D values of the C4S mutant were unchanged under diamide and HOCl stress compared to the untreated QsrR, indicating the unresponsiveness of the C4S mutant towards thiol stress. In contrast, the QsrR WT protein and the C29S and C32S mutants showed similar increased K_D values after quinone and disulfide stress, supporting their capability to respond to thiol stress. However, the inhibition of the QsrR DNA-binding activity by diamide, HOCl and MHQ stress was reversible with DTT, providing confirmation that thiol switch models are involved in QsrR regulation.

The thiol switch mechanisms of the QsrR repressor resemble the redox-sensing mechanisms of the OHP-sensing OhrR repressors of *B. subtilis* and *Xanthomonas campestris* (Antelmann and Helmann 2011; Hong et al, 2005; Lee et al, 2007; Mongkolsuk and Helmann 2002; Newberry et al, 2007). The one-Cys-type $OhrR_{BS}$ protein of *B. subtilis* senses OHP and HOCl stress via its single Cys15 residue by *S*-bacillithiolation (Antelmann and Helmann 2011; Chi et al, 2011; Lee et al, 2007), whereas the two-Cys-type $OhrR_{XC}$ homolog of *X. campestris* forms intermolecular disulfides between Cys22 and Cys127' leading to conformational changes in the winged HTH motif and dissociation of OhrR from the operator DNA (Newberry et al, 2007; Panmanee et al, 2006). Moreover, the one-Cys OhrR protein could be converted to a two-Cys-type redox sensor by introduction of a C-terminal Cys residue by either G120C

or Q124C mutations, resulting in intersubunit disulfide formation as alternative thiol switch mechanism (Soonsanga et al, 2008). Similarly as QsrR, the YodB repressor of *B. subtilis* was demonstrated to sense quinones and diamide by intersubunit disulfide formation between Cys6 and either of the C-terminal Cys101' or Cys108' residues *in vitro* and *in vivo* (Chi et al, 2010a; Linzner et al, 2021).

The structural mechanism of YodB inactivation by intersubunit disulfide formation under diamide treatment and by *S*-alkylation of Cys6 with methyl-*p*-benzoquinone (MPBQ) has been resolved *in vitro* (Lee et al, 2016). Interestingly, while *S*-alkylation of Cys6 does not cause major conformational changes in the HTH motifs of YodB, the oxidation to the Cys6-Cys101' intersubunit disulfides under diamide stress was accompanied by large structural rearrangements (Lee et al, 2016). The structural changes of *S*-alkylated QsrR with menadione involved steric clashes with the DNA backbone, a 10° rigid-body rotation and 9Å elongation of the two QsrR monomers, but no major conformational changes in the monomer structures (Ji et al, 2013). Since Cys4 and Cys29' of adjacent subunits are 15.2Å apart in the structure of the QsrR dimer **(Fig. S5)**, formation of the Cys4-Cys29' intersubunit disulfides will require structural rearrangements, which should be incompatible with DNA binding. While Cys4 is located at the N-terminal α1 helix in the QsrR dimer interface, Cys29 and Cys32 are located in the loop region between the α2 and α3 helices. The α3 and α4 helices form together with the ß1 and ß2 sheets the winged HTH DNA-binding domains (Ji et al, 2013). While mutation of Cys29 or Cys32 showed only minor effects on the DNA-binding activity of QsrR *in vivo*, the Cys4-Cys29' intersubunit disulfide might cause conformational changes in the winged HTH motifs, leading to dissociation of the QsrR repressor from the operator DNA as revealed by the gel shift assays.

Apart from the Cys4-Cys29' intermolecular disulfide, the MS data identified also Cys4-Cys4' crosslinks, which are most likely *in vitro* artefacts due to reshuffling of Cys4-Cys29' peptides. The distance between Cys4 and Cys4' of both subunits is 27Å **(Fig. S5)**, which is too far apart for disulfide bond formation. The Cys4-Cys4' disulfide is also not physiologically relevant because the Cys29,32S mutant did not respond to diamide and MHQ stress in

transcriptional studies *in vivo*. Moreover, in phenotype analyses both Cys4 and Cys29,32S mutants were sensitive in survival assays after oxidative stress, supporting that Cys4 and either Cys29' or Cys32' are important for redox sensing and engaged in intersubunit disulfide formation *in vivo*. Similar intermolecular thiol switch models were revealed as common redox-sensing mechanism in two-Cys-type MarR-family redox sensors, such as $OhrR_{XC}$ (Newberry et al, 2007), $HypR_{Bs}$ (Palm et al, 2012), $YodB_{Bs}$ (Chi et al, 2010a) and the Rrf2-family regulator $HypR_{Sa}$ (Loi et al, 2018b), supporting the Cys4-Cys29' intermolecular disulfide model of QsrR as revealed in this work.

In addition, we found that QsrR senses allicin by *S*-thioallyalation of all three Cys residues, leading to the reversible inactivation of the QsrR repressor. Since the C29,32S mutant still responded to allicin in transcriptional analyses *in vivo*, *S*-thioallylation of Cys4 might be sufficient for repressor inactivation, causing similar structural changes as observed for *S*-alkylation of Cys4 by quinones (Ji et al, 2013). The *S*-thioallylation of the redox-sensing Cys residues of YodB, HypR and $OhrR_{BS}$ was previously found in *B. subtilis* cells under allicin stress *in vivo*, resulting in up-regulation of the corresponding regulons in the transcriptome (Chi et al, 2019). In addition, the single Cys OhrR repressor of *B. subtilis* was shown to be inactivated by *S*-bacillithiolation under HOCl and OHP stress, resulting in derepression of the *ohrA* gene, encoding a peroxiredoxin, which confers resistance towards OHP and HOCl stress (Chi et al, 2011; Lee et al, 2007). Thus, *S*-thioallylation of QsrR at the conserved Cys4 might cause similar structural changes as observed for the *S*-bacillithiolated $OhrR_{BS}$ or the menadione-alkylated monothiol QsrR repressor (Ji et al, 2013).

Finally, the quinone-sensing QsrR and MhqR regulons were previously shown to confer resistance to antimicrobials with quinone-like elements, including ciprofloxacin, rifampicin and pyocyanin in *S. aureus* (Fritsch et al, 2019; Noto et al, 2017). While QsrR conferred stronger resistance to MHQ, the MhqR regulon showed a better protection against the quinone-like antimicrobials pyocyanin, ciprofloxacin, norfloxacin and rifampicin in *S. aureus* (Fritsch et al, 2019). Ciprofloxacin belongs to the fluoroquinolone antibiotics, which are frequently applied in the clinics for the treatment of patients with *S. aureus* infections. While the target of

ciprofloxacin is the DNA gyrase, the bacterial killing has been associated with ROS generation (Dwyer et al, 2007; Phillips-Jones and Harding 2018). Pyocyanin is a blue-colored redox-active phenazine antibiotic produced by the pathogen *Pseudomonas aeruginosa* (Price-Whelan et al, 2006), which causes cystic fibrosis and often co-occurs together with *S. aureus* during wound and respiratory tract infections in cystic fibrosis patients (Biswas and Gotz 2021). Pyocyanin was shown to generate ROS as toxicity mechanism (Mahajan-Miklos et al, 1999; Noto et al, 2017), but its redox-cycling activity further contributed to the proton motive force, ATP generation, redox homeostasis and biofilm formation in *P. aeruginosa* (Dietrich et al, 2008; Glasser et al, 2014; Price-Whelan et al, 2007). The resistance of the *qsrR* mutant to quinone-like antimicrobials might be caused either by diminishing ROS produced by the antibiotics or by the degradation or reduction of the compounds by the QsrR-controlled catechol-2,3-dioxygenases (CatE, CatE2) and quinone reductases (AzoR1, YodC) (Noto et al, 2017).

Taken together, our results revealed that two-Cys-type MarR-type redox sensors, such as QsrR, can sense different redox-active compounds via distinct thiol switches, including intersubunit disulfides or *S*-thiolations, which lead to inactivation of the repressor function and induction of detoxification pathways with broad specificities for thiol-reactive oxidants and electrophiles. While the *S*-alkylation model might be relevant under toxic quinone concentrations, QsrR might sense mainly the oxidative mode via thiol switches upon exposure of cells to sublethal doses of quinones or quinone-like antimicrobials. Future studies should be directed to elucidate the thiol-disulfide reductase pathways responsible to regenerate reduced QsrR upon recovery from quinone and oxidative stress in *S. aureus*.

INNOVATION

Staphylococcus aureus is a major human pathogen, which has to cope with oxidative and electrophile stress as well as redox-active antibiotics during infections. In this work, we have shown that the MarR/DUF24-family regulator QsrR senses and responds not only to quinones and quinone-like antimicrobials, but also to strong oxidants, such as diamide, HOCl and allicin stress. Using transcriptional studies, DNA binding assays and mass spectrometry, QsrR was

shown to sense disulfide stress by diamide and allicin via different thiol-switches, which involve Cys4 and Cys29'. Thus, QsrR allows the adaptation of *S. aureus* towards quinones, antimicrobials and strong oxidants via reversible thiol-switch mechanisms.

MATERIALS AND METHODS

Bacterial strains, growth and survival assays. Bacterial strains and primers are listed in **Tables S2 and S3**. *Escherichia coli* strains were cultivated in Luria broth (LB) medium for plasmid construction and protein expression. For growth and survival assays, *S. aureus* strains were cultivated in RPMI medium with 0.75 µM $FeCl_3$ and 2 mM glutamine as supplements as described previously (Dorries and Lalk 2013). The strains were exposed to the thiol-reactive compounds during the exponential growth phase at an optical density at 500 nm (OD_{500}) of 0.5. Survival assays were performed by plating 100 µl of serial dilutions of *S. aureus* strains onto LB agar plates for CFUs counting. Statistical analysis was performed using the Student's unpaired two-tailed *t*-test. The chemicals MHQ, H_2O_2, diamide, methylglyoxal, formaldehyde and the antibiotics were purchased from Sigma Aldrich. NaOCl was purchased from Honeywell Fluka. NaOCl dissociates in aqueous solution to hypochlorous acid (HOCl) and hypochlorite (OCl^-) (Estrela et al, 2002). Thus, the concentration of HOCl was determined by absorbance measurements as described previously (Winter et al, 2008). Allicin and AGXX® were generated as reported previously (Linzner and Antelmann 2021; Loi et al, 2019).

Construction of the *S. aureus* COL Δ*qsrR* mutant as well as the *qsrR, qsrRC4S*, *qsrRC29S*, *qsrRC32S* and *qsrRC29,C32S* complemented strains. The *S. aureus* COL Δ*qsrR* (*SACOL2115*) deletion mutant was constructed previously by allelic replacement via the pMAD *E. coli/S. aureus* shuttle vector (Fritsch et al, 2019). For construction of the His-tagged *S. aureus qsrR*, *qsrRC4S, qsrRC29S, qsrRC32S* and *qsrRC29,32S* complemented strains, the pRB473 plasmid was used as described (Loi et al, 2018b). The *qsrRC29S* and *qsrRC32S* sequences were amplified from plasmids pET11b-*qsrRC29S-His* and pET11b-*qsrRC32S-His*. The *qsrR* and *qsrRC4S* sequences were amplified from *S. aureus* chromosomal DNA using the primers pRB-qsrR-for-BamHI or pRB-qsrRC4S-for-BamHI and pRB-qsrR-rev-KpnI **(Table S3)**. For construction of pRB473-*qsrRC29,32S-His,* two first-round PCR products were performed using the primer pairs qsrRC29,32S-for and pRB-qsrR-rev-KpnI as well as

qsrRC29,32S-rev and pRB-qsrR-for-BamHI, respectively. The purified PCR products were fused and amplified by a second-round PCR using the primers pRB-qsrR-rev-KpnI and pRB-qsrR-for-BamHI. The PCR products were digested with *Bam*HI and *Kpn*I and inserted into pRB473. The plasmids were introduced into the Δ*qsrR* mutant *via* phage transduction as described previously (Loi et al, 2018b).

RNA isolation and Northern blot analysis. For RNA isolation, *S. aureus* strains were cultivated in RPMI medium and treated with various thiol-reactive compounds and antibiotics at an OD_{500} of 0.5 for 30 and 60 min, respectively, as indicated in the figure legends. Northern blot hybridizations were performed as described (Tam le et al, 2006; Wetzstein et al, 1992) with the digoxigenin-labeled *catE2* and *qsrR*-specific antisense RNA probes, which were synthesized *in vitro* using the T7 RNA polymerase and the specific primer pairs as described previously (Busche et al, 2018; Imber et al, 2018) and in **Table S3**.

Cloning, expression and purification of His-tagged QsrR, QsrRC4S, QsrRC29S and QsrRC32S proteins in *E. coli.* To construct the plasmids pET11b-*qsrR-His* and pET11b-*qsrRC4S-His,* the *qsrR* gene (SACOL2115) was amplified from chromosomal DNA of *S. aureus* COL using primers pET-qsrR-for-NheI or pET-qsrRC4S-for-NheI and pET-qsrR-rev-BamHI **(Table S3)**. The PCR products were digested with *Nhe*I and *BamH*I and inserted into plasmid pET11b (Novagen) **(Table S2)**. For the construction of the plasmids pET11b-*qsrRC29S-His* and pET11b-*qsrRC32S-His,* two first-round PCR products were fused and amplified by a second round of PCR as described previously (Loi et al, 2018b). For the *qsrRC29S* mutant, the primer pairs pET-qsrRC29S-for-f2 and pET-qsrR-rev-BamHI as well as pET-qsrRC29S-rev-f1 and pET-qsrR-for-NheI were used. For the *qsrRC32S* mutant, the primers pET-qsrRC32S-for-f2 and pET-qsrR-rev-BamHI as well as pET-qsrRC32S-rev-f1 and pET-qsrR-for-NheI were applied **(Table S3)**. The second-round PCR products were digested and cloned into pET11b as described above. For expression and purification of His-tagged QsrR, QsrRC4S, QsrRC29S and QsrRC32S proteins, *E. coli* BL21(DE3) plysS strains with

plasmids pET11b-*qsrR-His*, pET11b-*qsrRC4S-His*, pET11b-*qsrRC29S-His* and pET11b-*qsrRC32S-His* were cultivated in 1.5 l LB medium until the log phase at an OD_{600} of 0.7, followed by addition of 1 mM iso-propyl-β-D-thiogalactopyranoside (IPTG) for 5 h at 30°C. Recombinant His-tagged proteins were purified using His Trap™ HP Ni-NTA columns and the ÄKTA purifier liquid chromatography system as described (Loi et al, 2018b).

Electrophoretic mobility shift assays (EMSAs) of QsrR and QsrR Cys mutant proteins. For EMSAs, the 210 bp and 185 bp DNA fragments containing the upstream regions of *qsrR* and *catE2,* respectively, were amplified by PCR. The DNA-binding reactions were performed with 15 ng of the promoter region and purified His-tagged QsrR, QsrRC4S, QsrRC29S and QsrRC32S proteins for 45 min, as described previously (Loi et al, 2018b). MHQ, diamide, HOCl and allicin were added to the DNA-QsrR-complex for 30 min to observe the dissociation of QsrR from the DNA. To analyze the reversibility of the QsrR inhibition by quinones and oxidants, DTT was added for 30 min as described previously (Loi et al, 2018b).

The percentage of the protein-DNA complex formation was determined according to the band intensities of 3-4 biological replicates of the EMSAs and quantified using Image J 1.52a. The K_D values of the QsrR, C4S, C29S and C32S mutant proteins for the *catE2* and *qsrR* promoter were determined using the Graph prism software version 7.03. The detailed individual data of percentage of DNA-protein complex formation of the QsrR, QsrRC4S, QsrRC29S and QsrRC32S proteins under control conditions, diamide and HOCl stress are shown in **Table S4, S5 and S6**, respectively.

Analyses of thiol-oxidation of QsrR and the QsrR Cys mutant proteins *in vitro*. Purified QsrR and its Cys mutant proteins QsrRC4S, QsrRC29S and QsrRC32S were first pre-reduced with 10 mM DTT for 15 min. Reduced QsrR proteins were treated with increasing amounts of MHQ, diamide, HOCl and allicin, followed by alkylation with 50 mM iodoacetamide (IAM) for 30 min in the dark due to the light sensitivity and instability of IAM. The reversible thiol-oxidation

of QsrR to intermolecular disulfides was analysed by separation of the reduced and oxidized QsrR and Cys mutant proteins by non-reducing and reducing SDS-PAGE.

Mass spectrometry for identification of the QsrR disulfides and *S*-thioallylations. To identify the post-translational thiol-modifications, 5 µg of the QsrR protein was treated with 320 µM diamide or 1 mM allicin for 30 min, alkylated with IAM and separated by non-reducing SDS-PAGE. Reduced and oxidized QsrR bands were cut and in-gel tryptic digested as described previously (Loi et al, 2018b). The tryptic peptides were dissolved in 30 µl of 0.05% trifluoroacetic acid (TFA) with 5% acetonitrile, diluted 1:30, and 6 µl were analyzed by an Ultimate 3000 reverse-phase capillary nano liquid chromatography system connected to an Orbitrap Q Exactive HF mass spectrometer (Thermo Fisher Scientific). Samples were injected and concentrated on a trap column (PepMap100 C_{18}, 3 µm, 100 Å, 75 µM i.d. x 2 cm; Thermo Fisher Scientific) equilibrated with 0.05% TFA in water. After switching the trap column in-line, LC separations were performed on a reverse-phase column (Acclaim PepMap100 C_{18}, 2 µm, 100 Å, 75 µm i.d. x 25 cm, Thermo Fisher Scientific) at an eluent flow rate of 300 nl/min. The mobile phase A contained 0.1% formic acid in water, and mobile phase B contained 0.1% formic acid in 80% acetonitrile / 20% water. The column was pre-equilibrated with 5% mobile phase B, followed by an increase of 5-44% mobile phase B in 35 min. Mass spectra were acquired in a data-dependent mode utilizing a single MS survey scan (m/z 200–2,000) with a resolution of 60,000 in the Orbitrap, and MS/MS scans of the 5 most intense precursor ions with a resolution of 15,000 and a normalized collision energy of 27. All spectra were recorded in the profile mode. The isolation window of the quadrupole was set to 2.0 m/z. The dynamic exclusion time was set to 10 seconds and automatic gain control was set to $3x10^6$ and $1x10^5$ for MS and MS/MS scans, respectively.

Data processing and identification of proteins was performed using the Mascot software package (Mascot Server version 2.7, Mascot Distiller version 2.8, Mascot Daemon version 2.7, Matrix Science). During MS/MS processing, the maximum charge state was set to the precursor charge state and singly charged fragment ions were used as an output.

Processed spectra were searched against the *S. aureus* COL QsrR protein sequence with the N-terminal extension (AS) and the C-terminal His_6-tag. The pre-existing disulfide bond crosslinking method from Mascot was used, which allows for the identification of possible intramolecular (Cys29-Cys32) and intermolecular (Cys4-Cys29', Cys4-Cys32' or Cys4-Cys4') disulfides in the oxidized QsrR protein. A maximum of two missed cleavages was allowed and the mass tolerance of precursor and sequence ions was set to 10 ppm and 0.02 Da, respectively. Methionine oxidation (Met+15.994915 Da), methionine dethiomethylation (Met–48.003371) and cysteine carbamidomethylation (Cys+57.021465 Da) were set as variable modifications. A significance threshold of 0.05 was used as a cut-off and the MS/MS spectra of the identified disulfide peptides were manually checked.

The peptides of the allicin-treated QsrR sample were analysed by matrix-assisted laser desorption ionization-time of flight mass spectrometry (MALDI-TOF-MS) using an Ultraflex-II TOF/TOF instrument (Bruker Daltonics, Bremen, Germany) equipped with a 200 Hz solid-state Smart beam™ laser. Alpha-Cyano-4-hydroxycinnamic acid was used as matrix substance and the mass spectrometer was operated in the positive reflector mode. Mass spectra were acquired over an m/z range of 600–4,000. Cysteine *S*-thioallylations by allicin were identified in the MS1 spectra by the mass shift of 72.00337 Da for $C_3H_5S_1$ at Cys peptides using the Mascot software.

Western blot analyses. *S. aureus* COL cells were harvested before and 30 min after treatment with 5 mM diamide as described (Loi et al, 2018b). After washing, protein lysates were prepared in TE-buffer (pH 8.0) with 50 mM IAM using the ribolyzer. Protein lysates were separated using 18% non-reducing SDS-PAGE and subjected to Western blot analysis using anti-His_6 monoclonal antibodies (Sigma) as described previously (Loi et al, 2021; Loi et al, 2018a).

DATA AVAILABILITY STATEMENTS

All data of this manuscript are available in the figures and supplementary figures and supplementary tables. Raw data are made available on request to the corresponding author. An electronic laboratory notebook by a specific platform was not used for data collection.

AUTHOR CONTRIBUTIONS

V.N.F. and H.A. designed the concept of this project. V.N.F performed the majority of the experiments and analyzed the data. V.V.L. and V.N.F. constructed the plasmids and mutants. B.K. and C.W. performed the mass spectrometry and data analysis. M.G. contributed with allicin synthesis. H.A. and V.N.F. wrote the manuscript. H.A. provided funding and supervised the project. All authors have read, edited and approved the final manuscript.

ACKNOWLEDGEMENTS

For mass spectrometry performed by C.W. and B.K., we would like to acknowledge the assistance of the Core Facility BioSupraMol supported by the Deutsche Forschungsgemeinschaft.

.

AUTHOR DISCLOSURE STATEMENT

No competing financial interests exist.

Funding information

This work was supported by an ERC Consolidator grant (GA 615585) MYCOTHIOLOME and grants from the Deutsche Forschungsgemeinschaft (AN746/4-1 and AN746/4-2) within the SPP1710 on “Thiol-based Redox switches”, by the SFB973 project C08 and TR84 project B06 to H.A.

LIST OF ABBREVIATIONS

BQ	1,4-benzoquinone
CFUs	colony forming units
DTT	dithiothreitol
EMSA	electrophoretic mobility shift assay
IAM	iodoacetamide
IPTG	isopropyl- β-D-thiogalactopyranoside
LB	Luria Bertani
H_2O_2	hydrogen peroxide
HTH	Helix-turn-helix
HOCl	hypochlorous acid
OCl^-	hypochlorite
K_D	dissociation constant
LC	liquid chromatography
MALDI-TOF-MS	matrix-assisted laser desorption ionization-time of flight-mass spectrometry
MarR	multiple antibiotic resistance regulator
MhqR	quinone-sensing MarR-type repressor
MHQ	methylhydroquinone
MPBQ	methyl-*p*-benzoquinone
MS/MS	tandem mass spectrometry
OD_{500}	optical density at 500 nm
QsrR	quinone-sensing MarR/DUF24 repressor
RES	reactive electrophilic species
ROS	reactive oxygen species
RCS	reactive chlorine species
TCA	trifluoroacetic acid

REFERENCES

1. Alghofaili F, Najmuldeen H, Kareem BO, et al. Host Stress Signals Stimulate Pneumococcal Transition from Colonization to Dissemination into the Lungs. mBio 2021;12(6):e0256921; doi:10.1128/mBio.02569-21.

2. Antelmann H, Hecker M, Zuber P. Proteomic signatures uncover thiol-specific electrophile resistance mechanisms in *Bacillus subtilis*. Expert Rev Proteomics 2008;5(1):77-90; doi:10.1586/14789450.5.1.77.

3. Antelmann H, Helmann JD. Thiol-based redox switches and gene regulation. Antioxid Redox Signal 2011;14(6):1049-63; doi:10.1089/ars.2010.3400.

4. Archer GL. *Staphylococcus aureus*: a well-armed pathogen. Clin Infect Dis 1998;26(5):1179-81.

5. Biswas L, Gotz F. Molecular Mechanisms of Staphylococcus and Pseudomonas Interactions in Cystic Fibrosis. Front Cell Infect Microbiol 2021;11:824042; doi:10.3389/fcimb.2021.824042.

6. Borlinghaus J, Albrecht F, Gruhlke MC, et al. Allicin: chemistry and biological properties. Molecules 2014;19(8):12591-618; doi:10.3390/molecules190812591.

7. Borlinghaus J, Foerster Nee Reiter J, Kappler U, et al. Allicin, the odor of freshly crushed garlic: A review of recent progress in understanding allicin's effects on cells. Molecules 2021;26(6); doi:10.3390/molecules26061505.

8. Busche T, Hillion M, Van Loi V, et al. Comparative secretome analyses of human and zoonotic *Staphylococcus aureus* isolates CC8, CC22, and CC398. Mol Cell Proteomics 2018;17(12):2412-2433; doi:10.1074/mcp.RA118.001036.

9. Chi BK, Albrecht D, Gronau K, et al. The redox-sensing regulator YodB senses quinones and diamide via a thiol-disulfide switch in *Bacillus subtilis*. Proteomics 2010a;10(17):3155-64; doi:10.1002/pmic.201000230.

10. Chi BK, Gronau K, Mäder U, et al. *S*-bacillithiolation protects against hypochlorite stress in *Bacillus subtilis* as revealed by transcriptomics and redox proteomics. Mol Cell Proteomics 2011;10(11):M111 009506; doi:10.1074/mcp.M111.009506.

11. Chi BK, Huyen NTT, Loi VV, et al. The disulfide stress response and protein *S*-thioallylation caused by allicin and diallyl polysulfanes in *Bacillus subtilis* as revealed by transcriptomics and proteomics. Antioxidants (Basel) 2019;8(12); doi:10.3390/antiox8120605.

12. Chi BK, Kobayashi K, Albrecht D, et al. The paralogous MarR/DUF24-family repressors YodB and CatR control expression of the catechol dioxygenase CatE in *Bacillus subtilis*. J Bacteriol 2010b;192(18):4571-81; doi:10.1128/JB.00409-10.

13. Dietrich LE, Teal TK, Price-Whelan A, et al. Redox-active antibiotics control gene expression and community behavior in divergent bacteria. Science 2008;321(5893):1203-6; doi:10.1126/science.1160619.

14. Dorries K, Lalk M. Metabolic footprint analysis uncovers strain specific overflow metabolism and D-isoleucine production of *Staphylococcus aureus* COL and HG001. PLoS One 2013;8(12):e81500; doi:10.1371/journal.pone.0081500.

15. Dwyer DJ, Kohanski MA, Hayete B, et al. Gyrase inhibitors induce an oxidative damage cellular death pathway in *Escherichia coli*. Mol Syst Biol 2007;3:91; doi:10.1038/msb4100135.

16. Estrela C, Estrela CRA, Barbin EL, et al. Mechanism of action of sodium hypochlorite. Brazilian Dental Journal 2002;13(2):113-117; doi:10.1590/s0103-64402002000200007.

17. Fritsch VN, Loi VV, Busche T, et al. The MarR-type repressor MhqR confers quinone and antimicrobial resistance in *Staphylococcus aureus*. Antioxid Redox Signal 2019;31(16):1235-1252; doi:10.1089/ars.2019.7750.

18. Glasser NR, Kern SE, Newman DK. Phenazine redox cycling enhances anaerobic survival in Pseudomonas aeruginosa by facilitating generation of ATP and a proton-motive force. Mol Microbiol 2014;92(2):399-412; doi:10.1111/mmi.12566.

19. Grove A. Regulation of metabolic pathways by MarR family transcription factors. Comput Struct Biotechnol J 2017;15:366-371; doi:10.1016/j.csbj.2017.06.001.

20. Gruhlke MCH, Antelmann H, Bernhardt J, et al. The human allicin-proteome: S-thioallylation of proteins by the garlic defence substance allicin and its biological effects. Free Radic Biol Med 2019;131:144-153; doi:10.1016/j.freeradbiomed.2018.11.022.

21. Hong M, Fuangthong M, Helmann JD, et al. Structure of an OhrR-ohrA operator complex reveals the DNA binding mechanism of the MarR family. Mol Cell 2005;20(1):131-41; doi:10.1016/j.molcel.2005.09.013.

22. Imber M, Loi VV, Reznikov S, et al. The aldehyde dehydrogenase AldA contributes to the hypochlorite defense and is redox-controlled by protein S-bacillithiolation in *Staphylococcus aureus*. Redox Biol 2018;15:557-568; doi:10.1016/j.redox.2018.02.001.

23. Imlay JA. Cellular defenses against superoxide and hydrogen peroxide. Annu Rev Biochem 2008;77:755-76; doi:10.1146/annurev.biochem.77.061606.161055.

24. Jacobs AT, Marnett LJ. Systems analysis of protein modification and cellular responses induced by electrophile stress. Acc Chem Res 2010;43(5):673-83; doi:10.1021/ar900286y.

25. Ji Q, Zhang L, Jones MB, et al. Molecular mechanism of quinone signaling mediated through *S*-quinonization of a YodB family repressor QsrR. Proc Natl Acad Sci U S A 2013;110(13):5010-5; doi:10.1073/pnas.1219446110.

26. Kumagai Y, Koide S, Taguchi K, et al. Oxidation of proximal protein sulfhydryls by phenanthraquinone, a component of diesel exhaust particles. Chem Res Toxicol 2002;15(4):483-9; doi:tx0100993 [pii].

27. Lee JW, Soonsanga S, Helmann JD. A complex thiolate switch regulates the *Bacillus subtilis* organic peroxide sensor OhrR. Proc Natl Acad Sci U S A 2007;104(21):8743-8; doi:10.1073/pnas.0702081104.

28. Lee SJ, Lee IG, Lee KY, et al. Two distinct mechanisms of transcriptional regulation by the redox sensor YodB. Proc Natl Acad Sci U S A 2016;113(35):E5202-11; doi:10.1073/pnas.1604427113.

29. Leelakriangsak M, Huyen NT, Towe S, et al. Regulation of quinone detoxification by the thiol stress sensing DUF24/MarR-like repressor, YodB in *Bacillus subtilis*. Mol Microbiol 2008;67(5):1108-24; doi:10.1111/j.1365-2958.2008.06110.x.

30. Liebeke M, Pöther DC, van Duy N, et al. Depletion of thiol-containing proteins in response to quinones in *Bacillus subtilis*. Mol Microbiol 2008;69(6):1513-29; doi:10.1111/j.1365-2958.2008.06382.x.

31. Linzner N, Antelmann H. The antimicrobial activity of the AGXX$^{(R)}$ surface coating requires a small particle size to efficiently kill *Staphylococcus aureus*. Front Microbiol 2021;12:731564; doi:10.3389/fmicb.2021.731564.

32. Linzner N, Fritsch VN, Busche T, et al. The plant-derived naphthoquinone lapachol causes an oxidative stress response in *Staphylococcus aureus*. Free Radic Biol Med 2020;158:126-136; doi:10.1016/j.freeradbiomed.2020.07.025.

33. Linzner N, Loi VV, Fritsch VN, et al. Thiol-based redox switches in the major pathogen *Staphylococcus aureus*. Biol Chem 2021;402(3):333-361; doi:10.1515/hsz-2020-0272.

34. Loi VV, Busche T, Fritsch VN, et al. The two-Cys-type TetR repressor GbaA confers resistance under disulfide and electrophile stress in *Staphylococcus aureus*. Free Radic Biol Med 2021;177:120-131; doi:10.1016/j.freeradbiomed.2021.10.024.

35. Loi VV, Busche T, Preuss T, et al. The AGXX antimicrobial coating causes a thiol-specific oxidative stress response and protein *S*-bacillithiolation in *Staphylococcus aureus*. Front Microbiol 2018a;9:3037; doi:10.3389/fmicb.2018.03037.

36. Loi VV, Busche T, Tedin K, et al. Redox-sensing under hypochlorite stress and infection conditions by the Rrf2-family repressor HypR in *Staphylococcus aureus*. Antioxid Redox Signal 2018b;29(7):615-636; doi:10.1089/ars.2017.7354.

37. Loi VV, Huyen NTT, Busche T, et al. *Staphylococcus aureus* responds to allicin by global *S*-thioallylation - role of the Brx/BSH/YpdA pathway and the disulfide reductase MerA to overcome allicin stress. Free Radic Biol Med 2019;139:55-69; doi:10.1016/j.freeradbiomed.2019.05.018.

38. Loi VV, Rossius M, Antelmann H. Redox regulation by reversible protein *S*-thiolation in bacteria. Front Microbiol 2015;6:187; doi:10.3389/fmicb.2015.00187.

39. Mahajan-Miklos S, Tan MW, Rahme LG, et al. Molecular mechanisms of bacterial virulence elucidated using a Pseudomonas aeruginosa-Caenorhabditis elegans pathogenesis model. Cell 1999;96(1):47-56; doi:10.1016/s0092-8674(00)80958-7.

40. Marnett LJ, Riggins JN, West JD. Endogenous generation of reactive oxidants and electrophiles and their reactions with DNA and protein. J Clin Invest 2003;111(5):583-93; doi:10.1172/JCI18022.

41. Mongkolsuk S, Helmann JD. Regulation of inducible peroxide stress responses. Mol Microbiol 2002;45(1):9-15.

42. Monks TJ, Hanzlik RP, Cohen GM, et al. Quinone chemistry and toxicity. Toxicol Appl Pharmacol 1992;112(1):2-16; doi:10.1016/0041-008x(92)90273-u.

43. Müller A, Eller J, Albrecht F, et al. Allicin induces thiol stress in bacteria through *S*-allylmercapto modification of protein cysteines. J Biol Chem 2016;291(22):11477-90; doi:10.1074/jbc.M115.702308.

44. Newberry KJ, Fuangthong M, Panmanee W, et al. Structural mechanism of organic hydroperoxide induction of the transcription regulator OhrR. Mol Cell 2007;28(4):652-64; doi:10.1016/j.molcel.2007.09.016.

45. Noto MJ, Burns WJ, Beavers WN, et al. Mechanisms of pyocyanin toxicity and genetic determinants of resistance in *Staphylococcus aureus*. J Bacteriol 2017;199(17); doi:10.1128/JB.00221-17.

46. O'Brien PJ. Molecular mechanisms of quinone cytotoxicity. Chem Biol Interact 1991;80(1):1-41; doi:10.1016/0009-2797(91)90029-7.

47. Palm GJ, Khanh Chi B, Waack P, et al. Structural insights into the redox-switch mechanism of the MarR/DUF24-type regulator HypR. Nucleic Acids Res 2012;40(9):4178-92; doi:10.1093/nar/gkr1316.

48. Panmanee W, Vattanaviboon P, Poole LB, et al. Novel organic hydroperoxide-sensing and responding mechanisms for OhrR, a major bacterial sensor and regulator of organic hydroperoxide stress. J Bacteriol 2006;188(4):1389-95; doi:10.1128/JB.188.4.1389-1395.2006.

49. Perera IC, Grove A. Molecular mechanisms of ligand-mediated attenuation of DNA binding by MarR family transcriptional regulators. J Mol Cell Biol 2010;2(5):243-54; doi:10.1093/jmcb/mjq021.

50. Phillips-Jones MK, Harding SE. Antimicrobial resistance (AMR) nanomachines-mechanisms for fluoroquinolone and glycopeptide recognition, efflux and/or deactivation. Biophys Rev 2018;10(2):347-362; doi:10.1007/s12551-018-0404-9.

51. Pi H, Helmann JD. Genome-wide characterization of the Fur regulatory network reveals a link between catechol degradation and bacillibactin metabolism in *Bacillus subtilis*. mBio 2018;9(5); doi:10.1128/mBio.01451-18.

52. Price-Whelan A, Dietrich LE, Newman DK. Rethinking 'secondary' metabolism: physiological roles for phenazine antibiotics. Nat Chem Biol 2006;2(2):71-8; doi:10.1038/nchembio764.

53. Price-Whelan A, Dietrich LE, Newman DK. Pyocyanin alters redox homeostasis and carbon flux through central metabolic pathways in Pseudomonas aeruginosa PA14. J Bacteriol 2007;189(17):6372-81; doi:10.1128/JB.00505-07.

54. Snell SB, Gill AL, Haidaris CG, et al. *Staphylococcus aureus* tolerance and genomic response to photodynamic inactivation. mSphere 2021;6(1); doi:10.1128/mSphere.00762-20.

55. Soonsanga S, Lee JW, Helmann JD. Conversion of *Bacillus subtilis* OhrR from a 1-Cys to a 2-Cys peroxide sensor. J Bacteriol 2008;190(17):5738-45; doi:10.1128/JB.00576-08.

56. Tam le T, Eymann C, Albrecht D, et al. Differential gene expression in response to phenol and catechol reveals different metabolic activities for the degradation of aromatic compounds in *Bacillus subtilis*. Environ Microbiol 2006;8(8):1408-27; doi:EMI1034 [pii] 10.1111/j.1462-2920.2006.01034.x.

57. Töwe S, Leelakriangsak M, Kobayashi K, et al. The MarR-type repressor MhqR (YkvE) regulates multiple dioxygenases/glyoxalases and an azoreductase which confer resistance to 2-methylhydroquinone and catechol in *Bacillus subtilis*. Mol Microbiol 2007;66(1):40-54; doi:10.1111/j.1365-2958.2007.05891.x.

58. Ulfig A, Leichert LI. The effects of neutrophil-generated hypochlorous acid and other hypohalous acids on host and pathogens. Cell Mol Life Sci 2021;78(2):385-414; doi:10.1007/s00018-020-03591-y.

59. Vestergaard M, Frees D, Ingmer H. Antibiotic resistance and the MRSA problem. Microbiol Spectr 2019;7(2); doi:10.1128/microbiolspec.GPP3-0057-2018.

60. Wetzstein M, Volker U, Dedio J, et al. Cloning, sequencing, and molecular analysis of the *dnaK* locus from *Bacillus subtilis*. J Bacteriol 1992;174(10):3300-10.

61. Wilkinson SP, Grove A. Ligand-responsive transcriptional regulation by members of the MarR family of winged helix proteins. Curr Issues Mol Biol 2006;8(1):51-62.

62. Winter J, Ilbert M, Graf PC, et al. Bleach activates a redox-regulated chaperone by oxidative protein unfolding. Cell 2008;135(4):691-701; doi:10.1016/j.cell.2008.09.024.

63. Yurimoto H, Hirai R, Matsuno N, et al. HxlR, a member of the DUF24 protein family, is a DNA-binding protein that acts as a positive regulator of the formaldehyde-inducible hxlAB operon in Bacillus subtilis. Mol Microbiol 2005;57(2):511-9; doi:10.1111/j.1365-2958.2005.04702.x.

64. Zhang Y, Martin JE, Edmonds KA, et al. SifR is an Rrf2-family quinone sensor associated with catechol iron uptake in Streptococcus pneumoniae D39. J Biol Chem 2022:102046; doi:10.1016/j.jbc.2022.102046.

Figure legends

Summary Graphic Illustration:

Redox-sensing mechanism of the two-Cys-type QsrR repressor under oxidative and quinone stress in *S. aureus*. QsrR senses HOCl, diamide and the oxidative mode of quinones by a thiol switch via intersubunit disulfide formation between Cys4 and Cys29'. In addition, QsrR is modified by *S*-thioallylations of Cys4, Cys29 and Cys32 under allicin stress. Thiol-oxidation of QsrR leads to derepression of the genes encoding dioxygenases (*catE, catE*2) and quinone reductases (*azoR1, yodC*). The QsrR regulon was shown to confer resistance against quinones, allicin and oxidative stress in *S. aureus*. While the dioxygenases were previously shown to function in the ring-cleavage of quinones, the quinone reductases could be more promiscuous to reduce quinones and the oxidants diamide and allicin.

Fig. 1. The QsrR regulon is induced by quinones and disulfide stress, which requires Cys4 and either Cys29' or Cys32'. (A) Northern blot analysis was used to analyze transcription of *catE2* and *qsrR* in *S. aureus* COL WT before (co) and after exposure to 0.25 µg/ml erythromycin (Ery), 0.5 µg/ml vancomycin (Van), 0.1 µg/ml rifampicin (Rif), 5 µg/ml tetracycline (Tet), 32 µg/ml ciprofloxacin (Cip), 50 µM methylhydroquinone (MHQ), 0.5 mM methylglyoxal (MG), 0.75 mM formaldehyde (FA), 2 mM diamide (Dia), 10 mM H_2O_2, 1.5 mM HOCl, 300 µM allicin (All) and 5 µg/ml AGXX®. Cells were treated at an OD_{500} of 0.5 for 30 min with the thiol-reactive compounds or exposed to antibiotics for 60 min. **(C,E,G)** Transcription of *catE2* was analyzed in *S. aureus* COL WT and *qsrR* mutant strains before (co) and 30 min after treatment with 50 µM MHQ **(C)**, 2 mM Dia **(E)** and 0.3 mM All **(G)** using Northern blots. The methylene blue bands denote the 16S and 23S rRNAs as RNA loading controls below the Northern blots. **(B,D,F,H)** Band intensities of the *catE2 and qsrR* transcripts of the Northern blot images were quantified in the WT before and after different stress and antibiotics treatments **(B)** and in the WT, *qsrR* mutant and the complemented strains in response to MHQ **(D)**, diamide **(F)** and allicin **(H)** stress using ImageJ version 1.52a from 1-2 biological replicates

with 2 technical replicates each and error bars represent the standard deviation. One representative Northern blot of each condition is shown in **A, C, E, G**. For comparison of the *catE2* and *qsrR* induction upon stress exposure, the statistics of the control and stress sample was calculated using the Student's unpaired two-tailed t-test. $p>0.05$, $^{*}p\leq0.05$, $^{**}p\leq0.01$ and $^{***}p\leq0.001$.

Fig. 2. The Cys residues are not essential for DNA-binding activity of QsrR *in vitro*. (A) EMSAs were used to analyze the DNA-binding activity of increasing amounts (0.002–0.4 μM) of QsrR to the *catE2* (P_{catE2}) **(A)** and *qsrR* (P_{qsrR}) **(B)** promoter *in vitro*. The free DNA probe is indicated with "0" and the shifted band show the DNA-QsrR promoter complex. **(C, D)** The percentage of the protein-DNA complex formation was determined according to the band intensities of 3-4 biological replicates of the EMSAs and quantified using Image J 1.52a. Dissociation constants (K_D) of the QsrR, C4S, C29S and C32S mutant proteins for the *catE2* promoter were calculated as 68.28 nM, 61.5 nM, 66.52 nM and 61.12 nM **(C)**, and for the *qsrR* promoter as 112.4 nM, 103.7 nM, 105.4 nM and 105.5 nM **(D)**, respectively, using the Graph prism software version 7.03. The detailed individual data of percentage of DNA-protein complex formation are shown in **Table S4**. **(E)** As a nonspecific control DNA probe, the *trxA* and *ycel* promoter region were used. To confirm the specificity of DNA-binding, two base substitutions were introduced in each half of the inverted repeat, underlined and labelled in gray (m1 and m2) in the QsrR-specific operator sequence.

Fig. 3. Quinones lead to reversible inhibition of the DNA-binding activity of QsrR *in vitro*, which requires Cys4 and Cys29. (A, B) EMSAs of the QsrR and QsrR Cys mutant proteins (0.3 μM) to the *catE2* (P_{catE2}) **(A)** and *qsrR* (P_{qsrR}) **(B)** promoter were performed to study the inactivation of QsrR by increasing amounts of MHQ (0.25–20 μM), leading to the loss of DNA binding. **(C, D)** QsrR inactivation by quinones could be partially reversed with 10 mM DTT, which was added to the QsrR-DNA-binding reaction 30 min after MHQ addition. "DNA" and

"co" denote the free DNA probe and the QsrR-DNA complex in the presence of DTT, respectively.

Fig. 4. Diamide leads to reversible inhibition of the QsrR DNA-binding activity *in vitro*, which requires Cys4. (A) EMSAs of the QsrR protein (0.3 µM) to the *catE2* (P_{catE2}) promoter were performed to study the inactivation of QsrR by increasing amounts of diamide (25–50 µM), leading to the partial loss of DNA binding. The addition of DTT restored the complete DNA binding. **(B, C)** The addition of 20 µM diamide to increasing QsrR protein concentrations (0.002-0.4 µM) lead to a decreased DNA-binding affinity of QsrR to the *catE2* (P_{catE2}) and *qsrR* (P_{qsrR}) promoter. **(D, E)** Dissociation constants (K_D) of the QsrR, C4S, C29S and C32S mutant proteins for the *catE2* promoter were calculated as 337.5 nM, 61.13 nM, 296.3 nM and 325.5 nM **(D)** and for the *qsrR* promoter as 291.9 nM, 102.9 nM, 266.2 nM and 295.6 nM **(E)**, respectively, using the Graph prism software version 7.03. While C29S and C32S mutant proteins show a similar response to diamide as the QsrR wild type protein, C4S cannot be inactivated by diamide. For comparison the DNA-binding activity of the QsrR, C4S, C29S and C32S mutant proteins under reducing conditions from **Fig 2C,D** are shown in grey. The detailed individual data of percentage of DNA-protein complex formation after diamide treatment are shown in **Table S5**.

Fig. 5. HOCl leads to a reversible inhibition of the QsrR DNA-binding activity *in vitro*, which requires Cys4. (A-D) EMSAs of increasing QsrR, C4S, C29S and C32S protein concentrations (0.002-0.4 µM) to the *catE2* (P_{catE2}) **(A,C)** and *qsrR* (P_{qsrR}) **(B, D)** promoter were performed to study the inactivation of QsrR by 20 µM HOCl. **(C, D)** The addition of HOCl decreased the QsrR binding affinity which could be reversed with 10 mM DTT. **(E, F)** Dissociation constants (K_D) of the QsrR, C4S, C29S and C32S mutant proteins for the *catE2* promoter were calculated as 176.3 nM, 63.3 nM, 167.8 nM and 175.5 nM **(E)** and for the *qsrR* promoter as 239.9 nM, 103 nM, 222 nM and 221 nM **(F)**, respectively, using the Graph prism software version 7.03. For comparison the DNA-binding activity of the QsrR, C4S, C29S and

C32S mutant proteins under reducing conditions from **Fig 2C,D** are shown in grey. The detailed individual data of percentage of DNA-protein complex formation after HOCl treatment are shown in **Table S6**.

Fig. 6. QsrR senses oxidants and quinones by formation of intermolecular disulfides *in vitro*, which requires Cys4. **(A-C)** The purified QsrR WT protein was treated with increasing concentrations of diamide (Dia) **(A)**, HOCl **(B)** and methylhydroquinone (MHQ) **(C)** *in vitro* and subjected to non-reducing SDS-PAGE analysis. The reduction of the QsrR disulfides after DTT treatment is shown in the reducing SDS-PAGE analysis. **(D,E)** Purified QsrR, C4S, C29S and C32S mutant proteins were treated with 320 µM Dia **(D)** and HOCl **(E)** for 15 min, followed by alkylation with 50 mM iodoacetamide (IAM) for 30 min in the dark and separation by non-reducing SDS-PAGE.

Fig. 7. QsrR senses diamide stress by formation of intermolecular disulfides *in vivo*, which requires Cys4. The *S. aureus qsrR* mutant, the *qsrR* complemented strain and the *qsrR* Cys-mutants were treated with 5 mM diamide (Dia) for 30 min, alkylated with 50 mM iodoacetamide (IAM) and the protein extracts were analyzed for thiol-oxidation of QsrR *in vivo* by non-reducing **(A)** and reducing **(B)** Western blot analysis using monoclonal anti-His_6 antibodies. The protein loading controls are shown in **Fig. S2**.

Fig. 8. QsrR is oxidised to intermolecular disulfides by diamide *in vitro*, which involve Cys4 and Cys29' as revealed by MS analysis. The tryptic peptides of reduced QsrR and the oxidized QsrR intersubunit disulfides were subjected to Orbitrap Q Exactive LC-MS/MS analysis. The MS/MS spectra **(A, B)** and extracted ion chromatograms **(C, D)** are shown for the disulfide-crosslinked Cys4-Cys29' peptides with the monoisotopic mass of 3089.221 Da **(A, C)** and for the Cys4-Cys4' intersubunit disulfide peptides with the monoisotopic mass of 3321.4477 Da **(B, D)**. XL indicates crosslinked Cys residues. The assigned fragment ion signals are labelled in red, all unassigned are in black. Carbamidomethylation and methionine oxidation are marked with "CA" and "Ox", respectively. **(A)** For the Cys4-Cys29' disulfide, the

monoisotopic masses of the α and β peptides were calculated as 1661.7317 Da and 1429.5060 Da, respectively. **(B)** For the Cys4-Cys4' peptide, the monoisotopic masses for the α and β peptides were calculated as 1661.7317 Da. **(C, D)** The extracted ion chromatograms for the observed Cys4-Cys29' peptides $[M+5H]^{5+}$ of m/z 618.8523 **(C)** and the observed Cys4-Cys4' peptides $[M+5H]^{4+}$ of m/z 831.3722 **(D)** indicate the relative abundance of the disulfide-linked peptides in the reduced and diamide treated (oxidized) samples.

Fig. 9. Allicin causes *S*-thioallylation of QsrR, leading to inhibition of DNA binding *in vitro*. (A) EMSAs of the QsrR protein (0.3 µM) to the *catE2* (P_{catE2}) and *qsrR* (P_{qsrR}) promoter were performed to study the inactivation of QsrR by increasing amounts of allicin (1–60 µM), leading to decreased DNA-binding activity. QsrR inactivation by allicin could be reversed with 10 mM DTT, which was added to the QsrR-DNA-binding reaction 30 min after allicin addition. **(B)** Purified QsrR was treated with increasing concentrations of allicin and separated by non-reducing and reducing SDS-PAGE. **(C, D)** The allicin-treated QsrR protein band was tryptic digested and subjected to MALDI-TOF-MS analysis. The upper panels show the MS1 Spectrum of the reduced QsrR Cys4 **(C)** and Cys29,32 peptides **(D)**, which were carbamidomethylated with IAM (CAM). The lower panel shows the MS1 spectrum of the allicin-treated QsrR Cys4 **(C)** and Cys29,32 peptides **(D)** with the thioallylations. The MS1 scans are displayed in the mass ranges of m/z 1650-1750 **(C)** and m/z 1440-1550 **(D)**, showing the Cys4 and Cys29,32 peptides, respectively. *S*-thioallylations cause a shift of 72 Da at Cys residues and of 15 Da compared with carbamidomethylated Cys (CAM).

Fig. 10. The QsrR regulon confers resistance towards quinones and oxidants, which depends on Cys4 and either Cys29 or Cys32. (A-D) For growth curves, *S. aureus* COL WT and the *qsrR* deletion mutant were grown in RPMI until an OD_{500} of 0.5 and treated with 50 µM MHQ **(A)**, 10 mM H_2O_2 **(B),** 1.5 mM HOCl **(C)** and 0.3 mM allicin **(D)**. The enhanced resistance of the *qsrR* mutant could be reversed to the WT level in the *qsrR* complemented strain as shown in **Fig. S3**. **(E-K)** For survival assays the wild type, the *qsrR* mutant and the *qsrR*

deletion mutant complemented with *qsrR, C4S, C29S, C32S and C29,32S* alleles were grown in RPMI medium until an OD_{500} of 0.5 and treated with 250 µM MHQ **(E)**, 40 mM H_2O_2 **(F,J)**, 2 mM HOCl **(G,K)**, 0.5 mM allicin **(H)** and 150 µM MHQ **(I)**. After 1, 2 and 4 h of stress exposure, 100 µl of serial dilutions were plated onto LB agar plates and the survival rates of CFUs for the treated samples were calculated relative to the control, which was set to 100%. The *qsrR* mutant is significantly more resistant to electrophiles and oxidants, which could be restored to wild type levels in the *qsrR* complemented strain. The Cys4 and one of the C-terminal Cys-residues of QsrR are required for resistance against these stressors. The results are from three to four biological replicates. Error bars represent the standard deviation. *$p < 0.05$; **$p < 0.01$; ***$p < 0.001$.

Supplemental Figure legends

Fig. S1. Northern blot and Western blot analysis of transcription and protein expression in the *qsrR* and *qsrR* Cys mutant complemented strains. (A) The complementation of the *qsrR* mutant with pRB473-encoded *qsrR*, *C4S*, *C29S*, *C32S* and *C29,32S* alleles under control (co) and 50 µM MHQ stress was confirmed using Northern blots with a *qsrR*-specific mRNA probe. **(B)** By Western blot analysis, protein expression was verified for the QsrR, C4S, C29S, C32S and C29,32S mutant proteins in the complemented strains after overnight growth in LB medium.

Fig. S2. Coomassie-stained SDS-PAGE loading control. The same protein extracts of the *S. aureus* COL *qsrR* mutant and the *qsrR*, *C4S*, *C29S*, *C32S* and *C29,32S* complemented strains after diamide (Dia) stress, which were used for Western blot analyses in Fig. 7, were separated by reducing SDS-PAGE and stained with Coomassie Blue as loading control.

Fig. S3. The phenotype of the *qsrR* mutant can be restored to the WT level in the *qsrR* complemented strain. For the growth curves, *S. aureus* COL WT and the *qsrR* complemented strain (*qsrR*) were grown in RPMI medium. At an OD_{500} of 0.5 the strains were exposed to 100 µM MHQ **(A),** 10 mM H_2O_2 **(B)**, 1.5 mM HOCl **(C)** and 0.3 mM allicin **(D)**. The results are from three to four biological replicates. Error bars represent the standard deviation. $p > 0.05$; $^*p < 0.05$.

Fig. S4. Cys4 is required for MHQ resistance, while Cys4 and either Cys29 or Cys32 are essential for HOCl tolerance. For growth curves, the *S. aureus* COL *qsrR* mutant complemented with the *qsrR, C4S, C29S, C32S* and *C29,32S* alleles were grown in RPMI until an OD_{500} of 0.5 and treated with 10 mM H_2O_2 **(A-D)**, 1.5 mM HOCl **(E-H)** and 50 µM methylhydroquinone (MHQ) **(I-L)**. The results are from three to four biological replicates. Error bars represent the standard deviation. $p > 0.05$; $^*p < 0.05$; $^{**}p < 0.01$; $^{***}p < 0.001$.

Fig. S5. The structure of the two-Cys-type QsrR repressor with the positions of the 3 Cys residues. The QsrR structure (PDB:4HQE) was previously resolved (Ji et al, 2013) and is visualized with PyMol. The α1-α5 helices and ß1 and ß2 sheets are labelled in both subunits of the QsrR dimer as in the previous study (Ji et al, 2013). The distance of Cys4 and Cys29' was calculated as ~15.2Å, whereas Cys4 and Cys4' are 27Å apart between the opposing subunits of the QsrR dimer. Cys4 and Cys29' are oxidized to intersubunit disulfides in the QsrR dimer under diamide stress.

Fig. S6. Sunburst view of 19719 species encoding the HxlR-type HTH domain proteins in bacteria and archaea (IPR002577) according to the InterPro database (https://www.ebi.ac.uk/interpro/entry/InterPro/IPR002577).

Fig. S7. ClustalW2 protein sequence alignment of selected QsrR (SACOL2115) homologs according to EMBL STRING (https://string-db.org/) and InterPro databases (https://www.ebi.ac.uk/interpro/entry/InterPro/IPR002577). The QsrR homologs harbor the HxlR-type HTH domain (IPR002577) with a conserved N-terminal Cys residue (*) (Cys4 of QsrR). The alignment and consensus is presented in Jalview. Intensity of the blue color gradient is based on 50% protein sequence. Cys residues are indicated by red boxes.

Supplemental Table legends

Table S1. Transcriptional induction of the QsrR-regulon under oxidative and electrophile stress according to published RNA-seq datasets. The published RNAseq datasets of S. aureus COL and USA300 strains exposed to 150 µM HOCl, 0.3 mM allicin, 5 µg/ml AGXX, 45 µM MHQ and 300 µM lapachol show strong induction of the QsrR regulon genes catE2, yodC and the catE-SACOL0409-azoR1 operon by oxidants and electrophiles.

Table S2. Bacterial strains, phages and plasmids

Table S3. Oligonucleotide (primer) sequences

Table S4. % protein-DNA complex formation of the untreated QsrR, C4S, C29S and C32S proteins. The percentage of the protein-DNA complex formation was determined according to the band intensities of 3-4 biological replicates of the EMSAs and quantified using Image J 1.52a. The calculated percentual values of all biological replicates are shown for 0-0.5 µM of the QsrR, C4S, C29S and C32S proteins bound to the *catE2* and *qsrR* promoters. These values were used for the nonlinear regression shown in **Fig. 2C, D** using the specific binding with Hill slope of the Graph prism software version 7.03 to determine the Dissociation constants (K_D).

Table S5. % protein-DNA complex formation of the QsrR, C4S, C29S and C32S proteins after diamide. The percentage of the protein-DNA complex formation was determined according to the band intensities of 3-4 biological replicates of the EMSAs and quantified using Image J 1.52a. The calculated percentual values of all biological replicates are shown for 0-0.5 µM of the QsrR, C4S, C29S and C32S proteins bound to the *catE2* and *qsrR* promoter after addition of 20 µM diamide. These values were used for the nonlinear regression shown in **Fig. 4D, E** using the specific binding with Hill slope of the Graph prism software version 7.03 to determine the Dissociation constants (K_D).

Table S6. % protein-DNA complex formation of the QsrR, C4S, C29S and C32S proteins after HOCl. The percentage of the protein-DNA complex formation was determined according to the band intensities of 3-4 biological replicates of the EMSAs and quantified using Image J 1.52a. The calculated percentual values of all biological replicates are shown for 0-0.5 µM of the QsrR, C4S, C29S and C32S proteins bound to the *catE2* and *qsrR* promoter after addition of 20 µM HOCl. These values were used for the nonlinear regression shown in **Fig. 5E, F** using the specific binding with Hill slope of the Graph prism software version 7.03 to determine the Dissociation constants (K_D).

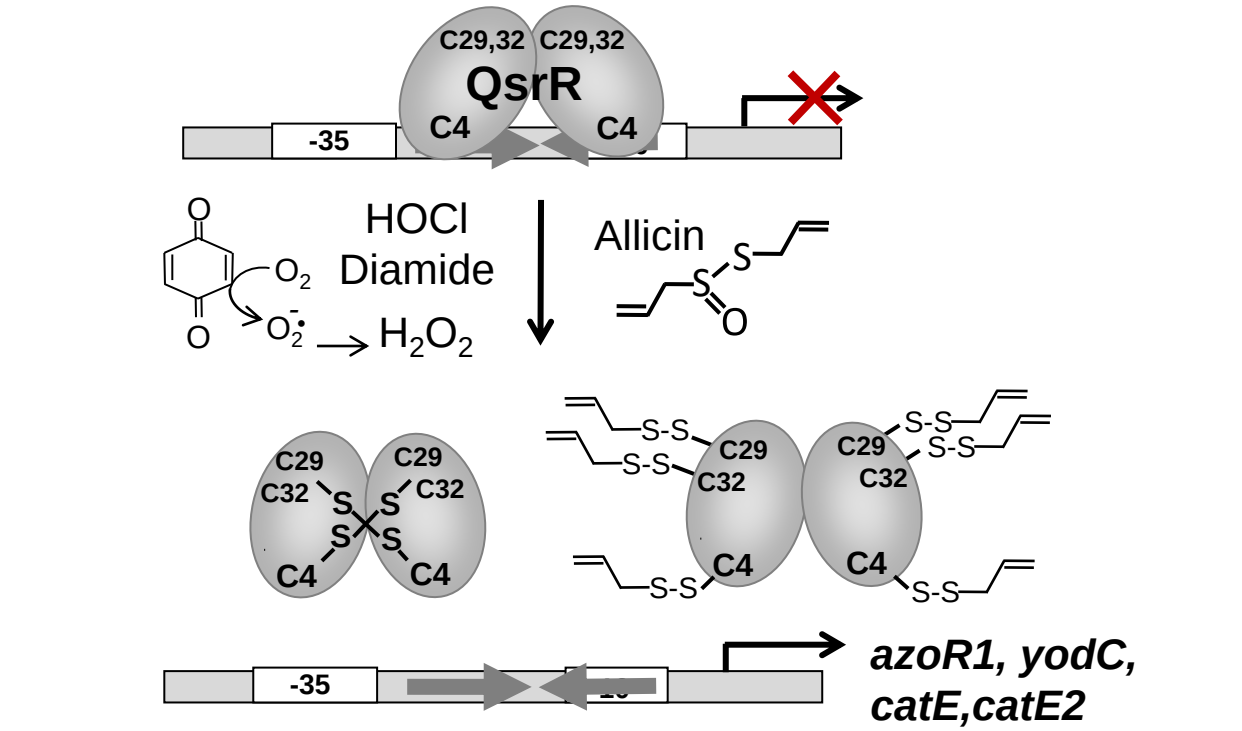
C29,32
C29,32
QsrR
C4
C4
-35
HOCl
Diamide
Allicin
O_2
$O_2^{\bullet-}$
H_2O_2
C29
C32
C4
S-S
azoR1, yodC,
catE,catE2

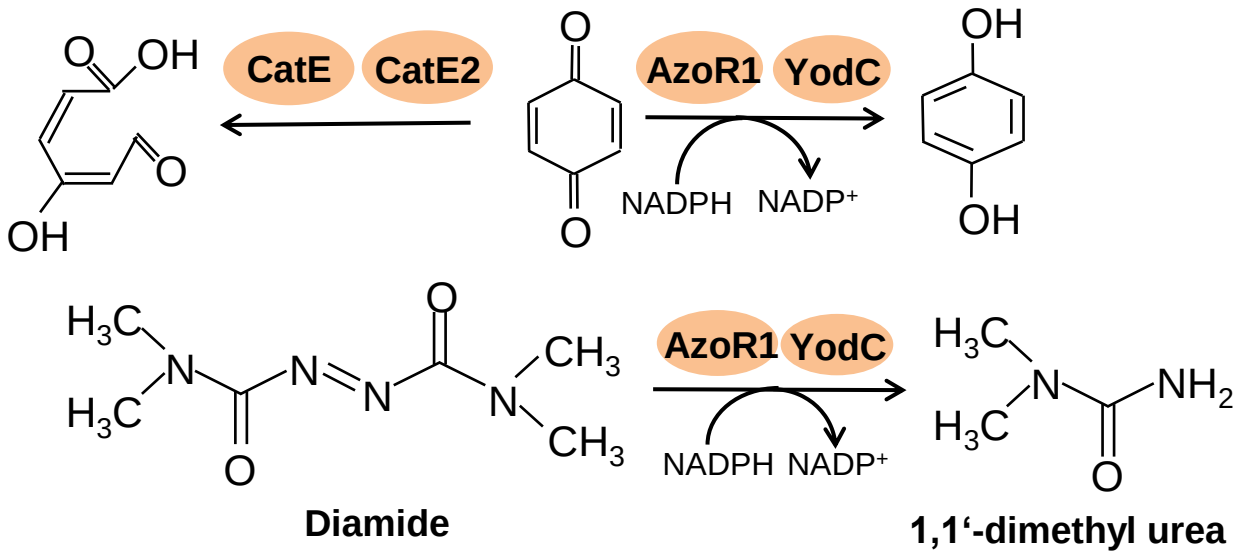
CatE
CatE2
AzoR1
YodC
NADPH
NADP+
OH
Diamide
1,1'-dimethyl urea

Fig. 1

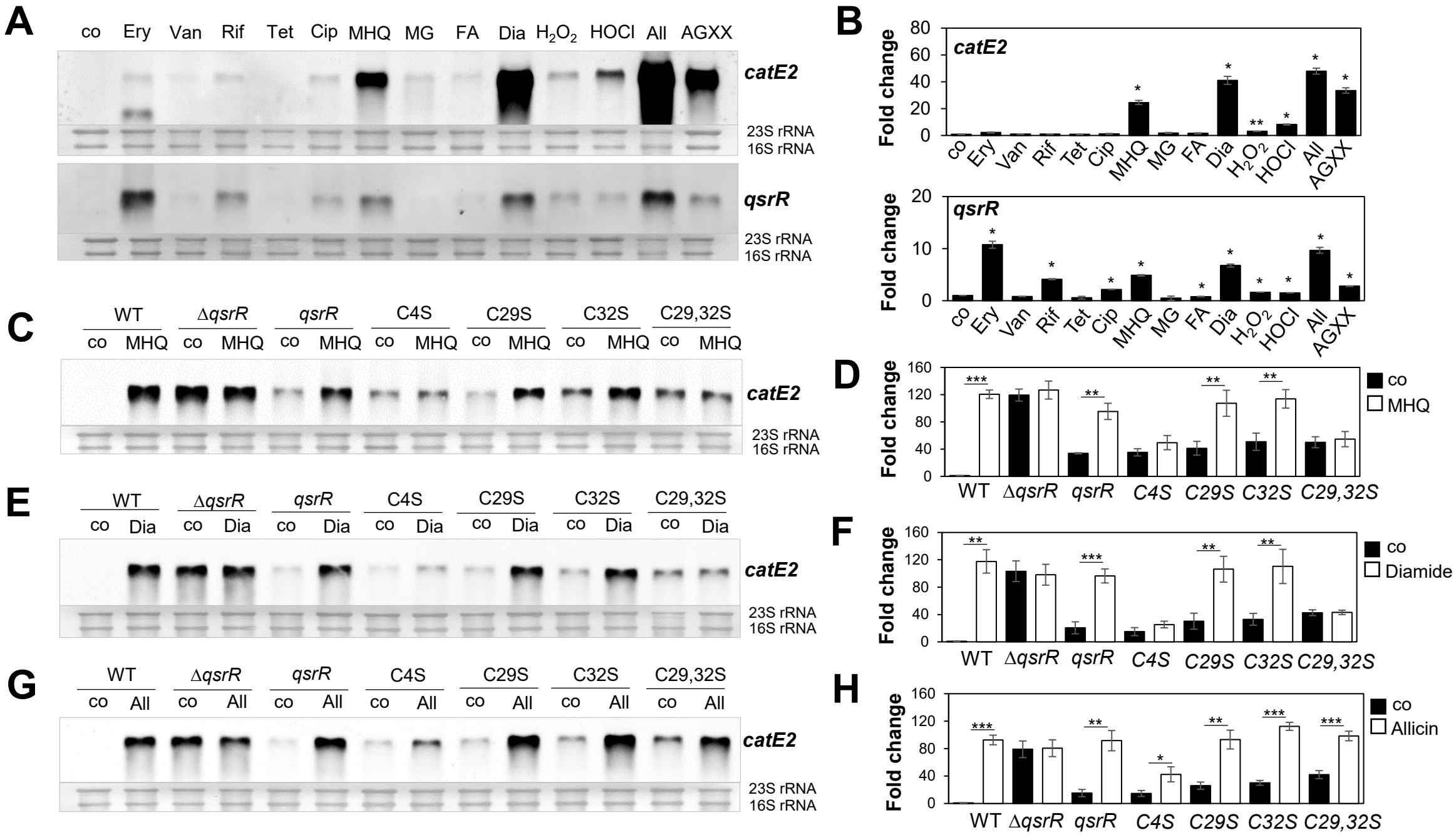
A
co Ery Van Rif Tet Cip MHQ MG FA Dia H2O2 HOCl All AGXX
catE2
23S rRNA
16S rRNA
qsrR
23S rRNA
16S rRNA
B
catE2
Fold change
co Ery Van Rif Tet Cip MHQ MG FA Dia H2O2 HOCl All AGXX
qsrR
Fold change
co Ery Van Rif Tet Cip MHQ MG FA Dia H2O2 HOCl All AGXX
C
WT ΔqsrR qsrR C4S C29S C32S C29,32S
co MHQ co MHQ co MHQ co MHQ co MHQ co MHQ co MHQ
catE2
23S rRNA
16S rRNA
D
Fold change
co
MHQ
WT ΔqsrR qsrR C4S C29S C32S C29,32S
E
WT ΔqsrR qsrR C4S C29S C32S C29,32S
co Dia co Dia co Dia co Dia co Dia co Dia co Dia
catE2
23S rRNA
16S rRNA
F
Fold change
co
Diamide
WT ΔqsrR qsrR C4S C29S C32S C29,32S
G
WT ΔqsrR qsrR C4S C29S C32S C29,32S
co All co All co All co All co All co All co All
catE2
23S rRNA
16S rRNA
H
Fold change
co
Allicin
WT ΔqsrR qsrR C4S C29S C32S C29,32S

Fig. 2

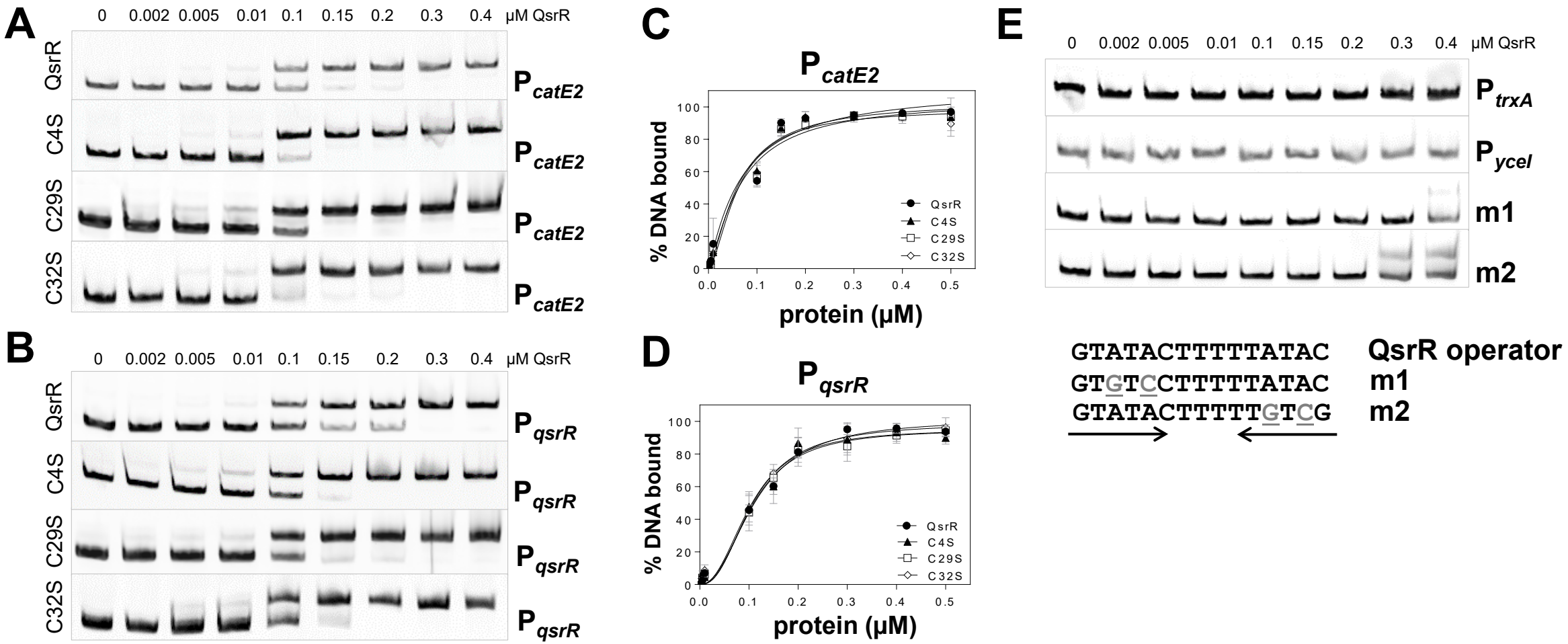
A
0 0.002 0.005 0.01 0.1 0.15 0.2 0.3 0.4 μM QsrR
QsrR
C4S
C29S
C32S
P catE2
P catE2
P catE2
P catE2
B
0 0.002 0.005 0.01 0.1 0.15 0.2 0.3 0.4 μM QsrR
QsrR
C4S
C29S
C32S
P qsrR
P qsrR
P qsrR
P qsrR
C
P catE2
% DNA bound
protein (μM)
QsrR
C4S
C29S
C32S
D
P qsrR
% DNA bound
protein (μM)
QsrR
C4S
C29S
C32S
E
0 0.002 0.005 0.01 0.1 0.15 0.2 0.3 0.4 μM QsrR
P trxA
P ycel
m1
m2
GTATACTTTTTATAC QsrR operator
GTGTCCTTTTTATAC m1
GTATACTTTTTGTCG m2

Fig. 3

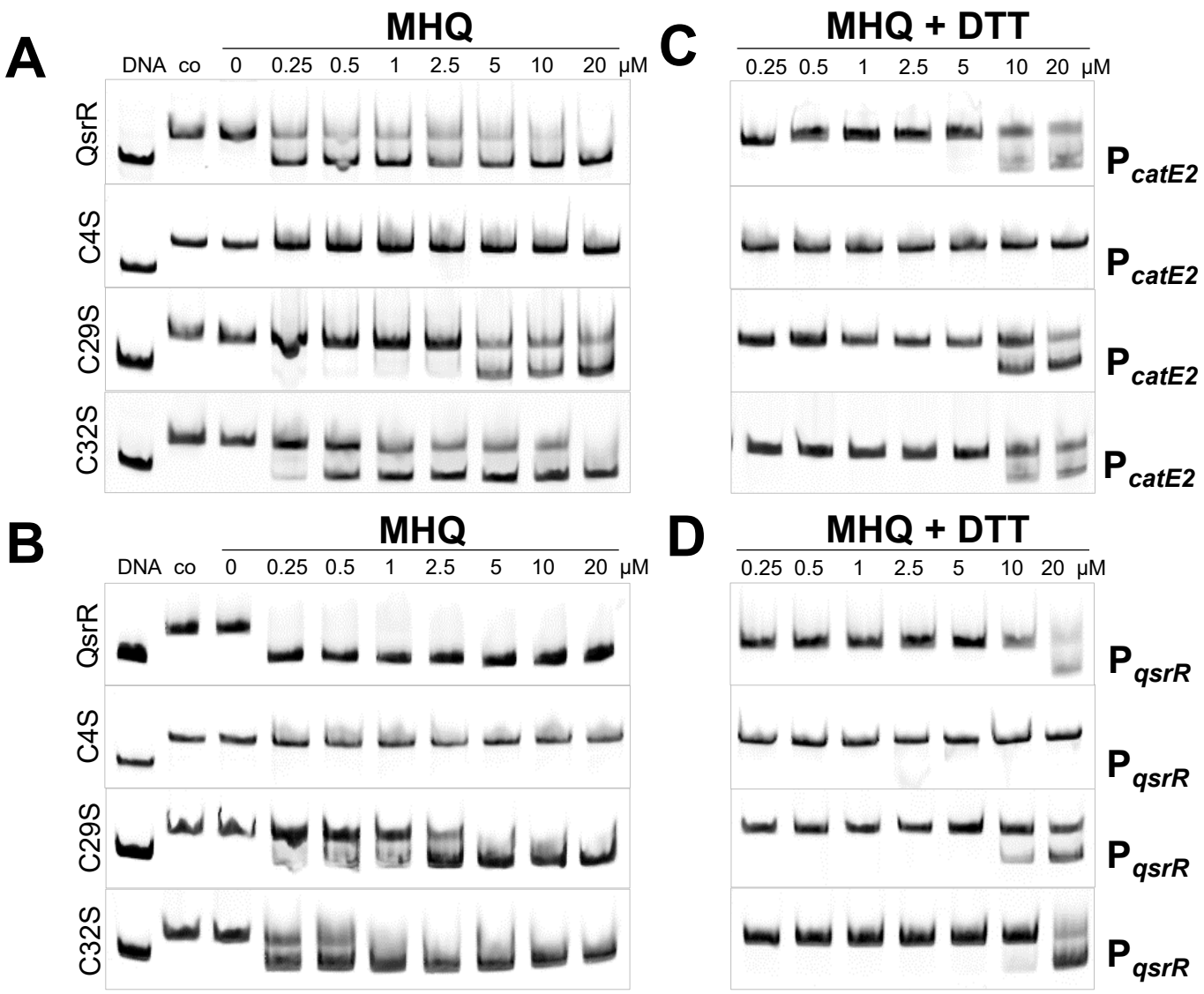
A
MHQ
DNA co 0 0.25 0.5 1 2.5 5 10 20 μM
QsrR
C4S
C29S
C32S
C
MHQ + DTT
0.25 0.5 1 2.5 5 10 20 μM
P catE2
P catE2
P catE2
P catE2
B
MHQ
DNA co 0 0.25 0.5 1 2.5 5 10 20 μM
QsrR
C4S
C29S
C32S
D
MHQ + DTT
0.25 0.5 1 2.5 5 10 20 μM
P qsrR
P qsrR
P qsrR
P qsrR

Fig. 4

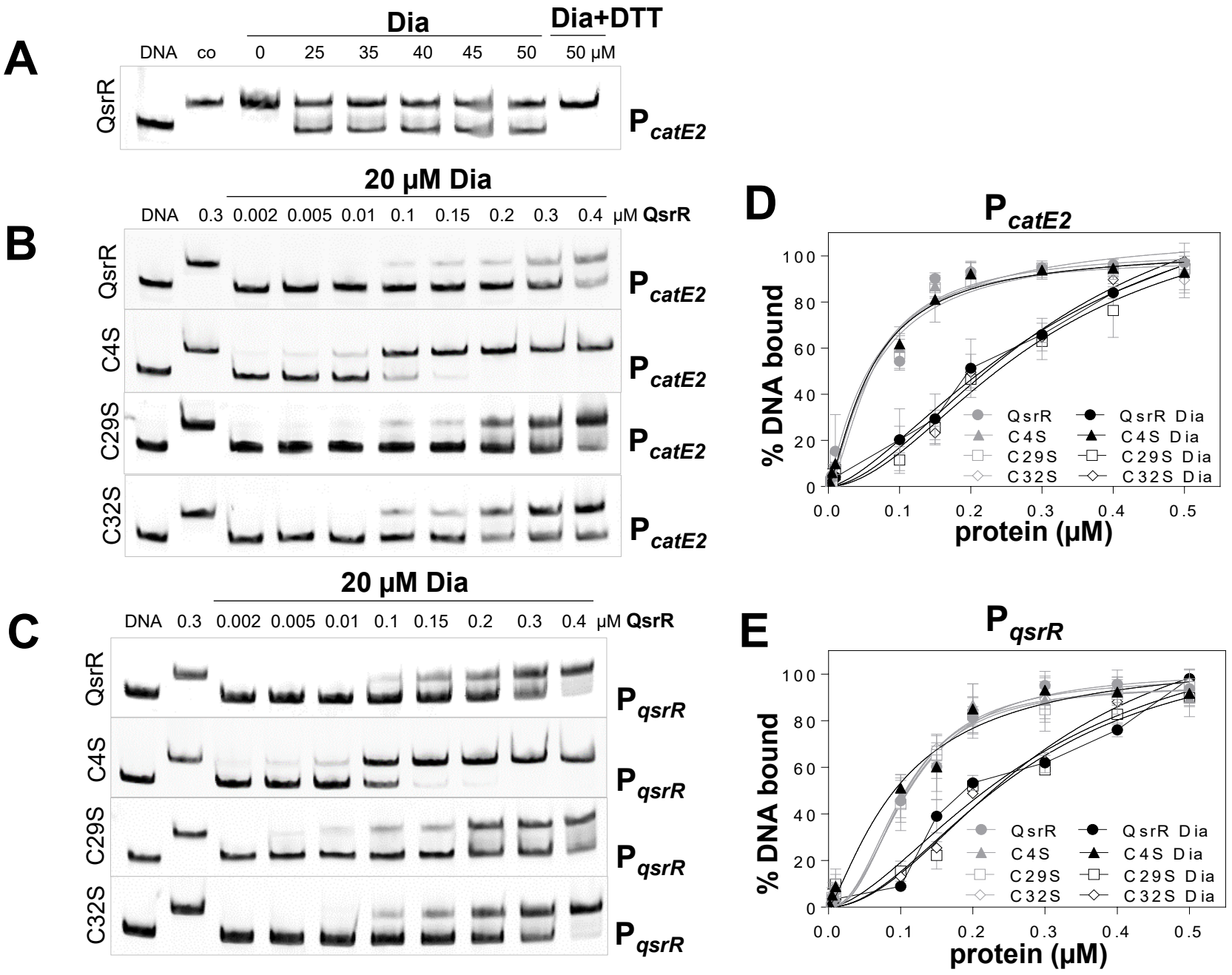
A
Dia
Dia+DTT
DNA co 0 25 35 40 45 50 50 μM
QsrR
P catE2
B
20 μM Dia
DNA 0.3 0.002 0.005 0.01 0.1 0.15 0.2 0.3 0.4 μM QsrR
QsrR
C4S
C29S
C32S
P catE2
C
20 μM Dia
DNA 0.3 0.002 0.005 0.01 0.1 0.15 0.2 0.3 0.4 μM QsrR
QsrR
C4S
C29S
C32S
P qsrR
D
P catE2
% DNA bound
protein (μM)
QsrR
C4S
C29S
C32S
QsrR Dia
C4S Dia
C29S Dia
C32S Dia
E
P qsrR
% DNA bound
protein (μM)
QsrR
C4S
C29S
C32S
QsrR Dia
C4S Dia
C29S Dia
C32S Dia

Fig. 5

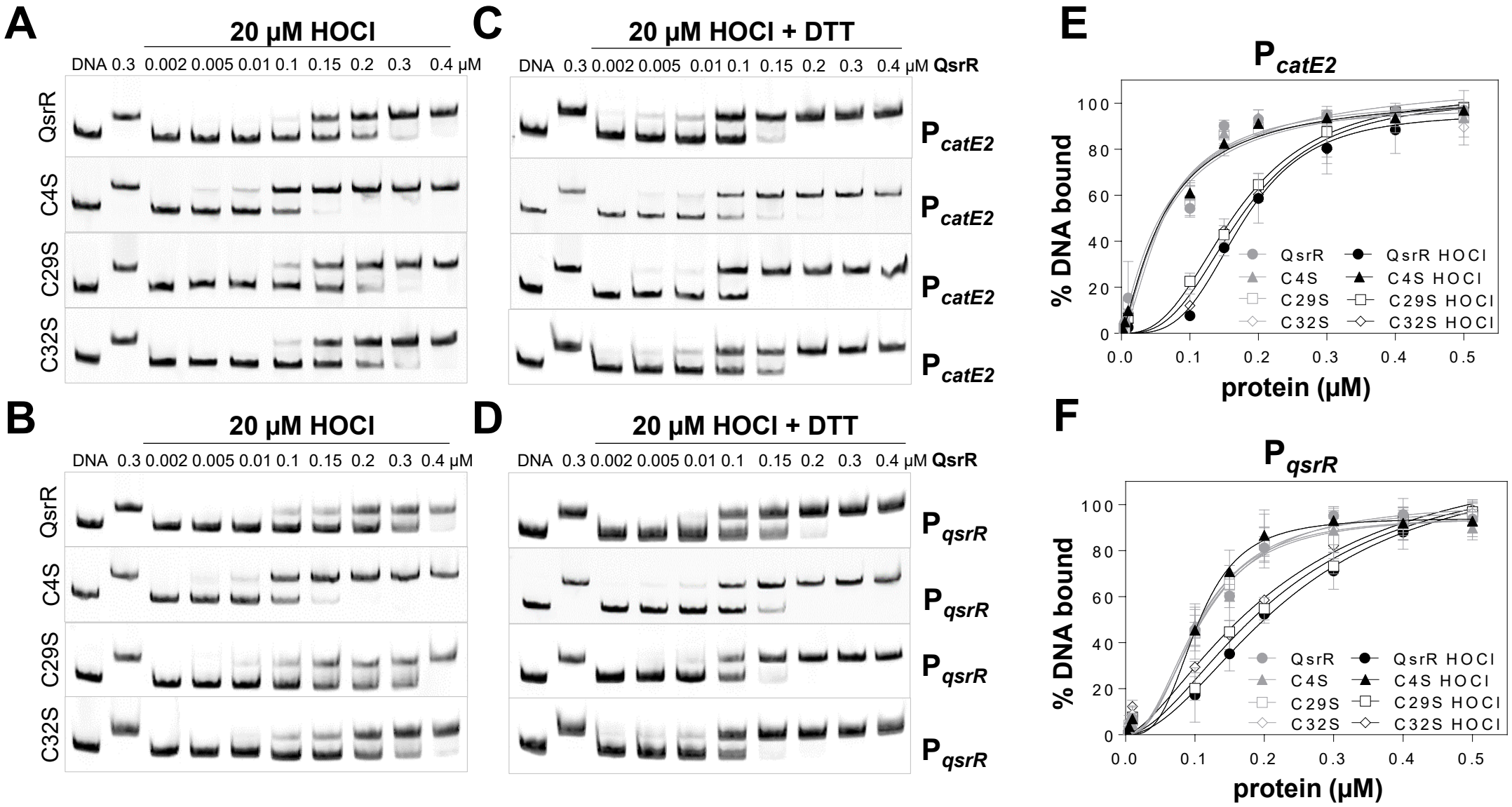
A
20 μM HOCl
DNA 0.3 0.002 0.005 0.01 0.1 0.15 0.2 0.3 0.4 μM
QsrR
C4S
C29S
C32S
B
20 μM HOCl
DNA 0.3 0.002 0.005 0.01 0.1 0.15 0.2 0.3 0.4 μM
QsrR
C4S
C29S
C32S
C
20 μM HOCl + DTT
DNA 0.3 0.002 0.005 0.01 0.1 0.15 0.2 0.3 0.4 μM QsrR
P catE2
P catE2
P catE2
P catE2
D
20 μM HOCl + DTT
DNA 0.3 0.002 0.005 0.01 0.1 0.15 0.2 0.3 0.4 μM QsrR
P qsrR
P qsrR
P qsrR
P qsrR
E
P catE2
% DNA bound
protein (μM)
QsrR
C4S
C29S
C32S
QsrR HOCl
C4S HOCl
C29S HOCl
C32S HOCl
F
P qsrR
% DNA bound
protein (μM)
QsrR
C4S
C29S
C32S
QsrR HOCl
C4S HOCl
C29S HOCl
C32S HOCl

Fig. 6

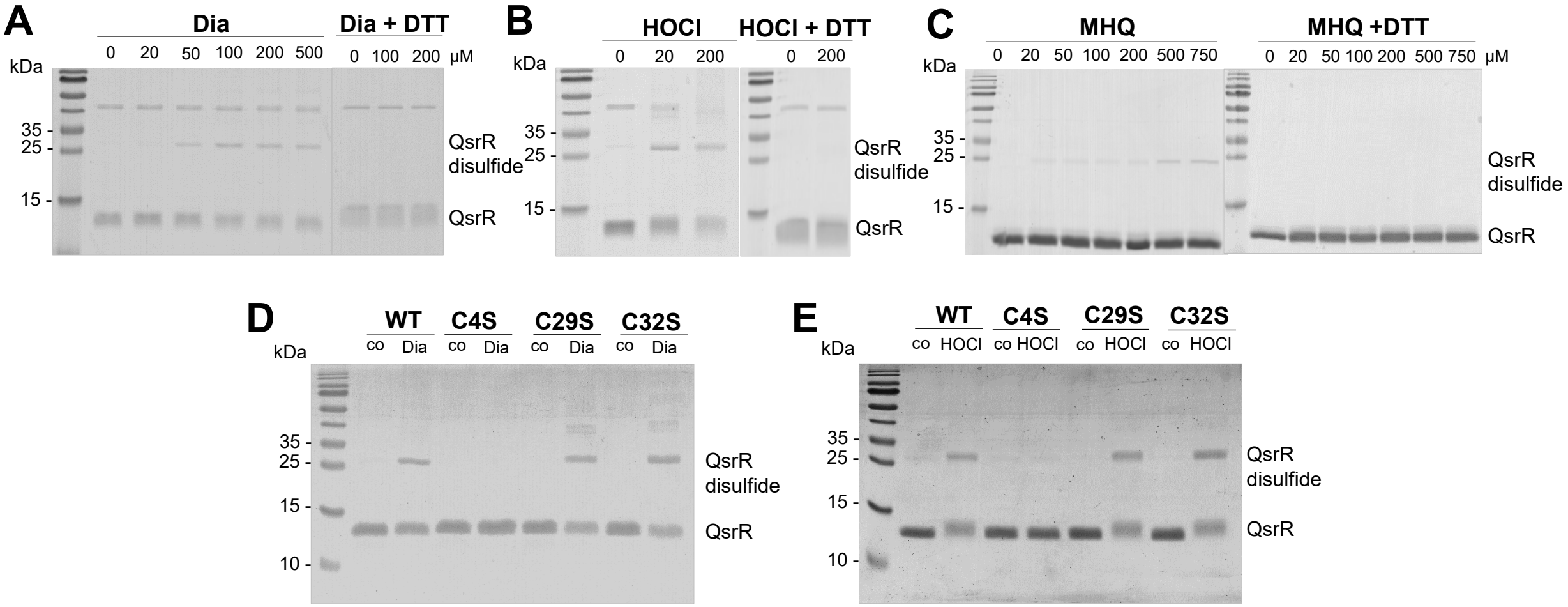
A
Dia
Dia + DTT
0 20 50 100 200 500
0 100 200 μM
kDa
35
25
15
QsrR disulfide
QsrR
B
HOCl
HOCl + DTT
0 20 200
0 200
kDa
35
25
15
QsrR disulfide
QsrR
C
MHQ
MHQ +DTT
0 20 50 100 200 500 750
0 20 50 100 200 500 750 μM
kDa
35
25
15
QsrR disulfide
QsrR
D
WT
C4S
C29S
C32S
co Dia co Dia co Dia co Dia
kDa
35
25
15
10
QsrR disulfide
QsrR
E
WT
C4S
C29S
C32S
co HOCl co HOCl co HOCl co HOCl
kDa
35
25
15
10
QsrR disulfide
QsrR

Fig. 7

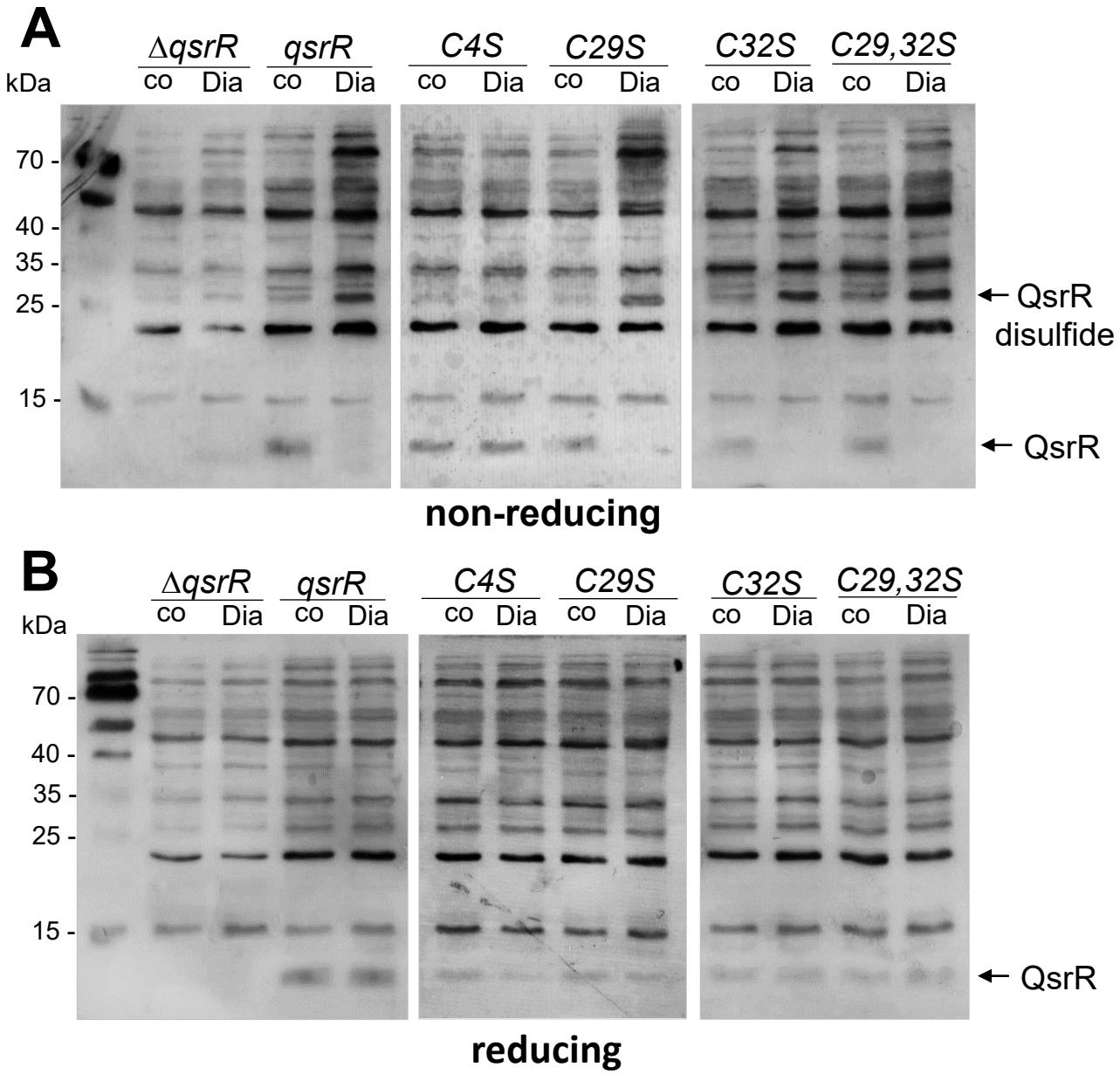
A
ΔqsrR
qsrR
C4S
C29S
C32S
C29,32S
co
Dia
kDa
70
40
35
25
15
QsrR disulfide
QsrR
non-reducing
B
reducing

Fig. 8

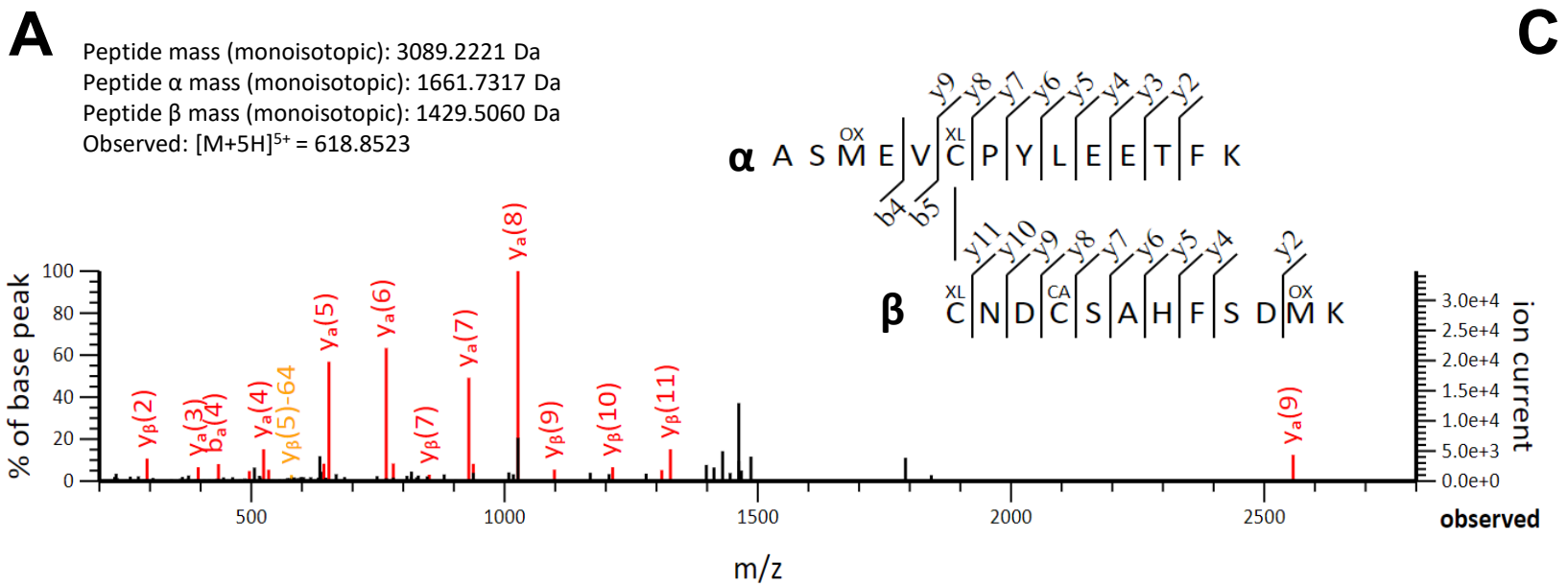
A
Peptide mass (monoisotopic): 3089.2221 Da
Peptide α mass (monoisotopic): 1661.7317 Da
Peptide β mass (monoisotopic): 1429.5060 Da
Observed: [M+5H]5+ = 618.8523
α A S M E V C P Y L E E T F K
β C N D C S A H F S D M K
OX
XL
CA
% of base peak
m/z
ion current
observed

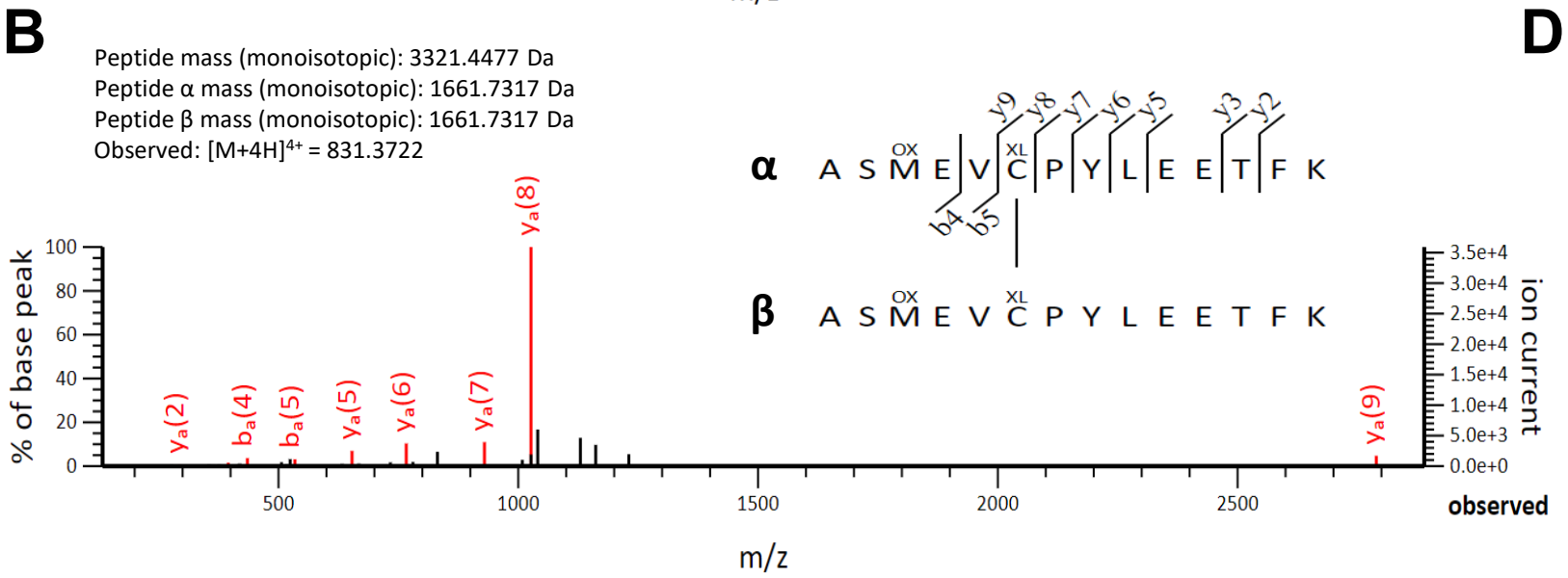
B
Peptide mass (monoisotopic): 3321.4477 Da
Peptide α mass (monoisotopic): 1661.7317 Da
Peptide β mass (monoisotopic): 1661.7317 Da
Observed: [M+4H]4+ = 831.3722
α A S M E V C P Y L E E T F K
β A S M E V C P Y L E E T F K
OX
XL
% of base peak
m/z
ion current
observed

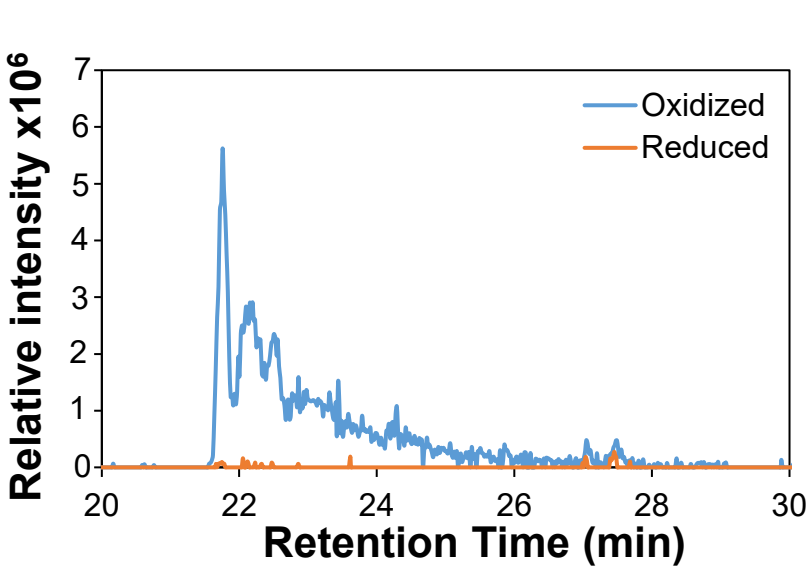
C
Relative intensity x10^6
Retention Time (min)
Oxidized
Reduced

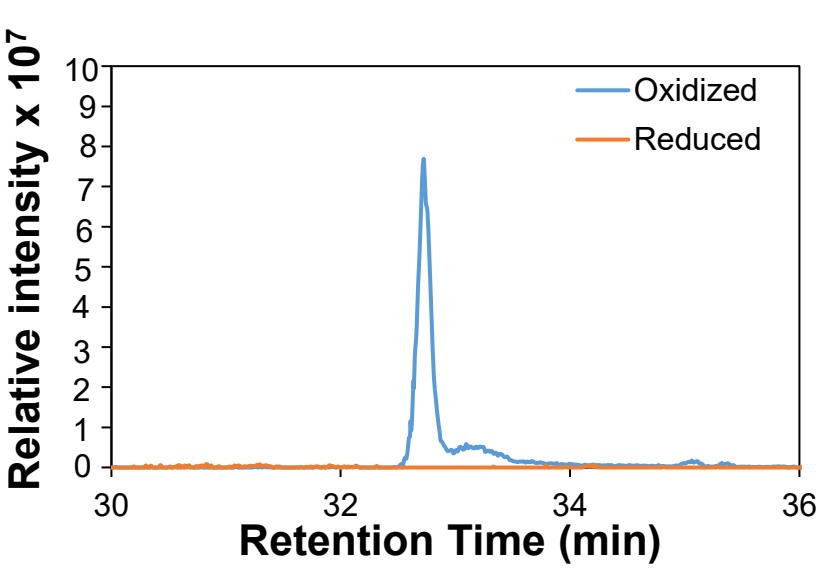
D
Relative intensity x 10^7
Retention Time (min)
Oxidized
Reduced

Fig. 9

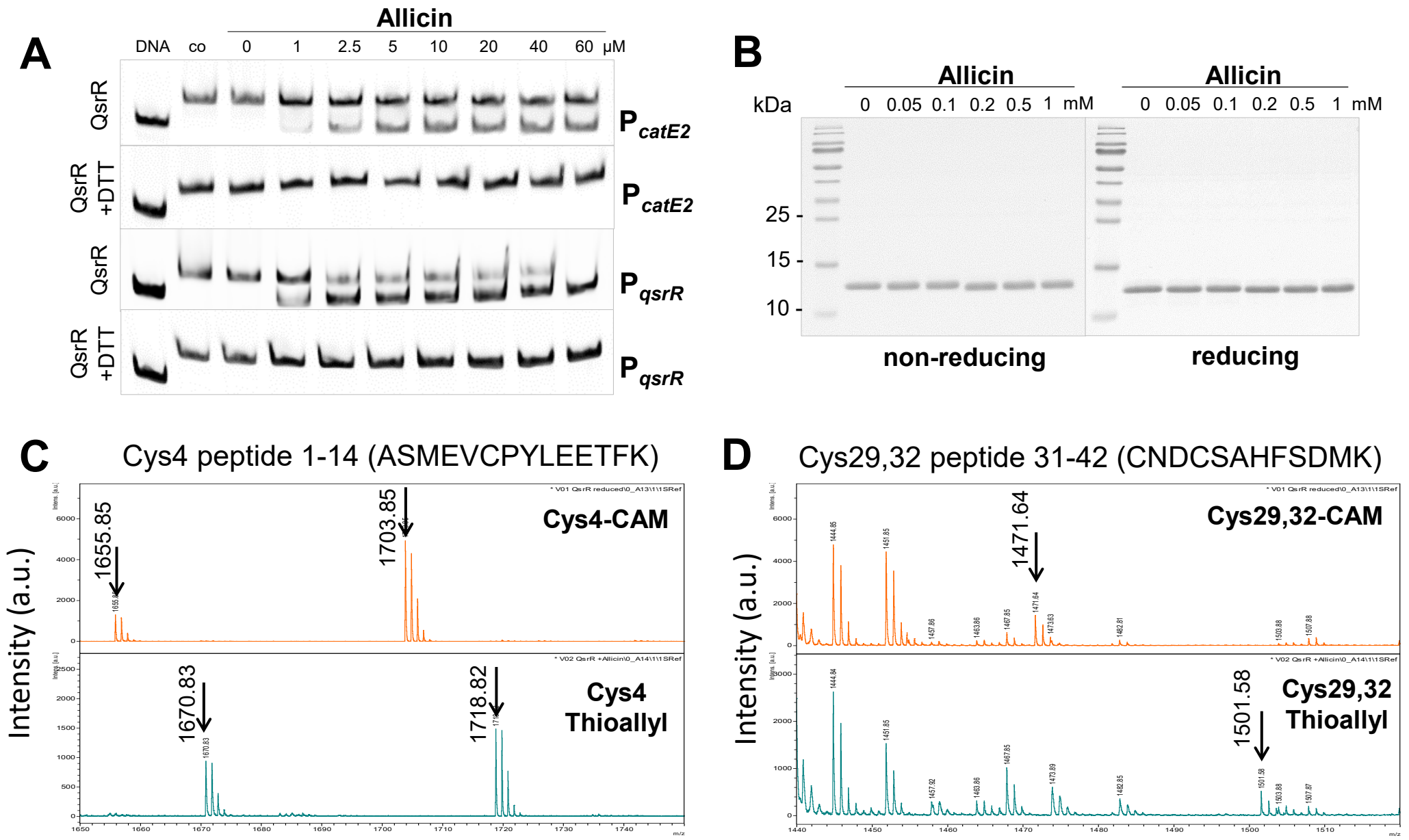
A
Allicin
DNA
co
0
1
2.5
5
10
20
40
60
μM
QsrR
QsrR +DTT
QsrR
QsrR +DTT
P catE2
P catE2
P qsrR
P qsrR
B
Allicin
Allicin
kDa
0 0.05 0.1 0.2 0.5 1 mM
0 0.05 0.1 0.2 0.5 1 mM
25
15
10
non-reducing
reducing
C
Cys4 peptide 1-14 (ASMEVCPYLEETFK)
Intensity (a.u.)
1655.85
1703.85
Cys4-CAM
1670.83
1718.82
Cys4 Thioallyl
D
Cys29,32 peptide 31-42 (CNDCSAHFSDMK)
Intensity (a.u.)
1471.64
Cys29,32-CAM
1501.58
Cys29,32 Thioallyl

Fig. 10

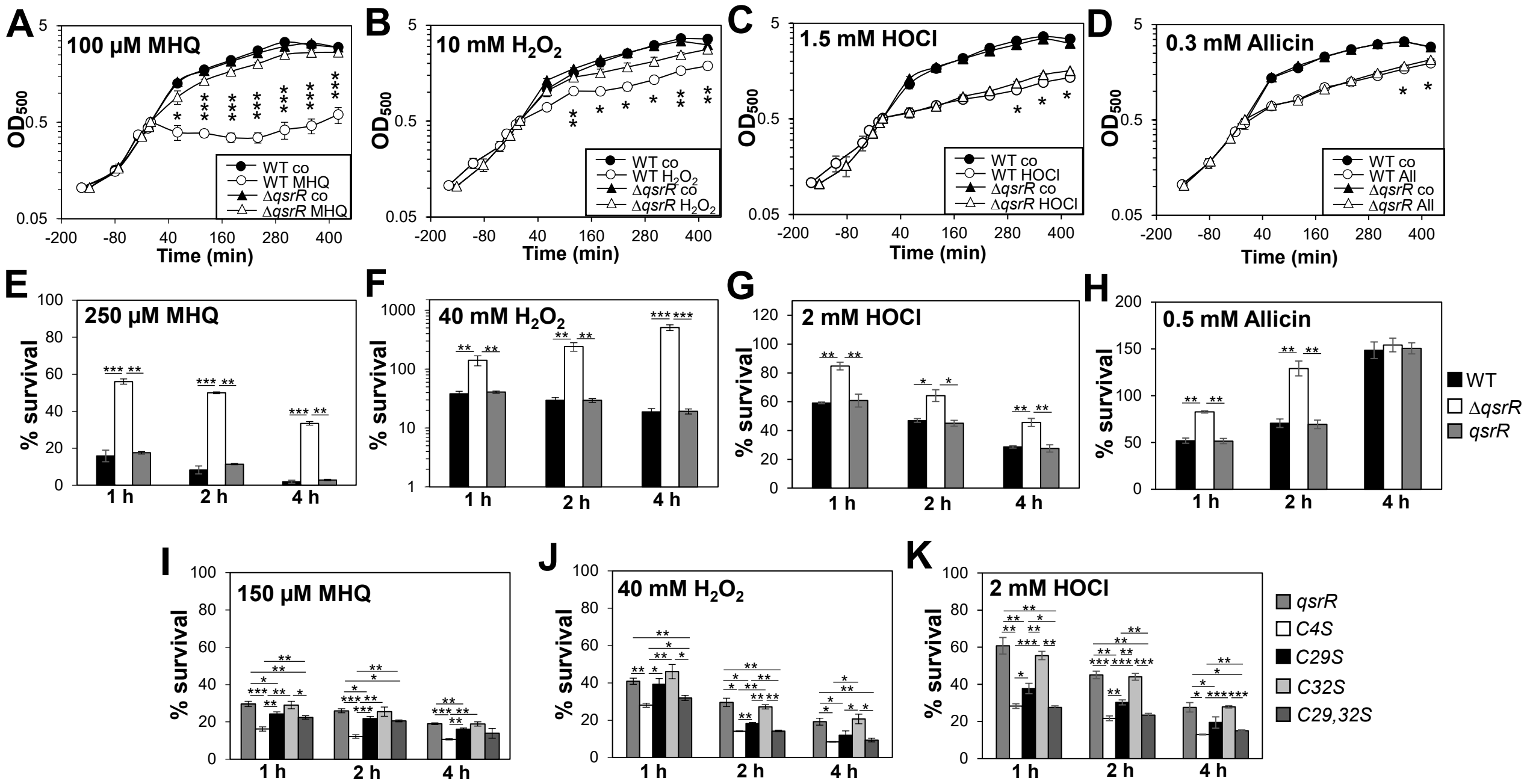
A
100 μM MHQ
OD500
Time (min)
WT co
WT MHQ
ΔqsrR co
ΔqsrR MHQ
B
10 mM H2O2
WT co
WT H2O2
ΔqsrR co
ΔqsrR H2O2
C
1.5 mM HOCl
WT co
WT HOCl
ΔqsrR co
ΔqsrR HOCl
D
0.3 mM Allicin
WT co
WT All
ΔqsrR co
ΔqsrR All
E
250 μM MHQ
% survival
1 h
2 h
4 h
F
40 mM H2O2
G
2 mM HOCl
H
0.5 mM Allicin
WT
ΔqsrR
qsrR
I
150 μM MHQ
J
40 mM H2O2
K
2 mM HOCl
qsrR
C4S
C29S
C32S
C29,32S

Fig. S1

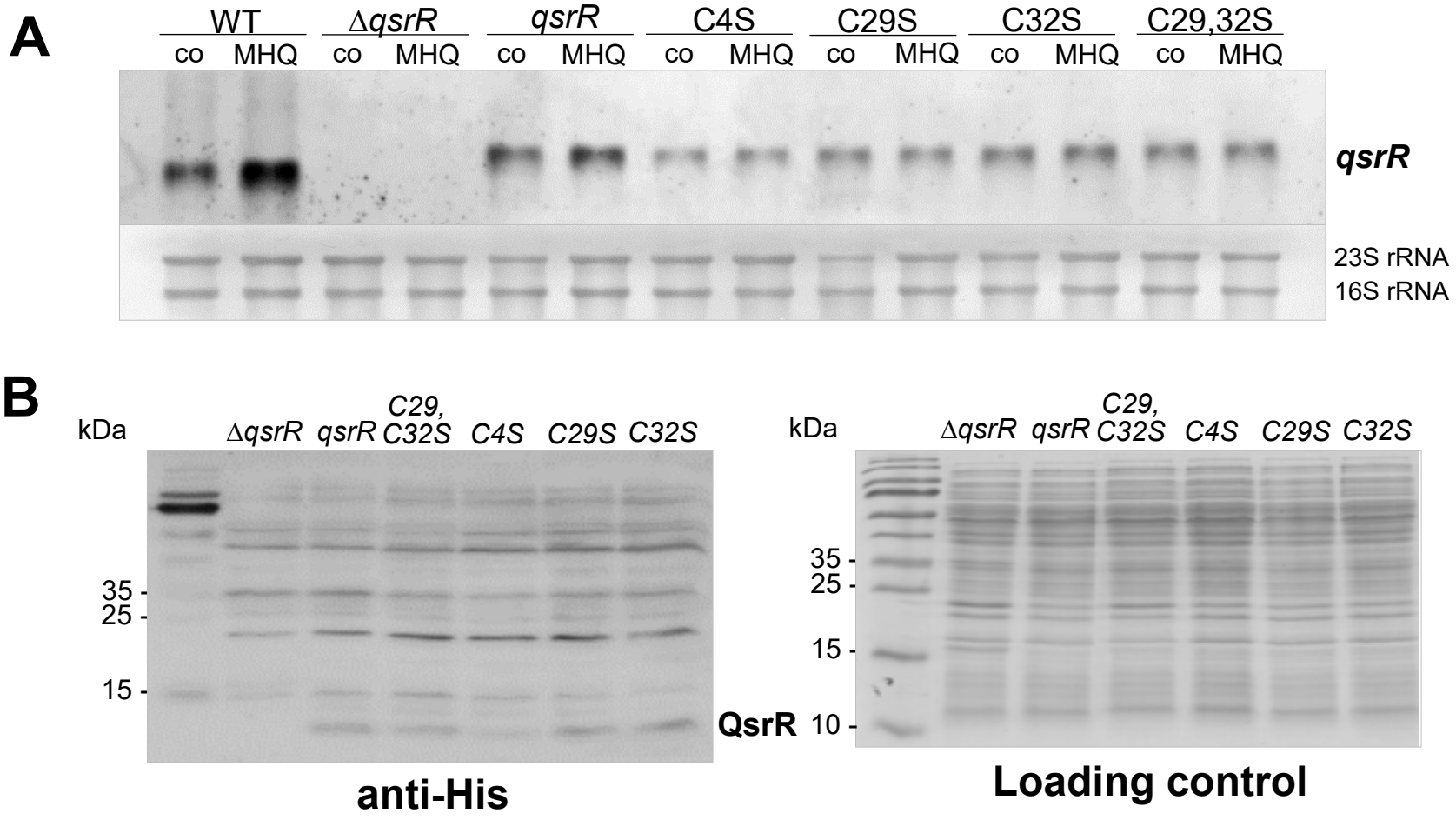

Fig. S1. Northern blot and Western blot analysis of transcription and protein expression in the *qsrR* and *qsrR* Cys mutant complemented strains. (A) The complementation of the *qsrR* mutant with pRB473-encoded *qsrR*, *qsrRC4S*, *qsrRC29S*, *qsrRC32S* and *qsrRC29,32S* alleles under control (co) and 50 µM methylhydroquinone (MHQ) stress was confirmed using Northern blots with a *qsrR*-specific mRNA probe. **(B)** By Western blot analysis, protein expression was verified for the QsrR, QsrRC4S, QsrRC29S, QsrRC32S and QsrRC29,32S mutant proteins in the complemented strains after overnight growth in LB medium.

Fig. S2

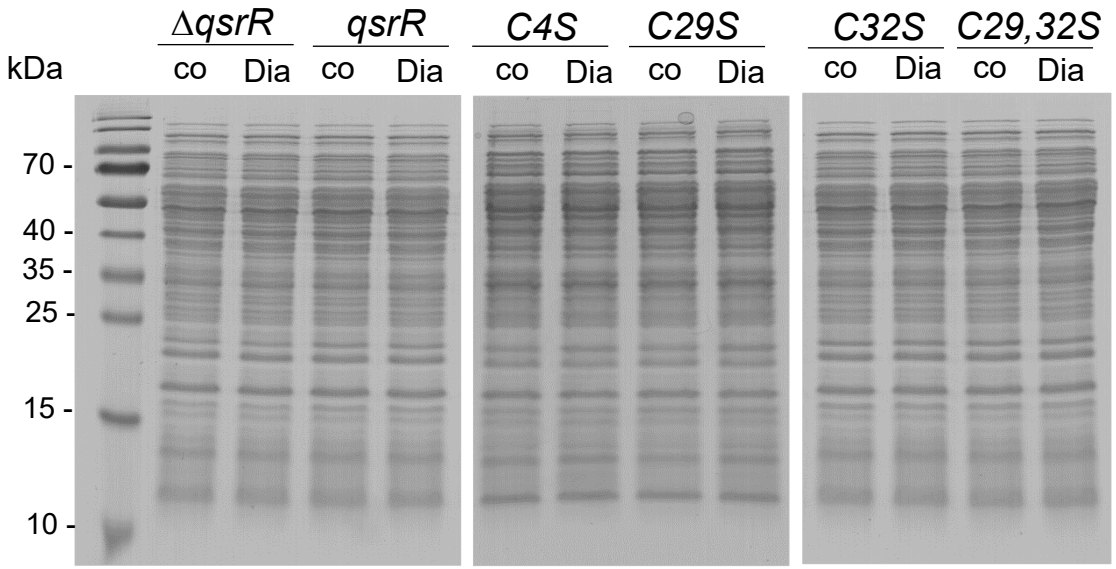

Fig. S2. Coomassie-stained SDS-PAGE loading control. The same protein extracts of the *S. aureus* COL *qsrR* mutant and the *qsrR*, *qsrRC4S*, *qsrRC29S*, *qsrRC32S* and *qsrRC29,32S* complemented strains after diamide (Dia) stress, which were used for Western blot analyses in Fig. 7, were separated by reducing SDS-PAGE and stained with Coomassie Blue as loading control.

Fig. S3

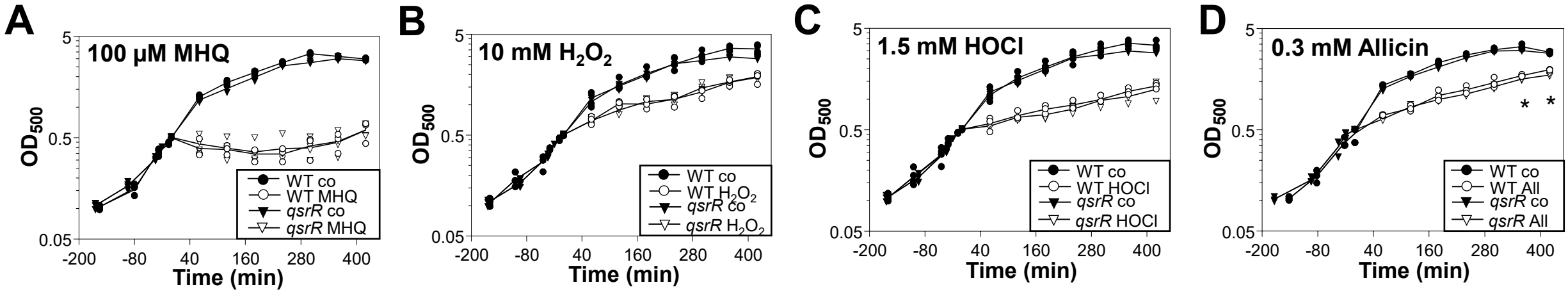

Fig. S3. The phenotype of the *qsrR* mutant can be restored to the WT level in the *qsrR* complemented strain. For the growth curves, *S. aureus* COL WT and the *qsrR* complemented strain (*qsrR*) were grown in RPMI medium. At an OD_{500} of 0.5 the strains were exposed to 100 µM methylhydroquinone (MHQ) **(A),** 10 mM H_2O_2 **(B)**, 1.5 mM HOCl **(C)** and 0.3 mM allicin **(D)**. The results are from three to four biological replicates. Error bars represent the standard deviation. $p > 0.05$; $^*p < 0.05$.

Fig. S4

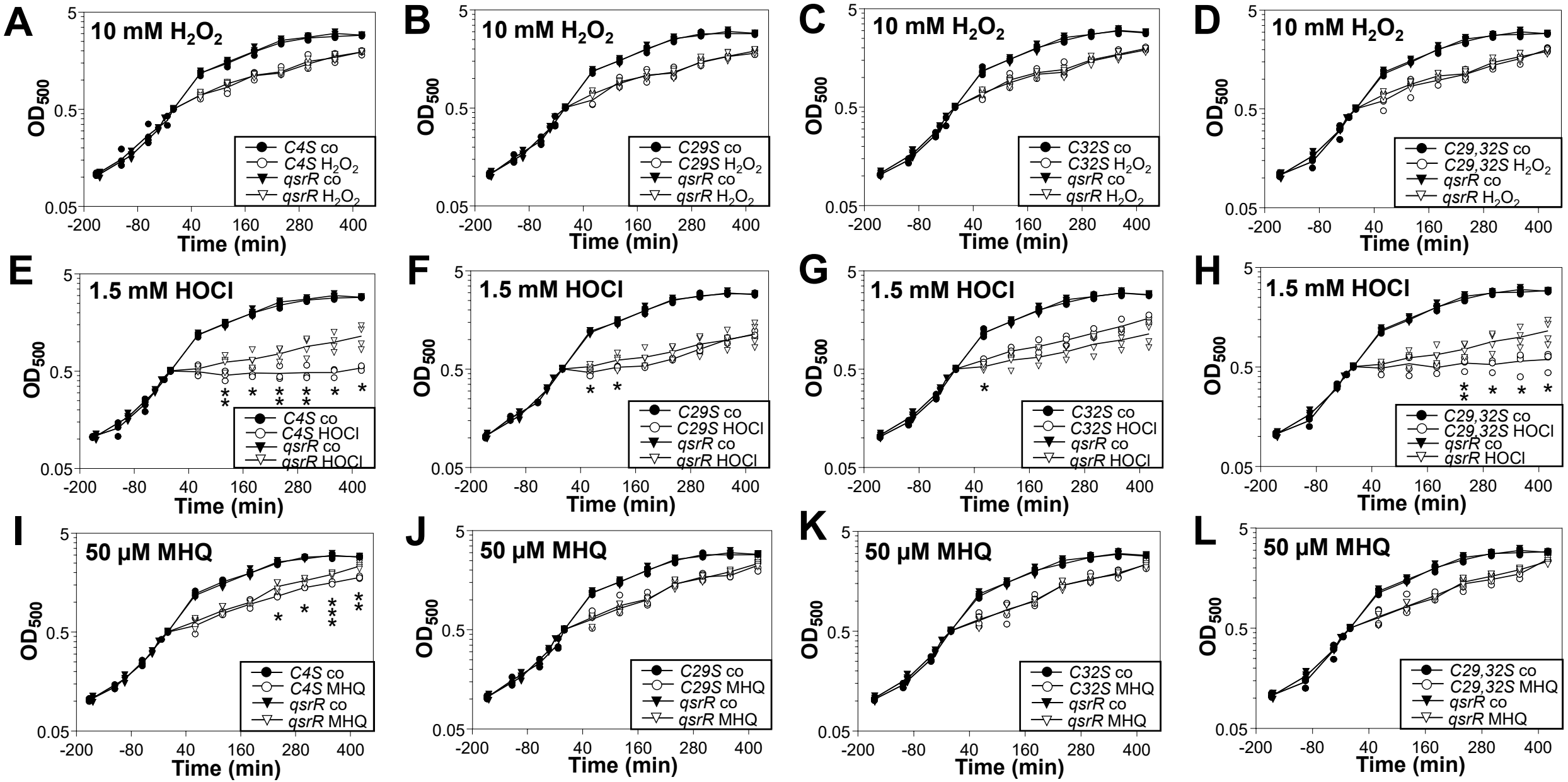

Fig. S4. Cys4 is required for MHQ resistance, while Cys4 and either Cys29 or Cys32 are essential for HOCl tolerance. For growth curves, the *S. aureus* COL *qsrR* mutant complemented with the *qsrR, qsrRC4S, qsrRC29S, qsrRC32S* and *qsrRC29,32S* alleles were grown in RPMI until an OD_{500} of 0.5 and treated with 10 mM H_2O_2 **(A-D)**, 1.5 mM HOCl **(E-H)** and 50 μM methylhydroquinone (MHQ) **(I-L)**. The results are from three to four biological replicates. Error bars represent the standard deviation. $p > 0.05$; $^*p < 0.05$; $^{**}p < 0.01$; $^{***}p < 0.001$.

Fig. S5

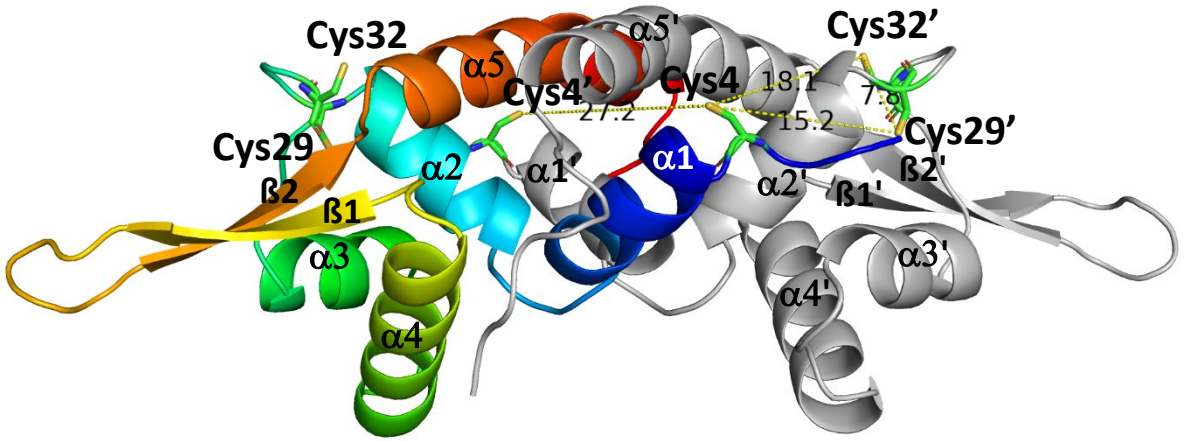

QsrR (PDB:4HQE)

Fig. S5. The structure of the 2-Cys-type QsrR repressor with the positions of the 3 Cys residues. The QsrR structure (PDB:4HQE) was previously resolved (Ji et al., 2013) and is visualized with PyMol. The α1-α6 helices and ß1-ß2 sheets are labelled in both subunits of the QsrR dimer. The distance of Cys4 and Cys29' was calculated as ~15.2Å, whereas Cys4 and Cys4' are 27Å apart between the opposing subunits of the QsrR dimer. Cys4 and Cys29' are oxidized to intersubunit disulfides in the QsrR dimer under diamide stress.

Fig. S6

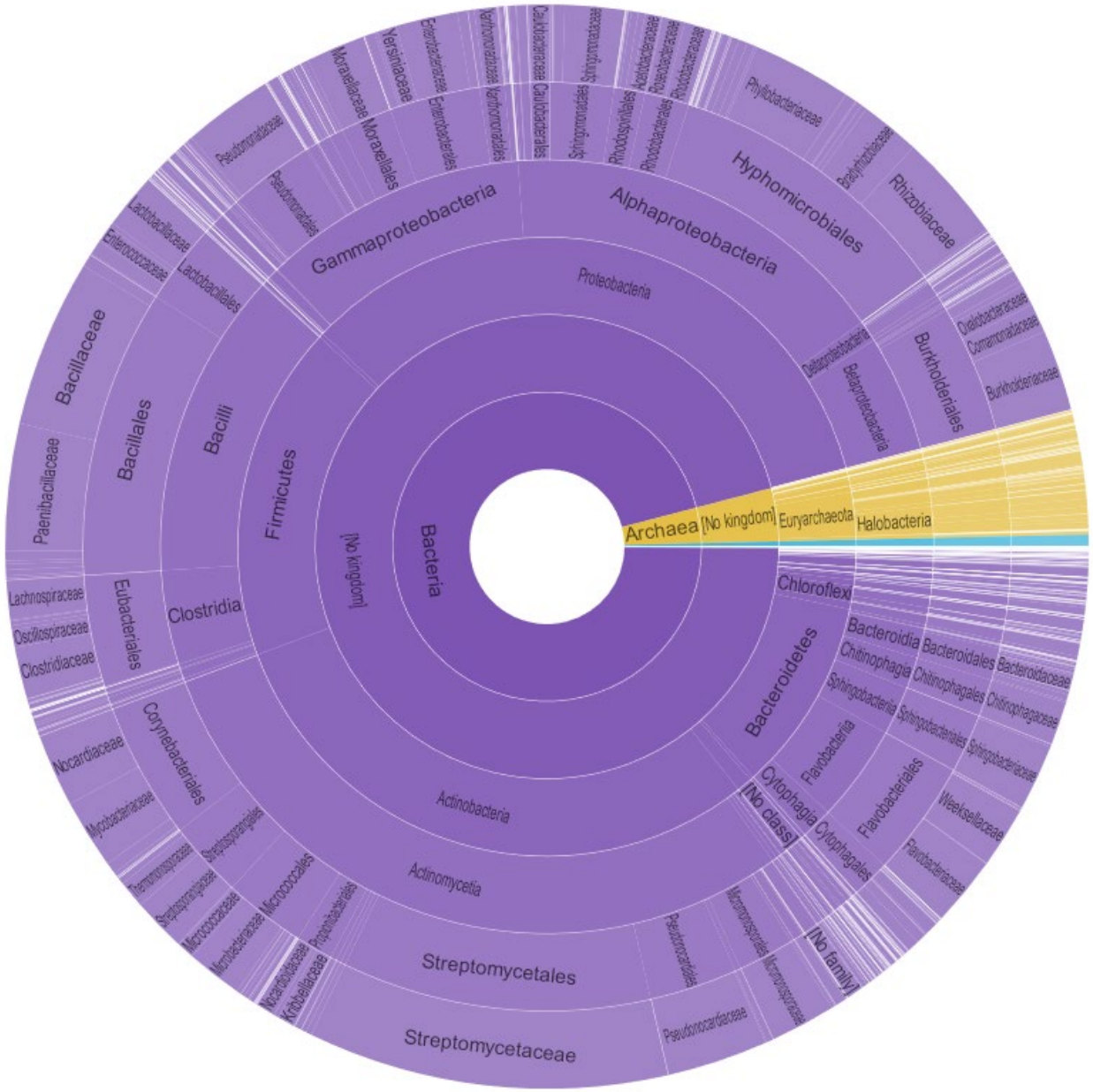

Fig. S6. Sunburst view of 19719 species encoding the HxIR-type HTH domain proteins in bacteria and archaea (IPR002577) according to the InterPro database (https://www.ebi.ac.uk/interpro/entry/InterPro/IPR002577).

Fig. S7

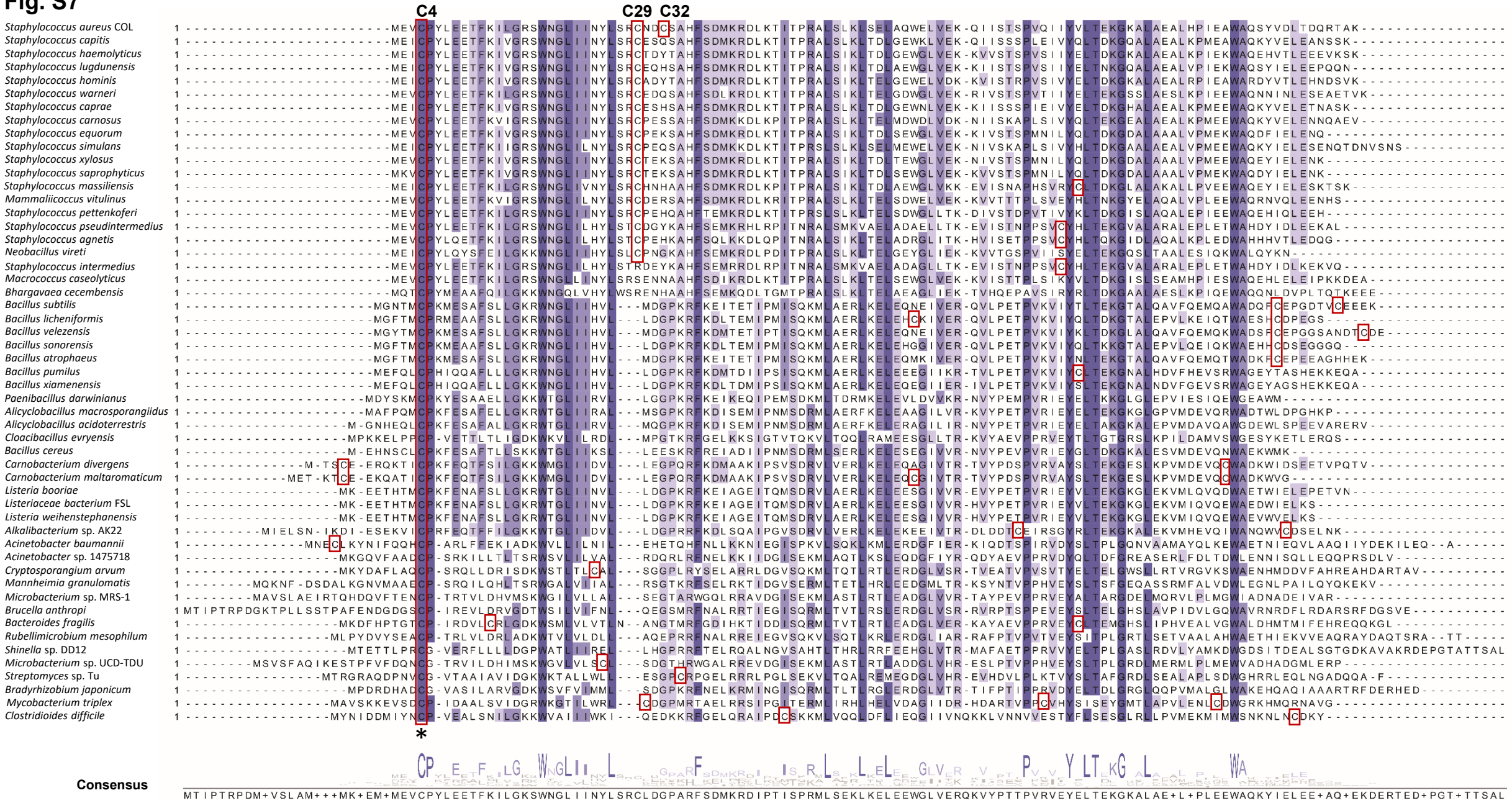

Fig. S7. ClustalW2 protein sequence alignment of selected QsrR (SACOL2115) homologs according to EMBL STRING (https://string-db.org/) and InterPro databases (https://www.ebi.ac.uk/interpro/entry/InterPro/IPR002577). The QsrR homologs harbor the HxlR-type HTH domain (IPR002577) with a conserved N-terminal Cys residue (*) (Cys4 of QsrR). The alignment and consensus is presented in Jalview. Intensity of the blue color gradient is based on 50% protein sequence. Cys residues are indicated by red boxes.

Table S1. Transcriptional induction of the QsrR-regulon under oxidative and electrophile stress according to published RNA-seq datasets

SACOL-No.	Gene symbol	Operon	Functions	log2-FC NaOCl	log2-FC Allicin	log2-FC AgXX	log2-FC MHQ	log2-FC Lapachol
SACOL2533	*catE2*	*catE2*	possible dioxygenase	3,25	6,33	6,71	8,12	2,29
SACOL2020	*yodC*	*yodC*	possible nitroreductase	2,79	4,09	3,86	4,68	0,81
SACOL0408	*catE*	*catE-SACOL0409-azoR1*	possible lactoylglutathione lyase/dioxygenase	2,08	5,89	5,53	6,19	1,89
SACOL0409	*SACOL0409*	*catE-SACOL0409-azoR1*	possible alkanal monooxygenase (FMN-linked)	2,24	5,99	5,71	6,58	2,12
SACOL0410	*azoR1*	*catE-SACOL0409-azoR1*	possible FMN reductase	2,28	5,78	5,88	6,92	2,05

Table S1. Transcriptional expression of the QsrR-regulon under oxidative and electrophile stress . The published RNAseq datasets of *S. aureus* COL and USA300 strains exposed to 150 µM HOCl (1), 0.3 mM allicin (2), 5 µg/ml AGXX (3), 45 µM MHQ (4) and 300 µM lapachol (5) show strong induction of the QsrR regulon genes *catE2, yodC* and the *catE-SACOL0409-azoR1* operon by oxidants and electrophiles.

References:

1) Loi VV, Busche T, Tedin K, Bernhardt J, Wollenhaupt J, Huyen NTT, Weise C, Kalinowski J, Wahl MC, Fulde M, Antelmann H. Redox-sensing under hypochlorite stress and infection conditions by the Rrf2-family repressor HypR in *Staphylococcus aureus* . Antioxid Redox Signal 29: 615-636, 2018.

2) Loi VV, Huyen NTT, Busche T, Tung QN, Gruhlke MCH, Kalinowski J, Bernhardt J, Slusarenko AJ, Antelmann H. *Staphylococcus aureus* responds to allicin by global S-thioallylation - role of the Brx/BSH/YpdA pathway and the disulfide reductase MerA to overcome allicin stress. Free Radic Biol Med 139: 55-69, 2019.

3) Loi VV, Busche T, Preuss T, Kalinowski J, Bernhardt J, Antelmann H. The AGXX(R) antimicrobial coating causes a thiol-specific oxidative stress response and protein *S* -bacillithiolation in *Staphylococcus aureus* . Front Microbiol 9: 3037, 2018.

4) Fritsch VN, Loi VV, Busche T, Sommer A, Tedin K, Nürnberg DJ, Kalinowski J, Bernhardt J, Fulde M, Antelmann H. The MarR-type repressor MhqR confers quinone and antimicrobial resistance in *Staphylococcus aureus* . Antioxid Redox Signal 31: 1235-1252, 2019.

5) Linzner N, Fritsch VN, Busche T, Tung QN, Van Loi V, Bernhardt J, Kalinowski J, Antelmann H. The plant-derived naphthoquinone lapachol causes an oxidative stress response in *Staphylococcus aureus* . Free Radic Biol Med 158: 126-136, 2020.

Table S2. Bacterial strains, phages and plasmids.

Strain	Description	Reference
Staphylococcus aureus		
RN4220	restriction negative strain/MSSA cloning intermediate derived from 8325-4	(1)
COL	archaic HA-MRSA strain	(2, 3)
COL-Δ*qsrR*	COL *qsrR* deletion mutant	(4)
COL-Δ*qsrR*-pRB473-*qsrR-His*	COL *qsrR* deletion mutant complemented with pRB473-*qsrR-His*	This study
COL-Δ*qsrR*-pRB473-*qsrRC4S-His*	COL *qsrR* deletion mutant complemented with pRB473-*qsrRC4S-His*	This study
COL-Δ*qsrR*-pRB473-*qsrRC29S-His*	COL *qsrR* deletion mutant complemented with pRB473-*qsrRC29S-His*	This study
COL-Δ*qsrR*-pRB473-*qsrRC32S-His*	COL *qsrR* deletion mutant complemented with pRB473-*qsrRC32S-His*	This study
COL-Δ*qsrR*-pRB473-*qsrRC29,32S-His*	COL *qsrR* deletion mutant complemented with pRB473-*qsrRC29,32S-His*	This study
Staphylococcus phage 81		(5)
Escherichia coli		
DH5α	F-φ80dlacZ Δ(lacZYA-argF) U169 deoRsupE44ΔlacU169 (f80lacZDM15) hsdR17 recA1 endA1 (rk- mk+) supE44gyrA96 thi-1 gyrA69 relA1	(6)
BL21(DE3)*plysS*	F- ompT hsdS gal (rb- mb+) DE3(Sam7 Δnin5 lacUV5-T7 Gen1)	(6)
BL21(DE3)*plysS* pET11b-*qsrR-His*	For overexpression of His-tagged QsrR	This study
BL21(DE3)*plysS* pET11b-*qsrRC4S-His*	For overexpression of His-tagged QsrRC4S	This study
BL21(DE3)*plysS* pET11b-*qsrRC29S-His*	For overexpression of His-tagged QsrRC29S	This study
BL21(DE3)*plysS* pET11b-*qsrRC32S-His*	For overexpression of His-tagged QsrRC32S	This study
plasmids		
pRB473	pRB373-derivative, *E. coli/ S. aureus* shuttle vector, containing xylose-inducible P_{Xyl} promoter Amp^R, Cm^R	(7, 8)
pRB473-*qsrR-His*	pRB473-derivative expressing *qsrR-His* under P_{Xyl}	This study
pRB473-*qsrRC4S-His*	pRB473-derivative expressing *qsrRC4S-His* under P_{Xyl}	This study
pRB473-*qsrRC29S-His*	pRB473-derivative expressing *qsrRC29S-His* under P_{Xyl}	This study
pRB473-*qsrRC32S-His*	pRB473-derivative expressing *qsrRC32S-His* under P_{Xyl}	This study
pRB473-*qsrRC29,32S-His*	pRB473-derivative expressing *qsrRC29,32S-His* under P_{Xyl}	This study
pET11b	*E. coli* expression plasmid	Novagen
pET11b-*qsrR-His*	pET11b-derivative for overexpression of His-tagged QsrR	This study
pET11b-*qsrRC4S-His*	pET11b-derivative for overexpression of His-tagged QsrRC4S	This study
pET11b-*qsrRC29S-His*	pET11b-derivative for overexpression of His-tagged QsrRC29S	This study
pET11b-*qsrRC32S-His*	pET11b-derivative for overexpression of His-tagged QsrRC32S	This study

^{R}: resistant, Amp: ampicillin, Cm: chloramphenicol

Table S3. Oligonucleotide (primer) sequences

Primer name	Sequence (5' to 3')
NB-qsrR-for	ATACTTGGTAGAAGTTGGAA
NB-qsrR-rev	CTAATACGACTCACTATAGGGAGAACGTTGATCTGTTAAATCGA
NB-catE2-for	ACATTTATTAGAAGACGGCC
NB-catE2-rev	CTAATACGACTCACTATAGGGAGAATGTATGTGTTGAGGCGTCG
EMSA-qsrR-for	GCTGAGGGTGTAACTACAAT
EMSA-qsrR-rev	CATACTTCCATCATCTTCAC
EMSA-catE2-for	ATAAATTTTGCGATGGTGCAAC
EMSA-catE2-rev	ATCGTGAAATGCCATTATGCAT
EMSA-qsrR-m1-for	GTGGT**G**T**C**ATAATTATACT
EMSA-qsrR-m1-rev	AGTATAATTAT**G**A**C**ACCAC
EMSA-qsrR-m2-for	GTGGTATAATAATT**G**T**C**CT
EMSA-qsrR-m2-rev	AG**G**A**C**AATTATTATACCAC
pRB-qsrR-for-BamHI	TAGGGATCCATTTATTGATGAGAGGTGAAGATGATGGAAGTATGTCCGTATC
pRB-qsrR-rev-KpnI	CGCGGTACCTTAGTGATGGTGATGGTGATGTTTAGCAGTACGTTGATCTGTT
pRB-qsrRC4S-for-BamHI	TAGGGATCCATTTATTGATGAGAGGTGAAGATGATGGAAGTATCTCCGTATC
qsrRC29SC32S-for	ATTAATTATCTCTCAAGA**TCT**AATGAC**TCT**TCAGCACAC
qsrRC29SC32S-rev	GTGTGCTGA**AGA**GTCATT**AGA**TCTTGAGAGATAATTAAT
pET-qsrR-for-NheI	CTAGCTAGCATGGAAGTATGTCCGTATCTC
pET-qsrR-rev-BamHI	CGCGGATC**C**TTAGTGATGGTGATGGTGATG
pET-qsrRC4S-for-NheI	CTAGCTAGCATGGAAGTA**TCT**CCGTATCTC
pET-qsrRC29S-rev-f1	CGGAAAAGTGTGCTGAACAGTCATT**AGA**TCTTGAGAGAT
pET-qsrRC29S-for-f2	ATCTCTCAAGA**TCT**AATGACTGTTCAGCACACTTTTCCG
pET-qsrRC32S-rev-f1	CGGAAAAGTGTGCTGA**AGA**GTCATTACATCTTGAGAGAT
pET-qsrRC32S-for-f2	ATCTCTCAAGATGTAATGAC**TCT**TCAGCACACTTTTCCG

References of Table S2

1. Kreiswirth BN, Lofdahl S, Betley MJ, O'Reilly M, Schlievert PM, Bergdoll MS, Novick RP. 1983. The toxic shock syndrome exotoxin structural gene is not detectably transmitted by a prophage. Nature 305:709-12.

2. Shafer WM, Iandolo JJ. 1979. Genetics of staphylococcal enterotoxin B in methicillin-resistant isolates of *Staphylococcus aureus*. Infect Immun 25:902-11.

3. Gill SR, Fouts DE, Archer GL, Mongodin EF, Deboy RT, Ravel J, Paulsen IT, Kolonay JF, Brinkac L, Beanan M, Dodson RJ, Daugherty SC, Madupu R, Angiuoli SV, Durkin AS, Haft DH, Vamathevan J, Khouri H, Utterback T, Lee C, Dimitrov G, Jiang L, Qin H, Weidman J, Tran K, Kang K, Hance IR, Nelson KE, Fraser CM. 2005. Insights on evolution of virulence and resistance from the complete genome analysis of an early methicillin-resistant *Staphylococcus aureus* strain and a biofilm-producing methicillin-resistant *Staphylococcus epidermidis strain*. J Bacteriol 187:2426-38.

4. Fritsch VN, Loi VV, Busche T, Sommer A, Tedin K, Nurnberg DJ, Kalinowski J, Bernhardt J, Fulde M, Antelmann H. 2019. The MarR-Type Repressor MhqR Confers Quinone and Antimicrobial Resistance in *Staphylococcus aureus*. Antioxid Redox Signal 31:1235-1252.

5. Rosenblum ED, Tyrone S. 1964. Serology, Density, and Morphology of Staphylococcal Phages. J Bacteriol 88:1737-42.

6. Studier FW, Moffatt BA. 1986. Use of bacteriophage T7 RNA polymerase to direct selective high-level expression of cloned genes. J Mol Biol 189:113-30.

7. Brückner R, Wagner E, Götz F. 1993. Characterization of a sucrase gene from *Staphylococcus xylosus*. J Bacteriol 175:851-7.

8. Pöther DC, Gierok P, Harms M, Mostertz J, Hochgräfe F, Antelmann H, Hamilton CJ, Borovok I, Lalk M, Aharonowitz Y, Hecker M. 2013. Distribution and infection-related functions of bacillithiol in *Staphylococcus aureus*. Int J Med Microbiol 303:114-23.

Table S4. % protein-DNA complex formation of the untreated QsrR, C4S, C29S and C32S proteins

***catE2* promoter**		**0**	**0.002**	**0.005**	**0.01**	**0.1**	**0.15**	**0.2**	**0.3**	**0.4**	**0.5**	**µM Protein**
QsrR	rep. 1	0.0086	3.8884	4.1365	7.8014	58.503	88.222	93.530	93.663	95.331	99.200	
	rep. 2	0.0092	3.1250	7.1315	39.224	53.417			93.164			
	rep. 3	0.0103			9.6442		92.952	92.936	95.450	95.361	97.190	
	rep. 4	0.0097	2.0423	3.1733	4.9015	51.023	89.159	92.598	97.527	97.904	98.981	
C4S	rep. 1	0.0106	2.9505	5.5035	8.9280	63.555	88.175	95.829	93.291	96.963	95.180	
	rep. 2	0.0106	1.7795	4.6287	10.499	53.206	90.767	89.778	93.303	95.542	100.00	
	rep. 3	0.0102	3.4959	4.4407	10.978	63.916	81.908	95.384	95.540	96.489	85.800	
C29S	rep. 1	0.0090	1.3219	2.7519	10.398	48.146	86.907	91.382	93.756	94.359	95.069	
	rep. 2	0.0084	0.6384	2.1962	14.617	61.428			96.937	96.922	93.681	
	rep. 3	0.0104	1.6413	2.5249	15.416	61.287	87.191	89.515	93.426	95.009	96.863	
	rep. 4	0.0055	1.7099	1.9438	10.655	59.245	84.449	85.517		90.074	90.667	
C32S	rep. 1	0.0094	0.7623	5.9537	9.2002	61.573	81.139	89.493	90.184	89.259	84.883	
	rep. 2	0.0104	3.8024	3.5632	7.7460	52.655	87.432	94.741	95.576	95.174	90.573	
	rep. 3	0.0048	2.7929	5.8944	11.023	64.033	89.617	96.379	95.220	95.683	93.087	
***qsrR* promoter**		**0**	**0.002**	**0.005**	**0.01**	**0.1**	**0.15**	**0.2**	**0.3**	**0.4**	**0.5**	**µM Protein**
QsrR	rep. 1	0.0082	0.7329	1.3004		49.565	59.062	81.162	92.183		94.598	
	rep. 2	0.0087	0.7329		9.5939	46.737		92.572	94.252	96.555	96.302	
	rep. 3	0.0090		2.6445	6.6217	43.831	55.897	79.94		92.39	90.263	
	rep. 4	0.0094	0.0092	3.3141	4.8608	42.121	65.779	71.192	98.784	98.061		
C4S	rep. 1	0.0107	1.8143	6.1601	7.6599	44.394	63.281	94.629	92.322	96.687	89.828	
	rep. 2	0.0115	1.8195	6.8332	2.4925	40.373	48.41	88.745	94.352	96.285	93.502	
	rep. 3	0.0119	1.2101	7.3252	4.1392	58.078	68.702	76.514	79.686	86.932	85.987	
C29S	rep. 1	0.0077	1.0362	3.4705	4.0262	49.422	66.108	83.362	81.438	88.363	92.096	
	rep. 2	0.0093	0.8563	2.6631	6.8683	56.475	68.643	89.794	96.984	98.38	98.53	
	rep. 3	0.0102	2.63	5.3793		30.337			74.854	89.896	93.127	
	rep. 4	0.008	1.3259	5.2874	7.2879	40.469	61.335	74.462	85.662	88.663		
C32S	rep. 1	0.0116	2.8891	7.8785	10.26	45.423	73.696	86.615	90.644	91.241	89.466	
	rep. 2	0.0041	1.6307	6.3756	11.063	36.394	68.148	79.956	78.693	92.427	99.995	
	rep. 3	0.01	1.7816	2.1302	5.0132	54.413	62.74	79.692	98.376	98.141	99.291	

Table S4. The percentage of the protein-DNA complex formation was determined according to the band intensities of 3-4 biological replicates of the EMSAs and quantified using Image J 1.52a. The calculated percentual values of all biological replicates are shown for 0-0.5 µM of the QsrR, C4S, C29S and C32S proteins bound to the catE2 and qsrR promoter. These values were used for the nonlinear regression shown in Fig. 2C, D using the specific binding with Hill slope of the Graph prism software version 7.03 to determine the Dissociation constants (KD).

Table S5. % protein-DNA complex formation of the QsrR, C4S, C29S and C32S proteins after diamide

***catE2* promoter**		**0**	**0.002**	**0.005**	**0.01**	**0.1**	**0.15**	**0.2**	**0.3**	**0.4**	**0.5**	**µM Protein**
QsrR	rep. 1	0.0080	4.0550	4.8436	8.6631	35.790	38.531	65.915	73.996	86.947	93.610	
	rep. 2	0.0106	1.1066	1.7413	2.2803	12.905	17.588	42.740	62.150	83.067	97.450	
	rep. 3	0.0109	0.1146	0.4018	1.3967	12.133	32.071	45.320	61.503	81.936	97.604	
C4S	rep. 1	0.0102	1.6417	3.3630	9.8417	69.542	91.017	96.109	96.934	97.262	97.929	
	rep. 2	0.0150	1.0655	2.4005	4.8149	58.598	87.222	91.339	95.827	97.274	97.283	
	rep. 3	0.0123	2.7037	8.4609	16.019	66.195	76.372	96.687	94.609	94.789	96.608	
	rep. 4	0.0108	3.1917	9.8581	8.8100	53.045	69.527	84.715	88.036	89.260	79.486	
C29S	rep. 1	0.0087	3.0922	4.4371	4.7301	6.7512	19.429	41.075	54.601	66.817	94.527	
	rep. 2	0.0112	0.8528	3.8966	7.3386	8.0707	29.730	47.616	69.455	77.467	92.607	
	rep. 3	0.0114	6.7466	9.2396	11.351	19.732	34.264	49.908	69.877	92.386	93.672	
	rep. 4	0.0109	2.4825	4.0939	6.4021	11.282	19.215	47.509	57.770	68.481	97.161	
C32S	rep. 1	0.0124	4.1421	1.7132	0.8258	26.981	24.308	58.598	62.479	87.605	97.138	
	rep. 2	0.0095	2.1336	2.8946	3.0593	18.247	19.859	44.985	67.069	91.329	97.857	
	rep. 3	0.0118	1.7296	3.0042	5.2796	16.030	25.495	45.094	64.727	90.210	98.183	
***qsrR* promoter**		**0**	**0.002**	**0.005**	**0.01**	**0.1**	**0.15**	**0.2**	**0.3**	**0.4**	**0.5**	**µM Protein**
QsrR	rep. 1	0.0107	2.4135	3.2071	4.1218	6.7143	46.286	56.322	66.779	77.926	98.605	
	rep. 2	0.0115	0.9846	1.9938	3.3787	10.864	38.759	49.946	60.601	77.517	98.068	
	rep. 3	0.0047	3.0439	2.4570	3.0310	9.2895	32.017	53.775	58.441	72.648	97.420	
C4S	rep. 1	0.0115	1.3869	2.0015	3.3465	48.377	39.974	75.859	95.473	98.354	98.354	
	rep. 2	0.0102	1.5727	2.7698	7.2213	53.122	68.132	94.305	97.619	96.195	97.297	
	rep. 3	0.0134	0.5091	2.4737	4.7776	44.794	61.756	94.242	98.181	96.213	94.281	
	rep. 4	0.0111	0.9855	13.35	19.901	58.056	70.917	75.62	81.102	78.125	76.93	
C29S	rep. 1	0.0109	1.2426	6.8603	7.2016	12.442	26.835	53.727	60.935	79.481	85.803	
	rep. 2	0.0126	0.0768	7.8458	15.295	21.771	27.395	50.133	58.133	87.298	93.872	
	rep. 3	0.0080	4.8533	3.4712	5.9802	13.921	15.250	51.612	57.767	78.271	89.079	
	rep. 4	0.0093	2.9269	4.0215	10.940	13.641	19.584	52.446	58.925	85.992	90.392	
C32S	rep. 1	0.0091	1.4360	3.4721	5.1606	12.830	23.817	48.778	65.259	87.936	98.267	
	rep. 2	0.0104	0.9047	2.6804	9.2301	12.711	26.443	50.523	60.660	88.724	97.266	
	rep. 3	0.0100	0.6412	1.5962	3.9630	13.593	26.104	47.020	62.684	87.463	98.575	

Table S5. The percentage of the protein-DNA complex formation was determined according to the band intensities of 3-4 biological replicates of the EMSAs and quantified using Image J 1.52a. The calculated percentual values of all biological replicates are shown for 0-0.5 µM of the QsrR, C4S, C29S and C32S proteins bound to the catE2 and qsrR promoter after addition of 20 µM diamide. These values were used for the nonlinear regression shown in Fig. 4D, E using the specific binding with Hill slope of the Graph prism software version 7.03 to determine the Dissociation constants (K_D).

Table S6. % protein-DNA complex formation of the QsrR, C4S, C29S and C32S proteins after HOCl

***catE2* promoter**		**0**	**0.002**	**0.005**	**0.01**	**0.1**	**0.15**	**0.2**	**0.3**	**0.4**	**0.5**	**µM Protein**
QsrR	rep. 1	0.0119	0.3819	0.4990	3.4134	5.7632	39.075	58.802	85.491	94.114	96.262	
	rep. 2	0.0103	0.8533	1.0121	1.3509	8.9194	39.308	47.774	67.658	76.544	96.955	
	rep. 3	0.0130	0.8182	1.4603	3.1153	8.3355	33.057	69.334	88.270	94.702	96.250	
C4S	rep. 1	0.0134	4.4306	5.3883	9.2735	61.774	78.406	89.305		84.040	94.856	
	rep. 2	0.0120	1.2405	5.3309	9.6000	57.404	80.330	93.532	96.555	95.032	96.462	
	rep. 3	0.0094	1.2317	3.9444	8.6692		88.490		94.217	98.100	98.248	
	rep. 4	0.0090	2.0172	5.1902	11.875	63.847		90.782	89.903	96.935	97.683	
C29S	rep. 1	0.0096	1.4648	1.2594	5.6423	20.465	42.620	64.472	96.671	94.626	98.968	
	rep. 2	0.0107	1.0061	2.3027	5.3782	20.572	46.964	69.623	90.880	95.725	98.927	
	rep. 3	0.0100	0.4570	0.5548	8.8501	26.680	39.053	59.719	75.300	97.737	96.540	
C32S	rep. 1	0.0102	0.2169	0.6154	0.2394	9.7608	39.482	57.909	80.523	93.400	99.338	
	rep. 2	0.0112	0.1192	0.3383	9.0154	8.5109	45.108	59.329	73.409	97.470	97.480	
	rep. 3	0.0101	0.0682	0.7756	4.1663	17.828	49.577	63.868	85.538	97.868	97.557	
***qsrR* promoter**		**0**	**0.002**	**0.005**	**0.01**	**0.1**	**0.15**	**0.2**	**0.3**	**0.4**	**0.5**	**µM Protein**
QsrR	rep. 1	0.0089	2.0251	3.9901	7.8328	11.724	30.716	56.854	73.456	82.449	92.401	
	rep. 2	0.0094	3.7926	6.3220	9.7509	30.833	43.720	49.327	62.333	85.165	99.863	
	rep. 3	0.0087	1.9414	3.7531	6.6605	9.2341	31.047	50.981	77.818	96.542	99.531	
C4S	rep. 1		2.5667	3.6409	7.7553	49.760	69.851	88.502	87.945	84.947	94.262	
	rep. 2	0.0085	1.0988	2.7411	5.4016	39.978	77.185	99.037	98.109	98.189	97.476	
	rep. 3	0.0110	1.9591	5.1157	9.8039	52.191	78.307	86.625	94.905	97.749	98.672	
	rep. 4	0.0112	1.1561	3.0393	4.5803	39.722	57.863	72.128	90.904	86.736	80.842	
C29S	rep. 1	0.0102	0.6550	5.0075	6.1947	22.600	46.912	51.534	72.605	97.253	99.199	
	rep. 2	0.0118	1.7427	1.4172	14.546	16.954	43.748	54.944	78.094	99.428	99.897	
	rep. 3	0.0111	1.5454	2.4134	2.9200	14.727	44.327	51.102	71.008	97.441	96.233	
	rep. 4	0.0117	1.9993	3.4480	7.0798	26.046	43.762	61.640	70.909	79.998	92.008	
C32S	rep. 1	0.0102	2.6060	2.9746	11.499	30.332	48.663	59.762	83.386	95.094	98.614	
	rep. 2	0.0104	1.6265	4.0131	15.326	31.265	44.976	59.584	84.485	96.009	96.368	
	rep. 3	0.0034	3.0706	6.2664	9.9593	26.464	36.301	56.229	78.770	95.320	94.578	

Table S6. The percentage of the protein-DNA complex formation was determined according to the band intensities of 3-4 biological replicates of the EMSAs and quantified using Image J 1.52a. The calculated percentual values of all biological replicates are shown for 0-0.5 µM of the QsrR, C4S, C29S and C32S proteins bound to the *catE2* and *qsrR* promoter after addition of 20 µM HOCl. These values were used for the nonlinear regression shown in Fig. 5E, F using the specific binding with Hill slope of the Graph prism software version 7.03 to determine the Dissociation constants (K_D).

Chapter 8

The two-Cys-type TetR repressor GbaA confers resistance under disulfide and electrophile stress in *Staphylococcus aureus*

Vu Van Loi[1], Tobias Busche[2], Verena Nadin Fritsch[1], Christoph Weise[3], Martin Clemens Horst Gruhlke[4], Alan John Slusarenko[4], Jörn Kalinowski[2], and Haike Antelmann[1]*

[1]Freie Universität Berlin, Institute of Biology-Microbiology, D-14195, Berlin, Germany

[2]Center for Biotechnology, Bielefeld University, D-33594, Bielefeld, Germany

[3]Freie Universität Berlin, Institute of Chemistry and Biochemistry, D-14195, Berlin, Germany

[4]Department of Plant Physiology, RWTH Aachen University, D-52056, Aachen, Germany

*Corresponding author: haike.antelmann@fu-berlin.de

Published in:
Free Radical Biology and Medicine 177:120-131, 2021
DOI: https://doi.org/10.1016/j.freeradbiomed.2021.10.024

Personal contribution:

I helped to elucidate the function of the GbaA regulon in *S. aureus* by performing phenotype analyses under different thiol-stress conditions (Fig. 8; S9). Additionally, I contributed to the clarification of the redox-sensing mechanism of GbaA *in vivo* by analyzing the survival of the GbaA Cys mutants (Fig. 9).

Free Radical Biology and Medicine 177 (2021) 120–131

Contents lists available at ScienceDirect

Free Radical Biology and Medicine

journal homepage: www.elsevier.com/locate/freeradbiomed

The two-Cys-type TetR repressor GbaA confers resistance under disulfide and electrophile stress in *Staphylococcus aureus*

Vu Van Loi [a], Tobias Busche [b], Verena Nadin Fritsch [a], Christoph Weise [c], Martin Clemens Horst Gruhlke [d], Alan John Slusarenko [d], Jörn Kalinowski [b], Haike Antelmann [a,*]

[a] Freie Universität Berlin, Institute of Biology-Microbiology, D-14195, Berlin, Germany
[b] Center for Biotechnology, Bielefeld University, D-33594, Bielefeld, Germany
[c] Freie Universität Berlin, Institute of Chemistry and Biochemistry, D-14195, Berlin, Germany
[d] Department of Plant Physiology, RWTH Aachen University, D-52056, Aachen, Germany

ARTICLE INFO

Keywords:
Staphylococcus aureus
GbaA
Thiol switches
Allicin
Diamide
Electrophiles

ABSTRACT

Staphylococcus aureus has to cope with oxidative and electrophile stress during host-pathogen interactions. The TetR-family repressor GbaA was shown to sense electrophiles, such as N-ethylmaleimide (NEM) via monothiol mechanisms of the two conserved Cys55 or Cys104 residues in vitro. In this study, we further investigated the regulation and function of the GbaA repressor and its Cys residues in *S. aureus* COL. The GbaA-controlled *gbaAB-SACOL2595-97* and *SACOL2592-nmrA-2590* operons were shown to respond only weakly 3-10-fold to oxidants, electrophiles or antibiotics in *S. aureus* COL, but are 57-734-fold derepressed in the *gbaA* deletion mutant, indicating that the physiological inducer is still unknown. Moreover, the *gbaA* mutant remained responsive to disulfide and electrophile stress, pointing to additional redox control mechanisms of both operons. Thiol-stress induction of the GbaA regulon was strongly diminished in both single Cys mutants, supporting that both Cys residues are required for redox-sensing in vivo. While GbaA and the single Cys mutants are reversible oxidized under diamide and allicin stress, these thiol switches did not affect the DNA binding activity. The repressor activity of GbaA could be only partially inhibited with NEM in vitro. Survival assays revealed that the *gbaA* mutant confers resistance under diamide, allicin, NEM and methylglyoxal stress, which was mediated by the *SACOL2592-90* operon encoding for a putative glyoxalase and oxidoreductase. Altogether, our results support that the GbaA repressor functions in the defense against oxidative and electrophile stress in *S. aureus*. GbaA represents a 2-Cys-type redox sensor, which requires another redox-sensing regulator and an unknown thiol-reactive ligand for full derepression of the GbaA regulon genes.

1. Introduction

Staphylococcus aureus is an opportunistic human pathogen, which colonizes the skin and the nose of one quarter of the human population [1], but can also cause life-threatening infections especially in immunocompromised persons, ranging from skin and soft tissue infections to systemic septic shock syndrome, chronic osteomyelitis, endocarditis and pneumonia [2–4]. Moreover, *S. aureus* rapidly acquires new antibiotic resistant elements resulting in an increased prevalence of multi-resistant *S. aureus* isolates with limited treatment options [5,6].

During infections and antibiotics treatments, *S. aureus* has to cope with reactive oxygen, chlorine and electrophile species (ROS, RCS, RES) [7]. Activated macrophages and neutrophils produce ROS, such as superoxide anion and H_2O_2 as well as the strong microbicidal agent hypochlorous acid (HOCl) in large quantities to kill invading pathogens in the acidic phagosome [8–10]. ROS and HOCl lead to oxidation of amino acids, unsaturated fatty acids, carbohydrates and nucleotides, resulting in RES with electron-deficient centers as secondary reactive metabolites, such as quinones, epoxides and the highly toxic dicarbonyl compounds glyoxal and methylglyoxal (MG) [11–13]. Enhanced levels of reactive aldehydes and MG are produced during infections in inflamed tissues, in the blood and in activated neutrophils, causing alkylation of lysine, arginine and cysteine residues in proteins [14,15]. Moreover, the host-derived electrophilic metabolite itaconate reprograms the host metabolism to stimulate macrophage immune responses and to promote biofilm formation in bacterial pathogens [16,17]. Thus,

* Corresponding author. Freie Universität Berlin, Institute for Biology-Microbiology, Königin-Luise-Strasse 12-16, D-14195 Berlin, Germany.
E-mail address: haike.antelmann@fu-berlin.de (H. Antelmann).

https://doi.org/10.1016/j.freeradbiomed.2021.10.024
Received 22 August 2021; Received in revised form 15 October 2021; Accepted 18 October 2021
Available online 19 October 2021

host-pathogen interactions generate various reactive species, which require the expression of efficient protection, detoxification and repair systems in *S. aureus* for successful infection, spread and survival in the human body.

These defense mechanisms are often controlled by redox-sensing regulators, such as SarZ, MgrA, HypR and QsrR, which utilize conserved Cys residues to sense and respond to ROS, RCS, RES or antibiotics via post-translational thiol-modifications, leading to activation of their specific regulons in *S. aureus* [7,18–24]. Redox-sensing transcription factors sense ROS, RCS and RES via one-Cys-type and two-Cys-type mechanisms, depending on the number of Cys residues [18,19]. The *Bacillus subtilis* MarR-type OhrR repressor is the prototype of the one-Cys-type redox sensor, which is inactivated by organic hydroperoxides and HOCl via *S*-bacillithiolation of the single Cys residue in both subunits [18,25,26]. In contrast, OhrR of *Xanthomonas campestris*, YodB of *B. subtilis* and HypR of *S. aureus* harbor more than one Cys residue and are regulated by intersubunit disulfide formation between the N-terminal redox-sensing Cys and the C-terminal Cys of opposing subunits according to the two-Cys-type model [18,21,27–29]. Thus, the number of Cys residues determines the regulatory mechanism of thiol-based redox regulators owing to different thiol-modifications.

In *S. aureus*, the TetR-family GbaA regulator was characterized as a negative regulator of glucose-induced biofilm formation, since a *gbaA* mutation enhanced the production of poly-*N*-acetylglucosamine (PNAG), required for polysaccharide intracellular adhesin (PIA)-dependent biofilm formation in a super-biofilm-elaborating *S. aureus* isolate TF2758 [30,31]. GbaA was shown to repress transcription of two divergent operons, including the upstream *SACOL2592-nmrA-90* and downstream *gbaAB-SACOL2595-97* operons [30,31]. The upstream operon encodes a putative glyoxalase, the NAD^+-dependent epimerase/dehydratase NmrA and the DUF2316 hypothetical protein. The downstream operon encodes the GbaA repressor, a short chain dehydrogenase/oxidoreductase GbaB, an amidohydrolase and an α,β-fold hydrolase [30–32]. GbaA binds to a 9-6-9 bp inverted repeat sequence ATAAACGGA-N_6-TCCGTTTGT in the upstream promoter regions of both divergent operons [30,31]. However, the physiological inducer for GbaA inactivation and the functions of the GbaA regulon genes are unknown in *S. aureus*.

In transcriptomic studies, the GbaA regulon was weakly upregulated under various disulfide and electrophile stress conditions, such as AGXX®, allicin, HOCl, methylhydroquinone (MHQ) and lapachol stress [33–36]. GbaA harbors two Cys55 and Cys104 residues, which are highly conserved across TetR/AcrR homologs of other Gram-positive bacteria (Fig. S1), and located close to the DNA binding and regulatory domains of the GbaA dimer as modelled based on the template of *Escherichia coli* AcrR (Fig. S2). Thus, we investigated the role of GbaA and its Cys residues for redox sensing under various thiol-stress conditions in vitro and in vivo. While our work was in progress, GbaA was described as monothiol electrophile sensor that senses N-ethylmaleimide (NEM) and oxidants via one of the two Cys residues in vitro, since DNA binding activity was only impaired in the single Cys55 and Cys104 mutants, but not in the two-Cys wild type protein [32]. Oxidation of GbaA by diamide, bacillithiol disulfide (BSSB) or *S*-nitroso glutathione (GSNO) led to formation of the intramolecular C55-C104 disulfide, which did not change the structure and DNA binding activity. Only the monothiol GbaA variants could be inactivated by *S*-bacillithiolation with BSSB or S-alkylation with NEM in vitro [32]. Therefore, GbaA was suggested to function as monothiol electrophile sensor under oxidative and electrophile stress. However, the physiological role of the GbaA regulon under electrophile stress, such as NEM and MG remained unclear in the previous study [32].

Here, we have further studied the function and regulation of GbaA under oxidative and electrophile stress in *S. aureus* COL. The GbaA regulon was only weakly induced under various disulfide, electrophile and antibiotics stress conditions in *S. aureus*. Moreover, the full derepression of the GbaA regulon depends on inactivation of a second thiol-redox regulator. While both Cys residues are required for redox sensing of GbaA in vivo, diverse thiol switches are not sufficient for inactivation of GbaA and the single Cys proteins in vitro. However, phenotype analyses revealed that the GbaA regulon conferred resistance under diamide, allicin, NEM and MG stress, indicating that the GbaA regulon functions in the defense under disulfide and electrophile stress.

2. Material and methods

2.1. Bacterial strains and cultivations

Bacterial strains, plasmids and primers are listed in Tables S1 and S2. *E. coli* strains were cultivated in Luria broth (LB) for plasmid construction and protein expression. For stress experiments, *S. aureus* strains were cultivated in RPMI medium and treated with thiol-reactive compounds and antibiotics during the exponential growth at an optical density at 500 nm (OD_{500}) of 0.5. Survival assays were performed by treatment of *S. aureus* cells with the thiol-reactive compounds at an OD_{500} of 0.5 and plating of 100 μl of serial dilutions onto LB agar plates, followed by counting of colony forming units (CFUs) after 24 h incubation. The statistics of the survival assays was calculated using Student's unpaired two-tailed *t*-test. Northern blot results were quantified with ImageJ and the statistics was calculated by the one-way ANOVA and Dunnet's multiple comparisons test using the Graph prism software.

2.2. Cloning, expression and purification of His-tagged GbaA, GbaAC55S and GbaAC104S proteins in E. coli

The *gbaA* (*SACOL2593*) gene was PCR amplified from chromosomal DNA of *S. aureus* COL using primers pET-gbaA-for-*Nhe*I and pET-gbaA-rev-*Bam*HI (Table S2). The PCR product was digested with *Nhe*I and *BamH*I and cloned into plasmid pET11b, generating pET11b-*gbaA*. The plasmids pET11b-*gbaAC55S* and pET11b-*gbaAC104S* were constructed using PCR mutagenesis with primers including the cysteine-serine mutation as previously described [21,37]. For the *gbaAC55S* mutant, the primers pET-gbaA-for-*Nhe*I, gbaAC55S-rev, gbaAC55S-for and pET-gbaA-rev-*Bam*HI were used in two first-round PCRs. For the *gbaAC104S* mutant, the primers pET-gbaA-for-*Nhe*I, gbaAC104S-rev, gbaAC104S--for and pET-gbaA-rev-*Bam*HI were used for two first-round PCRs (Table S2). The PCR products of each Cys mutant were fused by overlap extension PCR with primers pET-gbaA-for-*Nhe*I and pET-gbaA-rev-*Bam*HI to generate the *gbaAC55S* and *gbaAC104S* mutant alleles, which were cloned into pET11b as described above.

For expression and purification of His-tagged GbaA, GbaAC55S and GbaAC104S proteins, *E. coli* BL21(DE3) p*lysS* with plasmids pET11b-*gbaA,* pET11b-*gbaAC55S* and pET11b-*gbaAC104S* was cultivated in 1.5 l LB medium until an OD_{600} of 0.8 followed by addition of 1 mM isopropyl-β-D-thiogalactopyranoside (IPTG) for 16 h at 25 °C. Recombinant His-tagged proteins were purified using His Trap™ HP Ni-NTA columns and the ÄKTA purifier liquid chromatography system as described [21].

2.3. Construction of the S. aureus COL gbaA, gbaB and SACOL2590-92 mutants as well as the gbaA, gbaAC55S, gbaAC104S and gbaB complemented strains

The *S. aureus gbaA*, *gbaB* and *SACOL2590-92* mutants were constructed using the temperature-sensitive *E. coli-S. aureus* shuttle vector pMAD as described [21,38]. Around 500 bp of the up- and downstream flanking regions of the corresponding genes were amplified using primers (Table S2) and fused by overlap extension PCR. The fusion products were digested with *Bgl*II and *Sal*I and ligated into pMAD, which was cut with the same restriction enzymes. The methylated pMAD constructs from the intermediate strain *S. aureus* RN4220 were transferred into *S. aureus* COL by phage transduction. The clean deletion mutants of *gbaA, gbaB* and *SACOL2590-92* were selected as described before [21,38].

For construction of the His-tagged *S. aureus gbaA*, *gbaAC55S* and *gbaAC104S* complemented strains as well as the untagged *gbaB* complementation, the coding sequences including the C-terminal His6-tag of *gbaA, gbaAC55S* and *gbaAC104S* were PCR amplified from plasmids pET11b-*gbaA,* pET11b-*gbaAC55S* and pET11b-*gbaAC104S*, whereas *gbaB* was amplified from *S. aureus* chromosomal DNA. The purified PCR products were ligated into plasmid pRB473 after digestion with *Bam*HI and *Kpn*I resulting in plasmids pRB473-*gbaA,* pRB473-*gbaAC55S,* pRB473-*gbaAC104S* and pRB473-*gbaB* (Table S2). The plasmids were introduced into the corresponding *S. aureus gbaA* and *gbaB* mutants via phage transduction as described [21,37].

2.4. RNA isolation and Northern blot analysis

To investigate transcriptional regulation of the GbaA-controlled up- and downstream operons, *S. aureus* COL strains were cultivated in RPMI and treated with various thiol-reactive compounds at an OD_{500} of 0.5 for 30 min as well as with different antibiotics for 60 min as previously described [21]. The applied concentrations of the compounds are indicated in the figure legends of the Northern blots.

Northern blot hybridizations were conducted with digoxigenin-labeled *gbaB* and *SACOL2590*-specific antisense RNA probes, which were synthesized by in vitro transcription with the T7 RNA polymerase and the primer pairs NB-gbaB-for and NB-gbaB-rev as well as NB-SACOL2590-for and NB-SACOL2590-rev, respectively (Table S2) as described [39,40].

2.5. Whole RNA-seq transcriptomics analysis and primary 5' transcript mapping of the GbaA regulon genes

Whole RNA-seq transcriptomics was performed with RNA of *S. aureus* COL WT and the *gbaA* deletion mutant, which were harvested under control conditions at an OD_{500} of 0.5 as described [34]. Differential gene expression analysis of 3 biological replicates was performed using DESeq2 [41] with ReadXplorer v2.2 [42] as described [34]. Significant expression changes in the *gbaA* mutant versus WT cells were identified by an adjusted *p*-value cut-off of $p \leq 0.05$ and a signal intensity ratio (M-value) cut-off of ≥0.6 or ≤ -0.6 (fold-change of ± 1.5) as in earlier studies [34].

The primary 5′ transcripts of the GbaA-controlled up- and downstream operons were mapped in untreated and allicin-treated cells using the 5′ end enriched RNA-seq dataset of untreated cells as reported earlier [33] and of cells exposed to 0.3 mM allicin stress. The cDNAs enriched for primary 5′-transcripts were prepared as described [43]. cDNAs were sequenced paired end on an Illumina MiSeq system (San Diego, CA, USA) using 75 bp read length. The R1 cDNA reads were mapped to the *S. aureus* COL genome with bowtie2 v2.2.7 [44] using the default settings for single-end read mapping and visualized with Read Explorer v.2.2 [42]. The whole transcriptome of the *gbaA* mutant versus WT under control conditions and the 5' enriched RNA-seq raw data files of WT control and WT after allicin stress are available in the ArrayExpress database (www.ebi.ac.uk/arrayexpress) under the accession numbers E-MTAB-10887, E-MTAB-7385 and E-MTAB-10889, respectively.

2.6. Electrophoretic mobility shift assays (EMSAs) of GbaA and GbaA Cys mutant proteins

For DNA binding assays in vitro, EMSAs were performed with the DNA promoter probe containing the 150 bp upstream region of *gbaA* covering a region from −83 to +67 relative to the transcription start site (TSS). The DNA-binding reactions were performed with 15 ng of the promoter probe incubated with the purified His-tagged GbaA, GbaAC55S or GbaAC104S proteins for 45 min according to the EMSA protocol as described before [21].

2.7. Western blot analysis

S. aureus COL cells were collected before and after treatment with 2 and 5 mM diamide and 0.3 mM allicin for 30 min as described [21]. After harvesting, cells were washed and lysed in TE-buffer (pH 8.0) with 50 mM NEM using the ribolyzer. Protein lysates were separated using 15% non-reducing SDS-PAGE and subjected to Western blot analysis using His6 tag monoclonal antibodies (Sigma) as described previously [21,34,45].

2.8. MALDI-TOF mass spectrometry for identification of thiol-modifications of GbaA, GbaAC55S and GbaAC104S mutant proteins in vitro

The purified GbaA, GbaAC55S and GbaAC104S proteins were reduced with 10 mM DTT for 20 min, treated with 1 mM allicin or 1 mM diamide for 15 min, followed by alkylation of reduced thiols with 50 mM iodoacetamide (IAM) for 30 min in the dark. The post-translational thiol-modifications of GbaA and its Cys mutants were analyzed using non-reducing SDS–PAGE, in-gel tryptic digestion and mass spectrometry of the GbaA bands as described previously [21]. The peptides were measured using matrix-assisted laser desorption ionization-time of flight mass spectrometry (MALDI-TOF-MS) using an Ultraflex-II TOF/TOF instrument (Bruker Daltonics, Bremen, Germany) equipped with a 200 Hz solid-state Smart beam™ laser. The mass spectrometer was operated in the positive reflector mode. Mass spectra were acquired over an *m/z* range of 600–4,000. MS/MS spectra of selected peptides were acquired in the LIFT mode as described previously [21,46].

3. Results

3.1. The GbaA regulon is weakly induced by ROS, RES and antibiotics in S. aureus COL

The TetR family GbaA repressor was previously characterized as monothiol electrophile sensor, which possibly senses NEM and MG via one of its two conserved Cys residues in *S. aureus* USA300 [32]. GbaA controls two divergent operons, the downstream *gbaAB-SACOL2595-97* operon and the upstream *SACOL2592-nmrA-2590* operon, which were previously shown to respond weakly to thiol-reactive compounds and antibiotics as revealed by transcriptome analyses [21,32,34,35,47]. We used Northern blot analyses to investigate transcription of the *gbaAB--SACOL2595-97* operon after exposure to 5 μg/ml AGXX®, 50 μM MHQ, 2 mM diamide, 0.3 mM allicin, 1 mM HOCl, 0.75 mM formaldehyde (FA) and 10 mM H_2O_2, which were sub-lethal in growth and survival assays (Fig. 1A; Figs. S3A and S4A). Transcription of the *gbaAB* operon was further analyzed in *S. aureus* after treatment with sub-lethal and lethal doses of 0.05–0.5 mM NEM and 0.5–2 mM MG (Fig. 1B; Figs. S3B, S4B) as well as the antibiotics erythromycin, vancomycin, chloramphenicol, tetracycline, nalidixic acid, rifampicin, ciprofloxacin, gentamycin and linezolid (Fig. 1C, Figs. S3C and S4D). The Northern blot results revealed that transcription of the large 3.21 kb *gbaAB-SACOL2595-97* operon was only weakly 3-10-fold upregulated by these strong oxidants, electrophiles and antibiotics in *S. aureus* COL, which is in the range of stress-induced ratios of previous RNA-seq transcriptome datasets [21,32,34,35,47] (Fig. 1A–C, Figs. S4A,B,D; Table S3). No significant up-regulation of the *gbaAB* operon was quantified under MHQ, H_2O_2, formaldehyde, chloramphenicol, rifampicin and ciprofloxacin exposure in *S. aureus* COL (Fig. 1A,C; Figs. S4A and D). However, much stronger >50-100-fold derepression of transcription of both GbaA-controlled operons was quantified in the *gbaA* mutant versus the WT under control conditions using Northern blots (Figs. 1B, Fig. 2C,D, Fig. S4C, Figs. S5A and B). In agreement with these data, the *gbaAB-SACOL2595-97* and *SACOL2592-nmrA-2590* operons were 57–194-fold and 401–734-fold upregulated in the RNA-seq transcriptome of the *gbaA* mutant compared to the WT control (Tables S3–S4) [30]. Together, the

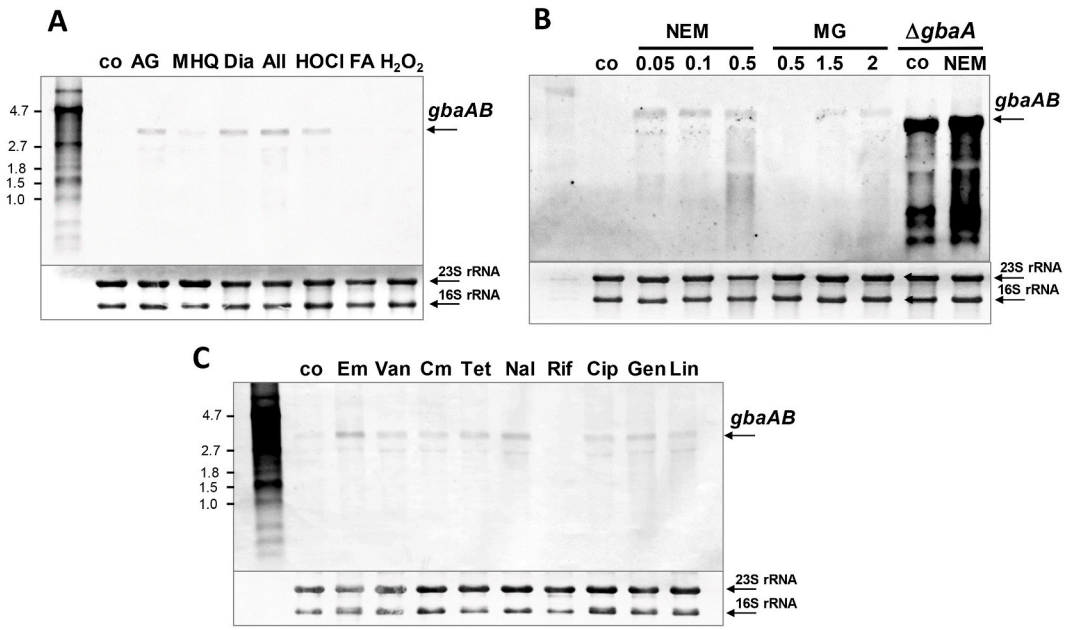

Fig. 1. Transcription of the *gbaAB-SACOL2595-97* operon is weakly up-regulated by oxidative, electrophile and antibiotic treatments in *S. aureus* COL. Northern blot analysis was carried out using RNA isolated from *S. aureus* COL WT before (co) and 30 min after exposure to different thiol-reactive compounds (A, B) or 60 min after antibiotic treatments (C). For stress experiments, cells were treated with 5 μg/ml AGXX® (AG), 50 μM methylhydroquinone (MHQ), 2 mM diamide (Dia), 300 μM allicin (All), 1 mM HOCl, 0.75 mM formaldehyde (FA) and 10 mM H_2O_2 (A) or to 0.05–0.5 mM N-ethylmaleimide (NEM), 0.5–2 mM methylglyoxal (MG) for 30 min (B). For comparison of the weak transcriptional induction of the *gbaAB* operon after 0.5 mM NEM and 2 mM MG stress in the WT, the Δ*gbaA* mutant was analyzed under control and 0.5 mM NEM stress showing full derepression of the *gbaAB* operon in the control (B). For antibiotics experiments, *S. aureus* WT was exposed to 0.25 μg/ml erythromycin (Em), 0.5 μg/ml vancomycin (Van), 4 μg/ml chloramphenicol (Cm), 5 μg/ml tetracycline (Tet), 128 μg/ml nalidixic acid (Nal), 0.1 μg/ml rifampicin (Rif), 32 μg/ml ciprofloxacin (Cip), 2 μg/ml gentamicin (Gen) and 2 μg/ml linezolid (Lin) (C). The arrows point toward the size of the *gbaAB-SACOL2595-97* specific operon transcript. The methylene blue stain is the RNA loading control indicating the 16S and 23S rRNAs. Band intensities of the *gbaAB* operon transcripts were quantified using ImageJ and the data shown in Figs. S4A–D.

Northern blot and RNA-seq results clearly indicate that the tested oxidants, electrophiles and antibiotics cause only a very weak derepression of the GbaA regulon genes, while full derepression in the *gbaA* mutant leads to up-regulation of transcription in the range of 57-734-fold versus WT control. Thus, the tested compounds are clearly not the physiological inducers for complete inactivation of the GbaA repressor as already pointed out in earlier studies [32]. Thus, the identification of the GbaA inducer remains an open question.

In addition, transcription of the *gbaAB-SACOL2595-97* operon was still significantly 3-6-fold up-regulated in the *gbaA* mutant under oxidative and electrophile stress, including diamide, AGXX®, NEM and MG (Figs. 1B, Fig. 2C,D; Fig. 4A and B; Figs. S6A and B). This points to the presence of another redox-sensing regulator involved in the transcriptional control of the GbaA regulon genes, which senses and responds to thiol-stress conditions.

3.2. Mapping of strong SigmaA-dependent promoters upstream of the divergent gbaAB-SACOL2595-97 and SACOL2592-nmrA-2590 operons

To study the transcriptional regulation by GbaA, we mapped the promoters of the upstream *SACOL2592-nmrA-2590* and downstream *gbaAB-SACOL2595-97* operons using RNA-seq of 5' primary transcripts under allicin stress in *S. aureus* COL (Fig. 3A). The *gbaA*-specific transcription start site TSS-1 was identified as an adenine, which is located 45 bp upstream of the ATG start codon. TSS-1 is preceded by a strong SigmaA-dependent promoter with the consensus sequence TATAAT-N_{17}-TTGCAT (Fig. 3A and B). The *SACOL2592*specific TSS-2 was mapped at a guanine located 65 bp upstream of the ATG start codon. TSS-2 is also preceded by a strong SigmaA-dependent promoter, which contains the consensus sequence TATTAT-N_{18}-TTGACA. Thus, both −10 promoter regions overlap at the opposite strands upstream regions of the divergent *gbaA* and *SACOL2592* genes (Fig. 3A). The GbaA repressor was previously shown to bind to the conserved 9-6-9 bp inverted repeat sequence ATAAACGGA-N_6-TCCGTTTGT [31], which overlapped with the TSS-1 and the −10 region upstream of *gbaA* and with the −10 and −35 promoter elements upstream of SACOL2592 (Fig. 3A–C). Thus, transcription of both operons from the overlapping SigmaA-dependent promoters is strongly repressed by GbaA. The GbaA operator and the perfect −10 promoter elements upstream of *gbaA* and *SACOL2592* are highly conserved across other staphylococci (Fig. 3B and C), indicating that both operons are highly transcribed under the specific inducing conditions.

3.3. Cys55 and Cys104 are both important for redox sensing of GbaA in response to oxidants and electrophiles in vivo

TetR/AcrR family repressors are composed of N-terminal helix-turn-helix (HTH) DNA-binding domains (α1-α3 helices) and C-terminal regulatory domains (α4ab-α9) in each subunit of the dimer [48–50]. The C-terminal domain is involved in dimerization and senses specific inducers or ligands, leading to inactivation of the TetR/AcrR repressor activity [48–50]. GbaA shares the two conserved Cys55 and Cys104 residues with GbaA homologs across staphylococci and TetR/AcrR homologs in other Gram-positive bacteria (Fig. S1) [32]. The structural model of GbaA, which is based on the template of *E. coli* AcrR, suggests that Cys55 is located in the α4a domain close to the HTH motif, while Cys104 is in helix α6 of the C-terminal regulatory domain (Fig. S2) [48–50]. The distance of Cys55 and Cys104 in each subunit was calculated as ~8.6 Å in this model, indicating that intramolecular disulfide formation will be possible as revealed previously [32].

To examine the function of the two Cys residues for DNA binding activity and redox-sensing of GbaA, the *gbaA* mutant was complemented with plasmid-encoded His-tagged *gbaA*, *gbaAC55S* and *gbaAC104S* alleles, expressed under a xylose-inducible promoter. Similar expression

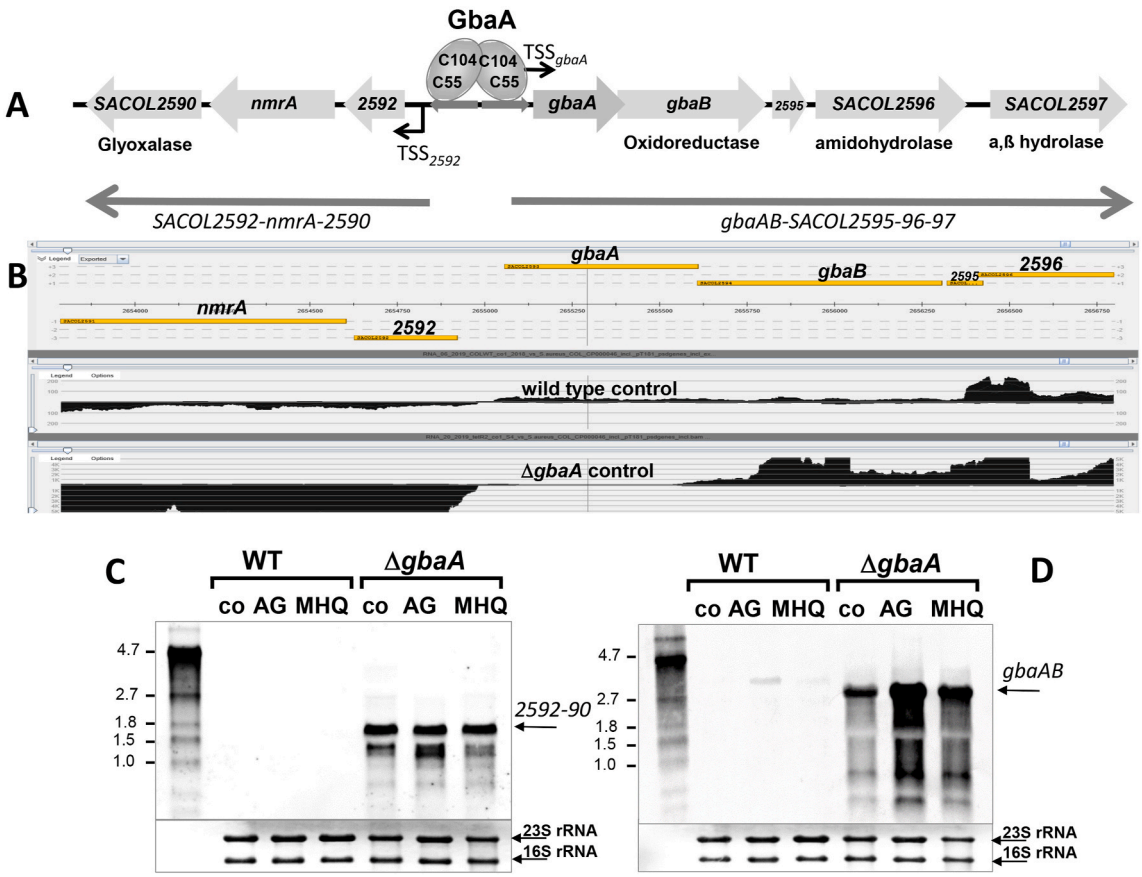

Fig. 2. Deletion of *gbaA* results in derepression of transcription of the downstream *gbaAB-SACOL2595-97* and upstream *SACOL2592-90* operons. (A, B) Transcriptional organization of the divergent *gbaAB-SACOL2595-97* and *SACOL2592-90* operons in *S. aureus*. The upstream *SACOL2592-nmrA-2590* operon encodes for a putative glyoxalase and NAD^+-dependent epimerase/dehydratase (NmrA). The downstream *gbaAB* operon encodes for the GbaA repressor, a putative short chain oxidoreductase, an amidohydrolase and an a,ß hydrolase. (B) Both operons are negatively regulated by GbaA as displayed by the RNA-seq data of *S. aureus* COL WT and the *gbaA* mutant under control conditions using Read-Explorer. (C, D) Transcription of the *SACOL2592-90* (C) and *gbaAB-SACOL2595-97* operons (D) was analyzed in *S. aureus* COL WT and *gbaA* mutant strains before (co) and 30 min after treatment with 5 μg/ml AGXX® (AG) and 50 μM MHQ using Northern blots. Both operons remained inducible by AGXX® and MHQ stress in the *gbaA* mutant. The arrows point toward the transcript sizes of the *gbaAB* and *SACOL2592-90* operons. The methylene blue bands denote the 16S and 23S rRNAs as RNA loading controls below the Northern blots. Band intensities of the *gbaAB* and *SACOL2592-90* operon transcripts were quantified using ImageJ and the data are shown in Figs. S5A and B. (For interpretation of the references to color in this figure legend, the reader is referred to the Web version of this article.)

of GbaA and Cys mutant proteins in the complemented strains was verified by Western blot analyses using anti-His6 tag monoclonal antibodies (see section 3.5). Northern blots were used to study the transcriptional response of GbaA and the Cys mutants under oxidative and electrophile stress (Fig. 4A–D; Figs. S6A–D). Complementation of the *gbaA* mutant with *gbaA* and its Cys mutant alleles restored the repression of the *gbaAB-SACOL2595-97* and *SACOL2592-nmrA-2590* operons under control conditions, indicating that the Cys mutations do not affect the DNA binding activity of GbaA (Fig. 4A–D; Figs. S6A–D). In addition, the *gbaAB-SACOL2595-97* operon was significantly 20-50-fold induced in the *gbaA* complemented strain, but non-significantly changed in the *gbaAC55S* and *gbaAC104S* mutants under AGXX®, diamide and NEM stress, indicating that both Cys residues are involved in redox sensing under disulfide and electrophile stress in vivo (Fig. 4A and B; Figs. S6A and B). In contrast to the *gbaAB* operon, the *SACOL2592-nmrA-2590* operon was not significantly up-regulated in the *gbaA* complemented strain and no transcript visible in the *gbaAC55S* and *gbaAC104S* mutants (Fig. 4C and D; Figs. S6C and D). The non-significant thiol-stress induction of the *SACOL2592-nmrA-2590* operon in the *gbaA* complemented strain is in agreement to the WT results (Fig. 2C, Fig. S5A). Together, these transcriptional results on the Cys55 and Cys104 mutants support that both Cys residues function in redox sensing of the GbaA repressor in vivo.

3.4. DNA binding activity of GbaA and the Cys mutants is not impaired under oxidative and MG stress in vitro

Next, gel-shift assays were used to study the effect of thiol-reactive compounds on DNA binding activity of purified GbaA and GbaA Cys mutant proteins to the *gbaA* promoter probe, which covered the −83 to +67 upstream region relative to TSS-1 (Fig. 3A and B). GbaA was shown to bind to the GbaA operator with a dissociation constant (K_D) of 15.24 nM (Fig. 5A and B). Both GbaAC55S and GbaAC104S mutant proteins showed similar K_D values, indicating that the Cys mutations do not affect the DNA binding activity of GbaA in vitro (Fig. 5A and B).

However, treatment of GbaA and the Cys mutants with diamide, allicin and the electrophile MG did not lead to dissociation of the proteins from the operator DNA in gel-shift assays in vitro (Fig. 5C–E). Thus, the oxidants and electrophiles do not cause major structural changes in the DNA binding domains of GbaA. This suggests that the second unknown regulator is responsive to thiol-stress conditions, while GbaA binds an unknown thiol-reactive compound as ligand. In contrast, exposure of GbaA and the GbaAC104S mutant protein to NEM resulted in partial relief from DNA binding, while the GbaAC55S mutant could be inactivated only weakly with NEM in vitro (Fig. 5F) [32]. These results confirm previous data [32], that GbaA responds only partially to NEM, but is not inactivated under disulfide and MG stress in vitro.

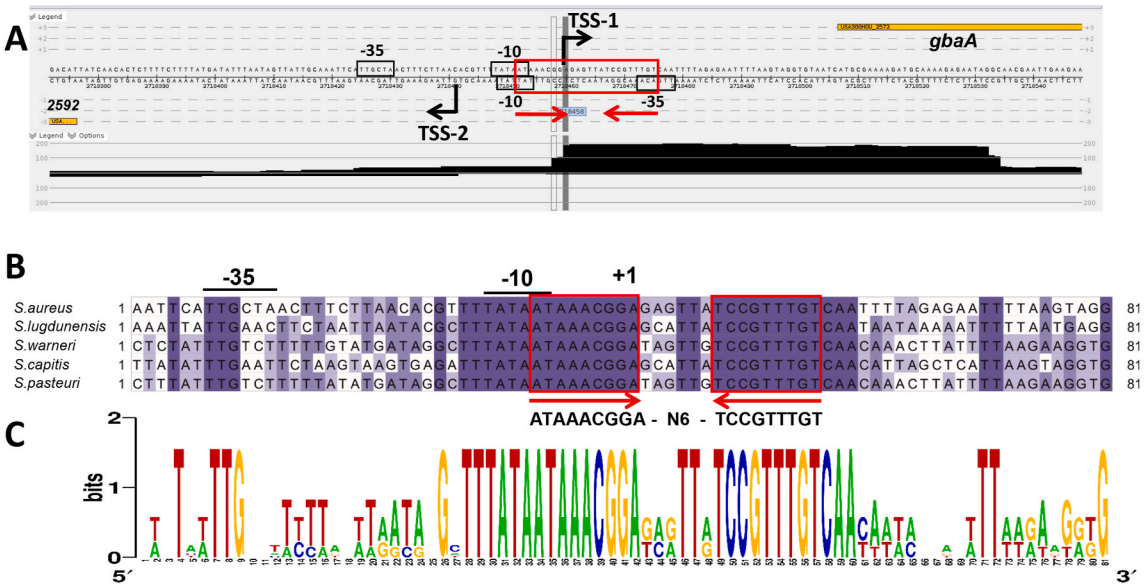

Fig. 3. Mapping of the 5′ ends of the *gbaAB-SACOL2595-97* and *SACOL2592-90* operons and the 9-6-9 bp inverted repeat as GbaA operator in *S. aureus* (A). 5′ RNA-seq was used to map TSS-1 and TSS-2 upstream of the divergent *gbaAB* and *SACOL2592-90* operons, respectively, which is displayed with Read-Explorer. (B) The promoter sequence of the *gbaAB* operon and the 9-6-9 bp inverted repeat are highly conserved across different *Staphylococcus* species. The promoter regions were aligned using Clustal Omega and presented in Jalview. Intensity of the blue color gradient is based on 50% nucleotide sequence identity. (C) The conservation of the *gbaA* −10 promoter region and the GbaA operator is further displayed with WebLogo. (For interpretation of the references to color in this figure legend, the reader is referred to the Web version of this article.)

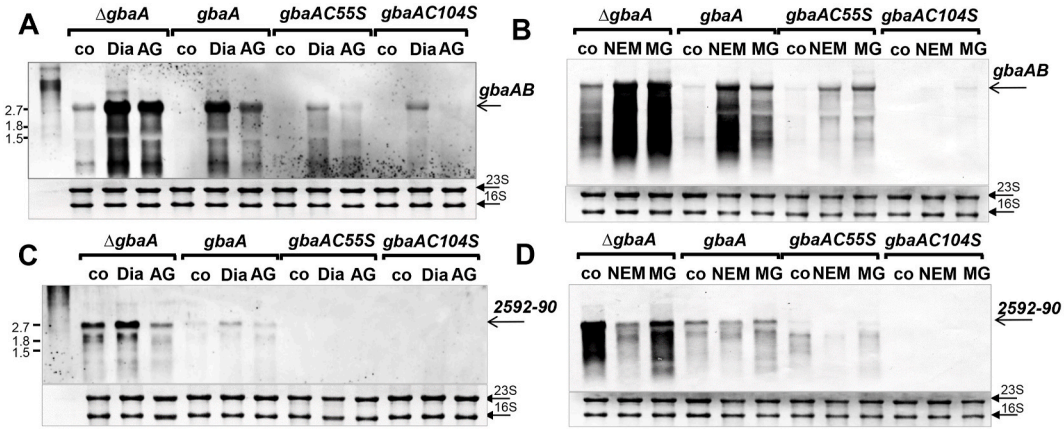

Fig. 4. Northern blot analysis of transcription of the *gbaAB-SACOL2595-97* and *SACOL2592-90* operons under diamide, AGXX®, NEM and MG stress in the *S. aureus* COL *gbaA* mutant and the *gbaA*, *gbaAC55S* and *gbaAC104S* complemented strains. Transcription of the *gbaAB-SACOL2595-97* (A,B) and *SACOL2592-90* operons (C,D) was analyzed in the *S. aureus gbaA* deletion mutant and in the *gbaA, gbaAC55S, gbaAC104S* complemented strains before (co) and 30 min after treatment with 2 mM diamide (Dia), 5 μg/ml AGXX® (AG), 0.3 mM NEM and 2 mM MG using Northern blots. The arrows point toward the transcript sizes of the *gbaAB-SACOL2595-97* or *SACOL2592-90* operons. The methylene blue bands denote the 16S and 23S rRNAs as RNA loading controls below the Northern blots. Band intensities of the *gbaAB* and *SACOL2592-90* operon transcripts were quantified using ImageJ and the data are shown in Figs. S6A–D.

3.5. GbaA and the Cys mutants are oxidized to different thiol switches under diamide and allicin stress

Non-reducing SDS-PAGE and MALDI-TOF-MS were used to monitor thiol-oxidation of GbaA and the Cys mutants after diamide and allicin stress in vitro (Fig. 6A–C, Fig. 7A–C, Fig. S7). The GbaA protein showed a slightly faster migration after diamide treatment compared to DTT-reduced GbaA, indicating the formation of an intramolecular disulfide between Cys55 and Cys104 in each subunit of the dimer (Fig. 6A). The intramolecular cross-link between Cys55 and Cys104 in the diamide-treated sample was confirmed by MALDI-TOF-MS, showing the corresponding mass peak of m/z= 2530.22 Da in the MS1 spectrum (Fig. S7C). In contrast, the diamide-treated GbaAC104S mutant was oxidized to the Cys55-Cys55′ disulfide-linked dimer, which migrates at the size of ~40 kDa (Fig. 6C). In addition, a small fraction of the GbaAC55S mutant formed weakly intermolecular Cys104-Cys104' disulfides, while the majority of the protein was not oxidized to the disulfide-linked dimer (Fig. 6B). These results demonstrate that GbaA responds to diamide by intramolecular disulfides, whereas the single Cys mutants are oxidized to intermolecular disulfides between both subunits. The weaker oxidation of the GbaAC55S mutant to intermolecular disulfides might indicate that the Cys104 residues in both subunits are less accessible for disulfide formation in vitro.

To analyze thiol-oxidation of GbaA and its Cys mutants under diamide stress in vivo, cell extracts from the *S. aureus gbaA* mutant and the *gbaA*, *gbaAC55S* and *gbaAC104* complemented strains were subjected to non-reducing anti-His-tag Western blot analysis (Fig. 6D). GbaA was oxidized to Cys55-Cys104 intramolecular disulfides by

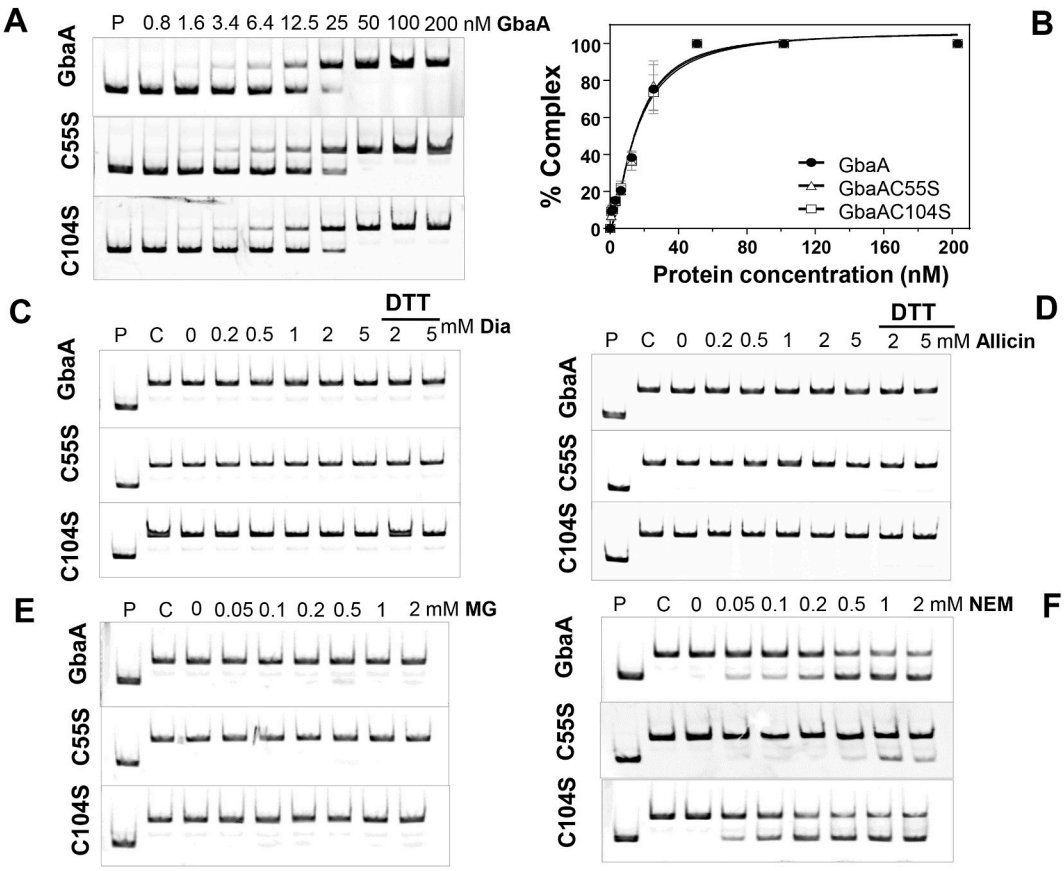

Fig. 5. The DNA binding activity of GbaA and the Cys mutant proteins is not inhibited under disulfide stress (diamide, allicin) and MG, but partially affected by NEM in vitro. (A) EMSAs were used to analyze the DNA binding activity of increasing concentrations of GbaA, GbaAC55S and GbaAC104S proteins to the 150 bp *gbaA* promoter probe. (B) The percentage of the GbaA-DNA complex formation was determined according to the band intensities of five biological replicates of the EMSAs in A) and quantified using Image J 1.48v. Dissociation constants (K_D) were calculated as 15.24 nM, 15.24 nM and 15.79 nM for GbaA, GbaAC55S and GbaAC104S mutant proteins, respectively using the Graph prism software version 6.01. (C-F) The DNA binding activity of GbaA, GbaAC55S and GbaAC104S proteins was not affected by diamide, allicin and MG (C–E), but partially inhibited with NEM (F).

diamide as shown by the slower mobility band compared to reduced GbaA under control conditions. While the *gbaAC55S* mutant was strongly oxidized to Cys104-Cys104' intermolecular disulfides, the *gbaAC104S* mutant did not form intermolecular disulfides (Fig. 6D). The Cys mutant results are in contrast to the in vitro disulfide data, but confirm that Cys104 is the more reactive and redox-sensing Cys in vivo. The reversibility of the intra- and intermolecular thiol switches in GbaA and GbaAC55S proteins was shown in the reducing Western blot analyses with DTT (Fig. 6E).

We further analyzed possible thiol-modifications of GbaA and the Cys mutants after allicin treatment (Fig. 7A–E). Allicin treatment of GbaA protein resulted in a slightly faster mobility, which might indicate intramolecular disulfide formation (Fig. 7A). The same slight mobility shift was also observed in the *S. aureus gbaA* strain in vivo (Fig. 7D). However, no intermolecular disulfide was detected in the monothiol GbaAC55S and GbaAC104S mutants after allicin exposure in vitro or in vivo (Fig. 7B–D). Since allicin causes *S*-thioallylation of protein thiols, the allicin-treated GbaA and the Cys mutant proteins were subjected to MALDI-TOF-MS (Fig. S7). Interestingly, allicin caused formation of the intramolecular C55-C104 disulfide peptide (m/z=2530.31) and *S*-thioallylations of the Cys55 and Cys104 peptides with mass shifts of 72 Da (m/z=1331.63 Da and m/z=1345.65 Da) (Fig. S7). In conclusion, our data support that GbaA is oxidized to intramolecular disulfides by diamide, while allicin causes *S*-thioallylation and intramolecular disulfides, which, however, does not affect the DNA binding activity of the GbaA repressor in vitro.

3.6. *GbaA controls defense mechanisms against oxidative and electrophile stress*

GbaA was shown to regulate two short chain dehydrogenases/oxidoreductases, GbaB and NmrA, and the putative glyoxalase (SACOL2590), which could be involved in the defense against oxidative and electrophile stress in *S. aureus*. The putative glyoxalase might be involved in MG detoxification in *S. aureus*. Since the GbaA regulon is induced by diamide, allicin, MG and NEM, we analyzed the survival phenotypes of the *gbaA, gbaB* and *SACOL2592-nmrA-SACOL2590* deletion mutants under these thiol-stress conditions.

The survival assays revealed that the *S. aureus* COL *gbaA* mutant was significantly more resistant under diamide, allicin, MG and NEM stress as compared to the WT (Fig. 8A–E). While the % survival rate of the *gbaA* mutant was 1.5–2.7-fold increased with 0.5 mM allicin, 0.3 mM NEM and 2 mM MG compared to the WT, no significantly enhanced tolerance towards MHQ stress could be determined in the absence of *gbaA* (Fig. 8A–E). This enhanced survival of the *gbaA* mutant under diamide, allicin, NEM and MG could be reversed to the WT level in the *gbaA* complemented strain. In addition, both GbaA Cys mutants showed a significantly 1.6–3.4 -fold decreased survival after 4h of treatment with NEM and MG in relation to the *gbaA* complemented strain, while no difference in viability was measured with allicin (Fig. 9A–C). These results support the role of the Cys55 and Cys104 residues of the GbaA repressor in the control of electrophile resistance. To clarify the involvement of the GbaA-regulon genes in stress tolerance, the survival of the *SACOL2590-92* and *gbaB* mutants was investigated (Fig. 8A–E).

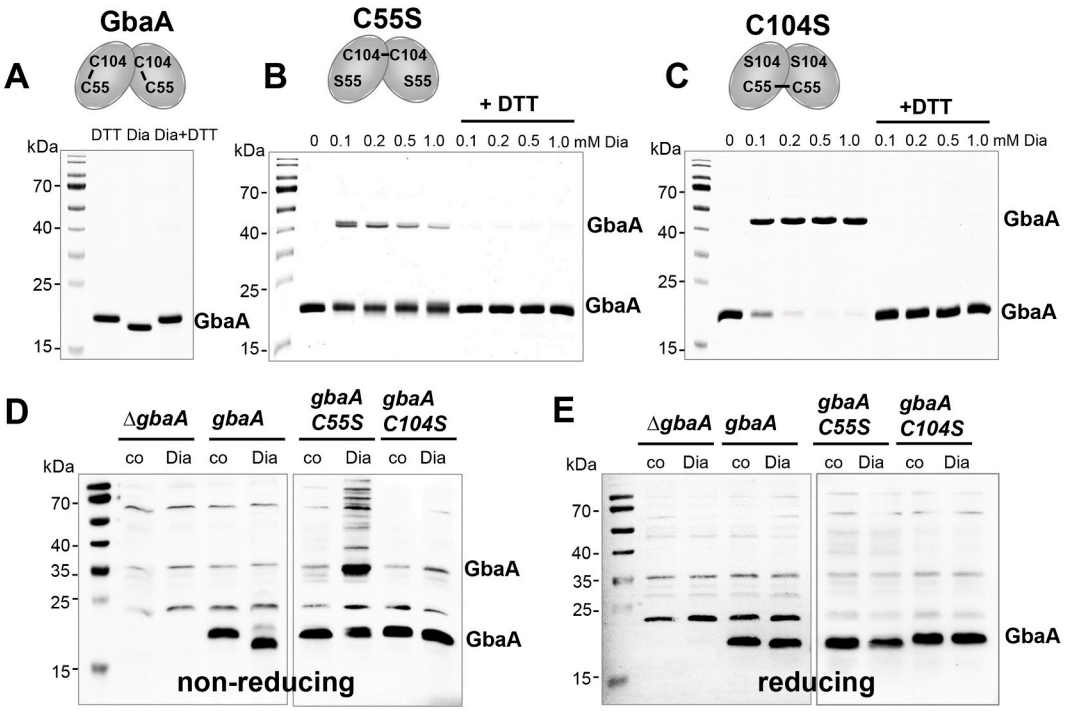

Fig. 6. GbaA and the GbaA Cys mutants are oxidized to intra- and intermolecular disulfides by diamide in vitro and in vivo, respectively. (A–C) Purified GbaA was treated with 1 mM diamide (A), while the GbaAC55S (B) and GbaAC104S mutant proteins (C) were exposed to increasing concentrations of diamide for 15 min, followed by alkylation with 50 mM IAM for 30 min in the dark and separation by non-reducing SDS-PAGE. The non-reducing SDS-PAGE gels are stained with Coomassie Blue. To assess the reversibility, diamide-treated samples were reduced with 20 mM DTT for 15 min before alkylation and analysis by non-reducing SDS-PAGE. GbaA is oxidized to intramolecular C55-C104 disulfides by diamide as confirmed by MALDI-TOF MS (Fig. S7), while the C55S and C104S mutants form intermolecular disulfides as shown in the schematics above the gel images. (D, E) The *S. aureus gbaA* mutant and the *gbaA* complemented strain were treated with 5 mM diamide and the *gbaAC55S* and *gbaAC104S* complemented strains were exposed to 2 mM diamide for 30 min, alkylated with NEM and the protein extracts analyzed for thiol-oxidation of GbaA in vivo by non-reducing (D) and reducing (E) Western blot analysis with monoclonal anti-His6 tag antibodies. The protein loading controls are shown in Fig. S8.

The *SACOL2590-92* mutant was significantly impaired in viability after exposure to diamide, allicin, MG and NEM compared to the WT, whereas the *gbaB* mutant showed only a slight survival defect under MG and MHQ stress (Fig. 8A–E). However, we did not observed growth phenotypes of the *gbaA* and *SACOL2590-92* mutants in response to these high concentrations of allicin, MG and NEM in comparison to the WT (Fig. S9). Overall, the survival results support that GbaA confers tolerance under disulfide and electrophile stress in *S. aureus* via control of the upstream *SACOL2592-nmrA-SACOL2590* operon, which might be involved in allicin, diamide, MG and NEM detoxification. Future analyses will be directed to investigate the functions of these hypothetical proteins under oxidative and MG stress in *S. aureus*.

4. Discussion

The TetR family GbaA repressor controls the *SACOL2592-nmrA-2590* and *gbaAB-SACOL2595-97* operons [30,31]. Biochemical studies revealed that GbaA functions as monothiol redox sensor, which senses electrophiles via one of its two Cys residues in the single Cys mutants, while the intramolecular disulfide of GbaA did not play a regulatory role [32]. In this work, we investigated the regulation and function of GbaA and its Cys mutants in *S. aureus* COL under various thiol-stress conditions. Northern blot results revealed that the *gbaAB-SACOL2595-97* operon is only weakly 3-10-fold induced under oxidative, electrophile and antibiotics stress in *S. aureus* COL (Fig. 1; Figs. S4A,B,D), which is far below the high level of 57-734-fold derepression as observed in the transcriptome of the *gbaA* deletion mutant and in the Northern blot analyses (Fig. 1B; Fig. 2C and D; Tables S3–S4). Moreover, induction of the *SACOL2592-nmrA-2590* operon under these thiol-stress conditions was not visible in *S. aureus* COL using Northern blots, although this upstream operon is clearly regulated by GbaA (Fig. 2A–C).

Based on these findings, we conclude that GbaA does not sense directly any of these thiol-reactive compounds, including AGXX®, diamide, allicin, NEM and MG, which lead only to a weak inactivation of GbaA in vivo. The impact of the *gbaA* deletion and GbaA Cys mutants on transcriptional regulation of the *gbaAB-SACOL2595-97* operon was studied under diamide, AGXX®, allicin, NEM and MG stress in vivo. Here, we made the surprising observation that the *gbaA* mutant still responds strongly to thiol-stress conditions, such as diamide, AGXX®, NEM and MG, indicating that regulation of the GbaA-controlled operons is more complex and involves another yet unknown (co)regulator. The transcriptional analyses suggest that inactivation of the GbaA repressor is the prerequisite for much faster inactivation of the secondary regulator under thiol-stress conditions, as requirement for full derepression of the *gbaAB-SACOL2595-97* operon (Fig. 4A–D).

Using 5' RNA-seq, TSS-1 and TSS-2 of the divergent transcripts were mapped at the opposing strands, respectively. Since both operons are transcribed from strong SigmaA-dependent promoters, which overlap at both strands in the −10 region, we hypothesize that the secondary regulator might represent another transcriptional repressor. One scenario could be that the primary regulator GbaA requires a specific ligand for inactivation as shown for other TetR-family regulators [49,51]. The secondary regulator likely senses thiol-stress conditions only, as shown by the full derepression of the *gbaAB-SACOL2595-97* operon in the *gbaA* mutant under various disulfide and electrophile stress conditions. The physiological inducers of GbaA could be also combinations of electrophiles, antibiotics or oxidants.

GbaA belongs to the TetR/AcrR family of transcriptional regulators, consisting of a DNA binding HTH motif and a regulatory core domain, which is responsible for dimerization and interacts with different

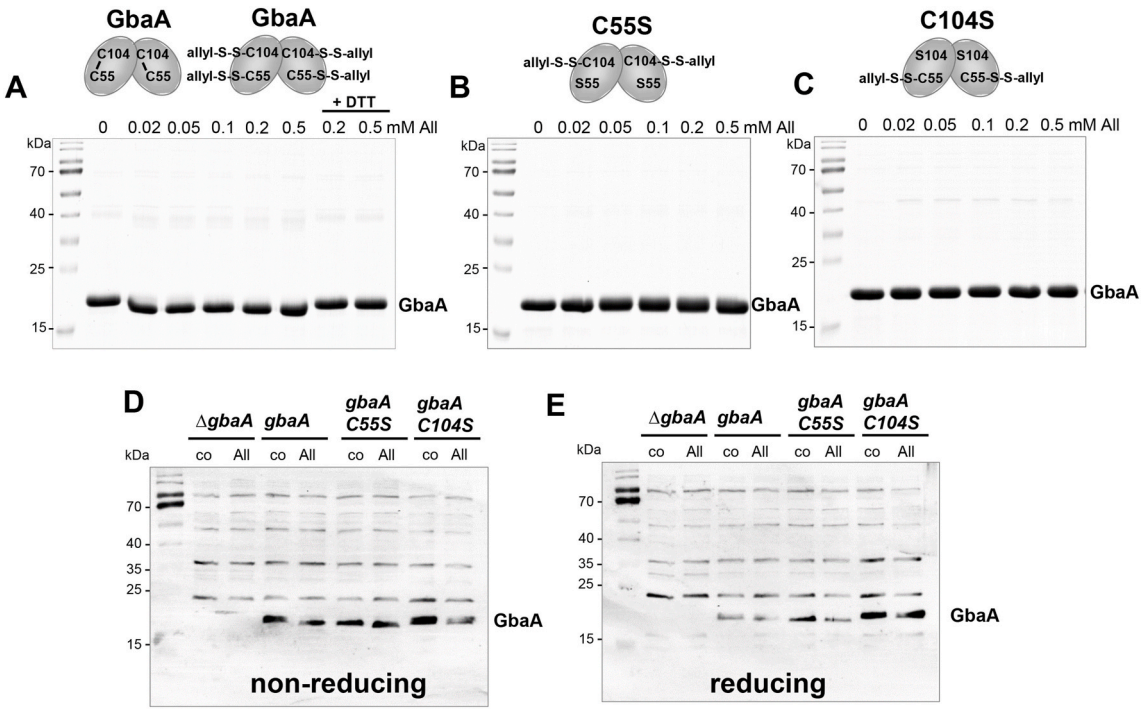

Fig. 7. GbaA is oxidized to intramolecular disulfides and *S*-thioallylations by allicin in vitro. (A–C) Purified GbaA (A), GbaAC55S (B) and GbaAC104S mutant proteins (C) were treated with increasing concentrations of allicin for 15 min, followed by alkylation with 50 mM IAM for 30 min in the dark and separation by non-reducing SDS-PAGE. The non-reducing SDS-PAGE gels are stained with Coomassie Blue. For the analysis of reversibility, allicin-treated samples were reduced by 20 mM DTT for 15 min, alkylated and subjected to non-reducing SDS-PAGE. GbaA was oxidized to intramolecular disulfides and *S*-thioallylations. The GbaA Cys mutants are *S*-thioallylated under allicin stress as revealed by MALDI-TOF MS (Fig. S7) and shown in the schematics above the images. (D, E) The *S. aureus gbaA* mutant and *gbaA*, *gbaAC55S* and *gbaAC104S* complemented strains were treated with 0.3 mM allicin stress for 30 min, alkylated with NEM and the protein extracts were used to analyze thiol-oxidation of GbaA in vivo by non-reducing (D) and reducing (E) Western blot analysis with monoclonal anti-His6 tag antibodies. The protein loading controls are shown in Fig. S8.

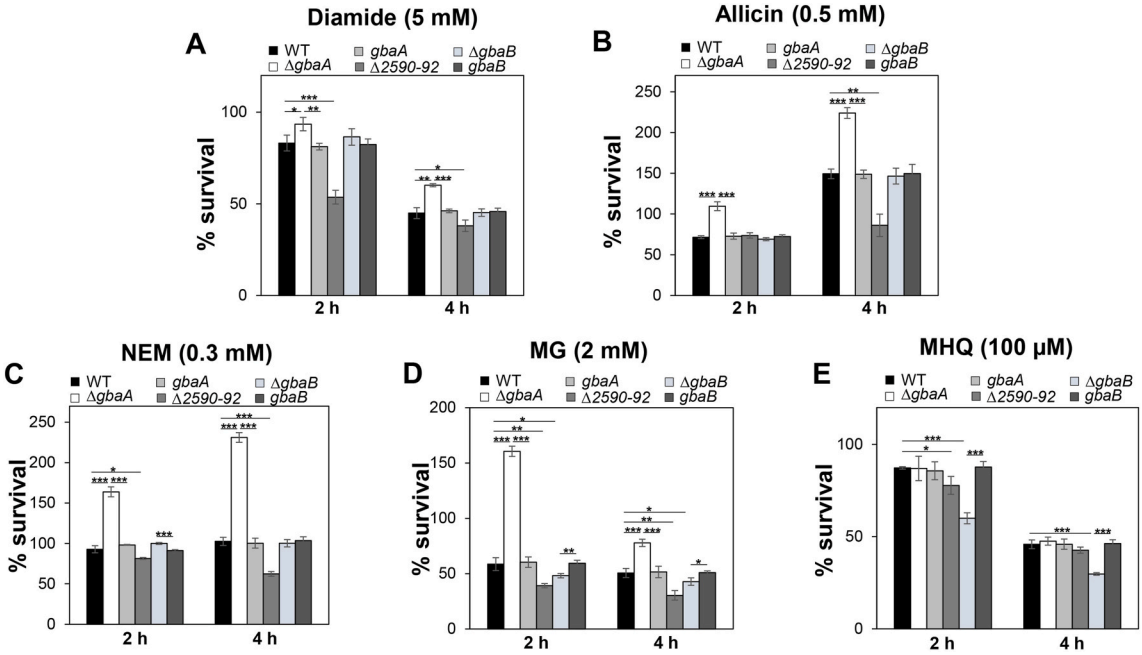

Fig. 8. The GbaA regulon confers resistance under disulfide stress (diamide, allicin) and electrophiles (NEM, MG) in *S. aureus*. For survival assays, *S. aureus* COL WT, the *gbaA*, *gbaB* and *SACOL2592-90* deletion mutants and *gbaA, gbaB* complemented strains were grown in RPMI medium until an OD_{500} of 0.5 and treated with 5 mM diamide (A), 0.5 mM allicin (B), 0.3 mM NEM (C), 2 mM MG (D) and 100 μM MHQ (E). CFUs were counted after plating 100 μl of serial dilutions onto LB agar plates after 2 and 4 h of stress exposure. The survival of treated cells was normalized to the untreated control, which was set to 100%. The results are from four biological replicates. Error bars indicate the standard deviation (SD) and the statistics was calculated using a Student's unpaired two-tailed *t*-test. Symbols are: $*p \leq 0.05$, $**p \leq 0.01$ and $***p \leq 0.001$.

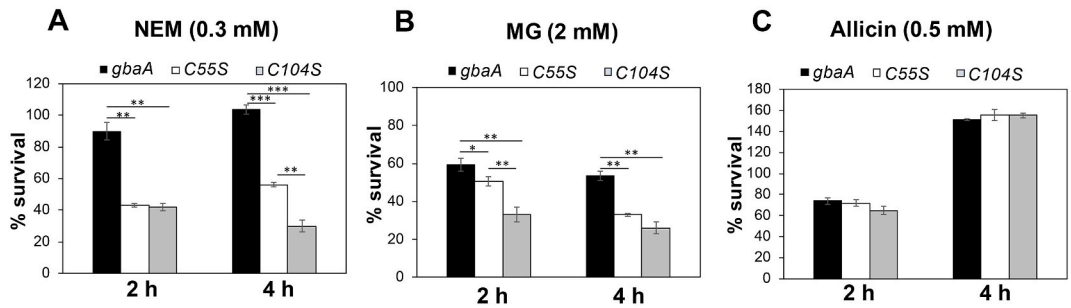

Fig. 9. The Cys55 and Cys104 residues of GbaA are required for NEM and MG tolerance. Survival assays were performed for the *S. aureus gbaA* mutant complemented with *gbaA, gbaAC55S* and *gbaAC104S* alleles. Strains were grown in RPMI until an OD_{500} of 0.5 and treated with 0.3 mM NEM (A), 2 mM MG (B) and 0.5 mM allicin (C) to determine CFUs after 2 and 4 h of stress exposure. The percentage survival was normalized to the control. Error bars represent the standard deviation (SD) calculated from three biological replicates. The statistics was determined using a Student's unpaired two-tailed *t*-test. Symbols are: $*p \leq 0.05$, $**p \leq 0.01$ and $***p \leq 0.001$.

ligands, such as tetracycline and multiple antibiotics, disinfectants and other toxic compounds [48,49,51]. TetR/AcrR family regulators control various functions, including resistance to multiple antibiotics, catabolism of organic compounds, lipid metabolism, iron homeostasis, osmotic stress and virulence functions [48,49,51]. A main feature of the *E. coli* AcrR structure is the presence of a large cavity in the ligand binding pocket, which was shown to accommodate many different ligands, such as ethidium bromide, proflavin, and rhodamine 6G and ciprofloxacin to inhibit DNA binding activity [49,52]. Similarly, the multidrug efflux pump regulator QacR of *S. aureus* responds to many cationic lipophilic antiseptics and disinfectants, such as rhodamine 6G, crystal violet, palmatine, nitidine as well as antimicrobial plant alkaloids [53–55]. However, QacR and AcrR control multidrug resistance via their specific efflux pumps, which is not the case for GbaA. Thus, GbaA might be inactivated by specific thiol-reactive compounds or metabolites, which bind to the ligand pocket, leading to oxidation of GbaA and a second redox regulator to induce the upstream and downstream operons.

Transcriptional analyses further revealed that both GbaA single Cys mutants showed non-significant induction of the *gbaAB-SACOL2595-97* operon under diamide, AGXX® and NEM stress as compared to the *gbaA* complemented strain (Fig. 4A and B; Figs. S6A and B). In addition, the Cys55 and Cys104 mutants showed decreased resistance under NEM and MG stress (Fig. 9), indicating that both Cys55 and Cys104 are required for redox sensing in vivo, supporting previous findings [32]. In previous biochemical studies, Cys104 was shown to be more reactive towards electrophiles compared to Cys55 [32], which is in line with the abolished transcription of the *gbaAB-SACOL2595-97* operon and the increased susceptibility of the Cys104 mutant after NEM and MG stress compared to the Cys55 mutant (Fig. 4B; Fig. S6B; Fig. 9). While diamide leads to formation of the Cys55–Cys104 intramolecular disulfide in GbaA in vivo and in vitro, allicin caused a mix of intramolecular disulfides and *S*-thioallylation of both Cys residues (Fig. S7). However, the different thiol switches are not sufficient for GbaA inactivation in vitro, which probably explains the weak transcription of the *gbaAB-SACOL2595-97* operon under thiol stress conditions in *S. aureus* COL WT. Thus, our results demonstrate that thiol switches occur in GbaA and the single Cys mutants in vivo, but they do not alter the structure and abolish the DNA binding activity completely, which is in agreement with previous results [32]. However, NEM caused partial inhibition of the DNA binding activity of GbaA and the GbaAC104S mutant in vitro, while the GbaAC55S mutant was less responsive to NEM (Fig. 5F) [32]. Our in vitro results suggest that in the GbaAC104S mutant, Cys55 is more accessible for C55–C55′ intersubunit disulfide formation by diamide or NEM alkylation, while the C104–C104' disulfide or C104 alkylation are not favored in the GbaAC55S mutant in vitro. We further were unable to detect any effect of MG on the DNA binding activity of GbaA or the GbaA Cys mutants in vitro, perhaps since MG might cross-link amino-acid side chains with cytosine bases [56]. Altogether, our data show that GbaA functions as two-Cys-type redox sensor, which senses disulfide and electrophile stress via both Cys residues in vivo. However, an unknown thiol-reactive ligand and an additional redox-sensing (co)regulator are required for full derepression of the GbaA regulon, which are subjects of our future studies.

The phenotype analyses of GbaA regulon mutants support that strong oxidants or electrophiles could serve as physiological ligands and are perhaps detoxified by GbaA-controlled genes. The *gbaA* mutant was resistant to diamide, allicin, NEM and MG, while the deletion of the upstream *SACOL2592-nmrA-2590* operon enhanced the susceptibility of *S. aureus* towards oxidants and electrophiles (Fig. 8). However, deletion of *gbaB* did not confer sensitivity to diamide, allicin and NEM, while the *gbaB* mutant was more sensitive to quinones and MG. The sensitivity of the *SACOL2592-nmrA-2590* deletion mutant under MG stress is intriguing, since *SACOL2590* encodes a glyoxalase enzyme, which could be involved in detoxification of MG. MG is a toxic α, β-unsaturated dicarbonyl compound, which is generated as a byproduct of glycolysis [57–59]. In *B. subtilis*, MG detoxification involves a bacillithiol-dependent glyoxalase pathway, consisting of the glyoxalase-I (GlxA) generating *S*-lactoyl bacillithiol, which is hydrolyzed by the glyoxalase-II (GlxB) to lactate [59,60]. The glyoxalase encoded by *SACOL2590* belongs to the vicinal oxygen chelate (VOC) family of enzymes, which includes glyoxalase-I enzymes involved in the first step of MG detoxification.

In addition, NmrA and GbaB are both annotated as $NAD(P)^+$-dependent oxidoreductases/short chain dehydrogenases (SDR). SDR enzymes were shown to catalyze oxidation-reduction reactions of various compounds, such as aldehydes, steroids, alcohols, sugars, xenobiotics and aromatic compounds using $NAD(P)^+$ or NADP(H) cofactors [58,60]. Increasing intracellular NADH concentrations were previously determined in the *gbaA* mutant, suggesting that NmrA or GbaB might catalyze the oxidation of an electrophilic metabolite leading to NADH production [30]. However, since NmrA is lacking the essential tyrosine in the YxxxK active-site motif, it was suggested to function rather as regulator of the $NAD(P)^+$/NADP(H) redox balance [61]. Future analyses will reveal the roles of the glyoxalase and SDR/oxidoreductases in detoxification of MG, allicin, diamide and unknown thiol-reactive metabolites to maintain the cellular redox homeostasis.

Similarly, the redox-sensitive TetR-family regulator NemR of *E. coli* was shown to sense oxidants and electrophiles, such as HOCl, NEM and MG [58,62,63]. NemR contains 6 cysteine residues and was inactivated by intermolecular disulfides, resulting in induction of the NEM reductase NemA and the glyoxalase I (GloA) to confer resistance under HOCl and MG stress in *E. coli* [63]. While there are functional links to MG detoxification between NemR of *E. coli* and GbaA of *S. aureus*, the regulation of GbaA is far more complex, since the physiological inducer and the additional redox-sensitive (co)regulator are unknown and both are required for full derepression of the GbaA regulon genes. Future

studies will be directed to investigate combinations of thiol-reactive antimicrobials as inducers and to utilize *gbaA* promoter mutations to shed light on the genetic basis for full derepression.

Declaration of competing interest

The authors declare that there is no conflict of interest.

Acknowledgements

This work was supported by an European Research Council (ERC) Consolidator grant (GA 615585) MYCOTHIOLOME and grants from the Deutsche Forschungsgemeinschaft (AN746/4-1 and AN746/4-2) within the SPP1710 on "Thiol-based Redox switches", by the SFB973 project C08 and TR84 project B06 to H.A. For mass spectrometry (C.W.) we would like to acknowledge the assistance of the Core Facility Bio-SupraMol supported by the Deutsche Forschungsgemeinschaft.

Appendix A. Supplementary data

Supplementary data to this article can be found online at https://doi.org/10.1016/j.freeradbiomed.2021.10.024.

References

[1] T.J. Foster, The *Staphylococcus aureus* "superbug, J. Clin. Invest. 114 (12) (2004) 1693–1696.
[2] F.D. Lowy, *Staphylococcus aureus* infections, N. Engl. J. Med. 339 (8) (1998) 520–532.
[3] H.W. Boucher, G.R. Corey, Epidemiology of methicillin-resistant *Staphylococcus aureus*, Clin. Infect. Dis. 46 (Suppl 5) (2008) S344–S349.
[4] G.L. Archer, *Staphylococcus aureus*: a well-armed pathogen, Clin. Infect. Dis. 26 (5) (1998) 1179–1181.
[5] H.F. Chambers, F.R. Deleo, Waves of resistance: *Staphylococcus aureus* in the antibiotic era, Nat. Rev. Microbiol. 7 (9) (2009) 629–641.
[6] M. Vestergaard, D. Frees, H. Ingmer, Antibiotic resistance and the MRSA problem, Microbiol. Spectr. 7 (2) (2019).
[7] N. Linzner, V.V. Loi, V.N. Fritsch, H. Antelmann, Thiol-based redox switches in the major pathogen *Staphylococcus aureus*, Biol. Chem. 402 (3) (2021) 333–361.
[8] A. Ulfig, L.I. Leichert, The Effects of Neutrophil-Generated Hypochlorous Acid and Other Hypohalous Acids on Host and Pathogens, Cell Mol Life Sci, 2020.
[9] C.C. Winterbourn, A.J. Kettle, Redox reactions and microbial killing in the neutrophil phagosome, Antioxidants Redox Signal. 18 (6) (2013) 642–660.
[10] C.C. Winterbourn, A.J. Kettle, M.B. Hampton, Reactive oxygen species and neutrophil function, Annu. Rev. Biochem. 85 (2016) 765–792.
[11] L.J. Marnett, J.N. Riggins, J.D. West, Endogenous generation of reactive oxidants and electrophiles and their reactions with DNA and protein, J. Clin. Invest. 111 (5) (2003) 583–593.
[12] A.T. Jacobs, L.J. Marnett, Systems analysis of protein modification and cellular responses induced by electrophile stress, Acc. Chem. Res. 43 (5) (2010) 673–683.
[13] M. Delmastro-Greenwood, B.A. Freeman, S.G. Wendell, Redox-dependent anti-inflammatory signaling actions of unsaturated fatty acids, Annu. Rev. Physiol. 76 (2014) 79–105.
[14] S.W. Vetter, Glycated serum albumin and AGE receptors, Adv. Clin. Chem. 72 (2015) 205–275.
[15] S.L. Hazen, A. d'Avignon, M.M. Anderson, F.F. Hsu, J.W. Heinecke, Human neutrophils employ the myeloperoxidase-hydrogen peroxide-chloride system to oxidize alpha-amino acids to a family of reactive aldehydes. Mechanistic studies identifying labile intermediates along the reaction pathway, J. Biol. Chem. 273 (9) (1998) 4997–5005.
[16] S.A. Riquelme, K. Liimatta, T. Wong Fok Lung, B. Fields, D. Ahn, D. Chen, C. Lozano, Y. Saenz, A.C. Uhlemann, B.C. Kahl, C.J. Britto, E. DiMango, A. Prince, *Pseudomonas aeruginosa* utilizes host-derived itaconate to redirect its metabolism to promote biofilm formation, Cell Metabol. 31 (6) (2020) 1091–1106 e6.
[17] K.L. Tomlinson, T.W.F. Lung, F. Dach, M.K. Annavajhala, S.J. Gabryszewski, R. A. Groves, M. Drikic, N.J. Francoeur, S.H. Sridhar, M.L. Smith, S. Khanal, C. J. Britto, R. Sebra, I. Lewis, A.C. Uhlemann, B.C. Kahl, A.S. Prince, S.A. Riquelme, *Staphylococcus aureus* induces an itaconate-dominated immunometabolic response that drives biofilm formation, Nat. Commun. 12 (1) (2021) 1399.
[18] H. Antelmann, J.D. Helmann, Thiol-based redox switches and gene regulation, Antioxidants Redox Signal. 14 (6) (2011) 1049–1063.
[19] M. Hillion, H. Antelmann, Thiol-based redox switches in prokaryotes, Biol. Chem. 396 (5) (2015) 415–444.
[20] Q. Ji, L. Zhang, M.B. Jones, F. Sun, X. Deng, H. Liang, H. Cho, P. Brugarolas, Y. N. Gao, S.N. Peterson, L. Lan, T. Bae, C. He, Molecular mechanism of quinone signaling mediated through *S*-quinonization of a YodB family repressor QsrR, Proc. Natl. Acad. Sci. U. S. A. 110 (13) (2013) 5010–5015.
[21] V.V. Loi, T. Busche, K. Tedin, J. Bernhardt, J. Wollenhaupt, N.T.T. Huyen, C. Weise, J. Kalinowski, M.C. Wahl, M. Fulde, H. Antelmann, Redox-sensing under hypochlorite stress and infection conditions by the Rrf2-family repressor HypR in *Staphylococcus aureus*, Antioxidants Redox Signal. 29 (7) (2018) 615–636.
[22] P.R. Chen, S. Nishida, C.B. Poor, A. Cheng, T. Bae, L. Kuechenmeister, P. M. Dunman, D. Missiakas, C. He, A new oxidative sensing and regulation pathway mediated by the MgrA homologue SarZ in *Staphylococcus aureus*, Mol. Microbiol. 71 (1) (2009) 198–211.
[23] C.B. Poor, P.R. Chen, E. Duguid, P.A. Rice, C. He, Crystal structures of the reduced, sulfenic acid, and mixed disulfide forms of SarZ, a redox active global regulator in *Staphylococcus aureus*, J. Biol. Chem. 284 (35) (2009) 23517–23524.
[24] P.R. Chen, T. Bae, W.A. Williams, E.M. Duguid, P.A. Rice, O. Schneewind, C. He, An oxidation-sensing mechanism is used by the global regulator MgrA in *Staphylococcus aureus*, Nat. Chem. Biol. 2 (11) (2006) 591–595.
[25] J.W. Lee, S. Soonsanga, J.D. Helmann, A complex thiolate switch regulates the *Bacillus subtilis* organic peroxide sensor OhrR, Proc. Natl. Acad. Sci. U. S. A. 104 (21) (2007) 8743–8748.
[26] B.K. Chi, K. Gronau, U. Mäder, B. Hessling, D. Becher, H. Antelmann, *S*-bacillithiolation protects against hypochlorite stress in *Bacillus subtilis* as revealed by transcriptomics and redox proteomics, Mol. Cell. Proteomics 10 (11) (2011). M111 009506.
[27] S. Mongkolsuk, J.D. Helmann, Regulation of inducible peroxide stress responses, Mol. Microbiol. 45 (1) (2002) 9–15.
[28] B.K. Chi, D. Albrecht, K. Gronau, D. Becher, M. Hecker, H. Antelmann, The redox-sensing regulator YodB senses quinones and diamide via a thiol-disulfide switch in *Bacillus subtilis*, Proteomics 10 (17) (2010) 3155–3164.
[29] S.J. Lee, I.G. Lee, K.Y. Lee, D.G. Kim, H.J. Eun, H.J. Yoon, S. Chae, S.H. Song, S. O. Kang, M.D. Seo, H.S. Kim, S.J. Park, B.J. Lee, Two distinct mechanisms of transcriptional regulation by the redox sensor YodB, Proc. Natl. Acad. Sci. U. S. A. 113 (35) (2016) E5202–E5211.
[30] Y. You, T. Xue, L. Cao, L. Zhao, H. Sun, B. Sun, *Staphylococcus aureus* glucose-induced biofilm accessory proteins, GbaAB, influence biofilm formation in a PIA-dependent manner, Int J Med Microbiol 304 (5–6) (2014) 603–612.
[31] L. Yu, J. Hisatsune, I. Hayashi, N. Tatsukawa, Y. Sato`o, E. Mizumachi, F. Kato, H. Hirakawa, G.B. Pier, M. Sugai, A novel repressor of the *ica* Locus discovered in clinically isolated super-biofilm-elaborating *Staphylococcus aureus*, mBio 8 (1) (2017).
[32] A. Ray, K.A. Edmonds, L.D. Palmer, E.P. Skaar, D.P. Giedroc, *Staphylococcus aureus* glucose-induced biofilm accessory protein A (GbaA) is a monothiol-dependent electrophile sensor, Biochemistry 59 (31) (2020) 2882–2895, https://doi.org/10.1021/acs.biochem.0c00347.
[33] V.N. Fritsch, V.V. Loi, T. Busche, A. Sommer, K. Tedin, D.J. Nürnberg, J. Kalinowski, J. Bernhardt, M. Fulde, H. Antelmann, The MarR-type repressor MhqR confers quinone and antimicrobial resistance in *Staphylococcus aureus*, Antioxidants Redox Signal. 31 (16) (2019) 1235–1252.
[34] V.V. Loi, T. Busche, T. Preuss, J. Kalinowski, J. Bernhardt, H. Antelmann, The AGXX antimicrobial coating causes a thiol-specific oxidative stress response and protein *S*-bacillithiolation in *Staphylococcus aureus*, Front. Microbiol. 9 (2018) 3037.
[35] V.V. Loi, N.T.T. Huyen, T. Busche, Q.N. Tung, M.C.H. Gruhlke, J. Kalinowski, J. Bernhardt, A.J. Slusarenko, H. Antelmann, *Staphylococcus aureus* responds to allicin by global *S*-thioallylation - role of the Brx/BSH/YpdA pathway and the disulfide reductase MerA to overcome allicin stress, Free Radic. Biol. Med. 139 (2019) 55–69.
[36] N. Linzner, V.N. Fritsch, T. Busche, Q.N. Tung, V. Van Loi, J. Bernhardt, J. Kalinowski, H. Antelmann, The plant-derived naphthoquinone lapachol causes an oxidative stress response in *Staphylococcus aureus*, Free Radic. Biol. Med. 158 (2020) 126–136.
[37] V.V. Loi, M. Harms, M. Müller, N.T.T. Huyen, C.J. Hamilton, F. Hochgräfe, J. Pane-Farre, H. Antelmann, Real-time imaging of the bacillithiol redox potential in the human pathogen *Staphylococcus aureus* using a genetically encoded bacilliredoxin-fused redox biosensor, Antioxidants Redox Signal. 26 (15) (2017) 835–848.
[38] M. Arnaud, A. Chastanet, M. Debarbouille, New vector for efficient allelic replacement in naturally nontransformable, low-GC-content, gram-positive bacteria, Appl. Environ. Microbiol. 70 (11) (2004) 6887–6891.
[39] M. Wetzstein, U. Volker, J. Dedio, S. Lobau, U. Zuber, M. Schiesswohl, C. Herget, M. Hecker, W. Schumann, Cloning, sequencing, and molecular analysis of the *dnaK* locus from *Bacillus subtilis*, J. Bacteriol. 174 (10) (1992) 3300–3310.
[40] T. Tam le, C. Eymann, D. Albrecht, R. Sietmann, F. Schauer, M. Hecker, H. Antelmann, Differential gene expression in response to phenol and catechol reveals different metabolic activities for the degradation of aromatic compounds in *Bacillus subtilis*, Environ. Microbiol. 8 (8) (2006) 1408–1427.
[41] M.I. Love, W. Huber, S. Anders, Moderated estimation of fold change and dispersion for RNA-seq data with DESeq2, Genome Biol. 15 (12) (2014) 550.
[42] R. Hilker, K.B. Stadermann, O. Schwengers, E. Anisiforov, S. Jaenicke, B. Weisshaar, T. Zimmermann, A. Goesmann, ReadXplorer 2-detailed read mapping analysis and visualization from one single source, Bioinformatics 32 (24) (2016) 3702–3708.
[43] K. Pfeifer-Sancar, A. Mentz, C. Ruckert, J. Kalinowski, Comprehensive analysis of the *Corynebacterium glutamicum* transcriptome using an improved RNAseq technique, BMC Genom. 14 (2013) 888.
[44] B. Langmead, S.L. Salzberg, Fast gapped-read alignment with Bowtie 2, Nat. Methods 9 (4) (2012) 357–359.
[45] B.K. Chi, A.A. Roberts, T.T. Huyen, K. Basell, D. Becher, D. Albrecht, C.J. Hamilton, H. Antelmann, *S*-bacillithiolation protects conserved and essential proteins against

hypochlorite stress in firmicutes bacteria, Antioxidants Redox Signal. 18 (11) (2013) 1273–1295.
[46] D. Suckau, A. Resemann, M. Schuerenberg, P. Hufnagel, J. Franzen, A. Holle, A novel MALDI LIFT-TOF/TOF mass spectrometer for proteomics, Anal. Bioanal. Chem. 376 (7) (2003) 952–965.
[47] U. Mäder, P. Nicolas, M. Depke, J. Pane-Farre, M. Debarbouille, M.M. van der Kooi-Pol, C. Guerin, S. Derozier, A. Hiron, H. Jarmer, A. Leduc, S. Michalik, E. Reilman, M. Schaffer, F. Schmidt, P. Bessieres, P. Noirot, M. Hecker, T. Msadek, U. Völker, J. M. van Dijl, *Staphylococcus aureus* transcriptome architecture: from laboratory to infection-mimicking conditions, PLoS Genet. 12 (4) (2016), e1005962.
[48] J.L. Ramos, M. Martinez-Bueno, A.J. Molina-Henares, W. Teran, K. Watanabe, X. Zhang, M.T. Gallegos, R. Brennan, R. Tobes, The TetR family of transcriptional repressors, Microbiol. Mol. Biol. Rev. 69 (2) (2005) 326–356.
[49] W. Deng, C. Li, J. Xie, The underling mechanism of bacterial TetR/AcrR family transcriptional repressors, Cell. Signal. 25 (7) (2013) 1608–1613.
[50] M. Li, R. Gu, C.C. Su, M.D. Routh, K.C. Harris, E.S. Jewell, G. McDermott, E.W. Yu, Crystal structure of the transcriptional regulator AcrR from *Escherichia coli*, J. Mol. Biol. 374 (3) (2007) 591–603.
[51] L. Cuthbertson, J.R. Nodwell, The TetR family of regulators, Microbiol. Mol. Biol. Rev. 77 (3) (2013) 440–475.
[52] C.C. Su, D.J. Rutherford, E.W. Yu, Characterization of the multidrug efflux regulator AcrR from *Escherichia coli*, Biochem. Biophys. Res. Commun. 361 (1) (2007) 85–90.
[53] K. Takeuchi, M. Imai, I. Shimada, Conformational equilibrium defines the variable induction of the multidrug-binding transcriptional repressor QacR, Proc. Natl. Acad. Sci. U. S. A. 116 (40) (2019) 19963–19972.
[54] S. Grkovic, M.H. Brown, N.J. Roberts, I.T. Paulsen, R.A. Skurray, QacR is a repressor protein that regulates expression of the *Staphylococcus aureus* multidrug efflux pump QacA, J. Biol. Chem. 273 (29) (1998) 18665–18673.
[55] S. Grkovic, K.M. Hardie, M.H. Brown, R.A. Skurray, Interactions of the QacR multidrug-binding protein with structurally diverse ligands: implications for the evolution of the binding pocket, Biochemistry 42 (51) (2003) 15226–15236.
[56] M.P. Kalapos, The tandem of free radicals and methylglyoxal, Chem. Biol. Interact. 171 (3) (2008) 251–271.
[57] G.P. Ferguson, S. Totemeyer, M.J. MacLean, I.R. Booth, Methylglyoxal production in bacteria: suicide or survival? Arch. Microbiol. 170 (4) (1998) 209–218.
[58] M.J. Gray, W.Y. Wholey, B.W. Parker, M. Kim, U. Jakob, NemR is a bleach-sensing transcription factor, J. Biol. Chem. 288 (19) (2013) 13789–13798.
[59] P. Chandrangsu, V.V. Loi, H. Antelmann, J.D. Helmann, The role of bacillithiol in Gram-positive firmicutes, Antioxidants Redox Signal. 28 (6) (2018) 445–462.
[60] P. Chandrangsu, R. Dusi, C.J. Hamilton, J.D. Helmann, Methylglyoxal resistance in *Bacillus subtilis*: contributions of bacillithiol-dependent and independent pathways, Mol. Microbiol. 91 (4) (2014) 706–715.
[61] D.K. Stammers, J. Ren, K. Leslie, C.E. Nichols, H.K. Lamb, S. Cocklin, A. Dodds, A. R. Hawkins, The structure of the negative transcriptional regulator NmrA reveals a structural superfamily which includes the short-chain dehydrogenase/reductases, EMBO J. 20 (23) (2001) 6619–6626.
[62] M.J. Gray, Y. Li, L.I. Leichert, Z. Xu, U. Jakob, Does the transcription factor NemR use a regulatory sulfenamide bond to sense bleach? Antioxidants Redox Signal. 23 (9) (2015) 747–754.
[63] C. Lee, J. Shin, C. Park, Novel regulatory system *nemRA-gloA* for electrophile reduction in *Escherichia coli* K-12, Mol. Microbiol. 88 (2) (2013) 395–412.

Chapter 9

Thiol targets in drug development to combat bacterial infections

Verena Nadin Fritsch[1], and Haike Antelmann[1]*

[1]Freie Universität Berlin, Institute of Biology-Microbiology, Berlin, Germany

*Corresponding author: haike.antelmann@fu-berlin.de

Published in:
Book chapter no. 28, p. 679-711, Book title "Redox Chemistry and Biology of Thiols", Academic Press, Elsevier Inc., 2022
DOI: https://doi.org/10.1016/B978-0-323-90219-9.00003-0

Personal contribution:

My work on this book chapter included the literature search to develop, together with Prof. Dr. Haike Antelmann, the outline of this review article. During the writing process, I drafted most parts of the manuscript and created the blueprints for Fig. 2-6.

Chapter 10

The effect of allicin on the proteome of SARS-CoV-2 infected Calu-3 cells

Kirstin Mösbauer[1#], Verena Nadin Fritsch[2#], Lorenz Adrian[3], Jörg Bernhardt[4], Martin Clemens Horst Gruhlke[5], Alan John Slusarenko[5], Daniela Niemeyer[1], and Haike Antelmann[2]*

[1]Institute of Virology, Berlin Institute of Health, Charité-Universitätsmedizin Berlin, Freie Universität Berlin, Berlin, Germany; German Centre for Infection Research (DZIF), Berlin, Germany

[2]Institute for Biology-Microbiology, Freie Universität Berlin, Berlin, Germany

[3]Department Environmental Biotechnology, Helmholtz Centre for Environmental Research-UFZ, Leipzig, Germany; Fachgebiet Geobiotechnologie, Technische Universität Berlin, Berlin, Germany

[4]Institute for Microbiology, University of Greifswald, Greifswald, Germany

[5]Department of Plant Physiology, RWTH Aachen University, Aachen, Germany

*Corresponding author: haike.antelmann@fu-berlin.de
#These authors have contributed equally to this work.

Published in:
Frontiers in Microbiology 12:746795, 2021
DOI: https://doi.org/10.3389/fmicb.2021.746795

Personal contribution:

Prof. Dr. Haike Antelmann and I conducted the study and wrote the manuscript. My experimental research part included the sample preparation for the proteomics study and the measurement of the glutathione and glutathione disulfide levels (Fig. 1C). I was heavily involved in the analysis and interpretation of the proteomic data (Tables 1; S1-3; Fig. 5). Further, I did the statistical data analysis of all experiments and drafted figures 1-4.

frontiers in Microbiology

ORIGINAL RESEARCH
published: 28 October 2021
doi: 10.3389/fmicb.2021.746795

The Effect of Allicin on the Proteome of SARS-CoV-2 Infected Calu-3 Cells

*Kirstin Mösbauer[1,2†], Verena Nadin Fritsch[3†], Lorenz Adrian[4,5], Jörg Bernhardt[6], Martin Clemens Horst Gruhlke[7], Alan John Slusarenko[7], Daniela Niemeyer[1,2] and Haike Antelmann[3]**

[1] Institute of Virology, Berlin Institute of Health, Charité-Universitätsmedizin Berlin, Freie Universität Berlin, Berlin, Germany, [2] German Centre for Infection Research (DZIF), Berlin, Germany, [3] Institute for Biology-Microbiology, Freie Universität Berlin, Berlin, Germany, [4] Department Environmental Biotechnology, Helmholtz Centre for Environmental Research-UFZ, Leipzig, Germany, [5] Fachgebiet Geobiotechnologie, Technische Universität Berlin, Berlin, Germany, [6] Institute for Microbiology, University of Greifswald, Greifswald, Germany, [7] Department of Plant Physiology, RWTH Aachen University, Aachen, Germany

OPEN ACCESS

Edited by:
M. Pilar Francino,
Fundación Para el Fomento de la Investigación Sanitaria y Biomédica de la Comunitat Valenciana (FISABIO), Spain

Reviewed by:
Alvaro Mourenza Flórez,
University of Southern California, United States
Bruno Andrade,
Universidade Estadual do Sudoeste da Bahia, Brazil

***Correspondence:**
Haike Antelmann
haike.antelmann@fu-berlin.de

[†] These authors have contributed equally to this work

Specialty section:
This article was submitted to Virology, a section of the journal Frontiers in Microbiology

Received: 24 July 2021
Accepted: 04 October 2021
Published: 28 October 2021

Citation:
Mösbauer K, Fritsch VN, Adrian L, Bernhardt J, Gruhlke MCH, Slusarenko AJ, Niemeyer D and Antelmann H (2021) The Effect of Allicin on the Proteome of SARS-CoV-2 Infected Calu-3 Cells. Front. Microbiol. 12:746795. doi: 10.3389/fmicb.2021.746795

Allicin (diallyl thiosulfinate) is the major thiol-reactive organosulfur compound produced by garlic plants (*Allium sativum*) upon tissue damage. Allicin exerts its strong antimicrobial activity against bacteria and fungi via *S*-thioallylation of protein thiols and low molecular weight thiols. Here, we investigated the effect of allicin on SARS-CoV-2 infected Vero E6 and Calu-3 cells. Toxicity tests revealed that Calu-3 cells showed greater allicin tolerance, probably due to >4-fold higher GSH levels compared to the very sensitive Vero E6 cells. Exposure of infected Vero E6 and Calu-3 cells to biocompatible allicin doses led to a ∼60–70% decrease of viral RNA and infectious viral particles. Label-free quantitative proteomics was used to investigate the changes in the Calu-3 proteome after SARS-CoV-2 infection and the effect of allicin on the host-virus proteome. SARS-CoV-2 infection of Calu-3 cells caused a strong induction of the antiviral interferon-stimulated gene (ISG) signature, including several antiviral effectors, such as cGAS, Mx1, IFIT, IFIH, IFI16, IFI44, OAS, and ISG15, pathways of vesicular transport, tight junctions (KIF5A/B/C, OSBPL2, CLTCL1, and ARHGAP17) and ubiquitin modification (UBE2L3/5), as well as reprogramming of host metabolism, transcription and translation. Allicin treatment of infected Calu-3 cells reduced the expression of IFN signaling pathways and ISG effectors and reverted several host pathways to levels of uninfected cells. Allicin further reduced the abundance of the structural viral proteins N, M, S and ORF3 in the host-virus proteome. In conclusion, our data demonstrate the antiviral and immunomodulatory activity of biocompatible doses of allicin in SARS-CoV-2-infected cell cultures. Future drug research should be directed to exploit the thiol-reactivity of allicin derivatives with increased stability and lower human cell toxicity as antiviral lead compounds.

Keywords: allicin, SARS-CoV-2, proteome, Vero E6, Calu-3

INTRODUCTION

The Severe Acute Respiratory Syndrome Coronavirus 2 (SARS-CoV-2) causes Coronavirus disease (COVID-19), which represents a global health burden (Zhou et al., 2020). COVID-19 is often associated with immunopathology since severely ill patients had decreased levels of T lymphocytes, including regulatory T cells, cytotoxic and helper T cells, and natural killer cells (Qin et al., 2020; Wei et al., 2020). Patients with severe illness showed a cytokine storm syndrome associated with a dysregulated immune activation and hyperinflammation (Fara et al., 2020). High levels of pro-inflammatory cytokines IL-1ß, IL-2, IL-6, IL-7, IL-10, macrophage inflammatory protein-1A (MIP-1A), TNF-α, and INF-γ have been detected, connecting the uncontrolled inflammation and dysregulation of the immune response with the high mortality in severely ill COVID-19 patients (Fara et al., 2020; Qin et al., 2020; Wei et al., 2020). While mild infections were characterized by highly activated HLA-DR^{hi}CD11c^{hi} inflammatory monocytes with the interferon-stimulated gene (ISG) signature, severe illness was manifested by dysfunctional neutrophil precursors, and HLA-DR^{lo} monocytes with pro-inflammatory functions (Schulte-Schrepping et al., 2020). These immunological markers of pro-inflammatory cytokines and the dysfunctional myeloid compartment might help to identify drug targets to prevent progression to severe illness (Fara et al., 2020; Schulte-Schrepping et al., 2020).

While global vaccination campaigns are underway, the development of efficient therapies to prevent COVID-19 disease progression is an urgent need. Garlic plants (*Allium sativum*) produce volatile organosulfur compounds, such as diallyl thiosulfinate (allicin) and diallyl polysulfanes, which are known for their antimicrobial, antiviral, anticancer, anti-inflammatory and immunomodulatory effects (Borlinghaus et al., 2014, 2021; Schäfer and Kaschula, 2014). Garlic compounds showed broad-spectrum antimicrobial activity against several pathogenic bacteria, viruses, fungi, and parasites (Rabinkov et al., 1998; Münchberg et al., 2007; Block, 2010; Borlinghaus et al., 2014, 2021; Reiter et al., 2017; Arbach et al., 2019; Loi et al., 2019; Rouf et al., 2020).

Allicin is a thiol-reactive compound, which reacts with Cys thiols via thiol-disulfide exchange reactions, leading to *S*-thioallylations of proteins (Miron et al., 2000, 2010). Widespread *S*-thioallylations of redox-sensitive Cys residues in proteins were identified in the proteome of human Jurkat cells, *Escherichia coli*, *Staphylococcus aureus*, and *Bacillus subtilis* (Rabinkov et al., 1998; Miron et al., 2010; Müller et al., 2016; Chi et al., 2019; Gruhlke et al., 2019; Loi et al., 2019). In Jurkat cancer cells, 332 *S*-thioallylated proteins were identified 10 min after allicin treatment, including highly abundant cytoskeleton proteins, HSP90 chaperones, translation elongation factors and glycolytic enzymes. Allicin caused disruption of the actin cytoskeleton, enzymatic inactivation and Zn^{2+} release to stimulate the IL-1-dependent IL-2 secretion by T cells as an immunomodulatory effect (Gruhlke et al., 2019).

In addition, *S*-thioallylations deplete low molecular weight thiols, such as glutathione (GSH) and bacillithiol (BSH) in bacteria and yeast cells (Gruhlke et al., 2010, 2019; Arbach et al., 2019). Thus, allicin leads to oxidative stress responses, inhibition of protein functions and an impaired cellular redox balance. Since SARS-CoV-2 is rich in Cys residues in its surface spike glycoprotein, a reduced state of the host cell cytoplasm is required for efficient virus entry and membrane fusion. Moreover, allicin is cell permeable and has been shown to cause transient pore formation in phospholipid membranes (Miron et al., 2000; Gruhlke et al., 2015). The antiviral effect of allicin has been previously investigated against several respiratory viruses, including influenza, SARS-CoV and rhinovirus (Rouf et al., 2020).

In this work, we show that allicin at biocompatible doses decreases infectious viral particles and viral RNA of SARS-CoV-2 in the primate kidney-derived cell line Vero E6 and the human lung cell line Calu-3. We further identified proteome changes caused by SARS-CoV-2 infection and the effect of allicin on these host pathways. While the interferon-stimulated gene (ISG) signature was most prominently upregulated in SARS-CoV-2 infected Calu-3 cells, the ISG response and several host cellular pathways were restored to levels of untreated cells by allicin. Thus, allicin exerts an antiviral and immunomodulatory effect when applied in infected cell cultures *in vitro*, which is supported at the proteome level.

MATERIALS AND METHODS

Cultivation of Cell Lines and Infection Experiments With SARS-CoV-2

Vero E6 (ATCC CRL-1586) and Calu-3 (ATCC HTB-55) cell lines were cultivated in Dulbecco's Modified Eagle's Medium (DMEM), supplemented with 10% fetal bovine serum (FBS), 1% non-essential amino acids and 1% sodium pyruvate (Gibco), and grown at 37°C and 5% CO_2. Cell lines were free of mycoplasma, authenticated based on morphology and growth properties and confirmed by PCR. The cell cultures were used for viability or infection assays below cell passage 20. No antibiotics have been used during cultivation of eukaryotic cells.

The infection experiments were performed with SARS-CoV-2 Munich isolate (CSpecVir985) under biosafety level 3 conditions with appropriate respiratory personal protection equipment. Vero E6 and Calu-3 cells were seeded at densities of 3.5×10^5 or 6×10^5 cells/ml in 12-well TC plates (TPP Techno Plastic Products AG), respectively. After 24 h, cells were infected at a MOI of 0.01 or 0.005, diluted in serum-free OptiPro medium for 1 h at 37°C. The medium was removed and cells were washed twice with phosphate-buffered saline (PBS) followed by addition of DMEM and supplements. Samples were taken at 16 and 24 h p.i. for further analysis.

Allicin Synthesis and Treatment

Allicin was synthesized by oxidation of 3-[(Prop-2-en-1-yl)disulfanyl]prop-1-ene (diallyl disulfide, Sigma-Aldrich, Germany) with peracetic-acid (glacial acetic acid/H_2O_2) as described previously (Gruhlke et al., 2010). To analyze the antiviral effect of allicin, SARS-CoV-2 infection experiments were performed with an allicin pre- and post-treatment of Vero

E6 cells. For the pre-treatment, either the cells or the virus dilution were incubated with 50 μM allicin for 30 min. We have chosen 50 μM allicin since this concentration was determined as sub-lethal for Vero E6 cells. Pre-treated cells were washed with PBS and infected according to the infection protocol as described above. Pre-treated virus was used in the infection experiment according to the protocol above. Post-treatment of SARS-CoV-2 infected cells was accomplished by adding the indicated concentration of allicin into the medium after infection. Thus, in the post-treatment protocol, the added allicin remained on the infected cells until sample collection after 16 and 24 h.

Cell Viability Assay

The cell viability of Vero E6 and Calu-3 cells was analyzed by quantification of ATP levels using the CellTiter-Glo® Luminescent Cell Viability Assay (Promega) according to the instructions of the manufacturer. The cells were cultivated as described above in 96-well flat clear bottom black TC-treated microplates (Corning®) and exposed to different amounts of allicin for 24 h. Cell viability of treated cells was normalized to non-treated cells.

Determination of the Levels of Glutathione and Glutathione Disulfide in Vero E6 and Calu-3 Cells

Vero E6 and Calu-3 cells were cultivated as described above in 96-well white opaque flat bottom tissue culture plate (Falcon) and seeded at densities of 1×10^4 cells/well. After washing with PBS, the intracellular GSH and glutathione disulfide (GSSG) concentrations were determined using the GSH/GSSG-Glo™ assay (Promega) according to the instructions of the manufacturer for adherent cells. Briefly, total GSH levels were measured in one sample by reduction of GSSG to GSH using DTT. Total GSSG amounts were measured in a second sample by blocking reduced GSH with *N*-ethylmaleimide (NEM), followed by GSSG reduction with DTT. The GSH transferase (GST) uses GSH as cofactor to convert luciferin-NT to GSH-NT resulting in the release of luciferin. Luciferin is oxidized to oxyluciferin by the Ultra-Glo™ rLuciferase, leading to emission of chemiluminescence, which was measured using an integration time of 1 s/well by the CLARIOstar microplate reader (BMG Labtech). GSH levels were calculated based on GSH standard curves. For determination of the cellular GSH levels, the GSSG amounts were subtracted from the total GSH level.

Plaque Titration Assay

The number of infectious virus particles was determined by a plaque titration assay. Vero E6 monolayers were seeded in 24-well TC plates (TPP Techno Plastic Products AG) and infected with 200 μl of serial dilutions of SARS-CoV-2 containing cell culture supernatants of infected Vero E6 or Calu-3 cells, which were diluted in OptiPro serum-free medium. After 1 h adsorption, the supernatant was removed and cells overlaid with 1.2% Avicel (FMC BioPolymers) diluted in DMEM. After 72 h, the overlay was removed, cells were fixed in 6% formaldehyde and plaques were visualized by crystal violet staining.

Viral RNA Extraction and Real-Time Reverse-Transcription PCR

Viral RNA extraction was performed from 50 μl culture supernatant of SARS-CoV-2 infected Vero E6 and Calu-3 cells using the viral RNA kit (Macherey-Nagel) according to the instructions of the manufacturer. SARS-CoV-2 genome equivalents (GE) were detected by quantitative RT–PCR [LightCycler 480 Real-Time PCR System and Software version 1.5 (Roche)], targeting the SARS-CoV-2 *E* gene using the primers *E* gene-F (5′-ACAGGTACGTTAATAGTTAATAGCGT-3′) and *E* gene-R (5′-ATATTGCAGCAGTACGCACACA-3′). Absolute quantification was performed using SARS-CoV-2 specific *in vitro*-transcribed RNA standards as described previously (Corman et al., 2020).

Proteome Analysis of SARS-CoV-2 Infected Host Cells Using Orbitrap Fusion Mass Spectrometry

6×10^5 Calu-3 cells per sample were infected with SARS-CoV-2 as described above and treated with 150 μM allicin for 24 h. Calu-3 cells were harvested by centrifugation. The cell pellets were washed with PBS and alkylated for 15 min at room temperature (RT) under denaturing conditions in 200 μl of UCE-IAM buffer, consisting of 8 M urea, 1% (w/v) CHAPS, 1 mM EDTA, 200 mM Tris–HCl pH 8.0 and 100 mM IAM as described (Rossius et al., 2018). Subsequently, the alkylated protein extracts were precipitated with trizol and 96% ethanol and washed four times with 1 ml 70% ethanol. The protein pellets were separated by a short 15% non-reducing SDS-PAGE, which was running for 15 min and stained with Colloidal Coomassie Blue. The gel fractions were cut and in-gel tryptic digested as described previously (Rossius et al., 2018). The eluted peptides were desalted using ZipTip-μC18 material (Merck Millipore) and dissolved in 0.1% (v/v) formic acid before LC-MS/MS analysis. The peptide samples of non-infected Calu-3 cells (Mock) and SARS-CoV-2 infected Calu-3 cells with and without allicin treatment were subjected to nLC-MS/MS analysis using an Orbitrap Fusion (Thermo Fisher Scientific) coupled to a TriVersa NanoMate (Advion, Ltd.) as described previously (Kublik et al., 2016). Peptide identification of the human and SARS-CoV-2 proteome was performed by Proteome Discoverer (version 2.2, Thermo Fisher Scientific) using the SequestHT search engine as described (Seidel et al., 2018). Human and SARS-CoV-2 proteins were identified by searching all tandem MS/MS spectra against the human proteome protein sequence database (20,286 entries) extracted from UniprotKB release 12.7 (UniProt Consortium, Nucleic acids research 2007, 35, D193-197) as well as against the European Virus Archive Global # 026V-03883 sequence database. Peptides were considered to be identified with high confidence at a target false discovery rate of $\leq$0.01 and with a medium confidence at $\leq$0.05, based on the *q*-values. Identified proteins were quantified by the "Percursor Ions Quantifier" implemented in Proteome Discoverer 2.2 based on peak intensities to estimate the abundance of the human and SARS-CoV-2 proteins in the peptide samples. Error tolerance

for precursor ion and fragment ion *m/z* values was set to 3 ppm and 0.5 Da, respectively. Two missed cleavage sites were allowed. Methionine oxidation (+15.994915 Da), cysteine carbamidomethylation (+57.021464 Da) and cysteine *S*-thioallylation by allicin (+72.00337 Da for $C_3H_5S_1$) were set as variable modifications. The mass spectrometry data have been deposited to the ProteomeXchange Consortium via the PRIDE partner repository (Perez-Riverol et al., 2019; Deutsch et al., 2020) with the dataset identifier PXD024375.

Statistical Analyses

Statistical analysis of the cell viability assays, the GSH and GSSG measurements as well as the determination of viral RNA and infectious particles were performed from 3–4 biological replicates with 1–3 technical replicates using the Student's unpaired two-tailed *t*-test for two samples with unequal variance. Proteomics analyses were performed from 3–4 biological replicates with 1–3 technical replicates. For calculation of the statistics of the proteomics data, the LFQ intensity values of each proteomics sample and every single treatment were tested for normality by using Jarque Bera (testing for kurtosis and skewness) (Jarque and Bera, 1980) and Anderson Darling (based on Kolmogorov-Smirnov) tests (Anderson and Darling, 1954). Accordingly, *p*-values for pairwise treatment comparisons were calculated by the Welsh test (Student's unpaired two-tailed *t*-test for two samples with unequal variance and heteroscedastic data). The *p*-values and significance levels are included in the figure and table legends.

RESULTS

Biocompatible Allicin Concentrations Correlate With the Intracellular Glutathione Levels in Vero E6 and Calu-3 Cells

While allicin has many beneficial effects for human health, crushed garlic is also toxic and harmful for human cells. Fresh garlic can cause severe cellular and tissue damage upon direct exposure to the epithelial cells and mucous membranes of the respiratory tract and the skin, such as garlic burns (Bautista et al., 2005; Al-Qattan, 2009; Vargo et al., 2017; Hitl et al., 2021; Muniz et al., 2021). Thus, we first assessed the toxicity of allicin in Calu-3 and Vero E6 cells, which are used here as cell culture models for SARS-CoV-2 infection. Using cell viability assays, the biocompatible, non-harmful doses of allicin in Calu-3 and Vero E6 cells were determined. Both cell lines differed strongly in their susceptibilities toward allicin. Calu-3 cells showed high viability rates of ∼85% after treatment with 200 μM allicin. Even concentrations of 300 μM allicin decreased the viability rate of Calu-3 cells only non-significantly to ∼70% (**Figure 1A**). Treatment of Vero E6 cells with 75 μM allicin led to a cell viability rate of 84% (**Figure 1B**), whereas 150 μM allicin resulted in killing of 99% of Vero E6 cells. Thus, the sub-lethal biocompatible doses of allicin were determined as 50–75 μM in Vero E6 cells and 100–200 μM in the more tolerant Calu-3 cells.

Previous studies already revealed strong variations in the susceptibilities of different cell lines toward allicin, which correlated with different intracellular GSH contents (Gruhlke et al., 2016, 2019). Thus, we measured the intracellular GSH and GSSG levels in Vero E6 and Calu-3 cells (**Figure 1C**). The GSH content of the more tolerant Calu-3 cells was determined as 3.2 μM, which was 4.2-fold higher compared to only 0.77 μM GSH as measured in Vero E6. As expected, the amounts of GSSG were very low with 0.05 μM and 0.009 μM in Calu-3 and Vero E6 cells, respectively. These data suggest that Calu-3 cells show greater allicin tolerance in part due to their higher GSH levels compared to Vero E6 cells.

Allicin Leads to Decreased Infectious Viral Particles and Viral RNA in SARS-CoV-2 Infected Vero E6 and Calu-3 Cells

The antiviral effect of allicin against SARS-CoV-2 was analyzed using pre- and post-treatment options for the more allicin-sensitive infected Vero E6 cells: (1) Cells were pre-exposed to 50 μM allicin for 30 min before SARS-CoV-2 infection. (2) The virus was treated with 50 μM allicin for 30 min prior to infection. (3) SARS-CoV-2 infected Vero E6 cells were treated with 50 μM allicin post infection (p.i.) (**Figure 2A**). We have chosen 50 μM allicin since this concentration did not affect viability of Vero E6 cells (**Figure 1B**). The number of infectious SARS-CoV-2 particles (PFU, plaque forming units) was determined 24 h p.i. by the plaque titration assay. However, only post-treatment with 50 μM allicin led to a significant 70% decrease in the amount of infectious virus particles, whereas the pre-treatment of cells or virus caused only a 16–21% reduction of viral plaques (**Figure 2A**). These results suggest that allicin might affect host-virus interactions by its antiviral and immunomodulatory activities.

In addition, viral RNA genome equivalents (GE) were determined from the supernatant of infected Vero E6 cells using quantitative RT-PCR. In agreement with the plaque assays, the qRT-PCR results revealed a 72% lower amount of viral RNA after addition of 50 μM allicin to SARS-CoV-2 infected Vero E6 cells (**Figures 2B,C**). Moreover, virus plaque assays and qRT-PCR results showed an almost complete >99% inhibition of SARS-CoV-2 replication after exposure to 75 μM allicin, supporting the strong antiviral activity of allicin in infected Vero E6 cells (**Figures 2B,C**).

The antiviral effects of biocompatible doses of allicin were further analyzed in the more allicin-resistant Calu-3 cells. After infection with SARS-CoV-2 at a multiplicity of infection (MOI) of 0.01 and 0.005, Calu-3 cells were treated with biocompatible doses of 100 and 200 μM allicin and analyzed 16 and 24 h p.i., respectively (**Figure 3**). Treatment of infected Calu-3 cells with 100 μM allicin did not significantly inhibit viral replication (**Figures 3A–D**). However, exposure of infected Calu-3 cells to 200 μM allicin led to a significant >60% decrease of viral RNA (**Figures 3A,B**) and a >65% reduction of infectious particles (**Figures 3C,D**).

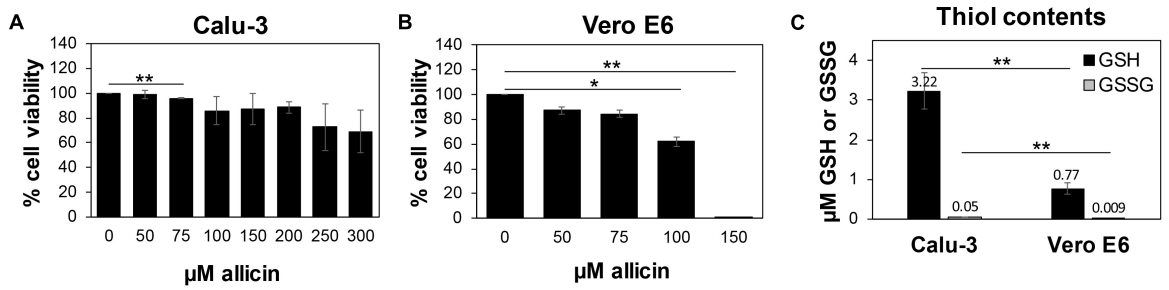

FIGURE 1 | Human Calu-3 cells are more resistant to allicin compared to Vero E6. **(A,B)** Cell viability of untreated and allicin treated Calu-3 **(A)** and Vero E6 cells **(B)** was measured after 24 h using the CellTiter-Glo® Luminescent Cell Viability Assay (Promega) according to the manufacturer's instructions. The viability of the control without allicin was set to 100%. The viability of Calu-3 cells was not significantly decreased upon exposure to 100–200 µM allicin, while concentrations of ≥100 µM allicin interfered with Vero E6 cell viability. **(C)** The levels of glutathione (GSH) and glutathione disulfide (GSSG) were determined in untreated Calu-3 and Vero E6 cells using the GSH/GSSG-Glo Assay (Promega) according to the manufacturer's instructions. The results are from 4 biological replicates with 3 technical replicates for **(C)**. Error bars represent the standard deviation (SD). *p*-values were calculated using an unpaired two-tailed *t*-test.*$p < 0.05$; **$p < 0.01$.

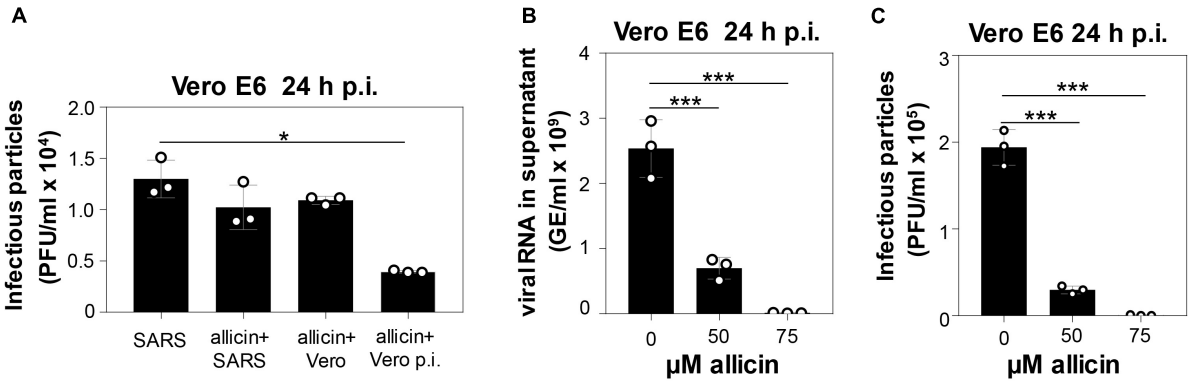

FIGURE 2 | Allicin treatment of SARS-CoV-2 infected Vero E6 cells reduced the levels of infectious viral particles and viral RNA. **(A–C)** Vero E6 cells were infected with SARS-CoV-2 at a MOI of 0.01. After 24 h p.i. viral replication was analyzed by determination of infectious viral particles or viral RNA in the supernatant. **(A)** Comparison of different allicin treatments: Untreated Vero E6 cells infected with SARS-CoV-2 as control (SARS); SARS-CoV-2 pre-treated with 50 µM allicin for 30 min prior to infection of host cells (allicin + SARS); host cells pre-treated with 50 µM allicin for 30 min prior to infection with SARS-CoV-2 (allicin + Vero); and SARS-CoV-2 infected host cells treated with 50 µM allicin p.i. (allicin + Vero p.i.). **(B,C)** The amount of viral RNA **(B)** and infectious viral particles **(C)** was determined after treatment of SARS-CoV-2 infected Vero E6 cells with 50 and 75 µM allicin p.i. The results **(A–C)** are from three biological replicates with two technical replicates for panel **(B)**. Error bars represent the SD. *p*-values were calculated using an unpaired two-tailed *t*-test.*$p < 0.05$; ***$p < 0.001$.

The antiviral effect of allicin on SARS-CoV-2 infected Calu-3 cells was further supported by microscopy imaging (**Figures 4A–C**). While SARS-CoV-2 infection at a MOI of 0.01 resulted in cellular damage of Calu-3 cells after 24 h p.i., the addition of 150 µM allicin partially protected the cells against this damage (**Figures 4B,C**). Taken together, our results indicate that biocompatible allicin doses exert an antiviral effect against SARS-CoV-2 in both Vero E6 and Calu-3 cells.

Changes in the Calu-3 Proteome After SARS-CoV-2 Infection

Label-free quantitative (LFQ) proteomics by Orbitrap Fusion LC-MS/MS analysis was used to investigate the changes in the proteome of Calu-3 cells after SARS-CoV-2 infection and the effect of 150 µM allicin. The concentration of 150 µM allicin was chosen since this was sub-lethal for Calu-3 cells (**Figure 1A**), and protected the cells against SARS-CoV-2 damage (**Figure 4C**). The proteome samples of Calu-3 cells were analyzed before infection (Mock) and 24 h p.i. with SARS-CoV-2 at a MOI of 0.01 in the absence or presence of 150 µM allicin in 3–4 biological and 1–3 technical replicates. The total LFQ intensities of all proteins in each sample were normalized and represent 100% of the total protein abundance. Overall, we quantified 4,251 proteins, including 4,243 Calu-3 host proteins and 8 SARS-CoV-2 proteins in the total proteome (**Supplementary Tables 1,2**). After infection, about 207 and 329 proteins were ≥1.5-fold induced and <0.66-fold decreased, respectively (**Supplementary Table 3**). These 536 differentially expressed proteins contribute to only 2.73% of the total proteome abundance in SARS-CoV-2 infected Calu-3 cells (**Supplementary Table 3**). The proteins were sorted into KEGG Ontology (KO) or Uniprot categories and their fold-changes, *p*-values and averaged abundances were visualized in Voronoi treemaps as color gradients and

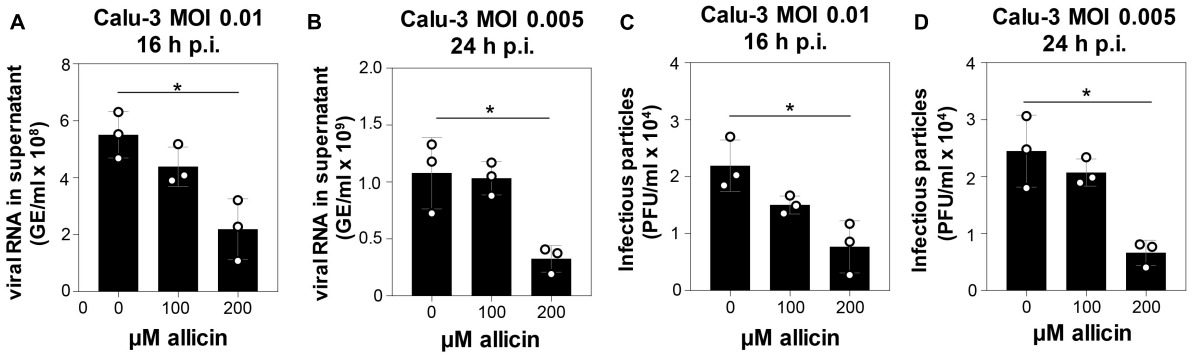

FIGURE 3 | Allicin treatment of SARS-CoV-2 infected Calu-3 cells leads to decreased amounts of infectious viral particles and viral RNA. **(A–D)** SARS-CoV-2 infected Calu-3 cells were treated with 100 and 200 µM allicin p.i. The amount of viral RNA **(A,B)** and infectious viral particles **(C,D)** was determined 16 h **(A,C)** and 24 h **(B,D)** p.i. with SARS-CoV-2 at a MOI of 0.01 **(A,C)** and 0.005 **(B,D)**. The results are from three biological replicates with two technical replicates for panels **(A,B)**. Error bars represent the SD. *p*-values were calculated using an unpaired two-tailed *t*-test. $^*p < 0.05$.

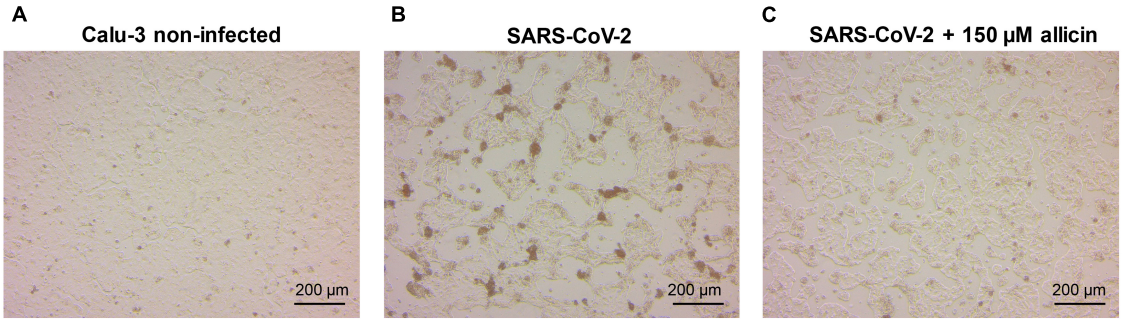

FIGURE 4 | Cellular effect of 150 µM allicin on SARS-CoV-2 infected Calu-3 cells. Non-infected Calu-3 cells were cultivated for 24 h and served as controls **(A)**. Calu-3 cells were infected with SARS-CoV-2 at a MOI of 0.01 and the SARS-CoV-2 induced cellular effects were studied at 24 h p.i. without **(B)** or with 150 µM allicin treatment **(C)** after infection as described in the "Materials and Methods" section. At 24 h p.i. infected Calu-3 cells showed cellular damages, including cell rounding, detachment and cell death **(B)**. Allicin treatment decreased some cellular damages **(C)**. Cells were imaged with a Nikon Ts2R-FL inverted microscope.

cell sizes, respectively (**Figures 5A–D** and **Supplementary Table 3**). A subset of the most strongly induced proteins in the Calu-3 proteome after SARS-CoV-2 infection is listed in **Table 1**.

The proteome after SARS-CoV-2 infection revealed altered expression of various cellular pathways, including the interferon-stimulated gene (ISG) signature, transcription, translation and protein degradation, the cytoskeleton, vesicular trafficking and tight junctions, apoptosis, signal transduction pathways as well as carbon, lipid and nucleotide metabolism (**Figure 5A**, **Table 1**, and **Supplementary Table 3**). In addition, the eight detected SARS-CoV-2 proteins were induced after 24 h p.i. of Calu-3 cells, with the ribonucleocapsid protein (N-protein) as one of the most abundant proteins in the proteome of infected Calu-3 cells with 0.35% of the total proteome. The N-protein was 29- and 21-fold higher expressed compared to the membrane protein (M-protein) (0.012%) and spike protein (S-protein) (0.016%), respectively (**Figure 6A** and **Supplementary Table 3**), confirming previous data with infected Vero E6 cells (Zecha et al., 2020). The viral proteins Nsp1, Nsp2, ORF3, ORF9b, and the papain-like protease PLP were low abundant, contributing from 0.00022% (PLP) to 0.0043% (ORF3) to the total proteome (**Figure 6B** and **Supplementary Table 3**), while other viral proteins were not detected.

SARS coronaviruses have been shown to enter the cell via endocytosis and direct fusion with the cell membrane (Wang et al., 2008; Ou et al., 2020). In agreement with these reports, 18 proteins involved in vesicular transport and cytoskeleton regulation, such as formation of lysosomes, phagosomes, and exosomes were 1.5–5.2-fold higher expressed after infection in the Calu-3 proteome (**Figure 5A**, **Table 1**, and **Supplementary Table 3**). Among these proteins are the abundant and highly induced kinesins (KIF5A/B/C), clathrin (CLTCL1), and tubulin (TUBAL3), which are microtubule-associated proteins and participate in endocytosis and traffic of viral RNA and vesicles. The 1.7-fold induced highly abundant Rho GTPase-activating protein 17 (ARHGAP17) could be involved in the repair of tight junctions, which are often damaged in COVID-19 patients (De Maio et al., 2020; Tian et al., 2020).

About 21 proteins of the interferon (IFN) and ISG response were strongly induced, including sensors of viral RNA, the

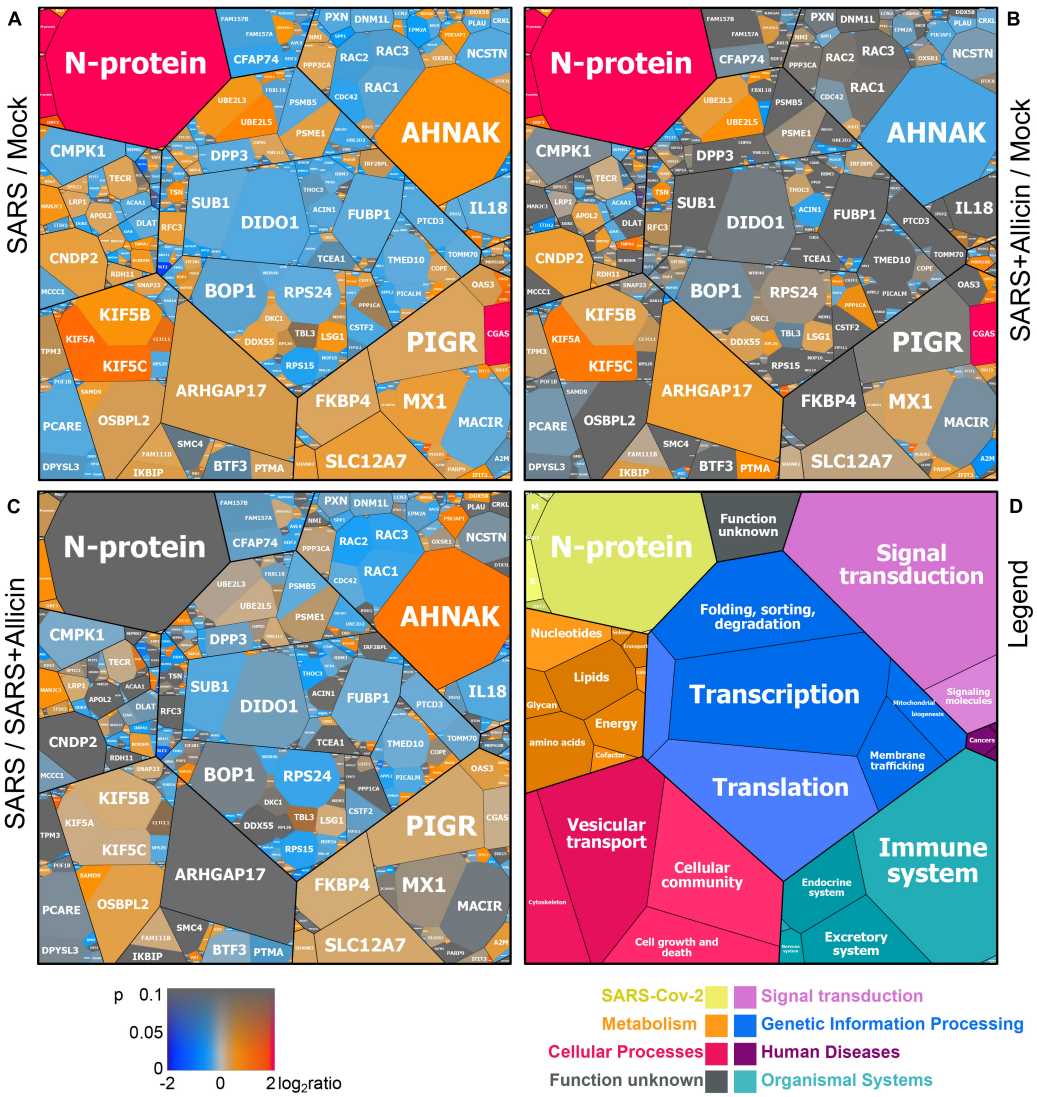

FIGURE 5 | The effect of allicin on the proteome of SARS-CoV-2 infected Calu-3 cells. The host-viral proteome treemaps **(A–C)** show the 536 differentially expressed proteins upon SARS-CoV-2 infection and were constructed by the Paver software (Mehlan et al., 2013). The treemaps visualize the following proteome changes: **(A)** SARS-CoV-2 infection/Mock, **(B)** SARS-CoV-2 infection + Allicin/Mock and **(C)** SARS-CoV-2 infection −/+ Allicin. The treemap **(D)** serves as legend for the functional KEGG categories displayed in different colors for level 1 and sublevel 2 as listed in **Supplementary Table 3**. The cell sizes in panels **(A–C)** denote the average abundances of 207 proteins with ≥1.5-fold inductions and 329 proteins with <0.66-fold decreased expression after SARS-CoV-2 infection. The log2 ratios of the proteins are shown by a red-blue color gradient (red – induction, blue – repression) **(A–C)**. *p*-values ($p < 0.05$; $p < 0.01$) were calculated using an unpaired two-tailed *t*-test from 3 to 4 biological replicates with 1–3 technical replicates (**Supplementary Table 3**).

JAK-STAT signal transduction pathway and antiviral effectors that interfere with the viral life cycle (**Figure 5A**, **Table 1**, and **Supplementary Table 3**) (Schneider et al., 2014). For a better understanding, the RNA sensing receptors, IFN and ISG signaling cascades and the previously described antiviral functions of the ISG effectors are displayed in a schematic (**Figures 7A,B**). The cyclic GMP-AMP (cGAMP) synthase (cGAS) was most strongly 98-fold upregulated upon infection, acting as sensor of viral RNA (**Table 1**, **Supplementary Table 3**, and **Figure 5A**) (Schneider et al., 2014). cGAMP activates the stimulator of interferon genes (STING) (**Figure 7A**). The 2′-5′-oligoadenylate synthases (OAS1-3, OASL) were 1.6–7-fold induced upon infection to produce 2′-5′-adenylic acid as second messenger and activator of RNaseL for viral RNA degradation. The IFN-induced helicase C-domain-containing protein (IFIH) was 6.5–fold upregulated, which activates the mitochondrial antiviral signaling protein (MAVS) to induce the IFN response. Other IFN-induced effector proteins with tetratricopeptide repeats (IFIT1-3, IFIT5) were 1.6–3.5-fold induced after infection and function in RNA degradation and inhibition of translation. Further effectors are the Interferon-induced myxoma resistance protein 1

(MX1) and the Polymeric immunoglobulin receptor (PIGR), which represented 0.05 and 0.1% of the total proteome abundance and were 1.8 and 1.5-fold induced, respectively. MX1 is a dynamin-like GTPase, which forms ring-like structures and traps incoming ribonucleocapsids, thereby blocking uncoating and vesicular trafficking to direct them for degradation (**Figure 7B**) (Schneider et al., 2014). MX1 was also reported to be up-regulated in COVID-19 patients (Bizzotto et al., 2020).

Furthermore, the abundant cytokine IL18, the IL-1 receptor antagonist protein (IL1RN), the macrophage immunometabolism regulator MACIR and the Alpha-2-macroglobulin (A2M) were ∼0.6-fold lower expressed in infected cells. MACIR is implicated in the regulation of macrophages and autoimmune diseases (McGauran et al., 2020).

An important role in signal transduction and regulation of the antiviral response plays the abundant ISG15 effector, which was 1.8-fold induced after SARS-CoV-2 infection in the proteome. ISG15 functions amongst others as Ubiquitin-like modifier in ISGylation of RIG-I and IRF-3, which are targeted for degradation or activated to regulate IFN and ISG production (**Figure 7A**) (Masucci, 2020). Widespread ISGylation of newly synthesized viral proteins is proposed to inhibit viral replication and translation (Durfee et al., 2010).

Additionally, post-translational modification by polyubiquitination of host signaling factors, such as RIG-I, STING and MAVS is important for regulation of the IFN response upon SARS-CoV-2 infection (**Figure 7A**). Thus, several ubiquitin-conjugating E2 enzymes (UBE2L3 and UBE2L5), the E3 ubiquitin ligases (TRIM21, TRIM38, and ARIH2) and the ubiquitin specific protease or deconjugases (USP13) are 1.5–3.2-fold induced in the infected cells, while other E2, E3 enzymes and deconjugases (e.g., UBE2D2/3, RNF214, USP4, USP47, and USP48) are 0.2–0.62-fold lower expressed (**Table 1**, **Supplementary Table 3**, and **Figure 5A**). Since host and viral targets of ubiquitination and ISGylation are often directed to degradation, components of the proteasome, proteases, protein folding factors, and chaperones are 1.5–1.8-fold upregulated. The folding factors include the highly abundant peptidyl-prolyl *cis-trans* isomerase FKBP4, which functions as immunophilin and co-chaperone to interact with HSP90.

Apart from protein modification, the virus relies on protein synthesis and translation by the host machinery for its successful replication and infectivity. Accordingly, 24 proteins involved in translation were 1.5–2.8-fold upregulated under SARS-CoV-2 infection, including the translation factor EIF2B1, ribosomal proteins (RPL26, MRPS30, RRP8, PDCD11, and MRPL4), RNA helicases (DDX55 and DDX56), RNAses (POP1 and XRN1) and other regulatory factors, such as phosphatases (PPP1CC, PPP1CA, and PPP2R5A) (**Supplementary Table 3** and **Figure 5A**).

In addition, 16 proteins involved in transcription and the spliceosome were upregulated in infected Calu-3 cells, including the pre-mRNA splicing factors Slu7, PRPF40B, SCAF11, and the U1 small nuclear ribonucleoprotein C (SNRPC), which were 1.6–1.8-fold higher expressed. The transcription factors GABPA, ZNF579, SP110, and TSC22D2 were also induced after infection. However, the majority of differentially expressed proteins involved in transcription (48) and translation (30) were repressed after SARS-CoV-2 infection, including the highly abundant proteins DIDO1, SUB1, FUBP1, TCEA1, BOP1, RPS24, and RPS15 (**Supplementary Table 3** and **Figure 5A**).

Moreover, virus replication and proliferation inside host cells requires reprogramming of the host metabolism, which was evident by the upregulation of 34 proteins and downregulation of 43 proteins involved mainly in lipid, energy, glycan, and nucleotide metabolism (**Table 1**, **Supplementary Table 3**, and **Figure 5A**). The induced proteins might function in the biosynthesis of the building blocks for viral phospholipid membranes, glycosylation of surface proteins and viral RNA genomes. Since the nucleotide pool is essential for coronavirus replication (Bojkova et al., 2020), some purine and pyrimidine biosynthesis proteins were 1.7–2.3-fold induced (NT5C2, UPP1, and PPAT), while others were 0.5-0.65-fold repressed (CMPK1, AK6, and ENPP4) (**Supplementary Table 3** and **Figure 5A**).

Furthermore, expression of several signaling pathways, including JAK-STAT, MAPK, Wnt, Ras, and Rap1 signaling were affected by SARS-CoV-2 infection. The JAK-STAT pathway senses and transduces IFN-signals via a phosphorylation cascade to activate ISG expression (**Figure 7A**). Thus, STAT2, N-myc interactor NMI and the RIG-I receptor were 1.6–1.8-fold induced upon infection (**Supplementary Table 3** and **Figure 5A**). Proteins of the MAPK signaling pathways were activated in response to infections with SARS-CoV (Bouhaddou et al., 2020) and 1.6–1.8-fold induced in the proteome of SARS-CoV-2 infected cells. Proteins of the PI3K/Akt signaling pathway were 2.3–2.6-fold upregulated in infected cells, controlling apoptosis of host cells for successful viral replication. The highly abundant neuroblast differentiation-associated protein AHNAK was 2.6-fold induced after SARS-CoV-2 infection. AHNAK is required for calcium signaling and might regulate the immune response (Matza et al., 2009). Proteins of the Ras-signaling pathway were 0.5–0.64-fold downregulated upon virus infection, including three Rac GTPases Rac1-3 that are implicated in the regulation of cell morphology, migration and invasion, by transducing signals from cell surface receptors to the actin and microtubule cytoskeletons (Wheeler et al., 2006). Similarly, other proteins involved in the cytoskeleton organization were 0.3–0.66-fold lower expressed, indicating re-organization of the cytoskeleton for transport of virus particles.

Allicin Leads to a Decreased Antiviral Interferon Response in the Proteome of Infected Calu-3 Cells

Next, we investigated the effect of allicin on the proteome changes upon SARS-CoV-2 infection. Quantification of the 8 viral proteins in infected Calu-3 cells after allicin treatment revealed a significantly 18–59% decreased abundance of the structural proteins N, M, and S and ORF3, supporting the antiviral effect of allicin in the proteome (**Figures 6A,B**).

Allicin treatment resulted in a diminished IFN-response in infected cells, since expression of innate immune receptors

TABLE 1 | Selected most strongly induced proteins in the Calu-3 proteome after SARS-CoV-2 infection and the effect of allicin treatment p.i.

Protein informations			Expression ratios			log2 Expression ratios						*T*-Test *p*-value					
Protein name	Accession number	Protein function	SARS/ Mock	SARS + All/ Mock	SARS/ SARS + All	SARS/ Mock	SARS + All/ Mock	SARS/ SARS + All	SARS/ Mock	SARS + All/ Mock	SARS/ SARS + All	*T*-Test SARS/ Mock	*T*-Test SARS + All/ Mock	*T*-Test SARS + All/ SARS	SARS/ Mock	SARS + All/ Mock	SARS/SARS + All
Protein folding and ubiquitination																	
UBE2L5	A0A1B0GUS4	Ubiquitin-conjugating enzyme E2 L5	3.02	2.45	1.23	1.59	1.29	0.30				0.000	0.000	0.036			
UBE2L3	P68036	Ubiquitin-conjugating enzyme E2 L3	2.06	1.79	1.15	1.04	0.84	0.20				0.000	0.000	0.139			
FKBP4	Q02790	Peptidyl-prolyl *cis-trans* isomerase FKBP4	1.51	1.10	1.37	0.59	0.14	0.45				0.003	0.550	0.032			
Tight junctions, endocytosis and phagosome																	
ARHGAP17	Q68EM7	Rho GTPase-activating protein 17	1.66	1.88	0.88	0.73	0.91	−0.18				0.092	0.028	0.462			
KIF5A	Q12840	Kinesin heavy chain isoform 5A	5.24	4.13	1.27	2.39	2.05	0.34				0.000	0.000	0.016			
KIF5C	O60282	Kinesin heavy chain isoform 5C	4.97	3.91	1.27	2.31	1.97	0.34				0.000	0.000	0.016			
KIF5B	P33176	Kinesin-1 heavy chain	2.20	1.61	1.36	1.14	0.69	0.45				0.001	0.009	0.036			
TUBAL3	A6NHL2	Tubulin alpha chain-like 3	5.24	0.73	7.14	2.39	−0.45	2.84				0.025	0.251	0.019			
Calcium signaling																	
AHNAK	Q09666	Neuroblast differentiation-associated protein	2.55	0.60	4.28	1.35	−0.74	2.10				0.012	0.055	0.004			
O- and N-glycan biosynthesis and degradation																	
GALNT4	Q8N4A0	Polypeptide N-acetylgalactosaminyltransferase 4	2.10	0.97	2.16	1.07	−0.05	1.11				0.003	0.801	0.002			
GALNT12	Q8IXK2	Polypeptide N-acetylgalactosaminyltransferase 12	1.67	1.00	1.66	0.74	0.01	0.73				0.003	0.215	0.020			
ALG3	Q92685	Dol-P-Man:Man(5)GlcNAc(2)-PP-Dol α-1,3-mannosyltransferase	1.67	0.85	1.97	0.74	−0.24	0.98				0.064	0.481	0.024			
FUT8	Q9BYC5	Alpha-(1,6)-fucosyltransferase	1.62	0.90	1.79	0.69	−0.15	0.84				0.027	0.704	0.015			
MAN2C1	Q9NTJ4	Alpha-mannosidase 2C1	2.08	0.92	2.25	1.06	−0.12	1.17				0.039	0.761	0.026			
RNA sensing, interferon (IFN) and ISG effectors																	
CGAS	Q8N884	Cyclic GMP-AMP synthase	97.90	80.16	1.22	6.61	6.32	0.29				0.000	0.000	0.028			
OAS1	P00973	2′–5′-oligoadenylate synthase 1	6.97	4.26	1.64	2.80	2.09	0.71				0.000	0.003	0.031			
OAS2	P29728	2′–5′-oligoadenylate synthase 2	4.32	2.31	1.87	2.11	1.21	0.90				0.000	0.038	0.010			
OAS3	Q9Y6K5	2′–5′-oligoadenylate synthase 3	1.61	0.95	1.70	0.69	−0.08	0.77				0.091	0.843	0.073			
OASL	Q15646	2′–5′-oligoadenylate synthase-like protein	6.13	3.49	1.76	2.62	1.80	0.81				0.000	0.014	0.015			
MX1	P20591	Interferon-induced GTP-binding protein	1.80	1.50	1.20	0.85	0.59	0.26				0.000	0.063	0.251			
IFI16	Q16666	Gamma-interferon-inducible protein 16	4.55	1.77	2.57	2.18	0.82	1.36				0.019	0.345	0.086			
IFI44	Q8TCB0	IFN-induced protein 44	8.00	5.56	1.44	3.00	2.48	0.52				0.000	0.009	0.145			
IFI44L	Q53G44	IFN-induced protein 44-like	5.77	3.19	1.81	2.53	1.67	0.85				0.000	0.037	0.033			
IFIH1	Q9BYX4	IFN-induced helicase C domain protein 1	6.59	2.28	2.89	2.72	1.19	1.53				0.011	0.139	0.029			
IFIT1	P09914	IFN-induced protein with tetratricopeptide repeats 1	2.53	1.05	2.41	1.34	0.07	1.27				0.003	0.237	0.008			
IFIT2	P09913	IFN-induced protein with tetratricopeptide repeats 2	1.69	1.02	1.66	0.76	0.03	0.73				0.026	0.298	0.041			
IFIT3	O14879	IFN-induced protein with tetratricopeptide repeats 3	2.33	1.85	1.26	1.22	0.89	0.33				0.002	0.004	0.189			
IFIT5	Q13325	IFN-induced protein with tetratricopeptide repeats 5	3.54	2.46	1.44	1.83	1.30	0.53				0.000	0.017	0.040			
ISG15	P05161	Ubiquitin-like protein ISG15	1.83	1.81	1.01	0.87	0.86	0.01				0.000	0.001	0.934			
PARP14	Q460N5	Protein mono-ADP-ribosyltransferase PARP14	3.59	0.42	8.54	1.84	−1.25	3.09				0.009	0.066	0.003			
PIGR	P01833	Polymeric immunoglobulin receptor	1.51	1.08	1.40	0.59	0.11	0.48				0.001	0.368	0.002			
SARS-CoV-2 proteins																	
S-protein	spike	protein surface glycoprotein SARS-CoV-2	440.36	180.28	2.44	8.78	7.49	1.29				0.002	0.000	0.033			
N-protein	Nucleocapsid	phosphoprotein SARS-CoV-2	130.33	106.28	1.23	7.03	6.73	0.29				0.000	0.000	0.684			
M-protein	Membrane	protein glycoprotein SARS-CoV-2	99.01	60.94	1.62	6.63	5.93	0.70				0.001	0.000	0.150			
ORF3	ORF3	structural protein SARS-CoV-2	9.80	5.18	1.89	3.29	2.37	0.92				0.000	0.000	0.036			
ORF9b	ORF9b	structural protein SARS-CoV-2	8.77	9.41	0.93	3.13	3.23	−0.10				0.001	0.000	0.251			
Nsp1	Nsp1	Non-structural protein1 SARS-CoV-2	6.54	7.09	0.92	2.71	2.83	−0.12				0.003	0.001	0.451			

The proteome samples of Calu-3 Mock cells (Mock), SARS-CoV-2 infected Calu-3 cells (SARS) and SARS-CoV-2 infected Calu-3 cells treated with 150 μM allicin p.i. (SARS + All) were harvested after 24 h p.i. and separated by non-reducing SDS PAGE for prefractionation. Protein fractions were tryptic in-gel digested and peptides analyzed by Orbitrap Fusion LC-MS/MS analysis as described in the "Materials and Methods". The table lists 37 out of 207 identified proteins with >1.5-fold induction upon SARS-CoV-2 infection. These proteins are most strongly induced after SARS-CoV-2 infection, affected by allicin treatment and/or are present at high abundance in the Calu-3 proteome. The proteins were classified according to their KEGG ontologies and UniprotKB annotations. The full set of up- and downregulated proteins after SARS-CoV-2 infection is listed in ***Supplementary Table 3****. The table includes protein names, accession numbers, protein functions, expression ratios, log2 expression ratios and p-values. The log2 ratios and p-values are visualized with a blue-orange and red-gray color code, respectively. p-values were calculated using an unpaired two-tailed t-test for two samples with unequal variance.*

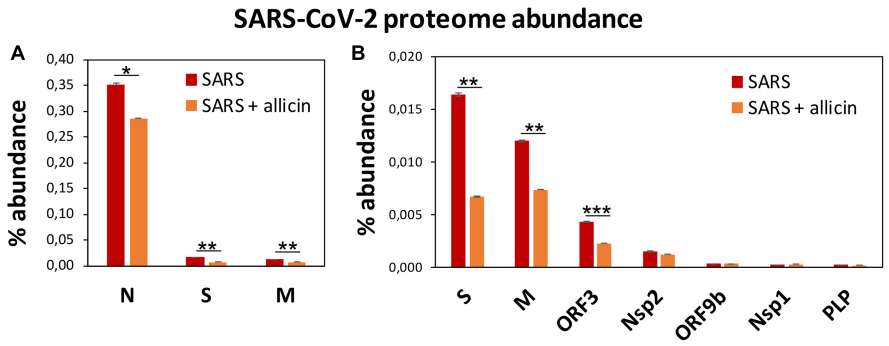

FIGURE 6 | The effect of allicin on the abundance of SARS-CoV-2 proteins in the proteome of infected Calu-3 cells. **(A,B)** The abundance of the SARS-CoV-2 proteins (N, S, M, ORF3, Nsp2, ORF9b, Nsp1, and PLP) at 24 h p.i. relative to the total proteome abundance of infected Calu-3 cells was calculated in the absence (SARS) or presence of 150 μM allicin exposure p.i. (SARS + allicin). The N-protein showed a 21–29-fold higher abundance compared to the structural proteins S and M as shown in panel **(A)**. The lower abundant S, M, ORF3, Nsp2, ORF9b, Nsp1, and PLP proteins are separately displayed in panel **(B)**. The proteome results were obtained from 3–4 biological replicates with 1–3 technical replicates (**Supplementary Table 3**). Error bars represent the SD. *p*-values were calculated using an unpaired two-tailed *t*-test. $^{*}p < 0.05$; $^{**}p < 0.01$; $^{***}p < 0.001$.

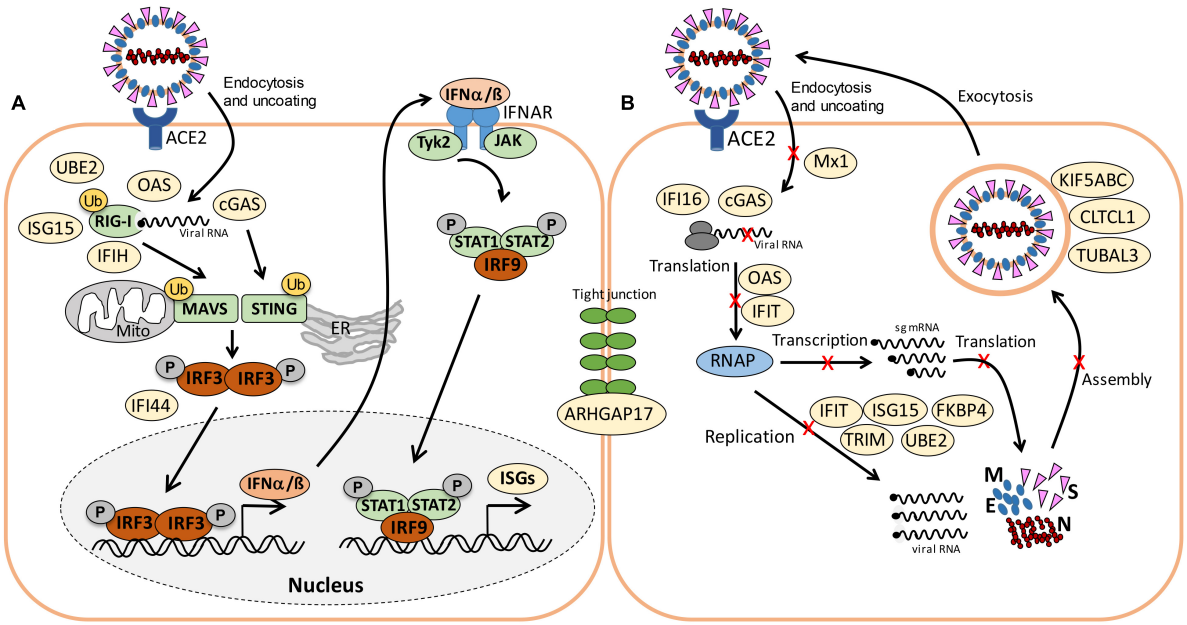

FIGURE 7 | Schematic of viral RNA recognition, activation of the IFN and ISG signaling pathways **(A)** and antiviral functions of the identified ISG effectors **(B)** in this host-virus proteome study. **(A)** SARS-CoV-2 enters host cells via endocytosis. RIG-I is a cytosolic receptor to recognize viral RNA. cGAS and OAS are ISG effectors that function as RNA sensors. RIG-I, IFIH, and cGAS activate the mitochondrial antiviral-signaling protein (MAVS) and stimulator of IFN genes (STING), leading to phosphorylation of IFN responsive factors (e.g., IRF3), followed by IRF3 dimerization, translocation into the nucleus and transcriptional activation of IFN expression. IRF3 is negatively regulated by IFI44. RIG-I, MAVS, and STING can be regulated by ubiquitination (UBE2) and ISGylation (ISG15). Type-I IFN a/ß bind to the IFNAR receptor, resulting in phosphorylation of signal transducers and activators of transcription (STAT1/2) by the JAK and TYK kinases. Phosphorylated STAT1/2 form dimers and bind to IRF9, which triggers transcription of IFN-stimulated genes (ISGs) in the nucleus. **(B)** Antiviral ISG effectors affect different stages of the viral life cycle. Mx1 inhibits virus endocytosis and uncoating of the ribonucleocapsid. IFI16, OAS, and IFIT function in viral RNA degradation and block translation. IFIT, ISG15, TRIM, and UBE2 inhibit transcription, replication, translation or virus assembly. FKBP4 promotes protein folding. Kinesins (KIFA/B/C), Clathrin (CLTCL1), and TUBAL3 are involved in transport of virus vesicles. ARHGAP17 facilitates the formation or repair of tight junctions. The figure is adapted from reference (Schneider et al., 2014).

and ISG effectors of the JAK-STAT signaling pathways were decreased, including FKBP4, PIGR, MX1, cGAS, OAS1-3, and IFIT1-3 (**Table 1**, **Supplementary Table 3**, and **Figures 5B,C**). In addition, proteins involved in ubiquitination (UBE2L3/5) and the JAK-STAT, MAPK, PI3K/Akt, and Ras signaling pathways showed lower expression changes after allicin treatment. The abundant calcium-signaling protein AHNAK was repressed after allicin exposure, while it was induced in infected cells. Allicin resulted in decreased expression of kinesins KIFA/B/C, clathrin CLTCL1 and tubulin TUBAL3, indicating reduced endocytosis

and traffic of vesicles. Moreover, prothymosin alpha (PTMA) was 2.6-fold upregulated after allicin exposure. PTMA showed antiviral activity to inhibit replication of human deficiency virus type-1 (Mosoian et al., 2006; Teixeira et al., 2015), indicating that PTMA induction by allicin might contribute to the antiviral effect against SARS-CoV-2.

Similarly, the expression of proteins involved in transcription, spliceosome and translation was reversed to the levels of uninfected (Mock) cells after allicin exposure of SARS-CoV-2 infected cells, including the abundant proteins DIDO1, SUB1, FUBP1, TCEA1, BOP1, RPS24 and RPS15. Finally, expression of metabolic enzymes involved in glycan, nucleotide, and lipid metabolism was restored by allicin, including GALNT4/12, ALG3, FUT8, MAN2C1, CMPK1, and TECR (**Table 1**, **Supplementary Table 3**, and **Figures 5B,C**). Overall, allicin showed antiviral effects in the host proteome as revealed by the diminished IFN-dependent antiviral response and the effects on signal transduction, transcription, translation, and metabolism.

DISCUSSION

Garlic organosulfur compounds showed antiviral activity against several enveloped viruses, including herpes simplex, parainfluenza, vaccinia, and rhinovirus (Weber et al., 1992; Rouf et al., 2020). These virucidal effects of garlic compounds were proposed to depend on the disruption of the viral envelope and inhibition of viral replication (Weber et al., 1992; Rouf et al., 2020).

In this work, we explored the antiviral effect of allicin on SARS-CoV-2 infected Vero E6 and Calu-3 cells. By determining >60–70% decreased levels of viral RNA and infectious viral particles, the antiviral effect of biocompatible allicin doses against SARS-CoV-2 was demonstrated in both cell lines. However, Calu-3 cells showed a greater allicin tolerance compared to the more sensitive Vero E6 cells. Different cell lines were previously shown to vary in their allicin susceptibilities, which correlated with their intracellular GSH levels (Gruhlke et al., 2016, 2019). Allicin leads to *S*-thioallylation of GSH and the formation of *S*-allylmercaptoglutathione (GSSA), which is accompanied by GSH depletion and an oxidative shift in the GSH redox potential (Gruhlke et al., 2010, 2019; Müller et al., 2016). The measurement of GSH levels confirmed that Calu-3 cells have 4.2-fold higher GSH levels compared to the allicin-sensitive Vero E6 cells.

Since Vero E6 cells are more sensitive toward allicin compared to Calu-3 cells, we first analyzed the effect of low levels of 50 μM allicin on SARS-CoV-2 infected Vero E6 cells using pre- and post-infection treatments of host cells or pre-exposure of the virus before infection. Interestingly, treatment of Vero E6 cells with 50 μM allicin showed only antiviral effects if applied after infection with SARS-CoV-2. The number of infectious viral particles was not affected if virus or Vero E6 host cells were pretreated with 50 μM allicin for 30 min before infection. This missing antiviral effect of allicin in the pre-treatment experiments might be explained by the washing step of Vero E6 cells after the 1 h infection, leading to the removal of the remaining allicin from the cells. During post-infection treatment, allicin remained in the cell culture until sample harvesting. These results suggest that allicin might disrupt early steps of viral replication in Vero E6 cells, which requires further investigation. Further experiments revealed the significant reduction in viral plaques and RNA copies in both SARS-CoV-2 infected Vero E6 and Calu-3 cell lines after exposure to sub-lethal doses allicin p.i.

To better understand the effect of allicin, we investigated the proteome changes of Calu-3 cells upon SARS-CoV-2 infection and the impact of 150 μM allicin on the host-virus proteome. In agreement with previous proteome studies, SARS-CoV-2 reprograms major host pathways, including signaling pathways, transcription, splicing, translation, protein modification and folding, lipid, glycan, and nucleotide metabolism (**Table 1**, **Supplementary Table 3**, and **Figures 5A**, **7A,B**) (Bojkova et al., 2020; Bouhaddou et al., 2020; Zecha et al., 2020). The ribonucleocapsid protein was the most abundant viral protein in the infected cell, indicating that a large portion of the translation capacity goes to the N-protein for package of the viral RNA genome.

In addition, our proteome data highlight the importance of the IFN pathway and ISG effectors to prevent virus replication by interacting with various stages of the viral life cycle. Antiviral ISG effectors were among the most highly induced and abundant proteins in the infected host cells, such as MX1, cGAS, OAS1-3, IFIT1-3, ISG15, FKBP4, PIGR, and UBE2L3/5, which function in sensing and degradation of viral RNA, inhibition of ribonucleocapsid uncoating, translation and promote the innate immune response (**Table 1**, **Supplementary Table 3**, and **Figures 5A**, **7A,B**). Apart from IFN signaling, proteins involved in motility, tight junction and membrane trafficking are highly induced host proteins, supporting the importance of vesicular transport for virus endocytosis and exocytosis. Thus, our proteomics studies reflect all described host pathways known to be altered after viral infections, suggesting new host targets for SARS-CoV-2 interventions.

At the same time, the proteomic profiling gave the opportunity to monitor the responses of infected Calu-3 cells after allicin treatment. The proteome results of allicin-treated infected host cells revealed an 18–59% reduced abundance of the structural proteins N, M, S, and ORF3. Several expression changes dedicated to virus proliferation are reversed to Mock levels in allicin-treated cells. Allicin affected virus-responsive expression of JAK-STAT, MAPK, PI3K/Akt, and Ras signaling pathways, IFN and ISG effectors, transcription, splicing, translation, ubiquitination, vesicular transport, tight junctions as well as glycan, lipid, and nucleotide metabolism. Thus, our results confirm the antiviral effect of allicin in host cells in agreement with the infection assays.

The mode of action of allicin involves *S*-thioallylation of proteins and low molecular weight thiols in bacteria and human Jurkat cells, which was observed already 10–30 min after allicin treatment (Gruhlke et al., 2019; Loi et al., 2019). The majority of *S*-thioallylated Jurkat proteins were abundant cellular proteins, involved in the cytoskeleton, translation and protein folding, although also low abundant redox-sensitive transcription factors, such as MgrA, SarZ, OhrR, HypR, and YodB were targets for

allicin modification in *S. aureus* and *B. subtilis* cells (Chi et al., 2019; Gruhlke et al., 2019; Loi et al., 2019). In this study, we did not detect *S*-thioallylated Cys peptides in SARS-CoV-2 infected Calu-3 cells after 24 h of allicin exposure using label-free proteomics and MS/MS spectrum verification. In addition, no viral *S*-thioallylated Cys peptides were identified, although the spike protein is a Cys-rich glycoprotein exposed on the surface of the virus envelope (Ou et al., 2020). Given the long duration of allicin treatment, this is not surprising since cells have the capacity to reduce allicin and the majority of *S*-thioallylations within 24 h. In human Jurkat cells, allicin led to a rapid depletion of the cellular GSH pool within 10 min (Gruhlke et al., 2019). Efficient allicin detoxification and removal of *S*-thioallylations were confirmed in yeast and bacterial cells, as supported by fast recovery of growth after a short allicin-induced lag phase (Gruhlke et al., 2010, 2019; Müller et al., 2016; Loi et al., 2019). In *S. aureus*, allicin can be reduced by the disulfide reductase MerA, while the bacillithiol disulfide reductase YpdA enables the recycling of *S*-allylmercaptobacillithiol, formed in the reaction of BSH with allicin (Loi et al., 2019). Furthermore, YpdA was shown to function in the Brx/BSH/YpdA pathway in regeneration of *S*-thioallylated proteins (Loi et al., 2019). Similarly, Calu-3 cells should have reduced GSSA via the glutathione disulfide reductase and *S*-thioallylated proteins by the glutaredoxin/GSH/glutathione disulfide reductase system within 24 h.

Finally, the question arises about the antiviral mechanism of allicin on SARS-CoV-2 infected Calu-3 cells during host-pathogen interactions. Garlic organosulfur compounds were shown to exert their immunomodulatory activity via inhibition of the transcription factor NF-κB, leading to decreased levels of pro-inflammatory cytokines, such as TNF-α, IL-1β, IL-6, MCP-1, and IL-12 (Arreola et al., 2015). Allicin further stimulates the release of Zn^{2+} from proteins in murine EL-4 T-cells, possibly due to *S*-thioallylation of Zn^{2+} coordinating Cys thiolates (Gruhlke et al., 2019). Thus, the immunomodulatory effect of allicin on cytokine secretion in cell cultures could be mediated by elevated Zn^{2+} levels due to inactivation of host proteins by *S*-thioallylation.

On the other hand, allicin could also target Cys-containing virus proteins, such as the Cys-rich spike glycoprotein, the viral RNA-dependent RNA polymerase RdRp (Nsp12), the main protease M^{pro} (also termed as 3C-like protease) and the papain-like protease PLP. M^{pro} and PLP are both involved in proteolytic processing of the large pp1a and pp1ab polyproteins to produce functional polypeptides, which assemble into the replicase-transcriptase complex (Jin et al., 2020; Zhang et al., 2020; Amin et al., 2021). Since M^{pro} and RdRp are important for viral replication and transcription, these could be antiviral drug targets. M^{pro} has a catalytic active site motif consisting of His41 and Cys145 residues (Jin et al., 2020; Zhang et al., 2020; Amin et al., 2021). Several *in silico* docking studies with allicin revealed the formation of *S*-thioallylations at Cys145, Cys85 and Cys156 of M^{pro} and of Cys622 of RdRp, indicating the potential of allicin to attenuate SARS-CoV-2 replication (Bastikar et al., 2020; Shekh et al., 2020). Further docking studies with the garlic compounds alliin and ajoene revealed strong ligand-protein binding stabilities and many interactions at the M^{pro} active site (Bastikar et al., 2020; Cheng and Li, 2020). In total, 17 garlic organosulfur compounds, accounting for 99.4% of substances found in garlic oil, showed interactions with ACE2 receptor and M^{pro} *in silico*, including the diallyl di- and trisulfides with promising docking scores (Thuy et al., 2020). Furthermore, elevated Zn^{2+} levels released from host proteins inhibited the RdRp of SARS coronavirus (te Velthuis et al., 2010) and the host ACE2 enzyme (Polak and Speth, 2021), indicating that allicin could target either host and viral proteins directly via *S*-thioallylation or via elevated Zn^{2+} levels to exert immunomodulatory and antiviral effects.

Thus, allicin might inhibit SARS-CoV-2 infection at different stages of the viral life cycle, preventing receptor binding, replication or transcription by *S*-thioallylation of host or viral proteins. However, in our host-virus proteome we could not identify the M^{pro} or RdRp proteins, indicating that these are low abundant proteins. Thus, possible *S*-thioallylations of M^{pro} and RdRp will be difficult to verify upon allicin exposure of infected host cells *in vivo*. Nevertheless, these *in silico* docking studies highlight the potential of garlic organosulfur compounds as inhibitors of viral Cys proteins, which could be further developed as possible future COVID-19 therapeutics.

Taken together, our results demonstrate that allicin shows antiviral and immunomodulatory activity in SARS-CoV-2 infected Vero E6 and Calu-3 cell cultures, supported on the proteome level by the decreased antiviral interferon response. However, allicin is unstable and quickly decomposes to polysulfanes, ajoene, and other sulfur compounds during heating (Block, 2010; Borlinghaus et al., 2021). The half-life of allicin is 30–40 days in water at 23°C, but decreases in garlic extracts with increased concentrations (Koch and Lawson, 1996). In the acidic stomach, the majority of allicin is degraded to 2-propenethiol and allyl methyl sulfide, which are excreted (Block, 2010; Borlinghaus et al., 2021). In the blood, the effective dose of allicin is reduced by its reaction with GSH (Block, 2010; Borlinghaus et al., 2021). In our experiments, the viral load was only reduced by 60–70% after allicin treatment in Calu-3 cells, which is below 1-log scale and would not satisfy the desired antiviral effect required for therapeutics to enter pre-clinical trials. Future drug research should be directed to exploit the thiol-reactive activity of allicin derivatives with reduced toxicity, increased stability and higher antiviral activity as antiviral lead compounds.

DATA AVAILABILITY STATEMENT

The mass spectrometry data have been deposited to the ProteomeXchange Consortium via the PRIDE partner repository (Perez-Riverol et al., 2019; Deutsch et al., 2020) with the dataset identifier PXD024375.

AUTHOR CONTRIBUTIONS

KM performed the infection experiments and analyzed the data. VF and LA measured and analyzed the proteomic data. JB

constructed the Voronoi treemaps. MG and AS synthesized allicin. DN supervised the infection experiments and gave critical advise. VF and HA conducted the study and wrote the initial manuscript. All authors contributed to the final manuscript.

FUNDING

This work was supported by an European Research Council (ERC) Consolidator grant (GA 615585) MYCOTHIOLOME and grants from the Deutsche Forschungsgemeinschaft, Germany (AN746/4-1 and AN746/4-2) within the SPP1710 on "Thiol-based Redox switches," by the SFB973 (project C08) and TR84 (project B06) to HA. Infections experiments were supported by the TR84 (project A07) to DN. Mass spectrometry was performed by LA at the Centre for Chemical Microscopy (ProVIS) at the Helmholtz Centre for Environmental Research, which is supported by European regional development funds (EFRE-Europe Funds Saxony) and the Helmholtz Association. Support for allicin synthesis was provided by internal funding from the RWTH Aachen University to MG and AS. We further acknowledge support by the Open Access Publication Initiative of Freie Universität Berlin.

SUPPLEMENTARY MATERIAL

The Supplementary Material for this article can be found online at: https://www.frontiersin.org/articles/10.3389/fmicb.2021.746795/full#supplementary-material

REFERENCES

Al-Qattan, M. M. (2009). Garlic burns: case reports with an emphasis on associated and underlying pathology. *Burns* 35, 300–302. doi: 10.1016/j.burns.2008.01.004

Amin, S. A., Banerjee, S., Singh, S., Qureshi, I. A., Gayen, S., and Jha, T. (2021). First structure-activity relationship analysis of SARS-CoV-2 virus main protease (Mpro) inhibitors: an endeavor on COVID-19 drug discovery. *Mol. Divers* 25, 1827–1838. doi: 10.1007/s11030-020-10166-3

Anderson, T. W., and Darling, D. A. (1954). A test of goodness of fit. *J. Am. Statist. Assoc.* 49, 765–769. doi: 10.1080/01621459.1954.10501232

Arbach, M., Santana, T. M., Moxham, H., Tinson, R., Anwar, A., Groom, M., et al. (2019). Antimicrobial garlic-derived diallyl polysulfanes: interactions with biological thiols in Bacillus subtilis. *Biochim Biophys. Acta Gen. Subj.* 1863, 1050–1058. doi: 10.1016/j.bbagen.2019.03.012

Arreola, R., Quintero-Fabian, S., Lopez-Roa, R. I., Flores-Gutierrez, E. O., Reyes-Grajeda, J. P., Carrera-Quintanar, L., et al. (2015). Immunomodulation and anti-inflammatory effects of garlic compounds. *J. Immunol. Res.* 2015:401630. doi: 10.1155/2015/401630

Bastikar, V. A., Bastikar, A. V., and Chhajed, S. S. (2020). Understanding the role of natural medicinal compounds such as curcumin and allicin against SARS-CoV-2 proteins as potential treatment against COVID-19: an in silico approach. *Proteom. Bioinform* 13:7.

Bautista, D. M., Movahed, P., Hinman, A., Axelsson, H. E., Sterner, O., Hogestatt, E. D., et al. (2005). Pungent products from garlic activate the sensory ion channel TRPA1. *Proc. Natl. Acad. Sci. U S A.* 102, 12248–12252. doi: 10.1073/pnas.0505356102

Bizzotto, J., Sanchis, P., Abbate, M., Lage-Vickers, S., Lavignolle, R., Toro, A., et al. (2020). SARS-CoV-2 infection boosts MX1 antiviral effector in COVID-19 patients. *iScience* 23:101585. doi: 10.1016/j.isci.2020.101585

Block, E. (2010). *Garlic and Other Alliums-the Lore and the Science*. Cambridge: RSC Publishing.

Bojkova, D., Klann, K., Koch, B., Widera, M., Krause, D., Ciesek, S., et al. (2020). Proteomics of SARS-CoV-2-infected host cells reveals therapy targets. *Nature* 583, 469–472. doi: 10.1038/s41586-020-2332-7

Borlinghaus, J., Albrecht, F., Gruhlke, M. C., Nwachukwu, I. D., and Slusarenko, A. J. (2014). Allicin: chemistry and biological properties. *Molecules* 19, 12591–12618. doi: 10.3390/molecules190812591

Borlinghaus, J., Foerster, J., Kappler, U., Antelmann, H., Noll, U., Gruhlke, M., et al. (2021). Allicin, the odor of freshly crushed garlic: a review of recent progress in understanding allicin's effects on cells. *Molecules* 26:1505. doi: 10.3390/molecules26061505

Bouhaddou, M., Memon, D., Meyer, B., White, K. M., Rezelj, V. V., Correa Marrero, M., et al. (2020). The global phosphorylation landscape of SARS-CoV-2 infection. *Cell* 182, 685–712.e19. doi: 10.1016/j.cell.2020.06.034

Cheng, B., and Li, T. (2020). Discovery of alliin as a putative inhibitor of the main protease of SARS-CoV-2 by molecular docking. *Biotechniques* 69, 108–112. doi: 10.2144/btn-2020-0038

Chi, B. K., Huyen, N. T. T., Loi, V. V., Gruhlke, M. C. H., Schaffer, M., Mäder, U., et al. (2019). The disulfide stress response and protein S-thioallylation caused by allicin and diallyl polysulfanes in Bacillus subtilis as revealed by transcriptomics and proteomics. *Antioxidants (Basel)* 8:605. doi: 10.3390/antiox8120605

Corman, V. M., Landt, O., Kaiser, M., Molenkamp, R., Meijer, A., Chu, D. K., et al. (2020). Detection of 2019 novel coronavirus (2019-nCoV) by real-time RT-PCR. *Euro. Surveill.* 25:2000045. doi: 10.2807/1560-7917.ES.2020.25.3.2000045

De Maio, F., Lo Cascio, E., Babini, G., Sali, M., Della Longa, S., Tilocca, B., et al. (2020). Improved binding of SARS-CoV-2 Envelope protein to tight junction-associated PALS1 could play a key role in COVID-19 pathogenesis. *Microbes Infect.* 22, 592–597. doi: 10.1016/j.micinf.2020.08.006

Deutsch, E. W., Bandeira, N., Sharma, V., Perez-Riverol, Y., Carver, J. J., Kundu, D. J., et al. (2020). The ProteomeXchange consortium in 2020: enabling 'big data' approaches in proteomics. *Nucleic Acids Res.* 48, D1145–D1152. doi: 10.1093/nar/gkz984

Durfee, L. A., Lyon, N., Seo, K., and Huibregtse, J. M. (2010). The ISG15 conjugation system broadly targets newly synthesized proteins: implications for the antiviral function of ISG15. *Mol. Cell* 38, 722–732. doi: 10.1016/j.molcel.2010.05.002

Fara, A., Mitrev, Z., Rosalia, R. A., and Assas, B. M. (2020). Cytokine storm and COVID-19: a chronicle of pro-inflammatory cytokines. *Open Biol.* 10:200160. doi: 10.1098/rsob.200160

Gruhlke, M. C., Hemmis, B., Noll, U., Wagner, R., Luhring, H., and Slusarenko, A. J. (2015). The defense substance allicin from garlic permeabilizes membranes of *Beta vulgaris*, *Rhoeo discolor*, *Chara corallina* and artificial lipid bilayers. *Biochim. Biophys. Acta* 1850, 602–611. doi: 10.1016/j.bbagen.2014.11.020

Gruhlke, M. C., Nicco, C., Batteux, F., and Slusarenko, A. J. (2016). The effects of allicin, a reactive sulfur species from garlic, on a selection of mammalian cell lines. *Antioxidants (Basel)* 6:1. doi: 10.3390/antiox6010001

Gruhlke, M. C., Portz, D., Stitz, M., Anwar, A., Schneider, T., Jacob, C., et al. (2010). Allicin disrupts the cell's electrochemical potential and induces apoptosis in yeast. *Free Radic. Biol. Med.* 49, 1916–1924. doi: 10.1016/j.freeradbiomed.2010.09.019

Gruhlke, M. C. H., Antelmann, H., Bernhardt, J., Kloubert, V., Rink, L., and Slusarenko, A. J. (2019). The human allicin-proteome: S-thioallylation of proteins by the garlic defence substance allicin and its biological effects. *Free Radic. Biol. Med.* 131, 144–153. doi: 10.1016/j.freeradbiomed.2018.11.022

Hitl, M., Kladar, N., Gavaric, N., Srdenovic Conic, B., and Bozin, B. (2021). Garlic burn injuries- a systematic review of reported cases. *Am. J. Emerg. Med.* 44, 5–10. doi: 10.1016/j.ajem.2021.01.039

Jarque, C. M., and Bera, A. K. (1980). Efficient tests for normality, homoscedasticity and serial independence of regression residuals. *Econ. Lett.* 6, 255–259. doi: 10.1016/0165-1765(80)90024-5

Jin, Z., Du, X., Xu, Y., Deng, Y., Liu, M., Zhao, Y., et al. (2020). Structure of M(pro) from SARS-CoV-2 and discovery of its inhibitors. *Nature* 582, 289–293. doi: 10.1038/s41586-020-2223-y

Koch, H. P., and Lawson, L. D. (1996). *Garlic: The Science and Therapeutic Application of Allium sativum L. and Related Species*. Baltimore, MD: Williams & Wilkins.

Kublik, A., Deobald, D., Hartwig, S., Schiffmann, C. L., Andrades, A., Von Bergen, M., et al. (2016). Identification of a multi-protein reductive dehalogenase complex in Dehalococcoides mccartyi strain CBDB1 suggests a protein-dependent respiratory electron transport chain obviating quinone involvement. *Environ. Microbiol.* 18, 3044–3056. doi: 10.1111/1462-2920.13200

Loi, V. V., Huyen, N. T. T., Busche, T., Tung, Q. N., Gruhlke, M. C. H., Kalinowski, J., et al. (2019). Staphylococcus aureus responds to allicin by global S-thioallylation - role of the Brx/BSH/YpdA pathway and the disulfide reductase MerA to overcome allicin stress. *Free Radic. Biol. Med.* 139, 55–69. doi: 10.1016/j.freeradbiomed.2019.05.018

Masucci, M. G. (2020). Viral ubiquitin and ubiquitin-like deconjugases-swiss army knives for infection. *Biomolecules* 10:1137. doi: 10.3390/biom10081137

Matza, D., Badou, A., Jha, M. K., Willinger, T., Antov, A., Sanjabi, S., et al. (2009). Requirement for AHNAK1-mediated calcium signaling during T lymphocyte cytolysis. *Proc. Natl. Acad. Sci. U S A.* 106, 9785–9790. doi: 10.1073/pnas.0902844106

McGauran, G., Dorris, E., Borza, R., Morgan, N., Shields, D. C., Matallanas, D., et al. (2020). Resolving the interactome of the human macrophage immunometabolism regulator (MACIR) with enhanced membrane protein preparation and affinity proteomics. *Proteomics* 20:e2000062. doi: 10.1002/pmic.202000062

Mehlan, H., Schmidt, F., Weiss, S., Schuler, J., Fuchs, S., Riedel, K., et al. (2013). Data visualization in environmental proteomics. *Proteomics* 13, 2805–2821. doi: 10.1002/pmic.201300167

Miron, T., Listowsky, I., and Wilchek, M. (2010). Reaction mechanisms of allicin and allyl-mixed disulfides with proteins and small thiol molecules. *Eur. J. Med. Chem.* 45, 1912–1918. doi: 10.1016/j.ejmech.2010.01.031

Miron, T., Rabinkov, A., Mirelman, D., Wilchek, M., and Weiner, L. (2000). The mode of action of allicin: its ready permeability through phospholipid membranes may contribute to its biological activity. *Biochim. Biophys. Acta* 1463, 20–30. doi: 10.1016/S0005-2736(99)00174-1

Mosoian, A., Teixeira, A., High, A. A., Christian, R. E., Hunt, D. F., Shabanowitz, J., et al. (2006). Novel function of prothymosin alpha as a potent inhibitor of human immunodeficiency virus type 1 gene expression in primary macrophages. *J. Virol.* 80, 9200–9206. doi: 10.1128/JVI.00589-06

Müller, A., Eller, J., Albrecht, F., Prochnow, P., Kuhlmann, K., Bandow, J. E., et al. (2016). Allicin induces thiol stress in bacteria through S-allylmercapto modification of protein cysteines. *J. Biol. Chem.* 291, 11477–11490. doi: 10.1074/jbc.M115.702308

Münchberg, U., Anwar, A., Mecklenburg, S., and Jacob, C. (2007). Polysulfides as biologically active ingredients of garlic. *Org. Biomol. Chem.* 5, 1505–1518. doi: 10.1039/B703832A

Muniz, I. A. F., Campos, D. E. S., Shinkai, R. S. A., Trindade, T. G. D., and Cosme-Trindade, D. C. (2021). Case report of oral mucosa garlic burn during COVID-19 pandemic outbreak and role of teledentistry to manage oral health in an older adult woman. *Spec Care Dentist* 41, 639–643. doi: 10.1111/scd.12605

Ou, X., Liu, Y., Lei, X., Li, P., Mi, D., Ren, L., et al. (2020). Characterization of spike glycoprotein of SARS-CoV-2 on virus entry and its immune cross-reactivity with SARS-CoV. *Nat. Commun.* 11:1620. doi: 10.1038/s41467-020-15562-9

Perez-Riverol, Y., Csordas, A., Bai, J., Bernal-Llinares, M., Hewapathirana, S., Kundu, D. J., et al. (2019). The PRIDE database and related tools and resources in 2019: improving support for quantification data. *Nucleic Acids Res.* 47, D442–D450. doi: 10.1093/nar/gky1106

Polak, Y., and Speth, R. C. (2021). Metabolism of angiotensin peptides by angiotensin converting enzyme 2 (ACE2) and analysis of the effect of excess zinc on ACE2 enzymatic activity. *Peptides* 137:170477. doi: 10.1016/j.peptides.2020.170477

Qin, C., Zhou, L., Hu, Z., Zhang, S., Yang, S., Tao, Y., et al. (2020). Dysregulation of immune response in patients with Coronavirus 2019 (COVID-19) in Wuhan. China. *Clin. Infect. Dis.* 71, 762–768. doi: 10.1093/cid/ciaa248

Rabinkov, A., Miron, T., Konstantinovski, L., Wilchek, M., Mirelman, D., and Weiner, L. (1998). The mode of action of allicin: trapping of radicals and interaction with thiol containing proteins. *Biochim. Biophys. Acta* 1379, 233–244. doi: 10.1016/S0304-4165(97)00104-9

Reiter, J., Levina, N., Van Der Linden, M., Gruhlke, M., Martin, C., and Slusarenko, A. J. (2017). Diallylthiosulfinate (Allicin), a volatile antimicrobial from garlic (*Allium sativum*), kills human lung pathogenic bacteria including MDR strains as a vapor. *Molecules* 22:1711. doi: 10.3390/molecules22101711

Rossius, M., Hochgräfe, F., and Antelmann, H. (2018). Thiol-redox proteomics to study reversible protein thiol oxidations in bacteria. *Methods Mol. Biol.* 1841, 261–275. doi: 10.1007/978-1-4939-8695-8_18

Rouf, R., Uddin, S. J., Sarker, D. K., Islam, M. T., Ali, E. S., Shilpi, J. A., et al. (2020). Antiviral potential of garlic (*Allium sativum*) and its organosulfur compounds: a systematic update of pre-clinical and clinical data. *Trends Food Sci. Technol.* 104, 219–234. doi: 10.1016/j.tifs.2020.08.006

Schäfer, G., and Kaschula, C. H. (2014). The immunomodulation and anti-inflammatory effects of garlic organosulfur compounds in cancer chemoprevention. *Anticancer Agents Med. Chem.* 14, 233–240. doi: 10.2174/18715206113136660370

Schneider, W. M., Chevillotte, M. D., and Rice, C. M. (2014). Interferon-stimulated genes: a complex web of host defenses. *Annu. Rev. Immunol.* 32, 513–545. doi: 10.1146/annurev-immunol-032713-120231

Schulte-Schrepping, J., Reusch, N., Paclik, D., Bassler, K., Schlickeiser, S., Zhang, B., et al. (2020). Severe COVID-19 is marked by a dysregulated myeloid cell compartment. *Cell* 182, 1419–1440.23.

Seidel, K., Kühnert, J., and Adrian, L. (2018). The complexome of *Dehalococcoides mccartyi* reveals its organohalide respiration-complex is modular. *Front. Microbiol.* 9:1130. doi: 10.3389/fmicb.2018.01130

Shekh, S., Reddy, K. K. A., and Gowd, K. H. (2020). In silico allicin induced S-thioallylation of SARS-CoV-2 main protease. *J. Sulphur Chem.* 42, 1–12. doi: 10.1080/17415993.2020.1817457

te Velthuis, A. J., Van Den Worm, S. H., Sims, A. C., Baric, R. S., Snijder, E. J., and Van Hemert, M. J. (2010). Zn(2+) inhibits coronavirus and arterivirus RNA polymerase activity in vitro and zinc ionophores block the replication of these viruses in cell culture. *PLoS Pathog* 6:e1001176. doi: 10.1371/journal.ppat.1001176

Teixeira, A., Yen, B., Gusella, G. L., Thomas, A. G., Mullen, M. P., Aberg, J., et al. (2015). Prothymosin alpha variants isolated from CD8+ T cells and cervicovaginal fluid suppress HIV-1 replication through type I interferon induction. *J. Infect. Dis.* 211, 1467–1475. doi: 10.1093/infdis/jiu643

Thuy, B. T. P., My, T. T. A., Hai, N. T. T., Hieu, L. T., Hoa, T. T., Thi Phuong, et al. (2020). Investigation into SARS-CoV-2 resistance of compounds in garlic essential oil. *ACS Omega* 5, 8312–8320. doi: 10.1021/acsomega.0c00772

Tian, W., Zhang, N., Jin, R., Feng, Y., Wang, S., Gao, S., et al. (2020). Immune suppression in the early stage of COVID-19 disease. *Nat. Commun.* 11: 5859.

Vargo, R. J., Warner, B. M., Potluri, A., and Prasad, J. L. (2017). Garlic burn of the oral mucosa: a case report and review of self-treatment chemical burns. *J. Am. Dent. Assoc.* 148, 767–771. doi: 10.1016/j.adaj.2017.02.053

Wang, H., Yang, P., Liu, K., Guo, F., Zhang, Y., Zhang, G., et al. (2008). SARS coronavirus entry into host cells through a novel clathrin- and caveolae-independent endocytic pathway. *Cell Res.* 18, 290–301. doi: 10.1038/cr.2008.15

Weber, N. D., Andersen, D. O., North, J. A., Murray, B. K., Lawson, L. D., and Hughes, B. G. (1992). In vitro virucidal effects of *Allium sativum* (garlic) extract and compounds. *Planta Med.* 58, 417–423. doi: 10.1055/s-2006-961504

Wei, L. L., Wang, W. J., Chen, D. X., and Xu, B. (2020). Dysregulation of the immune response affects the outcome of critical COVID-19 patients. *J. Med. Virol.* 92, 2768–2776. doi: 10.1002/jmv.26181

Wheeler, A. P., Wells, C. M., Smith, S. D., Vega, F. M., Henderson, R. B., Tybulewicz, V. L., et al. (2006). Rac1 and Rac2 regulate macrophage morphology but are not essential for migration. *J. Cell Sci.* 119, 2749–2757. doi: 10.1242/jcs.03024

Zecha, J., Lee, C. Y., Bayer, F. P., Meng, C., Grass, V., Zerweck, J., et al. (2020). Data, reagents, assays and merits of proteomics for SARS-CoV-2 research and testing. *Mol. Cell. Proteom.* 19, 1503–1522. doi: 10.1074/mcp.RA120.002164

Zhang, L., Lin, D., Sun, X., Curth, U., Drosten, C., Sauerhering, L., et al. (2020). Crystal structure of SARS-CoV-2 main protease provides a basis for design

of improved alpha-ketoamide inhibitors. *Science* 368, 409–412. doi: 10.1126/science.abb3405

Zhou, P., Yang, X. L., Wang, X. G., Hu, B., Zhang, L., Zhang, W., et al. (2020). A pneumonia outbreak associated with a new coronavirus of probable bat origin. *Nature* 579, 270–273. doi: 10.1038/s41586-020-2012-7

Author Disclaimer: Crushed garlic acts as strong irritant and activates the transient receptor potential channel (TRPA1) in pain-sensing neurons, resulting in pain, inflammation and neurotoxic effects (Bautista et al., 2005). Garlic can be highly toxic to human cells and caused severe garlic burns by its direct exposure to the skin or mucous membranes of the respiratory tract (Bautista et al., 2005; Al-Qattan, 2009; Vargo et al., 2017; Hitl et al., 2021; Muniz et al., 2021). Consequently, any ingestion, inhalation or introduction of fresh garlic can clearly be harmful and hazardous for patients, causing even more severe damage of the lung or the skin. This work does in no way suggest the use of garlic for self-medication of respiratory tract infections, including COVID-19. The authors explicitly warn against any form of self-medication with garlic or garlic compounds.

Conflict of Interest: The authors declare that the research was conducted in the absence of any commercial or financial relationships that could be construed as a potential conflict of interest.

Publisher's Note: All claims expressed in this article are solely those of the authors and do not necessarily represent those of their affiliated organizations, or those of the publisher, the editors and the reviewers. Any product that may be evaluated in this article, or claim that may be made by its manufacturer, is not guaranteed or endorsed by the publisher.

Curriculum vitae

For reasons of data protection, the curriculum vitae is not included in the electronic version.